LA-UR-11-04610

Approved for public release;
distribution is unlimited.

Title:	SEISMIC HAZARDS EVALUATION OF THE LOS ALAMOS NATIONAL LABORATORY 24 February 1995 Volume 1 of 3 (consists of 3 volumes)
Author(s):	Steven L. Reneau Leigh S. House Ivan Wong Keith Kelson
Intended for:	Reference



Los Alamos National Laboratory, an affirmative action/equal opportunity employer, is operated by the Los Alamos National Security, LLC for the National Nuclear Security Administration of the U.S. Department of Energy under contract DE-AC52-06NA25396. By acceptance of this article, the publisher recognizes that the U.S. Government retains a nonexclusive, royalty-free license to publish or reproduce the published form of this contribution, or to allow others to do so, for U.S. Government purposes. Los Alamos National Laboratory requests that the publisher identify this article as work performed under the auspices of the U.S. Department of Energy. Los Alamos National Laboratory strongly supports academic freedom and a researcher's right to publish; as an institution, however, the Laboratory does not endorse the viewpoint of a publication or guarantee its technical correctness.

Form 836 (7/06)

Final Report
Volume I

SEISMIC HAZARDS EVALUATION OF THE LOS ALAMOS NATIONAL LABORATORY



Prepared for

Los Alamos National Laboratory
University of California
Los Alamos, New Mexico 87545

24 February 1995

Woodward-Clyde

Woodward-Clyde Federal Services
500 12th Street
Suite 100
Oakland, California 94607-4014

Woodward-Clyde
Engineering & sciences applied to the earth & its environment

24 February 1995

Mr. Doug Volkman
Los Alamos National Laboratory
University of California
P.O. Box 1663, MS M984
Los Alamos, New Mexico 87544

Subject: **Final Report on the "Seismic Hazards Evaluation of the Los Alamos National Laboratory"; LANL Contracts 9-XT1-092K-1 and 5175F0013-9Y**

Dear Doug:

On the behalf of Woodward-Clyde Federal Services, I am very pleased to submit to you 50 copies of the final report on the "Seismic Hazards Evaluation of the Los Alamos National Laboratory." We have very much appreciated the opportunity to perform these studies. We feel that they represent an important contribution and a major step toward the mitigation of seismic hazards at the LANL. In this regard, we are particularly grateful to you and Dean Keller for your leadership and enthusiastic support of our studies.

Please call me if you have any questions or require further assistance.

Best regards,
WOODWARD-CLYDE FEDERAL SERVICES

Ivan

Ivan G. Wong
Vice President and Manager
Seismic Hazards Branch

H:\CONTRACT\91C0509F.L5\1

M0217951421

Woodward-Clyde Federal Services • A subsidiary of Woodward-Clyde Group, Inc.
500 12th Street, Suite 100 • Oakland, California 94607-4014
510-893-3600 Fax 510-874-3268

FINAL REPORT
VOLUME I

SEISMIC HAZARDS EVALUATION OF THE LOS ALAMOS NATIONAL LABORATORY

by

Ivan Wong[1], Keith Kelson[2], Susan Olig[1], Tom Kolbe[1]
Mark Hemphill-Haley[1], Jacqueline Bott[1], Robert Green[3],
Helen Kanakari[3], Janet Sawyer[1], Walter Silva[4], Cathy Stark[4]
Colleen Haraden[2], Clark Fenton[1], Jeffrey Unruh[2],
Jamie Gardner[5], Steven Reneau[5], and Leigh House[5]

Woodward-Clyde Federal Services
500 12th Street, Suite 100
Oakland, CA 94607

Prepared for the

Los Alamos National Laboratory
University of California
Los Alamos, New Mexico 87545

and the

U.S. Department of Energy

24 February 1995

[1]Woodward-Clyde Federal Services, 500 12th Street, Suite 100, Oakland, CA 94607
[2]William Lettis & Associates, 1000 Broadway, Suite 612, Oakland, CA 94607
[3]Woodward-Clyde Consultants, 500 12th Street, Suite 100, Oakland, CA 94607
[4]Pacific Engineering & Analysis, 311 Pomona Avenue, El Cerrito, CA 94530
[5]Los Alamos National Laboratory, University of California, Los Alamos, NM 87545

TABLE OF CONTENTS

Section			Page
	EXECUTIVE SUMMARY		ES-1
	ACKNOWLEDGMENTS		
1.0	INTRODUCTION		1-1
	1.1 Objectives		1-1
	1.2 DOE Seismic Design Criteria		1-4
	1.3 Scope of Work		1-7
		1.3.1 Phase II	1-8
		1.3.2 Phase III	1-12
		1.3.3 Phase IV	1-14
	1.4 Project Team and Review Panel		1-16
	1.5 Previous Studies		1-18
2.0	GEOLOGIC AND SEISMOTECTONIC SETTING		2-1
	2.1 Structure and Seismotectonics of Continental Rift Systems		2-2
	2.2 Seismotectonic Provinces in the LANL Region		2-6
		2.2.1 The Rio Grande Rift Province	2-6
		2.2.2 The Valles Volcanic Province	2-7
		2.2.3 The Colorado Plateau Transition Zone	2-8
		2.2.4 The Southern Rocky Mountains Province	2-9
		2.2.5 The Great Plains Province	2-9
	2.3 Principal Components of the Rio Grande Rift in the LANL Region		2-10
		2.3.1 The San Luis Basin	2-11
		2.3.2 The Española Basin	2-11
		2.3.3 The Santo Domingo Basin	2-13
		2.3.4 The Albuquerque Basin	2-14

Section			Page
	2.4	Geology and Faults of the Pajarito Plateau	2-15
	2.4.1	Bedrock Geology of the Pajarito Plateau	2-16
	2.4.2	Major Faults of the Pajarito Plateau	2-19
3.0	HISTORICAL SEISMICITY		3-1
	3.1	Earthquake Detection and Location Accuracy	3-1
	3.1.1	Pre-Instrumental Seismicity	3-2
	3.1.2	Instrumental Seismicity	3-3
	3.2	Significant Earthquakes	3-4
	3.2.1	1906-1907 Socorro Swarm	3-4
	3.2.2	1918 Cerrillos Earthquakes	3-7
	3.2.3	1930 Earthquakes	3-7
	3.2.4	1931 Earthquake	3-8
	3.2.5	1947 Earthquake	3-8
	3.2.6	1966 Dulce Earthquake	3-8
	3.2.7	1970 Earthquake	3-10
	3.2.8	1971 Earthquake	3-10
	3.2.9	1978-1979 Albuquerque Volcanoes Swarm	3-11
	3.2.10	Earthquakes Felt in Los Alamos	3-11
	3.2.11	Reservoir-Induced Seismicity at Heron and El Vado Reservoir	3-12
	3.3	Earthquake Recurrence	3-13
	3.3.1	Sensitivity Tests	3-17
4.0	GEOLOGIC INVESTIGATIONS		4-1
	4.1	Regional Surficial Geology Investigations	4-1
	4.1.1	Generalized Late Quaternary Surficial Geology of the Pajarito Plateau	4-1

Section			Page
	4.1.1.1	Methods	4-2
	4.1.1.2	Results	4-4
	4.1.1.3	Interpretations	4-6
4.1.2	Topographic Profiling of the Pajarito Fault System		4-7
	4.1.2.1	Methods	4-7
	4.1.2.2	Results of Regional Profiles	4-9
	4.1.2.3	Results of Detailed Profiles of the Pajarito Fault Escarpment	4-10
4.1.3	Regional Investigations of Nearby Potential Seismogenic Sources		4-14
	4.1.3.1	Embudo Fault	4-14
		4.1.3.1.1 Introduction	4-14
		4.1.3.1.2 Mesa West of Hernandez	4-17
		4.1.3.1.3 The Arroyo Ocole Drainage	4-20
		4.1.3.1.4 Rio Embudo Area	4-21
		4.1.3.1.5 Arroyo Hondo Area	4-22
		4.1.3.1.5.1 Roadcut I	4-23
		4.1.3.1.5.2 Roadcut II	4-23
		4.1.3.1.5.3 Roadcut III	4-24
		4.1.3.1.5.4 Roadcut IV	4-24
		4.1.3.1.6 Summary of Embudo Fault Investigation	4-26
	4.1.3.2	Faults of Black Mesa	4-26
4.2	Paleoseismic Investigations of the Pajarito Fault System		4-28
	4.2.1	Pajarito Fault	4-29
	4.2.1.1	Water Canyon Site	4-32

Section			Page
		4.2.1.1.1 Site Geology	4-32
		4.2.1.1.2 Trench Description	4-33
		4.2.1.1.3 Event Chronology	4-35
	4.2.1.2	Water Tanks Site	4-35
		4.2.1.2.1 Site Geology	4-35
		4.2.1.2.2 Trench Description	4-38
		4.2.1.2.2.1 Water Tanks Trench 1	4-38
		4.2.1.2.2.2 Water Tanks Trench 2	4-40
		4.2.1.2.3 Event Chronology	4-41
	4.2.1.3	Pajarito Canyon Site	4-44
		4.2.1.3.1 Site Geology	4-45
		4.2.1.3.2 Trench Description	4-45
		4.2.1.3.3 Event Chronology	4-50
		4.2.1.3.4 Shallow Drilling Investigation	4-50
	4.2.2	Rendija Canyon Fault	4-52
	4.2.2.1	Guaje Pines Site	4-54
		4.2.2.1.1 Late Quaternary Stratigraphy	4-55
		4.2.2.1.2 Structure	4-62
		4.2.2.1.3 Paleoseismic Characteristics, Guaje Pines Site	4-63
		4.2.2.1.3.1 Number & Timing of Paleoearthquakes	4-63
		4.2.2.1.3.2 Surface Rupture Recurrence	4-67
		4.2.2.1.3.3 Displacement per Earthquake	4-69
	4.2.2.2	County Landfill Site	4-69

Section				Page
			4.2.2.2.1 Quaternary Stratigraphy	4-71
			4.2.2.2.2 Structure	4-73
			4.2.2.2.3 Paleoseismic Characteristics	4-75
		4.2.3 Guaje Mountain Fault		4-78
		4.2.3.1 Rendija Canyon Area		4-79
			4.2.3.1.1 Late Quaternary Stratigraphy	4-81
			4.2.3.1.2 Fault Exposures	4-84
			4.2.3.1.3 Paleoseismic Characteristics	4-85
		4.2.3.2 Sportsmen's Club Site		4-87
			4.2.3.2.1 Holocene Stratigraphy	4-88
		4.2.3.3 Summary		4-90
	4.3 Potential for Surface Rupture			4-91
5.0	EVALUATION OF THE LOS ALAMOS SEISMOGRAPHIC NETWORK DATA			5-1
	5.1 Evaluation of Network Data			5-1
	5.2 Contemporary Seismicity and Tectonic Stresses			5-5
6.0	SITE GEOLOGY CHARACTERIZATION			6-1
	6.1 Subsurface Geology of the Pajarito Plateau			6-1
		6.1.1 Pre-Rift Subsurface Geology		6-2
		6.1.2 Rift Sediments, Volcanics, and Volcaniclastics		6-2
			6.1.2.1 Santa Fe Group	6-3
			6.1.2.2 Puye Formation	6-3
			6.1.2.3 Basalts	6-4
			6.1.2.4 Tschicoma Dacite	6-4
			6.1.2.5 Bandelier Tuff - Otowi Member	6-4

Section			Page
	6.1.2.6	Cerro Toledo Rhyolite/Epiclastic Reworked Pyroclastics	6-5
	6.1.2.7	Bandelier Tuff - Tshirege Member	6-5
6.2	Site-Specific Subsurface Geology		6-5
6.2.1	Core Hole Exploration		6-6
	6.2.1.1	SHB-1 (TA-55)	6-6
	6.2.1.2	SHB-2 (TA-3)	6-7
	6.2.1.3	SHB-3 (TA-16)	6-7
	6.2.1.4	SHB-4 (TA-18)	6-8
6.2.2	Downhole Geophysical Measurements		6-8
6.2.3	Dynamic Laboratory Testing		6-11
	6.2.3.1	Dynamic Laboratory Testing Procedures	6-11
	6.2.3.2	Test Results and Discussion	6-12
		6.2.3.2.1 Effects of Confining Pressure	6-13
		6.2.3.2.2 Effects of Confinement Duration	6-13
		6.2.3.2.3 Effects of Loading Frequency	6-14
		6.2.3.2.4 Effect of Number of Loading Cycles	6-14
6.2.4	Other Borehole Data		6-14
6.2.5	Summary of Site-Specific Velocity Profiles		6-15
	6.2.5.1	TA-2	6-15
	6.2.5.2	TA-3	6-17
	6.2.5.3	TA-16	6-18
	6.2.5.4	TA-18	6-18
	6.2.5.5	TA-21	6-19
	6.2.5.6	TA-41	6-19
	6.2.5.7	TA-46	6-20

Section			Page
	6.2.5.8	TA-55	6-20
	6.2.5.9	P-Wave Velocity Profiles	6-21
7.0	SEISMIC SOURCE CHARACTERIZATION		7-1
7.1	Potentially Seismogenic Faults		7-1
7.1.1	Pajarito Fault System		7-4
7.1.2	Sawyer Canyon Fault		7-8
7.1.3	Puye Fault Zone		7-9
7.1.4	Lobato Mesa Fault Zone		7-10
7.1.5	La Bajada Fault		7-10
7.1.6	Embudo Fault		7-11
7.1.7	La Cañada del Amagre-Clara Peak Fault Zone		7-13
7.1.8	San Francisco Fault		7-13
7.1.9	Pojoaque Fault		7-14
7.1.10	San Felipe Fault		7-15
7.1.11	Jemez-San Ysidro Fault System		7-16
7.1.12	Cañones Fault		7-17
7.1.13	Nambe Fault		7-18
7.1.14	Faults of Black Mesa		7-19
7.1.15	Tijeras-Cañoncito Fault		7-19
7.1.16	Nacimiento Fault		7-20
7.1.17	Picuris-Pecos Fault		7-21
7.1.18	West Mesa Fault Zone		7-22
7.1.19	Puerco Fault		7-22
7.1.20	Gallina Fault		7-23
7.1.21	Sandia-Rio Grande Fault Zone		7-24
7.1.22	Sangre de Cristo Fault		7-25
7.1.23	Los Cordovas Fault		7-25
7.2	Seismic Source Zones		7-26
7.2.1	Rio Grande Rift		7-27
7.2.2	Colorado Plateau Transition Zone		7-28
7.2.3	Valles Volcanic Province		7-29
7.2.4	Southern Rocky Mountains		7-29
7.2.5	Great Plains		7-30

Section				Page
8.0	DETERMINISTIC GROUND MOTION ESTIMATES			8-1
	8.1	Empirical Approach		8-1
		8.1.1	Selection of Attenuation Relationships	8-2
		8.1.2	Peak Accelerations and Acceleration Response Spectra	8-3
	8.2	Stochastic Approach		8-3
		8.2.1	Methodology	8-4
			8.2.1.1 Band-Limited-White-Noise Point Source Model	8-4
			8.2.1.2 Random Vibration Theory	8-5
			8.2.1.3 Stress Drop	8-6
			8.2.1.4 Near-Surface Crustal Amplification and Damping	8-6
			8.2.1.5 Path Attenuation	8-7
			8.2.1.6 Finite Source Model	8-8
			8.2.1.7 Equivalent-Linear Approach for Soil Response	8-10
			8.2.1.8 Model Validation and Uncertainties	8-12
		8.2.2	Analysis of Kappa	8-13
		8.2.3	Input Parameters	8-14
			8.2.3.1 Earthquake Sources	8-14
			8.2.3.2 Propagation Path	8-16
			8.2.3.3 Sites	8-16
		8.2.4	Site-Specific Ground Motion Estimates	8-18
		8.2.5	Site-Specific Attenuation Relationships	8-20
	8.3	Review of Site Effects at the Nevada Test Site		8-21
	8.4	Evaluation of Topographic Effects		8-22

Section			Page
	8.4.1	Description of the Numerical Code	8-22
	8.4.2	Topographic Model	8-23
	8.4.3	Results of Analyses	8-24
8.5	Assessment of Vertical Motions		8-26
9.0	PROBABILISTIC SEISMIC HAZARD ANALYSES		9-1
9.1	Seismic Hazard Methodology		9-1
9.2	Seismic Sources		9-3
	9.2.1	Source Geometry	9-4
	9.2.2	Recurrence	9-5
9.3	Attenuation Relationships		9-8
9.4	Seismic Hazard Results		9-8
	9.4.1	Peak Acceleration	9-8
	9.4.2	Response Spectral Acceleration	9-9
9.5	Sensitivity of the Hazard Results		9-9
	9.5.1	Seismic Source Contributions	9-10
	9.5.2	Sensitivity to Attenuation Relationship	9-10
	9.5.3	Magnitude and Distance Contributions	9-11
	9.5.4	Sensitivity to Site Location	9-12
9.6	Equal Hazard Spectra		9-12
9.7	Comparison with Other Probabilistic Estimates		9-12
9.8	Comparison with Deterministic Estimates		9-13
10.0	DESIGN BASIS EARTHQUAKE PARAMETERS		10-1
10.1	Design Basis Earthquake Response Spectra		10-1

Section		Page
10.2	Design Basis Earthquake Time Histories	10-2
10.2.1	Recommended Stochastic Time Histories	10-2
10.2.2	Recommended Empirical Time Histories	10-3
11.0	RECOMMENDATIONS FOR FUTURE STUDIES	11-1
11.1	Pajarito Fault System	11-1
11.1.1	Faulting History	11-1
11.1.2	Tectonic Model	11-3
11.1.3	Surface Rupture Potential	11-3
11.2	GROUND MOTION EVALUATIONS	11-4
11.2.1	Site Response of Other Technical Areas	11-4
11.3	SEISMIC MONITORING	11-4
11.3.1	LANL Seismographic Network	11-4
11.3.2	LANL Strong Motion Network	11-5
REFERENCES		

LIST OF TABLES

Table 3-1 Abridged Modified Mercalli Intensity Scale
Table 3-2 Earthquake Catalogue Completeness Estimates and Number of Events Used in Recurrence
Table 3-3 Recurrence Parameters for LANL Compared with Other Estimates
Table 3-4 Earthquake Completeness Estimates and Number of Events Used in Recurrence for Circular Source Regions Around Los Alamos
Table 3-5 Recurrence Parameters for Circular Regions Around Los Alamos
Table 4-1 Net Vertical Tectonic Displacements Estimated From Topographic Profiles Across the Pajarito Fault System
Table 4-2 Radiocarbon Samples and Analyses from Trench Investigations
Table 4-3 Luminescence Data and Age Estimates for Samples from Trenches Along the Pajarito Fault System
Table 5-1 Velocity Model for the LANL Region
Table 6-1 Index Properties of Tested Samples
Table 7-1 Footnotes to Logic Trees for Potential Earthquake Sources
Table 7-2 Commonly Cited Characteristics of Segment Boundaries Along Normal Faults
Table 7-3 Slip Rates and Normalized Slip Rates for Faults in the Rio Grande Rift
Table 7-4 Weighted-Mean Maximum Magnitudes for Rupture Scenarios of the Pajarito Fault System
Table 7-5 Depth (in km) of Intersection for the Pajarito (PAF) and Rendija Canyon (RC) Faults for the Intersecting Structural Model
Table 7-6 Depth (in km) of Intersection for the Pajarito (PAF) and Guaje Mountain (GM) Faults for the Intersecting Structural Model
Table 7-7 Historical Surface-Faulting Earthquakes with Primarily Normal Slip
Table 7-8 Estimation of a Long-Term Average Net Slip Rate for the Southwest Section of the Embudo Fault
Table 8-1 Estimated Median (50th Percentile) Peak Horizontal Accelerations from the Pajarito Fault M_w 7 Earthquake
Table 8-2 Earthquake Recordings Used for Kappa Estimates
Table 8-3 Kappa Values at LANL
Table 8-4 Input Parameters and Uncertainties for Parametric Variations in Stochastic Modeling
Table 8-5 Comparison of Empirical and Stochastic Peak Horizontal Accelerations from the Pajarito Fault M_w 7 Earthquake
Table 8-6 Input Parameters and Weights for Stochastic Attenuation Relationships
Table 9-1 Probabilistic Peak Horizontal Accelerations (in g's) for LANL
Table 9-2 Dominant Earthquakes
Table 10-1 Recommended Empirical Time Histories

LIST OF FIGURES

Figure 1-1 Map of the LANL Region Showing Important Technical Areas and Major Faults
Figure 1-2 Location Map of Physiographic Provinces in Relation to the LANL region
Figure 2-1 Tectonic Map of the LANL Region
Figure 2-2 Generalized Geologic Map of the Pajarito Plateau
Figure 3-1 Population Growth Around the LANL Region
Figure 3-2 Significant Seismograph Stations and Networks in the LANL Region
Figure 3-3 Los Alamos Seismograph Network Locations and Approximate Operational Periods
Figure 3-4 Isoseismal Map for the 15 November 1906 Socorro Earthquake
Figure 3-5 Isoseismal Map for the 28 May 1918 Cerrillos Earthquake
Figure 3-6 Isoseismal Map for the 22 January 1966 M_s 4.9 Dulce Earthquake
Figure 3-7 Locations of Reservoir Induced Seismicity at Heron-El Vado Reservoirs and Correlation Between Reservoir Volume and Earthquake Occurrence
Figure 3-8 Annual Cumulative Rates of Independent Earthquake Occurrence for the Rio Grande Rift
Figure 3-9 Annual Cumulative Rates of Independent Earthquake Occurrence for the Colorado Plateau Transition Zone
Figure 3-10 Annual Cumulative Rates of Independent Earthquake Occurrence for the Southern Rocky Mountains
Figure 3-11 Annual Cumulative Rates of Independent Earthquake Occurrence for the Great Plains
Figure 3-12 Historical Seismicity Used in Recurrence for the Seismotectonic Provinces
Figure 3-13 Earthquake Recurrence for the Rio Grande Rift Province and the Colorado Plateau Transition Zone
Figure 3-14 Earthquake Recurrence for the Southern Rocky Mountains and Great Plains Provinces
Figure 3-15 Historical Seismicity Used in Recurrence for Selected Radii Around Los Alamos
Figure 3-16 Earthquake Recurrence for 20 and 40 km Radius Circles Around Los Alamos
Figure 3-17 Earthquake Recurrence for 60 and 80 km Radius Circles Around Los Alamos
Figure 4-1 Location Map of Topographic Profiles Across the Pajarito Fault System
Figure 4-2a Topographic Profile of the top of Bandelier Tuff Along Frijoles Mesa (Western Part of Profile P6)
Figure 4-2b Topographic Profile of the top of Bandelier Tuff West of Mesita del Potrillo (Profile P18)
Figure 4-2c Topographic Profile of the top of Bandelier Tuff west of Twomile Mesa (Profile P17)

Figure 4-2d Topographic Profile of the top of Bandelier Tuff Along Barranca Mesa (Profile P1)
Figure 4-2e Topographic Profile of the top of Bandelier Tuff Along South Mesa (Western Part of Profile P4)
Figure 4-3a Net Vertical Tectonic Displacement of Upper Bandelier Tuff Along the Pajarito Fault
Figure 4-3b Net Vertical Tectonic Displacement of Upper Bandelier Tuff Along the Rendija Canyon Fault
Figure 4-3c Net Vertical Tectonic Displacement of Upper Bandelier Tuff Along the Guaje Mountain Fault
Figure 4-4 Topographic Profiles and Slope Angle Plots for Profiles M7 and M2 Across the Pajarito Fault
Figure 4-5 Simplified Geologic Map of the Unnamed Mesa West of Hernandez
Figure 4-6 Fault Map of the Arroyo Honda Area
Figure 4-7 Topographic Profiles of Scarps Along Faults on Black Mesa
Figure 4-8 Geologic Map of the Water Canyon Site Showing Trench and Soil Pit Locations
Figure 4-9 Sequence of Depositional and Faulting Events Inferred from the Water Tanks Trenches
Figure 4-10 Location of Shallow Drill Holes in Pajarito Canyon
Figure 4-11 Cross-Section for Drill Holes in Pajarito Canyon
Figure 4-12 Sequence of Depositional and Faulting Events Inferred from the Pajarito Canyon Trench
Figure 4-13 Oblique Aerial Photograph of the Guaje Pines Site
Figure 4-14 Surficial Geologic Map of the Guaje Pines Site on the Rendija Canyon Fault
Figure 4-15 Schematic Cross-Section A-A' at the Guaje Pines Site
Figure 4-16 Sequence of Depositional and Faulting Events on the Rendija Canyon Fault at the Guaje Pines Site
Figure 4-17 Inferred Timing of Surface-Faulting Earthquakes, Rendija Canyon Fault at Guaje Pines Site
Figure 4-18 Palinspastic Reconstruction of Trench GPT1 to Time Immediately Following the Most-Recent Earthquake
Figure 4-19 Inferred Recurrence Values for Rendija Canyon Fault at Guaje Pines Site
Figure 4-20 Ground Photograph of the County Landfill Site
Figure 4-21 Schematic Diagram Showing Relative Soil Development on Terraces in the Rendija Canyon Area
Figure 4-22 Surficial Geologic Map of the Sportsmen's Club Site
Figure 5-1 Seismicity Cross-Sections - North-South
Figure 5-2 Seismicity Cross-Sections - East-West
Figure 5-3 Focal Depth Distribution for Well-Located Earthquakes in the LANL Region

Figure 5-4 Focal Depth Distribution for Well-Located Earthquakes in the Rio Grande Rift
Figure 5-5 Focal Mechanisms and Faults Within the LANL Region
Figure 6-1 Locations of Existing Water-Supply and Test Wells, Test Holes, Core Holes, and Seismic Hazards Borings at LANL
Figure 6-2 Map Showing Location of Seismic Hazards Borings
Figure 6-3 Schematic Logs for Core Holes SHB-1, SHB-2, SHB-3 and SHB-4
Figure 6-4 Pajarito Plateau Cross-Sections A-A' and B-B'
Figure 6-5 Pajarito Plateau Cross-Section C-C'
Figure 6-6 Downhole Travel Times for P- and S-Wave Signals and the Resulting Velocity Profiles for SHB-1
Figure 6-7 Downhole Travel Times for P- and S-Wave Signals and the Resulting Velocity Profiles for SHB-2
Figure 6-8 Downhole Travel Times for P- and S-Wave Signals and the Resulting Velocity Profiles for SHB-3
Figure 6-9 Downhole Travel Times for P- and S-Wave Signals and the Resulting Velocity Profiles for SHB-4
Figure 6-10 S-Wave Damping Measurements in SHB-1
Figure 6-11 Percentage Core Recovery Versus Velocity for Core Holes SHB-1 Through SHB-4
Figure 6-12 Variation in Normalized Shear Modulus with Shearing Strain from Resonant Column and Torsional Shear Tests
Figure 6-13 Variation in Material Damping Ratio with Shearing Strain for $\gamma \leq 0.1\%$ from Resonant Column and Torsional Shear Tests
Figure 6-14 Variation in Low-Amplitude Shear Modulus with Effective Confining Pressure from Resonant Column Tests
Figure 6-15 Variation in Low-Amplitude Material Damping Ratio with Effective Confining Pressure from Resonant Column Tests
Figure 6-16 TA-2 and TA-3 Geologic and S-Wave Velocity Profiles
Figure 6-17 TA-16 and TA-18 Geologic and S-Wave Velocity Profiles
Figure 6-18 TA-21 and TA-41 Geologic and S-Wave Velocity Profiles
Figure 6-19 TA-46 and TA-55 Geologic and S-Wave Velocity Profiles
Figure 6-20 TA-2 and TA-3 Geologic and P-Wave Velocity Profiles
Figure 6-21 TA-16 and TA-18 Geologic and P-Wave Velocity Profiles
Figure 6-22 TA-21 and TA-41 Geologic and P-Wave Velocity Profiles
Figure 6-23 TA-46 and TA-55 Geologic and P-Wave Velocity Profiles
Figure 7-1a Logic Tree for Pajarito Fault System: PAF Independent Branch
Figure 7-1b Logic Tree for Pajarito Fault System: RC Independent Branch
Figure 7-1c Logic Tree for Pajarito Fault System: GM Independent Branch
Figure 7-1d Logic Tree for Pajarito Fault System: PAF and RC Dependent and GM Independent Branch

Figure 7-1e Logic Tree for Pajarito Fault System: PAF and GM Dependent and RC Independent Branch
Figure 7-1f Logic Tree for Pajarito Fault System: RC and GM Dependent and PAF Independent Branch
Figure 7-1g Logic Tree for the Pajarito Fault System: PAF, RC, and GM Dependent Branch
Figure 7-2 Logic Tree for Sawyer Canyon Fault
Figure 7-3 Logic Tree for Puye Fault Zone
Figure 7-4 Logic Tree for Lobato Mesa Fault Zone
Figure 7-5 Logic Tree for La Bajada Fault
Figure 7-6 Logic Tree for Embudo Fault
Figure 7-7 Logic Tree for La Cañada Del Amagre-Clara Peak Fault Zone
Figure 7-8 Logic Tree for San Francisco Fault
Figure 7-9 Logic Tree for Pojoaque Fault
Figure 7-10 Logic Tree for San Felipe Fault Zone
Figure 7-11 Logic Tree for Jemez-San Ysidro Fault System
Figure 7-12 Logic Tree for Cañones Fault
Figure 7-13 Logic Tree for Nambe Fault
Figure 7-14 Logic Tree for Faults of Black Mesa
Figure 7-15 Logic Tree for Tijeras-Cañoncito Fault
Figure 7-16 Logic Tree for Nacimiento Fault
Figure 7-17 Logic Tree for Picuris-Pecos Fault
Figure 7-18 Logic Tree for West Mesa Fault Zone
Figure 7-19 Logic Tree for Puerco Fault
Figure 7-20 Logic Tree for Gallina Fault
Figure 7-21 Logic Tree for Sandia-Rio Grande Fault Zone
Figure 7-22 Logic Tree for Sangre De Cristo Fault
Figure 7-23 Logic Tree for Los Cordovas Fault
Figure 7-24 Previous Segmentation Models for the Pajarito Fault System
Figure 7-25a to 7-25f Schematic Diagram of Rupture Scenarios for the Pajarito Fault System
Figure 7-26 Slip Rates for Faults in the Rio Grande Rift
Figure 7-27 Logic Tree for the Rio Grande Rift
Figure 7-28 Logic Tree for the Colorado Plateau Transition Zone
Figure 7-29 Logic Tree for the Southern Rocky Mountains
Figure 7-30 Logic Tree for the Great Plains
Figure 8-1 Comparison of LANL Profiles With Generic Empirical Profiles
Figure 8-2 TA-2 Median Empirical Acceleration Response Spectra for Pajarito Fault M_w 7 Earthquake

Figure 8-3 TA-3 Median Empirical Acceleration Response Spectra for Pajarito Fault M_w 7 Earthquake
Figure 8-4 TA-16 Median Empirical Acceleration Response Spectra for Pajarito Fault M_w 7 Earthquake
Figure 8-5 TA-18 Median Empirical Acceleration Response Spectra for Pajarito Fault M_w 7 Earthquake
Figure 8-6 TA-21 Median Empirical Acceleration Response Spectra for Pajarito Fault M_w 7 Earthquake
Figure 8-7 TA-41 Median Empirical Acceleration Response Spectra for Pajarito Fault M_w 7 Earthquake
Figure 8-8 TA-46 Median Empirical Acceleration Response Spectra for Pajarito Fault M_w 7 Earthquake
Figure 8-9 TA-55 Median Empirical Acceleration Response Spectra for Pajarito Fault M_w 7 Earthquake
Figure 8-10 Stochastic Finite Fault Methodology
Figure 8-11 Least-Squares Fits to the Vector-Sum Fourier Spectra for 26 October 1989 Earthquake
Figure 8-12 Least-Squares Fits to the Vector-Sum Fourier Spectra for 27 October 1989 Earthquake
Figure 8-13 Least-Squares Fits to the Vector-Sum Fourier Spectra for 27 April 1990 Earthquake
Figure 8-14 Least-Squares Fits to the Vector-Sum Fourier Spectra for 24 May 1990 Earthquake
Figure 8-15 Least-Squares Fits to the Vector-Sum Fourier Spectra for 5 July 1990 Earthquake
Figure 8-16 Least-Squares Fits to the Vector-Sum Fourier Spectra for 3 September 1990 Earthquake
Figure 8-17 Least-Squares Fits to the Vector-Sum Fourier Spectra for 13 September 1990 Earthquake
Figure 8-18 Sample of Randomized Slip Models for the Pajarito Fault M_w 7 Earthquake
Figure 8-19 Acceleration Response Spectra for M_w 5.9 Earthquake at 6 km at Mesa Top Sites
Figure 8-20 Acceleration Response Spectra for M_w 5.9 Earthquake at 6 km at Canyon Sites
Figure 8-21 Average Response Spectra for M_w 5.9 Earthquake at 6 km at Canyon and Mesa Top Sites
Figure 8-22 Stochastic Acceleration Response Spectra for Pajarito Fault M_w 7 Earthquake at TA-2
Figure 8-23 Stochastic Acceleration Response Spectra for Pajarito Fault M_w 7 Earthquake at TA-3

Figure 8-24 Stochastic Acceleration Response Spectra for Pajarito Fault M_w 7 Earthquake at TA-16
Figure 8-25 Stochastic Acceleration Response Spectra for Pajarito Fault M_w 7 Earthquake at TA-18
Figure 8-26 Stochastic Acceleration Response Spectra for Pajarito Fault M_w 7 Earthquake at TA-21
Figure 8-27 Stochastic Acceleration Response Spectra for Pajarito Fault M_w 7 Earthquake at TA-41
Figure 8-28 Stochastic Acceleration Response Spectra for Pajarito Fault M_w 7 Earthquake at TA-46
Figure 8-29 Stochastic Acceleration Response Spectra for Pajarito Fault M_w 7 Earthquake at TA-55
Figure 8-30 Stochastic Peak Acceleration Attenuation Relationships for Mesa Top Sites
Figure 8-31 Stochastic Peak Acceleration Attenuation Relationships for Canyon Sites
Figure 8-32 Generalized Mesa Cross-Section Used in Topographic Modeling
Figure 8-33 Two-dimensional Model Used in the Finite Difference Simulations
Figure 8-34 Simulated Displacement Time Histories at Sites 1-10 for a Vertically Propagating Plane SH Wave
Figure 8-35 Site 1 Fourier Amplitude Spectral Ratio (2D/1D)
Figure 8-36 Site 2 Fourier Amplitude Spectral Ratio (2D/1D)
Figure 8-37 Site 3 Fourier Amplitude Spectral Ratio (2D/1D)
Figure 8-38 Site 4 Fourier Amplitude Spectral Ratio (2D/1D)
Figure 8-39 Site 5 Fourier Amplitude Spectral Ratio (2D/1D)
Figure 8-40 Site 6 Fourier Amplitude Spectral Ratio (2D/1D)
Figure 8-41 Site 7 Fourier Amplitude Spectral Ratio (2D/1D)
Figure 8-42 Site 8 Fourier Amplitude Spectral Ratio (2D/1D)
Figure 8-43 Site 9 Fourier Amplitude Spectral Ratio (2D/1D)
Figure 8-44 Site 10 Fourier Amplitude Spectral Ratio (2D/1D)
Figure 8-45 Log Average V/H Ratios for M_w 6 and Mesa Top Sites
Figure 8-46 Log Average V/H Ratios for M_w 7 and Mesa Top Sites
Figure 8-47 Log Average V/H Ratios for M_w 6 and Canyon Sites
Figure 8-48 Log Average V/H Ratios for M_w 7 and Canyon Sites
Figure 8-49 Log Average V/H Ratios for M_w 6 and All Sites
Figure 8-50 Log Average V/H Ratios for M_w 7 and All Sites
Figure 8-51 Log Average V/H Ratios for M_w 6 and 7 and All Sites
Figure 8-52 Recommended 5% Damped V/H Ratios
Figure 8-53 Ratios of Vertical to Horizontal Response Spectra 500 Year Return Period
Figure 8-54 Ratios of Vertical to Horizontal Response Spectra 1,000 and 2,000 Year Return Period
Figure 8-55 Ratios of Vertical to Horizontal Response Spectra 10,000 Year Return Period

Figure 8-56 Recommended Ratios of Vertical to Horizontal Response Spectra
Figure 9-1 Seismic Hazard Model Logic Tree
Figure 9-2 Seismic Source Recurrence
Figure 9-3 Attenuation Relationships Peak Ground Acceleration
Figure 9-4 Attenuation Relationships Horizontal Spectral Acceleration at 0.1 sec
Figure 9-5 Attenuation Relationships Horizontal Spectral Acceleration at 0.2 sec
Figure 9-6 Attenuation Relationships Horizontal Spectral Acceleration at 0.3 sec
Figure 9-7 Attenuation Relationships Horizontal Spectral Acceleration at 0.5 sec
Figure 9-8 Attenuation Relationships Horizontal Spectral Acceleration at 1 sec
Figure 9-9 Attenuation Relationships Horizontal Spectral Acceleration at 2 sec
Figure 9-10 Attenuation Relationships Horizontal Spectral Acceleration at 4 sec
Figure 9-11 Mean and 5th to 95th Percentile Seismic Hazard Curves for Peak Horizontal Acceleration at TA-2
Figure 9-12 Mean and 5th to 95th Percentile Seismic Hazard Curves for Peak Horizontal Acceleration at TA-3
Figure 9-13 Mean and 5th to 95th Percentile Seismic Hazard Curves for Peak Horizontal Acceleration at TA-16
Figure 9-14 Mean and 5th to 95th Percentile Seismic Hazard Curves for Peak Horizontal Acceleration at TA-18
Figure 9-15 Mean and 5th to 95th Percentile Seismic Hazard Curves for Peak Horizontal Acceleration at TA-21
Figure 9-16 Mean and 5th to 95th Percentile Seismic Hazard Curves for Peak Horizontal Acceleration at TA-41
Figure 9-17 Mean and 5th to 95th Percentile Seismic Hazard Curves for Peak Horizontal Acceleration at TA-46
Figure 9-18 Mean and 5th to 95th Percentile Seismic Hazard Curves for Peak Horizontal Acceleration at TA-55
Figure 9-19 Mean and 5th to 95th Percentile Seismic Hazard Curves for 0.2 sec Horizontal Spectral Acceleration, TA-2
Figure 9-20 Mean and 5th to 95th Percentile Seismic Hazard Curves for 0.2 sec Horizontal Spectral Acceleration, TA-3
Figure 9-21 Mean and 5th to 95th Percentile Seismic Hazard Curves for 0.2 sec Horizontal Spectral Acceleration, TA-16
Figure 9-22 Mean and 5th to 95th Percentile Seismic Hazard Curves for 0.2 sec Horizontal Spectral Acceleration, TA-18
Figure 9-23 Mean and 5th to 95th Percentile Seismic Hazard Curves for 0.2 sec Horizontal Spectral Acceleration, TA-21
Figure 9-24 Mean and 5th to 95th Percentile Seismic Hazard Curves for 0.2 sec Horizontal Spectral Acceleration, TA-41

Figure 9-25 Mean and 5th to 95th Percentile Seismic Hazard Curves for 0.2 sec Horizontal Spectral Acceleration, TA-46
Figure 9-26 Mean and 5th to 95th Percentile Seismic Hazard Curves for 0.2 sec Horizontal Spectral Acceleration, TA-55
Figure 9-27 Mean and 5th to 95th Percentile Seismic Hazard Curves for 1 sec Horizontal Spectral Acceleration, TA-2
Figure 9-28 Mean and 5th to 95th Percentile Seismic Hazard Curves for 1 sec Horizontal Spectral Acceleration, TA-3
Figure 9-29 Mean and 5th to 95th Percentile Seismic Hazard Curves for 1 sec Horizontal Spectral Acceleration, TA-16
Figure 9-30 Mean and 5th to 95th Percentile Seismic Hazard Curves for 1 sec Horizontal Spectral Acceleration, TA-18
Figure 9-31 Mean and 5th to 95th Percentile Seismic Hazard Curves for 1 sec Horizontal Spectral Acceleration, TA-21
Figure 9-32 Mean and 5th to 95th Percentile Seismic Hazard Curves for 1 sec Horizontal Spectral Acceleration, TA-41
Figure 9-33 Mean and 5th to 95th Percentile Seismic Hazard Curves for 1 sec Horizontal Spectral Acceleration, TA-46
Figure 9-34 Mean and 5th to 95th Percentile Seismic Hazard Curves for 1 sec Horizontal Spectral Acceleration, TA-55
Figure 9-35 Contribution of Seismic Sources to the Mean Seismic Hazard for Peak Horizontal Acceleration, TA-2
Figure 9-36 Contribution of Seismic Sources to the Mean Seismic Hazard for Peak Horizontal Acceleration, TA-3
Figure 9-37 Contribution of Seismic Sources to the Mean Seismic Hazard for Peak Horizontal Acceleration, TA-16
Figure 9-38 Contribution of Seismic Sources to the Mean Seismic Hazard for Peak Horizontal Acceleration, TA-18
Figure 9-39 Contribution of Seismic Sources to the Mean Seismic Hazard for Peak Horizontal Acceleration, TA-21
Figure 9-40 Contribution of Seismic Sources to the Mean Seismic Hazard for Peak Horizontal Acceleration, TA-41
Figure 9-41 Contribution of Seismic Sources to the Mean Seismic Hazard for Peak Horizontal Acceleration, TA-46
Figure 9-42 Contribution of Seismic Sources to the Mean Seismic Hazard for Peak Horizontal Acceleration, TA-55
Figure 9-43 Contribution of Seismic Sources to the Mean Seismic Hazard for 0.2 sec Horizontal Spectral Acceleration, TA-2
Figure 9-44 Contribution of Seismic Sources to the Mean Seismic Hazard for 0.2 sec Horizontal Spectral Acceleration, TA-3

Figure 9-45 Contribution of Seismic Sources to the Mean Seismic Hazard for 0.2 sec Horizontal Spectral Acceleration, TA-16
Figure 9-46 Contribution of Seismic Sources to the Mean Seismic Hazard for 0.2 sec Horizontal Spectral Acceleration, TA-18
Figure 9-47 Contribution of Seismic Sources to the Mean Seismic Hazard for 0.2 sec Horizontal Spectral Acceleration, TA-21
Figure 9-48 Contribution of Seismic Sources to the Mean Seismic Hazard for 0.2 sec Horizontal Spectral Acceleration, TA-41
Figure 9-49 Contribution of Seismic Sources to the Mean Seismic Hazard for 0.2 sec Horizontal Spectral Acceleration, TA-46
Figure 9-50 Contribution of Seismic Sources to the Mean Seismic Hazard for 0.2 sec Horizontal Spectral Acceleration, TA-55
Figure 9-51 Contribution of Seismic Sources to the Mean Seismic Hazard for 1 sec Horizontal Spectral Acceleration, TA-2
Figure 9-52 Contribution of Seismic Sources to the Mean Seismic Hazard for 1 sec Horizontal Spectral Acceleration, TA-3
Figure 9-53 Contribution of Seismic Sources to the Mean Seismic Hazard for 1 sec Horizontal Spectral Acceleration, TA-16
Figure 9-54 Contribution of Seismic Sources to the Mean Seismic Hazard for 1 sec Horizontal Spectral Acceleration, TA-18
Figure 9-55 Contribution of Seismic Sources to the Mean Seismic Hazard for 1 sec Horizontal Spectral Acceleration, TA-21
Figure 9-56 Contribution of Seismic Sources to the Mean Seismic Hazard for 1 sec Horizontal Spectral Acceleration, TA-41
Figure 9-57 Contribution of Seismic Sources to the Mean Seismic Hazard for 1 sec Horizontal Spectral Acceleration, TA-46
Figure 9-58 Contribution of Seismic Sources to the Mean Seismic Hazard for 1 sec Horizontal Spectral Acceleration, TA-55
Figure 9-59 Effect of Attenuation Relationships on Mean Seismic Hazard for Peak Acceleration and Spectral Accelerations of 0.2 and 1.0 second, TA-2
Figure 9-60 Effect of Attenuation Relationships on Mean Seismic Hazard for Peak Acceleration and Spectral Accelerations of 0.2 and 1.0 second, TA-3
Figure 9-61 Effect of Attenuation Relationships on Mean Seismic Hazard for Peak Acceleration and Spectral Accelerations of 0.2 and 1.0 second, TA-16
Figure 9-62 Effect of Attenuation Relationships on Mean Seismic Hazard for Peak Acceleration and Spectral Accelerations of 0.2 and 1.0 second, TA-18
Figure 9-63 Effect of Attenuation Relationships on Mean Seismic Hazard for Peak Acceleration and Spectral Accelerations of 0.2 and 1.0 second, TA-21
Figure 9-64 Effect of Attenuation Relationships on Mean Seismic Hazard for Peak Acceleration and Spectral Accelerations of 0.2 and 1.0 second, TA-41

Figure 9-65 Effect of Attenuation Relationships on Mean Seismic Hazard for Peak Acceleration and Spectral Accelerations of 0.2 and 1.0 second, TA-46
Figure 9-66 Effect of Attenuation Relationships on Mean Seismic Hazard for Peak Acceleration and Spectral Accelerations of 0.2 and 1.0 second, TA-55
Figure 9-67 Magnitude and Distance Contributions to Mean Seismic Hazard for Peak Acceleration, TA-2
Figure 9-68 Magnitude and Distance Contributions to Mean Seismic Hazard for Peak Acceleration, TA-3
Figure 9-69 Magnitude and Distance Contributions to Mean Seismic Hazard for Peak Acceleration, TA-16
Figure 9-70 Magnitude and Distance Contributions to Mean Seismic Hazard for Peak Acceleration, TA-18
Figure 9-71 Magnitude and Distance Contributions to Mean Seismic Hazard for Peak Acceleration, TA-21
Figure 9-72 Magnitude and Distance Contributions to Mean Seismic Hazard for Peak Acceleration, TA-41
Figure 9-73 Magnitude and Distance Contributions to Mean Seismic Hazard for Peak Acceleration, TA-46
Figure 9-74 Magnitude and Distance Contributions to Mean Seismic Hazard for Peak Acceleration, TA-55
Figure 9-75 Magnitude and Distance Contributions to Mean Seismic Hazard for 0.2 sec Horizontal Spectral Acceleration, TA-2
Figure 9-76 Magnitude and Distance Contributions to Mean Seismic Hazard for 0.2 sec Horizontal Spectral Acceleration, TA-3
Figure 9-77 Magnitude and Distance Contributions to Mean Seismic Hazard for 0.2 sec Horizontal Spectral Acceleration, TA-16
Figure 9-78 Magnitude and Distance Contributions to Mean Seismic Hazard for 0.2 sec Horizontal Spectral Acceleration, TA-18
Figure 9-79 Magnitude and Distance Contributions to Mean Seismic Hazard for 0.2 sec Horizontal Spectral Acceleration, TA-21
Figure 9-80 Magnitude and Distance Contributions to Mean Seismic Hazard for 0.2 sec Horizontal Spectral Acceleration, TA-41
Figure 9-81 Magnitude and Distance Contributions to Mean Seismic Hazard for 0.2 sec Horizontal Spectral Acceleration, TA-46
Figure 9-82 Magnitude and Distance Contributions to Mean Seismic Hazard for 0.2 sec Horizontal Spectral Acceleration, TA-55
Figure 9-83 Magnitude and Distance Contributions to Mean Seismic Hazard for 1 sec Horizontal Spectral Acceleration, TA-2
Figure 9-84 Magnitude and Distance Contributions to Mean Seismic Hazard for 1 sec Horizontal Spectral Acceleration, TA-3

Figure 9-85 Magnitude and Distance Contributions to Mean Seismic Hazard for 1 sec Horizontal Spectral Acceleration, TA-16
Figure 9-86 Magnitude and Distance Contributions to Mean Seismic Hazard for 1 sec Horizontal Spectral Acceleration, TA-18
Figure 9-87 Magnitude and Distance Contributions to Mean Seismic Hazard for 1 sec Horizontal Spectral Acceleration, TA-21
Figure 9-88 Magnitude and Distance Contributions to Mean Seismic Hazard for 1 sec Horizontal Spectral Acceleration, TA-41
Figure 9-89 Magnitude and Distance Contributions to Mean Seismic Hazard for 1 sec Horizontal Spectral Acceleration, TA-46
Figure 9-90 Magnitude and Distance Contributions to Mean Seismic Hazard for 1 sec Horizontal Spectral Acceleration, TA-55
Figure 9-91 Mean Equal Hazard Spectra at TA-2
Figure 9-92 Mean Equal Hazard Spectra at TA-3
Figure 9-93 Mean Equal Hazard Spectra at TA-16
Figure 9-94 Mean Equal Hazard Spectra at TA-18
Figure 9-95 Mean Equal Hazard Spectra at TA-21
Figure 9-96 Mean Equal Hazard Spectra at TA-41
Figure 9-97 Mean Equal Hazard Spectra at TA-46
Figure 9-98 Mean Equal Hazard Spectra at TA-55
Figure 9-99 Comparison of the Mean Equal Hazard Spectra for a 500-year Return Period
Figure 9-100 Comparison of the Mean Equal Hazard Spectra for a 1000-year Return Period
Figure 9-101 Comparison of the Mean Equal Hazard Spectra for a 2000-year Return Period
Figure 9-102 Comparison of the Mean Equal Hazard Spectra for a 10,000-year Return Period
Figure 10-1 Average Empirical Acceleration Response Spectra for 500-year Dominant Earthquake at 0.2 sec
Figure 10-2 Average Empirical Acceleration Response Spectra for 500-year Dominant Earthquake at 1.0 sec
Figure 10-3 Average Empirical Acceleration Response Spectra for 1000-year Dominant Earthquake at 0.2 sec
Figure 10-4 Average Empirical Acceleration Response Spectra for 1000-year Dominant Earthquake at 1.0 sec
Figure 10-5 Average Empirical Acceleration Response Spectra for 2000-year Dominant Earthquake at 0.2 sec
Figure 10-6 Average Empirical Acceleration Response Spectra for 2000-year Dominant Earthquake at 1.0 sec
Figure 10-7 Average Empirical Acceleration Response Spectra for 10,000-year Dominant Earthquake at 0.2 sec

Figure 10-8 Average Empirical Acceleration Response Spectra for 10,000-year Dominant Earthquake at 1.0 sec
Figure 10-9 Normalized Empirical Acceleration Response Spectra for 500-year Dominant Earthquake at 0.2 sec
Figure 10-10 Normalized Empirical Acceleration Response Spectra for 500-year Dominant Earthquake at 1.0 sec
Figure 10-11 Normalized Empirical Acceleration Response Spectra for 1000-year Dominant Earthquake at 0.2 sec
Figure 10-12 Normalized Empirical Acceleration Response Spectra for 1000-year Dominant Earthquake at 1.0 sec
Figure 10-13 Normalized Empirical Acceleration Response Spectra for 2000-year Dominant Earthquake at 0.2 sec
Figure 10-14 Normalized Empirical Acceleration Response Spectra for 2000-year Dominant Earthquake at 1.0 sec
Figure 10-15 Normalized Empirical Acceleration Response Spectra for 10,000-year Dominant Earthquake at 0.2 sec
Figure 10-16 Normalized Empirical Acceleration Response Spectra for 10,000-year Dominant Earthquake at 1.0 sec
Figure 10-17 Recommended DBE Horizontal Response Spectrum for 500-year Return Period
Figure 10-18 Recommended DBE Horizontal Response Spectrum for 1000-year Return Period
Figure 10-19 Recommended DBE Horizontal Response Spectrum for 2000-year Return Period
Figure 10-20 Recommended DBE Horizontal Response Spectrum for 10,000-year Return Period
Figure 10-21 Recommended DBE Vertical Response Spectrum for 500-year Return Period
Figure 10-22 Recommended DBE Vertical Response Spectrum for 1000-year Return Period
Figure 10-23 Recommended DBE Vertical Response Spectrum for 2000-year Return Period
Figure 10-24 Recommended DBE Vertical Response Spectrum for 10,000-year Return Period
Figure 10-25 Spectral Match to DBE Horizontal Response Spectrum for 500-year Return Period
Figure 10-26 Spectral Match to DBE Horizontal Response Spectrum for 1000-year Return Period
Figure 10-27 Spectral Match to DBE Horizontal Response Spectrum for 2000-year Return Period
Figure 10-28 Spectral Match to DBE Horizontal Response Spectrum for 10,000-year Return Period

Figure 10-29 Spectral Match to DBE Vertical Response Spectrum for 500-year Return Period
Figure 10-30 Spectral Match to DBE Vertical Response Spectrum for 1000-year Return Period
Figure 10-31 Spectral Match to DBE Vertical Response Spectrum for 2000-year Return Period
Figure 10-32 Spectral Match to DBE Vertical Response Spectrum for 10,000-year Return Period
Figure 10-33 Recommended DBE Horizontal Time Histories for 500-year Return Period
Figure 10-34 Recommended DBE Horizontal Time Histories for 1000-year Return Period
Figure 10-35 Recommended DBE Horizontal Time Histories for 2000-year Return Period
Figure 10-36 Recommended DBE Horizontal Time Histories for 10,000-year Return Period
Figure 10-37 Recommended DBE Vertical Time Histories for 500-year Return Period
Figure 10-38 Recommended DBE Vertical Time Histories for 1000-year Return Period
Figure 10-39 Recommended DBE Vertical Time Histories for 2000-year Return Period
Figure 10-40 Recommended DBE Vertical Time Histories for 10,000-year Return Period

LIST OF PLATES

Plate 1 Map of Quaternary and Pliocene Faults and Seismotectonic Provinces
Plate 2 Map of Major Fault Traces and Lineaments on the Pajarito Plateau in the LANL Region
Plate 3 Historical Seismicity (1873-1992), Quaternary and Pliocene Faults, and Seismotectonic Provinces in the LANL Region
Plate 4 Surficial Deposit Map Along the Pajarito Fault Between Twomile Canyon and Water Canyon
Plate 5 Logs of Water Canyon Trenches
Plate 6 Logs of Water Tanks Trenches
Plate 7 Logs of Pajarito Canyon Trenches
Plate 8 Logs of Guaje Pines Trenches
Plate 9 Logs of County Landfill Trenches
Plate 10 Map and Long-Profiles of Fluvial Terraces and Surficial Deposits, Rendija Canyon Area
Plate 11 Logs of Sportsmen's Club Trenches
Plate 12 Relocated Earthquakes, Quaternary and Pliocene Faults, and Seismotectonic Provinces in the LANL Region

LIST OF APPENDICES

Appendix A	Historical Earthquake Catalogue for the LANL Region
Appendix B	Historical Earthquake Catalogue for the Rio Grande Rift Used in Recurrence
Appendix C	Historical Earthquake Catalogue for the Colorado Plateau Transition Zone Used in Recurrence
Appendix D	Historical Earthquake Catalogue for the Southern Rocky Mountains Used in Recurrence
Appendix E	Historical Earthquake Catalogue for the Great Plains Used in Recurrence
Appendix F	Earthquake Recurrence Parameters
Appendix G	Lithologic Descriptions of Deposits Exposed in Trenches
Appendix H	Descriptions of Selected Soil Profiles in Trenches
Appendix I	Relocated Earthquakes in the LANL Region, 1973-1992
Appendix J	Core Hole Field Logs
Appendix K	Subsurface Geological and Geotechnical Data in the LANL Region
Appendix L	Empirical Attenuation Relationships
Appendix M	Shear Modulus Reduction and Damping Curves
Appendix N	Stochastic Attenuation Response Spectra - Variation of Parameters
Appendix O	Stochastic Attenuation Relationships for LANL Sites
Appendix P	Evaluation of Site Effects at the Nevada Test Site

A state-of-the-art seismic hazard evaluation of the Los Alamos National Laboratory (LANL) has been performed and is described and summarized in this report. Site-specific ground motions have been estimated both probabilistically and deterministically for eight facility sites including TA-2, TA-3, TA-16, TA-18, TA-21, TA-41, TA-46, and TA-55. The objective of this evaluation is to update the current seismic design criteria for LANL in response to new DOE Standards.

The LANL is located within the northern Rio Grande rift, a tectonically, volcanically, and seismically active seismotectonic province in the western U.S. Although active on the microearthquake level, only six historic earthquakes of estimated Richter magnitude (M_L) 5.0 or greater have occurred in the LANL region. The most significant event was the 1918 Cerrillos earthquake of estimated M_L 5½ which occurred approximately 50 km southeast of LANL.

Although surface-faulting earthquakes have not occurred historically in the LANL region (within 100 km), geologic evidence indicates they have occurred during the Quaternary (1.6 million years). Therefore, both faults and areal sources (to account for background seismicity not associated with known geologic structures) were considered in the evaluation. We identified 25 faults and four seismic source zones within the LANL region as potential seismic sources significant to the laboratory in terms of ground shaking. In particular, the three most significant and closest faults to the LANL were the focus of these studies: the Pajarito, Guaje Mountain, and Rendija Canyon faults, which comprise the Pajarito fault system. The Pajarito fault system is a 41-km-long, north-striking discontinuous fault system that defines the active western boundary of a portion of the Rio Grande rift. The main 41-km-long Pajarito fault is located along the western margin of the LANL and is a down-to-the-east normal fault, dipping beneath the laboratory. The 14-km-long Rendija Canyon fault is located 3 km east of the Pajarito fault, strikes north-south across the LANL site, dips steeply to the west and shows dominantly normal slip down to the west. The 12-km-long Guaje Mountain fault is located 1 to 2 km east of the Rendija Canyon fault, and is similar in its orientation, structural style, and sense of slip.

From 34 topographic profiles across the Pajarito fault system, we estimated net vertical tectonic displacements (NVTD) of the upper surface of the 1.2 million-year-old Tshirege member of the Bandelier Tuff. Along the Pajarito fault, we estimated a maximum NVTD of 154 $\pm$ 4 m and an average NVTD of about 81 m. These values yield a maximum vertical slip rate of about 0.13 mm/yr and an average vertical slip rate of about 0.07 mm/yr on the Pajarito fault for the past 1.2 million years. Along the Rendija Canyon fault, we estimated a maximum NVTD of 36 $\pm$ 10 m and an average NVTD of about 22 m. These displacements yield a maximum vertical slip rate of 0.03 mm/yr and an average vertical slip rate of 0.02 mm/yr for the past 1.2 million years on the Rendija Canyon fault. Finally, the maximum and average displacements estimated for the Guaje Mountain fault were 27 $\pm$ 4 m and 15 m, respectively. These displacements yield maximum and average vertical slip rates of 0.02 and 0.01 mm/yr, respectively, for the past 1.2 million years on the Guaje Mountain fault.

Detailed paleoseismic investigations were conducted during this study along the Pajarito, Rendija Canyon and Guaje Mountain faults. Evidence from trenches along the base of the Pajarito fault escarpment suggests faulting probably occurred between 45,000 and 55,000 years ago but, because exposures of the fault zone are incomplete, we cannot preclude the possibility of younger surface ruptures. We found both direct and indirect evidence at two different sites for five faulting events since 1.2 million years ago, but this can only account for a very small percentage of the total NVTD estimated from topographic profiles at these sites. Therefore, the paleoseismic record for the Pajarito fault remains too incomplete to determine reliable recurrence intervals.

Evidence from trenches on the Rendija Canyon fault shows that it has repeatedly ruptured during the late Quaternary, with the most recent event occurring at either 8,000 to 9,000 years ago or around 23,000 years ago. Estimated recurrence intervals on the Rendija Canyon fault range from 10,500 to 110,000 years, with preferred values ranging from 20,500 to 55,500 years and averaging about 36,000 years. The Guaje Mountain fault exhibits evidence of multiple surface ruptures during the past approximately 150,000 to 300,000 years and estimated slip rates for this time period range from 0.01 to 0.03 mm/yr. Previous paleoseismic trenching along the Guaje Mountain fault also shows evidence for repeated late Quaternary surface faulting, with the most-recent event having occurred about 4,000 to 6,000 years ago (Gardner et al., 1990).

The wide range of recurrence intervals and rates of activity for all three local faults demonstrates the considerable uncertainty in the timing of past surface-faulting events. Therefore, to better account for possible variations in rates of activity, slip rates for well-studied faults in the Rio Grande rift were compiled. For many faults, there was more than an order of magnitude difference between long-term and short-term rates, with the latter generally being much higher. We used this distribution of slip rates to characterize uncertainties in rates for all faults whose short-term rates are not well-constrained.

The source geometry, orientation, capability or activity potential, rupture scenarios, sense of slip, slip rate, and recurrence intervals (where appropriate) were characterized for each fault considered in the hazard analysis. Maximum magnitudes were estimated using empirical relations for rupture lengths, rupture areas and, where appropriate, displacements. Because available information suggests the most recent activity on the three principal faults of the Pajarito fault system was not contemporaneous, we considered both independent and dependent behavior for these faults, resulting in 22 rupture scenarios for the Pajarito fault system. Additional paleoseismic investigations are needed to simplify this preliminary model.

An evaluation of the seismicity recorded by the LANL network from 1973 to 1992 was performed. As is commonly observed throughout the Basin and Range province, seismicity is generally not associated with mapped faults or structures. Some microearthquakes, however, appear to correlate with a few faults including the Puye, La Bajada, and La Cañada del Amagre-Clara Peak fault zones. Only one well-located earthquake has occurred in the vicinity of LANL and the three local faults. The Valles caldera also appears to be seismically quiescent. The maximum depth of seismicity in the northern Rio Grande rift is 12 to 15 km, which is consistent with elevated crustal temperatures. Focal mechanisms show normal and strike-slip faulting generally on northerly-striking planes. The tectonic stress field is characterized by approximate east-west extension.

Seismic source zones considered in the evaluation include the Rio Grande rift, the Colorado Plateau transition zone, the Southern Rocky Mountains, and Great Plains provinces. Maximum magnitudes for the random earthquakes within these provinces range from M_w 6 to 6½. Recurrence for these seismic source zones was computed based upon an evaluation of the historical and contemporary seismicity.

The subsurface geology beneath the LANL was investigated through a program of core hole exploration, downhole velocity measurements, dynamic laboratory testing of core hole samples, and compilation and evaluation of all available LANL borehole and geotechnical data. Based on site-specific geologic and shear-wave velocity profiles developed in this study (compressional wave velocity profiles were also developed), the LANL sites were grouped into two categories: mesa top and canyon sites. The profiles were used in either one of these two groups in the stochastic modeling of ground motions. Kappa, a measure of the near-surface attenuation used in the modeling, was computed by analyzing earthquakes recorded at LANL seismographic stations whose near-surface geology is similar to that beneath the laboratory. A kappa value of 0.035 sec was estimated, which is typical for the western U.S.

Based on these site-specific geologic data and the seismic source characterization, deterministic and probabilistic ground motions were estimated in terms of peak horizontal accelerations and response spectra. The deterministic ground motions for the most significant earthquake to LANL, a M_w 7 event on the Pajarito fault, were evaluated through empirical and state-of-the-art stochastic approaches. Average empirical peak horizontal accelerations for such an event generally ranged from 0.47 to 0.53 g at the eight facility sites. Based on the site-specific shear-wave velocity profiles, the LANL sites are most similar to deep soil sites and thus empirical attenuation relationships appropriate for such site conditions were used in this analysis.

Site-specific stochastic acceleration response spectra were computed based upon the Band-Limited-White-Noise source model and random vibration theory. The stochastic peak horizontal accelerations (0.60 to 0.62 g) computed for a M_w 7 Pajarito fault event and the mesa top sites were similar to the empirical values. In contrast, high-frequency site amplification occurs at the three canyon sites, TA-2, TA-18, and TA-41 with peak horizontal accelerations ranging from 0.8 to 0.9 g, significantly exceeding the empirical values. The site-specific stochastic spectra exhibit significant effects of both high-frequency site amplification and long-period material damping, the latter due to the presence of the Bandelier Tuff beneath the mesa top sites.

Based on the stochastic modeling approach, site-specific attenuation relationships and vertical to horizontal response spectral ratios were also computed. The ratios were used to scale the horizontal design ground motions to arrive at vertical design motions. In addition to the

effects of site geology, the possible effects of the mesa topography on ground motions were analyzed using a numerical finite difference modeling technique. Based upon this first-order analysis, topographic amplification on the order of 10 to 20% is likely to occur at LANL mesa top sites in the frequency range of 1 to 5 Hz.

Seismic hazard curves were developed for each LANL site for peak horizontal acceleration and response spectral accelerations at periods of 0.2 and 1.0 sec. These curves were computed based upon a probabilistic seismic hazard analysis using a logic tree approach. This approach allows the incorporation of the full range of possible source, path, and site parameters and their uncertainties. The following summarizes the peak horizontal accelerations at the annual exceedance probabilities specified in DOE Standard 1020-94 for the four Performance Categories (PC):

PROBABILISTIC PEAK HORIZONTAL ACCELERATIONS (in g's) for LANL

Site	Annual Exceedance Probability (Return Period)			
	PC1-$2x10^{-3}$ (500 yrs)	PC2-$1x10^{-3}$ (1,000 yrs)	PC3-$5x10^{-4}$ (2,000 yrs)	PC4-$1x10^{-4}$ (10,000 yrs)
TA-2	0.14	0.22	0.31	0.57
TA-3	0.14	0.21	0.30	0.56
TA-16	0.14	0.21	0.29	0.53
TA-18	0.14	0.22	0.31	0.57
TA-21	0.15	0.22	0.31	0.55
TA-41	0.14	0.22	0.31	0.57
TA-46	0.15	0.22	0.30	0.55
TA-55	0.15	0.22	0.30	0.56

The principal seismic source contributors to hazard at the LANL are the Pajarito fault system and the random earthquake within the Rio Grande rift source zone. To a much lesser degree, other seismic sources which contribute to the ground shaking hazard at LANL include the Embudo, Puye, Lobato Mesa, Sawyer Canyon, and La Bajada faults.

Based on the results of the probabilistic analysis, equal hazard spectra were computed, deaggregation was performed to characterize the dominant earthquakes at three selected frequencies (1, 5, and 33 Hz), and Design Basis Earthquake response spectra and time histories were developed.

ACKNOWLEDGMENTS

This study was performed by the personnel of Woodward-Clyde Federal Services (WCFS); its subcontractors, William Lettis & Associates (WLA) and Pacific Engineering & Analysis (PE&A); and members of the Earth and Environmental Sciences Division of LANL. Many individuals in addition to the authors contributed to this study and to them we would like to express our sincere gratitude: Andy Gorton, Doug Wright, Sue Penn, and Norma Biggar of WCFS; Susan Chang, Sadako McInerney, Fumiko Goss, Anita Quintana, Said Salah-Mars, Jim Springer, and Perry Jung of Woodward-Clyde Consultants; Gary Simpson, Jay Noller, Tom Sawyer, and William Lettis of WLA; Sylvia Li and Ky Lang of PE&A; Suzanne Meuret, John Carney, James Lakings, Larry Goen, Scott Baldridge, and Karen Carter of LANL; and John Hawley of the New Mexico Bureau of Mines and Mineral Resources. Our thanks to Bruce Redpath of Redpath Geophysics for performing the downhole shear wave velocity measurements, Ken Stokoe and his associates of the University of Texas for the dynamic laboratory testing, Steve Forman of The Ohio State University for analysis of thermoluminescence samples and helpful discussions on interpreting results, and Jim McCalpin of GEO-HAZ Consultants who provided a compilation of slip rate data and valuable assistance in incorporating uncertainties. Our appreciation to Robert Remillard of the U.S. Forest Service, Ellen McGehee, Anne Pendergrass, Bev Larson, and Cathy Bennett of LANL for their assistance in permitting the trench sites. Celina Mae Vigil and Mike Pierotti of LANL provided valuable assistance in the management of this contract. Special gratitude to Dean Keller and Doug Volkman for their leadership and enthusiastic support of our efforts. Our sincere thanks to Jeff Kimball of DOE Headquarters for his insights, guidance, and fortitude in the ever evolving field of DOE seismic hazards. Jamie Gardner, Leigh House, and Dan Cash of LANL deserve special recognition for their early significant efforts in establishing a seismic hazards evaluation program at LANL. Without their diligent work, this study would not have been possible. The early efforts of Ken Olsen of LANL and Al Sanford of New Mexico Tech also are greatly appreciated. Technical reviews of various aspects of this study were provided by Michael Machette of the U.S. Geological Survey, James McCalpin, Al Sanford, Michael Cline of WCFS, Robert Youngs of Geomatrix Consultants, Jeff Kimball, William Lettis, Tom Cardonne of EG&G Idaho Inc., and Carl Costantino of City College of New York. These studies were supported by LANL Contracts 9-XT1-092K-1 and 5175F0013-9Y.

1.0
INTRODUCTION

At the request of the Los Alamos National Laboratory (LANL), the following report describes and summarizes a state-of-the-art seismic hazards evaluation of the LANL. Probabilistic earthquake ground motion assessments have been made for eight specific Technical Areas (TA) including TA-2, TA-3, TA-16, TA-18, TA-21, TA-41, TA-46, and TA-55 (Figure 1-1). This evaluation was performed by Woodward-Clyde Federal Services (WCFS); its prime subcontractors, William Lettis & Associates and Pacific Engineering & Analysis; and members of the Earth and Environmental Sciences Division at LANL. The purpose of this study is to update the seismic design criteria presently being used at LANL, particularly in light of the recognition in 1990 that the nearby Guaje Mountain fault has been active in the Holocene (past 11,000 years) (Gardner et al., 1990). This evaluation also was performed in response to recently published U.S. Department of Energy (DOE) Standards on seismic hazards.

1.1 OBJECTIVES

The objective of this study was to perform a state-of-the-art seismic hazard assessment based on the identification and characterization of seismic sources and probabilistic evaluations of ground motions, and to develop appropriate seismic design criteria for LANL. This project originally consisted of two phases (originally called "Tasks"): Phase I involved a review of existing information to identify specific seismic hazard issues and to develop a focused program to evaluate seismic hazards at LANL. The results of our Phase I evaluation is presented in the report "Data Review and Evaluation and Recommendations for Phase II Seismic Hazard Studies" (Woodward-Clyde Consultants, 1991) submitted to LANL in May 1991.

Phase II studies, which were initiated in June 1991, were performed using a systematic approach to address the most significant issues and to maximize critical data. Based on this program, any remaining unresolved issues could, therefore, be addressed in a similar systematic, cost-effective manner as part of future studies.

It was recognized in Phase I that only a few seismic sources may be significant to LANL in terms of earthquake hazards. To provide a comprehensive evaluation and to confirm this observation, all seismic sources, which could generate strong ground shaking at LANL, were incorporated into the hazard analysis. Thus, the results contained in this report represent a current assessment of the total hazard at LANL. Given both time and cost constraints, we designed a Phase II program that would address those seismic sources that pose the **highest** hazard and would probably control the seismic design criteria for LANL. These sources are three faults or fault segments that either border or intersect LANL: the Pajarito, Rendija Canyon and Guaje Mountain faults (Figure 1-1). Thus these three local faults were the focus of the Phase II as well as Phase III studies described in this report. As will be described in this report, the Pajarito fault system (includes the Rendija Canyon and Guaje Mountain faults) does indeed dominate the hazard at the LANL justifying our initial approach to this study.

As a result of the reviews of the draft final report issued on 11 June 1993 and review meetings held with DOE Headquarters and the Defense Nuclear Facility Safety Board (DNFSB), several additional issues were raised which required addressing.

- Whether the draft report provided sufficiently detailed documentation of the assumptions and analyses performed (e.g., the bases for values in the logic trees) such that the results could be properly reviewed by regulatory agencies.

- Whether sufficient uncertainty had been incorporated into the characterization of potential fault sources where adequate data was lacking regarding age and rates of most recent activity.

- Whether the lack of a more complete exposure of the Pajarito fault, and hence, an incomplete record of surface faulting earthquakes, provided an adequate basis for characterizing rates of activity on the Pajarito fault.

- Whether the behavioral and structural model for the Pajarito fault system was appropriate or was a more complex model required to allow independent and dependent rupture of the Pajarito, Rendija Canyon, and Guaje Mountain faults.

- Whether there was an adequate characterization of nearby regional faults such as the Embudo, Puye, and Sawyer Canyon faults.

- Whether the limited core-hole program provided sufficient data to adequately characterize the near-surface geology at the Technical Areas and hence, site response effects on ground motions.

- Whether the current approach of incorporating site response effects into the probabilistic seismic hazard analysis (using both empirical and numerical modeling techniques) was adequate to capture the variability and uncertainties in ground motions across a Technical Area.

These issues were the focus of the Phase III and IV studies. In addition, Phase III activities included evaluating topographic effects on ground motions, investigating the Embudo fault, and additional age-dating of faulting-related sediments in trenches. Phase IV activities, which focused on issues regarding ground motion evaluation such as compiling and evaluating all available geotechnical and borehole at LANL, were also performed. Details of these additional activities are described in the Scope of Work.

The specific objectives of the LANL seismic hazards evaluation were:

1) Identify active faults or other potential earthquake sources in the LANL region that may significantly contribute to the seismic hazard at the laboratory;

2) Characterize the location, geometry, orientation, maximum earthquake magnitude and earthquake recurrence of these seismic sources;

3) Assess the effects of the subsurface geology on strong ground shaking (>0.05 g) especially in the near-surface beneath each major facility site;

4) Estimate the probability of exceeding selected values of ground motion values by performing a probabilistic seismic hazard analysis which will incorporate parametric uncertainties;

5) Estimate deterministic ground motion parameters (e.g. peak acceleration, response spectra, time histories) from the most significant earthquake sources to compare with the probabilistic ground motion estimates; and

6) Develop site-specific seismic design and seismic safety criteria for LANL.

According to DOE Standard 1022-94: "as defined in NRC DG-1015, an active fault is part of capable tectonic source which is essentially characterized by the presence of surface or near surface deformation of geologic deposits of a recurring nature within the last approximately 500,000 years or at least once in the last approximately 50,000 years or/and an association with one or more large earthquakes or sustained earthquake activity which are usually accompanied by significant surface deformation." In addition, "all Quaternary faults within about 25 to 50 km of a site should be assessed to determine if they are significant contributors to the seismic hazard of the site."

The LANL region as referred to in this report is defined in Figure 1-2. The boundaries of this region were selected to include all seismic sources capable of generating strong ground shaking at the sites. This encompasses an area out to a radial distance of about 100 km from LANL.

1.2 DOE SEISMIC DESIGN CRITERIA

In recent years, the DOE through their Natural Phenomena Hazards Project has focused on addressing the potential hazards that might affect their facilities due to earthquakes, wind, tornadoes and floods. As part of this project, standards, orders and guidance documents have been revised and/or issued which requires compliance from DOE facilities. Specifically, DOE Order 5480.28 on "Natural Phenomena Hazards Mitigation" requires that all structures, systems and components at DOE facilities be designed and constructed to withstand the effects of natural hazards including earthquakes. The seismic effects include ground shaking, fault rupture and ground failure such as liquefaction and landsliding. The following DOE documents include criteria for which this study was designed and has been performed:

- DOE Standard 1020-94 Natural Phenomena Hazards Design and Evaluation Criteria for DOE Facilities (formerly UCRL-15910)

- DOE Standard 1022-94 Natural Phenomena Hazards Site Characterization Criteria

- DOE Standard 1023-94 Natural Phenomena Hazards Assessment Criteria (draft dated January 1995)

The Standards have been developed to aid in the definition of seismic design basis vibratory ground motion for DOE facilities. Appropriate methods and acceptance criteria for evaluating seismic hazards are described in these documents to insure a consistent approach across DOE sites and that state-of-the-art techniques are being used to evaluate facility design. Previously the current design criteria for LANL and all other DOE sites were specified in UCRL-15910.

According to the DOE Standards:

1) For DOE sites with Category 3 (moderate hazard) and 4 (high hazard) facilities, a state-of-the-art site-specific probabilistic evaluation of seismic hazards should be performed;

2) An accurate site-specific geologic and seismic data base should be available when computing estimates of seismic hazard. The following activities need to be considered:

   a) Characterization of Quaternary faults within 40 km (25 miles) of the site. Active Quaternary faults within 320 km (200 miles) of the site need to be identified and incorporated into the hazard analysis;

   b) Detailed characterization of all faults that occur within 8 km (5 miles) of the site and determination if they have been active in the Quaternary. This factor is particularly important in terms of assessing the potential for fault displacement;

c) Evaluation of liquefaction potential of soils supporting facilities;

d) Assessment of potential slope instability and failure, soil compaction, ground subsidence and ground collapse; and

e) Evaluation of the potential for site-specific amplification of vibratory ground motion.

3) For vibratory ground motion, a Design/Evaluation Basis Earthquake (DBE) in terms of a design response spectrum shall be defined in order to perform seismic design and seismic safety evaluations.

DOE Standard 1020-94 provides guidelines to evaluate, modify or upgrade existing DOE facilities or to design new DOE facilities for the effects of natural phenomena hazards including those from earthquakes. Previous seismic design criteria for LANL were specified in UCRL-53582 which contains the seismic hazard curves produced by Tera Corporation prior to 1984 under contract to Lawrence Livermore National Laboratory. The UCRL-53582 annual probabilities of exceedance and the peak horizontal ground surface accelerations (average soil/rock conditions) for LANL are specified below for four Performance Categories:

Usage Category	Hazard Exceedance Probability (Return Period)	Peak Horizontal Ground Surface Acceleration (g)
General Use (1)	2×10^{-3} (500 yrs)	0.18
Important or Low Hazard (2)	1×10^{-3} (1,000 yrs)	0.22
Moderate Hazard (3)	1×10^{-3} (2,000 yrs)	0.22
High Hazard (4)	2×10^{-4} (5,000 yrs)	0.38

DOE recognized that the Tera Corporation seismic hazard curves are outdated and that new site-specific curves need to be developed using state-of-the-art techniques (DOE-STD-1024-92). It should be noted that during the performance of this study, the hazard exceedance

probabilities for Performance Categories 3 and 4 were revised downward to 5×10^{-4} and 1×10^{-4}, respectively, based on the new Standard 1020-94. Thus in this study, the hazard was calculated at these new probabilities.

Specific regulations governing surface fault rupture are not explicitly addressed in the current DOE Standards. However, surface faulting is of obvious concern and it is an adverse condition recognized by DOE that must be avoided. The siting, design and construction of the waste treatment facilities including those at DOE sites, must comply with U.S. Environmental Protection Agency (EPA) regulations for seismic hazards. According to EPA 40 CFR Chapter 1 (7-1-90 Edition) Subpart B (General Facility Standards):

> "Portions of new facilities where treatment, storage or disposal of hazardous waste will be conducted must not be located within 200 feet (61 m) of a fault which has had displacement in Holocene time."

If Holocene faults (including limitations) are present within 3000 feet (914 m) of a facility, a comprehensive geologic analysis of the site is required by the EPA. Specifically,

> "Unless a site analysis is otherwise conclusive concerning the absence of faults within 200 feet (61 m) of such portions of the facility, data shall be obtained from subsurface exploration (trenching) of the area within a distance no less than 200 feet (61 m) from portions of the facility where treatment, storage, or disposal of hazardous waste will be conducted. Such trenching shall be performed in a direction that is perpendicular to known faults (which have had displacement in Holocene time) passing within 3,000 feet (914 m) of the portions of the facility where treatment, storage, or disposal of hazardous waste will be conducted. Such investigation shall document with supporting maps and other analyses, the location of faults found."

1.3 SCOPE OF WORK

To meet the objectives of this study as described in Section 1.1, the following studies were performed in Phase II. These studies were recommended based on a review of existing data and field reconnaissance in the LANL site area performed in the Phase I evaluation (Woodward-Clyde Consultants, 1991). These tasks were designed to provide an investigative

framework that encouraged flexibility and constant refocusing of the seismic hazard assessment. Phases III and IV tasks are also described below.

1.3.1 Phase II

Task 1 Acquisition and Analysis of Aerial Photography

Aerial photography was interpreted to refine existing maps of geologic units and potentially fault-related geomorphic features along the Pajarito, Rendija Canyon, and Guaje Mountain faults. Five sites for paleoseismic investigations along these faults were identified on the basis of geomorphic expression of deformation, availability of Quaternary deposits to record late-Pleistocene and Holocene fault activity, and potential for obtaining well-constrained data on fault behavior and geometry. Activities in this task included analysis of conventional black-and-white and color photography and acquisition and analysis of low-sun-angle aerial photography along the Pajarito, Embudo and La Bajada fault zones.

Task 2 Regional Quaternary Investigations

Field investigations were conducted to: (1) verify tectonic and geomorphic features identified during the aerial photography and imagery analysis; (2) identify additional potentially fault-related features or other significant landforms; (3) narrow the focus of subsequent investigations; and (4) assess the feasibility of using various geologic, geomorphic, and paleoseismic techniques to investigate the prehistoric rupture history of specific seismic sources. The objective of this task based on these investigations was to: (1) refine the regional chronostratigraphy of Quaternary surficial deposits and geomorphic surfaces; (2) prepare a regional Quaternary fault map along the Pajarito (including the Rendija Canyon and Guaje Mountain), Embudo, and La Bajada fault zones; and (3) provide additional subsurface information on the amount of deformation of the Bandelier Tuff in the Los Alamos area. These activities enabled development of a stratigraphic framework from which to assess the ages and origins of deposits that lie along the Pajarito fault and to better constrain the amount and location of post-Bandelier deformation. Activities in this task included aerial reconnaissance, regional field mapping, and analysis of existing borehole data.

Task 3 Detailed Characterization of Investigation Areas

The purpose of this task was to characterize Quaternary deposits and landforms that will yield information on the nature, amount, and timing of Quaternary deformation at selected areas of investigation. Information collected during this and previous tasks was used to select specific localities for exploratory trenches. Activities in this task included exploratory test pits and detailed field mapping of geomorphic features, such as fault scarps, fluvial terraces, alluvial fans, and deflected stream channels, at three investigation areas.

Task 4 Paleoseismic Trenching

Trenching investigations were conducted to provide detailed site-specific information on the nature, amount, and timing of late-Quaternary displacements on the Pajarito and the Rendija Canyon faults. Activities in this task included exploratory trenching at three investigation areas along the Pajarito fault zone, two areas along the Rendija Canyon fault, and one area along the Guaje Mountain fault. Design of the trenching program at each area was dependent on specific site characteristics, which were assessed during previous tasks. One to four trenches were excavated at each site, each up to about 100 m long and 5 m deep.

Task 5 Age-Estimation Studies

Estimation of ages of displaced and undisplaced surficial deposits and landforms is critical for assessing the timing of paleoseismic earthquakes. Based on numerical dating techniques (e.g., radiocarbon), correlative techniques (e.g., tephrochronology), and relative techniques (e.g., relative topographic position, relative soil development, relative scarp or surface morphology), the purpose of this task was to provide data from which to assess the age of faulted, unfaulted, and fault-related deposits, and consequently the timing and rates of deformation. Suitable dateable material were collected from the trenches.

Task 6 Characterization of Regional Tectonic Setting

The purpose of this task was to understand the role of potential seismic sources within the context of the regional geologic and tectonic framework, to aid in the development of fault segmentation models, and to assess possible interactions among regional structures. Understanding the regional tectonic setting is critical for assessing the nature and location of inherited deformational structures and for characterizing the contemporary seismotectonic setting of the site area. This task included a comprehensive review and analysis of literature and data relevant to Quaternary deformation, seismicity, and tectonic stresses in the site

region. The characterization included analysis of data concerning the nature, amount, rate and timing of fault or fold deformation along regionally significant structures. A major result of this task was a map illustrating the distribution of known and potential seismic sources and other related tectonic elements in the LANL region.

Task 7 Evaluation of Historical and Contemporary Seismicity

This task consisted of an evaluation of the historical and contemporary seismicity in the LANL region. The latter extends back to 1973 as recorded by the LANL network and adjacent networks operated by agencies such as the USGS and New Mexico Institute of Mining and Technology (NMT). The objective of such an evaluation was to characterize: (1) seismogenic sources in the Los Alamos region in terms of faulting parameters; (2) the possible association of seismicity with faults or other geologic structures; and (3) the regional tectonic stresses. The network data was reviewed for its accuracy, earthquakes were relocated using an improved velocity model and station corrections, and focal mechanisms were determined. Regional earthquake recurrence rates also were estimated.

Task 8 Seismic Source Characterization

All seismic sources in the LANL region were characterized in terms of capability, maximum magnitude, sense of slip, fault geometry, slip rate, and recurrence intervals. Such characterizations were based primarily on data developed from the previous tasks. A logic tree approach was used to capture the range of interpretations for each fault parameter. This approach also enabled explicit quantification of uncertainty for each fault parameter and the performance of sensitivity analyses to evaluate which parameters are critical in terms of the seismic hazard to LANL.

Task 9 Characterization of LANL Site Geology

Based on empirical data and observations, it is well known that near-surface geology can significantly influence, if not dominate, the level and spectral content of strong ground motions. Specifically, the Bandelier Tuff beneath the LANL may be capable of strongly affecting ground motions. The objective of this task was to characterize the subsurface geology beneath the eight technical areas at least to depths beneath the tuff. Core holes were drilled at four of these sites (TA-3, TA-16, TA-18, and TA-55) and logged for lithology and structure. Downhole shear-wave velocity and damping measurements were performed in each hole to provide the data necessary for strong ground motion estimates. Laboratory

testing for dynamic properties of undisturbed samples also were performed. The objective was to assess the range of properties with lithology and depth, particularly for soils and unconsolidated sediments.

Task 10 Deterministic Ground Motion Estimates

Site-specific deterministic ground motions estimates were made for each of the eight technical areas. The effects of being in the near-field of the earthquake source and site response were incorporated into the estimates. Both empirical and stochastic numerical modeling techniques were used to estimate ground motions. These estimates are in the form of acceleration response spectra.

Task 11 Probabilistic Seismic Hazard Analyses

In the implementation of UCRL-15910, DOE has used probabilistic seismic hazard analyses (UCRL-53582) as the basis for the seismic design of its facilities. The use of a probabilistically-based hazard analysis is especially appropriate for tectonic regions such as the northern Rio Grande rift where the recurrence intervals of faults may be on the order of several to many thousands of years. A state-of-the-art probabilistic seismic hazard analysis was thus performed that incorporated the most up-to-date information on seismic sources significant to LANL. Stochastically-determined site-specific attenuation relationships were also developed and used in the analysis. Site-specific probabilistic hazard curves were calculated for all eight sites.

Task 12 Development of Seismic Design Criteria

Seismic design criteria based on up-to-date assessments of potential strong ground motions were developed for the eight technical areas and the LANL as a whole. Based on the level of hazard for each existing facility (low, moderate, or high), design spectra were developed from probabilistic criteria. Existing facilities can then be evaluated for seismic safety based on their structural performance under loading during the estimated strong ground shaking, as characterized in previously described tasks.

Task 13 Report Preparation

An interim report and draft final report were produced and submitted to LANL and DOE for review and acceptance.

1.3.2 Phase III

Task 1 1992-1993 Meetings and Trench Extension at Water Tanks Site

During Phase II studies, two meetings with the DNFSB, one meeting with LANL management and DOE Albuquerque, and one meeting with DOE Headquarters (DP-621) were convened and attended by WCFS personnel. Also upon the recommendation of DP-621, the paleoseismic trench at the Water Tanks site along the Pajarito fault was extended upslope in an effort to expose the main fault zone.

Task 2 Peer Review and Meetings

Peer reviews of the draft final report were performed by a selected external panel of experts focusing on three specific areas: seismic geology, seismology, and ground motions. The panel consisted of Michael Machette (U.S. Geological Survey), Jim McCalpin (GEO-HAZ Consultants), Al Sanford (NMT), Mike Cline (WCFS), and Robert Youngs (Geomatrix Consultants). Three review meetings with staff of DOE Headquarters were also held. These review meetings specifically addressed: (1) seismic source characterization; (2) ground motions and site response; and (3) resolution of other outstanding issues. In addition, meetings with LANL Senior Management and with the DNFSB were also held.

Task 3 Sensitivity Analyses for Probabilistic Analysis

As a result of the review meetings in Task 2, changes to the source and ground motion parameters used in the probabilistic seismic hazard analysis were required. The sensitivities to various parameters were evaluated to assess the effects on the results of probabilistic hazard analysis.

Task 4 Evaluation of Topographic Effects on Ground Motions

At the recommendation of the DNFSB, the effects of the mesa and canyon topography beneath the LANL on ground motions were evaluated using a two-dimensional finite difference modeling approach. In addition, an analysis of earthquake recordings made at the LANL by the local seismograph network was performed to assess whether differences in the near-surface geology between the mesa tops and canyons could explain the amplification observed by House and Phillips (1989).

Task 5 Design Response Spectra and Time Histories

Upon approval of the probabilistic seismic hazard analysis results by LANL management and DOE Headquarters, site-specific seismic design parameters in the form of peak values, response spectra and/or time histories were developed.

Task 6 Age-Dating

Additional age-dating, specifically thermoluminescence (TL) dating, was recommended to provide better constraints on the age of displaced and undisplaced deposits along the Pajarito, Rendija Canyon, and Guaje Mountain faults. These data were crucial in assessing the slip rates, recurrence intervals, and the dependence or independence of these faults. Dr. Steven Forman of The Ohio State University collected samples from the paleoseismic trenches and performed the TL dating.

Task 7 Fault Location Boreholes Within Pajarito Canyon

It was recommended that possibly up to ten relatively shallow (less than 10 m) boreholes be drilled along the Pajarito Canyon Road within the canyon to the north of the trench site. The purpose of these boreholes was to constrain the locations of significant late Pleistocene displacements in the Bandelier Tuff. The placement of the boreholes within the low-gradient canyon floor allowed avoidance of the large, steep escarpment.

Task 8 Scarp Profiling and Geologic Mapping Along the Central Pajarito Fault

Detailed scarp profiling was recommended from the crest to the base of the Pajarito fault escarpment in at least two locations. The most promising sites for the profiles were the existing paleoseismic study areas at Pajarito Canyon and at Water Tanks. Monuments were already established and some tectonic information was known at these locations. These profiles were used to identify changes and inflections in the scarp slope that may be related to significant fault traces. Geologic mapping along the profiles provided information on faulting and the deposits they do and do not offset.

Task 9 Regional Fault Evaluation

Based on the preliminary probabilistic seismic hazard analysis, the Puye and Embudo faults are significant seismic sources to the LANL at annual exceedance probabilities of 10^{-3} to 10^{-4}. As with many of the regional faults in the Rio Grande rift, the paleoseismic

characteristics of the Puye and Embudo faults are unknown, with the exception that both exhibit evidence of late Quaternary displacement. Helicopter and ground reconnaissance was thus performed along the Puye and Embudo faults in an attempt to refine available source characterization data and to develop a recommended program for future detailed paleoseismic studies.

Task 10 Finalization and Issuance of the Final Report

Review comments of the draft final report were addressed and incorporated into the final report. The results of additional studies were also included in the final report.

1.3.3 Phase IV

Task 1 Review Meetings

Two additional meetings were required prior to issuance of the Final Report. A workshop organized by DOE DP-621 was held to discuss ground motion issues at western U.S. DOE sites including LANL. In particular, the role of stochastic ground motion model in estimating site-specific ground motions and site effects was reviewed and evaluated at this workshop. The second meeting was a review of (1) the field of activities being performed in the Fall 1993 along the Pajarito and Embudo faults and (2) the seismic source logic trees to be used in the probabilistic seismic hazard analysis.

Task 2 Evaluation of LANL Geotechnical Data

Site effects, in the case of LANL, the influence of the near-surface volcanic geology on ground motions, appear to be significant. However, the data collected to date appears to be inadequate to accurately characterize the physical and dynamic properties of geologic units, especially the Bandelier Tuff and Guaje Pumice. All available geotechnical data, collected principally in site exploration activities for facilities at LANL, were compiled and evaluated to aid in the characterization of the near-surface geology.

Task 3 Evaluation of NTS Data

Both surface and downhole seismic monitoring of nuclear explosions and earthquakes has been performed for several years at the Nevada Test Site (NTS), which is underlain in part by silicic volcanic rocks, including ash-flow tuffs that are similar in many respects to tuff at LANL. Much, if not all, of these data including several reports were archived at the

Sandia National Laboratories in Albuquerque. Seismic and borehole velocity data and reports to assess the effects of volcanic tuff on ground motions at NTS were collected and evaluated. This information aided in the characterization of possible similar effects at LANL.

Task 4 Review of Dynamic Laboratory Testing

Dr. Ken Stokoe of the University of Texas performed dynamic laboratory testing of six selected core samples collected in the drilling of the TA-55 borehole during Phase II. Based on those test results, site-specific shear modulus reduction and damping curves were developed by Walt Silva for several facility sites. Dr. Silva met with Dr. Stokoe to discuss the laboratory results and their uncertainties and to review the site-specific curves.

Task 5 Evaluation of Borehole Data

The variability in ground motions due to variation in site geology across a technical area is a potential issue for LANL. To examine possible ground motion variability, all available borehole data for the eight LANL sites were collected and evaluated. Sensitivity tests to the stochastic ground motion estimates to characterize the range in ground motion parameters for a given site were also performed.

Task 6 Probabilistic Seismic Hazard Recomputations

The probabilistic seismic hazard calculations were performed several times prior to issuance of the Final Report. The calculations were based on the revised logic trees and recommended changes to date including final input parameters, revised site-specific stochastic attenuation relationships at minimum magnitudes of M 4 and 5 to allow comparison of results with current NEHRP ground motion maps. (Note: the national maps currently being developed for the western U.S. will have a minimum of M 5.)

Task 7 Reevaluation of Attenuation Relationships

Both soil and rock empirical attenuation relationships were used in the preliminary probabilistic seismic hazard analysis. This approach required classification of eight technical areas into soil or rock sites. The complex volcanic geology at LANL, however, makes such a classification difficult. The site geology beneath the technical areas were compared to a database of shear-wave profiles to determine whether available rock or soil (stiff or deep)

attenuation relationships were appropriate. Site-specific stochastic relationships were recomputed based on revisions to the site-specific geologic and shear-wave profiles.

Task 8 Evaluation of Kappa

Kappa, the parameter which characterizes the near-surface attenuation beneath a site using the stochastic approach, was evaluated. Values of κ were derived from an analysis of locally recorded earthquakes where the site geology beneath the seismograph station is similar to the technical areas. Such information was vital to constraining one of the most important parameters used in the ground motion estimates.

Task 9 Vertical Design Motions

Vertical ground motion parameters are required for seismic design at LANL. Typical factors, such as 2/3 of peak horizontal acceleration, are typically used to estimate vertical motions. Such empirical factors may not be appropriate for the LANL because it is located in the near-field of three seismic sources where vertical motions could exceed the horizontal. Correction factors for the vertical/horizontal motions appropriate for LANL were estimated through an examination of the available and relevant strong motion data and stochastic modeling.

Task 10 Final Report Documentation

As a result of the September 1993, Ground Motion Peer Review Meeting, the level of detail and documentation in the Final Report was increased significantly. The level of documentation being required is similar to what is contained in a NRC licensing document, e.g., Safety Analysis Report. The Final Report was expanded to meet this requirement.

1.4 PROJECT TEAM AND REVIEW PANEL

DOE Standard 1023-94 recommends that the input into a probabilistic seismic hazard analysis be derived though either (1) the elicitation of multiple experts, or (2) peer review. The objective of both processes is to ensure that the diversity (or uncertainty) of opinion on how to model both earthquake occurrence and the propagation of seismic energy is properly incorporated into hazard analysis. In this study, the latter approach was used. A Project Team ("single analyst" as referred to in DOE Standard 1023-94) developed the probabilistic hazard analysis input which was then reviewed by an independent panel of experts.

Members of both the Project Team and the Review Panel were very well qualified, many of whom are nationally or internationally known in their fields. In the seismic source characterization, which requires the more multi-disciplinary approach, both geologists, whose expertise were in paleoseismology and structural geology and seismologists participated. Additionally, not only was expertise in the Rio Grande rift contained in the Project Team and Panel but also considerable knowledge of the Basin and Range province and the western U.S. The members of the Project Team who developed the input into the probabilistic analysis and the reviewers were as follows:

Seismic Source Characterization Participants

Keith Kelson	Paleoseismology and Structural Geology
Susan Olig	Paleoseismology and Structural Geology
Mark Hemphill-Haley	Paleoseismology
Jamie Gardner	Paleoseismology, Volcanology and Structural Geology
Steven Reneau	Paleoseismology
Ivan Wong	Seismology
Jackie Bott	Seismology
Leigh House	Seismology

Seismic Source Characterization Reviewers

Michael Machette	Paleoseismology
James McCalpin	Paleoseismology
Michael Cline	Paleoseismology
Alan Sanford	Seismology

Ground Motion Characterization Participants

Walter Silva	Seismology
Ivan Wong	Seismology
Cathy Stark	Seismology
Jacqueline Bott	Seismology
Bob Green	Earthquake Engineering
Helen Kanakari	Earthquake Engineering

Ground Motion Characterization Reviewers

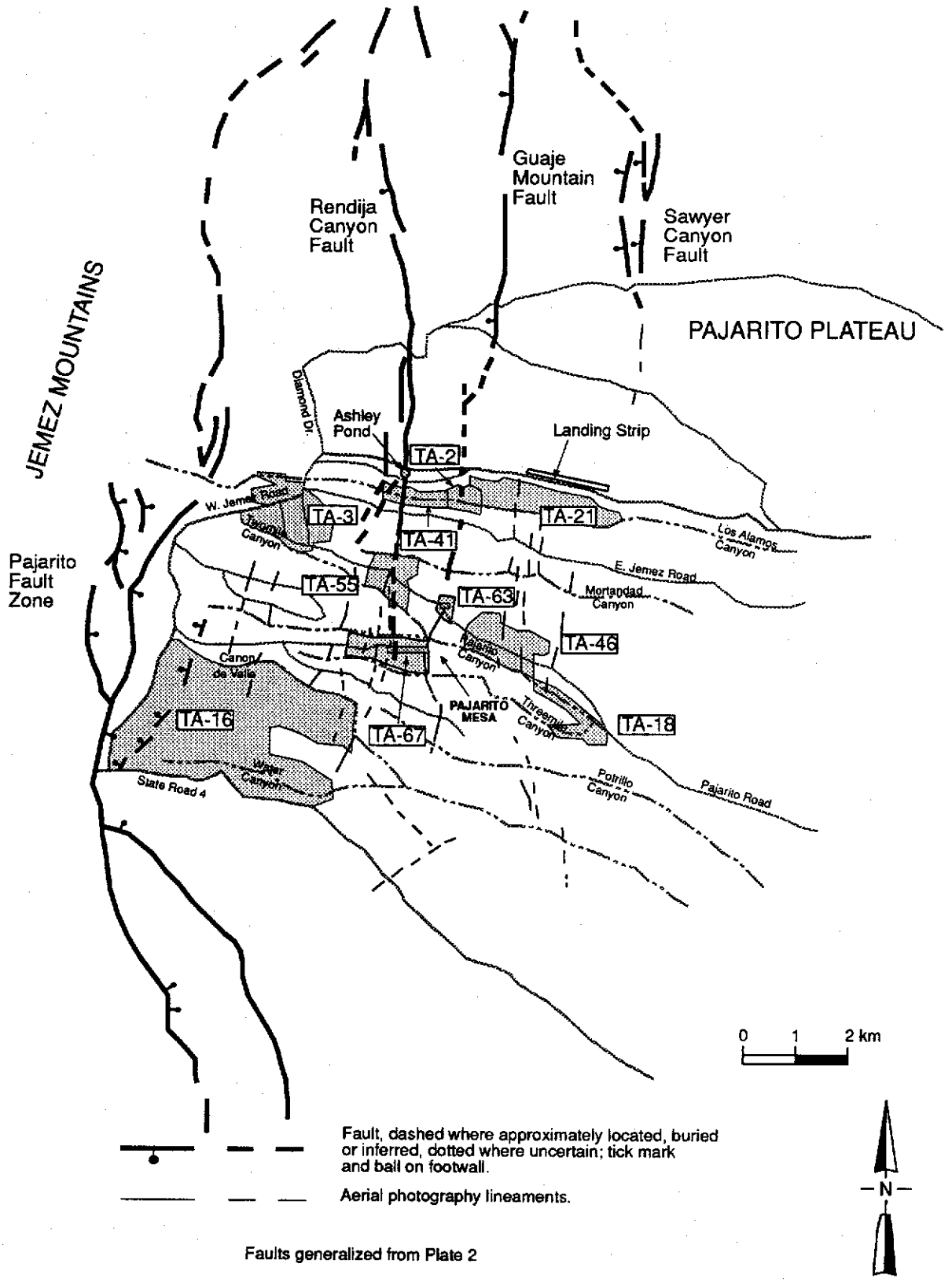
Bob Youngs	Earthquake Engineering
Jeffrey Kimball	Seismology
Carl Costantino	Earthquake Engineering

1.5 PREVIOUS STUDIES

Only two previous studies have focused on aspects of the seismic hazards at the LANL. These studies were performed by Dames and Moore (1972) for the Plutonium Facility (TA-55) and Tera Corporation (UCRL-53582). A detailed review of these studies can be found in Gardner and House (1987) and House and Cash (1988).

The Dames and Moore (1972) study was the first and most comprehensive seismic hazard evaluation of a site at the LANL. Their analysis was purely deterministic. Based solely on the 100-year historical earthquake record, Dames and Moore (1972) selected a maximum Modified Mercalli (MM) intensity of VIII as the strongest ground motions that might be expected at the TA-55 site during the design life of the Plutonium Facility. This is believed to be the highest intensity associated with a New Mexico earthquake; specifically, the 1918 Cerrillos earthquake and the three largest events in the 1906 Socorro swarm. According to Dames and Moore (1972), a MM VIII corresponds to peak horizontal accelerations ranging from 0.08 to 0.33 g. Thus, they defined the Safe Shutdown Earthquake (SEE) as having a peak value of 0.33 g and the Operating Basis Earthquake (OBE), a value of 0.17 g.

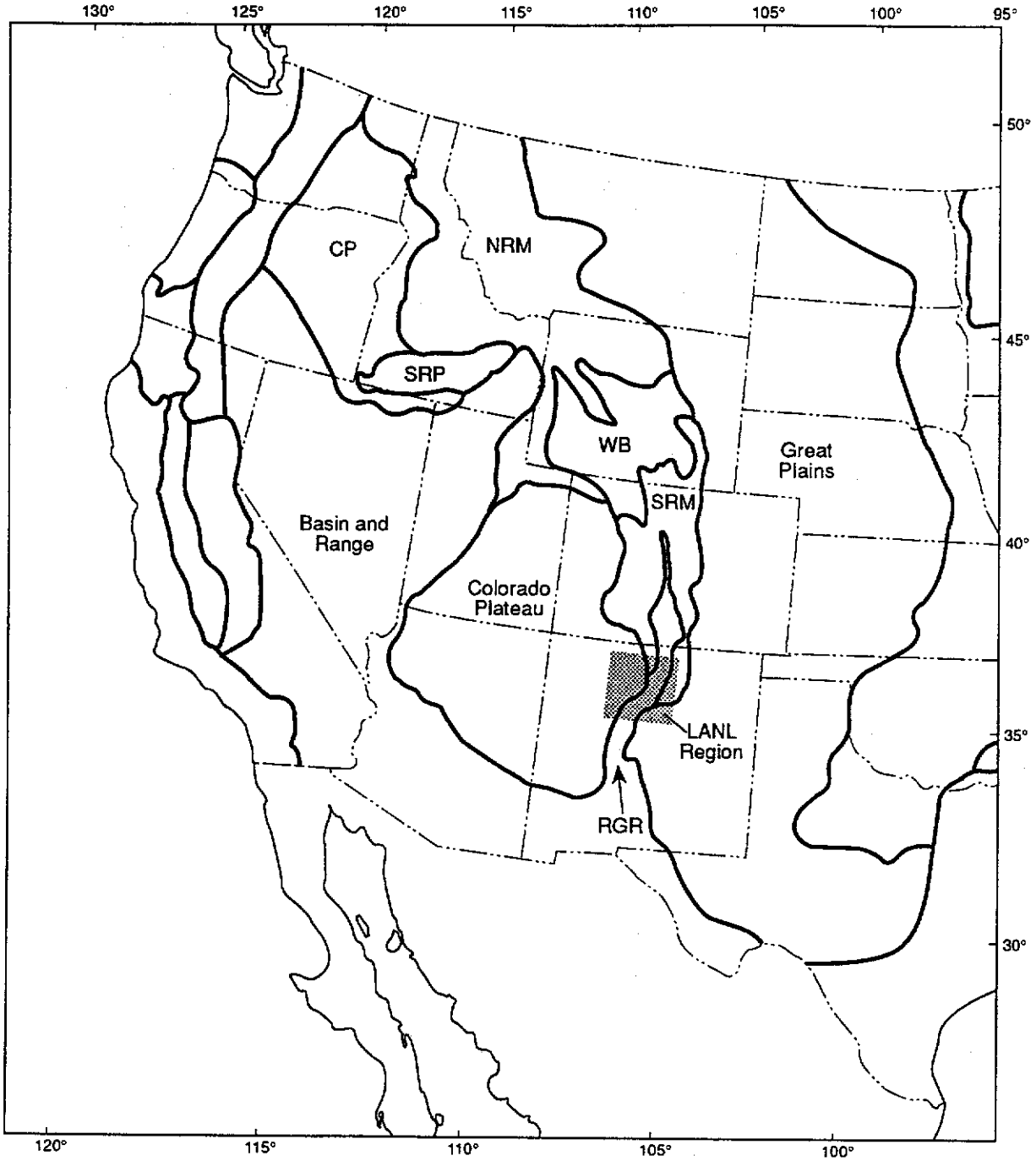
Dames and Moore (1972) also developed a spectral shape by enveloping two actual strong motion records, the 1935 M_L 6.0 Helena, Montana and 1957 M_L 5.3 Daly City, California earthquakes and three synthetic accelerograms. The strong motion records were corrected for site conditions. The spectral shape was anchored to the SSE and OBE peak horizontal accelerations to provide design spectra for TA-55.



Faults generalized from Plate 2

Project No. 91C0509	Los Alamos Seismic Hazards	MAP OF THE LANL REGION SHOWING IMPORTANT TECHNICAL AREAS AND MAJOR FAULTS	Figure 1-1
Woodward-Clyde Federal Services			

91C0509A-1300/060193



RGR Rio Grande Rift
SRM Southern Rocky Mountains
WB Wyoming Basin
NRM Northern Rocky Mountains
SRP Snake River Plain
CP Columbia Plateau

—— Physiographic Province Boundaries

Source: Zoback and Zoback (1980)

Project No. 91C0509	Los Alamos Seismic Hazards	LOCATION MAP OF PHYSIOGRAPHIC PROVINCES IN RELATION TO THE LANL REGION	Figure 1-2
Woodward-Clyde Federal Services			

91C0509A-1300/052893

2.0
GEOLOGIC AND SEISMOTECTONIC SETTING

The LANL is located along the western margin of the Española Basin in northern New Mexico, which is a major structural basin within the Rio Grande rift (Figure 2-1; Plate 1). The Rio Grande rift in north-central New Mexico and south-central Colorado is a broad physiographic and structural depression bordered by the southern Rocky Mountains, the Colorado Plateau transition zone, and the Great Plains. The rift in north-central New Mexico is composed of a series of north-trending, elongate topographic and structural basins that are collapsed parts of a broad area of Laramide structural uplift (Baltz, 1978). The elongate structural basins are arranged in a right-stepping, *en echelon* pattern (Figure 2-1), and are characterized by high heat flow, late Quaternary faulting, Quaternary volcanism, and thick basin fills (Seager and Morgan, 1978; Morgan et al., 1986). From north to south, the basins in southern Colorado and north-central New Mexico are the San Luis, Española, Santo Domingo, and Albuquerque basins (Plate 1). In general, these basins are broad half-grabens up to 80 km wide that are tilted either to the east or west and typically have a deep, narrow inner graben or half-graben. Although the basins are more or less distinct, they merge into each other at structural and physiographic constrictions and form a continuous topographic depression (Bryan, 1938; Kelley, 1952; Baltz, 1978). The present distribution of the Miocene to Pliocene rift-fill sediments of the Santa Fe Group and other time-equivalent sediments and rocks reasonably delineates the margins of the present rift basins (Baltz, 1978).

Many basins of the northern and central Rio Grande rift have resulted from the collapse of Laramide uplifts (Tweto, 1979; Cather, 1992). In general, the tectonic and stratigraphic development of the rift may be divided into three phases (Chapin and Cather, 1994). Sedimentation began in most of the rift basins in the late Oligocene to early Miocene (about 30 to 26 Ma), with moderate rates of strain (Cather et al., 1994.) Lozinsky (1994) estimates sedimentation rates of 20 to 30 m/m.y. in the Albuquerque Basin during this phase of rifting. During the middle Miocene (16 to 10 Ma), rates of extensional strain increased and sedimentation was rapid (Chapin and Cather, 1994). Lozinsky (1994) estimates sedimentation rates up to 600 m/m.y. in the Albuquerque Basin during this phase. Rapid extension began to wane in the late Miocene, and there was net aggradation in the rift during

the Pliocene (Chapin and Cather, 1994), with sedimentation rates comparable to those during the first phase of rifting (Lozinksy, 1994). Overall, strain rates and basin subsidence have been relatively modest since the late Miocene (Keller and Cather, 1994). In some rift basins, the rate of movement along major basin-controlling faults has decreased an order of magnitude since the late Pliocene (Menges, 1990a).

2.1 STRUCTURE AND SEISMOTECTONICS OF CONTINENTAL RIFT SYSTEMS

The Rio Grande rift exhibits geologic and geophysical characteristics that are similar to continental rifts throughout the world, such as the Kenya rift of the East African rift system and the Baikal rift of the Mongolian Plateau (Keller et al., 1991; Sherman, 1992). Thus, investigations of worldwide rifts provide important information on the geologic and seismotectonic setting of the Rio Grande rift. For example, both the Rio Grande rift and the Kenya rift are examples of continental rifting associated with lithospheric thinning and upwelling or diapirism of the asthenosphere (Davis, 1991; Keller et al., 1991). Both rifts are associated with regions of broad uplift and arching, with elevations of rift flanks locally as high as 4 km. Gravity, seismic refraction, magnetotelluric, and other geophysical studies show that the lithospheric mantle is anomalously thin or absent beneath the axes of the Rio Grande and Kenya rifts (Eaton, 1987; Achauer et al., 1992). The replacement of mantle lithosphere beneath the rifts with warm, buoyant asthenospheric mantle probably accounts for the regional elevated topography, high heat flow, low gravity and late Cenozoic magmatism (Eaton, 1987; Keller et al., 1991). The Baikal rift of the Mongolian Plateau exhibits many of the same geological and geophysical characteristics, and also is thought to overlie an asthenospheric diapir or zone of mantle upwelling (Logatchev and Zorin, 1992; Windley and Allen, 1993). Crustal extension in these rift zones may be a consequence of forcible intrusion of the asthenosphere into the lithosphere (Davis, 1991), or may be a more passive response to the regional domal uplift and arching (Eaton, 1987).

Continental rift systems share many common structural elements such as normal faults, half grabens, and transverse structures known as accommodation zones. Rosendahl (1987) proposed a hierarchy for the tectonic "architecture" of rift systems. At the broadest scale, regions of continental rifting consist of systems of bifurcating rift "branches". This scale of rifting is observed in the East African rift system. Individual branches of the rift system

may be characterized by differences in orientation, magnitude of extension, or volume of magmatism. Rift system branches are, in turn, subdivided into "rift zones". Individual rift zones generally have lengths of 500 to 700 km and are terminated along strike by offsets, kinks, complex zones of faulting, or major changes in orientation. Using Rosendahl's hierarchy (1987), the 1000-km-long Rio Grande rift probably represents a "rift zone".

Rift zones, in turn, consist of discrete structural basins with typical lengths of 80 to 160 km, and length-to-width ratios of approximately two to four (Rosendahl, 1987). Examples of such basins in the Rio Grande rift zone include the San Luis, Albuquerque, and Española basins. Basins may consist of a series of smaller asymmetric half-grabens that are bounded or linked by high-angle strike-slip or oblique-slip faults termed accommodation zones. The trends of accommodation zones generally are oblique to the regional strike of the rift zone, and the sense of half-graben asymmetry commonly changes across the accommodation zones. Rosendahl (1987) proposed that the geometry and kinematics of accommodation zones depend on the manner in which asymmetric half-grabens overlap with each other.

Detailed studies of asymmetric basins in the Kenya rift (Rosendahl, 1987) show that the steep sides of the grabens typically are bounded by moderately to gently-dipping normal faults. Seismic reflection profiles show that many of the basin-bounding faults have listric geometry (i.e., they flatten downward). Similar fault geometries have been reported for the Albuquerque Basin in the Rio Grande rift. For example, Gridley and Keller (1990) interpreted seismic reflection profiles to infer that basin-bounding listric normal faults may flatten at depths of approximately 10 km beneath the Albuquerque Basin. Seismic reflection data from the Kenya rift show that numerous sympathetic normal faults are commonly present in the hanging wall of the major basin-bounding faults (Rosendahl, 1987). Progressive slip on the normal fault systems results in domino-style tilting of fault blocks and asymmetric subsidence adjacent to the major basin-bounding fault. Clear evidence for synsedimentary subsidence in the basins can be seen in the progressive tilting or synformal "rollover" of older strata in the direction of a major basin-bounding fault (Rosendahl, 1987).

The locations of rift-related faults may be influenced by pre-existing structural trends. Tweto (1979) noted that many faults of the Rio Grande rift in Colorado are reactivated faults of Laramide (late Cretaceous-early Tertiary), late Paleozoic and Precambrian origin. To the south, the north-northeast trend of the Rio Grande rift in New Mexico does not appear to

parallel the strike of Precambrian structures, but northwest-striking faults within the rift may be, in part, reactivated Paleozoic faults (Tweto, 1979). Similar relationships have been observed in other rift systems. The Baikal rift developed along trends of pre-Cenozoic basement faults, and extension in the rift is locally accommodated by reactivation of pre-existing faults (Sherman, 1992). Rosendahl (1987) noted that a strong correlation exists between the location of pre-existing structures and the trend of rift branches and individual tilt-blocks in the East African Rift system.

A comparative study of seismicity in the Baikal, East Africa and western U.S. rift systems (Doser and Yarwood, 1991) reveals that earthquakes in these regions occur almost exclusively in the upper crust above 10 to 12 km. The relatively shallow base of seismicity probably is related to the high heat flow observed in these rifts. Despite geologic and geophysical evidence for listric normal faulting, most earthquakes with dip-slip focal mechanisms occur on faults with dips of 25° or greater. Analysis of focal mechanisms from the Baikal, East Africa and Rio Grande rifts shows that rakes are distributed nearly evenly between dip-slip, oblique-slip and strike-slip events (Doser and Yarwood, 1991). A detailed study of seismicity in the Baikal rift (Sherman, 1992) showed that mixed strike-slip, dip-slip and oblique-slip faulting occurs on basin-bounding faults, and on transverse faults that are probably accommodation zones. In general, earthquakes are not limited to or necessarily concentrated on, faults oriented perpendicular to the inferred regional extension direction. Doser and Yarwood (1991) concluded that the variable slip directions may indicate that pre-existing faults or other zones of crustal weakness may be preferentially activated, and that strike-slip faulting within rift systems does not necessarily imply a "youthful" stage of rifting prior to development of laterally-extensive, basin-bounding normal fault systems.

Sanford et al. (1991) summarized the results of several detailed studies of seismicity in the New Mexico portion of the Rio Grande rift zone. In general, seismicity is diffuse throughout this portion of the Rio Grande rift and only locally associated with discrete structural or tectonic features. Detailed studies of the Albuquerque and Socorro areas show that seismicity is limited to the upper 12 to 13 km of the crust (Sanford et al., 1991), consistent with observations from other rift systems that seismicity typically is concentrated in the upper crust (Doser and Yarwood, 1991). Focal mechanisms from the Albuquerque and Socorro areas show both strike-slip and dip-slip motions. These data also suggest that the direction of extensional stress may vary within the rift. Based on the orientation of

T-axes from focal mechanisms, the orientation of the minimum principal stress is interpreted to be approximately WNW-ESE near Albuquerque, and approximately NE-SW near Socorro. Sanford et al. (1991) noted that local areas of high seismicity in the Albuquerque area may be correlated with magmatic activity rather than tectonism. Similarly, active crustal deformation in the Socorro area determined by geodetic studies appears to be centered over an inferred magmatic intrusion. Several focal mechanisms obtained from this region had large non-double-couple components, possibly indicating that the seismicity is related to magmatism. Notably, Sanford et al. (1991) conclude that modern patterns of seismicity in Rio Grande rift may not necessarily be representative of long-term activity.

Although active continental rifts occur throughout the world, the record of moderate to large magnitude earthquakes in rifts is relatively sparse. Most historical large magnitude earthquakes within rift zones occurred prior to the establishment of the Worldwide Standardized Seismographic Network in 1962 (Doser and Yarwood, 1991). The 1928 Sabukia earthquake (M_w 7.0) in the Kenya rift is the largest historic earthquake recorded in eastern Africa, and the only large earthquake that has occurred in the well-developed graben of the central portion of the rift during this century. The Sabukia earthquake thus may be the best-studied analogue to date for large magnitude earthquakes in continental rifts. Based on waveform modeling, Doser and Yarwood (1991) showed that the mainshock consisted of two events separated by approximately 10 seconds and that rupture occurred at 10 km depth or less. The earthquake produced 18 to 20 km of surface rupture along a pre-existing escarpment, with a maximum of approximately 3.3 m of normal dip-slip displacement and local reverse displacement. However, variations in scarp height and morphology along strike suggest that there may have been a substantial component of lateral slip. Doser and Yarwood (1991) also concluded from waveform modeling that the Sabukia mainshock primarily was a strike-slip event. They noted that the Sabukia event may have been similar to the 1954 M_w 6.8 Rainbow Mountain, Nevada earthquake in the northern Basin and Range province, where coseismic strike-slip motion at depth was accompanied by significant dip-slip faulting at the surface.

To summarize, regions of continental rifting such as the Rio Grande, Kenya, and Baikal rifts appear to reflect thinning of the crust and mantle lithosphere above zones of upwelling asthenospheric mantle. Rift systems commonly exhibit a hierarchy of scale, with rift zones such as the Rio Grande, Kenya, and Baikal rifts consisting of smaller, asymmetric structural

basins bordered by moderately to gently-dipping normal faults. These asymmetric structural basins commonly are linked by transverse accommodation zones that transfer strain between major basin-border faults on opposite sides of the rift. In addition, pre-existing structures may influence the location and orientation of rift basins and associated border fault systems. Seismicity in rift zones generally is limited to the upper 10 to 12 km of the crust. Analysis of focal mechanisms from several rifts indicate that a large proportion of earthquakes occur on strike-slip and oblique-slip faults. The 1928 Sabukia earthquake in the Kenya rift was primarily a strike-slip event at seismogenic depths that produced an approximately 18- to 20-km-long surface rupture. These characteristics provide information pertinent to the assessment of the geologic and seismotectonic setting, and potential seismic hazards of the LANL region.

2.2 SEISMOTECTONIC PROVINCES IN THE LANL REGION

The LANL region includes several seismotectonic provinces that are differentiated on the basis of geologic and geophysical characteristics and historical and contemporary seismicity (Plates 1 and 3). The LANL is located at the western margin of the Rio Grande rift province, where it abuts the Valles Volcanic province to the west. These provinces are bordered on the west by the Colorado Plateau transition zone. To the north and east of the LANL, two prongs of the Southern Rocky Mountains province extend southward into the region from Colorado and border both sides of the Rio Grande rift province (Plate 1). Lastly, the southeastern corner of the LANL region includes part of the Great Plains province. As described briefly below, each of these provinces has fairly distinct geologic, geophysical, and seismologic properties. The seismicity and seismogenic potential of these provinces are discussed in Section 7.2.

2.2.1 The Rio Grande Rift Province

The Rio Grande rift province is characterized by regional elevated topography, high heat flow, low gravity, and late Cenozoic magmatism and fault displacement (Eaton, 1987; Keller et al., 1991). The rift consists of several north-trending, elongate topographic and structural basins that are arranged in a right-stepping, en echelon pattern (Figure 2-1). These basins are collapsed parts of a broad area of Laramide structural uplift (Baltz, 1978). In general, these basins are broad asymmetric half-grabens up to 65 km wide and 240 km long. The

grabens are tilted either to the east or west and typically have deep, narrow inner grabens or half-grabens. The inner half-grabens contain up to 10 km of late Cenozoic volcanic deposits and rift-fill sediments derived from the flanks of basin-border uplifts. The top of Precambrian basement is substantially deeper in the rift than in the adjacent parts of the Colorado Plateau transition zone and Great Plains provinces (Baltz, 1978). The half-grabens are typically bordered on one side by down-to-the-east or down-to-the-west faults, such as the Pajarito and Sangre de Cristo faults, that exhibit evidence of late Pleistocene to Holocene displacement. Heat flow in the rift is typically high (Eaton, 1987; Keller et al., 1991), with values locally more than 180 mW/m^2.

The Rio Grande rift province is characterized by low to moderate levels of historic seismicity (Sanford et al., 1979). The central portion from Belen to Socorro has been the focus of the most intense historic seismic activity including the 1906-1907 swarm (Section 3.2.1), which included three moderate-sized earthquakes (MM VII-VIII). Since 1962, instrumental studies have revealed a continued low to moderate level of contemporary background seismicity within the Rio Grande rift, but intensity of activity appears to vary both spatially and temporally. Areas of concentrated microseismicity, especially from Belen to Socorro and also northwest of Española, may be associated with magma bodies and magma movement (Sanford et al., 1979). Focal mechanisms indicate predominantly normal faulting with some strike-slip faulting and the average T-axis is oriented east-west (Sanford et al. 1979).

2.2.2 The Valles Volcanic Province

The Valles Volcanic province is bordered by the Rio Grande rift province on the east and by the Colorado Plateau transition zone on the west (Plate 1). The province is a late Cenozoic volcanic edifice that coincides with the intersection of the Rio Grande rift and the Jemez lineament, a northeast-trending crustal flaw and alignment of Miocene to Quaternary volcanic centers between southeastern Colorado and central Arizona (Aldrich, 1986; Goff et al., 1989). The volcanic edifice is the product of more than 13 Ma of volcanic activity (Gardner et al., 1986) that culminated in the formation of the Valles caldera, which is the "type" example of an intercontinental resurgent caldera (Smith and Bailey, 1968; Self et al., 1988). The volcanism is intimately related to tectonic activity associated with the rift and the Jemez lineament (Goff et al., 1989). The province is characterized by very high heat flow, with values of generally more than 180 mW/m^2 (Reiter et al., 1979), and a low

Bouguer gravity anomaly (Keller et al., 1984). Because of the high heat flow, there have been several exploratory investigations of the hydrothermal characteristics of the crust beneath the Valles caldera (Goff et al., 1989). The Valles Volcanic province is absent of significant microearthquake activity, a contrast to intense activity observed in other parts of the rift where magma bodies are thought to exist (Sanford et al., 1979). The lack of seismicity is probably related to the elevated temperatures and high heat flow at shallow crustal depths (Sanford et al., 1979).

2.2.3 The Colorado Plateau Transition Zone

The Colorado Plateau transition zone encompasses the western part of the LANL region and represents the southeastern portion of a relatively coherent uplifted crustal block bordered on the east by the Valles Volcanic and Rio Grande rift provinces (Plate 1). Geologically and geophysically, however, the transition zone possesses characteristics that are transitional between the Colorado Plateau and the Rio Grande rift. Physiographically, the Colorado Plateau is an elevated region related to epeirogenic uplift during the late Cenozoic. Precambrian bedrock beneath the Colorado Plateau is structurally higher than in the adjacent parts of the rift (Baltz, 1978), and overlying Mesozoic and early Tertiary rocks are relatively undeformed. In general, the plateau has low heat flow, with values generally less than 80 mW/m^2, relative to the Rio Grande rift and Valles Volcanic provinces to the east that have high heat flow (Reiter et al., 1979). The Colorado Plateau in general is characterized by northeast to southwest extensional crustal stresses, normal faulting, and low to moderate levels of seismicity (Wong and Humphrey, 1989). Within the LANL region, no evidence of Quaternary activity has been recognized along any of the faults in the Colorado Plateau transition zone province.

The diffuse seismicity characteristic of the Colorado Plateau transition zone (mostly microseismicity) is relatively high compared with the Colorado Plateau. The transition zone has historical seismicity comparable to the Rio Grande rift, but the rift has experienced more larger earthquakes. Focal mechanisms from within the Colorado Plateau transition zone, southwest of the Valles Caldera, indicate a predominance of strike-slip faulting with some normal faulting (Section 5.2). This contrasts with the predominant normal faulting observed within the Rio Grande rift. T-axes of focal mechanisms of the Colorado Plateau transition zone also indicate an average east-west extension, similar to the Rio Grande rift, but the

P-axes are oriented approximately north-south. The transition zone appears to be a locus of contemporary deformation, similar to that observed at the boundary between the Basin and Range province and Colorado Plateau in the southern Intermountain Seismic Belt in Utah.

2.2.4 The Southern Rocky Mountains Province

The Southern Rocky Mountains province in the LANL region consists of two prongs that extend southward from Colorado and border both sides of the Rio Grande rift province (Plate 1). The western prong is coincident with the Brazos uplift of northern New Mexico and southern Colorado, and is bordered on the west by the Colorado Plateau transition zone. The eastern prong coincides with the Taos and Santa Fe Ranges of the Sangre de Cristo Mountains. These ranges are elevated, in part, as a result of Laramide uplift, although the Sangre de Cristo Mountains have been elevated during the late Cenozoic (Kelley and Duncan, 1984). Both the eastern and western prongs of the province are composed of Precambrian crystalline rocks overlain by younger volcanic and sedimentary rocks. Precambrian rocks in the core of the Brazos uplift reach elevations of more than 3200 m (Wobus, 1984), whereas Precambrian rocks in the Sangre de Cristo Mountains are over 4000 m high (Kelley and Duncan, 1984). Although there is no evidence of Quaternary displacement along faults within the Brazos uplift, a few high-angle, northwest-striking faults displace Pliocene rift-fill deposits (Manley et al., 1987). The western margin of the Sangre de Cristo Mountains, in contrast, contains abundant evidence of late Pleistocene and possibly Holocene activity (Machette and Personius, 1984; Menges, 1988, 1990a,b). The southern extent of the Sangre de Cristo Mountains, and therefore of the Southern Rocky Mountains, is located at Glorieta Pass east of Santa Fe, where Precambrian rocks are buried by Tertiary and older sedimentary rocks (Figure 2-1). In contrast to the western flank of the Rio Grande rift, the Southern Rocky Mountains are characterized by low levels of diffuse seismicity with no apparent transition zone with the rift.

2.2.5 The Great Plains Province

The Great Plains province encompasses the southeastern part of the LANL region and is bordered on the west by the Rio Grande rift province and on the north by the Southern Rocky Mountains province (Plate 1). In general, this province has low heat flow, with values generally less than 80 mW/m^2, relative to the Rio Grande rift and Southern Rocky

Mountains provinces to the west that generally have heat flow values higher than 80 mW/m^2 (Reiter et al., 1979). Similar to the Colorado Plateau transition zone to the west of the Rio Grande rift, Precambrian bedrock beneath the Great Plains is higher than in the adjacent parts of the rift (Baltz, 1978), and overlying Mesozoic rocks are relatively undeformed. Within the Great Plains province, there is no recognized evidence of Quaternary activity along any of the faults in the LANL region. The Great Plains within New Mexico are noted as having nearly comparable levels of seismicity to the Rio Grande rift since 1962 (Sanford et al., 1991). Within the LANL region, the Great Plains Province has a low level of seismicity. However, the boundary between the Great Plains and the Rio Grande rift appears to exhibit slightly elevated levels of seismicity in comparison (Plate 3). This may be due in part, to the poor locations, especially for pre-instrumental earthquakes, or it may reflect a diffuse boundary or transition zone.

2.3 PRINCIPAL COMPONENTS OF THE RIO GRANDE RIFT IN THE LANL REGION

The Rio Grande rift in north-central New Mexico consists of several north-trending asymmetric structural basins (Plate 1). The LANL region includes the three largest structural basins in the northern and central Rio Grande rift (the San Luis, Española, and Albuquerque basins) as well as the Santo Domingo basin between the Española and Albuquerque Basins. As noted above, these rift basins are half graben that are tectonically inverted Laramide upthrust blocks (Keller and Cather, 1994). The polarity (sense of regional stratigraphic dip) changes between these major basins, with differential movement taken up by accommodation zones that traverse the rift at high angles. Importantly, the amount of extension within each major basin increases southward, with about 8 to 12 % extension in the San Luis Basin, at least 17% in the northern Albuquerque Basin, and a minimum of 28% in the southern Albuquerque Basin (Keller and Cather, 1994; Kluth and Schaftenaar, 1994; Russell and Snelson, 1994). This north-south variation in extension can be explained by 1 to 1.5 degrees of counter clockwise rotation of the Colorado Plateau about a Euler pole in northeastern Utah (Chapin and Cather, 1994), with greater extension in the southern and central rift basins because of greater distances from the Euler pole. As summarized below, there are several similarities and differences among the basins in the northern and central Rio Grande rift.

2.3.1 The San Luis Basin

The San Luis Basin is a 240-km-long, elongate structural basin that extends from Poncha Pass in south-central Colorado to near the town of Taos in north-central New Mexico (Keller et al., 1984). The San Luis Basin is flanked by the San Juan and Tusas Mountains on the west and by the Sangre de Cristo Mountains on the east, and the Española Basin borders it to the south. Precambrian basement rocks beneath the basin are overlain by pre-rift Oligocene volcanic rocks (Steven, 1975) and Miocene to Recent rift-fill sedimentary and volcanic deposits. Seismic reflection and gravity data show that the depth to the base of the rift-fill sediments is greatest (about 6 km) along the eastern margin of the basin near Alamosa, Colorado (Kluth and Schaftenaer, 1994; Brister and Gries, 1994). The Sangre de Cristo fault exhibits prominent geologic and geomorphic evidence of late Pleistocene and possibly Holocene displacement (Machette and Personius, 1984; Menges, 1988, 1990a,b). The San Luis Basin is an east-tilted, asymmetric half-graben, with several kilometers of down-to-the-west displacement on the Sangre de Cristo fault along its eastern margin and a gentle homocline along its western margin (Chapin and Cather, 1994). Compared with other major half grabens in the Rio Grande rift, the San Luis Basin is structurally uncomplicated, with few or no major faults within the basin (Chapin and Cather, 1994; Kluth and Schaftenaer, 1994). Syn-rift sediments within the basin dip up to 12 degrees eastward. Kluth and Schaftenaar (1994) estimate that there has been about 8 to 12% extension across the basin, based on seismic reflection data. The southern margin of the San Luis basin coincides with the Embudo fault, which is an accommodation zone that transfers strain between the east-tilted San Luis Basin and the west-tilted Española Basin to the south (Figure 2-1; Plate 1). The Embudo fault shows evidence of late Pleistocene displacement near its intersection with the Sangre de Cristo fault (Muehlberger, 1979; Machette and Personius, 1984), but has poor geomorphic expression and lateral continuity to the southwest where it traverses the rift and separates the southernmost San Luis Basin and the northernmost Española Basin (Plate 1).

2.3.2 The Española Basin

The Española Basin is a 90-km-long, approximately 40-km-wide structural basin that extends from the southern San Luis Basin on the north to the northern Albuquerque and Santo Domingo basins on the south (Figure 2-1; Plate 1). The nearly 4000-m-high Sangre de

Cristo uplift borders the eastern side of the basin, and the 3400-m-high Jemez volcanic edifice borders the western side of the basin. Similar to the San Luis and Albuquerque basins, the Española Basin is an asymmetric structural depression that contains a deep, narrow graben along one margin. In contrast, however, the Española Basin is tilted to the west, having the greatest amount of late Cenozoic displacement and thickest section of rift-fill sediments (about 3 km) along its western margin near Española and Los Alamos (Manley, 1979a; Cather, 1992). The Española Basin is unusual compared to other basins in the northern and central Rio Grande rift in that it is structurally and topographically higher on its hinged side, rather than on the side associated with the master basin-controlling fault. This likely is related to structural and topographic relief inherited from Laramide uplift (Chapin and Cather, 1994). The down-to-the-east Pajarito fault system forms the western margin of the basin (Plate 1), along which possibly more than 1.5 km of late Cenozoic displacement has occurred (Gardner and Goff, 1984). As noted by several previous workers and documented during this investigation, faults within the Pajarito fault system display geologic and geomorphic evidence of late Pleistocene and, in some cases, Holocene displacement (Section 4).

The eastern margin of the Española Basin is poorly defined, similar to the western margin of the San Luis Basin and likely is not delineated by a well-defined, continuous fault, (Baltz, 1978). Manley (1979a) notes that the eastern margin of the Española Basin appears to lack a throughgoing border fault, and Baltz (1976) notes that there is little or no evidence of significant down-to-the-west fault displacement. Syn-rift sediments in the eastern part of the basin dip about 6 to 8 degrees westward, and thicken to the west from an eroded homoclinal edge of the basin (Chapin and Cather, 1994). Discontinuous faults in the central and eastern parts of the basin exhibit down-to-the-east displacement and are probably related to middle or late Pliocene tilting to the west (Baltz, 1976). Most likely, there is no discrete eastern boundary of the Española Basin, and relatively minor structures such as the Nambe and Pojoaque faults (Vernon and Riecker, 1989; Plate 1) accommodate minor distributed strain related to westward tilting of the basin.

Several workers have postulated that the Española Basin is characterized by counterclockwise rotation (Muehlberger, 1979; Brown and Golombek, 1986; Aldrich, 1986). This model is based, in part, on observations of reverse displacement at the acute ends of a diamond-shaped block bordered by the Embudo fault on the northeast, the Pajarito and La

Bajada faults on the west, the Tijeras fault zone on the southeast, and the Pecos-Picuris fault on the east (Figure 2-1; Plate 1). However, recent paleomagnetic data collected at several sites within the Española Basin suggest that rigid block rotation is not applicable to Neogene deformation in the northern Rio Grande rift (Salyards et al., 1994). These workers show that there is considerable variability in vertical-axis rotations within the basin, which can be explained by dip slip on the Pajarito fault system and intra-rift faults, and by strike-slip on the Embudo accommodation zone (Salyards et al., 1994). An alternative model to the Española Basin block rotation model is one in which the Embudo fault is an accommodation zone between the San Luis and Española basins, and the Santo Domingo Basin is an accommodation zone between the Española and Albuquerque basins. This model is more consistent with geologic evidence that the Española Basin is primarily a west-tilted basin that lacks a discrete eastern boundary. Slight changes in the orientations of fault planes, local block rotations, and local interactions among faults and between faults and range blocks may explain evidence of local reverse displacements, such as that on the northernmost Embudo fault (Muehlberger, 1979). In addition, field evidence collected during this investigation suggests that the Embudo fault near Taos may be a high-angle strike-slip structure rather than a reverse fault (Section 4.1.3.1).

2.3.3 The Santo Domingo Basin

The 50-km-long Santo Domingo Basin is located between the southwestern part of the Española Basin and the northeastern part of the Albuquerque Basin (Plate 1). The basin may be a northeastern sub-basin of the Albuquerque Basin, because it also is an east-tilted half-graben bordered on the east by a relatively large-displacement fault and on the west by a distributed zone of faulting and flexuring. The down-to-the-west La Bajada fault borders the eastern margin of the basin (Stearns, 1953; Kelley, 1978). The San Felipe fault zone, which is up to 8-km-wide and consists of several down-to-the-east and down-to-the-west faults (Smith et al., 1970), may be associated with a broad, anticlinal bend or hinge along the western margin of the basin (Baltz, 1978). This pattern is similar to evidence of distributed strain in the eastern part of the Española Basin and in the western parts of the Albuquerque Basin. Intersections between the La Bajada and Pajarito faults at the northern end of the basin and between the San Felipe and Sandia fault zones at the southern end of the basin (Plate 1) suggest that the Santo Domingo Basin itself may be an accommodation zone between the Española Basin and the northern Albuquerque Basin. The basin contains

several features that are characteristic of accommodation zones, such as interfingering fault traces of opposite senses of displacement, the presence of a major through-going fluvial system in the central part of the zone, and its location between two structural basins with opposite senses of tilt (Morley et al., 1990; Bosworth, 1985; Rosendahl, 1987). No evidence of late Pleistocene or Holocene displacement has been documented along the La Bajada or San Francisco faults, although aerial reconnaissance and analysis of aerial photography conducted during this investigation suggests that there are several potentially fault-related lineaments, including west- or southwest-facing topographic scarps, along both of these faults. In addition, the intersections of these faults with the Pajarito fault system and the Rio Grande-Sandia fault provide supporting evidence that these faults may have had late Quaternary displacement. Overall, the Albuquerque Basin is considerably more complex than rift basins to the north. The basin is a single topographic feature, but consists of two major structural basins. Both the northern and southern Albuquerque sub-basins contain deep inner half-grabens flanked by shallow structural benches (Lozinsky, 1994).

2.3.4 The Albuquerque Basin

The 150-km-long Albuquerque Basin is one of the largest and deepest basins of the Rio Grande rift (Figure 2-1). The basin extends from the San Felipe fault zone on the north to the Joyita uplift near Socorro on the south, and from the Sandia-Manzano-Los Pinos uplift on the east to the Ladron-Lucero uplift and the Colorado Plateau on the west (Lozinsky et al., 1991). The northern Albuquerque sub-basin is a half-graben tilted to the east, with about 4,400 m of syn-rift sediments in the deepest part of the sub-basin (Lozinsky, 1994). Structural relief between this sub-basin and the adjacent Sandia Mountains to the east is over 10,000 m. The Sandia fault forms the eastern border of the basin, but the majority of the stratigraphic throw is present across the Rio Grande fault located about 5 km basin-ward of the base of the Sandia Mountains. The western margin of the northern Albuquerque Basin is marked by the topographically subdued Puerco fault (Slack and Campbell, 1976; Lozinsky, 1994), to the west of which lies a gently east-dipping monoclinal ramp of the Colorado Plateau transition zone (Plate 1). The San Ysidro fault may also form the western margin of the northern sub-basin (Figure 2-1). The western part of the northern Albuquerque Basin is characterized by distributed faulting within the West Mesa fault zone, which consists of a series of down-to-the-east faults (Bryan and McCann, 1937, 1938; Kelley, 1977; Hawley and Galusha, 1978; Lambert, 1978; Machette, 1978a, b; Lozinsky, 1988; Hawley and

Haase, 1992). Evidence of late Quaternary activity is present along the County Dump fault, which is herein included in the West Mesa fault zone (Machette, 1978a). It is possible that evidence for late Quaternary activity along the Rio Grande fault may not be preserved because of its location in the recent floodplain of the Rio Grande.

The northern Albuquerque sub-basin is separated from the west-tilted southern Albuquerque sub-basin by the northeast-trending Tijeras accommodation zone (Lozinsky et. al., 1991; Lozinsky, 1994; Russell and Snelson, 1990, 1994). This poorly defined zone of distributed strain lies along the southwestern projection of the Tijeras fault (Lozinsky, 1994; Plate 1). It accommodates differential movement between the northern and southern sub-basins, and is interpreted as a lateral-slip negative flower structure (Russell and Snelson, 1990, 1994). As with the Embudo accommodation zone between the San Luis and Española basins, the Tijeras accommodation zone has poor geomorphic expression and is inferred primarily on the need to explain differential basin polarities.

The southern Albuquerque sub-basin is more complex than the northern sub-basin and lies outside of the LANL region. It is a west-tilted half graben that is controlled along its western margin by a system of major east-dipping, ramp-like and largely planar normal faults that may extend to deep crustal levels (Russell and Snelson, 1994). The eastern margin includes the Manzano fault along the base of the Manzano Mountains, and the late Quaternary Hubbell Springs fault located several kilometers basin-ward of the range front.

2.4 GEOLOGY AND FAULTS OF THE PAJARITO PLATEAU

The LANL is located in the western most part of the Española structural basin upon the eastern flank of the Jemez Mountains volcanic field (Figure 2-1; Plate 1). The volcanic field is coincident with the intersection of the Rio Grande rift and an alignment of late Cenozoic volcanic centers between central Arizona and southeastern Colorado and referred to as the Jemez lineament (Aldrich, 1986; Goff et al., 1989). The Pajarito Plateau, which is a gently sloping, highly dissected surface that extends from the Pajarito fault eastward to the Rio Grande, is underlain by the 1.6 to 1.2 Ma Bandelier Tuff (Spell et al., 1990; Izett and Obradovich, 1994). The plateau consists of numerous narrow, finger-like mesas, upon which LANL and the town of Los Alamos are located. These mesas are separated by steep-walled canyons formed by incision along many east-flowing tributaries of the Rio

Grande. Along the eastern margin of the plateau, the Rio Grande flows in a 300-m-deep gorge incised into rift-fill sediments and volcanic rocks. Along the western margin of the plateau, the north-striking Pajarito fault forms a 100- to 120-m-high, east-facing escarpment developed in the Bandelier Tuff (Figure 2-2). In contrast, the north-striking Rendija Canyon and Guaje Mountain faults exhibit smaller, but still prominent, west-facing escarpments in the northern part of the plateau. The following sections provide a brief overview of the subsurface geology and structural features of the Pajarito Plateau.

2.4.1 Bedrock Geology of the Pajarito Plateau

Based on exposures within the uplifted flanks of the rift to the north and east, basement rocks beneath the Pajarito Plateau probably are composed of Proterozoic crystalline rocks overlain by Paleozoic and Mesozoic mudstone, sandstone, conglomerate, and carbonate rocks (Ingersoll et al., 1990). Lowermost Cenozoic volcanic and nonmarine sedimentary deposits that pre-date initiation of the rift also are present beneath the Pajarito Plateau. Initiation of rifting in the late Oligocene to early Miocene resulted in deposition of a complex sequence of intercalated volcanic, volcaniclastic, and sedimentary deposits in the area now occupied by the Pajarito Plateau and the Española Basin. The western margin of the rift during this time was located along the now inactive Cañada de Cochiti fault south of the Jemez Mountains (Gardner and Goff, 1984) and the Cañones fault to the north (Manley, 1976a; Gonzalez and Dethier, 1991). Mantle-derived volcanic and volcaniclastic rocks of the Miocene (16- to 6-Ma) Keres Group are located in the southern part of the Jemez Mountains volcanic edifice and interfinger with rift-fill sediments of the Santa Fe Group (Bailey et al., 1969; Smith et al., 1970; Gardner and Goff, 1984). The Santa Fe Group sediments consist of silt, sand, and gravel derived from and intercalated with the Keres Group rocks, and of fluvial gravel deposited by the ancestral Rio Grande (Ingersoll et al., 1990).

Stratigraphically overlying the Keres Group rocks and intercalated with the Santa Fe group sediments are rocks of the Polvadera Group, which in the vicinity of the Pajarito Plateau consist of dacites, latites, quartz latites, and andesites of the Tschicoma Formation and volcaniclastic fan deposits of the Puye Formation (Griggs, 1964; Gardner et al., 1986). These 4- to 1.7-Ma old rocks are exposed in the headwaters of tributaries that drain the eastern flank of the Jemez Mountains, as well as along several incised drainages on the Pajarito Plateau (Smith et al., 1970; Waresback and Turbeville, 1990). Approximately 5 Ma

ago, the western rift margin shifted to the east from the Cañada de Cochiti fault to the Pajarito fault (Golombek, 1981, 1983; Gardner and Goff, 1984).

After this eastward shift in the location of the western rift margin, basalts of the Cerros del Rio field were extruded at about 2.6 to 2.5 Ma (Bachman and Mehnert, 1978; Aubele, 1978). This field is adjacent to the southeastern margin of the Pajarito Plateau on the eastern side of the Rio Grande, although basalt flows are present beneath younger rocks in the vicinity of White Rock (Smith et al., 1970; Dethier and Manley, 1993). These flows interfinger with the Puye Formation north of about Los Alamos Canyon (Dransfield and Gardner, 1985; Gardner and House, 1987).

The Pajarito Plateau is underlain primarily by the rhyolitic Bandelier Tuff, which consists of the lower, approximately 1.6 Ma Otowi Member and the upper, approximately 1.2 Ma Tshirege Member (Smith et al., 1970; Spell et al., 1990; Gardner et al., 1993; Izett and Obradovich, 1994). The Otowi Member consists of an unconsolidated, massive basal air-fall pumice bed (the Guaje Pumice), which is overlain by a sequence of nonwelded, pumiceous pyroclastic flows. These deposits apparently filled east-trending paleovalleys developed in the Tschicoma and Puye Formations and the Cerros del Rio basalt. Locally, deposits of unconsolidated, pumice-rich sand and gravel occur stratigraphically between the Otowi and Tshirege Members, and are correlated with the Cerro Toldeo Rhyolite of the Valles caldera (Bailey et al., 1969; Smith et al., 1970, Heiken et al., 1986). The Tshirege Member unconformably overlies the Otowi Member and the Cerro Toledo Rhyolite (equivalent), and consists of an unconsolidated basal air-fall pumice bed (the Tsankawi Pumice), overlain by multiple pyroclastic flows. This member filled paleovalleys and aggraded to a smooth, easterly- to southeasterly-dipping surface represented by present-day mesa tops. The degree of welding of these flows varies across the plateau, with proximal deposits near the Jemez Mountains typically being welded to moderately welded and distal deposits near the Rio Grande being nonwelded. The flows also decrease in thickness from several tens of meters along the western plateau to zero near the Rio Grande (Smith et al., 1970). Along the western and northern margins of the plateau, knobs of Tschicoma Formation protrude out of the tuff (Smith et al., 1970).

The youngest volcanic deposit present on the Pajarito Plateau is the El Cajete Pumice (Smith et al., 1970; Self et al., 1988). This air-fall deposit of interbedded tan to white pumice was

derived from the El Cajete crater in the southern part of the Valles caldera, and is distinct in hand sample from other pumice deposits on the plateau by the presence of mesoscopic biotite grains. Pumice deposits on the plateau are present locally along the base of east- and southeast-facing escarpments, as well as on relatively flat mesa tops in the central part of the plateau (Reneau et al., 1994). This distribution, however, may be a result of rapid erosion off escarpments and redeposition at their bases (Self et al., 1988).

Although uranium-thorium disequilibrium and fission-track dates support an age for the El Cajete pumice of 130 to 180 ka (Marvin and Dobson, 1979; Miyachi et al., 1985; Self et al., 1988), recent investigations (including results from this study) support a much younger age (Reneau et al., 1994). Spell and Harrison (1993) pointed out that numerous attempts to date biotite in the pumice, using K-Ar and Ar-Ar methods has yielded unequivocal results, probably due to contamination of xenocrystic material. As a result, they report an age of <520 ka based on stratigraphic relations. Electron spin resonance (ESR) analyses yield age estimates between 45 and 73 ka for the El Cajete Pumice (Toyoda et al., 1995). Radiocarbon analyses of charcoal entrained within a pumice bed in the Jemez Mountains yield ages ranging from 50.1 ± 1.3 yr BP to >58 yr BP (Reneau et al., 1994).

Thermoluminescence analyses of a soil Av horizon exposed in trenches at TA-67 and buried by air-fall deposits of El Cajete Pumice on Pajarito Mesa yield ages between 48 ± 10 (2 sigma error) and 52 ± 10 ka (S.L. Forman, the Ohio State University, written communication, 1994). Finally, in this study thermoluminescence analyses of slopewash colluvium underlying a deposit of El Cajete pumice yield ages of 55 ± 9 and 57.0 ± 18 ka (Section 4.2.1.2). Thus, there is considerable evidence that suggests fission-track ages are too old and that eruption of the El Cajete Pumice actually occurred sometime between 45 and 73 ka, probably around 60 ka (Reneau et al., 1994).

Generally, there are relatively few late Quaternary surficial deposits preserved on the Pajarito Plateau. Mesa tops typically are mantled by less than 3 m of either fine-grained fluvial or eolian deposits. Coarse-grained fluvial gravels are present along the rims of some large drainages, although very few valleys contain substantial fluvial terrace deposits. Frijoles and Rendija Canyons, where developed into either nonwelded tuff or the Cerro Toldeo Rhyolite epiclastic deposits, contain fluvial gravel deposits up to about 10 m thick

(Section 4.2.3; Reneau et al., 1993). In addition, substantial colluvial deposits are present along the east-facing escarpment of the Pajarito fault.

2.4.2 Major Faults of the Pajarito Plateau

The Pajarito fault system is the main structural boundary along the western side of the Española Basin (Plate 1). The north-trending fault system consists of three main faults, and numerous secondary faults that cross the western part of the Pajarito Plateau (Plate 2). The main faults include the down-to-the-east Pajarito fault and the down-to-the-west Rendija Canyon and Guaje Mountain faults. The 41-km-long Pajarito fault extends from an intersection with the Embudo fault north of Santa Clara Canyon to an intersection with the La Bajada and San Francisco faults near Cochiti Lake (Plate 2). Where the fault traverses the Pajarito Plateau near Los Alamos, a nearly 200-m-high, east-facing escarpment is developed in the Bandelier Tuff. The fault is associated with up to about 150 m of post-Bandelier, down-to-the-east displacement and has had a long-term slip rate of approximately 0.1 to 0.2 mm/yr (Gardner and House, 1987). Subsurface geologic data show progressively more displacement of older rocks, providing evidence that the Pajarito fault pre-dates the Bandelier Tuff and has had recurrent activity (Dransfield and Gardner, 1985). The fault escarpment, as well as results of this investigation, provide strong evidence of late Quaternary activity along the Pajarito fault (Section 4.2.1).

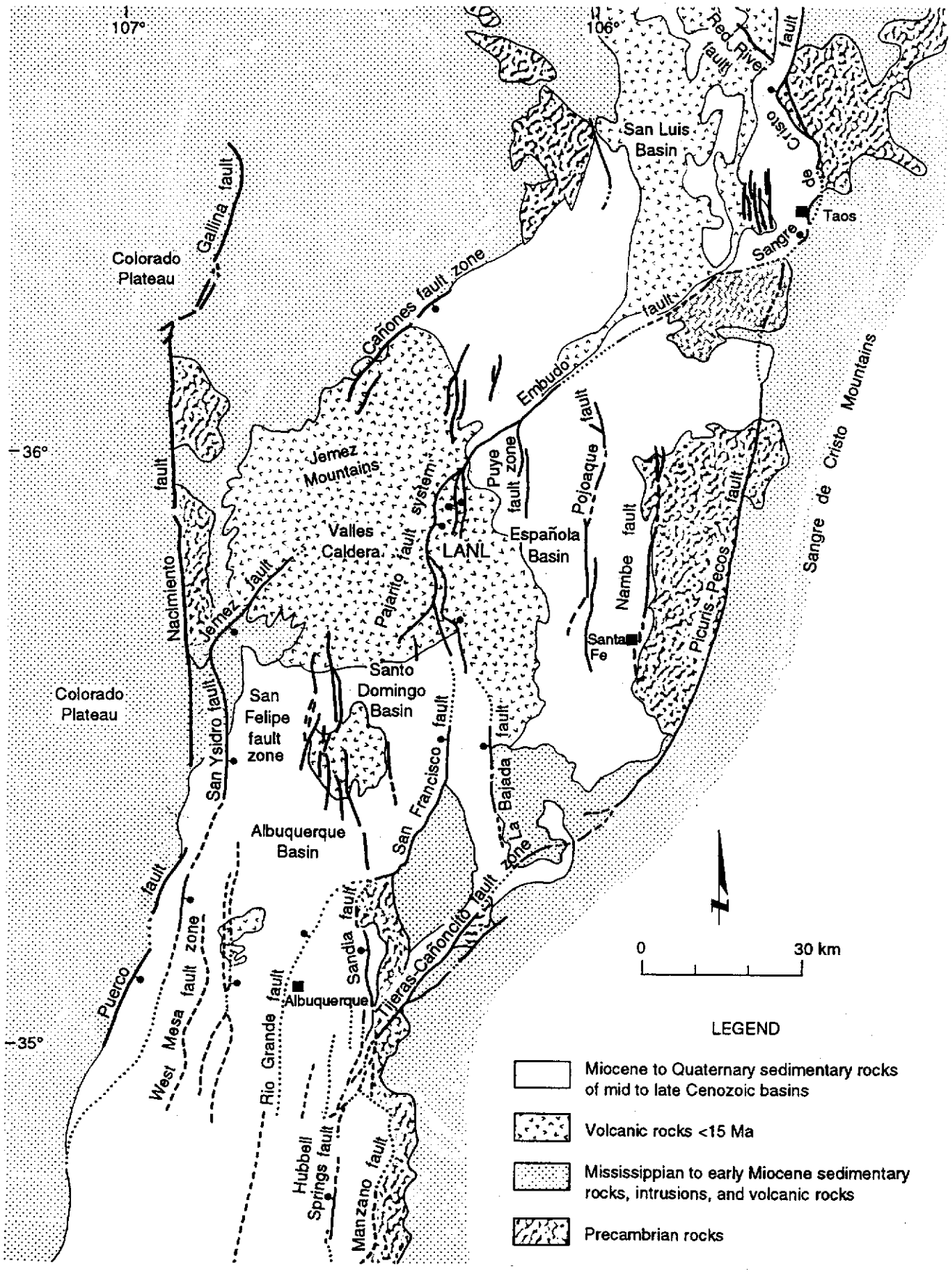
The 14-km-long Rendija Canyon fault is subparallel to and located approximately 3 km east of the Pajarito fault (Figure 2-2; Plate 2). The north-trending, steeply west-dipping fault exhibits down-to-the-west displacement of the 1.2 Ma upper Bandelier Tuff (Kelley, 1954; Griggs, 1964; Smith et al., 1970; Budding and Purtyman, 1976; Kelley, 1978; Golombek, 1981, 1983; Gardner and House, 1987). Down-to-the-west net vertical tectonic displacement of the 1.2 Ma-old Bandelier Tuff is about 36 m in the central part of the fault (Section 4) which agrees well with vertical stratigraphic offsets of 34 m also measured along the central section in the Bandelier Tuff (Carter and Gardner, 1993). Structural data given by Carter and Winter (1995) reveal predominantly dip-slip normal movement on the Rendija Canyon fault. As noted in Section 4.2.2, the fault exhibits evidence of repeated late Quaternary activity, including a most-recent event that occurred either 8 to 9 ka or around 23 ka.

The 12-km-long Guaje Mountain fault is subparallel to and located approximately 4 to 5 km east of the Pajarito fault (Figure 2-2; Plate 2). The north-trending, steeply west-dipping fault exhibits down-to-the-west displacement of the Bandelier Tuff and, thus, is structurally similar to the subparallel Rendija Canyon fault. Net vertical tectonic displacement of the upper Bandelier Tuff is as much as about 27 m at the northern end of the fault (Section 4). Carter and Winter (1995) found evidence for dominantly dip-slip normal movement on the Guaje Mountain fault. There is geomorphic and paleoseismologic evidence of repeated late Quaternary activity (Section 4.2.3), including a most-recent event at about 4,000 to 6,000 years ago (Gardner et al., 1990).

Subsurface geologic data show that the Rendija and Guaje Mountain faults also pre-date the Bandelier Tuff and have had recurrent activity (Dransfield and Gardner, 1985; Budding and Purtyman, 1976). Based on similar senses and amounts of post-1.2 Ma displacement, the Rendija Canyon and Guaje Mountain faults likely are structurally related to each other and to the Pajarito fault. Baldridge et al. (1990) note that a topographic low between the northern Pajarito fault and the Guaje Mountain and Rendija Canyon faults, and possible lateral slip along these faults, suggests that the west-dipping faults accommodate right-lateral strain between the Embudo fault and the central Pajarito fault. Alternatively, the west-dipping faults may be antithetic to the east-dipping Pajarito fault and the topographic low is a 3- to 5-km-wide graben in the hanging wall of the predominantly dip-slip Pajarito fault. Slickenside data, suggesting predominantly dip-slip on the Rendija Canyon and Guaje Mountain faults (Carter and Winter, 1995), support this model, although Baldridge et al. (1990) note that oblique slickensides plunge shallowly to the north and to the south and offer conflicting senses of lateral offset. These differences in observed sense of slip may be related to dip-slip along fault planes that have minor variations in orientation relative to local stress directions. Clearly, paleoseismic data on the sense of slip of the Pajarito, Rendija Canyon, and Guaje Mountain faults are required to assess interactions among these faults and to evaluate their roles in the late Quaternary deformation of the LANL region.

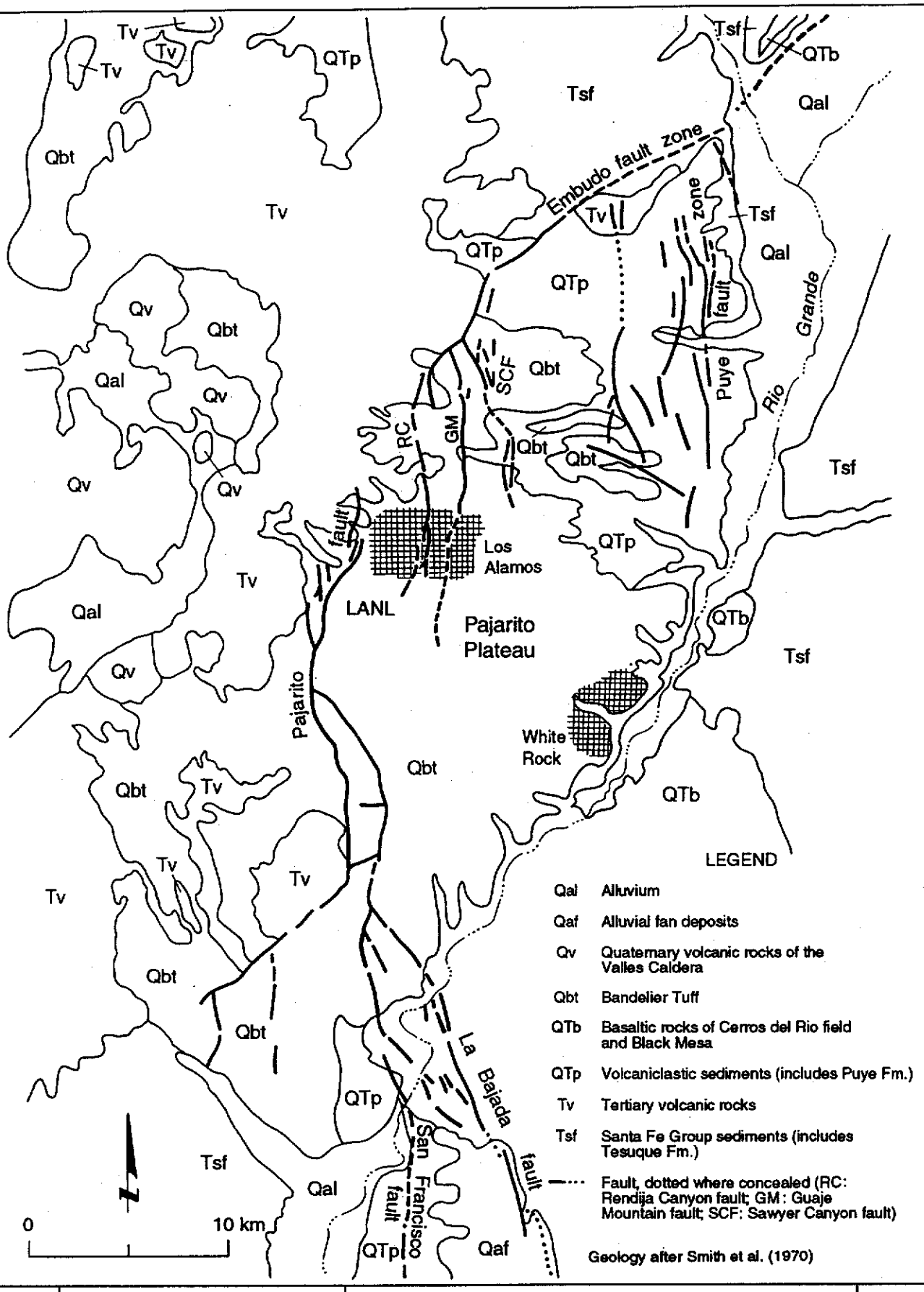
Interestingly, the Pajarito fault system differs from other major rift-border faults to the north and south in that it does not lie at the base of a Precambrian-cored range block originally uplifted during Laramide deformation. Perhaps the lack of a major range block on the footwall of the Pajarito fault system is related to a displacement history that spans only about 5 Ma (Gardner and Goff, 1984; Golombek, 1983), rather than about 15 to 30 Ma as along

the Sangre de Cristo fault in northern New Mexico and southern Colorado (Kelley and Duncan, 1984; Menges, 1990a,b; Lindsey et al., 1983), or to a thin crust and high heat flow associated with the Valles caldera (Goff et al., 1989). In essence, the 200-m-high Pajarito "fault scarp" (Gardner and House, 1987) is equivalent to mountain-front escarpments along late Quaternary faults elsewhere in the Rio Grande rift (Machette, 1986; McCalpin, 1982; Menges, 1990a,b) and the Basin and Range province (Machette et al., 1992; Ramelli and dePolo, 1993; Turko and Kneupfer, 1991). Thus, the escarpment along the Pajarito fault is distinct from late Quaternary fault scarps commonly developed in piedmont alluvium along or basin-ward from other rift-margin or Basin and Range mountain fronts.



Project No. 91C0509	Los Alamos Seismic Hazards	TECTONIC MAP OF THE LANL REGION	Figure 2-1
Woodward-Clyde Federal Services			

91C0509A-1300/121494



Project No. 91C0509	Los Alamos Seismic Hazards	GENERALIZED GEOLOGIC MAP OF THE PAJARITO PLATEAU	Figure 2-2
Woodward-Clyde Federal Services			

91C0509A-1300/121494

3.0
HISTORICAL SEISMICITY

A historical earthquake catalogue (Appendix A) was compiled for the LANL region and is shown in Plate 3. Recurrence estimates were computed for the four seismotectonic provinces defined in Section 2.0 and the earthquakes used are listed in Appendices B through E. Appendix F includes recurrence plots and tables of recurrence parameters.

Several primary data sources were used in the compilation of historical seismicity. These include the Decade of North American Geology (DNAG) catalogue (Engdahl and Rinehart, 1988) for the time period from about 1800 through 1985; the catalogue compiled for New Mexico by the National Earthquake Information Center (NEIC) (an earlier version is contained in Stover et al., 1988); the NEIC Preliminary Determination of Epicenters from 1985 to date; Los Alamos Seismographic Network (LASN) catalogue from 1973 through 1990; and a catalogue compiled by Woodward-Clyde Consultants for the Paradox Basin region from 1893 through 1984.

The historical catalogue (Appendix A) contains 1351 earthquakes of approximate Richter magnitude (M_L) greater than or equal to 0. The majority of events before 1961 occurred prior to adequate seismographic coverage and are thus based on felt reports; hence, they have been assigned maximum Modified Mercalli (MM) intensities (see Table 3-1 for explanation of the MM scale).

3.1 EARTHQUAKE DETECTION AND LOCATION ACCURACY

With regard to our knowledge of earthquake occurrence, the historical record can be divided into pre-instrumental and instrumental periods. In New Mexico, uniform instrumental detection and location of earthquakes did not begin until about 1961. Prior to that time, the detection of earthquakes was generally based on direct observations and felt reports. This capability is strongly dependent on population distribution and density. The LANL region, typical of many areas of the western U.S., was sparsely populated in the 1800's (Figure 3-1), and, thus, the detection of pre-instrumental earthquakes is of variable completeness as described below.

3.1.1 Pre-Instrumental Seismicity

About 25 earthquakes in the historical catalogue occurred within the pre-instrumental period (prior to 1961) and were located within the LANL region based principally on felt reports. An examination of population growth shows a very gradual growth for the majority of counties around the study region except Santa Fe County which has undergone significant growth since 1940 (Figure 3-1). In central New Mexico, only Bernalillo County, which contains the city of Albuquerque, has undergone significant growth, and only since about 1930. In the counties east of Los Alamos, Torrance County has had moderate growth, also since about 1930. Similarly San Juan, Valencia and McKinley Counties sustained moderate growth from around 1950. The region of today's Los Alamos County was originally settled in 1880 and grew in the early 1940s with the advent of weapons research at LANL. Since then, the population has increased slowly from about 10,000 to its present-day size of 18,000 people.

As is most often the case, growth in the region was concentrated in the larger towns and cities. Many of the towns in the vicinity were originally founded and settled by Spaniards in the early 17th and 18th centuries including: Santa Fe in 1609 on the site of an ancient Indian village, Taos in the early 17th century, Albuquerque in 1706, Belen in 1740, and Las Vegas in 1833. After New Mexico became a territory of the U. S., post offices were established in most of the major towns in the 1850s to 1880s, before which little is known about earthquake occurrence.

Based on this population distribution and growth, we judge that the historical record for the LANL region is complete for earthquakes of $M_L \geq 5.5$ since about 1850 (Table 3-2). Earthquakes smaller than M_L 5.5 have varied completeness due to varying population in the different parts of the region. Engdahl and Rinehart (1991) estimate completeness of $M \geq 5¾$ since 1900 and $M \geq 5$ since 1925 for the New Mexico region. On the whole, significant increases in population occurred in 1880, 1900, 1930 and 1950 and these form part of the basis for the completeness estimates shown in Table 3-2. The periods of completeness are generally smaller for the Southern Rocky Mountains and Colorado Plateau provinces due to lower populations overall in these regions and few major towns being established early on.

3.1.2 Instrumental Seismicity

The majority of earthquakes contained in the historical catalogue (Appendix A) were instrumentally recorded and located by LANL from about 1973 to present. A detailed discussion of New Mexico's historical seismicity and related aspects are discussed by Northrop (1961; 1976) and Sanford et al. (1979; 1981).

For New Mexico, uniform detection and location of earthquakes did not begin until the early 1960s when stations at Albuquerque (ALQ), Las Cruces (LCN), and Payson, Arizona (TFO) went into continuous operation (Sanford et al., 1979) (Figure 3-2). These stations supplemented those at Lubbock (LUB), Socorro (SNM), and Tucson (TUC) permitting the location of many more earthquakes. A recent unpublished report (A. Sanford, New Mexico Tech., written communication, 1994) indicates that the whole of New Mexico had a complete record of events of $M_L \geq 2.7$, the minimum magnitude for detection at the edges of the state, from 1962 to 1986. Engdahl and Rinehart (1991) estimate completeness for earthquakes of $M \geq 2.5$ since the early 1960s for the whole of New Mexico. In 1973, the LASN began operation along with the Albuquerque Seismological Laboratory (ASL) and New Mexico Institute of Mining and Technology (NMT) networks, which greatly increased the level of detection (Figure 3-2). This monitoring allowed for the recording of earthquakes of $M_L < 0$ within the bounds of the LASN (Figures 3-2 and 3-3). The network was at its peak from 1976 to 1983 (Figure 3-3) when the largest number of stations were operating and providing the greatest areal coverage. From 1973 to 1984, $M_L \geq 1.5$ events could probably be detected in most parts of the study area. From 1983 to 1985, many of the LASN stations were closed due to increasing costs and lack of funding. As a result, the detection level and location accuracy decreased, despite the installation of several new stations in 1985 and 1986. The new stations were generally installed near Los Alamos and so decreased the areal coverage (Figure 3-3). Most of the earthquakes since 1985 have poorly-constrained locations due to a lack of azimuthal coverage.

The Great Plains province completeness ranges are generally shorter than for the other provinces due to its even poorer seismographic coverage.

3.2 SIGNIFICANT EARTHQUAKES

In historical times, six earthquakes of estimated M_L 5.0 (or MM VI) or greater have occurred within the LANL region (Plate 3 and Appendix A). In this section, a description of these events is presented. The largest event to occur within the LANL region in pre-instrumental times is the 1918 Cerrillos earthquake which had a maximum MM intensity of VII. Several MM intensity VI events occurred in the 1930s to 1940s and again in the early 1970s. In addition, the 1906-1907 Socorro swarm and the 1966 Dulce earthquake are discussed. Although not within the LANL region, these events are of significance to this study because they are the largest events to occur in the Rio Grande rift and Colorado Plateau transition zone provinces, respectively.

3.2.1 1906-1907 Socorro Swarm

The largest earthquake to occur within the Rio Grande rift province was the MM VIII (Rossi-Forel VIII) earthquake of 15 November 1906. Though not within the LANL region, this event is important for estimating a maximum magnitude for random earthquakes within the Rio Grande rift province.

The region around Socorro is known to be the source of intermittent bursts of seismic activity in New Mexico throughout the historic and instrumental record. Although the area was occupied by the Spanish and native Americans, no record of any earthquakes has been recovered prior to 1849. The earliest activity near Socorro was a swarm of 22 moderate sized earthquakes (MM $\leq$ IV) (Sanford et al., 1981) which occurred from 11 December 1849 to 8 February 1850 as reported by a U.S. Army surgeon (Hammond, 1966). Again, events of MM V and MM VII occurred on 28 April 1868 and April 1869 (date unknown) (Sanford et al., 1981). The latter, the most serious earthquake known to that date in Socorro (Bagg, 1904), shifted the flow of water along the base of the Socorro Mountains northwards and caused it to flow muddy for many weeks. Again in 1886 and 1897 earthquakes caused significant shaking in Socorro, awakening many people (MM V) but causing no damage (Bagg, 1904).

The 1906-1907 sequence began on 2 July 1906 with two jolting earthquakes at 3:15 a.m. and 3:30 a.m. MDT which were felt within a 80-km radius of Socorro (Reid, 1911). Earthquakes were then felt almost daily from 2 July 1906 to 21 July 1907, the most severe occurring on 12 July, 16 July and 15 November 1906 (Reid, 1911). The 12 July earthquake lasted 15 to 20 seconds causing adobe walls to crack, some chimneys to fall and a rockslide to cause some damage to the nearby railroad (MM VII-VIII). Many aftershocks followed, including the 16 July earthquake which damaged additional chimneys and houses, caused a brick gable to partially fall down and the southeast corner of the brick post office to be thrown out (Reid, 1911). Newspaper accounts apparently exaggerated the damage, which appeared severe, partly due as Reid (1911) notes, to houses overlying saturated alluvium and built of poor construction material (uncemented adobe). There are felt reports from as far northeast as Raton (380 km) and as far southwest as Douglas, Arizona (400 km) although Reid (1911) questions their validity.

The strongest earthquake occurred at 5:15 a.m. MDT on 15 November and was felt throughout central New Mexico over an area of approximately 245,000 km^2 (Sanford et al., 1981; Reid, 1911; Figure 3-4). It was felt as far north as Gallup, Sante Fe and Cerrillos and would have probably been felt in the Los Alamos area. The maximum intensity of this earthquake is estimated as MM VIII (Rossi-Forel VIII) and it caused additional damage to that already sustained in the 12 and 16 July earthquakes. Reid (1911) notes that the event was not much more severe than the other earthquakes; however, the felt area of the 15 November event is considerably larger than the felt areas for the 12 and 16 July earthquakes, both estimated around 105,000 km^2 (Reid, 1911). Estimated property loss was only around $3,000 and no one was seriously injured (Ashcroft, 1974).

A wide range of magnitudes has been suggested for this event (M_L 4.9 to 6.5) due to the large uncertainties involved (Sanford et al., 1979). Using relationships between magnitude and maximum intensity or felt area from Toppozada (1975), an M_L 5.8 is estimated based on a I_{max} of VIII, an M_L 6.4 using total felt area and M_L 5.6 from the felt area of MM V and greater. However, the use of the Toppozada (1975) relationships is questionable given that it was developed for Nevada and northern California where the average crustal Q_o is on the order of 140 to 200, at least a factor of two less than for the LANL region for which Q_o is about 370 (Singh and Herrmann, 1983). It is likely that an overestimation of magnitude should be expected when using these relationships. La Forge and Anderson (1988)

performed a regression on 36 New Mexico earthquakes relating magnitude and maximum MM intensity. Using their relationship, a M_L 4.9 results for the Socorro earthquake (MM VIII), about one magnitude unit less than the value from the Toppozada (1975) relationship. However, La Forge and Anderson (1988) estimate a M_L 6 for this earthquake based on comparison of the Socorro swarms with the 1906 Flagstaff earthquake, as their relationship appears to underestimate earthquake size.

Reid (1911) deduced that the source of these earthquakes was probably within the Socorro Mountain horst block in the rift west of Socorro. Sanford et al. (1979) believe that the swarm activity in the central portion of the Rio Grande rift around Socorro may be associated with magma injection. However, another source could be the abundant north-south-trending Quaternary normal faults in the region, one of which bounds the eastern edge of the Socorro Mountains. More recent instrumental observations of microseismicity in the Socorro region (1974 to 1983) showed increased diffuse seismicity within the Socorro caldera and also in the region above a postulated mid-crustal magma body defined by Rinehart et al. (1979). Some of these epicenters could be associated with the Socorro Basin-bounding normal faults, but some of the active normal faults in the region appear to have no associated seismicity.

Composite focal mechanisms from some of the Socorro microearthquakes indicate east-west extension on north- to west-northwest striking, moderately-dipping planes (Sanford et al., 1979). However, a geodetic survey by Prescott et al. (1979) reveals zero extension across the rift near Socorro. Other leveling data indicate an average uplift rate of 5 mm/yr from 1909 to 1979, coincident with the region above a mid-crustal magma body (Reilinger et al., 1980), which was later confirmed from crustal reflection profiling (Brown et al., 1979; Brown et al., 1980). Sanford et al. (1979) conclude from the seemingly conflicting data that the seismic activity, significant uplift and zero horizontal extension can be explained by the intrusion of a sill-like magma body at midcrustal depths. This could also cause reactivation of pre-existing north-south-striking faults without the necessity of regional extension.

In summary, the Rio Grande rift to the south of Los Alamos is characterized by recurrent moderate-sized earthquakes (MM VI-VII) and swarm activity probably due to the existence of a magma body. The likelihood of this style and intensity of seismic activity within the rift near Los Alamos is probably low. However, activity may vary temporally and spatially

within the rift, so we cannot totally preclude such activity in the future, especially within an actively extending area and with a geologic history of sporadic volcanism and active Quaternary normal faulting.

3.2.2 1918 Cerrillos Earthquakes

The Cerrillos earthquake, the largest historical earthquake within the LANL region and the northern portion of the Rio Grande rift, occurred at 5:30 a.m. MDT on 28 May 1918 (Coffman et al., 1982). It was strongly felt in Cerrillos where chimneys fell, plaster cracked, windows broke, people were thrown off their feet and a large crack in the earth's surface appeared at the edge of town (Olsen, 1979). In Stanley, doors rattled, a piano sounded and walls and plaster cracked (Coffman et al., 1982). At Lamy and Estancia, a rapid twisting motion, and in Moriarty, a noise like distant thunder were reported (Olsen, 1979). A MM VII-VIII has been assigned to this event by Coffman et al. (1982), but the MM VIII depends on the observed ground breakage. Olsen (1979) believes that MM VII is more appropriate and that the crack probably resulted from ground settling not surface rupture. A felt area of 31,000 km^2 (Figure 3-5) determined by Olsen (1979) may be on the conservative side due to low population density at this time, being post-mining boom time.

Olsen (1979) analyzed the amplitudes, or lack thereof, on available seismograms and those of a calibration event on 23 May 1918, and determined an upperbound of M_L 4.5 to 5.0. Similarly, felt area information indicated a M_L 4.5 to 5.5 using various magnitude-felt area relationships (Olsen, 1979). Olsen (1979) concludes that the Cerrillos earthquake was comparable to the M_L 5.2 (m_b 4.9) 1966 Dulce earthquake (Section 3.2.6) and that the epicenter was very close to Cerrillos. We concur with the estimate of Olsen (1979) of a M_L 5¼ for this earthquake.

3.2.3 1930 Earthquake

A MM VII earthquake was reported felt in Albuquerque on 3 December 1930 (Plate 3). Two distinct shocks were felt at 14:36 MST, causing plaster and dishes to crack (Neumann and Bodle, 1932). It was felt over an area of 47,160 km^2 (Newton et al., 1976). Sanford (1976) assigns a M_L 4½ to this event using a magnitude-intensity-radius relationship

developed by Richter, which was probably originally applicable to California. We agree with this estimate.

3.2.4 1931 Earthquake

On 4 February 1931 at 21:48 MST, many people in Albuquerque (Plate 3) left their houses and some reported being thrown from their beds. In theaters, people panicked and tried to leave. Goods were thrown from shelves in stores and a 3 m crack appeared in a bakery (Neumann, 1932). A hot water tank fell and mirrors and plaster cracked (Neumann, 1932). We have assigned a M_L 4½ to this event based on Sanford's (1976) estimate using the Richter magnitude-intensity-radius relationship.

3.2.5 1947 Earthquake

At 9:50 a.m. MST, a MM VI earthquake rattled through San Antonito (Plate 3) causing dishes to jar from shelves and desks to rattle in a school. A small survey, however, found the earthquake was only locally felt (within a 16 km radius). In Zamora, a fireplace was cracked as well as plaster and windows, and doors and dishes rattled (MM VI) (Murphy, 1950). Northrop stated that the epicenter was in the vicinity of the Tijeras Coal Basin, a graben on the eastern side of the Sandia Mountains fault block (Murphy, 1950). Sanford (1976) estimated a M_L 4¼ for this earthquake, also based on Richter's magnitude-intensity-radius relationship. We have also assigned a M_L 4¼ to this earthquake.

3.2.6 1966 Dulce Earthquake

The 23 January 1966 Dulce earthquake, though located just north of the LANL region, is the largest earthquake to occur within the Colorado Plateau transition zone which lies to the northwest and west of LANL. The maximum intensity was reported as MM VII in Dulce, a small town with a population around 2,000 (von Hake and Cloud, 1968). This earthquake has been assigned a body-wave magnitude (m_b) 5.1, surface-wave magnitude (M_s) 4.9 (Cash, 1971), Nuttli magnitude (m_{bLg}) 5.1, M_s 4.6 (Nuttli et al., 1979), m_b 5.5 by the U.S. Coast and Geodetic Survey, and M_L 5.5 by Sanford et al. (1972). The earthquake, which occurred at about 18:56 MST and located north of Dulce and west of Edith, on the New Mexico-Colorado border, was felt over an area of 39,000 km^2 (Figure 3-6). It was felt as far south

as Los Alamos at MM I-III. The earthquake caused major damage to the Bureau of Indian Affairs School and Dormitory Complex amounting to $200,000 and also to the Dulce Independent Schools in Dulce (von Hake and Cloud, 1968). The damage was mostly to interior and exterior walls in the form of cracks and fractures and falling plaster. The steam-heating plant appeared to be damaged beyond repair with brick walls displaced by 5 cm and two 10-ton boilers shifting 1 cm at their base. A 20-m smoke stack also buckled, held in place only by guy wires (von Hake and Cloud, 1968).

No injuries or deaths were reported but most buildings in Dulce were affected and many were damaged. Some chimneys were damaged and spalling stucco was common. Damage appeared to be accentuated by poor design and inferior construction material (von Hake and Cloud, 1968). Some rockfalls and earthslides occurred on Highway 17 and some minor cracks appeared on the road.

A lively aftershock sequence of 119 earthquakes was recorded at Albuquerque from 22 to 28 January. An additional 218 events were recorded on three temporary seismograph stations deployed for a week beginning on 28 January. Twenty-three of the aftershocks were felt locally. Relocations of some of the aftershocks from a joint hypocenter determination technique using "Gasbuggy," a nearby explosion in 1967, as the calibration event form a cluster around the mainshock in the vicinity of some mapped Miocene normal faults (Herrmann et al., 1980). Herrmann et al. (1980) postulate reactivation of these older structures under the present extensional stress regime. Several focal mechanisms have been computed of varying quality (Cash, 1975; Hoffman and Northrop, 1977) the most reliable of which appears to be by Herrmann et al. (1980). They used surface-wave modeling and some first motions and the resulting focal mechanism indicates normal faulting on north-northwest-striking planes which is consistent with the orientation of the mapped Miocene faults. The estimated focal depth of 3 km (Herrmann et al., 1980) appears shallow for typical earthquakes of the Colorado Plateau. Surface-wave modeling, however, is not particularly sensitive to hypocentral depth and so the depth is probably greater, but less than 15 km, which is typically observed for moderate-sized earthquakes occurring in the western U.S.

3.2.7 1970 Earthquake

On 28 November 1970 at 00:40 a.m. MST, a MM VI earthquake occurred close to Albuquerque (Plate 3). Coffman et al. (1982) report a felt area of 3,150 km^2. Thousands of people were awakened and explosion-like noises were reported. There were many reports of minor damage to buildings such as cracked plaster and block wall fences, a cracked garage floor, and broken windows. There was one report of an air conditioner, which had shaken loose, falling through a skylight. Several burglar alarms also were activated (Coffman and von Hake, 1972). A barn roof collapsed and animals at the zoo were disturbed. Coffman and von Hake (1972) and NEIC report a M_L 3.8 for this earthquake and a hypocentral depth of 9 km.

3.2.8 1971 Earthquake

On 4 January 1971 at 00:30 a.m. MST, another MM VI earthquake struck northwest of Albuquerque (Plate 3). The felt area was approximately 1,600 km^2. The University of Albuquerque sustained $30,000 to $40,000 in damage, mostly due to spillage of chemicals which corroded the floor tiling and molding (Coffman and von Hake, 1973). Steel shelves were bent and twisted and thousands of books were thrown to the floor in the library. In the university chapel, a baptismal font split in two. Other damage included a 1.2-m-long crack in a wall of Bernalillo Jail, many cracked walls and plaster, and broken windows (Coffman and von Hake, 1973). A Persian gazelle reportedly ran into a wall and died at the zoo in Albuquerque (USGS, 1974). Magnitudes of m_b 4.7 (Coffman and von Hake, 1973) and M_L 3.8 (Sanford, 1976), and a hypocentral depth of 9 km (Coffman and von Hake, 1973) were reported. We agree with the magnitude determination of Sanford (1976). Sanford (1976) indicates it was most strongly felt at Corrales, whereas Coffman and von Hake (1973) report the town as only having an intensity MM V. Both the 1970 and 1971 earthquakes probably occurred near the University of Albuquerque, west of the Rio Grande River (A. Sanford, New Mexico Tech., written communication, 1994). The locations in the historical catalogue (Appendix A) and those shown on the map were obtained from the DNAG catalogue and the actual location should be further west; however, there are no alternative published locations.

3.2.9 1978-1979 Albuquerque Volcanoes Swarm

A sequence of about 300 earthquakes of $M_L \leq 2.5$ occurred between 28 September 1978 and 30 April 1979 in the vicinity of the Albuquerque Volcanoes (Jaksha et al., 1981), a region previously described as seismically quiet (Sanford et al., 1979). The swarm occurred in two major bursts of activity, a short intense initial burst and a more prolonged period of less frequent events, separated by a couple of months of seismic quiescence. The largest earthquake (M_L 2.5) occurred towards the end of the second burst of activity. Jaksha et al. (1981) were able to locate about 90 earthquakes in the sequence using data recorded by both the USGS ASL network and a temporary field network. A local velocity model and station corrections were developed and used in the locations. The epicenters were located in a north-south elongate zone, about 2.5 km west of the fissures from which the 0.19 m.y. Albuquerque Volcanoes erupted (Bachman and Mehnert, 1978), at an average focal depth of 9.5 km. A composite focal mechanism for three of the largest events recorded on both networks, indicates normal slip on a N5° E striking, west-dipping fault plane, in response to east-west extension. The swarm may be related to the County Dump fault, described by Machette (1978a) as a steeply east-dipping normal fault, which lies near the swarm and is shown on Plates 3 and 12 as part of the West Mesa fault zone.

3.2.10 Earthquakes Felt in Los Alamos

Five additional earthquakes have been reported felt by residents of Los Alamos, all of which were located nearby. The first event occurred at 3:45 MDT on 17 August 1952 and awakened and frightened all the residents of Los Alamos (MM V) (Murphy and Cloud, 1954). There were reports of minor damage to walls and a bassinet shifted (Murphy and Cloud, 1954). It was also reported as felt in Santa Fe Forest near Santa Fe and in Española. Sanford (1976) assigns a M_L 4 to this earthquake.

On 17 February 1971, a MM II event was reported in Los Alamos (Dames and Moore, 1972); however, Coffman and von Hake (1973) only record an m_b 3.7 earthquake occurring at 4:28 a.m. MST on 18 February approximately 70 km east-northeast of Los Alamos (House and Cash, 1988). Sanford (1976) also only lists the latter event with M_L 3.4 and 3.3 from Stations ALQ and SNM, respectively. It appears that there was a mistake in reported timing of this earthquake in Los Alamos, unless a very small localized earthquake occurred.

Another earthquake of M_L 3.2 and maximum intensity MM V occurred near Mendales about 25 km north of Los Alamos on 5 December 1971 at 22:18 MDT, causing adobe walls to crack at Mendales. It was felt at Los Alamos with intensity MM I-II (Coffman and von Hake, 1973).

On 17 March 1973, Coffman et al. (1975) describe an earthquake felt in the Los Alamos area. The depth is given as 6 km and with an m_b 4.5. House and Cash (1988) assign a M_L 3.6 to this event and a maximum intensity of MM V in Los Alamos. The epicenter lies very close to that of the 5 December 1971 earthquake. More recently, a sequence of small earthquakes, the two largest with coda duration magnitudes of (M_D) 1.9 to 2.0, occurred on the evening of 3 February 1991 (Gardner and House, 1994). The two largest events occurred at 8:31 and 10:14 p.m. MST and had shallow focal depths of 3.7 and 2.4 km, respectively. The earthquakes were located at the intersection of the Rendija Canyon fault and the trend of the Pajarito fault, approximately 13 km north of Los Alamos and were felt over an area of 6 km^2 and with a maximum MM intensity of V-VI (Gardner and House, 1994). Damage was minimal, mostly cracks in plaster. The isoseismal pattern indicates a significant effect of the mesa topography on the ground motions, with higher intensities felt towards the center of Barranca mesa. A rapid decrease in intensities over short distances indicates high attenuation of ground motions with distance and reflects the shallow focal depth (Gardner and House, 1994). A poorly constrained focal mechanism indicates a north-south-trending nodal plane consistent with right-lateral strike-slip faulting.

3.2.11 Reservoir-Induced Seismicity at Heron and El Vado Reservoirs

A large temporal cluster of seismicity is located in the northwest corner of the study region, in the vicinity of Heron and El Vado Reservoirs (Plate 3). The timing and intensity of the seismicity has been related to the filling cycles of the two reservoirs (El-Hussain and Carpenter, 1990). The earthquakes were limited to a small diffuse region around the reservoirs and occurred between 1976 and 1984, often occurring in swarms. A correlation between swarm activity and filling to new maximum volumes was observed especially for Heron Reservoir (Figure 3-7). A total of 264 locatable earthquakes occurred in 1982 with magnitudes up to M_L 2.7 (m_b 3.8) during one of these filling cycles (El-Hussain and Carpenter, 1990). The overwhelming spatial and temporal association with the reservoir filling cycles offers a convincing reservoir-induced seismicity scenario (Figure 3-7). We

believe these earthquakes are not representative of the Colorado Plateau transition zone in which they occurred as they are not wholly tectonic in origin and so would bias any recurrence estimates. The b-value determined for the reservoir-induced seismicity at these two reservoirs was 0.92 $\pm$ 0.03 (El-Hussain and Carpenter, 1990), comparable to the value (0.9) used in this study to characterize the recurrence for the Colorado Plateau transition zone. Earthquakes located within a polygon surrounding the reservoirs within the time period 1976 and 1984 were removed from the historical catalogue prior to the determination of recurrence.

3.3 EARTHQUAKE RECURRENCE

In order to assess the effects of background earthquakes on the LANL (Section 5.2), estimates of earthquake recurrence in the region are required. Ideally, it is preferable to calculate separate earthquake recurrence estimates for each of the seismotectonic provinces in the LANL region (Plate 3). Thus, the historical catalogue was divided into separate catalogues, one for each of the seismotectonic provinces except for the Valles Volcanic province which is almost aseismic. It was not considered as a separate seismic source zone but was incorporated into the Rio Grande rift zone. Based on our analysis of catalogue completeness (Section 3.1.2), completeness intervals were estimated (Table 3-2) and used in the evaluation of earthquake recurrence. The time periods represent the time span for which we believe earthquakes within that magnitude range are completely reported in the catalogues.

The recurrence relationships were estimated following the maximum-likelihood procedure developed by Weichert (1980) and the estimated completeness intervals and for a range of minimum magnitudes (Table 3-2). The relationships are in the form of a truncated exponential distribution for the occurrence of independent earthquakes. Dependent events, either foreshocks, aftershocks or smaller events within an earthquake swarm (the largest event is assumed to be a mainshock) were identified using empirical criteria for the size in time and space of mainshock-foreshock-aftershock sequences developed by Arabasz and Robinson (1976), Gardner and Knopoff (1974), and Uhrhammer (1986). This procedure has been adopted from Youngs et al. (1987). If an event was identified as dependent by two of the three criteria, it was deleted from the catalogue. The resulting catalogues of independent

events were then used to develop the recurrence relationships. Occurrence of independent earthquakes is assumed to be a Poissonian process.

Plots of annual cumulative rates of independent earthquake occurrence (Figures 3-8 to 3-11), based on the four earthquake catalogues of independent earthquakes, were used to corroborate the catalogue completeness estimates (Section 3.1; Table 3-2). For all provinces, the curves (Figures 3-8 to 3-11) indicate that there is a poor representation in the 1990s, except for the Rio Grande rift province, and this may reflect the shrinking seismographic coverage of the region. The recurrence curves for earthquakes of $M_L \geq 0.5$ for all provinces are peaked and so the magnitude range M_L 0.5-0.99 is probably incomplete in all cases.

For the Rio Grande rift province (Figure 3-8), the curves appear to indicate that the data is not complete for events of $M_L < 2.0$; however, both the $M_L \geq 2.0$ and $M_L \geq 2.5$ curves have two levels of activity for 1970 to date and prior to 1970 which may reflect a temporal change in the rate of earthquake occurrence. It may also be the result of a change in seismographic coverage or method of earthquake magnitude determination. For the Colorado Plateau transition zone (Figure 3-9), the recurrence curves indicate that the estimated values are probably reasonable even down to as low as $M_L \geq 1.0$. The Southern Rocky Mountains curves (Figure 3-10) give some indication of completeness down to $M_L \geq 1.0$. The curves for the Great Plains province (Figure 3-11), however, indicate completeness for possibly only $M_L \geq 1.5$ and greater.

The annual cumulative rates of independent earthquake occurrence generally indicate the lack of data available in the study region. Each of the provinces appear to only be complete above levels for which there are too few earthquakes to provide a reasonable level of confidence in the recurrence parameters. We have, therefore, computed recurrence parameters for a range of minimum magnitudes which can be found in Table F-1 (Appendix F).

For many of the events in the catalogues, the magnitudes are M_D values; a few earthquakes were assigned intensity-based (M_I), M_L and m_b values. The M_D values for many of the recently recorded smaller earthquakes are coda-duration based magnitudes calculated from the LASN using a relationship developed by Newton et al. (1976). The M_D and M_I values

were assumed to be equivalent to M_L for this study. For the purpose of including felt events with no assigned magnitudes in the recurrence estimates, their maximum intensities (I_o) were converted to M_I using the relationship $M_I = 2/3\ I_o + 1$ developed by Gutenberg and Richter (1956). Such magnitudes have an uncertainty of at least 0.5 to 1 magnitude unit. We chose not to use the relationships of Toppozada (1975) or La Forge and Anderson (1988) as the former tends to overestimate and the latter appears to underestimate earthquake size (Section 3.2.1).

Adjusting the available historical record for dependent events and incompleteness, the numbers of earthquakes remaining in the various ranges from which to estimate recurrence for the four seismotectonic provinces are summarized in Table 3-2 (Appendices B through F). Independent earthquakes for the study region ranging from M_L 0.5 to 5.5 are shown in Figure 3-12. Although there is no specific requirement on the number of events necessary to constitute an adequate data base which would justify the assumption of a Poisson process (hence, provide an accurate assessment of earthquake recurrence), the small number of events for some of the provinces (Southern Rocky Mountains and Great Plains provinces) suggests that large uncertainties must be associated with those resulting estimates.

Earthquakes were placed into 0.5 magnitude unit bins (Table 3-2) and the number of earthquakes was normalized on an annual basis and per km^2. The areas of the provinces used in this study vary from 2,100 to 10,650 km^2 and are summarized in Table 3-3. A regression was performed on the resulting data points for each separate province, as described in Weichert (1980). Based on these earthquakes, the recurrence relationships for the four provinces, assuming the usual form of the Gutenberg-Richter relationship of $\log N = a - bM$, are shown in Figures 3-13 through 3-14.

For each seismotectonic province, the range of recurrence parameters estimated using a range of minimum magnitudes (Table F-1) was utilized in deciding the final b-values chosen for the probabilistic analyses. Standard uniform error bars of $\pm$ 0.1 were used for the b-values loosely based on the range of standard deviations computed (Table F-1). To determine the corresponding a-values and normalized activity rates for M_w 5.0, each b-value was fixed and the maximum likelihood curve was fit to the data (Figure F-1). Resulting activity rates for M_w 5.0 for minimum magnitudes ranging from 0.5-1.5 are shown in Table F-2. Minimum magnitudes used in the final data fit and used in the probabilistic analysis

varied from province to province and these were based on the annual cumulative rates of occurrence curves (Figures 3-8 to 3-11) and recurrence plots (Figures 3-13 and 3-14).

Standard deviations of the estimated activity rates vary from about 1/2 to 1/13 of the mean activity rate (Table F-2). To incorporate the uncertainty in the data, the completeness estimates and the maximum likelihood fit to the data, we used an upper bound of twice the mean activity rate and a lower-bound of ½ the mean activity rate. All nine recurrence combinations plotted with the data points generally span the data points and the standard errors (Figures F-1 to F-4). Return periods for the maximum random earthquake for each province were computed for each of the nine combinations of a- and b-values (Tables F-3 to F-6).

The mean b-values chosen for the four seismotectonic provinces range from 0.7 to 0.9 with error bars of $\pm$ 0.1 (Table 3-3). The b-values chosen in this study compare well with those of La Forge and Anderson (1988) and Anderson et al. (1987) who determined b-values of 0.86 for the whole of New Mexico using 47 earthquakes and 0.83 for Arizona using 34 earthquakes, respectively (Table 3-3). Sanford (1976) and House and Cash (1988) both determined b-values of approximately 1.0, but it is difficult to compare with the values obtained in this study, as they did not correct their catalogue for dependent events.

Based on the recurrence parameters chosen in this study, the return period for the occurrence of an $M_L \geq 6.0$ earthquake varies from 794 years (200 to 3162 years) for the Rio Grande Rift province to 4,786 years (1,202 to 19,055 years) for the Southern Rocky Mountains province (Table 3-3). The lower and upper bounds shown in brackets are determined by incorporating the error assumed for the b-values (Table 3-3). The recurrence for the northern portion of the Rio Grande rift within the LANL region seems reasonable and consistent with the historic record of only one event of M_L 5.5 occurring in historic times, the 1918 Cerrillos earthquake. Return periods for the other provinces are shown in Table 3-3 and ranges of return periods incorporating the chosen uncertainties in the a- and b-values are listed in Table F-3.

3.3.1 Sensitivity Tests

To justify determining a separate recurrence estimate for each of the seismotectonic provinces within the study region, a sensitivity analysis was performed. A plot of the earthquakes used in recurrence for the study region (Figure 3-12) illustrates the variation in seismicity levels within each seismotectonic province. One exception is the western portion of the Great Plains province which is more active compared to that of the eastern portion and more similar in character to the Rio Grande rift province. Some of the historical earthquakes at the western edge of the Great Plains may also have been mislocated and may actually have occurred within the rift. Similarly, the seismicity in the northern portion of the eastern Southern Rocky Mountains province appears to be more active than the southern portion and is more similar in character to the Rio Grande rift. Both the Rio Grande rift and the Colorado Plateau transition zone have moderate levels of seismicity; however, the transition zone has a greater number of smaller magnitude earthquakes, and fewer large magnitude earthquakes. In contrast, the rift has several larger magnitude events and fewer small magnitude earthquakes. This is reflected in the b-values of the two provinces. The b-value chosen for the Colorado Plateau transition zone is 0.9 compared to 0.75 for the Rio Grande rift. The a-values of the two provinces are -2.29 and -2.45, respectively. The return periods indicated for M_w 5 earthquake is 457 years for the transition zone but only 141 years for the rift. The Southern Rocky Mountains and the Great Plains, in contrast, are regions of sparse seismicity.

The seismicity within the circle areas of radii of 20, 40, 60 and 80 km from LANL was determined from the catalogue of independent events (Figure 3-15). Recurrence was determined for each of these circular areas, applying uniform completeness intervals based on the network size and on the population growth in the study region (Figures 3-1 and 3-2; Tables 3-4 and F-1). Recurrence parameters are listed in Table 3-5. The b-values are surprisingly similar for the 20, 40 and 60 km circles, comparable to that chosen for the Rio Grande rift (Tables 3-3 and 3-5). As the radius increases, a larger proportion of seismicity from the Colorado Plateau transition zone and less from the Rio Grande rift are included in the recurrence estimate (Figure 3-15). The result is an increase in b-value. The b-value for the 80-km radius circle is 0.81, closer to the chosen value for the Colorado Plateau transition zone of 0.9 (Figure 3-15). The a-values also vary with circle radius. The a-value is higher

for the 40 and 60-km circles, because these contain the largest number of earthquakes from both the rift and the transition zone. Recurrence of the seismicity of the 20-km radius circle is the most unreliable because of the small number of earthquakes (13) and points (3) on the recurrence plot (Table 3-4; Figure 3-16). The a-value of the 80-km circle is about the same as that for the Rio Grande rift province. Recurrence curves for the circular areas are shown in Figures 3-16 and 3-17.

TABLE 3-1
ABRIDGED MODIFIED MERCALLI INTENSITY SCALE

I	Not felt except by a few under especially favorable circumstances (RF* I)
II	Felt only by a few persons at rest, especially on upper floors of buildings. Delicately suspended objects may swing. (RF I to II)
III	Felt quite noticeably indoors, especially on upper floor of buildings, but many people do not recognize it as an earthquake. Standing motorcars may rock slightly. Vibration like passing of truck. Duration estimated. (RF III)
IV	Felt indoors by many, outdoors by few during the day. Some awakened at night. Dishes, windows, door disturbed; walls make creaking sound. Sensation like heavy truck striking building. Standing motorcars rocked noticeably. (RF IV to V).
V	Felt by nearly everyone, many awakened. Some dishes, windows, and other fragile objects broken; cracked plaster in a few places; unstable objects overturned. Disturbances of trees, poles, and other tall objects sometimes noticed. Pendulum clocks may stop. (RF V to VI)
VI	Felt by all, many frightened and run outdoors. Some heavy furniture moved; a few instances of fallen plaster and damaged chimneys. Damage slight. (RF VI to VII)
VII	Everybody runs outdoors. Damage negligible in buildings of good design and construction; slight to moderate in well built ordinary structures; considerable in poorly built or badly designed structures; some chimneys broken. Noticed by persons driving cars. (RF VIII)
VIII	Damage slight in specially designed structures; considerable in ordinary substantial buildings with partial collapse; great in poorly built structures. Panel wall thrown out of frame structures. Fall of chimneys, factory stacks, columns, monuments, walls. Heavy furniture overturned. Sand and mud ejected in small amounts. Changes in well water levels. Persons driving cars disturbed. (RF VIII + to IX)
IX	Damage considerable in specially designed structures; well designed frame structures thrown out of plumb; great in substantial buildings; with partial collapse. Buildings shifted off foundations. Ground cracked conspicuously. Underground pipes broken. (RF IX +)
X	Some well built structures destroyed; most masonry and frame structures destroyed with foundations; ground badly cracked. Rails bent. Landslides considerable from river banks and steep slopes. Shifted sand and mud. Water splashed, slopped over banks. (RF X)
XI	Few, if any, [masonry] structures remain standing. Bridges destroyed. Broad fissures in ground. Underground pipelines completely out of service. Earth slumps and land slips in soft ground. Rails bent greatly.
XII	Damage total. Waves seen on ground surface. Lines of sight and level distorted. Objects thrown into the air.

* Equivalent Rossi-Forel (RF) intensities.

TABLE 3-2

EARTHQUAKE CATALOGUE COMPLETENESS ESTIMATES AND NUMBER OF EVENTS USED IN RECURRENCE

Magnitude Range (M_L)	Time Period and Number of Events			
	Rio Grande Rift	Colorado Plateau Transition Zone	Great Plains	Southern Rocky Mountains
.5 - 0.99	1976 - 1983? 52	1976 - 1983? 90	not complete	1976 - 1983? 12
1.0 - 1.49	1975 - 1983 45	1975 - 1983 54	1976 - 1983 12	1975 - 1983 7
1.5 - 1.99	1973 - 1984 38	1973 - 1984 27	1975 - 1983 5	1973 - 1984 9
2.0 - 2.49	1973 - 1985 14	1973 - 1985 6	1973 - 1984 0	1973 - 1985 0
2.5 - 2.99	1973 - Date 3	1973 - Date 5	1973 - Date 1	1973 - Date 2
3.0 - 3.49	1973 - Date 0	1973 - Date 1	1973 - Date 0	1973 - Date 0
3.5 - 3.99	1961 - Date 2	1973 - Date 0	1961 - Date 0	1973 - Date 0
4.0 - 4.49	1930 - Date 3	1961 - Date 0	1950 - Date 1	1950 - Date 1
4.5 - 4.99	1880 - Date 1	1900 - Date 0	1900 - Date 1	1940 - Date 0
5.0 - 5.49	1850 - Date 1	1880 - Date 0	1850 - Date 0	1900 - Date 0
5.5 - 5.99	1850 - Date 0	1850 - Date 0	1850 - Date 0	1850 - Date 0
6.0 - 6.49	1850 - Date 0	1850 - Date 0	1850 - Date 0	1850 - Date 0

TABLE 3-3
RECURRENCE PARAMETERS FOR LANL COMPARED WITH OTHER ESTIMATES

Study Region	Area (km^2)	Total Number of earthquakes and magnitude range	Recurrence Parameters			Return Periods+(yrs)			
			a_{norm}*	a_{unnorm}**	b	$T_{M\,5}$	$T_{M\,5.5}$	$T_{M\,6}$	$T_{M\,6.3}$
Rio Grande Rift in N. New Mexico (this study)	11,250	24 M 2.0-5.5	-2.45	1.60	0.75 ± 0.1	141 (45-447)	335 (94-1189)	794 (200-3162)	1334 (313-5689)
Colorado Plateau Transition Zone (this study)	10,375	93 M 1.0-3.5	-2.17	1.84	0.9 ± 0.1	457 (145-1445)	1288 (363-4571)	3631 (912-14,454)	-
Southern Rocky Mountains (this study)	8,325	12 M 1.5-4.5	-2.80	1.12	0.8 ± 0.1	759 (240-2399)	1905 (537-6761)	4786 (1202-19,055)	8318 (1950-35,481)
Great Plains Province (this study)	4,650	8 M 1.5-5.0	-2.84	0.83	0.7 ± 0.1	468 (148-1479)	1047 (295-3715)	2344 (589-9333)	-
Whole of New Mexico La Forge and Anderson (1988)x	317,800	47 M 3.0-6.0	-2.76	2.74	0.86	36	98	266	717
New Mexico Region Sanford et al. (1976)x	697,000	68 M 2.5-4.1	-2.00	3.84	1.0	14	46	143	454
Arizona Anderson et al. (1987)x	368,000	34 M 3.0-5.5	-2.56	3.00	0.83	14	38	98	257

*a_{norm} is the normalized a-value at M 0
**a_{unnorm} is the unnormalized a-value at M 0
+Intervals incorporate the standard error of the b-value
xNote that the return periods in these regions are for a much larger area.

TABLE 3-4

EARTHQUAKE COMPLETENESS ESTIMATES AND NUMBER OF EVENTS USED IN RECURRENCE FOR CIRCULAR SOURCE REGIONS AROUND LOS ALAMOS

Magnitude Range (M_L)	Time Period and Number of Events			
	20-km Radius Circle	40-km Radius Circle	60-km Radius Circle	80-km Radius Circle
.5 - 0.99	1976-1983 3	1976-1983 29	1976-1983 69	1976-1983 109
1.0 - 1.49	1975-1983 5	1975-1983 25	1975-1983 56	1975-1983 84
1.5 - 1.99	1973-1984 5	1973-1984 15	1973-1984 29	1973-1984 49
2.0 - 2.49	1973-1985 0	1973-1985 5	1973-1985 9	1973-1985 9
2.5 - 2.99	1973-Date 0	1973-Date 2	1973-Date 3	1973-Date 6
3.0 - 3.49	1973-Date 0	1973-Date 0	1973-Date 1	1973-Date 1
3.5 - 3.99	1961-Date 0	1961-Date 0	1961-Date 0	1961-Date 0
4.0 - 4.49	1930-Date 0	1930-Date 2	1930-Date 2	1930-Date 2
4.5 - 4.99	1880-Date 0	1880-Date 0	1880-Date 0	1880-Date 0
5.0 - 5.49	1850-Date 0	1850-Date 0	1850-Date 1	1850-Date 1
5.5 - 5.99	1850-Date 0	1850-Date 0	1850-Date 0	1850-Date 0
6.0 - 6.49	1850-Date 0	1850-Date 0	1850-Date 0	1850-Date 0

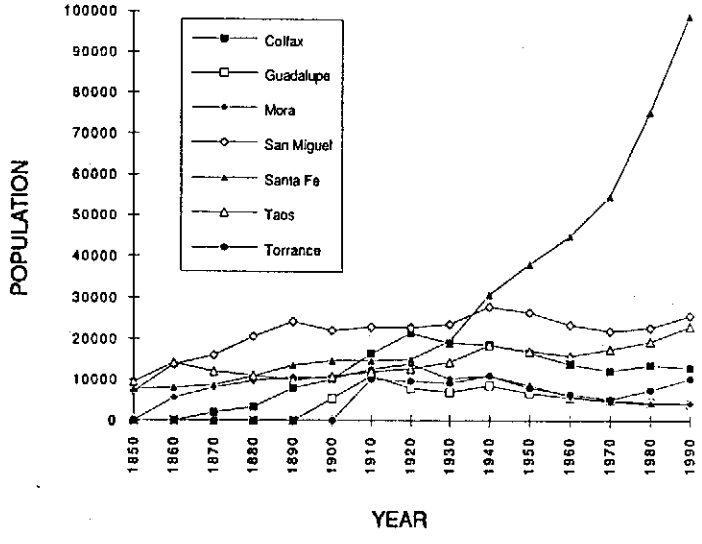
TABLE 3-5

RECURRENCE PARAMETERS FOR CIRCULAR REGIONS AROUND LOS ALAMOS

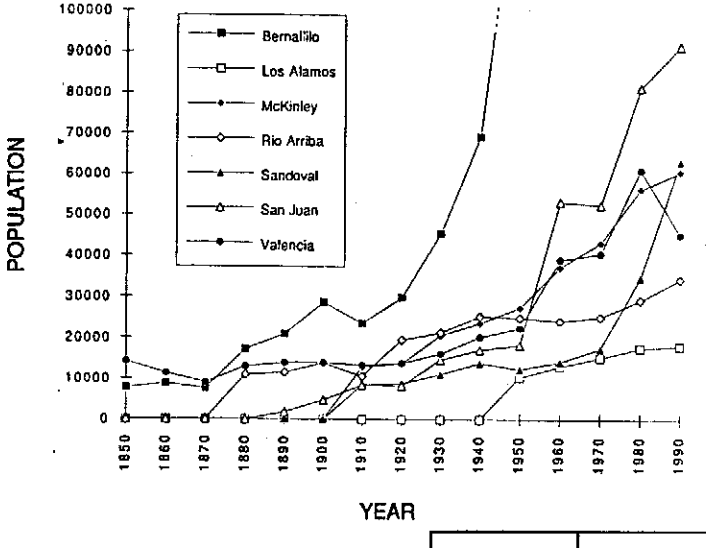
Study Region	Area (km^2)	Number of earthquakes and magnitude range	Recurrence Parameters			Return Periods+ (yrs)		
			a_{norm}*	a_{unnorm}**	b	T_{M5}	$T_{M5.5}$	T_{M6}
20 km radius circle	1257	13 (0.5-2.0)	-2.59	0.51	0.75 ± 0.14	1738 (347-8710)	4121 (700-24266)	9772 (1413-67608)
40 km radius circle	5027	78 (0.5-4.5)	-2.42	1.28	0.75 ± 0.06	295 (148-589)	700 (327-1496)	1650 (724-3802)
60 km radius circle	11,310	170 (0.5-5.5)	-2.40	1.65	0.78 ± 0.04	178 (112-282)	437 (263-724)	1072 (617-1862)
80 km radius circle	20,106	261 (0.5-5.5)	-2.45	1.85	0.81 ± 0.04	158 (100-251)	403 (243-668)	1023 (587-1778)

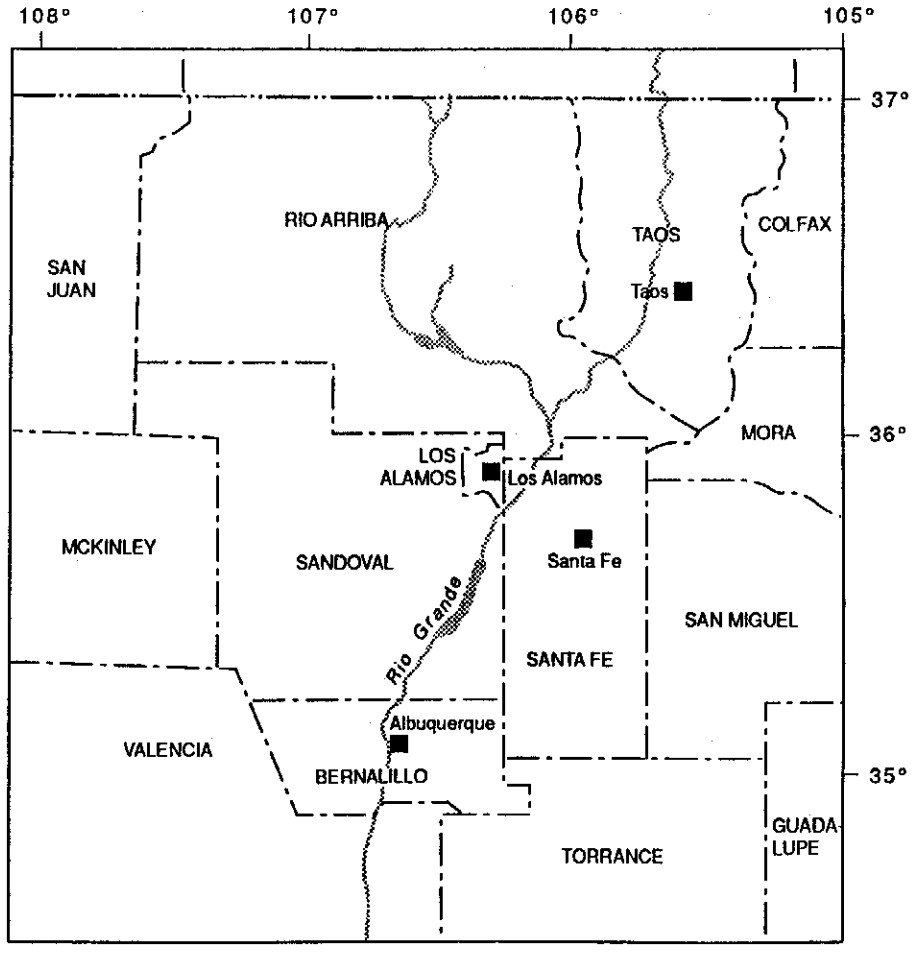
*a_{norm} is the normalized a-value at M 0
**a_{unnorm} is the unnormalized a-value at M 0
+Intervals incorporate the standard error of the b-value

EASTERN COUNTIES



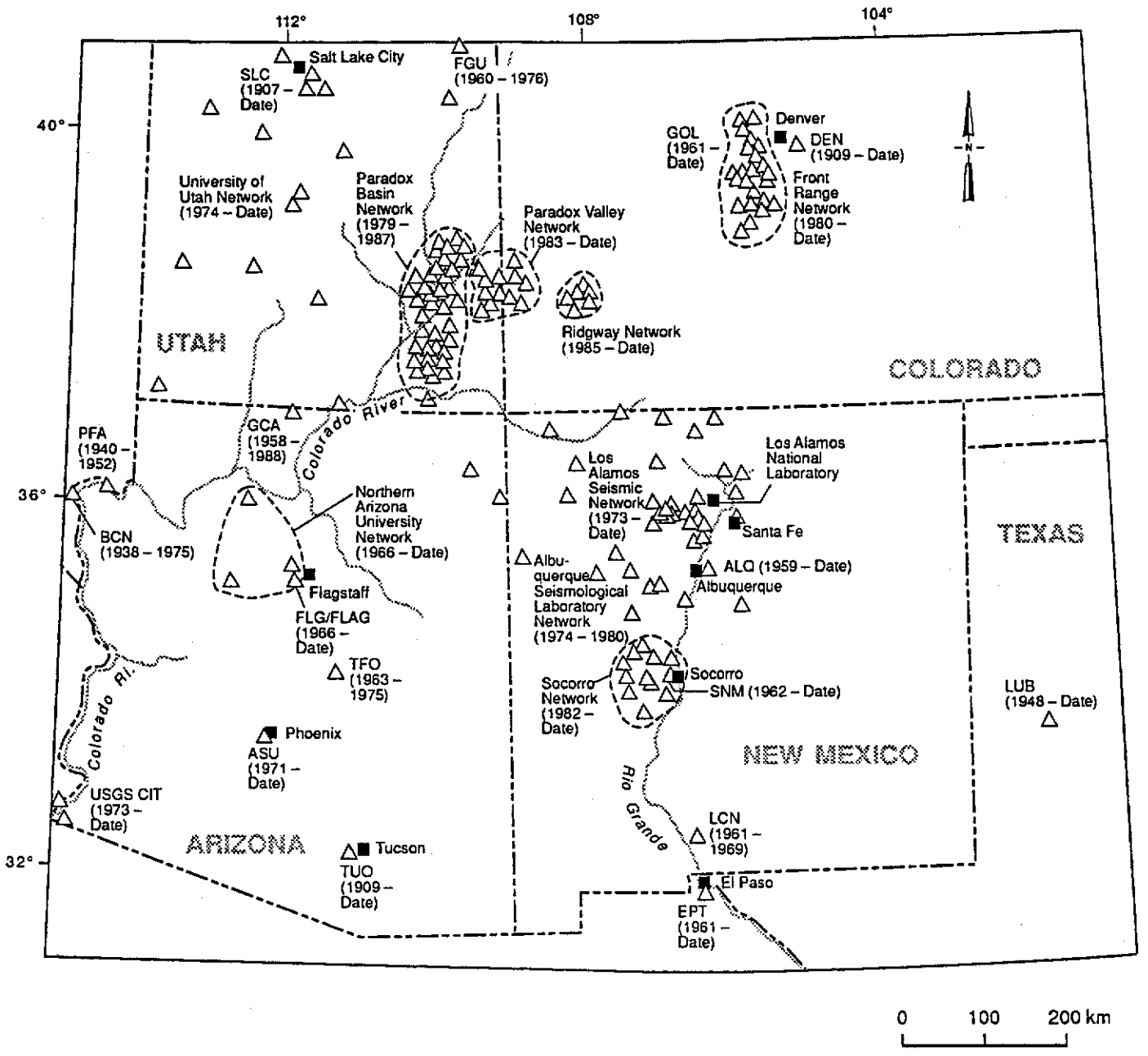
WESTERN COUNTIES





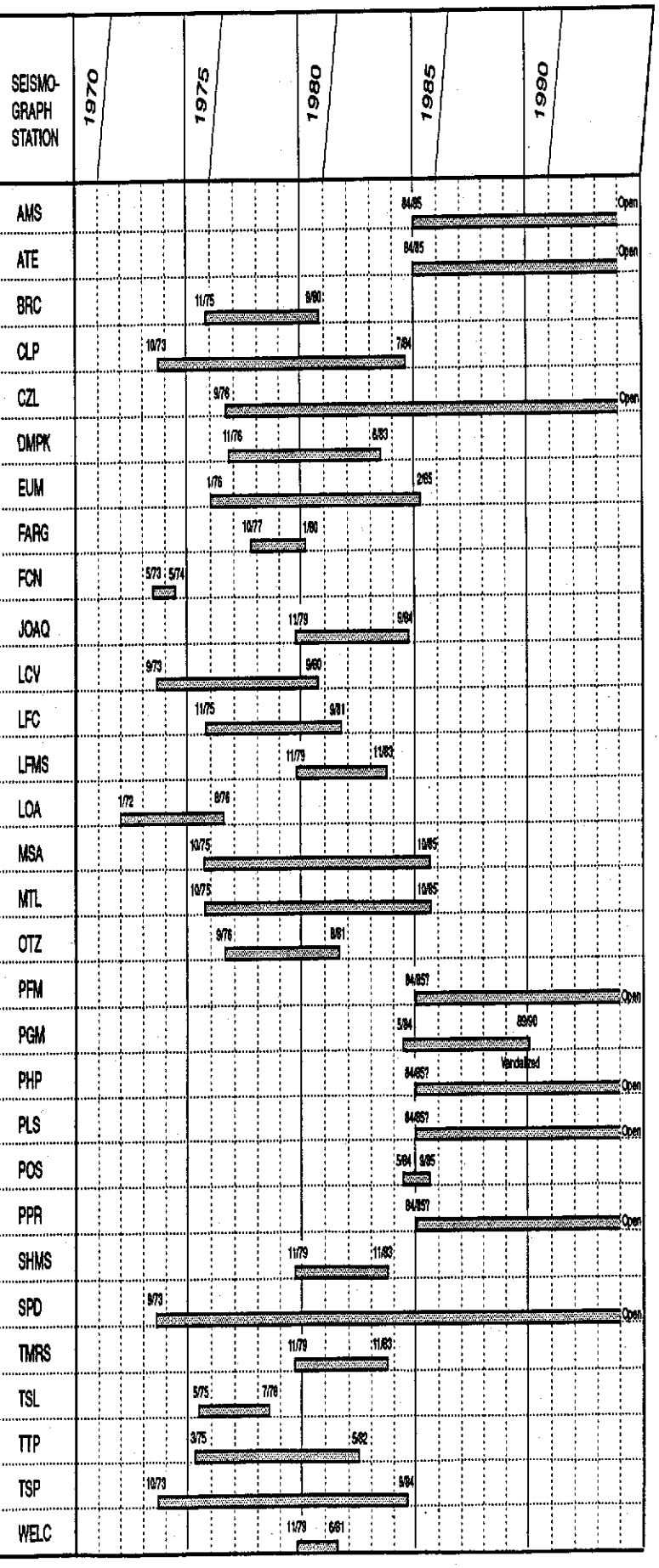
Project No. 91C0509	Los Alamos Seismic Hazards	POPULATION GROWTH AROUND THE LANL REGION	Figure 3-1
Woodward-Clyde Federal Services			

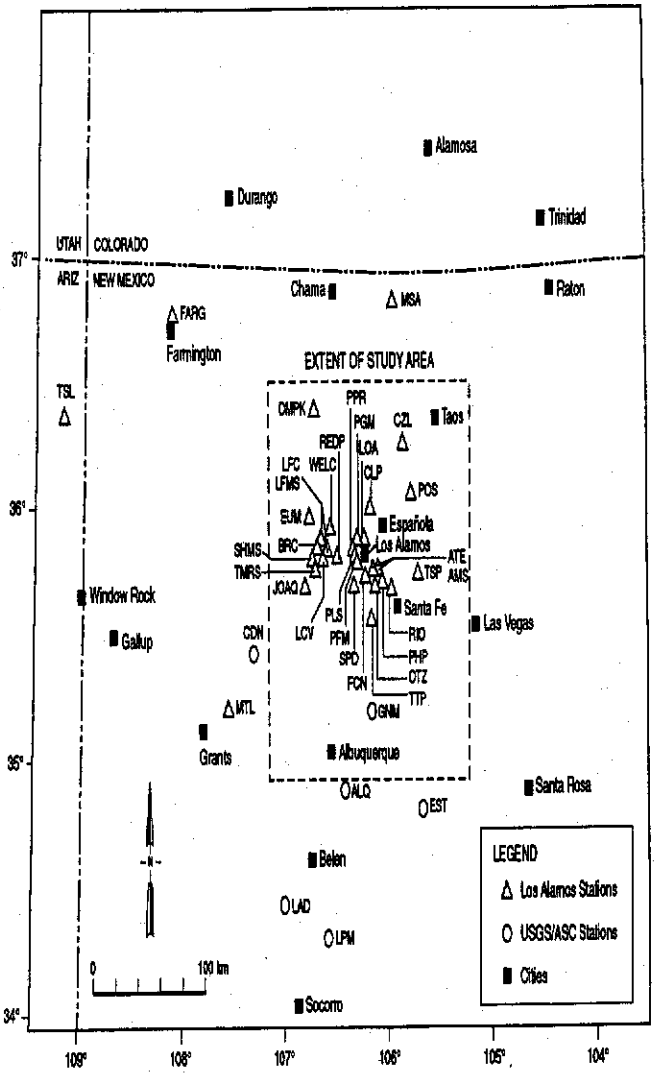
91C0509A-1300/053093



Project No. 91C0509	Los Alamos Seismic Hazards	SIGNIFICANT SEISMOGRAPH STATIONS AND NETWORKS IN THE LANL REGION	Figure 3-2
Woodward-Clyde Federal Services			

91C0509A-1300/053093

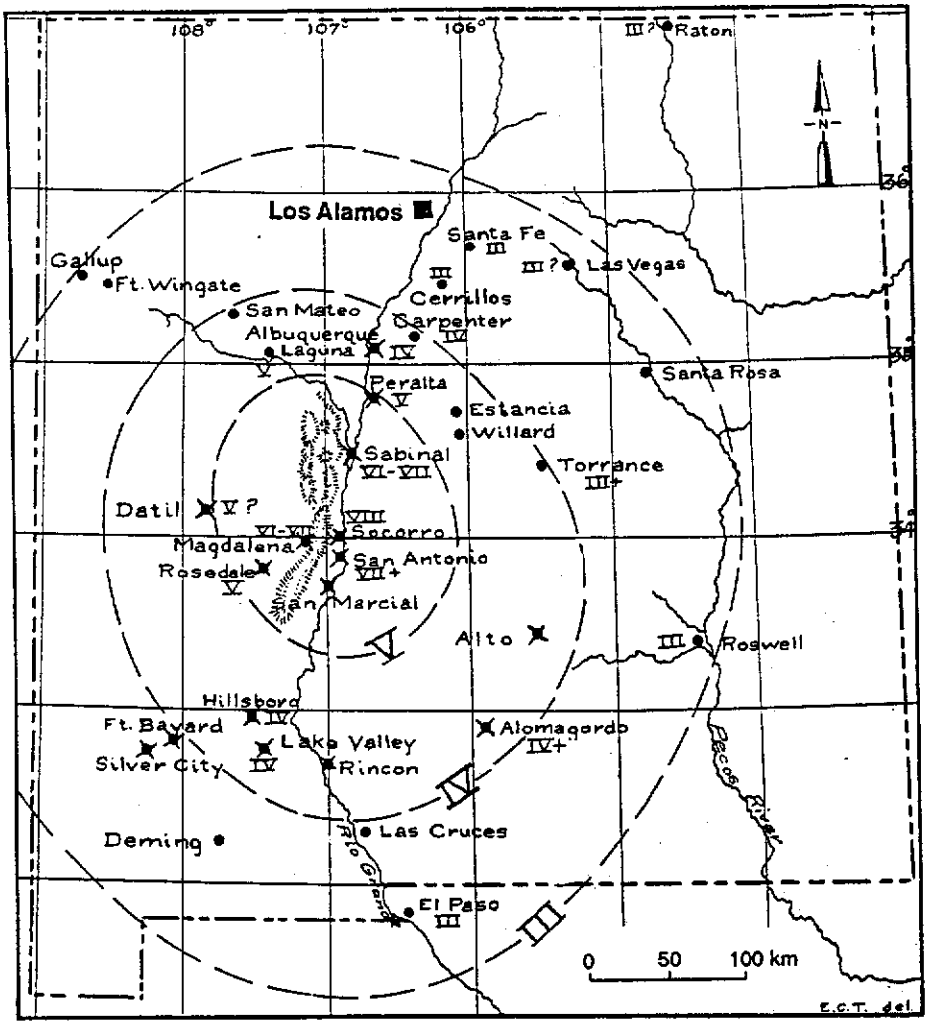




Source: Modified from Wolff et al. (1984)

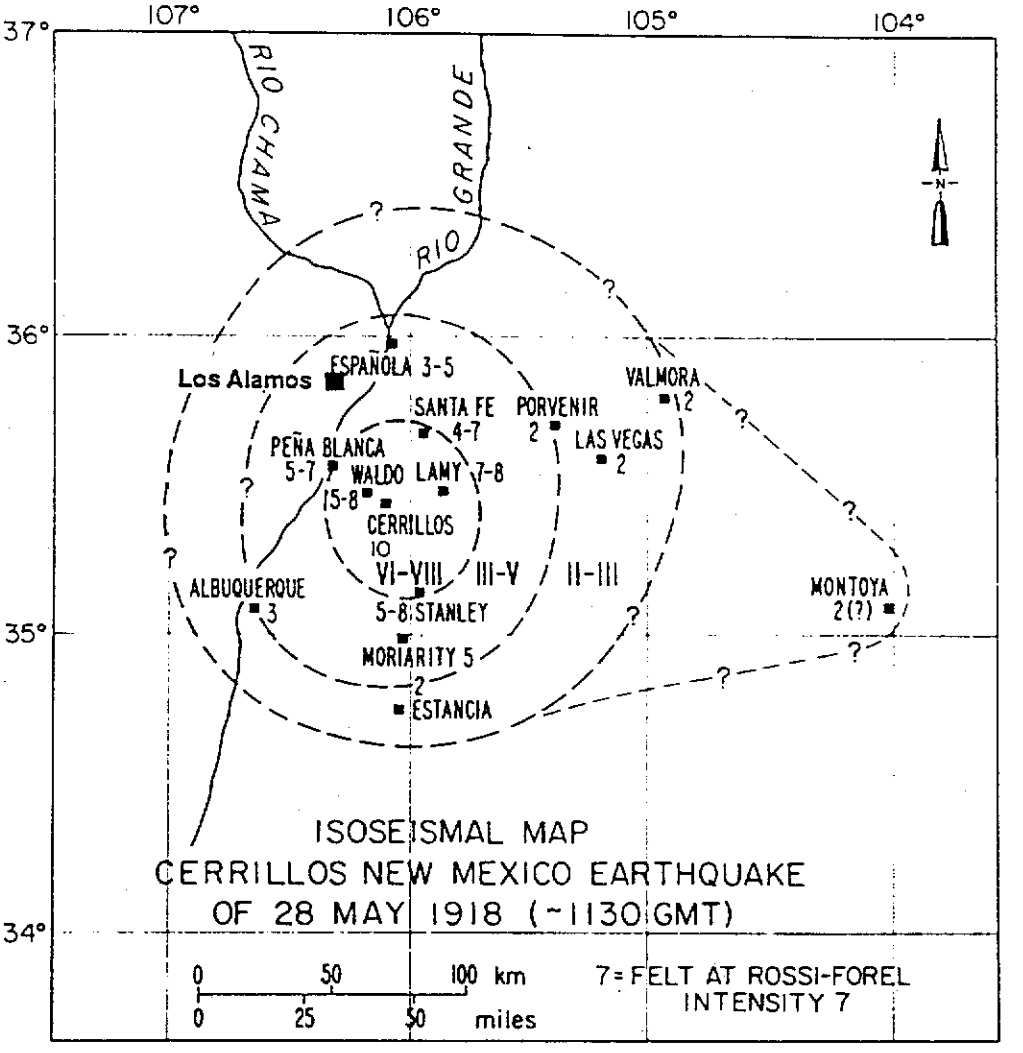
Project No. 91C0509	Los Alamos Seismic Hazards	LOS ALAMOS SEISMOGRAPH NETWORK LOCATIONS AND APPROXIMATE OPERATIONAL PERIODS	Figure 3-3
	Woodward-Clyde Federal Services		

1300/052993



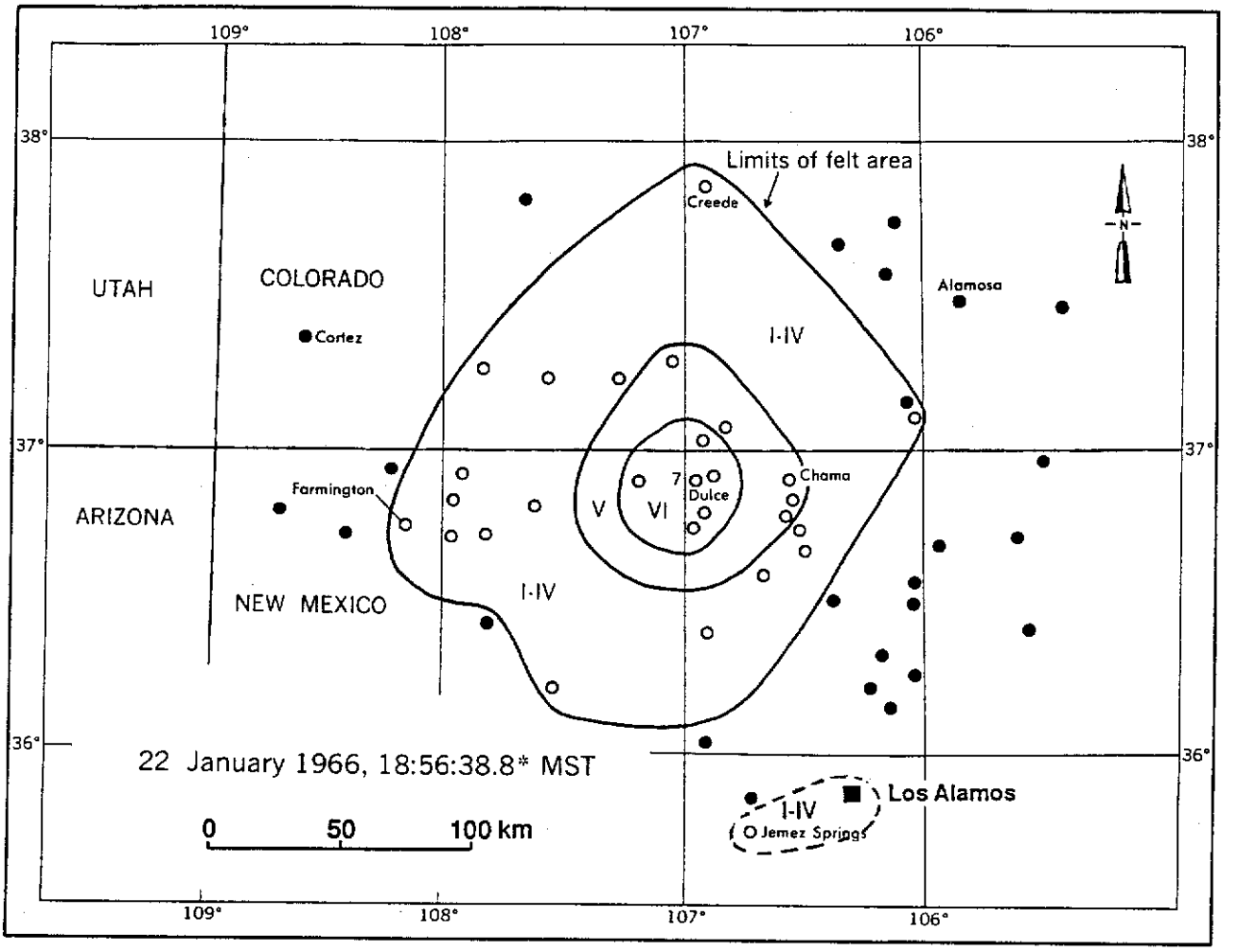
Source: Reid, 1911

Project No. 91C0509	Los Alamos Seismic Hazards	ISOSEISMAL MAP FOR THE 15 NOVEMBER 1906 SOCORRO EARTHQUAKE	Figure 3-4
Woodward-Clyde Federal Services			



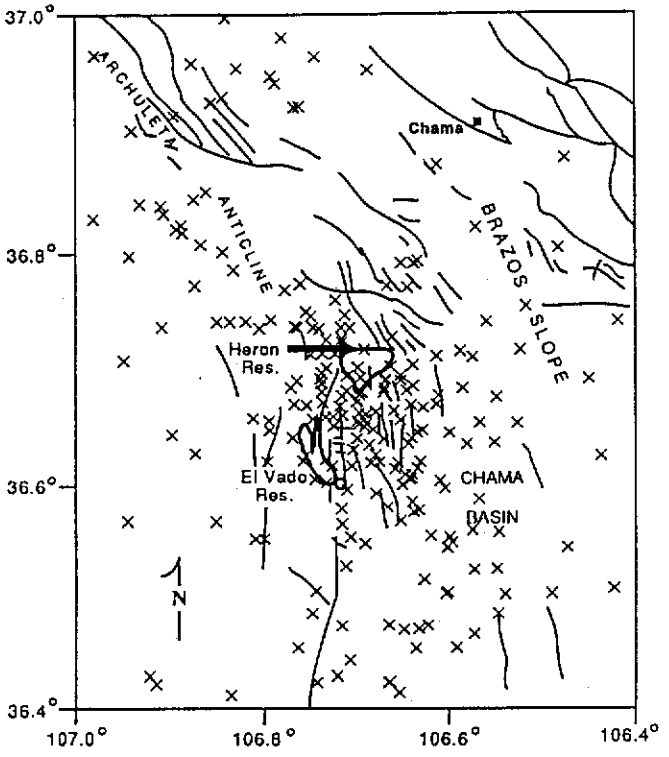
Source: Olsen, 1979

Project No. 91C0509	Los Alamos Seismic Hazards	ISOSEISMAL MAP FOR THE 28 MAY 1918 CERRILLOS EARTHQUAKE	Figure 3-5
Woodward-Clyde Federal Services			

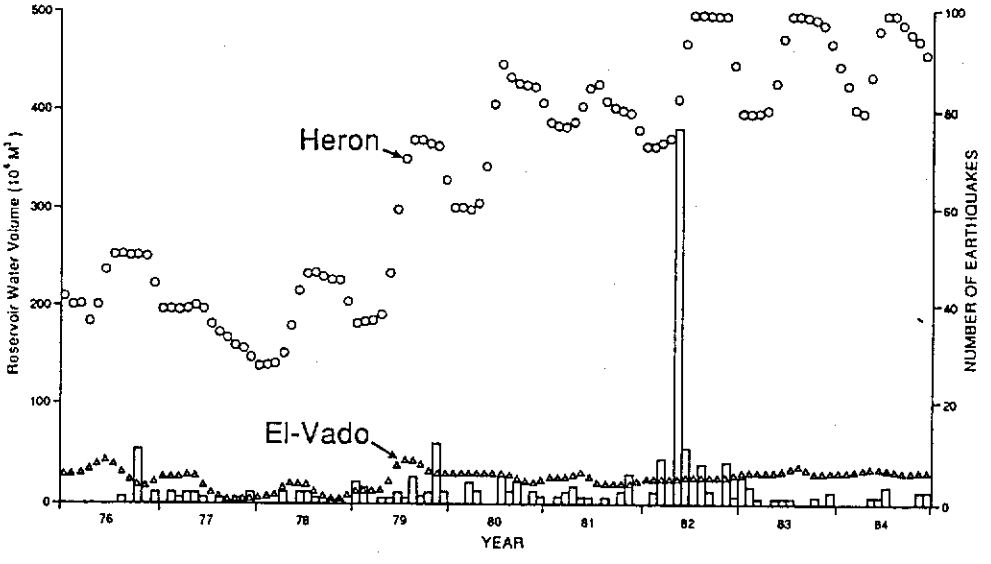


Source: von Hake and Cloud, 1968

Project No. 91C0509	Los Alamos Seismic Hazards	ISOSEISMAL MAP FOR THE 22 JANUARY 1966 Ms 4.9 DULCE EARTHQUAKE	Figure 3-6
Woodward-Clyde Federal Services			



Seismotectonic map of the study area, showing all epicenters, mapped faults and the maximum extent of the Heron-El Vado reservoirs. Faults and structure are from Smith and Muehlberger (1960).

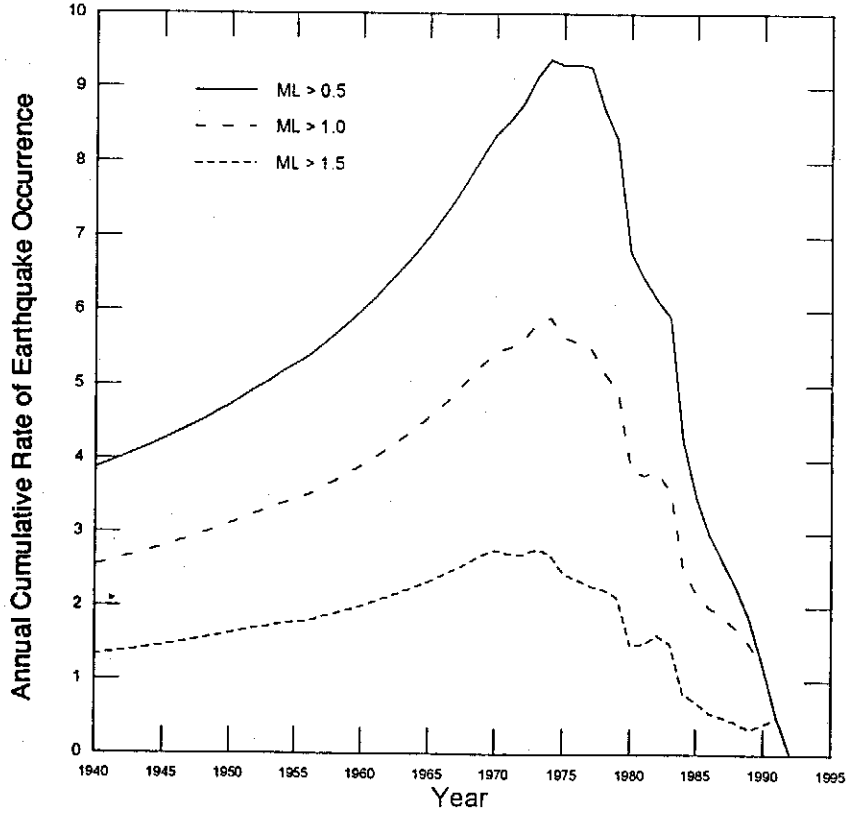


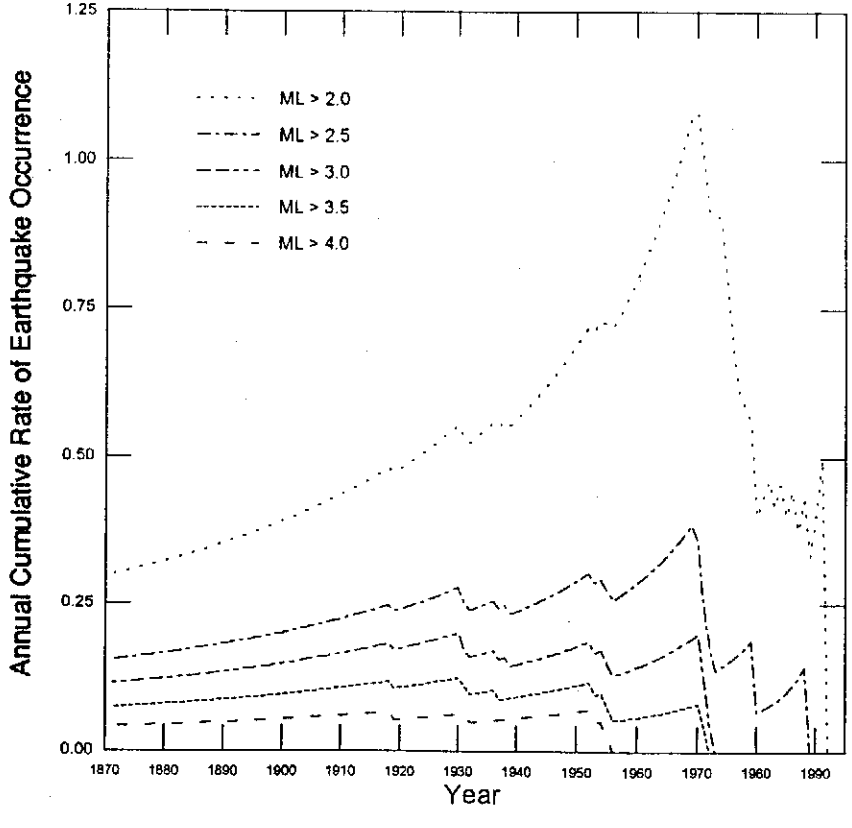
Average reservoir volumes (m^3) for each month plotted as a function of seismicity. Bars represent monthly number of shocks within the study area (within 35 km of reservoirs).

Source: El-Hussain and Carpenter (1990)

Project No. 91C0509	Los Alamos Seismic Hazards	LOCATIONS OF RESERVOIR INDUCED SEISMICITY AT HERON-EL VADO RESERVOIRS AND CORRELATION BETWEEN RESERVOIR VOLUME AND EARTHQUAKE OCCURRENCE	Figure 3-7
Woodward-Clyde Federal Services			

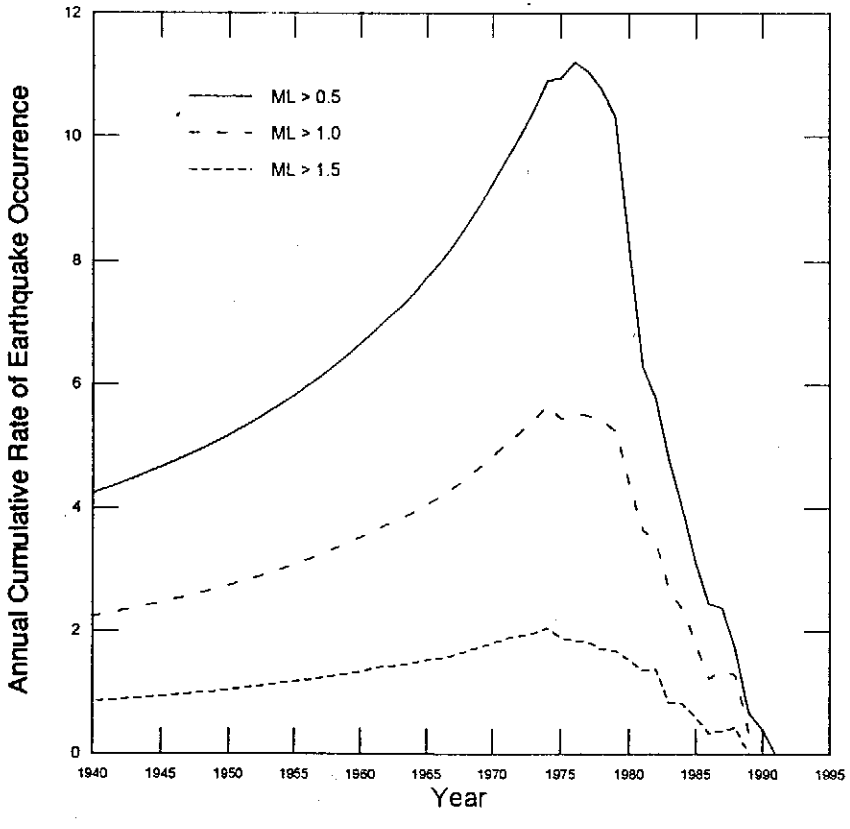
Rio Grande Rift Province

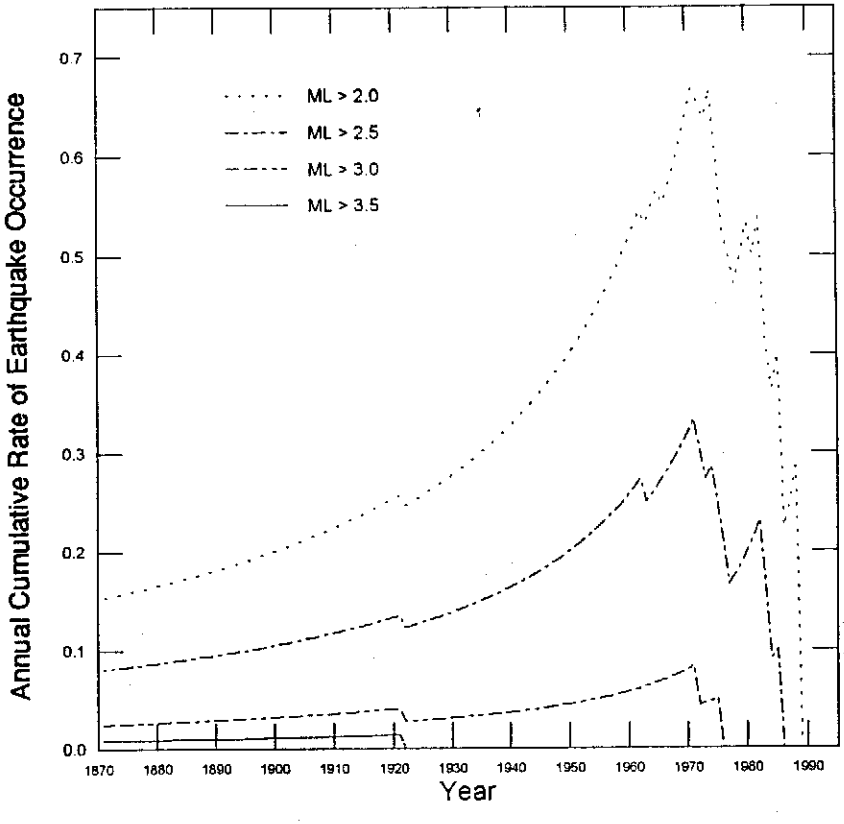




Project No. 91C0509	Los Alamos Seismic Hazards	ANNUAL CUMULATIVE RATES OF INDEPENDENT EARTHQUAKE OCCURRENCE FOR THE RIO GRANDE RIFT	Figure 3-8
Woodward-Clyde Federal Services			

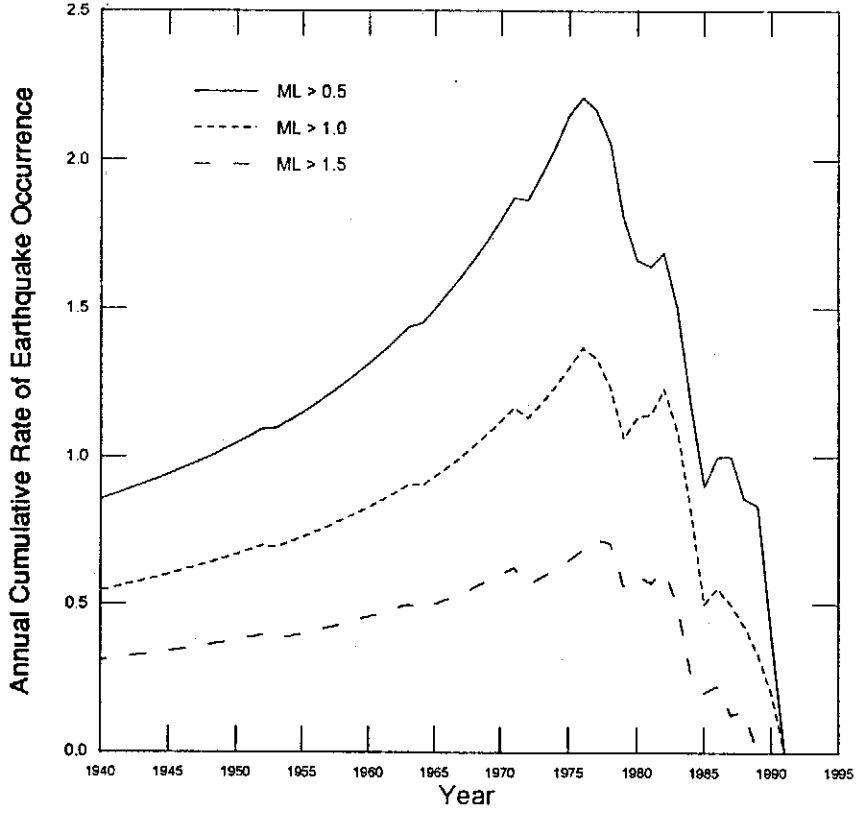
Colorado Plateau Transition Zone

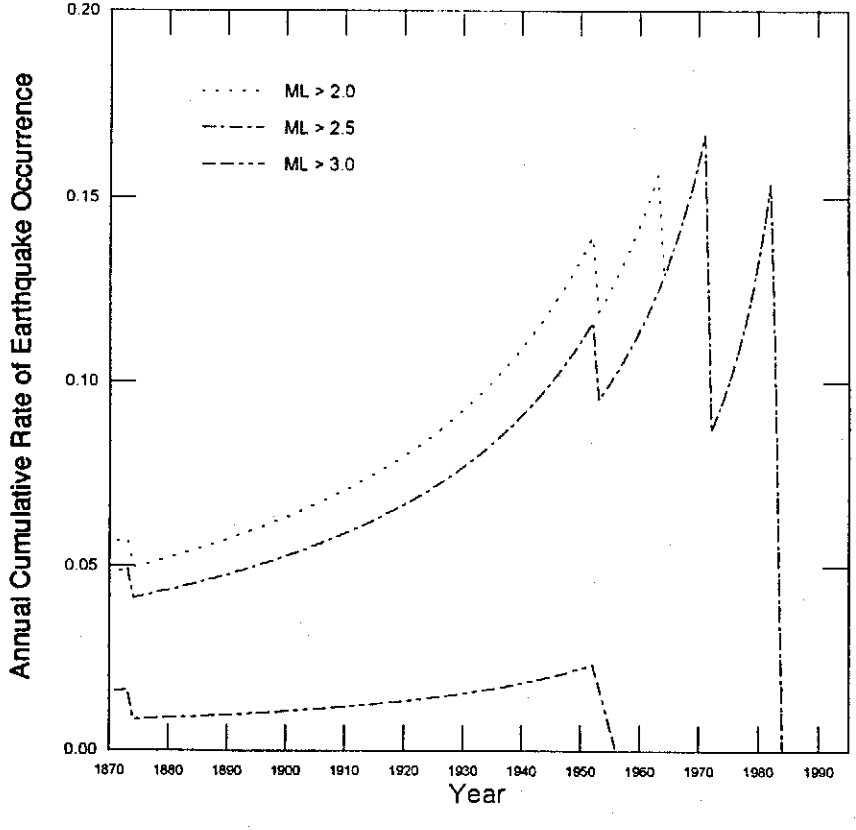




Project No. 91C0509	Los Alamos Seismic Hazards	ANNUAL CUMULATIVE RATES OF INDEPENDENT EARTHQUAKE OCCURRENCE FOR THE COLORADO PLATEAU TRANSITION ZONE	Figure 3-9
Woodward-Clyde Federal Services			

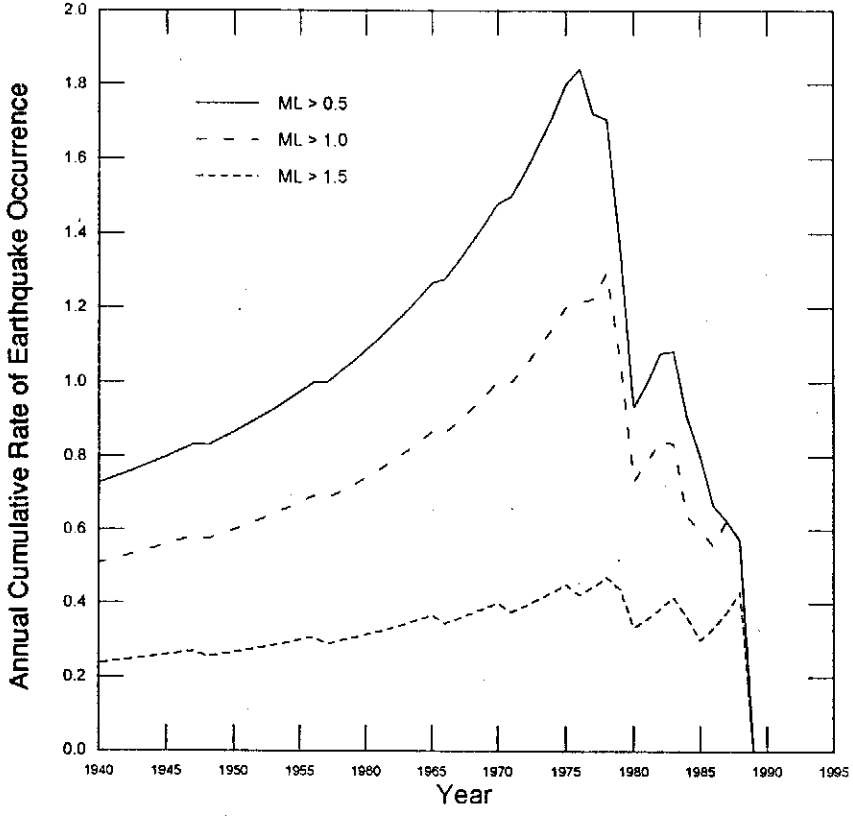
Southern Rocky Mountains Province

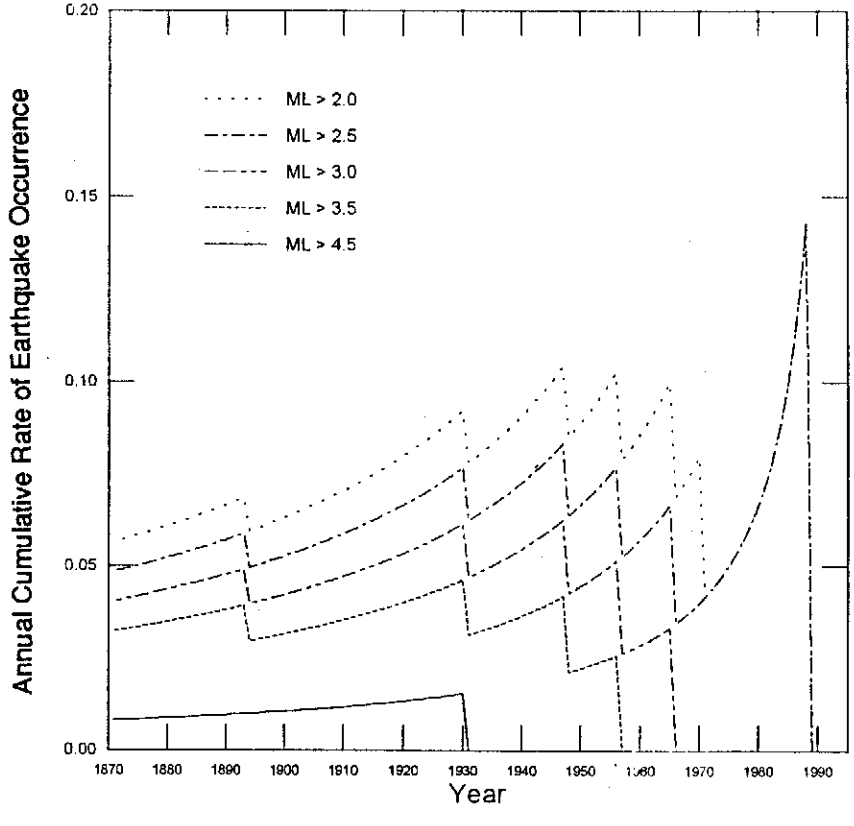




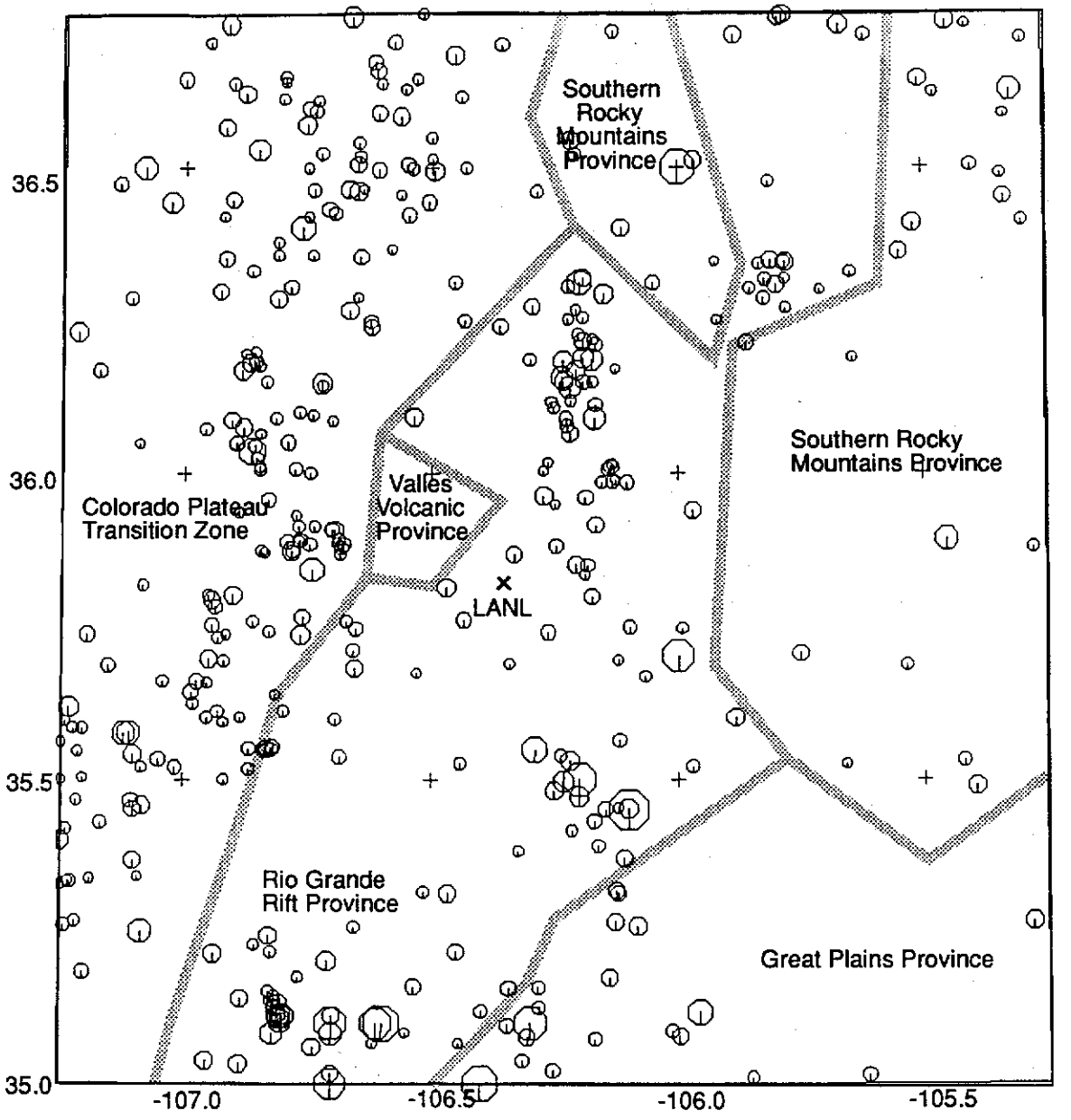
Project No. 91C0509	Los Alamos Seismic Hazards	ANNUAL CUMULATIVE RATES OF INDEPENDENT EARTHQUAKE OCCURRENCE FOR THE SOUTHERN ROCKY MOUNTAINS	Figure 3-10
Woodward-Clyde Federal Services			

Great Plains Province





Project No. 91C0509	Los Alamos Seismic Hazards	ANNUAL CUMULATIVE RATES OF INDEPENDENT EARTHQUAKE OCCURRENCE FOR THE GREAT PLAINS	Figure 3-11
Woodward-Clyde Federal Services			



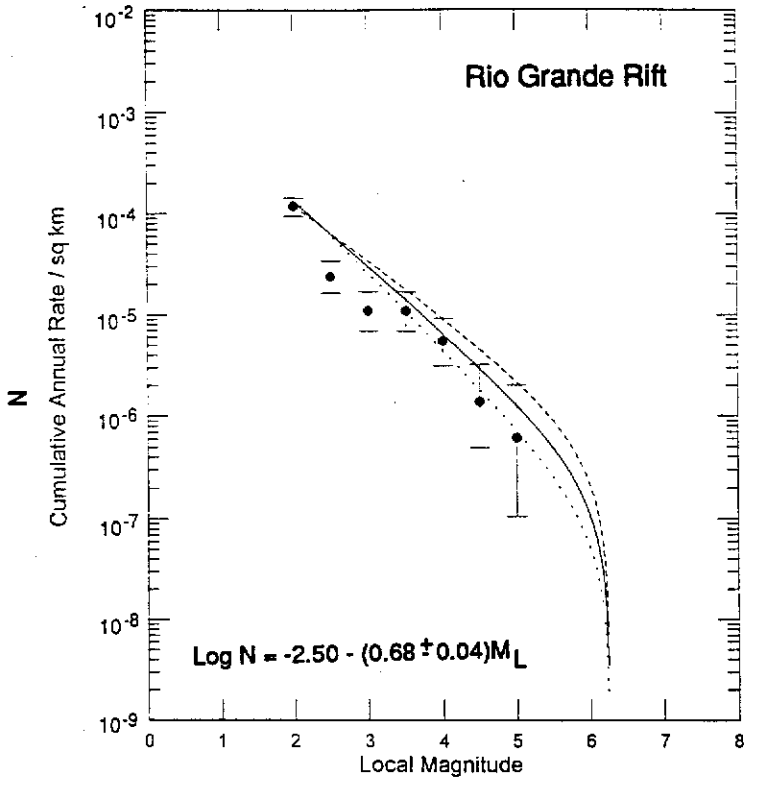
Magnitude

.0
1.0
2.0
3.0
4.0
5.0
6.0
7.0

0 20
kilometers

N

Project No. 91C0509	Los Alamos Seismic Hazards	HISTORICAL SEISMICITY USED IN RECURRENCE FOR THE SEISMOTECTONIC PROVINCES	Figure 3-12
Woodward-Clyde Federal Services			



Rio Grande
Magnitude cutoff 2.0
Maximum magnitude 6.25

b fixed at 0.65; a = -2.466

b fixed at 0.75; a = -2.333

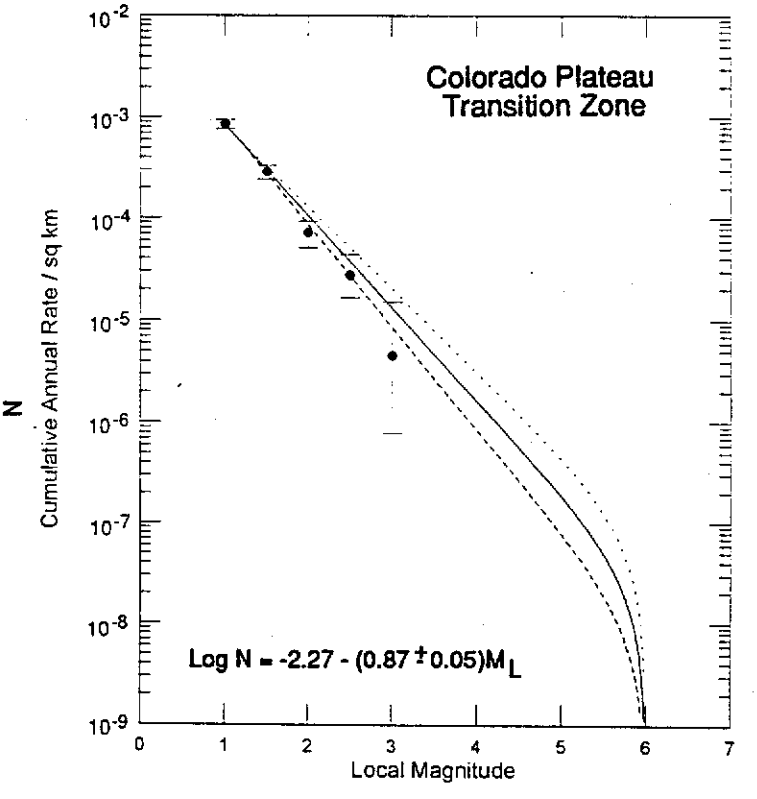
b fixed at 0.85; a = -2.211

Colorado Transition Zone
Magnitude cutoff 1.0
Maximum magnitude 6.0

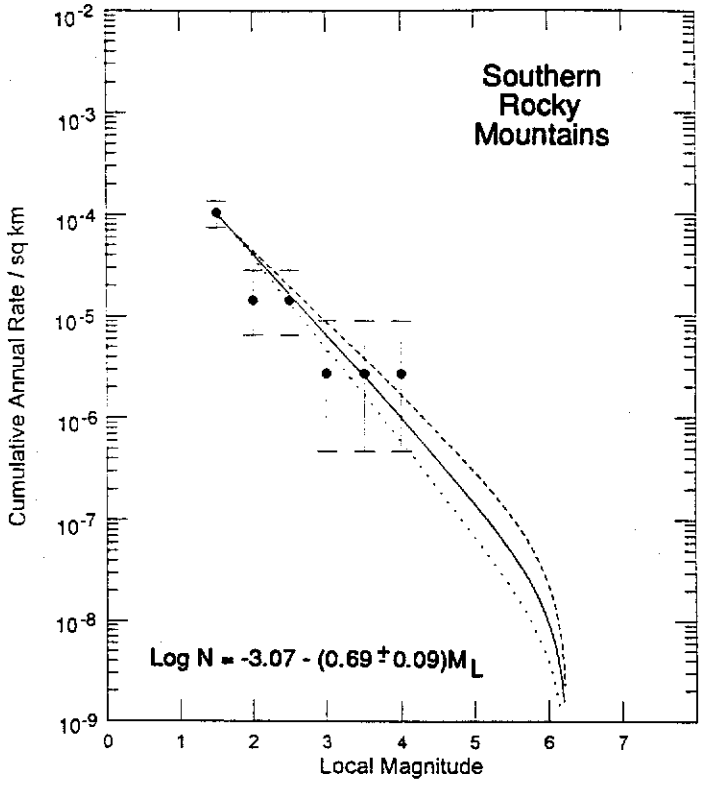
b fixed at 0.8; a = -2.290

b fixed at 0.9, a = -2.174

b fixed at 1.0; a = -2.062



Project No. 91C0509	Los Alamos Seismic Hazards	EARTHQUAKE RECURRENCE FOR THE RIO GRANDE RIFT PROVINCE AND THE COLORADO PLATEAU TRANSITION ZONE	Figure 3-13
Woodward-Clyde Federal Services			

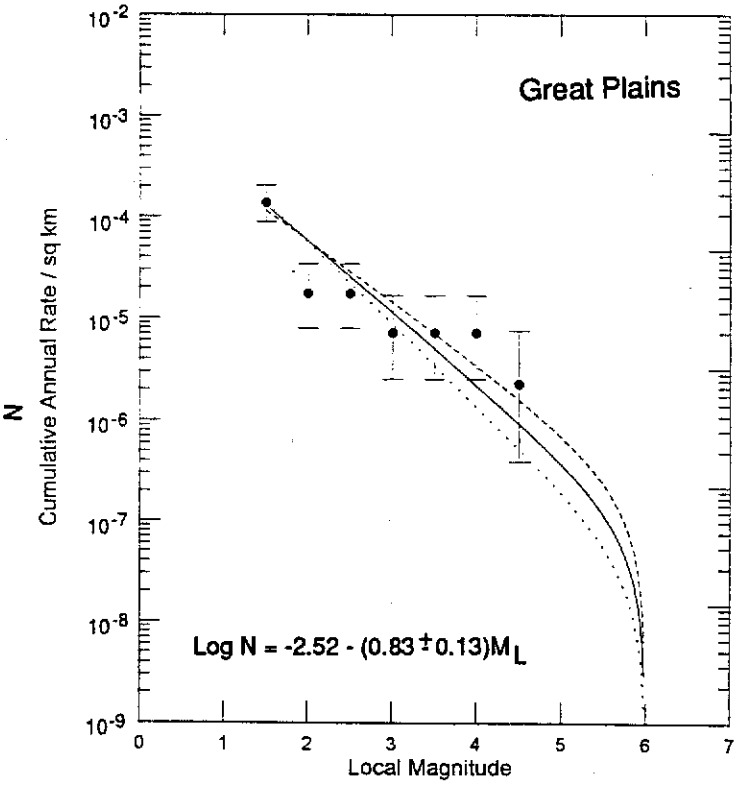


Southern Rocky Mountains
Magnitude cutoff 1.5
Maximum magnitude 6.25

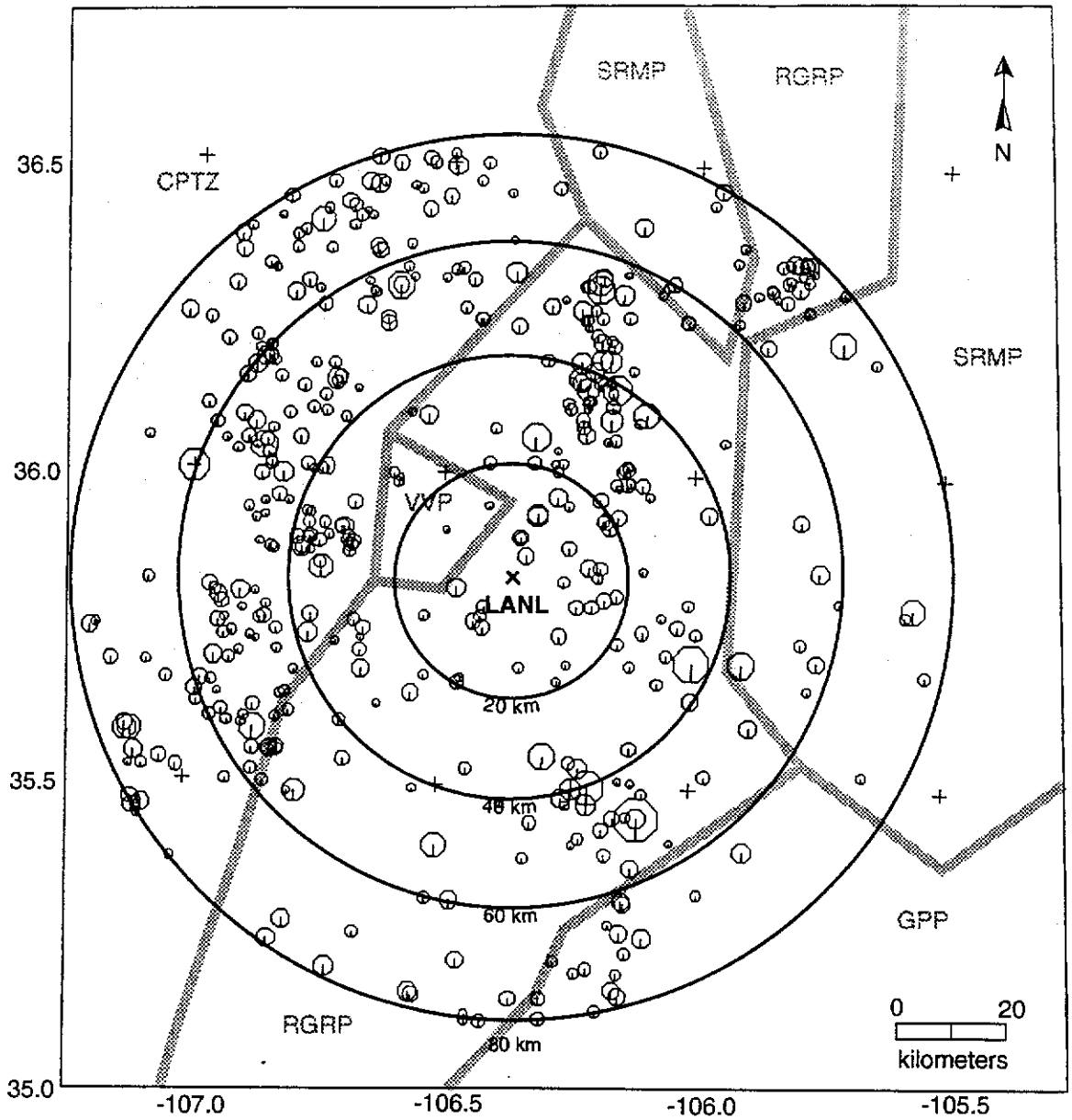
- b fixed at 0.7; a = -2.959
- b fixed at 0.8; a = -2.788
- b fixed at 0.9; a = -2.623

Great Plains
Magnitude cutoff 1.5
Maximum magnitude 6.0

- b fixed at 0.6; a = -2.478
- b fixed at 0.7; a = -3.308
- b fixed at 0.8 a = -2.654



Project No. 91C0509	Los Alamos Seismic Hazards	EARTHQUAKE RECURRENCE FOR THE SOUTHERN ROCKY MOUNTAINS AND GREAT PLAINS PROVINCES	Figure 3-14
Woodward-Clyde Federal Services			



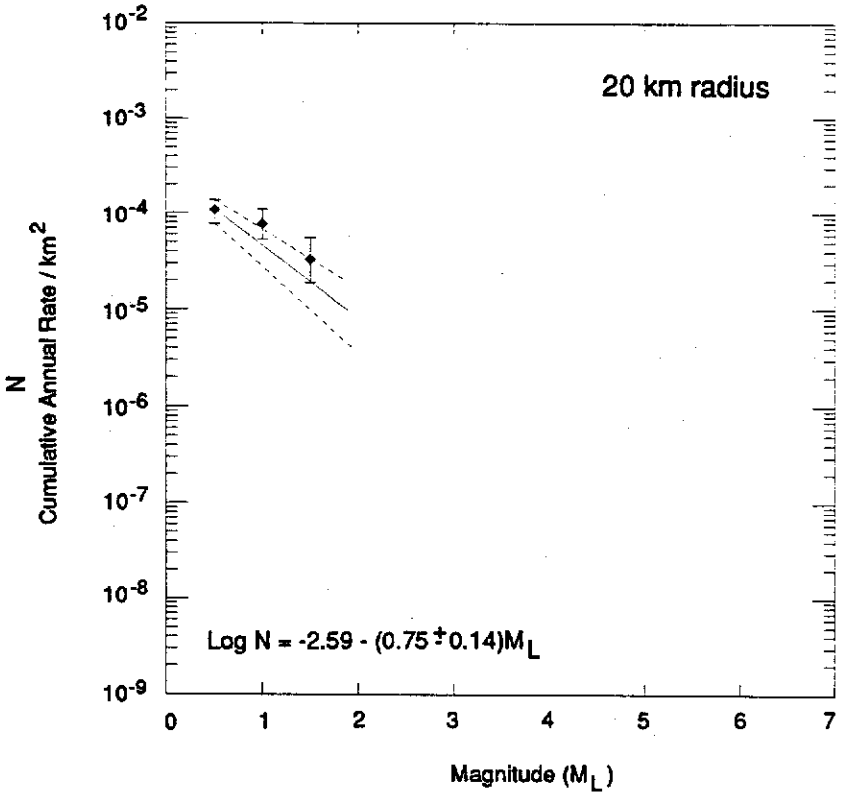
LEGEND

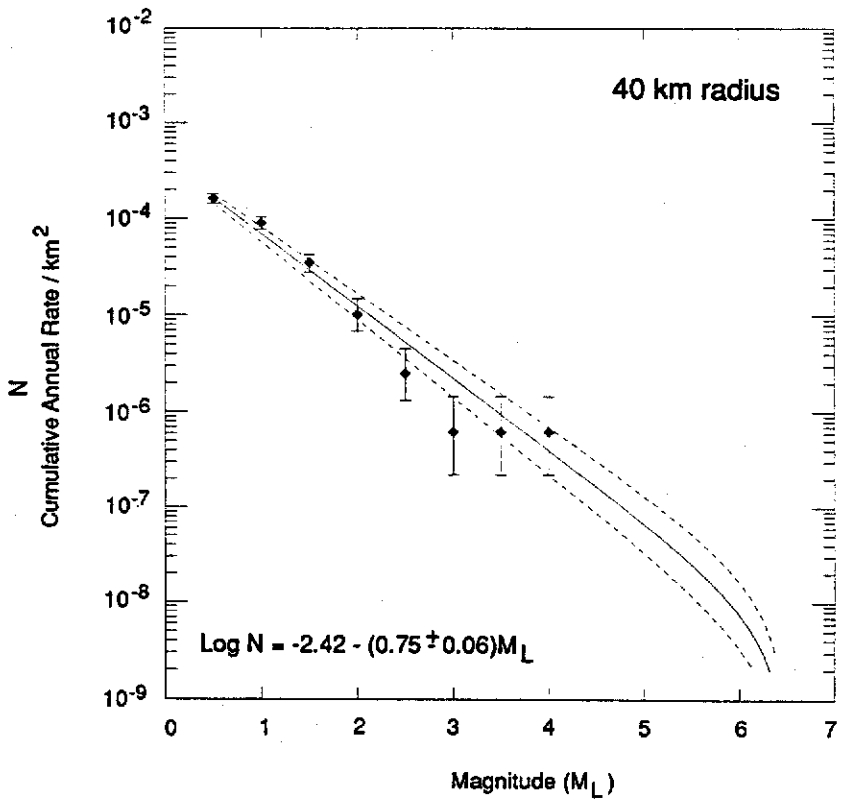
CPTZ	Colorado Plateau Transition Zone
GPP	Great Plains Province
RGRP	Rio Grande Rift Province
SRMP	Southern Rocky Mountains Province
VVP	Valles Volcanic Province
LANL	Los Alamos National Laboratory

Magnitude

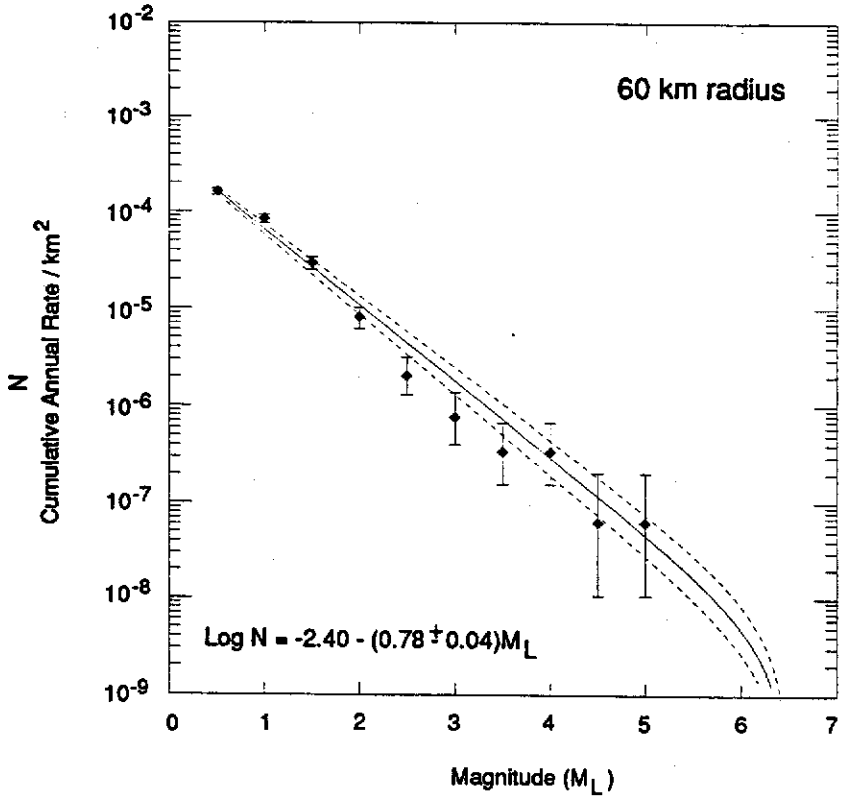
.0
1.0
2.0
3.0
4.0
5.0
6.0
7.0

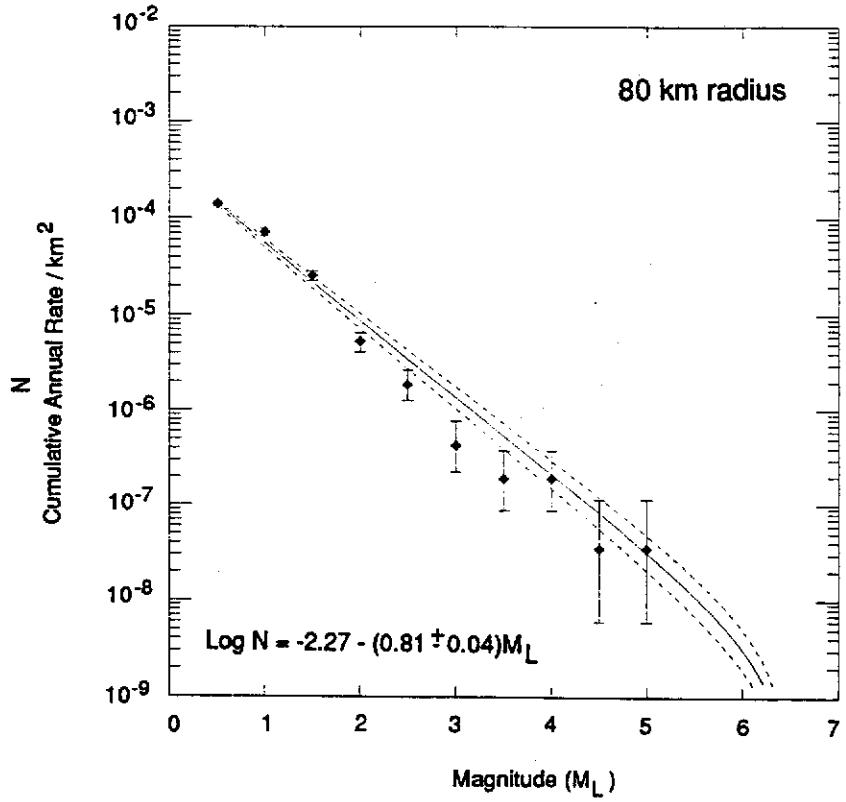
Project No. 91C0509	Los Alamos Seismic Hazards	HISTORICAL SEISMICITY USED IN RECURRENCE FOR SELECTED RADII AROUND LOS ALAMOS	Figure 3-15
Woodward-Clyde Federal Services			





Project No. 91C0509	Los Alamos Seismic Hazards	EARTHQUAKE RECURRENCE FOR 20 AND 40 KM RADIUS CIRCLES AROUND LOS ALAMOS	Figure 3-16
Woodward-Clyde Federal Services			





Project No. 91C0509	Los Alamos Seismic Hazards	EARTHQUAKE RECURRENCE FOR 60 AND 80 KM RADIUS CIRCLES AROUND LOS ALAMOS	Figure 3-17
Woodward-Clyde Federal Services			

4.0
GEOLOGIC INVESTIGATIONS

A critical element of the evaluation of seismic hazards at a specific location is the geologic characterization of potentially significant seismogenic sources. We focused our geologic investigations on the three closest and most significant faults to LANL: the Pajarito, Rendija Canyon, and Guaje Mountain faults. These studies included detailed investigations at specific sites along each of these three faults. In order to provide a regional surficial geologic framework for data collected at these sites, we also conducted reconnaissance-level surficial mapping along the Pajarito fault adjacent to LANL. In addition, we constructed several topographic profiles of fault scarps along the Pajarito, Rendija Canyon, and Guaje Mountain faults in order to assess the style and amount of late Cenozoic deformation. We also conducted reconnaissance-level studies of the Embudo fault and faults of Black Mesa, in order to better understand these potentially seismogenic sources. The sections below describe our regional surficial geology investigations (Section 4.1), which included surficial mapping (Section 4.1.1), topographic profiling (Section 4.1.2), and reconnaissance fault studies (Section 4.1.3), as well as detailed site-specific paleoseismologic investigations (Section 4.2).

4.1 REGIONAL SURFICIAL GEOLOGY INVESTIGATIONS

Investigations of surficial deposits at a regional scale are an important element in the assessment of paleoseismic characteristics of individual faults, because they provide a regional framework to interpret surficial processes at specific paleoseismic sites. Such a framework allows for the assessment of erosional and depositional processes that are related to or influenced by fault displacements. Thus, an understanding of the regional geomorphology and near-surface stratigraphy is essential for the evaluation of the nature, timing, and amount of surface displacements along faults in the LANL region. In addition, regional surficial geologic investigations allow for the identification of sites that are most likely to yield important paleoseismic information.

4.1.1 Generalized Late Quaternary Surficial Geology of the Pajarito Plateau

The primary goals of the reconnaissance mapping of surficial deposits were to identify paleoseismic sites and to provide information on the types and relative ages of surficial deposits at these potential sites. The following sections describe the methods, results, and interpretations of this investigation.

4.1.1.1 Methods

Our investigation of the surficial geology of the Pajarito Plateau consisted of analysis of aerial photography, aerial reconnaissance, and reconnaissance-level field mapping. Analysis of aerial photography is a commonly used technique to rapidly and efficiently assess the presence or absence of potentially fault-related geomorphic features throughout a large area. In addition, aerial photography provides a means to quickly target areas or localities that promise to provide important information on paleoseismic fault characteristics.

Several types and vintages of aerial photography and remote sensing imagery were employed during the regional investigations. These included color infrared imagery of the Pajarito fault system, the southern part of the Embudo fault, and the northern parts of the Puye, La Bajada and San Francisco faults. This imagery, which was obtained from the U.S. Department of Interior, consists of 26 images of stereo coverage from the National High-Altitude Program (NHAP2), taken in July 1986 and July 1987 at a scale of 1:58,000. Vertical color photography available from the U.S. Forest Service also was interpreted. These photographs were taken in 1975 at a scale of 1:24,000, and covered the western Pajarito Plateau. Lastly, vertical stereo black-and-white photography of the Pajarito, Rendija Canyon, and Guaje Mountain faults was obtained during this investigation at a scale of 1:12,000. This photography consists of 119 images taken under low-sun-angle conditions on the mornings of 16 and 23 July 1991. The low-sun-angle photography covers the area along the three major fault traces between Peralta Canyon on the south and Santa Clara Canyon on the north.

Geomorphic features that are potentially related to faults and/or surface deformation were identified on the imagery or aerial photography. These features include: 1) alignments of vegetation; 2) linear valleys or stream segments; 3) knickpoints or waterfalls along streams;

4) alignments of ponds, springs, or marshy areas; 5) linear changes in vegetation, photographic tone of soils and deposits, drainage, or erosional texture; 6) deflected drainages; and 7) alignments of topographic elements such as facets, scarps, depressions, or saddles. Geologic and geomorphic interpretations were recorded on mylar overlays attached to individual photographs and were checked during subsequent field studies.

An aerial reconnaissance flight was conducted to assist in the identification and delineation of potentially fault-related surficial features, to help identify possible sites for detailed investigations, and to provide additional information on the geomorphic expression of major faults within the LANL region. The flight occurred on the morning of 21 July 1991 during low-sun-angle conditions, which typically provide shadowing and other lighting conditions that promote identification of potentially fault-related features. The aerial reconnaissance included overflights of the entire Pajarito fault between Peralta Canyon on the south and Clara Peak on the north, the Rendija Canyon and Guaje Mountain faults, the Embudo fault from its intersection with the northern part of the Pajarito fault near Clara Peak to its intersection with the Sangre de Cristo fault near Taos, the Sangre de Cristo fault directly east of Taos, and the La Bajada fault between Cochiti Lake and Highway 25 (Plate 2). This reconnaissance provided an excellent comparison of the relative geomorphic expression of these major rift structures and helped identify sites for later detailed investigation. For example, the reconnaissance showed the presence of a prominent lineament across the floor of the Los Alamos County Landfill coincident with a strand of the Rendija Canyon fault (Section 4.2.2).

Field investigations were conducted to verify tectonic and geomorphic features identified during aerial reconnaissance and analysis of aerial photography, to identify additional potentially fault-related features or other significant landforms, to delineate surficial deposits present across fault traces, and to help develop a preliminary assessment of Quaternary surficial deposits. In addition, the field studies included selection of sites for detailed paleoseismic investigations (Section 4.2). Field mapping was conducted intermittently during the summers of 1991 and 1992, using the USGS Frijoles and Guaje Mountains quadrangles enlarged to a scale of 1:12,000. The emphasis of the mapping was on the deposits along the section of the Pajarito fault between Los Alamos and Water Canyons (Plate 4).

4.1.1.2 Results

Primary and secondary fault traces traversing the Pajarito Plateau were delineated based on aerial reconnaissance, analysis of aerial photography, and field mapping (Plate 2). Many of these traces are coincident with traces identified by previous investigations (Griggs, 1964; Smith et al., 1970; Kelley, 1978; Golombek, 1983; Gardner and House, 1987), particularly along the easily-identified west- and east-facing scarps associated with major fault traces.

The distribution and characteristics of surficial deposits identified by previous investigations along the Pajarito fault (J. Gardner, LANL, unpublished data, 1989) were assessed and revised during this investigation. Surficial deposits along the Pajarito fault between Los Alamos Canyon and Water Canyon include several alluvial-fan and fluvial deposits overlying the Bandelier Tuff and dacite of the Tschicoma Formation (Plate 4). The ages of these alluvial and fluvial deposits are poorly constrained, and correlation between deposits is based solely on limited clast size and lithology data, topographic and stratigraphic position, and relative amounts of erosional modification of geomorphic surfaces associated with the deposits.

The oldest surficial deposit identified during the mapping is a coarse-grained alluvium that consists of rounded and subrounded cobbles and boulders in a sandy matrix, with clasts composed mostly of tuff (Unit Qao, Plate 4). This deposit is exposed primarily on a structural bench between two major strands of the Pajarito fault, at elevations close to 2440 m. Stratigraphically above this alluvium is a fine-grained basin-fill deposit (Unit Qbf), which consists primarily of sand, silt, and pebble-size clasts of Bandelier Pumice. The absence of El Cajete Pumice clasts in this unit demonstrates that Unit Qbf was deposited before 73 ka (see below). Unit Qbf is identified only on the eastern (downthrown) side of the eastern fault strand, although it may be buried on the structural bench between the fault strands. The basin-fill sediments are interpreted to have been deposited in a small graben at the base of the fault strand. Included in Unit Qbf is a very coarse-grained deposit of limited areal extent exposed in a roadcut east of the eastern strand (center of section 19, Plate 4). Dacite clasts exposed in this roadcut are up to 2 m in diameter, and may be correlative with Qao deposits on the upthrown side of the eastern fault strand (Plate 4). However, clasts within the Qao deposits typically are composed of tuff rather than dacite.

Overlying the fine-grained basin-fill deposits are older alluvial-fan deposits that consist of cobbles and pebbles in a sandy matrix (Unit Qfo, Plate 4). In contrast to the Qao deposits, clasts within this unit are composed predominantly of dacite. The Qfo deposits extend eastward from the mouths of moderate to large drainages at the base of the eastern fault escarpment, such as Twomile, Pajarito, and Cañon del Valle canyons. The deposits are probably several meters to tens of meters thick at the base of the escarpment, but they pinch out and rarely extend more than 1 km to the east of the escarpment. The moderate-size drainages, such as Cañon del Valle, have deposited larger fans at the base of the fault escarpment than the larger drainages. This is probably because the larger drainages flow in incised valleys to the east of the escarpment, whereas the moderate-size drainages are not integrated with incised canyons to the east. The Qfo deposits, therefore, appear to post-date at least some of the substantial incision along the larger drainages. In addition, the predominance of dacite clasts suggests that the older alluvial-fan deposits had source areas within headwater regions underlain by the Tschicoma Formation.

The older alluvial-fan deposits are overlain by pumice of the El Cajete Series, an airfall deposit which probably erupted from the Valles caldera between 45 and 73 ka (see Section 2.4.1 for discussion of age). The El Cajete Pumice deposit is identified primarily along the base of the eastern fault escarpment, suggesting that it was deposited on the leeward side of the escarpment or that substantial amounts of the deposit have been eroded. The pumice is exposed along the north wall of a small, southeast-flowing tributary approximately 500 m north of Water Canyon, where it is overlain by coarse-grained younger alluvial-fan gravel. This relation shows that the pumice, although unconsolidated and very loose, may be preserved even in environments that clearly have the capability of substantial erosion.

Along major drainages that are integrated with canyons to the east of the Pajarito fault escarpment, such as Pajarito and Water Canyons, there are sequences of two to three fluvial terrace deposits inset into older alluvial-fan deposits and bedrock (Plate 4). These fluvial deposits (Unit Qt) are coarse-grained and contain clasts of dacite and tuff. Younger alluvial-fan deposits (Unit Qfy) interfinger with the axial terrace deposits, and consist primarily of dacite clasts (Plate 4).

4.1.1.3 Interpretations

Based on our field mapping of surficial deposits and fault traces, a preliminary sequence of events has been interpreted for the area along the Pajarito fault between Los Alamos Canyon and Water Canyon (Plate 4). This geologic history is poorly constrained and should be revised as additional stratigraphic and age data become available. After deposition of the Bandelier Tuff on the Tschicoma Formation about 1.2 Ma (event A, Plate 4), an episode of down-to-the-east faulting occurred along the western trace of the Pajarito fault, exposing Bandelier Tuff in an east-facing escarpment (event B). Older alluvium (Qao) was deposited on the downthrown side of the escarpment by drainages that, based on the presence of tuff but no dacite clasts, drained only Bandelier Tuff in headwater regions (event C). Following deposition of Unit Qao, displacement on down-to-the-east fault strands and subsidiary down-to-the-west strands produced localized, north-trending grabens along the base of the eastern Pajarito fault escarpment (event D, Plate 4). Unit Qbf was deposited within these grabens, and may have aggraded up to the top of the graben (event E). Down-to-the-east displacement likely continued on the main fault strands. Drainages that eventually tapped into the dacite terrain west of the fault incised into the escarpment and deposited Unit Qfo on the downthrown side of the eastern strand (event F). Incision of the drainages into bedrock between the fault strands may explain the absence of Unit Qfo on the structural bench.

Deposition of the El Cajete Pumice occurred sometime between 45 and 73 ka, mantling the bases of the east-facing escarpments (event G, Plate 4). Based on the presence of El Cajete Pumice in roadcuts along West Jemez Road and in trenches at the base of the eastern fault strand (Section 4.2.1), the pumice was deposited on scarp-derived colluvium at the base of the escarpment. The presence of younger alluvial-fan deposits (Unit Qfy) overlying El Cajete Pumice shows that moderate-size drainages continued to develop alluvial fans at the base of the escarpment, whereas larger drainages such as Pajarito and Water Canyons episodically incised into bedrock and formed axial stream terraces (event H). Large drainages integrated both with headwater regions to the west and with incised canyons to the east. Displacement on down-to-the-east and down-to-the-west fault strands likely continued. Thus, the western part of the Pajarito Plateau has experienced a series of complex depositional events strongly influenced by displacements along the Pajarito fault and by incision of drainages to the east.

The distribution of surficial deposits along the Pajarito fault between Los Alamos and Water Canyons is substantially different than that typically present along the base of other major late Quaternary faults in the Rio Grande rift and the Basin and Range province. Along many range fronts in the rift and the Basin and Range, surficial deposits consist of broad, coalescent late Quaternary alluvial fans that display prominent evidence of late Pleistocene and/or Holocene displacement (e.g., Machette, 1986; McCalpin, 1982; Menges, 1990a,b; Ramelli and dePolo, 1993). In contrast, the Pajarito fault is associated with laterally limited fans separated by deeply incised drainages. Thus, the preserved record of late Quaternary displacement along the Pajarito fault is strongly influenced by incision along drainages that flow east to the Rio Grande. Ultimately, the lack of broad alluvial fans along the Pajarito fault may be a result of substantial middle to late Pleistocene incision of the Rio Grande (Hawley, 1978; Dethier and Demsey, 1984; Wells et al., 1987), and concomitant incision of tributaries that drain the Pajarito Plateau. The lack of alluvial deposits along the western Pajarito Plateau is likely also related to the poorly-resistant Bandelier Tuff, into which the tributary drainages could easily incise.

In summary, subsequent to deposition of the Bandelier Tuff 1.2 Ma, the western part of the Pajarito Plateau experienced a series of complex depositional events strongly influenced by displacements along the Pajarito fault and by incision of fluvial systems draining the plateau. Surficial deposits present along the escarpment provide a preliminary stratigraphic framework for detailed investigations (Section 4.2). In particular, eruption of the El Cajete Pumice sometime between 45 and 73 ka, provided a key stratigraphic marker that is distributed over much of the plateau. The preserved record of the late Quaternary displacement along the Pajarito fault is strongly influenced by incision along drainages that flow east to the Rio Grande and by the poorly resistant Bandelier Tuff.

4.1.2 Topographic Profiling of the Pajarito Fault System

4.1.2.1 Methods

The Pajarito Plateau is underlain by the 1.2 Ma upper member of the Bandelier Tuff, which forms a smooth, gently east-sloping surface on the eastern flank of the Jemez Mountains. This deposit provides an excellent stratigraphic and geomorphic datum from which to estimate the amount and location of post-1.2 Ma vertical displacements along faults that

traverse the plateau. As a first approximation, the mesa surfaces on the plateau provide an estimate of the uppermost stratigraphic level of the Bandelier Tuff. To this end, 34 topographic profiles were constructed along several mesas underlain by the Bandelier Tuff (Figure 4-1; Table 4-1). To construct profiles we used: 1) 1:24,000-scale topographic maps with 12 m (40 ft) contour intervals (USGS Frijoles and Guaje Mountain 7.5 minute quadrangles) and 1:12,000-scale enlargements of these maps; 2) 1:1,200-scale topographic maps with 2-foot contour intervals that were generated by the Facility for Information Management, Analysis and Display (FIMAD) at LANL; and 3) an abney level, a 50-m tape measure, and a 5-m telescoping stadia rod to measure profiles in the field. The profiles cross escarpments and scarps present along the Pajarito, Rendija Canyon, and Guaje Mountain faults (Figure 4-1). We estimate that the limit of resolution to detect vertical displacements on profiles constructed from 7.5 minute quadrangles is about 3 m. Although precision for the FIMAD maps is between one to two feet, we found in practice the accuracy is less, particularly for steep, densely-forested areas. While measuring one of the profiles in the field, we discovered a gully nearly 2 m deep that was not shown on the FIMAD topographic map, and so we estimate that the limit of resolution for these profiles can be as high as 2 m. We measured profiles in the field to the nearest tenth of a meter and slopes angles to the nearest degree. We estimate that the resolution for these profiles is about 0.5 m, depending primarily on the nature of the surfaces and underlying deposits.

Normal fault zones commonly have associated antithetic faults and grabens with backtilted areas on the downthrown side of the fault, resulting in accentuated scarp (or escarpment) heights and wide deformation zones. Therefore, to adequately account for backtilting and graben formation in quantifying vertical displacements on all the topographic profiles, we measured net vertical tectonic displacements (NVTD) of surfaces. Surfaces on the upthrown and downthrown side of the scarp or escarpment were projected from outside the zone of deformation to the fault, and NVTD was measured as the vertical displacement between the projected surfaces measured at the fault (Swan et al., 1980).

Several assumptions were made in using the profiles to estimate vertical slip along the faults. First, it is assumed that mesa surfaces have been essentially unmodified, there has been negligible erosion or deposition on the mesas, and that the topographic surface of the mesas reflects the uppermost stratigraphic level of the Bandelier Tuff. There is substantial colluvial deposition at the base of the Pajarito fault escarpment (Plate 4) and there is clear evidence

of local deposition up to 4 m on some mesas (see Section 4.2.2.2, County Landfill Site). However, extensive trench investigations at TA-63 and TA-67 (Plate 2) indicate only a thin layer of sediment (<2 m) overlies the Bandelier Tuff (Kolbe et al., 1994, 1995) on other mesas. Although erosion of the upper tuff units is substantial in the eastern part of the plateau, mesa widths increase to the west and suggest that mesa surfaces in the western part of the plateau are valid approximations of the upper aggradational surface of the tuff. In the absence of substantial erosion and deposition, the topographic profiles are proxies for detailed mapping of individual volcanic flow units throughout the western Pajarito plateau.

Second, it is assumed that there is little or no warping or tilting of the mesa tops that might affect the mesa-top slopes projected across fault traces. Because field observations show that upper tuff units are warped down to the east along the Pajarito fault, north of Los Alamos Canyon, we attempt to capture the total amount of deformation (including brittle and ductile deformation) by projecting surface gradients toward faults only from areas having constant gradients. In this way, surface displacement estimates account for the possible amount of warping along fault traces. Third, the original gradient of the uppermost tuff unit most likely decreased gradually from west to east, so that along some profiles surface gradients west of the Pajarito fault are greater than those east of the fault. In such cases, amounts of displacement are estimated by assuming gradual eastward gradient changes. Fourth, we are assuming that during deposition, the tuff filled in any topographic relief along pre-existing fault escarpments, so that there was no significant remnant relief from pre-1.2 Ma movement along the faults.

4.1.2.2 Results of Regional Profiles

Figures 4-2a through 4-2b show some of the profiles constructed from 7.5 minute topographic maps. In general, topographic profiles show that there is substantial variation along strike in the amount of NVTD along the Pajarito, Rendija Canyon, and Guaje Mountain faults (Table 4-1 and Figures 4-3a through 4-3c). This apparent along-strike variation generally precludes comparison of results for different methodologies except for profiles F1 and M2, which traversed the same location (Figure 4-1). Except for minor differences, profile morphologies for F1 and M2 were very similar and best estimates of NVTD differed by only 2.5 m, well within the ranges of estimates for each profile of $\pm$ 15.6 m and $\pm$ 12 m.

Along the Pajarito fault, down-to-the-east NVTD of the Bandelier Tuff is generally more than 40 m along each of two or more individual fault strands, and cumulative NVTD across all traces along a given profile is as high as 154 ± 5 m (P5 on Figure 4-1 and Table 4-1). The amount of NVTD is highest in the central part of the fault, where it is located along the western boundary of LANL (Figures 4-1 and 4-3a). The maximum displacement of 154 m yields a maximum vertical slip rate for the past 1.2 million years of about 0.13 mm/yr. To calculate an average slip rate along the Pajarito fault, we used the NVTD data to plot a displacement curve that generally envelopes the data (Figure 4-3a). The area under this curve yields an average NVTD of 81 m along the Pajarito fault and a vertical slip rate of about 0.07 mm/yr for the past 1.2 million years.

The Rendija Canyon fault exhibits as much as 36 ± 10 m of down-to-the-west NVTD (P1 on Figure 4-1 and Table 4-1) along its central part, although NVTD decreases to zero within about 6 km to the north and south (Figure 4-3b). The maximum displacement of 36 m yields a maximum vertical slip rate of 0.03 mm/yr for past 1.2 million years on the Rendija Canyon fault. We calculated an average NVTD of about 22 m for the Rendija Canyon fault, which yields an average vertical slip rate of about 0.02 mm/yr for the past 1.2 million years.

The Guaje Mountain fault shows as much as 27 ± 4 m of down-to-the-west NVTD at its northern end, where it intersects the Pajarito fault (Figure 4-3c). NVTD on the Guaje Mountain fault progressively decreases southward to zero in the vicinity of the town of Los Alamos. The maximum displacement of 27 m yields a maximum vertical slip rate of about 0.02 mm/yr for the past 1.2 million years on the Guaje Mountain fault. We calculate an average NVTD of 15 m (Figure 4-3c), which yields an average vertical slip rate of about 0.01 mm/yr for the Guaje Mountain fault for the past 1.2 million years.

Thus, both maximum and average NVTDs estimated from the topographic profiles are greatest on the Pajarito fault, and slightly less on the Guaje Mountain fault than the Rendija Canyon fault. Several profiles (P5, P6, P7, and P8) cross the southern projections of the Rendija Canyon and Guaje Mountain faults, and show no evidence of vertical displacement of the Bandelier Tuff (Figures 4-1, 4-3b, and 4-3c). The amounts and distribution of NVTD shown in Table 4-1 and on Figures 4-3a through 4-3c were utilized in characterizing slip rates and in assessing potential rupture scenarios for the Pajarito fault system (Section 7.1).

4.1.2.3 Results of Detailed Profiles of the Pajarito Fault Escarpment

Two detailed topographic profiles of the Pajarito fault escarpment were surveyed in the field during September and October of 1994. The primary purpose of measuring these profiles was to characterize the escarpment morphology in enough detail to identify breaks in slope (inflection points) that may represent individual fault strands, and possibly identify potential future paleoseismic investigation sites. We selected two locations to measure profiles based on: interpretation of 1:7,500-scale color aerial photographs provided by LANL, construction of topographic profiles from 1:1,200-scale maps provided by FIMAD, and ground reconnaissance. Profile M2 was located north of Cañon de Valle and profile M7 was located south of Highway 4 (Figure 4-1). Profiles were originally plotted at scales of 1:1,200 and 1:500, and Figure 4-4 shows reduced versions of these plots.

North of Cañon de Valle along profile M2, the Pajarito fault is characterized by two east-facing escarpments roughly 675 m apart (Figure 4-4). Both escarpments are developed in bedrock (1.2 Ma Bandelier Tuff) and are mantled by a thin veneer of colluvium and eolian deposits. The surface of the upthrown side of the fault (west of the western escarpment) slopes 4° to 5° east and the surface on the downthrown side (east of the eastern escarpment) slopes 3° to 4° east. Estimates of the total NVTD measured across both escarpments range from 92.4 m to 123.6 m. However, these estimates may be too large because although backtilting was not evident on the profile, S.L. Reneau (LANL, personal communication, 1994) has observed exposures of surge beds just east of profile M2 that indicate the Bandelier Tuff is backtilted at least a couple of degrees to the west of this area. The larger, steeper eastern escarpment is 91 m high, with an average slope of 32° and a maximum slope of 41° near its crest. In comparison, the western escarpment is roughly 48 m high, slopes average 20° to 25°, and the maximum slope is 31° near the base (Figure 4-4). A steeper slope and narrower, sharper crest for the eastern escarpment than the western escarpment was also visible in profiles F1 and F3, which were constructed from FIMAD maps north of Cañon de Valle (Figure 4-1).

The crest of the western escarpment in profile M2 is highly degraded, forming a broad, 150-m-wide crestal zone, and giving an asymmetry to the profile (Figure 4-4). As scarp faces degrade with time, crestal zones widen and slope angles decrease for both scarps on alluvium and scarps on fractured bedrock (Wallace, 1977). Slopes of faceted spurs on fault-bounded

range-fronts also generally decrease with time (Wallace, 1978), which would suggest that the western escarpment is generally older than the eastern escarpment. As the escarpments, and in particular their crests, were presumably formed in the same units of the Bandelier Tuff with a similar degree of welding, it seems likely that their resistance to erosion was similar, and thus, the more subdued morphology for the western escarpment suggests a greater overall age for this escarpment.

The morphology of the eastern escarpment shows a narrow (22-m-wide) well-defined crestal zone, a maximum slope angle of 41° near the crest, and multiple segments (seven) throughout the escarpment face with slope angles of 37° or more. Wallace (1978) found that slopes of 25° to 35° in fractured bedrock can remain relatively stable along faulted range-fronts for long periods of time, but angles of slopes above 37° tend to decrease rapidly. Thus, the eastern escarpment does not appear to match the pattern of typical normal faults that repeatedly rupture near the base of a range-front and form faceted-spurs that are steepest near the base where faulting rejuvenates slopes to steeper angles (eg., Menges, 1990a,b).

Instead, the steep slopes near the crest and throughout the eastern escarpment face suggest that faulting may have occurred most recently high above the base of the escarpment and perhaps just below the crest. The maximum slope occurs at an outcrop of moderately welded Bandelier Tuff (at 1,100 m on Figure 4-4) that appears to be *in situ* and contains flattened pumice clasts, oriented N25°E 4°SE, that are subparallel to a pervasive set of joints. It is possible that the maximum slope angle here is a result of more densely welded tuff being more resistant to erosion. However, many of the other steeper sections within the escarpment occur where a thin (<0.5 m) veneer of slopewash and debris colluvium mantle less-welded tuff, and so it seems unlikely that all of these breaks in slope are related to differential erosion.

Although the western escarpment may be generally older than the eastern escarpment, it does show some characteristics that suggest further investigation of the western escarpment is warranted and so we discuss it here in more detail. These characteristics are: a graben on the downthrown side (Figure 4-4), which has trapped a significant amount of eolian sediment, good material for thermoluminescence dating; and 2) breaks in slope near the base, both in bedrock and alluvium, which may be remnants of individual fault scarps. In

addition, access via a dirt road up Cañon de Valle, and the smaller less-steep escarpment makes a trench investigation at this site logistically feasible.

Morphologically, the western escarpment can be separated into six sections: an upper crest, a middle crest, a lower crest, an upper face, a lower face, and an alluvial apron at the base. The upper crest slopes 6°, extending from the crestal break at 210 to 270 m and having a thin (<0.5 m) veneer of slopewash overlying the Bandelier Tuff. The middle section of the crest slopes 7° to 10°, is convex and extends from 270 to 320 m (Figure 4-4). It is underlain by a coarser, thinner veneer of colluvium. The break between the middle and lower crest is marked by a striking change in vegetation from chiefly pine trees to scrub oak. The lower crest is very convex, sloping between 10° and 17° from 320 to 360 m, and it generally exposes bedrock at the surface.

The upper section of the face is degraded, sloping on average 20°, and generally exposes bedrock. The lower, steeper section of the face generally slopes 25° from 360 to 409 m, but contains two breaks in slope at roughly 392 and 407 m, each with the maximum slope angle of 31°. These breaks may represent remnants of more recent fault scarps. This section is generally underlain by colluvium except at the lower break in slope where bedrock is exposed. The alluvial apron at the base of the escarpment slopes 15° to 8°, is concave, and extends into the western side of the graben (Figure 4-4). During our reconnaissance along the base of the escarpment, we observed breaks in slope that have a relatively linear trend subparallel to the escarpment, but are very discontinuous. These breaks may be remnants of small fault scarps on alluvium that have been extensively modified by deposition and erosion. Detailed mapping of these features in relation to surficial deposits and possible stratigraphic offsets in the Bandelier Tuff elsewhere along the escarpment may provide better insight into their origin.

South of Highway 4, along profile M7, the Pajarito fault is characterized by one large east-facing escarpment that is 117 m high (Figure 4-4). Estimates of NVTD across this escarpment range from 106.2 to 110.4 m. The escarpment is also developed in the 1.2 Ma Bandelier Tuff, but is mantled by a generally thicker veneer of alluvium, colluvium, and eolian deposits than along profile M2. Except for an area at the east end of M7 that had been burned by a forest fire, tree cover is also generally denser, including mostly pine trees and much fewer scrub oak.

Along profile M7, the surface on the upthrown side of the escarpment slopes 2° to 4° east and the surface on the downthrown side slopes 2° east. Analysis of aerial photographs indicates a wide zone of backtilting toward the Pajarito fault (to the west) on the downthrown side of the escarpment, extending perhaps as far east as 1400 m (Figure 4-4). However, significant erosion by two drainage channels that run parallel to the backtilted zone precluded identification of any individual antithetic fault scarps. Detailed mapping by Reneau (1991) revealed no stratigraphic evidence for faults in this area. However, to the south, on Escobas Mesa, Reneau (1991) found numerous secondary faults offsetting contacts within the Bandelier Tuff as much as 30 m. He also observed stratigraphic evidence for backtilting toward the main escarpment.

Morphologically, the escarpment can be separated into four sections along profile M7: a broad crestal zone, a steep bedrock face, a debris slope, and an alluvial apron. The crestal zone extends from about 188 m to roughly 340 m and consists of a convex slope with angles from 6° to 17°. Its underlain by colluvium that grades coarser downslope.

From 345 to 405 m, welded Bandelier Tuff is exposed, forming a steep bedrock face. The upper portion of this face slopes an average of 25°, but the lower portion slopes an average of 37° with three segments sloping over 37° and one segment at 390 m, forming an approximate 90° cliff that is over 2.5 m high (Figure 4-4). Outcrops were rounded, eroded, and mantled by large boulders. The tuff was homogeneous, slightly welded, and appeared to be *in situ* bedrock, but this is not conclusive. It was relatively undeformed containing sparsely-distributed, irregular fractures that showed no evidence for faulting such as slickensides, or offsets. The cliff is visible in aerial photographs, forming a discontinuous linear feature that extends along much of the escarpment between Highway 4 and the Frijoles benchmark (Plate 4). Below the bedrock face is a steep colluvial debris slope that grades into an alluvial apron at about 460 m (Figure 4-4). The debris slope is concave, sloping from 28° to 20°. The alluvial apron extends east of 480 m and slopes 12° to 14°.

Based on the escarpment morphology and distribution of surficial deposits, the break in slope at the contact between the bedrock face and the debris slope ($\approx$ 405 m) may represent a significant fault strand. Evidence is equivocal as to whether the cliff at 390 m is another fault strand, is related to differential erosion, or is related to mass wasting along this steeper section of the escarpment. The profile morphology and linear geomorphic expression

support either faulting or differential erosion. The lack of deformation and numerous large boulders along this section support either the mass wasting or differential erosion.

During our reconnaissance of potential sites to profile, we observed numerous slope failures along the Pajarito fault escarpment including large deep-seated slumps, rock falls, topple failures, slab failures, and landslide blocks. Often these failures can be easily identified by their morphology (e.g., slumps) or by the identification of blocks. The latter often show pervasive joints and flattened pumice clasts dipping at much steeper angles than in *in situ* bedrock, which are typically 2° to 5°. Dips in translated blocks typically are parallel to the local slope, often greater than 15°. However, when topple and slab failures, and landslide blocks occur in homogeneous tuff and large blocks are partially buried, they can be mistaken for *in situ* bedrock. Depending on the dimensions of the block, either toppling or sliding failures can occur on slopes greater than 35° (Hoek and Bray, 1977). Thus, the evidence suggests that the cliff along this section of the escarpment could actually be a result of multiple processes such as mass wasting or uniform retreat along a bedrock scarp initially created by faulting. Detailed mapping along this section of the escarpment to identify potential translated blocks, stratigraphic units within the tuff and potential offsets, or other definitive evidence for faulting may better define the origin of the cliff face.

4.1.3 Regional Investigations of Nearby Potential Seismogenic Sources

Based on the initial seismic hazard evaluation conducted by Wong et al. (1993), the Embudo fault was identified as a potentially significant seismogenic source to LANL. The seismic source characteristics of the Embudo fault, however, are poorly known. During the fall of 1993, additional reconnaissance-level studies were conducted to provide additional information on the characteristics of the Embudo fault. These studies are summarized in Section 4.1.3.1 below. During these studies, several prominent topographic scarps were identified on Black Mesa, located about 35 km northeast of LANL and within 5 km north of the Embudo fault (Plate 1). Reconnaissance studies of these scarps yielded limited information on these faults, informally named herein as the faults of Black Mesa. These studies are summarized in Section 4.1.3.2 below.

4.1.3.1 Embudo Fault

4.1.3.1.1 Introduction. The Embudo fault is an approximately 64-km-long, northeast-striking system of faults that forms the structural boundary between the Española and San Luis basins (Plate 1). The Embudo fault lies along the Jemez lineament, a northeast-trending zone of Plio-Pleistocene volcanic fields extending from central Arizona to northeastern New Mexico. This lineament probably is related to a zone of crustal weakness that has controlled faulting, fracturing, and the locus of Tertiary volcanism in the Jemez Mountains and the Rio Grande rift (Aldrich, 1986).

The Embudo fault was recognized by Kelley (1978), and subsequently mapped along its southwestern end by Harrington and Aldrich (1984), as the Santa Clara fault zone and by Dethier and Manley (1985). The northeastern part of the fault is mapped by Muehlberger (1979) and Leininger (1982). These studies suggest that the fault is a transfer zone between predominantly down-to-the-east faulting along the western margin of the Española Basin and the down-to-the-west faulting along the eastern margin of the San Luis Basin (Dungan et al., 1984). The geometry of the Embudo fault, and its relationship to the Española and San Luis basins, are similar to characteristics of accommodation zones in other continental rift systems (Rosendahl, 1987; Morley et al., 1990). If the fault is an accommodation zone between the Española and San Luis basins, then it should display opposite senses of vertical separation at its northeastern and southwestern ends, and it should display a consistent sense of sinistral strike separation along its entire length.

Many workers have identified reversals in sense of vertical separation along the Embudo fault, although there is some disagreement as to the location of the possible hinge point. For example, Kelley (1978) shows several reversals along the fault. Muehlberger (1979) notes a "pivot point" near Cerro Azul, a Precambrian basement outlier at the southern end of the San Luis Basin. Leininger (1982) notes a hinge point near the town of Pilar, and Personius and Machette (1984) suggest a hinge point near Embudo. Clearly, there are several possible reversals in dip separation along the entire trace of the fault.

Field relationships along the northeastern section of the Embudo fault, however, indicate that the kinematics of deformation may be more complicated than suggested by the simple model

that the fault is an accommodation zone. Muehlburger (1979) reports evidence that Precambrian basement rocks of the Picuris mountains are thrust northward over late Miocene and Quaternary sediments along the northeastern end of the Embudo fault. This suggests that the fault locally accommodates crustal shortening rather than differential crustal extension. Along the southeastern part of the fault, the Embudo fault displays a left-stepping en echelon geometry between the Rio Chama and Clara Peak (Dethier and Manley, 1985; Aldrich, 1986; Gonzalez and Dethier, 1991). Blocks between the left-stepping traces of the fault have been deformed by folding and reverse faulting. Aldrich (1986) and Aldrich and Dethier (1990) interpret the zones of crustal shortening as contractional left-stepovers associated with right-lateral, strike-slip faulting along the Embudo fault. Right-lateral slip on the Embudo fault is inconsistent with the model that the fault is an accommodation zone.

In order to reconcile the evidence for local thrust faulting and possible dextral slip along the Embudo fault, previous workers suggested that the Española Basin is undergoing counterclockwise vertical axis rotation driven by oblique extension within the Rio Grande rift. Muehlberger (1979) proposed that the Española Basin is underlain by a rigid, diamond-shaped crustal block that is being rotated counterclockwise in response to left-oblique extension of the Rio Grande rift. He interpreted the contraction along the northeastern part of the Embudo fault to be the consequence of impingement of the corner of the diamond-shaped block during rotation. Brown and Golombek (1986) presented paleomagnetic data from numerous sites in the Española Basin suggesting that Pliocene and older rocks have been rotated counterclockwise, and elaborated on Muehlberger's model (1979) of counterclockwise rigid block rotation. Salyards and Ni (1990) noted, however, that the magnitude of the vertical axis rotations indicated by paleomagnetic data are not uniform throughout the Española Basin and instead are greatest near the major basin-bounding faults. These relationships suggest that the entire basin may not have rotated as a single, rigid block as proposed by Muehlberger (1979).

These models have different implications for the kinematics of coseismic rupture along the Embudo fault. If the fault is an accommodation zone between the Española and San Luis basins, then the opposite senses of vertical separation expressed by the northeastern and southwestern parts of the fault imply that it consists of at least two kinematically distinct reaches, associated with either the Española Basin or the San Luis Basin. If so, then it is unlikely that the fault would rupture independently along its entire length during a single

event. Alternatively, if the Embudo fault is primarily a right-lateral strike-slip fault that is accommodating the counterclockwise rotation of the entire Española Basin, then the inferred direction of slip and rate of strain accumulation are consistent along the length of the fault, and it is more likely that a large rupture involving both the northeast and southwest reaches could occur.

We conducted an analysis of aerial photography, aerial reconnaissance and field studies to: (1) assess evidence for late Quaternary deformation along the Embudo fault; (2) determine the style and rate of slip, if possible, and (3) assess the potential for large rupture involving both the southwestern and northeastern sections of the fault. Based on analysis of aerial photography and aerial reconnaissance, we selected four sites for detailed field investigations:

1) an unnamed mesa south of the confluence of Arroyo de la Presa and the Rio Chama, west of the town of Hernandez;
2) the northeast-trending reach of Arroyo Ocole northeast of the town of Velarde;
3) the Rio Embudo area near the town of Dixon; and
4) the Arroyo Hondo area in the southern San Luis Basin.

The following sections describe the results of aerial and field reconnaissance studies of these areas.

4.1.3.1.2 Mesa West of Hernandez. Previous workers (Kelley, 1978; Machette and Personius, 1984; Gonzalez and Dethier, 1991) interpreted several northeast-striking faults east of Clara Peak as part of the Embudo fault. The faults are located south of the Arroyo de la Presa between Clara Peak and Black Mesa. As mapped in detail by Dethier and Manley (1985), the faults generally cut sediments of the late Miocene-early Pliocene Chamita Formation, with down-to-the-southeast displacement. The faults project toward a small, northeast-trending mesa that lies between the confluence of Arroyo de la Presa and Rio Chama, approximately 1.3 km northwest of the town of Hernandez (Figure 4-5). The mesa is underlain by deformed strata of the Chamita Formation and capped by a sequence of Quaternary sand and silt interbedded with fluvially derived tephra (Unit Qs of Dethier and Manley, 1985). The northeast-striking faults are mapped by Dethier and Manley (1985) as underlying the Quaternary deposits (Figure 4-5).

Wachs et al. (1988) observed a 0.5-m-high, south-facing scarp along the north wall of an arroyo draining the upper surface of the unnamed mesa. Based primarily on an inferred down-to-the-south displacement of mesa surface across the scarp, Wachs et al. (1988) interpreted the feature as a result of movement on a strand of the Embudo fault. They further noted that the scarp is undissected and is not crossed by any drainage channels, and speculated that the latest surface faulting event occurred relatively recently.

We analyzed small-scale aerial photographs of the reach of the Embudo fault between Clara Peak and Black Mesa. We observed no conspicuous topographic, tonal or vegetation lineaments, or other anomalous northeast-trending geomorphic features, in the vicinity of the mapped fault zone. Short tributaries to the Arroyo de la Presa locally trend northeast and may reflect some structural control on drainage development, but these tributaries are not associated with obvious photo lineaments or scarps. Aerial reconnaissance confirmed the lack of scarps, lineaments or other anomalous geomorphic features along the mapped trend of the Embudo fault between Clara Peak and the Rio Grande.

We conducted limited field reconnaissance of the unnamed mesa west of Hernandez and the area south of Arroyo de la Presa. The Quaternary sandy alluvium (Unit Qs) of Dethier and Manley (1985) underlies a smooth, undeformed surface on the top of the mesa (Figure 4-5). Vertical exposures of the Quaternary sandy alluvium are present in gullies eroding headward on the southwestern and northeastern sides of the mesa. We examined these exposures for evidence of faulting and observed that bedding generally is horizontal and undeformed. We thus conclude that any movement on northeast-striking faults mapped through the mesa must predate deposition of the Quaternary sandy alluvium.

Specifically, we examined the south-facing scarp on the mesa surface interpreted as a fault by Wachs et al. (1988). Analysis of aerial photographs and helicopter reconnaissance revealed that the feature is marked by a linear alignment of vegetation and a linear topographic depression. Field examination showed that the depression has a constant width along its length that is approximately equivalent to the typical width of a dirt track (Site A, Figure 4-5). We traced the depression to the northeast and southwest margins of the mesa and observed in bluff exposures that the soil developed on the mesa surface is not deformed along the projections of the feature. Based on these observations, we interpret the depression to be an abandoned road or similar cultural feature. This interpretation is consistent with

the observation of Wachs et al. (1988) that the depression is a very young, undissected feature. The abandoned road surface is apparently being eroded by channelization of drainage from the surface of the mesa. The higher moisture content of the soil along the depression probably attracts juniper trees, and thus contributes to the associated tonal and vegetation alignments visible in aerial photographs.

Soil profile development in the Quaternary alluvium provides some constraint on the age of this unit. A soil profile exposed on the southwestern side of the mesa consists of a reddened B horizon with moderately hard consistency and subangular blocky ped structure (Site B, Figure 4-5). The development of soil structure suggests that some clay translocation has occurred, although field textural analysis indicates that insufficient clay accumulation has occurred for development of an argillic (Bt) horizon. The B horizon also shows evidence of carbonate accumulation in the form of mineralized root casts, nodules and disseminated lime, consistent with stage II carbonate accumulation in late Pleistocene soils for the northern New Mexico region (Machette, 1985). Current models for clay accumulation in B horizons require that soil carbonate must be leached from the profile prior to downward movement of the clay colloids (Soil Survey Staff, 1975). If these models are correct, clay translocation in the soil profile probably occurred prior to carbonate accumulation. These soil relations suggest that the soil profile is late Pleistocene in age. Other exposures of the Quaternary sandy alluvium in the vicinity of the soil profile reveal fragments of a water-lain ash. This ash is most likely the 610-ka Lava Creek B ash (D. Dethier, Williams College, personal communication, 1994), and is undisplaced across the projection of the fault mapped by Dethier and Manley (1985).

We studied exposures of the Chamita Formation in an attempt to locate the northeast-striking faults mapped by Dethier and Manley (1985). South of Arroyo de la Presa, the faults are shown as separating packages of strata that have significantly different bedding dips (Dethier and Manley, 1985). Bedding in outcrops of the Chamita Formation nearest to Arroyo de la Presa dips 60-80° southeast (Site C, Figure 4-5). The beds dip less steeply with increasing distance south of Arroyo de la Presa, and thus show evidence of dips shallowing upsection. Based on reconnaissance of exposures in ephemeral, north-draining stream gullies south of Arroyo de le Presa, some of these dip variations occur abruptly across angular unconformities within the Chamita Formation. In particular, one intraformational angular unconformity is shown by east-striking beds dipping 50° south that are overlain by a

sequence of cobble conglomerate and coarse sand deposits dipping 25° south (Site C, Figure 4-5). The base of the cobble conglomerate truncates the more steeply-dipping underlying strata. This pattern of dips shallowing upsection across unconformities can be observed in other nearby exposures, indicating that abrupt changes in bedding dip may be a result of syndepositional subsidence and tilting rather than post-depositional faulting. In addition to the angular unconformities, high-angle faults with several meters of dip-slip separation are present in the Chamita Formation south of Arroyo de la Presa. These faults may have formed during active subsidence within the Chamita Basin, and thus may be related to syndepositional, rather than post-depositional, tectonism. During our field reconnaissance, we observed no evidence to suggest that faults mapped by Dethier and Manley (1985) have had late Quaternary displacement.

Field reconnaissance, however, confirms the presence of deformed basalt along the northern margin of the mesa. Dethier and Manley (1985) mapped the basalt as the Lobato Basalt, which yielded a K-Ar age of 9.9$\pm$1.0 Ma (Manley and Mehnert, 1981). The steep dip of the basalt supports the possibility of a fault strand beneath the active channel of Arroyo de la Presa, as mapped by Kelley (1978). Aerial reconnaissance and analysis of aerial photography showed no geomorphic evidence of late Quaternary faulting in the areas northeast and southwest of this basalt exposure, although these areas are characterized by a high degree of dissection. The possibility that a major strand of the Embudo fault is present beneath Arroyo de la Presa cannot be precluded (D. Dethier, Williams College, personal communication, 1994).

4.1.3.1.3 <u>The Arroyo Ocole Drainage</u>. Kelley (1978) mapped several northeast-striking faults in the valley of Arroyo Ocole, a southwest-draining tributary to the Cañada de las Entrañas, northeast of the town of Velarde (locality A; Plate 1). The faults cut strata mapped as the Miocene-Pliocene Tesuque Formation (Kelley, 1978), and are interpreted to be strands of the Embudo fault by Machette and Personius (1984). We conducted aerial and field reconnaissance investigations to assess evidence for late Quaternary activity on the faults.

The mapped fault traces cross a saddle that forms a drainage divide between the Arroyo Ocole and Embudo Creek. Aerial reconnaissance showed that the faults have no prominent geomorphic expression. We observed no scarps, lineaments or other potentially fault-related

geomorphic features within the stream valleys, across fluvial terraces or across the drainage divide. Field reconnaissance showed that in some cases the faults are mapped between stratigraphic packages with beds that dip at different angles (Kelley, 1978). We did not observe any discrete faults or zones of shearing in outcrop exposures during the field reconnaissance. It is possible that some of the bedding dip changes within strata of the Tesuque Formation are due to syndepositional tilting rather than faulting, similar to the angular unconformities present in the vicinity of Arroyo de la Presa (see discussion above). Based on lack of geomorphic expression of the northeast-striking faults, and evidence for no faulting of late Quaternary deposits or surfaces in valley of Arroyo Ocole, we postulate that the northeast-striking faults mapped in this region are not active strands of the Embudo fault.

4.1.3.1.4 Rio Embudo Area. Kelley (1978) mapped several northeast-striking strands of the Embudo fault across Rio Embudo. Based on the presence of numerous fluvial terraces flanking Rio Embudo, we conducted aerial and field reconnaissance studies to assess whether faults mapped by Kelley (1978) deform the terraces.

During aerial and field reconnaissance, we observed a sequence of at least four fluvial terraces on the northern side of Rio Embudo valley (locality B, Plate 1). The highest terrace surface is approximately 100 m above the modern floodplain of Rio Embudo and consists of numerous discontinuous remnants. The second-highest terrace is a continuous surface denoted as La Pareia on the Dixon USGS 7.5 minute quadrangle, and is about 60 to 70 m above Rio Embudo. Two lower terraces are about 24 m and 30 m high, respectively. The terrace heights increase slightly down valley as Rio Embudo flows into a narrow bedrock gorge at the Embudo fault. The terrace surfaces are underlain by approximately 1 to 3 m of fluvial conglomerate. The conglomerates were not differentiated from the underlying Miocene-Pliocene Tesuque Formation by Kelley (1978). Field reconnaissance conducted for this study, however, shows that the base of the fluvial conglomerates is an angular unconformity that post-dates tilting and folding of the underlying Tertiary Tesuque Formation. Pedogenic carbonate in the gravel underlying the second-highest terrace surface consists of disseminated $CaCO_3$ as well as rinds on the surfaces of larger clasts. The degree of pedogenic carbonate accumulation corresponds to stage II of Machette (1985). Based on these relationships, we interpret the upper two terrace remnants to be late Pleistocene in age or older.

Aerial reconnaissance showed the absence of lineaments or other anomalous geomorphic features in the terraces. During field reconnaissance, however, we observed a fault in a roadcut into deposits associated with the second-highest terrace. The fault in the roadcut exposure strikes N50E, dips 85° northwest to vertical, and displaces the base of the gravel approximately 2 m down-to-the-southeast. Bedding in the Tertiary Tesuque Formation on the southeastern side of the fault appears to be dragged upward along the fault, consistent with the observed northwest-side-up displacement of the overlying fluvial conglomerate. The component of strike-slip, if any, is unknown. The fault has no discernible geomorphic expression, although the projection of the fault on strike to the southwest may coincide with a southeast-facing break in slope along the back edge of the second-highest terrace surface. We were not able to trace the fault to the northeast due to landsliding on the northwest side of La Pareia Mesa. We re-examined La Pareia Mesa during a subsequent aerial reconnaissance, and observed no tonal or vegetation lineaments in the vicinity of the fault exposure. There is no geomorphic expression of faulting across the lower terrace of Rio Embudo, and there is no displacement of the bedrock strath surface beneath the terrace.

4.1.3.1.5 **Arroyo Hondo Area**. The northeastern part of the Embudo fault lies along the southern margin of the San Luis Basin, near the towns of Taos and Pilar. Muehlburger (1979) described and mapped a series of northeast-striking faults in several roadcuts along U.S Highway 64 near Arroyo Hondo, which he interpreted as part of the Embudo fault. Machette and Personius (1984) correlated these faults with northeast-striking faults mapped by Kelley (1978) in the Arroyo Ocole and Rio Embudo areas to the southwest.

According to Muehlburger (1979), the Embudo fault in the Arroyo Hondo area (locality C, Plate 1) consists of a series of southeast-dipping thrust or reverse faults that displace strata of the Santa Fe Group. This interpretation has been cited as evidence for late Cenozoic thrusting of the Picuris Mountains over the southern margin of the San Luis Basin, and has been incorporated into models for deformation of the Española Basin via late Cenozoic counterclockwise rigid block rotation (Muehlburger, 1979; Brown and Golombek, 1986).

We conducted aerial and field reconnaissance studies to assess the style and recency of faulting in the Arroyo Hondo area. Aerial reconnaissance shows that the Embudo fault is marked by a northwest-facing scarp and other lineaments that can be traced southwest for about 5 km from Arroyo Hondo toward the town of Pilar (Leininger, 1982). The

topographic expression of the scarp dies out in the upper Rito Cienguilla drainage, near Pilar. The scarp continues to the northeast of Arroyo Hondo for at least 4 km (Muehlburger, 1979), and merges with a prominent break in slope at the base of the Picuris Mountains. Leininger (1982) maps the fault trace in the Arroyo Hondo area, and shows a right step in the fault where it crosses Arroyo Hondo and U.S. Highway 64 (Figure 4-6).

We examined four roadcut exposures on U.S. Highway 64 near Arroyo Hondo (locality C on Plate 1 and Figure 4-6), which previously were sketched by Muehlburger (1979) and mapped by Leininger (1982). The roadcuts expose high-angle and low-angle faults cutting strata mapped by Muehlburger (1979) as the Santa Fe Group and the Servilleta Formation. Because these outcrops expose critical stratigraphic and structural relationships, we discuss them in detail below. As described below, we refer to the roadcuts as numbers I through IV, which correspond to the numbered designations in Muehlburger (1979).

4.1.3.1.5.1 Roadcut I. Roadcut I is located approximately 0.5 km east of Arroyo Hondo, on the northwestern side of Highway 64 (Figure 4-6). Muehlburger (1979) showed a single, southeast-dipping thrust or reverse fault cutting a southeast-dipping cobble conglomerate of the Santa Fe Group. We observed no discrete southeast-dipping fault in the outcrop, although bedding is difficult to discern in the conglomerate and the exposure probably has degraded since it was sketched by Muehlburger (1979). The mapped fault trace coincides with the hinge of a synformal flexure in the cobble conglomerate, and thus may be associated with folding.

4.1.3.1.5.2 Roadcut II. Roadcut II is located approximately 0.3 km east of Arroyo Hondo on the southeastern side of Highway 64 (Figure 4-6). As previously sketched by Muehlburger (1979), several southeast-dipping thrust or reverse faults are present in roadcut II. We concur with the strike, dip and location of these faults as shown by Muehlburger (1979). Based on correlation of bedding sequences across the faults, maximum displacements on the thrust faults are approximately 2 m or less.

In addition to the thrust faults, we observed a previously unmapped, high-angle fault in roadcut II that strikes N68°E, dips 70° northwest, and lies several meters southeast of the thrust faults. The fault consists of a 0.5 to 2.0 m wide zone of shearing, and juxtaposes moderately southwest-dipping Santa Fe Group strata on the southeast against vertical Santa

Fe Group strata on the northwest. The trace of the fault is coincident with an ephemeral gully that drains the slope above the outcrop. The fault is partly obscured by colluvium and slopewash in the gully. We confirmed the presence of the fault within the channel by excavating approximately 2 m of the fault plane near the top of the outcrop. We were unable to determine the sense or amount of separation because of a lack of correlative bedding or other features across the fault. Thus, vertical separation on this strand is probably greater than the height of the roadcut (approximately 4 m).

The high-angle fault also is present in an east-facing roadcut on the western side of Highway 64, directly opposite roadcut II. In this exposure, the fault strikes N68°E, dips 88° northeast, and juxtaposes moderately northeast-dipping strata on the northwest against gently southwest-dipping strata on the southeast. The similar orientation, structural relationships, and projection of the fault northeast across Highway 64 demonstrates that this fault and the high-angle fault in roadcut II are correlative. We excavated portions of the fault plane in an attempt to find slickensides or other kinematic indicators. Although we did not observe slickensides, the fault plane contains subhorizontal undulations or shallow grooves that may indicate a lateral component of slip. Small, poorly-developed sigmoidal "s" shears in the fault zone suggest left-lateral slip. The high-angle fault is the only structure visible in the roadcut on the western side of Highway 64. The thrust and reverse faults observed in roadcut II (Muehlburger, 1979) are not present in the exposure on the western side of Highway 64.

5.1.3.1.5.3 Roadcut III. Roadcut III is located approximately 100 m west of Arroyo Hondo on the western side of Highway 64 (Figure 4-6). Based on our field reconnaissance, we concur with Muehlburger's (1979) interpretation that the Embudo fault consists of a single high-angle fault that juxtaposes strata of different orientations and sedimentary textures. The fault in roadcut III projects northeastward to the high-angle fault exposed in roadcut II.

5.1.3.1.5.4 Roadcut IV. Roadcut IV is located approximately 1.0 km west of Arroyo Hondo on the east side of Highway 64. We examined roadcut IV and concur with Muehlburger's (1979) interpretation that the Embudo fault consists of a single, high-angle fault. The fault trace in roadcut IV is associated with a northwest-facing scarp (Muehlburger, 1979) that can be traced for approximately 0.9 km northeast toward the fault

exposure in roadcut III. Stratigraphic and structural relationships in roadcut IV indicate that the Embudo fault has accommodated a component of northwest-side-down displacement.

The northwest-facing scarp above roadcut IV is associated with a prominent down-to-the-northwest topographic step in the surface of a dissected alluvial fan. This topographic step crosses Arroyo Hondo and can be traced northeast of roadcuts I and II. Based on our brief field reconnaissance in the Arroyo Hondo region, we postulate that the topographic step is formed by one or more northwest-facing scarps associated with the Embudo fault. A pace-and-compass profile of a scarp several hundred meters northeast of roadcut II shows approximately 8.5 m of northwest-side-down displacement of the fan surface. We interpret the scarp to be the result of northwest-side-down movement on the Embudo fault.

A cobble conglomerate exposed on both sides of the fault at roadcut IV shows evidence of pedogenic carbonate accumulation. Disseminated $CaCO_3$ is present in the conglomerate matrix, and calcium carbonate rinds coat upper and lower surfaces of the clasts. The pedogenic carbonate horizon is 1 to 2 m thick on the northwestern side of the fault and 1 m or less in thickness on the southeastern side of the fault. We attribute the difference in thickness to erosional stripping of the surface on the upthrown (southeast) side of the fault. The thickness and morphology of the carbonate horizon are consistent with stage III pedogenic development for middle Pleistocene carbonate soils in northern New Mexico (Machette, 1985). The carbonate accumulation indicates that deposition waned or stopped and the alluvial fan ceased to be a constructive landform in the middle Pleistocene or later. Significant deposition on the fan surface probably ceased when Arroyo Hondo began to deepen its channel in response to regional incision by the Rio Grande (Muehlburger, 1979).

Based on field reconnaissance of the Arroyo Hondo area, we interpret that the Embudo fault is a high-angle, oblique-slip fault with a component of northwest-side-down vertical separation. Possible kinematic indicators in the exposure opposite roadcut II suggest that the fault may accommodate a component of left-lateral slip. We interpret the thrust faults mapped by Muehlburger (1979) in roadcuts I and II to splay upward from the trace of the high-angle fault and form a flower structure. We thus infer that the thrust faults are secondary features and that the principal fault trace is a steeply-dipping to vertical structure. This interpretation is consistent with relationships in roadcuts II and IV showing that greater displacements have occurred on the high-angle fault rather than the low-angle thrust faults.

If the Embudo fault is primarily a left-lateral oblique-slip fault, then the origin of the transpressional thrust faults may be a result of the right step in the trace of the fault between Arroyo Hondo and the southern end of the Sangre de Cristo fault in the southern Taos Basin (Figure 4-6).

4.1.3.1.6 Summary of Embudo Fault Investigation. Based on our reconnaissance investigations, we conclude the following:

1) Geomorphic expression of the Embudo fault is most prominent at its northeastern end, near Arroyo Hondo, but then decreases in prominence to the southwest. Thus, vertical separation along the Embudo fault zone probably is greatest at the northeastern end of the fault and diminishes toward the southwest;

2) The Embudo fault in the Arroyo Hondo area is most simply and directly characterized as a steeply-dipping to near vertical left-oblique fault with a component of northwest-side-down movement. Thrust faults associated with the Embudo fault probably are related to a locally transpressional right-restraining bend in the fault trace near Arroyo Hondo.

We conclude that the Embudo fault forms a transfer or accommodation zone between the Española and San Luis structural basins, as previously suggested by Muehlberger (1979) and Dungan et al. (1984). The data collected for this reconnaissance study do not support the hypothesis that the Embudo fault zone presently is a through-going, right-lateral strike-slip fault system that accommodates counterclockwise rotation of the Española Basin (Muehlburger, 1979; Brown and Golombek, 1986). We conclude that the local counterclockwise rotations measured adjacent to the Embudo fault are consistent with left-lateral shearing, and thus support the hypothesis that the fault is an accommodation zone.

4.1.3.2 Faults of Black Mesa

Previous workers (Kelley, 1978; Machette and Personius, 1984) mapped several northeast-striking faults across the upper surface of Black Mesa, an approximately 15-km-long, northeast-trending mesa northwest of the Rio Grande that is capped by a 3.6 Ma basalt (Laughlin et al., 1993). As mapped, the faults display both northwest-down and southeast-

down displacements of the basalt beneath the surface of Black Mesa (Kelley, 1978; Machette and Personius, 1984).

Analysis of aerial photography performed for this study confirmed the presence of several prominent northeast-striking scarps on the surface of Black Mesa. In many cases, the scarps appear to be headwall scarps of large landslides. The entire southeastern slope of Black Mesa is a large landslide complex consisting of rotational block slides, slumps and rockfalls. One 8-km-long set of scarps, however, strikes northeast, faces southeast, and is located near the northwestern rim of Black Mesa. Based on analysis of the 20-ft contour topographic map, this scarp is about 19 m high (locality D, Plate 1). The scarps locally display an en echelon, left-stepping pattern and are associated with small graben. This system of scarps was mapped as a series of Quaternary faults by Machette and Personius (1984), and shown as extending beyond the northwestern rim of Black Mesa for a total length of approximately 15 km. Based primarily on linearity, length, and position along the northwestern mesa rim, these scarps cannot be unequivocally attributed to landsliding. This would require that the entire mesa, with the exception of a narrow remnant along the northwestern rim, is sliding as a single block into the Rio Grande canyon.

We conducted aerial and field reconnaissance investigations to assess whether the system of scarps is a result of faulting or landsliding. A profile of a southeast-facing scarp at locality E (Plate 1) shows a surface displacement of 8.5 m (Figure 4-7a). The scarp projects southwest to a dissected drainage basin along the northwestern rim of Black Mesa, adjacent to Vallito Peak (Plate 1). Bedding in strata of the Santa Fe Group are well-exposed in this drainage basin. The presence of faulted bedding in the drainage would support a tectonic origin for the scarp, but we could not identify marker horizons and trace them across the downward projection of the scarp during helicopter aerial reconnaissance. In addition, we did not observe unequivocal evidence of faulted beds in the cliff exposures. Additional field reconnaissance is necessary to determine if faulting has deformed bedding of the Santa Fe Group along the southwestern projection of the scarp.

Directly east of this southeast-facing scarp are two short, northwest-facing scarps (localities F and G, Plate 1). Pace-and-compass surveys show that the minimum vertical separations of the basalt surface across these scarps are approximately 5.5 and 19 m (Figures 4-7b and 4-7c). Based on the 20-ft contour topographic map, the basalt surface on the upthrown side

of the northwest-facing scarp (locality G) is about 18 m (60 ft) higher than the surface on the upthrown side of the southeast-facing scarp to the north (locality D). If the southeast-facing scarp is associated with a large landslide, the northwest-facing scarp to the south would be an antithetic failure in the slide mass. Because the upthrown side of the scarp at locality G is higher than at locality D, however, it is very unlikely that the scarps are related to a large, deep-seated landslide.

Based on these observations, we conclude that the system of northeast-striking scarps of Black Mesa mapped by Machette and Personius (1984) are results of surface faulting. The precise timing of displacements is unknown, but the faulting occurred after deposition of the basalt at about 3.6 Ma. Because there were no data available to characterize these faults prior to this study, we use scarp heights to estimate possible fault slip rates (Section 7.1).

4.2 PALEOSEISMIC INVESTIGATIONS OF THE PAJARITO FAULT SYSTEM

Since the early 1960's, several investigations have been conducted to evaluate the structure, stratigraphy, and potential seismic hazard of the Pajarito fault system (Griggs, 1964; Keller, 1968; Kelley, 1979; Muehlberger, 1979; Boden, 1980; Golombek, 1981, 1983; Gardner and Goff, 1984; Harrington and Aldrich, 1984; Gardner, 1985; Gardner and House, 1987; Wachs et al., 1988; Gardner et al., 1990). This fault system consists of several generally north-striking faults that define the active western boundary of the Española Basin portion of the Rio Grande rift (Gardner and House, 1987). Gardner and House (1987) refer to the "Pajarito fault system" as a broad, complex system of faults which they suggest constitute a single structural entity. As defined here, the fault system is comprised of three principal faults and numerous secondary faults that cross the western Pajarito Plateau (Figure 2-2; Plate 2). These main faults are the down-to-the-east, 41-km-long Pajarito fault, the down-to-the-west 14-km-long Rendija Canyon fault, and the down-to-the-west 12-km-long Guaje Mountain fault (Sections 4.2.1, 4.2.2, and 4.2.3, respectively).

Based on findings in previous studies (e.g., Wachs et al., 1988; Gardner, 1986), and our analysis of aerial photographs, aerial reconnaissance and field mapping, several possible sites for detailed investigations of the Pajarito fault system were identified and the process of obtaining permits for subsurface investigations was initiated. Sixteen sites along the Pajarito, Rendija Canyon, and Guaje Mountain faults were identified for further studies. The sites

are located on land owned or administered by the U.S. Forest Service, LANL, Los Alamos County, the General Services Administration, and Bandelier National Monument. Of the sixteen sites, seven were selected for detailed investigations, on the basis of geomorphic expression of faulting, availability of surficial deposits to record late Quaternary displacement, potential for obtaining data on deposit ages and fault characteristics, and permission to conduct subsurface excavations. The following sections describe the investigations at three sites along the Pajarito fault, two sites along the Rendija Canyon fault, and two sites along the Guaje Mountain fault.

4.2.1 Pajarito Fault

The lateral extent of the Pajarito fault has not been well-documented previously. Although Aldrich and Dethier (1990) show that the Pajarito and Embudo faults intersect near Clara Peak (Plate 2), Gardner and House (1987) consider the Pajarito fault and Embudo fault to be continuous structures. Based on analysis of aerial photography, aerial reconnaissance, and review of geologic mapping, we extend the Pajarito fault as far northeast as Clara Peak (Plate 2). Northeast of Clara Peak, there is little or no geomorphic evidence of discrete normal slip (Section 4.1.3.1). Sense of slip at this location appears to change to predominately strike-slip with minimal down-to-the-southeast vertical slip. This junction of the Embudo and Pajarito faults is also near the intersection of other faults, including the La Cañada del Amagre-Clara Peak fault zone to the north and the Puye fault zone to the south (Plate 2). We define the southern end of the Pajarito fault at its intersection with the La Bajada fault (Plate 2), near Cochiti Lake, where the sense of slip changes from down-to-the-east to down-to-the-west.

Where the Pajarito fault traverses the Pajarito Plateau near the LANL, a complex range-front almost 200 m high is present in the 1.2 Ma Bandelier Tuff. Topographic profiles indicate that the maximum NVTD of the Bandelier Tuff along this portion of the Pajarito fault is 154 $\pm$ 5 m down-to-the-east, whereas the average NVTD is about 81 m (Section 4.1.2). This clearly indicates that recurrent Quaternary movement has occurred along the fault and these displacements yield maximum and average vertical slip rates of about 0.13 and 0.07 mm/yr, respectively, for the Pajarito fault since 1.2 Ma. Subsurface geologic data are interpreted to show progressively larger displacements of older rocks, suggesting that the Pajarito fault was active prior to Bandelier Tuff deposition 1.2 Ma (Dransfield and Gardner,

1985). However, the age of most recent activity on the fault is unknown and it is unclear whether activity along the fault zone has been evenly distributed through Quaternary time or has shown an increase or decrease during the late Quaternary. Gardner and House (1987) report up to 6 m of apparent vertical separation of Quaternary alluvium along the Bland-Sanchez Canyon section of the Pajarito fault about 11 km south of Los Alamos (locality 11, Plate 2). Although Keller (1968) suggests that displacements south of Los Alamos post-date deposition of the El Cajete Pumice (45 to 73 ka), Wachs et al. (1988) indicate that the relationship of the pumice to the fault zone is unclear.

Although the Pajarito fault shows a significant amount of normal slip, how much lateral slip has occurred and its sense is not well constrained. Gardner and House (1987) report a northward change in sense of slip from dip-slip to oblique to lateral slip along the fault toward its intersection with the Embudo fault. Golombek (1981, 1983) reports slickenside data that suggest predominantly dip-slip motion along the central part of the Pajarito fault. Salyards and Ni (1990) and Salyards et al. (1991) interpret paleomagnetic data as evidence of left-lateral slip along the Pajarito fault. However, Baldridge et al. (1990) note that oblique slickensides plunge to the north and to the south, offering different senses of lateral offset. In addition, a substantial change in fault strike north of Santa Clara Canyon, the presence of several fault splays and cross structures between Los Alamos and Santa Clara Canyon (Golombek, 1983; Gardner and House, 1987), the change in geomorphic expression from prominent fault escarpments south of Los Alamos Canyon to a more subdued monoclinal flexure north of the canyon, and the possible connection with the Embudo fault (Aldrich, 1986; Aldrich and Dethier, 1990) suggest that kinematic characteristics along the fault between Los Alamos Canyon and Santa Clara Canyon may be different than that along the central part of the fault.

Interestingly, the Pajarito fault differs from other major rift-border faults to the north and south in that it does not lie at the base of a Precambrian-cored range block, many of which were originally uplifted during Laramide deformation. Perhaps the absence of a major range block along the footwall of the Pajarito fault is related to thin crust and high heat flow associated with the Jemez Volcanic province (Goff et al., 1989), or to a possibly shorter displacement history that spans about 16 Ma (Gardner and Goff, 1984), rather than about 15 to 30 Ma as along the Sangre de Cristo fault in northern New Mexico and southern Colorado (Kelley and Duncan, 1984; Menges, 1990a,b; Lindsey et al., 1983). Regardless, the

development of the Pajarito fault in Quaternary rocks (albeit "soft" rocks) rather than in Tertiary unconsolidated or semiconsolidated sediments at the surface, has influenced the geomorphic expression of the fault. Along much of its length, it is characterized by multiple bedrock escarpments forming a complex range-front that morphologically is similar to many other late Quaternary range-bounding normal faults in the Rio Grande rift (e.g., Sangre de Cristo fault) and elsewhere in the Basin and Range province, with steep, faceted spurs forming linear mountain fronts (Wallace, 1978). However, the Pajarito fault is noticeably different in two respects. First, total structural and topographic relief are much less, a few hundreds of meters, compared to a couple of thousand of meters that is typical of many range-bounding faults in the Rio Grande rift and Basin and Range province (e.g., Wallace, 1978; Schwartz and Coppersmith, 1984; Menges, 1990a,b). Second, the Pajarito fault apparently does not have prominent single- or multiple-event fault scarps developed in late Quaternary alluvium at the base of a range front, as do most late Quaternary faults in the Rio Grande rift (Machette, 1986; McCalpin, 1982; Menges, 1990a,b) and the Basin and Range province (Machette et al., 1992; Ramelli and dePolo, 1993). Although Boden (1980) identified a fault scarp on older alluvium at the southern end of the fault, we did not observe definite evidence for prominent fault scarps on alluvium along the central section of the fault, closest to the LANL. Perhaps this lack of scarps on alluvium is because of substantial incision by streams draining the Pajarito Plateau and an absence of well-preserved late Pleistocene to Holocene alluvial-fan deposits. Regardless of the reason, due to this general lack of fault scarps on alluvium along the Pajarito fault escarpment, it is more difficult to constrain the age of most recent activity on the fault.

To better understand recent fault behavior, we excavated four exploratory trenches and three test pits at three sites along the central section of the Pajarito fault near the base of the easternmost escarpment (localities 1, 2, and 3; Plate 2). The purpose of the excavations was to expose faulted and unfaulted stratigraphic units to assess the recency of activity, particularly evidence of Holocene faulting. In addition, we sought to estimate the late Quaternary slip rate and recurrence of surface faulting earthquakes.

Reasons for selection of paleoseismic investigations were different for each location because of unique stratigraphic and/or structural characteristics. However, general criteria that were applied for all potential sites include: 1) the simplest fault geometry to avoid complex, multiple fault splays; 2) minimal scarp modification by stream erosion, gullying, or human

alteration; 3) potential for encountering datable material; 4) presence of fluvial, colluvial or volcanic deposits that may be either faulted or post-date the most recent surface rupture; and 5) avoidance of cultural artifacts and threatened and endangered species habitats.

The eastern escarpment along the central part of the Pajarito fault is generally about 100 m high and therefore, posed significant logistical and interpretive problems for this investigation. In lieu of trenching the entire escarpment with a single or multiple overlapping trenches, we limited this investigation to trenches located near the base of the escarpment where critical colluvial wedge deposits may occur and the most recent activity may be preserved. We realized at the outset that the most recent event(s) may have occurred on other fault escarpments, or elsewhere on the eastern escarpment. However, the morphology of the eastern escarpment suggests it includes the youngest faults (Section 4.1.2.3) with the greatest amount of displacement (Table 4-1). In addition, we thought that it was most likely that geologic evidence for surface faulting would be more difficult to identify and not as well preserved on the face of the escarpment than at the base because of erosion on the extremely steep, bedrock-supported slope of the escarpment face. Based on our experience in paleoseismic investigations of Basin and Range-style faults, we excavated trenches near the base of the escarpment, a location with a higher probability of preserving colluvial wedge deposits and providing paleoseismic information.

We emphasize here that because the record from the trenches at the base of the eastern escarpment is incomplete, we did not directly use this information to develop recurrence intervals for the hazard analysis (Section 7.1). Instead, the information presented here forms a beginning in better understanding the surface faulting behavior of the Pajarito fault, but much additional work is needed to develop a comprehensive paleoseismic record and to better characterize the Pajarito fault as a potential earthquake source for the LANL. Moreover, although the available evidence would suggest that the most recent faulting events on the Rendija Canyon and Guaje Mountain faults are younger than any faulting observed so far in trenches on the Pajarito fault, there is still great uncertainty as to whether the various components of the Pajarito fault system behave dependently or independently of each other.

4.2.1.1 Water Canyon Site

The Water Canyon site is the southernmost paleoseismic investigation along the Pajarito fault (locality 3, Plate 2). The Water Canyon drainage is a perennial stream that originates near the eastern margin of the Valles caldera and flows east in a deeply incised canyon to the Rio Grande. Access to the site is gained along U.S. Forest Service trail #281 which heads west from Highway 501 (West Jemez Road). The objective at this site was to trench through the oldest, apparently unfaulted, inset fluvial terrace deposits that extend up canyon and possibly cross the easternmost main splay of the fault. If the fault could be located and overlying deposits were undeformed, then a minimum-limiting age for movement of that structure might be constrained.

4.2.1.1.1 Site Geology. The Water Canyon site is located along the central part of the fault at the base of the main Pajarito fault escarpment and on the northern side of Water Canyon (locality 3, Plate 2; Figure 4-8). Topographic profiles indicate about 103 to 124 m of NVTD of the top of the Bandelier Tuff across the entire Pajarito fault at the Water Canyon site (P6 and F6 in Table 4-1). The fault is characterized by a main escarpment that is over 120 m high and over 270 m wide, and a smaller, more subdued scarp about 150 m to the west that is about 18 m high (Plate 4) (Gardner and House, 1987).

At the trench site, near the base of the main escarpment, remnants of a flight of inset fluvial terraces are preserved. These terraces formed as a result of the progressive incision of Water Canyon Creek toward its present elevation (Plate 4) and have been extensively modified by erosion and burial. The highest and oldest terrace at the site is approximately 14 m above the present elevation of the creek. Based on evidence of eroded soils exposed in soil test pits excavated at three locations (TP1 through TP3 on Figure 4-8), an undetermined amount of the upper sections of the terrace deposits have been stripped (Plate 5). This is substantiated by the presence of broad, deep swales dissected into the present day topography (Figure 4-8). In addition, the western parts of the terrace deposits are buried by a colluvial apron and alluvium from fans derived from small ephemeral drainages along the base of the escarpment (Figure 4-8). The colluvium burying the terrace gravels contains abundant reworked fragments of El Cajete Pumice. Samples of charcoal from colluvium in

test pit TP2 (WCSP2-RC1 and WCSP2-RC2 on Plate 5) yielded radiocarbon ages of 8,060 ± 160 yr B.P. and 9,490 ± 110 yr B.P., respectively (Table 4-2).

One terrace located at the base of the escarpment can be traced as discontinuous remnants upstream (westward) across the escarpment along the northern margin of the valley (Qc/Qay near WCT1 on Figure 4-8). This is the only location along the central part of the fault where inset fluvial terrace deposits are located upstream of the projected base of the escarpment. These deposits were exposed in the trench and are discussed in the next section.

4.2.1.1.2 Trench Description. One exploratory trench (WCT1) was excavated within the inset fluvial deposits along the northern valley margin (Figure 4-8; Plate 5). The objective of the excavation was to expose deposits that bury a southern projection of the fault, which is inferred to be at the base of the escarpment (Figure 4-8) based on a significant break in slope coincident with a relatively linear bedrock-alluvium contact at this location. No scarps were observed on the inset terrace deposits along the valley margin or on younger fluvial deposits at a lower elevation. The west-trending trench WCT1 was 38 m long and as deep as 4 m (Plate 5). We cleaned and logged the entire south wall and 10 m of the north wall of the trench. Contacts, structures and other pertinent features were flagged, digitally surveyed, and then logged on a mylar base at a scale of 1 inch = 0.5 m. Detailed lithologic descriptions of units are provided in Appendix G and a soil profile description is in Appendix H.

The trench exposed boulders of Bandelier Tuff, fluvial gravels, and overlying colluvium (Plate 5, Appendix G). The base of the eastern 21 m of the trench is located within fluvial gravels and coarse colluvium. The gravels at the eastern end of the trench are more than 4 m thick and are comprised of distinct beds ranging in thickness from less than 0.25 m to more than 1 m. The base of the western 17 m of the trench is founded in Bandelier Tuff. Along portions of the trench, the tuff clearly consists of large colluvial boulders (eg. Stations 29-31 m), whereas in other areas (eg. Stations 16-21 m on the north wall), the possibility that the tuff is actually *in situ* bedrock cannot be precluded. Between Stations 31 and 35 m, a large gravel-filled pocket was excavated within the confines of extremely competent tuff. Clasts within the depression (Units 12 and 13) have an inclined texture that parallels the margins of the depression and suggests that they were deposited within an open hole or void between very large boulders. The origin of this depression is ambiguous. It may have been

related to bioturbation or it may be a fissure associated with slope failure or faulting, although it appeared unusually large for the latter.

No faults, shear fabric or fractures were observed within any of the units above the Bandelier Tuff boulders in the trench. Along the north wall of the trench, between Stations 16-21 m, Bandelier Tuff near the base of the trench contains many east-dipping fractures (Plate 5). The strike of the fractures nearly parallels that of the escarpment. These fractures are possibly related to faulting of *in situ* bedrock prior to deposition of the inset terrace gravels or they could be fractures within a large block-failure deposited at the base of the escarpment. Numerous such blocks containing slope-parallel fractures are present along many sections of the Pajarito fault escarpment (Section 4.1.2.2).

Regardless of the interpretation of these fractures or the depression between Stations 31 and 35 m, the alluvium and colluvium exposed in the trench appears unfaulted. Although these deposits could not be directly dated, based on map (Figure 4-8) and stratigraphic relations, we infer that colluvium in the trench correlates with colluvium in TP2 (Plate 5) and thus, the underlying alluvial deposits (and inset terrace) are older than roughly 9,000 to 10,000 years (see calendar-calibrated ages in Table 4-2).

4.2.1.1.3 Event Chronology. No shearing, fracturing, or deformation was observed in the trench in alluvium that was deposited after the El Cajete Pumice (45 to 73 ka), and probably before 9 to 10 ka. Thus, evidence of no Holocene faulting was observed in the trench at this location. However, we recognize that the most recent surface faulting might have occurred within any part of the escarpment to the west of the trench and although there is no apparent geomorphic evidence for young (Holocene) faulting within the valley floor fluvial deposits or elsewhere on the escarpment, the possibility of Holocene displacement on the Pajarito fault cannot be precluded based on evidence solely from this trench.

4.2.1.2 Water Tanks Site

The Water Tanks site (named for two large water-holding tanks immediately to the south of the site) is located adjacent to the west side of Highway 501 (West Jemez Road) and lies approximately 400 m south of Cañon de Valle (locality 2, Plate 2). The mean elevation of the site is about 2360 m. The site is located at the base of a roughly 110-m-high, 300-m-

wide east-facing fault escarpment (Figure 4-2b), which is the largest and easternmost escarpment in a complex fault zone that is over 500 m wide (Plate 2). Here, two fault escarpments are separated by a large relatively flat structural bench. The strands merge approximately 400 m to the southwest of the site to form a single large escarpment (Plates 2 and 4). Two trenches (WTT1 and WTT2) were excavated at this site and the main objective for trenching was to evaluate whether a pumiceous unit that was previously exposed at the nearby Water Tanks excavations was faulted along the base of the escarpment (Plate 4).

4.2.1.2.1 Site Geology. Geologic units at the Water Tanks site consist of welded and nonwelded flow units of 1.2 Ma Bandelier Tuff exposed in the escarpment that are overlain by tectonic and non-tectonic colluvium. The lower portion of the site is mantled by an unstratified homogeneous deposit at least 1.3 m thick comprised of pumice fragments (Unit 15 in WTT1 and Unit 4 in WTT2; Plate 6). Where exposed in the exploratory trenches, the pumice unit gradually thins upslope where it becomes mixed with relatively recent colluvium and ultimately pinches out. Based on their mineralogy, the pumice fragments are identified as part of the El Cajete series, which was erupted between 45 and 73 ka (see Section 2.4 for discussion of age). These deposits are significant for interpreting the history of surface rupture at the Water Tanks site because they are the oldest unfaulted deposits that were exposed.

Although lithologic characteristics suggest that Units 14 (WTT2) and 15 (WTT1) were primary air-fall deposits (Appendix G) and therefore, were deposited between 45 and 73 ka, radiocarbon age estimates for underlying colluvium were anomalously young. Two internally consistent radiocarbon age estimates, 19,070 $\pm$ 160 yr B.P. and 22,420 $\pm$ 690 yr B.P. (Table 4-2), were obtained from charcoal samples (WTT1-RC5 and WTT1-RC1) collected from colluvium (Unit 13 in WTT1 and Unit 11 in WTT2), which is buried by the El Cajete Pumice deposits (Plate 6). These samples provide a maximum age of about 19 to 22 ka for Units 14 and 15 (Table 4-2). Charcoal extracted from near the base of overlying colluvium (Unit 16 in WTT1) provides a minimum age for the pumice deposits of about 6.7 ka (sample WTT1-RC6, Table 4-2).

Thus, there is a disparity between the probable age for the El Cajete Pumice (between 45 and 73 ka) and the maximum age, based on radiocarbon analyses, for the pumice deposits

in the trenches. Four possible explanations for this disparity include: 1) the age-estimate for eruption of the El Cajete Pumice is too old; 2) the pumice in the trenches comprise a primary air-fall deposit but not from the El Cajete eruption; 3) the radiocarbon age estimates for charcoal from colluvium below the pumice incorrectly constrains the maximum age of the pumice because the charcoal is either contaminated or intrusive; or 4) Units 14 and 15 consist of reworked El Cajete Pumice and are considerably younger than the eruption. To provide an independent check of the radiocarbon age estimates, we collected thermoluminescence samples, WTT1-TL8 and WTT1-TL9, from Units 13 and 11, respectively (WTT1 on Plate 6). Analyses yielded respective age estimates of 55 $\pm$ 9 ka and 57 $\pm$ 18 ka (S.L. Forman, The Ohio State University, written communication, 1994) (Table 4-3). These ages and the evidence discussed below best support the explanation that the radiocarbon samples were probably either contaminated or were intrusive and introduced by bioturbation.

As previously discussed in Section 2.4, charcoal samples from logs entrained within the El Cajete Pumice in the Valles caldera yielded a minimum age of greater than 50 ka for the pumice (Reneau et al., 1994) and ESR age estimates for quartz phenocrysts in the pumice range between 45 and 73 ka (Toyoda et al., 1995). These results are consistent with a previous age estimate of $>$42 ka obtained for charcoal from within El Cajete deposits in the Valles caldera (Bailey and Smith, 1978). Additionally, thermoluminescence samples collected from an Av horizon buried by primary air-fall deposits of El Cajete Pumice on Pajarito Mesa yield ages of 48 $\pm$ 10, 51 $\pm$ 10, and 52 $\pm$ 10 ka ($\pm$ 2σ) (S.L. Forman, The Ohio State University, written communication, 1994). Therefore, primary El Cajete Pumice is at least older than 45 ka.

The pumice in the trenches is clearly identified as the El Cajete Pumice based on its unique mineralogy, specifically an abundance of biotite, that distinguishes it from other pumice deposits erupted from the Valles caldera. In addition, no younger eruptions ($\sim$19 ka to 22 ka) have been identified within the Valles caldera (J. Gardner, LANL, personal communication, 1992). Therefore, there seems little doubt that the pumice observed in the trench is derived from the El Cajete eruption.

The third explanation requires that the charcoal samples were contaminated or have been introduced into the colluvium after eruption of the pumice, and thus yield an erroneously

young age for the overlying pumice. Although roots can contaminate charcoal samples with younger carbon, and younger charcoal can be introduced into a deposit by bioturbation (such as by burrowing animals), the two internally consistent age-estimates from samples within two trenches would suggest that this possibility is less likely. WTT2-RC1 was a bulk sediment sample and thus, the age represents a composite for organics in the deposit matrix, which may have been contaminated by younger carbon from roots. Sample WTT1-RC5 was a very small piece of charcoal that required analysis by an accelerator mass spectrometer. A small amount of contamination during analysis of very small and old samples can yield unreliably young finite radiocarbon ages and we cannot preclude this possibility for sample WTT1-RC5.

Finally, if Units 14 and 15 are reworked pumice and not primary air-fall deposits, this would require monolithologic redistribution of the sediments because virtually no other clasts are present in the deposits. Also, no pumice fragments occur within underlying deposits. The reworking scenario requires eruption of El Cajete Pumice between 45 and 73 ka, no reworking of the pumice along the base of the escarpment for about 20,000 to 50,000 years, then sudden reworking of almost pure El Cajete Pumice at about 19 to 22 ka. This scenario is deemed possible, but highly unlikely because of the low probability that a large volume of pumice would be stored for so long and then redeposited without inclusion of other clast sizes and lithologies or without recognizable stratification being developed in the deposit.

4.2.1.2.2 Trench Descriptions. Two trenches were excavated near the base of the easternmost fault scarp (Plate 4). The upper end of the first trench (WTT1) was located to intersect the lowest position on the slope where bedrock might be exposed, thus potentially coinciding with a major fault strand. This position was located based on geologic mapping, position of bedrock outcrops, and inflection of the slope. The second trench (WTT2) was excavated after WTT1 was logged and interpreted. Based on our interpretation that tectonically-derived colluvial deposits were associated with a possible structure at a higher elevation than that of the upper end of WTT1, we excavated WTT2 about 8 m north and slightly upslope of the initial trench. The trench WTT2 was positioned so as to overlap trench WTT1 by about 10.6 m (marked near Station 11 m, WTT2, Plate 6).

4.2.1.2.2.1 Water Tanks Trench 1. Water Tanks Trench 1 is 47 m long and extends almost 13 m up the base of the escarpment (Plate 6). At its steepest location, the

trench crosses slopes of almost 30°. The average depth of the excavation is about 3 m; the depth ranges from 2 m, to 4 m, to 3.5 m in the upper, middle and lower portions of the trench, respectively. The south wall of the trench was cleaned, and contacts, structures and other pertinent features were flagged, digitally surveyed, and logged on a mylar base at a scale of 1 inch = 0.5 m. Detailed lithologic descriptions of units are provided in Appendix G and a soil profile description is included in Appendix H.

Moderately welded, pinkish-gray Bandelier Tuff (ca. 1.2 Ma) is exposed in three locations along the base of the trench (Stations 10-11 m, 34-36 m, and 39 m). The tuff may represent bedrock, or instead possibly large colluvial boulders. At Station 34-36 m, possible bedrock appears sheared with near vertical fractures. It terminates eastward and is buried by coarse-grained colluvium (Unit 3). The tuff exposures are overlain by numerous relatively thin (<1 to 1.5 m) colluvial units that roughly parallel the present slope and comprise almost the entire trench exposure (Plate 6). In general, these deposits are laterally continuous, with several units traceable along almost the entire length of the excavation (Units 6, 11, and 13). The colluvium is divided into coarse- and fine-grained deposits. The coarse-grained deposits consist of relatively large (up to 0.5 m-long) angular Bandelier Tuff clasts.

Unit 1a (Station 43-45 m) represents the oldest colluvial deposit in the exposure. It is moderately- to well-consolidated and has abundant $CaC0_3$ within the matrix. Both the eastern and western contacts of the deposit appear faulted. Unit 1b has an inclined texture commonly found within fissure-fill deposits and is located along a possible shear that terminated the upper end of Unit 1a. Unit 2 also appears to be a fissure-fill deposit that is buried by Unit 11 and may be related to the faulting event that produced Unit 11. At the upper 4 to 5 m of the trench, basal colluvium (Unit 3) has a clast-supported texture. This suggests a source of loose, coarse material that was transported mainly by gravity (toppling, sliding, falling, etc.). The overlying deposits (Units 5a, 5b) contain an abundance of large clasts at their upslope end that gradually decrease in number and size downslope. They have matrix-supported textures, indicative of the dominance of finer grained sand and silt fractions that have been translocated principally during wet periods. Units 3, 5a, and 5b probably represent debris- and wash-facies tectonic colluvium associated with surface displacement along the Pajarito fault (Appendix G).

Colluvial deposits 3, 5a, and 5b contain a strongly developed soil Bt horizon (not explicitly shown on Plate 6), requiring a relatively long period of stabilization and surface exposure prior to burial by Unit 6 colluvium. The soil is characterized by a high clay content, thick clay skins, well developed ped structure, and strong pervasive rubification (reddish brown, 5YR 4/4). In contrast, Units 6 and 11, both comprised of a similar parent material, have a moderately developed soil Bt horizon (not explicitly shown on Plate 6) consisting of some clay, minor clay skins, and moderate rubification (generally brown, 7.5YR 5/6). Thus, the soils in these younger deposits did not appear to have as much time to form.

Unit 15 is a nearly monolithologic unstratified pumiceous deposit up to 1.3-m-thick. The pumice is located in the upper part of the lower three-fourths of the extent of the trench (Stations 2-40 m; Plate 6). As discussed previously in Section 4.2.1.2.1, this deposit is probably an air-fall deposit of El Cajete Pumice that was deposited between 45 and 73 ka. There is a small possibility that Unit 15 is actually reworked pumice deposited around 19 to 22 ka. The deposit consisted of well-sorted pumice that has similar texture throughout the trench exposure. As with the underlying colluvium, the base of the deposit nearly parallels the present slope, however, at about three-fourths of the way up the slope the unit tapers and pinches out. Thin, discontinuous bands of clay are located throughout the unit and are subparallel to the present slope. These features may be lamellae of incipient pedogenic Bt horizons resulting from variable depths of wetting within the permeable pumice.

Unit 15 is overlain by two fine-grained colluvial deposits (Units 16 and 17) along its lower half (Plate 6). Both of these units are thin, less than 0.5 to 1 m thick, and pinch out upslope. The irregular, wavy base of the lower colluvium, Unit 16, and the abundance of pumice clasts provide strong evidence that this unit is reworked from Unit 15 upslope. Unit 16 has a poorly developed Bt horizon, while Unit 17 has a weakly-developed Bw horizon.

Structures in the WTT1 trench consist primarily of: fractures and faults with apparent small vertical displacements located in the eastern half of the trench (Stations 8-10 m and 15-21 m; Plate 6), and faults in Units 3 and 1a at the west end of the trench (Stations 42 to 45 m; Plate 6). The latter had associated shear fabric that did not appear to extend into overlying sediments (Unit 5b), but any fabric in Unit 5b may have been masked by the well-developed Bt horizon in this unit. Faults in the easternmost part of the trench strike N30°E to N45°W and have dips that are greater than 80° to both the east and west. These faults are

concentrated within a narrow zone less than about 2 m wide (Stations 8-10 m) and offset Units 6, 10, 11, 12 and 13 by small amounts. Likewise, the fractures are also steeply dipping and are located within a zone less than 6 m wide (Stations 15-21 m). Fracturing of possible bedrock was observed at Station 34 m where Bandelier Tuff is exposed at the base of the trench. Nearly vertical fractures and shears are visible within the tuff but do not extend upward into the overlying colluvium.

4.2.1.2.2.2 Water Tanks Trench 2. The second trench at the Water Tanks site was located about 8 m north of WTT1 and extended an additional 8 m further to the west. The trench was approximately 20 m long and up to 5 m deep (Plate 6). The ground surface along the trench excavation sloped almost 30° at its steepest location. As with trench WTT1, the south wall of the trench was cleaned, and contacts, structures and other pertinent features were then flagged, digitally surveyed, and logged on a mylar base at a scale of 1 inch = 0.5 m. Detailed lithologic descriptions of units are presented in Appendix G.

In general, geologic units exposed in trench WTT2 were similar to those described from trench WTT1, however, there were some notable differences. Of primary note was the presence of thick, irregularly-shaped, colluvial deposits in the westernmost third of the trench (Stations 14-20 m, Units 3, 4 and 5), which were coarse, unsorted, unstratified, and had a variable texture ranging from matrix-supported in Unit 4 to clast-supported openwork in Unit 3. Large clasts (up to 1 m wide) of Bandelier Tuff were jumbled within a loose sandy matrix in these sediments and definitive shear fabric or other clear evidence for faults was not observed, but would be difficult to identify in this type of material.

The lithology and shape of these deposits, along with the cross-cutting relations between deposits suggest they are either large fissure-fill deposits related to earthquakes or are landslide deposits. The shape and texture of Unit 3 strongly suggests it is a fissure-fill deposit. In addition, the shape and texture of Unit 6, which is associated with a part of Unit 5, strongly suggests that Unit 6 forms the debris facies of a colluvial wedge derived from a normal fault scarp (Appendix G). However, given the location of this site between large landslides (Plate 4) and without more definitive evidence for faulting directly associated with these deposits, we cannot preclude the possibility that Unit 3 is a fissure and Units 4 and 5 are jumbled blocks of material, all related to mass wasting.

The probable oldest deposit, Unit 4, (Plate 6) contained substantial secondary calcium carbonate (Stage III-IV) that was derived through pedogenesis and/or meteoric percolation and precipitation from water along fractures or downslope. The matrix and coatings of almost all clasts consist primarily of calcium carbonate. A probable intermediate-age deposit (Unit 5) comprised the majority of the eastern 7 m of the trench. The unit is comprised of three packages surrounded by Units 3, 4, and 6 (Plate 6). It is distinguished from other colluvial deposits by slight textural differences, and by Stage II-III calcium carbonate, which is abundant in the matrix (except where queried on Plate 6) and commonly coats many clasts. The youngest package (Unit 3) is distinguished from the older deposits based on its extremely loose character, open lattice matrix, and lack of carbonate. Unit 3 cuts through Unit 5 near the western end of the trench and probably is comprised largely of clasts from that deposit.

The other prominent difference between the WTT2 trench and WTT1 is the presence of pumice exposed at the present ground surface (Unit 14, Plate 6). In comparison, Unit 15 does not extend as far upslope in trench WTT1 and the difference may only reflect the local variability of deposition and/or preservation of the pumice along the base of the escarpment.

4.2.1.2.3 Event Chronology. Indirect evidence for probably at least three and possibly as many as five surface faulting earthquakes is interpreted from the stratigraphic and structural relationships observed in the two trenches (WTT1, WTT2) at the Water Tanks site (Figure 4-9). Although the primary scarp-forming fault could not clearly be identified in the trenches for any of these events, secondary faults, fissure fills, and potential scarp-derived colluvium that buries soil horizons is supporting evidence for the occurrence of at least three events (Earthquakes W, X, and Z). Apparent warping and possible fissure fills and/or scarp-derived colluvium is speculative evidence for the occurrence of Earthquakes V(?) and Y(?). It is important to emphasize that the earthquake record interpreted from trenches WTT1 and WTT2 can only account for a small fraction of the total 110 m of NVTD estimated for the eastern escarpment. Thus, additional earlier and/or distributed surface faulting events must have occurred along the Pajarito fault and, therefore, the record of surface faulting events discussed here is a minimum.

The oldest possible fissure-fill deposit (Unit 4) in the upslope end of trench WTT2 (Plate 6) provides indirect evidence of the oldest tectonic surface rupture (Earthquake V[?], Figure

4-9). A remnant of a possible colluvial wedge deposit (Unit 1a) associated with this event was identified in trench WTT1 (Plate 6). Both the fissure fill and colluvium are characterized by their abundance of pedogenic or possibly meteoric carbonate (Stage III-IV). If pedogenic, the extensive carbonate development suggests that a relatively long period of time occurred since that event and its burial by colluvium from the next event.

The next surface faulting earthquake (Earthquake W, Figure 4-9) is suggested by: secondary faults bounding Unit 1a, a fissure fill in WTT1 (Unit 1b), a possible fissure fill in WTT2 (Unit 5), and probable scarp-derived colluvium (Units 3, 5a and 5b, WTT1 and Units 1, 2, 6, and 7, WTT2). The matrix of the colluvium contains a significant amount of clay, well-developed ped structure and is reddish brown (up to 5YR 4/4, dry), suggesting there was a relatively long period of post-event soil development and slope stability after Earthquake W. The fissure fill deposit is relatively loose, but contains abundant carbonate (Stage II-III). Colluvium potentially associated with this event can be traced along the base of approximately ½ of the upslope portion of WTT1 (Stations 21-44 m; Plate 6). At Station 34 m, a step in Bandelier Tuff of approximately 2 m occurs, with coarse colluvium (Unit 3) deposited directly over it. Although it is unclear whether Unit 3 was deposited immediately after faulting at the bedrock step, an absence of faults or shears in Unit 3 indicate that no events occurred at that step subsequent to deposition of Unit 3.

Indirect evidence for the next surface rupture earthquake (Earthquake X, Figure 4-9) at the Water Tanks site includes fissure-fill deposits (Plate 6, Unit 3, WTT2; Unit 2, WTT1), secondary faults in Unit 3 (WTT1), and probable scarp-derived, debris- and slopewash-facies colluvium (Plate 6, Units 6 and 11, WTT1; Units 8 and 9, WTT2). Although the fissure-fill deposits in WTT2 (Unit 3) appear to be associated with the proximal debris-facies colluvium (Unit 8), the upslope termination of that deposit against a buried fault free-face was not exposed in the trench. Therefore, either the main fault zone associated with that event lies farther upslope beyond the western limit of the trench or the colluvium is not tectonic in origin. Soil development is not as pronounced in Unit 8 as it is in underlying deposits, suggesting that less time elapsed since the slope became stable. A detrital charcoal sample (WTT1-RC1D) extracted from the base of the proximal-facies colluvium (Unit 6) exposed in WTT1 (Station 32.5 m; Plate 6) yielded an infinite radiocarbon age of older than 47,500 yr B.P. (Table 4-2). This is consistent with an age of 57 $\pm$ 18 ka for a thermoluminescence

sample (WTT1-TL9, Table 4-3) collected from an overlying unit (Unit 11). Thus, Earthquake X most likely occurred more than 57 ka.

Speculative evidence for the penultimate surface rupture earthquake at this site (Earthquake Y[?], Figure 4-9) includes a possible 0.5 m of down-to-the-east warping of the base of Unit 8 in WTT2, and deposition of colluvial deposits (Plate 6; Units 12 and 13 in WTT1, and Units 10, 11 and 12 in WTT2) that could be tectonic in origin. No fault was positively identified at Station 16 m in WTT2 possibly because of the loose, chaotic texture of Units 4 and 5 (WTT2), which may contain the shear zone associated with this postulated event. Two radiocarbon samples were extracted from the coarse colluvium in each trench (Unit 11, WTT2; Unit 13, WTT1). Sample WTT2-RC1 (Table 4-2) provided an age estimate of 22,420 $\pm$ 690 yr B.P. Sample WTT1-RC5 (Table 4-2) provided an age estimate of 19,070 $\pm$ 160 yr B.P. As noted previously, these ages do not agree with the thermoluminescence age of 55 $\pm$ 9 ka (Table 4-3) for Unit 13 (WTT1), or the age of the El Cajete Pumice (45 to 73 ka) and interpretation of overlying Units 14 (WTT2) and 15 (WTT1) as primary air-fall deposits of this eruption. Thus, these radiocarbon samples were probably either contaminated or were intrusive. If so, Earthquake Y(?) possibly occurred around 55 to 57 ka (Figure 4-9). Alternatively, a small possibility remains that the pumice was reworked and the thermoluminescence age is erroneous. If so, Earthquake Y(?) possibly occurred some time between 19 and 57 ka (Figure 4-9).

Evidence for the most recent surface faulting earthquake (Earthquake Z, Figure 4-9) recorded within the Water Tanks trenches includes small, down-to-the-east displacements along a zone of faults and fractures between Stations 8-10 m within the eastern half of WTT1 (Plate 6). Total apparent net vertical separation is less than 20 cm. Faulting extends through Unit 13, colluvium possibly deposited as a result of Earthquake Y(?), but faulting does not displace the base of the El Cajete Pumice deposit (Unit 15) that overlies Unit 13. This is most easily explained by erosion of the top of Unit 13 subsequent to faulting. Therefore, the most recent event occurred after deposition of Unit 13 and prior to deposition of Unit 15. A charcoal sample (WTT1-RC6, Table 4-2) extracted from near the base of Unit 16, colluvium directly overlying the pumice deposit provides a radiocarbon age of 5840 $\pm$ 90 yr B.P. and a calendar-calibrated age of 6,670 (6,290-7,160) cal B.P. Thus, the unfaulted pumice deposit is older than about 6.7 ka.

Similar to Earthquake Y(?), the apparent discrepancies between radiocarbon ages and other information result in two different possibilities for the age of Earthquake Z. Unit 15 is probably a primary air-fall deposit of El Cajete Pumice and thus, was probably deposited between 45 and 73 ka. If so, Earthquake Z occurred between 45 and 55 ka. Alternatively, there is a small possibility that Units 14 and 15 are reworked pumice deposits and are younger than 19 to 22 ka. If so, Earthquake Z occurred sometime between 6.7 and 22 ka (Figure 4-9).

4.2.1.3 Pajarito Canyon Site

The Pajarito Canyon site is our northernmost paleoseismic study area along the Pajarito fault (Plate 2, location 1). The site is located directly west of State Highway 501 (West Jemez Road) and about 100 m south of the Pajarito Canyon drainage, a perennial stream that originates near the eastern rim of the Valles caldera. We excavated a trench and drilled 13 shallow holes at this site (Figure 4-10). The objective for trenching was to excavate into stream-terrace and colluvial deposits that cross the inferred projection of the fault near the base of the easternmost escarpment (Plate 4). Although the trench did not expose the primary fault of this escarpment, it did expose compelling evidence that a significant fault lies just west of the west end of the trench. The objective for drilling in Pajarito Canyon (Figures 4-10 and 4-11) was to locate this or other significant faults of the easternmost escarpment.

4.2.1.3.1 Site Geology. The Pajarito Canyon site is located along the eastern base of the range front formed in 1.2 Ma Bandelier Tuff (Plate 2). At this location, the Pajarito fault consists of two escarpments that reach a total height of about 180 m (Figure 4-2c). The trench was located just south of Pajarito Canyon, about 40 m west of Highway 501 (Figure 4-10) along the lower 12 m of the easternmost escarpment, which is about 80 m high. The site consists of a bedrock escarpment mantled by a thin (<1 m) veneer of colluvium, slopewash colluvium shed from the escarpment, and debris-flow and fluvial sediments that were deposited by the Pajarito Canyon drainage near the mouth of the canyon. Pajarito Canyon is deeply incised and terraces are preserved along the drainage, mainly on the downthrown side of the Pajarito fault (Plate 4). One such terrace at the east end of the trench site is roughly 10 m above the present thalweg of the drainage. We did not observe any evidence for fault scarps on unconsolidated sediments at the Pajarito Canyon site, and

in particular we observed no geomorphic evidence for faulting of the younger deposits within the drainage. However, the Holocene surfaces have been modified by construction of a dirt road along the southern side of the drainage in the canyon. In the absence of apparent fault scarps on unconsolidated deposits, we inferred the location of the primary fault associated with the eastern escarpment at the Pajarito Canyon site to be located near the base of the escarpment, where a relatively linear bedrock-colluvium contact is coincident with a significant break in slope.

4.2.1.3.2 Trench Description. Exploratory trench PCT1 (Trench 1 on Figure 4-10) was excavated to expose a primary strand of the Pajarito fault. It was oriented approximately east-west, nearly perpendicular to the inferred trace of the fault. The trench was 47 m long, 2.5 to 4 m deep, and was deepest at its western and easternmost ends where it exposed only unconsolidated deposits (Plate 7; Units 14a and 14b; Units 4-9). It was shallowest between Stations 15 to 31 m, where the relatively competent Tshirege member of the Bandelier Tuff (Unit 12) apparently has been upthrown relative to adjacent unconsolidated sediments (Plate 7). The entire south wall of the trench was cleaned, and contacts, structures and other pertinent features were flagged, digitally surveyed, and logged on a mylar base at a scale of 1 inch = 0.5 m. Detailed lithologic descriptions of units are presented in Appendix G and a soil profile description is in Appendix H.

The stratigraphy exposed in the trench consisted of: 1) young unfaulted colluvium that mantled the present slope and was exposed along the entire trench (Units 1 and 2); 2) an underlying buried soil, consisting of a Bt horizon, that also extends the entire length of the trench and appears unfaulted; 3) coarse colluvium that may have been shed from fault scarps associated with surface faulting earthquakes (Units 15 and 16); 4) a thick package of faulted, fine-grained sediments (Units 14a and 14b) at the west end of the trench that may be graben fill; 5) colluvium (Unit 3) (west of Station 34 m); 6) underlying faulted channel deposits (Units 18 and 13); 7) also underlying Unit 3, interbedded colluvial, eolian and alluvial deposits at the east end of trench and the base of the slope (Units 4 through 8); 8) faulted debris-flow and alluvial deposits (Units 11, 17, and 10) only exposed in the central part of the trench (between Stations 10 and 38 m); and 9) the Bandelier Tuff and associated pyroclastic deposits (Units 12a through 12e), also only exposed in the central part of the trench (between Stations 15 and 28 m).

Also exposed in the trench were numerous secondary faults and indirect evidence for at least two, and possibly as many as four events since deposition of the Bandelier Tuff 1.2 Ma (Figure 4-12). However, the primary fault responsible for 64 $\pm$ 5 m of NVTD on the easternmost escarpment (Figure 4-2c) of the Pajarito fault was not exposed in Trench PCT1. Therefore, the earthquake record for this strand remains incomplete and the number of events discussed here are a minimum for this escarpment.

Exposed at the west and of the trench was compelling evidence for the youngest earthquake event, Earthquake Z (Figure 4-12). Units 14 and 15 were deformed and cut by numerous, densely spaced, high-angle fractures and faults that showed small, primarily down-to-the-west displacements (Plate 7). In addition, we observed an intense and pervasive shear fabric developed in Unit 14 at the west end of the trench. An overlying, coarse, poorly-sorted colluvium (Unit 16) did not appear faulted and exhibited characteristics similar to colluvial wedge deposits associated with surface faulting events (Appendix G). The back (west) wall of the trench exposed Unit 16 nearly at the base of the trench, showing that the deposit thickened abruptly to the west. Additionally, Unit 16 contained clasts that were imbricated upslope to the west, suggesting that it may be part of a fissure-fill deposit associated with Earthquake Z. However, trench PCT1 did not extend far enough west to expose the primary scarp-forming fault for this event.

Similar to Unit 16, Unit 15 also was a coarse, poorly-sorted colluvial deposit that may have been associated with a separate earlier surface faulting event, Earthquake Y(?) (Figure 4-12). Evidence suggestive of an earlier event, distinct from Earthquake Z, includes some fault terminations in Unit 14 (Plate 7), apparently more intense deformation in Unit 14 than in Unit 15 (between Stations 45 and 46.5 m), and the gross morphology and lithologic characteristics of Unit 15 suggest it was a colluvial-wedge deposit that was subsequently deformed during Earthquake Z. In addition, the top of Unit 14 between Stations 45 and 46 was redder, more clay-rich, and contained peds, suggesting a buried soil horizon was developed below Unit 15. However, the intense deformation in this area precluded definitive identification and mapping of this horizon. Similar to Unit 16, the primary scarp-forming fault associated with Unit 15 was not exposed and we speculate it lies just west of the trench exposure.

Although the primary down-to-the-east fault was not exposed, based on multiple lines of indirect evidence, we interpret the area west of Station 27 m to be a graben, and evidence for all earlier earthquake events exposed in Trench PCT1, Earthquakes X(?), W and V(?) (Figure 4-12), was directly or indirectly related to faulting along this structure. Evidence for the graben includes: 1) west-dipping, down-to-the-west faults near Station 27 m that are interpreted to be the easternmost antithetic faults bounding the graben; 2) shallow bedrock (Bandelier Tuff) exposed east of these faults, between Stations 15 and 28 m, but not west of 28 m, suggesting the bedrock is an uplifted block or horst east of the graben; 3) Unit 11 is much thicker (>1.5 m) west of Station 28 m (in the graben) than where it overlies bedrock between Stations 15 and 28 m; 4) west of Station 27 m, apparent backtilting to the west of Units 10, 11, 14 and 15, provides additional indirect evidence, to that previously discussed, for a significant down-to-the-east fault west of the trench exposure; and finally, 5) the thickness, shape, and location of Unit 14 indicate it was deposited in a large paleodepression.

Unit 14 was unusually fine-grained and interpretation of the origin of this unit is equivocal. It consisted of a thick (>4 m) package of silty sand that occupied most of the western end of the trench. It was generally homogeneous and lacking in sedimentary structures (Unit 14a), with the exception of sandier pods (Unit 14b) that grossly defined gently west-dipping interbeds (Plate 7). At its eastern end, Unit 14 overlies Unit 10, and appears to overlie Unit 3, although the nature of this contact is somewhat obscured by subsequent overprinting of the Bt horizon developed in the top of both Units 14 and 3. The shape of the base of Unit 14 suggests it was either the base of a channel or the base of a deposit burying a degraded, west-facing scarp (between Stations 38 and 34 m), possibly associated with a west-dipping antithetic fault buried below the base of the trench. In either case, Unit 14 was deposited in a paleodepression that is no longer expressed in the present landscape except for perhaps a subtle break in slope near Station 35 m. The presence of a large depression in this slope position is most easily explained by the formation of a graben at this location. Alternatively, a depression could have formed at the base of a landslide scarp.

The fine-grained texture of Unit 14 and its presence above the base of the escarpment on a slope greater than 20° is anomalous. Fine-grained deposits almost completely devoid of clasts greater than sand-size are rarely found on such slopes that are mantled by coarse material. One possible explanation is that Unit 14 is alluvium deposited by a channel that

flowed parallel to a graben. The shape and sandy interbeds of Unit 14 would support this interpretation. Another possibility is that it is graben fill primarily composed of eolian and colluviated eolian sediments that accumulated during a time of intense loess deposition, resulting in a small percentage of gravel within the colluvium. Finally, Unit 14 could represent a combination of both alluvium and eolian deposits.

Thermoluminescence analysis of sample PCT1-TL12 from Unit 14 (Plate 7) yielded an age of 137 $\pm$ 22 ka (Table 4-3), providing the most reliable absolute age constraints for deposits overlying the Bandelier Tuff in this trench. However, the sample was near saturation and the age may be a minimum (S. L. Forman, The Ohio State University, written communication, 1994). In contrast, radiocarbon sample PCT1-RC1, collected near the top of Unit 14 (Plate 7), yielded an anomalous age of 700 $\pm$ 90 years B.P. (Table 4-2). The presence of the overlying Bt horizon indicates that this age estimate is most likely too young, suggesting either the sample was intrusive or it was contaminated by nearby young roots (Plate 7).

Based on the nature of Unit 14 and its relation to surrounding deposits, we speculate that at least one faulting event, Earthquake X(?) (Figure 4-12), occurred prior to deposition of Unit 14 to form a graben where Unit 14 was deposited. Graben formation would require movement on both a down-to-the-east main fault and a down-to-the-west antithetic fault, neither of which were exposed in trench PCT1. However, the base of Unit 14 may bury a degraded fault scarp associated with an antithetic fault buried below the base of the trench near Station 38 m and based on indirect stratigraphic and structural evidence previously discussed, we infer that the main graben-bounding fault lies just west of the trench.

Evidence for an earlier event, Earthquake W, is more direct and includes subvertical secondary faults near Station 27 m that offset Units 12, 11, 17, and 13, but not Unit 3 (Plate 7). Units 13 and 18 were channel-fill deposits inset into stream alluvium (Unit 11) and probable debris-flow deposits (Units 10 and 17). The location of channels coincident with the fault and western exposed end of bedrock may be evidence of faulting and local erosion along a former fissure.

Apparent vertical separation on the fault at Station 27 m was down to the west and measurements of slickensides suggest dextral normal-oblique slip (Plate 7). A component

of strike-slip movement may explain the inconsistencies in amounts of apparent vertical separation and thicknesses of deposits (note base of Unit 17 versus base of Unit 18) and the apparently small, if any, amount of vertical separation projected across the fault for Unit 10. Alternatively, we may have miscorrelated units or there may have been differential erosion between multiple faulting events on this strand. Ideally, to discern if a significant component of dextral slip has occurred repeatedly on this fault, additional data, such as measurements of piercing points offset by the fault, are needed.

Indirect evidence for a possible earlier faulting event, Earthquake V(?) (Figure 4-12) that occurred prior to deposition of Unit 10, includes fault and fracture terminations within Unit 11 and possible differential erosion of Unit 11 between Station 15 and 28 m (Plate 7). However, larger boulders in the trench floor prevented exposure of Unit 11 near Stations 28 and 29 m, and without a more complete exposure, we cannot preclude the possibility that variations in thickness were entirely depositional and not related to faulting and erosion. The base and top of Unit 11 dip nearly 20° between Stations 15 and 24 m, an orientation that is somewhat enigmatic for stream alluvium unless it is faulted and tilted. However, Unit 11 changes laterally which is common in alluvial-fan deposits. In this area, Unit 11 lacked the distinctive bedding structures present farther to the west and texturally it appeared more like debris-flow or possibly even colluvial sediments. A few faults were observed between Stations 15 and 27 m that offset the top of bedrock a small amount and terminated in or at the top of Unit 11 (Plate 7). These high-angle faults ranged in strike between N88°E to N15°W and slickenside measurements indicated a component of oblique slip (Plate 7).

No faults were observed in the sediments overlying the Bandelier Tuff east of Station 16 m, although numerous fractures were observed east of Station 9 m. Deposits at this end of the trench were primarily slopewash colluvium and loess except for Unit 6. The alluvial gravels that comprise Unit 6 probably correlate to the deposits that form the terrace at the east end of the site (Qt on Plate 4).

4.2.1.3.3 Event Chronology. The record of surface faulting events (Figure 4-12) represented by structures and deposits exposed in the Pajarito Canyon trench (PCT1) is minimal and equivocal because primary scarp-forming faults were not exposed, although units of probable fault-scarp colluvium were present. Based on the available data, two post-Bandelier Tuff surface faulting events (Earthquakes W and Z) and three equivocal events

(Earthquakes V[?], X[?] and Y[?]) can be interpreted from the PCT1 trench data (Figure 4-12).

The timing of events in trench PCT1 is loosely constrained by the age of the Bandelier Tuff (1.2 Ma), the thermoluminescence age for Unit 14 (137 $\pm$ 22 ka), and the moderately-developed Bt horizon that postdates all events. Earthquake V(?) possibly occurred on several small secondary faults after 1.2 Ma and deposition of Unit 11 over the Bandelier Tuff, but before deposition of Unit 10 sometime before 137 ka (Figure 4-12). Earthquake W also occurred on secondary faults sometime after Earthquake V(?) and subsequent deposition of Unit 18, but before deposition of Unit 3, also presumably sometime before 137 ka (Figure 4-12).

Earthquake X (?) possibly formed the graben in which Unit 14 was deposited about 137 ka (Figure 4-12). This event apparently occurred after deposition of Unit 3 and therefore, after Earthquake W. After deposition of Unit 14, 137 ka, Earthquake Y(?) possibly occurred on a primary, scarp-forming fault inferred to lie just west of the trench exposure (Figure 4-12). Finally, Earthquake Z occurred on numerous secondary faults and probably involved movement on the same primary fault inferred to lie west of the trench (Figure 4-12). A Bt horizon developed in colluvium that post-dates this event suggests that the slope was stable for at least some time (at least a few thousand years) since Earthquake Z occurred.

4.2.1.3.4 Shallow Drilling Investigation. Although a primary fault of the easternmost Pajarito escarpment was not exposed in trench PCT1, as previously discussed in Section 4.2.1.3.2, there was compelling evidence in the trench that a significant fault could be close to the west end of this trench. Shallow drilling was conducted to test this hypothesis and assist in the location of possible fault strands at the Pajarito Canyon trench site. Drilling was carried out on November 8 and 9, 1993 using an 8" hollow-stem auger, later enhanced with a center bit in order to allow greater penetration through a bouldery horizon. Thirteen holes were drilled along a transect up Pajarito Canyon, directly west of Highway 501 (Figure 4-10). It was hoped that drilling would reveal discontinuities in the bedrock-alluvium contact and perhaps discontinuities in the overlying alluvium that may be indicative of the location of recent faulting. The drill hole locations extended westward up the canyon, from a small alluvial terrace surface adjacent to the highway, for a distance of roughly 200 m. The slope of the ground surface along the transect is between 3° and 4° to the southeast.

Each drill hole encountered 0.3 to 0.5 m of silty clay, overlying a mixture of sandy clay, sandy gravels and silty gravels to a depth of 1.0 to 1.3 m (Figure 4-11). This in turn overlies a bouldery horizon, about 1.0 m thick, comprised mainly of tuff boulders, with occasional cobbles and boulders of dacite, especially in the more eastern holes (Figure 4-11). This boulder horizon resulted in refusal at a depth of about 1.3 m in all but two drill holes, even when using the center-bit and percussion drilling. From the two holes that encountered bedrock (2b and 3), it appears that the tuff boulders lie directly on top of bedrock (Figure 4-11), probably indicating that they form some sort of regolith. When encountered, bedrock was pinkish-grey, moderately welded Bandelier Tuff. No evidence of faulting was discovered within the tuff. Bedrock was possibly encountered in two other holes (4 and 4a); however, the lack of recovered core prevented definitive identification of the lithology.

Evidence from shallow drill holes was equivocal in regard to locating a main strand of the Pajarito fault because no significant discontinuities or offsets were observed in the alluvium or the alluvium-bedrock contact. All contacts are approximately parallel to each other and the ground surface (Figure 4-11), exhibiting apparent dips of 3° to 4° (Figure 4-11 is vertically exaggerated approximately ten times in order to show each unit). Although the shallow depths at which bedrock was encountered in holes suggest that drill sites were located on the upthrown side of the fault, the data is inconclusive because bedrock could only be positively identified in two holes due to limitations in recovery and penetration. Additionally, the bedrock could also be shallow on the downthrown side of the fault if the alluvium was eroded away during incision of Pajarito Canyon. Thus, although drilling revealed no definitive evidence for a splay of the Pajarito fault in Pajarito Canyon, neither does the evidence preclude the presence of a fault strand in the canyon.

4.2.2 Rendija Canyon Fault

The 14-km-long Rendija Canyon fault is subparallel to and located approximately 3 km east of the Pajarito fault (Figure 2-2; Plate 2). The north-trending, steeply west-dipping fault exhibits down-to-the-west displacement of the 1.2-Ma-old Bandelier Tuff, and thus is antithetic to the Pajarito fault (Kelley, 1954; Griggs, 1964; Smith et al., 1970; Budding and Purtymun, 1976; Kelley, 1978; Golombek, 1981, 1983; Gardner and House, 1987). The fault consists of a single strand north of Barranca Mesa, of two primary strands and

numerous secondary strands through the town of Los Alamos, and of a zone of distributed deformation south of Los Alamos Canyon (Plate 2).

Smith et al. (1970), Budding and Purtymun (1976), and Gardner and House (1987) show no connection between the Rendija Canyon fault and the Pajarito fault. Although several lineaments identified during our analysis of aerial photography provide possible evidence that the Pajarito fault may extend north of Los Alamos Canyon (Section 4.2.1), a possible intersection between the Pajarito fault and the northern end of the Rendija Canyon fault cannot be demonstrated at present. Thus, it is unclear whether the Rendija Canyon fault merges with or intersects the Pajarito fault north of Los Alamos Canyon (Plate 2). Nevertheless, the northern termination of the Rendija Canyon fault is identified herein at a possible intersection with the Pajarito fault near Rincon del Cuervo (Plate 2).

Smith et al. (1970) and Kelley (1978) show the southern end of the Rendija Canyon fault at about Los Alamos Canyon, whereas Dransfield and Gardner (1985) and Gardner and House (1987) continue the fault to the south of Los Alamos Canyon beneath the Bandelier Tuff. The presence of post-Bandelier displacement exposed in the Los Alamos County Landfill (Section 4.2.2.2) shows that major fault splays exist south of Los Alamos Canyon. Topographic profiles suggest that the net vertical tectonic displacement of the upper member of the Bandelier Tuff decreases to zero progressively south of Los Alamos Canyon (Figures 4-1 and 4-2b) and is distributed over a zone about 1 km wide. The southernmost prominent geomorphic evidence of the Rendija Canyon fault is located at Mortandad Canyon, although there are north- and northeast-trending aerial photograph lineaments along the projection of the Rendija Canyon fault further south to Water Canyon (Plate 2).

Vaniman and Wohletz (1990) inferred that the fault extends about to Cañon del Valle, which is about 3 km south of Mortandad Canyon, based on the presence of a broad zone of abundant, open fractures in the Bandelier Tuff. Recent trenching across their projection of the Rendija Canyon fault on Pajarito Mesa, at TA-67 (Plate 2), exposed several faults that form a 30-m-wide zone that offsets alluvium overlying the Bandelier Tuff (Kolbe et al., 1994). Apparent vertical offsets are small (60 cm or less) and generally down to the west, consistent with the sense of displacement on the Rendija Canyon fault. However, these faults do not offset air-fall and associated deposits of El Cajete Pumice. Therefore, movement on these faults occurred prior to 45 ka and prior to the most recent surface

faulting event on the Rendija Canyon fault identified at the Guaje Pines site to the north (see Section 4.2.2.1 below). Thus, the most recent event on the Rendija Canyon fault apparently did not rupture as far south as Pajarito Mesa; this may explain the lack of geomorphic expression between Mortandad Canyon and Pajarito Mesa, and the zero NVTD measured on profile P5 (Table 4-1) across the Rendija Canyon fault on Pajarito Mesa.

Net vertical tectonic displacement of the top of the 1.2 Ma upper Bandelier Tuff by the Rendija Canyon fault is greatest (36 $\pm$ 10 m) near Rendija Canyon, but decreases to zero within about 6 km to the north and south (Figure 4-3b). Based on the distribution of NVTD along the fault, the average displacement is 22 m. These data and the 1.2 Ma age of the upper Bandelier Tuff (Izett and Obradovich, 1994) yield an average long-term vertical slip rate of 0.018 mm/yr for the fault. The maximum vertical slip rate based on 36 m of displacement is 0.030 mm/yr. As previously noted (Section 4.1.2), slip rate estimates for the Rendija Canyon fault are slightly higher than estimates for the Guaje Mountain fault, but are lower than estimates for the Pajarito fault.

Prior to this investigation, there was no information concerning the paleoseismic characteristics of the Rendija Canyon fault. The primary goals of this investigation of the Rendija Canyon fault were to assess the timing of late Quaternary surface ruptures and to document the presence or absence of Holocene rupture along the fault. In addition, a major goal was to estimate the slip rates and recurrence intervals along the fault for probabilistic analyses of strong ground motion. The following section presents results of investigations at two sites (Plate 2): the Guaje Pines site, located along the central section of the fault where the amount of post-1.2 Ma displacement is greatest (Figure 4-2d); and the County Landfill site, located along a major fault strand in the area of distributed faulting south of Los Alamos Canyon.

4.2.2.1 Guaje Pines Site

The Guaje Pines site is located along the Rendija Canyon fault where it crosses Rendija Canyon northeast of the Guaje Pines Cemetery (Plate 2). The surrounding area contains a pine-juniper woodland, although the site itself contains grassland vegetation. The site was cleared of trees and farmed in the early 1900s (E. McGehee, LANL archaeologist, personal communication, 1992). The site includes a prominent west-facing fault scarp (Figure 4-13)

along the western side of a small bedrock knoll bordered on the north by the east-flowing Rendija Canyon drainage and on the south by a small unnamed tributary. These drainages merge along the eastern side of this knoll and are incised into Tertiary volcanic rocks of the Tschicoma Formation. On the western (downthrown) side of the fault, alluvial-fan sediments deposited by these drainages are associated with a broad, gently east-sloping geomorphic surface upon which the cemetery is located (Qfy in Figure 4-14). These deposits most likely overlie the Bandelier Tuff, although during this investigation no natural or artificial exposures of the bedrock directly beneath the younger alluvium was encountered. On the eastern (upthrown) side of the fault, older alluvium (Qfo) is present on the surface and is underlain by dacite of the Tschicoma Formation. A vertical, north-striking fault in the dacite exposed along the northern side of the knoll lies along the projection of the topographic scarp and faults exposed in the trenches (Figure 4-14).

The primary purpose of the investigation of the Guaje Pines site was to assess the nature and timing of late Quaternary displacements along the Rendija Canyon fault. Activities consisted of topographic surveying and geomorphic mapping to characterize the site geomorphology, followed by subsurface exploration to assess possible paleoseismic displacement. The exploration consisted of excavation of three soil pits into the younger fluvial deposits (SP1, SP2, and SP3), two east-west-oriented trenches across the fault scarp (GPT1 and GPT2), and two north-south oriented trenches parallel to and on opposite sides of the fault (GPT3 and GPT4) (Figure 4-14). The purpose of the two fault-normal trenches was to expose fault-related features and displaced and undisplaced stratigraphy and thus to obtain data on the nature and timing of surface ruptures. The purpose of the two fault-parallel trenches was to investigate two linear geomorphic features as possible indicators of lateral slip along the fault. The soil pits were excavated to assess soil development on the Qfy terrace surface and to extrapolate to the west stratigraphic and soil contacts exposed in the fault-normal trenches. Excavation and the main phase of documentation of these trenches and soil pits occurred during July and August, 1992, followed by technical review of the exposures in March 1993. We collected samples for thermoluminescence analysis in September 1993, and trenches were backfilled by summer 1994.

4.2.2.1.1 <u>Late Quaternary Stratigraphy</u>. The oldest surficial deposit exposed at the Guaje Pines site was Unit 21, which unconformably overlies dacite of the Tschicoma Formation on the eastern (upthrown) side of the fault in trench GPT2 (Plate 8). This clayey gravel

contained oxidized clasts of tuff and dacite, which probably were derived from the Rendija Canyon drainage and nearby dacite outcrops. This unit probably was a debris-flow or fluvial deposit. A pebble layer at the base of this deposit suggested that it was fluvial rather than colluvial in origin. Unit 21 was overlain unconformably in trench GPT2 by an olive gray sandy clay (Unit 20, Plate 8). This clay pinches out to the east and was faulted along its western contact with younger colluvial units. Minor shearing also was present through the western and central part of the unit, but did not extend into the overlying alluvial deposit (Station 7 m, Plate 8). Several pedogenic features, such as prismatic and angular blocky soil structure, clay films, and manganese oxide nodules, show that a well-developed soil formed in this deposit, and thus that the deposit was exposed at the surface for a substantial period of time. The gleyed colors of the deposits strongly suggest that there was ponding of groundwater on the eastern side of the fault. This unit is interpreted as a sag-pond deposit that may be related to surficial deformation along the fault. The location and extent of this deposit on the western side of the fault is unknown, but if delineated may provide information on the sense and amount of late Quaternary slip. The age of Unit 20 is estimated on the basis of one thermoluminescence sample (GPT2-TL5, Table 4-3, Plate 8). This sample yielded an age estimate of $>140 \pm 26$ ka (2 sigma uncertainty; S.L. Forman, The Ohio State University, written communication, 1994).

Unconformably overlying Units 21 and 20 was a package of relatively well-bedded, oxidized alluvial deposits that were exposed in trenches GPT1, GPT2, and GPT4 (Units 6a, 6b, 6c, 7, 8, 9, 10, 10a, 11, 12, 19, 19a, 19b, 19c, 19d, 19x, and 22; Plate 8). Based on trench exposures, this sequence of alluvium was more than 5 m thick and consisted primarily of oxidized sandy gravel with minor interbeds of silty sand. Clasts within this package were primarily tuff and dacite pebbles, although rare dacite boulders up to 1.5 m in diameter are present. There are dacite boulders of similar size at the surface on the crest of the knoll, although in greater abundance than in the deposits exposed in the trench. These relations, and the lack of soil development in the exposed deposits, suggest that the top of the knoll is degraded and that many of the boulders at the crest likely are an erosional lag deposit. Notably, this older package of oxidized alluvial deposits was exposed only on the eastern (upthrown) side of the fault. Along the main fault strand, Units 6a, 6b, 6c, and 6 were faulted in GPT1, and Units 19 and 19x were faulted in GPT2 (Plate 8). Minor faulting of Units 9, 10, 11, and 12 was present between Stations 8 and 11 m in GPT1. In contrast, as noted above, Unit 19 in GPT2 was not displaced by minor faults that do displace Unit 20.

The basal contact of Unit 19 is clear and smooth, and easily identifiable throughout its extent. Removal of the shore present at Station 6.0 m (Plate 8) allowed observation of this contact along the upward projection of the minor fault, and demonstrated that the fault did not displace Unit 19. The age of this older package of alluvial deposits is unknown, although thermoluminescence samples from overlying deposits suggest an age of more than about 64 ka (see below).

Stratigraphically above the oxidized package of alluvial deposits, but on the western (downthrown) side of the fault, were alluvial sediments deposited by the Rendija Canyon drainage or its tributaries. These sediments (Units 4b, 4c, and 4d in GPT1 and Unit 18 in GPT2; Plate 8) were informally termed the lower alluvium. These deposits primarily were gravel with dacite and tuff clasts up to 1.5 m in diameter within a silty sand matrix. A high percentage of tuff clasts relative to deposits on the top of the knoll to the east (Units 6 to 12, Plate 8) suggests a source to the west rather than the east. There was little or no distinct imbrication or bedding in Units 4b and 4d, although Unit 4c contains alignment of sandy and pebbly strata that dip gently to the west, parallel to the contact between Units 4b and 4c. In the western part of the trench, Unit 4b decreases in elevation from west to east, which is consistent with deposition via the Rendija Canyon drainage. In the central part of the trench, this deposit increases in elevation close to the fault (Figure 4-15). Based on lithologic similarities and stratigraphic position, we correlate Unit 4b in trench GPT1 with Unit 18 in trench GPT2. Units 4b, 4c and 4d are faulted along a subsidiary shear in trench GPT1, and Unit 18 is faulted by the main shear in trench GPT2 (Plate 8). Unit 4d, in particular, is interpreted as a faulted, down-dropped block of Unit 4b, based on lithologic similarity and structural relations (see below). Because of unclear lithologic relations, the lower part of what is mapped as Unit 4d may include some parts of Unit 4c (Plate 8). Notably, Units 4b, 4c, 4d and 18 are not present east of the fault. Based on thermoluminescence analyses of overlying deposits and on the amount of development of two soils formed in overlying deposits (see below), Units 4b, 4c, and 18 are more than about 64 ka.

Overlying the lower alluvium is a package of colluvial and alluvial deposits grouped together and informally termed the lower colluvium/alluvium (Units 5 and 4a in GPT1; Units 16 and 16a in GPT2; and Unit 16 in GPT3; Plate 8; Figure 4-15). In general, the package consists of three units that are finer grained upward and away from the shear zone exposed in

trenches GPT1 and GPT2. Unit 16a, the stratigraphically lowest unit in this package, is a coarse gravel containing dacite clasts up to 0.5 m in diameter that is very limited in extent and present only adjacent to the main fault strand in GPT2. This deposit is interpreted as scarp-derived debris colluvium that was produced shortly following a surface-rupture earthquake. In trench GPT2, Unit 16a grades upward into Unit 16, which is a gravelly silt that, based on lithologic similarities and stratigraphic position, is correlative with Unit 4a in trench GPT1. The easternmost 4 or 5 m of Units 4a and 16 are interpreted as wash colluvium (Appendix G) derived from the fault scarp following a surface rupture event. The western part of Unit 4a contains thin gravelly interbeds and is interpreted as contemporaneous alluvium derived from the Rendija Canyon drainage that interfingers with the scarp-derived colluvium. Both Units 4a and 16 are displaced by the main fault strand. The age of Unit 4a was estimated on the basis of two thermoluminescence samples collected from the base of the deposit (GPT-1-TL1 and GPT1-TL2, Table 4-3, Plate 8). These samples yielded age estimates of 69 $\pm$ 14 and 58 $\pm$ 52 ka, respectively (S.L. Forman, The Ohio State University, written communication, 1994). The root-mean-square average of these two samples is 64 $\pm$ 54 ka.

Unit 5 was a gravelly silt that overlies Unit 4a and represents the upper part of the fining-upward sequence of the lower colluvium/alluvium. As in Unit 4a, the westernmost part of Unit 5 contained thin gravelly interbeds that suggest deposition by an east-flowing fluvial system. The majority of Unit 5 likely was fluvial, although it may have contained fine-grained scarp-derived colluvium close to the fault as well as some eolian silt or sand.

A prominent soil horizon (Unit 5a) is developed on the upper parts of Units 4a and 5 (Plate 8). This soil horizon was up to 33 cm thick and exhibited evidence of secondary clay accumulation, such as medium subangular blocky structure, reddening (7.5YR 4.5/5 dry color), and clay film (horizon 2Bt1b; Soil Profile GPT1, 17 m; Appendix H). Units 4, 4a and 5 also exhibited evidence of clay accumulation and together with Unit 5a comprised a moderately developed buried soil. The total thickness of the Bt horizons (2Bt1b and 2Bt2b, Appendix H) within this buried soil is about 103 cm, from a depth of 137 to 240 cm (Fig. 4-12). Although there are few or no suitably dated comparable soils elsewhere in the northern Rio Grande rift from which to estimate the age of these deposits, we postulate that the properties of this soil are consistent with several tens of thousands of years of soil

development and the age-estimate of about 64 ka for the base of Unit 4a, based on thermoluminescence samples GPT1-TL1 and GPT1-TL2 (Table 4-3).

Directly overlying the lower colluvium/alluvium on the western (downthrown) side of the fault was a package of colluvial and alluvial deposits informally termed the upper colluvium/alluvium (Plate 8; Figure 4-15). This package consisted of Units 2a, 2b, 3, 3y, 3x, and 3z in trench GPT1, and Units 15 and 17 in trenches GPT2 and GPT3 (Plate 8). As with the lower colluvium/alluvium, this package was a fining-upward series of gravel, silty gravel, and silt with gravel that in general was finer grained away from the fault. In GPT1, Unit 3z was a gravelly silt that had a triangular cross-section suggestive of deposition in a depression along the fault trace. This stratigraphic position and the lithologic similarity between Unit 8 on the upthrown side of the fault and Unit 3z are evidence that Unit 3z was probably derived from Unit 8 immediately after a surface-faulting event. Based on clast lithologies and sizes and on stratigraphic position, Unit 3x was derived from the older alluvium exposed in a scarp face (Units 8 through 12), and was deposited at the base of the scarp. Based on the fining upward nature of Units 3x, 3y, 15, and 17, and the decrease in the size and abundance of dacite and tuff clasts in these units away from the fault, we interpret Units 3x and 17 as debris colluvium and Units 3y and 15 as wash colluvium (Appendix G) derived from the fault scarp formed during surface rupture. Units 2b, 3, and 15 are silts with sand and gravel, and are finer grained than underlying Units 3y and 3x. These units are interpreted as alluvial deposits derived from the Rendija Canyon drainage that interfinger with the scarp-derived colluvium of Units 3x and 3y. In addition, the abundance of silt in Units 2b, 3 and 15 suggests that they may also contain a substantial component of eolian material, either as primary airfall or a secondary (reworked) deposit.

Notably, the upper debris colluvium exposed in trench GPT2 (Unit 17, Plate 8) is anomalous because it is present upslope of the upward projection of the main fault strand, but did not appear faulted. Typically, little or no scarp-derived colluvium is present on upthrown fault blocks, with the exception of relatively thin hillslope deposits, such as Units 13 and 14 in trench GPT2 (M. Machette, U.S. Geological Survey, and J. McCalpin, GEO-HAZ Consultants, written communication, 1993). Thus, it is possible that the eastern part of Unit 17 east of the upward projection of the fault (east of Station 9 m in trench GPT2) is an upfaulted part of either Unit 16, 17, or another unit not exposed on the downthrown side of the fault. Such interpretations require that Unit 17 is faulted, which is inconsistent with the

observed lack of faulting in the correlative Unit 3x in trench GPT1. Based on the lack of observable shearing in Unit 17 above the projection of the main fault strand, it is most likely that Unit 17 extends upslope onto the upthrown block of the fault, as shown on Plate 8. Although atypical, this relation probably is a result of colluvial transport down the scarp face that is not in the plane of the trench exposure. The present ground surface near the central part of the trench slopes to the northwest, approximately N50°W. This is about 40° to 50° more northerly than the strike of the trench wall (Figure 4-14). Thus, an oblique sediment transport direction may have resulted in the anomalous presence of Unit 17 in GPT2 on the upthrown side of the fault. The absence of Unit 3x, which is correlative with Unit 17, on the upthrown side of the fault in trench GPT1 supports this model, because trench GPT2 is generally downslope from trench GPT1.

Unit 2a was delineated during documentation of the GPT1 trench exposure to show a moderately developed Bt horizon formed on Units 2b, 3, and 3y. This soil horizon was about 28 cm thick and exhibited evidence of moderate clay accumulation in the form of clay films, angular blocky structure and reddening (7.5YR 6/4 dry color). This soil was interpreted to have begun developing across Units 2b, 3, and 3y after degradation of the scarp slowed and the lower parts of the scarp became a relatively stable surface. The correlative soil horizon in trenches GPT2 and GPT3 was developed on Units 15 and 17 on the downthrown side of the fault, and on Units 19 and 19a on the upthrown side of the fault (Plate 8). Because of differences in the original texture of Units 19a, 19b, and 19c in trench GPT2, the base of the prominent Bt horizon coincides with the basal contact of Unit 19a in the eastern part of the trench.

Several radiocarbon and thermoluminescence analyses were conducted to estimate the age of the upper colluvium/alluvium (Tables 4-2 and 4-3), and two soil profiles were described to provide qualitative information on the relative age of the deposit. Unfortunately, these analyses provide conflicting results and make estimation of the age equivocal. As described below, two cases are considered for the age of the upper colluvium/alluvium, on the basis of either the radiocarbon or thermoluminescence analyses.

Five charcoal samples from the upper colluvium/alluvium were analyzed (Table 4-2). Of these, three samples taken from the basal part of Unit 15 in trench GPT2 yielded very consistent results (numbers GPT2-RC1, -RC2, and -RC3, Table 4-2). The average of these

three calendar-calibrated ages is 8100 ± 200 cal B.P. (see Table 4-2 for details on calibration). The charcoal fragments analyzed from these samples was scattered in an area tens of centimeters wide, and there was no indication of discoloration of the soil matrix or textural differences between the sampled area and the rest of Unit 15. Samples GPT2-RC2 and GPT2-RC3 were collected by S.L. Reneau (LANL), and were submitted separately by Reneau and Woodward-Clyde to Beta Analytic for radiometric analysis. Independent of the thermoluminescence results there is no reason to suspect that these ages were contaminated or out of context. Two charcoal fragments likely were intrusive into Units 2a and 2b in trench GPT1 (samples GPT1-RC5 and GPT1-RC8, Table 4-2) as they yielded ages of about 1170 cal BP and 780 cal BP, respectively. These ages are inconsistent with the age estimate of about 8 ka for Unit 15, and from the moderate amount of soil development in the upper colluvium/alluvium. These charcoal fragments likely were emplaced into Units 2a and 2b by burrowing animals.

Two thermoluminescence analyses were conducted on samples from the upper colluvium/alluvium in trenches GPT1 and GPT2. The preferred age-estimate from the Unit 3y sample (GPT1-TL4, Table 4-3) was 26 ± 6 ka, and the preferred age-estimate from the Unit 15 sample (GPT1-TL7) was 20 ± 4 ka. The average of these estimates was 23 ± 7 ka. This value is significantly higher than the age-estimate for the upper colluvium/alluvium based on radiocarbon analyses. S.L. Forman (The Ohio State University, written communication, 1994) notes that the thermoluminescence samples showed no evidence for anomalous fading and were characterized by low percentages of laboratory error. Comparison between results for total-bleach analyses and optically-stimulated analysis or partial-bleach analysis of the same sample shows no statistical difference between age estimates (Table 4-3), suggesting that the sediments analyzed were completely or nearly solar reset prior to deposition. The assumed moisture content for the samples was 15 ± 5% (Table 4-3), but even if a moisture content as low as 5% was assumed, this would only decrease thermoluminescence age-estimates by about 10% and there would still be a significant difference between the thermoluminescence and the radiocarbon age-estimates. Thus, there is no reason, independent of the radiocarbon results, to suspect the thermoluminescence ages.

Thus, the upper colluvium/alluvium is either about 8 ka (assuming that the radiocarbon analyses are valid) or about 23 ka (assuming that the TL analyses are valid). The amount

of soil development is consistent with an early Hologene age for the deposit if eolian influx rates are high enough to contribute silt and clay particles to the soil profile. This seems likely based on abundant accumulations of loess in valleys to the north of the Guaje Pines site and on mesa tops throughout the Pajarito Plateau (L.D. McFadden, The University of Mexico, personal communication, 1994). However, there is sufficient uncertainty in the rates and characteristics of soil development in the Los Alamos area, that the amount of soil development within the upper colluvium/alluvium is also consistent with the late Pleistocene age of about 23 ka. Although there were no field conditions that suggested the charcoal samples dated at about 8 ka were emplaced after deposition of Unit 15, the possibility that pedogenesis (soil development) has masked such evidence cannot be precluded. In addition, the presence of anomalously young dates from two charcoal samples from Units 2a and 2b shows that this process has been active in the recent past. On the other hand, the application of thermoluminescence methods to assess the timing of colluvial events in temperate, forested areas is still somewhat experimental. In conclusion, the available data are sufficient only to determine that the upper colluvium/alluvium was either deposited about 8 ka or about 23 ka.

Because Unit 17 (and correlative Units 3x and 3z) underlie Unit 15 (and correlative Unit 3y), the deposition of the basal part of the upper colluvium/alluvium occurred prior to either 8 or 23 ka by an unknown amount. Because this proximal colluvium probably was deposited relatively rapidly as a result of scarp degradation, it is likely that these units are at most about 1 ka older than the dated Unit 15.

Unit 1 in trench GPT1 is a silty colluvium that contains sand, gravel, and historic and reworked prehistoric artifacts and most likely reflects the material being transported by active slope processes. Based on lithologic similarities and the presence of historic artifacts, Unit 1 is correlative with Units 13 and 14 in trenches GPT2 and GPT3. Acceleration of slope transport along the scarp probably occurred within the past hundred years, possibly following initial clearing and cultivation of the scarp and the Qfy terrace surface. Two radiocarbon dates on charcoal sampled from Unit 1 (GPT1-RC7 and GPT1-RC10, Plate 8) provide an age-estimate of about 650 cal BP (Table 4-2). The presence of historic artifacts in this deposit shows that this age-estimate probably is too old. Thus, the charcoal fragments likely were reworked from an older deposit or were contaminated.

4.2.2.1.2 Structure. The main strand of the Rendija Canyon fault was exposed in trench GPT1 at about Station 17 m and in trench GPT2 at about Station 9.5 m (Plate 8). In both trenches, the fault dips about 70° to the west, and strikes about N20°W. A subsidiary strand exposed in GPT2 has a shallow to moderate dip (27°SW to 57°SW) and strikes between N16° W and N20° W. Slickensides were not encountered on the main shear plane, but faint lineations on the subsidiary shear in GPT2 trend to the southwest, providing limited evidence of left-lateral oblique slip on the subsidiary strand. Slickensides on the subsidiary strand exposed (but not mapped) on the northern trench wall (Plate 8) also were consistent with left-lateral oblique slip. Without piercing-line or other structural data on the main trace of the fault, however, an interpretation of the Rendija Canyon fault as a left-oblique normal fault presently is not conclusive.

Trenches GPT3 and GPT4 were excavated parallel to the fault scarp on the downthrown and upthrown sides of the fault, respectively (Figure 4-14), in order to assess lateral slip on the fault. Topographic surveying and geomorphic mapping at the site revealed the presence of a west-trending break in slope across the fault trace. This break in slope was interpreted to be a possible backedge of the Qfy terrace surface, and thus may have been a piercing line across the fault from which to constrain the sense and amount of lateral slip, if any. The locations of these breaks in slope suggested right-lateral slip on the fault of about 2 to 4 m. Trenches GPT3 and GPT4 were located to assess the origin of these features. As shown on Plate 8, trenches GPT3 and GPT4 exposed no evidence of a terrace back-edge, or any other linear features that might provide information on the sense of slip. Thus, the west-trending breaks in slope possibly are related to historic cultural modification, perhaps clearing of the area for cultivation or road construction.

There was evidence that Units 4b and 4c on the downthrown side of the fault were folded within a zone about 10 m wide (Figure 4-15; Plate 8). The westerly dip of Unit 4b in trench GPT1 between Stations 18 m and 26 m is opposite in direction to that for a fluvial deposit derived from the Rendija Canyon drainage. In addition, bedding within Unit 4c dip to the west and are parallel to the upper contact of the unit. Notably, this deformation is not present in overlying stratigraphy. This deformation is interpreted as contemporaneous with surface rupture immediately preceding deposition of the lower scarp-derived colluvium (Units 4a, 16a, and 16).

4.2.2.1.3 Paleoseismic Characteristics, Guaje Pines Site. Stratigraphic and structural relations exposed in the trenches and soil pits at the Guaje Pines site provide evidence of four surface rupture earthquakes along the Rendija Canyon fault during the past approximately 140 ka, and evidence of possible surface rupture prior to this time. The trenches also yield limited information that helps assess the average time interval between surface ruptures, as well as the possible range in displacement that occurred during some of these earthquakes. Assessment of the number of paleoseismic surface ruptures at the Guaje Pines site is based primarily on stratigraphy exposed in trenches GPT1 and GPT2 (Plate 8). Because of the complex history of late Quaternary tectonic, depositional, and erosional events at the Guaje Pines site, the earliest events are inferred on the least amount of evidence and are poorly characterized. Later events are better understood because of better deposit preservation, and thus are viewed with greater confidence, although there remains considerable uncertainty in the ages of deposits and therefore the timing of surface ruptures. The following section provides information on the number, timing, and size of surface ruptures on the Rendija Canyon fault at the Guaje Pines site.

4.2.2.1.3.1 Number and Timing of Paleoearthquakes. The stratigraphically lowest surficial deposit identified at the Guaje Pines site is Unit 21, which was exposed at the base of the eastern part of trench GPT2 (Plate 8). As noted above, this unit likely was deposited by the ancestral Rendija Canyon drainage, as it flowed to the east across the site. The eastern end of trench GPT2 shows that the base of this deposit presently dips about 21 degrees to the west (upstream). Assuming that the original depositional gradient of the drainage was similar to the present-day gradient (about 2 degrees to the east), this westward dip suggests that deposits on the eastern side of the fault have been backtilted about 23 degrees to the west since the Rendija Canyon drainage deposited Unit 21. The timing of this rotation can be constrained qualitatively based on the presence of a prominent soil horizon at the top of overlying quiet-water deposits (Unit 20, Plate 8). The base of this soil dips about 7 degrees to the west, which suggests that about 16 degrees of rotation occurred prior to formation of the soil and thus prior to the deposition of Unit 20. Based on thermoluminescence analysis of a sample from Unit 20, this deposition prior to 140 $\pm$ 26 ka. Therefore, a large part of the westward tilt of Unit 21 is a result of surface deformation prior to about 140 ka (Earthquake V[?], Figure 4-16). The number of individual surface ruptures, if any, and the amount of displacement associated with this deformation are

unknown. Notably, this deformation may have resulted in the formation of a closed depression within which Unit 20 was deposited.

The quiet-water deposit (Unit 20) and the soil developed in it are displaced by a west-dipping, subsidiary fault strand east of the main fault (Plate 8). Because overlying fluvial deposits (Unit 19) are not displaced by this strand, it is interpreted that a surface rupture earthquake occurred after deposition of Unit 20 but prior to deposition of Unit 19 (Earthquake W, Figure 4-16). The age of Unit 19 is poorly constrained, so that the minimum-limiting age of this deformation is constrained only by the age-estimate of 64 $\pm$ 54 ka for Unit 4a (Figures 4-16 and 4-17). The amount of displacement along the subsidiary strand is within the mapping resolution of the base of the soil horizon, which is about 10 cm. However, the amount of displacement along the main fault strand associated with this rupture is unknown.

Earthquake W was followed by deposition of Units 19, 19a, 19b in trench GPT2, and by deposition of Units 6 through 12 in trench GPT1 (Figure 4-16). Additional units that are not preserved in the trench exposures also may have been deposited, and subsequently eroded. Alternatively, the lowermost units on the western side of the fault (Units 4b, 4c, and 4d, Plate 8) may have been deposited on top of Unit 19a (in trench GPT1) and Unit 12 (in trench GPT2). If so, palinspastic reconstruction of the trench stratigraphy suggests that the total vertical separation of Unit 4b is about 6 m. Based on exposure in soil pit GPSP2 and in the western end of trench GPT1, the gradient of Unit 4b most likely was 2 $\pm$ 1 degrees to the east, which is comparable to the present-day gradient of the Rendija Canyon drainage. Adjacent to the fault, Unit 4b dips about 21 $\pm$ 2 degrees to the west. These relations suggest a cumulative westward tilt of the block west of the fault, since deposition of Unit 4b, of 23 $\pm$ 2 degrees. As discussed below, all of this tilt was produced by two or three earthquakes (Earthquakes X, Y[?], and Z, Figure 4-16).

The presence of the lower colluvium/alluvium (Units 4a and 5 in trench GPT1, and Units 15 and 17 in GPT2; Plate 8) provides evidence of a surface rupture since the deposition of Unit 4b (Earthquake X, Figure 4-16). As noted above, two thermoluminescence samples (GPT1-TL1 and GPT1-TL2, Table 4-3) provide an age-estimate of 64 $\pm$ 54 ka for Unit 4a, which likely was deposited immediately following this surface rupture. Based on this age-estimate, it is interpreted that Earthquake X occurred at about 64 ka (Figure 4-16). Because

there is a moderately developed soil on the lower colluvium/alluvium, it is interpreted that the maximum-limiting age for this event is about 30 ka (Figure 4-17).

There is indirect evidence of a previously unrecognized surface rupture earthquake at the Guaje Pines site (Earthquake Y[?], Figure 4-16). This possible rupture is inferred based on structural relations among Units 4b (the lower fluvial deposit), Units 4a and 5 (the lower colluvium/alluvium), and Unit 5a (the soil developed on Units 4a and 5). As noted above, the lowermost fluvial deposit on the western side of the fault (Unit 4b) dips about 21 degrees to the west, which is opposite in direction to that expected for alluvium deposited by the east-flowing Rendija Canyon drainage. In addition, the basal contacts of both Units 4a and 5 in trench GPT1 dip 20 to 25 degrees to the west (Plate 8). Our previous interpretation of the trench stratigraphy (Wong et al., 1993) assumed that this westward dip was the original depositional gradient for the lower colluvium, and that the dip of the lower alluvium (Units 4b, 4c and 18) was a result of the rupture that immediately preceded deposition of Unit 4a (Earthquake X, Figure 4-16). However, the concordant dips of the lower scarp-derived colluvium and the underlying lower alluvium are permissive of the interpretation that tilting of the downthrown side of the fault occurred after deposition of Units 4a, 5, and 16. Because the soil developed on the lower colluvium/alluvium (Unit 5a, Plate 8) is nearly horizontal and is developed across the upper parts of Units 4a and 5, it must have formed after the earthquake that tilted Units 4a and 5. This scenario thus includes the following sequence of events: (1) Earthquake X, with little or no westward tilting of Units 4b, 4c and 18; (2) deposition of Units 4a, 5, and 16 as scarp-derived colluvium/alluvium; (3) surface rupture Earthquake Y and tilting of Units 5 and below; (4) degradation of the scarp and deposition of an intermediate scarp-derived colluvium (that was not preserved); (5) soil development in this colluvium and the underlying lower scarp-derived colluvium/alluvium; and (6) fluvial erosion of the upper part of the soil and the (non preserved) middle scarp-derived colluvium. This final step is required to produce the nearly horizontal upper surface of Unit 5a (Plate 8).

Although the above scenario requires many steps to explain the observed stratigraphic and structural relations, our previously assumed scenario similarly requires multiple steps. In this scenario, the following sequence of events took place: (1) Earthquake X, with substantial westward tilting of Units 4b and 4c; (2) deposition of Units 4a and 5 as scarp-derived colluvium/alluvium, on a 20- to 25-degree west-dipping slope; (3) fluvial erosion that

removes the upper parts of Units 4a and 5 in trench GPT1 and Unit 16 in trench GPT2; (4) soil development in the remaining lower colluvium/alluvium; and (5) another round of fluvial erosion, which removes the upper part of the soil and produces the nearly horizontal upper surface of Unit 5a (Plate 8). Clearly, a complex sequence of events occurred at the Guaje Pines site to produce the stratigraphic and structural relations exposed in the trenches. Because of a lack of information that precludes or favors either of these scenarios, both are considered plausible. The age of this possible surface rupture (Earthquake Y[?], Figure 4-16 and 4-17) is unknown, other than it must have occurred after deposition of Unit 4a at about 64 ka and before deposition of Unit 15 at about 8 or 23 ka (Figure 4-17).

The presence of the upper colluvium/alluvium in trenches GPT1 and GPT2 provides evidence of a surface rupture earthquake following the erosion of the upper part of the soil developed in Units 4a and 5 (Earthquake Z, Figure 4-16). Figure 4-18 illustrates the probable configuration of the GPT1 trench site immediately following the most recent surface rupture. This sketch shows a presumed amount of material on the upthrown side of the fault, which was subsequently eroded from the scarp to form Units 3z, 3x, 3y, and parts of 2b. The source of this material was, in part, the older alluvium (including Units 7 through 12, Plate 8). Based on the volume of Units 3z and 3x, the colluvial material also may have been derived from deposits that previously were above Unit 12 prior to erosion of the scarp crest. These deposits may have included Units 4b, 4c and 18, which stratigraphically were the next highest units preserved in the trenches, and/or deposits stratigraphically between Units 12 and 4c that were not preserved in the trench exposures. At the time of the rupture, deposits at the surface west of the fault included Units 4a and 5 in trench GPT1 (Figure 4-18), and Unit 16 in trench GPT2. The land surface east of the fault likely also was underlain by a soil correlative to the preserved remnant on the downthrown side of the fault (Unit 5a, Plate 8).

The amount of vertical separation associated with the most recent rupture can be estimated based on the thickness of the coarse-grained debris colluvium derived from the scarp (Units 3x and 17, Plate 8). As noted above, it may be reasonable to use the scarp-degradation model (Appendix G) to estimate the amount of displacement per surface rupture earthquake at the Guaje Pines site. In trench GPT1, the coarse-grained debris colluvium (Unit 3x) is approximately 0.75 m thick, and in trench GPT2 the correlative deposit (Unit 17) at the fault is about 0.5 m thick. Because of the possibility that deposition of Unit 17 may have

involved a component of transport that was not parallel to the trench exposure (see above), the thickness of Unit 3x provides a better estimate of original scarp height. Thus, it is interpreted that the scarp height immediately following the most recent rupture was approximately twice the thickness of Unit 3x, or about 1.5 m (Figure 4-18). To account for the possibility that the scarp actually was higher than twice the thickness of the colluvial deposits and to account for other unknown sources of uncertainty, it is estimated that the surface displacement during this earthquake was 1.5 + 0.5 m.

Following Earthquake Z, erosion of the topographic scarp at the site resulted in deposition of the upper scarp-derived colluvium/alluvium (Figure 4-16). Deposition of the coarse-grained debris colluvium (Unit 3z and 3x in trench GPT1 and Unit 17 in trench GPT2) likely occurred immediately after formation of the scarp. These units are overlain by finer-grained Units 3y and 15, which were deposited beginning at about 8 or 23 ka, as discussed in Section 4.2.2.1.1 above. The amount of time elapsed between this surface rupture and the deposition of Units 3y and 15 is unknown. Deposition of debris colluvium at the base of fault scarps can typically occur in a geologically short period of time (Nelson, 1992; Appendix G). In the absence of data on the timing and rate of deposition of Units 3z, 3x, and 17, it is estimated that these units were deposited in less than 1,000 years. Considering uncertainties in the age-estimates and the time interval represented by the debris colluvium, it is interpreted that the most recent surface rupture occurred between 8 and 9 ka, or at about 23 $\pm$ 7 ka.

4.2.2.1.3.2 <u>**Surface Rupture Recurrence**</u>. Structural and stratigraphic relations from subsurface investigations at the Guaje Pines site provide information on the number and timing of surface rupture earthquakes along the Rendija Canyon fault. Evidence in the trenches and soil pits suggest the occurrence of at least three and as many as five surface ruptures (Figure 4-16). Three or four of these events (Earthquakes W, X, Y[?], and Z) occurred since deposition of a fine-grained deposit exposed in trench GPT2, which is estimated to be more than 140 $\pm$ 26 ka. Of these, the timing of oldest rupture (Earthquake W) is unknown. Earthquake X occurred between 30 and 118 ka (Figure 4-17). The timing of Earthquake Y[?] is unknown. The most recent rupture (Earthquake Z) occurred at about 8 to 9 ka or at 23 $\pm$ 7 ka on the basis of age-estimates of the upper scarp-derived colluvium.

Given this estimated timing of rupture events, the intervals between earthquakes large enough to break the ground surface can be estimated (Figure 4-19). The calculation of recurrence intervals along a fault based on the timing of paleoseismic events requires consideration of two important constraints. First, it is important to use intervals defined by dated earthquakes, rather than to estimate the number of earthquakes that occurred within a set time period (Machette et al., 1992). Otherwise, the calculation uses undefined intervals: between the most recent event and the present, and between the oldest earthquake and the beginning of the time period considered. For example, the occurrence of three ruptures within the past 300,000 years may suggest an average recurrence of 100,000 years. However, if these events occurred at, for example, 200, 125, and 50 ka, the actual average recurrence interval is 75,000 years, because there were two interseismic intervals over a period of 150,000 years. Second, temporal clustering of paleoearthquakes has been recognized on faults in the Basin and Range province (e.g., Machette et al., 1992; Olig et al., 1994) and in other tectonic settings (Grant and Sieh, 1994). Preferably, the possibility of temporal clustering should be evaluated through sufficient dating of individual paleoearthquakes. In the absence of adequate timing information, the possibility of clustering can be incorporated through inclusion of adequate uncertainties into the hazard analysis. This discussion acknowledges these potential sources of error and attempts to quantify the recurrence interval for the Rendija Canyon fault.

Overall, there have been as many as four surface rupture earthquakes since deposition of Unit 20 sometime before 140 $\pm$ 26 ka (Figure 4-13). Based on the possible timing of each of these four ruptures, recurrence values can be calculated considering the number of interseismic intervals over various time periods and including cases in which Earthquake Y(?) did or did not occur. Based on this analysis, possible recurrence intervals range from about 10,500 to 110,000 years (Figure 4-19). Assuming that Earthquake Y(?) did not occur, the interval between the two most recent ruptures (Earthquakes X and Z) is less than 110,000 years, with preferred values of 41,000 or 55,000 years depending on the assumed age for the upper colluvium/alluvium (Figure 4-19). Estimated recurrence intervals for the case in which Earthquake Y(?) did occur are one-half of these values.

Between Earthquakes V and Z, there were three interseismic intervals (if Earthquake Y[?] did not occur) or four intervals (if Earthquake Y[?] did occur). Earthquake V must have occurred before deposition of Unit 20, and thus, considering uncertainties in the age-estimate

of this unit, cannot be younger than about 114 ka. These data provide four minimum recurrence values, again depending on whether Earthquake Y(?) occurred or not, and on the assumed age of the upper colluvium. These average minimum recurrence values range from 21,000 to 35,000 years (Figure 4-19).

The lower part of Figure 4-19 graphically shows the distribution of these recurrence values for each case. Clearly, there is considerable variability in the recurrence values, which is a result of substantial uncertainties in the age estimates of faulted deposits and uncertainty concerning the number of paleoearthquakes. As noted above, whether Earthquake Y(?) occurred or not is considered equally plausible, and thus all of these cases are considered equally plausible. Based on this analysis, possible recurrence intervals range from about 10,500 to 110,000 years. Preferred values range from 20,500 to 55,500 years, with an average preferred value of about 36,000 years.

4.2.2.1.3.3 Displacement Per Earthquake. The amount of vertical separation associated with Earthquake X can be estimated based on the thickness of the scarp-derived colluvium (Unit 4a, Plate 8). Based on theoretical models of scarp degradation, the thickness of material deposited at the base of the scarp is approximately one-half of original scarp height (Appendix G), and can be used to estimate the original scarp height (and thus the amount of vertical separation). The Guaje Pines site is characterized by an alluvial fan surface that slopes gently in a direction opposite to that of the scarp, and by a lack of integrated drainage along the base of the scarp. Although some deposits at the site may contain a component of loess (and thus will provide maximum estimates of scarp height), it may be reasonable to use the scarp-degradation model to estimate the amount of displacement per surface rupture earthquake at the site. In trench GPT1, Unit 4a is approximately 1 m thick, and in trench GPT2 the correlative deposit (Unit 16) at the fault is about 0.75 m thick. Thus, the scarp height immediately following this rupture probably was about twice the thickness of these units, or about 1.5 to 2 m. To account for the possibility that the scarp actually was higher than twice the thickness of the colluvial deposits and to account for other unknown sources of uncertainty, such as backtilting, it is estimated that the surface displacement during Earthquake X was 2.0 ± 0.5 m.

4.2.2.2 County Landfill Site

The County Landfill site is located along the southern part of the Rendija Canyon fault where it crosses South Mesa (locality 5, Plate 2). This site, which was investigated during late July and early August 1991, provided the opportunity to document an exposure produced during enlargement of the Los Alamos County Landfill. Aerial reconnaissance of the Rendija Canyon fault in June 1991, showed a prominent northeast-trending lineament across the floor of the landfill excavation near the southern end of the fault (Figure 4-20). At the time of investigation, the excavation was about 190 m long, 40 wide, and 13 m deep, and was oriented along the crest of South Mesa at an elevation of about 2235 m. The central 57 m of the northern wall of this exposure was mapped in detail. Subsequent to our investigations the excavation was expanded to the north and the northern wall was destroyed.

In the vicinity of the County Landfill site, South Mesa slopes gently to the east and is bordered on the north by the 100-m-deep Los Alamos Canyon and on the south by the 40-m-deep Sandia Canyon (Plate 2). The site has been disturbed prior to and during landfill operations. The mesa is composed of moderately welded pyroclastic deposits of the upper member of the Bandelier Tuff (the 1.2 Ma Tshirege Member) and younger, fine-grained, pumice-rich fluvial deposits. A topographic profile along the mesa shows that there is little or no down-to-the-west NVTD of the mesa surface (Figure 4-2e). Analysis of high-altitude aerial photography taken in 1981 shows the presence of a series of north- to northeast-trending lineaments that occur in a zone up to about 1 km wide. Notably, the strikes of main fault strands in the exposure are about N30°E to N35°E, which is consistent with these northeast-trending lineaments and with an inferred zone of distributed deformation between the southern part of the Rendija Canyon fault and the Pajarito fault (Baldridge et al., 1990). Because the southern end of the Rendija Canyon fault consists of several splays, the fault exposed in the landfill is only one of perhaps many traces of the fault. However, the strand exposed in the landfill is coincident with the most prominent lineament along the Rendija Canyon fault at this latitude and is probably a main strand within the fault zone.

The northern wall of the excavation was mapped at a scale of 1:20 using an aerial lift for access and electronic surveying equipment to locate stratigraphic and structural features relevant to assessment of faulting at the site (Figure 4-20). A reconnaissance of the

southern, western, and eastern walls of the excavation was conducted to assess the possibility of obtaining additional geologic data. The northern wall was chosen for investigation because the upper 5 to 10 m of the southern wall was disturbed by landfill operations, and the western and eastern walls lacked prominent evidence of post-Bandelier displacement. Surficial deposits exposed in the northern wall, which was up to 5 m deep, were mapped in detail. However, major faults and shear zones within the underlying Bandelier Tuff were mapped throughout the entire 13 m exposure at a reconnaissance level. The western and eastern limits of mapping were determined by the presence of faults. Beyond the western limit of mapping, surficial deposits are unfaulted and laterally continuous. The eastern limit was chosen to include the fault at Station 55 m; surficial deposits are laterally continuous east of this fault.

4.2.2.2.1 Quaternary Stratigraphy. In general, the landfill excavation exposed the Tshirege Member of the Bandelier Tuff, overlain by as much as 5 m of semi-consolidated fluvial deposits (Plate 9). The northern wall of the excavation exposed approximately 7 m of tuff on the western side of the 25-m-wide main fault zone, and up to 13 m of tuff on the eastern side of the main fault zone (Unit B1a, Plate 9). The tuff at the site is a massive, moderately welded to welded rhyolite containing common crystal and lithic fragments (Table G-8). A zone of weathered tuff (Unit B1b) as much as about 30 cm thick is present where the tuff is overlain unconformably by the semi-consolidated fluvial deposits. Zones of oxidation are common, particularly along fractures. Abundant vertical and near-vertical fractures in the tuff are present throughout the exposure, although the continuity, width, and density of fractures is highest in the main fault zone mapped between Stations 2 and 24 m (Plate 9).

Between Stations 18 m and 24 m, Bandelier Tuff is overlain by two laterally discontinuous deposits (Units PC and FC, Plate 9). Unit PC consists of angular clasts of tuff in a loose, sandy and silty matrix (Table G-8). Many of the clasts in Unit PC are broken and have a sandy matrix between clast faces. Unit PC is either a zone of weathered and fractured bedrock, slightly reworked weathered bedrock, or a coarse-grained colluvium. Between Stations 21 m and 24 m, Unit PC dips steeply to the west and has about 1 m of structural relief on its base. Unit PC also is present between Stations 10 m and 13 m, where it is overlain by Unit B2 (Plate 9). Unit FC is a silty sand containing few pebbles of welded tuff. This unit is either a fine-grained, well-sorted alluvial deposit or an eolian (loess) deposit.

There is no evidence of soil development in Units PC, FC, or B2. Units FC and PC between Stations 18 m and 24 m are deformed within a fault-bounded graben. These relations suggest deposition in a structural depression, perhaps in a north- or south-trending swale along the fault trace. If Unit PC is a course-grained colluvium, it probably was shed off the walls of the swale, and subsequently was buried by Unit FC either through eolian or fluvial deposition filling in the swale.

On the western (downthrown) side of the fault at Station 23.5 m, approximately 4 m of bedded, pumice-rich gravel, sand, and silt are preserved above the Bandelier Tuff (Units B2 to B12, Plate 9). Where Units PC and FC are absent, these deposits rest unconformably on a zone of weathered tuff. Units B2 through B9 are a series of fine sandy silts and pumice-rich gravel and sand that are as much as 40 cm thick, but typically are 10 to 15 cm thick (Table G-8). The clasts in the gravels are medium to fine pumice fragments, although Units B8 and B9 contain pumice and dacite pebbles. None of the pumice clasts observed contained mesoscopic biotite characteristic of the 45 to 73 ka El Cajete Pumice. Planar laminations and bedding in these deposits are common, and some cross-beds are present, providing evidence that the deposits are fluvial. Unit B7 is a powdery silt that likely is a reworked ash deposit, although it may by a primary air-fall deposit. Each of these units is distinct in grain size, lithology, degree of sorting, or continuity of laminations or cross-bedding, and is correlated easily throughout the exposure. Thus, these deposits provide an excellent opportunity to assess the style of deformation within the fault zone. Unit B10 is a massive silty sand within which fractures and faults are difficult to trace. Units B11 and B12 overlie Unit B10 and consist of bedded, pumice-rich fluvial deposits. These two units are preserved only in the central part of the graben between Stations 21 and 23 m.

On the eastern (upthrown) side of the fault at Station 23.5 m, only thin remnants of Unit B10 are preserved between bedrock and the overlying artificial fill (Plate 9). The upper part of Unit B10, Units B11 and 12, and any other overlying units probably were stripped by erosion or cultural activities. Remnants of a well-developed soil Bt horizon and overlying loess and pumice-rich fluvial deposits are preserved locally east of the fault zone (Units B13 through B16, Plate 9, Table G-8). These units are displaced by a minor down-to-the-east fault at the eastern end of the exposure (Station 55.5 m, Plate 9). Based on lithologic characteristics and the presence of the well-developed soil in Unit 13, these deposits may be

correlative with deposits exposed west of the fault at Station 23.5 m. It is interpreted that Unit B14 is correlative with Unit B10, and Units B15 and B16 are correlative with Units B11 and B12, respectively. If these correlations are valid, then the weathered bedrock within and west of the shear zone (Unit B1b) may be the lower part of a (now stripped) soil correlative with Unit 13 east of the shear zone.

Units PC, FC, B2 through B12, and B14 through B16 are most likely older than the 45 to 73 ka El Cajete Pumice. None of these units contains pumice clasts that have biotite crystals characteristic of the El Cajete Pumice. In addition, small dacite clasts within the deposits show that the fluvial system responsible for depositing these units contained drainage area in dacite terrane in the Jemez Mountains. Because the County Landfill is located on a mesa top, this fluvial system preceded substantial incision of Los Alamos and Sandia canyons. Although the timing of this incision is poorly constrained, Units B2 through B12, and B14 through B16, are interpreted as at least several hundred thousands of years old.

Artificial fill up to about 80 cm thick is present along the top of the entire exposure (Plate 9). The fill overlies native materials with an abrupt, wavy contact and contains cultural artifacts (pipe, bricks, nails, etc.). The sandy to silty fill is distinct from native material because it is loose, very poorly sorted, and has a greater moisture content. Unfortunately, cultural modifications prior to emplacement of the fill destroyed native material that might have yielded information on the timing of faulting events.

4.2.2.2.2 Structure. The County Landfill site provides an excellent exposure of a main strand of the Rendija Canyon fault south of Los Alamos Canyon. Reconnaissance of the entire exposure showed that although vertical and near-vertical fractures are abundant in the tuff, the continuity, width, and density of fractures is several times higher in a 22-m-wide shear zone mapped in the central part of the northern wall. This zone, which lies between Stations 2 m and 24 m (Plate 9), is associated with approximately 4 m of down-to-the-west cumulative vertical separation of the top of Bandelier Tuff. The main shear zone consists of a series of faults within bedrock and overlying surficial deposits, a central horst, and an associated graben (Plate 9). Two primary fault strands are exposed at Stations 13 m and 23.5 m, both of which are vertical and strike about N35°E. Additional minor faulting is present east of the graben at Stations 26 m, 47 m, and 55.5 m.

The main fault strand is exposed at Station 13 m (Plate 9) and based on a similar amount and sense of vertical separation of the top of bedrock, was identified in the southern wall of the excavation. The strike of the vertical fault plane in bedrock near the base of the exposure is N35°E, which is the same orientation obtained via measurement across the excavation to the southern wall. The fault exhibits about 2.5 m of down-to-the-west vertical separation of the top of bedrock, and is associated with a sandy, 20-cm-wide fissure-fill deposit between strands within the surficial deposits. The fault extends into the lower part of Unit B10, where it dies out or is truncated by the overlying artificial fill (Plate 9). The main fault strand forms the western border of the 6-m-wide bedrock horst in the central part of the shear zone.

West of the main fault strand at 13 m (Plate 9), the shear zone consists of a small graben between Stations 2 m and 6 m, and several major and minor fault splays. The small graben is bordered by vertical to steeply-dipping faults in bedrock that strike between N33°E and N52°E, splay upward, and die out within the massive silty sand of Unit B10. Well-bedded surficial deposits overlying the fault splays are complexly deformed, with many of the beds showing evidence of minor reverse separation. This deformation may be a result of downdropping of the graben and complex interaction of the fault splays in the overlying, less-competent sediments. Between Stations 9 m and 11 m, a fault splay dips to the east and joins the main fault strand at the base of the entire exposure at about Station 13 m. Several west-dipping splays antithetic to this strand are present within the surficial deposits. The dip of the major splay decreases upsection from 75°SE at the base of the exposure to 59°SE at the top of bedrock (Plate 9). The strike of the splay also changes upsection, from N30°E at the base of the exposure to N14°E at the top of bedrock. If there is lateral slip along the main fault strand, this counterclockwise rotation of the plane of the splay upsection may reflect a component of left-lateral slip.

The graben exposed between Stations 17 m and 24 m is bordered on the west by an east-dipping fault and on the east by a vertical to 85°NW-dipping fault that strikes N34°E (Plate 9). These faults likely merge at a level below the excavation floor. The graben was not observed on the southern wall of the excavation, although this is probably a result of removal of the upper 5 to 6 m of native material by landfill operations. There are many shears in bedrock exposed in the southern wall and along the southwestern projection of these faults that may correlate with the graben-bordering faults. As noted above, this graben

may have been a structural depression prior to deposition of Unit B2, based on the presence of a fine-grained alluvial or loess deposit in the base of the graben (Unit FC, Plate 9).

A minor fault at the eastern end of the exposure (Station 55.5 m, Plate 9) exhibits about 45 cm of down-to-the-east vertical separation of Units B13 and B14. This vertical fault strikes N8°E and is associated with a clay gouge zone near the top of bedrock. Possible slickensides in a similar clay gouge at the base of the exposure plunge shallowly to the southwest (two measurements: 20°, S9°W and 4°, S4°W). Given the down-to-the-east vertical separation of Units B13 and B14, these data provide evidence of right-lateral slip on this fault strand.

4.2.2.2.3 Paleoseismic Characteristics. In general, the exposure at the County Landfill provides an excellent opportunity to assess the style of faulting along the Rendija Canyon fault, but it yields little information on the number, timing, and amount of late Quaternary surface-rupture events. Based on the exposure, the top of Bandelier Tuff has about 4 m of cumulative down-to-the-west vertical separation. This amount of separation and the 1.2 Ma age of the tuff yield an average long-term vertical slip rate of less than 0.01 mm/yr. This is a minimum fault slip rate because of the possibility of lateral slip and the possibility of other fault strands beyond the limits of the landfill exposure. If the 4° to 20° plunge of slickensides on the vertical minor fault at the eastern end of the exposure are representative of the true slip direction on the main fault strand, then the 4 m of cumulative vertical separation was produced by approximately 10 to 60 m of oblique slip. If the above assumptions are correct, these data in turn yield an estimated post-1.2 Ma slip rate of about 0.01 to 0.05 mm/yr.

The County Landfill exposure is located near the southern end of the Rendija Canyon fault, where deformation is distributed within a 1-km-wide zone and may be related to transfer of strain between the Rendija Canyon and Pajarito faults (Baldridge et al., 1990). The fault zone exposed in the excavation therefore is only one of possibly several traces. Nevertheless, the location of the exposure along the southern projection of the fault and the presence of prominent lineaments on aerial photographs through the landfill strongly suggest that the shear zone exposed in the excavation is a major strand of the Rendija Canyon fault. In addition, the cumulative amounts of vertical separation in the exposure (4m) and derived from the regional topographic profile (3 ± 3 m; Figure 4-15) are comparable. Therefore,

the amount of deformation shown in the exposure probably makes up a substantial part, if not the majority, of the deformation associated with the Rendija Canyon fault at this latitude.

The County Landfill exposure provides limited information on the number and timing of post-Bandelier surface ruptures. Based on stratigraphic and structural relations in the exposure, there have been at least three, and perhaps many more, episodes of surface rupture at the site since deposition of the upper Bandelier Tuff. There is considerable uncertainty in the sequence and timing of events that occurred at the site over the past 1.2 Ma, primarily because of the lack of continuous depositional record, a lack of well-defined age-estimates, and cultural modifications that destroyed the upper part of the stratigraphic section. Using the available information contained in the exposure, the following sequence of events is interpreted for the site. This sequence likely is incomplete, and only the relative timing of the events is reasonably constrained.

After deposition of the upper Bandelier Tuff at about 1.2 Ma, an episode of surface rupture is interpreted based on the presence of Unit PC within grabens at Stations 9 to 13 m and 18 to 23 m. As noted above, this unit is either weathered and fractured bedrock, slightly reworked bedrock, or coarse-grained colluvium. If this unit is interpreted either as fractured bedrock filling a rupture-related fissure or as a scarp-derived colluvium, its presence suggests a surface rupture. Fractured bedrock between two fault splays and beneath Unit B13 (Stations 54 to 55.5 m, Plate 9) may be a time-correlative unit. Unit FC then was deposited via eolian or fluvial processes within the graben. It is possible that Unit FC extended outside of the graben and was the parent material for the soil developed in Unit B13. If so, the lack of soil development in Unit FC suggests that the unit originally was thicker than the remnants preserved in the graben, and that the upper part (perhaps containing a soil) was eroded prior to deposition of the overlying Unit B2. In addition, the weathered bedrock mapped as Unit B1b (Plate 9) may reflect the lower part of the soil, which extended through surficial deposits and into bedrock.

After the period of surface stability indicated by the soil developed in Unit 13, it is inferred that the upper part of Unit FC (and the soil developed in it) was eroded in the area west of Station 46 m. Because Unit B2 rests directly on weathered bedrock (Unit B1b) west of Station 9 m, it appears that erosion was greater on the western part of the site. This erosion also may have stripped the top of the horst block between Stations 13 and 17 m. Unit B2

then was deposited, followed by deposition of Units B3 through B9. Lithologic characteristics of these units suggest deposition by a fluvial system carrying primarily pumice clasts, possibly alternating with eolian or reworked eolian deposits.

Stratigraphic relations in the exposure are permissive of an interpretation of a rupture event between deposition of Units B9 and B10. Units B2 through B9 terminate abruptly against faults at Stations 13 m, 18 m, and 23 m. These units are absent on the horst block between Stations 13 m and 18 m and on the block east of Station 23 m. Because Unit B8 rests directly on Unit FC at Station 22 m (Plate 9), it is likely that Units B2 through B9 were deposited onto a west-sloping surface in the vicinity of Stations 21 m to 23 m. Importantly, it is likely that Units B2 through B9 once were continuous across the horst block and have since been eroded from the top of the block prior to deposition of Unit B10. If the initiation of this erosion was a result of uplift of the horst, then the exposures suggests the occurrence of another surface rupture. Although there is no evidence of a scarp produced during this rupture because of the absence of a scarp-derived colluvium, the scarp was developed in unconsolidated sand and pumice pebbles, and probably was small enough to have been eroded completely prior to or during deposition of Unit B10.

Deposition continued at the site with the fluvial and/or eolian Unit B10, followed by deposition of Units B11 and B12 (and the correlative Units B15 and B16) across the site. Additional units may have been laid down above Units B12 and B16, and are no longer preserved. Unit B10 is extensively faulted throughout the exposure. In addition, Units B11 and B12 are faulted within the graben at Stations 20.5 m and 22.5 m (Plate 9), and Units B15 and B16 are faulted at Station 55.5 m. Therefore, a third episode of faulting is interpreted from the exposure. The number of individual surface ruptures associated with this deformation is unknown; it is likely that this deformation is a result of multiple paleoearthquakes. There is no record of scarp-derived colluvium preserved at the site, probably because of substantial erosion on the mesa top following incision of Los Alamos Canyon and more recently, cultural modification during the past 50 years.

In conclusion, the County Landfill site provides limited information on the paleoseismic characteristics of the Rendija Canyon fault. Down-to-the-west vertical separation of the top of Bandelier Tuff is about 4 m. There is evidence of lateral slip along fault strands exposed in the excavation, although there are conflicting data on whether the lateral component is

left- or right-lateral. Considering the possible occurrence of lateral slip and the presence of multiple fault traces, we estimate that the post-1.2 Ma slip rate on the fault at this latitude is about 0.01 to 0.05 mm/yr. There is evidence of at least three surface-rupture earthquakes during the past several hundred thousand years. It is possible that there have been several ruptures during this period. The timing of these events and the amounts of displacements during each event are unknown.

4.2.3 Guaje Mountain Fault

The 12-km-long Guaje Mountain fault is subparallel to and located approximately 4 to 5 km east of the Pajarito fault in northern Los Alamos County (Figure 2-2; Plate 2). The north-striking, steeply dipping fault exhibits down-to-the-west displacement of the 1.2-Ma upper Bandelier Tuff and thus is structurally similar to the subparallel Rendija Canyon fault (Kelley, 1954; Griggs, 1964; Smith et al., 1970; Budding and Purtymun, 1976; Kelley, 1978; Golombek, 1981, 1983). Gardner and House (1987) mapped the 5-km-long central part of the Guaje Mountain fault as a single continuous strand between Guaje Canyon and Bayo Canyon (Plate 2). To the north and south of this central section, the location of the fault is approximate because of structural complexities or a lack of prominent geomorphic expression (Gardner and House, 1987).

The northern termination of the fault occurs at its intersection with the Pajarito fault just south of the border between Los Alamos and Sandoval counties (Plate 2). This intersection is characterized by complex deformation in the area between the down-to-the-east Pajarito fault and the down-to-the-west Guaje Mountain fault. NVTD of the 1.2 Ma upper Bandelier Tuff by the Guaje Mountain fault is greatest (27 $\pm$ 4 m) near this intersection, based on topographic profiles on the top of the tuff. The amount of displacement decreases progressively southward to zero near South Mesa (Figures 4-1 and 4-3c; Table 4-1). Although to the south of Los Alamos Canyon, there is little or no geomorphic expression of the fault across mesas underlain by the Bandelier Tuff (Figure 4-2e), aerial photograph lineaments in Pajarito and Threemile Canyons and vertical fractures along the mapped trace of the fault in Twomile Canyon suggest that near-surface faulting may extend further south. Vaniman and Wohletz (1990) interpreted that the fault extends to Threemile Canyon based on fracture density within the upper Bandelier Tuff and geomorphic features. However, trench investigations across their projected traces of the Guaje Mountain fault at TA-63

(Kolbe et al., 1995) and TA-67 (Kolbe et al., 1994) revealed no evidence for faulting. Therefore, we interpret the southern termination of the Guaje Mountain fault to be near TA-63 (Plate 2).

Subsurface geologic data show that movement on the Guaje Mountain fault pre-dates the Bandelier Tuff and that the fault had recurrent activity in the early Quaternary (Dransfield and Gardner, 1985; Budding and Purtymun, 1976; Griggs, 1964). The average post-1.2 Ma vertical slip rate along the Guaje Mountain fault is about 0.01 mm/yr, based on an average of 15 m of NVTD measured along the fault (Figure 4-3c). The maximum NVTD of 27 m yields a maximum long-term vertical slip rate of about 0.02 mm/yr. As previously noted, these rates are slightly lower than the average and maximum vertical slip rates estimated for the Rendija Canyon fault, and are much less than the average and maximum vertical rates estimated for the Pajarito fault.

As with the Rendija Canyon fault, the role of the Guaje Mountain fault in the tectonic setting of the Pajarito Plateau is unresolved. The fault likely is intimately related to the Rendija Canyon fault, which has a similar sense and amount of post-1.2 Ma displacement and which is located 1 to 2 km to the west. Baldridge et al. (1990) note that the topographic depression between the northern Pajarito fault and the Guaje Mountain and Rendija Canyon faults is a possible pull-apart basin within a right-lateral shear system. Baldridge et al. (1990) note that oblique slickensides plunge to the north and to the south and thus provide conflicting evidence for the sense of lateral offset. Alternatively, the west-dipping faults may be antithetic to the east-dipping Pajarito fault and the topographic low is a 3- to 5-km-wide graben in the hanging wall of the predominantly dip-slip Pajarito fault. Slickenside data that suggest predominantly dip slip on the Pajarito (Golombek, 1983), Guaje Mountain, and Rendija Canyon faults (K. Carter, LANL, personal communication, 1994) support the graben model.

A previous trench along the central part of the fault at Cabra Canyon provides evidence of late Quaternary displacement (Gardner et al., 1990). This trench yielded stratigraphic and structural evidence of a Holocene rupture about 4 to 6 ka. Therefore, the Guaje Mountain fault had recurrent late Quaternary displacement and a middle Holocene surface rupture.

The primary goals of our investigation of the Guaje Mountain fault were to refine the timing of late Quaternary ruptures along the fault and to better constrain the late Quaternary slip rate and recurrence interval of the fault. The following section presents results of investigations at two sites (Plate 2): the Rendija Canyon area, located where the fault traverses the alluviated valley of Rendija Canyon; and the Sportsmen's Club site (Figure 4-22), located within Rendija Canyon where the fault projects into late Holocene alluvial deposits.

4.2.3.1 Rendija Canyon Area

The Rendija Canyon investigation area includes the alluviated valley of Rendija Canyon where it crosses the Guaje Mountain fault (Plate 2). The area is directly north of Barranca Mesa and encompasses the reach of Rendija Canyon approximately 450 m upstream and 850 m downstream of the Guaje Mountain fault (Plate 10). This northeast-trending reach encompasses a 3-km-long, approximately 300- to 500-m-wide canyon that is about 14 km upstream of the Rio Grande. This relatively wide reach of the canyon is bordered by narrow gorges at its upstream and downstream ends. The Rendija Canyon area was targeted for detailed investigation because of the presence of several late Pleistocene and Holocene fluvial terraces that cross the fault and provide the opportunity to assess the location, amount, and timing of late Quaternary displacement. The investigation included analysis of aerial photography, detailed field mapping of surficial deposits, description of soil profiles, and radiometric dating. These activities occurred following trenching investigations at the Sportsmen's Club site (Section 4.2.3.2), which is located along the Guaje Mountain fault in the north-central part of the Rendija Canyon investigation area (Plate 10). The Cabra Canyon trench site of Gardner et al. (1990) is located approximately 1 km north of the Rendija Canyon investigation area.

In the investigation area, Rendija Canyon is incised about 120 m into the 1.2 Ma Tshirege member of the Bandelier Tuff and in the lowest part of the valley, pumice-rich sands, gravel, and ash beds that were mapped as part of the Cerro Toledo Rhyolite (Smith et al., 1970; Kelley, 1978; Heiken et al., 1986; see Section 2.4). The upper flow units of the Bandelier Tuff in the area are moderately welded, and form steep, near-vertical cliff faces along the flanks of the canyon (Plate 10). Stratigraphically and topographically lower tuff units are progressively less welded, and form shallower slopes typically mantled by slopewash or

colluvium. At the base of the Bandelier Tuff in the area is a loose, friable pumice deposit that likely is the basal Tsankawi air-fall pumice. The unconsolidated epiclastic deposits of the Cerro Toledo Rhyolite in the area are easily eroded and typically are overlain by thin slopewash or colluvium. Exposures of these deposits in the area are limited to rare stream cuts and artificial excavations. Upstream of the investigation area, resistant dacite of the Tertiary Tschicoma Formation crops out in the narrow gorge directly east of the Rendija Canyon fault at the Guaje Pines site, and farther west in the headwaters of the drainage along the eastern flank of the Jemez Mountains (Figure 2-2). Tschicoma Formation dacite also crops out in the extreme northeastern corner of the area (Plate 10) and along the northern canyon wall approximately 1 km downstream of the investigation area. The narrow gorge downstream of the investigation area is underlain by volcaniclastic-rich sediments of the Puye Formation (see Section 2.4).

The type and distribution of bedrock, as well as microclimatic differences between the northern and southern valley walls, have strong influences on the canyon's morphology and the type and distribution of surficial deposits in the area. As in many canyons throughout the Pajarito Plateau, the northern wall of the area is steep and relatively dry, whereas the southern wall has a less steep slope, is wetter, and contains more vegetation. The southern wall typically also is mantled with a greater amount of colluvium.

The Guaje Mountain fault crosses the central part of the investigation area (Plate 10). There is approximately 15 $\pm$ 5 m of apparent down-to-the-west separation of the top of the Bandelier Tuff along Barranca Mesa (Figure 4-2e). Although the sense of throw on the fault is opposite to the gradient direction of Rendija Canyon, there is only limited geomorphic expression of the fault across the valley. Analysis of color aerial photography taken in 1975 shows the presence of a subtle alignment of vegetation along the valley floor that may be associated with the fault, although this lineament is not present on low-sun-angle black-and-white photography taken in 1991 for this investigation. The fault also is associated with a linear north-trending tributary valley that drains the southern side of the canyon, and a prominent east-facing topographic scarp in bedrock on the northern side of the canyon (Plate 10). This east-facing scarp is probably a result of differential erosion of rock types juxtaposed along the fault, rather than down-to-the-east vertical separation. Seismic refraction data cited by Gardner and House (1987) and Wachs et al. (1988) suggest that the

top of bedrock across the Guaje Mountain fault in Rendija Canyon has at least 5 m of down-to-the-west vertical separation.

4.2.3.1.1 Late Quaternary Stratigraphy. A previous investigation identified several late Quaternary fluvial terrace surfaces and associated deposits within the Rendija Canyon investigation area (M. Gonzalez, LANL, unpublished data, 1990). Gonzalez's geomorphic and surficial-deposit mapping, at a scale of 1:6,000, identified two prominent geomorphic surfaces associated with fluvial gravel at heights of 160 to 180 m and 25 to 30 m above the canyon floor. Based on correlation to geomorphic surfaces present along the Rio Grande approximately 7 to 24 km to the northeast (Dethier et al., 1988a), the surfaces in Rendija Canyon were estimated to be 350 ka to 1.2 Ma and 150 to 240 ka, respectively (M. Gonzalez, LANL, unpublished data, 1990). Gonzalez also identified two "landscape assemblages" that include fluvial terraces at heights of 4 to 10 m and 2 to 4 m above the present-day channel. These surfaces were estimated to be 60 to 130 ka and 10 to 25 ka, respectively. Gonzalez (LANL, unpublished data, 1990) estimated that the 25- to 30-m-high (150- to 240-ka) surface is displaced about 13 m by the Guaje Mountain fault.

Based on analysis of aerial photography (1:24,000-scale color and 1:12,000-scale low-sun-angle, black-and-white) and detailed field mapping, we recognize eight fluvial geomorphic surfaces in the Rendija Canyon area (Plate 10). The terrace surfaces and associated fluvial gravels, together with bedrock and fault exposures, were mapped on 2-ft-contour intervals, 1:1200-scale topographic maps and reduced to the scale of Plate 10. The terrace surfaces are up to 36 m above the present-day channel and typically consist of small, discontinuous remnants inset into bedrock or older fluvial deposits. The unconsolidated terrace gravels associated with these surfaces consist of cobble- to boulder-size clasts of dacite and tuff within a sandy matrix, and are typically about 6 to 12 m thick. The base of the gravel beneath each terrace surface was readily identified and mapped by exposing the coarse gravel overlying fine-grained, unconsolidated Cerro Toledo deposits or Bandelier Tuff.

Surface remnants were correlated on the basis of height above the present-day channel, preservation of original bar- and swale-topography, amount of dissection, and relative soil development. The highest three terrace levels (Qt1, Qt2, and Qt3; Plate 10) are represented by surface remnants along the southern margin of the valley. Qt2 and Qt3 remnants, and

remnants of the next lower surface (Qt4), are relatively extensive on the upthrown (eastern) side of the fault. Elsewhere, these remnants are moderately degraded. Remnants of surfaces Qt5 and Qt6 are limited in extent, although the next lowest surface (Qt7) is nearly continuous along the margin of the Rendija Canyon drainage throughout the area. Terrace Qt7 is characterized by well-preserved original depositional morphology, including large boulder bars and intervening swales. The present-day floodplain is the Qt8 surface, and is continuous throughout the area (Plate 10). In general, all of the terrace levels represented by these remnants are slightly divergent downstream (Plate 10).

Six soil test-pits were excavated into the terraces to provide correlation between terrace remnants and to help estimate deposit ages via relative amounts of soil-profile development. Test-pit TP2 was excavated on the highest terrace remnant (Qt1) on the upthrown eastern side of the fault (Plate 10). This pit exposed a 34-cm-thick upper soil with evidence of slight secondary clay accumulation, such as common subangular blocky structure, a 7.5YR hue, and few clay films (Appendix H; Figure 4-21). The lower soil developed on Qt1 deposits consists of two well-developed argillic Bt horizons that total 71 cm in thickness and have prismatic or angular blocky structure, many thick clay films, and 5YR hues (Figure 4-21). On the basis of these soil characteristics, an age of approximately 150 to 300 ka is estimated for the Qt1 surface.

Two soil test-pits were excavated on the Qt2 surface, one on a remnant on the eastern (upthrown) side of the fault (TP1, Plate 10) and one on a remnant on the western (downthrown) side of the fault (TP3). Both of these profiles are very similar, containing an upper, 61- to 62-cm-thick moderately developed soil characterized by Bw horizons, subangular blocky structure, thin clay films, and 7.5YR hues (Figure 4-21). This soil is probably correlative with the upper soil observed in TP2 on Qt1, and likely represents a period of accretion and surface stability after an episode of substantial loess accumulation or fine-grained hillslope colluviation. Beneath this soil both in TP1 and TP3 is a buried soil with a well-developed, 43- to 44- cm-thick Bt horizon. This buried argillic horizon contains evidence of substantial secondary clay accumulation, such as angular blocky soil structure, thick clay films, and 5YR hues. On the basis of these soil characteristics, we estimate an age of approximately 100 to 200 ka for the Qt2 surface. Gonzalez (LANL, unpublished data, 1990) estimated that terraces mapped herein as Qt1 and Qt2 are 150 to 240 ka, based on height correlations with terraces along the Rio Grande.

Test-pit TP5 was excavated on a very small remnant of terrace Qt3 in the northern part of the canyon (Plate 10), and yielded little or no information on the age of this surface. The small pit exposed about 60 cm of sandy loam and loamy sand that lacked substantial soil development and likely was deposited via hillslope processes onto an eroded remnant of the Qt3 surface. Test-pit TP6, which was excavated on terrace Qt4, exposed a moderately developed soil with a 22-cm-thick A horizon, a 27-cm-thick Bt horizon, and a 14-cm-thick Bk horizon (Figure 4-21). The argillic Bt horizon is characterized by angular blocky structure, thin to moderately thick clay films, and 7.5YR hues. The Bk horizon has subangular blocky structure and Stage I secondary carbonate morphology. Based on these characteristics, we estimate an age of 20 to 100 ka for the Qt4 surface. Gonzalez (LANL, unpublished data, 1990) estimated that terraces mapped herein as Qt4 through Qt6 are 60 to 130 ka.

Test pit TP4 was located on terrace Qtb in the western part of the area (Plate 10). The profile exposed in this pit contains very little evidence of soil development. The soil consisted of a 10-cm-thick A horizon and a 26-cm-thick AB horizon with subtle evidence of pedogenesis. Two radiocarbon analyses performed on samples taken from excavations SCSP3 and SCSP4 at the Sportsmen's Club site provide age estimates for deposits associated with surface Qt6 (samples SCSP-RC3 and SCSP-RC4, Table 4-2). These analyses yielded an average calibrated age of about 7170 cal B.P., which shows that the Qt6 deposits are middle to early Holocene in age and that the Qt6 surface is about 6 to 7 ka (Reneau et al., 1993).

One piece of charcoal from the base of deposits associated with terrace Qt7 in trench SCT2 at the Sportsmen's Club was dated (sample SCT1-1, Plate 11). This sample yielded a calibrated age of about 2750 cal B.P. (Table 4-2). In addition, a charcoal fragment collected from stream deposits overlying the 5-m-high Qt7 surface yielded a calibrated age of about 2120 cal B.P. (sample GM-5; Table 4-2). These data suggest that Qt7 is a late Holocene surface (Reneau et al., 1993). This is consistent with the prominent boulder-bar and swale topography associated with the Qt7 surface. Gonzalez (LANL, unpublished data, 1990) estimated that the Qt7 surface mapped herein is 10 to 25 ka.

4.2.3.1.2 Fault Exposures. During field mapping of the geomorphic surfaces and associated deposits, several exposures of strands of the Guaje Mountain fault were encountered. Within

the extreme southern part of the investigation area along the northern rim of Barranca Mesa, three fault strands were identified within moderately welded units of the Bandelier Tuff (Plate 10). All of these strands are near-vertical fractures, with sheared rock present along the middle strand. This middle strand has a strike of N20°E and a dip of 86°SE, (locality A, Plate 10), and could not be traced continuously to the north because of colluvial cover on the southern valley wall. A substantial shear zone in an arroyo wall about 200 m to the north is the likely northern projection of this strand. This shear zone is exposed in the left bank of the arroyo where it abruptly changes orientation from an east-flowing arroyo to a north-trending arroyo (locality B, Plate 10). Reneau (LANL, personal communication, 1994) observed that one shear in this zone strikes N10°E, dips 67°NW and exhibited slickensides that trend N50°W, and one shear strikes N27°E, dips 63°NW, and exhibited slickensides that trend N78°W. Given the down-to-the-west sense of separation, these data suggest right-lateral oblique slip on the Guaje Mountain fault. A secondary fault trace that dips moderately to the east is exposed about 35 m west of this shear zone (locality C, Plate 10).

A vertical fault striking N7°W is exposed along the northern side of the Rendija Canyon road and along the eastern wall of the small, north-trending arroyo (locality D, Plate 10). Fluvial terrace deposits are juxtaposed on the west against Cerro Toledo deposits along this fault strand. The gravel consists of dacite and tuff cobbles and likely are sediments deposited by the tributary arroyo rather than the axial Rendija Canyon drainage. Based on height above the actual channel, this deposit is likely younger than Qt2 and probably correlative with the Qt3, Qt4, or Qt5 deposits. No correlative deposit was identified on the eastern side of the fault, and therefore the amount of displacement on this strand is unknown.

Lastly, two parallel fault strands are present within a small drainage channel at the northern margin of the investigation area, to the north and upslope of trench SCT2 (locality E, Plate 10). These vertical strands strike N10°E and are within the Cerro Toledo deposits. The southern projection of these strands trend through trench SCT2, although only minor faults were exposed in this excavation (see below). In summary, exposures of fault strands in the Rendija Canyon area provide evidence of the approximate location of the zone within which the main fault is located. Because the Guaje Mountain fault consists of several strands within a zone at least 10 m wide (Gardner et al., 1990), it is likely that most of the strands mapped on Plate 10 are faults within the zone of deformation.

4.2.3.1.3 Paleoseismic Characteristics. The primary purpose of delineating the terrace surfaces and associated bedrock strath surfaces in the Rendija Canyon area was to provide datums from which to assess the location and amount of displacement along the Guaje Mountain fault. From this mapping and age estimates of displaced and undisplaced deposits, the timing of displacements and the late Quaternary slip rate along the Guaje Mountain fault can be evaluated. Longitudinal profiles of the terrace surfaces and associated bedrock strath surfaces provide evidence of at least two and possibly three surface-faulting events since the formation of the highest terrace surface (Qt1, Plate 10). Based on projection of the gradients of the surfaces downstream and upstream toward the zone within which the fault is constrained, there is about 2.5 to 4 m of down-to-the-west vertical separation of terrace surface Qt1 and the associated bedrock strath surface. The Qt2 surface has slightly less vertical separation, about 1.8 to 2.5 m (Plate 10).

Because of the lack of surface continuity close to the fault, the amount of vertical separation of surfaces Qt3 through Qt6 is poorly constrained. The resolution of the faultward projections of the longitudinal profiles is permissive of as much as 2.5 m of displacement of these younger terraces (Plate 10). Based on trench exposures in Cabra Canyon, the most recent rupture along the Guaje Mountain fault occurred between about 4 and 6 ka and had about 1.5 to 2 m of vertical displacement (Gardner et al., 1990). This site is located about 1 km to the north of the Rendija Canyon area. Thus, it is likely that there is about 1.5 to 2 m of vertical separation of terrace surfaces Qt3 through Qt6. There is no evidence of displacement of the Qt7 and Qt8 deposits. Trench SCT1, which was located across a prominent west-facing scarp along the projection of the fault, showed no evidence of displacement of the Qt7 deposits (Section 4.2.3.2).

The age-estimates of the terrace surfaces and the amounts of displacement derived from the terrace mapping provide rough estimates of the late Quaternary slip rate on the Guaje Mountain fault. The Qt1 surface is displaced approximately 2.5 to 4 m, and has an estimated age of about 150 to 300 ka. These data yield a range in slip rate of about 0.01 to 0.03 mm/yr. A similar range in slip rate is estimated from the 1.8 to 2.5 m of displacement of the estimated 100- to 200-ka Qt2 surface. Slip rates calculated from the amount of displacement of younger surfaces are higher than these rates, but these are maximum values because they probably do not represent complete interseismic cycles.

The greater amount of displacement of the Qt1 surface than the Qt2 and younger surfaces is strong evidence that there were at least two late Quaternary rupture events on the Guaje Mountain fault. The oldest of these events occurred between the formation of the Qt1 and Qt2 surfaces, and was associated with less than about 1.5 m of vertical separation. A second rupture occurred after formation of the Qt2 surface at about 100 to 200 ka. This event may be the 4 to 6 ka rupture interpreted by Gardner et al. (1990). However, the amounts of terrace displacement are permissive of a second, post-Qt2 event on the fault. It is possible that the 1.8 to 2.5 m of displacement of the Qt2 surface and associated bedrock strath is a result of two events, especially considering the possibility of lateral slip along the fault and the maximum separation of 1.5 m produced by the pre-Qt2 rupture. Thus, it is possible that there have been three surface-rupture earthquakes along the Guaje Mountain fault since formation of the Qt1 surface approximately 150 to 300 ka, each producing about 1 to 1.5 m of vertical separation. There is paleoseismic evidence that the most-recent of these events occurred between about 4 and 6 ka (Gardner et al., 1990). In this three event scenario, the penultimate event post-dates formation of the 100- to 200-ka Qt2 surface but occurred prior to the most recent event at about 4 to 6 ka.

4.2.3.2 Sportsmen's Club Site

The Sportsmen's Club site is located within the central part of the Rendija Canyon investigation area, along the Guaje Mountain fault (Plates 2 and 10). The site is located north of the Rendija Canyon drainage in an area underlain by late Holocene fluvial and alluvial-fan deposits (Figure 4-22). As noted above, the 120-m-deep Rendija Canyon in this area is incised into the Tshirege member of the Bandelier Tuff, and in the lowest part of the valley, pumice-rich sands, gravel, and ash beds mapped as part of the Cerro Toledo Rhyolite (Smith et al., 1970; Kelley, 1978; Heiken et al., 1986; Section 2.4). Unconsolidated epiclastic deposits of the Cerro Toledo Rhyolite underlie surficial deposits at the site. The cuspate embayment along the northern margin of the canyon at the site was probably formed by lateral erosion of the Rendija Canyon drainage during or immediately prior to the formation of terrace Qt7 (Plate 10). Directly northwest of the site, easily erodible pumice of the Cerro Toledo deposits and the upper Bandelier Tuff compose the lower parts of the valley walls and contribute large amounts of low density, pumice-rich alluvium to the valley floor.

Based on previous investigations (Smith et al., 1970; Kelley, 1978; Gardner and House, 1987; Wachs et al., 1988; M. Gonzalez, LANL, unpublished data, 1990), analysis of aerial photography, and field mapping, the Guaje Mountain fault traverses the northwestern part of the site (Figure 4-22, Plate 10). Analysis of color aerial photography taken in 1975 shows the presence of a subtle alignment of vegetation along the valley floor that was interpreted to be related to the fault, although this lineament is not present on low-sun-angle black-and-white photography taken in 1991 for this investigation. Seismic refraction data cited by Gardner and House (1987) and Wachs et al. (1988) suggest that the top of bedrock across the Guaje Mountain fault in Rendija Canyon has at least 5 m of down-to-the-west vertical separation. The Cabra Canyon trench site of Gardner et al. (1990) is located approximately 1 km north of the Sportsmen's Club site along trend of the Guaje Mountain fault.

The Sportsmen's Club site was targeted for detailed investigation because of: (1) the presence of a 1- to 2-m-high west-facing topographic scarp in Holocene fluvial deposits; (2) the presence of vegetation lineament identified on the 1975 aerial photographs; and (3) an apparent truncation of Cerro Toledo deposits and middle Holocene fluvial deposits along the northern valley wall. The purpose of our investigation was to assess the location, amount, and timing of Holocene displacement on the Guaje Mountain fault. The investigation took place during August 1992, and included excavation of four shallow trenches and four soil test-pits (Figure 4-22).

4.2.3.2.1 Holocene Stratigraphy. Trench SCT1 was excavated along a 1-m-high west-facing topographic scarp within deposits associated with the Qt7 fluvial terrace, on the northern side of the Rendija Canyon drainage. Field mapping conducted after the trenching shows that this surface is underlain by late Holocene deposits (Qt7, Figure 4-21). The topographic scarp is coincident with a vegetation lineament identified on aerial photography and lies along the eastern margin of a small closed depression on the present-day canyon floor. The scarp borders the western margin of a linear boulder bar that parallels the Rendija Canyon drainage for approximately 50 m downstream. A main goal of trench SCT1 was to assess if the scarp is a product of surface faulting or fluvial processes. The 7-m-long, west-trending trench exposed approximately 2 m of coarse-grained fluvial deposits overlying Cerro Toledo epiclastic deposits (Plate 11). The lower fluvial deposits consist primarily of gravelly sand and gravel, which are overlain by thin overbank silt with gravel (Units 2 and

3), and pumice-rich distal slopewash from the slopes to the north (Unit 1). Clasts within the channel gravel are predominantly subrounded dacite and subordinate rounded tuff, and are typical in size, rounding, and lithology to those in fluvial deposits throughout the Rendija Canyon investigation area. Radiocarbon sample SCT1-1, which was taken from the lowermost part of the fluvial deposits, yielded a calibrated age of about 2750 cal B.P. (Table 4-2). The abrupt basal contact of the fluvial deposits is continuous and undisplaced across the trench exposure, and there is no evidence of displacement or shearing of the Cerro Toledo deposits in the trench (Plate 11). Thus, the west-facing topographic scarp is related to original fluvial deposition of the boulder bar located along the eastern margin of the scarp, rather than to faulting.

The 35-m-long trench SCT2 was located across valley-floor deposits along the inferred location of the Guaje Mountain fault based on analysis of aerial photography, field reconnaissance, and small hand-dug excavations along the northern margin of the valley (Plate 11). Prior to excavation of trench SCT2, manual excavation exposed several distinct ash beds within the Cerro Toledo deposits that are abruptly terminated along the inferred location of the fault. Coincident with the terminations of these ash marker beds is the western termination of a coarse-grained fluvial gravel that crops out along the northern margin of the canyon (Figure 4-22). On the basis of these relations, trench SCT2 was excavated to locate the fault and to assess the presence or absence of Holocene fault displacement. The trench was excavated as far west and as deep as possible without failure of the trench walls. Although the trench was stabilized using hydraulic shores, the extremely poorly consolidated deposits exposed in the trench precluded excavation deeper than about 2 m. The trench exposed approximately 2 m of late Holocene, pumice-rich alluvial fan deposits and did not expose underlying bedrock or fluvial deposits associated with terrace Qt7. The deposits are moderately well-bedded pumice gravel and sand derived from small gullies that drain the canyon wall directly to the northwest (Figure 4-22). These gullies produce substantial amounts of pumice-rich alluvium during individual rainstorm events. The deposits exposed in the trench are most likely a result of this intermittent sedimentation on top of Qt7 fluvial deposits. Two radiocarbon samples from Unit 7 and one from Unit 6 show that all of the surficial deposits exposed in the trench are less than about 300 years old (Table 4-2). There is no evidence of fault displacement of surficial deposits exposed in trench SCT2.

Cerro Toledo bedrock was exposed in the western part of trench SCT2 (Plate 11). Thin sandy interbeds within the bedrock exhibit minor faulting that may be correlative with faults exposed in the small gully to the north (Figure 4-22). The west-dipping contact between bedrock and alluvial-fan deposits at Station 30.5 m is a depositional contact, with pumice-rich sand and gravel buttressed against bedrock (Plate 11). Although no fault was exposed, it is possible that the fault is present, but is buried by unfaulted alluvial-fan pumice deposits. The buttress unconformity at Station 30 m may, in fact, reflect erosion along fractured bedrock. Nevertheless, because trench SCT2 exposed only latest Holocene deposits, the exposure only precludes fault displacement within the past few hundred years, which is readily apparent on the basis of the lack of geomorphic expression of the fault across terrace Qt7 (Plate 10).

Trenches SCT3 and SCT4 were excavated to assess the western termination of the Holocene terrace gravels exposed in the northern canyon wall. Soil test-pits SCSP1, SCSP2, SCSP3, and SCSP4 were excavated to trace the basal contact of the fluvial gravel to the east, in order to assess possible displacement by the Guaje Mountain fault (Figure 4-22). These excavations exposed Cerro Toledo bedrock and as much as 1 m of overlying coarse-grained fluvial deposits (Unit 3). The fluvial deposits in all of the excavations are overlain by hillslope colluvium. Two radiocarbon samples from the fluvial deposits and overlying basal colluvium exposed in these excavations yielded an average calibrated age of 7170 cal B.P. (Table 4-2). The abrupt basal contact of the fluvial deposits is undisplaced along the series of excavations, and there is no evidence of displacement or shearing of the Cerro Toledo bedrock in the trenches SCT3 or SCT4 (Plate 11). Thus, the termination of the fluvial deposits at Station 10 m in trench SCT3 is unrelated to faulting and instead reflects the back edge of the terrace gravel deposit where the paleochannel eroded into Cerro Toledo bedrock exposed in a paleocanyon wall. This back edge likely trends obliquely into the hillslope along the present-day northern canyon wall.

Trench SCT1 shows that the 1-m-high west-facing scarp present along the surface projection of the Guaje Mountain fault is related to fluvial rather than tectonic processes. Trench SCT2 provides little or no information on the Holocene paleoseismic characteristics of the fault. Trenches SCT3 and SCT4, and soil pits SCSP1 through SCSP4 show no evidence of faulting in bedrock or 7 ka fluvial deposits. The Guaje Mountain fault, therefore, is located to the west of the western end of trench SCT3. Because distinct beds within the Cerro Toledo

Rhyolite are undisplaced across the slope to the north of trench SCT2, the fault probably is located directly west of the western end of the trench, along trend of the fault exposed in the small gully northwest of the trench (Plate 10).

4.2.3.3 Summary

The 12-km-long Guaje Mountain fault is subparallel to and located approximately 4 to 5 km east of the Pajarito fault in northern Los Alamos County (Plate 2). The north-trending, steeply west-dipping fault exhibits down-to-the-west displacement of the 1.2-Ma upper Bandelier Tuff and Quaternary terrace deposits. The fault is believed to extend from a complex intersection with the Pajarito fault on the north to as far south as near TA-63 (Plate 2). Cumulative down-to-the-west displacement of the Bandelier Tuff is greatest (27 $\pm$ 4 m) at the northernmost part of the fault near its intersection with the Pajarito fault, but decreases progressively southward to less than 3 m south of Rendija Canyon (Figures 4-1 and 4-3c). Amounts of NVTD of the 1.2-Ma upper Bandelier Tuff measured along the fault yield an average of 15 m resulting in a vertical slip rate of 0.01 mm/yr, whereas the maximum NVTD of 27 m yields a maximum vertical rate of 0.02 mm/yr. Slip rates based on amounts of displacement and age estimates of middle to late Pleistocene terrace surfaces in Rendija Canyon are similar, 0.01 to 0.03 mm/yr. Geomorphic and geologic mapping in the Rendija Canyon area show that there were at least two and possibly three late Quaternary surface-rupture earthquakes along the Guaje Mountain fault. These events are believed to have occurred within the past 150 to 300 ka, with one rupture event after about 150 to 300 ka, but prior to about 100 to 200 ka, and the most recent event at about 4 to 6 ka (Gardner et al., 1990). The amount of vertical separation produced by each of these events probably averages about 1 to 1.5 m.

4.3 POTENTIAL FOR SURFACE RUPTURE

Surface faulting with displacements of ¾ m or more can cause building collapse (Youd, 1980). Additionally, waste disposal facilities can be disrupted by surface faulting and federal regulations (e.g., 40 CFR Part 264) require that such facilities be located a minimum set-back distance from active faults to reduce potential hazards from surface rupture. Finally, surface faulting can significantly damage lifelines, such as gas and water pipelines, electric and telephone lines, and roads. This can cause disruption of services critical to emergency

response after an earthquake. Thus, there is much at risk from potential surface faulting hazards at the LANL and those hazards are generally discussed here.

Several major fault strands and secondary fault splays are located on or project toward the LANL (Plate 2; Figure 1-2), based on aerial reconnaissance, analysis of aerial photography, field mapping, and detailed trench investigations conducted for this and other studies (Gardner and House, 1987; Gardner et al., 1990; Vaniman and Wohletz, 1990; Kolbe et al., 1994; Vaniman and Chipera, 1994; Kolbe et al., 1995). These faults are part of the Pajarito fault system and include strands and splays of the Pajarito, Rendija Canyon, and Guaje Mountain faults. All of these faults show clear evidence for repeated late Quaternary surface rupture (Section 4.2) and thus, pose a potential threat from surface rupture in the future.

Major strands of the Pajarito fault are located along the western margin of the LANL, and there is evidence that secondary splays traverse westernmost parts of the LANL (Plate 2). This area also appears to be backtilted toward the Pajarito fault. The Rendija Canyon fault is interpreted to extend at least as far south as Pajarito Mesa and perhaps as far south as Water Canyon (Section 4.2.2). Thus, the Rendija Canyon fault extends about 3 km or more into the LANL (Plate 2). In this area, the fault consists of a wide and variable zone of deformation with many fault splays. It may be over 1 km wide at Mortandad Canyon. The Guaje Mountain fault is interpreted to terminate south of Mortandad Canyon (Section 4.2.3) and thus, traverses approximately 2 km of the north-central part of the LANL (Plate 2; Figure 1-2). The zone of deformation may be several hundred meters wide at the southern end of the Guaje Mountain fault.

Available information suggests the age of the most recent activity on each fault is different; however, the record is incomplete for the Pajarito fault and age constraints are equivocal for the Rendija Canyon fault. Radiocarbon ages from a trench exposure across the Guaje Mountain fault indicate that the fault was active in the Holocene and the most recent surface rupture probably occurred between 4 to 6 ka (Gardner et al., 1990). Trench investigations from this study indicate that the most recent surface rupture on the Rendija Canyon fault occurred either 8 to 9 ka or around 23 ka (Section 4.2.2). However, this event did not extend the entire length of the fault (Kolbe et al., 1994). Finally, the youngest activity exposed so far in trenches on the Pajarito fault probably occurred between 45 and 55 ka

(Section 4.2.1). However, because exposures were incomplete, we cannot preclude the occurrence of younger surface ruptures on the Pajarito fault.

Because the Rendija Canyon and Guaje Mountain faults extend southward into the LANL, the potential for surface faulting may exist at some facilities. Splays of the Pajarito fault in the westernmost part of the LANL may also experience surface rupture during a moderate to large earthquake along any of the local faults. Characterization of the potential for surface rupture at specific sites requires assessment of the presence or absence of major fault strands and secondary splays, and evaluation of the width of secondary deformation (e.g., fracturing, tilting), usually on a site-specific basis. Such studies have been conducted at TA-63 (Kolbe et al., 1995), TA-67 (Kolbe et al., 1994), and TA-55 (Dames and Moore, 1972). Unfortunately, trench logs from the investigation at TA-55 are missing from the LANL archives and the Dames and Moore files, but information from these and other studies (e.g., Reneau, 1991; Carter and Winter, 1995) still provides useful insights into evaluating surface faulting hazards at the LANL. In particular, these studies demonstrate the need for both: 1) detailed mapping of the LANL area to develop a surface faulting hazards map that defines areas of potential hazard at an adequate scale (1:10,000 or larger); and 2) additional site-specific investigations to evaluate the potential for surface rupture at specific facilities, such as TA-55 (Figure 1-2).

Results from this and previous studies provide caveats and additional information for developing a surface faulting hazards map for the LANL and conducting future site-specific investigations of surface faulting hazards. In particular, the investigation at TA-67 found evidence for faulting associated with lineaments along the Rendija Canyon fault, but evidence for no faulting associated with lineaments associated with the Guaje Mountain fault (Kolbe et al., 1994). These results emphasize the caveat that although lineaments can be used as indicators for potential surface faulting hazards, they are not completely reliable in evaluating the potential hazard.

In addition, detailed mapping and trenching studies have identified numerous fault strands on the Pajarito Plateau, many of which show no geomorphic expression (e.g., Reneau, 1991; Vaniman and Wohletz, 1990; Kolbe et al., 1994; Carter and Winter, 1995). Nevertheless, these faults offset the 1.2 Ma Tshirege Member of the Bandelier Tuff, suggesting that Quaternary faulting was more distributed throughout the Pajarito Plateau than was previously

thought. Results from these studies highlight the need for a detailed surface faulting hazards map for the LANL and the town of Los Alamos.

Many of the fault strands may be older and less active, and therefore not necessarily pose a significant surface rupturing threat to lower-risk lab facilities (e.g., Kolbe et al., 1994); however, the age of the most recent activity on most fault strands is unknown. Thus, even with the development of a detailed surface faulting hazards map, some additional site-specific studies will be necessary because fault strands are extensively distributed, not always expressed geomorphically, and do not all show the same age. A good example of the latter is the evidence from trenches at the Guaje Pines site (Section 4.2.2.1) and the trench investigation on Pajarito Mesa (Kolbe et al., 1994), which suggests that the most recent surface rupture on the Rendija Canyon fault, which occurred 8 to 9 ka or around 23 ka, did not extend as far south as Pajarito Mesa because the most recent surface faulting there predates deposition of El Cajete air-fall pumice 45 to 73 ka (Kolbe et al., 1994).

Finally, evaluating surface faulting hazards for many areas on the Pajarito Plateau is complicated by the presence of fractures throughout the Bandelier Tuff (e.g., Dames and Moore, 1972; Vaniman and Wohletz, 1990, 1994; Kolbe et al., 1994, 1995) and the thin cover of overlying sediments. Although many of the fractures may be cooling-related and show no evidence for displacements (e.g., Kolbe et al., 1994), this may be difficult to evaluate when the tuff is homogeneous and overlying sediments are non-stratified and thin (e.g., Kolbe et al., 1995). These potential complications should be considered in conducting future site-specific surface faulting investigations on mesas where sediments overlying the tuff are especially thin (e.g., TA-55).

Table 4-1. Net Vertical Tectonic Displacements Estimated from Topographic Profiles Across the Pajarito Fault System

		Net Vertical Tectonic Displacement of the Top of the Bandelier Tuff (m)					
Profile	Profile Location*	Pajarito Fault		Total	Rendija	Guaje	Total
No.	(Listed from North to South)	West Splay	East Splay	(Down-to-E)	Canyon Fault	Mtn. Fault	(Down-to-W)
P20	North Rim of Santa Clara Canyon						
P22	North Rim of Sawyer Canyon			38 +/- 12		17 +/- 10	17 +/- 10
P15	North of Alamitos Canyon			7 +/- 2			
P13	Alamitos					27 +/- 4	27 +/- 4
P0	South Rim of Chupaderos Canyon				6 +/- 3	23 +/- 8	29 +/- 8
P12	North of Guaje Canyon						21 +/- 2
P14	Guaje Ridge Trail						25 +/- 2
P1	Barranca Mesa				36 +/- 10	15 +/- 5	51 +/- 10
P2	North Mesa				35 +/- 5	3 +/- 2	38 +/- 5
P3	Los Alamos Mesa			81 +/- 81	24 +/- 10	3 +/- 3	27 +/- 10
P4	South Mesa			100 +/- 20	3 +/- 3	0	3 +/- 3
P17	Twomile Mesa			114 +/- 9			
P5	Pajarito Mesa	54 +/- 4	100 +/- 5	154 +/- 5	0	0	
F1	West of TA-67			110.5 +/- 12			
M2	West of TA-67			108 +/- 15.6			
F3	North of Canon de Valle			115 +/- 24			
P18	Water Tanks Trench Site	42 +/- 10	110 +/- 5	152 +/- 10			
F4	South of Canon de Valle			118 +/- 4			
F5	North of Water Canyon			106 +/- 10.5			
F6	Water Canyon Trench Site			124 +/- 24			
P6	Water Canyon			103 +/- 7			
M7	South of Highway 4			108.3 +/- 2.1			
P7	Burnt Mesa	76 +/- 5	36 +/- 7	112 +/- 7			
P8	Rim of Lummis Canyon	91 +/- 23	17 +/- 4	108 +/-23			
P9a	Rim of Frijoles Canyon	80 +/- 10	12 +/- 4	92 +/- 10			
P9b	Stone Lion's Shrine	36 +/- 8	65 +/- 7	101 +/- 8			
P9c	St. Peter's Dome			37 +/- 5			
P9d	San Miguel Ruins	71 +/- 10	15 +/- 10	86 +/- 10			
P9g	Medio Mesa			22 +/- 5			
P9e	Sanchez Canyon South			30 +/- 10			
P9f	Horn Mesa			85 +/- 15			
P9h	Southern Horn Mesa			65 +/- 5			
P10	North Rim of Sanchez Canyon			17 +/-3			
P11	Grande Confluence			50 +/- 50			
*See Figure 4-1 for location on map							

TABLE 4-2. RADIOCARBON SAMPLES AND ANALYSES FROM TRENCH INVESTIGATIONS

Submitted By[1]	Laboratory Numbers	Field Number	14-C Age (yr B.P.)[2]	Calibrated Age (cal B.P.)[3]	Notes[4]
Water Canyon Site					
WCFS	TO-3415	WCSP2-RC1	8060±160	8980 (8163-9647)	1.0 m deep, silty sand, AMS, Unit TP2-3
WCFS	Beta-55318	WCSP2-RC2 (CAMS-3717)	9490±110	10480-10530 (9995-11071)	Detrital, 0.5 m deep, silty sand, AMS, Unit TP2-3
Water Tanks Site					
WCFS	Beta-56176	WTT1-RC4	1120±80*	1060 (723-1342)	0.25 m deep, E. end trench, loess or reworked loess in Unit 18
WCFS	TO-3413	WTT1-RC5	19,070±160	too old for calibration	1.45 m deep, below El Cajete, Unit 13 (intrusive or contaminated?), AMS
WCFS	TO-3414	WTT1-RC6	5840±90	6670 (6289-7156)	0.65 m deep, E. end trench, Unit 16, AMS
WCFS	Beta-60220	WTT2-RC1	22,420±690	too old for calibration	Bulk sediment sample, 1.05 m deep, below El Cajete, Unit 11 (intrusive or contaminated?)
WCFS	Beta-55313 CAMS-3715	WTT1-RC1D	>47,500	too old for calibration	Burn layer, 1.8 m deep, below El Cajete, Unit 6, AMS, infinite age
Pajarito Canyon Site					
WCFS	Beta-55312 CAMS-3714	PCT1-RC1	700±90	660 (323-954)	0.55 m deep, W. end trench; below Bt horizon, Unit 14b (intrusive or contaminated?), AMS

TABLE 4-2. RADIOCARBON SAMPLES AND ANALYSES FROM TRENCH INVESTIGATIONS (Continued)

Submitted By[1]	Laboratory Numbers	Field Number	14-C Age (yr B.P.)[2]	Calibrated Age (cal B.P.)[3]	Notes[4]
Guaje Pines Site					
WCFS	Beta-55314 CAMS-3716	GPT1-RC5	1250±70	1170 (918-1403)	0.25 m deep, Unit 2b, W. end trench (intrusive or contaminated?), AMS
WCFS	Beta-55319 CAMS-3718	GPT1-RC7	630±70	560-640 (329-789)	0.25 m deep, Unit 1, upper soil W. of fault, AMS
WCFS	Beta-56175	GPT1-RC8	860±80*	780 (547-1130)	0.55 m deep, Unit 2a, below RC-7 in Bt horizon (root? contaminated?)
WCFS	TO-3416	GPT1-RC10	710±50	660 (523-789)	0.15 m deep, Unit 1, upper soil E. of fault, AMS
WCFS	Beta-55320 CAMS-3719	GPT2-RC1	7270±70	8000-8060 (7767-8335)	Detrital, 0.75 m deep, Unit 15, AMS
WCFS	Beta-59678 ETH-10052	GPT2-RC2	7375±90	8130 (7800-8484)	0.75 m deep, Unit 15, AMS
SLR	Beta-59675 ETH-10058	GPT2-RC3	7345±85	8120 (7792-8414)	0.6 m deep, Unit 15, AMS
Sportsmen's Club Site/Rendjia Canyon Area					
SLR	Beta-59676 ETH-10059	SCT1-RC1	2615±70	2750 (2344-2990)	1.7 m below Qt7 terrace; near base of stream gravels, AMS
WCFS	Beta-55316	SCT2-RC1	120±90*	0-260 (0-525)	1.4 m deep, Unit 7
WCFS	TO-3417	SCT2-RC1	150±50	0-260 (0-435)	1.4 m deep, Unit 7, AMS
SLR	AA-9417	SCT2-RC5b	230±75*	300 (0-546)	Pine cone, 1.65 m deep, Unit 6, AMS

TABLE 4-2. RADIOCARBON SAMPLES AND ANALYSES FROM TRENCH INVESTIGATIONS (Continued)

Submitted By[1]	Laboratory Numbers	Field Number	14-C Age (yr B.P.)[2]	Calibrated Age (cal B.P.)[3]	Notes[4]
SLR	AA-9418	SCSP-RC3	6290±80*	7210 (6811-7518)	Soil test pit SCSP3 at Sportsmen's Club site; basal slopewash above terrace Qt6 deposits (3.5 m strath), AMS
SLR	AA-9419	SCSP-RC4	6110±100*	7010 (6499-7391)	Soil test pit SCSP4 at Sportsmen's Club site; terrace Qt6 deposit, 0.4 m above 3.5 m high strath, AMS
SLR	Beta-59672 ETH-10056	GM-RC5	2140±65	2120 (1820-2357)	0.5 m below Qt7 terrace, above 3.3 m high strath

Average Ages

Geologic Unit	Average 14-C Age[5] (yr B.P.)	Average Calibrated Age[5] (cal B.P.)	Lab Sample Numbers	Notes
Qt6 terrace deposits	6249 + 126	7170 (6810-7385)	AA-9418; AA-9419	adjacent units
GPT-1: Unit 1	683 + 82	650 (528-732)	Beta-55319, TO-3416	same unit
GPT-2: Unit 15	7321 + 94	8030-8110 (7918-8319)	Beta-55320, 59675, 59678	same unit

Notes:

1 WCFS: Woodward-Clyde Federal Services; SLR: Steven L. Reneau, Los Alamos National Laboratory.

2 All radiocarbon ages corrected for $\delta^{13}C$ in laboratory except where noted with an asterisk. Laboratory errors are $\pm 1\sigma$.

3 Radiocarbon ages were calendar-calibrated using CALIB 3.0 (Stuiver and Reimer, 1993) with an error multiplier of 2.0 and 2σ uncertainty. Ages in parentheses are 2σ range. For samples not corrected for $\delta^{13}C$ in laboratory, the $\delta^{13}C$ value was assumed to be -23.2 ± 0.9 o/oo based on $\delta^{13}C$ values of 16 samples collected from the Pajarito Plateau by S.L. Reneau and WCFS.

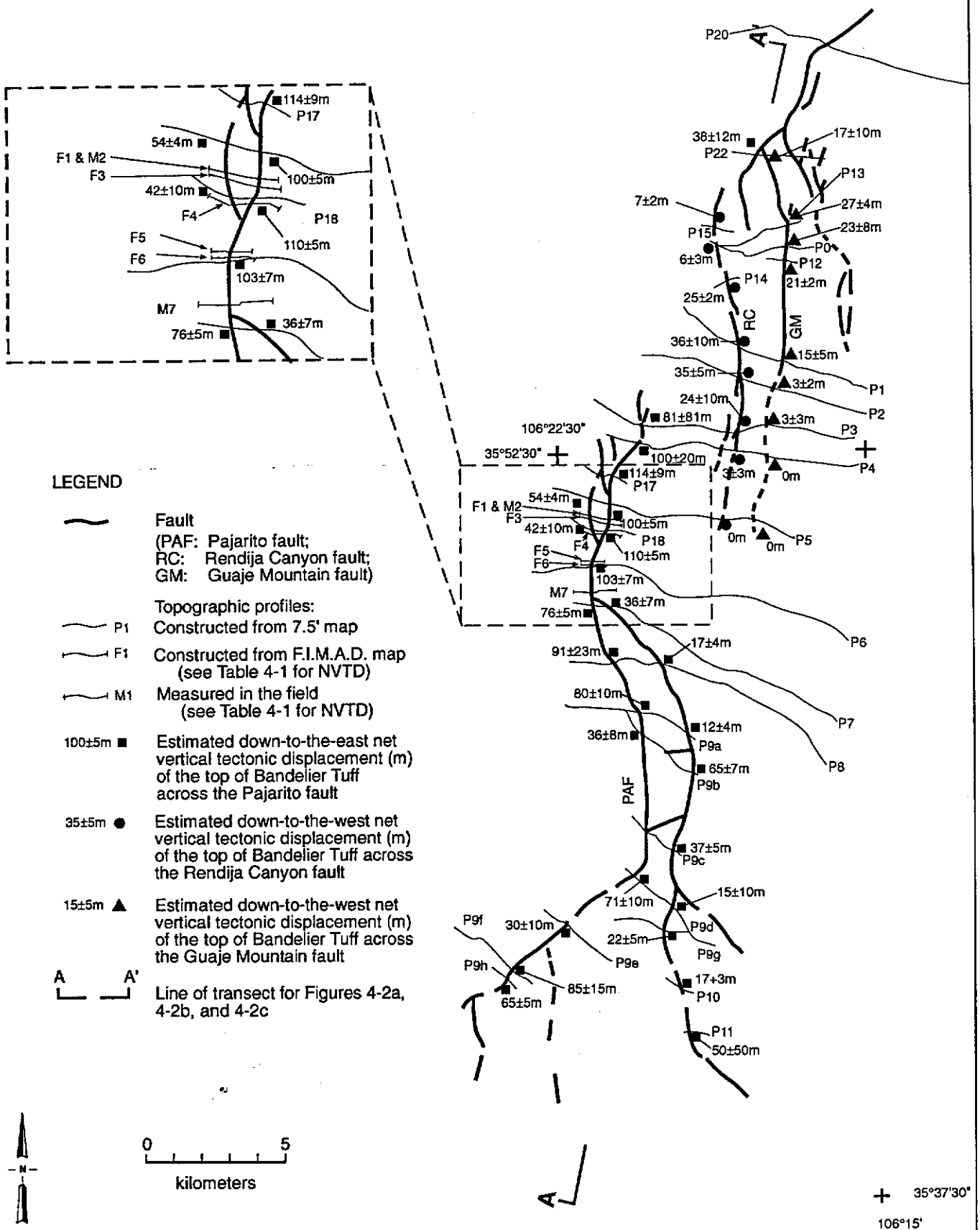
4 All ages are for conventional analyses of charcoal except where noted.

5 Averaged radiocarbon and calendar-calibrated ages were obtained using CALIB 3.0 with an error multiplier of 2.0 for the original analyses. Average ages were only obtained from split samples or from samples from the same or potentially correlative units at a site where there is no statistically significant difference between sample ages.

FOR SAMPLES FROM TRENCHES ALONG THE PAJARITO FAULT SYSTEM

Field No.	Lab No.	Strat. Unit	Equivalent Dose Method[2]	Light Exposure[3]	Temp. (°C)[4] or Time	Equivalent Dose (grays)[5]	TL age est. (ka)[6]
RENDIJA CANYON FAULT							
Guaje Pines Trench 1							
GPT1-TL1	OTL-518	Unit 4a	TL-Total Bleach	16h sun	260-360	385.40 ± 6.82	71.0 ± 14.0
			TL-Total Bleach	8h UV	non-calculable; no plateau	383.97 ± 6.99	**69 ± 14.0**
			OSL-Infrared	1h sun	2-23 sec.		
GPT1-TL2	OTL-463	Unit 4a	TL-Total Bleach	16h sun	300-390	338.10 ± 6.76	59.0 ± 10.0
			Partial Bleach	1h sun	300-390	337.6 ± 214.7	**58.0 ± 52.0**
GPT1-TL4	OTL-519	Unit 3y	TL-Total Bleach	16h sun	250-400	108.70 ± 2.35	24 ± 6
			TL-Total Bleach	8h UV	250-400	118.60 ± 1.43	**26 ± 6**
			OSL-Infrared	1h sun	3-59 sec	113.20 ± 1.27	26 ± 6
Guaje Pines Trench 2							
GPT2-TL5	OTL-477	Unit 20	TL-Total Bleach	16h sun	290-400	2026.9 ± 126.4	<140 ± 26
GPT2-TL7	OTL-478	Unit 15	TL-Total Bleach	16h sun	280-400	79.09 ± 2.63	15.0 ± 3
			TL-Total Bleach	8h UV	280-400	106.70 ± 2.08	**20 ± 4**
			TL-Partial Bleach	1h sun	280-400	109.10 ± 3.07	21 ± 4
PAJARITO FAULT							
Water Tanks Trench 1							
WTT1-TL8	OTL-464	Unit 13	TL-Total Bleach	16h sun	250-400	253.30 ± 5.02	51.0 ± 8.0
			TL-Partial Bleach	1h sun	250-400	272.40 ± 3.39	**55.0 ± 9.0**
WTT1-TL9	OTL-465	Unit 11	TL-Total Bleach	16h sun	280-400	259.80 ± 13.89	51.0 ± 10.0
			TL-Partial Bleach	1h sun	280-400	290.40 ± 51.92	**57.0 ± 18.0**
Pajarito Canyon Trench 1							
PCT1-TL12	OTL-479	Unit 14a	TL-Total Bleach	16h sun	280-400	731.8 ± 19.8	137 ± 22
			OSL-Infrared	1h sun		saturated signal; age not calculated	

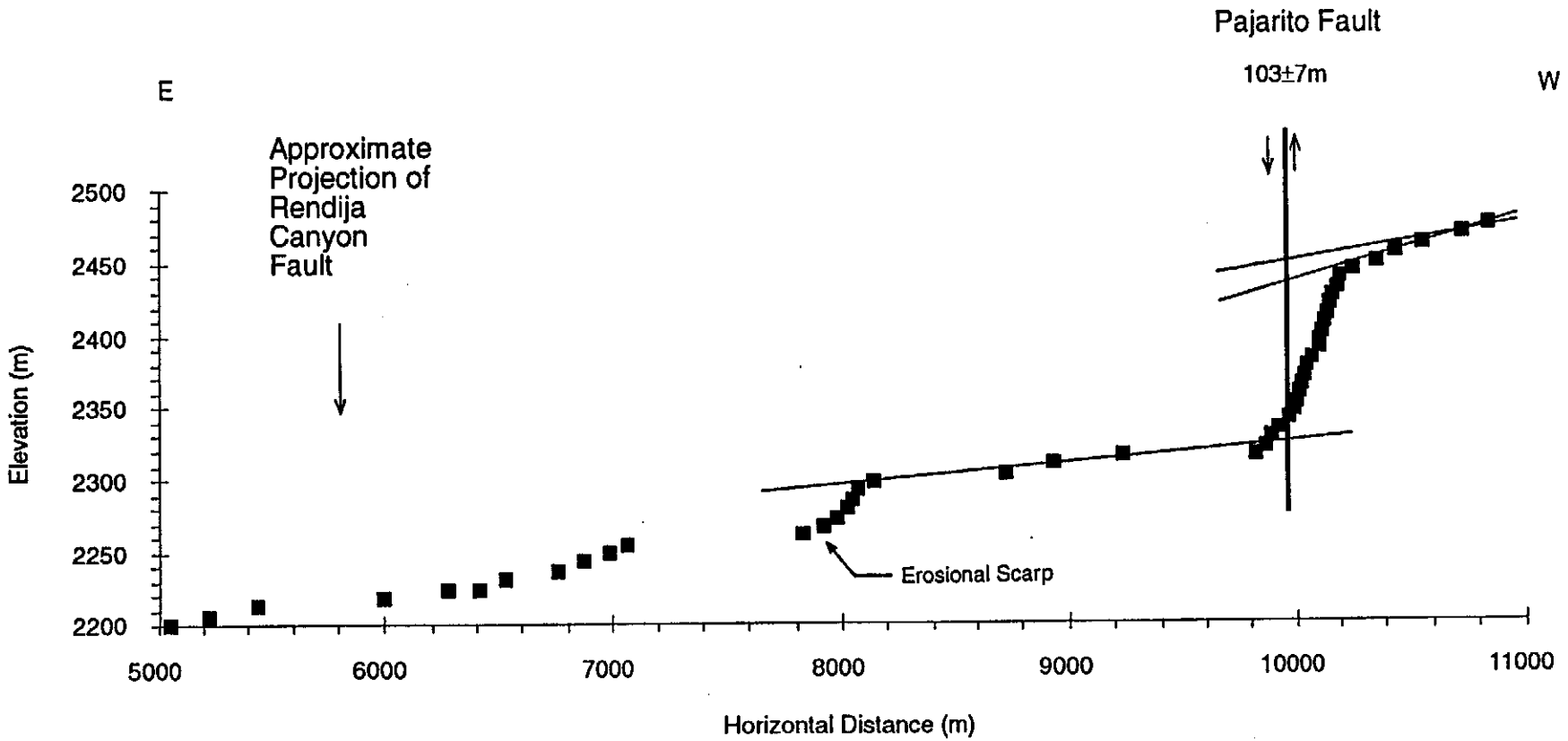
[1] Results of analyses provided by S.L. Forman, Byrd Polar Research Center, The Ohio State University, written communication, 1994.
[2] All thermoluminescence (TL) measurements were made with a Corning 5/58 and HA-3 filters in front of the photomultiplier tube. Samples were preheated to 124°C for 48 hours prior to analysis. Optically stimulated luminescence (OSL) measurements were made with BG-39 filter in front of the photomultiplier tube. OSL samples were preheated to 160°C for 5 hours prior to analysis.
[3] Hours of light exposure to define residual level. "Sun" is natural sunlight in Columbus, Ohio. UV is light exposure from 275 watt General Electric "sunlamp".
[4] Temperature range used to calculate equivalent dose.
[5] All errors are at one sigma and calculated by averaging the errors across the temperature range.
[6] Preferred age estimates are shown in bold. All errors are at two sigma. A moisture content of 15 ± 5% was assumed for all samples in the final age calculation.



Note: See Table 4-1 for geographic location names of profiles

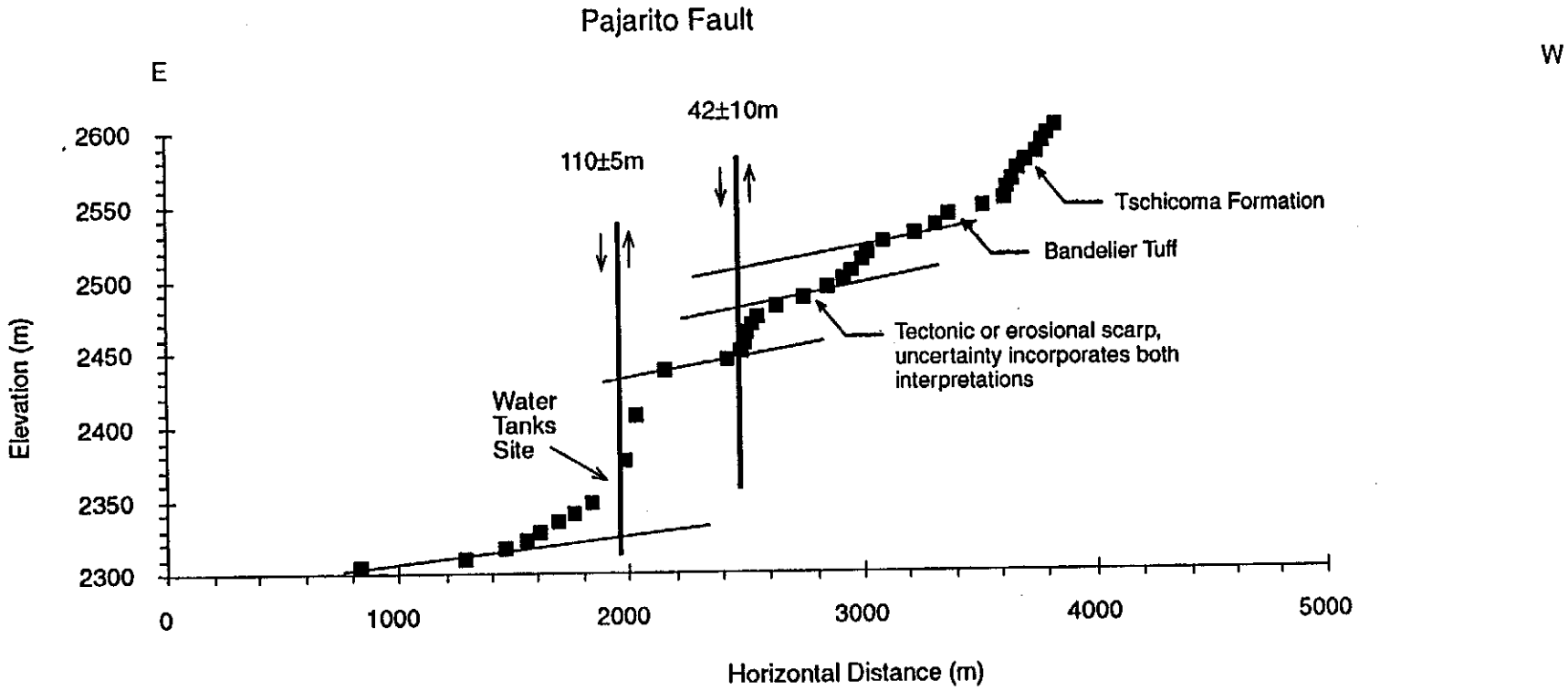
Project No. 91C0509	Los Alamos Seismic Hazards	LOCATION MAP OF TOPOGRAPHIC PROFILES ACROSS THE PAJARITO FAULT SYSTEM	Figure 4-1
Woodward-Clyde Federal Services			

91C0509A-1300/060893



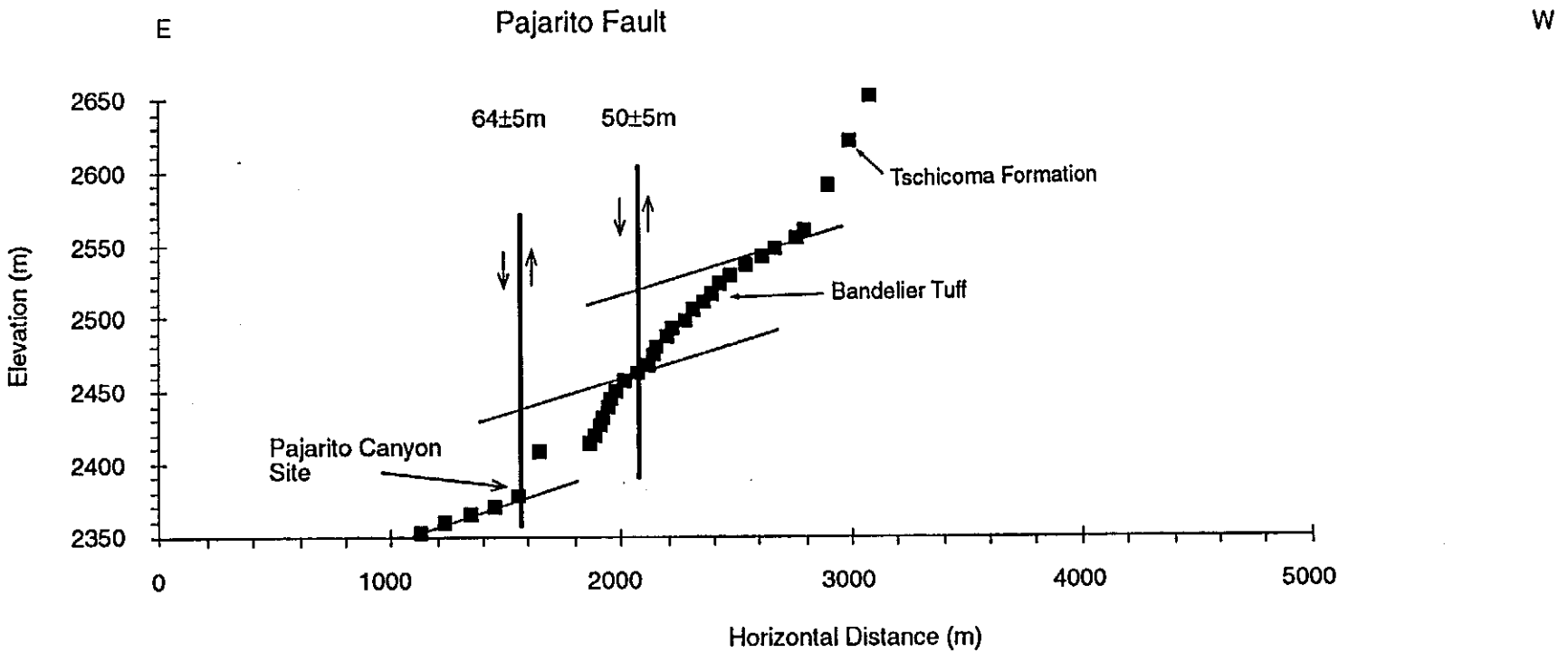
Note: Profile location shown on Figure 4-1.

Project No. 91C0509	Los Alamos Seismic Hazards	TOPOGRAPHIC PROFILE OF THE TOP OF BANDELIER TUFF ALONG FRIJOLES MESA (WESTERN PART OF PROFILE P6)	Figure 4-2a
Woodward-Clyde Federal Services			



Note: Profile location shown on Figure 4-1.

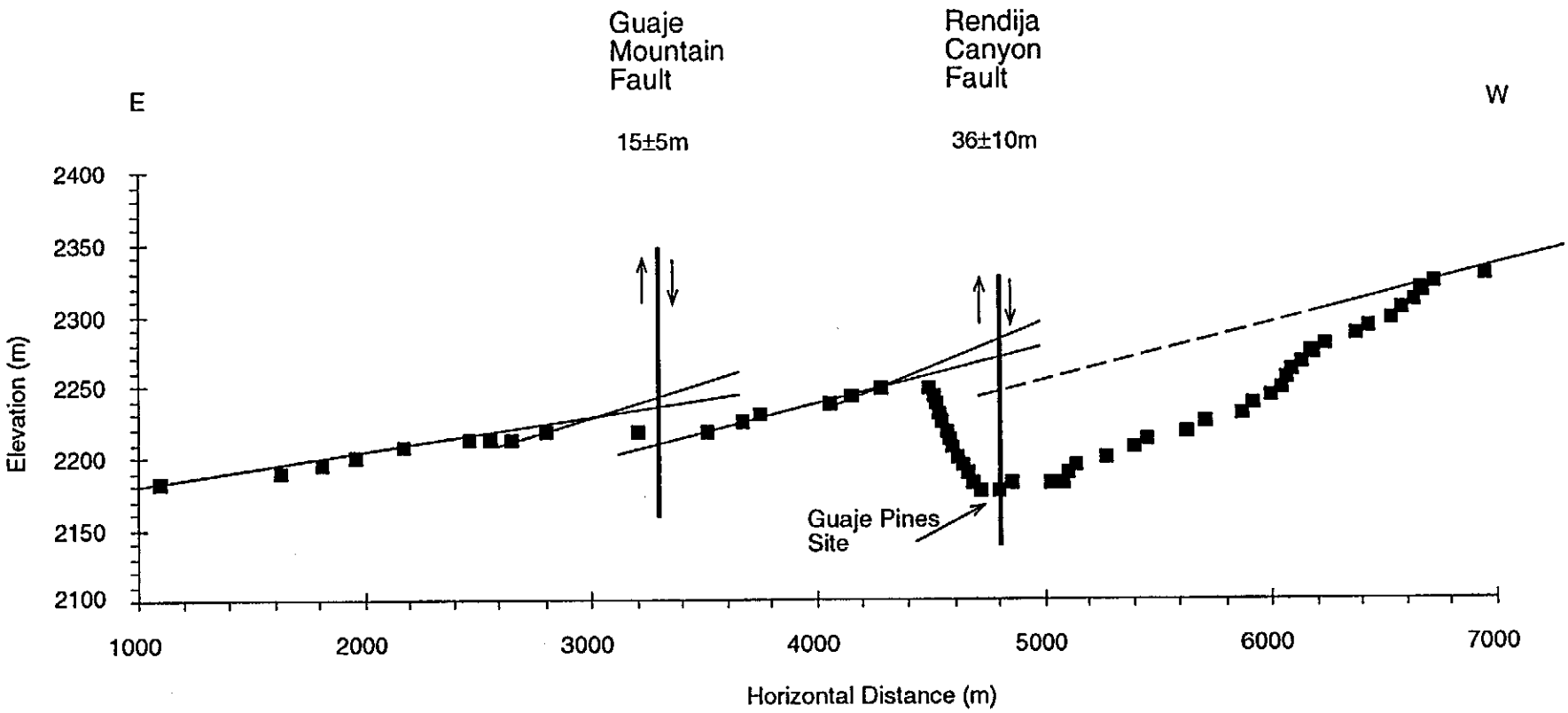
Project No. 91C0509	Los Alamos Seismic Hazards	TOPOGRAPHIC PROFILE OF THE TOP OF BANDELIER TUFF WEST OF MESITA DEL POTRILLO (PROFILE P18)	Figure 4-2b
Woodward-Clyde Federal Services			



Note: Down-to-the-east flexure on upthrown block.

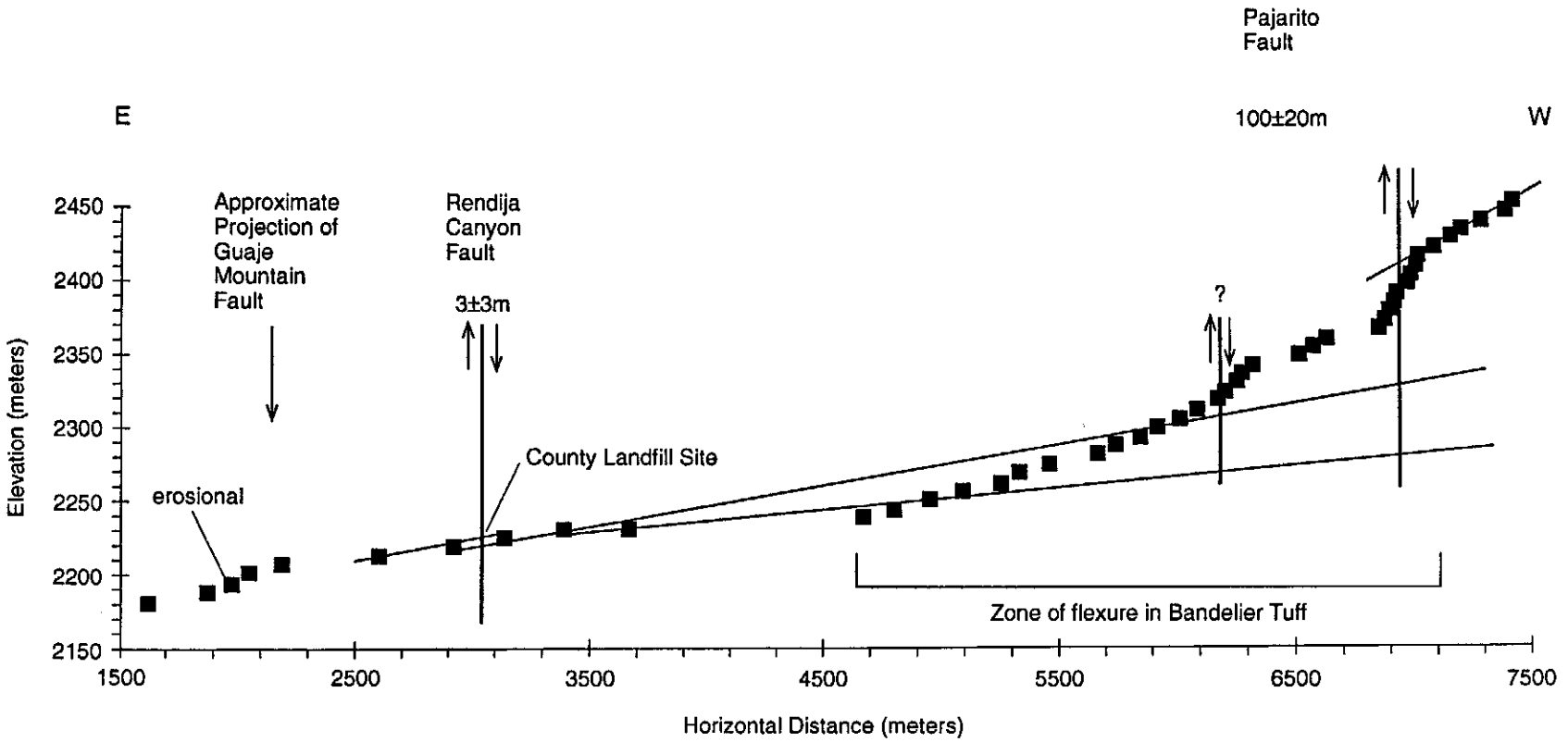
See Figure 4-1 for profile location.

Project No. 91C0509	Los Alamos Seismic Hazards	TOPOGRAPHIC PROFILE OF THE TOP OF BANDELIER TUFF WEST OF TWO MILE MESA (PROFILE P17)	Figure 4-2c
Woodward-Clyde Federal Services			



See Figure 4-1 for profile location.

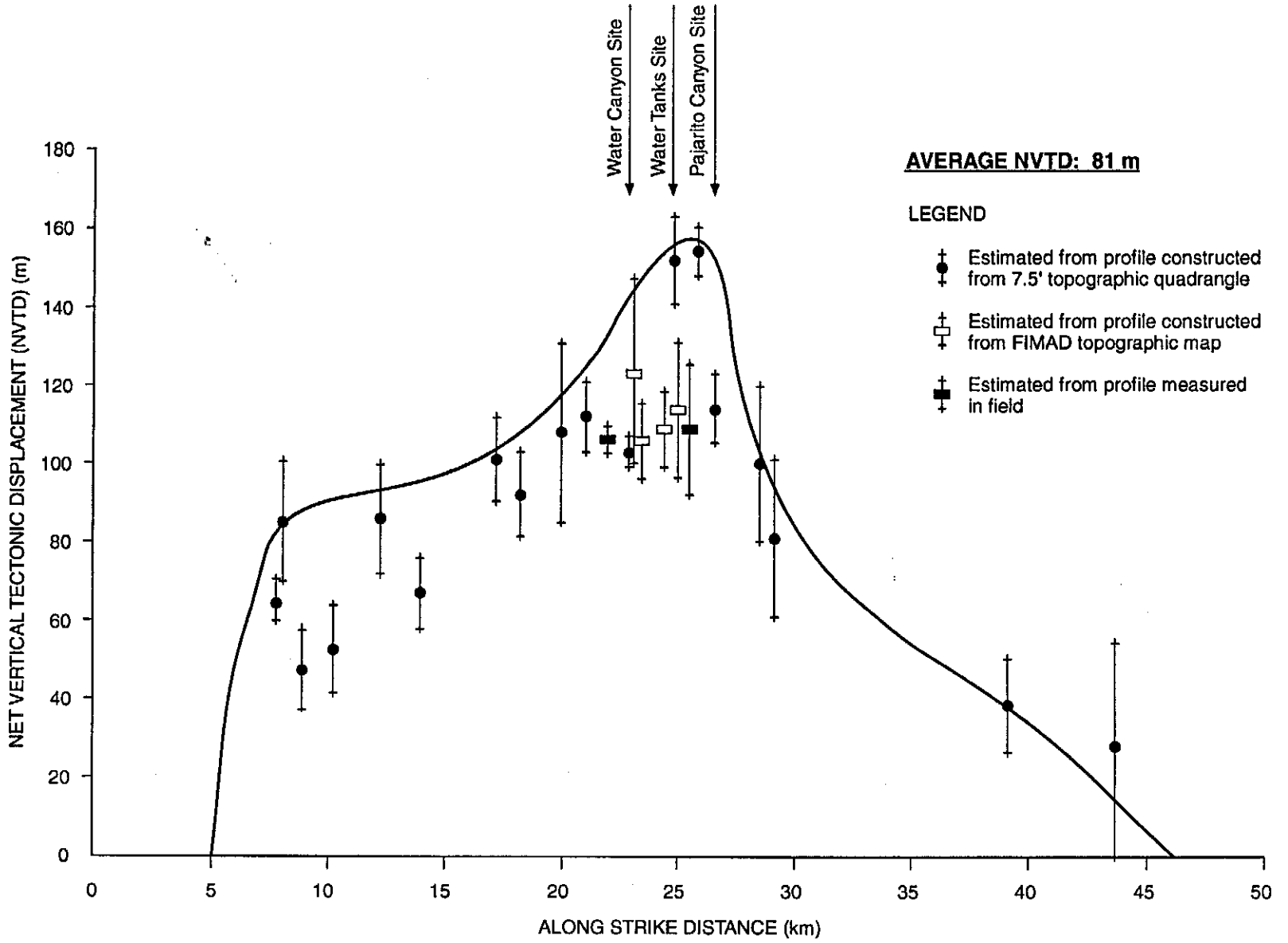
Project No. 91C0509	Los Alamos Seismic Hazards	TOPOGRAPHIC PROFILE OF THE TOP OF BANDELIER TUFF ALONG BARRANCA MESA (PROFILE P1)	Figure 4-2d
	Woodward-Clyde Federal Services		



See Figure 4-1 for profile location.

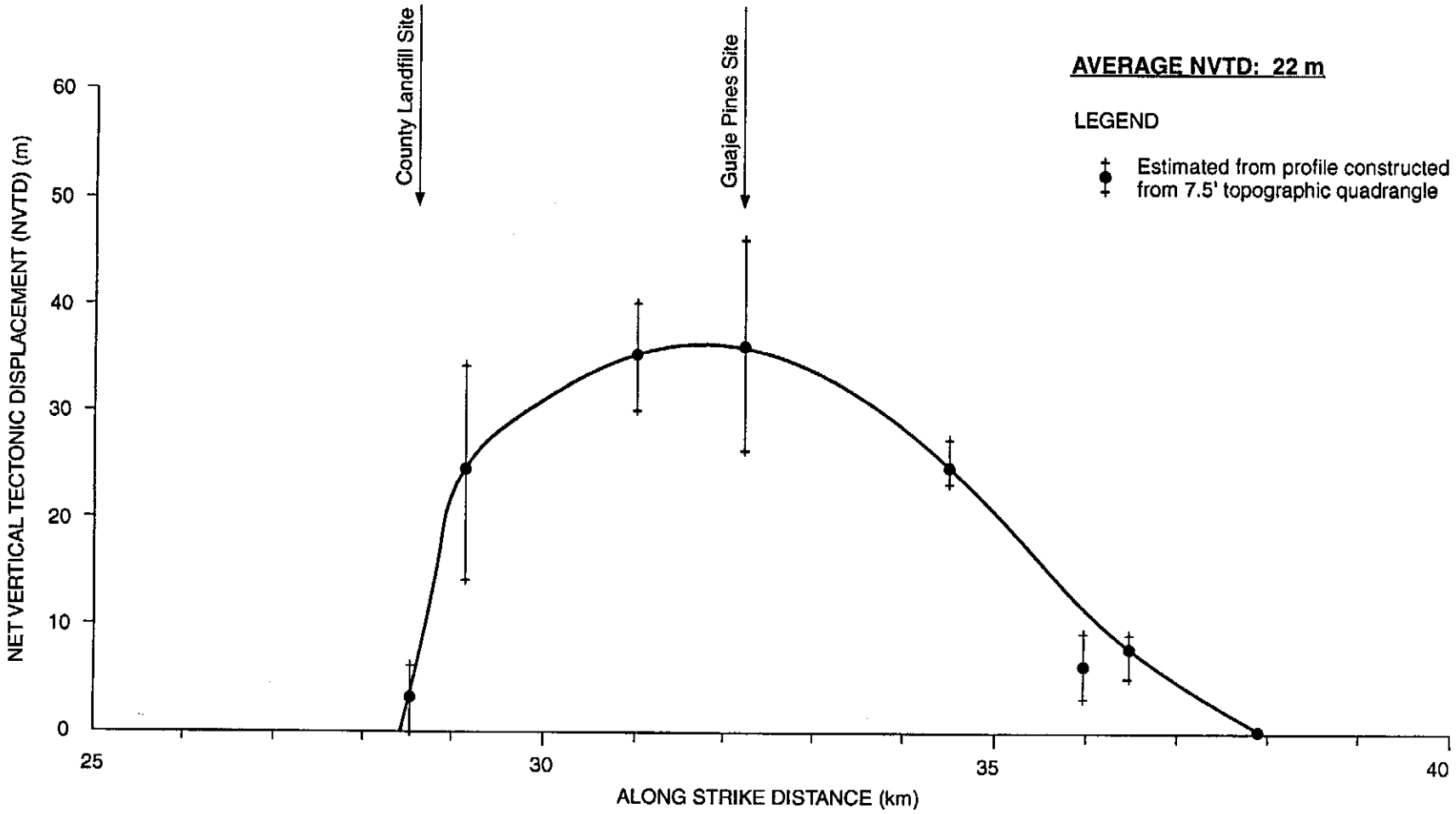
Project No. 91C0509	Los Alamos Seismic Hazards	TOPOGRAPHIC PROFILE OF THE TOP OF BANDELIER TUFF ALONG SOUTH MESA (WESTERN PART OF PROFILE P4)	Figure 4-2e
Woodward-Clyde Federal Services			

SK9423-9500/111794



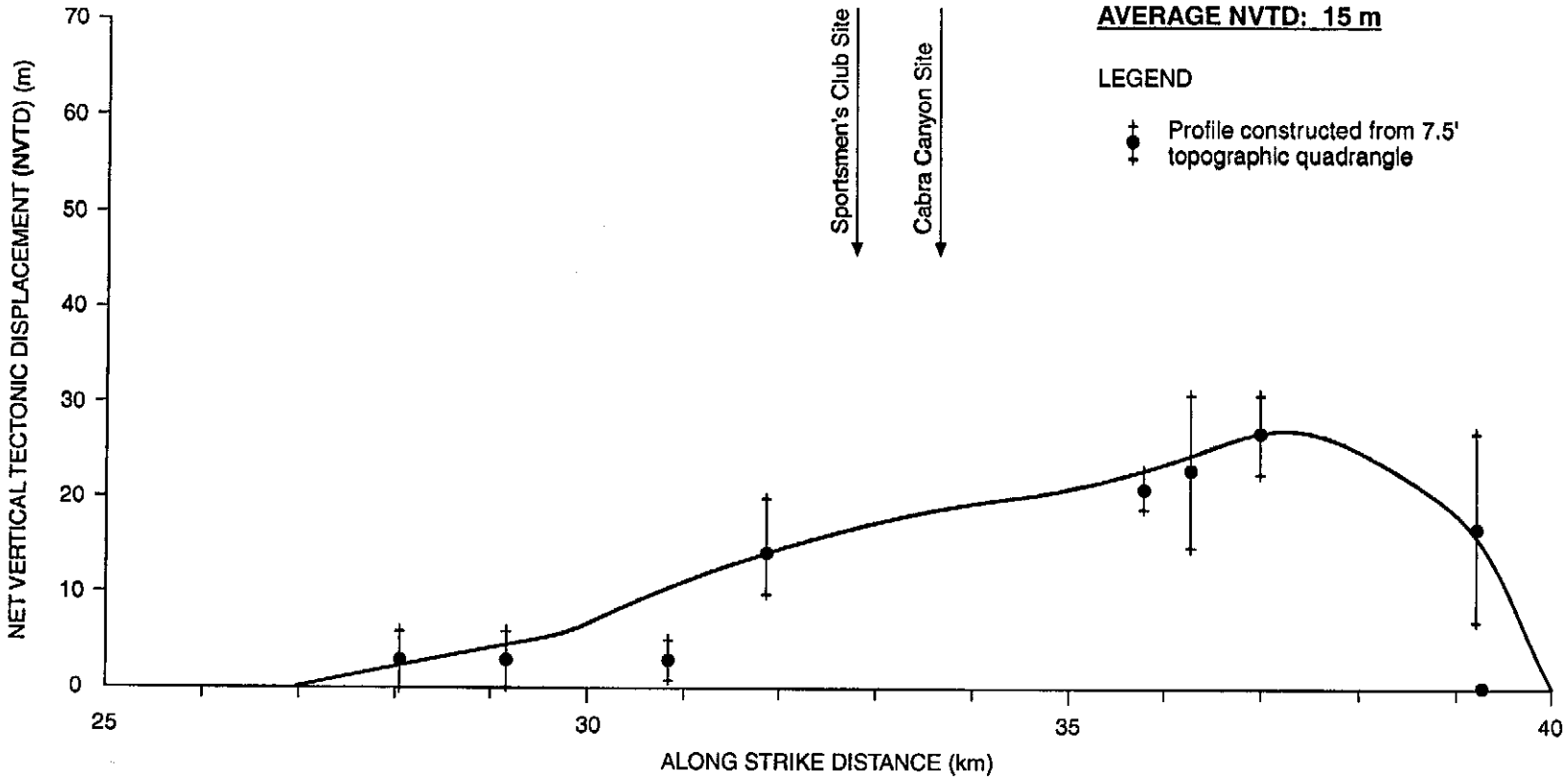
Project No. 91C0509	Los Alamos Seismic Hazards	NET VERTICAL TECTONIC DISPLACEMENT OF UPPER BANDELIER TUFF ALONG THE PAJARITO FAULT	Figure 4-3a
Woodward-Clyde Federal Services			

SK9423-A9500/011795/jun



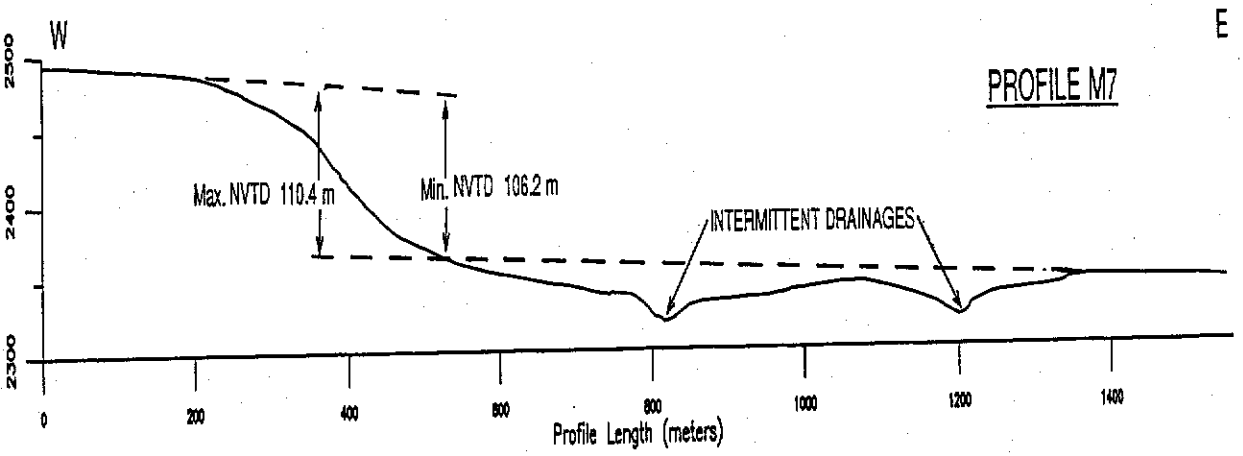
Project No. 91C0509	Los Alamos Seismic Hazards	NET VERTICAL TECTONIC DISPLACEMENT OF UPPER BANDELIER TUFF ALONG THE RENDIJA CANYON FAULT	Figure 4-3b
Woodward-Clyde Federal Services			

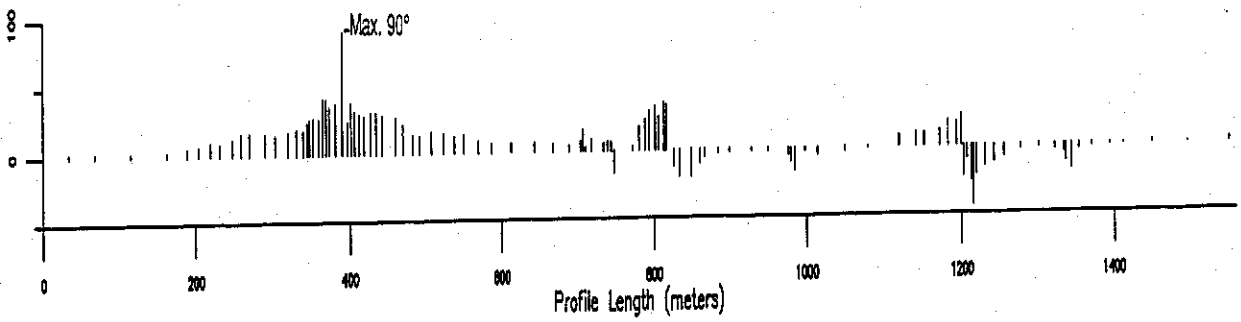
SK9423-A9500/111794

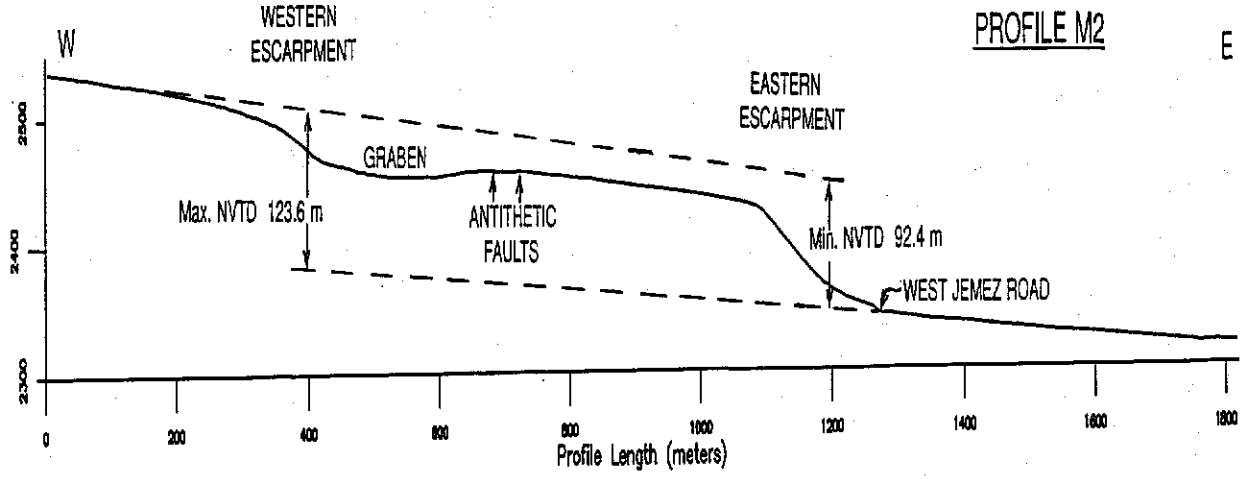


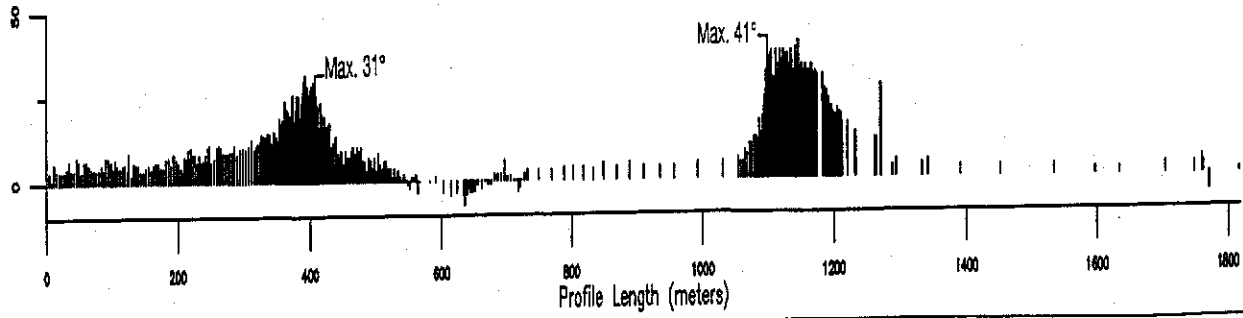
Project No. 91C0509A	Los Alamos Seismic Hazards	NET VERTICAL TECTONIC DISPLACEMENT OF UPPER BANDELIER TUFF ALONG THE GUAJE MOUNTAIN FAULT
Woodward-Clyde Federal Services		Figure 4-3c

SK9423-A9500/111794

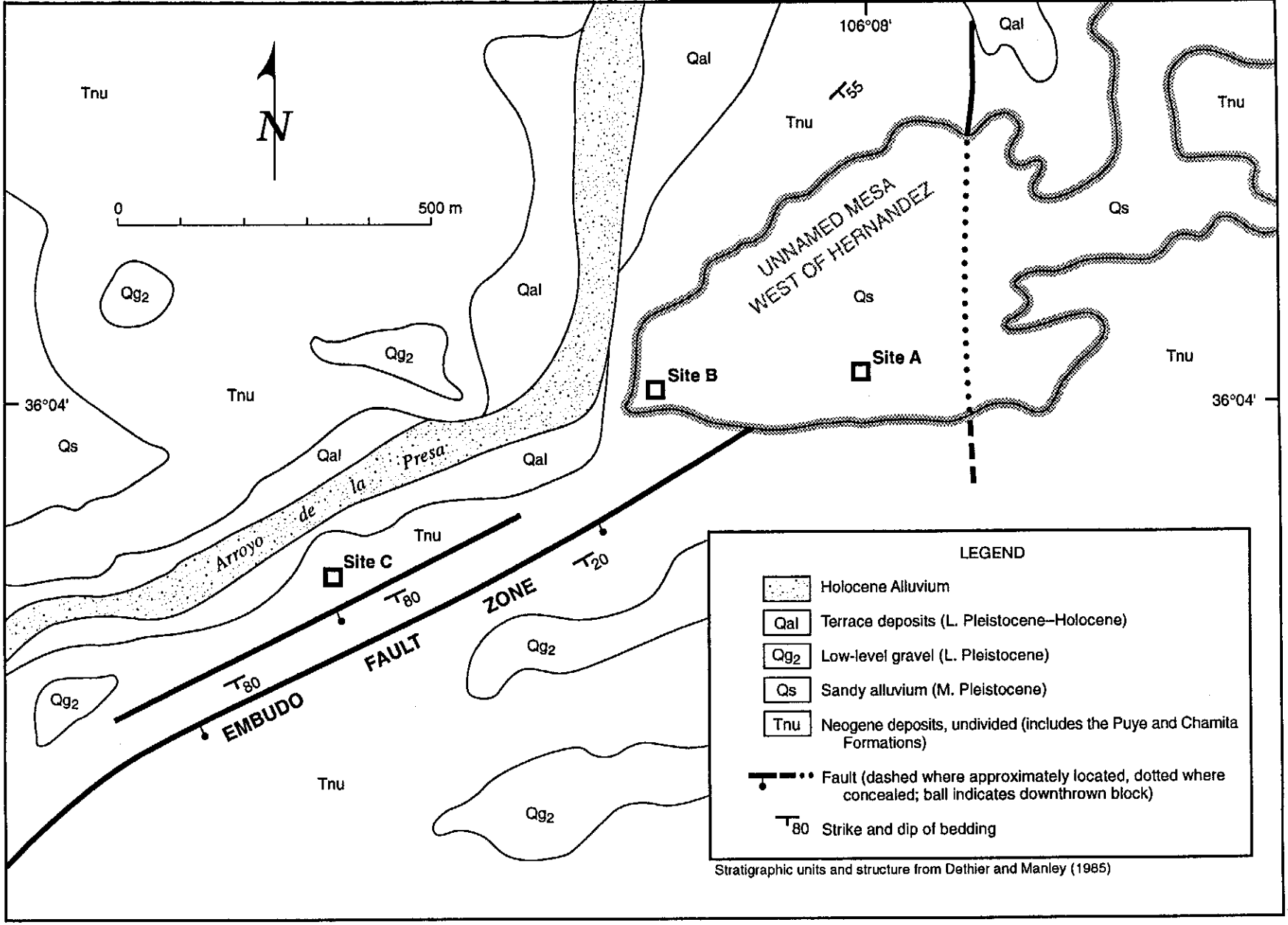






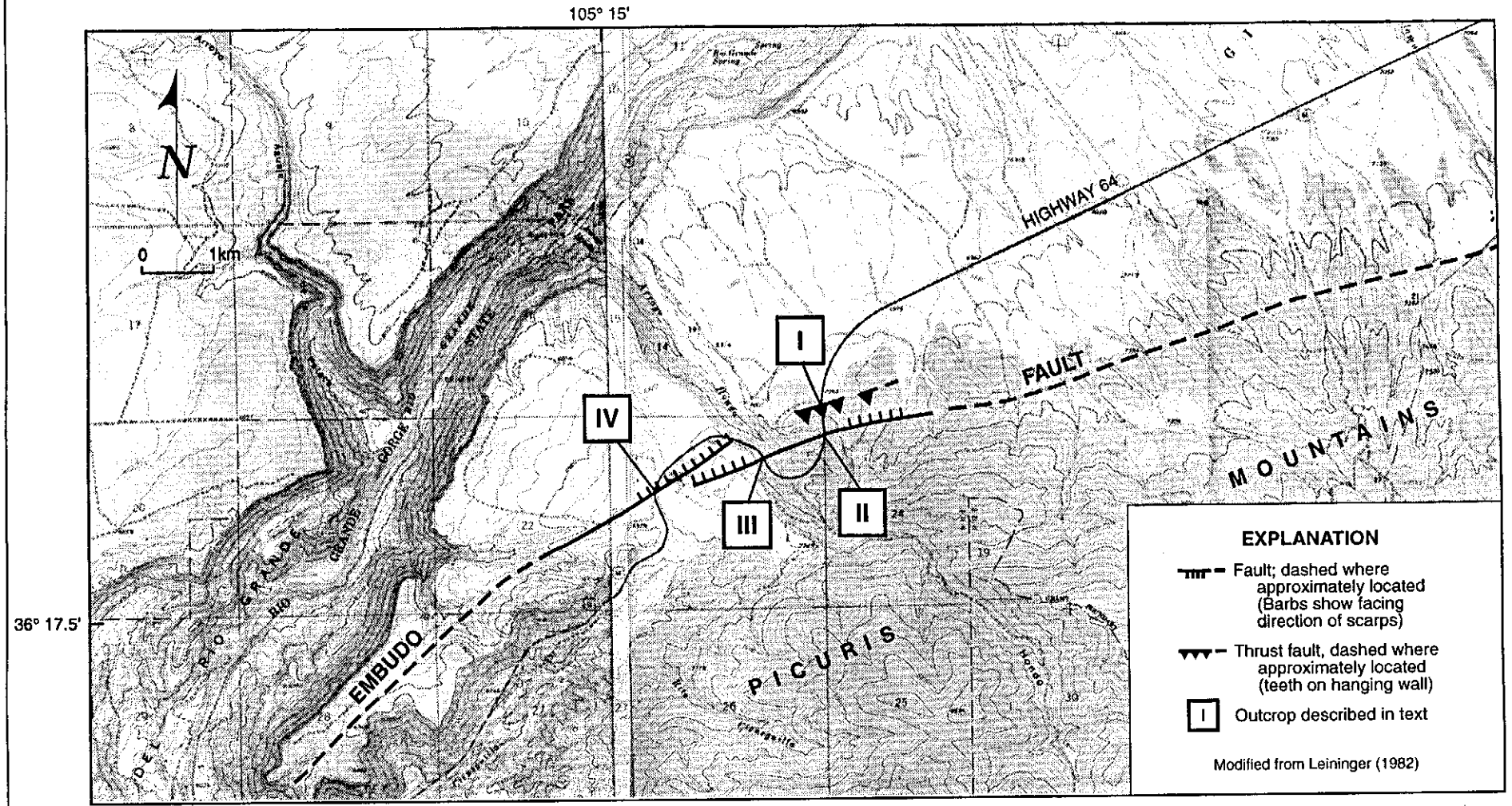


Project No. 91C0509	Los Alamos Seismic Hazards	TOPOGRAPHIC PROFILES AND SLOPE ANGLE PLOTS FOR PROFILES M7 AND M2 ACROSS THE PAJARITO FAULT	Figure 4-4
Woodward-Clyde Federal Services			

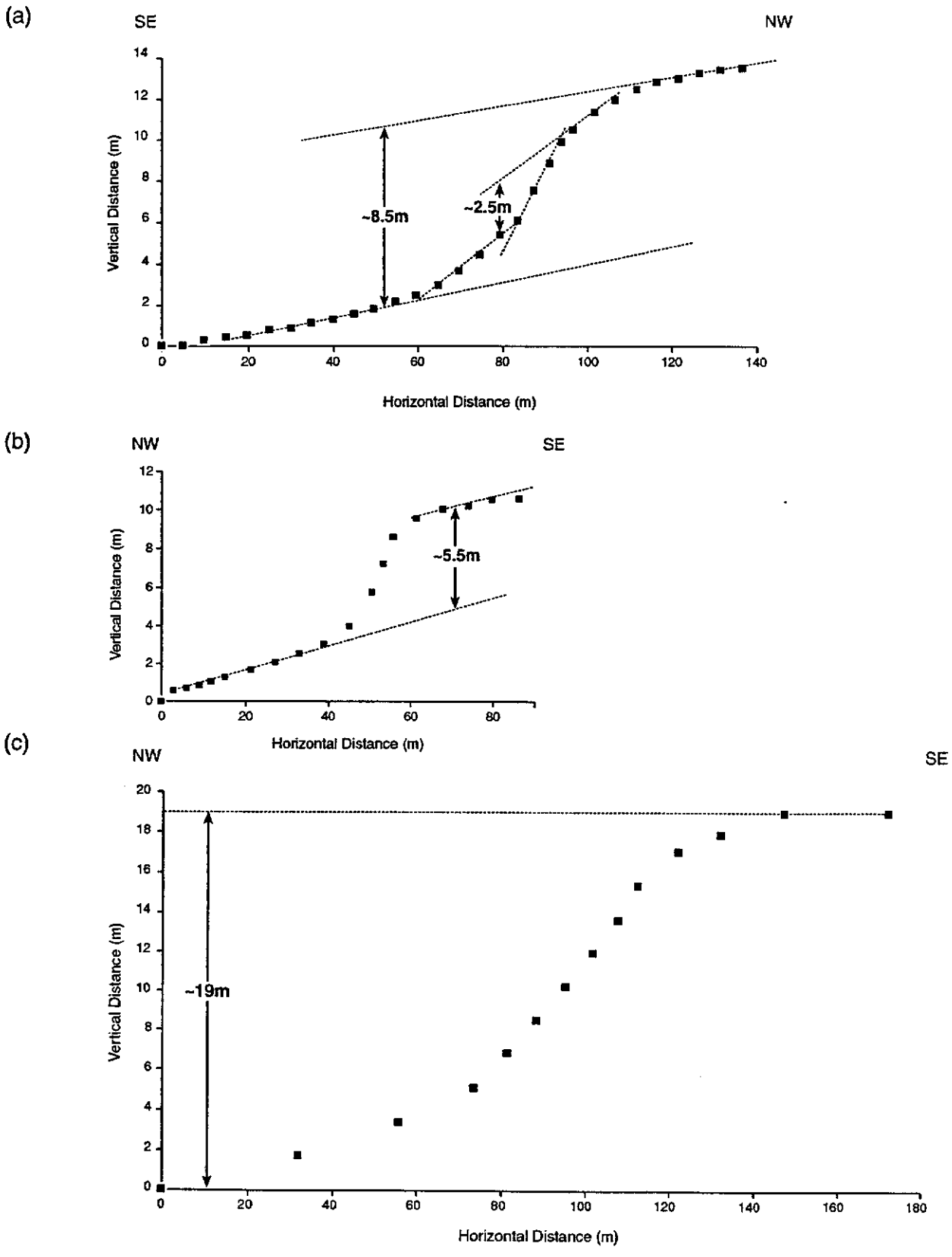


Stratigraphic units and structure from Dethier and Manley (1985)

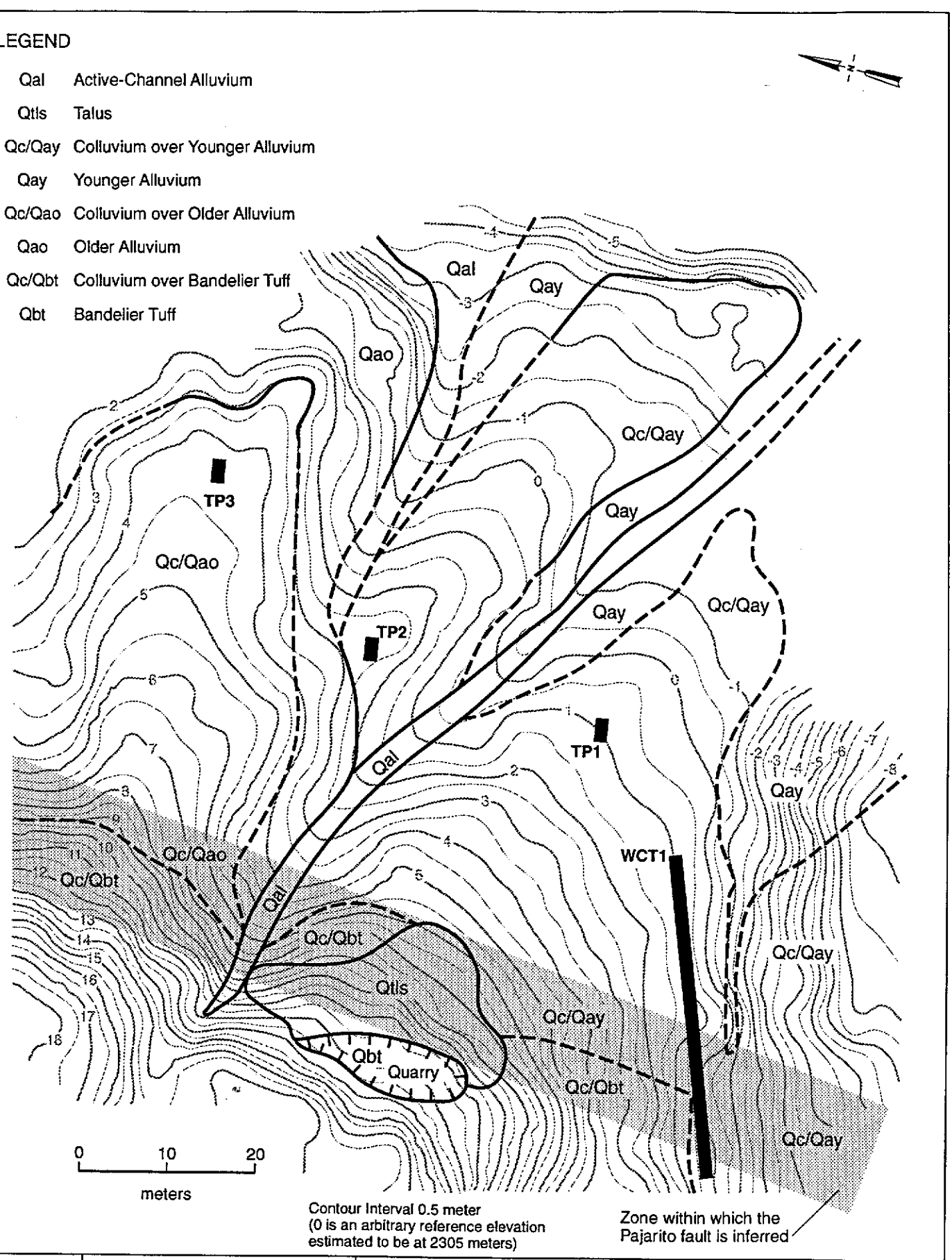
Project No. 91C0509	Los Alamos Seismic Hazards	SIMPLIFIED GEOLOGIC MAP OF THE UNNAMED MESA WEST OF HERNANDEZ	Figure 4-5
Woodward-Clyde Federal Services			



Project No. 91C0509	Los Alamos Seismic Hazards	FAULT MAP OF THE ARROYO HONDA AREA	Figure 4-6
Woodward-Clyde Federal Services			

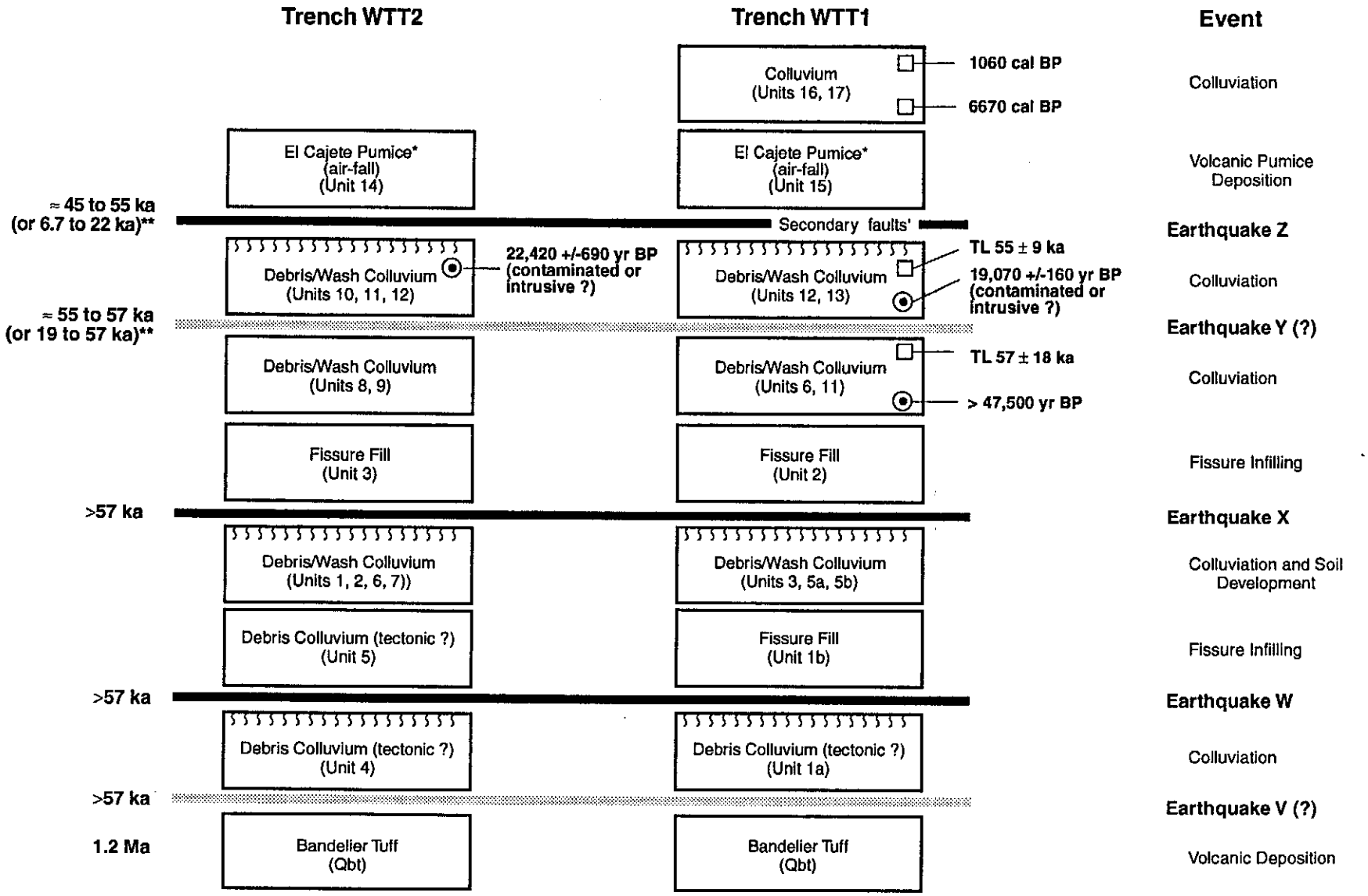


Project No. 91C0509	Los Alamos Seismic Hazards	TOPOGRAPHIC PROFILES OF SCARPS ALONG FAULTS ON BLACK MESA	Figure 4-7
Woodward-Clyde Federal Services			



Project No. 91C0509	Los Alamos Seismic Hazards	GEOLOGIC MAP OF THE WATER CANYON SITE SHOWING TRENCH AND SOIL PIT LOCATIONS	Figure 4-8
Woodward-Clyde Federal Services			

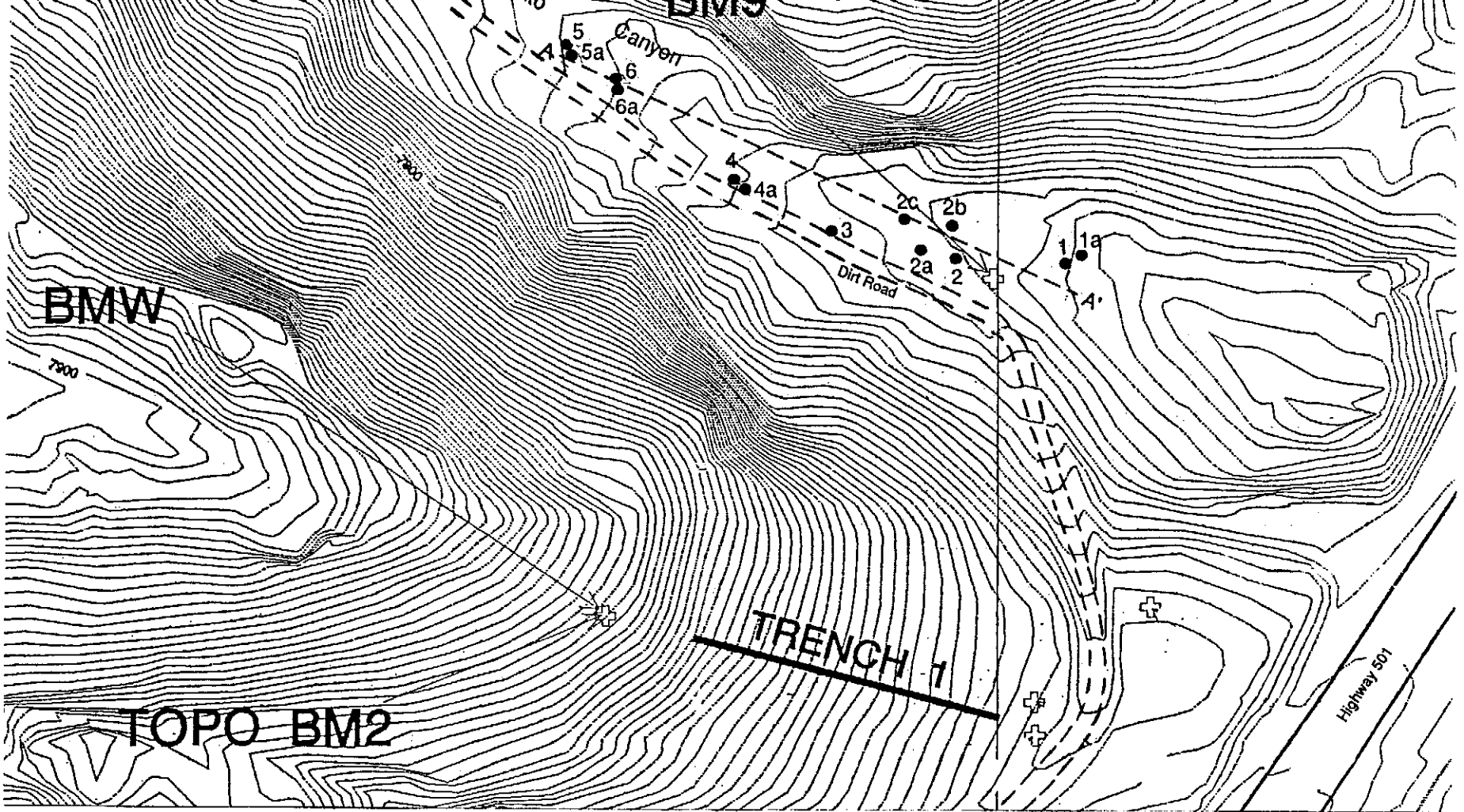
C0509A-1300/011795/jun



* Erupted between 45 and 73 ka
** See text for discussion of uncertainty

Project No. 91C0509	Los Alamos Seismic Hazards	SEQUENCE OF DEPOSITIONAL AND FAULTING EVENTS INFERRED FROM THE WATER TANKS TRENCHES	Figure 4-9
Woodward-Clyde Federal Services			

SK9423-A9500/021795/gos



- 5a — Drill hole
- A - - - - A' — Line of cross section in Figure 4-8
- BM9 — Bench mark

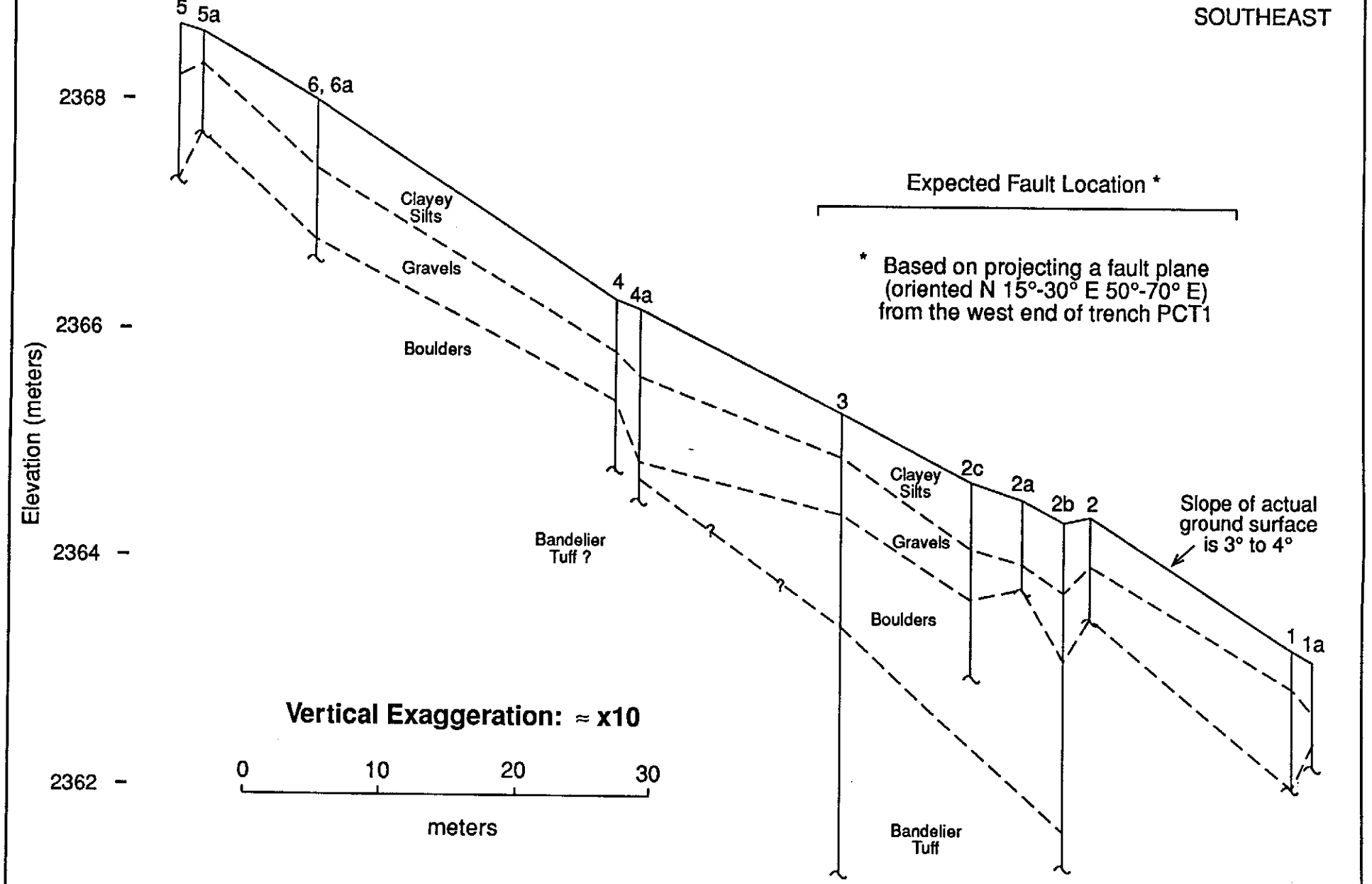
Contour interval - 2 feet

Base map from FIMAD - LANL

0 30
meters

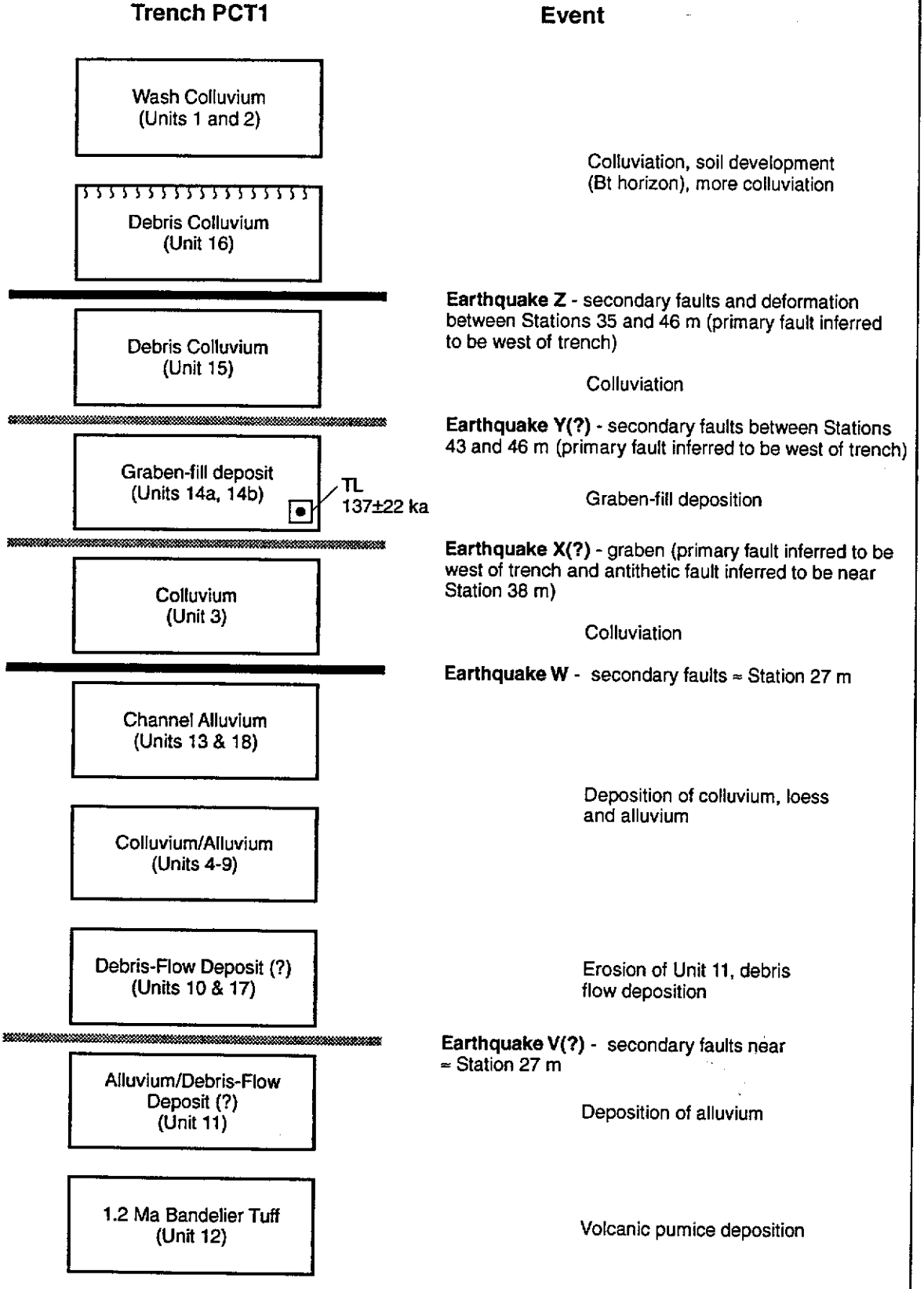
N

Project No. 91C0509	Los Alamos Seismic Hazards	LOCATION OF SHALLOW DRILL HOLES IN PAJARITO CANYON	Figure 4-10
Woodward-Clyde Federal Services			



Drill hole locations shown on Figure 4-7

Project No. 91C0509	Los Alamos Seismic Hazards	CROSS-SECTION FOR DRILL HOLES IN PAJARITO CANYON	Figure 4-11
Woodward-Clyde Federal Services			



Project No. 91C0509	Los Alamos Seismic Hazards	SEQUENCE OF DEPOSITIONAL AND FAULTING EVENTS INFERRED FROM THE PAJARITO CANYON TRENCH	Figure 4-12
Woodward-Clyde Federal Services			

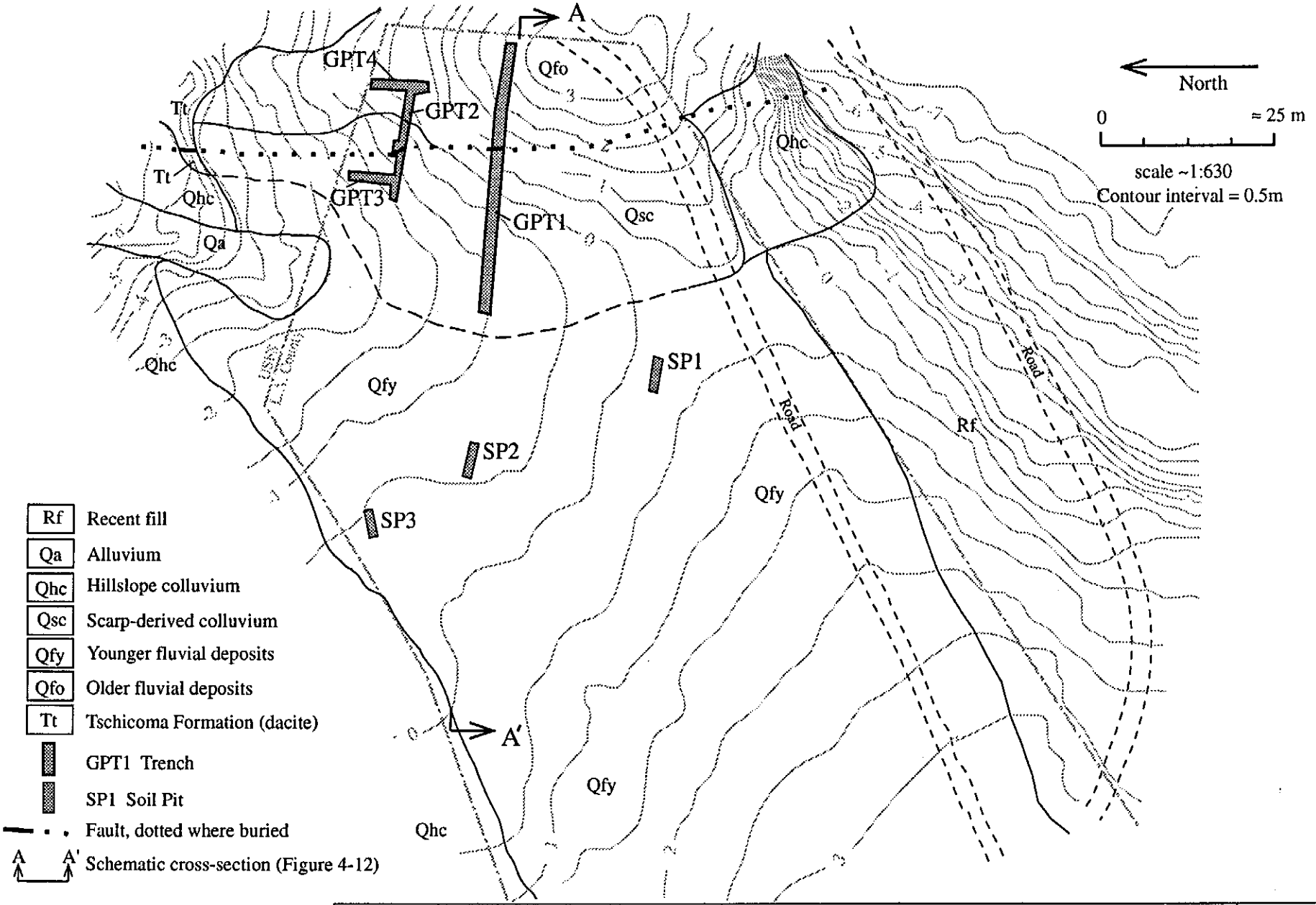
SK9423-A9500/020995/jun



Rendija Canyon Fault

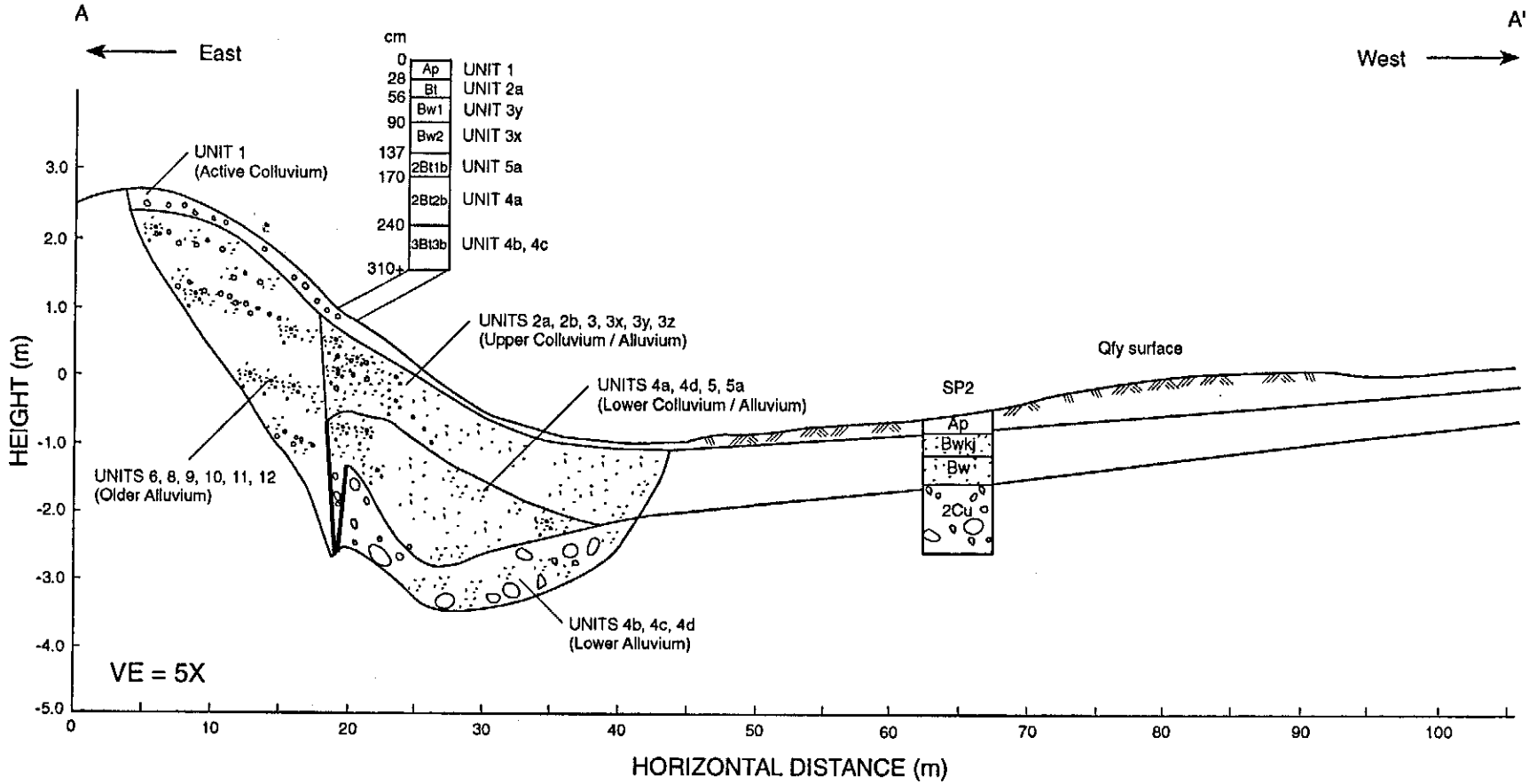
View to the South-Southeast

Project No. 91C0509	Los Alamos Seismic Hazards	OBLIQUE AERIAL PHOTOGRAPH OF THE GUAJE PINES SITE	Figure 4-13
Woodward-Clyde Federal Services			



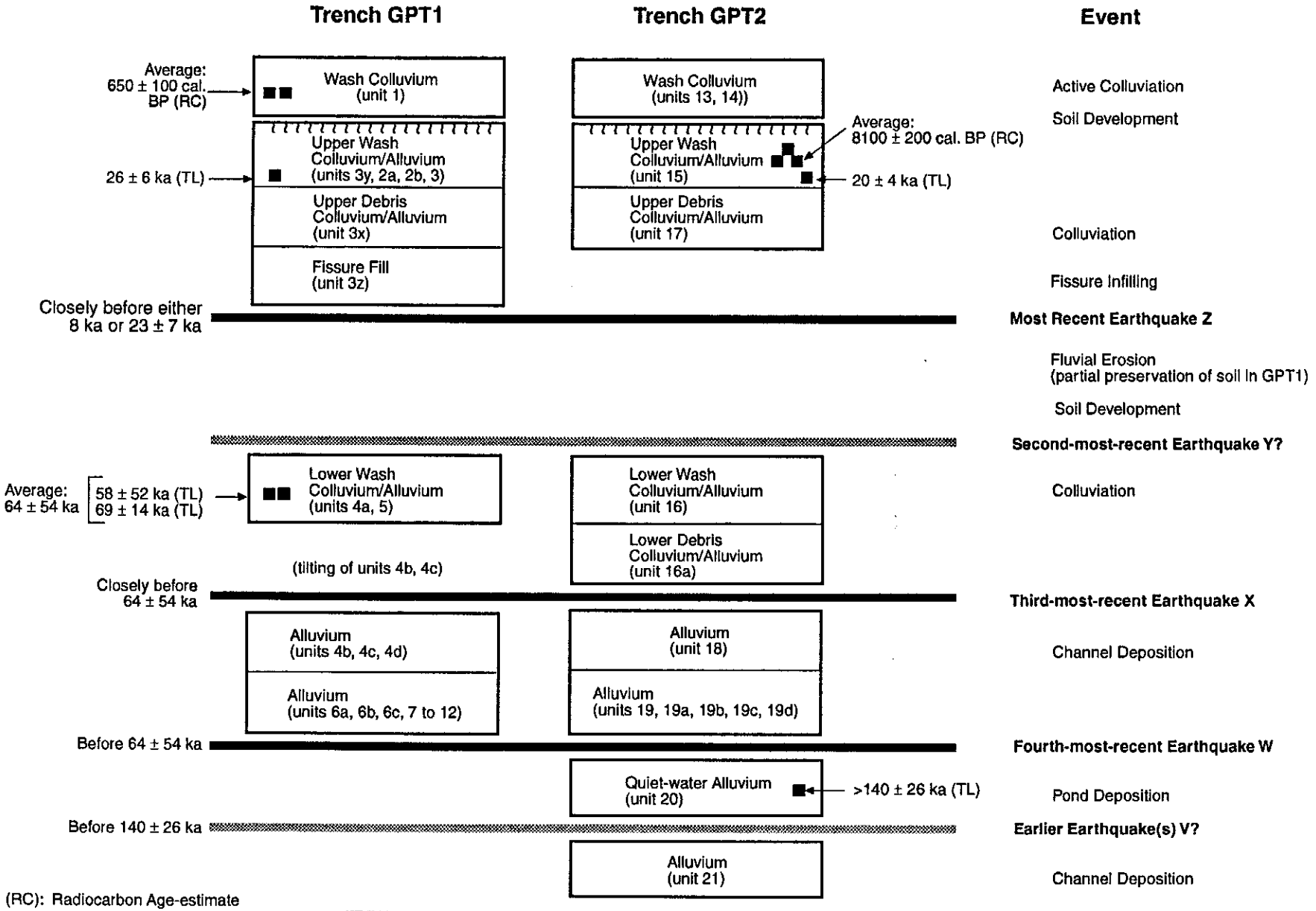
Project No. 91C0509	Los Alamos Seismic Hazards	SURFICIAL GEOLOGIC MAP OF THE GUAJE PINES SITE ON THE RENDIJA CANYON FAULT	Figure 4-14
Woodward-Clyde Federal Services			

91C0509A-1300/121494



Project No. 91C0509	Los Alamos Seismic Hazards	SCHEMATIC CROSS SECTION A-A' AT THE GUAJE PINES SITE	Figure 4-15
Woodward-Clyde Federal Services			

91C0509A-1300/010695

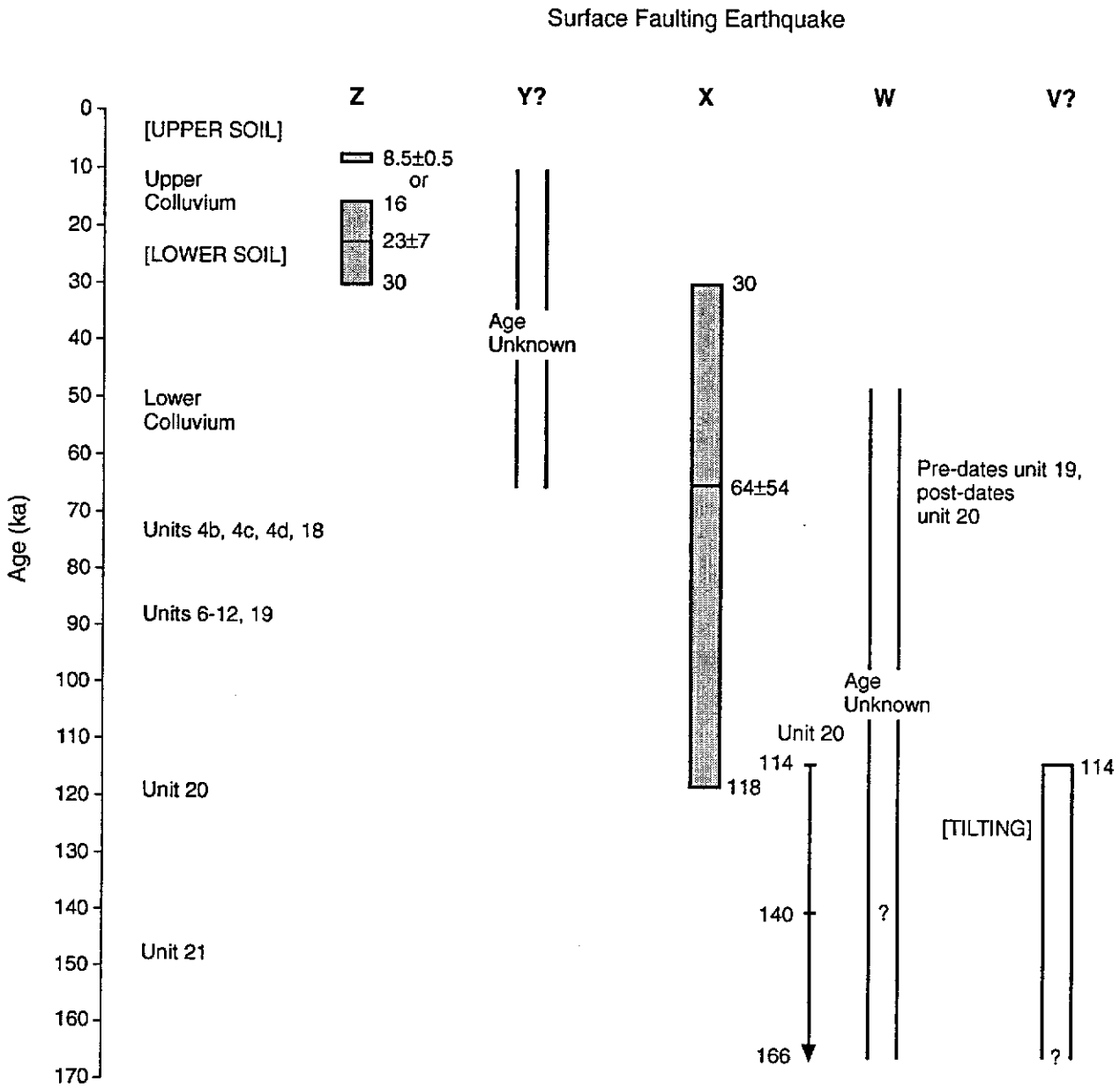


(RC): Radiocarbon Age-estimate

(TL): Thermoluminescence Age-estimate

Project No. 91C0509	Los Alamos Seismic Hazards	SEQUENCE OF DEPOSITIONAL AND FAULTING EVENTS ON THE RENDIJA CANYON FAULT AT THE GUAJE PINES SITE	Figure 4-16
Woodward-Clyde Federal Services			

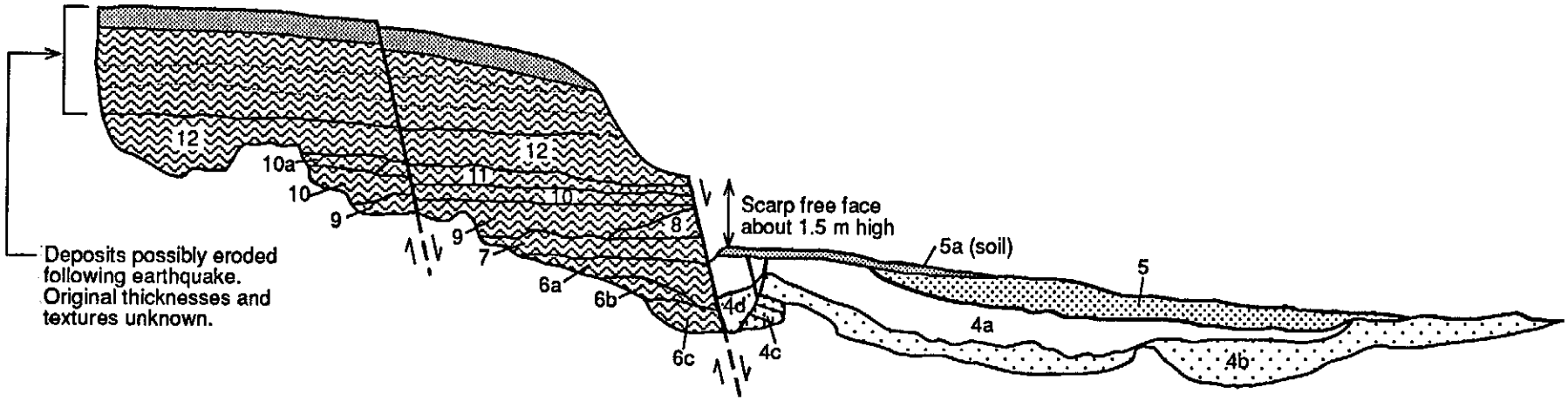
SK9423-A9500/020995/jun



Project No. 91C0509	Los Alamos Seismic Hazards	INFERRED TIMING OF SURFACE-FAULTING EARTHQUAKES, RENDIJA CANYON FAULT AT GUAJE PINES SITE	Figure 4-17
Woodward-Clyde Federal Services			

SK9423-9500/011295/gos

West



Unit Descriptions

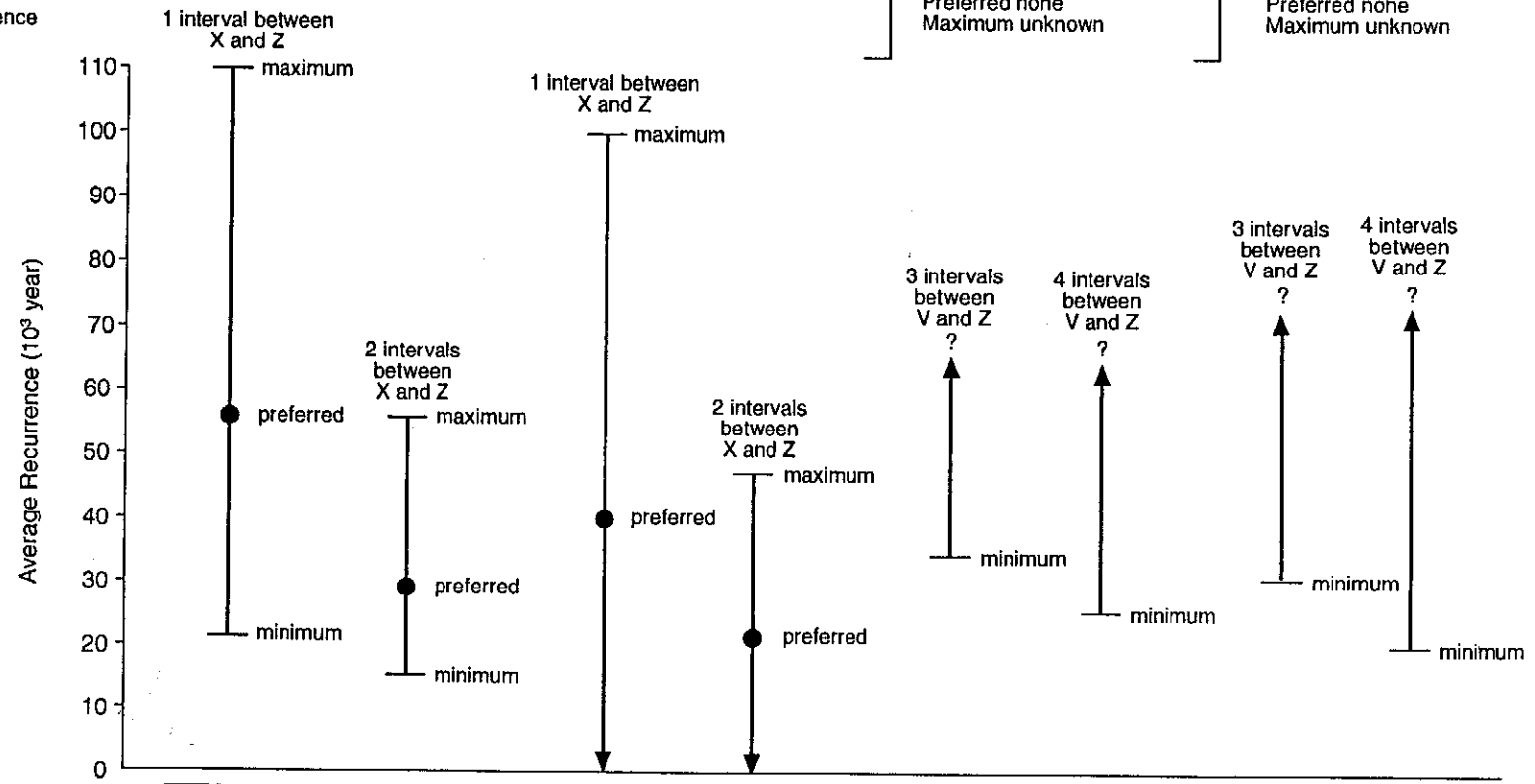
4a	Colluvium / alluvium	7	Alluvium
4b	Alluvium	8	Alluvium
4c	Alluvium	9	Alluvium
4d	Colluvium	10	Alluvium
5	Alluvium	10a	Alluvium
5a	Btb soil horizon	11	Alluvium
6a	Alluvium	12	Alluvium
6b	Alluvium		
6c	Alluvium		

0 1 2 3 4
meters

No vertical exaggeration

Project No. 91C0509	Los Alamos Seismic Hazards	PALINSPASTIC RECONSTRUCTION OF TRENCH GPT1 TO TIME IMMEDIATELY FOLLOWING THE MOST RECENT EARTHQUAKE	Figure 4-18
Woodward-Clyde Federal Services			

EARTHQUAKE	PREFERRED AGE (age range)	INTERVAL BETWEEN X AND Z		INTERVAL BETWEEN V AND Z	
		Assume 8 ka for upper colluvium	Assume 23 ka for upper colluvium	Assume 8 ka for upper colluvium	Assume 23 ka for upper colluvium
Z	8.5 ka (8 to 9 ka) or 23 ka (16 to 30 ka)	1 INTERVAL Minimum 21,000 years Preferred 55,500 years Maximum 110,000 years	1 INTERVAL Minimum none Preferred 41,000 years Maximum 102,000 years	3 INTERVALS Minimum 35,000 years Preferred none Maximum unknown	3 INTERVALS Minimum 32,667 years Preferred none Maximum unknown
Y?	Age unknown	or	or	or	or
X	64 ka (30 to 118 ka)	2 INTERVALS (assumes Y occurred) Minimum 10,500 years Preferred 27,750 years Maximum 55,000 years	2 INTERVALS (assumes Y occurred) Minimum none Preferred 20,500 years Maximum 51,000 years	4 INTERVALS (assumes Y occurred) Minimum 26,250 years Preferred none Maximum unknown	4 INTERVALS (assumes Y occurred) Minimum 21,000 years Preferred none Maximum unknown
W	Age unknown				
V?	No preference (>114 ka)				



Project No. 91C0509	Los Alamos Seismic Hazards	INFERRED RECURRENCE VALUES FOR RENDIJA CANYON FAULT AT GUAJE PINES SITE	Figure 4-19
Woodward-Clyde Federal Services			

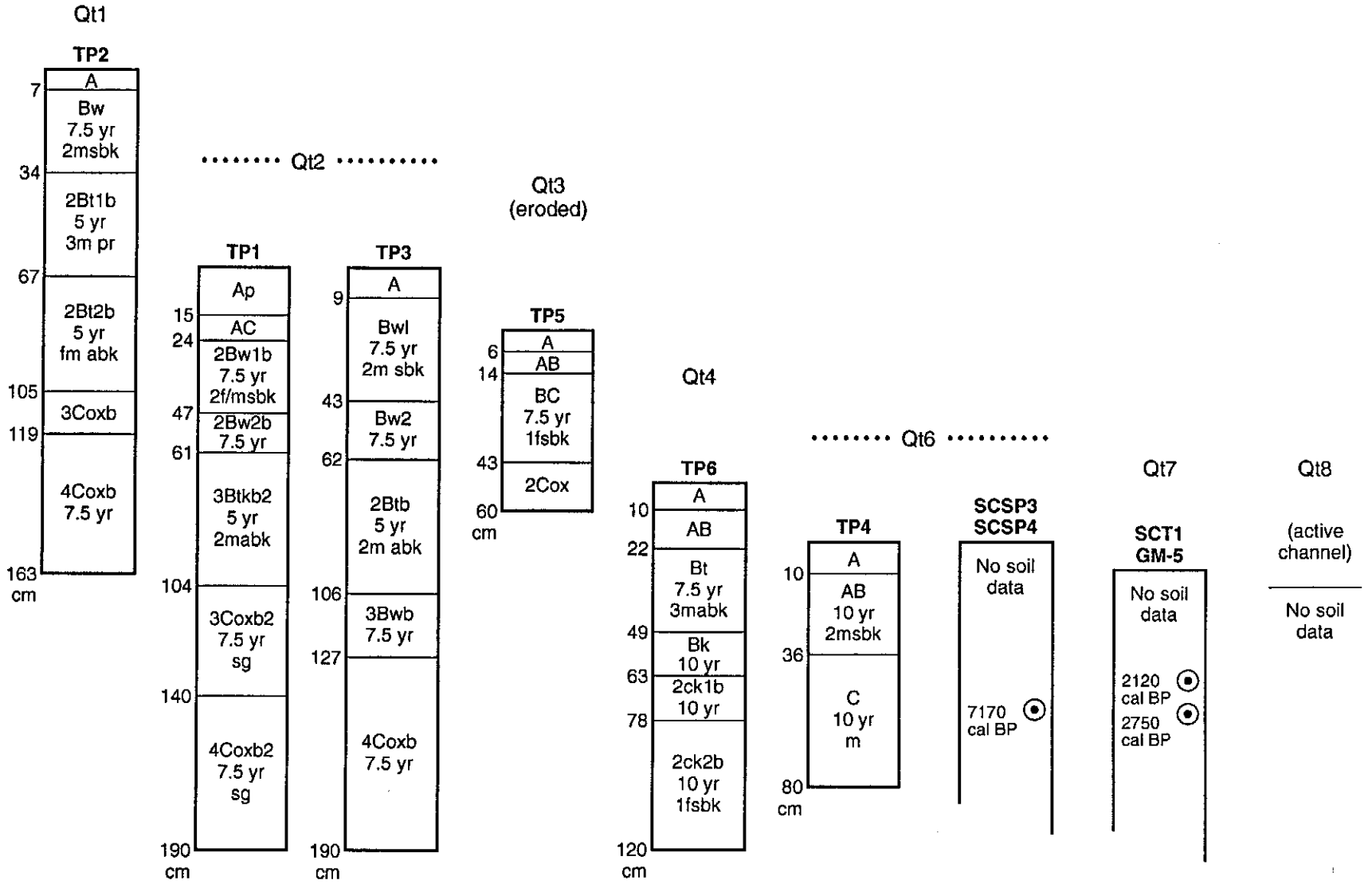
SK9423-9500/011295/gos



View to the east. Workers located at exposure of main fault strand.

Project No. 91C0509	Los Alamos Seismic Hazards	GROUND PHOTOGRAPH OF THE COUNTY LANDFILL SITE	Figure 4-20
Woodward-Clyde Federal Services			

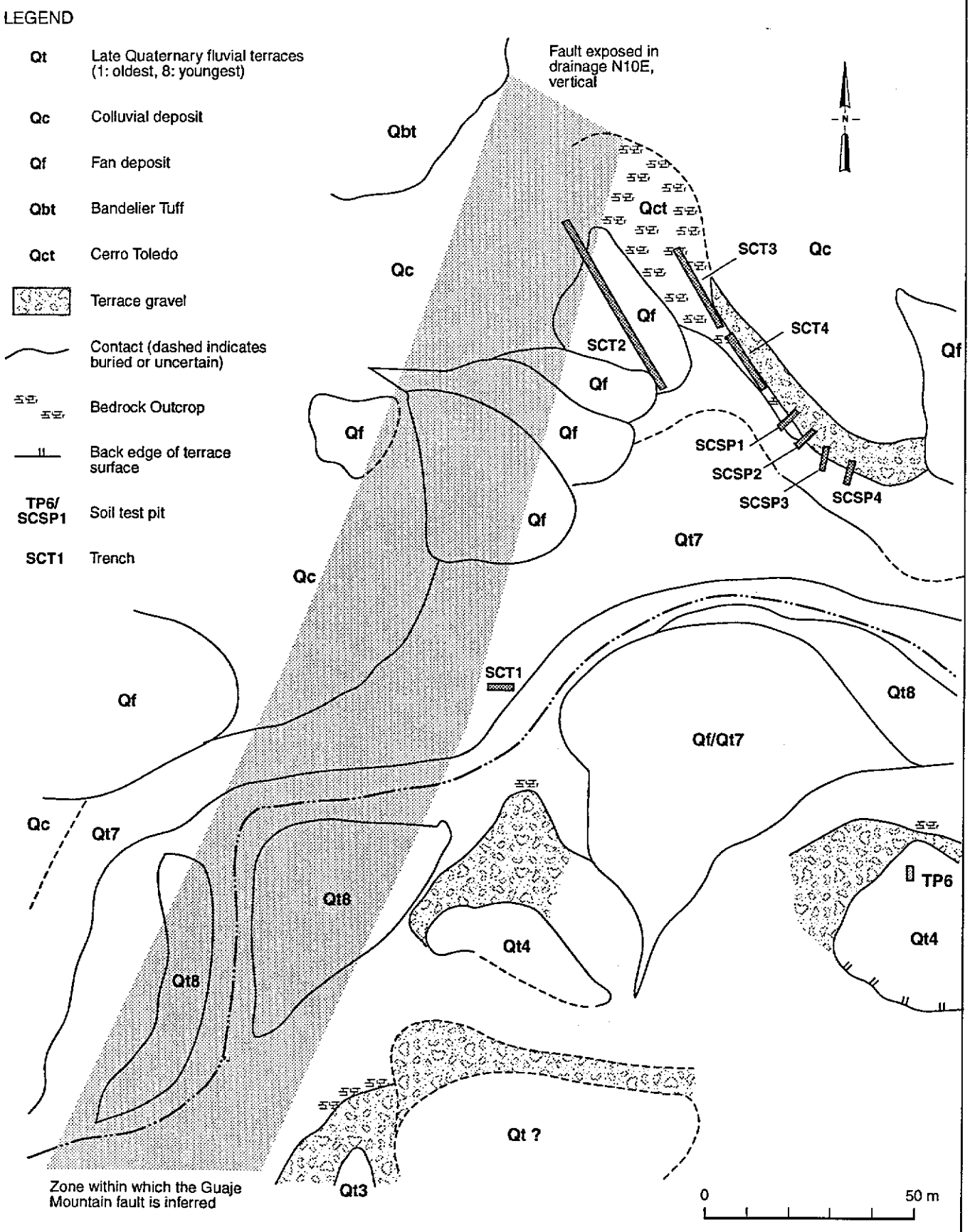
K9423-9500/120194



Note: Profiles arranged vertically to approximate vertical spacing between terraces directly downstream of Guaje Mountain fault.

Project No. 91C0509	Los Alamos Seismic Hazards	SCHEMATIC DIAGRAM SHOWING RELATIVE SOIL DEVELOPMENT ON TERRACES IN THE RENDIJA CANYON AREA	Figure 4-21
Woodward-Clyde Federal Services			

SK9423-9500/111794



Project No. 91C0509	Los Alamos Seismic Hazards	SURFICIAL GEOLOGIC MAP OF THE SPORTSMEN'S CLUB SITE	Figure 4-22
Woodward-Clyde Federal Services			

C0509A-1300/010695

5.0 EVALUATION OF THE LOS ALAMOS SEISMOGRAPHIC NETWORK DATA

Seismic monitoring can provide data that will allow for the spatial, temporal, and source characterization of recorded seismicity, the possible association with geologic structures (hence, the possible identification and characterization of active faults), and an evaluation of the styles of deformation and tectonic stresses. This information provides the basic data for any seismic hazards evaluation. The following describes efforts to reevaluate the seismicity recorded by the LASN since its installation in 1973.

5.1 EVALUATION OF NETWORK DATA

The LASN operated continuously from 1973 to 1984. During this 11-year period, earthquake locations from the LASN were routinely determined and published (Section 3). These data are summarized in House and Cash (1988). However, throughout the operational period, several different location procedures, velocity structures, and analysts were used, resulting in a data set of non-uniform quality. Accurate locations of earthquakes are necessary in order to determine whether certain structures and faults are active and whose last movement is not well-constrained from geologic data.

P-wave first motions also were not routinely picked and thus, in general, no focal mechanisms had been determined from this data set (L. House, LANL, written communication, 1992). Only a few earthquake focal mechanisms have been determined to date for northern New Mexico (Herrmann et al., 1980; Sanford et al., 1979; Wong et al., 1984).

House and Cash (1988) suggested that the accuracy of earthquakes previously located by LASN were on the order of ± 5 km, but of variable quality. However, House (LANL, written communication, 1992) noted that the 1978-1979 Albuquerque Volcanoes swarm, which occurred southwest of Los Alamos, was systematically mislocated by LASN on the order of 8 km to the north of the more accurately determined locations of Jaksha et al. (1981) which incorporated data from stations very close to the source region. House (LANL, written communication, 1992) systematically repicked both P- and S-wave arrival times and P-wave

first motions for earthquakes within a chosen study area between 35.2° to 36.6° N. latitude and 105.4° to 107.2° W. longitude, a 160 x 160 km square centered on LANL. This was done in order to improve the accuracy of the earthquake locations, determine new focal mechanisms and produce a more uniform data set.

To obtain accurate locations, only earthquakes with 10 or more arrival times (P and S waves) used in the original locations were repicked (L. House, LANL, written communication, 1992). This threshold was reduced to eight or more arrival times used in the original locations for earthquakes recorded between 1984 and 1989 due to a decrease in number of operating seismographic stations. Earthquakes between October 1989 and September 1990 had not been previously analyzed and so were located for the first time in his study. Events after September 1990 have not been analyzed. In addition, the earthquake coda durations were measured to determine more uniform magnitudes using the magnitude-coda duration relationship developed by Newton et al. (1976). P-wave first motions also were weighted according to how impulsive the first arrival was. From September 1973 to March 1982, earthquake waveforms were recorded on 16-mm develocorder film, and the repicks from these records resulted in a precision of 0.05 sec. Between 1982 to date, the waveform data was recorded digitally with reading pick errors ranging from 0.01 to 0.02 sec depending on the exact digital sampling rate used. In some cases, only heliocorder (paper) records were available for certain earthquakes and arrival times on these could only be read to the nearest 0.1 sec.

In order to reliably locate earthquakes in the chosen study region, a region-specific velocity model is required. Several authors have previously studied the velocity structure in northern and central New Mexico (Roller, 1965; Toppozada and Sanford, 1976; Keller et al., 1979; Olsen et al., 1979; Murdock and Jaksha, 1981; Davis et al., 1984; Ankeny et al., 1986; Spence and Gross, 1990; Roberts et al., 1991); however, these studies usually have low raypath density or have been determined for small areas not necessarily relevant to the LANL region.

House (LANL, written communication, 1992) used a simultaneous location-velocity model inversion to determine an appropriate region-specific velocity model. Only earthquakes with eight or more arrival times from six or more stations, an azimuthal gap less than 270°, minimum source-to-station distance (DMIN) of less than 25 km, and standard errors in

epicentral location and depth of less than 5 km and 7.5 km respectively, were used in the inversion. This was done to prevent a bias in the number of raypaths used from one small portion of the study region. A high density of raypaths using 104 earthquakes was obtained across the central portion of the study region. Several inversions were performed before the resulting velocity model shown in Table 5-1 was obtained. A 40-km thick crust overlying an upper-mantle half-space of velocity 8.0 km/sec was used as a starting model, and the velocity of the upper layer was allowed to vary. The resulting upper-layer velocity was 5.90 km/sec. Station corrections were not incorporated, and the resulting average root mean square (rms) error was 0.48 sec. A similar inversion incorporating station corrections resulted in an upper-layer velocity of 5.96 km/sec, and the average rms dropped to 0.31 sec. Station corrections provide a way to account for the differences in the actual velocity structure of the earth from the plane layer velocity model used in the location program. A final four layer over a half-space velocity model was input into the inversion in which the layers were fixed at 10 km depth intervals and the velocities within each layer allowed to vary. The average rms error was reduced to 0.29 sec. This velocity model (Table 5-1) appears to best fit the arrival times and so was chosen for the relocation analyses.

All earthquakes whose arrival times were reread in the study region were relocated using the velocity model and station corrections obtained in the simultaneous location-velocity model inversion. To evaluate the accuracy of the relocations, the locations of the Albuquerque Volcanoes swarm (Section 3.2.9) was compared to the locations of Jaksha et al. (1981). The center of the relocated swarm locates within 2 km of that determined by Jaksha et al. (1981). This suggests a notable improvement in location accuracy considering that the swarm locates towards one corner of the study region. House (LANL, written communication, 1992) believes that the relocations have an improved accuracy with errors in epicenter and focal depth averaging $\pm$ 2 km and $\pm$ 5 km, respectively, within the network.

In this study, we relocated 632 earthquakes employing the computer location program HYPOELLIPSE (Lahr, 1984) using House's repicked arrival times, velocity model and station delays. The average rms error for a randomly selected set of 100 earthquakes from our relocations was 0.15 sec compared to 0.18 sec for the same events relocated by House. The difference between the two relocation sets being a function of location program and solution refinement. We prefer our relocations because of the slightly lower rms errors. Most of the

locations did not change significantly with the exception of those events located towards the edges of the LANL region. These events had unstable solutions in both relocation schemes.

The earthquakes were screened for location quality, and those events which met the following criteria were used in the following spatial analysis: azimuthal gap $\leq 270°$, rms error ≤ 0.25 sec, number of arrivals ≥ 5. The 457 earthquakes that met these criteria are shown on Plate 12 and listed in Appendix I. North-south and east-west cross-sections of this data set are shown in Figures 5-1 and 5-2. To the left of each cross-section is its location within the LANL region. Focal depths are fairly well-constrained when a station occurs within a distance of about 1.5 times the focal depth of the event. To better characterize the depth distribution, we further discarded events with DMIN $\geq$ 1.5 focal depths. The depth distributions of the remaining earthquakes for the whole study region and the Rio Grande rift, respectively, are shown in Figures 5-3 and 5-4, respectively. Very few earthquakes met all the criteria necessary to be considered as well-located; only 63 for the whole study region and 35 within the Rio Grande rift. A larger, more dense seismographic network will be necessary in the future to better characterize the spatial aspects of contemporary crustal seismicity in the northern Rio Grande rift.

Station polarities were reexamined by House (LANL, written communication, 1992) in an effort to determine reliable focal mechanisms. Station polarities are often changed during network maintenance. Polarities are reliably known for the period 1973 to 1977. House (LANL, written communication, 1992) utilized teleseismic earthquakes for the period from 1977 to 1990 as recorded by the NEIC and the International Seismological Center (ISC) to verify polarities on the LASN network. Heliocorder polarities could not be reliably determined and so were excluded from the focal mechanism determinations.

Using the P-wave first motions, House (LANL, written communication, 1992) determined focal mechanisms of 72 earthquakes which each had at least eight first motions, using the computer program FPFIT (Reasenberg and Oppenheimer, 1985). We have examined these mechanisms and judge only 12 of them to be well-determined, with a sufficient number of first motions and adequate focal sphere coverage; these are shown in Figure 5-5.

5.2 CONTEMPORARY SEISMICITY AND TECTONIC STRESSES

Examination of the seismicity relocated in this study, which ranged up to M_L 2.9, shows that earthquakes generally are diffusely distributed throughout the LANL region with a few concentrations of events (Plate 12). With a few exceptions, the spatial distribution of events is similar to what is commonly observed throughout the Basin and Range province, that is, seismicity occurring with no apparent spatial correlation with mapped faults or structures. This "background" seismicity probably represents low-level strain release on low-slip rate faults or short faults for which repeated ruptures are too small to manifest themselves at the earth's surface.

Although a few historical earthquakes have been located in the vicinity of the Pajarito, Guaje Mountain and Rendija Canyon faults (Plate 3), only one well-located event has been observed to date, near the intersection between the Guaje Mountain and Embudo faults (Plate 12). A few clusters of events are observed along the Puye and La Bajada faults suggesting that these two structures may be active. A tight cluster of events is located adjacent to the Jemez Sierrita fault, possibly on this fault or a north-trending structure which has been mapped directly to the south (Plate 12).

A north-trending somewhat linear zone of epicenters appears to occur north of the Embudo fault along the La Cañada del Amagre-Clara Peak fault zone. This activity has been previously suggested to be associated with the Embudo (Velarde) fault (Sanford et al., 1991). House (LANL, written communication, 1993) notes that the La Cañada del Amagre-Clara Peak fault zone locates near the western edge of an area of subsidence identified from geodetic data (Reilinger et al., 1979). Reilinger et al. (1979) discount water well extraction as a cause for this subsidence.

As observed in previous studies (e.g., Sanford et al., 1991), earthquakes cluster in the vicinity and just to the east of the Nacimiento and Gallina faults (Plate 12). Historically, seismicity appears to be concentrated on a northward, but somewhat diffuse, extension of the Gallina fault (Plate 3). Interestingly, three events seem to mimic the eastward bend of the Sangre de Cristo fault (segment 4). No other mapped faults appear to exhibit any significant seismicity to date (Plate 12).

Although not evident in the distribution of well-located earthquakes, Sanford et al. (1979, 1981, 1991) noted that portions of the Jemez lineament, particularly the Taylor volcanic field, appear to be seismically active (Plate 3). One particular area within the lineament that seems to be characterized by seismic quiescence, both in historical and contemporary times, is the Valles caldera (Plates 3 and 12). Elevated crustal temperatures due to high heat flow or stress release on surrounding fault zones may explain this quiescence (Sanford et al., 1991).

Earthquakes in the LANL region, typical of the majority of western U.S. seismicity, appear to be confined to the brittle upper crust (Wong and Chapman, 1990). Cross-sections through the LANL region suggest that most events occur at focal depths less than about 12 km (Figures 5-1 and 5-2). A few scattered earthquakes occur as deep as 20 km with an occasional event as deep as 40 km; however, these focal depths are poorly constrained. Although deep earthquakes (20-40 km+) have been observed within the Colorado Plateau, where crustal temperatures conducive to brittle failure (less than 350° $\pm$ 100°C.) extend to depths of 20 to 30 km (Wong and Humphrey, 1989; Wong et al., 1984), we believe it is highly unlikely that significant seismicity can occur beneath a depth of 17 km within the Rio Grande rift.

Within the northern rift, the few measurements available suggest that heat flow values range from a moderate 70 mW/m^2 to a high 130 mW/m^2 (Reiter et al., 1991). The highest values are observed within the Española Basin and may be associated with young volcanics. In general, Blackwell et al. (1991) characterize the rift as an area of high heat flow. Based on an average heat flow of 90 $\pm$ 10 mW/m^2 (Blackwell et al., 1991), the 350° C isotherm would occur at a depth of about 12 km within the northern Rio Grande rift (Wong and Chapman, 1990). This observation is consistent with the distribution of well-located earthquakes in the northern Rio Grande rift which exhibit a cut-off at about 12 km depth (Figures 5-1 and 5-2) and seismicity within the central and southern portions of the rift (Sanford et al., 1991). Events within the whole LANL region, which includes the rift, the adjacent Colorado Plateau transition zone and the Southern Rocky Mountains, appear to be generally confined to focal depths of less than 20 km (Figure 5-4).

The well-determined focal mechanisms for the LANL region selected from those computed by House (LANL, written communication, 1993) exhibit both normal and strike-slip faulting similar to what is often observed throughout the Basin and Range province (Figure 5-5). At

least one, sometimes both nodal planes of the focal mechanisms trend in a northerly direction (ranging from northwest to northeast) parallel to the structures of the Rio Grande rift. For example, the two focal mechanisms north of Los Alamos suggest predominantly normal faulting on the north-trending La Cañada del Amagre-Clara Peak fault zone (Plate 12 and Figure 5-5). Two of the three focal mechanisms in the earthquake cluster north of the Jemez-San Ysidro fault system possess one nodal plane that strikes to the north and dips to the east. The strike-slip focal mechanisms indicate either left-lateral strike-slip faulting on northeast-trending, steeply-dipping planes or right-lateral strike-slip faulting on northwest-trending, near-vertical planes.

A possibly significant focal mechanism is for an event located south-southeast of Los Alamos (Plate 12 and Figure 5-5). The mechanism exhibits normal faulting on north-striking planes consistent with the mapped extent of the Puye fault zone 10 km to the north. The focal mechanisms from events within the Rio Grande rift exhibit predominantly normal faulting, but those from within the Colorado Plateau transition zone appear to have a predominately strike-slip component. Strike-slip focal mechanisms also predominate within the southern Intermountain Seismic Belt (ISB) in central Utah, which marks the transition zone between the Basin and Range extensional province and the relatively stable Colorado Plateau province. The two transition zones appear similar, both having diffuse microseismicity not associated with specific faults and characterized by strike-slip faulting, but the activity rate in the transition zone in the LANL region is much lower than that of the southern ISB. The Rio Grande rift transition with the Southern Rocky Mountains does not exhibit a comparable level of elevated seismicity as that observed at the transition zone with the Colorado Plateau.

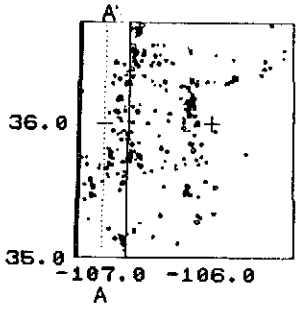
The few previously determined focal mechanisms for the northern Rio Grande rift are generally consistent with these observations (Wong and Humphrey, 1989) and are consistent with the model that the north-trending normal faults within the rift and along its boundaries are active. Focal mechanisms in the central and southern rift near Socorro (Sanford et al., 1991) are similar to those observed in the LANL region.

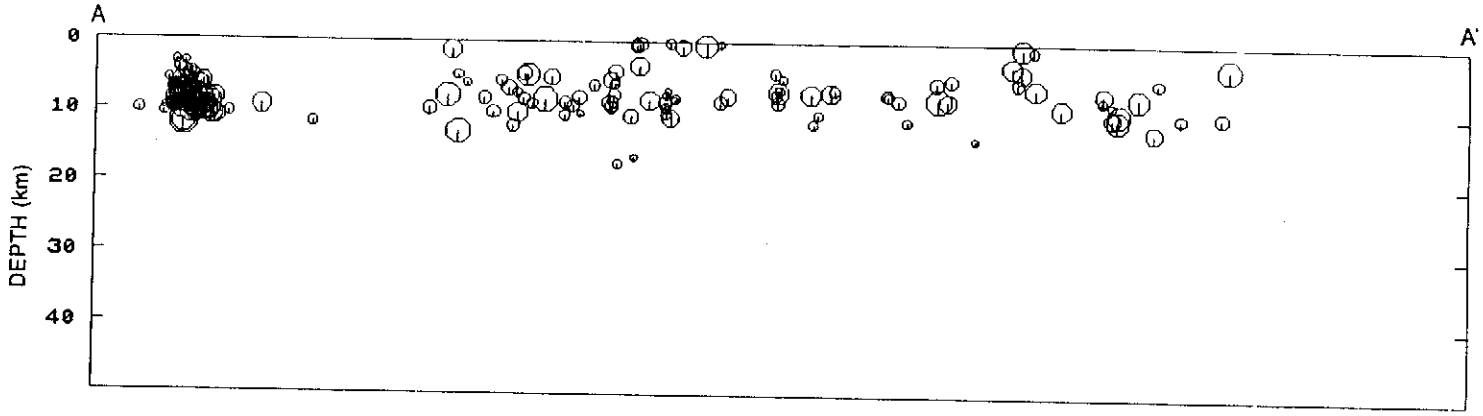
The mix of both normal and strike-slip faulting suggests a tectonic stress field which can be characterized as

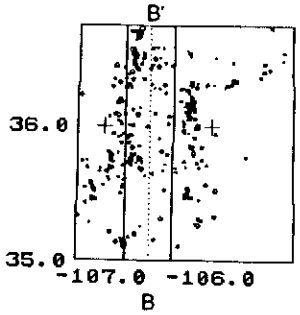
$$S_1 \approx S_2 >> S_3$$

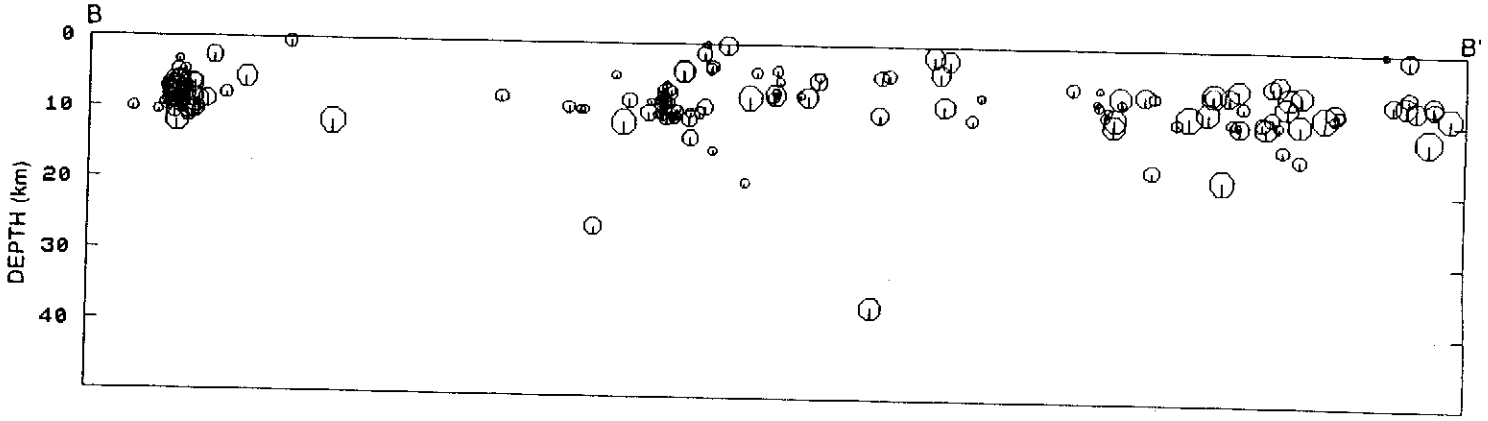
where S_1, S_2 and S_3 are the maximum, intermediate, and minimum principal stresses (Zoback and Zoback, 1989). S_1 and S_2 are nearly equivalent and either could be oriented vertically resulting in normal and strike-slip faulting, respectively.

The available focal mechanisms exhibit T-axes which are oriented in a direction consistent with the approximate east-west regional extensional stress field of the Rio Grande rift as previously characterized by Zoback and Zoback (1989). Although such a stress field is consistent with a model of active rifting, the whole of the Basin and Range province is also characterized by extensional stresses oriented similar to the minimum principal stress direction observed in the Rio Grande rift.



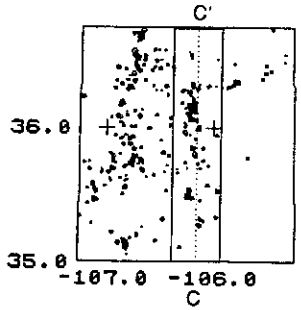


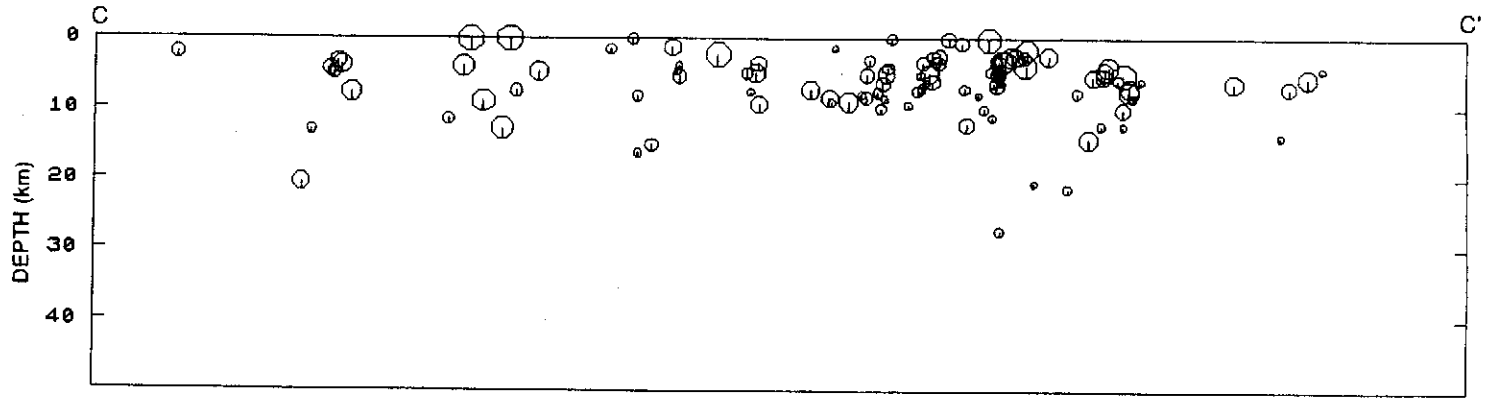


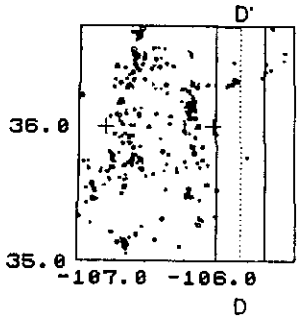


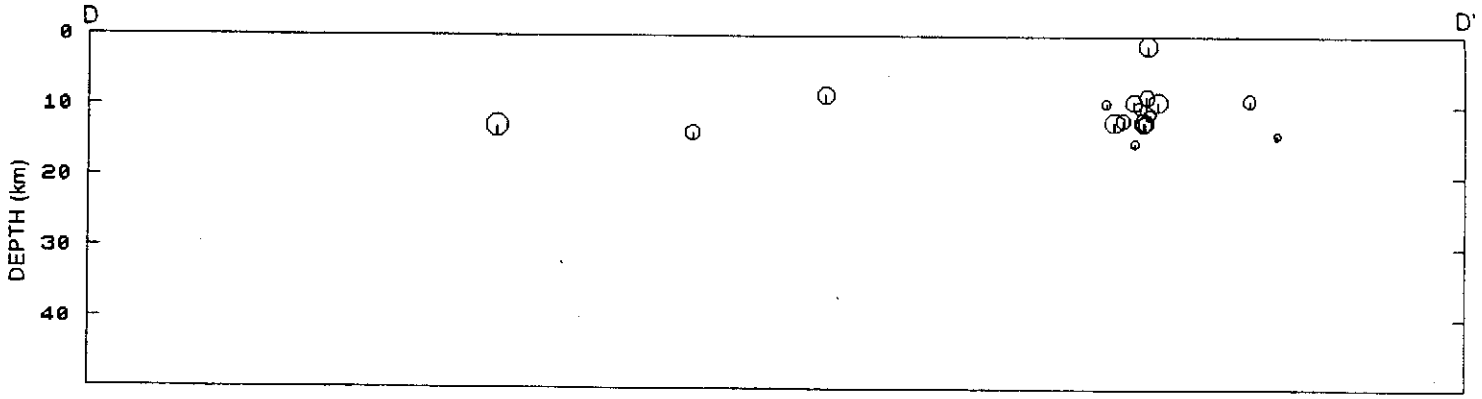
Project No. 91C0509	Los Alamos Seismic Hazards	SEISMICITY CROSS-SECTIONS NORTH-SOUTH	Figure 5-1
Woodward-Clyde Federal Services			

91C0509A-2200/052793



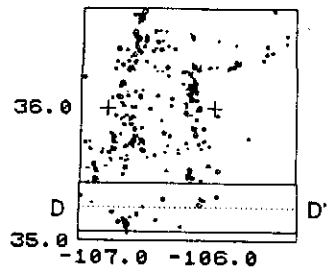


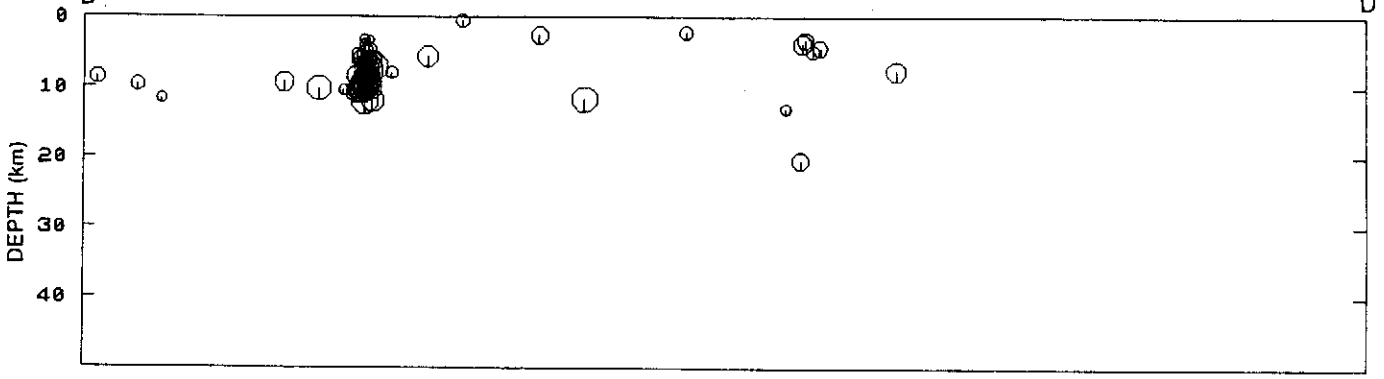


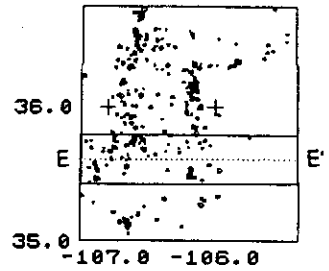


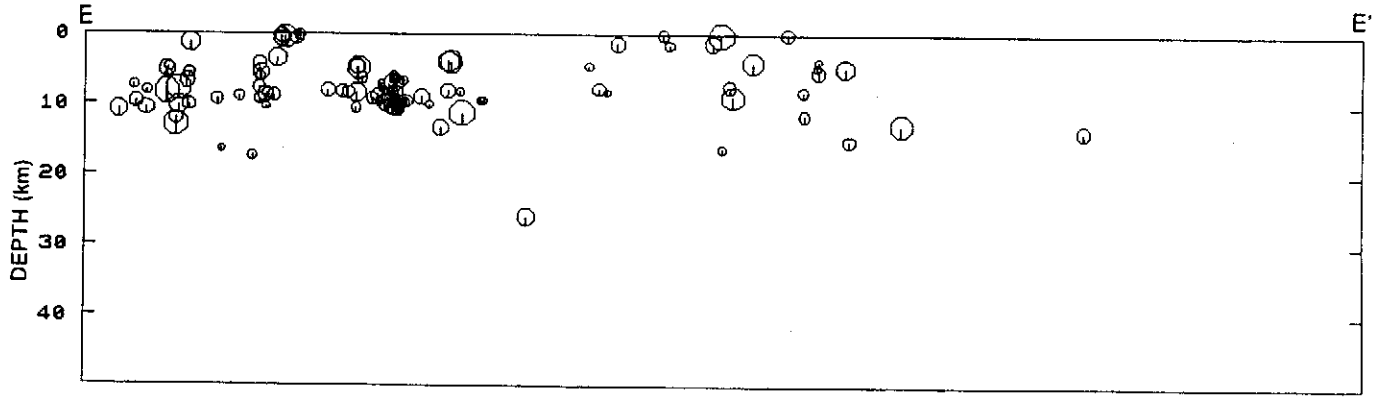
Project No. 91C0509	Los Alamos Seismic Hazards	SEISMICITY CROSS-SECTIONS NORTH-SOUTH (concluded)	Figure 5-1
Woodward-Clyde Federal Services			

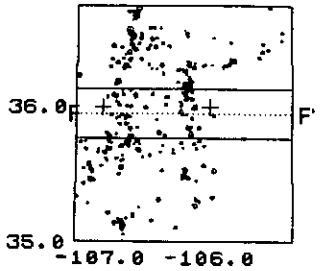
91C0509A-1300/053193

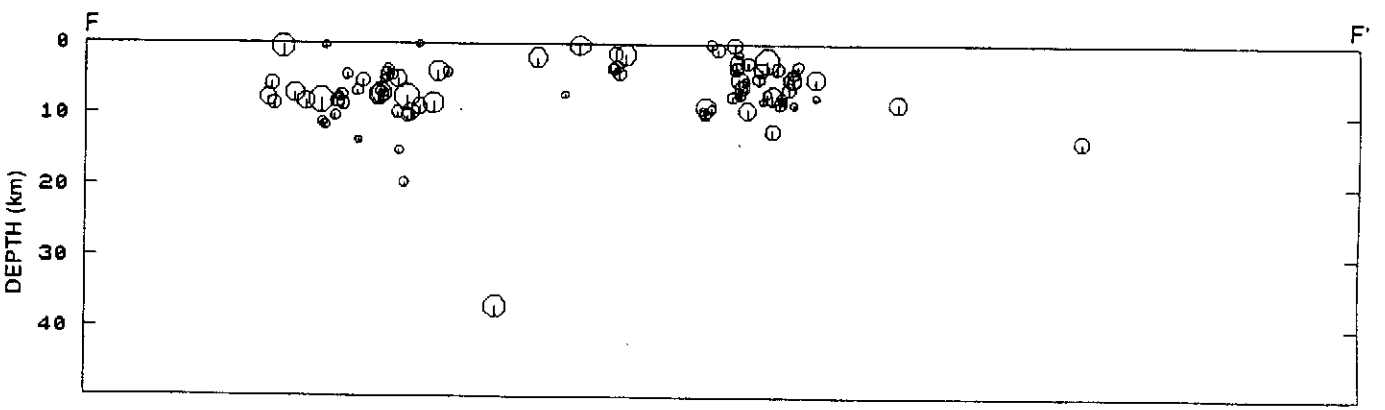






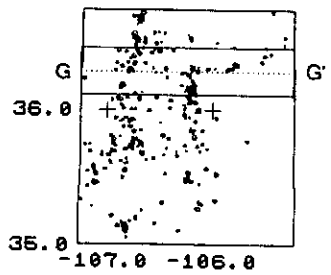


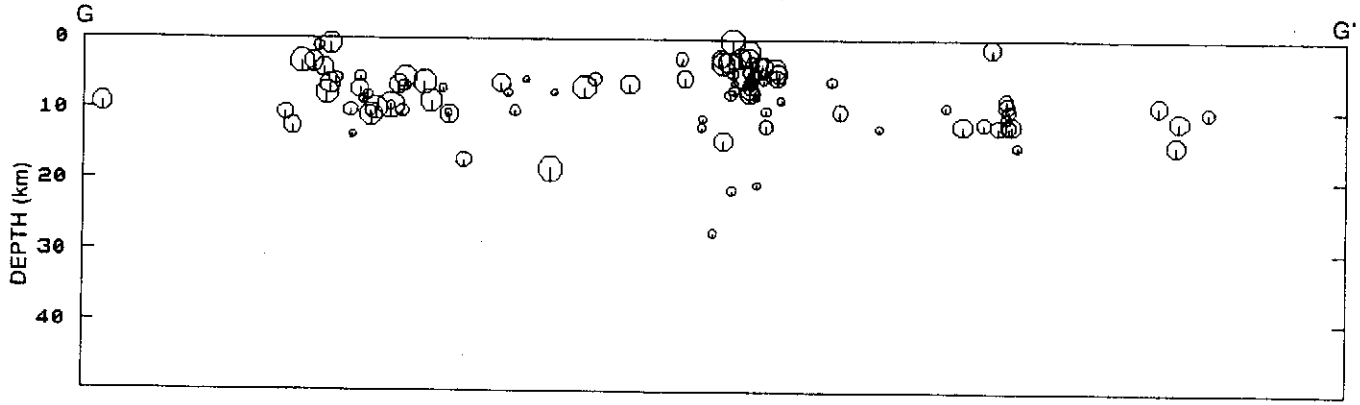


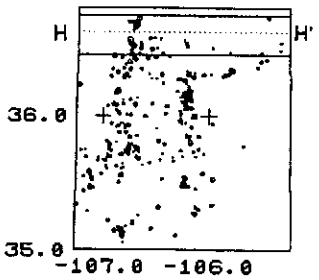


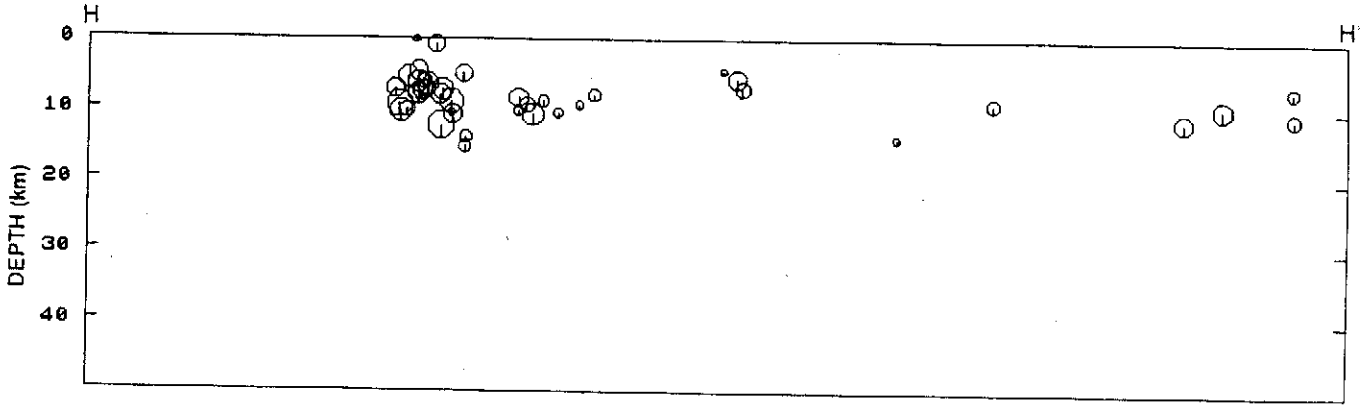
Project No. 91C0509	Los Alamos Seismic Hazards	SEISMICITY CROSS-SECTIONS EAST-WEST	Figure 5-2
Woodward-Clyde Federal Services			

91C0509A-1300/053193



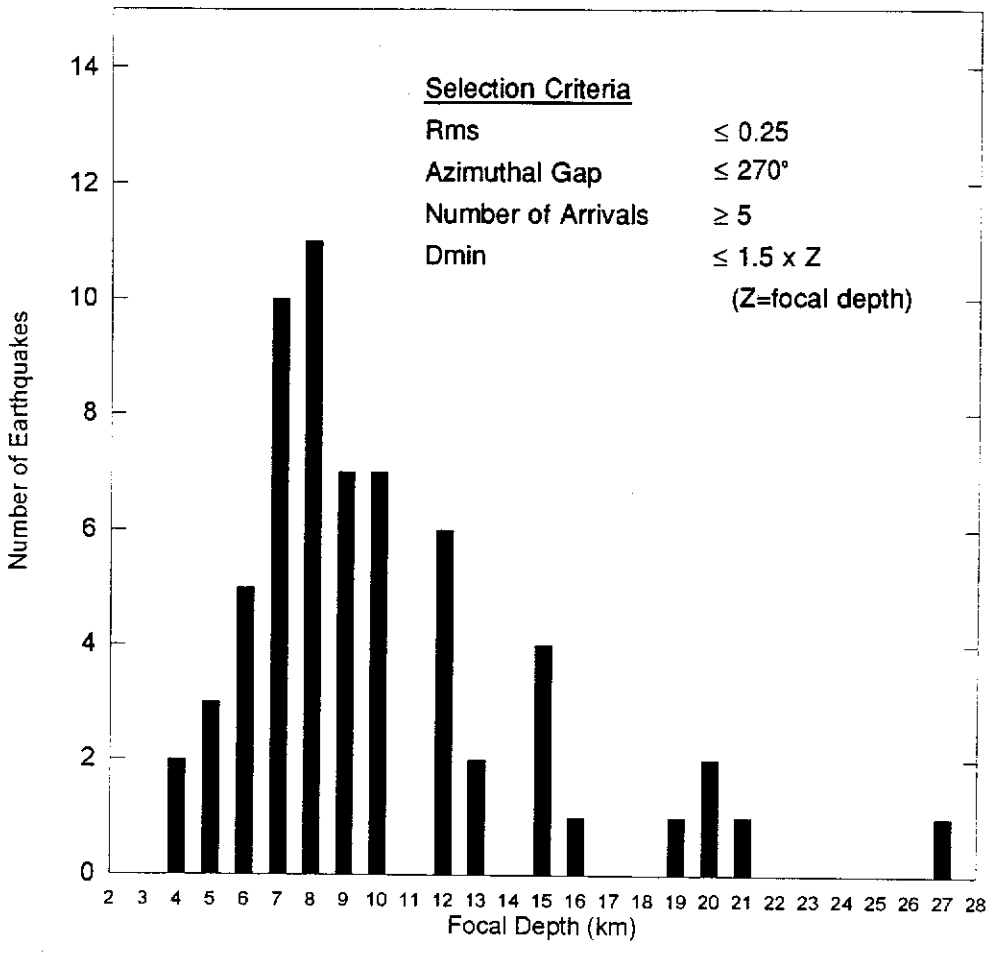




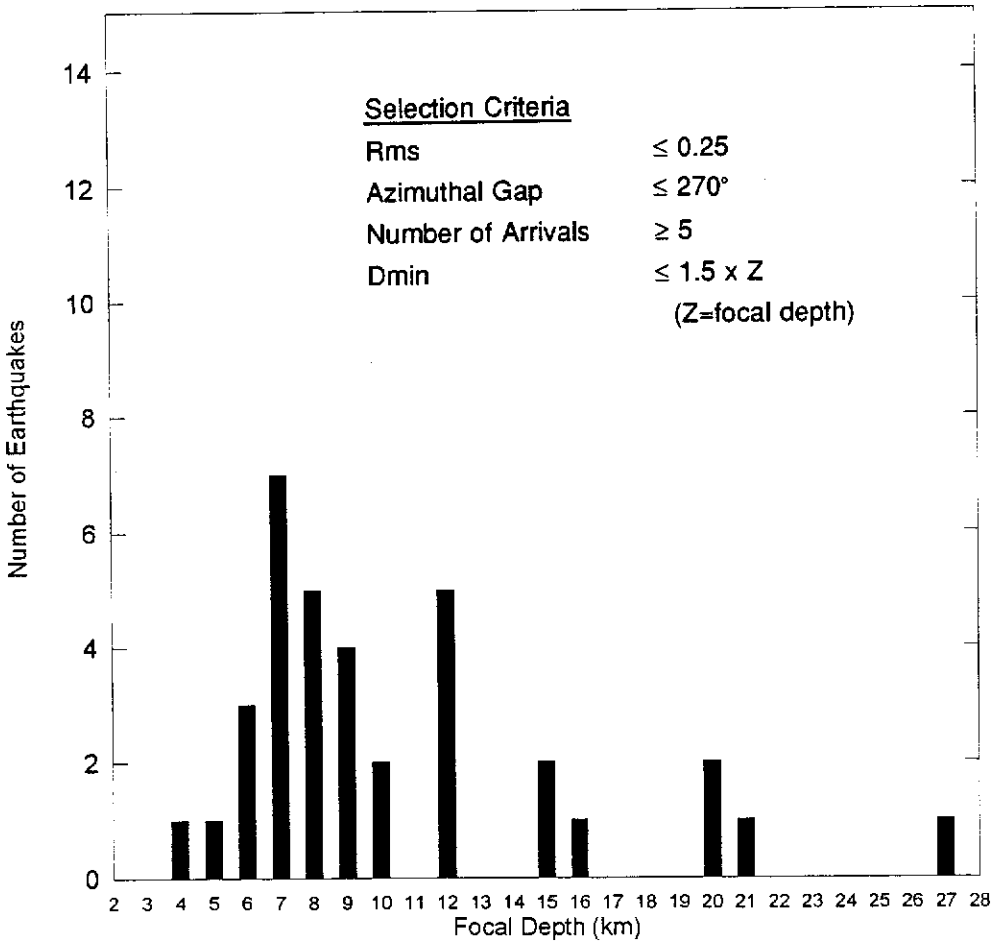


Project No. 91C0509	Los Alamos Seismic Hazards	SEISMICITY CROSS-SECTIONS EAST-WEST (concluded)	Figure 5-2
Woodward-Clyde Federal Services			

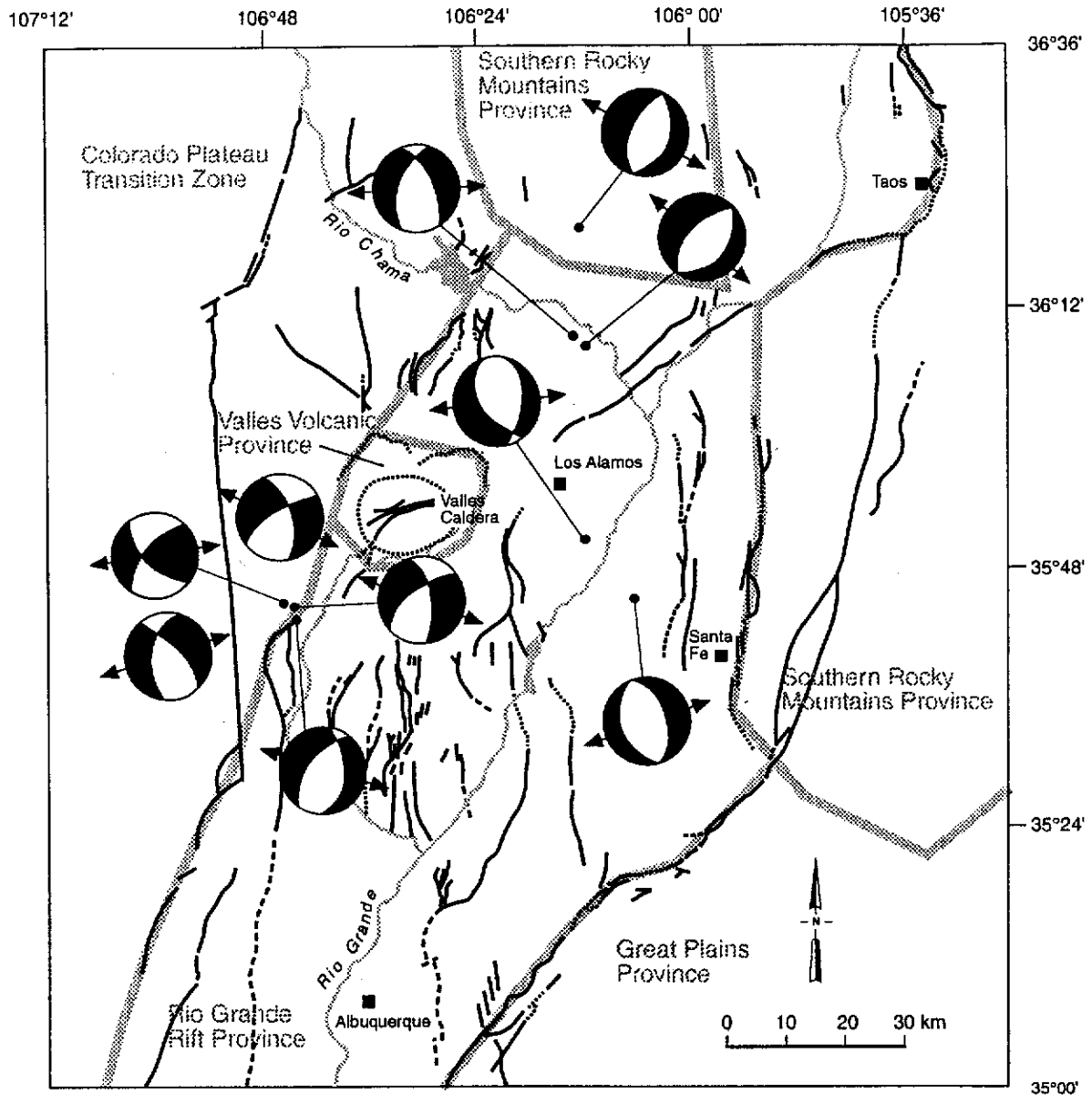
91C0509A-1300/053193



Project No. 91C0509	Los Alamos Seismic Hazards	FOCAL DEPTH DISTRIBUTION FOR WELL-LOCATED EARTHQUAKES IN THE LANL REGION	Figure 5-3
Woodward-Clyde Federal Services			



Project No. 91C0509	Los Alamos Seismic Hazards	FOCAL DEPTH DISTRIBUTION FOR WELL–LOCATED EARTHQUAKES IN THE RIO GRANDE RIFT	Figure 5-4
Woodward-Clyde Federal Services			



EXPLANATION

Normal faulting

Strike-slip faulting

Reverse faulting

Seismotectonic Province Boundary

Note: Outward arrows indicate approximate direction of the minimum principal stress.

Data from L. House, LANL

Project No. 91C0509	Los Alamos Seismic Hazards	FOCAL MECHANISMS AND FAULTS WITHIN THE LANL REGION	Figure 5-5
Woodward-Clyde Federal Services			

6.0
SITE GEOLOGY CHARACTERIZATION

The subsurface geology beneath a specific site can significantly influence ground motions through two opposing effects: site amplification and material damping. Dames and Moore (1972) recognized that the range in physical properties of the nonwelded to welded Bandelier Tuff could have major effects on strong ground motions. Therefore, a program to characterize the subsurface geology beneath the technical areas was undertaken and is described below.

6.1 SUBSURFACE GEOLOGY OF THE PAJARITO PLATEAU

The Pajarito Plateau is located at the base of the Jemez Mountains on the western margin of the Española Basin of the Rio Grande rift. It has a gently-sloping surface that extends from the Pajarito fault, eastward to the Rio Grande. The plateau is underlain by Bandelier Tuff that has been deeply incised by many east-trending tributaries of the Rio Grande, leaving finger-like mesas radiating out from the base of the Jemez Mountains. Most of the LANL technical areas are located on these mesas.

In general, the subsurface geology of the Pajarito Plateau consists of igneous and metamorphic basement rocks typical of the Sangre de Cristo Mountains to the east, and pre-rift Paleozoic-Mesozoic rocks typical of the Colorado Plateau to the west (e.g., Stearns, 1953; Griggs, 1964). These rocks are overlain by rift-fill sediments that are, in part, concomitant with volcanism associated within the Jemez volcanic field (e.g., Galusha and Blick, 1971; Gardner, 1985).

The subsurface geology of the LANL was investigated by collecting and evaluating all available data and information including geophysical and borehole data and by drilling four continuously cored boreholes to depths of up to 258 m (846 ft). Figure 6-1 shows the approximate locations of existing water supply and test wells, test holes and core holes, including those drilled for this study, that exceeded a depth of 61 m (200 ft). Figure 6-2 shows the generalized location of the core holes drilled as part of this study (SHB-1 to SHB-4), in relation to LANL facilities, main roads and towns, as well as site-specific maps in the

vicinity of each core hole. Figure 6-3 shows the schematic lithologic logs for the four core holes. Figures 6-4 and 6-5 show geologic cross-sections of the Pajarito Plateau based on the available data. Table 6-1 shows the results of laboratory analyses of core samples from seismic hazards core hole SHB-1. Appendix J contains the core hole field logs and Appendix K summarizes previous subsurface geologic and geotechnical investigations undertaken within the LANL boundaries.

6.1.1 Pre-Rift Subsurface Geology

Pre-rift stratigraphy beneath the Española Basin and Pajarito Plateau consists of Precambrian crystalline basement rocks, which are overlain by pre-rift rocks and sediments that range in age from Pennsylvanian to Tertiary (Stearns, 1953; Griggs, 1964). Because no borings penetrated the complete stratigraphic column beneath Pajarito Plateau, depth to crystalline basement rocks, and depths and thicknesses of pre-rift rocks and rift-fill sediments are poorly constrained. Based on gravity measurements (Budding, 1978; Cordell, 1976; 1979) and subsurface geologic investigations (e.g., Griggs, 1964; Galusha and Blick, 1971; Budding, 1978; Golombek, 1983; Dransfield and Gardner, 1985), the depth to Precambrian crystalline rocks is estimated to be approximately 3700 m ($\approx$12,100 ft) and the depth to pre-rift deposits about 1400 m ($\approx$4600 ft).

6.1.2 Rift Sediments, Volcanics and Volcaniclastics

Data from deep water-well borings, other boreholes, and seismic and gravity surveys (Appendix K) have improved the understanding of the rift-fill stratigraphy beneath the Pajarito Plateau. Generally, the stratigraphy is composed of the Santa Fe Group and volcanic and volcaniclastic rocks associated with the Jemez volcanic field. The Santa Fe Group includes sediments that began to accumulate at the onset of rifting and, in part, include intercalated volcanic rocks and associated volcaniclastic sediments of the Keres Group. These rocks and sediments are overlain discontinuously by members of the Polvadera Group, which include Cerros del Rio basalt, the Puye and Tschicoma Formations, and the Bandelier Tuff and Cerro Toledo Rhyolite of the Tewa Group (Griggs, 1964; Bailey et al., 1969; Dransfield and Gardner, 1985; Gardner et al., 1986).

The following description of rift-fill stratigraphy beneath Pajarito Plateau adopts the stratigraphic nomenclature of Bailey et al. (1969) as refined by Gardner et al. (1986); and the unit descriptions of Stearns (1953), Griggs (1964), Galusha and Blick (1971), Crowe et al. (1978), Gardner et al. (1986), and Vaniman and Wohletz, (1990). The rift-fill stratigraphy is based on the integrated borehole and gravity data of Budding (1978), geologic cross-sections based on LANL borehole data (Cooper et al., 1965; John et al., 1967; Weir and Purtymun, 1962; Purtymun, 1993) and the core holes drilled for this study (Gardner et al., 1993).

6.1.2.1 Santa Fe Group

Sediments of the Santa Fe Group are largely derived from rift-bounding highlands that shed debris into the developing Rio Grande rift. The sediments include alluvial-fan deposits of loose to moderately cemented arkosic silt, sand and gravel, as well as fluvial gravel of the ancestral Rio Grande. The Santa Fe Group, in the vicinity of Pajarito Plateau, consists of the Tesuque and Chamita formations of Galusha and Blick (1971). Here the younger fluvial and alluvial-fan deposits of the Santa Fe Group are intercalated, in part, with Keres Group volcanics (Canovas Canyon Rhyolite and Paliza Canyon Formation) and volcaniclastics (Cochiti Formation) of the developing Jemez volcanic complex. Members of the Keres Group were not recorded in any borehole logs within LANL, and thus do not appear on the geologic cross-sections in Figures 6-4 and 6-5. Within and overlying the Santa Fe Group lie two formations: the Puye Formation which is interbedded with basalts and the Tschicoma Formation (Dransfield and Gardner, 1985).

6.1.2.2 Puye Formation

The Puye Formation is a broad alluvial fan deposit composed of a silty sandy conglomerate mixed with lahars and tuffs. It has two recognized members, the basal Totavi Lentil and an overlying fanglomerate member which constitutes the main portion of the Puye Formation (Galusha and Blick, 1971). However, Kelley (1978) states that because of its lithology, the Totavi Lentil Member may actually be part of the Tesuque Formation. The Puye Formation thickens toward its source in the northwest and locally interfingers with basalts to the southeast and dacite and andesite flows of the Tschicoma Formation to the west. At the north end of White Rock Canyon, it is 18 to 24 m thick and in Pueblo Canyon, a thickness

of 221 m was recorded in well 19.6.14.221 (Griggs, 1964). The Puye Formation was encountered at 256 m (840 feet) in core hole SHB-3 (Figure 6-3).

6.1.2.3 Basalts

Olivine basalt flows erupted from centers southeast of the Pajarito Plateau and flowed northwestward into the Los Alamos area, where they interfinger with the Puye Formation. Five separate flows were identified by Griggs (1964) with most described as thinning to the north. Basalt is exposed near the town of White Rock at the surface and within Los Alamos Canyon, where a 37-m-thick flow is characterized as massive and commonly brecciated at its base and edges. Basalt was encountered at 196 m (644 feet) near the bottom of core hole SHB-1 (Figure 6-3).

6.1.2.4 Tschicoma Formation

The Tschicoma Formation is composed of dacite with some pyroxene andesite flows (Griggs, 1964) that unconformably overly Abiquiu Tuff and the Santa Fe Group in the northern Jemez Mountains (Gardner et al., 1986). It is exposed at the surface in the upper parts of the canyons that drain the eastern Jemez Mountains. Flows of the Tschicoma Formation underlie the Bandelier Tuff on the western side of the plateau and interfinger with the Puye Formation. This formation was not penetrated by any of the seismic hazards core holes.

6.1.2.5 Bandelier Tuff - Otowi Member

The Otowi Member of the Bandelier Tuff (Griggs, 1964) consists of a basal air-fall pumice bed, the Guaje Pumice Bed, which is overlain by a sequence of pyroclastic flows. The Guaje Pumice Bed consists of unconsolidated air-fall pumice that is massive to poorly bedded and lithic poor. Clasts range in size from silt to 5 cm in diameter. The overlying pyroclastic-flow deposit consists of two sequences of a nonwelded, highly pumiceous, comparatively lithic-rich, poorly sorted tuff to lapilli tuff. Locally, vapor phase alteration has caused induration of the tuff.

6.1.2.6 Cerro Toledo Rhyolite/Epiclastic Reworked Pyroclastics

As referred to in this study and discussed by Gardner et al. (1993) and Heiken et al. (1986), the Cerro Toledo Rhyolite is a sequence of epiclastic deposits between the Otowi and Tshirege Members of the Bandelier Tuff that best correlates with the Cerro Toledo Rhyolite inside the Toledo caldera. The deposits consist of unconsolidated sand and gravel with interbeds of Cerro Toledo Rhyolite pyroclastic deposits.

6.1.2.7 Bandelier Tuff - Tshirege Member

The Tshirege Member of the Bandelier Tuff (Griggs, 1964) forms the surface of the Pajarito Plateau and rests unconformably on the Otowi Member. It also rests both unconformably and conformably on Cerro Toledo Rhyolite epiclastic deposits. The Tshirege Member forms the major part of the canyon cliffs of the plateau. It consists of a basal air-fall pumice, the Tsankawi Pumice Bed, which is overlain by ash-flow deposits. The Tsankawi Pumice consists of loose, tuff to lapilli tuff, air-fall deposits similar to the Guaje Pumice, but contains larger pumice clasts. Ash-flow deposits typically become moderate to densely welded westward towards the Jemez Mountains. These units were penetrated in all seismic hazards borings.

6.2 SITE-SPECIFIC SUBSURFACE GEOLOGY

Based on empirical data and observations, it is well known that near-surface geology can significantly influence the level and spectral content of strong ground motions. With this consideration in mind, core holes were drilled, logged and downhole seismic wave velocity and damping measurements performed to better characterize the near-surface seismic response beneath the moderate- and high-risk LANL facilities. Laboratory tests were performed on six undisturbed core samples to assess dynamic properties at high strain levels, and the range of properties with lithology and depth, particularly for soils and unconsolidated sediments. In addition, all available geotechnical and geophysical data, collected principally in site exploration activities for the eight technical areas, was compiled, tabulated and evaluated to aid in the characterization of the near-surface geology. All of this data was then used to develop site-specific geologic and seismic wave velocity profiles.

6.2.1 Core Hole Exploration

Four core holes were drilled at TA-55 (core hole SHB-1), TA-3 (core hole SHB-2), TA-16 (core hole SHB-3), and TA-18 (SHB-4) (Figures 6-1 and 6-2). All core holes were drilled with conventional coring techniques. Air was primarily used as the circulating fluid in the shallow holes (SHB-2 and SHB-4), whereas water, with viscosifier and mud additives, was used in the deep holes (SHB-1 and SHB-3) after circulation had been lost. After coring, each hole was reamed to a diameter of 6 inches and a PVC casing was lowered and set with cement slurry. The PVC casing (approximately 2.8 inches inside diameter) provided a conduit for lowering instruments to measure downhole shear (S-wave) and compressional-wave (P-wave) velocities (v_s and v_p, respectively) discussed in Section 6.2.2 below.

Core recovery varied depending on depth and lithology. Recovery was greatest in rocks of higher strength and higher degree of welding of the tuff. There is a reasonably strong positive correlation between downhole velocities versus core recovery (Section 6.2.2). Characterization of the degree of welding and/or lithification in penetrated ignimbrites was based on relative hardness and the flattening of pumices observed in hand sample and thus is subjective.

6.2.1.1 SHB-1 (TA-55)

SHB-1 is located just to the west of TA-55 at 2230 m (7,314 feet) elevation (Figure 6-2). The boring was drilled to a total depth of 213 m (700 feet), completely penetrating both members of the Bandelier Tuff, and terminating in the underlying Cerro del Rio basalts (Figure 6-3). Approximately 37% of the core was recovered.

In SHB-1, the Tshirege Member of the Bandelier Tuff extended from the surface to 94 m (310 feet). The upper 91 m consisted of approximately 43% nonwelded tuff, 34% moderately welded tuff, 10% moderate to densely welded tuff, and 13% densely welded tuff. The Tsankawi Pumice, between approximately 91 to 94 m (300 to 310 feet), marks the base of the Tshirege Member. Beneath the Tshirege Member were epiclastic sediments that correlate with the Cerro Toledo Rhyolite. This unit extended from approximately 94 m (310 feet) to the top of the Otowi Member of the Bandelier Tuff at 136 m (445 feet) (Figure 6-3).

The Otowi Member consisted of approximately 47 m of nonwelded tuff that overlies possibly 9 m of the basal Guaje Pumice Bed. Between 197 m (645 feet) and the bottom of the hole at 213 m (700 feet), SHB-1 penetrated basalts of upper flow units of the Cerros del Rio volcanic field (Figure 6-3).

6.2.1.2 SHB-2 (TA-3)

SHB-2 was drilled entirely within the Tshirege Member, north of SM-40 (Figure 6-2), to a total depth of 61 m (200 feet). The collar elevation of the hole was 2267 m (7,436 feet). Total core recovered was approximately 62%. At this location, the Tshirege Member consisted of about 42% nonwelded tuff, 45% moderately welded tuff, 7% moderate to densely welded tuff, and 6% densely welded tuff (Figure 6-3).

6.2.1.3 SHB-3 (TA-16)

SHB-3 was drilled to 258 m (848 feet) at TA-16 (Figure 6-2) on the west side of the tritium facility (Bldg 16-205) and close to the base of the Jemez Mountains to the west. The boring completely penetrated both members of the Bandelier Tuff and terminated in the underlying Puye Formation or a correlative conglomerate (Figure 6-3). Approximately 68% of the core was recovered.

The Tshirege Member of the Bandelier Tuff in SHB-3 extended from the surface, at an elevation of 2319 m (7,607 feet), to a depth of 98 m (321 feet). It consisted of approximately 64% densely welded tuff, 23% light to moderately welded tuff and 13% welded tuff. Between 98 and 103 m (321 and 338 feet), no core was recovered. The stratigraphic position of this interval suggests that it may be occupied by the Tsankawi Pumice Bed. From about 103 to 129 m (338 to 424 feet), a loose epiclastic unit is present similar to that observed in SHB-1 between the Tsankawi Pumice and the Otowi Member. It is assumed to correlate with the Cerro Toledo Rhyolite.

The Otowi Member extends from about 129 to 256 m (424 to 839 feet). It consists of about 124 m of lithified but nonwelded tuff and 2.4 m of pumice at the base. The basal pumice is probably the Guaje Pumice Bed. Beneath the Guaje Pumice, the hole penetrates 2.7 m of the Puye Formation.

6.2.1.4 SHB-4 (TA-18)

SHB-4, the easternmost of the four borings (Figure 6-2), was drilled to a depth of 61 m (200 feet). The boring is located in the TA-18 parking lot at an elevation of 2043 m (6701 feet). Only about 15% of core was recovered from SHB-4, thus characterization of the stratigraphy was uncertain (Figure 6-3). However, recovered core indicates that nonwelded tuff is dominant. The abundance of pumice and pumice fragments between about 35 and 37 m (115 and 120 feet), may represent the Tsankawi Pumice Bed. If this is correct, the core hole penetrated nonwelded tuff of the lowermost Tshirege Member and the uppermost Otowi Member of the Bandelier Tuff.

6.2.2 Downhole Geophysical Measurements

A downhole velocity survey was carried out by Redpath Geophysics, from 25 through 30 May 1992, in the four core holes to measure v_s and v_p as a function of depth. *In situ* S-wave damping measurements were also performed in core hole SHB-1.

Three-inch outer diameter PVC casing was inserted initially into the holes and grouted in place to provide a smooth passage for the geophones (Redpath Geophysics, 1992). To generate the S-wave signals, 16-lb hammer blows were subsequently made to each end of a 2.1-m-long steel-capped 6" x 6" wood beam, held firmly to the ground by the weight of a truck. This configuration produced both a negative and a positive signal, which when superimposed, graphically enhanced S-wave identification and travel-time picks. A variable-azimuth horizontal geophone was used to record the S-wave signals (Redpath Geophysics, 1992). It was oriented parallel to the S-wave source motion at 3 m intervals and locked against the PVC casing wall with a nitrogen-inflated bladder. A backup triaxial transducer was used to extend the survey depth (to a maximum of 174 m [570 ft] when narrowing of the PVC casing prevented further lowering of the slightly larger variable-azimuth geophone. Because the orientation of this triaxial transducer with respect to the source could not be controlled, recordings on both of the two orthogonal horizontal components were required for picking arrival times.

P-wave signals were generated from vertical blows to a striker plate at the surface and a vertical geophone was used to record the P-wave arrival times (Redpath Geophysics, 1992). Both P-wave and S-wave signals were recorded on a Geometrics 1210F, 12-channel digital seismograph and stacked where necessary to improve the signal-to-noise ratio. The resulting travel times as a function of depth for both P- and S-waves are shown in Figures 6-6 through 6-9. Least-square fits to straight line segments of the data points, the corresponding velocities, and the interpreted velocity profiles as a function of depth are also depicted in Figures 6-6 through 6-9 (Redpath Geophysics, 1992).

P- and S-wave velocities were obtained for the top 122, 61, 168, and 55 m of core holes SHB-1, SHB-2 , SHB-3 and SHB-4, respectively. The v_s and v_p profiles correlate very well to the thickness of geologic units (Figures 6-3 and 6-6 through 6-9). In general, the v_s strongly correlates with the degree of welding in the Bandelier Tuff: v_s ranges from 200 to 300 m/sec for the nonwelded tuff in the near surface, about 500 m/sec for moderately welded tuff, and on the order of 600 to 1000 m/sec for moderately to densely welded tuff (Figures 6-6 through 6-9). The v_s typically increases with depth for a given lithology, for example, for nonwelded tuff, v_s increases from 230 m/sec in the near surface to 500 m/sec at a depth of about 70 m (230 ft) in SHB-1 (Figure 6-6). The v_s of the Cerro Toledo epiclastic reworked pyroclastics is generally the highest velocity recorded in the survey, approximately 800 to 1000 m/sec as recorded in SHB-1 and SHB-3 (Figures 6-6 and 6-8).

S-wave damping was measured in borehole SHB-1. Recordings of "clean" S waves were necessary at several depths in the borehole to obtain good measurements. Spectral ratios were calculated with respect to a reference depth and spectral decay as a function of distance and frequency was determined (Redpath Geophysics, 1992). Inspection of the S-wave records from SHB-1 showed "clean" S waves at depths of 9, 21, 55, 70, 91 and 107 m (30, 70, 180, 230, 300, and 350 ft, respectively). Fourier spectra were computed for each of these S-wave signals and ratios were determined with respect to the spectrum recorded at a depth of 9 m (30 ft) (Figure 6-10). The least-squares slope of the logarithm of each spectral ratio slope was calculated over the bandwidth of 20 to 90 Hz and plotted as a function of depth (Figure 6-10).

Two possible interpretations result from the scatter in the data shown in Figure 6-10. First, a constant S-wave damping of 2.9% down to a depth of 107 m (350 ft) can explain the data

if more emphasis is placed on the deeper measurements (Redpath Geophysics, 1992). In contrast, a two layer attenuation model with 4.4% damping between 9 and 37 m (30 and 120 ft) and 0.6% damping between 37 and 107 m (120 and 350 ft) could also explain the data, the boundary of which corresponds to the observed velocity increase at 37 m (120 ft) (Figure 6-6). The cumulative damping of 2.9% at 107 m (350 ft) is the same in both cases (Redpath Geophysics, 1992). These values are higher than the results of the dynamic laboratory testing which are around 1% at 10^{-4}% shear strain for the same depth range (Section 6.2.3). These differences are not significant considering the uncertainties inherent in damping measurements. In particular, the *in situ* damping measurements assume a simple 1/R geometric attenuation and neglect layer boundary effects. The actual geometrical attenuation in the presence of a velocity gradient is greater than 1/R and would result in increased apparent damping if 1/R is assumed. Since the small strain damping does not control strong ground motions, the difference between the *in situ* and laboratory measurements is not a significant issue and the laboratory values are considered to be more appropriate.

During the core drilling, the variability in the percentage of core recovered within and between borings was cause for some concern. It was not known at the time of drilling whether coring methods and techniques, core-bit selection, other drilling-related causes or lithologic variations were responsible for the wide fluctuations in core recovery. Similarly, during the downhole velocity survey phase of the core hole exploration, questions arose over whether or not some of the variability in velocity measurements was due to poor coupling of energy from the surrounding lithology, through the annular casing grout, to the transducer (Section 6.2.1). In an attempt to resolve these questions, the percentage of core recovered was plotted against velocities for each hole (Figure 6-11).

In general, results of the comparison indicate a reasonably strong positive correlation between recovery percentages and velocities. In general, when v_s decreased, there was a corresponding drop in core recovery, suggesting core recovery variability was more dependent on rock strength than coring methods, and that the condition of the annular grout was probably not a significant factor in velocity variability.

One exception was for SHB-4, where there appeared to be little correlation between velocities and core recovery (Figure 6-11). One possible explanation for the lack of correlation may be that when core recovery dropped below a minimum threshold value, it

became difficult to resolve significant trends in the percentage of core recovered. In general, however, results from velocity/recovery comparisons in the other core holes suggest that both velocity and core recovery appear to reasonably reflect changes in lithologic characteristics. Thus, the v_p and v_s measurements in core hole SHB-4 probably reflect changes in rock characteristics and are not due to energy coupling problems.

6.2.3 Dynamic Laboratory Testing

Dynamic laboratory testing of core samples extracted during the core hole program was performed to aid in characterizing the dynamic properties of the subsurface geology beneath the technical areas. Ten samples were recovered from the SHB-1 core hole at TA-55 on November 1991. The samples were visually inspected in the field, sealed and transported by automobile to the University of Texas at Austin in February 1992 for dynamic laboratory testing. The dynamic properties to be evaluated consisted of shear moduli and damping ratios for various levels of shear strains. The samples were tested by Dr. Ken Stokoe during the period February 1992 and January 1993.

Upon visual inspection of the ten samples, only six appeared to be sufficiently intact and representative of undisturbed samples. The remaining four appeared to be disturbed, presumably during the sampling process and thus only the six samples were tested. The locations at which these samples were collected, along with their corresponding index properties, are summarized in Table 6-1. Based on their physical appearance, three samples were handled as soil samples (HQ63, HQ82, and HQ114). The other three samples (HQ5, HQ30, and HQ146) were handled as rock samples and were trimmed with a rock saw. Generally the samples sizes were kept within a ratio of 2:1 between the height and diameter.

6.2.3.1 Dynamic Laboratory Testing Procedures

Resonant column and torsional shear (RCTS) equipment was used to analyze the shear modulus (G) and the damping coefficient (D). The sensitivities of the dynamic properties, G and D, to the following parameters were investigated:

- Isotropic confining stresses. The samples were tested under four to seven isotropic pressures, including values at *in situ* effective mean pressures and below.

- Duration of the confining isotropic pressure. Confinement time varied between 1 hour and 3 days. The rock samples were tested for 1 hour and the soil samples were tested for 1 to 3 days at each confining pressure.

- Shearing strain amplitude. Shear strains during testing were varied from small levels of about 0.001% to large shear strain levels of about 0.1%.

- Number of loading cycles. One to ten cycles of loading were used in the torsional shear test followed by 500 to 1000 cycles in the resonant column test.

- Excitation frequency. Frequencies ranging from 0.1 Hz to about 10 Hz were used in the torsional shear test while the excitation frequency used in the resonant column test varied with soil/rock stiffness and ranged between 20 Hz to about 400 Hz.

The low-amplitude dynamic properties (G_{max} and D_{min}) were tested for shearing strains less than 0.001% using the resonant column procedure. The high-amplitude dynamic properties (G and D) were tested for shearing strains between 0.001% and 0.1%, using both resonant column and torsional shear test procedures. The resonant column testing procedure consisted of applying cyclical torque to the sample at frequencies above 20 Hz (fast cycling), whereas the torsional shear testing procedure consisted of applying cyclic torque to the sample at frequencies below 5 Hz (slow cycling). Further details on the equipment and procedures used in this testing program are described in the report entitled "Dynamic Properties of Undisturbed Soil Samples from Los Alamos, New Mexico" (Stokoe et al., 1993).

6.2.3.2 Test Results and Discussion

This section summarizes the results of the testing program and discusses the sensitivity of the dynamic properties (G and D) to various parameters. The full set of test results and specific sensitivity evaluation can be found in the laboratory test report (Stokoe et al., 1993).

The index soil/rock properties were tested first and are summarized in Table 6-1. After the index properties were evaluated, G and D were measured for low- and high-amplitude shear strains as previously described. The results of these dynamic tests indicate that the

normalized (G/G_{max}) secant shear moduli decay with higher amplitude shear strain as shown in Figure 6-12. The shape of the moduli reduction values are compared with the empirical modulus reduction curves by Seed and Idriss (1970) for sands, which seem to fit the upper range of their curve. The damping ratios of the six samples increase with increasing shear strain as shown in Figure 6-13. The damping ratios appear to fit the lower range of the empirical values for sands presented by Seed and Idriss (1970). These results indicate that the material tested are generally stiffer and consequently dissipate less hysteretic energy than the average sands described by Seed and Idriss (1970). These results are consistent with the classification of the specimens as being more rock-like than soil-like. It is further observed that the basalt rock sample (HQ146) exhibits a slower shear modulus decay and consequently a little increase in damping ratio over the other five samples.

6.2.3.2.1 Effects of Confining Pressure. The sensitivity of G_{max} to isotropic confining pressure is illustrated in Figure 6-14. The tests were performed for a range of confining pressures varying between 100 psf and 100,000 psf. G_{max} for the rhyolite tuff and basalt samples (HQ5, HQ30 and HQ146) appears to have a negligible sensitivity to different isotropic stress levels. However, the samples of silty sand, pumice sand and rhyolite sand (HQ63, HQ82 and HQ114) show a typical increasing trend with increasing isotropic pressure. Within the range of applied confining pressures, the G_{max} varied by one log cycle from about 1,000 ksf to 10,000 ksf. The soil-like G_{max} versus confining pressure relationships for soil-like samples appear to follow the equations of Hardin (1978). In contrast, D_{min} generally shows a decreasing trend with higher confining pressure, independent of the soil or rock type as shown in Figure 6-15. One exception is the silty sand sample (HQ63), which overall shows an increasing trend with confining pressure. This trend may not be reliable, however, because of the low quality of the sample at higher confining pressures. Finally, it is interesting to note that all D_{min} values are less than 1.5%.

6.2.3.2.2 Effects of Confinement Duration. Generally the test results show that G_{max} and D_{min} are relatively unaffected by variations in the duration of the application of confining pressures (Stokoe et al., 1993). There is, however, a slight trend indicating that G_{max} increases with longer duration of application of confining pressures while D_{min} decreases. This effect appears to be negligible because of the low degree of saturation and also because of the granular (high permeability) nature of the samples. The duration of applied confining

pressure may have a more pronounced affect on saturated low-permeability soils such as clays.

6.2.3.2.3 Effects of Loading Frequency. The loading frequency during testing was varied from 0.05 Hz to about 400 Hz using the torsional shear test for small strain levels between 0.0001% to 0.008%. Although there is a slight increase in both the shear moduli and damping ratios with higher loading frequency, the results of the tests indicate that generally the frequency of loading has no significant effects (Stokoe et al., 1993).

6.2.3.2.4 Effect of Number of Loading Cycles. The number of load cycles applied to the torsional shear tests were varied between 1 and 10 cycles whereas for the resonant column tests, the number of cycles varied between 500 to 1000 cycles. Comparable tests for different cycles were taken up to 0.01% shear strain. The results of these tests show that G and D were not very sensitive to the number of load cycles within the shear strain range tested ($< 0.01\%$) (Stokoe et al., 1993). These results also indicate that within the test range of shear strain, the shear moduli degradation and damping was insignificant.

6.2.4 Other Borehole Data

To supplement the subsurface data provided by water and other deep-test well boring logs on Pajarito Mesa (Figure 6-1), shallow site-specific geotechnical boring logs were also compiled. These shallow boreholes were reviewed to assess the range of physical and dynamic properties for specific near-surface geologic units. All available site-specific geotechnical and geophysical data were compiled and reviewed for the LANL, which included ten technical areas (TA-2, TA-3, TA-16, TA-18, TA-21, TA-35, TA-41, TA-46, TA-53, and TA-55), containing moderate- and high-hazard facilities. This compilation included 61 foundation, subsurface, soil or geotechnical investigation reports generated as part of site exploration activities for proposed facilities at LANL, and four geophysical investigations. These reports are described in Appendix K. Data from this compilation that was used in site-specific characterization is discussed in the next section.

6.2.5 Summary of Site-Specific Velocity Profiles

Site-specific seismic velocity profiles developed for the eight LANL technical areas are shown in Figures 6-16 through 6-23. The development of geologic and v_s profiles is discussed in detail for each of the technical areas in the following sections (Sections 6.2.5.1 through 6.2.5.8). The development of v_p profiles is generally discussed in Section 6.2.5.9. All profiles were developed using the geologic and geotechnical data previously described in this chapter. Cross sections A-A', B-B' and C-C'(Figures 6-4 and 6-5), which provide generalized stratigraphy beneath specific sites, were constructed using all available data from deep (> 61 m) borehole logs in the LANL area. Physical and dynamic properties of the near-surface geologic units for the eight specific sites were obtained mainly from foundation geotechnical reports, the seismic hazard boreholes, and the dynamic laboratory testing. Physical and dynamic properties for deeper subsurface geologic units beneath the eight technical areas of interest were obtained from the literature and by extrapolation of data from the seismic hazard boreholes.

6.2.5.1 TA-2

TA-2 is located near the base of the northern flank of Los Alamos Canyon above canyon-bottom alluvium (Figure 6-1). There is no available subsurface information for any of the buildings at TA-2; however, conditions should be similar to those at TA-41 (D. Keller, LANL, personal communication, 1994), which is located approximately 500 m to the west further up Los Alamos Canyon. Therefore, geologic and shear-wave velocity profiles for both TA-2 and TA-41 were primarily based on extrapolation of data from nearby borehole SHB-1 (in TA-55 on Figure 6-1) and the cross-sections. Specifically, the upper portion of the profile for TA-2 (Figure 6-16), above the Guaje Pumice, was modified from SHB-1 data, and the rest of the profile was constructed by using the cross-section A-A' (Figure 6-4) and assuming velocities appropriate for the various rock types.

In general, welding within cooling units of pyroclastic flows increases towards the source and the thickness of the cooling units decreases away from the source (Fisher and Schmincke, 1984) and therefore, the lithologic units within the Bandelier Tuff are assumed to be generally uniform across the Pajarito Plateau from north to south, at similar distances

from their source, the Valles Caldera. TA-2 is located close enough to SHB-1 that v_s, densities, and thicknesses measured in SHB-1, can be extrapolated with some degree of confidence to TA-2. However, there are some differences between geologic conditions at TA-2 and TA-55 that required modifications to the seismic profile used for TA-2, and these are discussed below.

The epiclastic reworked pyroclastics associated with the Cerro Toledo Rhyolite were encountered in SHB-1 at a depth of about 95 m, below the Tshirege Member and above the Otowi Member of the Bandelier Tuff (Figure 6-3). The Cerro Toledo Rhyolite is not depicted as a separate unit on the map of Vaniman and Wohletz (1990), but grouped with the underlying Otowi Member and their map depicts this unit outcropping in Los Alamos Canyon in the vicinity of TA-2. Therefore, buildings at TA-2 probably rest on the epiclastic deposits of the Cerro Toledo Rhyolite, based on interpretation of their mapping and extrapolation between boreholes.

Because TA-2 is in a canyon and SHB-1 is on a mesa top, the v_s of the two layers of the Otowi Member of the Bandelier Tuff in the TA-2 velocity profile (Figure 6-16) were reduced from those measured in SHB-1 by 200 to 350 m/sec to account for the lack of overburden pressure. A v_s estimate of 700 m/sec for the Guaje Pumice Bed is extrapolated from a 730 m/sec v_s measurement from a nonwelded, pumice-rich and vapor-phase altered tuff unit that occurs at a depth of 78 m in SHB-1. The v_s and density of the Tschicoma dacitic rocks were based on velocity measurements by Press (1966) and from downhole velocity measurements compiled by R. Nigbor (Agbabian Associates, written communication, 1994) assuming that these properties were similar to those of andesitic rocks (v_s ~3000 m/sec and a density of ~2.8 g/cm^3). The v_s and density of dacites will not vary significantly within the depth range of the profiles. Gardner and House (1987) reported P-wave velocity measurements of 1000 m/sec (v_s of 580 m/sec for a Poisson's ratio of 0.25), based on refraction of fractured and weathered near-surface possible Tschicoma dacite. This appears to be significantly low for this rock type and so these values were not used. The depth to the base of the Tschicoma dacitic rocks is poorly constrained, but is known to reach at least 700 m in well EGH-LA-1. The v_s and density of the Totavi Lentil Member are assigned values similar to the rest of the Puye Formation because of their similar lithologies. The v_s of the Puye Formation and the Tertiary Santa Fe group, consisting of sandstone, siltstone and gravel, are estimated to range from 1000 to 1600 m/sec, increasing with depth. The velocity gradient used to construct the

profiles was 100 m/sec per 150 m-depth-increments, starting with a v_s of 1000 m/sec for the 50 to 200 m depth interval. This gradient is based on sonic velocity measurements from the Baldwin Hills borehole, which cuts through Pleistocene and Pliocene sediments and sandstones. (v_p ranges from 2.0 to 3.0 km/sec and using a Poisson's ratio of 0.25 yields v_s values from 1.15 to 1.73 km/sec). Densities of these rocks range from 2.2 g/cm^3 to 2.5 g/cm^3 as depth and velocity increase. These values are based on *in situ* measurements performed by Agbabian Associates for similar lithologies (R. Nigbor, written communication, 1994).

6.2.5.2 TA-3

Data from core hole SHB-2 and various investigations provides constraints for profile TA-3 (Figure 6-16). Subsurface investigations conducted at various building sites within TA-3 indicate the thickness of soil is variable across TA-3 and is between 0 and 12.5 m (Appendix K). This soil is comprised of sandy clay to silty and clayey sands and overlies the Tshirege Member of the Bandelier Tuff. About 1.5 m of this soil was encountered in boring SHB-2 (Figure 6-3), which was drilled 61 m into the Bandelier Tuff. Due to the great expense in removing large thicknesses of soil and the variability in required foundation bearing capacities, some structures were constructed on the ground surface. Downhole velocity measurements (Section 6.2.2) were obtained for most of the drilled depth and densities were extrapolated from the velocities. Lithologies and thicknesses of units beneath the bottom of SHB-2 (Figure 6-16) were estimated from cross-section B-B' (Figure 6-4), which is constrained to the northwest by the relatively deep borehole H-19 (1501 m) and to the southeast and east by SHB-1 and EGH-LA-1 (Figure 6-1). The Guaje Pumice is estimated to have a v_s of 1000 m/sec, and a density of 2.9 g/cm^3, as it occurs at a depth of over 200 m.

Subsurface v_s determined from refraction surveys (Appendix K) for the design upgrade of the CMR Building, SM-297, indicate a v_s of 250 to 655 m/sec for the upper units of the Tshirege Member of the Bandelier Tuff in this area of LANL, which is consistent with the downhole v_s determined in this study. Near-surface dry densities obtained for the Bandelier Tuff range from 1.15 to 1.89 g/cm^3 (Appendix K). At TA-53, Keller (1968) determined densities of 1.28 to 1.76 g/cm^3 for Unit 3a and 1.6 to 1.9 g/cm^3 for Unit 2b, both of which are part of the Tshirege Member of the Bandelier Tuff as described by Vaniman and Wohletz

(1990). Dames and Moore obtained a v_s of 230 to 655 m/sec for the Bandelier Tuff (Appendix K), which can significantly vary in degree of welding within a particular cooling unit from densely to nonwelded tuff. From seismic data collected at TA-53 and TA-55, SHB-Agra Inc. estimated a v_s of 655 m/sec for the Otowi Member of the Bandelier Tuff and the Guaje Pumice Bed, and a v_s of 1190 m/sec for the underlying Puye Formation and interfingered basalt (Appendix K). Dames and Moore estimated a v_s of 915 m/sec for the Puye fanglomerate (Appendix K), close to our estimate of 1000+ m/sec, and 1220 m/sec for the Santa Fe Group which we estimate to be in the range of 1300 to 1500 m/sec. SHB-Agra Inc. estimated a v_s of 1190 m/sec for the Tschicoma dacite, which we believe to be far too low (Appendix K).

6.2.5.3 TA-16

The Tritium facility at TA-16 is located approximately 0.4 km east of West Jemez Road and 0.7 km north of Highway 4 on the mesa top between Water Canyon and Canon de Valle (Figure 6-1). The facility rests on the Tshirege Member of the Bandelier Tuff. Foundation investigation reports indicate that most of the buildings at TA-16 are underlain by approximately 2 to 4 m of soil (Appendix K). However, the WX-4 Office Building overlies approximately 13 m of soil and Building 200, overlies approximately 16 m of soil. The v_s profile for TA-16 (Figure 6-17), however, reflects conditions at boring SHB-3, where less than 1 m (3.3 ft) of soil was encountered (Figure 6-3). We assume that soil was removed from the Tritium facility site prior to construction.

Borehole SHB-3 was drilled to a depth of 258 m and included *in situ* v_s measurements, which were incorporated into the geologic and shear-wave velocity profile (Figure 6-17). Densities for the geologic profile beneath TA-16 were again estimated from Hauksson et al. (1987), Press (1966), and downhole measurements of similar lithologies by R. Nigbor (Agbabian Associates, written communication, 1994). Geologic units below the depth of penetration of SHB-3 were estimated from the cross-section C-C' (Figure 6-5).

6.2.5.4 TA-18

TA-18 is located at the bottom of a shallow canyon at the confluence of Threemile and Pajarito Canyons (Figure 6-1). Borehole SHB-4 was drilled near the north wall of Pajarito

Canyon, therefore, valley fill alluvium was not encountered in the boring. Several boreholes drilled at the Accelerator Development Laboratory Building 227, near the north edge of the canyon bottom, indicate that approximately 2 m (6.6 ft) of fill overlies 3 m (9.8 ft) of alluvial silt, sand and gravel (Appendix K).

SHB-4 was drilled to a depth of 61 m and v_s was measured for most of its depth (Figures 6-9 and 6-17). The stratigraphy below the bottom of the borehole was estimated from cross-section B-B' (Figure 6-4). Logs from water well borings PM-2 and PM-4 provide fairly good constraints on the thicknesses of the various geologic units underneath TA-18. The basaltic rocks found in both PM-4 and PM-2, below the Guaje Pumice, were assumed to similarly occur at TA-18. The velocity and density of these rocks were estimated based on comparisons with geophysical measurements of other basaltic rocks (Press, 1966; R. Nigbor, Agbabian Associates, written communication, 1994).

6.2.5.5 TA-21

TA-21 is located on top of DP Mesa, a relatively short and narrow mesa approximately 0.5 km south of the Los Alamos landing strip between Los Alamos Canyon and an unnamed fork that dead ends in the Los Alamos townsite (Figure 6-1). Two geotechnical studies encountered about 1 m (3.3 ft) of soil overlying the Bandelier Tuff at TA-21 (Appendix K). We assume that soil was removed prior to construction of buildings at this site.

TA-21 is located close to boring LADP-4 on cross-section A-A' (Figure 6-4). The thicknesses of geologic units were estimated from cross-section A-A' and SHB-1. The v_s values (Figure 6-18) for this site were estimated from borehole SHB-1 for the Tshirege and Otowi Members of the Bandelier Tuff. The v_s values and densities of the rest of the profile were estimated in a similar manner to those of the profiles described previously.

6.2.5.6 TA-41

TA-41 is located within Los Alamos Canyon about 1.5 to 2 km northeast of SHB-1 and west of TA-2 (Figure 6-1). The geologic and v_s profiles (Figure 6-18) were developed in a similar fashion to that of TA-2 from SHB-1 and from cross-section A-A' for units below the depth of SHB-1. To compensate for the lack of overburden pressure, the velocities were

reduced by 200 to 350 m/sec in the upper two layers for the TA-41 geologic profile. The base of the Otowi Member outcrops on the canyon walls about 10 m above TA-41 (Vaniman and Wohletz, 1990). Thus, similar to TA-2, TA-41 is probably underlain by Cerro Toledo epiclastic deposits. This interpretation is supported by the presence of water-deposited pumice and ash found at depths of 1 to 10 m (3.3 to 33 ft) at this site with densities of approximately 1.63 to 2.05 g/cm^3 (see Appendix K). Other boreholes drilled at TA-41 found alluvium and/or colluvium up to depths of 5 m (1.5 ft).

6.2.5.7 TA-46

TA-46 is located on Mesita del Buey, about 1 km south of cross-section B-B'(Figures 6-1 and 6-4). Albuquerque Testing Laboratory drilled several holes at TA-46 and found less than 2 m of soil overlying the Bandelier Tuff (Appendix K). Consequently, we presume all sites at TA-46 are built on bedrock. Southward extrapolation from B-B' provides the basis for estimating the thicknesses of geologic units, which are constrained by two relatively deep boreholes, PM-5 to the east, and EGH-LA to the west (Figures 6-4 and 6-19). The v_s values of the Bandelier Tuff units were estimated from those measured in boreholes SHB-1 and SHB-4 (Figures 6-6 and 6-9).

6.2.5.8 TA-55

TA-55 is located on Mesita del Buey between Mortandad and Pajarito Canyons (Figure 6-1). Many shallow drill holes indicate a soil thickness of up to 6 m (Appendix K). Borehole SHB-1, located just west of the TA-55 security perimeter, encountered less than 2 m of soil and was drilled to a depth of 213 m (Figure 6-3). Downhole v_s values were determined for the upper 137 m of the borehole (Figure 6-6). Only a few samples from this borehole were analyzed in the laboratory to measure densities and these were not included in the TA-55 geologic and v_s profile (Figure 6-19) because they were not measured *in situ* and did not appear consistent with the velocities and lithologic descriptions. Instead, we assumed densities based on velocities and measurements of similar lithologies determined by R. Nigbor (Agbabian Associates, written communication, 1994). Thicknesses of units below the bottom of the borehole are estimated from cross-section B-B' (Figure 6-4).

6.2.5.9 P-wave Velocity Profiles

To model the vertical ground motions at LANL, P-wave velocity profiles were constructed for the eight sites (Figures 6-20 to 6-23). The profiles were based on the v_p measurements in the boreholes (Figures 6-6 to 6-9); however, some of the measurements appear to be less reliable than others and so were not incorporated. This degree of scatter is not uncommon in downhole P-wave surveys (B. Redpath, Redpath Geophysics, personal communication, 1995). The P-wave velocity measurements are thought to be accurate to within 20% to 30% (B. Redpath, Redpath Geophysics, personal communication, 1995). P-wave velocities for the rock below the boreholes, for sites without boreholes, and for unreliable velocity measurements, were determined from the S-wave velocity profiles. For the Bandelier Tuff, a regression between measured v_s and v_p values gives the relationship $v_s = 0.618\ v_p - 0.60$, assuming the same gradient developed for *in situ* acoustic properties of densely-welded tuffaceous volcanic rocks in central Nevada (Carroll and Paul, 1970). To estimate v_p for the other formations, we used a Poisson's ratio of 0.35 ($v_p/v_s = 2.08$) for the Puye Formation and the Santa Fe Group, 0.30 ($v_p/v_s = 1.87$) for the basaltic sediments, and 0.25 ($v_p/v_s = 1.73$) for the basalt and dacite.

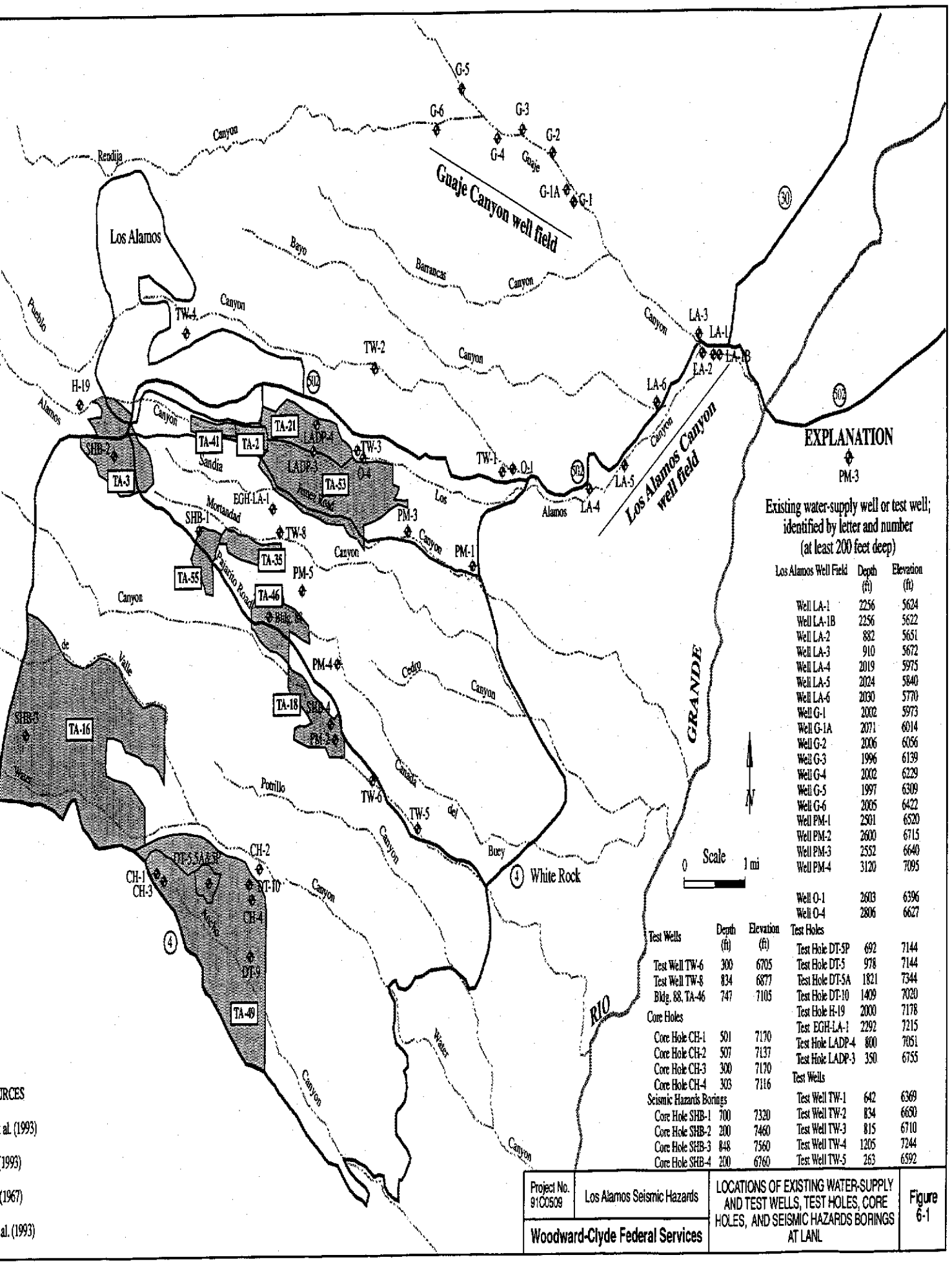
TABLE 6-1

INDEX PROPERTIES OF TESTED SAMPLES

Sample Number[a]	Depth ft(m)	Soil Type[b]	R_{200}[c] %	Water Content %	Total Unit Weight pcf(g/cm^3)	Void Ratio e	Dia. cm	Height cm	Specific Gravity G_s[d]	Degree of Saturation %
HQ5 [1]	23(7.01)	Rhyolite Tuff	-	0.15[e]	92(1.47)	0.80	5.7	11.12	2.65	0.5
HQ30 [1]	146(44.5)	Rhyolite Tuff	-	0.12[e]	116(1.86)	0.43	6.05	11.45	2.65	0.7
HQ63	310(94.5)	Silty Sand	54	9.2	91(1.46)	1.00	5.05	8.23	2.65	24
HQ82 [2]	400(122)	Pumice Sand	78	38.0	108(1.73)	1.12	6.1	11.0	2.65	90
HQ114 [2,3]	515(157)	Rhyolite Tuff	75	24.0	102(1.63)	1.01	6.1	11.5	2.65	63
HQ146 [1]	662(202)	Basalt	-	_[f]	143(2.29)	0.20	2.54	4.99	2.75	_[g]

1. Epoxy glue was used to fix the specimen to the end platens of the test equipment.
2. Stopped during testing due to leakage of the rubber membrane.
3. Sample grouted with hydrostone to the end platens of the test equipment.

a. Sample number used in boring log supplied by Woodward-Clyde Federal Services, Inc.
b. Identification based on description given in the boring log supplied by Woodward-Clyde Federal Services, Inc.
c. R_{200} = Percent of soil sample by weight remaining on #200 sieve
d. Specific gravity was assumed.
e. Water content was determined using sample next to the specimen used for RCTS tests.
f. Water content not determined because water was used to cut the ends of the specimen.
g. Degree of saturation not calculated because water content was not determined.



EXPLANATION

PM-3

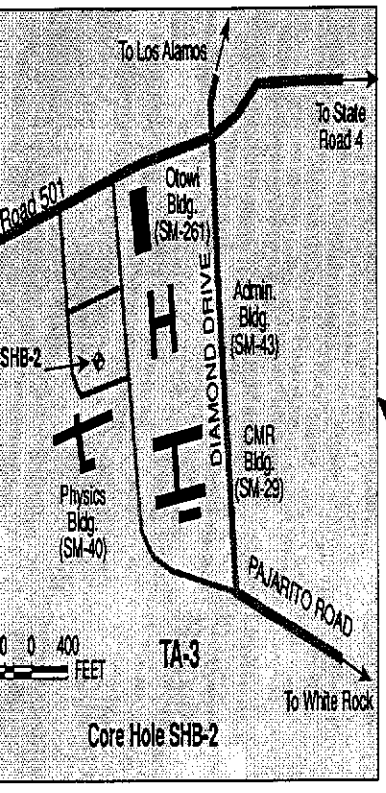
Existing water-supply well or test well; identified by letter and number (at least 200 feet deep)

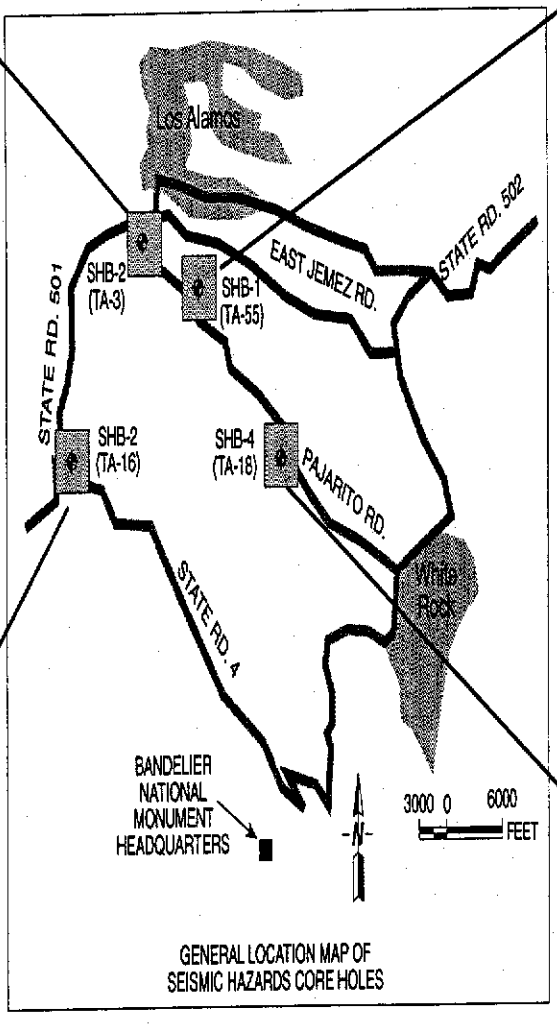
Los Alamos Well Field	Depth (ft)	Elevation (ft)
Well LA-1	2256	5624
Well LA-1B	2256	5622
Well LA-2	882	5651
Well LA-3	910	5672
Well LA-4	2019	5975
Well LA-5	2024	5840
Well LA-6	2030	5770
Well G-1	2002	5973
Well G-1A	2071	6014
Well G-2	2006	6056
Well G-3	1996	6139
Well G-4	2002	6229
Well G-5	1997	6309
Well G-6	2005	6422
Well PM-1	2501	6520
Well PM-2	2600	6715
Well PM-3	2552	6640
Well PM-4	3120	7095
Well O-1	2603	6396
Well O-4	2806	6627
Test Holes		
Test Hole DT-5P	692	7144
Test Hole DT-5	978	7144
Test Hole DT-5A	1821	7344
Test Hole DT-10	1409	7020
Test Hole H-19	2000	7178
Test Hole EGH-LA-1	2292	7215
Test Hole LADP-4	800	7051
Test Hole LADP-3	350	6755
Test Wells		
Test Well TW-1	642	6369
Test Well TW-2	834	6650
Test Well TW-3	815	6710
Test Well TW-4	1205	7244
Test Well TW-5	263	6592

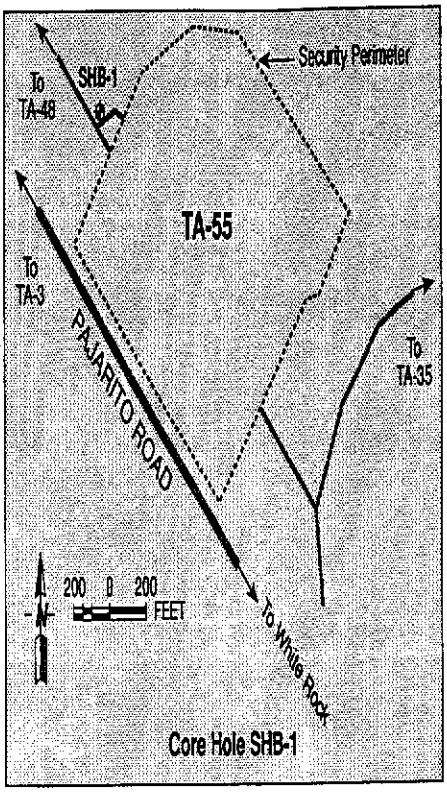
Test Wells	Depth (ft)	Elevation (ft)
Test Well TW-6	300	6705
Test Well TW-8	834	6877
Bldg. 88, TA-46	747	7105
Core Holes		
Core Hole CH-1	501	7170
Core Hole CH-2	507	7137
Core Hole CH-3	300	7170
Core Hole CH-4	303	7116
Seismic Hazards Borings		
Core Hole SHB-1	700	7320
Core Hole SHB-2	200	7460
Core Hole SHB-3	848	7560
Core Hole SHB-4	200	6760

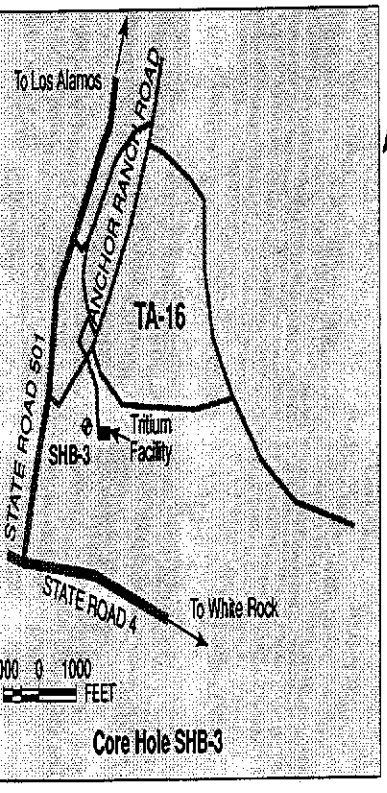
Project No. 91C0509	Los Alamos Seismic Hazards	LOCATIONS OF EXISTING WATER-SUPPLY AND TEST WELLS, TEST HOLES, CORE HOLES, AND SEISMIC HAZARDS BORINGS AT LANL	Figure 6-1
Woodward-Clyde Federal Services			

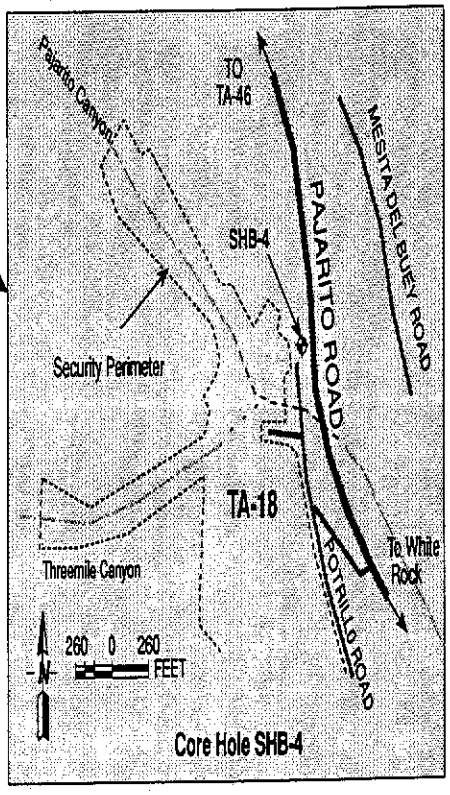
URCES
al. (1993)
1993)
(1967)
al. (1993)



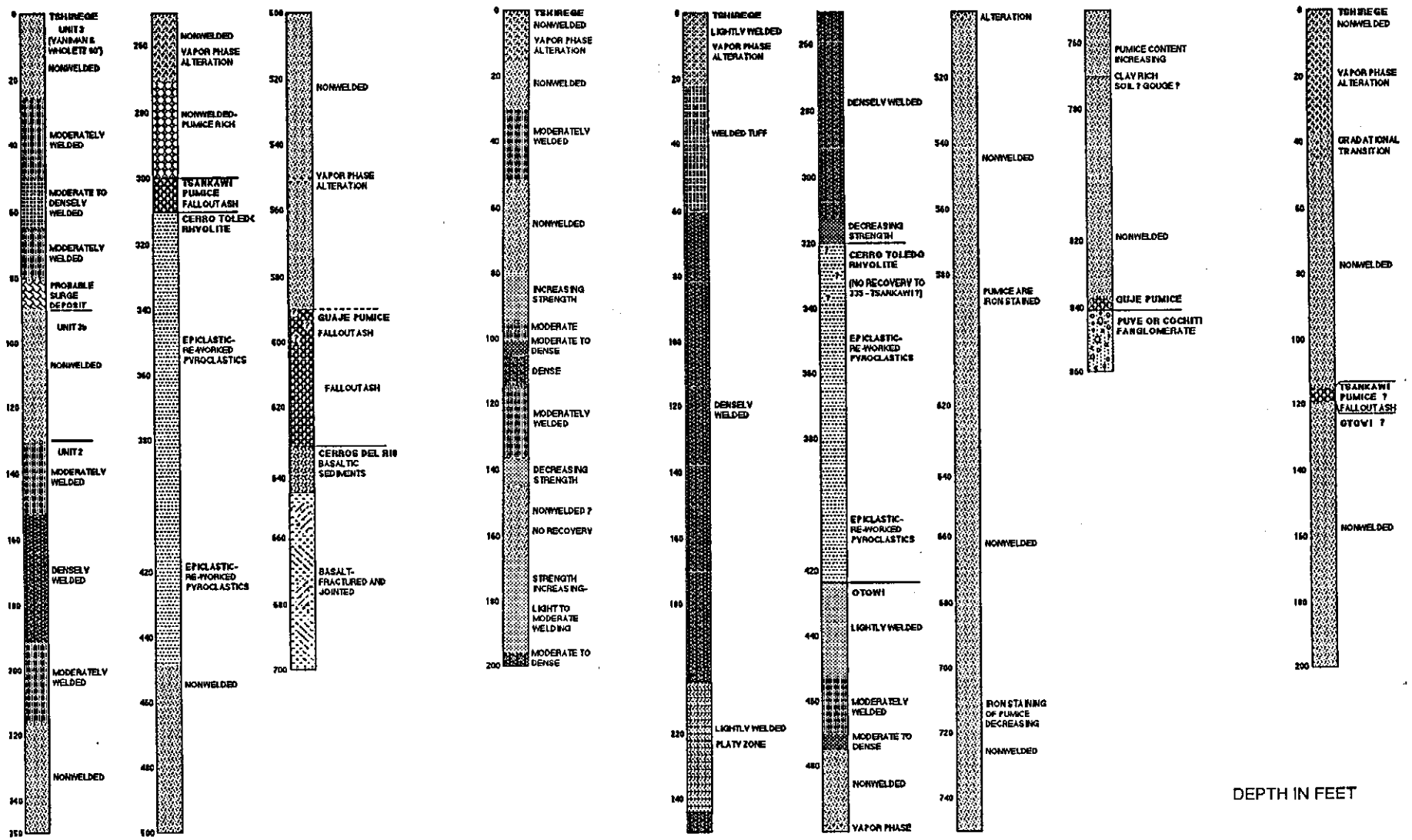






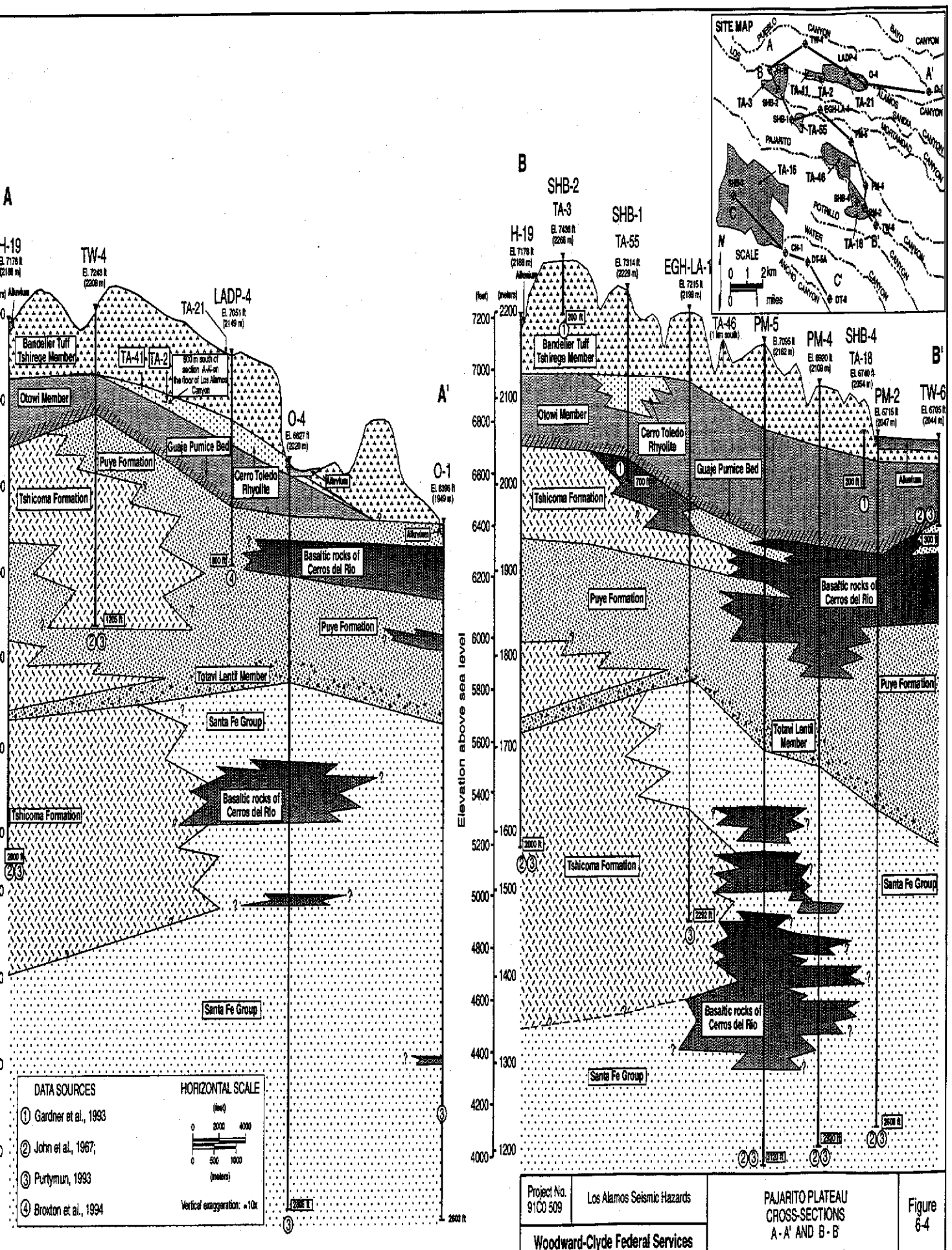


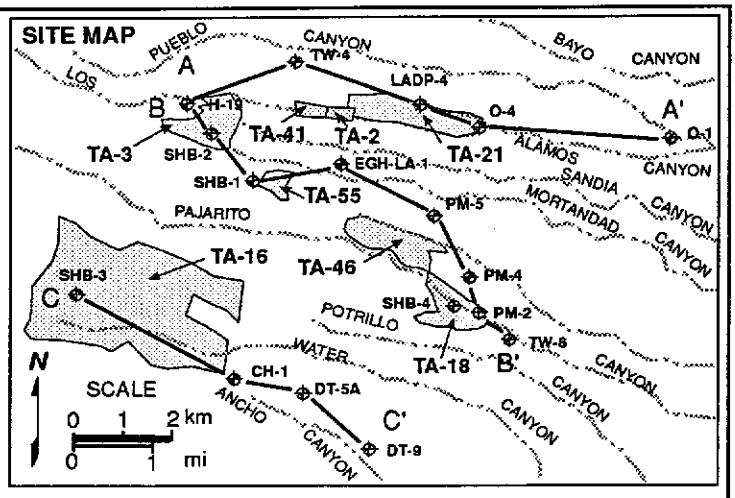
Project No. 91C0509	Los Alamos Seismic Hazards	MAP SHOWING LOCATION OF SEISMIC HAZARDS BORINGS	Figure 6-2
Woodward-Clyde Federal Services			

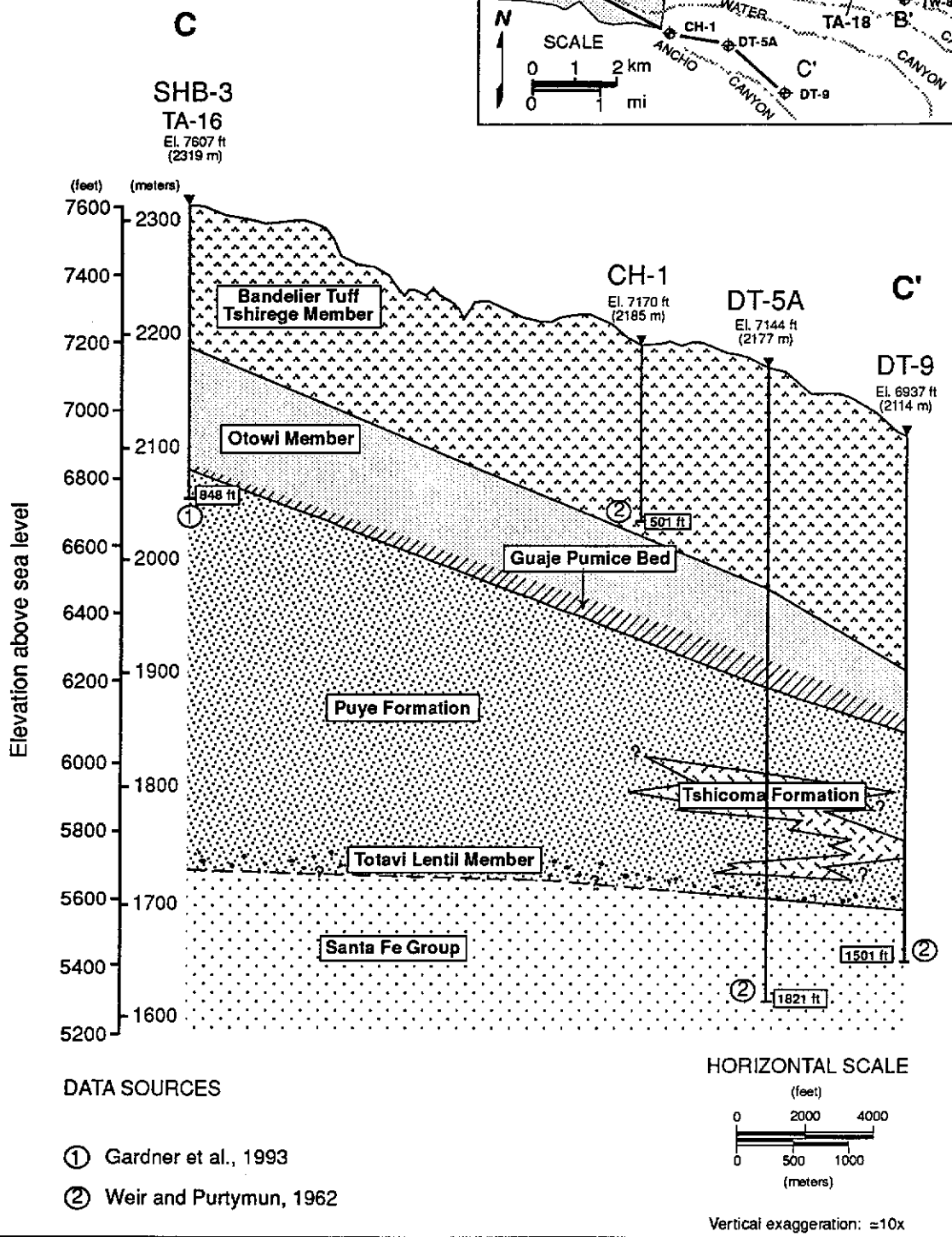


Project No. 91C0509	Los Alamos Seismic Hazards	SCHEMATIC LOGS FOR CORE HOLES SHB-1, SHB-2, SHB-3 AND SHB-4	Figure 6-3
Woodward-Clyde Federal Services			

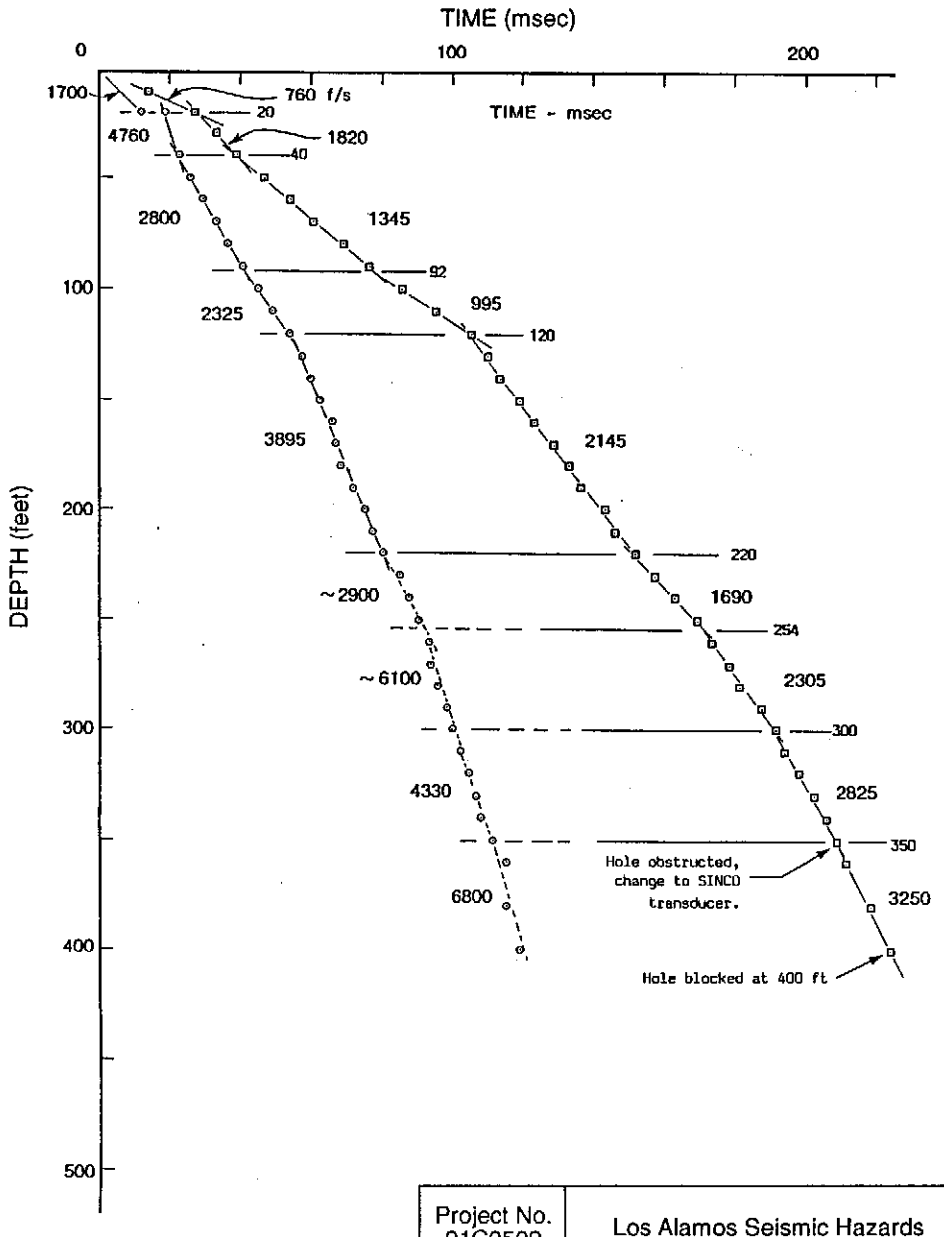
91C0509A-1300/101994

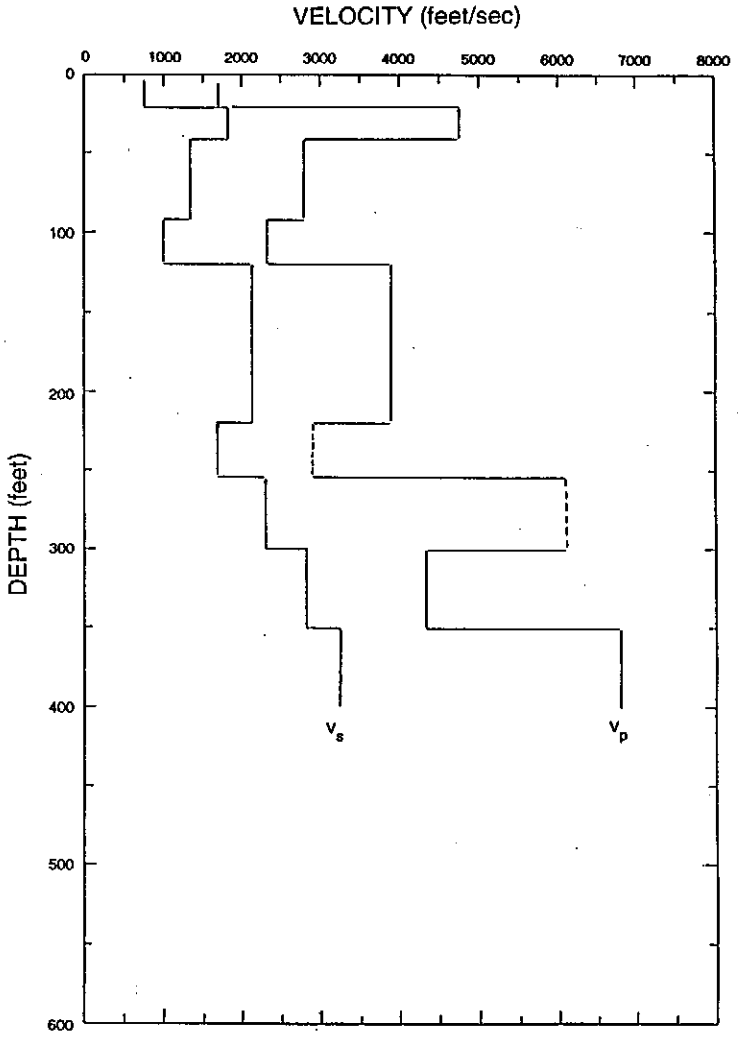

SITE MAP
A
A'
B
B'
C
C'
TW-4
LADP-1
O-1
TA-1
TA-2
TA-21
TA-3
SHB-2
EGH-LA-1
TA-55
PM-5
TA-16
TA-46
SHB-1
PM-1
PM-2
SHB-4
TA-18
TW-6
CH-1
DT-5A
DT-4
PAJARITO
POTRILLO
WATER
ANCHO
CANYON
SANDIA
MORTANDAD
LOS
PUEBLO
BAYO
SCALE
0 1 2km
0 1 miles
A
A'
B
B'
H-19
El. 7178 ft (2188 m)
Alluvium
TW-4
El. 7249 ft (2208 m)
LADP-4
El. 7651 ft (2149 m)
TA-21
TA-41
TA-2
800 m south of section A-A' on the floor of Los Alamos Canyon
O-4
El. 6627 ft (2020 m)
O-1
El. 6396 ft (1949 m)
Bandelier Tuff Tshirege Member
Otowi Member
Guaje Pumice Bed
Puye Formation
Cerro Toledo Rhyolite
Tshicoma Formation
Basaltic rocks of Cerros del Rio
Totavi Lentil Member
Santa Fe Group
1205 ft
800 ft
2800 ft
2600 ft
SHB-2
TA-3
El. 7436 ft (2266 m)
SHB-1
TA-55
El. 7314 ft (2229 m)
EGH-LA-1
El. 7215 ft (2199 m)
TA-46 (1 km south)
PM-5
El. 7295 ft (2182 m)
PM-4
El. 6920 ft (2109 m)
SHB-4
TA-18
El. 6740 ft (2054 m)
PM-2
El. 6715 ft (2047 m)
TW-6
El. 6705 ft (2044 m)
Elevation above sea level
(feet) (meters)
7200 2200
7000 2100
6800 2000
6600 1900
6400 1800
6200 1700
6000 1600
5800 1500
5600 1400
5400 1300
5200 1200
5000
4800
4600
4400
4200
4000
390 ft
700 ft
300 ft
2000 ft
2292 ft
2720 ft
2920 ft
2608 ft
DATA SOURCES
① Gardner et al., 1993
② John et al., 1967;
③ Purtymun, 1993
④ Broxton et al., 1994
HORIZONTAL SCALE
(feet)
0 2000 4000
0 500 1000
(meters)
Vertical exaggeration: ≈10x
Project No. 9100 509
Los Alamos Seismic Hazards
Woodward-Clyde Federal Services
PAJARITO PLATEAU CROSS-SECTIONS A - A' AND B - B'
Figure 6-4



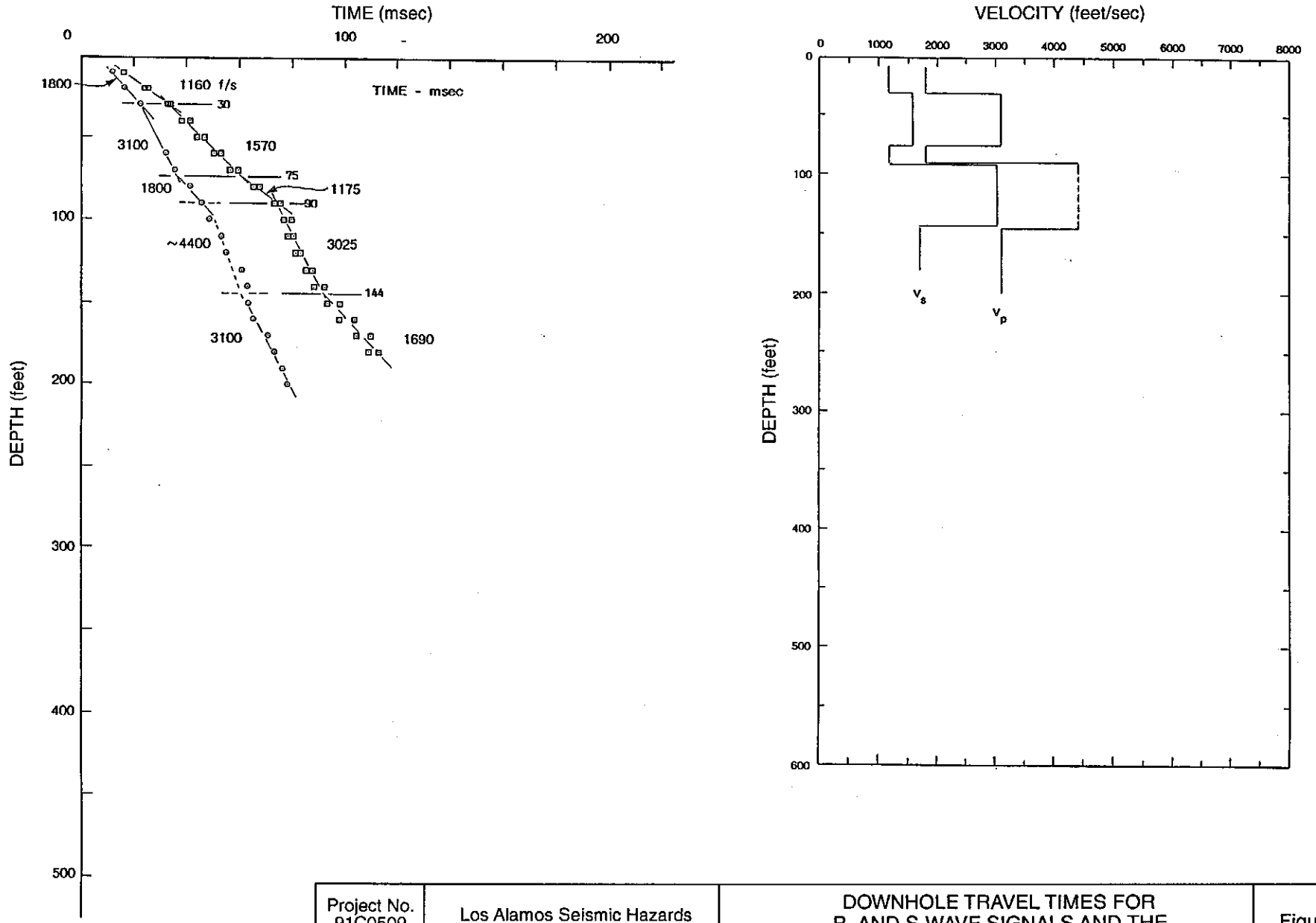


Project No. 91C0509	Los Alamos Seismic Hazards	PAJARITO PLATEAU CROSS-SECTION C - C'	Figure 6-5
Woodward-Clyde Federal Services			



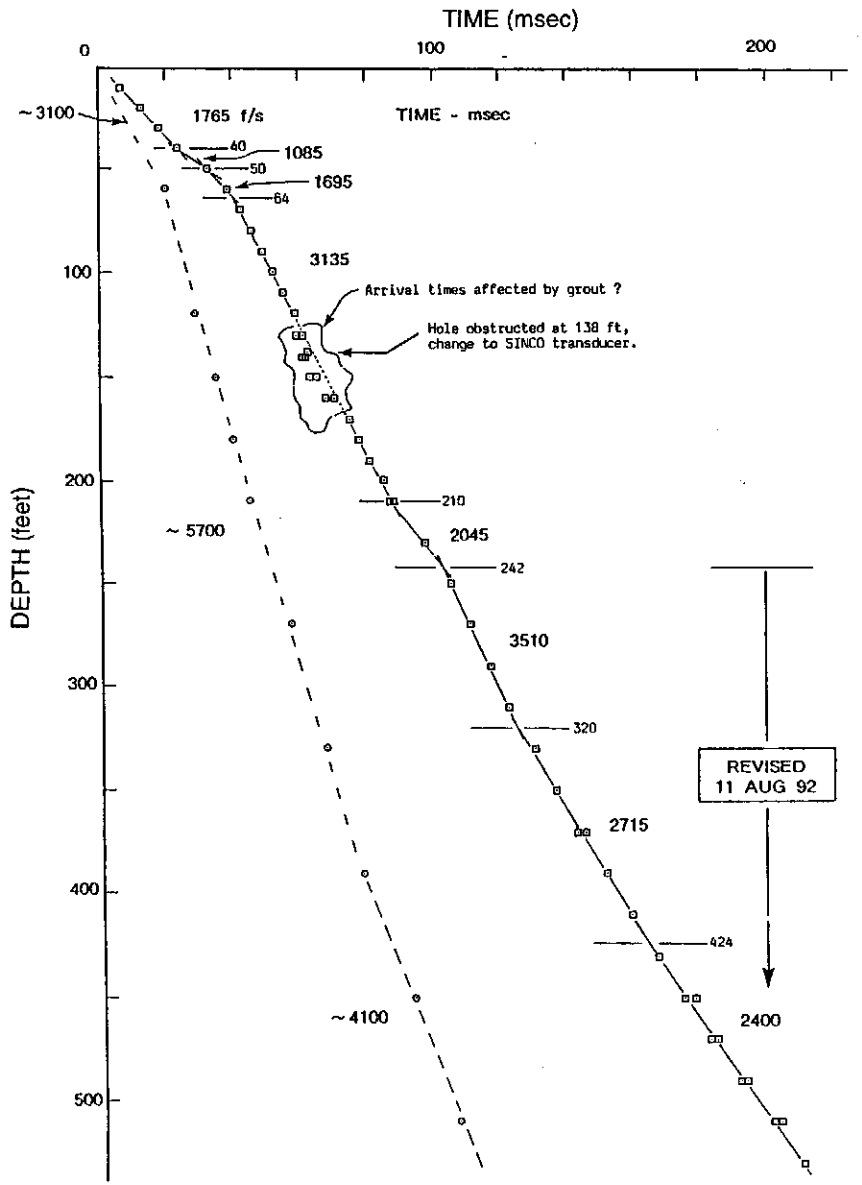


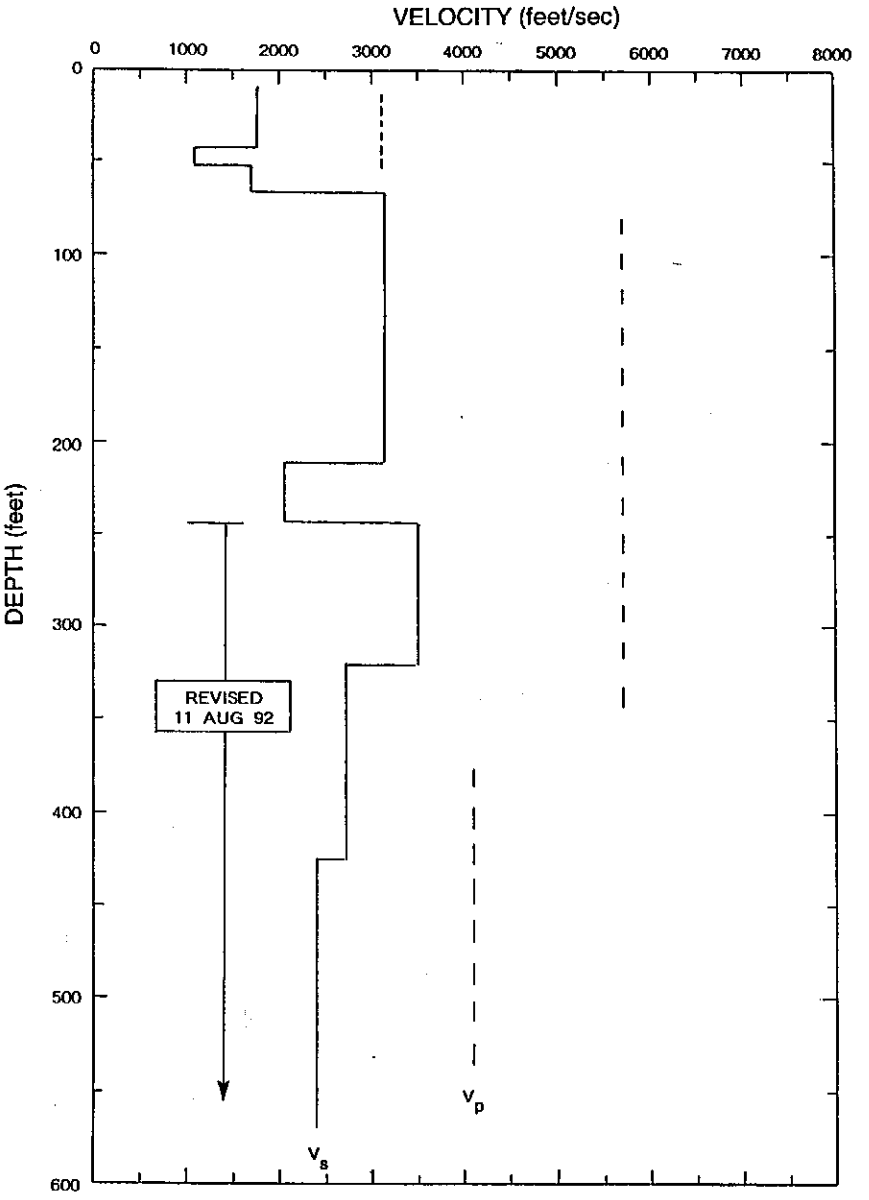
Project No. 91C0509	Los Alamos Seismic Hazards	DOWNHOLE TRAVEL TIMES FOR P- AND S-WAVE SIGNALS AND THE RESULTING VELOCITY PROFILES FOR SHB-1	Figure 6-6
Woodward-Clyde Federal Services			



Project No. 91C0509	Los Alamos Seismic Hazards	DOWNHOLE TRAVEL TIMES FOR P- AND S-WAVE SIGNALS AND THE RESULTING VELOCITY PROFILES FOR SHB-2	Figure 6-7
Woodward-Clyde Federal Services			

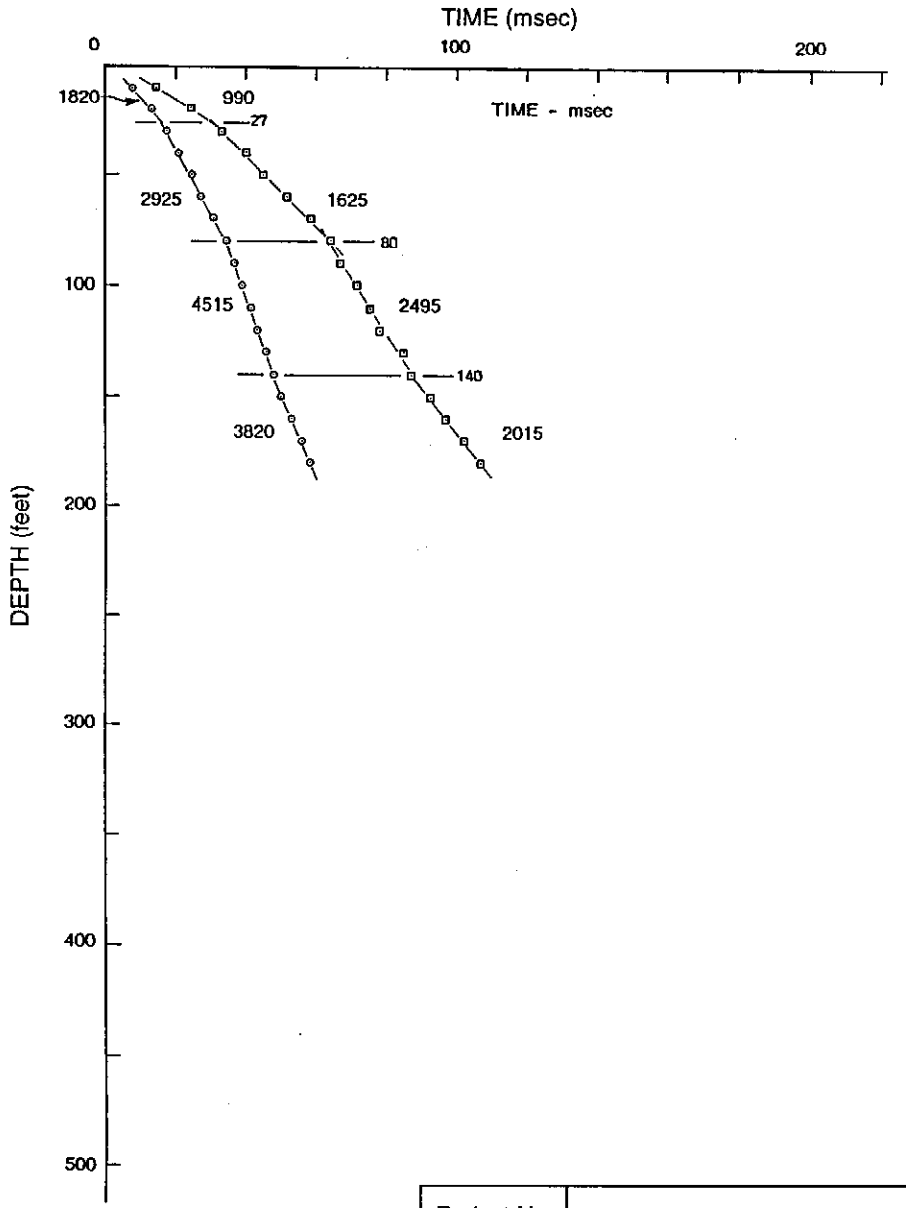
91C0509A-1300/101994

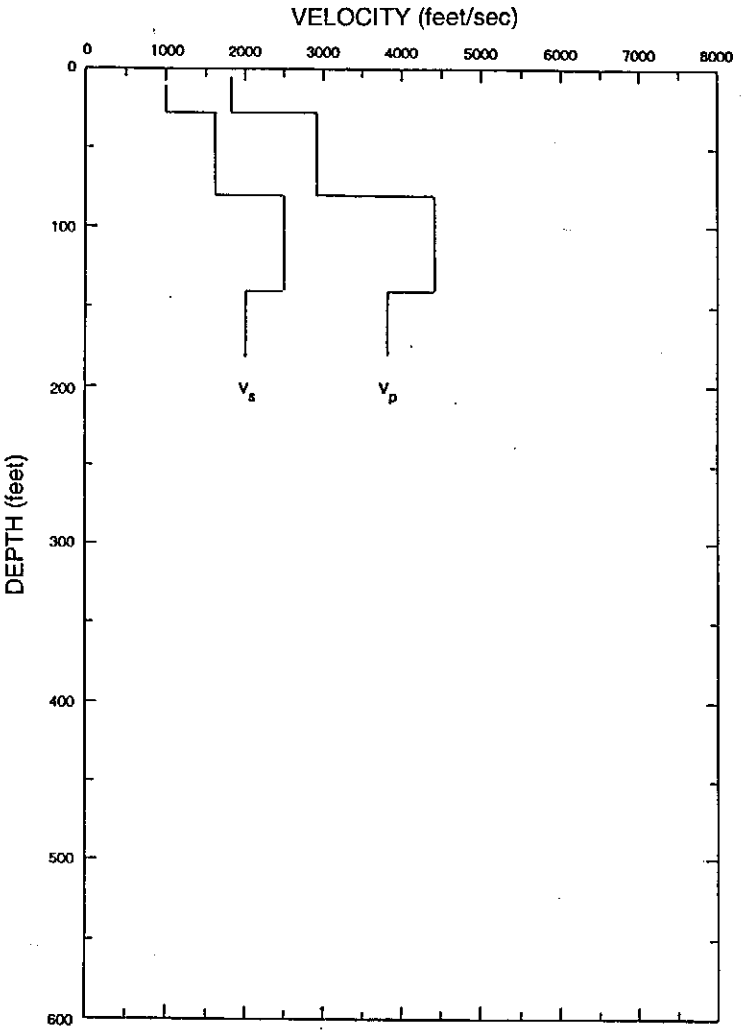




Project No. 91C0509	Los Alamos Seismic Hazards	DOWNHOLE TRAVEL TIMES FOR P- AND S-WAVE SIGNALS AND THE RESULTING VELOCITY PROFILES FOR SHB-3	Figure 6-8
Woodward-Clyde Federal Services			

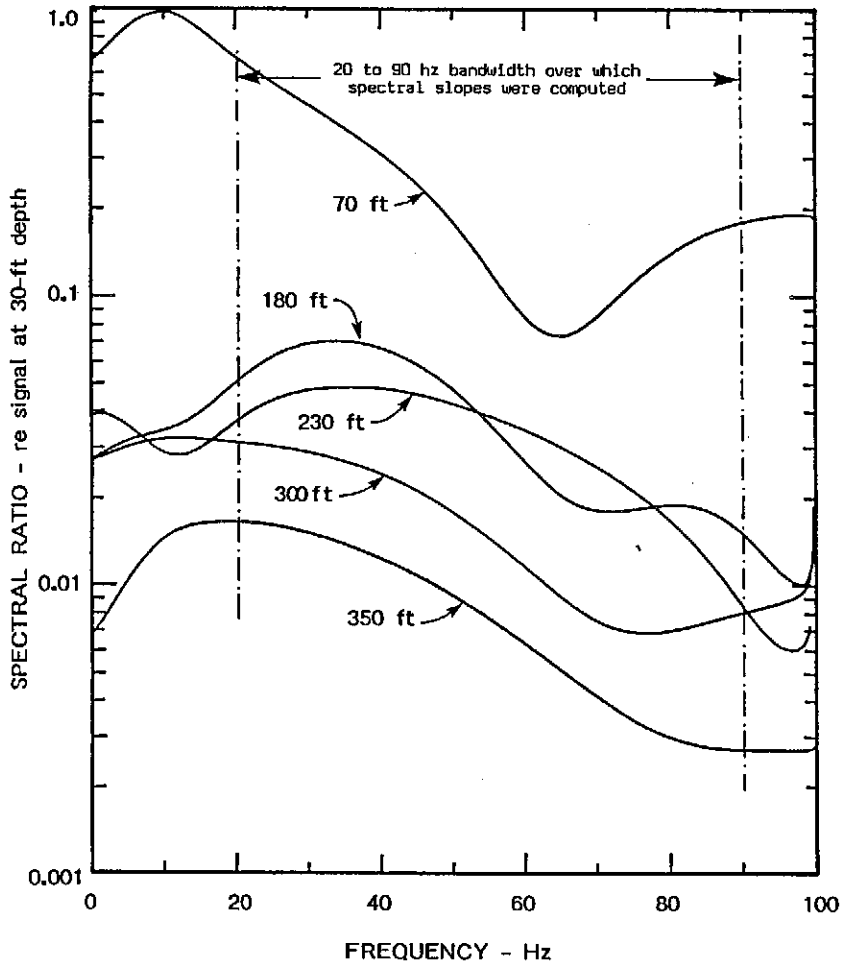
91C0509A-1300/101994



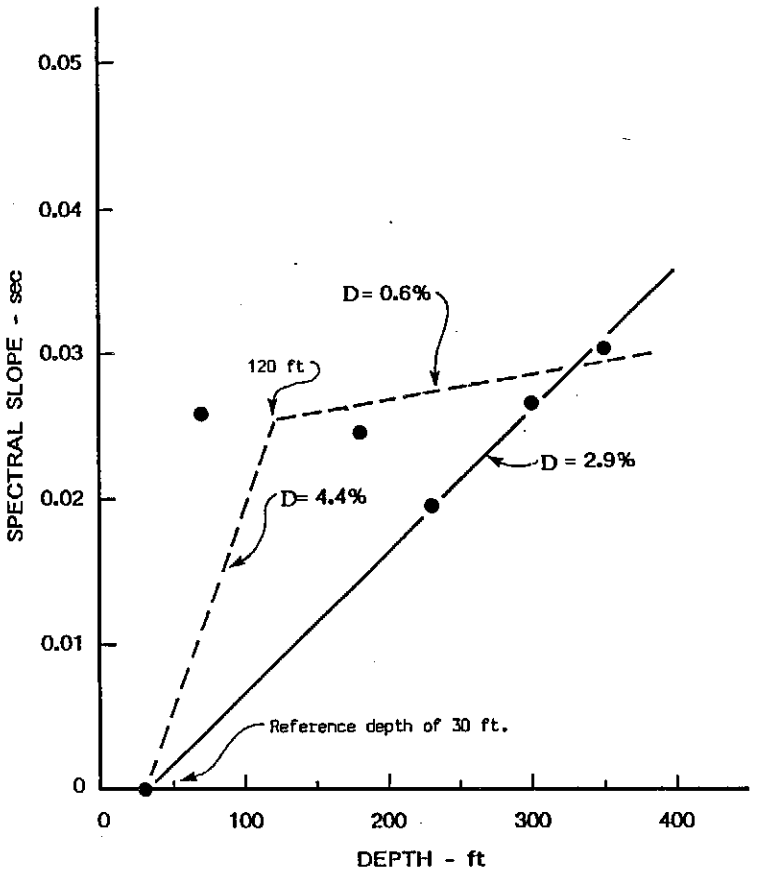


Project No. 91C0509	Los Alamos Seismic Hazards	DOWNHOLE TRAVEL TIMES FOR P- AND S-WAVE SIGNALS AND THE RESULTING VELOCITY PROFILES FOR SHB-4	Figure 6-9
Woodward-Clyde Federal Services			

91C0509A-1300/101994



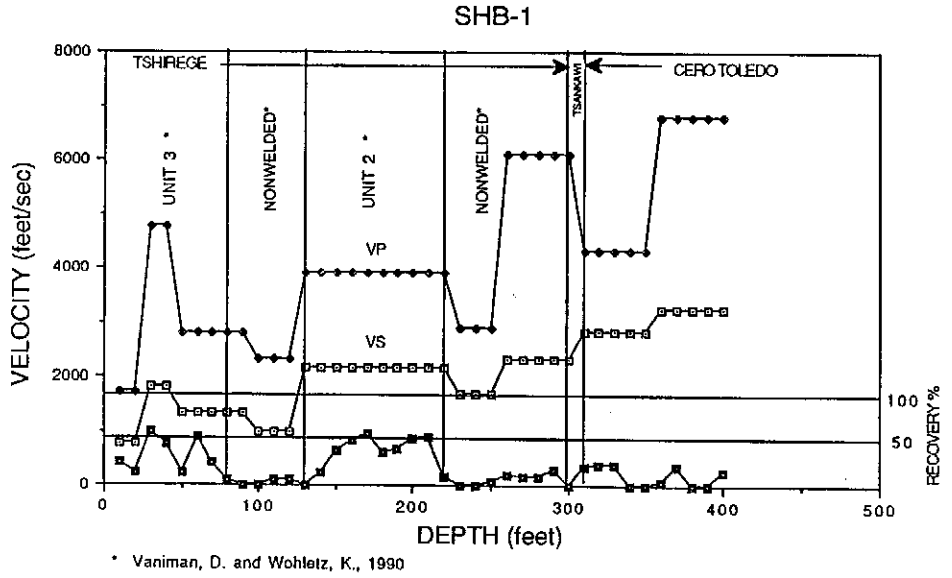
(a) Spectral ratios of downhole S-wave signals in SHB-1 computed with respect to the spectrum at 30-ft

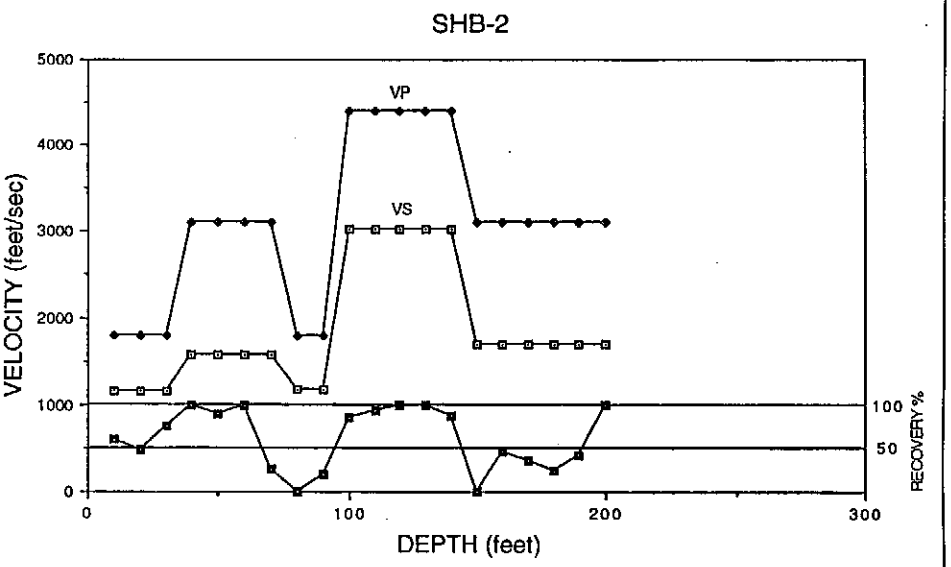


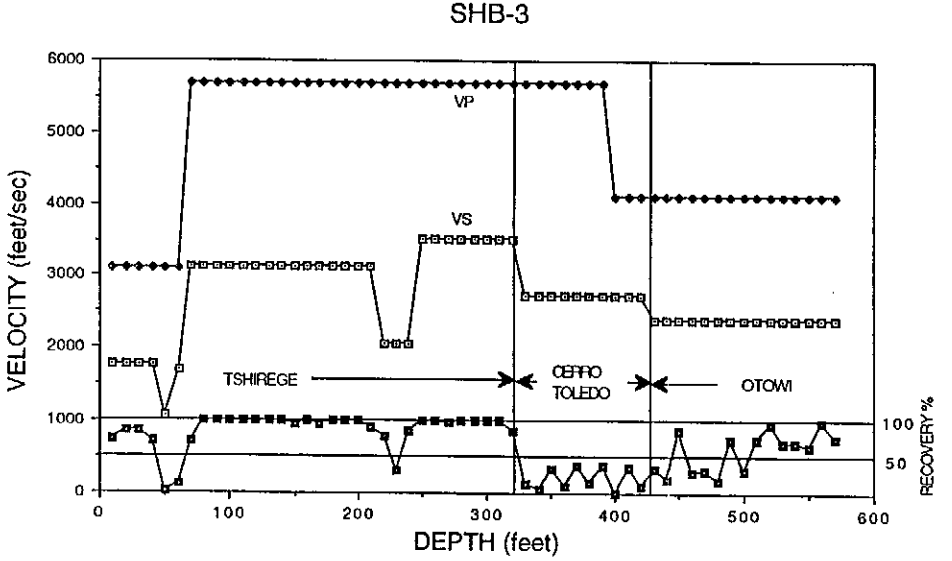
(b) The spectral slopes as a function of depth and the two possible damping scenarios

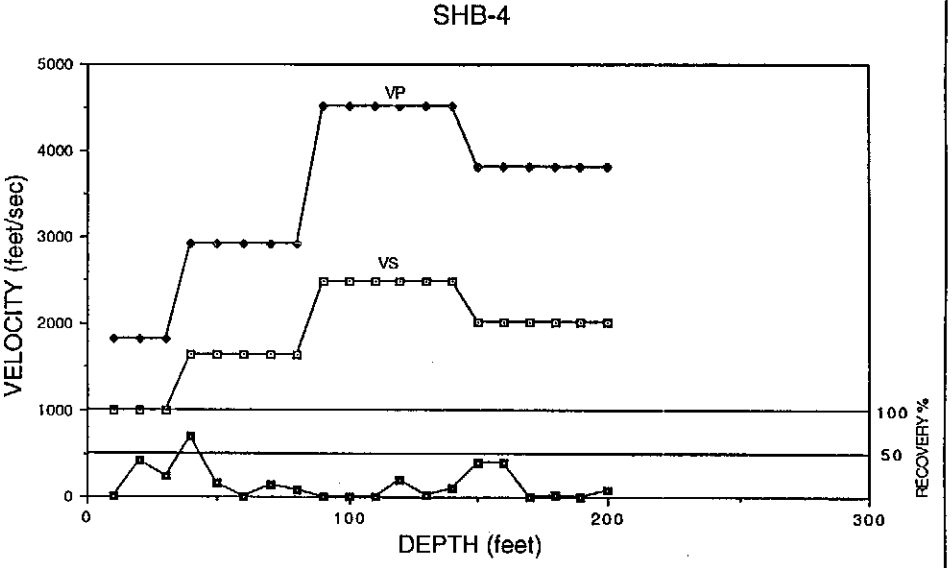
Project No. 91C0509	Los Alamos Seismic Hazards	S-WAVE DAMPING MEASUREMENTS IN SHB -1	Figure 6-10
Woodward-Clyde Federal Services			

91C0509A-1300/101994

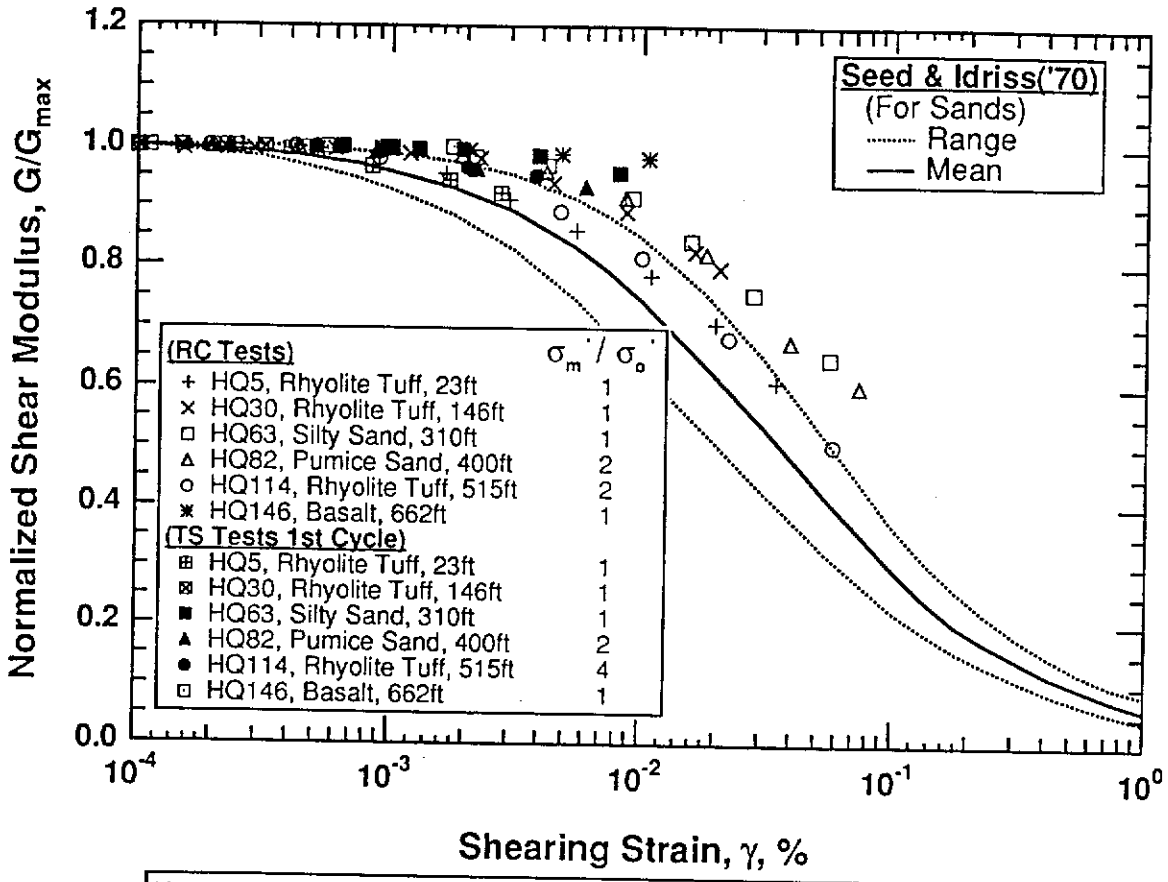








Project No. 91C0509	Los Alamos Seismic Hazards	PERCENTAGE CORE RECOVERY VERSUS VELOCITY FOR COREHOLES SHB-1 THROUGH SHB-4	Figure 6-11
Woodward-Clyde Federal Services			

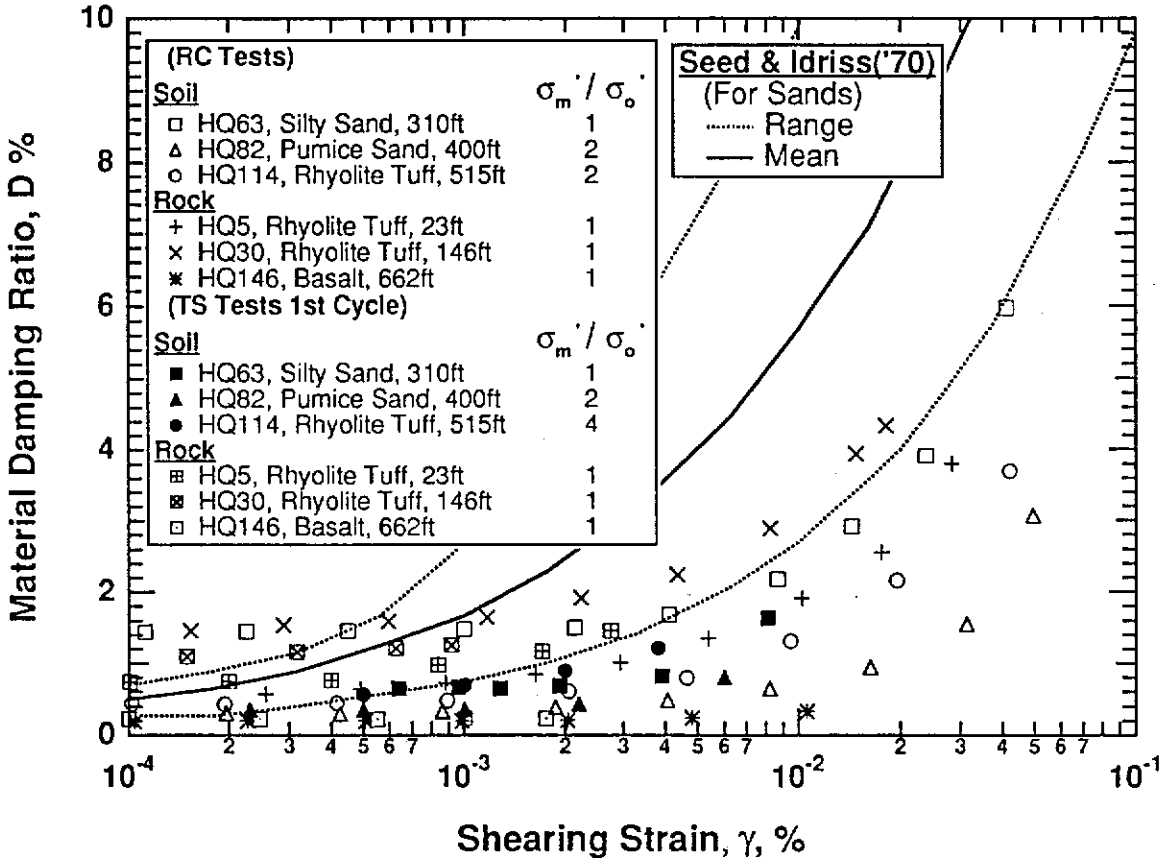


Note:

1. Only results at a confining pressure within a factor of four of the estimated in situ mean effective stress are plotted.
2. σ_m' = estimated in situ mean effective stress using K_o = 0.5.
3. σ_o' = effective confining pressure of the test.

Source: Stokoe et al., 1993

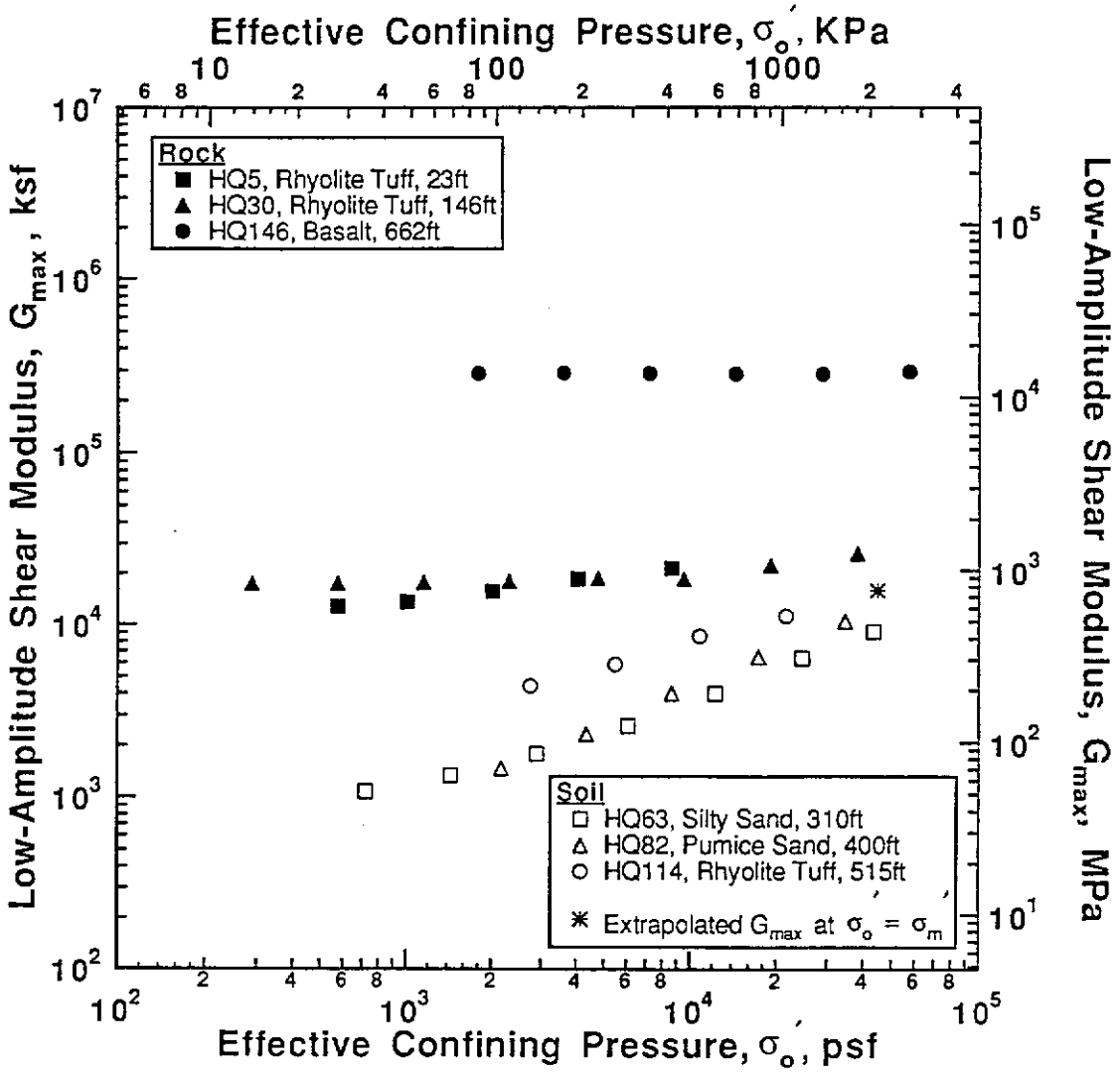
Project No. 91C0509	Los Alamos Seismic Hazards	VARIATION IN NORMALIZED SHEAR MODULUS WITH SHEARING STRAIN FROM RESONANT COLUMN AND TORSIONAL SHEAR TESTS	Figure 6-12
Woodward-Clyde Federal Services			



Note:
1. Only results at a confining pressure within a factor of four of the estimated in situ mean effective stress are plotted.
2. σ_m' = estimated in situ mean effective stress using $K_o = 0.5$.
3. σ_o' = effective confining pressure of the test.
4. Shearing strains were corrected to the average of the first 3 free-vibration cycles.

Source: Stokoe et al., 1993

Project No. 91C0509	Los Alamos Seismic Hazards	VARIATION IN MATERIAL DAMPING RATIO WITH SHEARING STRAIN FOR $\gamma \leq 0.1\%$ FROM RESONANT COLUMN AND TORSIONAL SHEAR TESTS	Figure 6-13
Woodward-Clyde Federal Services			

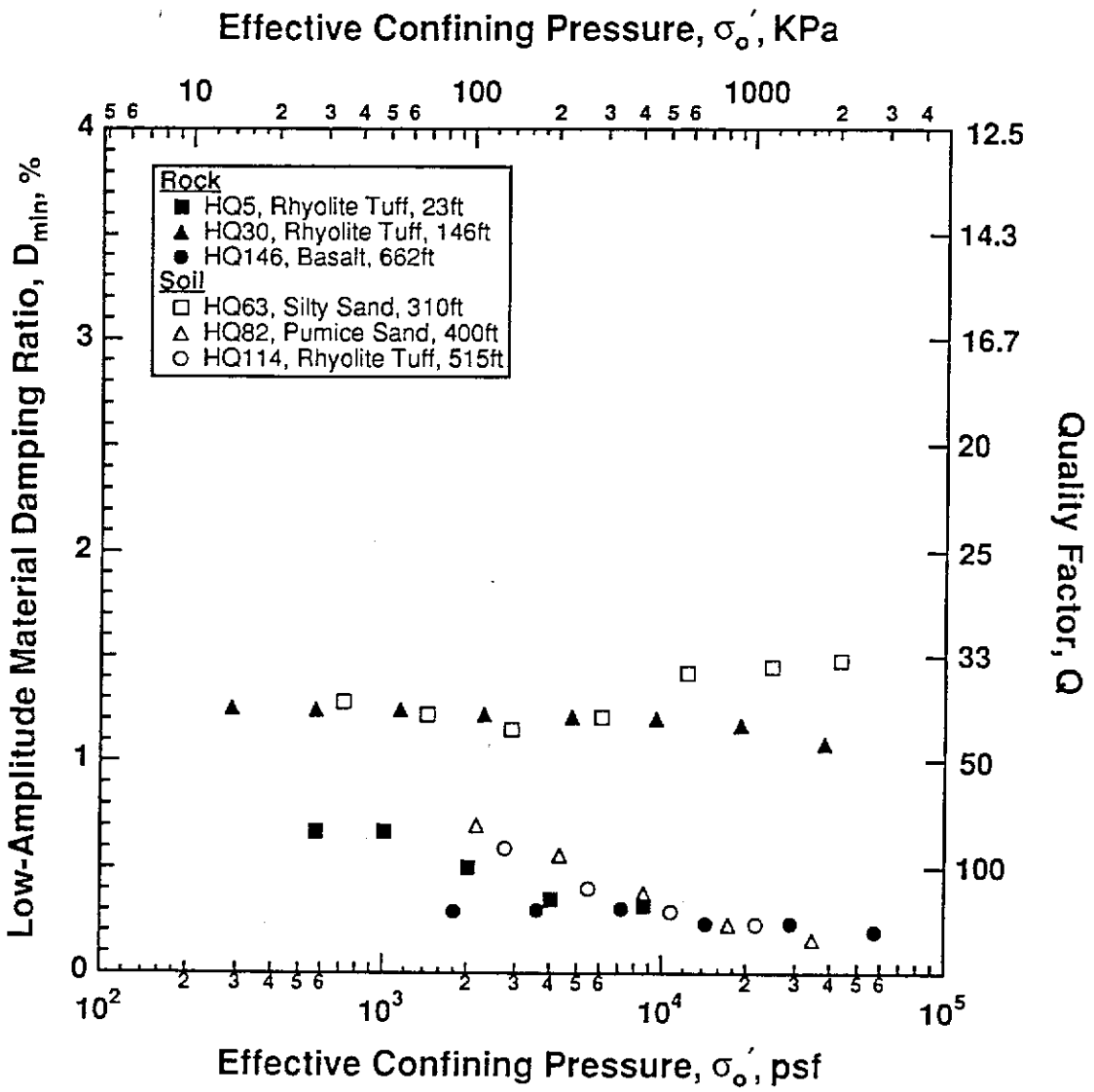


Notes:

1. G_{max} measured at t = 1000 min. at each σ_o' for each soil specimen (HQ63, HQ82 and HQ114) and at 50 min. for rock specimens HQ5 and HQ30 and at 20 min. for rock specimen HQ146.

Source: Stokoe et al., 1993

Project No. 91C0509	Los Alamos Seismic Hazards	VARIATION IN LOW-AMPLITUDE SHEAR MODULUS WITH EFFECTIVE CONFINING PRESSURE FROM RESONANT COLUMN TESTS	Figure 6-14
Woodward-Clyde Federal Services			



Notes:

1. D_{min} measured at t = 1000 min. at each σ_o' for each soil specimen (HQ63, HQ82 and HQ114) and at 50 min. for rock specimens HQ5 and HQ30 and at 20 min. for rock specimen HQ146.

Source: Stokoe et al., 1993

Project No. 91C0509	Los Alamos Seismic Hazards	VARIATION IN LOW-AMPLITUDE MATERIAL DAMPING RATIO WITH EFFECTIVE CONFINING PRESSURE FROM RESONANT COLUMN TESTS	Figure 6-15
Woodward-Clyde Federal Services			

TA-2

Elevation 2097 m

Depth (m)	Lithology	V_s (m/sec)	ρ (g/cm^3)	
10	Cerro Toledo	600	1.7	Otowi Member of Bandelier Tuff
60	Nonwelded tuff	500	1.6	
72	Guaje Pumice	700	1.7	
145	Puye Formation (Fanglomerate)	1000	2.2	
255	Tschicoma Formation (Dacitic rocks)	3000	2.8	
320	Puye Formation (Fanglomerate)	1100	2.3	
340	Totavi Lentil (Conglomerate)	1100	2.3	
625	Tschicoma Formation (Dacitic rocks)	3000	2.8	
650	Santa Fe Group (Sandstone, siltstone and conglomerate)	1300	2.5	
800		1400	2.5	
950		1500	2.5	
1000		1600	2.5	

TA-3 SHB2

Elevation 2268 m

Depth (m)	Lithology	V_s (m/sec)	ρ (g/cm^3)	
9	Nonwelded tuff	354*	1.6	Tshirege Member of Bandelier Tuff
23	Moderately to nonwelded tuff	479*	1.6	
28	Nonwelded tuff	358*	1.6	
44	Moderately to densely welded tuff	923*	1.8	
60	Nonwelded tuff	515*	1.7	
138	Moderately to nonwelded tuff	700	1.7	
210	Nonwelded tuff	700	1.7	Otowi Member of Bandelier Tuff
225	Guaje Pumice	1000	1.9	
330	Tschicoma Formation (Dacitic rocks)	3000	2.8	
350	Puye Formation (Fanglomerate)	1100	2.3	
450		1200	2.4	
520	Tschicoma Formation (Dacitic rocks)	3000	2.8	
530	Totavi Lentil (Conglomerate)	1300	2.5	
900	Tschicoma Formation (Dacitic rocks)	3000	2.8	
950	Santa Fe Group (Sandstone, siltsone and conglomerate)	1500	2.5	
1000		1600	2.5	

Note: Profiles below depth of borehole penetration or sites with no boreholes are estimated from other boreholes and geologic cross-sections

* Downhole velocity measurements

Project No. 91C0509	Los Alamos Seismic Hazards	TA-2 & TA-3 GEOLOGIC AND S-WAVE VELOCITY PROFILES	Figure 6-16
Woodward-Clyde Federal Services			

TA-16
SHB3

Elevation 2320 m

Depth (m)	Lithology	V_s (m/sec)	ρ (g/cm^3)	
12	Lightly welded tuff	538*	1.6	Tshirege Member of Bandelier Tuff
15	Welded tuff	331*	1.6	
18	Welded tuff	517*	1.6	
64	Densely welded tuff	956*	1.8	
74	Lightly welded tuff	624*	1.7	
98	Densely welded tuff	1071*	1.8	
129	Cerro Toledo Rhyolite	828*	1.7	
175	Lightly welded to nonwelded tuff and Guaje Pumice bed	732*	1.7	Otowi Member of Bandelier Tuff
		900	1.8	
256	Puye Formation (Fanglomerate)	1100	2.3	
350		1200	2.4	
500		1300	2.5	
575	Totavi Lentil (Conglomerate)	1300	2.5	
585	Santa Fe Group (Sandstone, siltstone and conglomerate)	1300	2.5	
650		1400	2.5	
800		1500	2.5	
950		1600	2.5	
1000				

Note: Profiles below depth of borehole penetration or sites with no boreholes are estimated from other boreholes and geologic cross-sections

TA-18
SHB4

Elevation 2044 m

Depth (m)	Lithology	V_s (m/sec)	ρ (g/cm^3)	
8	Nonwelded tuff	302*	1.6	Tshirege Member of Bandelier Tuff
24	Nonwelded tuff	496*	1.6	
43	Nonwelded tuff & Tsankawi Pumice	761*	1.7	
85	Nonwelded tuff	615*	1.7	Otowi Member of Bandelier Tuff
125		700	1.7	
135	Guaje Pumice	1000	1.9	
245	Cerros del Rio Basaltic rocks	3000	2.8	
315	Puye Formation (Fanglomerate)	1100	2.3	
350		1200	2.4	
395	Totavi Lentil (Conglomerate)	1200	2.4	
425	Santa Fe Group (Sandstone, siltstone and conglomerate)	1200	2.5	
500		1300	2.5	
650		1400	2.5	
800		1500	2.5	
950		1600	2.5	
1000				

* Downhole velocity measurements

Project No. 91C0509	Los Alamos Seismic Hazards	TA-16 & TA-18 GEOLOGIC AND S-WAVE VELOCITY PROFILES	Figure 6-17
Woodward-Clyde Federal Services			

TA-21

Elevation 2179 m

Depth (m)	Non-welded tuff Lithology	V_s (m/sec)	ρ (g/cm^3)	
10	Moderately to densely welded tuff	250	1.6	Tshirege Member of Bandelier Tuff
15	Nonwelded tuff	550	1.7	
30	Moderately to densely welded tuff	400	1.6	
40	Nonwelded tuff	300	1.6	
70	Moderately to densely welded tuff	650	1.7	Otowi Member of Bandelier Tuff
85	Nonwelded tuff	500	1.7	
100	Nonwelded/vapor phase altered tuff	700	1.7	
130	Cerro Toledo	900	1.8	
190	Nonwelded tuff	700	1.7	
200	Guaje Pumice	1000	1.9	
350	Puye Formation (Fanglomerate)	1100	2.3	
385		1200	2.4	
415	Totavi Lentil (Conglomerate)	1200	2.4	
510	Santa Fe Group (Sandstone, siltstone and conglomerate)	1200	2.4	
570	Cerros del Rio Basaltic Rocks	3000	2.8	
650	Santa Fe Group (Sandstone, siltstone and conglomerate)	1300	2.5	
800		1400	2.5	
950		1500	2.5	
1000		1600	2.5	

Note: Profiles below depth of borehole penetration or sites with no boreholes are estimated from other boreholes and geologic cross-sections

TA-41

Elevation 2112 m

Depth (m)	Lithology	V_s (m/sec)	ρ (g/cm^3)	
10	Cerro Toledo Rhyolite	600	1.7	
52	Nonwelded Tuff	500	1.6	Otowi Member of Bandelier Tuff
62	Guaje Pumice	700	1.7	
135	Puye Formation (Fanglomerate)	1000	2.2	
270	Tschicoma Formation (Dacitic rocks)	3000	2.8	
345	Puye Formation (Fanglomerate)	1100	2.3	
360	Totavi Lentil (Conglomerate)	1200	2.4	
650	Tschicoma Formation (Dacitic rocks)	3000	2.8	
800	Santa Fe Group (Sandstone, siltstone and conglomerate)	1400	2.5	
950		1500	2.5	
1000		1600	2.5	

* Downhole velocity measurements

roject No. 01C0509	Los Alamos Seismic Hazards	TA-21 & TA-41 GEOLOGIC AND S-WAVE VELOCITY PROFILES	Figure 6-18
Woodward-Clyde Federal Services			

TA-46

Elevation 2164 m

Depth (m)	Lithology	V_S (m/sec)	ρ (g/cm^3)	
10	Moderately to densely welded tuff	400	1.6	Tshirege Member of Bandelier Tuff
20	Nonwelded tuff	300	1.6	
50	Moderately to densely welded tuff	650	1.7	
65	Nonwelded tuff	500	1.6	
80	Nonwelded/vapor phase altered tuff	700	1.7	
200	Nonwelded tuff	700	1.7	Otowi Member of Bandelier Tuff
215	Guaje Pumice	1000	1.9	
240	Puye Formation (Fanglomerate)	1100	2.2	
275	Tschicoma Formation (Dacitic rocks)	3000	2.8	
350	Puye Formation (Fanglomerate)	1100	2.3	
415		1200	2.4	
435	Totavi Lentil (Conglomerate)	1200	2.4	
500	Santa Fe Group (Sandstone, siltsone and conglomerate)	1200	2.4	
535		1300	2.5	
555	Cerros del Rio Basaltic Rocks	3000	2.8	
590	Santa Fe Group (Sandstone, siltstone and conglomerate)	1300	2.5	
635	Cerros del Rio Basaltic Rocks	3000	2.8	
670	Santa Fe Group (Sandstone, siltstone and conglomerate)	1350	2.5	
820	Cerros del Rio Basaltic Rocks	3000	2.8	
950	Santa Fe Group (Sandstone, siltstone and conglomerate)	1500	2.5	
1000		1600	2.5	

Note: Profiles below depth of borehole penetration or sites with no boreholes are estimated from other boreholes and geologic cross-sections

TA-55 SHB1

Elevation 2230 m

Depth (m)	Lithology	V_S (m/sec)	ρ (g/cm^3)	
6	Nonwelded tuff	232*	1.6	Tshirege Member of Bandelier Tuff
12	Moderately welded tuff	555*	1.6	
28	Moderately to densely welded tuff	410*	1.6	
37	Nonwelded tuff	303*	1.6	
67	Moderately to densely welded tuff	654*	1.7	
78	Nonwelded tuff	515*	1.6	
95	Nonwelded/vapor phase altered tuff	703*	1.7	
107	Cerro Toledo Rhyolite epiclastic reworked pyroclastics	862	1.7	
137		991*	1.8	
180	Nonwelded tuff	700	1.7	Otowi Member of Bandelier Tuff
192	Guaje Pumice	1000	1.9	
197	Basaltic sediments	1500	2.5	
225	Cerros del Rio Basaltic rocks	3000	2.8	
310	Tschicoma Formation (Dacitic rocks)	3000	2.8	
350	Puye Formation (Fanglomerate)	1100	2.3	
460		1200	2.4	
475	Totavi Lentil (Conglomerate)	1200	2.4	
820	Tschicoma Formation (Dacitic rocks)	3000	2.8	
950	Santa Fe Group (Sandstone, siltstone and conglomerate)	1500	2.5	
1000		1600	2.5	

* Downhole velocity measurements

Project No. 91C0509	Los Alamos Seismic Hazards	TA-46 & TA-55 GEOLOGIC AND S-WAVE VELOCITY PROFILES	Figure 6-19
Woodward-Clyde Federal Services			

TA-2

Elevation 2097 m

Depth (m)	Lithology	V_P (m/sec)	ρ (g/cm^3)	
10	Cerro Toledo	1070	1.7	Otowi Member of Bandelier Tuff
60	Nonwelded tuff	905	1.6	
72	Guaje Pumice	1230	1.7	
145	Puye Formation (Fanglomerate)	2080	2.2	
255	Tschicoma Formation (Dacitic rocks)	5190	2.8	
320	Puye Formation (Fanglomerate)	2290	2.3	
340	Totavi Lentil (Conglomerate)	2290	2.3	
625	Tschicoma Formation (Dacitic rocks)	5190	2.8	
650	Santa Fe Group (Sandstone, siltstone and conglomerate)	2705	2.5	
800		2910	2.5	
950		3120	2.5	
1000		3330	2.5	

Note: Profiles below depth of borehole penetration or sites with no boreholes are estimated from other boreholes and geologic cross-sections

TA-3 SHB2

Elevation 2268 m

Depth (m)	Lithology	V_P (m/sec)	ρ (g/cm^3)	
9	Nonwelded tuff	549*	1.6	Tshirege Member of Bandelier Tuff
23	Moderately to non-welded tuff	946*	1.6	
28	Nonwelded tuff	549*	1.6	
44	Moderately to densely welded tuff	1590	1.8	
60	Nonwelded tuff	946*	1.7	
138	Moderately to non-welded tuff	1230	1.7	
210	Nonwelded tuff	1230	1.7	Otowi Member of Bandelier Tuff
225	Guaje Pumice	1715	1.9	
330	Tschicoma Formation (Dacitic rocks)	5190	2.8	
350	Puye Formation (Fanglomerate)	2290	2.3	
450		2495	2.4	
520	Tschicoma Formation (Dacitic rocks)	5190	2.8	
530	Totavi Lentil (Conglomerate)	2705	2.5	
900	Tschicoma Formation (Dacitic rocks)	5190	2.8	
950	Santa Fe Group (Sandstone, siltsone and conglomerate)	3120	2.5	
1000		3330	2.5	

* Downhole velocity measurements

Project No. 91C0509	Los Alamos Seismic Hazards	TA-2 & TA-3 GEOLOGIC AND P-WAVE VELOCITY PROFILES	Figure 6-20
Woodward-Clyde Federal Services			

TA-16
SHB3

Elevation 2320 m

Depth (m)	Lithology	Vp (m/sec)	ρ (g/cm³)	
	Lightly welded tuff	970	1.6	Tshirege Member of Bandelier Tuff
12	Welded tuff	630	1.6	
15	Welded tuff	935	1.6	
18	Densely welded tuff	1645	1.8	
64	Lightly welded tuff	1105	1.7	
74	Densely welded tuff	1830	1.8	
98	Cerro Toledo Rhyolite	1435	1.7	
129	Lightly welded to non-welded tuff and Guaje Pumice bed	1280	1.7	Otowi Member of Bandelier Tuff
175		1555	1.8	
256	Puye Formation (Fanglomerate)	2290	2.3	
350		2495	2.4	
500		2705	2.5	
575	Totavi Lentil (Conglomerate)	2705	2.5	
585	Santa Fe Group (Sandstone, siltstone and conglomerate)	2705	2.5	
650		2910	2.5	
800		3120	2.5	
950		3330	2.5	
1000				

Note: Profiles below depth of borehole penetration or sites with no boreholes are estimated from other boreholes and geologic cross-sections

TA-18
SHB4

Elevation 2044 m

Depth (m)	Lithology	Vp (m/sec)	ρ (g/cm³)	
8	Nonwelded tuff	555*	1.6	Tshirege Member of Bandelier Tuff
24	Nonwelded tuff	892*	1.6	
43	Nonwelded tuff & Tsankawi Pumice	1377*	1.7	
85	Nonwelded tuff	1090	1.7	
125		1230	1.7	
135	Guaje Pumice	1715	1.9	Otowi Member of Bandelier Tuff
245	Cerros del Rio Basaltic Rocks	5190	2.8	
315	Puye Formation (Fanglomerate)	2290	2.3	
350		2495	2.4	
395	Totavi Lentil (Conglomerate)	2495	2.4	
425	Santa Fe Group (Sandstone, siltstone and conglomerate)	2495	2.5	
500		2705	2.5	
650		2910	2.5	
800		3120	2.5	
950		3330	2.5	
1000				

* Downhole velocity measurements

Project No. 91C0509	Los Alamos Seismic Hazards	TA-16 & TA-18 GEOLOGIC AND P-WAVE VELOCITY PROFILES	Figure 6-21
Woodward-Clyde Federal Services			

TA-21

Elevation 2179 m

Depth (m)	Lithology	Vp (m/sec)	ρ (g/cm³)	
10	Moderately to densely welded tuff	500	1.6	Tshirege Member of Bandelier Tuff
15	Nonwelded tuff	990	1.7	
30	Moderately to densely welded tuff	745	1.6	
40	Nonwelded tuff	580	1.6	
70	Moderately to densely welded tuff	1150	1.7	Otowi Member of Bandelier Tuff
85	Nonwelded tuff	905	1.7	
100	Nonwelded/vapor phase altered tuff	1230	1.7	
130	Cerro Toledo	1555	1.8	
190	Nonwelded tuff	1230	1.7	
200	Guaje Pumice	1715	1.9	
350	Puye Formation (Fanglomerate)	2290	2.3	
385		2495	2.4	
415	Totavi Lentil (Conglomerate)	2495	2.4	
510	Santa Fe Group (Sandstone, siltstone and conglomerate)	2495	2.4	
570	Cerros del Rio Basaltic Rocks	5190	2.8	
650	Santa Fe Group (Sandstone, siltstone and conglomerate)	2705	2.5	
800		2910	2.5	
950		3120	2.5	
1000		3330	2.5	

Note: Profiles below depth of borehole penetration or sites with no boreholes are estimated from other boreholes and geologic cross-sections

TA-41

Elevation 2112 m

Depth (m)	Lithology	Vp (m/sec)	ρ (g/cm³)	
10	Cerro Toledo Rhyolite	1070	1.7	Otowi Member of Bandelier Tuff
52	Nonwelded Tuff	905	1.6	
62	Guaje Pumice	1715	1.7	
135	Puye Formation (Fanglomerate)	2080	2.2	
270	Tschicoma Formation (Dacitic rocks)	5190	2.8	
345	Puye Formation (Fanglomerate)	2290	2.3	
360	Totavi Lentil (Conglomerate)	2495	2.4	
650	Tschicoma Formation (Dacitic rocks)	5190	2.8	
800	Santa Fe Group (Sandstone, siltstone and conglomerate)	2915	2.5	
950		3120	2.5	
1000		3330	2.5	

* Downhole velocity measurements

Project No. 91C0509	Los Alamos Seismic Hazards	TA-21 & TA-41 GEOLOGIC AND P-WAVE VELOCITY PROFILES	Figure 6-22
Woodward-Clyde Federal Services			

TA-46

Elevation 2164 m

Depth (m)	Lithology	Vp (m/sec)	ρ (g/cm³)	
10	Moderately to densely welded tuff	745	1.6	Tshirege Member of Bandelier Tuff
20	Nonwelded tuff	580	1.6	
50	Moderately to densely welded tuff	1150	1.7	
65	Nonwelded tuff	905	1.6	
80	Nonwelded/vapor phase altered tuff	1230	1.7	
200	Non-welded tuff	1230	1.7	Otowi Member of Bandelier Tuff
215	Guaje Pumice	1715	1.9	
240	Puye Formation (Fanglomerate)	2290	2.2	
275	Tschicoma Formation (Dacitic rocks)	5190	2.8	
350	Puye Formation (Fanglomerate)	2290	2.3	
415		2495	2.4	
435	Totavi Lentil (Conglomerate)	2495	2.4	
500	Santa Fe Group (Sandstone, siltsone and conglomerate)	2495	2.4	
535		2705	2.5	
555	Cerros del Rio Basaltic Rocks	5190	2.8	
590	Santa Fe Group (Sandstone, siltstone and conglomerate)	2705	2.5	
635	Cerros del Rio Basaltic Rocks	5190	2.8	
670	Santa Fe Group (Sandstone, siltstone and conglomerate)	2910	2.5	
820	Cerros del Rio Basaltic Rocks	5190	2.8	
950	Santa Fe Group (Sandstone, siltstone and conglomerate)	3120	2.5	
1000		3330	2.5	

Note: Profiles below depth of borehole penetration or sites with no boreholes are estimated from other boreholes and geologic cross-sections

TA-55 SHB1

Elevation 2230 m

Depth (m)	Lithology	Vp (m/sec)	ρ (g/cm³)	
6	Nonwelded tuff	519*	1.6	Tshirege Member of Bandelier Tuff
12	Moderately welded tuff	995	1.6	
28	Moderately to densely welded tuff	854*	1.6	
37	Nonwelded tuff	709*	1.6	
67	Moderately to densely welded tuff	1188*	1.7	
78	Nonwelded tuff	885*	1.6	
95	Nonwelded/vapor phase altered tuff	1235	1.7	
107	Cerro Toledo Rhyolite epiclastic reworked pyroclastics	1490	1.7	
137		1700	1.8	
180	Non-welded tuff	1230	1.7	Otowi Member of Bandelier Tuff
192	Guaje Pumice	1715	1.9	
197	Basaltic sediments	2805	2.5	
225	Cerros del Rio Basaltic Rocks	5190	2.8	
310	Tschicoma Formation (Dacitic rocks)	5190	2.8	
350	Puye Formation (Fanglomerate)	2290	2.3	
460		2495	2.4	
475	Totavi Lentil (Conglomerate)	2495	2.4	
820	Tschicoma Formation (Dacitic rocks)	5190	2.8	
950	Santa Fe Group (Sandstone, siltstone and conglomerate)	3120	2.5	
1000		3330	2.5	

* Downhole velocity measurements

Project No. 91C0509	Los Alamos Seismic Hazards	TA-46 & TA-55 GEOLOGIC AND P-WAVE VELOCITY PROFILES	Figure 6-23
Woodward-Clyde Federal Services			

7.0
SEISMIC SOURCE CHARACTERIZATION

In this section, seismic sources including seismogenic faults and area sources (seismic source zones) significant to the LANL are identified and characterized. Source parameters for these seismic sources provide the basic input into both the deterministic and probabilistic ground motion estimates. Discussions of how these source parameters are used in the deterministic and probabilistic evaluations are included in Sections 8 and 9, respectively. Although surface faulting earthquakes have not occurred historically in the LANL region, geologic evidence indicates they have occurred prehistorically (e.g., Gardner and House, 1987; Gardner et al., 1990; Menges, 1988; 1990a,b). Therefore, we included two types of potential seismic sources: 1) fault sources that are considered capable of producing moderate to large surface faulting earthquakes (larger than M_w 6.0-6.5); and 2) seismic source zones that are considered not capable of producing large surface faulting earthquakes. In the following, we first describe the source parameters for identified active and potentially active faults in the LANL region (i.e., within about 100 km). We then describe source parameters for the seismic source zones identified in the region.

7.1 POTENTIALLY SEISMOGENIC FAULTS

Within the LANL region, we identified 25 faults as potential seismic sources capable of generating significant ground shaking at the LANL. In this section, we describe the source parameters for each fault, including location, geometry, orientation, capability or activity potential, rupture scenarios, maximum magnitude, slip rate, and recurrence intervals for each fault. Fault source parameters are summarized in logic trees (Figures 7-1 through 7-23), which include extensive footnotes (Table 7-1) that document the basis for the specific values and weights that were chosen. Sections 7.1.1 through 7.1.23 provide an overview of each fault, which are discussed in order according to their proximity to TA-55. Plates 1 and 2 show the locations of faults. We attempted to keep fault nomenclature consistent with previous literature (including the use of "fault" versus "fault zone"), with some exceptions as noted in the following sections.

In regard to fault capability or activity potential, we considered all known fault zones with evidence for demonstrable Quaternary (1.6 Ma) displacement as 100% active. This criteria is actually more conservative than DOE Standard 1022-94 that uses a 500,000-year time period for assessing fault activity (Section 1.1). Therefore, we used this more conservative criteria to ensure satisfying the DOE standard. However, many faults in the region offset Quaternary deposits, but whether they moved repeatedly during the past 500,000 years is unknown. The activity potential for faults that have no evidence for Quaternary displacement or evidence for no Quaternary displacement was evaluated on a case-by-case basis. In assigning these activity weights, we considered availability and quality of data on: 1) orientation and kinematic compatibility with the contemporary stress field; 2) any associated historical seismicity; 3) age and rates of most recent activity; and 4) the scale and tectonic role of the structure in accommodating extension within the Rio Grande rift.

All faults were modeled as single planes with the exception of the Pajarito fault system (PFS), which included multiple plane ruptures for some rupture scenarios. For faults with multiple traces at the surface that were modeled as a single plane, we assumed splays merge into one plane at a shallow depth (e.g., Puye fault zone). Rupture scenarios and dips were considered for each fault on an individual basis. To develop rupture scenarios, we used available information and criteria outlined in Table 7-2 to delineate likely rupture segment boundaries, where appropriate. Depths on the logic trees refer to seismogenic depths, which were used with dips to calculate down-dip fault widths. Down-dip fault widths are used to determine source-to-site distances, and in calculating rupture areas of faults that are used in estimating maximum magnitudes.

To estimate maximum magnitudes for each fault, we used the empirical relations of Wells and Coppersmith (1994) that relate M_w to surface rupture length (L in km) or rupture area (RA in km^2) for all fault types (see footnote 5 in Table 7-1). When data on displacement per event were available, we also used their appropriate relation for estimating M_w from displacement. Fault lengths are straight-line distances measured on Plates 1 or 2 and are shown on the logic trees (Figures 7-1 through 7-23). Areas were computed from lengths and down-dip widths. We then calculated a weighted-mean magnitude as our best estimate maximum magnitude for each rupture scenario of each fault, which we weighted 0.6. To adequately account for the error in the regression relations and the uncertainty in the input

values, we considered values at ± 0.3 of a magnitude unit around our best estimate, each weighted at 0.2 (see footnote 6 in Table 7-1 for more details).

We considered both characteristic and exponential recurrence models for fault sources. These models are discussed further in Sections 7.2 and 9.2.2. We characterized rates of surface faulting activity by slip rate and, where data were available, recurrence intervals. Slip rates are for average net slip over the fault plane in mm/yr. For faults that we modeled as multiple planes (e.g., certain rupture scenarios of the PFS), we averaged slip rates for each fault plane together to properly characterize average slip for the source.

In characterizing slip rates, we found that faults in the Rio Grande rift fall into three categories: A-faults with data on both long- and short-term slip rates; B-faults with data only on long-term rates; and C-faults with no available data on slip rates. We assigned values and weights for faults in Category A on an individual basis according to available data (e.g., Sangre de Cristo fault - see Figure 7-22 and footnote 107 in Table 7-1).

To assign values for faults in Category B, we needed to account for possible differences between known long-term and unknown short-term slip rates. To do this, we compared long-term and short-term slip rates for Category A faults in the Rio Grande rift (Table 7-3, J. McCalpin, GeoHaz Consultants, written communication, 1994). To develop a histogram of these slip rate data, McCalpin normalized the data to the long-term rate of interest. For example, for the PFS, the data were normalized to the long-term, average vertical slip rate of 0.07 mm/yr (Table 7-3 and footnote 9 in Table 7-1). We then plotted a cumulative frequency distribution of the normalized slip rates (e.g. Figure 7-26). These plots were then used to characterize variability from long-term rates. For faults in Category C with no available slip rate data, we assumed a long-term rate similar to other appropriate faults in the rift, and then assigned values and weights using the methodology for Category B faults.

For all Category B faults except the PFS, we chose a three-point approximation of the slip-rate distribution by assuming the long-term rate as a best estimate, weighted at 0.6, and using the 5th and 95th percentiles from the cumulative frequency plots, each weighted at 0.2. Where appropriate, we then resolved these values into dip slip values by assuming the fault dip that was given the greatest weight in the logic tree for each fault. We characterized the PFS with a three- to six-point approximation because of its importance to seismic hazards

at LANL (Figures 7-1a through g). Associated footnotes in Table 7-1 discuss the various distributions chosen for the PFS.

By using slip rate data from Category A faults in the Rio Grande rift to characterize uncertainty in short-term slip rates for Category B faults, we assumed that temporal variations in the behavior of a particular fault can be modeled by the cumulative behavior of the better understood faults in the rift. Acquiring short-term slip rate data for Category B faults is ultimately the best way to test this assumption. However, given the available data, this substitution of space for time appears to be a reasonable assumption and it provides an internally consistent means of characterizing uncertainty in slip rates.

7.1.1 Pajarito Fault System

The PFS consists of several generally north-striking faults that define the active western boundary of the Española Basin of the Rio Grande rift (Plate 1) (Gardner and House, 1987). We consider the fault system to be comprised of three principal faults: 1) the down-to-the-east, 41-km-long Pajarito fault (PAF); 2) the down-to-the-west 14-km-long Rendija Canyon fault (RC); and 3) the down-to-the-west 12-km-long Guaje Mountain fault (GM) (Plate 2). Although Gardner and House (1987) include the Embudo fault as part of the Pajarito fault system, we interpret the Embudo fault to be a separate, distinct seismic source and describe this fault separately in Section 7.1.6. Similarly, at the southern end of the PFS, we considered the La Bajada fault as an independent seismic source, which is described in Section 7.1.5. Each of the three main faults of the PFS clearly displaces the 1.2 Ma Tshirege Member of the Bandelier Tuff and therefore, the fault system was considered 100% active. Paleoseismic investigations for this study focused on components of the PFS which are described in more detail in Section 4. This section provides an overview of the Pajarito, Rendija Canyon, and Guaje Mountain faults. We considered both independent and dependent rupture of these faults. Seismic source characteristics are summarized in Figures 7-1a through 7-1g, and associated footnotes in Table 7-1 outline the bases for the chosen values.

Based on analysis of aerial photography, aerial reconnaissance and review of geologic mapping, we interpret the length of the Pajarito fault to be 41 km. We interpret the fault to extend as far northeast as Clara Peak (Plate 2), with faulting northeast of Clara Peak occurring on the Embudo fault, distinct from that along the rift-bordering Pajarito fault.

Aldrich and Dethier (1990) identified the area near Clara Peak as a complex intersection of northeast-, north-, and north-northwest-striking faults including the Pajarito, Embudo, and La Cañada del Amagre-Clara Peak faults (Plate 1). Northeast of Clara Peak, there is little or no geomorphic evidence of discrete, continuous Quaternary fault displacement. In contrast, geomorphic expression of the Pajarito fault in Quaternary deposits is generally very prominent (Section 4.1).

Similarly, the southern end of the Pajarito fault probably coincides with its intersection with a major rift accommodation zone. Near Cochiti Lake, the down-to-the-east Pajarito fault intersects the down-to-the-west La Bajada and San Francisco faults (Plate 2). As noted in Section 4.1, several northwest-trending lineaments in this complex intersection are probably a result of transfer of strain from the Pajarito fault to the La Bajada and San Francisco faults. We interpret the southern end of the Pajarito fault to be where the sense of slip changes at this intersection.

The 14-km-long Rendija Canyon fault is subparallel to and located approximately 3 km east of the Pajarito fault (Figure 2-2; Plate 2). The north-striking, steeply west-dipping fault exhibits down-to-the-west displacement of the 1.2 Ma upper Bandelier Tuff, and thus is antithetic to the Pajarito fault. Geologic and geomorphic evidence suggests that the Rendija Canyon fault extends from a possible intersection with the Pajarito fault on the north to at least Pajarito Mesa on the south (Section 4.2.2). The fault consists of a single strand north of Barranca Mesa, of two primary strands and numerous secondary strands through the town of Los Alamos, and a zone of distributed deformation south of Los Alamos Canyon (Section 4.2.2). Although there is little geomorphic expression of the fault south of Mortandad Canyon, we extended the Rendija Canyon fault south to Water Canyon in our model for the hazard evaluation, primarily based on evidence for post-1.2 Ma faulting exposed in trenches at TA-67 (Kolbe et al., 1994) and lineaments extending south of Pajarito Mesa to Water Canyon (Plate 2). Smith et al. (1970), Budding and Purtymun (1976), and Gardner and House (1987) show no connection between the Rendija Canyon fault and the Pajarito fault. It is unclear whether the Rendija Canyon fault merges with or intersects the Pajarito fault north of Los Alamos Canyon (Plate 2). Nevertheless, the northern termination of the Rendija Canyon fault is identified herein at a possible intersection with the Pajarito fault near Rincon del Cuervo (Plate 2).

Smith et al. (1970) and Kelley (1978) show the southern end of the Rendija Canyon fault at about Los Alamos Canyon, whereas Dransfield and Gardner (1985) and Gardner and House (1987) continue the fault to the south of Los Alamos Canyon beneath the Bandelier Tuff. The presence of post-Bandelier displacement exposed in the Los Alamos County Landfill (Section 4.2.2.2) shows that major fault splays exist south of Los Alamos Canyon. Vaniman and Wohletz (1990) inferred that the fault extends about to Cañon del Valle, which is about 3 km south of Mortandad Canyon, based on the presence of a broad zone of abundant, open fractures in the Bandelier Tuff. Recent trenching along Pajarito Mesa at TA-67 (Kolbe et al., 1994), shows evidence for several minor, near-vertical faults that form a 30-m-wide zone which is roughly coincident with a lineament that extends south of Mortandad Canyon to Water Canyon, along strike of the easternmost trace of the Rendija Canyon fault (Plate 2). These faults show small offsets (apparent vertical separations of 60 cm or less), that overall are down-to-the-west, in alluvium overlying the Bandelier Tuff, but these faults do not offset air-fall and associated deposits of 45 to 73 ka El Cajete Pumice (Kolbe et al., 1994). Thus, although these faults may have formed during a surface rupturing earthquake on the Rendjia Canyon fault, they apparently did not rupture during the most recent surface rupture on the Rendija Canyon fault, that was identified at the Guaje Pines site and is much younger, either about 8 or 23 ka (Section 4.2.2.1). Therefore, the most recent surface rupture on the Rendija Canyon fault apparently did not extend as far south as Pajarito Mesa (Kolbe et al., 1994). Geomorphic evidence suggests that the southern termination of this most recent event along the Rendija Canyon fault was probably near Mortandad Canyon. Notably, this southern termination coincides with a change in character of the Pajarito fault, from monoclinal flexuring on the north to brittle displacement on the south. Although the most recent surface faulting event may have only ruptured to Mortandad Canyon, we extended the Rendija Canyon fault south to Water Canyon in our model to include possible rupture of the older faults found at TA-67.

The 12-km-long Guaje Mountain fault is subparallel to and located approximately 4 to 5 km east of the Pajarito fault in northern Los Alamos County (Figure 2-2; Plate 2). The north-striking, steeply west-dipping fault exhibits down-to-the-west displacement of the 1.2-Ma upper Bandelier Tuff and thus, is structurally similar to the subparallel Rendija Canyon fault. Gardner and House (1987) map the 5-km-long central part of the Guaje Mountain fault as a single continuous strand between Guaje Canyon and Bayo Canyon (Plate 2). To the north

and south of this central section, the location of the fault is approximate because of structural complexities or a lack of prominent geomorphic expression (Gardner and House, 1987).

The northern termination of the fault occurs at its intersection with the Pajarito fault just south of the border between Los Alamos and Sandoval counties (Plate 2). This intersection is characterized by complex deformation in the area between the down-to-the-east Pajarito fault and the down-to-the-west Guaje Mountain fault. NVTD of the 1.2 Ma upper Bandelier Tuff by the Guaje Mountain fault is greatest (27 $\pm$ 4 m) near this intersection, based on topographic profiles on the top of the tuff. The amount of NVTD decreases progressively southward to zero at South Mesa (Figure 4-3c and Table 4-1). Although there is little or no geomorphic expression of the fault across mesas underlain by the Bandelier Tuff to the south of Los Alamos Canyon, aerial photograph lineaments in Pajarito and Threemile Canyons suggest that near-surface faulting may extend further south. Vaniman and Wohletz (1990) interpreted that the fault extends to Threemile Canyon based on fracture density within the upper Bandelier Tuff and geomorphic features. However, trench investigations across their projected traces of the Guaje Mountain fault at TA-63 (Kolbe et al., 1995) and TA-67 (Kolbe et al., 1994) revealed no evidence for faulting. Therefore, we considered the southern termination of the Guaje Mountain fault to be near TA-63 (Plate 2).

Previous segmentation models of the PFS were based primarily on along-strike differences in structural (geometric and kinematic) characteristics. Golombek (1983) proposed a segmentation model of the Pajarito fault on the basis of marked changes in the character of the fault zone along strike and on bedrock units cut by the fault at the surface (Figure 7-24). This four-segment model, which included the Rendija Canyon and Guaje Mountain faults in its "Guaje Mountain segment," did not address potential rupture lengths. In contrast, Gardner et al. (1990) identified fault segments based on scarp height, average vertical slip rate, and fault trace complexity. This five-segment model also did not explicitly identify specific rupture segments. However, both the Rendija Canyon and Guaje Mountain faults were identified as discrete fault segments (Figure 7-24). Based on aerial photographic interpretation, geologic reconnaissance, variations in amount of NVTD along strike (Figure 4-3a,b,c), available paleoseismic data from trench investigations, and previous geologic mapping, we developed possible rupture scenarios for the PFS (Figures 7-25a through f). General criteria used to delineate possible segment boundaries (Table 7-2) are described by dePolo et al. (1991) and Knuepfer (1989). The bases for specific scenarios and weights are

given in associated footnotes in Table 7-1 and are shown, in part, on Figures 7-25a through f.

The complexity in the rupture scenarios and the overall behavioral model, including five behavioral branches and twenty-two rupture scenarios for the PFS, results from uncertainty in the relationship among the three principal faults. In particular, there is considerable uncertainty in the rupture histories of each fault. Ideally, fault segmentation models and associated rupture scenarios are based on detailed and comprehensive rupture histories all along a fault (e.g., Machette et al., 1992) that are assessed in the context of patterns of other physical characteristics along the fault (e.g., Wheeler and Krystinik, 1988). Additional work is necessary to develop such a model for the PFS. In particular, paleoseismic studies during this project were concentrated along the central part of Pajarito fault, closest to LANL, and even along this section the record remains incomplete. It is likely that additional data on rupture histories for the PFS would allow significant simplification of our behavioral model and rupture scenarios for this fault.

7.1.2 Sawyer Canyon Fault

The Sawyer Canyon fault (as named in this study) is a short, north-northwest-striking normal fault that roughly parallels the Guaje Mountain fault, and lies about 1 to 2 km to the west (Plates 1 and 2). This previously unnamed fault dips to the east and has down-to-the-east displacement (Smith et al., 1970; Gardner and House, 1987). The Sawyer Canyon fault shows clear evidence for Quaternary activity, offsetting not only the Bandelier Tuff (Carter and Winter, 1995), but also exhibiting scarps on overlying younger alluvial gravels (K.E. Carter, LANL, personal communication, 1993). In fact, displacement patterns and kinematic analysis of the Rendija Canyon, Guaje Mountain, and Sawyer Canyon faults suggests the latter may be the youngest of these faults (Carter and Gardner, 1993, although paleoseismic data on the Sawyer Canyon fault are necessary to substantiate this hypothesis. A few historical earthquakes and one well-located event have occurred in the vicinity of the Sawyer Canyon fault (Plates 3 and 12).

We characterize the Sawyer Canyon fault as an active source, independent of the Pajarito fault system. Although the Sawyer Canyon fault may rupture with all or part of the Pajarito fault system, we considered it as a separate source for simplicity and because it dips away

from the Pajarito fault system. Source parameters are summarized in Figure 7-2 and associated footnotes in Table 7-1 outline the bases for the chosen values.

7.1.3 Puye Fault Zone

The 20-km-long Puye fault zone is located within the northeastern part of the Pajarito Plateau, southwest of the town of Hernandez (Plates 1 and 2). The zone consists of several discontinuous down-to-the-east, north-striking faults that are up to 11 km long (Smith et al., 1970; Kelley, 1978; Machette and Personius, 1984; Harrington and Aldrich, 1984; Dethier and Manley, 1985). Gardner and House (1987) informally refer to the northern traces within the zone as the "fault zone southwest of Hernandez." LaForge and Anderson (1988) refer to the zone between the Embudo fault zone and Highway 4 as the Puye fault zone, and this name is used herein (Plates 1 and 2).

Based on our aerial reconnaissance and analysis of aerial photography, several traces of the Puye fault zone are associated with prominent topographic scarps and vegetation and tonal lineaments. One of the highest and most prominent scarps shows 11.5 m of down-to-the-east displacement and a maximum scarp angle of 13° (LaForge and Anderson, 1988) . This scarp crosses the Q1 surface of Harrington and Aldrich (1984), which is estimated to be 275 to 500 ka. The scarp profile suggests multiple Pleistocene ruptures but no Holocene displacement (LaForge and Anderson, 1988). The scarp height and maximum scarp angle suggest that the most recent faulting event could be as old as 100,000 years. For this study, we measured a fault-scarp profile on a main strand of the Puye fault zone in the northeast quarter of Section 21, T.20N., R.7E., approximately 1.1 km south of the site investigated by LaForge and Anderson (1988). Our profile shows a scarp height of 7.5 m and a maximum scarp angle of 18°. The profile displays a subtle but distinct bevel, suggesting multiple Pleistocene surface ruptures. Machette and Personius (1984) note 5 to 20 m of early Pleistocene to Pliocene displacement on the fault zone. A clustering of several microearthquakes in the vicinity of the Puye fault also suggests that the structure is active (Section 5.2).

Harrington and Aldrich (1984) and Gardner and House (1987) note recurrent down-to-the-east late Pleistocene displacement on north-striking faults within the Puye fault zone at or directly south of its intersection with the Embudo fault zone. Harrington and Aldrich (1984)

note that there is 10 m of displacement of a 22 ka gravel and that soil profiles are different across the fault. These data yield a late Pleistocene slip rate of about 0.5 mm/yr, which probably is substantially higher than the long-term slip rate given a likely recurrence interval on the order of 100,000 years (LaForge and Anderson, 1988). It is uncertain if displacement along the Embudo fault zone has influenced sympathetic faulting along adjacent or intersecting strands of the Puye fault zone. Source characteristics for the Puye fault zone are summarized in Figure 7-3 and accompanying footnotes.

7.1.4 Lobato Mesa Fault Zone

The Lobato Mesa fault zone is comprised of several faults that generally strike north, dip to the west, are located north of the Pajarito fault system (Plate 1), and may be structurally part of the system (Gardner and House, 1987). The fault zone can be defined as far north as the town of Abiquiu for a total length of about 22 km. The age of most recent activity on most splays is unknown (Machette and Personius, 1984), but Dethier and Martin (1984) did observe less than 15 m of offset on the Bandelier Tuff along one spray. Additionally, a few historical earthquakes and one well-located contemporary event locate near the fault (Plates 3 and 12). We characterize the Lobato Mesa fault zone as active and model it as a single, west-dipping plane. Source parameters are summarized in Figure 7-4 and associated footnotes in Table 7-1 give the bases for the chosen values.

7.1.5 La Bajada Fault

The 40-km-long La Bajada fault is located along the eastern margin of the Santo Domingo Basin (Plate 1) and, as used herein, includes the La Bajada fault of Blatz (1976) and the Rosario fault of Stearns (1953). Although no evidence of late Quaternary displacement has been documented, the fault may be associated with microseismicity (Section 5.2, Plates 3 and 12). Although mapped as separate structures by Stearns (1953) and Baltz (1976), we interpret the La Bajada and Rosario faults as one fault based on structural similarities and their nearly continuous trace. The down-to-the-southwest northern part of the fault, the La Bajada fault, extends about 14 km south-southeast from its intersection with the Pajarito fault near Cochiti Lake to a connection with the Rosario fault near the Santa Fe River (Plate 1). Maximum vertical displacements of up to 1520 m near the southern end of the fault have been estimated based on juxtaposed Miocene Santa Fe group and Eocene to Oligocene rocks

(Baltz, 1976). Near the north end of the fault, 2.5 to 2.6 Ma basalts of the Cerros del Rio volcanic field cap the 160-m-high La Bajada escarpment (Aubele, 1978). Analysis of aerial photography conducted during this investigation shows that there are several potentially fault-related lineaments, including west- and southwest-facing topographic scarps along the La Bajada fault.

To the south, the La Bajada fault becomes the Rosario fault of Stearns (1953), which also displays down-to-the-west normal displacements but strikes more southward than the La Bajada fault. It can be traced approximately 23 km from Tetilla Peak (near the Santa Fe River) to about 2 km south of Rosario Siding where the fault reportedly is concealed by Quaternary gravels near the base of the Ortiz Mountains. Baltz (1976) speculates that throw along the Rosario fault diminishes to the south. Overall, the La Bajada fault probably transfers strain from the Pajarito fault along the western margin of the Española Basin to the San Francisco fault and perhaps the Sandia-Rio Grande fault zone along the eastern margin of the Albuquerque Basin (Section 2.3). Seismic source characteristics for the La Bajada fault are summarized in Figure 7-5 and accompanying footnotes.

7.1.6 Embudo Fault

The Embudo fault is an approximately 64-km-long, northeast-striking system of faults that forms the structural boundary between the Española and San Luis basins (Plate 1). The fault separates the predominantly down-to-the-east faulting along the western margin of the Española Basin from the down-to-the-west faulting along the eastern margin of the San Luis Basin (Dungan et al., 1984). The geometry of the Embudo fault, and its relationship to the Española and San Luis basins, are similar to characteristics of accommodation zones in other continental rift systems (Section 2.1).

However, field relations indicate that the kinematics of deformation may be more complicated than suggested by the simple model that the fault is an accommodation zone (Section 4.1.3). Field evidence for local thrust faulting along the northern part of the Embudo fault suggests that the fault locally accommodates crustal shortening rather than differential crustal extension (Muehlberger, 1979). Along the southeastern part of the fault, the Embudo fault displays a left-stepping en echelon geometry that is interpreted to be associated with right-lateral strike-slip faulting (Aldrich, 1986; Aldrich and Dethier, 1990).

Right-lateral slip on the Embudo fault is inconsistent with the model that the fault is an accommodation zone. In order to reconcile these issues, previous workers suggested that the Española Basin is undergoing counterclockwise vertical axis rotation driven by oblique extension within the Rio Grande rift (Muehlburger, 1979; Aldrich, 1986; Brown and Golombek, 1986).

These models have different implications for the kinematics of coseismic rupture along the Embudo fault. If the fault is an accommodation zone between the Española and San Luis basins, then the opposite senses of vertical separation expressed by the northeastern and southwestern parts of the fault imply that it consists of at least two kinematically distinct reaches, associated with either the Española Basin or the San Luis Basin. If so, then it is unlikely that the fault would rupture independently along its entire length during a single event. Alternatively, if the Embudo fault is primarily a right-lateral strike-slip fault that is accommodating the counterclockwise rotation of the entire Española Basin, then the inferred direction of slip and rate of strain accumulation are consistent along the length of the fault, and it is more likely that a large rupture involving both the northeast and southwest reaches could occur.

Based on our reconnaissance investigations (Section 4.1.3), the Embudo fault in the Arroyo Hondo area is most simply characterized as a steeply-dipping to near-vertical left-oblique fault with a component of northwest-side-down motion. Thrust faults associated with the Embudo fault near Arroyo Hondo probably are related to a locally transpressional restraining bend in the fault trace.

We conclude that the Embudo fault forms a transfer or accommodation zone between the Española and San Luis structural basins, as previously suggested by Muehlberger (1979) and Dungan et al. (1984). The data collected for this reconnaissance study do not support the hypothesis that the Embudo fault zone presently is a through-going, right-lateral strike-slip fault system that accommodates counterclockwise rotation of the Española Basin (Muehlberger, 1979; Aldrich, 1986; Brown and Golombek, 1986). We conclude that the local counterclockwise rotations measured adjacent to the Embudo fault are consistent with left-lateral shearing, and thus support the hypothesis that the fault is an accommodation zone. Seismic source characteristics of the Embudo fault are summarized in Figure 7-6 and accompanying footnotes.

7.1.7 La Cañada del Amagre-Clara Peak Fault Zone

Machette and Personius (1984) mapped several, short, north-striking, east-dipping faults north of Clara Peak and the intersection between the Embudo fault and the Pajarito fault system. Aldrich and Dethier (1990) mapped these faults slightly differently and specifically identified the La Cañada del Amagre and Clara Peak faults (Plate 2). We collectively refer to the faults as the La Cañada del Amagre-Clara Peak fault zone (Plate 1). Individual faults within the zone are about 3 to 7 km long, whereas the entire fault zone is approximately 12 km long. Observations of slickensides and offset of a basalt dike indicate dominantly dextral slip with minor normal slip across the La Canada del Amagre fault, possibly as a consequence of intra-rift block rotation in this part of the rift (Aldrich and Diether, 1990).

Although the age of most recent activity on the La Cañada del Amagre-Clara Peak fault zone is not well-constrained, some splays offset Pliocene to Pleistocene-age sediments (Machette and Personius, 1984). Additionally, the area is seismically active and the La Canada del Amagre Clara Peak fault zone may have associated historical seismicity (Section 5.2). We, therefore, characterize this fault zone as potentially active with a 0.5 weighting. We modeled it as a single plane, steeply dipping to the east. Source parameters are summarized in Figure 7-7 and the basis for the chosen values is detailed in associated footnotes of Table 7-1.

7.1.8 San Francisco Fault

The 42-km-long San Francisco fault extends from Placitas on the south to just north of Cochiti Lake on the north (Plate 1). The fault, as mapped by Stearns (1953), Kelley and Northrop (1975), Baltz (1976), and Kelley (1977) is subparallel to the La Bajada-Rosario fault, has normal, down-to-the-west displacement, and traverses the Santo Domingo Basin. The southern end of the fault is a complex intersection with the Sandia-Rio Grande fault zone. The northern end, based on analysis of aerial photographs and aerial reconnaissance conducted for this study, is a complex intersection with the down-to-the-east Pajarito fault. Kelley and Northrop (1975) report a maximum displacement of 4300 m of the base of the Miocene Santa Fe group, however, vertical separation along the northern end of the San Francisco fault is minor. This complex intersection likely is a transfer zone (Gibbs, 1984) between the Pajarito and San Francisco faults.

Hoge (1970) and Kelley (1978) map splays of the San Francisco fault offsetting Quaternary deposits, but the age of most recent activity is poorly constrained. Hoge (1970) considered the last movement along the fault to be early Quaternary based on deposition of older Quaternary gravels north of Placitas, although Kelley (1977) notes a lack of evidence of displacement of the early (?) Pleistocene Ortiz pediment. A few earthquakes have been located near the fault (Plates 3 and 12). Primarily because some evidence suggests possible Quaternary activity, but also because of its structural association with the late Pleistocene Sandia-Rio Grande fault zone to the south and the Pajarito fault system to the north, we characterize the San Francisco fault as an active, moderately-west-dipping fault (Figure 7-26). Source parameters are summarized in Figure 7-8 and the bases for the chosen values are outlined in associated footnotes in Table 7-1.

7.1.9 Pojoaque Fault

The 49-km-long Pojoaque fault is located in the central part of the Española Basin about 7 km east of the town of Española (Plate 1). The fault consists of several subparallel strands in a zone approximately 5 km wide (Kelley, 1978). As in the San Luis Basin to the north and the Albuquerque Basin to the south, the Española Basin includes a narrow, deep, asymmetric graben on one side of the basin. Manley (1979a,b) identified this part of the Española Basin as the Velarde graben, which is bordered by the Pajarito fault system on the west and the (herein named) Pojoaque fault zone on the east. There is considerable uncertainty regarding the precise location, activity, and amount of displacement along the eastern margin of the Velarde graben.

Kelley (1978) shows that major faults in the zone have down-to-the-west displacement, although Galusha and Blick (1971) and Baltz (1976) show faults with both down-to-the-west and down-to-the-east displacement. The cumulative amount of displacement across the zone is unknown, although geophysical data show that the Española Basin is likely a west-tilted basin that lacks faults of more than 100 m of throw along its eastern margin (Biehler et al., 1991). These data are consistent with Manley's (1979a) assertion that the eastern border of the Española Basin is a series of small-displacement faults or a tilted, unfaulted depositional onlap. Given the amount of uncertainty in the presence or absence of late Cenozoic activity, it is not surprising that there are no available data on paleoseismic characteristics of the Pojoaque fault zone. A few historical earthquakes have been located near the fault but only

one event is well-located (Plates 3 and 12). Seismic source characteristics for the Pojaque fault are summarized in Figure 7-9 and accompanying footnotes.

7.1.10 San Felipe Fault

The 47-km-long San Felipe fault zone consists of several subparallel, north-trending faults within the San Felipe volcanic field at the southern margin of the Jemez Mountains (Plate 1). The fault zone forms the border between the northeastern corner of the Albuquerque Basin and the western Santo Domingo Basin, which is a structural transition zone between the Albuquerque and Española basins (Section 2.3). Major faults within the fault zone include the Santa Ana, Cocida, Luce, Algodones, and Borrego faults (Smith et al., 1970; Kelley, 1977; Hawley and Galusha, 1978). The Santa Ana and Algodones faults form the western and eastern margins, respectively, of the San Felipe graben within the San Felipe volcanic field. This graben diverges southward, having a width of about 3 km at its northern end and a width of about 8 km at its southern end. Although there are no published measurements on the dips of faults within the zone, the linear traces of the faults across areas of topographic relief suggest that the faults are high angle. Kelley (1977) and Soister (1952) note that all of the faults exhibit less than about 100 m of throw of late Pliocene basalt flows on the surface of Santa Ana Mesa, which are about 2.5 to 2.6 Ma old (Bachman and Mehnert, 1978). The average displacements range from about 12 to 46 m (Soister, 1952). Notably, May et al. (1994) suggest that all of these faults may represent deformation in the hanging wall of the Rio Grande fault (see below).

All of the major, north-striking faults within the zone have prominent geomorphic expression, primarily where they displace resistant basalt flows. Hawley and Galusha (1978) note that the faults have little or no geomorphic expression south of the volcanic field, where they project into areas underlain by the less resistant Santa Fe Group sediments. Kelley (1977) indicates that the Algodones fault extends across the Rio Grande to the south and merges with the Rincon fault at the base of the Sandia Mountains near the town of Placitas (Plate 1). At the present time, there are no data addressing the presence or absence of Quaternary activity on the San Felipe fault zone, and there are no published data on paleoseismic characteristics of faults within the zone. Only one well-located earthquake has occurred within the fault zone (Plates 3 and 12). Seismic source characteristics for the San Felipe fault are summarized in Figure 7-10 and accompanying footnotes.

7.1.11 Jemez-San Ysidro Fault System

Numerous faults exist south-southwest of the Valles caldera, which we refer to collectively here as the Jemez-San Ysidro fault system (Plate 1). The geometry and nomenclature of these faults is somewhat complex (see Aldrich, 1986). Based primarily on changes in geometry, we consider a possible rupture boundary near Jemez Springs, separating the 26-km-long Jemez fault to the north from the 24-km-long San Ysidro fault to the south (Plate 1).

The Jemez fault, as defined in this study, extends southwest of the Valles caldera, trending southwest along the Cañon de San Diego to join the northern end of the north-trending San Ysidro fault (Plate 1). As such, it includes the zone of northwest-striking faults referred to as the Jemez fault zone by Goff and Kron (1980) and Goff et al. (1981), and also the curved, northwest- to north-striking Sierrita fault described by Woodward and DuChene (1975), Aldrich (1986), and Woodward (1987). The Jemez fault is a normal fault with down-to-the-east displacement and it forms the western boundary of the Albuquerque Basin (Woodward and DuChene, 1975; Aldrich, 1986). It displaces the Tshirege Member of the 1.2 Ma Bandelier Tuff more than 50 m in Cañon de San Diego (Goff et al., 1989). Woodward (1987) reports that up to 460 m of vertical separation is present along the central portion of the Jemez fault. Historical seismicity has occurred near the Jemez fault (Section 5.2).

Woodward (1987) and Golombek (1981) state that the southern, curvilinear portion of the Jemez fault (Sierrita fault) is vertical where it displaces Bandelier Tuff but at its structurally lowest exposure it dips 50°SE, suggesting a possible listric nature to the fault. Woodward (1987) reports up to 680 m of vertical displacement in Permian strata and about 12 m of separation in Bandelier Tuff. Based on slickenside observations, Woodward and DuChene (1975) characterize movement along the Sierrita fault as dominantly dip-slip with a minor right-slip component. Aldrich (1986) states that the Sierrita fault was the western margin of the Rio Grande rift during the Oligocene, and that activity eventually stepped eastward to the Pajarito fault system.

The San Ysidro fault (Sierrita fault of Galusha, 1966) includes two slightly overlapping sections that strike north and dip to the east (Plate 1). Hawley and Galusha (1978) and Woodward and Ruetschilling (1976) describe the San Ysidro fault as the western margin of

the Rio Grande rift. The northern terminus of the fault is located slightly northwest of Jemez Springs. The southern terminus is identified at the northern margin of the Llano de Albuquerque, a 500,000-year-old geomorphic surface along the western flank of the Albuquerque Basin that apparently is not displaced by the fault. The fault is present along the east rim of White Mesa where Cretaceous Dakota and Mancos formations are downfaulted to the east approximately 275 m against Jurassic Entrada, Todilto and Morrison formations (Hawley and Galusha, 1978). Woodward (1987) reports a maximum of 460 m of vertical separation along a steep east-dipping fault near San Ysidro. Because of this and its close proximity and possible structural connection with the Jemez fault, we considered the San Ysidro fault to be active. We also considered both independent and dependent ruptures of the Jemez and San Ysidro faults within this fault system. Specific source characteristics and weights are shown in Figure 7-11 and the bases for the values are outlined in the respective footnotes within Table 7-1.

7.1.12 Cañones Fault

The 30-km-long Cañones fault strikes northeast along the eastern margin of the Colorado Plateau, in the vicinity of Cerro Pedernal and Abiquiu (Plate 1). Kelley (1979), Manley (1982), Manley et al. (1987), and Gonzalez and Dethier (1991) show that the fault includes eastern and western strands that join north of Cañones Mesa. It is likely that the Cañones fault was the western margin of the Rio Grande rift between about 10 and 5 Ma, after which the primary activity shifted to the east onto the Pajarito fault system (Golombek, 1983). The fault does not displace basalt flows, mapped by Manley (1982) as the 8 Ma Lobato Basalt, although they are more likely the 3 Ma El Alto flows (M. Gonzalez, University of Denver, personal communication, 1994). Smith et al. (1970) show the fault is buried by the 1.2 Ma upper Bandelier Tuff. Nevertheless, we acknowledge that the Cañones fault is similar to the active Jemez-San Ysidro fault system (see above) in that both structures are pre-5 Ma margins of the rift that are still favorably oriented to accommodate strain in the present stress field.

The average rake of lineations on the main fault indicate down-to-the-east dip-slip movement, with evidence of a small left-lateral component, along near-vertical fault planes (Gonzalez and Dethier, 1991). Gonzalez and Dethier (1991) estimate a minimum vertical slip rate of 0.07 to 0.08 mm/yr over 8 Ma. However, the majority of the slip likely took place during

the rapid phase of rifting during the middle Miocene (M. Gonzales, University of Denver, personal communication, 1994), and thus probably is not applicable to the present day tectonic setting. There is no published information on the late Quaternary paleoseismic behavior of the Cañones fault. One well-located earthquake has occurred along the Cañones fault zone (Plate 12). Seismic source characteristics for the Cañones fault zone are summarized in Figure 7-12 and accompanying footnotes.

7.1.13 Nambe Fault

The 50-km-long Nambe fault lies along the western margin of the Sangre de Cristo Range between the towns of Chimayo and Santa Fe, in the eastern part of the Española Basin (Plate 1). We prefer the term Nambe for the fault rather than the term Santa Fe to avoid confusion with the Coyote Springs-Santa Fe fault zone located along the western margin of the southern Albuquerque Basin (Machette and McGimsey, 1983). There is considerable uncertainty as to the presence and activity of the Nambe fault, with several interpretations of the nature of the contact between the Miocene rift-fill sediments (Tesuque Formation) and Precambrian crystalline rocks at the base of the Sangre de Cristo Range. For example, analysis of aerial photography by Kelley (1978) shows faults along nearly the entire range front. In contrast, field mapping by Cabot (1938), Spiegel and Baldwin (1963), Galusha and Blick (1971), and Baltz (1976) show that the contact is only partially faulted. Miller et al. (1963) map the contact entirely as depositional, and Manley (1979a) notes that the eastern margin of the Española Basin appears to lack a border fault.

Because of the uncertainty in the presence of the fault, there also are various interpretations of the physical characteristics of the zone. Galusha and Blick (1971) show numerous short faults having down-to-the-east or down-to-the-west displacement of the Tesuque Formation. Baltz (1976) notes that there is little or no evidence of significant down-to-the-west displacement, and that most of the faults exhibit down-to-the-east displacement. Baltz (1976) attributes the discontinuous faulting to middle or late Pliocene west-tilting of the Española Basin. More recently, Vernon and Riecker (1989) interpret aerial photograph lineaments and faceted spurs along the range front as evidence of late Cenozoic displacement, and infer displacement of gravels estimated as about 150 ka old. Detailed mapping by R. Klinger (U.S. Bureau of Reclamation, personal communication, 1992) could not confirm or preclude displacement of the pediment gravels. LaForge and Anderson (1988) did not consider the

fault zone as a potentially seismogenic source. No microearthquakes have been observed to occur in the vicinity of the Nambe fault (Plates 3 and 12). Seismic source characteristics of the Nambe fault are summarized in Figure 7-13 and accompanying footnotes.

7.1.14 Faults of Black Mesa

Previous workers (Kelley, 1978; Machette and Personius, 1984) mapped several northeast-striking faults across the upper surface of Black Mesa, an approximately 15-km-long, northeast-trending mesa northwest of the Rio Grande. Black Mesa is capped by a 3.6 Ma basalt (Laughlin et al., 1993). As mapped, the 18-km-long, northeast-trending zone of faults displays both northwest-down and southeast-down displacements of the basalt beneath the surface of Black Mesa (Kelley, 1978; Machette and Personius, 1984). In contrast to north-striking fault within the Abiquiu embayment to the north and the Española Basin to the south, the faults of Black Mesa strike northeast and are parallel to the Embudo fault. The westernmost and easternmost faults within the fault zone border a small northeast-trending graben.

Aerial reconnaissance and limited field studies performed for this study confirmed the presence of several prominent northeast-striking scarps on the surface of Black Mesa (Section 4.1.3.2). The scarps locally display an *en echelon*, right-stepping pattern and are associated with small grabens. This system of scarps are mapped as a series of Quaternary faults by Machette and Personius (1984) and are shown as extending beyond the northwestern rim of Black Mesa. The scarps developed in the 3.6 Ma basalt are as high as about 19 m. The timing of displacements is unknown, but the faulting occurred after deposition of the basalt at about 3.6 Ma. At the present time, there are no data addressing the presence or absence of Quaternary activity on the faults of Black Mesa, and there are no data on paleoseismic characteristics of any of the faults. Seismic source characteristics for the faults of Black Mesa are summarized in Figure 7-14 and accompanying footnotes.

7.1.15 Tijeras-Cañoncito Fault

The 93-km-long Tijeras-Cañoncito fault (Plate 1) trends north and northeast along the eastern margin of the postulated Española block (Brown and Golombek, 1986) between Albuquerque and the town of Lamy (Plate 1). The fault consists of several fault strands that have

near-vertical dips, exhibit evidence of normal and left-lateral displacement and have variable amounts and senses of separation along strike (Kelly and Northrop, 1975; Lisenbee et al., 1979; Maynard et al., 1991). Lisenbee et al. (1979) separated the Tijeras-Cañoncito fault into five sections on the basis of structural style, fault trace complexity, and sense and amount of separation. For ease of description, we informally name these sections (from north to south) the Lamy, San Pedro/Ortiz, Monte Largo, Tijeras, and Four Hills sections (Plate 1). Lisenbee et al. (1979) note that late-Quaternary colluvium is displaced along the fault in Tijeras Canyon. No other evidence of Quaternary activity is documented for other segments of the fault, although analysis of aerial photography shows the presence of a prominent tonal lineament along the Four Hills section of the fault near Albuquerque, which may be related to late Quaternary fault activity. In addition, the fault south of Albuquerque strongly influences near-surface groundwater conditions (Hawley and Haase, 1992), and thus may have had late Quaternary displacement. Other than these reports of possible late Quaternary activity, no data on paleoseismic characteristics are available for the Tijeras-Cañoncito fault. Seismicity has occurred along and adjacent to the fault zone although the locations are poorly constrained (Plates 3 and 12). Seismic source characteristics for the Tijeras-Cañoncito fault zone are summarized in Figure 7-15 and accompanying footnotes.

7.1.16 Nacimiento Fault

The 80-km-long Nacimiento fault extends northward from Mesa Prieta to the northern end of Sierra Nacimiento where it connects with the Gallina fault (Plate 1). It forms the western margin of the Laramide Nacimiento uplift, a north-south elongate structural block that lies beneath Cretaceous rocks to the north in Chama Basin and beneath Miocene rocks of the Santa Fe Group to the south. The block lies east of the Jemez Mountains and forms the western margin of the San Juan Basin of the Colorado Plateau (Baltz, 1976). Woodward (1987) maps the northern part of the fault as a shallow dipping, up-on-the-east thrust fault and the southern part as a reverse fault. However, the linear map trace (Plate 1; Woodward, 1987) suggests that the fault has a steep near-surface dip throughout its length. We considered both an unsegmented model and Woodward's (1987) segmentation model, with a 34-km-long northern section and a 44-km-long southern section. The rupture boundary is at San Miguel Canyon, approximately 2 km east of the village of San Miguel. Although Woodward et al. (1972) referred to the northern section as the Nacimiento fault and the

southern section as the Pajarito fault, we prefer to not use this nomenclature to avoid confusion with the Pajarito fault closer to Los Alamos (Plate 1).

Cumulative vertical stratigraphic separation ranges from 1220 m near Vallecito del Rio Puerco to about 30 m near Señorito Creek. Right-lateral strike-slip faulting produced a maximum horizontal displacement of 770 m (Woodward et al., 1972). There is no reported evidence of Quaternary activity on the Nacimiento fault, although there is a relatively high rate of distributed seismicity within the Sierra Nacimiento that could possibly be related to deformation in the hanging wall block of the fault (Plates 3 and 12). Baltz (1976) reports that the fault has had Pleistocene activity, but does not provide any supporting evidence. We characterize the Nacimiento fault as a potentially active source primarily based on the possibly associated historical seismicity in the Sierra Nacimiento. Source characteristics are summarized in Figure 7-16 with associated footnotes in Table 7-1.

7.1.17 Picuris-Pecos Fault

The 96-km-long Picuris-Pecos fault strikes north-northeast within the central part of the Sangre de Cristo Range about 15 km east of Santa Fe (Plate 1). The steeply dipping fault has had several episodes of movement, including right-lateral displacement of about 37 km during the Precambrian followed by down-to-the-east dip slip during the Pennsylvanian and the late Cretaceous (Miller et al., 1963; Moench et al., 1988). Although the fault is associated with a prominent series of linear valleys and other linear geomorphic features, evidence for Quaternary activity has not been documented. Several investigators (Muehlberger, 1979; Manley, 1979a; Aldrich, 1986; Brown and Golombek, 1986) suggest that the Picuris-Pecos fault forms the eastern boundary of the Española block, which may have undergone late Cenozoic counterclockwise rotation. Biehler et al. (1991) and Baldridge and Jiracek (1992) provide geophysical evidence that the eastern margin of the Española block could possibly be along the Picuris-Pecos fault. However, P. Bauer (New Mexico Bureau of Mines and Mineral Resources, personal communication, 1993) notes that the Picuris-Pecos fault does not displace the Tertiary Picuris Formation near the town of Vadito. Salyards et al. (1994) provide paleomagnetic data that suggest that the rigid block rotation model of Muehlberger (1979) and Aldrich (1986) is not applicable to the Española Basin. These relations suggest that the Picuris-Pecos fault is not an active element in the deformation of the Española Basin. LaForge and Anderson (1988) did not acknowledge the

fault as a potential seismogenic source. The fault exhibits no definitive associated historical seismicity although a few events have occurred near the fault (Plates 3 and 12). Based on the available data, we conservatively assign a 50% probability that the Picuris-Pecos fault is active. Seismic source characteristics of the fault are summarized in Figure 7-17 and accompanying footnotes.

7.1.18 West Mesa Fault Zone

The seismically active West Mesa fault zone (Section 3.2.9) consists of several down-to-the-east normal faults along the central part of the Albuquerque Basin, in the vicinity of Albuquerque (Plate 1). For the purposes of this study, several east-dipping faults are included in the West Mesa fault zone: the Sand Hill, County Dump, Zia, Doval, Star Heights, Atrisco, and Garcia faults, and other minor or associated structures (Bryan and McCann, 1937, 1938; Kelley, 1977; Hawley and Galusha, 1978; Lambert, 1978; Machette, 1978a; 1978b; Lozinsky, 1988; Hawley and Haase, 1992). Many of these faults show geomorphic evidence of displacement since formation of the 500-ka-old Llano de Albuquerque geomorphic surface (Bryan and McCann, 1937; 1938; Hawley et al., 1976; Machette, 1978a; 1978b). Based on analysis of seismic reflection data and deep drillholes, Lozinsky (1988) and Russell and Snelson (1990, 1994) show that the major faults within the West Mesa fault zone are down-to-the-east and listric at depths below about 10 to 12 km. The total amount of Pliocene-Quaternary displacement on these faults is several kilometers (Lozinsky et al., 1991), although this amount is less than that across faults forming the eastern margin of the Albuquerque Basin (herein grouped as the Sandia-Rio Grande fault zone, see above). The County Dump fault is one of the few faults within the central Rio Grande rift for which paleoseismic data are available. Machette (1978a; 1978b) shows that there was recurrent normal displacement along the fault during the Quaternary. Seismic source characteristics for the West Mesa fault zone are summarized in Figure 7-18 and accompanying footnotes.

7.1.19 Puerco Fault

The 80-km-long Puerco fault consists of many en echelon faults that trend N30°E to N60°E directly west of the western margin of the Albuquerque Basin (Bryan and McCann, 1938; Wright, 1946; Baltz, 1976; Slack and Campbell, 1976; Kelley, 1977). The fault extends

from the northern end of the Lucero uplift on the south to the southern end of the Nacimiento uplift on the north (Kelley, 1977; Plate 1). The faults are exposed in pre-Santa Fe Group rocks within the easternmost part of the Colorado Plateau, and appear to be truncated by faults within the West Mesa fault. Fault dips range from 45° to 80° to the west, and striae on fault planes show evidence of dip-slip displacement (Hunt, 1936, cited in Kelley, 1977). Cumulative down-to-the-west displacement along most of the faults is generally less than a few hundred feet, and is opposite in sense to the down-to-the-east faults along the western margin of the Rio Grande rift. It is likely that the majority of faults in the Puerco fault developed during Laramide deformation in the late Cretaceous. There is no evidence of Quaternary activity identified along splays of the Puerco fault. Machette (U.S. Geological Survey, unpublished data, 1983) did not consider the Puerco fault as an active Quaternary structure. There is no published information on the paleoseismic behavior of splays within the Puerco fault. The fault appears to lack significant seismicity (Plates 3 and 12). Seismic source characteristics for the Puerco fault are summarized in Figure 7-19 and accompanying footnotes.

7.1.20 Gallina Fault

The Gallina-Archuleta arch forms the northern boundary of the Nacimiento uplift and separates the Chama Basin from the San Juan Basin (Woodward, 1987). The arch is an anticlinorium that extends northward for about 145 km into southern Colorado. It is bounded along its western margin by the north-northeast-striking, 40-km-long Gallina fault (Plate 1). About 1200 m of structural relief is estimated between the Gallina-Archuleta arch and the San Juan Basin to the east (Woodward, 1987). The arch, which Woodward (1987) characterizes as a steeply-dipping monocline, is separated from the bounding basin to the west by high-angle normal faults that have up to 300 m of down-to-the-west stratigraphic separation. The east side of the arch is formed by a gently dipping limb that merges with the Chama basin and has probably no more than about 150 m of structural relief (Woodward, 1987). The Gallina-Archuleta arch, along with the Nacimiento Uplift, probably originally formed during Laramide time and was rejuvenated during Miocene formation of the Rio Grande rift which also may have marked the initiation of the Gallina fault (Kelley, 1954; Woodward, 1987). Although there is no geologic evidence for Quaternary activity along the Gallina fault, the spatial coincidence of contemporary seismicity suggests that the fault may be active (Plate 12; Section 5.2). We characterize the Gallina fault as a potentially

active fault with an activity weighting of 0.5, primarily based on possible associated seismicity. Source parameters are summarized in Figure 7-20 and associated footnotes in Table 7-1 outline the bases for the chosen values.

7.1.21 Sandia-Rio Grande Fault Zone

The 45-km-long Sandia-Rio Grande fault zone as defined in this study includes all of the major, down-to-the-west faults along the eastern margin of the northern Albuquerque Basin, west of the Tijeras-Cañoncito fault (Plate 1). These north-trending faults include the Sandia fault along the base of the Sandia Mountains (Kelley, 1977; Cordell, 1978), the Rincon fault along the base of the Rincon Ridge part of the Sandia Mountains (Kelley, 1977; Hawley, 1978), the Rio Grande fault beneath the Holocene inner valley of the Rio Grande (Lozinsky, 1988; Hawley and Haase, 1992), and an unnamed fault beneath Albuquerque mapped by Lozinsky (1988) and Hawley and Haase (1992). Based on deep drillhole and oil-industry seismic reflection data, all of these west-dipping faults have down-to-the-west normal displacement and are listric at depths below about 10 to 12 km (Lozinsky, 1988; Russell and Snelson, 1990, 1994). Russell and Snelson (1994) suggest that the fault zone is decoupled at the top of the brittle-ductile transition in the crust. Collectively, these faults form the eastern margin of the Rio Grande rift and the east-tilted half graben of the northern Albuquerque Basin. The Sandia fault displaces upper Tertiary sediments and is structurally associated with the Rincon and Rio Grande faults (Cordell, 1978; Lambert et al., 1982; Lozinsky, 1988). The Rio Grande fault, which is located several kilometers basin-ward from the topographically high margin of the rift, borders the deep, inner half-graben of the basin, and exhibits the greatest amount of vertical separation of the base of rift-fill sediments (Lozinsky et al., 1991; Russell and Snelson, 1994). This fault exhibits over 4,400 m of Cenozoic displacement and clearly has played a major role in the development of the Albuquerque Basin.

The structural block between the Sandia and Rio Grande faults likely contains several down-to-the-west normal subsidiary faults, and is a structurally high suballuvial bench between the rift-flanking Sandia Mountains and the deep, inner half graben of the northern Albuquerque Basin (May and Russell, 1994). According to Chapin and Cather (1994) this bench, and others in the central Rio Grande rift, may be a result of basin-ward migration of displacement. Considering that the Rio Grande fault is the main rift-bordering structure in

the Albuquerque Basin and that similar rift-margin structures to the north (the Pajarito, La Bajada and Sangre de Cristo faults) and to the south (the Coyote Springs-Santa Fe, Hubbell Springs, and La Jencia faults) exhibit evidence of Quaternary displacement, it is likely that the Rio Grande fault is an active Quaternary structure. Identification and assessment of late Quaternary displacement along this fault is hampered by the parallelism between the fault and numerous topographic scarps thought to be terrace back-edges formed by the Rio Grande. Hawley (New Mexico Bureau of Mines, personal communication, 1993) suggests that some of these features may be late Pleistocene fault scarps. A few historical and well-located contemporary earthquakes have been located near the fault zone (Plates 3 and 12). There are no published data on the paleoseismic behavior of any faults within the Sandia-Rio Grande fault zone. Seismic source characteristics for the Sandia-Rio Grande fault zone are summarized in Figure 7-21 and accompanying footnotes.

7.1.22 Sangre de Cristo Fault

The 160-km-long Sangre de Cristo fault forms the primary tectonic boundary along the eastern margin of the San Luis Basin, which is a major structural basin of the northern Rio Grande rift (Plate 1). As noted in Section 2.3.1, the San Luis Basin is an asymmetric half-graben tilted to the east that contains a narrow (5 to 15 km wide) graben bordered on the east by the Sangre de Cristo fault (Keller et al., 1984; Chapin and Cather, 1994; Kluth and Schaftenaar, 1994). Pleistocene and Holocene fault scarps and faulted bedrock benches are present along most of the fault (Machette and Personius, 1984; Menges, 1988; 1990a,b). Along the section of the fault in New Mexico, Menges (1988; 1990a,b) identified four possible rupture segments that range from 16 to 23 km long. Each of these segments exhibits evidence of recurrent late Quaternary movement. Consistent with the geologic evidence for activity, a few well-located earthquakes appear to have occurred in the vicinity of the Sangre de Cristo fault (Section 5.2). Seismic source characteristics of the Sangre de Christo fault are summarized in Figure 7-22 and accompanying footnotes.

7.1.23 Los Cordovas Fault

The 12-km-long Los Cordovas fault consists of several parallel, north-trending faults within the southeastern San Luis Basin between the Rio Grande and Taos (Plate 1). The faults dip steeply to the west, forming an 8-km-wide zone on the Taos Plateau, and located along the

northward projection of the Picuris-Pecos fault (Lambert, 1966). Personius and Machette (1984) and Machette and Personius (1984) named the fault, and reported that it displaces alluvium no older than late Pliocene or early Pleistocene. Kelson (1986a) and Kelson and Wells (1987) mapped late Quaternary fluvial terraces across the zone, and showed that the highest geomorphic surface on the Taos Plateau (about 1.2 Ma) is displaced approximately 15 m across the fault. The oldest unfaulted terraces are estimated as younger than 0.69 Ma, because they post-date the initiation of Rio Grande incision into the Taos plateau volcano field (Wells, et al., 1987). This incision must have occurred after 0.69 Ma, the age-estimate for pre-incision fluviolacustrine deposits near Alamosa, Colorado (Rogers et al., 1985). No microearthquakes have been observed near the Los Cordovas fault (Plates 3 and 12). Seismic source characteristics for the Los Cordovas fault are summarized in Figure 7-23 and accompanying footnotes.

7.2 SEISMIC SOURCE ZONES

Seismic source zones, or in this case, seismotectonic provinces are area sources defined by unique tectonic, geologic and seismologic characteristics. Earthquakes not associated with distinct tectonic features (e.g., faults or folds) are assumed to occur randomly throughout the province. Five provinces occur within the LANL region: the Rio Grande rift, the Colorado Plateau transition zone, the Valles Volcanic province, the Great Plains, and Southern Rocky Mountains. The purpose of incorporating seismic source zones in this seismic hazard evaluation is to address the potential hazard from background (random) earthquakes. The background earthquake is defined as an event that occurs without an apparent association to a known or recognized tectonic feature (e.g., 1994 M_w 6.7 Northridge, California earthquake). In the western U.S., the maximum magnitude for the background earthquake usually ranges between M_L 6 to 6½. In most regions of the western U.S., events larger than M_L 6½ are usually accompanied by surface rupture and thus repeated events of this size will produce recognizable fault or fold-related features at the earth's surface (Doser, 1985; C. dePolo, 1994). Logic trees developed for four of the five seismic source zones are shown in Figures 7-27 through 7-30, and their components are discussed in detail in this section. Recurrence estimates were also determined for circles of increasing radii around LANL (Section 3.3.1) to determine the uniqueness of the a- and b-values for each of the separate provinces. Uncertainty in the exact position of province boundaries is not addressed specifically but is probably insignificant in comparison to the large uncertainty in the

recurrence parameters themselves, which have been incorporated into the probabilistic seismic hazard analysis.

For the LANL region, earthquakes displaying a possible association with mapped faults were still included in the recurrence calculations for the background earthquakes. We do not believe that the relocated epicenters (Section 5) are accurate enough to distinguish whether the earthquakes actually occurred on the mapped faults or structures or on smaller, similarly oriented buried faults close to the mapped fault (e.g., Nacimiento fault and associated seismicity). For example, background seismicity along the Wasatch fault in Utah occurs in a broad diffuse zone surrounding the fault with very few, if any, earthquakes located on the main fault itself (Arabasz and Julander, 1986).

7.2.1 Rio Grande Rift

As described in Sections 3.2 and 5.2, the Rio Grande rift is seismically active, with earthquakes distributed throughout much of the region. Much of the activity observed to date can be characterized as background seismicity apparently not associated with mapped faults or structures. The largest earthquake in the rift in the LANL region was the 1918 M_L 5½ Cerrillos event (Section 3.2.2). A maximum magnitude of M_w 6.3 $\pm$ 0.3 was chosen for the random earthquake within the Rio Grande rift province, a typical threshold value for surface faulting in the seismically and tectonically similar Basin and Range province. The Rio Grande rift covers an area of 11,250 km^2 within the central portion of the LANL region. The a- and b-values were determined for this province based on various minimum magnitudes (Table 3-3; Figure 3-12). The a-value is the log of the annual activity per km^2 for earthquakes of $M \geq 0$ and the b-value is the slope of the log of the annual activity per km^2 with magnitude (Section 3.3). For input into the probabilistic analyses, a b-value of 0.75 $\pm$ 0.10 was used (Figure 7-27), based on the range of b-values obtained from varying the minimum magnitudes for the recurrence estimates (Table F-1) and the fit with the data. The three chosen b-values were fixed and the corresponding a-values were computed from the truncated exponential fit to the data (see Section 3.3 for a more detailed discussion and Appendix F for tables and plots). The b-values were weighted 0.4, 0.4., 0.2 thus emphasizing the lower b-values which give more reasonable return periods for a M_w 6.3 earthquake (Table F-3). To incorporate the uncertainty in the a-value estimates, each of the three computed values was halved and doubled and the three a-values weighted 0.3, 0.4, 0.3.

All nine a- and b-value combinations span the data points (Figure F-1) and we believe the distribution adequately describes the large uncertainties associated with such a small data set. A focal depth distribution of 12, 15 and 17 km for the background earthquake was determined from the focal depth distribution observed for the best relocated earthquakes (Figures 5-1 to 5-3), with weights of 0.3, 0.4 and 0.3, respectively (Figure 7-27).

7.2.2 Colorado Plateau Transition Zone

The Colorado Plateau transition zone is characterized by low to moderate levels of background seismicity. Abundant seismicity occurs in the vicinity of the Nacimiento and Gallina faults but is diffuse and may not be directly associated with these faults. Thus, we have conservatively included these events in the recurrence analysis (Section 5.2). Elevated seismicity observed around El Vado and Heron reservoirs has been correlated with the filling cycles of these reservoirs (El-Hussain and Carpenter, 1990) and the associated seismicity for the appropriate time period (1976-1984) was removed before recurrence parameters were estimated (Section 3.2.11). A maximum magnitude of M_w 6.0 $\pm$ 0.3 was assigned to the random earthquake for the Colorado Plateau transition zone (Figure 7-28). The largest historical earthquake to occur in the transition zone is the 1966 M_L 5.5 Dulce event, which occurred just north of the LANL region. Within the LANL region, the largest event in the transition zone was the 31 July 1921 MM IV earthquake (Appendix A).

The transition zone covers an area of about 10,375 km^2 in the western portion of the LANL region (Plate 3). The a- and b-values determined for this province for various minimum magnitudes, based on the occurrence of up to 185 independent earthquakes between M_L 0.5 and 3.0, are shown in Table F-1. A b-value of 0.90 $\pm$ 0.10 was used for the probabilistic analyses based on these estimates and a visual fit to the data (Figure F-1). The b-values were weighted 0.4, 0.4, 0.2 similar to the Rio Grande rift as the highest b-value gave unrealistically large return periods for the background earthquake (Table F-4). The three corresponding a-values and their uncertainties were calculated as described above (Section 7.2.1). Focal depths of 12 to 20 km were assigned to the background earthquake. This distribution is slightly deeper than that observed within the rift because the seismogenic crust is thicker and has a lower heat flow.

7.2.3 Valles Volcanic Province

The Valles Volcanic province encompasses the Valles caldera and is located just to the west of LANL. The Valles Volcanic province is characterized by a distinct lack of seismicity, probably a result of the high heat flow beneath the caldera (Section 5.2). The Valles Volcanic province is, therefore, considered aseismic and not a significant seismic source zone in the probabilistic analysis; only three earthquakes have been located in this province (Plate 3). The province is conservatively included with the Rio Grande rift province for purposes of assigning a background earthquake.

7.2.4 Southern Rocky Mountains

The Southern Rocky Mountains province borders the northern portion of the Rio Grande rift within the LANL region and covers an area of about 8,325 km^2 (Plate 3). The province is characterized by low levels of diffuse seismicity, the majority of which locates to the east of Taos in the Sangre de Cristo Range. No significant historical earthquakes of M_L 5 or MM VI and greater have occurred in this province within the LANL region. The largest event to occur in the Southern Rocky Mountains was the 3 August 1952 maximum intensity MM V earthquake (Appendix A).

A maximum magnitude of M_w 6.3 $\pm$ 0.3 is assigned to the background earthquake of the Southern Rocky Mountains province. The b-values determined for this province, based on recurrence of earthquakes between M_L 0.5 and 4.5, vary from 0.69 to 0.93 for the various minimum magnitudes used in the recurrence estimates (Table F-1). A b-value of 0.80 $\pm$ 0.10 was chosen for the probabilistic analysis, the three corresponding a-values and their uncertainties were computed and weighted 0.4, 0.4, 0.2 (Figure 7-29). A focal depth distribution of 12 to 20 km was assigned to the background earthquake, similar to that for the Colorado Plateau transition zone. The b-value weights were estimated based on a comparison with the expected return periods of moderate size events (Table F-5).

7.2.5 Great Plains

The Great Plains seismotectonic province is characterized by low levels of seismicity (Plate 3). The most seismically active region lies just to the east of the Tijeras fault, which borders the western edge of the southern portion of the Rio Grande rift province in the LANL region (Plate 3). Two pre-instrumental earthquakes in 1930 and 1947 (Sections 3.2.3 and 3.2.5) are located just within the Great Plains province; however, given their early dates, they may be mislocated by 10 km or more. The 1930 event is the largest known earthquake (MM VI) in the Great Plains province within the LANL region. There is very little seismicity within the Great Plains province to the south and east of the LANL region.

A maximum magnitude of M_w 6.0 $\pm$ 0.3 was chosen for the background earthquake based on the general absence of significant historical seismicity. The Great Plains province covers an area of 4,650 km^2 of the southeast corner of the LANL region. The range of a- and b-values determined for this province are shown in Table F-1 and the return periods for a M 6.0 earthquake are shown in Table F-6. A b-value of 0.70 $\pm$ 0.10 was adopted for the Great Plains based on the few available data and weighted 0.4, 0.4, 0.2. Corresponding a-values and their uncertainties were again determined for each of the three b-values in a similar to fashion as described above. A focal depth distribution of 12 to 20 km is assumed for this province (Figure 7-30), similar to that for the Colorado Plateau transition zone and the Southern Rocky Mountains.

TABLE 7-1. FOOTNOTES TO LOGIC TREES FOR POTENTIAL EARTHQUAKE SOURCES

[1]The Pajarito fault system (PFS) includes the Pajarito (PAF), Rendija Canyon (RC), and Guaje Mountain (GM) faults. We considered dependent, independent, and various combinations of behavior for these three faults. Behavioral dependence branches and weightings were determined in review meetings by group consensus. The close proximity of all the faults, the dips of the RC and GM toward the PAF, and the relatively large displacements per event observed on the RC and GM, suggest dependent behavior for the three faults within the PFS. In contrast, the greater cumulative displacement on the PAF than on the RC or GM suggests at least partially independent behavior for PAF (unless displacements per event on the PAF are large and consistently exceed 3 m). Available information on timing of events suggests that, at least during the most recent event, the RC and GM ruptured independently of each other. Weights are based on consideration of overall geometry, paleoseismic information, and the assumption that out of the three cases: (1) all three faults are independent; (2) any two of the three faults are co-dependent; and (3) all three faults are co-dependent, the last case is slightly more likely. The model results in an equal likelihood that the RC is either independent or co-dependent of the GM.

[2]Rupture scenarios and lengths for the PFS are shown in Figures 7-25a through 7-25f. Scenarios and weights were based on considering criteria outlined in Table 7-2, including: fault trace geometry, sense of slip, cumulative displacement, geomorphic expression, and basin configuration. Scenarios were selected to encompass a reasonable range of likely ruptures and lengths; they do not necessarily reflect all possibilities for surface rupture. Rupture lengths are shown in brackets and were measured along a straight line end to end, on Plate 2.

[3]Deep subsurface data on the PAF is lacking but interpretation of seismic reflection data across the Albuquerque Basin indicates that, to the south, many rift-related normal faults flatten with depth (Russell and Snelson, 1990). Some of these listric faults shallow at 10 km depth, with upper portions dipping 60° and deeper portions dipping as low as 20°. In contrast, based on seismic, gravity, and geologic data, Baldridge et al. (1994) found that rift-

bounding structures near the Abiquiu embayment in the northern rift were high-angle planar normal faults. In addition, observations of historical earthquakes in the western U.S. (including the Rio Grande rift) show no evidence for earthquakes rupturing low-angle (<35°) or listric fault planes (Doser and Smith, 1989). Therefore, we assumed faults are planar in this analysis and used dips that represent averages throughout the seismogenic crust. Based on existing data, the likely average dip is about 60°. A value of 50° is included to allow for lower average dips. A value of 70° is also included to account for cases in which faults flatten deeper than 10 to 15 km and/or have a possible component of lateral slip. Weights are assumed based on a symmetric distribution about 60°.

[4]Depths and weights based on observations of historical seismicity in both the Basin and Range province (typically about 15 km) and Rio Grande rift (typically about 12 km) (see Section 5), and to reflect uncertainty and variability in observations (i.e., the possibility of ruptures as deep as 17 km for large magnitude events which tend to nucleate at or slightly below the base of the seismogenic crust).

[5]Maximum magnitudes for fault sources can be estimated using empirical relations and surface rupture lengths, surface rupture areas, displacements, or a combination of these parameters (see dePolo and Slemmons [1990] for more discussion on estimating maximum magnitudes). We use empirical relations from Wells and Coppersmith (1994) and for all fault types because they found no statistically significant difference between relations for faults with different types of slip. The Wells and Coppersmith's relations were selected for use because they compiled the most up-to-date database on historical surface ruptures, verifying observations from original reports and maps. However, we recognize that data from large normal-faulting earthquakes are still lacking, particularly from continental rift environments similar to the Rio Grande rift. Rupture length and rupture area relations were used for all faults and appropriate displacement relations were used when displacement data were available. Relations are as follows:

$M_w = 5.08+1.16 \log L$, s = 0.28;
$M_w = 4.07+0.98 \log RA$, s = 0.24;
$M_w = 6.69+0.74 \log MD$, s = 0.40; and
$M_w = 6.93+0.82 \log AD$, s = 0.39

TABLE 7-1. FOOTNOTES TO LOGIC TREES (CONTINUED)

(where L is surface rupture length measured end to end in a straight line in kilometers, s is the standard deviation, RA is rupture area in square kilometers, MD is maximum displacement in meters, and AD is average displacement in meters).

Weights were as follows: (1) where only length and area relations were used, relations were weighted equally or (2) where displacement relations were also used, these relations were weighted slightly less (0.3) because of the variability in displacement per event along a fault and the limited amount of data regarding displacements per event for the PFS and most other faults in the Rio Grande rift.

[6]Maximum magnitudes and their associated weights were calculated for each fault geometry and displacement branch. A weighted-mean maximum magnitude was then calculated from the distribution for each rupture scenario of each fault (for PFS values see Table 7.4). We used this weighted-mean, weighted at 0.6, as our best estimate, and then included values at ± 0.3 of a magnitude unit around this best estimate, weighted at 0.2, to adequately account for uncertainty. The reason for choosing these values was to use the best three-point approximation of the cumulative probability distribution for maximum magnitude. Keefer and Bodily (1983) found that the best such approximation for continuous random variables was the 5th, 50th, and 95th percentiles weighted at 0.185, 0.63, and 0.185, respectively. We rounded weights to the nearest 0.05 and used the calculated weighted-mean maximum magnitude as our best estimate of the 50th percentile, with the -0.3 and +0.3 values as best estimates of the 5th and 95th percentiles, respectively.

[7]Observations of historical seismicity and paleoseismic investigations suggest that characteristic behavior is considered more likely for individual faults and exponential behavior is more appropriate for modeling seismicity in regions (e.g., Schwartz and Coppersmith, 1984; Arabasz et al., 1992).

[8]Only the slip rate method was used because of a lack of well-constrained recurrence information.

[9]Slip rate values for the Pajarito fault are based on measurements of the NVTD of the top of the 1.2 Ma upper Bandelier Tuff (Figure 4-3a), and on comparison with published slip

TABLE 7-1. FOOTNOTES TO LOGIC TREES (CONTINUED)

rates within the Rio Grande rift (Table 7-3). The average NVTD of the upper Bandelier Tuff along the Pajarito fault is approximately 81 m, which suggests an average long-term slip rate of 0.07 mm/yr (Figure 4-3a). To account for temporal variations in slip rate, this long-term average vertical slip rate was compared to 34 short-term slip rate measurements along faults in the rift. Table 7-3 provides site-specific slip rate values (compiled by J. McCalpin, 1994) for certain time periods, and long-term average slip rates derived at each of 11 sites in the rift. We assume that this population of slip rates is an adequate representation of the likely temporal variation in slip rate along the Pajarito fault, and normalize each long-term rate to that of the Pajarito fault. To do this, we divided the site-specific long-term slip rate by the Pajarito fault long-term rate (0.07 mm/yr) to obtain a normalization factor. This factor is multiplied with the slip rates for certain time periods at each site, which yields a normalized short-term slip rate (Table 7-3). The normalized slip rates thus represent the likely temporal variations in slip rate along the Pajarito fault. A cumulative frequency plot of these data shows the probability distribution of these rates (Figure 7-26). To estimate slip rate values for the logic tree, we chose to use five branches having probabilities of 10%, 20%, 40%, 20% and 10%. These probabilities correspond to the 5th, 20th, 50th, 80th, and 95th percentiles of the slip rate cumulative frequency plot. Based on the normalized regional slip rate values, these percentiles correspond to 0.01, 0.04, 0.07, 0.16, and 0.77 mm/yr, respectively. This distribution yields a weighted mean of 0.146 mm/yr, which is slightly higher than the maximum long-term vertical slip rate for the PAF of 0.13 mm/yr based on the greatest NVTD of the upper Bandelier Tuff (Figure 4-3a). The weighted mean vertical slip rate of 0.146 mm/yr for the PFS compares favorably with the mean of normalized slip rate data in Table 7-3, which is 0.157 mm/yr.

To convert this distribution of vertical slip rates to net slip rates, the trend and plunge of the net slip vector must be accounted for. This vector can be resolved into a vertical component, a fault dip component, and a lateral component. Trigonometry shows that the net slip is equal to the vertical slip divided by the product of the size of the fault dip and the rake angle. For this analysis, we assume a fault dip of 60° (see footnote 3). Rake angle is estimated based on field data collected by K. Carter (LANL, personal communication, 1994) along the RC and GM faults. These data show that most rake angles on primary fault planes are 80° to 90°, suggesting dominantly dip-slip. However, she did observe a few rakes of about 70°. To be conservative, we assume a rake angle of 70° for this analysis. Based on

these assumptions, the net slip rate is approximately 123% of the vertical slip rate. Therefore, net slip rates of 0.01, 0.05, 0.09, 0.20, and 0.95 mm/yr are used. These data yield a weighted mean slip rate for the Pajarito fault of 0.182 mm/yr.

[10]The RC and GM faults are included here with the PAF as part of the PFS because of their close spatial association and geometry (i.e., they dip to the west toward the PAF). Although the Sawyer Canyon fault also is close to the PFS and could be part of this fault system, it was modeled as a separate source for simplicity and because it dips to the east, away from the PFS.

[11]Four rupture scenarios are included for independent ruptures of the PAF (Figure 7-25a). Rupture scenarios and weights are based on: (1) change in the sense of slip at the southern end of the fault; (2) intersection with the RC or Embudo faults at the northern end; (3) the likelihood that surface ruptures in the rift extend for tens of kilometers (Machette, 1982; Menges, 1990a,b); (4) the interpretation that structural complexities south of St. Peter's Dome are insufficient to consistently terminate rupture propagation; and (5) the significant change in geomorphic expression at Los Alamos Canyon. In the absence of paleoseismic data from each fault section, we considered RS-B as the least likely because of number (4) above.

[12]There are no data to constrain displacement per event for the PAF as an independent source. Therefore, we did not use the empirical relation for estimated maximum magnitude from displacement as we did when the PAF ruptures with either the RC or GM.

[13]Based on available fault geometry and paleoseismic data, two structural models were considered equally likely for the PFS: an intersecting and a non-intersecting model. In the intersecting model, the PAF is the master fault and truncates both the RC and GM at depths dictated by fault dips. Because geomorphic expression changes and cumulative displacement decreases on the PAF at the same latitude where cumulative displacement increases on both the RC and GM, we also considered a non-intersecting structural model. In this model, the RC and GM faults are not truncated by the PAF, but are through-going crustal structures with slip on the PAF being transferred to the RC and GM faults somewhere near the latitude of Los Alamos Canyon.

TABLE 7-1. FOOTNOTES TO LOGIC TREES (CONTINUED)

[14]Displacements estimated from the Guaje Pines Cemetery site are 1.5 to 2.5 m. Values of 2 and 2.5 m are determined from trench logs and models of scarp degradation. A value of 1.5 m is included because eolian or overbank deposits may have thickened colluvial wedges, resulting in overestimation of displacement, which were based on colluvial wedge thickness. This site is along the central part of the RC where the maximum NVTD was observed on topographic profiles (Figure 4-3b). Carter and Gardner (1993) also observed maximum stratigraphic separations of the Bandelier Tuff across the RC near this location. Therefore, we considered these values maximum displacements in estimating maximum magnitudes.

[15]Although recurrence information may be more indicative of recent activity along the PFS than the post-1.2 Ma slip rate, data on recurrence intervals are limited to only the RC and are not well-constrained. Therefore, we weighted slip rate and recurrence methods equally.

[16]Slip rate values for the Rendija Canyon fault are based on measurements of the NVTD of the 1.2 Ma upper Bandelier Tuff (Figure 4-3b), and on comparison with published slip rates within the Rio Grande rift. The average NVTD of the upper Bandelier Tuff along the Rendija Canyon fault is 21 m (Figure 4-3b), which suggests an average long-term slip rate of 0.02 mm/yr. To account for temporal variations in slip rate, this long-term rate was compared to 34 short-term rates within the Rio Grande rift (see footnote 9). Similar to the Pajarito fault (footnote 9), we normalized long-term rates at other sites to the Rendija Canyon fault long-term rate (0.02 mm/yr). This approach yielded vertical slip rate values of 0.01, 0.02, 0.05, and 0.20 mm/yr, and a weighted mean of 0.041 mm/yr. Based on conversion of these rates to net slip rates (see footnote 9), the slip rate values for this analysis are 0.01, 0.02, 0.06, and 0.25 mm/yr. The weighted mean for this distribution is 0.048 mm/yr.

[17]Recurrence values and weights for the RC are based primarily on paleoseismic data from the Guaje Pines Cemetery site. From stratigraphic relations, thermoluminescence ages, and radiocarbon ages, recurrence values range from about 13,000 to 67,000 years (Figure 4-19). Values are chosen to encompass this range, with an interval of 10,000 years included to allow for the possibility of temporal clustering. Weights are chosen based on temporal constraints shown on Figures 4-17 and 4-19.

TABLE 7-1. FOOTNOTES TO LOGIC TREES (CONTINUED)

[18]Fault plane measurements made during detailed bedrock mapping along the RC show dips ranging from 60° W to 90° and averaging about 79° W (K.E. Carter, LANL, personal communication, 1993). Shallow dips are consistent with interpretations of the RC as a rift-bounding structure and steeper dips are consistent with its linear trace and the possibility of lateral slip on the RC.

[19]For short faults less than 15 km long, shallower seismogenic depths were assumed to maintain more reasonable rupture plane aspect ratios (length:width). Weights were based on an assumed symmetric distribution of depths. Although empirical data indicates aspect ratios can be less than one, a typical value is greater than one and as high as 4 (D. Wells, Geomatrix Consultants, personal communication, 1994). Thus, we have assumed that for shorter faults, maximum depths of faulting less than 15 km to maintain ratios greater than one.

[20]In the intersecting model, the RC is truncated by the PAF at a depth determined by fault dips (Table 7-5). As a minimum rupture area is necessary to generate an earthquake of significant size, we only considered geometric scenarios with depths greater than 6 km in our analysis. This constraint only permits a 90° dip for the RC and a 70° dip for the PAF with this intersecting model. These dips result in a 8 km depth.

[21]Data from the Cabra Canyon trench across the GM suggests displacements of 1.5 to 2 m per event (Gardner et al., 1990). Displacement data from terrace profiles in Rendija Canyon is permissive of 1.0 to 2.5 m of displacement per event. Weights were based on overlap of data sets. Empirical relations for average displacement were used because both Cabra and Rendija Canyons are located along the GM where post-1.2 Ma displacement is roughly equal to the average displacement along the fault.

[22]Slip rate values for the Guaje Mountain fault are based on measurements of the NVTD of the 1.2 Ma upper Bandelier Tuff (Figure 4-3c), and on comparison with published slip rates within the Rio Grande rift. The average NVTD of the upper Bandelier Tuff along the Guaje Mountain fault is 15 m (Figure 4-3c), which suggests an average long-term vertical slip rate of 0.01 mm/yr. To account for temporal variations in slip rate, this long-term rate was

compared to 34 short-term rates within the Rio Grande rift (see footnote 9). Similar to the Pajarito fault (footnote 9), we normalized long-term rates at other sites to the Guaje Mountain fault long-term rate (0.01 mm/yr). This approach yielded vertical slip rate values of 0.01, 0.02, and 0.11 mm/yr, and a weighted mean of 0.022 mm/yr. Based on conversion of these rates to net slip rates (see footnote 9), the slip rate values for this analysis are 0.01, 0.02, and 0.14 mm/yr. The weighted mean for this distribution is 0.025 mm/yr.

[23]Fault plane measurements made during detailed bedrock mapping along the GM indicate a range of dips similar to the RC (see footnote 18), with an average dip of about 75°W (K.E. Carter, LANL, personal communication, 1993). Weights were based on these data and an overall linear surface trace, which suggests a near-vertical dip.

[24]In the intersecting model, the GM is truncated by the PAF at a depth determined by fault dips (Table 7-6). As a minimum rupture area is necessary to generate an earthquake of significant size, we considered geometric scenarios with depths of 6 km or greater in our analysis. This constraint only permits 70° to 90° dips for the GM with this intersecting model (Table 7-6). We weighted deeper scenarios more because we considered surface rupturing events that only rupture the shallow crust as less likely.

[25]In the non-intersecting structural model for PAF and RC rupturing dependently, individual events were randomly distributed over both fault planes in the probabilistic analysis and proportioned according to total fault plane area.

[26]Two rupture scenarios are included for the case in which the PAF and RC are behaviorally dependent and non-intersecting. Scenario RS-G is similar to scenario RS-B for the independent PAF, with the exception that the RC ruptures instead of the north-central section of the PAF. Scenario RS-H is similar to scenario RS-C for the independent PAF, with the same exception. Weights are based on similarities to RS-B and RS-C (see footnote 11), normalized by excluding RS-A and RS-D.

[27]Displacement data for the RC was considered most appropriate for dependent rupture of the RC and PAF together because of a lack of displacement data for individual events on the PAF (see footnote 14 for discussion of the RC displacement data). We used the average

displacement empirical relation in this case because the Guaje Pines site is not at the location of peak displacement for the PFS (as it is for the RC) (Figures 4-3a and 4-3b) and measured displacements would probably be closer to averages for the PFS rather than maximums as they appear to be for the RC.

[28]Both slip rate and recurrence methods are used for this case based on the assumption that recurrence information for the RC is representative of dependent rupture of the PAF and RC together. However, we weighted the slip rate method greater than the recurrence method in this case because recurrence intervals are not well-constrained, especially for the PAF.

[29]For the PAF and RC rupturing together, we used recurrence information for the RC (see footnote 17) because of a lack of data on the recurrence intervals for the PAF.

[30]For the PAF and RC rupturing together, slip rates for the PAF were considered most appropriate (see footnote 9 on PAF slip rates).

[31]For the intersecting model where the PAF and RC rupture together, the PAF was modeled as the master fault, where essentially all of the seismic moment is released on the PAF, and the RC is a subsidiary structure that contributes negligible moment during an event.

[32]Rupture scenarios for the intersecting structural model (RS-I, RS-J, RS-K) are similar to rupture scenarios RS-B, RS-C, and RS-D where the PAF ruptures independently because the PAF is modeled as the master fault in the intersecting model. Weights were assumed similar to RS-B, RS-C and RS-D but normalized by excluding RS-A.

[33]For cases in which the Pajarito fault ruptures co-dependently in the intersecting structural model with either the RC or GM, or with both, empirical relations between magnitude and maximum displacement (Wells and Coppersmith, 1994) were used. However, for the intersecting structural model, we did not directly use displacement data from the RC and GM as we did in the non-intersecting structural model (cf. footnotes 27, 37, 48) because in the intersecting model, the RC and GM are subsidiary faults to the PAF. Instead, because there are not available data on the displacement per event for the Pajarito fault, we used data on displacement per event for the RC and GM (see footnotes 21 and 27) as minima for the

maximum displacement per event on the entire fault system. This is based on the assumption that if rupture occurred on the Pajarito fault and one or both of the other faults, displacement likely would be greater on the Pajarito fault for the intersecting structural model. Therefore, a minimum value of 1.0 m for maximum displacement per event is likely (see footnotes 21 and 27). To estimate the range in maximum displacement per event, data on maximum displacement per event from earthquakes on normal faults throughout the world having more than 10 km of surface rupture (Wells and Coppersmith, 1994) were used. Their database shows 19 normal-fault historical earthquakes having a range in maximum displacement from 0.2 to 6.6 m (Table 7-7). We assume that this population is applicable to the Pajarito fault system, with the exception of the displacements that are less than 1 m, which is below the minimum value cited above. We plotted the cumulative frequency distribution of the 14 measurements satisfying these criteria. To estimate displacement values for the logic tree, we chose to use the 10th, 50th, and 90th percentiles of the cumulative frequency plot weighted at 0.3, 0.4, 0.3, respectively, because this three-point approximation is best when the tails of a distribution are not well-defined (Keefer and Bodily, 1983). These percentiles correspond to displacement values of 1.1, 2.5, and 5.8 m, respectively. For simplicity, we assign values of 1.5, 2.5, and 5.5 m to the three branches, which yields a weighted mean of 3.1 m.

[34]Although the timing of the most recent events on the RC and GM suggests they may rupture independently, this behavioral branch is weighted low because the RC and GM are close to one another and have similar geometries and structural styles.

[35]We used a two-plane rupture model for the non-intersecting case in which the PAF and GM rupture dependently. Individual events were randomly distributed over both fault planes in the probabilistic analysis and proportioned according to fault plane area.

[36]Two rupture scenarios are included for the case in which the PAF and GM are behaviorally dependent and non-intersecting. Scenario RS-L is similar to scenario RS-B for the independent PAF, with the exception that the GM ruptures instead of the north-central section of the PAF. Scenario RS-M is similar to scenario RS-C for the independent PAF, with the same exception. Weights are based on similarities to RS-B and RS-C (see footnote 11), normalized by excluding RS-A and RS-D.

TABLE 7-1. FOOTNOTES TO LOGIC TREES (CONTINUED)

[37]Displacement data for the GM was considered most appropriate for dependent rupture of the GM and PAF because of a lack of displacement data for individual events on the PAF (see footnote 21 for discussion of GM displacement data).

[38]For the PAF and GM rupturing together as behaviorally-dependent structures, slip rates for the PAF were considered most appropriate (see footnote 9 on the PAF slip rates).

[39]For the intersecting model where the PAF and GM rupture together, the PAF was modeled as the master fault, in which case, essentially all of the seismic moment is released on the PAF, and the GM is a subsidiary structure that contributes negligible moment during an event.

[40]Rupture scenarios for the intersecting structural model (RS-N, RS-O, RS-P) are similar to rupture scenarios RS-B, RS-C, and RS-D where the PAF ruptures independently because the PAF is modeled as the master fault in the intersecting model. Weights were assumed similar to RS-B, RS-C and RS-D but normalized by excluding RS-A.

[41]To determine areas for maximum magnitude calculations when the RC and GM rupture together, all dips and depths were considered, and areas of both fault planes were added together. For geometries where the RC and GM intersect one another, the plane resulting in the maximum area was modeled as the through-going plane to determine the rupture area below where they intersect.

[42]Maximum displacement data is from the Guaje Pines Cemetery site along the RC (see footnote 14).

[43]Average displacement data is from sites along the GM (see footnote 21).

[44]We assumed recurrence information for the RC is applicable for dependent rupture of RC and GM (see footnote 17 on RC recurrence intervals).

[45]To determine average slip rates and weights for the GM and RC rupturing together, we averaged slip rate distributions for each fault together, weighted according to fault plane area

TABLE 7-1. FOOTNOTES TO LOGIC TREES (CONTINUED)

(see footnote 22 on the GM slip rate distribution and footnote 16 on the RC slip rate distribution).

[46]Two rupture scenarios are included for the case in which the PAF, RC and GM are behaviorally dependent and non-intersecting. Scenario RS-R is similar to scenario RS-B for the independent PAF, with the exception that the RC and GM rupture instead of the north-central section of the PAF. Scenario RS-S is similar to scenario RS-C for the independent PAF, with the same exception. Weights are based on similarities to RS-B and RS-C (see footnote 11), normalized by excluding RS-A and RS-D.

[47]To determine areas for maximum magnitude calculations when the PAF, RC, and GM rupture together, all dips and depths were considered and areas for all three fault planes were added together. For geometries where the RC and GM intersect one another, the plane resulting in the maximum rupture area was modeled as the through-going plane to determine the rupture area below where they intersect.

[48]Displacement data is from the Guaje Pines Cemetery site along the RC (see footnote 14) and sites along the GM (see footnote 21). In this case, all values were considered averages and weights were determined by averaging the RC and GM displacement probabilities.

[49]We assumed recurrence information for the RC is applicable for rupture of the PAF, RC, and GM together (see footnote 17 on the RC recurrence intervals).

[50]For the PAF, RC, and GM rupturing together, PAF slip rates were considered the most appropriate (see footnote 9 on PAF slip rates).

[51]For the intersecting model where the PAF, GM and RC rupture together, the PAF was modeled as the master fault, in which case essentially all of the seismic moment is released on the PAF, and the RC and GM are subsidiary structures that contribute negligible moment.

[52]Rupture scenarios for the intersecting structural model (RS-T, RS-U, RS-V) are similar to rupture scenarios RS-B, RS-C, and RS-D where the PAF ruptures independently because the

TABLE 7-1. FOOTNOTES TO LOGIC TREES (CONTINUED)

PAF is modeled as the master fault in the intersecting model. Weights were assumed similar to RS-B, RS-C and RS-D but normalized by excluding RS-A.

[53]During detailed bedrock mapping along the Sawyer Canyon fault, Carter measured over 30 orientations of faults in the Tshirege Member of the Bandelier Tuff, yielding average dips of 75° to 80°E and dips ranging as steep as 90° (K.E. Carter, LANL, personal communication, 1993). Weights were based on general distribution of fault dips and the assumption that dips do not significantly change with depth for the Sawyer Canyon fault.

[54]Rupture scenario 1 for the Sawyer Canyon fault terminates at the northern end of the fault where it intersects the PAF (Plate 2). Rupture scenario 2 of the Sawyer Canyon fault includes the northernmost part of the PAF north of the PAF-Sawyer Canyon fault intersection (Plate 2). We assigned a slightly higher weight to scenario 2 because the longer length seems more reasonable for surface faulting events, and because displacements measured in the Tshirege Member of the Bandelier Tuff increase to the north along the Sawyer Canyon fault (Carter and Gardner, 1993).

[55]Although weighted-mean maximum magnitudes of M_w 6.0 and M_w 6.3, respectively, were calculated for rupture Scenarios 1 and 2 of the Sawyer Canyon fault, we used maximum magnitude distributions the same as those calculated for the RC and GM as independent non-intersecting sources (RS-E and RS-F for the Pajarito Fault System). Our reasons for making this exception were two-fold: 1) calculated magnitudes for the Sawyer Canyon fault result in values as low as 5.7, far below the threshold for surface faulting; and, 2) the close proximity and similarity of the Sawyer Canyon fault to the RC and GM in structural style, geomorphic expression and long-term Quaternary rate of activity suggests that displacements per event and maximum magnitudes may also be similar.

[56]The Sawyer Canyon fault is classified as a slip rate Category B fault. Measured vertical stratigraphic displacements of the Tshirege Member of the Bandelier Tuff (1.2 Ma) range from 21 to 37 m (K.E. Carter, LANL, personal communication, 1993) yielding long-term vertical slip rates from 0.019 to 0.034 mm/yr for the Sawyer Canyon fault. Values chosen here allow for possible differences in the short-term rate of activity by using the distribution of slip rates within the Rio Grande rift, normalized to 0.03 mm/yr.

TABLE 7-1. FOOTNOTES TO LOGIC TREES (CONTINUED)

[57]Measurements of bedrock faults within the Puye fault zone indicate dips of dominant splays are similar to those measured for the Sawyer Canyon fault, averaging 75° to 80°E (K.E. Carter, LANL, personal communication, 1993). Weights were based on general distribution of fault dips and the assumption that dips do not significantly change with depth for the Puye fault zone.

[58]The Puye fault is classified as a slip rate Category B fault. Assessment of total displacement across all strands of the Puye fault zone is unknown because of restricted access to faults on Indian Reservations. K.E. Carter (LANL, personal communication, 1993) measured displacements of 3 to 14 m of the 1.2 Ma Tshirege Member of the Bandelier Tuff along individual strands of the Puye fault zone, yielding slip rates of 0.003 to 0.013 mm/yr. There is 9 m of NVTD across the primary scarp along the central part of the zone; this surface is probably between 350 ka and 1.12 Ma (Dethier et al., 1988b). This yields slip rates of 0.008 to 0.03 mm/yr for this primary strand. Assuming this primary splay accommodates most of the displacement at this latitude along the fault, we normalized the distribution of slip rates within the Rio Grande rift to 0.03 mm/yr to determine values of 0.01, 0.03, and 0.3 mm/yr weighted 0.2, 0.6, 0.2, respectively, for the Puye fault zone.

[59]Although the surficial expression of the Puye fault zone is a 6-km-wide zone of small faults, these splays may converge to a single plane at depth. To be conservative, we modeled this fault zone as a single plane coincident with the westernmost splay.

[60]Deep subsurface data is lacking on this fault so dips and weights were assumed based on similar arguments for the PAF (see footnote 3).

[61]The Lobato Mesa fault zone is classified as a slip rate Category B fault. Gardner and House (1987) estimated a long-term net slip rate of 0.05 mm/yr based on 490 to 520 m of slip on a 10.6 My old basalt dike. They also estimate a vertical rate of 0.02 mm/yr for a single splay on the zone based on a 15-m-high scarp on Bandelier Tuff. We modeled slip rate values using the distribution of slip rates within the Rio Grande rift, normalized to 0.05 mm/yr.

TABLE 7-1. FOOTNOTES TO LOGIC TREES (CONTINUED)

[62]The Lobato Mesa fault zone is a series of short, north-striking faults that generally dip to the west. These faults may converge to a single fault plane. To be conservative, we modeled the Lobato Mesa fault zone as a single plane coincident with the dominant, central splay.

[63]The La Bajada and San Francisco faults form the eastern margin of the Santo Domingo Basin. Vertical separation on the La Bajada fault decreases to the south from its intersection with the Pajarito fault at Cochiti Lake. Vertical separation on the San Francisco fault likely increases to the south from Cochiti Lake to its intersection with the Sandia-Rio Grande fault near Placitas. Thus, slip may be transferred from the Pajarito fault at Cochiti Lake onto the La Bajada and San Francisco faults, and then further to the south from the La Bajada fault onto the San Francisco fault. If so, then both the La Bajada and San Francisco faults likely are rift margin faults. We assume dips and weights similar to the PAF for both the La Bajada and San Francisco faults.

[64]The La Bajada fault is classified as a slip rate Category B fault. Aubele (1978) notes that the La Bajada escarpment is approximately 160 m high and is capped by Cerros del Rio basalt flows, which are dated at 2.5 to 2.6 Ma (Bachman and Mehnert, 1978). These data yield an average long-term vertical slip rate of 0.06 mm/yr. Baltz (1976) speculates that displacement "could have been about 2,000 feet since the La Bajada basalts were erupted on the Ortiz physiographic surface," approximately on the basis of a regional geologic cross-section given by Smith et al. (1970). Furthermore, he speculates that this displacement has occurred "at some time within the last 2 million years," and cites undisclosed "indirect reasoning concerning the geomorphic relations" as evidence that much of the 2,000 ft (610 m) of displacement could have occurred since deposition of the 1.2 Ma upper Bandelier Tuff. These unconstrained estimates yield a slip rate of 0.55 mm/yr, which we do not use because of the uncertainty in the basis for the amount and age of displacement. The slip rate values for the La Bajada fault are modeled using the distribution of slip rates within the Rio Grande rift, normalized to 0.06 mm/yr.

[65]Dips measured during our reconnaissance of exposures at the northern end of the northeast section of the Embudo fault range from 70° to 85° to the northwest. Dips for the southwest section were assumed to also be steep but to the southeast based on possible continuity with

the PAF at the southern end and geometry of the Española Basin. Weights were based on assuming a symmetric distribution about 90° and assuming dips do not significantly change with depth for the Embudo fault.

[66]Rupture scenarios for the Embudo fault are based on changes in geomorphic expression and sense of slip between northeastern and southwestern sections. The sense of vertical separation on the Embudo fault is interpreted to change near the town of Embudo (Machette and Personius, 1984; Personius and Machette, 1984). The northeastern section of the fault is located from this hinge point to an intersection with the Sangre de Cristo fault at Ranchos de Taos; the southwestern section extends from the hinge point to an intersection with the Pajarito fault near Clara Peak. The northeastern section of the Embudo fault exhibits evidence of late Quaternary activity near Hondo Canyon (Muehlberger, 1979) and based on our field reconnaissance, near the town of Dixon. During our reconnaissance along the southwestern section of the fault, we found no evidence of late Quaternary activity. However, to be conservative, we assume both sections are active. Rupture scenarios include these two sections as independent segments.

[67]There are several pieces of geologic and geomorphic data that allow estimation of the slip rate for the Embudo fault. However, none is of sufficient quality to adequately constrain an average long-term slip rate. First, field reconnaissance along Rio Embudo near Dixon (Section 4.1.3.1) shows that late Quaternary fluvial terrace deposits exhibit about 3 m of vertical separation across one strand of the fault. These deposits are probably late Pleistocene in age (about 10 to 150 ka), but better constrained data are not available to estimate a slip rate. In addition, the observed displacement is based on just one of two or three fault strands in the vicinity and thus, any slip rate estimate would be a minimum. Second, scarp height data are available along the northeastern end of the fault near Arroyo Hondo (Section 4.1.3.1.5). Personius and Machette (1984) note a non-eroded scarp along the fault is about 15 m high and has the form of a late Pleistocene normal fault scarp. Our field reconnaissance shows that further to the southeast, the scarp has a height of 8.5 m. The lateral components of slip associated with these vertical separations are unknown, which precludes estimation of a net slip rate for the Embudo fault from available field data. Thus, the Embudo fault is classified as a Category C fault and the net slip rate distribution is derived from regional relations, as described below.

The Embudo fault likely is a predominantly lateral-slip fault that acts as a zone of accommodation between the Española and San Luis basins. In this model, the slip rate along the southwestern section of the Embudo fault is a function of the slip rates on the Pajarito, Rendija Canyon, Guaje Mountain, and Sawyer Canyon faults. Slip rates for these faults must first be converted to rates of horizontal east-west extension, and then resolved into average net slip rates along the N60°E-striking Embudo fault (Table 7-8). Similarly, this model requires that the slip rate along the northeastern section of the fault is a function of the Sangre de Cristo fault, which has a weighted late Quaternary vertical slip rate of 0.13 mm/yr (based on data in footnote 107). This value translates to a net horizontal east-west extension rate of 0.075 mm/yr, assuming a 60°W dipping fault. This value translates to a net lateral slip rate along the strike of the Embudo fault of 0.09 mm/yr. Based on these data, a net slip rate for the Embudo fault of 0.09 mm/yr is estimated. This value is probably conservative given the lack of prominent geomorphic expression of the fault. Slip rate values and weights used in the logic tree are based on the distribution of slip rate values from throughout the Rio Grande rift, normalized to 0.09 mm/yr.

[68]The potential activity of several faults in the region is unknown or poorly constrained. Many faults displace Pliocene basalt and exhibit geomorphic expression but there are no data on the timing of most recent events or on elapsed time between surface rupture earthquakes. These poorly characterized faults include the La Cañada del Amagre-Clara Peak, Pojoaque, San Felipe, Cañones, Black Mesa, Nacimiento, Picuris-Pecos and Puerco faults and fault zones. In the absence of definitive evidence for Quaternary activity, it is assumed equally likely that these faults are active or inactive.

[69]Due to the large component of lateral displacement on the La Cañada del Amagre fault observed by Aldrich and Dethier (1990) and the dip they measured on one splay of 66° to the east at the surface, we assumed slightly steeper dips than typical rift faults (c.f. footnote 3).

[70]The La Cañada del Amagre-Clara Peak fault zone is classified as a slip rate Category B fault. Aldrich and Dethier (1990) estimate 530 m of net slip across the fault based on offset of 10.6 Ma basalt dikes. From kinematic arguments, they infer that all this slip occurred since 5 Ma, yielding a long-term slip rate of 0.1 mm/yr. Certainly all offset has occurred

since emplacement of the dike, 10.6 Ma, which yields a slip rate of 0.05 mm/yr. We modeled slip rate values using the distribution of rates within the Rio Grande rift, normalized to 0.1 mm/yr.

[71]The San Francisco fault is classified as a slip rate Category C fault. Due to the lack of slip rate or recurrence data for the San Francisco fault, we assumed rates and weights similar to the La Bajada fault (see footnote 64).

[72]The Pojaque fault is classified as a slip rate Category C fault. No data are available regarding the slip rate on the Pojoaque fault, which likely is part of distributed brittle deformation along the southeastern margin of the Velarde graben (Manley, 1979a,b). If the fault is active, it probably has a lower slip rate than the Pajarito fault because: (1) the Española Basin is a west-tilted asymmetric graben with lower amounts of slip on faults in the eastern part of the basin, and (2) a lack of fault trace continuity and prominent geomorphic expression. Manley (1979a,b) notes that the Velarde graben has subsided 60 m in 3 Ma, which yields a long-term slip rate of 0.02 mm/yr, some of which may have occurred on the Pojoaque fault. We consider an upper bound for the long-term average slip rate on the Pojoaque fault of 0.02 mm/yr, based on the assumption that a 1 to 2 m high fault scarp could survive at most only 100,000 to 150,000 years in this climatic and geologic environment. The slip rate values are modeled using the distribution of slip rates within the Rio Grande rift, normalized to 0.02 mm/yr.

[73]Because it is unknown whether the eastern or western boundary fault of the San Felipe graben is the master fault, the dip direction at seismogenic depths is unknown. It is assumed that either the Algodones or Santa Ana fault is the master fault, and thus, that the "fault zone" itself dips either to the east or the west. An average dip of 60° is assumed based on likely dips of major rift faults in the Albuquerque Basin (see footnote 60); a vertical dip is included to account for a high degree of uncertainty in dip direction. Weights were based on an assumed symmetric distribution about a vertical dip.

[74]There is no data available on the temporal or physical behavior of the San Felipe fault zone that addresses potential rupture segments and so we consider both the possibility that the faults rupture together and that they rupture independently. We assume that the scenario in

which the faults bordering the San Felipe graben rupture together is half as likely as that in which the faults rupture as independent segments because the two faults are separated by 3 km and dip in opposing directions.

[75]The San Felipe fault zone is classified as a slip rate Category B fault. Soister (1952) notes that scarps along faults in the San Felipe fault zone are up to 102 m high, although most are 12 to 46 m high. These scarps are developed in basalt dated at 2.5 to 2.6 Ma (Bachman and Mehnert, 1978). It is likely that these scarps represent late Pliocene and Pleistocene displacement because they are not expressed in areas not underlain by the resistant basalt. Nevertheless, these data yield long-term slip rates of 0.01 to 0.04 mm/yr. The slip rate values for the San Felipe fault zone are based on the distribution of slip rates throughout the Rio Grande rift, normalized to an assumed, conservative long-term rate of 0.04 mm/yr.

[76]The San Felipe fault zone consists of several north-striking faults that, in general, form a graben in the northernmost Albuquerque Basin. The eastern boundary fault is the west-dipping Algodones fault of Kelley (1977), which exhibits down-to-the-west separation of Pliocene basalt. The western boundary fault is the east-dipping Santa Ana fault of Kelley (1977), which exhibits down-to-the-east separation of Pliocene basalt. It is likely that this graben is a minor sub-basin of the Albuquerque Basin.

[77]The Jemez-San Ysidro fault system consists of a northeast-striking series of faults (the Jemez fault of Goff and Kron, 1980) and a north-striking fault along the northwestern margin of the Albuquerque Basin (the San Ysidro fault of Woodward and Ruetschilling, 1976). The boundary between these two faults is interpreted as the 45° change in fault strike north of the town of San Ysidro. These two faults are grouped as the Jemez-San Ysidro fault system because of lateral continuity. Although there are no data regarding potential rupture segments within the fault system, it is assumed that both faults could either rupture together or separately as independent segments. The independent rupture scenario is believed to be more likely based on the difference in geometry between the Jemez and San Ysidro faults.

[78]The Jemez fault appears to be near vertical at the surface and in the shallow subsurface based on relatively straight traces across rugged topography. Microseismicity in the vicinity of the Jemez fault appears to be aligned along a near-vertical zone, slightly to the west

(Leigh House, LANL, unpublished data, 1993), although as a probable ancestral rift margin, the fault may also dip to the east. Based on these relations, it is assumed that the Jemez fault dips either 80°E, 90° or 80°W, with weights based on a lack of a favored dip. The San Ysidro fault likely is a major rift-margin fault, with moderate easterly dips (see footnote 60). For the rupture scenario in which both faults rupture together, the fault dips are assumed to be in the range of dips for the two individual faults, with steep westerly dips derived from the Jemez fault and moderate easterly dips derived from the San Ysidro fault.

[79]The Jemez-San Ysidro fault system is classified as a slip rate Category B fault. Woodward (1987) reports 12 m of separation of 1.2 Ma Bandelier Tuff along the Jemez fault, and Goff and Shevenell (1987) and Goff et al. (1989) note 50 m of separation of the same unit along the fault. These data yield long-term separation rates of 0.01 to 0.05 mm/yr. Based on these data, we modeled slip rate values using the distribution of slip rates within the Rio Grande rift, normalized to 0.05 mm/yr.

[80]The Cañones fault is classified as a slip rate Category C fault. Gonzalez and Dethier (1991) estimate a minimum vertical slip rate of 0.07 to 0.08 mm/yr over 8 Ma. However, this structure likely was the rift margin prior to 5 Ma (Gardner and Goff, 1984; Gonzalez and Dethier, 1991). If so, the slip rate on the Cañones fault between 8 and 5 Ma may have been as high as 0.21 mm/yr, then has been negligible since 5 Ma. The fault does not displace basalt flows on Cañones Mesa mapped as the 8 Ma Lobato Basalt (Manley, 1982), although these basalts are more likely the 3 Ma flows associated with El Alto Mesa (M. Gonzalez, personal communication, 1994). Smith et al. (1970) show that the fault is buried by the 1.2 Ma upper Bandelier Tuff. Although the Cañones fault is no longer the primary active margin of the rift, we acknowledge the possibility that the fault may be active (see footnote 68). We consider an upper bound for the long-term average slip rate on the Cañones fault of 0.02 mm/yr based on the assumption that a 1 to 2 m high fault scarp could survive at most 100,000 to 150,000 years in this climatic and geologic environment.

[81]On the basis of air photo interpretation, Kelley (1978) and Vernon and Riecker (1989) postulate that there is a continuous, well-defined, potentially active fault along the western margin of the Sangre de Cristo Mountains near Santa Fe. However, detailed field studies (Cabot, 1938; Spiegel and Baldwin, 1963; Miller et al., 1963; Galusha and Blick, 1971;

Baltz, 1976; Manley, 1979a,b) show that this margin is likely a depositional onlap with little or no continuous Quaternary faulting. More recent studies (R. Klinger, U.S. Bureau of Reclamation, unpublished data, 1992; LaForge and Anderson, 1988) do not consider the fault as a potential seismic source. It is assumed that there is a small possibility that the fault, if present, is active based on its location along the eastern margin of the Española Basin.

[82]Previous workers note that short fault strands in the eastern part of the Española Basin are steeply dipping at the surface. These strands exhibit both down-to-the-east and down-to-the-west vertical separation. We assume that strands of the Nambe fault could dip to the west or to the east. Dips of 60° and 80° are assumed for both dip directions based on steep near-surface dips observed in the field and on the possibility that the dip is similar to other intra-rift and rift-margin faults (see footnote 60).

[83]The Nambe fault is classified as a slip rate Category C fault. There are no data available on the Quaternary slip rate of the Nambe fault. Slip rate values are assumed based on other intra-rift and rift-margin faults, and on the lack of fault trace continuity and geomorphic expression. We consider an upper bound for the long-term average slip rate on the Nambe fault of 0.02 mm/yr, based on the assumption that a 1 to 2 m high fault scarp could survive at most only 100,000 to 150,000 years in this climatic and geologic environment. The slip rate values are modeled using the distribution of slip rates within the Rio Grande rift, normalized to 0.02 mm/yr.

[84]There are no data available on the dip of the faults of Black Mesa. The linear traces of these faults across topographic relief at the mesa margins suggest high-angle dips near the surface. Faults exhibit topographic scarps that face southeast and northwest; it is uncertain which strand, if any, is a master fault representative of the dominant fault separation at depth. Dip directions to the northwest and southeast are considered, as well as a vertical dip because of the proximity and possible association with the Embudo fault. Dips of 70° are considered based on the possibility that the fault dips moderately. Weights are estimated based on the assumption that all cases are equally likely.

[85]The faults of Black Mesa are classified as a slip rate Category B faults. Topographic scarp heights were measured across three of the four scarps present on Black Mesa, and the fourth

scarp height is estimated from a 20-ft contour topographic map. The mesa is underlain by basalt estimated as 3.65 ± 0.09 Ma (Laughlin et al., 1993). A minimum slip rate is estimated based on the assumption that the highest scarp is the main strand of the fault, and that other strands are subsidiary. This strand has a 19 m high scarp, which yields a slip rate of 0.005 mm/yr. The sum of all four scarp heights is 52 m, which yields a maximum slip rate of 0.014 mm/yr. The distribution of slip rates for the faults of Black Mesa are modeled using distribution of slip rates within the Rio Grande rift, normalized to an assumed, conservative long-term rate of 0.02 mm/yr.

[86]Previous workers note that the Tijeras-Cañoncito fault north of Albuquerque dips steeply, exhibits evidence of lateral slip, and has a linear trace across rugged topography (Lisenbee et al., 1979; Kelley and Northrop, 1975). Based on these data, the dip of the fault was assumed to be vertical.

[87]Previous literature identifies several structural sections of the Tijeras-Canoncito fault based on large horsts, graben, and changes in fault zone complexity (Lisenbee et al., 1979; Maynard et al., 1991; Kelley and Northrop, 1975; Bachman, 1975). The southern sections of the fault (Tijeras and Four Hills) are grouped together because of potentially fault-related lineaments across late Quaternary surfaces (K. Kelson, WL&A, unpublished data, 1994) and possible evidence of faulted colluvium (Lisenbee et al., 1979). The central sections (Monte Largo and San Pedro/Ortiz) are grouped together for a possible rupture scenario based on structural complexity and the likelihood that these short sections would not rupture independently in large magnitude earthquakes. The northern section (Lamy) is treated as possible rupture segment because of its length and less prominent geomorphic expression than the adjacent sections.

[88]The Tijeras/Four Hills section is considered active based on geomorphic expression across late Quaternary surfaces and possible evidence of faulted colluvium. The activity of the Monte Largo/San Pedro/Oritz and the Lamy sections is unknown. Both sections exhibit geomorphic expression in bedrock terrane, but there are no data that address the presence or absence of Quaternary displacement. In the absence of more conclusive data, it is assumed equally likely that these sections are active or inactive.

TABLE 7-1. FOOTNOTES TO LOGIC TREES (CONTINUED)

[89]The Tijeras-Cañoncito fault is classified as a slip rate Category C fault. There are no data available on the Quaternary slip rate of the Tijeras-Cañoncito fault. Slip rate values and weights are assumed based on similarity with the Embudo fault, which probably also accommodates strain between two major rift basins. Current tectonic models interpret that the fault southwest of Albuquerque is an accommodation zone between the northern and southern Albuquerque Basins. If so, an average long-term rate for this section (outside the LANL region) may be comparable to the rate estimated for the Embudo fault. Because there are no data on the slip rate of the fault where it traverses the LANL region, we used slip rates similar to the Embudo fault (see footnote 67) with a long-term slip rate of 0.09 mm/yr.

[90]The Nacimiento fault is a west-vergent thrust fault that is responsible for much of the uplift of the Nacimiento Mountains. Woodward (1987) notes that the fault dips 45° to 60° beneath the range block, although the linear surface trace suggests a steep, near-surface dip. Dip values of 50° to 70° are considered based on these relations. Weights are based on the assumption that these values are equally likely.

[91]Woodward (1987) identifies northern and southern sections of the fault, based on a 1-km right-step of the fault trace. We assumed to be equally likely that these sections may rupture either independently or dependently.

[92]There are no data available on the Quaternary slip rates of the Nacimiento and Gallina faults and so these faults are classified as slip rate Category C faults. Although the faults have geomorphic expression, this is probably primarily related to lithologic resistance of west-dipping strata along the faults. Manley et al. (1987) show Quaternary gravel as not displaced by the Nacimiento fault, suggesting that if this fault is active, the slip rate is low. In the absence of definitive data, we assigned slip rates and weights similar to the Puerco fault (see footnote 99).

[93]Previous workers note that the Picuris-Pecos fault dips steeply, has a linear trace across rugged topography, and has had substantial lateral movement (Miller et al., 1963; Moench et al., 1988). Based on these relations, dip values and weights are considered to reflect the likelihood that the fault is vertical or near-vertical.

TABLE 7-1. FOOTNOTES TO LOGIC TREES (CONTINUED)

[94]The Picuris-Pecos fault is classified as a slip rate Category C fault. There are no data available on the Quaternary slip rate of the Picuris-Pecos fault. The prominent geomorphic expression of the fault is probably related to juxtaposition of different rock types and erosional resistance of sheared rock along the fault. In the absence of definitive data, we consider an upper bound of 0.05 mm/yr for the long-term average slip rate on the Picuris-Pecos fault, based on the assumption that a 5 m high scarp could survive at most only 100,000 to 150,000 years in this climatic and geologic environment. This assumed value of 5 m is higher for the Picuris-Pecos fault than for other faults in the LANL region because of its presence within the rugged Sangre de Cristo Mountains, which have higher erosion rates because of greater precipitation and topographic relief. The value of 0.05 mm/yr is considered conservative. The slip rate values are modeled using the distribution of slip rates within the Rio Grande rift, normalized to 0.05 mm/yr.

[95]Machette (1978b) provides data on vertical separation produced during the four most recent surface ruptures on the County Dump fault. The three most recent events averaged 3.1 m of separation, whereas the earliest event(s) produced more than 7.8 m. This earlier displacement may be a result of more than one earthquake. The range in separation of the three later events is 2.1 to 4.1 m. Average displacements per event of 2, 3, and 4 m were considered based on these data. Weights were based on an assumed symmetric distribution.

[96]Recurrence methods used for the West Mesa fault zone include geologic recurrence intervals and slip rate. Geologic recurrence information is available from paleoseismologic studies (Machette, 1978b). These data are available for the County Dump fault over the past approximately 500 ka. Slip rate data also are available over a similar time period (Machette, 1978b), and over the past approximately 19 Ma (Russell and Snelson, 1990). These methods are weighted equally based on the assumption that both data sets are equally valid.

[97]Machette (1978b) estimates a range in interseismic intervals of 90,000 to 190,000 years for the County Dump fault, which is a primary strand of the West Mesa fault zone. Because of the possibility that other faults within the fault zone may act independently, this interval range may be lower for the entire zone. Thus, recurrence values of 50,000 and 100,000 years are considered, as well as 200,000 years in the case where the County Dump fault is the primary fault. Weights are based on an assumed broad, symmetric distribution.

TABLE 7-1. FOOTNOTES TO LOGIC TREES (CONTINUED)

[98]The West Mesa fault zone is classified as a slip rate Category A fault. Paleoseismic data presented by Machette (1978b) suggests there has been about 17 m of vertical separation across the County Dump fault since 400 ka, which yields a late Quaternary slip rate of 0.04 mm/yr. However, a higher slip rate is estimated for the West Mesa fault as identified in the upper 10 km by Russell and Snelson (1990), which is coincident with the County Dump fault at the surface. Based on seismic reflection data, Russell and Snelson (1990) show approximately 1.5 to 2.4 km of vertical separation of the base of the rift-fill sediments on geologic sections north and south of Albuquerque. Assuming an age range of 19 to 28 Ma for the initiation of rifting, these data yield long-term slip rates of 0.05 to 0.13 mm/yr. Vertical separation rates of 0.01, 0.05, 0.10, and 0.15 mm/yr are considered to encompass the range in data. These rates are resolved to net slip rates of 0.01, 0.06, 0.12, and 0.17 mm/yr, respectively, based on an assumed fault dip of 60°E. Weights are based on the likelihood that lower rates are more representative of the current strain rate.

[99]As there are no data available on the slip rate of the Puerco fault, it is classified as a slip rate Category C fault. There is little or no geomorphic expression of the fault. We consider an upper bound for the long-term slip rate on this fault of 0.02 mm/yr, which is based on the assumption that a 1 to 2 m high fault scarp on alluvium could survive at most only 100,000 to 150,000 years in this environment. The absence of scarps and any other geomorphic evidence of Quaternary activity suggests this low slip rate. Based on this, we assigned slip rates using the distribution of slip rates for Rio Grande rift faults, normalized to 0.02 mm/yr.

[100]The activity of the Gallina fault is unknown. The fault is considered equally active or inactive on the basis of microseismicity in the area directly east of the surface trace.

[101]The Gallina fault is the northern extension of the Nacimiento fault (Woodward, 1987; Manley et al., 1987), and likely also is related to Laramide deformation. Based on this similarity, dip values of 50° to 70° are considered (see footnote 90). Weights are based on an assumed symmetric distribution.

[102]The Sandia-Rio Grande fault zone is classified as a slip rate Category B fault. The absence of prominent fault scarps along the Sandia fault in Pleistocene alluvium (K. Kelson,

TABLE 7-1. FOOTNOTES TO LOGIC TREES (CONTINUED)

WL&A, unpublished data, 1994) suggests that this strand of the fault zone may be relatively minor compared to the total slip on the entire zone. Based on seismic reflection and drillhole data, the Rio Grande fault has the greatest amount of displacement of faults within the Sandia-Rio Grande fault zone; the base of rift-fill sediments is interpreted to have between 1.5 and 4.6 km of displacement on two cross sections across the Albuquerque Basin presented by Russell and Snelson (1990). Assuming an age range of 19 to 28 Ma for the base of these sediments, vertical slip rates range from 0.05 to 0.24 mm/yr. However, we believe that the maximum rates calculated for the Rio Grande fault using the data of Russell and Snelson (1990) probably are high for the current tectonic setting. We assume 0.18 mm/yr for the average long-term vertical slip rate along the Sandia-Rio Grande fault, which we believe is a conservative estimate. The slip rate values are modeled using the distribution of slip rates within the Rio Grande rift, normalized to 0.16 mm/yr.

[103]Based on interpretation of seismic reflection data in the San Luis Basin, Kluth and Schaftenaar (1994) model that the most likely orientation for the Sangre de Cristo fault is 60°W to mid-crustal depths. Tandon (1992; cited in Chapin and Cather, 1994) interprets the same data set processed for deeper resolution, and concludes that the fault dips about 60° to at least 26 to 28 km, which is probably below the brittle-ductile transition zone. We assume a mean value of 60°W for the Sangre de Cristo fault, and assume other possible dips of 50°W and 70°W for fault within the seismogenic crust. Weights are assumed based on a symmetric distribution about 60°W.

[104]Rupture scenario A for the Sangre de Cristo fault includes segments 3 and 4 of Menges (1990a,b) and rupture scenario B includes segments 2, 3, and 4 of Menges (1990a,b) (Plate 1). Weights are based on the assumption that it is more likely that the entire fault does not rupture at once.

[105]Recurrence information for the Sangre de Cristo fault is available based on detailed studies conducted by Menges (1988, 1990a,b). Recurrence interval data are estimated but only moderately constrained, whereas slip rate data are better constrained. Weights of these data sets were based on a higher degree of confidence in slip rate data.

TABLE 7-1. FOOTNOTES TO LOGIC TREES (CONTINUED)

[106]Menges (1988) estimates a range in recurrence intervals of 10,000 to 50,000 years based on morphology of fault scarps in late Quaternary deposits. Values of 10,000, 30,000, and 50,000 years were considered based on these data; each of these values were considered equally likely.

[107]The Sangre de Cristo fault is classified as a slip rate Category A fault. Menges (1988, 1990a,b) estimates a post-Pliocene slip rate of 0.15 to 0.25 mm/yr on the Sangre de Cristo fault, as well as a late Quaternary rate of 0.03 to 0.06 mm/yr. This lower rate better reflects the past hundred thousand to several hundred years, and is more appropriate for the current tectonic setting. Personius and Machette (1984) estimate a rate of 0.06 to 0.12 mm/yr for the fault based on fault scarp height and surface age estimates. To encompass the entire range of published values, vertical separation rates of 0.05, 0.10, 0.15, and 0.25 mm/yr were considered. These values are converted to net slip rates of 0.06, 0.12, 0.17, and 0.29 mm/yr, respectively, based on an assumed fault dip of 60°W. Weights were based on these data, and reflect the likelihood that the Quaternary slip rate is more representative of the current tectonic setting. These data are consistent with recurrence interval estimates of 10,000 to 50,000 years (see footnote 106).

[108]The activity of the Los Cordovas fault is moderately constrained by fluvial terraces mapped across the southern end of the fault (Kelson, 1986a). The youngest displaced geomorphic surface is approximately 1.2 Ma. The oldest undisplaced surface is probably about 500 to 600 ka, but may be as young as 300 to 400 ka. Thus, it is likely that there have been no surface ruptures on the fault for several hundred thousand years, but the age control on the oldest undisplaced terrace is insufficient to preclude post-500 ka activity.

[109]The Los Cordovas fault is classified as a slip rate Category A fault, although the geologically based slip rate for the fault is poorly constrained. There is approximately 15 m of displacement of the highest geomorphic surface mapped near Taos (Kelson, 1986a). This is the youngest displaced surface and is probably 1.2 Ma, although it is possibly as young as 600 ka. These data yield a range in slip rate of 0.01 to 0.03 mm/yr. Weights are based on an assumed symmetric distribution.

TABLE 7-1. FOOTNOTES TO LOGIC TREES (CONTINUED)

[110]The distribution of depths in the Rio Grande Rift is based on the available hypocentral locations of earthquakes recorded by the LANL network since 1973 and other networks operated in the Rio Grande rift by the USGS and New Mexico Tech. The upper value is based on the maximum depth of earthquakes observed in the Basin and Range province, such as the 1983 Borah Peak event, which was located at a depth of about 16 km. The lower values are weighted higher because of the observation that focal depths for seismicity appear to be truncated at a depth of 12 km in the vicinity of LANL. The average seismogenic thickness in the western U.S. is 15 km (Wong and Chapman, 1990).

[111]Based on the limited data, the maximum magnitudes commonly considered appropriate for the background or random earthquake considered in the Basin and Range province range from M_w 6 to 6 1/2 (Doser, 1985; Arabasz et al., 1992; dePolo, 1994). We encompass this range and use a best estimate value of M_w 6.25, with an assumed symmetric distribution for probabilities.

[112]The b-value recurrence parameter was based on recurrence estimates using the limited historical seismicity data unique to each seismotectonic province (Section 3.3 and Appendix F). A standard uncertainty of $\pm$ 0.1 for the b-value was used for all provinces to characterize both the uncertainties in the maximum likelihood data fit as well as the uncertainty in the magnitude and completeness estimates. Weights of 0.4, 0.4, and 0.2 were assumed based on the unreasonably high return periods estimated for the highest b-value for each province (Tables F-3 to F-6).

[113]The normalized activity rates at M_w 5.0 (per km^2) were computed by fixing each of the three b-values for each province and computing the maximum likelihood fits through the data points. The mean activity rate in each case was doubled and halved to encompass the large computed uncertainty (Table F-2) and the three values weighted 0.3, 0.4 and 0.3 to represent the 10^{th}, 50^{th} and 90^{th} percentile activity rates (Figures F-1 to F-4).

[114]A minimum magnitude of M_L 2.0 was used in the computation of activity rates using fixed b-values.

TABLE 7-1. FOOTNOTES TO LOGIC TREES (CONTINUED)

[115]The distribution of focal depths is weighted heavier toward relatively deeper values of 15 to 20 km based on focal depth distributions for observed seismicity within the Colorado Plateau (Wong and Humphrey, 1989). The thicker seismogenic crust (and thicker crust) is consistent with the observed lower heat flow and hence lower crustal temperatures in the Plateau (Wong and Chapman, 1990).

[116]Although the relatively thicker seismogenic crust might suggest a potentially greater maximum magnitude for the background earthquake, the historical seismicity record suggests a relatively lower best estimate value of M_w 6 (Wong and Humphrey, 1989) is most appropriate with an estimated uncertainty of 0.3 of a magnitude unit.

[117]A minimum magnitude of M_L 1.0 was used in the computation of activity rates using fixed b-values.

[118]There are limited data on focal depths of earthquakes in the southern Rocky Mountains. Observations of seismicity beneath the Front Range of central Colorado (D. Butler, MicroGeophysics Corporation, personal communication, 1994) and of the 1984 Laramie Mountains sequence in south-central Wyoming (Langer et al., 1991), suggest that the seismogenic crust is 20 to 25 km thick in the southern Rocky Mountains. Similar to the Colorado Plateau, the Southern Rocky Mountains also are characterized by relatively low crustal temperatures and a thick crust. Thus, we adopt a depth range of 15 to 25 km and assume a symmetric distribution for probabilities.

[119]The largest historical earthquake in the southern Rocky Mountains not known to be associated with a geologic structure expressed at the surface is the 1882 M 6½ earthquake in Colorado. The uncertainty of this pre-instrumentally recorded event is at least $\pm$ ¼ of a magnitude unit. Therefore, we adopt a best estimate of M_w 6.3, with a range of $\pm$ 0.3 and an assumed symmetric distribution of probabilities as a reasonable characterization for maximum magnitudes in the southern Rocky Mountains.

[120]A minimum magnitude of M_L 1.5 was used in the computation of activity rates using fixed b-values.

TABLE 7-1. FOOTNOTES TO LOGIC TREES (CONTINUED)

[121]Accurate focal depth information is scarce for seismicity in the Great Plains. Based on similarities in crustal temperatures and crustal thickness with the Colorado Plateau, we adopt the same depth distribution (see footnote 115).

[122]The Great Plains exhibits a low level of seismicity. The largest known historical event was a m_b 5.1 event. Previous studies for EPRI have adopted a maximum magnitude of about M_w 6 to 6 1/4. Thus, we encompass the range M_w 5.7 to 6.3, with a best estimate of M_w 6.0.

TABLE 7-2

COMMONLY CITED CHARACTERISTICS OF SEGMENT BOUNDARIES ALONG NORMAL FAULTS

*[1]	Temporal variation in occurrence of surface-faulting events
*[1]	Temporal variation in scarps for substantial distances along strike
*[1,3]	Major gaps in surficial expression (special case of above)
*[1]	Temporal variation in rupture recurrence
*[1]	Fault terminations (provided distributed rupture of multiple faults may be discounted)
*[2]	Abrupt changes in fault strike (bends)
*[2]	Changes in fault zone width (aerial extent)
*[2]	Changes in the number of faults
*[2,3]	Changes in structural relief across fault
*[2]	Changes in slip rate
*[3]	Intersection of faults
*[2]	Intersection of folds (and other structural trends)
*[3]	Transverse bedrock ridges
*[2]	Geophysical anomalies (transverse gravity and areomagnetic saddles)
*[2,3]	Major en échelon steps (oversteps & understeps)
*[2,3]	Increased fault zone complexity
*[3]	Bedrock salients

[1] Defines rupture segment boundaries

[2] Defines structural segment boundaries, which can or cannot coincide with rupture segment boundaries

[3] Tend to form persistent segment boundaries

Sources: Bruhn et al., 1987; Crone et al., 1987; Crone and Haller, 1991; dePolo et al., 1991; King, 1986; Knuepfer, 1989; Knuepfer et al., 1987; Schwartz, 1988; Schwartz and Coppersmith, 1984, 1986; Sibson, 1985; Susong et al., 1990; Turko and Knuepfer, 1991; Wheeler, 1987; Wheeler and Krystinik, 1988; Zhang et al., 1991.

Table 7-3

Slip rates and normalized slip rate [1] for faults in the Rio Grande rift

Fault Zone	Site	Ref.	Slip Rate (mm/yr)	Time Period (ka) min	Time Period (ka) max	Long-term Slip Rate (mm/yr)	Normalization Factor [2] 0.07	Elapsed Time (ka)	Normalized Slip Rate [3] (mm/yr)
County Dump, NM	County Dump	Machette 1978	0.017	0	300	0.04	1.75	300	0.03
			0.12	300	400	0.04	1.75	100	0.21
S. Sangre de Cristo, NM		Menges 1990	0.03-0.06	0	140	0.17	0.41	140	0.02
			0.12-0.23	0	4000	0.17	0.41	4000	0.07
N. Sangre de Cristo, CO	Major Creek	McCalpin 1983	0.48	8	13	0.06	1.17	5	0.56
			0.43	13	25	0.06	1.17	12	0.50
			0.05	25	140	0.06	1.17	115	0.06
			0.035	140	400	0.06	1.17	260	0.04
	San Isabel Creek		0.24	8	30	0.1	0.70	22	0.17
			0.09	30	60	0.1	0.70	30	0.06
			0.1	60	140	0.1	0.70	80	0.07
			0.09	140	400	0.1	0.70	260	0.06
	Willow Creek		0.09	8	25	0.04	1.75	17	0.16
			0.38	25	35	0.04	1.75	10	0.67
			0.02	35	400	0.04	1.75	365	0.04
	Uracca Creek		0.18	8	25	0.08	0.88	17	0.16
			0.04	25	140	0.08	0.88	115	0.04
			0.09	140	400	0.08	0.88	260	0.08
	Blanca Creek		0.08	15	60	0.05	1.40	45	0.11
			0.01	60	140	0.05	1.40	80	0.01
			0.05	140	400	0.05	1.40	260	0.07
Caballo, NM	Ash Springs	Machette 1987a	0.029	10	125	0.035	2.00	115	0.06
			0.044	125	250	0.035	2.00	125	0.09
			0.02-0.037	250	750	0.035	2.00	500	0.06
San Andres NM	Central Section	Machette 1987b	0.018-0.087	10	125	0.105	0.67	115	0.04
			0.10-0.18	125	250	0.105	0.67	125	0.09
Organ NM	Cox Ranch	Machette 1987b	1.65	3	5	0.1	0.70	2	1.16
			0.43	5	15	0.1	0.70	10	0.30
			0.054	25	125	0.1	0.70	100	0.04
			0.085	125	250	0.1	0.70	125	0.06
East Franklin NM	Ft. Bliss	Machette 1987b	0.003	15	125	0.08	0.88	110	0.00
			0.064	125	250	0.08	0.88	125	0.06
			0.137	250	400	0.08	0.88	150	0.12
			0.078	400	750	0.08	0.88	350	0.07

[1] Normalized to 0.07 mm/yr

[2] Normalization factor derived by dividing the long-term average slip rate into 0.07 mm/yr

[3] Normalized slip rate for the given interval multiplied times the normalization factor for that fault

TABLE 7-4
WEIGHTED-MEAN MAXIMUM MAGNITUDES FOR RUPTURE SCENARIOS OF THE PAJARITO FAULT SYSTEM

Rupture Scenario[1] (structural model)	Participating Faults[2]	Maximum Moment Magnitude[3]
RS-A	PAF	6.7
RS-B	PAF	6.7
RS-C	PAF	6.8
RS-D	PAF	6.9
RS-E (non-intersecting)	RC	6.5
RS-E (intersecting)	RC	6.4
RS-F (non-intersecting)	GM	6.5
RS-F (intersecting)	GM	6.5
RS-G (non-intersecting)	PAF, RC	6.8
RS-H (non-intersecting)	PAF, RC	6.9
RS-I (intersecting)	PAF, RC	6.7
RS-J (intersecting)	PAF, RC	6.8
RS-K (intersecting)	PAF, RC	6.9
RS-L (non-intersecting)	PAF, GM	6.7
RS-M (non-intersecting)	PAF, GM	6.8
RS-N (intersecting)	PAF, GM	6.7
RS-O (intersecting)	PAF, GM	6.8
RS-P (intersecting)	PAF, GM	6.9
RS-Q (non-intersecting)	RC, GM	6.6
RS-Q (intersecting)	RC, GM	6.5
RS-R (non-intersecting)	PAF, RC, GM	6.8
RS-S (non-intersecting)	PAF, RC, GM	6.9
RS-T (intersecting)	PAF, RC, GM	6.7
RS-U (intersecting)	PAF, RC, GM	6.8
RS-V (intersecting)	PAF, RC, GM	6.9

1 Shown on Figures 7-25a through 7-25f

2 PAF = Pajarito fault; RC = Rendija Canyon fault; GM = Guaje Mountain fault

3 Weighted-mean calculated for each rupture scenario using geometries, displacements, empirical relations and weights shown in logic trees

Table 7-5. Depth (in km) of Intersection for the Pajarito (PAF) and Rendija Canyon (RC) Faults for the Intersecting Structural Model*

		RC Dip (° to west)			
		60	70	80	90
PAF Dip (° to east)	50	2.1	2.5	3.0	3.6
	60	2.6	3.2	4.0	5.2
	70	3.2	4.1	5.6	**8.2**

*Depths shown in **bold** round to 7 km or greater and corresponding geometries were included in probabilistic analysis.

Table 7-6. Depth (in km) of Intersection for the Pajarito (PAF) and Guaje Mountain (GM) Faults for the Intersecting Structural Model*

		GM Dip (° to west)			
		60	70	80	90
PAF Dip (° to east)	50	3.5	4.2	4.9	6.0
	60	4.3	5.3	**6.6**	**8.7**
	70	5.3	**6.9**	**9.3**	**13.7**

*Depths shown in **bold** are greater than 6 km and corresponding geometries were included in probabilistic analysis.

TABLE 7-7

HISTORICAL SURFACE-FAULTING EARTHQUAKES WITH PRIMARILY NORMAL SLIP[1]

Year	Location	Fault	Type[2]	M_s	Rupture Length (km)	Maximum Displacement (m)
1887	Mexico	Pitaycachi	N	7.4	75	4.5
1915	Italy	Avezzano	N	6.9	20	2.0
1915	Nevada	Pleasant Valley	N	7.6	62	5.8
1928	Kenya	Laikipia	N	7.0	31	3.3
1928	Bulgaria	Papazili	N	6.9	50	3.5
1946	Peru	Ancash	N	7.2	21	3.5
1954	Nevada	Rainbow Mountain	N	6.3	18	0.31
1954	Nevada	Stillwater	N	6.9	34	0.76
1954	Nevada	Dixie Valley	RL-N	6.8	45	3.8
1959	Montana	Hebgen Lake	N	7.6	27	6.1
1969	Turkey	Alasehir Valley	N	6.5	32	0.82
1970	Turkey	Gediz	N	7.1	41	2.8
1978	Greece	Thessaloniki	N	6.4	19.4	0.22
1980	Italy	South Apennines	N	6.9	26	1.15
1981	Greece	Corinth	N	6.4	19	1.5
1981	Greece	Corinth	N	6.4	13	1.1
1983	Idado	Borah Peak	N-LL	7.3	34	2.70
1986	Greece	Kalamata	N	5.8	15	0.18
1987	New Zealand	Edgecumbe	N	6.6	18	2.9

[1]From Wells and Coppersmith (1994). Included here are only those ruptures with lengths greater than 10 km.

[2]N = Normal, RL = Right-lateral, LL = Left-lateral

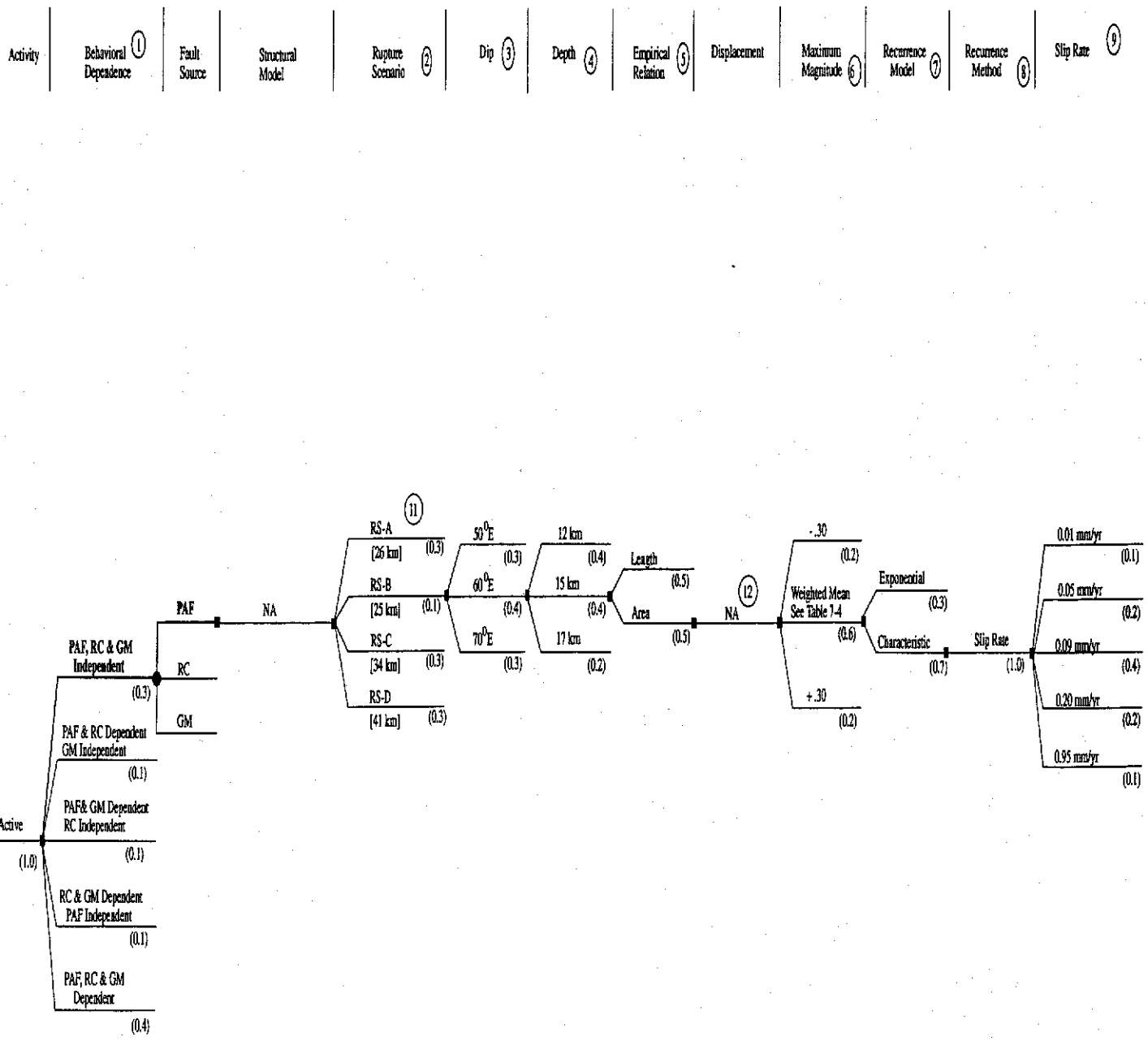
TABLE 7-8. ESTIMATION OF A LONG-TERM AVERAGE NET SLIP RATE FOR THE SOUTHWEST SECTION OF THE EMBUDO FAULT[1]

Fault	Vertical Slip Rate (mm/yr)	Horizontal East-West Extension Slip Rate (mm/yr)[2]	Embudo-Component of Lateral Slip Rate (mm/yr)[3]
Pajarito	0.07	0.040	0.046
Rendija Canyon	0.02	0.012	0.014
Guaje Mountain	0.01	0.006	0.007
Sawyer Canyon	0.03	0.017	0.020
TOTAL LATERAL COMPONENT			**0.087**

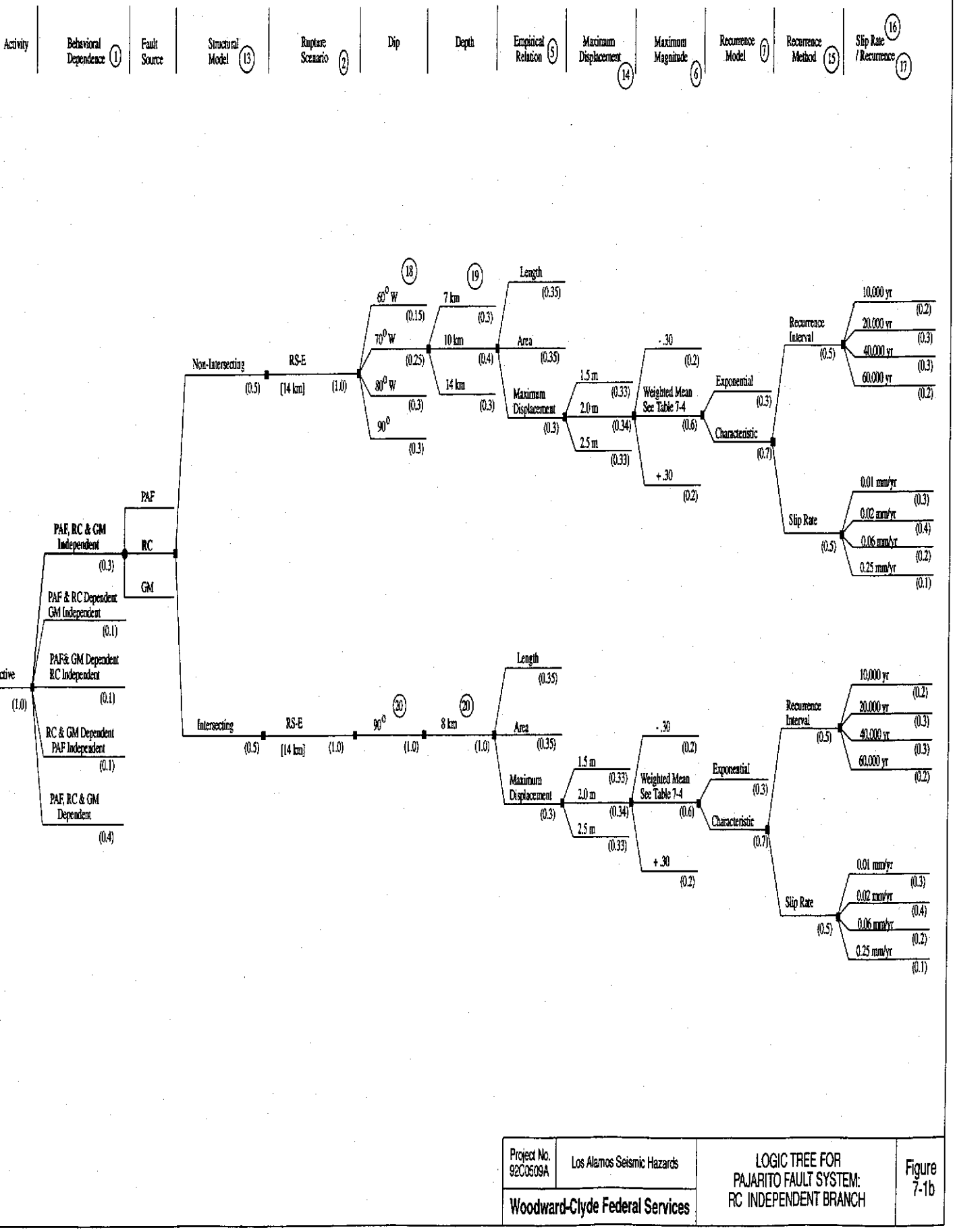
[1]Assuming dominantly lateral slip

[2]Assumed 60° fault dip, east-west extension

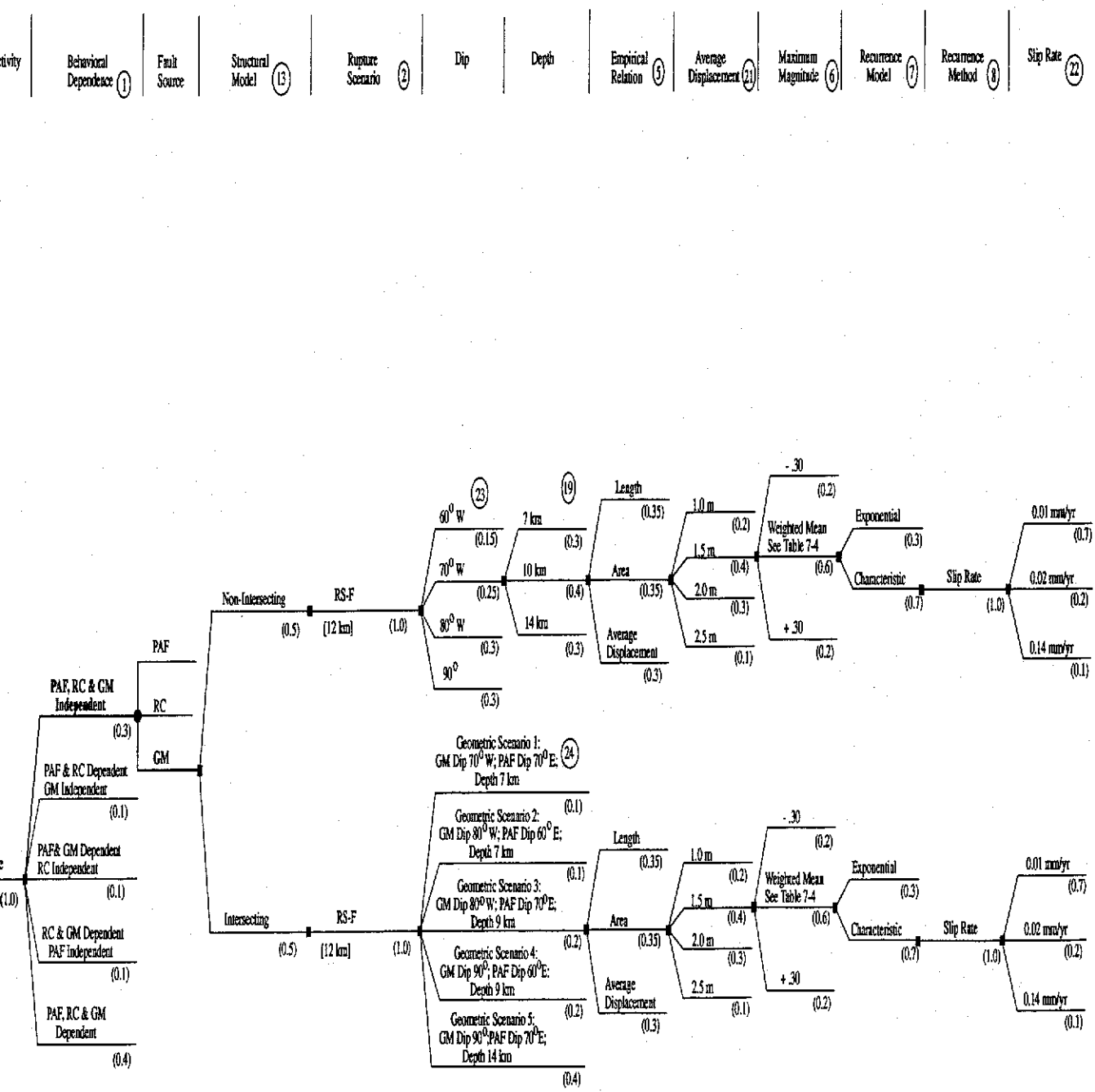
[3]Resolved along a strike of N60°E



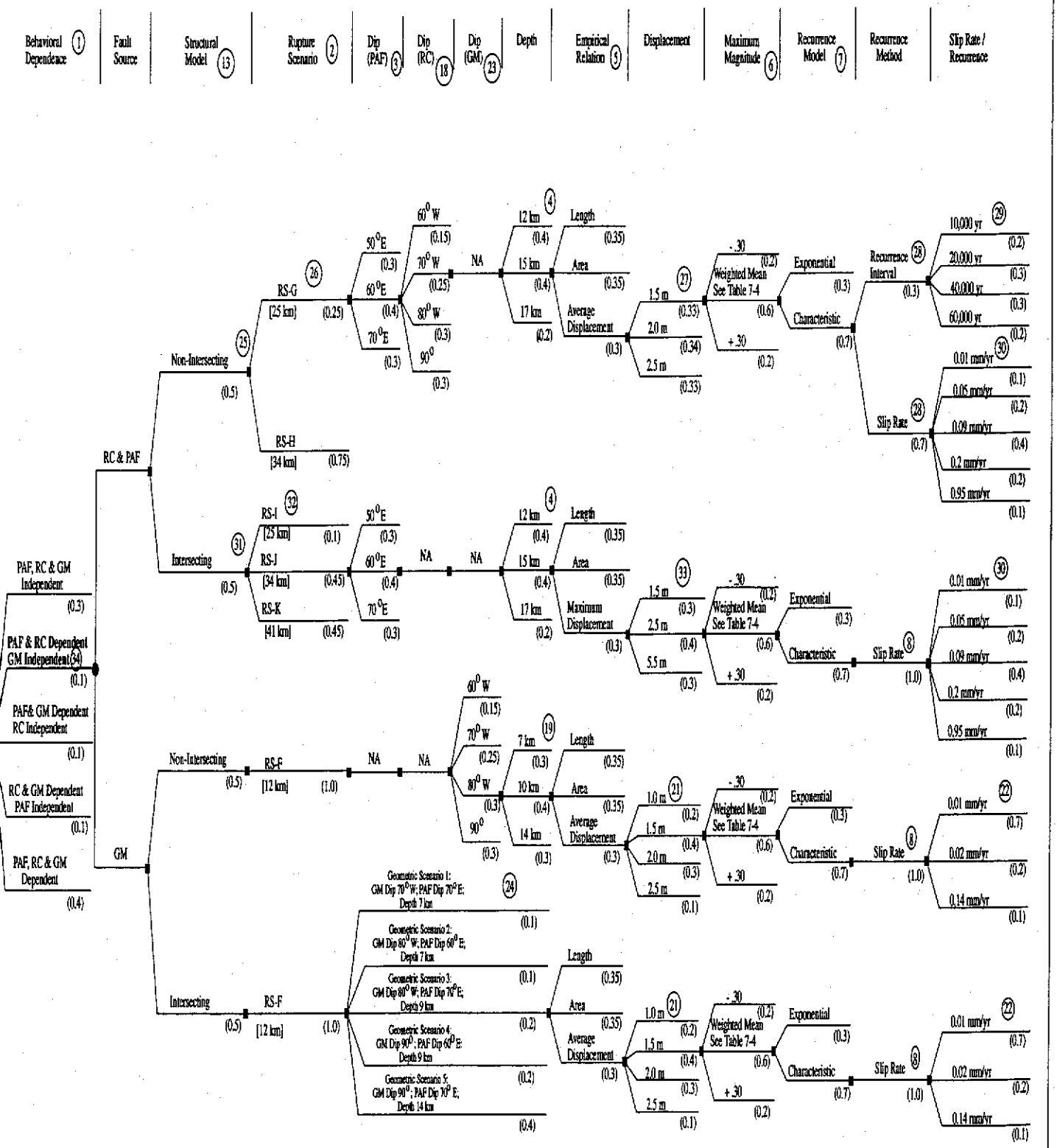
Project No. 92C0509A	Los Alamos Seismic Hazards	LOGIC TREE FOR PAJARITO FAULT SYSTEM: PAF INDEPENDENT BRANCH	Figure 7-1a
Woodward-Clyde Federal Services			



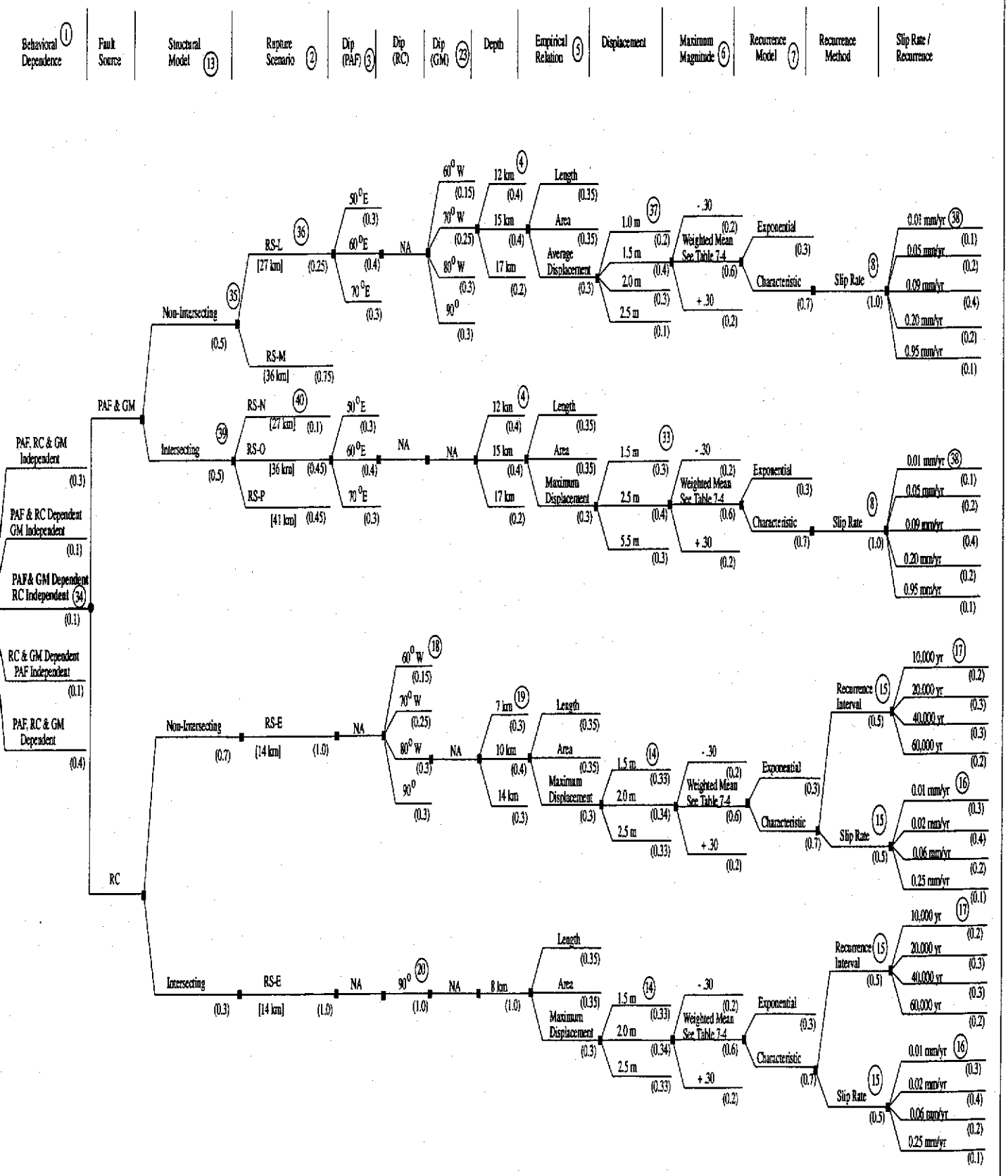
Project No. 92C0509A	Los Alamos Seismic Hazards	LOGIC TREE FOR PAJARITO FAULT SYSTEM: RC INDEPENDENT BRANCH	Figure 7-1b
Woodward-Clyde Federal Services			



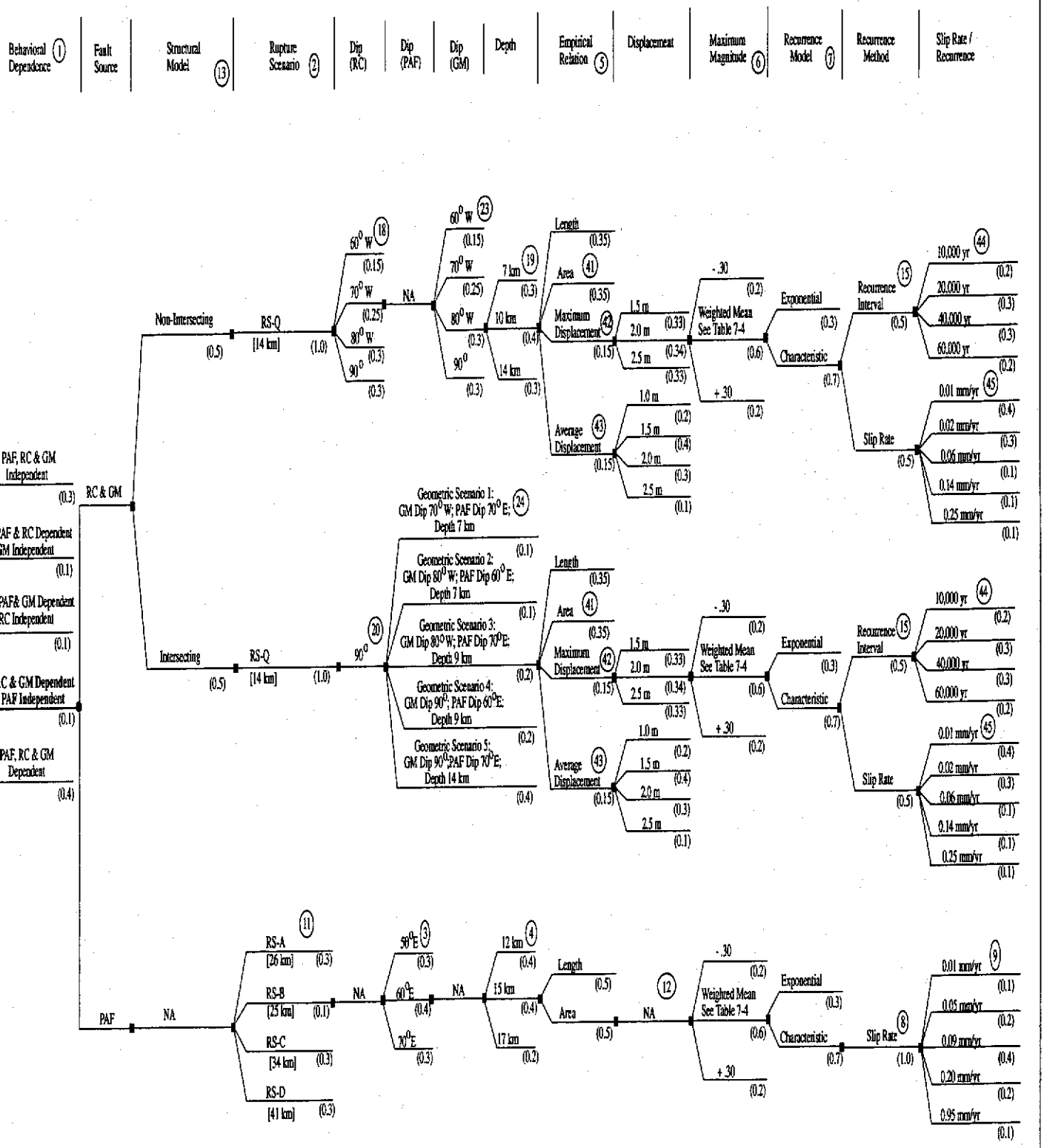
Project No. 92C0509A	Los Alamos Seismic Hazards	LOGIC TREE FOR PAJARITO FAULT SYSTEM: GM INDEPENDENT BRANCH	Figure 7-1c
Woodward-Clyde Federal Services			



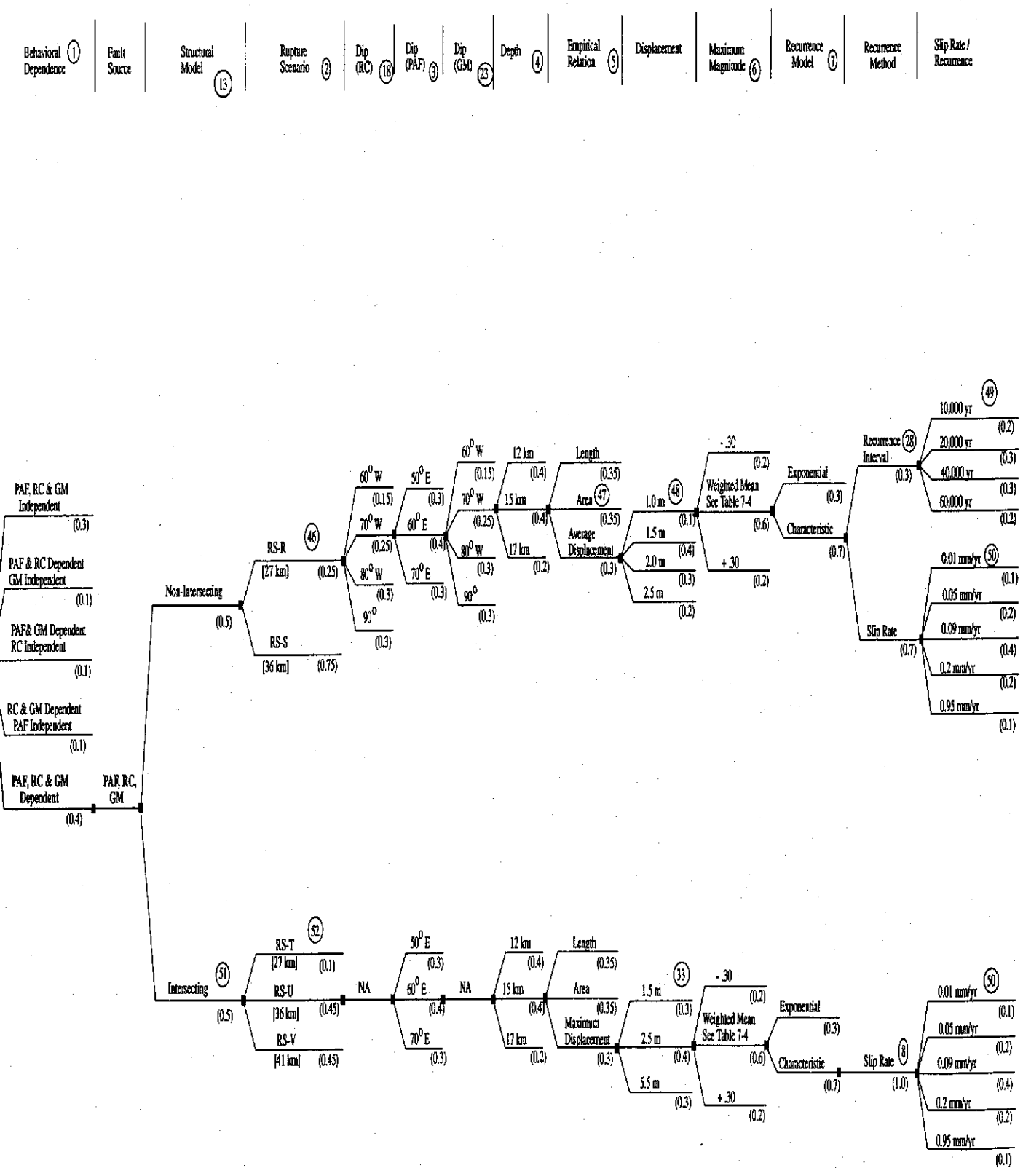
Project No. 92C0509A	Los Alamos Seismic Hazards	LOGIC TREE FOR PAJARITO FAULT SYSTEM: PAF AND RC DEPENDENT AND GM INDEPENDENT BRANCH	Figure 7-1d
Woodward-Clyde Federal Services			



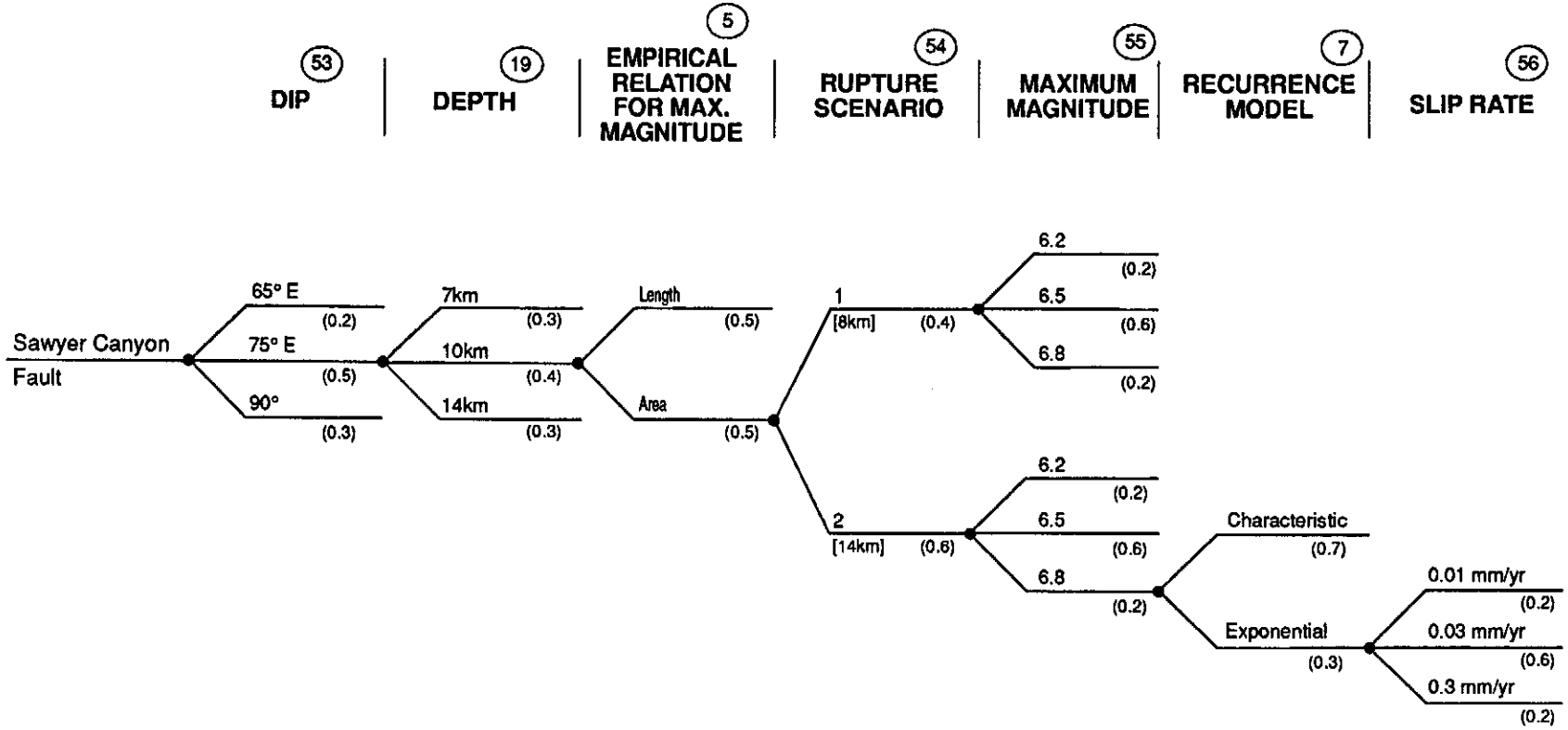
Project No. 92C0509A	Los Alamos Seismic Hazards	LOGIC TREE FOR PAJARITO FAULT SYSTEM: PAF AND GM DEPENDENT AND RC INDEPENDENT BRANCH	Figure 7-1e
Woodward-Clyde Federal Services			



Project No. 92C0509A	Los Alamos Seismic Hazards	LOGIC TREE FOR PAJARITO FAULT SYSTEM: RC AND GM DEPENDENT AND PAF INDEPENDENT BRANCH	Figure 7-1f
Woodward-Clyde Federal Services			

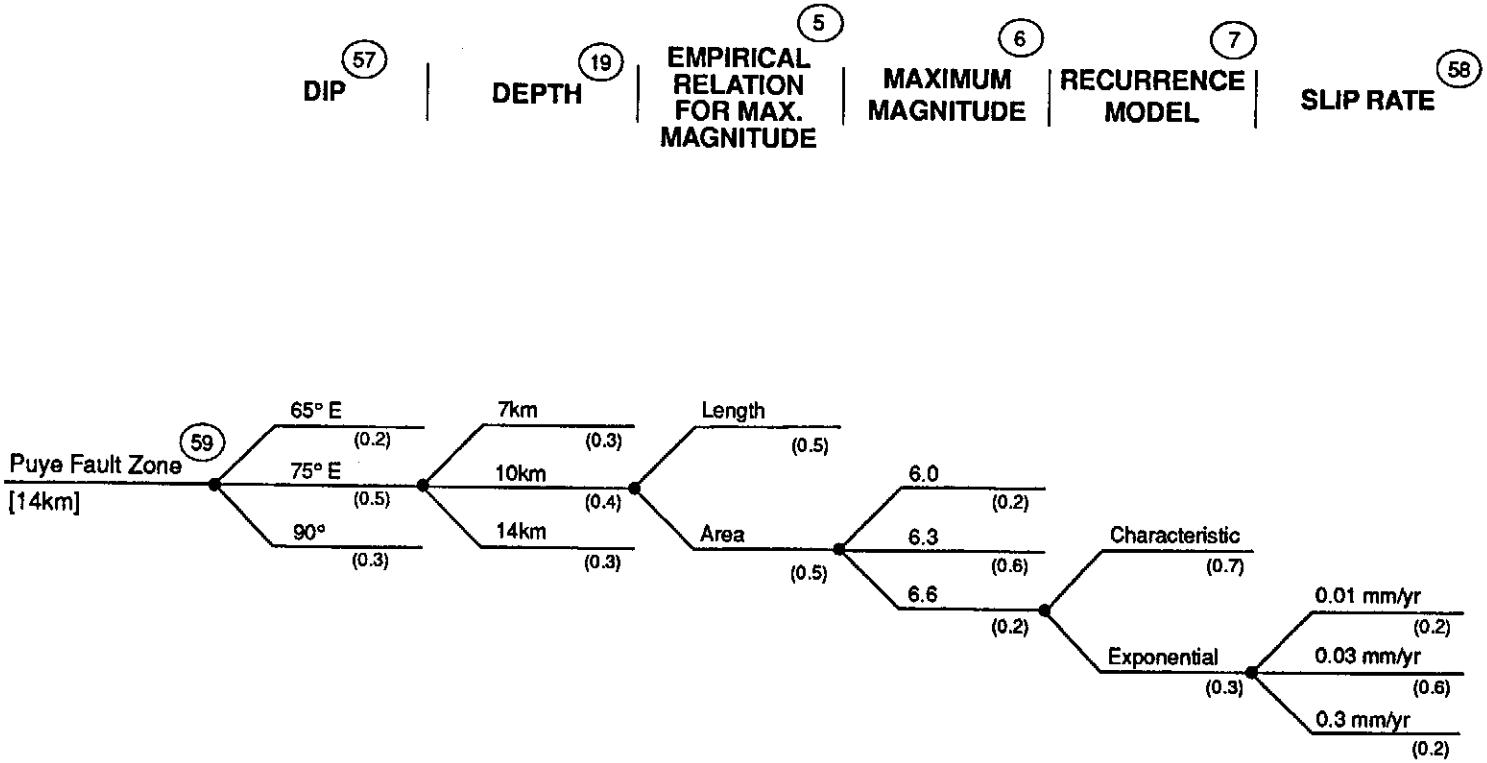


Project No. 92C0509A	Los Alamos Seismic Hazards	LOGIC TREE FOR THE PAJARITO FAULT SYSTEM: PAF, RC, AND GM DEPENDENT BRANCH	Figure 7-1g
Woodward-Clyde Federal Services			



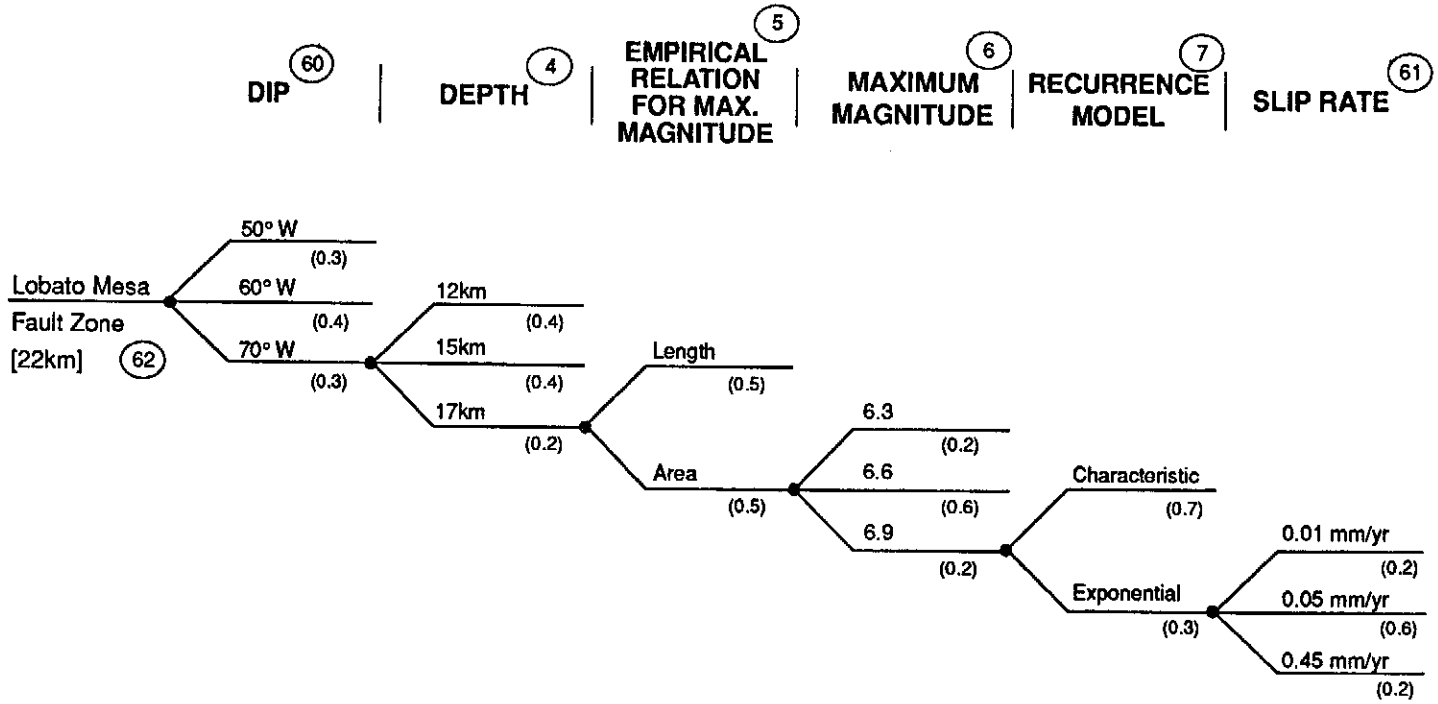
Project No. 91C0509	Los Alamos Seismic Hazards	LOGIC TREE FOR SAWYER CANYON FAULT	Figure 7-2
Woodward-Clyde Federal Services			

91C0509A-2200/052793



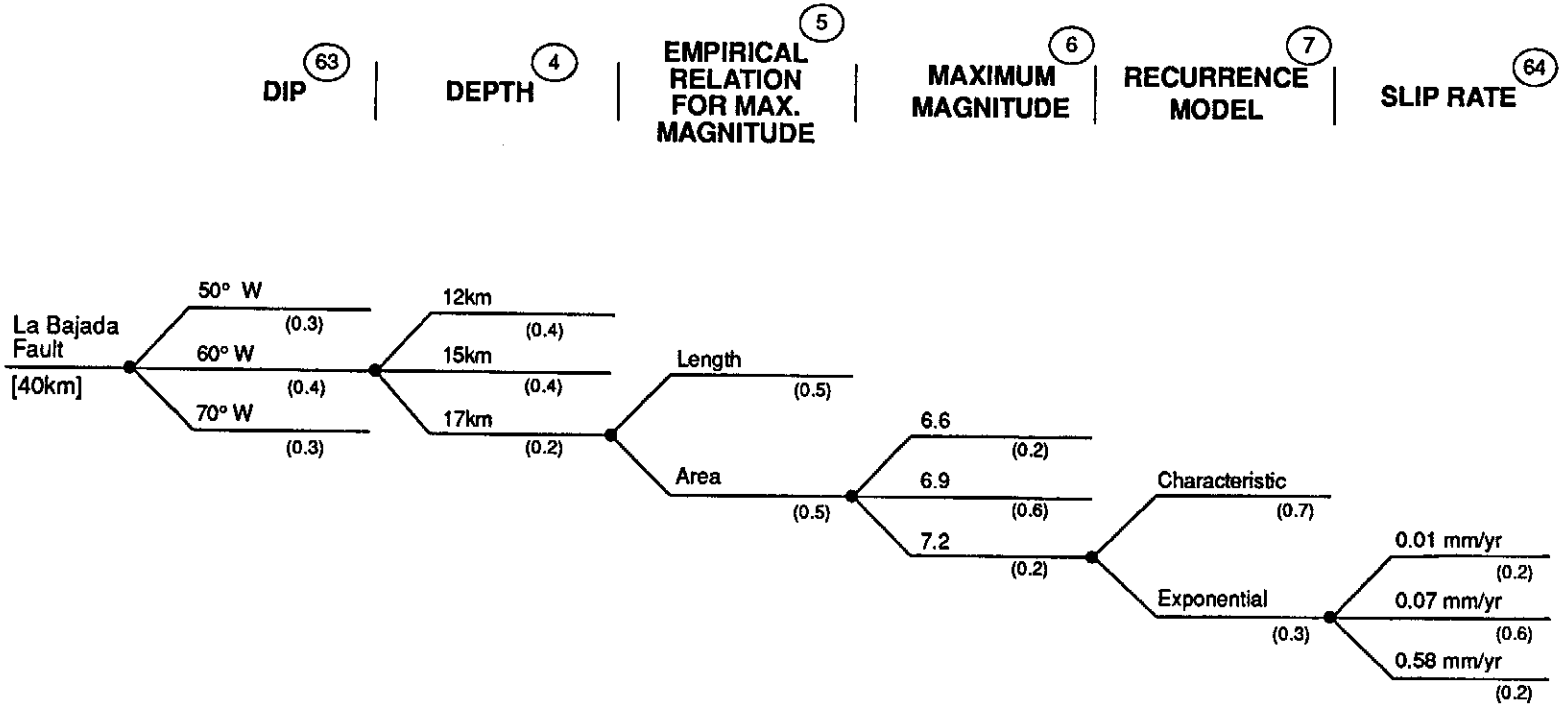
Project No. 91C0509	Los Alamos Seismic Hazards	LOGIC TREE FOR PUYE FAULT ZONE	Figure 7-3
Woodward-Clyde Federal Services			

91C0509A-2200/052793



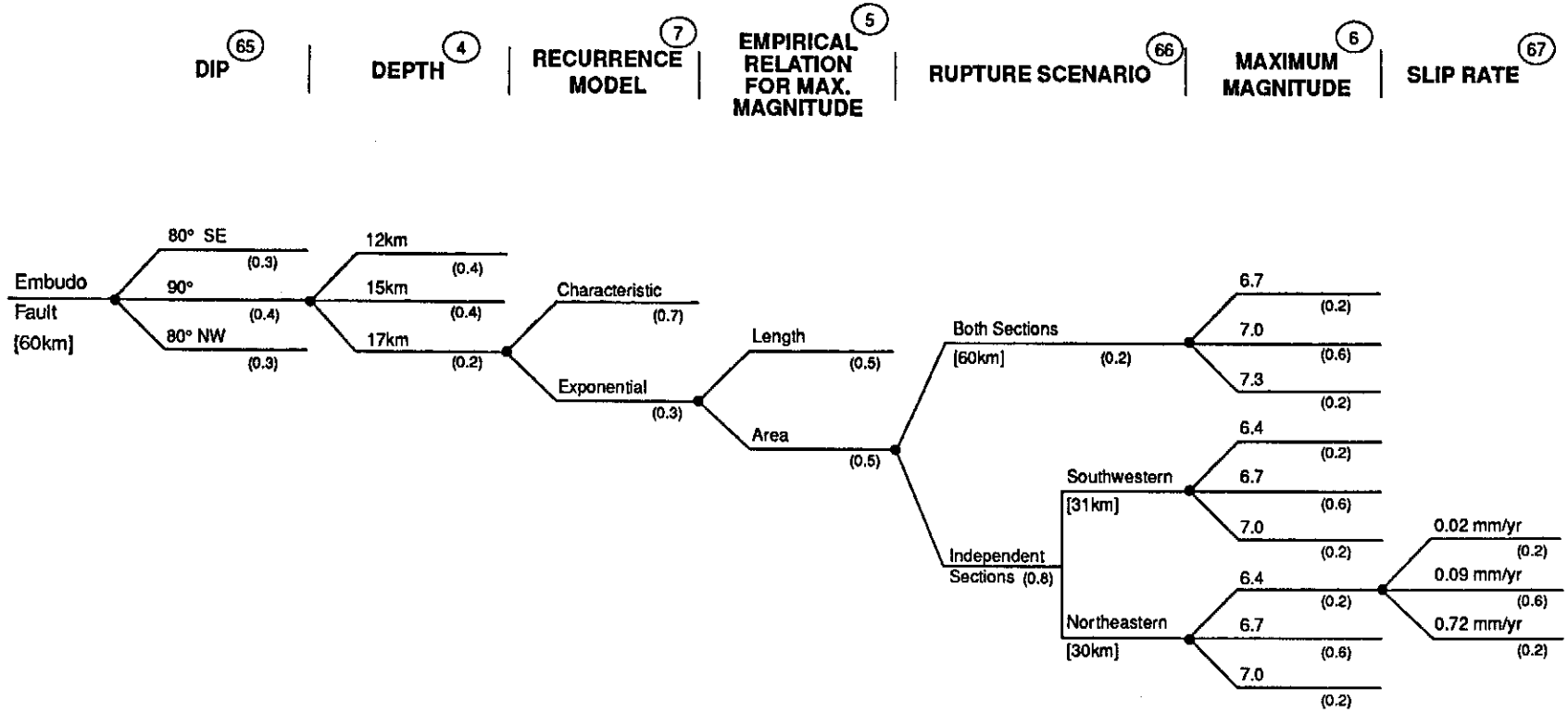
Project No. 91C0509	Los Alamos Seismic Hazards	LOGIC TREE FOR LOBATO MESA FAULT ZONE	Figure 7-4
Woodward-Clyde Federal Services			

91C0509A-2200/052793



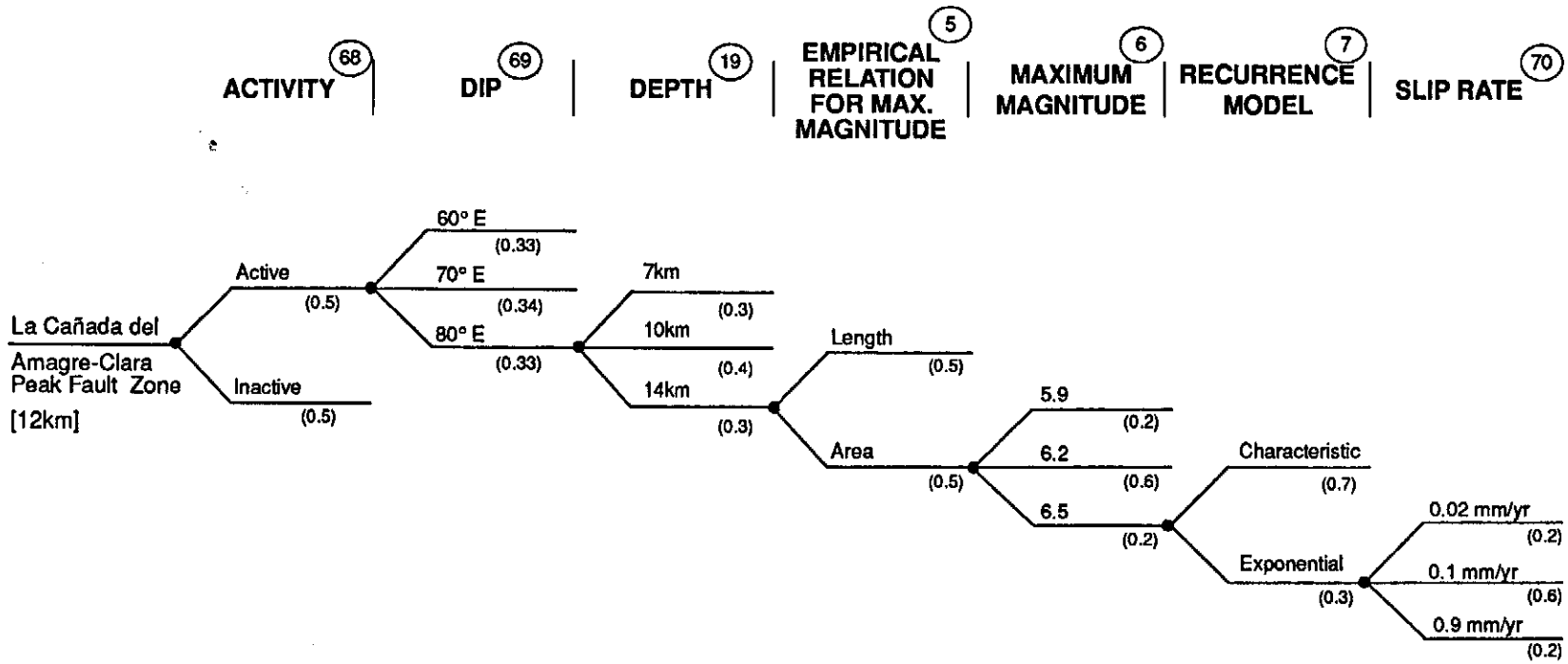
Project No. 91C0509	Los Alamos Seismic Hazards	LOGIC TREE FOR LA BAJADA FAULT	Figure 7-5
Woodward-Clyde Federal Services			

91C0509A-2200/052793



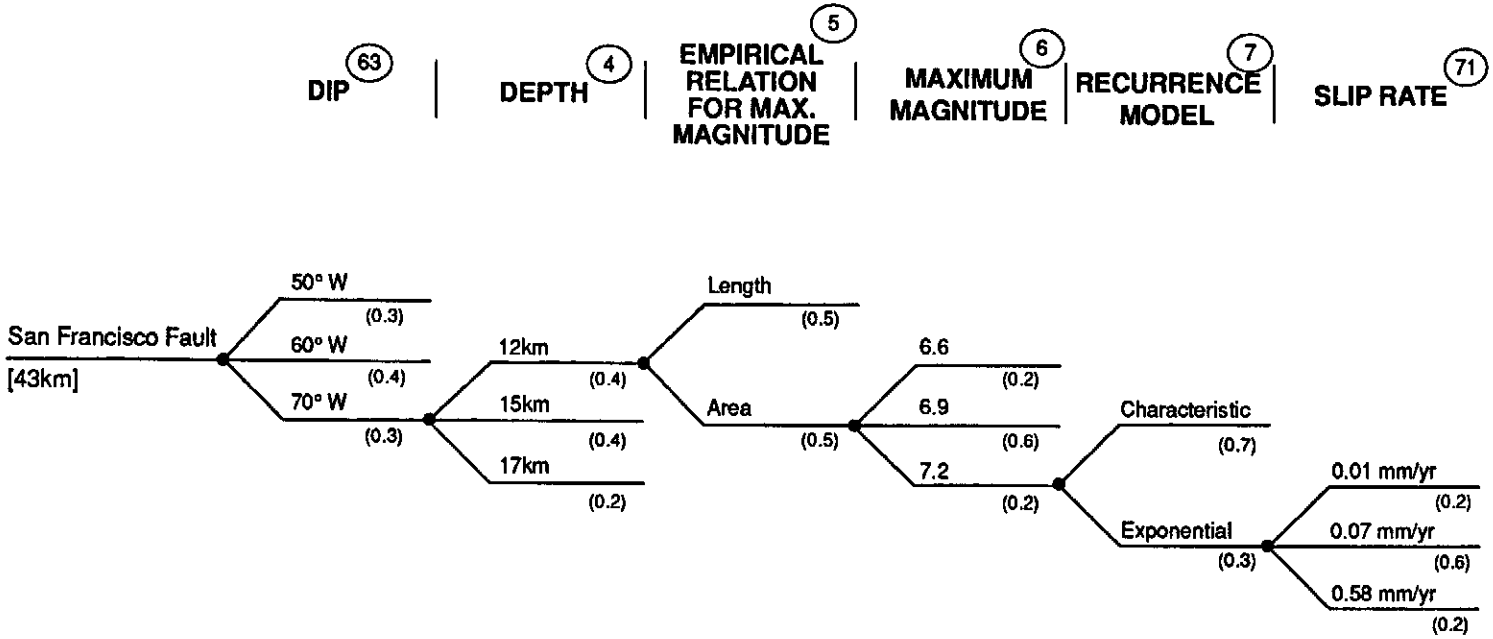
Project No. 91C0509	Los Alamos Seismic Hazards	LOGIC TREE FOR EMBUDO FAULT	Figure 7-6
Woodward-Clyde Federal Services			

91C0509A-2200/052793



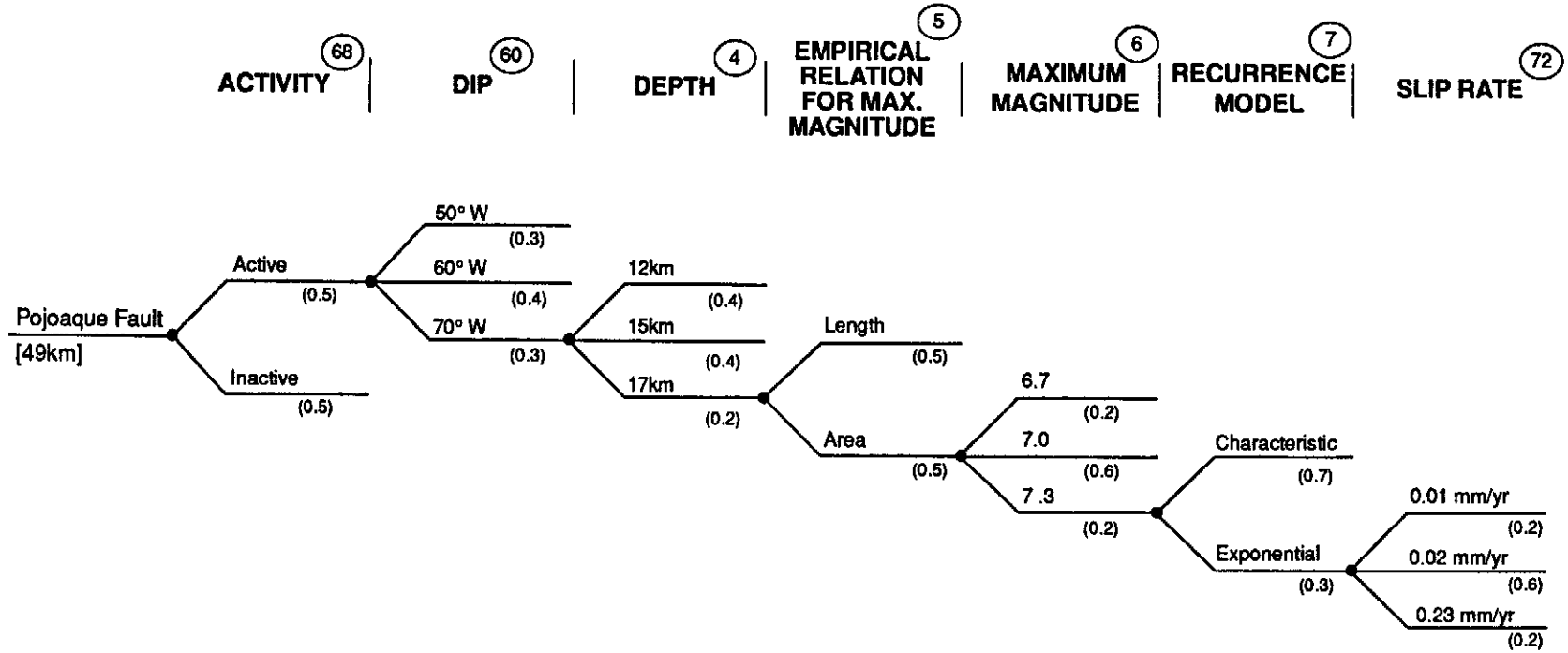
Project No. 91C0509	Los Alamos Seismic Hazards	LOGIC TREE FOR LA CAÑADA DEL AMAGRE-CLARA PEAK FAULT ZONE	Figure 7-7
Woodward-Clyde Federal Services			

91C0509A-2200/052793



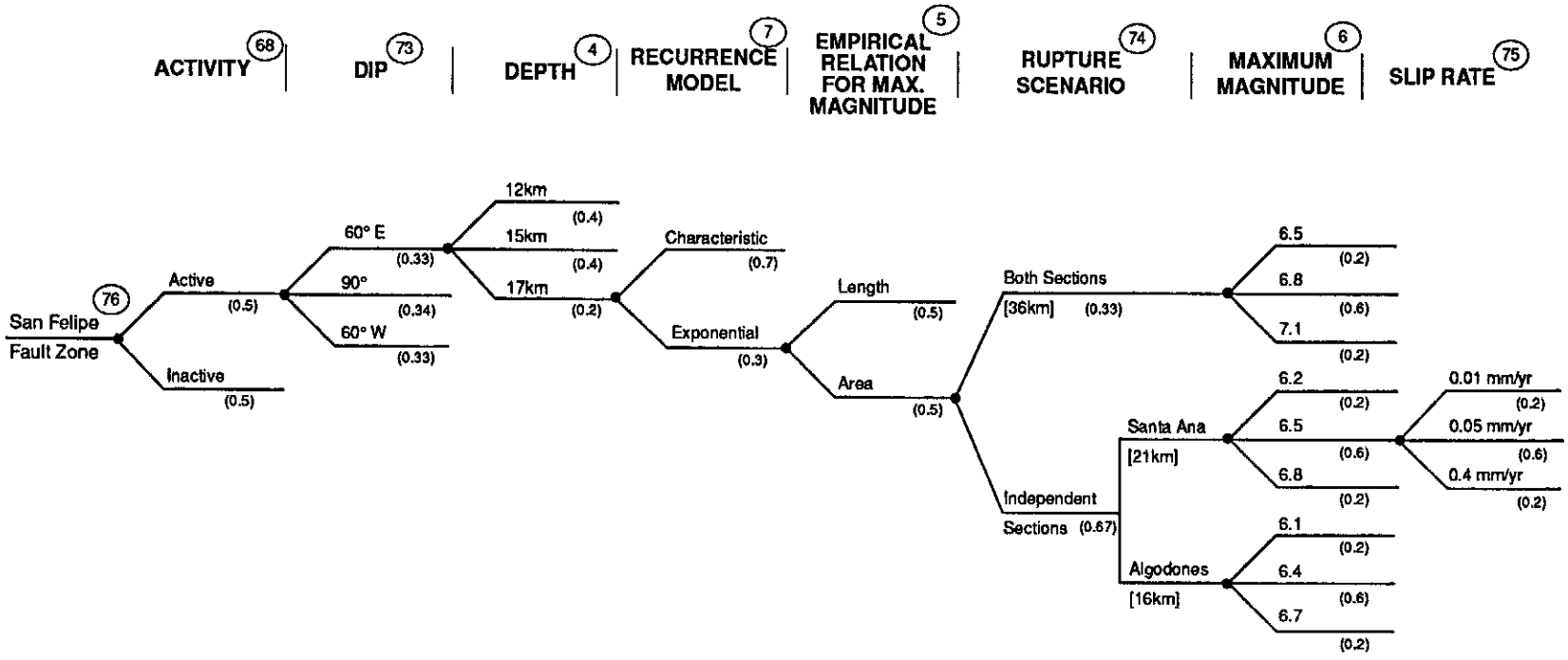
Project No. 91C0509	Los Alamos Seismic Hazards	LOGIC TREE FOR SAN FRANCISCO FAULT	Figure 7-8
Woodward-Clyde Federal Services			

91C0509A-2200/052793



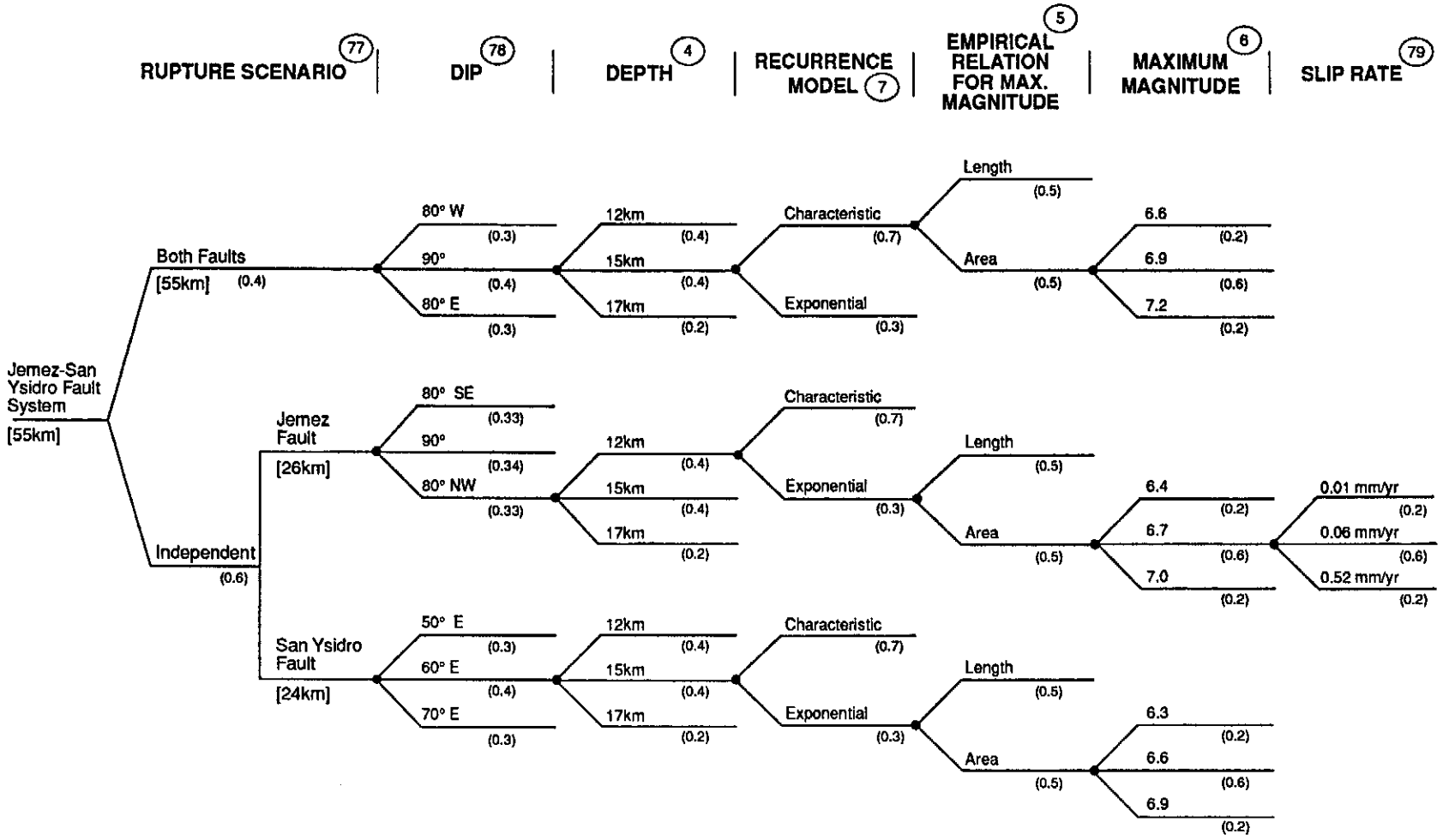
Project No. 91C0509	Los Alamos Seismic Hazards	LOGIC TREE FOR POJOAQUE FAULT	Figure 7-9
Woodward-Clyde Federal Services			

91C0509A-2200/052793



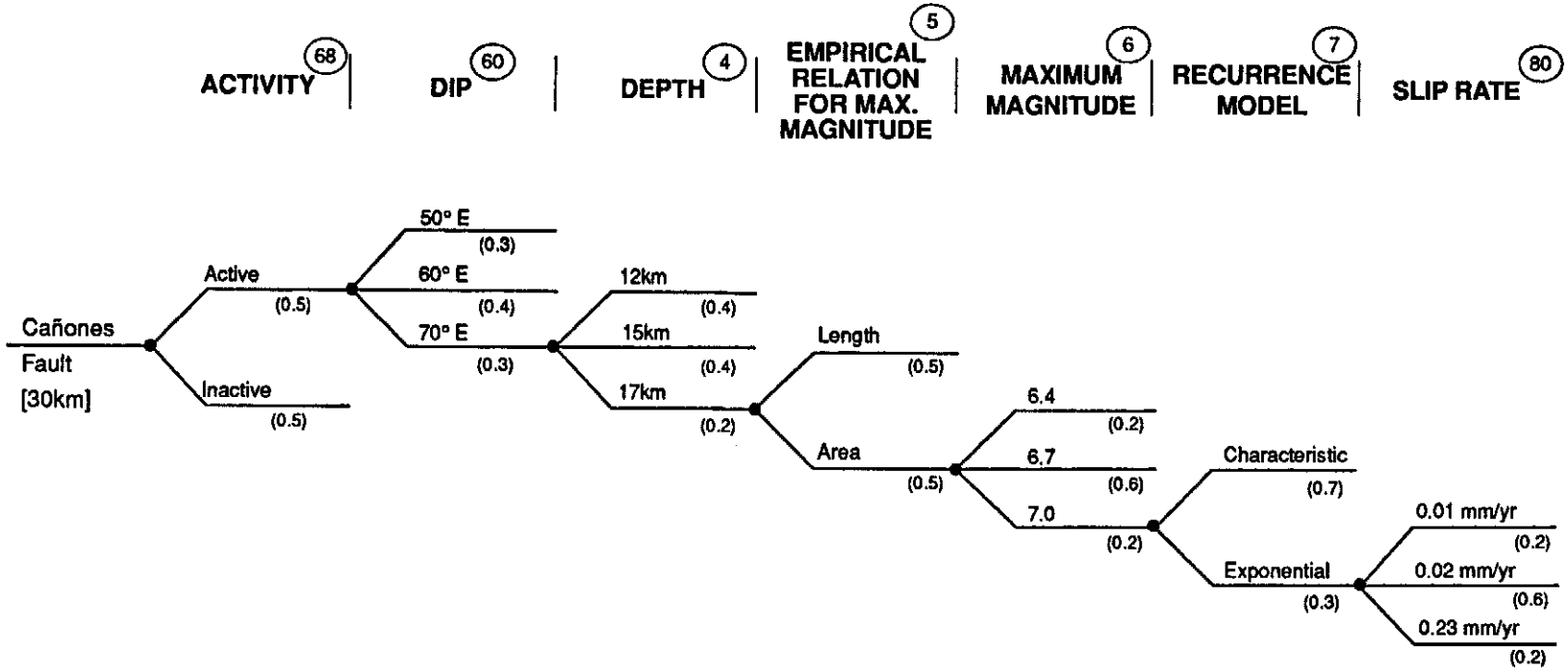
Project No. 91C0509	Los Alamos Seismic Hazards	LOGIC TREE FOR SAN FELIPE FAULT ZONE	Figure 7-10
Woodward-Clyde Federal Services			

91C0509A-2200/052793



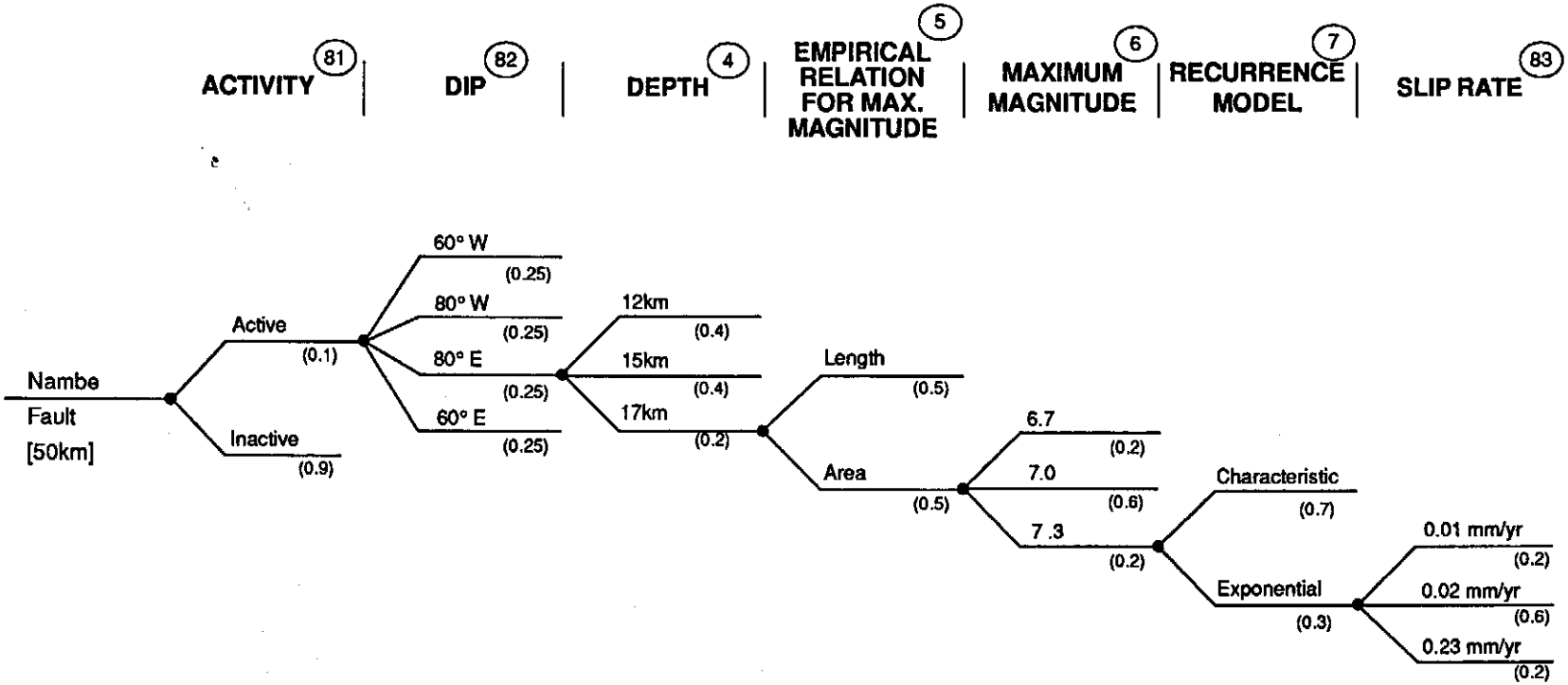
Project No. 91C0509	Los Alamos Seismic Hazards	LOGIC TREE FOR JEMEZ-SAN YSIDRO FAULT SYSTEM	Figure 7-11
Woodward-Clyde Federal Services			

91C0509A-2200/052793

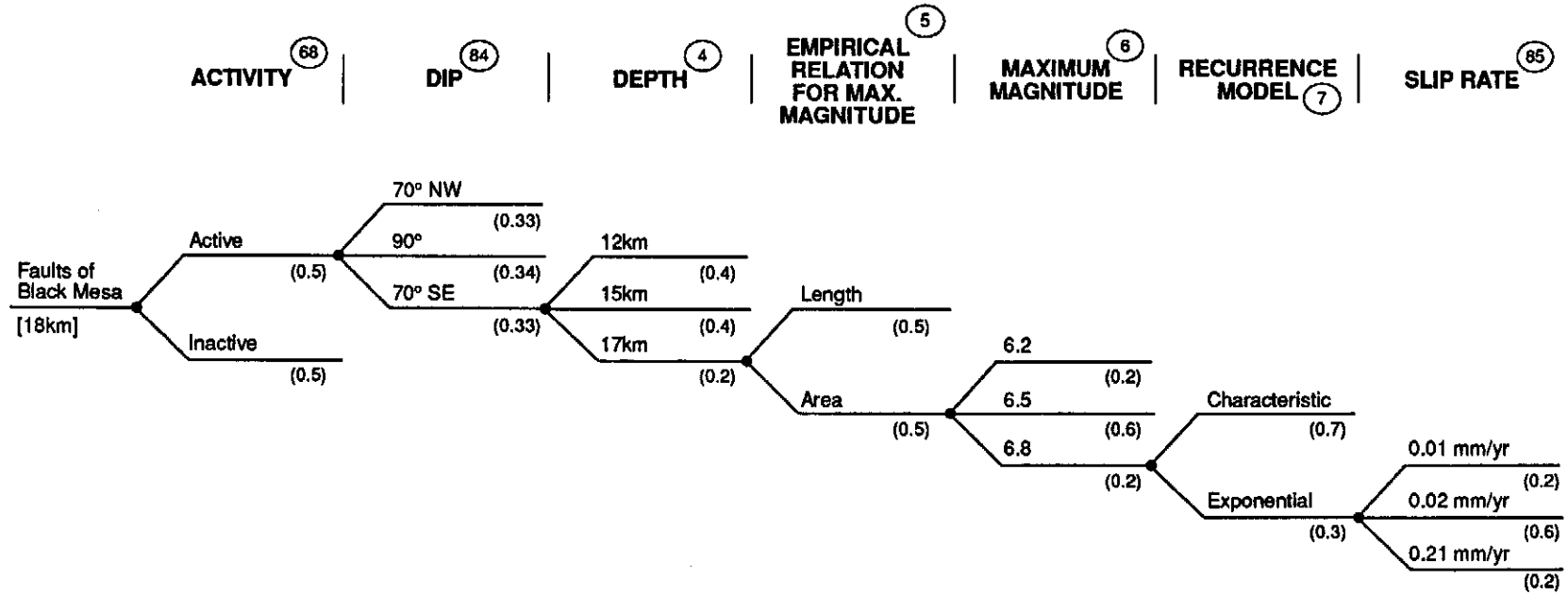


Project No. 91C0509	Los Alamos Seismic Hazards	LOGIC TREE FOR CAÑONES FAULT	Figure 7-12
	Woodward-Clyde Federal Services		

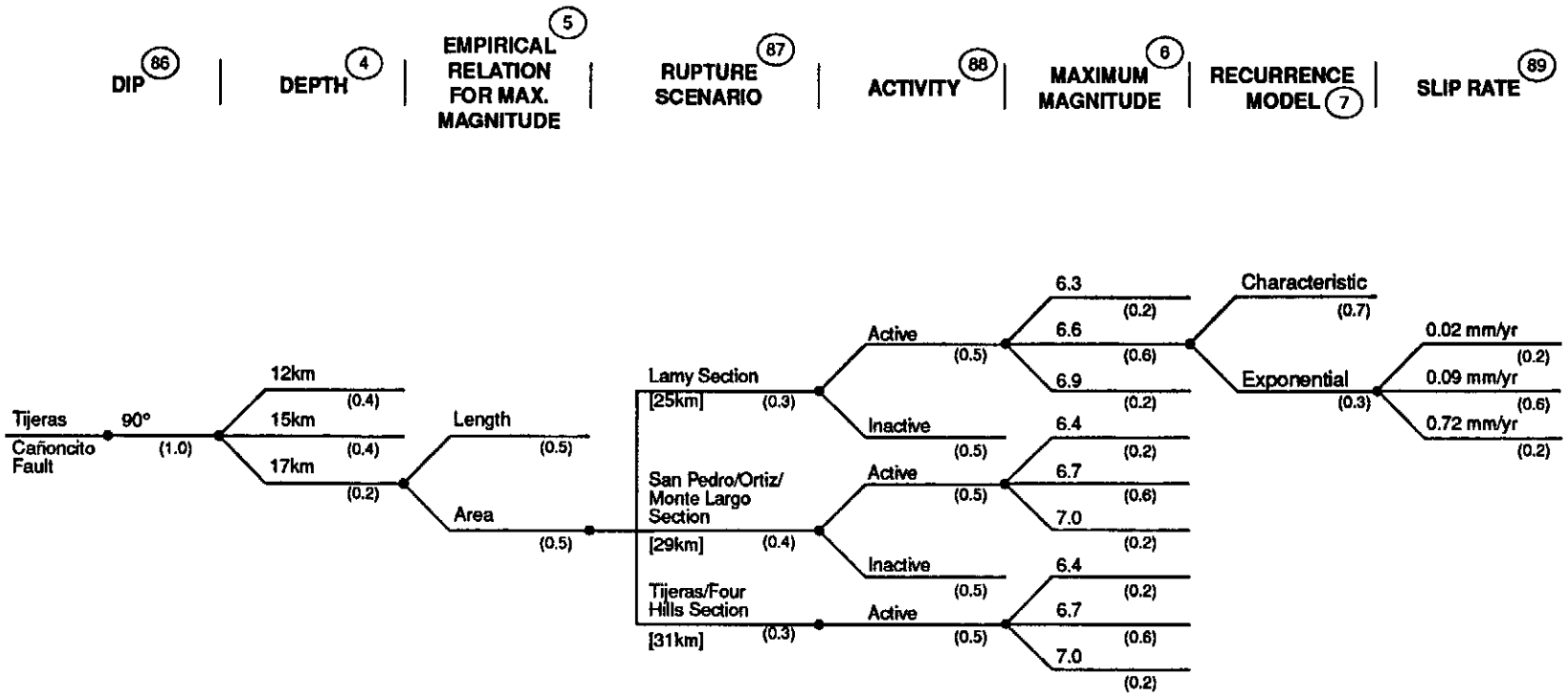
91C0509A-2200/052793



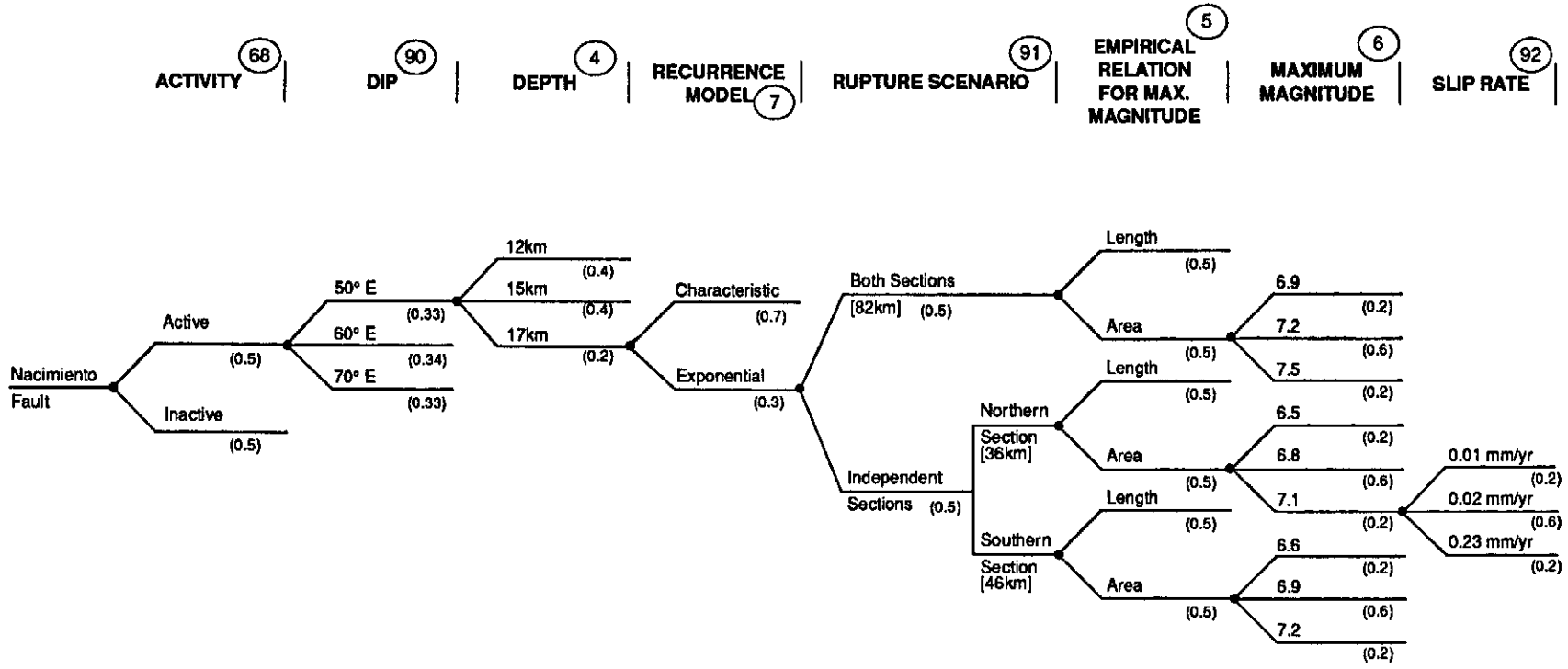
Project No. 91C0509	Los Alamos Seismic Hazards	LOGIC TREE FOR NAMBE FAULT	Figure 7-13
Woodward-Clyde Federal Services			



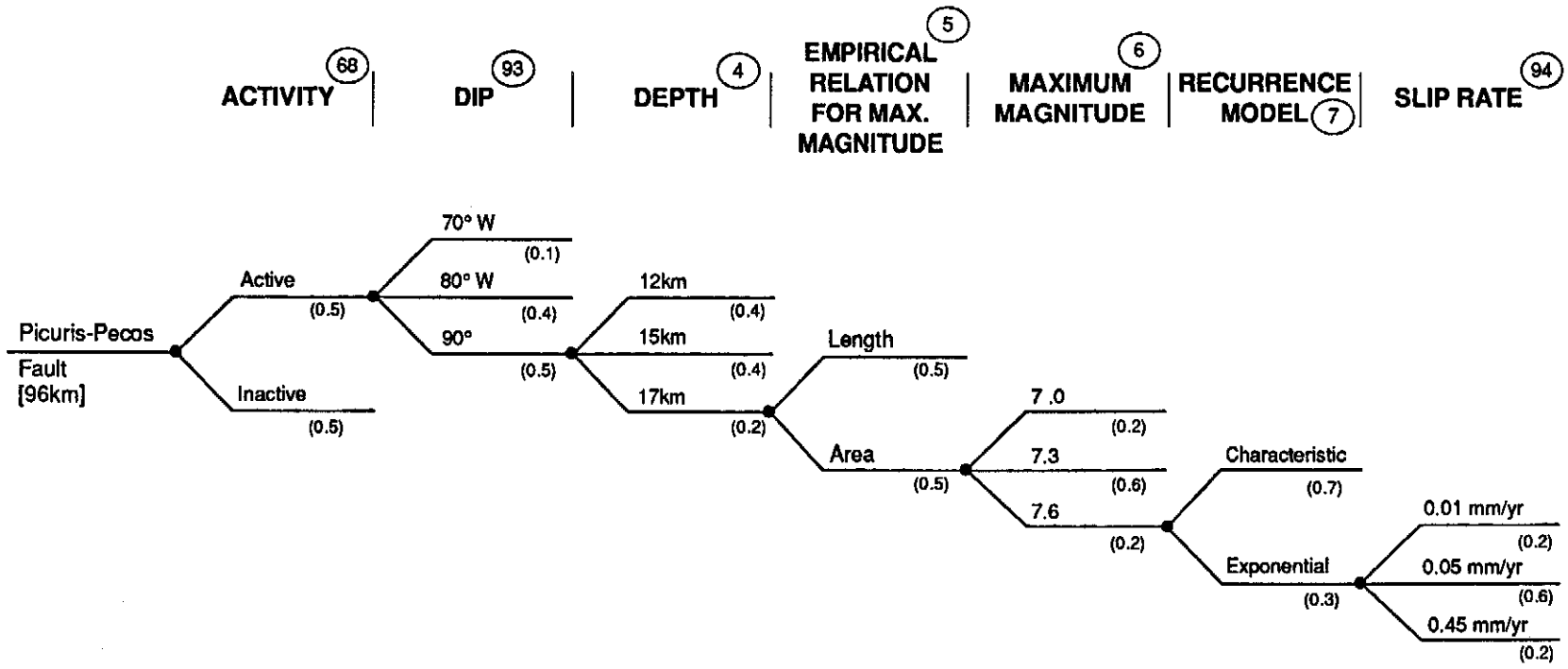
Project No. 91C0509	Los Alamos Seismic Hazards	LOGIC TREE FOR FAULTS OF BLACK MESA	Figure 7-14
Woodward-Clyde Federal Services			



Project No. 91C0509A	Los Alamos Seismic Hazards	LOGIC TREE FOR TIJERAS-CAÑONCITO FAULT	Figure 7-15
Woodward-Clyde Federal Services			

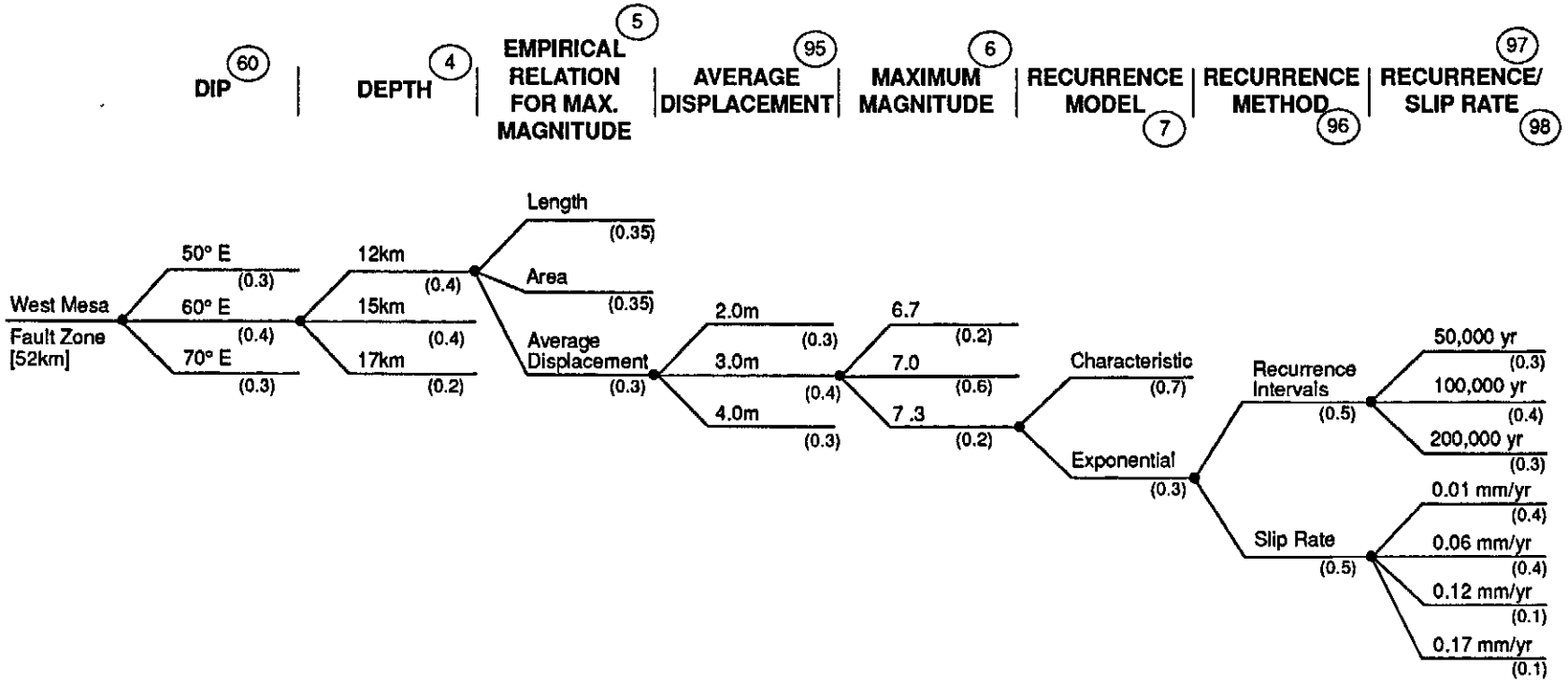


Project No. 91C0509	Los Alamos Seismic Hazards	LOGIC TREE FOR NACIMIENTO FAULT	Figure 7-16
Woodward-Clyde Federal Services			



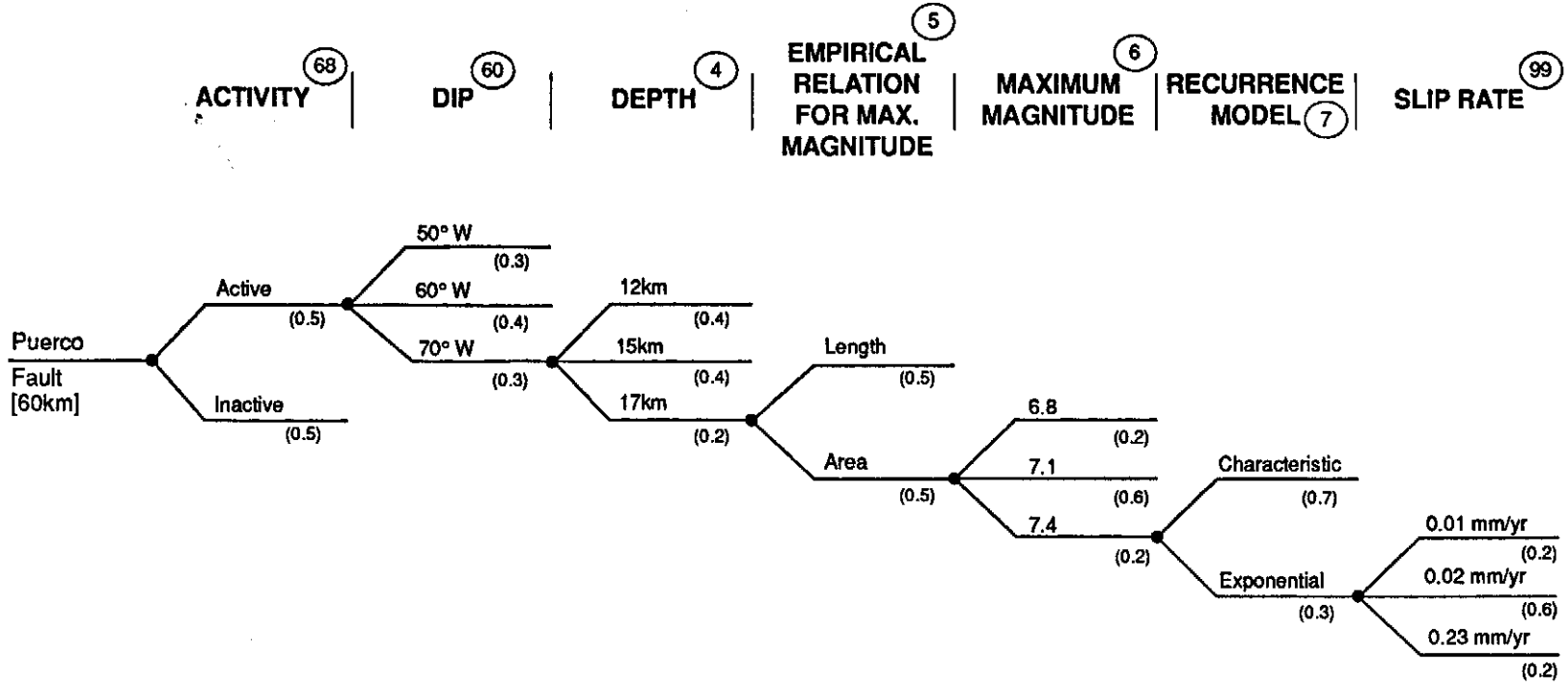
Project No. 91C0509	Los Alamos Seismic Hazards	LOGIC TREE FOR PICURIS-PECOS FAULT	Figure 7-17
Woodward-Clyde Federal Services			

91C0509A-2200/052793



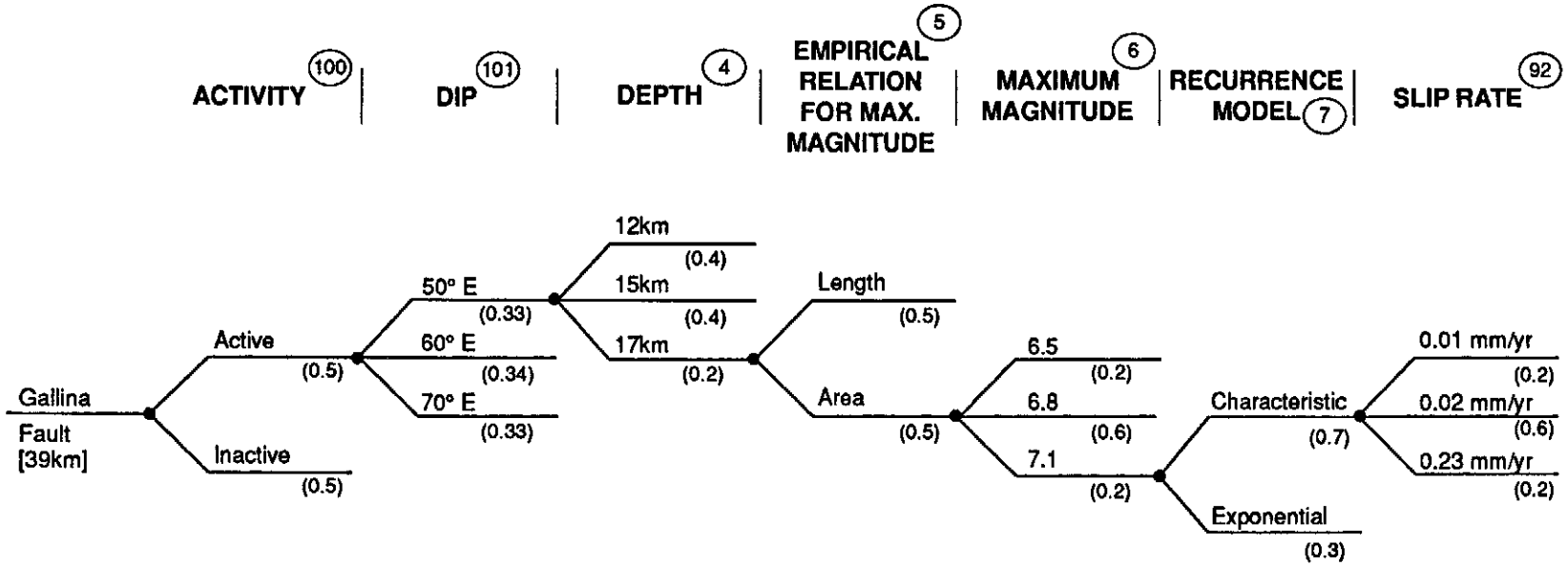
Project No. 91C0509	Los Alamos Seismic Hazards	LOGIC TREE FOR WEST MESA FAULT ZONE	Figure 7-18
Woodward-Clyde Federal Services			

91C0509A-2200/052793



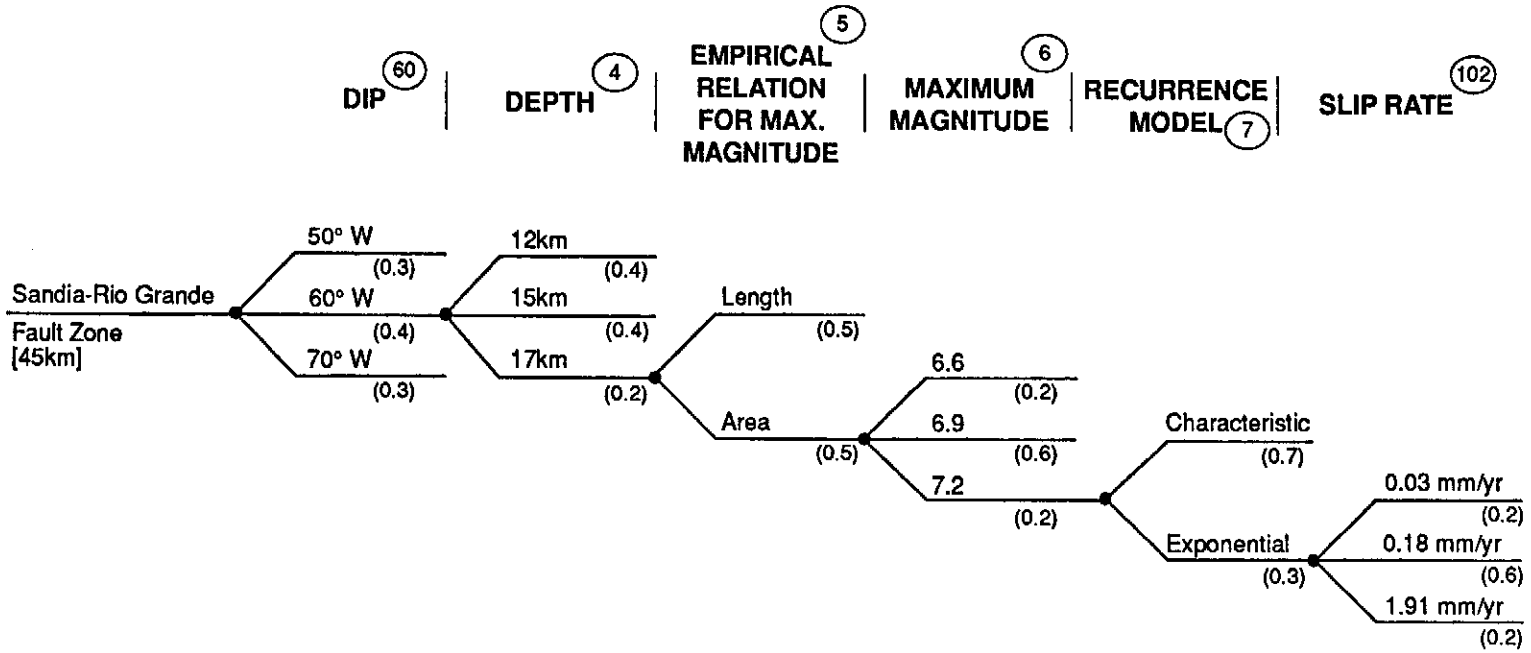
Project No. 91C0509	Los Alamos Seismic Hazards	LOGIC TREE FOR PUERCO FAULT	Figure 7-19
Woodward-Clyde Federal Services			

91C0509A-2200/052793



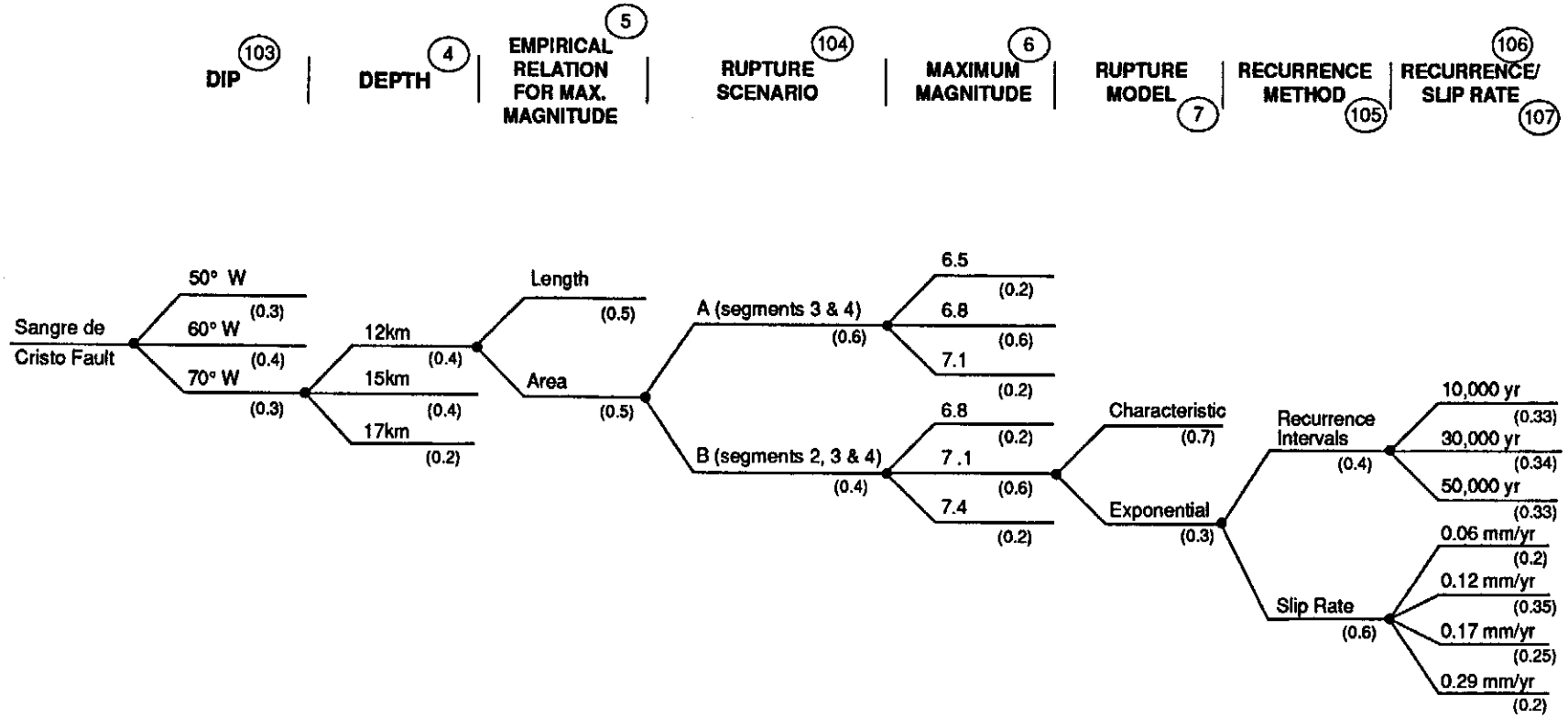
Project No. 91C0509	Los Alamos Seismic Hazards	LOGIC TREE FOR GALLINA FAULT	Figure 7-20
Woodward-Clyde Federal Services			

91C0509A-2200/052793



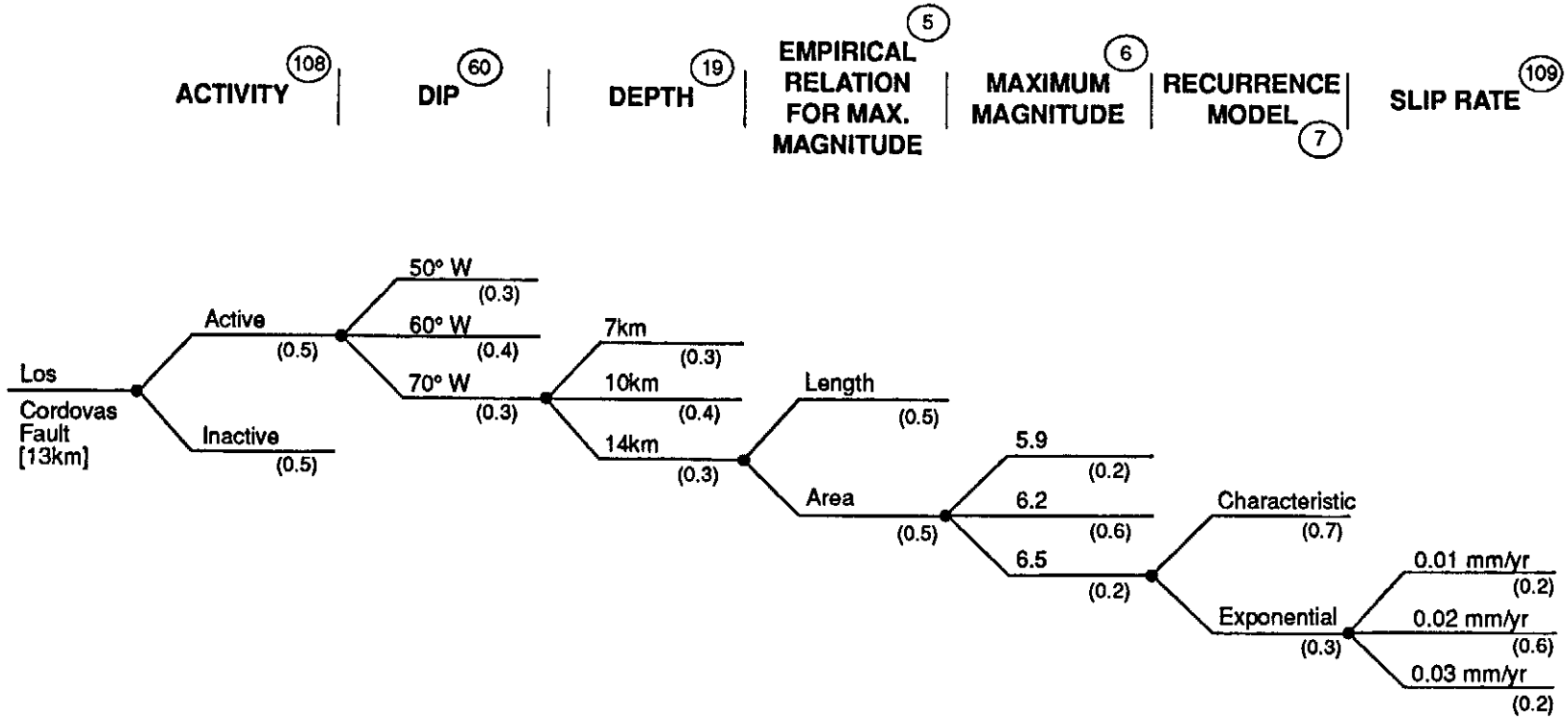
Project No. 91C0509	Los Alamos Seismic Hazards	LOGIC TREE FOR SANDIA-RIO GRANDE FAULT ZONE	Figure 7-21
Woodward-Clyde Federal Services			

91C0509A-2200/052793



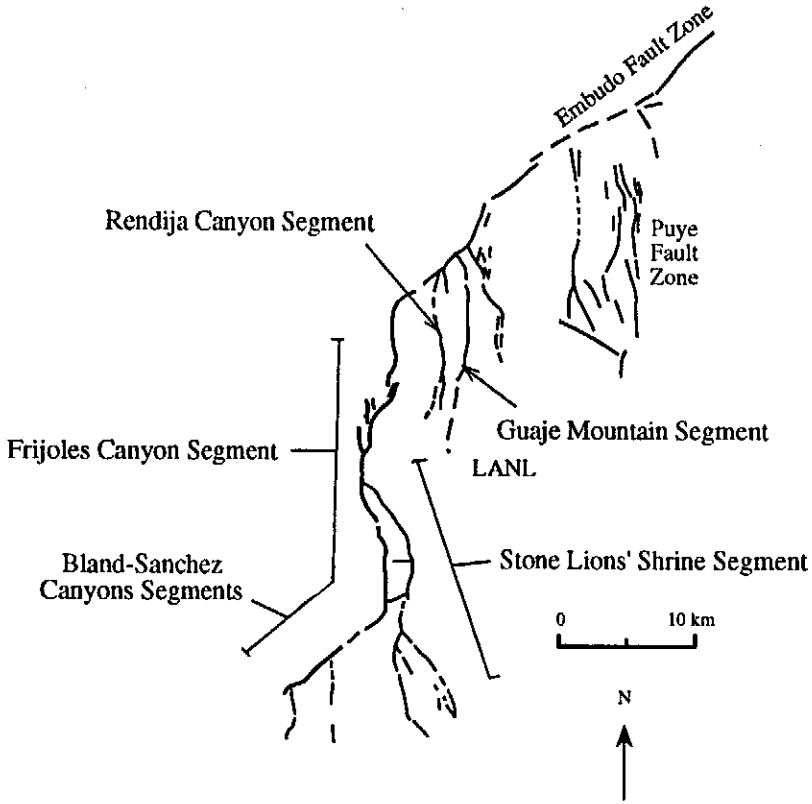
Project No. 91C0509	Los Alamos Seismic Hazards	LOGIC TREE FOR SANGRE DE CRISTO FAULT	Figure 7-22
Woodward-Clyde Federal Services			

91C0509A-2200/052793

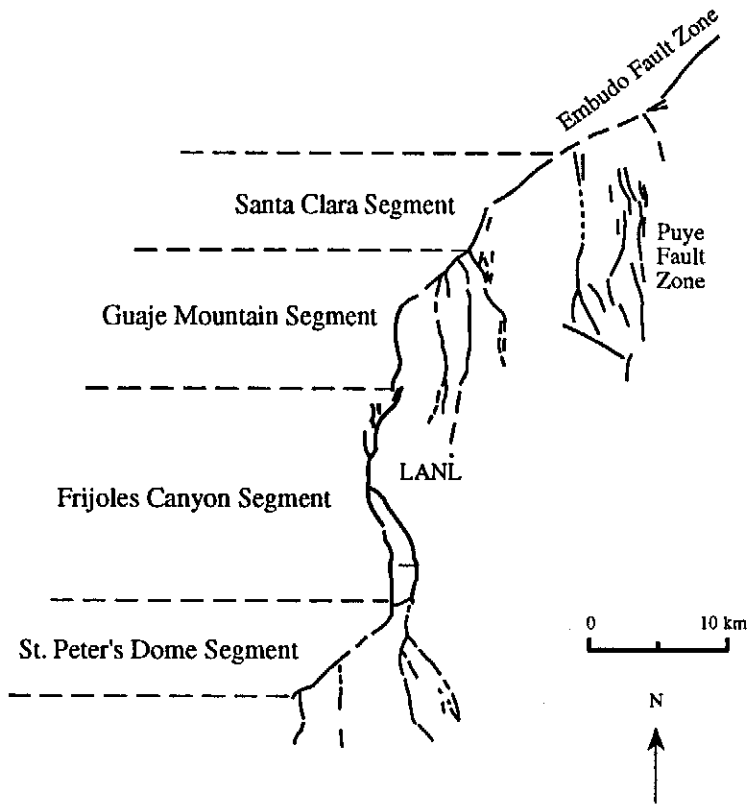


Project No. 91C0509	Los Alamos Seismic Hazards	LOGIC TREE FOR LOS CORDOVAS FAULT	Figure 7-23
Woodward-Clyde Federal Services			

91C0509A-2200/052793



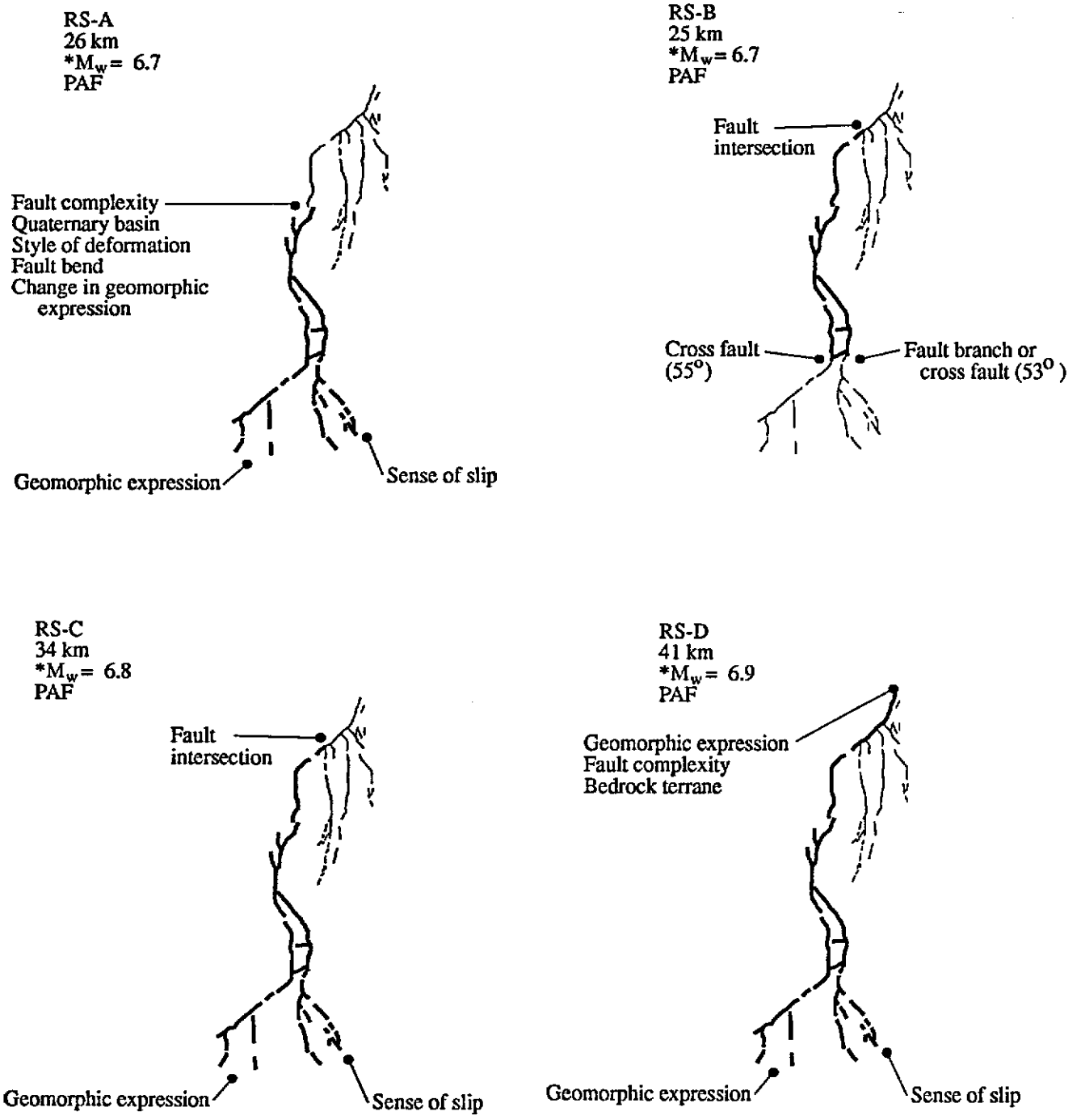
Structural Segmentation Model of Gardner et al. (1990)



Structural Segmentation Model of Golombek (1983)

Project No. 91C0509	Los Alamos Seismic Hazards	PREVIOUS SEGMENTATION MODELS FOR THE PAJARITO FAULT SYSTEM	Figure 7-24
Woodward-Clyde Federal Services			

91C0509A-1300/060493



PAF - Pajarito fault
RC - Rendija Canyon fault
GM - Guaje Mountain fault

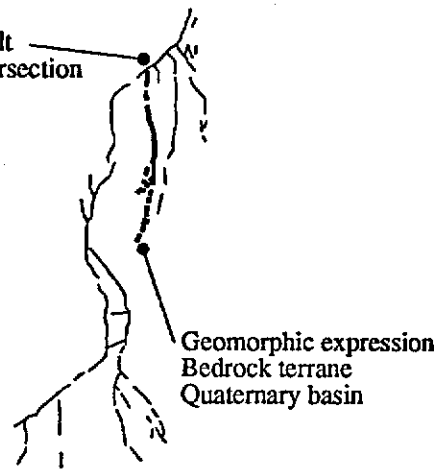
* Weighted mean calculated for each rupture scenario using geometries, empirical relations and associated probabilities shown in Figures 7-1a and 7-1f

0 10 km

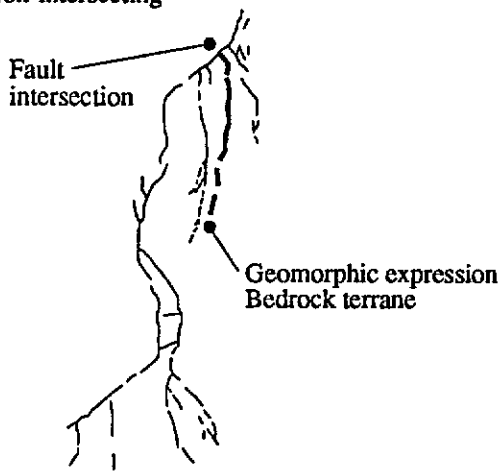
N

Project No. 91C0509	Los Alamos Seismic Hazards	SCHEMATIC DIAGRAM OF RUPTURE SCENARIOS FOR THE PAJARITO FAULT SYSTEM	Figure 7-25a
WOODWARD-CLYDE FEDERAL SERVICES			

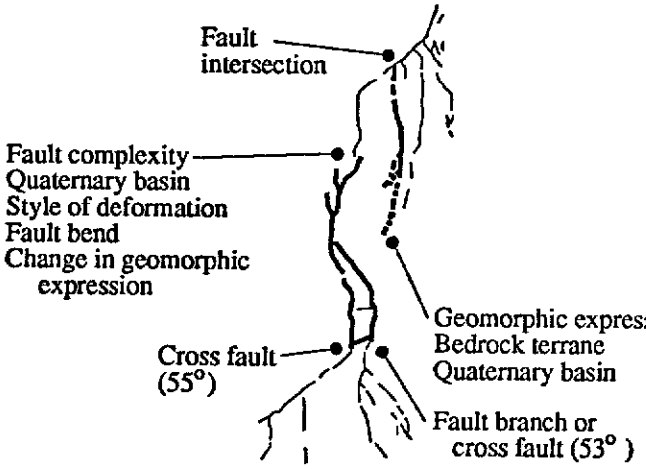
RS-E
14 km
*M_w = 6.5 (Non-intersecting)
*M_w = 6.4 (Intersecting)
RC



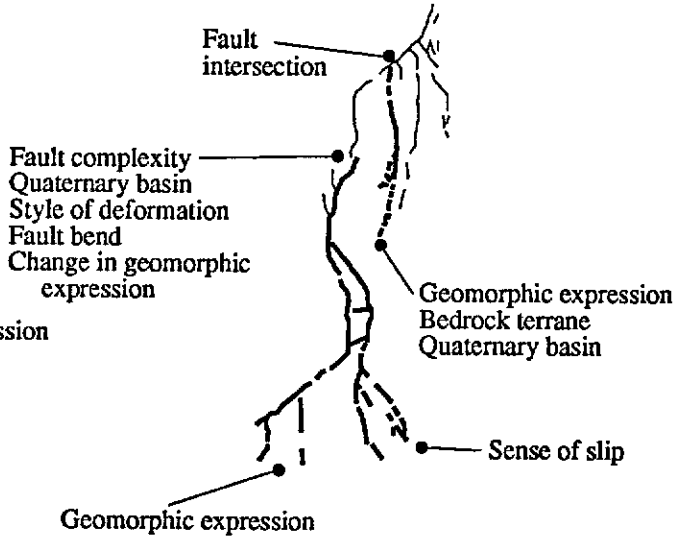
RS-F
12 km
*M_w = 6.5
GM
Intersecting &
Non-intersecting



RS-G
25 km
*M_w = 6.8
PAF & RC
Non-intersecting

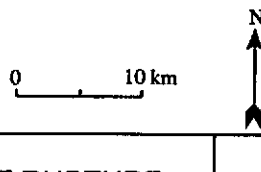


RS-H
34 km
*M_w = 6.9
PAF & RC
Non-intersecting



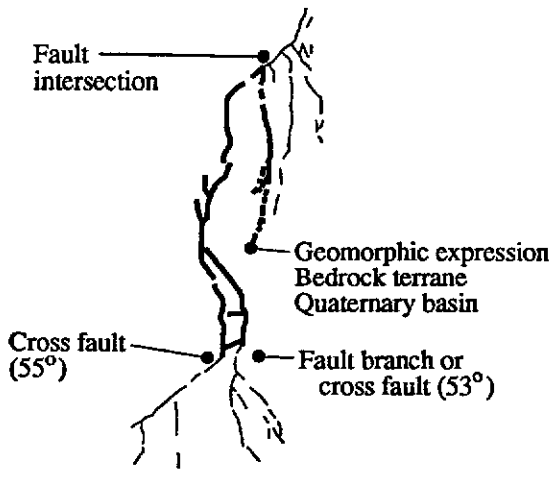
PAF - Pajarito fault
RC - Rendija Canyon fault
GM - Guaje Mountain fault

* Weighted mean calculated for each rupture scenario using geometries, displacements, empirical relations, and associated probabilities shown in Figures 7-1b through 7-1e

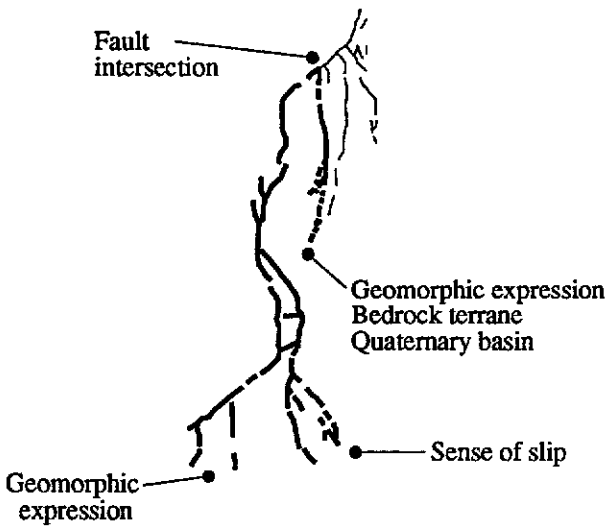


Project No. 91C0509	Los Alamos Seismic Hazards	SCHEMATIC DIAGRAM OF RUPTURE SCENARIOS FOR THE PAJARITO FAULT SYSTEM	Figure 7-25b
WOODWARD-CLYDE FEDERAL SERVICES			

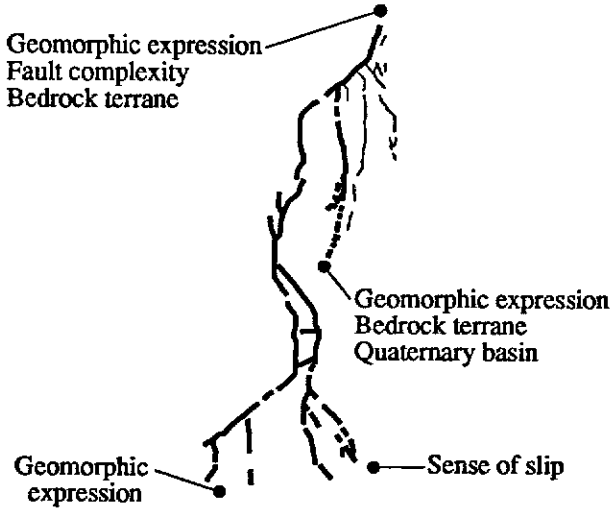
RS-I
25 km
*M_w = 6.7
PAF & RC
Intersecting



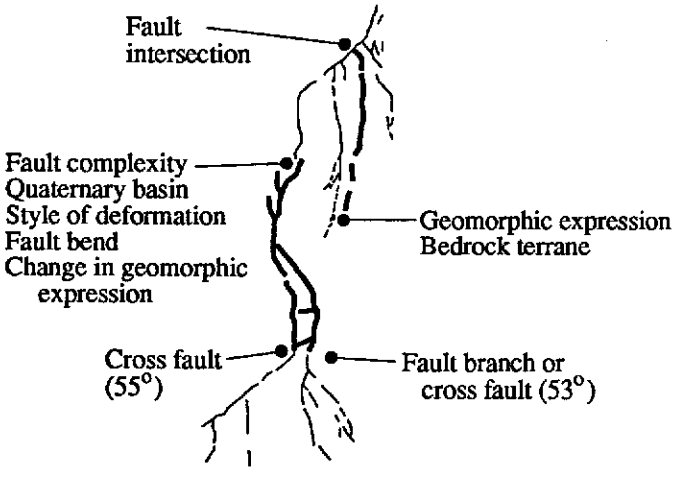
RS-J
34 km
*M_w = 6.8
PAF & RC
Intersecting



RS-K
41 km
*M_w = 6.9
PAF & RC
Intersecting

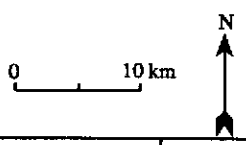


RS-L
27 km
*M_w = 6.7
PAF & GM
Non-intersecting



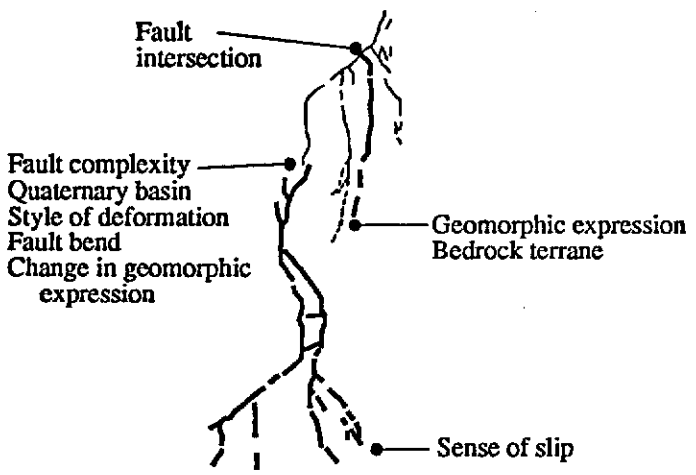
PAF - Pajarito fault
RC - Rendija Canyon fault
GM - Guaje Mountain fault

* Weighted mean calculated for each rupture scenario using geometries, displacements, empirical relations, and associated probabilities shown in Figures 7-1d and 7-1e

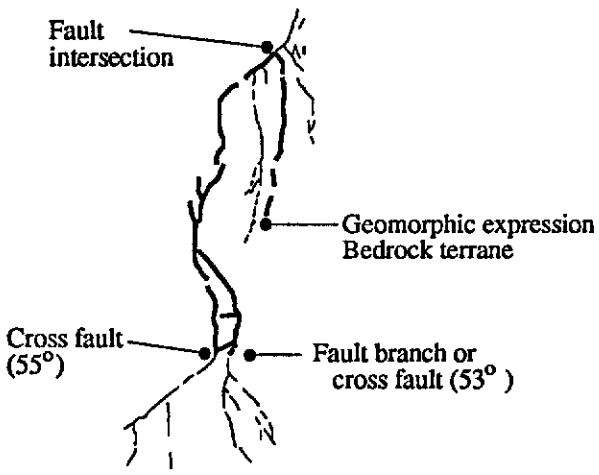


Project No. 91C0509	Los Alamos Seismic Hazards	SCHEMATIC DIAGRAM OF RUPTURE SCENARIOS FOR THE PAJARITO FAULT SYSTEM	Figure 7-25c
WOODWARD-CLYDE FEDERAL SERVICES			

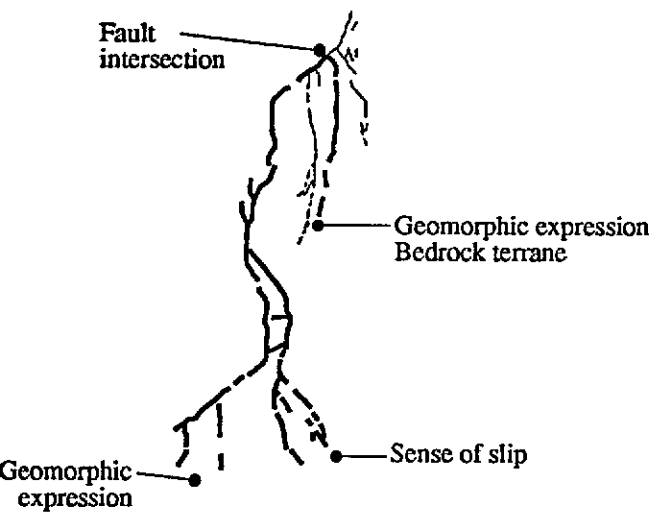
RS-M
36 km
*M_w = 6.8
PAF & GM
Non-intersecting



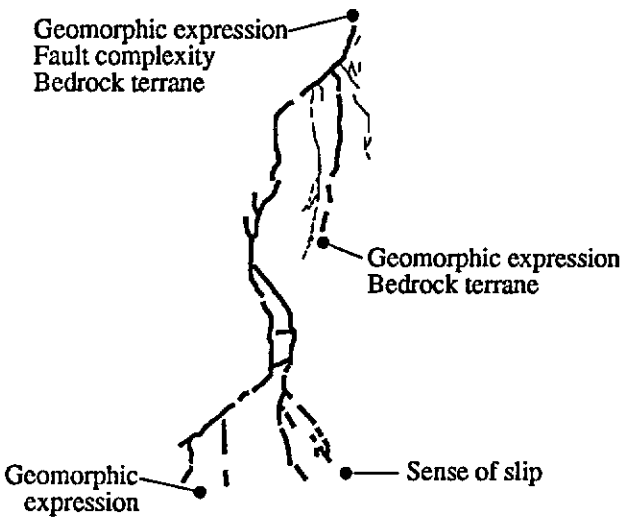
RS-N
27 km
*M_w = 6.7
PAF & GM
Intersecting



RS-O
36 km
*M_w = 6.8
PAF & GM
Intersecting



RS-P
41 km
*M_w = 6.9
PAF & GM
Intersecting



PAF - Pajarito fault
RC - Rendija Canyon fault
GM - Guaje Mountain fault

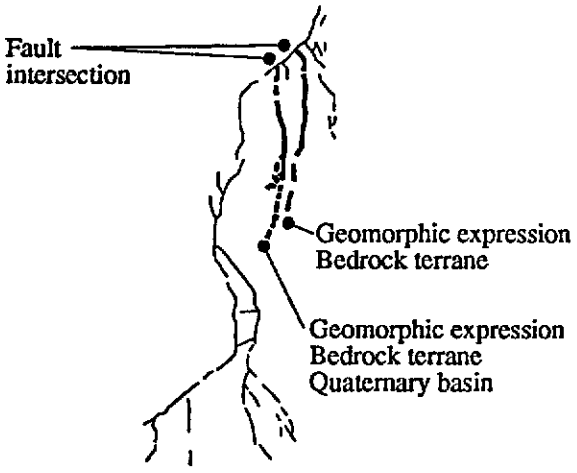
* Weighted mean calculated for each rupture scenario using geometries, displacements, empirical relations, and associated probabilities shown in Figure 7-1e

0 10 km

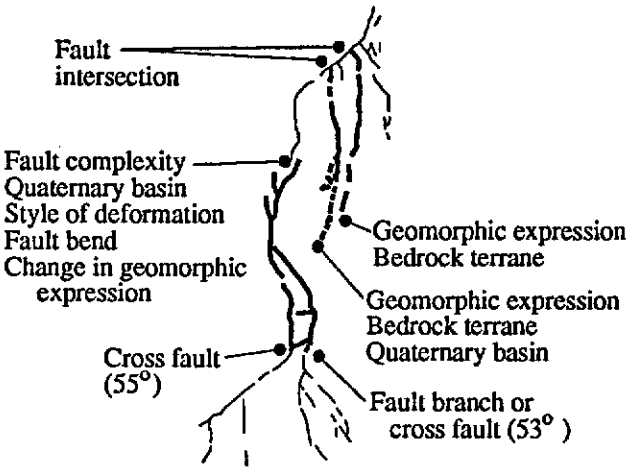
N

Project No. 91C0509	Los Alamos Seismic Hazards	SCHEMATIC DIAGRAM OF RUPTURE SCENARIOS FOR THE PAJARITO FAULT SYSTEM	Figure 7-25d
WOODWARD-CLYDE FEDERAL SERVICES			

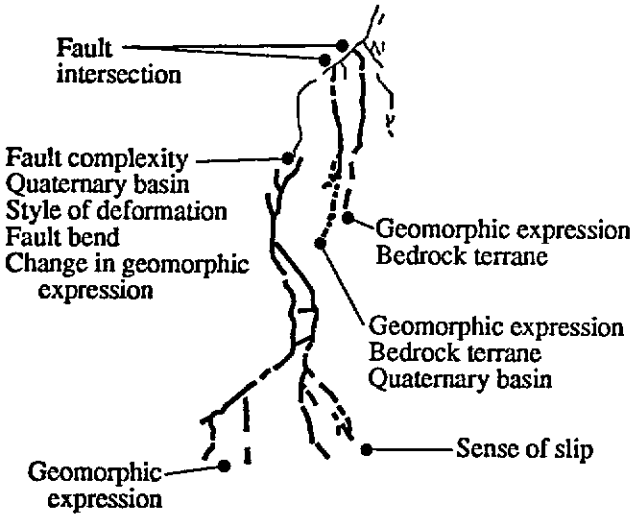
RS-Q
14 km
*M_w= 6.6 (Non-intersecting)
*M_w= 6.5 (Intersecting)
RC & GM



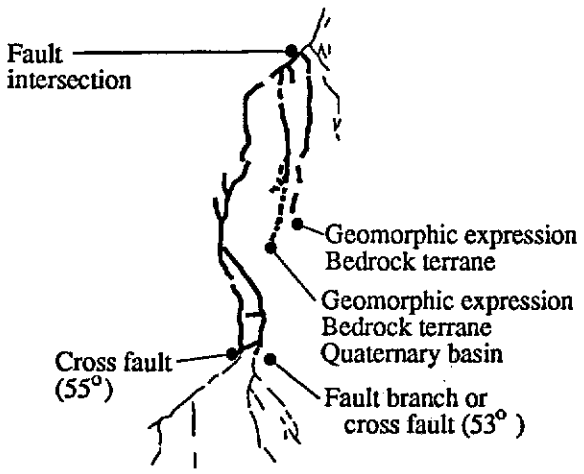
RS-R
27 km
*M_w= 6.8
PAF & RC & GM
Non-intersecting



RS-S
36 km
*M_w= 6.9
PAF & RC & GM
Non-intersecting

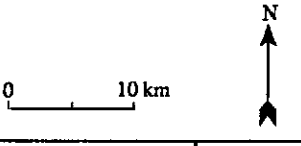


RS-T
27 km
*M_w= 6.7
PAF & RC & GM
Intersecting



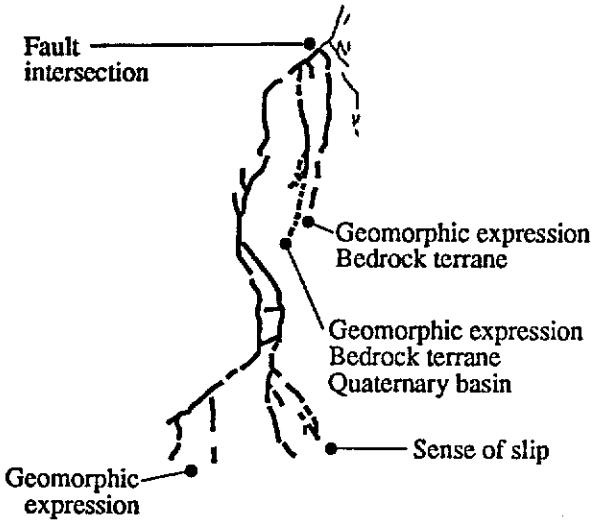
PAF - Pajarito fault
RC - Rendija Canyon fault
GM - Guaje Mountain fault

* Weighted mean calculated for each rupture scenario using geometries, displacements, empirical relations, and associated probabilities shown in Figures 7-1d through 7-1g

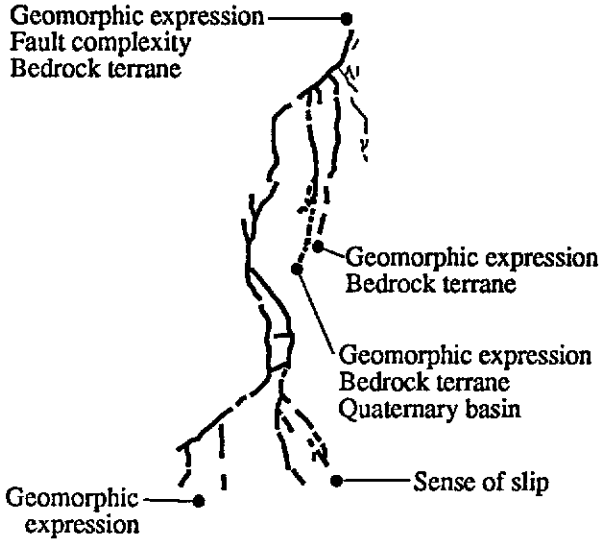


Project No. 91C0509	Los Alamos Seismic Hazards	SCHEMATIC DIAGRAM OF RUPTURE SCENARIOS FOR THE PAJARITO FAULT SYSTEM	Figure 7-25e
WOODWARD-CLYDE FEDERAL SERVICES			

RS-U
36 km
*M_w = 6.8
PAF & RC & GM
Intersecting

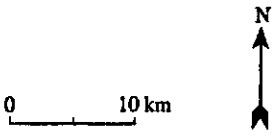


RS-V
41 km
*M_w = 6.9
PAF & RC & GM
Intersecting

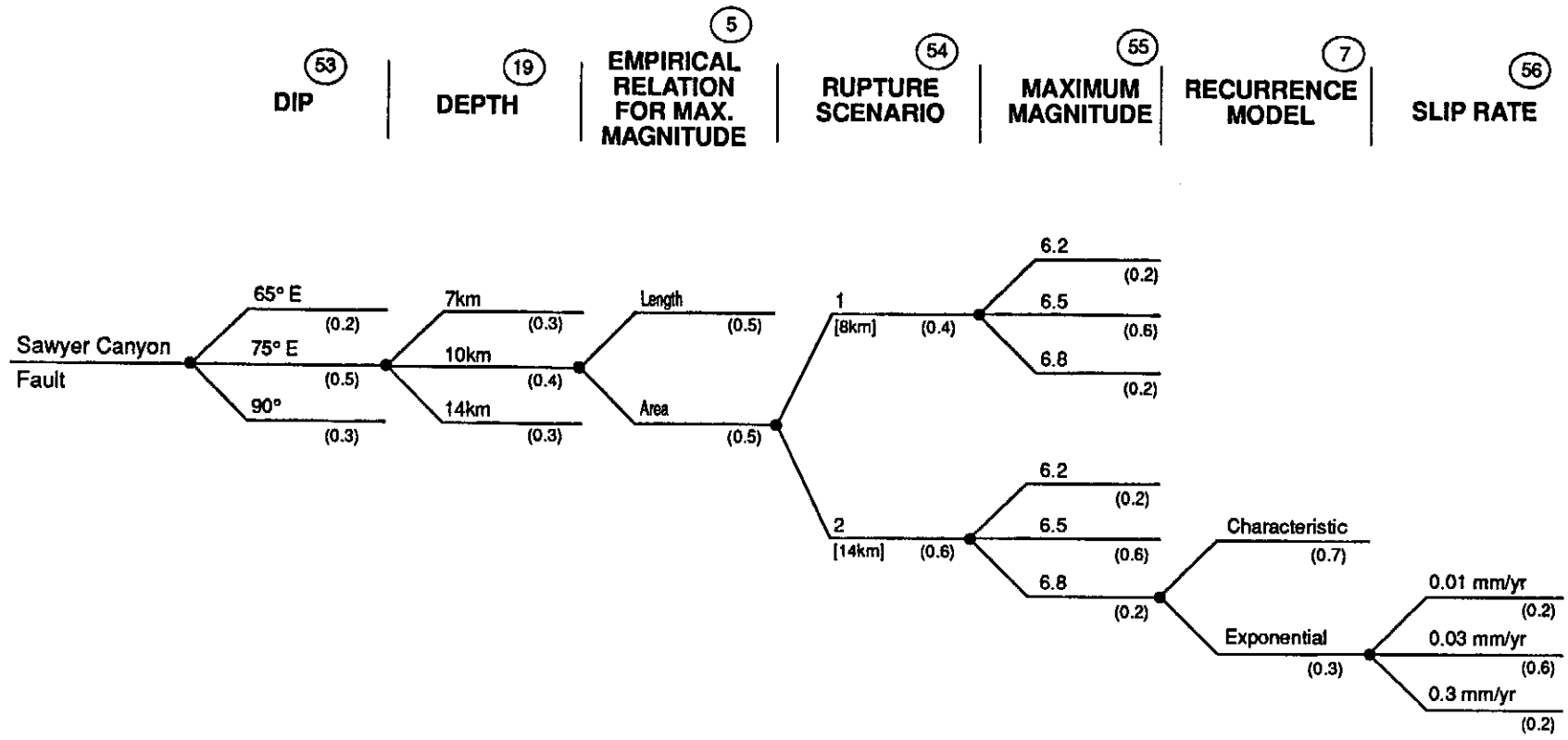


PAF - Pajarito fault
RC - Rendija Canyon fault
GM - Guaje Mountain fault

* Weighted mean calculated for each rupture scenario using geometries, displacements, empirical relations, and associated probabilities shown in Figure 7-1g

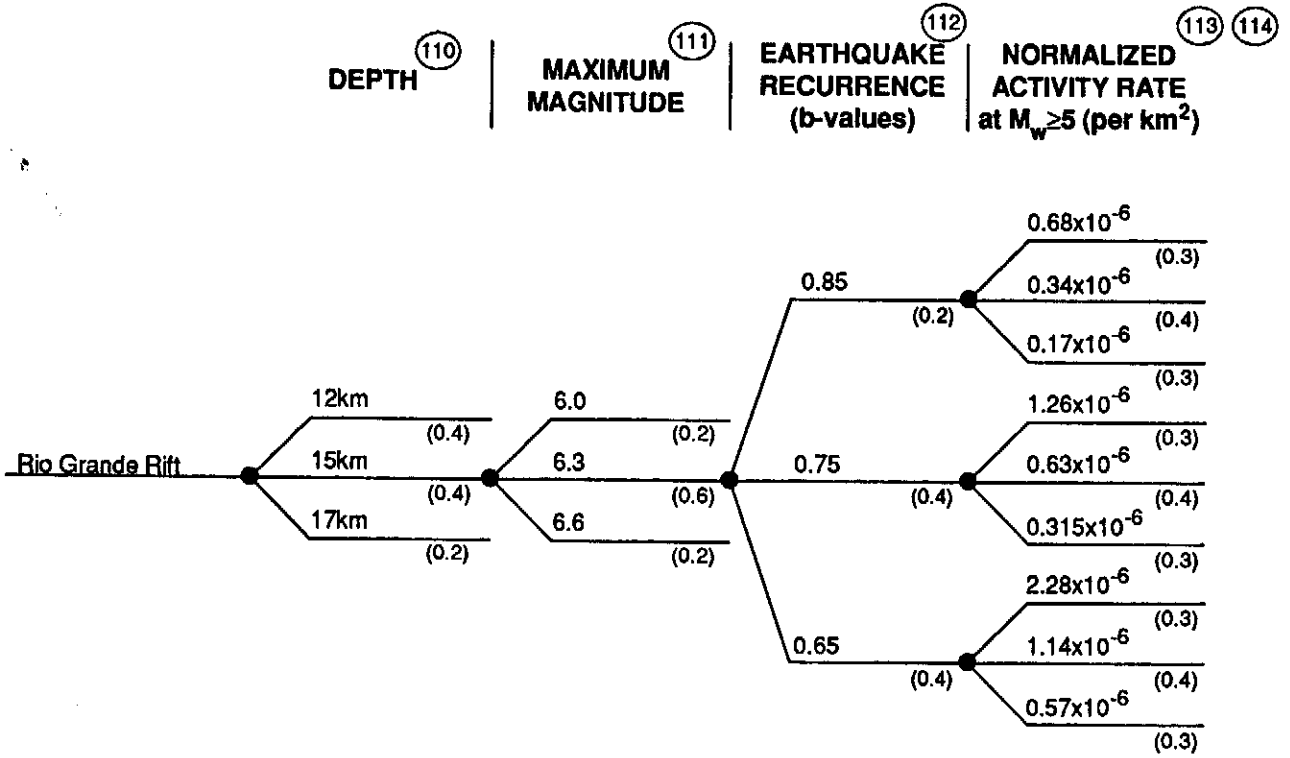


Project No. 91C0509	Los Alamos Seismic Hazards	SCHEMATIC DIAGRAM OF RUPTURE SCENARIOS FOR THE PAJARITO FAULT SYSTEM	Figure 7-25f
WOODWARD-CLYDE FEDERAL SERVICES			



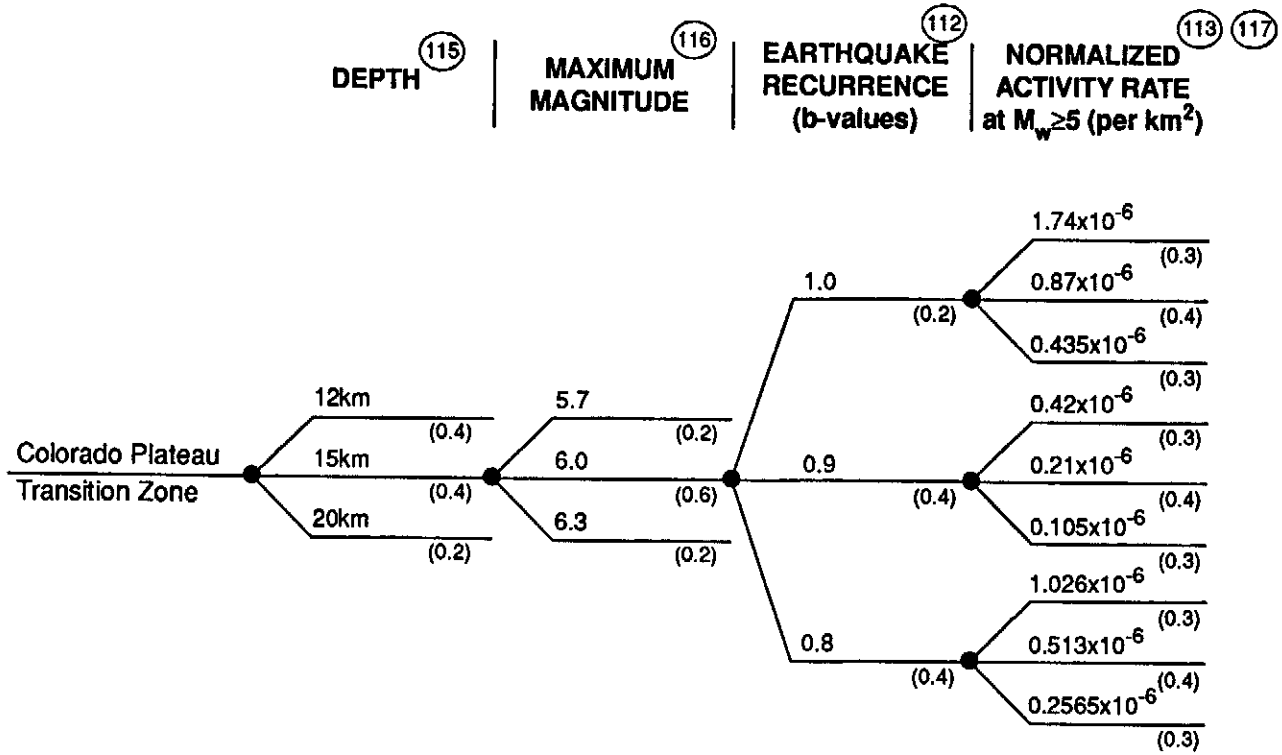
Project No. 91C0509	Los Alamos Seismic Hazards	LOGIC TREE FOR SAWYER CANYON FAULT	Figure 7-2
Woodward-Clyde Federal Services			

91C0509A-2200/052793



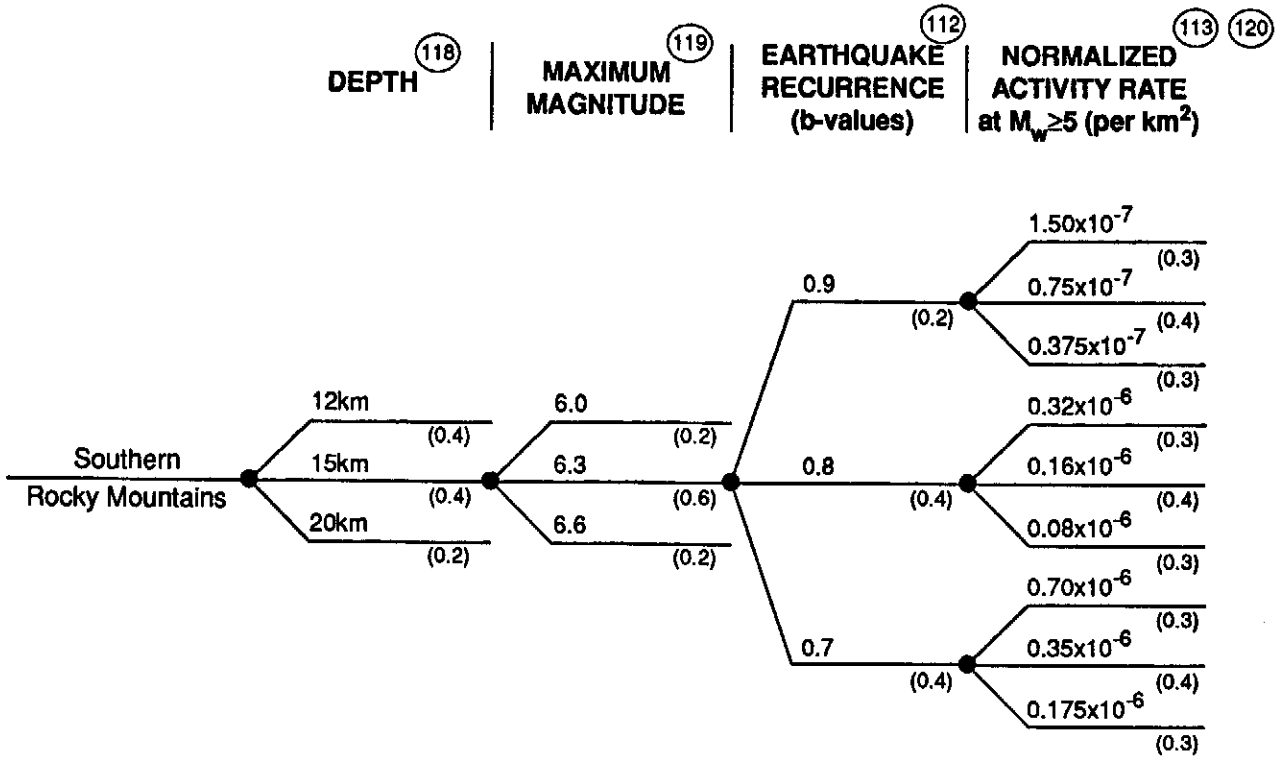
Project No. 91C0509	Los Alamos Seismic Hazards	LOGIC TREE FOR RIO GRANDE RIFT	Figure 7-27
Woodward-Clyde Federal Services			

91C0509A-1300/052993



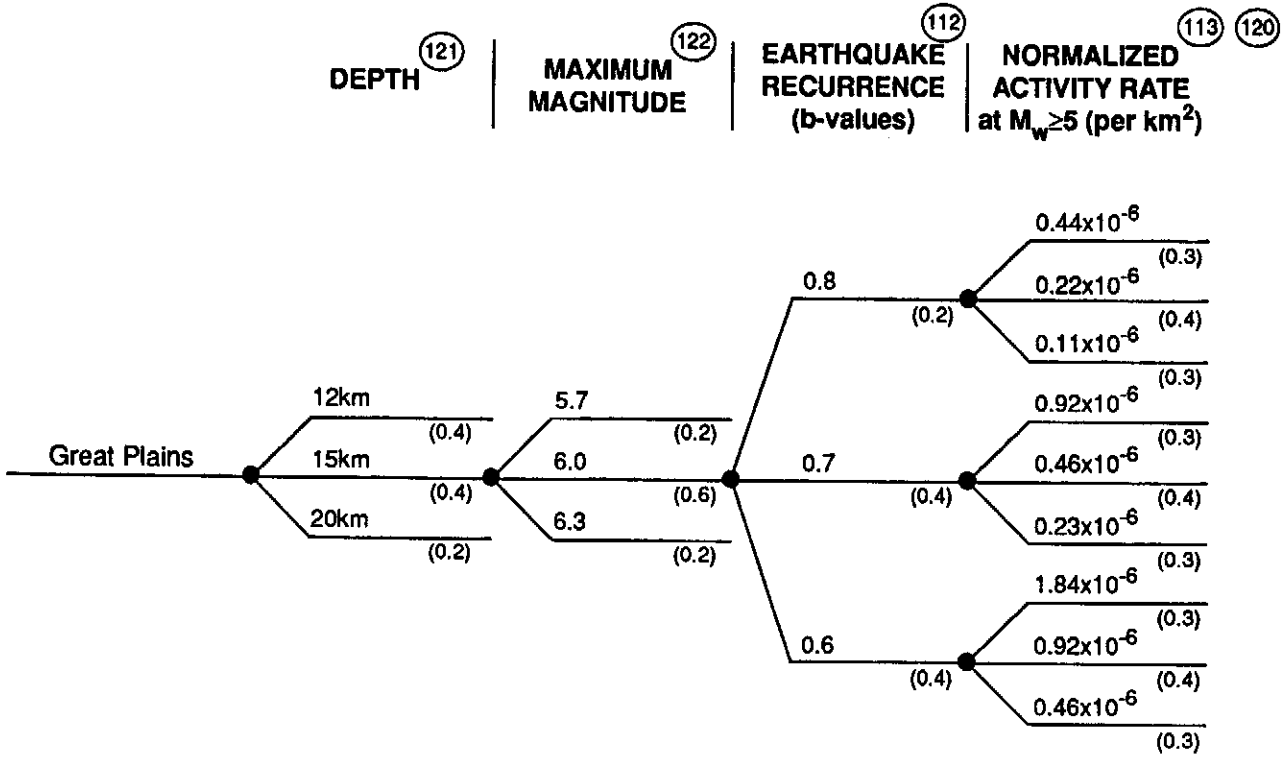
Project No. 91C0509	Los Alamos Seismic Hazards	LOGIC TREE FOR COLORADO PLATEAU TRANSITION ZONE	Figure 7-28
Woodward-Clyde Federal Services			

91C0509A-1300/052993



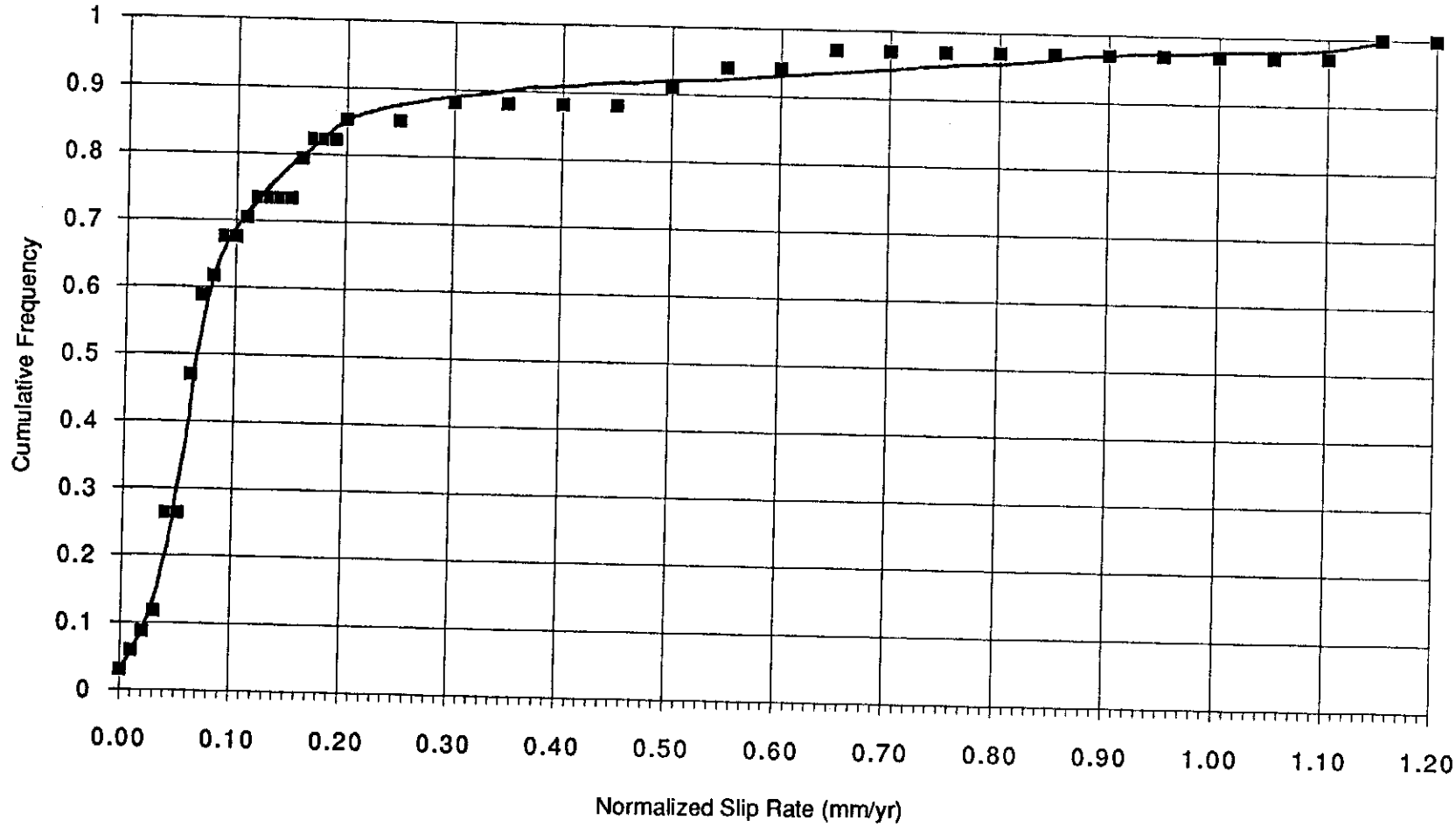
Project No. 91C0509	Los Alamos Seismic Hazards	LOGIC TREE FOR THE SOUTHERN ROCKY MOUNTAINS	Figure 7-29
Woodward-Clyde Federal Services			

91C0509A-1300/052993



Project No. 91C0509	Los Alamos Seismic Hazards	LOGIC TREE FOR THE GREAT PLAINS	Figure 7-30
Woodward-Clyde Federal Services			

91C0509A-1300/052993



Project No. 91C0509	Los Alamos Seismic Hazards	SLIP RATES FOR FAULTS IN THE RIO GRANDE RIFT	Figure 7-26
Woodward-Clyde Federal Services			

8.0
DETERMINISTIC GROUND MOTION ESTIMATES

In this section, deterministic ground motions for the maximum earthquake considered most significant to LANL were estimated by both empirical and stochastic approaches. Because of its proximity and the size of its maximum event (M_w 7), the Pajarito fault will produce the greatest ground shaking at LANL sites. The empirical approach consists of the use of attenuation relationships based on recorded strong motion data for both peak ground accelerations and response spectral accelerations. This is the traditional approach of estimating ground motions. Both peak accelerations and acceleration response spectra were developed for LANL sites using these empirical relationships. The stochastic ground motion modeling approach used in this study is based on the Band-Limited-White-Noise (BLWN) source model coupled with random vibration theory (RVT). This methodology, also called the stochastic approach, is appropriate for engineering characterizations of ground motions because it captures the general features of strong ground motion with a minimum of free parameters. In applications to strong ground motion, the methodology is especially effective in the frequency range of 0.25 to 35 Hz.

In addition, site-specific attenuation relationships were developed using the BLWN-RVT methodology for each of the technical areas. These relationships, which incorporate source and path effects appropriate for the LANL region, and site effects appropriate for the Technical Areas were used in the probabilistic seismic hazard analysis (Section 9). They are discussed in Section 8.2.5. Also included in this section is a review of site effects at the Nevada Test Site, an evaluation of topographic effects at the LANL, and an assessment of vertical ground motions.

8.1 EMPIRICAL APPROACH

The empirical approach to the characterization of potential ground motions uses attenuation relationships developed from strong motion records from past earthquakes. Ground motions typically are characterized by peak accelerations, peak velocities, peak displacements, response spectra, and/or durations. The strong motion data typically are analyzed statistically in a regression analysis to develop relationships between the ground motion value, distance

from the earthquake to the recording station, and magnitude of the earthquake. Other parameters used in these relationships often include the style of faulting and the soil conditions at the recording site.

Given maximum magnitude and source-to-site distance for a seismic source, published attenuation relationships can be used to define the median, and $\pm$ one standard deviation (16th and 84th percentile) ground motions for a site. The attenuation relationships used in this study were selected on the basis of the appropriateness of the site conditions and tectonic environment for which they were developed. The relationships selected generally represent recent efforts in modeling strong ground motion on the basis of empirical data, although many of the relationships employ theoretical arguments to constrain some of the model parameters.

The following describes the application of empirical ground motion attenuation relationships to the characterization of ground shaking expected at the LANL from the Pajarito fault. Peak accelerations and response spectral accelerations were estimated using multiple attenuation relationships. These relationships are described in detail in Appendix L.

8.1.1 Selection of Attenuation Relationships

To determine what site classification was appropriate for each Technical Area, the shear-wave profiles developed in Section 6.3 were compared with two generic shear-wave velocity profiles appropriate for a deep soil site in western North America (WNA) and a deep soil site in eastern North America (ENA) and a generic California rock profile (W. Silva, PE&A, written communication, 1994) (Figure 8-1). It is obvious that the LANL velocity profiles are most similar to the deep soil profiles.

Thus assuming a deep soil site classification for the LANL sites, appropriate attenuation relationships were selected to evaluate the peak acceleration and response spectral values. The relationships by Joyner and Boore (1988), Campbell and Bozorgnia (1994) for peak acceleration and Campbell (1989) for spectral ordinates, and Sadigh et al. (1987; described in Joyner and Boore, 1988) were selected. Although these relationships are based principally upon strong motion data from California strike-slip faulting earthquakes, studies suggest that they adequately characterize ground motion attenuation for normal faulting earthquakes and

for other areas within the western U.S. For example, Youngs et al. (1987) determined that the ground motion data from Basin and Range normal faulting earthquakes were adequately predicted by California-based attenuation relationships. Westaway and Smith (1989) compared a large worldwide data set of normal faulting ground motions with empirical attenuation relationships developed primarily from data consisting of compressional strike-slip strong motion records and found that they produce equivalent levels of ground motion. Thus, these empirical relationships were judged to be the most applicable for use in this study. Each of these relationships is described in Appendix L.

8.1.2 Peak Accelerations and Acceleration Response Spectra

Peak horizontal accelerations were estimated for each site for a M_w 7 earthquake occurring on the Pajarito fault. An examination of Table 8-1 shows that the average values lie in a narrow range between 0.47 to 0.53 g depending on the source-to-site distance. The individual peak accelerations also show a narrow range with the Joyner and Boore (1988) values being the highest.

Figures 8-2 through 8-9 show the 5% damped median empirical acceleration response spectra for the Pajarito fault earthquake for all eight sites. The spectra are similar in shape with the exception of the Joyner and Boore (1988) spectra, which have a higher peak amplitude and appear to be shifted to slightly longer periods. The data base used in their relationship contains both soil and rock recordings which may account for these differences.

8.2 STOCHASTIC APPROACH

In the near-field region of large earthquakes, the effects of a finite source including rupture propagation, directivity, and source-site geometry can be quite significant and thus should be incorporated into strong ground motion predictions. In this study, we have utilized an approach which combines the modeling of a finite source rupture with the BLWN-RVT methodology. In addition, because of the presence of low-velocity, nonwelded Bandelier Tuff at several of the technical areas, an equivalent-linear approach to estimate nonlinear soil response also was employed to estimate the site-specific ground motions. In this study, ground motions generated by a M_w 7 on the Pajarito fault have been estimated using the stochastic approach.

8.2.1 Methodology

The following is a detailed description of the Band-Limited-White-Noise ground motion methodology employed in this study. Both point source and finite fault versions of the methodology have been developed and are used in this study.

8.2.1.1 Band-Limited-White-Noise Point Source Model

The BLWN ground motion model first developed by Hanks and McGuire (1981) assumes a point source with energy distributed randomly over the duration of the source. The model has proven remarkably effective in modeling a wide range of ground motion observations. Time-domain measures such as peak accelerations and peak velocities, Wood-Anderson magnitudes, and short-period P- and S-wave amplitudes, as well as frequency-domain measures such as relative velocity response spectra and Fourier amplitude spectra, have been predicted with reasonable accuracy using the BLWN ground motion model (Hanks and McGuire, 1981; Boore, 1983, 1986; Boore and Atkinson, 1987; Silva and Lee, 1987; Toro and McGuire, 1987; Wong et al., 1991; Silva et al., 1991). The ground motion model employed here uses an ω^{-2} Brune source model (Brune, 1970, 1971) with a single corner frequency and a constant-stress parameter (Boore, 1983; Atkinson, 1984).

The acceleration spectral density a(f), where f is frequency, is given by (Figure 8-10):

$$a(f) = C \frac{f^2}{1+(f/f_c)^2} \frac{M_0}{R} P(f)\, A(f)\, e^{-\frac{\pi f R}{\beta_0 Q(f)}} \qquad (8\text{-}1)$$

where:

M_o = seismic moment
R = distance to the equivalent point source
β_o = shear-wave velocity at the source
$Q(f)$ = $Q_0 f^{\eta}$, frequency dependent quality factor model where Q_0 and η are model parameters

$A(f)$ = near-surface amplification factors
$P(f)$ = high-frequency truncation filter
f_c = source corner frequency and
C = $(1/\rho_o\beta_o^3)$ x (2) x (0.55) x $(1/\sqrt{2})$ x π.

C is a constant which contains source region density ρ_o and shear-wave velocity terms and accounts for the free-surface effect (factor of 2), the S-wave source radiation pattern averaged over a sphere (0.55) (Boore and Boatwright, 1984), and the partition of energy into two horizontal components $(1/\sqrt{2})$.

Source scaling is provided by specifying two independent parameters, M_o and the high-frequency stress parameter ($\Delta\sigma$). M_o is related to M_w through the relation

$$\log M_0 = 1.5\ M_w + 16.1 \qquad \text{(Hanks and Kanamori, 1979) (8-2)}$$

The stress parameter relates the corner frequency f_c to M_0 through the relation

$$f_c = \beta_o\ (\Delta\sigma/8.44\ M_o)^{1/3} \qquad \text{(Brune, 1970; 1971) (8-3)}$$

The spectral shape of the single-corner-frequency ω^{-2} source model is then described by the two free parameters M_o and $\Delta\sigma$. The corner frequency increases with the shear-wave velocity and with increasing stress, both of which are region dependent.

8.2.1.2 Random Vibration Theory

In order to compute peak time-domain values, i.e., peak acceleration, peak particle velocity, and peak oscillator response, RVT is used to relate rms calculations to peak value estimates (Boore, 1983; Boore and Joyner, 1984). The procedure, in general, involves computing the rms value by integrating the power spectrum from zero frequency to the Nyquist frequency and applying Parseval's relation. Extreme value theory is then used to estimate the expected ratio of the peak value to the rms value of a specified duration of the BLWN time history. The duration is generally taken as the inverse of the corner frequency (Boore, 1983).

8.2.1.3 Stress Drop

For earthquakes which have a source spectrum consistent with a single-corner-frequency-ω^{-2} model, the stress parameter is the stress drop of the earthquake. In this case, the stress drop may be computed by determining M_o and f_c and inverting Equation (8-3) and is generally referred to as the Brune stress drop. A convenient way of assessing the appropriateness of the BLWN source model used here is to compare stress drops using Equation (8-3), with the root-mean-square (rms) stress drops, both computed from data recorded in the region of interest (Stark et al., 1992).

The rms stress drop was introduced by Hanks (1979) and is defined as the stress drop required in the single-corner-frequency ω^{-2} Brune model to predict observed rms accelerations. If both the rms stress drops and the Brune stress drops are equivalent, then the observed source spectra are consistent with Equation (8-1).

8.2.1.4 Near-Surface Crustal Amplification and Damping

In a half-space model, the near-surface amplification factors, A(f), account for the increase in amplitude as the seismic energy travels through lower velocity crustal materials near the surface (Figure 8-10). These factors depend on average crustal and near-surface shear-wave velocity and density. In this study, amplification by near-surface velocity gradients is accounted for in the detailed velocity models.

The P(f) filter models the observation that acceleration spectral density appears to fall off rapidly beyond some region-dependent maximum frequency. This observed phenomenon truncates the high frequency portion of the spectrum and is responsible for the band-limited nature of the stochastic model. This spectral fall-off has been attributed to near-site attenuation (Hanks, 1982; Anderson and Hough, 1984) or to source processes (Papageorgiou and Aki, 1983) or perhaps to both effects. Hanks (1982) termed the phrase f_{max} to describe this site-dependent corner frequency. In the Anderson and Hough (1984) attenuation model, which is adopted in this study, the form of the P(f) filter is taken as

$$P(f) = e^{-\pi\kappa(r)f} \qquad (8\text{-}4)$$

$\kappa(r)$ is a site- and distance-dependent parameter that represents the effect of intrinsic attenuation on the seismic waves as they propagate through the crust from source to receiver (Figure 8-10). κ depends on epicentral distance (r) and on both the shear-wave velocity (v_s) and quality factor (Q_s) averaged over a depth of H beneath the receiver or site. At zero epicentral distance, κ is given by

$$\kappa(0) = \frac{H}{\overline{v_s}\,\overline{Q_s}} \tag{8-5}$$

The value of $\kappa(0)$ (herein referred to as kappa) is attributed to attenuation in the very shallow crust directly beneath the site (Hough and Anderson, 1988) (Figure 8-10). Silva and Darragh (1994) suggested that the predominant kappa effects extend from the surface down to several hundred meters and possibly as deep as 1 to 2 km. The intrinsic attenuation along this part of the path is thought to be frequency-independent, but site-dependent (Hough et al., 1988). Kappa has been determined for several rock and soil sites representative of western North America (Anderson and Hough, 1984; Anderson, 1986). For an average western North American rock site, a value between 0.02 and 0.06 sec is appropriate (Boore, 1986; Silva and Darragh, 1990).

The Fourier amplitude spectrum, a(f), models direct shear waves in a homogeneous half-space (with effects of a velocity gradient treated separately through the A(f) filter). For vertically inhomogeneous layered structures, the plane-wave propagators of Silva (1976) are used to propagate S_H motion through the layered structure.

8.2.1.5 Path Attenuation

The anelastic path attenuation from the source to just below the site is modeled with the frequency-dependent quality factor Q(f) (Figure 6-6). Geometric attenuation is taken as 1/R or $1/\sqrt{R}$ (for distances greater than 100 km).

8.2.1.6 Finite Source Model

Because LANL is located in the near-field of the Pajarito fault, possibly the most significant seismic source to the laboratory, source finiteness and rupture process must be incorporated into the ground motion estimates. A methodology that combines aspects of finite earthquake source modeling techniques (Hartzell, 1978; Irikura, 1983) with the BLWN-RVT ground motion model has been developed to produce response spectra as well as time histories appropriate for engineering design (Silva et al., 1990). This methodology is used in this study (Figure 8-10).

The approach is very similar to the empirical Green's functions methodology introduced by Hartzell (1978) and Irikura (1983). In this case, however, the stochastic point source is substituted for the empirical Green's function. Peak accelerations, peak velocities, and response spectra (when time histories are not produced) are estimated using RVT. Use of the stochastic point source as a Green's function is motivated by its demonstrated success in modeling ground motions in general and particularly strong ground motions (Boore, 1983, 1986; Silva and Stark, 1992) and the desire to have a model that is truly site- and region-specific. The model can accommodate a region-specific Q(f), Green's function sources of arbitrary moment or stress drop, and site-specific kappa values. The necessity of regional and site-specific recordings or the modification of possibly inappropriate empirical Green's functions is eliminated.

For the finite source characterization, a rectangular fault is discretized into NS subfaults where NS is the number of subfaults of moment M_o^s. The empirical relationship

$$\log A = -3.49 + 0.91\ M \text{ (Wells and Coppersmith, 1994)} \qquad (8\text{-}6)$$

where A is the rupture area in km^2 is used to assign areas to both the target earthquake (if its rupture surface is not fixed which was not the case in this study) as well as to the subfaults. Based on a validation of the model, the sub-event magnitude M^s is generally taken in the range of M_w 5.0 to 6.5 depending upon the size of the target event (Silva et al., 1990). The value of NS is determined as the ratio of the target event area to the subfault area. To constrain the proper seismic moment, the total number of events summed (N) is given by the

ratio of the target event moment to the sub-event moment. The sub-event rise time is determined by the equation

$$\log \tau_s = 0.33 \log M_o^s - 8.62 \qquad (8\text{-}7)$$

which results from a fit to the M_o - rise time data given in Heaton (1990). Slip on each subfault continues for a time τ_s multiplied by N/NS which is the modeled or target event rise time. Heterogeneity of the earthquake source process is modeled by randomizing the location of the sub-events within each subfault (Hartzell, 1978) as well as the sub-event rise time. The stress drop of the stochastic point-source Green's function is taken as

$$\Delta\sigma = \frac{7}{16}\left(\frac{M_e}{R_e^3}\right) \qquad (8\text{-}8)$$

where M_e is the seismic moment and R_e is the equivalent circular radius of the rectangular sub-event.

Different values of slip are assigned to each subfault as relative weights so that asperities or non-uniform slip can be incorporated into the methodology. The rupture velocity is taken as depth independent at a value of 0.8 times the shear-wave velocity generally at the half-depth of the slip surface. The rupture velocity is randomized within the range of $\pm$ 20%. The radiation pattern is computed for each subfault, a random component added, and the rms of the radiation pattern is applied to the motions computed at the site.

The ground motion time history at the receiver is computed by summing the contributions from each subfault associated with the closest Green's function, transforming to the frequency domain, and convolving with the Green's function spectrum (Equation 8-1). The locations of the Green's functions are generally taken at the center of each subfault for small subfaults or at a maximum separation of about 5 to 10 km for large subfaults. As a final step, the individual contributions associated with each Green's function are summed in the frequency domain multiplied by the rms radiation pattern, and the resultant power spectrum at the site is computed. The appropriate duration used in the RVT computations for peak acceleration

and oscillator response is computed by transforming the summed Fourier spectrum into the time domain and computing the 5 to 75%s Arias intensity (Ou and Herrmann, 1990).

As with the point-source model, crustal response effects are accommodated through the amplification factor (A[f]) or by using vertically propagating shear waves through a vertically heterogenous crustal structure. Propagation path damping, through the Q(f) model, is incorporated from each fault element to the site. Near-surface crustal damping is incorporated through the kappa operator (Equation 8-1). To model crustal propagation path effects, the method of Ou and Herrmann (1990) can be applied from each subfault to the site.

For fixed fault size, mechanism, and moment, the specific source parameters for the finite fault are slip distribution and location of nucleation point. Variability in these parameters may be thought of as replacing the variability in stress drop associated with the point source model. The propagation path and site parameters remain identical for both source models.

8.2.1.7 Equivalent-Linear Approach for Soil Response

It is well known from laboratory testing that soils exhibit pronounced nonlinear behavior under shear loading conditions. Shear modulus decreases with increasing strain with an accompanying increase in material damping (Seed and Idriss, 1970). If this observation is applicable to *in situ* soil properties subject to earthquake loading, then site-response calculations must accommodate these strain dependencies as material nonlinearities.

In general, strain dependence of moduli and damping would result in a nonlinear wave equation with the full finite-strain terms. In this case, superposition is invalid, the wave equation does not separate into P, SV, and SH fields, and Fourier analysis cannot be applied. The approach generally adopted is to assume infinitesimal displacements, utilize a linear wave equation, and confine the nonlinearity to the constitutive relation.

If a nonlinear constitutive relation is used, then velocities and damping become strain dependent. This can result in a wavefield and site response that depart significantly from linear one-dimensional theory. For high levels of ground motion, strain-dependent velocities would generally result in longer characteristic site periods. Strain-dependent damping would

generally reduce overall response at high strain levels. Depending upon site structure and input motion, these effects could be very large.

Departures of soil response from a linear constitutive relation may be treated in an approximate manner through the use of the equivalent linear approach introduced by Seed and Idriss (1970). Basically, the approach is to approximate a second-order nonlinear equation, over a limited range of its variables, by a linear equation. Formally this is done in such a way that an average of the difference between the two systems is minimized. This is done in an ad hoc manner for ground response modeling by defining an effective strain which is assumed to exist for the duration of the excitation. This value is usually taken as 65 percent of the peak time-domain strain calculated at the midpoint of each layer, using a linear analysis. Moduli and damping curves are then used to define new parameters for each layer. The linear response calculation is repeated, new effective strains evaluated, and iterations performed until the changes in parameters are below some tolerance level. Generally, a few iterations are sufficient to achieve a strain-compatible linear solution. This stepwise analysis procedure was formalized into a one-dimensional, vertically propagating shear-wave computer program called SHAKE (Schnabel et al., 1972). Subsequently, this program has become the most widely used analysis package for one-dimensional site response calculations. While the assumptions of vertically propagating shear-waves and equivalent-linear soil response certainly represent approximations to actual conditions, their combination has achieved demonstrated success in modeling observations of site effects (Schnabel et al., 1972; Silva et al., 1987).

The computational scheme incorporated in the BLWN-RVT code to estimate the site response uses the BLWN model to generate the power spectral density and spectral acceleration of the rock or input motion. This motion or power spectrum is then propagated through the one-dimensional soil profile using the plane-wave propagators of Silva (1976). The equivalent-linear formulation is employed in order to estimate possible material nonlinearities. RVT is used to predict peak time domain values of shear strain based upon the shear-strain power spectrum. In this sense, the procedure is analogous to the program SHAKE except that peak shear strains in SHAKE are measured in the time domain. The purely frequency-domain approach obviates a time-domain control motion and, perhaps just as significant, eliminates the need for a suite of analyses based on different input motions. This arises because each time domain analysis may be viewed as a simulation of a random process. Therefore, several

simulations of the random process must be sampled to have a statistically stable estimate of site response. The simulations are usually performed by employing different control motions with approximately the same level of peak acceleration.

In the case of the frequency-domain approach, the estimates of peak shear strain as well as oscillator response are fundamentally probabilistic in nature as a result of the RVT. The procedure of generating the BLWN power spectrum, computing the equivalent-linear layered-soil response, and estimating peak time domain values has been validated by comparison with SHAKE (Toro et al., 1988).

8.2.1.8 Model Validation and Uncertainties

An important aspect of any numerical modeling approach is a proper statistical estimate of uncertainty. A quantitative assessment of the modeling uncertainty (Abrahamson et al., 1990) associated with both the BLWN-RVT point-source and finite fault numerical predictions has been computed based on analyses of the 1987 Whittier Narrows and 1989 Loma Prieta, California earthquakes (Wong et al., 1992). This modeling uncertainty is incorporated into the stochastic ground motion estimates. For the Loma Prieta earthquake, strong ground motions recorded at ten rock and two soil sites for rupture distance of 1 to 55 km were modeled. For the Whittier Narrows earthquake, 12 sites were modeled, nine soil and three rock.

To provide a measure of the uncertainties in the ground-motion predictions, a simple goodness-of-fit was performed at each spectral period. The difference of the logarithms of the observed average 5% damped acceleration response spectrum and the predicted response spectrum was calculated at each period, squared, and summed over the total number of sites for both earthquakes (24 sites). Dividing this sum by the number of sites (assuming zero bias) results in an estimate of the model variance (Abrahamson et al., 1990). The results of this validation are detailed in Wong et al. (1992).

For both the finite fault and point source estimates, the uncertainty estimates are similarly low, indicating that both predict the observed motions with comparable accuracy (Silva and Stark, 1992). These results indicate that for magnitudes up to about M 7, the effects of

source finiteness, when averaged over several sites (distance, azimuth, and site conditions) are not particularly significant.

8.2.2 Analysis of Kappa

The subsurface geology beneath a site influence ground motions in two competing ways. A positive velocity gradient (velocity increasing with depth) amplifies motions, while material damping reduces the motions. In the stochastic ground motion model, the near-surface damping is parametized by κ and the amplification is modeled by propagation through a site-specific velocity profile. Because κ is such a critical factor affecting ground motions, we estimated its value by analyzing several earthquakes recorded at LANL.

Based on a search of all well-located events, only seven small earthquakes (including two possible explosions) were well-recorded at three 3-component stations of the LANL Seismograph Network. These events all occurred since 1986, when high-quality digital data was available to analyze. Table 8-2 lists the events, stations, magnitudes and distances used in these analyses. Magnitudes ranged from about coda duration magnitude (M_D) 0.0 to 1.5, and epicentral distances from 2 to 81 km. Two of the events, on 26 October and 27 October 1989 may be local explosions (Leigh House, LANL, personal communication, 1994), but were included because of the small amount of useable data.

Seismographic stations were selected on the basis of similarity of subsurface site conditions to those at LANL (Table 8-2). ATE is located on the northern part of Mesita del Buey, about 2.5 km east of TA-52 on the Pajarito Plateau. PLS and PFM are located on Pajarito Mesa; the former south of TA-52 and the latter about 3 km south-southwest of PLS. The stations were equipped with Mark Products L4-C and L4-3D seismometers with 1-Hz nominal frequency, and low-pass filtered at 30 Hz. The sampling rate was 100 samples/sec. The velocity recordings were corrected for gain and instrument response and differentiated to produce acceleration time histories.

Because these events are so small, their source corner frequencies are very high, making the estimation of kappa difficult. The RVT-based methods used in other studies (i.e., Silva and Darragh, 1994) break down with such small magnitudes. We thus estimated kappa from the slope of linear-log Fourier spectra which were first corrected for attenuation over the path.

Fourier amplitude spectra were calculated from the S-wave portions of the corrected time histories, and the two horizontal components of each recording set were combined by taking a vector sum of the two spectra. The vector-sum spectra were then corrected for the path attenuation by dividing the spectra by:

$$\exp[(\pi fr)/V_s Q(f))]$$

where f is the frequency, r is the hypocentral distance, V_s is the average shear-wave velocity (3.55 km/s), and Q is given by $Q(f)=370f^{0.35}$ (Singh and Herrmann, 1983). Least-square fits were made on the linear-log vector-sum spectra over the usable bandwidths, as estimated by visual examination. Plots of each fit are presented in Figures 8-11 to 8-17 and Table 8-3 lists the kappa values obtained from the slopes of the least-square fits with the associated standard deviations. The log-average kappa values at sites ATE, PFM, and PLS are 0.038, 0.033, and 0.034 sec, respectively, essentially the same at each site (Table 8-3). The overall log-average estimate of kappa is 0.035 sec, a value typical for sites in the western U.S. (Silva and Darragh, 1994).

For the two events that are possible explosions, the S-wave portions of the time histories were not clear, if they existed at all, suggesting that the kappa estimates may be contaminated by P-waves. Table 8-3 lists the median and standard deviations for the data set without these two events. The estimate of kappa without the possible explosions is a not too different 0.038 sec.

8.2.3 Input Parameters

The following describes the source, propagation path, and site parameters used to model a M_w 7 earthquake on the Pajarito fault.

8.2.3.1 Earthquake Sources

For the finite fault modeling of the maximum earthquake on the Pajarito fault, a rupture geometry and slip distribution need to be specified. The finite fault model was assumed to be a plane 49 km long and 16 km wide dipping 60° to a depth of 16 km (near the bottom of seismogenic crust) (Section 7). The estimated maximum surface rupture length of the fault

is 41 km. The subsurface length, which is the more appropriate dimension to use for the potential rupture length, is typically 33% longer than the surface rupture length (Wells and Coppersmith, 1994). As magnitude increases, however, the two dimensions become closer in value. In this study, we have chosen a subsurface rupture length of 49 km, which is consistent with the rupture area for a M_w 7 event based on Equation 8-6, assuming a downdip width of 16 km.

The top of the rupture model was placed at a depth of 2 km consistent with the assumption that negligible moment release occurs in the near-surface (Wong et al., 1992). The resulting rupture area of 784 km^2 is consistent with an approximate M_w 7 based on an empirical relationship for rupture area (Wells and Coppersmith, 1994).

Because there is obviously no *a priori* information on the slip characteristics of future earthquakes on the Pajarito fault, randomized slip distribution models were used in the finite fault modeling. Figure 8-18 shows a sample of such randomized models. The randomized slip models were generated in the spatial domain. The statistical properties of the asperities (regions of higher than average slip) such as area, aspect ratio, location, and number are based on an analysis of 12 published asperity slip distributions. The randomly-generated slip models are constrained to have the same statistical properties as the 12 slip distributions determined from inversions using both strong motion recordings and teleseismic data (Abrahamson et al., 1994).

In order to produce the slip distribution for the Pajarito fault, the slip in each patch is scaled relative to the average total slip across the fault. Fourteen elements were taken along strike with six elements along dip giving a 784 km^2 fault surface; 10 sub-events (equivalent to a M_w 5.0) are required per patch to generate a total M_w of 7.0. A mean rise time of 0.147 sec is assumed for each sub-event. This rise time is allowed to vary randomly with a lognormal distribution with a standard error of 0.8. Slip is initiated across the fault using a randomized rupture velocity with a mean value of 2.84 km/sec. The total rise time is 1.47 sec (10 sub-events per patch times 0.147 sec per sub-event rise time).

Points of rupture initiation were varied in the modeling of the Pajarito fault earthquake. Foci were randomized in a zone in the bottom half of the rupture plane extending 10% in from each end of the fault. Again this was done in the absence of any *a priori* knowledge of

where the actual rupture may initiate along the fault. For hypocenters located toward one end of the fault or the other, directivity becomes a factor (e.g. Wong and Silva, 1993).

8.2.3.2 Propagation Paths

For the propagation path, a half-space model characterized by a shear wave velocity (β_s) of 3.55 km/sec and a density (ρ) of 2.75 g/cm^3 was assumed based on values estimated from the LANL velocity model used in earthquake locations (L. House, LANL, written communication, 1992). Based on an analysis of Lg waves, Singh and Herrmann (1983) determined a crustal coda Q_o of 370 and a η of 0.35 for northern New Mexico to describe the frequency-dependent attenuation Q(f). The effects of anelastic attenuation on ground motions are, however, not expected to be significant for earthquakes on any of the local faults because the LANL sites are at near-field distances.

8.2.3.3 Sites

For each of the Technical Areas, a site-specific geologic and shear-wave velocity profile has been developed in this study (Section 6.3). It was recognized during the review process of this study, however, that these profiles may not be truly representative of the Technical Areas given the observations that the areas at LANL are in some cases quite large, variability in the subsurface stratigraphy across an area may be significant, and such variability may not be captured by a single profile. Although all available borehole and geotechnical data at LANL were collected, compiled, and evaluated (Section 6.2), the data were insufficient to characterize the variability across a Technical Area. Thus, it was decided to develop an approach which would incorporate the variability as well as the uncertainty in the geologic profiles in the ground motion estimates.

To accomplish this, an attempt was made to determine whether the site profiles could be grouped in terms of their site response effects. Acceleration response spectra were generated for each site by propagating the motions from a M_w 5.9 earthquake at a source-to-site distance of 6 km up through each profile using the stochastic point-source approach (Figures 8-19 and 8-20). This earthquake was selected because it approximates the dominant earthquake that will control the probabilistic hazard at LANL for return periods of 2000 years or less (Section 9.5.3). The profile velocities were varied in each run by about 50% for materials whose

shear-wave velocities were less than about 914 m/sec and 25% for higher velocity rock. These bounds were established by examining the velocities of similar materials (R. Nigbor, Agbabian Associates, written communication, 1994). Not unexpectedly because of their similar site profiles, the mesa top spectra (TA-3, 16, 21, 46, and 55) are similar in appearance given small variations in resonant peaks (Figure 8-19). The only "odd" spectrum is for site TA-16. It is low around 1 sec and high near 0.2 sec compared to the other mesa top sites. The low response near 1 sec is due to the absence of the dacite in the profile compared to the other mesa top sites (Figure 6-17) and the higher short-period response is likely due to the densely welded tuff (1,071 km/sec) at a depth of 74 m which is absent at the other sites. Given the uncertainties in the site profiles, the fact that dacite may actually exist beneath the site and the similarity in topographic position, TA-16 was classified as a mesa top site. Similarly, the spectra of the canyon sites (TA-2, 18, and 41) are similar in appearance (Figure 8-20).

The response spectra for the canyon sites are quite distinguishable from the mesa top spectra as illustrated in Figure 8-21. The average mesa top spectrum is lower at peak ground acceleration than the canyon spectrum most likely due to the damping effects of the Bandelier Tuff but higher at long periods due to amplification. The canyon sites also exhibit more pronounced resonant peaks and a valley at about a period of 0.4 sec due to site response.

A review of the shear-wave velocity profiles shows this same division based on the presence or absence of Bandelier Tuff. The canyon sites generally lack the tuff because they are located lower in stratigraphic position. It was then assumed in this study that the variability in the sites in each classification, mesa top versus canyon sites, could be used to capture the variability across any given Technical Area. The geologic and shear-wave velocity profiles were thus separated into these two groups and used directly in the site-specific stochastic ground motion estimates. For example, the ground motions based on the stochastic approach for the canyon site TA-2 were estimated using the TA-2 as well as the TA-18 and 41 profiles. A κ of 0.035 sec, as estimated in this study (Section 8.2.2), was assumed for all sites.

Based on laboratory testing of undisturbed samples from core hole TA-55 (Section 6.2.1.3), modulus reduction and damping curves were assigned to the various soil-like layers beneath each site (Appendix M). Results of the laboratory tests indicated that the sand-like material (pumice and rhyolite) showed generally less nonlinear behavior in modulus reduction and less

damping than the Bandelier Tuff samples. Consequently, two sets of curves were implemented, one set for sands and one for tuffs.

The effects of depth were also apparent in the laboratory testing, particularly for damping (Section 6.2.1.3). As a result, separate damping curves are used for the Bandelier Tuff above the rhyolite (shallow tuffs, higher damping) and below the rhyolite (deeper tuffs, lower damping) (Appendix M). For the sands, a significant difference in damping also was apparent in the laboratory testing. In this case, the pumice sands showed significantly higher levels of damping than the rhyolite sands. To accommodate these differences, separate damping curves were implemented for the pumice and rhyolite sands.

Because samples were obtained from only one hole and multiple samples from the same formation were not obtained, the variability of the curves over the site or within a formation could not assessed. However, variabilities of approximately 40% (at a shear-strain of $2x10^{-2}$%) were estimated by EPRI (1993) to apply on a generic basis to cohesionless materials. As a result, variability across a specific site is expected to be somewhat less and much less within a formation. This degree of uncertainty would represent a very small addition to the variability in ground motions resulting from combining the mesa and valley profiles.

8.2.4 Site-Specific Ground Motion Estimates

Stochastic acceleration response spectra were calculated for all sites based on a M_w 7 earthquake on the Pajarito fault. Selected input parameters were randomly varied to arrive at the parametric uncertainty which was then incorporated into the horizontal ground motion estimates. To achieve statistical stability of one-sigma estimates, 50 runs were made with all the parameters simultaneously randomized using the distributions shown in Table 8-4. To include all the canyon profiles at each canyon site and all the mesa profiles at each mesa site, each set of 50 runs was equally divided between profiles. For the canyon sites, 17 runs used the TA-2 profile, 17 runs used the TA-18 profile, and 16 runs used the TA-41 profile. For the mesa sites, 10 runs each were used for profiles TA-3, TA-16, TA-21, TA-46, and TA-55. Average mesa top and canyon profiles were not used in these analyses because the response of an average profile is not equivalent to the average of the responses of the individual profiles. The uncertainties of these sets of runs contain velocity variations as well as the

uncertainties in the modulus reduction and damping curves along with the specific parameters being varied. The uncertainties were calculated by repeating the same suite of analyses with the average canyon or mesa top profile at each site.

The 5%-damped absolute acceleration response spectra from the 50 runs were assumed to be lognormally distributed, and estimates of the 16th, median and 84th percentiles of the distribution were made, weighing the 50 spectra equally (Figures 8-22 to 8-29). The total uncertainty in the spectral acceleration is a combination of the parametric uncertainty and the modeling uncertainty described in Section 8.2.1.8. The two uncertainties were combined geometrically.

The site-specific median stochastic response spectra for the M_W 7 Pajarito fault earthquake differ significantly from the empirical spectra. The stochastic spectra peak at a period of about 1 sec (Figures 8-22 to 8-29) typical of deep soil sites in contrast to the empirical spectra which peak at about 0.3 sec characteristic of shallower and stiffer soil (Figures 8-2 to 8-9). The stochastic spectra show a characteristic site-specific response with strong multiple resonant peaks. The stochastic spectra for the mesa top sites are anchored at peak horizontal accelerations slightly larger than the empirical spectra (Table 8-5). In contrast, the canyon spectra exhibit considerable high-frequency site amplification significantly exceeding the empirical spectra (Table 8-5). The spectra for the mesa top sites would also significantly exceed their corresponding empirical spectra were it not for the presence of the Bandelier Tuff in the site profiles. The tuff appears to damp high-frequency ground motions similar to deep soils and this is evident in comparing the spectra, for example, between TA-2, a canyon site with TA-3, a mesa top site (Figures 8-22 and 8-23).

Appendix N illustrates the effects of individual and total parametric uncertainties for the twelve earthquakes modeled. The parameters Q(f), κ, rupture initiation, slip, and the site profile were varied. To evaluate whether directivity effects are significant, rupture was initiated at foci near the bottom of the center, northern, and southern ends of the rupture plane. As shown for the various sites, variations in the site profile have the greatest effects on the resulting ground motions out to long periods followed by the variations in slip (Appendix N). The variation in rupture initiation is significant at periods of 0.3 sec and longer. Variations in κ and, as expected, anelastic attenuation, Q(f), have negligible effect on ground motions because of the short source-to-site distances. Directivity does not appear

to have a strong effect on the ground motions. The very slightly higher motions, particularly at periods longer than 1 sec, are generated by a central focus. This result may be simply due to the locations of the sites near the center of the fault.

8.2.5 Site-Specific Attenuation Relationships

To incorporate source, path, and site-specific effects into the probabilistic seismic hazard analysis (Section 9), attenuation relationships were developed for peak acceleration (Figures 8-30 and 8-31) and spectral accelerations at 0.25, 0.5, 1.0, 2.0, 3.33, 5.0, and 10.0 Hz (Appendix O) for the two categories of sites (mesa top and canyon) using the point source version of the BLWN-RVT methodology. For four magnitude values, M_w 5, 6, 7, and 7.5, a range of weighted values for σ, κ, Q_o and point source focal depth (Table 8-6) were varied in a total of 50 runs. The resulting point source estimates were fit to an equation of the functional form

$$\ln y = C_1 + C_2 (M-6) + C_3 (M-6)^2 + C_4 \ln r + C_6 d \qquad (8\text{-}9)$$

for d less than or equal to 100 km and

$$\ln y = C_1 + C_2 (M-6) + C_3 (M-6)^2 + C_4 \ln r_c + C_5 [\ln (r) - \ln(r_c)] + C_6 d \qquad (8\text{-}10)$$

for d greater than 100 km where d is epicentral distance to the point source and

$$r = d + \exp (C_7 + C_8 M) \qquad (8\text{-}11)$$

$$r_c = 100 \text{ km} + \exp (C_7 + C_8 M) \qquad (8\text{-}12)$$

The range of parameter values reflects the estimated uncertainty (Table 8-6). The mean values for Q(f) and κ are described in Sections 8.2.3.2 and 8.2.3.3, respectively. A discussion of the assigned weights is contained in Section 9.2. The mean stress drop is, in our estimation, a conservative 75 bars. Previous studies of stress drops for historical Basin and Range normal faulting earthquakes suggest that 50 bars is a reasonable value to use in stochastic point source estimates of ground motions (Wong et al., 1992; Stark et al., 1992).

The individual profiles developed for each site were used in the attenuation analyses. The resulting predictions of spectral ordinates and peak acceleration for each site were then grouped according to whether the site was a mesa top or canyon site. Attenuation regressions were carried out on the two groups and these are shown graphically in Figures 8-30 and 8-31 and in Appendix O.

A comparison between the stochastic and empirical attenuation relationships is shown in Figures 9-3 through 9-10. The stochastic relationships, in general, show lower motions at peak acceleration and at periods less than 1 sec particularly at distances less than 10 km. This again is due to the damping effects of the low velocity volcanic rock, particularly the Bandelier Tuff for the mesa top sites. Also the presence of the high velocity dacite or basalt in the much lower velocity volcanic rocks may act as a reflector to upgoing seismic waves. At long periods of 1 sec or more, the stochastic relationships, particularly for the mesa top sites, nearly match or exceed the empirical relationships due to amplification.

8.3 REVIEW OF SITE EFFECTS AT THE NEVADA TEST SITE

At the Nevada Test Site (NTS) where the U.S. has conducted underground nuclear testing for several decades, the near-surface geology consists of silicic volcanic rocks including ash flow tuffs similar in many respects to the Bandelier Tuff at LANL. As part of the high-level nuclear waste repository siting program, both surface and downhole seismic monitoring of both nuclear explosions and earthquakes has been performed for several years. Because there appear to be significant site effects on ground motions at LANL due to the Bandelier Tuff, the available information on the NTS monitoring was compiled and evaluated. This evaluation is described in detail in Appendix P.

Unfortunately, based on the review of the available literature and discussions with Dr. Marianne Walck (Sandia National Laboratories, personal communication, 1994), no quantitative assessment of the site effects has been performed to date using the NTS surface/downhole data. Phillips (1991a) does make the following general observations: 1) the amplitude of downhole motions is generally less than the amplitude of the surface motions; 2) the frequency content of a surface/downhole pair is similar, but varies from component to component and from station to station; and 3) the radial and transverse components have larger surface/downhole ratios than the vertical component.

Site effects are apparent in the data, particularly amplification of the downhole to surface motions at one NTS station. At one NTS station, deamplification at high frequencies was observed similar to what is predicted by the stochastic modeling of the LANL site profiles. However, the lack of (1) shear-velocity data for the NTS stratigraphy and (2) modeling of the site response precludes any meaningful comparison of the possible effects of the volcanic geology on ground motions at the NTS with LANL.

8.4 EVALUATION OF TOPOGRAPHIC EFFECTS

Topographic effects are due to a focusing of energy near ridge crests and the interaction of the primary (incident) wavefield with outgoing scattered surface waves (Geli et al., 1988). The resulting total wavefield can show large amplifications at ridge crests, particularly for very steep topography, and is most pronounced for wavelengths which correspond roughly to the width of the structure, around 400 m for the generic Los Alamos mesa (Figure 8-32). Along the slopes and at the bases of elevated geologic structures, the interaction of the primary field with the scattered fields results in complicated patterns of amplification and deamplification. This varying pattern is associated with rapidly varying phase and may be expected to give rise to differential motions which could be of concern to long-period structures.

Due to the dimensions and average shear-wave velocities of the mesas and underlying materials (about 0.65 km/sec), the frequency range where maximum effects are expected is about 1 to 5 Hz (Geli et al., 1988). The purpose of the topographic modeling performed here is to determine whether or not stable features of mesa amplification are likely to exist over this frequency range.

8.4.1 Description of the Numerical Code

The computational algorithm used to model the effects of the two-dimensional structure is an elastic explicit time-domain-finite-difference formulation (Vidale and Helmberger, 1988). The algorithm was developed by Dr. John Vidale (USGS, Menlo Park). The computer code, AMOD, is fourth-order in accuracy of spatial derivatives resulting in minimal grid dispersion. Absorbing boundary conditions are imposed on the sides and bottom of the finite difference grid. In the SH mode implemented here, the top of the grid has free-surface boundary

conditions (reflection coefficient is equal to 1). In the analysis, the source is input as plane SH waves incident at specified angles from either the left or right side of the grid.

The effects of material damping have been implemented in the code in an approximate manner to attenuate high-frequency scattered wavefields. Because of the approximate nature of the damping algorithm, the effective damping is frequency dependent and only modest levels are permissible (1.25% at 3 Hz in this case). In general, for very high levels of ground motions, material damping is expected to increase substantially, especially in the shallow portions of the profiles ($\leq$ 300 m). As a result, the amplifications predicted by the modeling should not be viewed as average values.

8.4.2 Topographic Model

To model the effects of the mesa structures on strong ground motions, three-dimensional effects (along the mesa axes) are assumed to be less important than the effects from the generally steeper cross-sectional relief. For the purpose of modeling, a generic mesa cross-section was developed from topographic maps and is shown in Figure 8-32. This generic mesa is intended to represent an average mesa near the midpoint along its long axis. For more extensive modeling, necessary to quantify amplification effects, a large suite of structures and average velocities should be considered to define median values and their uncertainties. In this study, the generic mesa cross-section was simplified to straight line segments and is shown in Figure 8-33. The finite difference grid is 4.9 km wide and 4.9 km deep with a grid spacing of 6.5 m. Two mesas are modeled to allow for any coupling (scattering) effects between structures which may affect both mesa and canyon sites. Ten site locations are evaluated, representing canyon (1, 2, 7, and 10), mesa (4, 5, 8, and 9), and mesa side (3 and 6) sites. Canyon sites 1 and 10 are located a mesa dimension away from the closest mesa. This location was chosen to show minimum potential mesa effects while site 7 is located between the mesa at one-half mesa dimension. This site should show the maximum effect of the mesas on valley sites. The average shear-wave velocity for the mesas and underlying material is 0.65 km/sec and is based on measured velocity profiles.

8.4.3 Results of Analyses

To assess the effects of the mesa topography, Fourier amplitude spectra (smoothed over 2 Hz) are computed at each site using both the two-dimensional crustal structure and a one-dimensional structure for the same angles of incidence. The one-dimensional structure consists of simply the plane half-space. Taking the ratios of the two-dimension simulations to the one-dimension simulations cancels source and propagation effects thereby isolating the effects of the topographic structures.

For completeness, a suite of incidence angles and shear-wave velocities is considered. In the analyses, incident inclined plane SH waves are considered. Angles of incidence are at 0°, 10°, 20°, and 40° (corresponding to varying source distances and depths) and analyses are performed for the base case average velocity (0.65 km/sec) as well as a 50% variation (V_s x 1.5 = 0.98 km/sec and V_s/1.5 = 0.43 km/sec).

To present an example of time histories, Figure 8-34 shows both 1-D and 2-D displacement seismograms at the 10 site locations for a vertically propagating plane SH wave. For the mesa sites (3, 4, 5, 6, 8, and 9), the 2-D results show a delay relative to the 1D arrivals due to the additional propagation distance (35-70 m; Figure 8-33). There is also a slight decrease in amplitude of the initial dominant motion and an increase thereafter. In general, the effects of the topographic features are not strong for this case and suggest that the mesas do not have a strong or dominant influence on ground motions.

In order to better quantify these results and to include the effects of different incidence angles and shear-wave velocities, Fourier amplitude spectral ratios (2D/1D) were computed for a suite of deterministic analyses. For each incidence angle of 0°, 10°, 20°, and 40°, with the inclined waves incident from the right in Figure 8-33, analyses were performed for each velocity: 0.43, 0.65, and 0.98 km/sec. The results were then averaged (assuming a lognormal distribution) to compute median and one-sigma estimates of the Fourier amplitude ratios. Because a deterministic selection of incidence angles and velocities was used, the computed standard error should not be strictly interpreted as representing the range of 16th to 84th percentiles. It likely encompasses a broader range and should be viewed more as a qualitative estimate of the range of effects for the range of incidence angles and velocities.

A true parametric analyses would also vary the geometry as well as include incident inclined P-SV waves for a complete and thorough study. As previously mentioned, the intent of the current study is to determine whether or not stable features of amplification do exist which warrant further study, possibly resulting in accommodation into design motions.

The median and ± one-sigma estimates based on the deterministic analyses are shown for sites 1-10 in Figures 8-35 through 8-44 for frequencies from about 1 to 5 Hz. For most sites, a broad resonance is shown between 4 to 5 Hz. This is likely due to surface waves generated by the mesa topography. The resonance is strongest at the sites located on the mesa sides (sites 3 and 6, Figures 8-37 and 8-40) and has a peak of about 1.2, which is associated with a large variability. The large variability suggests a high degree of sensitivity to velocity and/or incidence angle and indicates that the variability of ground motions should be high at sites located on slopes. Interestingly, these sites also show a slight deamplification at lower frequencies indicating the effects of wave cancellation.

At the mesa sites (4, 5, 8, and 9; Figures 8-38, 8-39, 8-42, and 8-43), the average amplification between 4 to 5 Hz is approximately 15 to 20% for sites 5 and 9 and approximately 10% for sites 4 and 8. The difference is likely due to inclusion of waves incident from only the right in the analyses. Additional analyses for waves incident from the left would probably average the median amplifications and increase the variability. As with the sites on the mesa slopes, the variability is large near the resonance peak indicating a strong sensitivity to velocity and/or incidence angle. Unlike the sites on the slopes, however, the mesa top sites show a slight lower frequency amplification with a maximum of about 10% near 1 Hz. These results suggest that a more complete analysis may result in stable, perhaps broad-band amplification of ground motions at mesa sites.

At the canyon sites (1, 2, 7 and 10; Figures 8-35, 8-36, 8-41, and 8-44), similar patterns exist. There is an asymmetry in response between sites 1 and 10, again possibly due to the inclusion of incident waves from the right only. There is on average no net amplification for these sites, located at a distance corresponding to one mesa base dimension away. For site 2, located at the base of the mesa, the motions are generally deamplified with a maximum ratio slightly greater than one near 4 Hz. The remaining canyon site (7, Figure 8-41) is located symmetrically between the mesas at a distance of ½ base dimension and shows a slight broad-band amplification of 5 to 10%.

In general, the results of the 2-D topographic modeling suggest that stable features of topographic amplification are likely to occur at the Los Alamos National Laboratory. For mesa top sites, amplifications of 10 to 20% over the frequency range studied (1 to 5 Hz) are suggested. At canyon sites, the amplifications depend on distance from the mesas, being with either minimal amplification or deamplification at distant (≥ one base dimension) and adjacent sites and 5 to 10% for sites in between. These results are for a material damping of 1.25%. At high levels of motion, the damping will increase significantly which should result in a reduction of amplification.

To better quantify these topographic effects, further analytical as well as empirical studies are recommended. Analyses should consider ranges in mesa structure, velocities, damping values, and additional wave types (P-SV). Suggested empirical studies would involve deployment of recorders at mesa and valley sites at locations guided by results of the analytical studies.

8.5 ASSESSMENT OF VERTICAL MOTIONS

This section describes the evaluation of vertical ground motions through site response modeling and our recommendations for seismic design. Typically, the vertical component is seldom considered in the design of structures. When it is used in an analysis, the spectral ordinates of the vertical component are generally considered to be 2/3 of the spectral ordinates of the horizontal component. For some critical structures, and when the structure is within a short distance of the source, the spectrum of the vertical component is selected to be equal to or slightly larger than the horizontal spectrum for frequencies greater than about 2 Hz. In many instances, a set of actual recorded motions (two horizontal and one vertical component), obtained at close distances to the source, are used. Because of the scarcity of such data, however, it is not possible to utilize this procedure at many locations outside of California.

To model vertical motions, incident inclined compression (P) waves from the stochastic ground motion model (Section 8.2.1) are assumed incident at the top of the source layer and the P-SV (vertically polarized shear wave) propagators of Silva (1976) are used to model the crust and soil response to include P-SV wavefields. The angle of incidence at the top of the layer containing the source is computed by two-point ray tracing through the crust and soil

column assuming incident P-waves. To model soil response, the near-surface geologic profile is placed on top of the crustal structure, the incident P-SV wavefield is propagated to the surface, and the vertical (or radial) motions are computed.

At close distances, for typical crustal structures without strong near-surface P-wave velocity gradients, the predominant motion on the vertical component is principally due to the SV wavefield. In a soil column (particularly deep profiles), however, because there is usually a large P-wave velocity gradient (larger for P-waves than for S-waves as Poisson's ratio generally decreases with depth), the vertical component is usually controlled by the compression wavefield. The separation of rock and soil sites in terms of predominant wavefields in the vertical component depends on specific velocity profiles (soil as well as crustal), source depth and mechanism through their effect on incidence angles, as well as the depth of the water table.

The water table may be a significant factor at soil and perhaps soft rock sites because a significant increase in the P-wave velocity to values near the fluid phase (about 1524 m/sec) is generally encountered. Typically at soil and soft rock sites, beginning at the surface, a velocity gradient exists for both compression and shear waves with a Poisson's ratio in the range of about 0.3 to 0.4. Poisson's ratio may decrease with depth slightly until the water table is reached where it jumps to values approaching 0.5. At this point, the fluid phase controls the compression-wave velocity until a depth is reached where the compression-wave velocity of the skeleton material exceeds the fluid phase velocity. From this point on, the Poisson's ratio generally shows an overall slow decrease with depth.

On a generic basis, the most straightforward approach to model the vertical motions is to assume that the water table is at the surface. The effects of placing the water table at some depth below the surface will depend on the exact depth, the P-wave damping above the water table, and, to some degree, on source distance and depth, and may result in increased motions at high frequencies. Since these sensitivities are not yet resolved, the current analyses will assume the water table is at the surface and concentrate on general trends in the computed vertical-to-horizonal response spectral ratios. Conservative recommendations will then be given as a guide in assessing vertical motions. Site-specific analyses should be conducted with ranges of P- and S-wave velocities and water table depths based on measured values.

Commonly, equivalent-linear site response analyses for vertical motions have used strain iterated shear moduli from a horizontal motion analysis to adjust the P-wave velocities assuming either a strain independent Poisson's ratio or bulk modulus. Some fraction (generally 100% to 30%) of the strain iterated S-wave damping is used to model the P-wave damping and a linear analysis is performed for vertically propagating compression waves using the horizontal control motions scaled by 2/3 (I.M. Idriss, University of California at Davis, personal communication, 1993).

The equivalent-linear approach implicitly assumes some coupling between horizontal and vertical motions. This is necessitated by the lack of well determined degradation and damping curves for the constrained modulus. Ideally, the strain dependency of the constrained modulus should be determined independently of the shear modulus. Also, the approach assumes vertically-propagating P-waves and not inclined P-SV waves. Additionally, the use of some fraction of the horizontal control motion is an approximation and does not reflect the generally greater high-frequency content of vertical component motions at rock sites due to lower kappa values (Anderson, 1991).

Alternatively, fully nonlinear analyses can be made using two- or three-component control motions (Costantino, 1967; 1969; Li et al., 1992). These nonlinear analyses require two- or three-dimensional soil models which describe plastic flow and yielding and the accompanying volume changes as well as coupling between vertical and horizontal motions through Poisson's effect. While these analyses are important to examine expected dependencies of computed motions on material properties and may have applications in studies of soil compaction, deformation, slope stability, and component coupling, the models are very sophisticated and require specification of many parameters, at least some of which are poorly understood.

In the current implementation of the equivalent-linear approach to estimate vertical to horizontal (V/H) response spectral ratios, the horizontal component analyses are performed for vertically propagating shear waves using the RVT methodology. To compute the vertical motions, a linear analysis is performed for incident inclined P-SV waves using low-strain, P- and S-wave velocities derived from the profiles developed in Section 6. The P-wave damping is assumed to be equal to the low strain S-wave damping (Johnson and Silva, 1981). The horizontal component and vertical component analyses are assumed to be independent.

These approximations, linear analysis for the vertical component and uncoupled vertical and horizontal components, have been validated by comparing results of fully nonlinear analyses at reference sites Gilroy 2 and Treasure Island to recorded vertical and horizontal motions from the 1989 Loma Prieta earthquake (EPRI, 1993).

To compute the horizontal and vertical ground motions, the profiles derived in Section 6 were used. A stress drop of 75 bars was used along with a source depth of 8 km. A kappa value of ½ the shear wave kappa, 0.017 sec, is used for the vertical motions. The Q(f) model used was described in Section 8.2.3.2 and assumes S-wave propagation. This is not an important issue since motions are computed out to 50 km only and the crustal Q(f) models have very little effect at these distances in the frequency range of interest, 1-34 Hz.

Based on the computed motions, V/H response spectral ratios were computed for a distance range of 1 to 50 km. Because these ratios are a function of strain level (due to the soil-like layers in the profiles), ratios were also computed for two magnitudes, M_w 6 and 7. Shown in Figures 8-45 through 8-48 are the V/H ratios for M_w 6 and 7 for the mesa and canyon sites, respectively. Figures 8-49 and 8-50 illustrate the ratios for both magnitudes with the mesa and canyon profiles combined (assumes there are no significant differences in the ground motions between the two site categories; Section 10). Figure 8-51 shows the V/H ratios for the total of the combined cases, M_w 6 and 7 for all sites.

As expected, for all cases, the V/H ratio exceeds 1 at near-source distances less than 5 to 10 km and at frequencies greater than about 2 to 6 Hz. The ratios are highest at the near-source distances for the mesa sites compared to the canyon sites (Figures 8-46 and 8-48) and for M_w 7 compared to M_w 6 (Figures 8-45 and 8-46). For M_w 7 and the mesa sites, the V/H ratio exceeds a value of 3 (Figure 8-46). The trends in these V/H ratios are similar to what is observed in western North American empirical data for deep soil sites (EPRI, 1993), although the ratios are not as high as those computed for LANL. This may be due to the unique velocity profiles of the layered volcanic stratigraphy beneath the laboratory.

In this study, the V/H ratios for each magnitude and site profile were averaged. The combination is justified on the basis of the preliminary nature of the model and simplifies the recommendations. The V/H ratios for all sites are as follows (Figure 8-52): 0.6 for frequencies up to 1 Hz at all distances; from 1 to 5 Hz the ratios ramp up to 2 for distances

of 0 to 5 km, to 1.5 beyond 5 km to 10 km, and to 0.8 beyond 10 km. At 100 Hz (peak ground acceleration), the V/H ratios are 1.2, 0.9, and 0.6 for the distance ranges of 0 to 5 km, 5.1 to 10.0 km, and greater than 10 km, respectively.

The modeling results suggest that large vertical component motions are possible at close distances for large magnitude earthquakes. Although these results provide a source- and site-specific aspect to evaluating vertical ground motions, we also recognize that this approach is based on a single preliminary model which has not been widely used. Therefore, we have also investigated existing empirical approaches based on available strong motion data which albeit, lack the source- and site-specific nature of the above modeling results.

The following recent empirical evaluations of vertical motions were evaluated:

- Abrahamson and Litehiser (1989) - vertical peak accelerations and comparison with horizontal accelerations

- Campbell (1990) - regression analyses to develop attenuation relationships for peak acceleration and response spectra on soft rock and soil for both horizontal and vertical motions

- Sadigh et al. (1993) - development of attenuation relationships for peak acceleration and response spectra on rock for both horizontal and vertical motions

- Lew (1991) - ratio of vertical to horizontal response spectra from the 1989 Loma Prieta earthquake

- Ohtani (1993) - the ratio of the frequency of the peak vertical response to peak horizontal response

- Egan et al. (1994) - ratio of vertical to horizontal peak acceleration and response spectra from Northridge and several other earthquakes including effects of distance from the rupture

We evaluated the frequency dependent ratio of the vertical to horizontal response spectra using several of these relationships for the mean magnitude and distance contributing to the seismic hazard for the 500, 1000, 2000, and 10,000 year Design Basis Earthquakes (Sections 9 and 10). The ratios for these relationships showed similar trends. We selected the ratio from Campbell (1990) to represent the empirical relationships because soil sites were included in the data base used to develop his relationships, and they showed similar trends to the others. Due to the small differences in magnitudes (M_w 6.2 to M_w 6.5) and distances (3 km to 12 km) for the dominant events, the Campbell (1990) ratios were very similar in value. The ratios from the site response modeling and Campbell (1990) were thus averaged and smoothed to develop the recommended ratios of vertical to horizontal spectra for the four Performance Categories as shown in Figures 8-53 through 8-55. The recommended ratios of vertical to horizontal response spectra are compared in Figure 8-56.

TABLE 8-1

ESTIMATED MEDIAN (50th PERCENTILE) PEAK HORIZONTAL ACCELERATIONS FROM THE PAJARITO FAULT M_w 7 EARTHQUAKE

Site	Distances			Peak Ground Acceleration in g's			
	Horizontal[1] (km)	Seismogenic[2] (km)	Rupture[3] (km)	Joyner & Boore (1988)	Sadigh et al. (1987)	Campbell & Bozorgnia (1994)	Average
TA-2	0.0	3.5	3.5	0.54	0.44	0.49	0.49
TA-3	0.0	2.0	0.7	0.54	0.53	0.50	0.53
TA-16	0.0	2.3	0.0	0.54	0.55	0.50	0.53
TA-18	0.0	5.6	5.6	0.54	0.39	0.46	0.47
TA-21	0.0	3.7	3.7	0.54	0.44	0.49	0.49
TA-41	0.0	2.9	2.8	0.54	0.46	0.50	0.50
TA-46	0.0	4.5	4.5	0.54	0.42	0.48	0.48
TA-55	0.0	3.1	3.1	0.54	0.45	0.50	0.50

[1] M_w and horizontal distance used by Joyner and Boore (1988). Horizontal distance is defined as the shortest distance from the site to the vertical projection of the fault rupture on the earth's surface.

[2] M_w and seismogenic distance used by Campbell and Bozorgnia (1994). Seismogenic distance is the shortest distance from the site to the zone of seismogenic rupture. The top of this zone is assumed to be the top of crystalline basement rock at a depth of about 2 km in New Mexico.

[3] M_w and rupture distance used by Sadigh et al. (1987). Rupture distance is the shortest distance from the site to the rupture surface.

TABLE 8-2

EARTHQUAKE RECORDINGS USED FOR KAPPA ESTIMATES

Event Date	M_D	Focal Depth (km)	Station	Epicentral Distance (km)
26 Oct 89 (E)	0.0	0.0	PFM	3.6
			PLS	6.5
27 Oct 89 (E)	0.5	0.0	PFM	2.1
			PLS	5.3
27 Apr 90	0.9	10.0	ATE	78.4
			PFM	80.7
			PLS	80.2
24 May 90	1.2	10.0	ATE	8.0
			PFM	8.7
			PLS	7.0
5 July 90	1.5	14.9	ATE	11.4
			PFM	16.2
			PLS	13.3
3 Sept 90	1.0	13.7	ATE	12.3
			PFM	14.1
			PLS	13.8
13 Sept 90	1.4	10.0	ATE	44.5
			PFM	48.4
			PLS	46.6

E = Possible explosion

TABLE 8-3

KAPPA VALUES AT LANL

Event	Station	κ (sec)
26 Oct 89	PFM	0.019
	PLS	0.027
27 Oct 89	PFM	0.021
	PLS	0.028
27 April 90	ATE	0.063
	PFM	0.061
	PLS	0.058
24 May 90	ATE	0.037
	PFM	0.047
	PLS	0.029
5 July 90	ATE	0.032
	PFM	0.032
	PLS	0.039
3 Sept 90	ATE	0.024
	PFM	0.037
	PLS	0.024
13 Sept 90	ATE	0.042
	PFM	0.033
	PLS	0.042

	With Possible Explosions		Without Possible Explosions	
Station	Median (sec)	σ_{ln}	Median (sec)	σ_{ln}
ATE	0.038	0.32	--	--
PFM	0.033	0.38	0.041	0.24
PLS	0.034	0.29	0.037	0.31
Overall	0.035	0.34	0.038	0.29

TABLE 8-4

INPUT PARAMETERS AND UNCERTAINTIES FOR PARAMETRIC VARIATIONS IN STOCHASTIC MODELING

Parameter	Mean or Median Value	Distribution	σ*
Q_o	370	lognormal	0.18
η	0.35	normal	0.05
κ	0.035 sec	lognormal	0.30
Slip Models	Randomized	--	--
Rupture Initiation	Randomized in zone	--	--
Velocity Profiles	Randomized	--	--

*For lognormal distributions, σ is actually σ_{ln}

TABLE 8-5

COMPARISON OF EMPIRICAL AND STOCHASTIC PEAK HORIZONTAL ACCELERATIONS FROM THE PAJARITO FAULT M_w 7 EARTHQUAKE

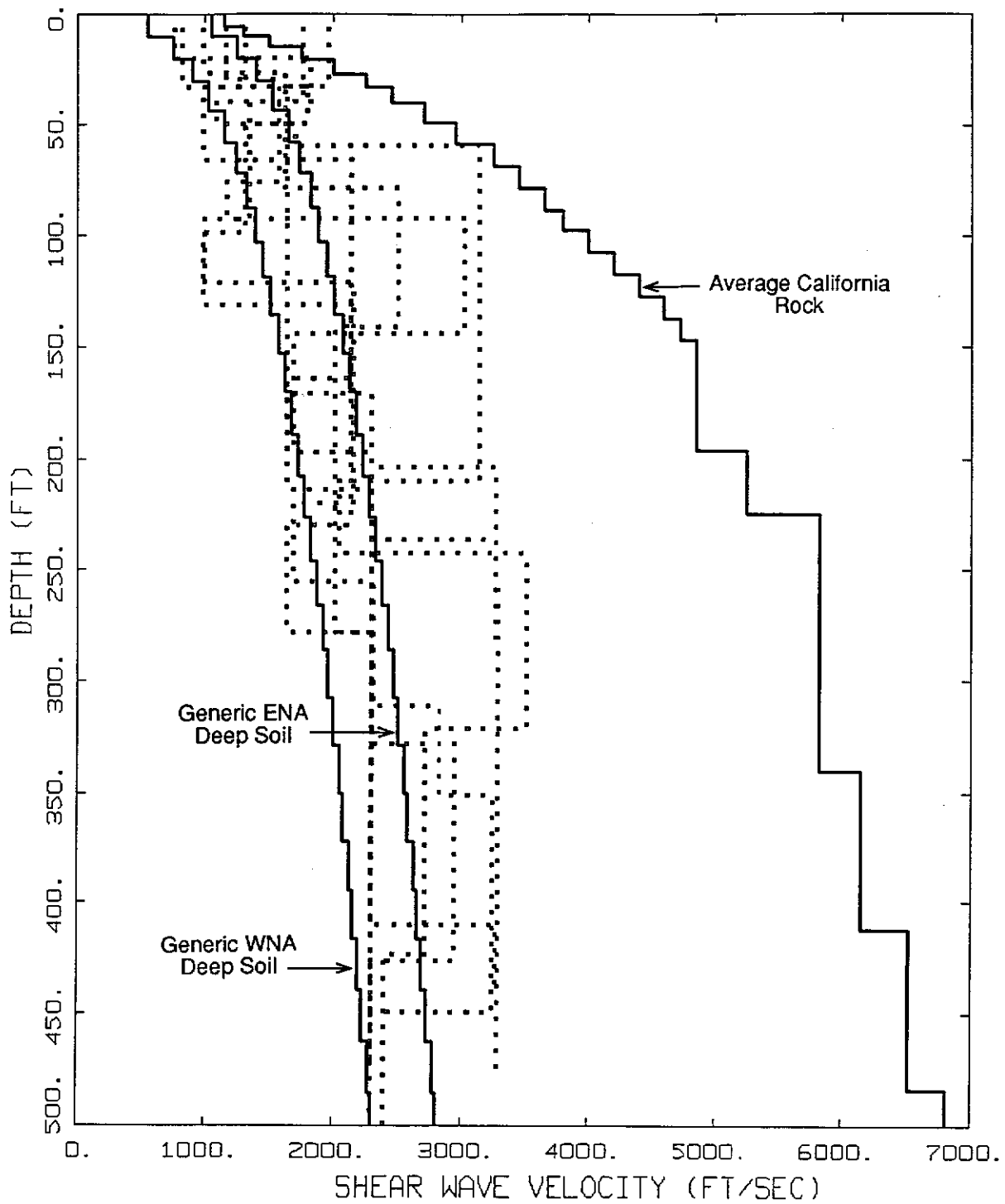
	Rupture Distance (km)	Average Empirical PHA (g)	Stochastic PHA (g)
TA-2	3.5	0.49	0.87
TA-3	0.7	0.53	0.62
TA-16	0.0	0.53	0.60
TA-18	5.6	0.47	0.81
TA-21	3.7	0.49	0.61
TA-41	2.8	0.50	0.90
TA-46	4.5	0.48	0.60
TA-55	3.1	0.50	0.62

PHA Peak Horizontal Acceleration

TABLE 8-6

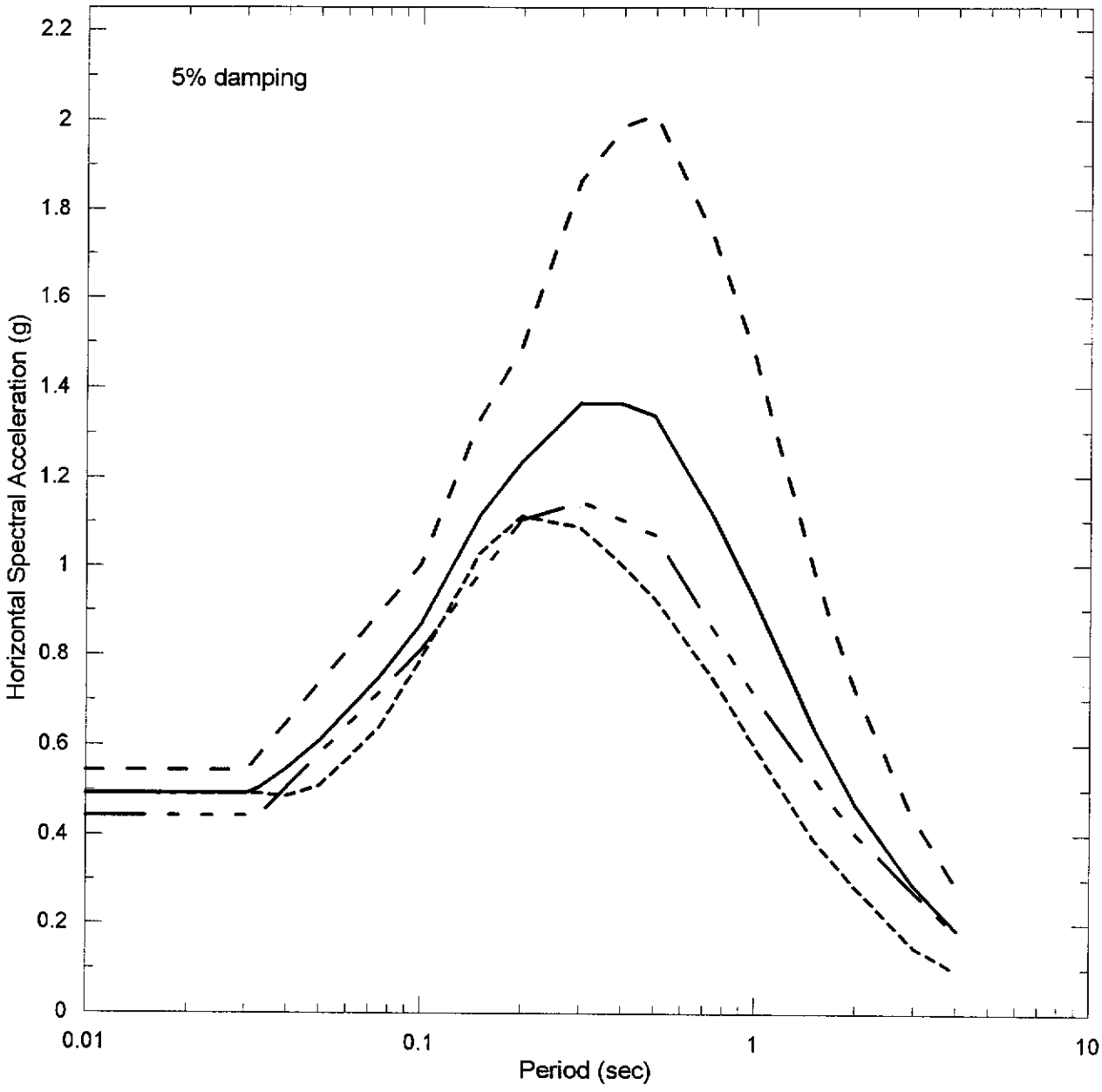
INPUT PARAMETERS AND WEIGHTS FOR STOCHASTIC ATTENUATION RELATIONSHIPS

Parameter	Value	Weight
σ	25 bars 75 bars 150 bars	0.185 0.63 0.185
κ	0.0175 sec 0.035 sec 0.070 sec	0.185 0.63 0.185
Q_o (η = 0.35 fixed)	150 370 670	0.185 0.63 0.185
M_w 5 Point Source Focal Depth	4 km 8 km 12 km	0.185 0.63 0.185
M_w 6 Point Source Focal Depth	6 km 9 km 12 km	0.185 0.63 0.185
M_w 7 and 7.5 Point Source Focal Depth	8 km 10 km 12 km	0.185 0.63 0.185



Note: LANL profiles are dotted lines

Project No. 91C0509	Los Alamos Seismic Hazards	COMPARISON OF LANL PROFILES WITH GENERIC EMPIRICAL PROFILES	Figure 8-1
Woodward-Clyde Federal Services			

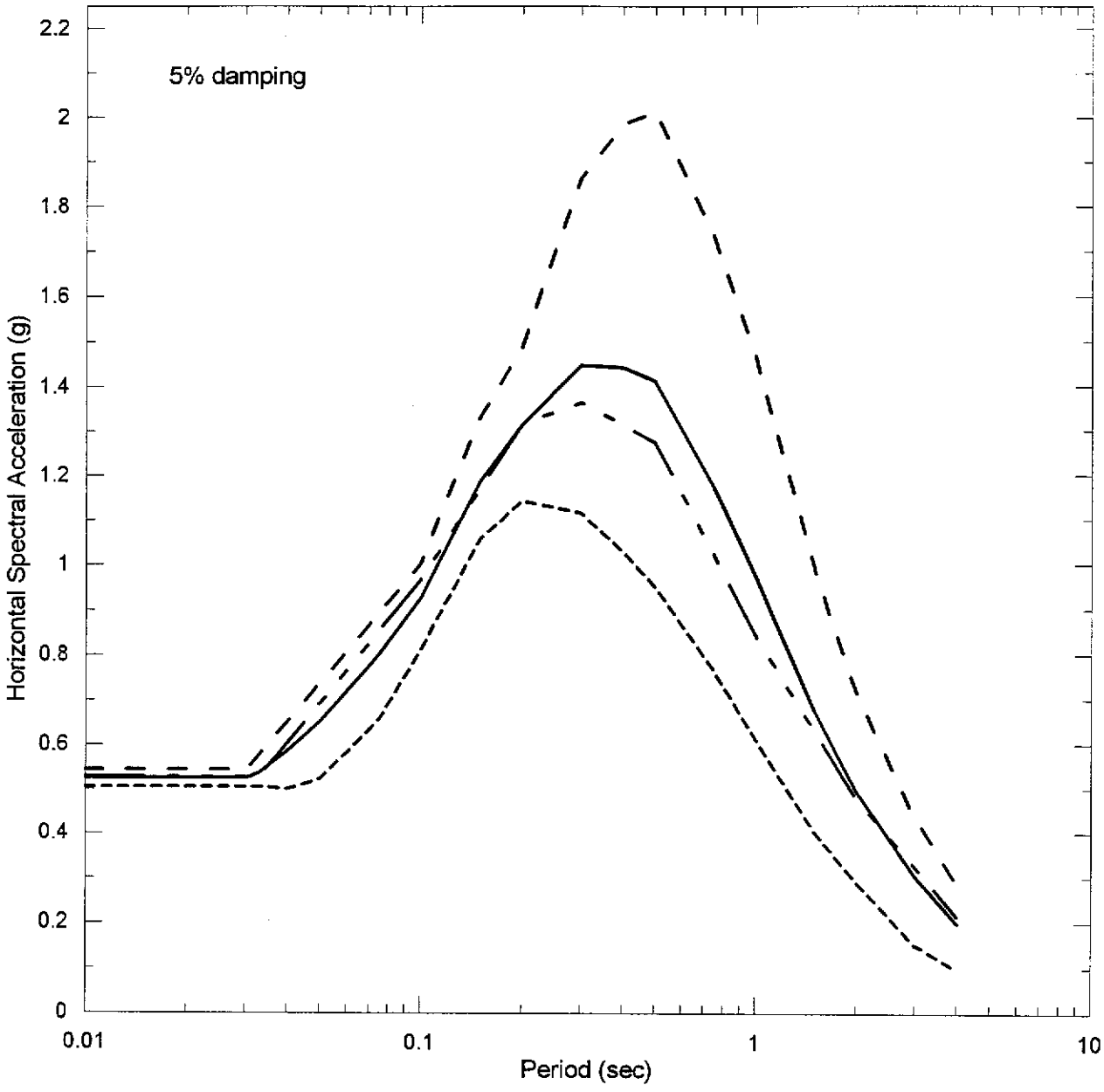


Horizontal Distance = 0.0 km
Seismogenic Distance = 3.5 km
Rupture Distance = 3.5 km

- Average (PGA = 0.49 g)
- Campbell and Bozorgnia (1994) and Campbell (1989)
- Joyner and Boore (1988)
- Sadigh et al. (1987)

Project No. 91C0509	Los Alamos Seismic Hazards	TA-2 MEDIAN EMPIRICAL ACCELERATION RESPONSE SPECTRA FOR PAJARITO FAULT Mw 7 EARTHQUAKE	Figure 8-2
Woodward-Clyde Federal Services			

MEAN.GRF

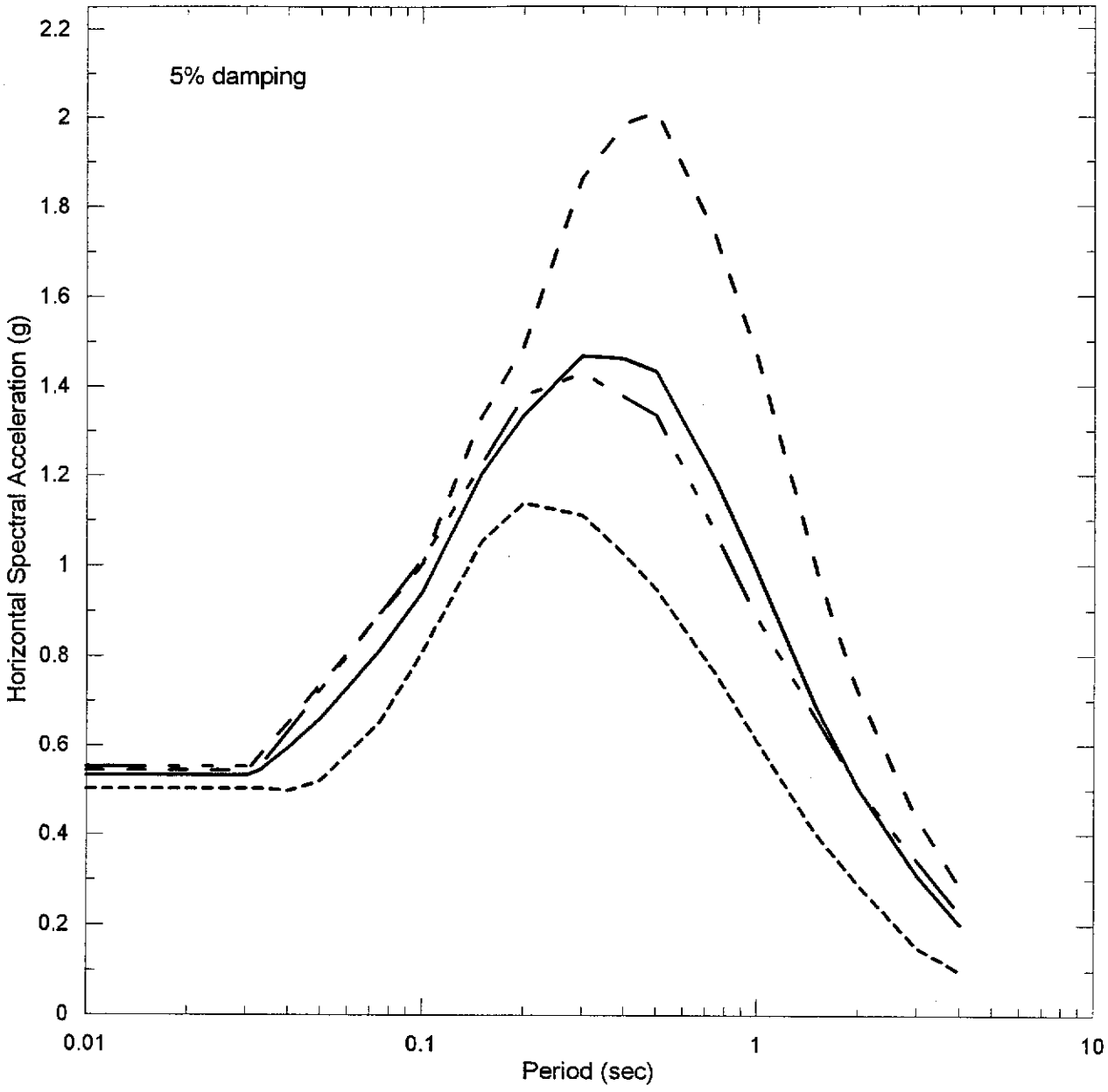


Horizontal Distance = 0.0 km
Seismogenic Distance = 2.0 km
Rupture Distance = 0.7 km

- Average (PGA = 0.53 g)
- Campbell and Bozorgnia (1994) and Campbell (1989)
- Joyner and Boore (1988)
- Sadigh et al. (1987)

Project No. 91C0509	Los Alamos Seismic Hazards	TA-3 MEDIAN EMPIRICAL ACCELERATION RESPONSE SPECTRA FOR PAJARITO FAULT Mw 7 EARTHQUAKE	Figure 8-3
Woodward-Clyde Federal Services			

MEAN.GRF

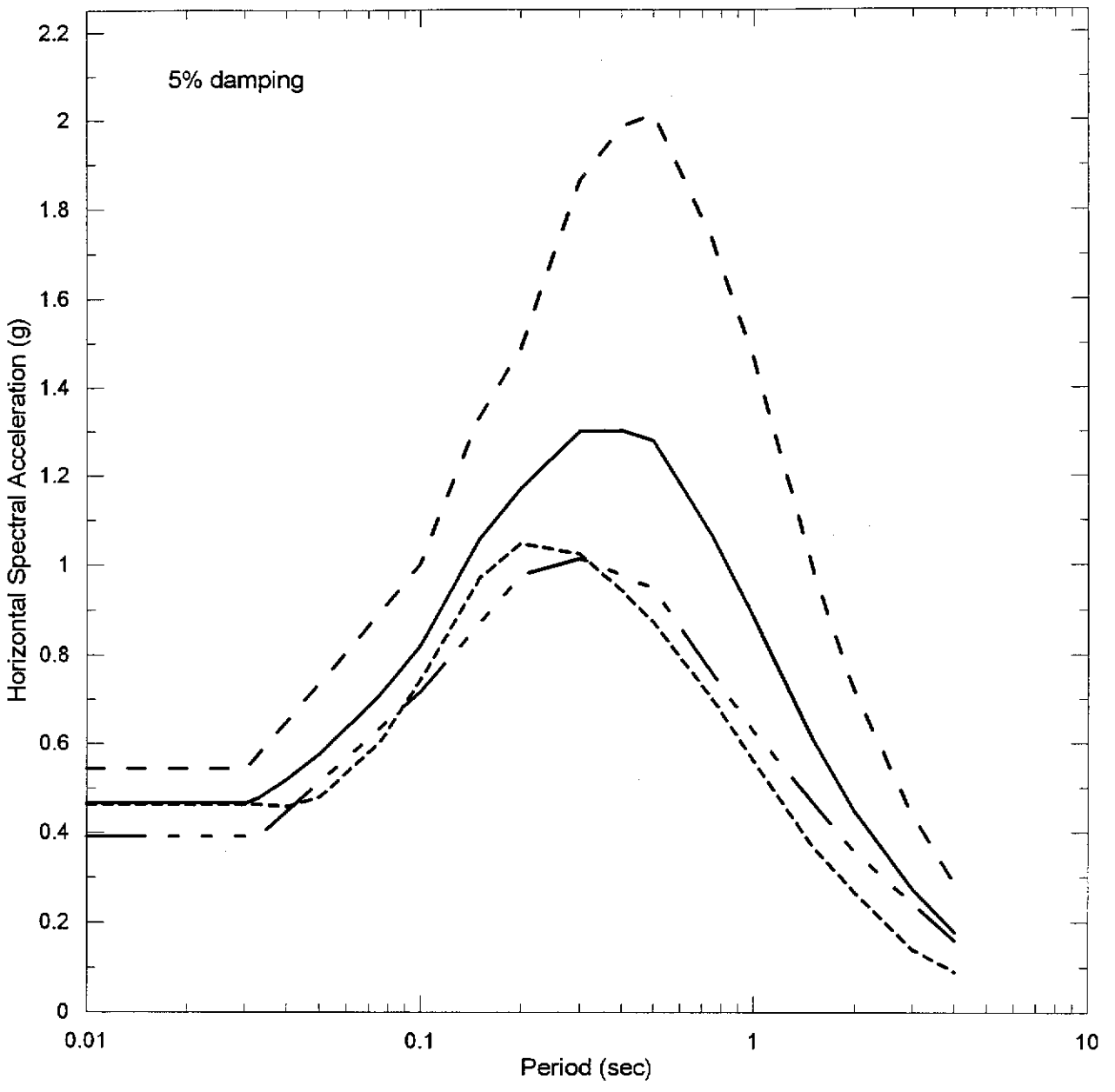


Horizontal Distance = 0.0 km
Seismogenic Distance = 2.3 km
Rupture Distance = 0.0 km

- Average (PGA = 0.53 g)
- Campbell and Bozorgnia (1994) and Campbell (1989)
- Joyner and Boore (1988)
- Sadigh et al. (1987)

Project No. 91C0509	Los Alamos Seismic Hazards	TA-16 MEDIAN EMPIRICAL ACCELERATION RESPONSE SPECTRA FOR PAJARITO FAULT Mw 7 EARTHQUAKE	Figure 8-4
Woodward-Clyde Federal Services			

MEAN.GRF

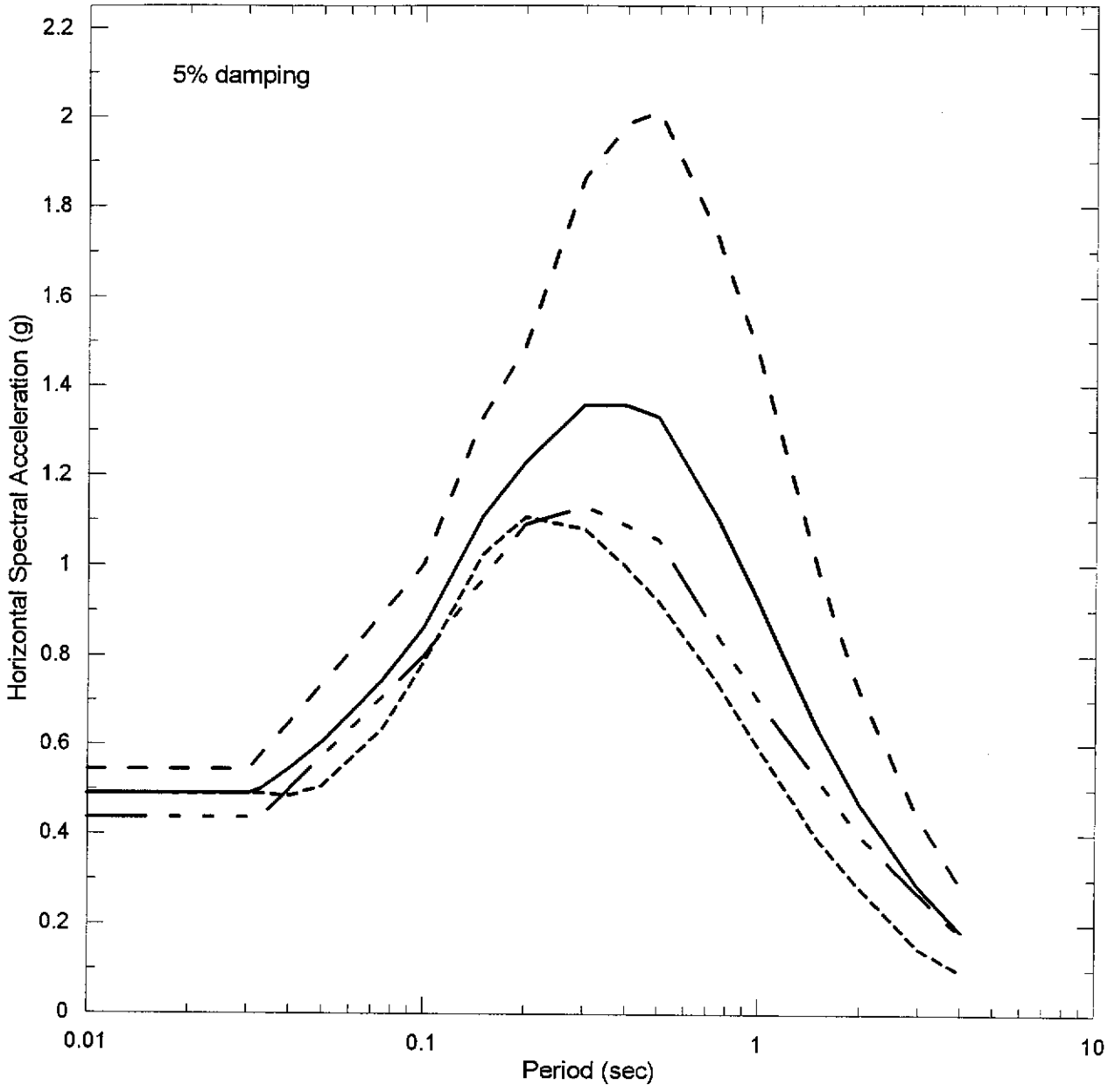


Horizontal Distance = 0.0 km
Seismogenic Distance = 5.6 km
Rupture Distance = 5.6 km

- Average (PGA = 0.47 g)
- Campbell and Bozorgnia (1994) and Campbell (1989)
- Joyner and Boore (1988)
- Sadigh et al. (1987)

Project No. 91C0509	Los Alamos Seismic Hazards	TA-18 MEDIAN EMPIRICAL ACCELERATION RESPONSE SPECTRA FOR PAJARITO FAULT Mw 7 EARTHQUAKE	Figure 8-5
Woodward-Clyde Federal Services			

MEAN.GRF

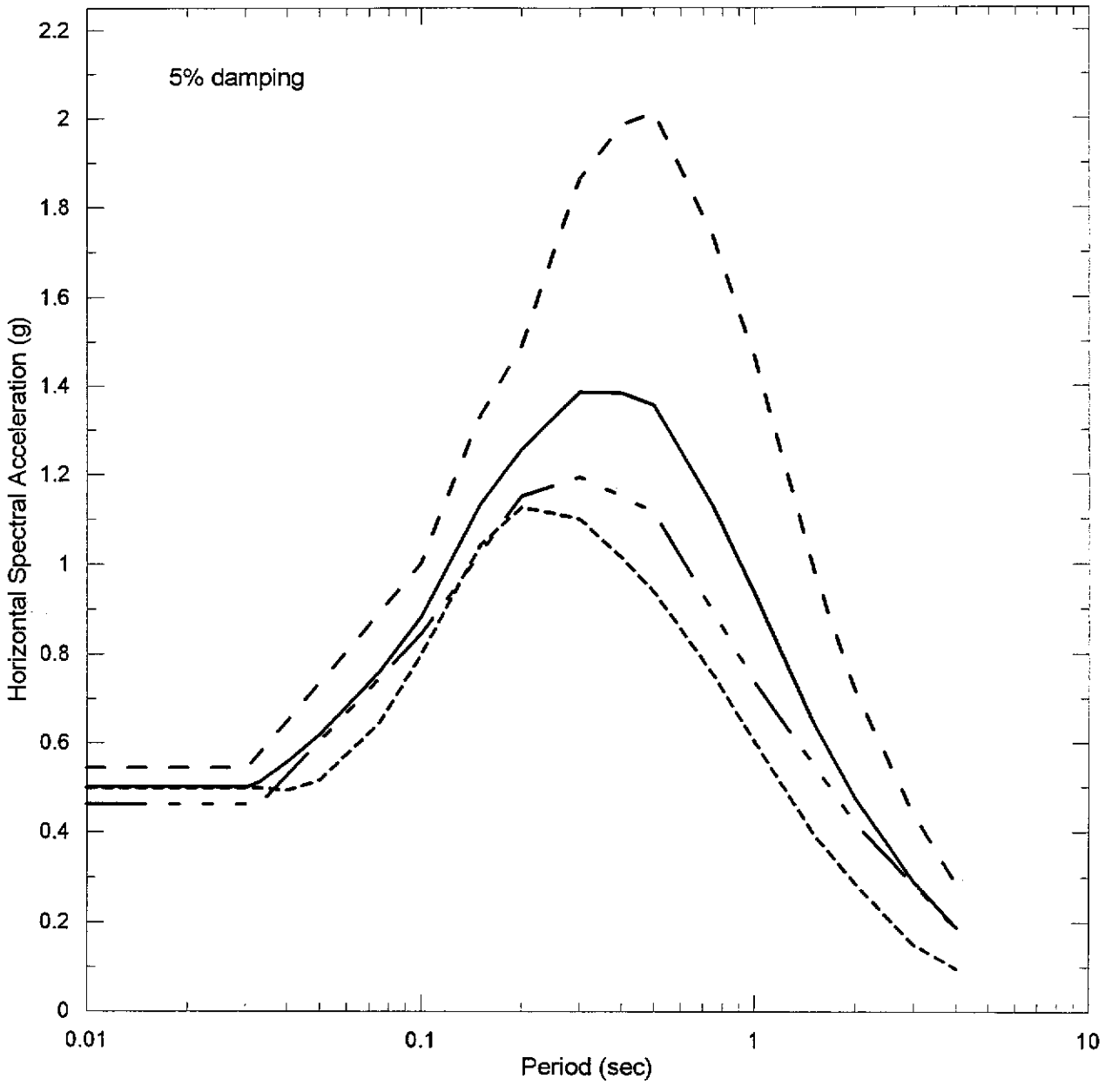


Horizontal Distance = 0.0 km
Seismogenic Distance = 3.7 km
Rupture Distance = 3.7 km

- Average (PGA = 0.49 g)
- Campbell and Bozorgnia (1994) and Campbell (1989)
- Joyner and Boore (1988)
- Sadigh et al. (1987)

Project No. 91C0509	Los Alamos Seismic Hazards	TA-21 MEDIAN EMPIRICAL ACCELERATION RESPONSE SPECTRA FOR PAJARITO FAULT Mw 7 EARTHQUAKE	Figure 8-6
Woodward-Clyde Federal Services			

MEAN.GRF

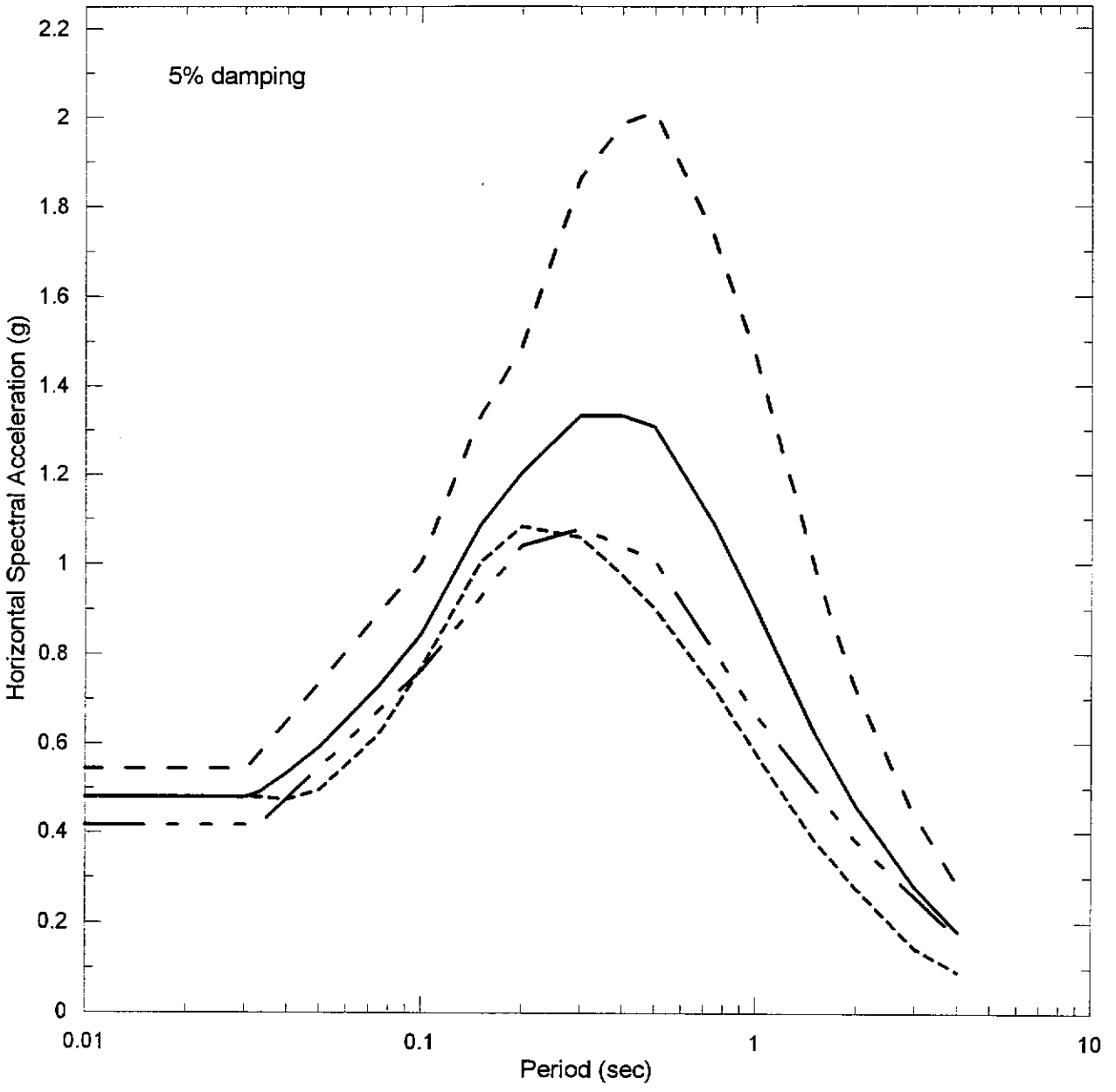


Horizontal Distance = 0.0 km
Seismogenic Distance = 2.9 km
Rupture Distance = 2.8 km

- Average (PGA = 0.50 g)
- Campbell and Bozorgnia (1994) and Campbell (1989)
- Joyner and Boore (1988)
- Sadigh et al. (1987)

Project No. 91C0509	Los Alamos Seismic Hazards	TA-41 MEDIAN EMPIRICAL ACCELERATION RESPONSE SPECTRA FOR PAJARITO FAULT Mw 7 EARTHQUAKE	Figure 8-7
Woodward-Clyde Federal Services			

MEAN.GRF

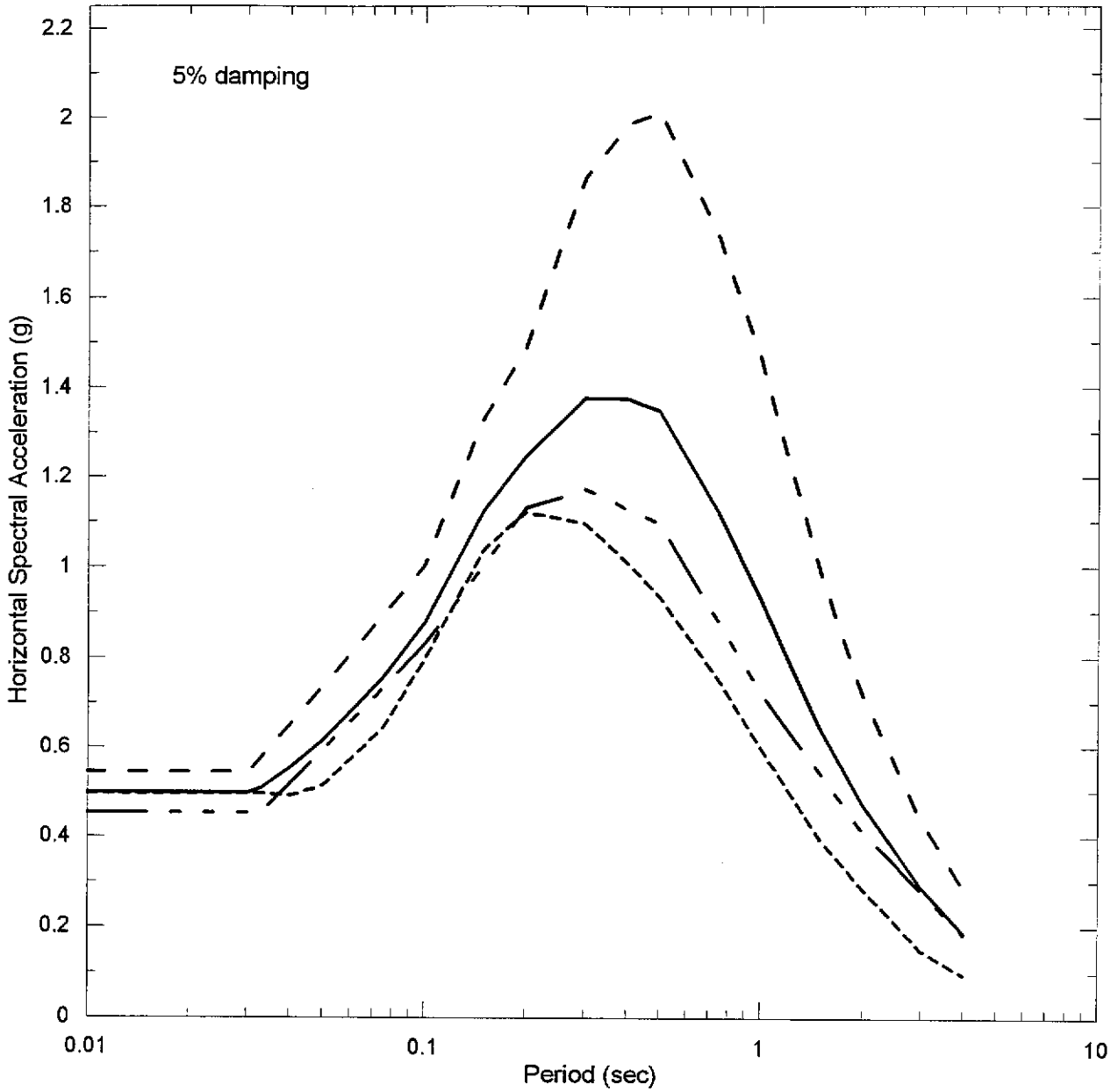


Horizontal Distance = 0.0 km
Seismogenic Distance = 4.5 km
Rupture Distance = 4.5 km

- Average (PGA = 0.48 g)
- Campbell and Bozorgnia (1994) and Campbell (1989)
- Joyner and Boore (1988)
- Sadigh et al. (1987)

Project No. 91C0509	Los Alamos Seismic Hazards	TA-46 MEDIAN EMPIRICAL ACCELERATION RESPONSE SPECTRA FOR PAJARITO FAULT Mw 7 EARTHQUAKE	Figure 8-8
Woodward-Clyde Federal Services			

MEAN.GRF



Horizontal Distance = 0.0 km
Seismogenic Distance = 3.1 km
Rupture Distance = 3.1 km

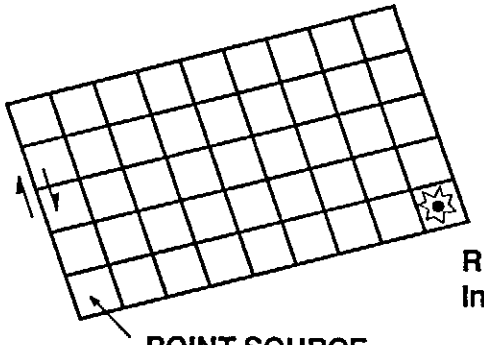
- Average (PGA = 0.50 g)
- Campbell and Bozorgnia (1994) and Campbell (1989)
- Joyner and Boore (1988)
- Sadigh et al. (1987)

Project No. 91C0509	Los Alamos Seismic Hazards	TA-55 MEDIAN EMPIRICAL ACCELERATION RESPONSE SPECTRA FOR PAJARITO FAULT Mw 7 EARTHQUAKE	Figure 8-9
Woodward-Clyde Federal Services			

MEAN.GRF



Geologic Profile (V_s, Q_s, ρ)



Finite Fault (Summation of point sources)

Rupture Initiation

POINT SOURCE

$$\frac{M_o f^2}{1+(f/f_c)^2}$$

where

$$f_c = \beta_s \left(\frac{\Delta\sigma}{8.44\, M_o}\right)^{\frac{1}{3}}$$

S-Waves

PATH OPERATOR

$$\frac{e^{\frac{-\pi f R}{\beta_s Q(f)}}}{R}$$

where

$$Q(f) = Q_o \left(\frac{f}{f_o}\right)^{\eta}$$

S-Waves

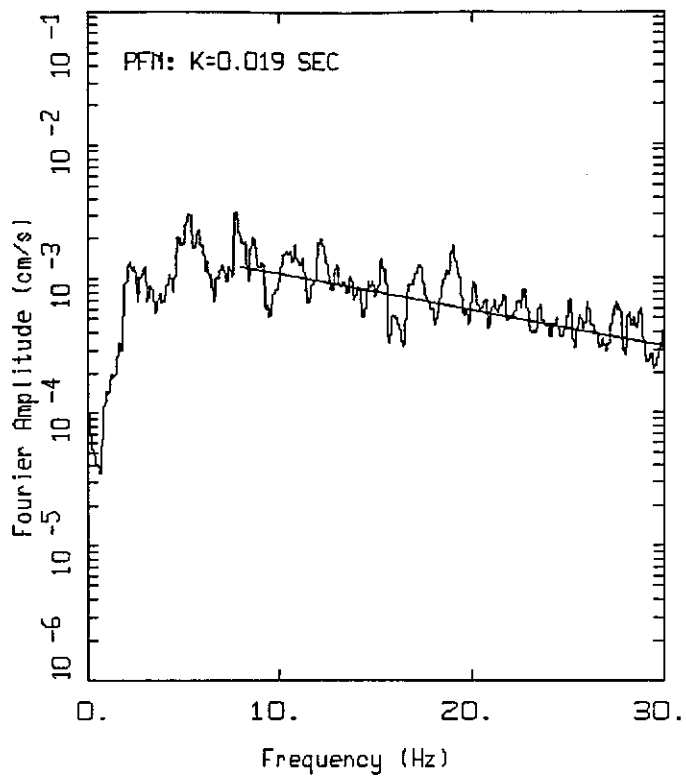
SITE OPERATOR

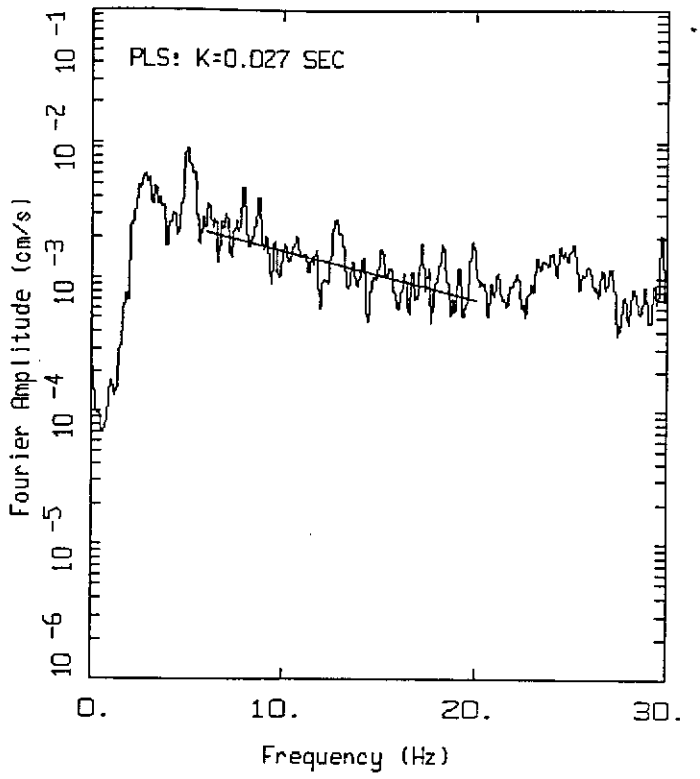
$$A(f)\, e^{-\pi\kappa f}$$

where

$$\kappa(0) = \frac{H}{\bar{V}_s \bar{Q}_s}$$

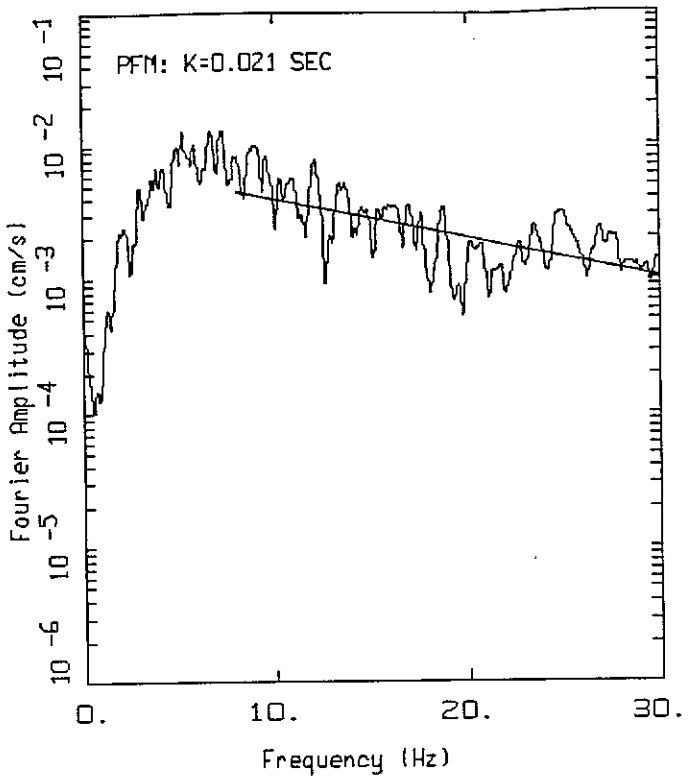
Project No. 91C0509	Los Alamos Seismic Hazards	STOCHASTIC FINITE FAULT METHODOLOGY	Figure 8-10
Woodward-Clyde Federal Services			

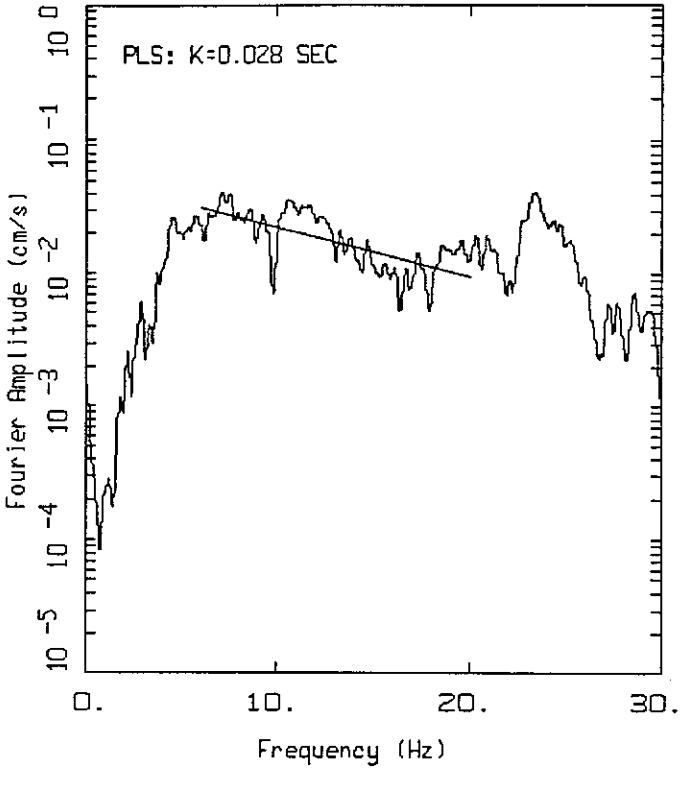




Note: 0.25 Hz smoothing

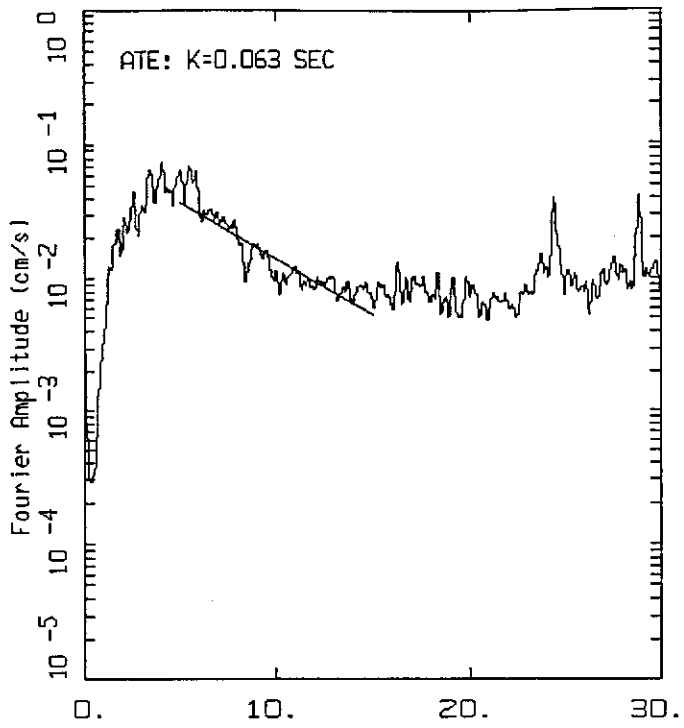
Project No. 91C0509	Los Alamos Seismic Hazards	LEAST-SQUARES FITS TO THE VECTOR-SUM FOURIER SPECTRA FOR 26 OCTOBER 1989 EARTHQUAKE	Figure 8-11
Woodward-Clyde Federal Services			

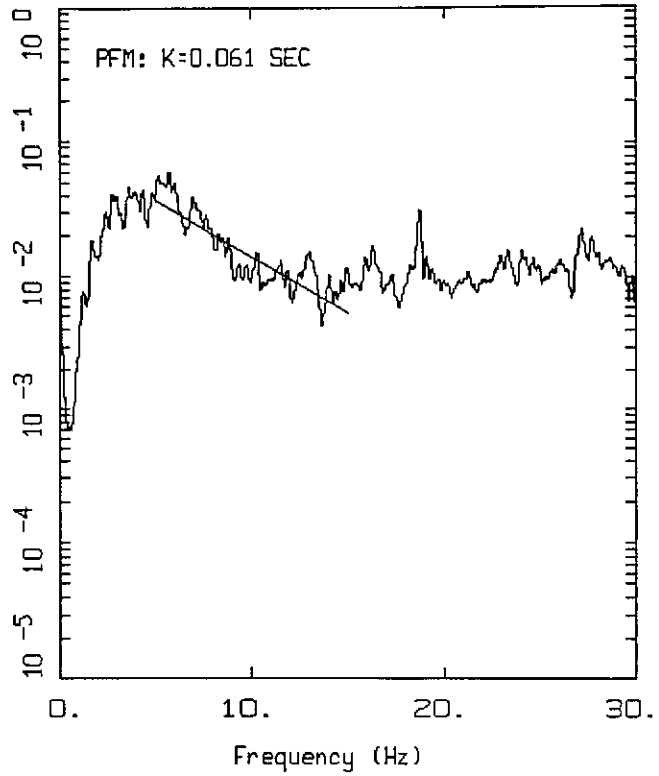


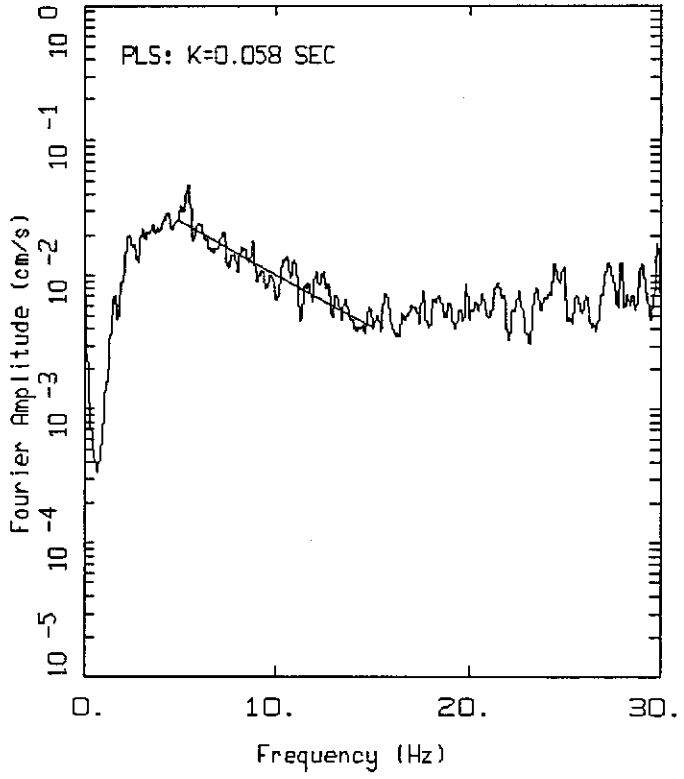


Note: 0.25 Hz smoothing

Project No. 91C0509	Los Alamos Seismic Hazards	LEAST-SQUARES FITS TO THE VECTOR-SUM FOURIER SPECTRA FOR 27 OCTOBER 1989 EARTHQUAKE	Figure 8-12
Woodward-Clyde Federal Services			

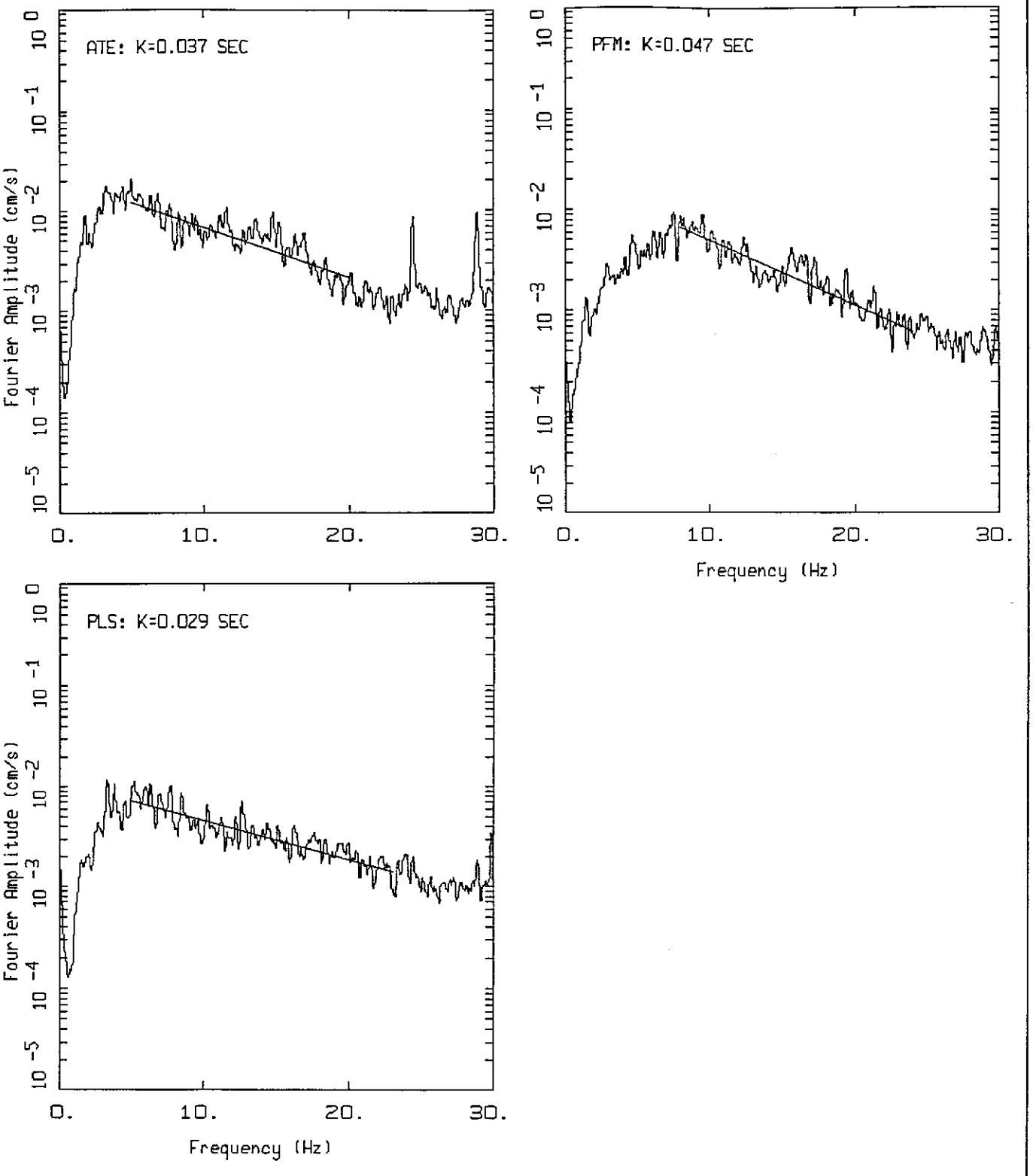






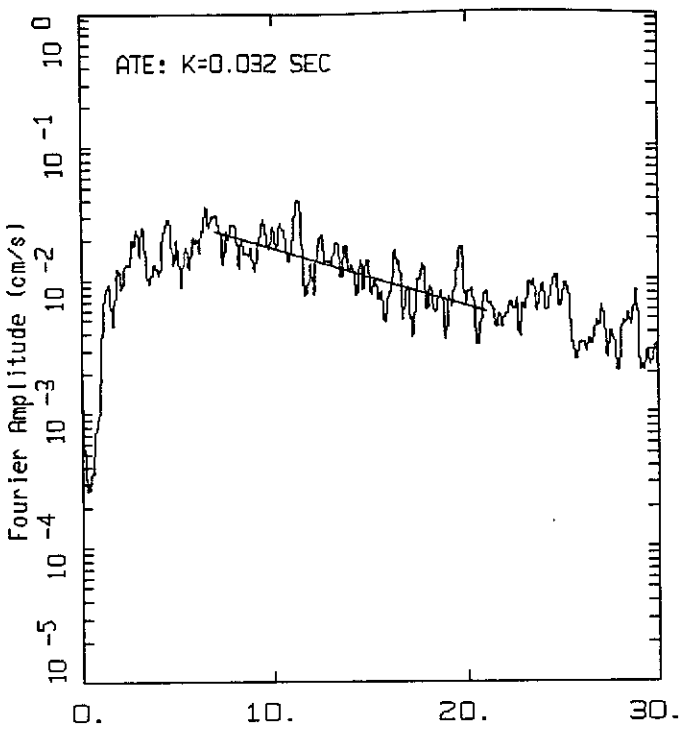
Note: 0.25 Hz smoothing

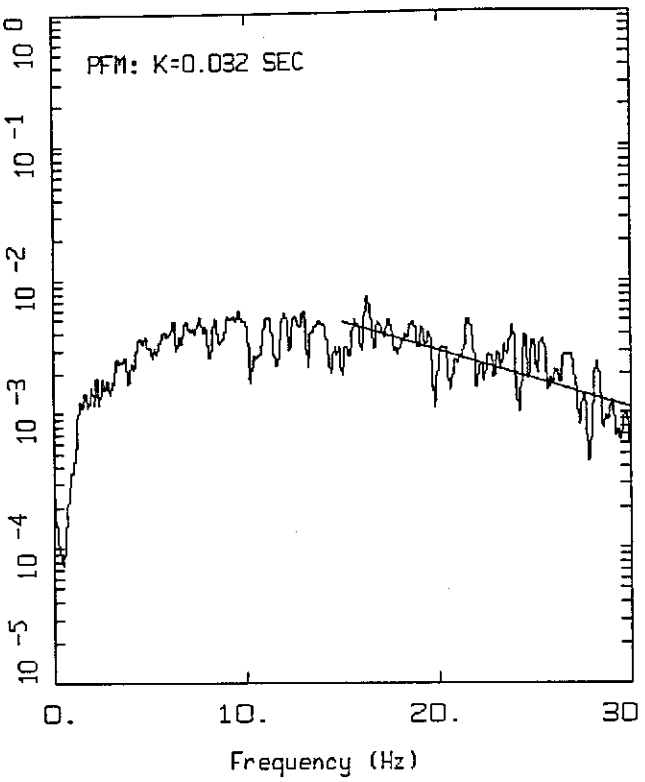
Project No. 91C0509	Los Alamos Seismic Hazards	LEAST-SQUARES FITS TO THE VECTOR-SUM FOURIER SPECTRA FOR 27 APRIL 1990 EARTHQUAKE	Figure 8-13
Woodward-Clyde Federal Services			

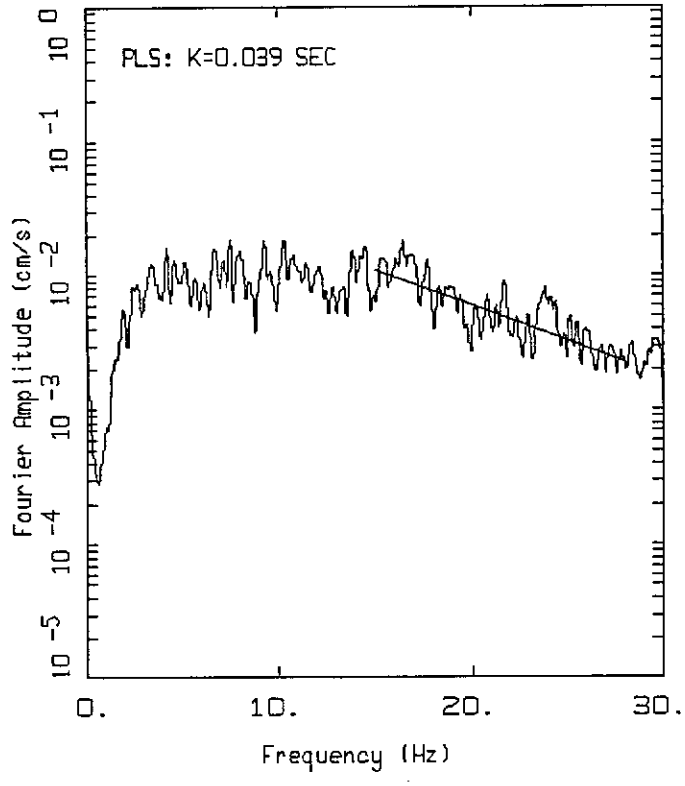


Note: 0.25 Hz smoothing

Project No. 91C0509	Los Alamos Seismic Hazards	LEAST-SQUARES FITS TO THE VECTOR-SUM FOURIER SPECTRA FOR 24 MAY 1990 EARTHQUAKE	Figure 8-14
Woodward-Clyde Federal Services			

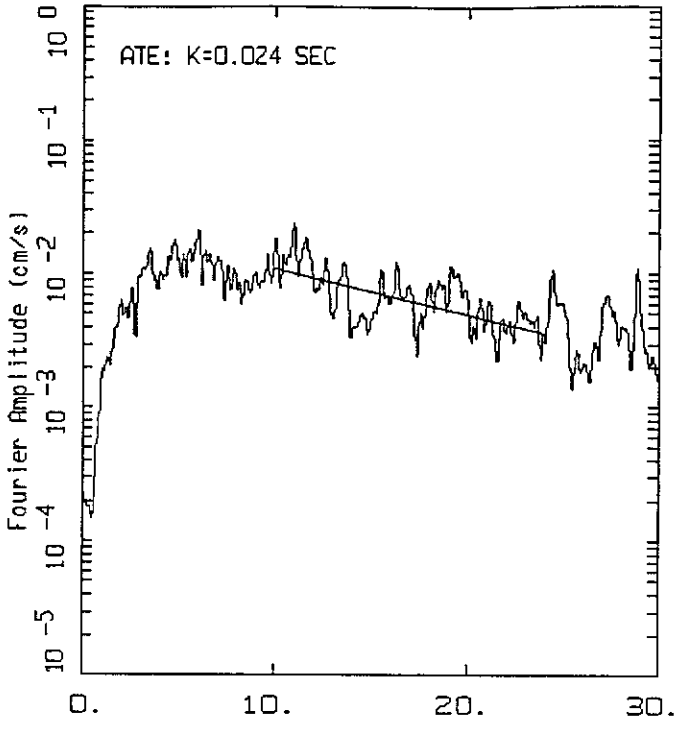


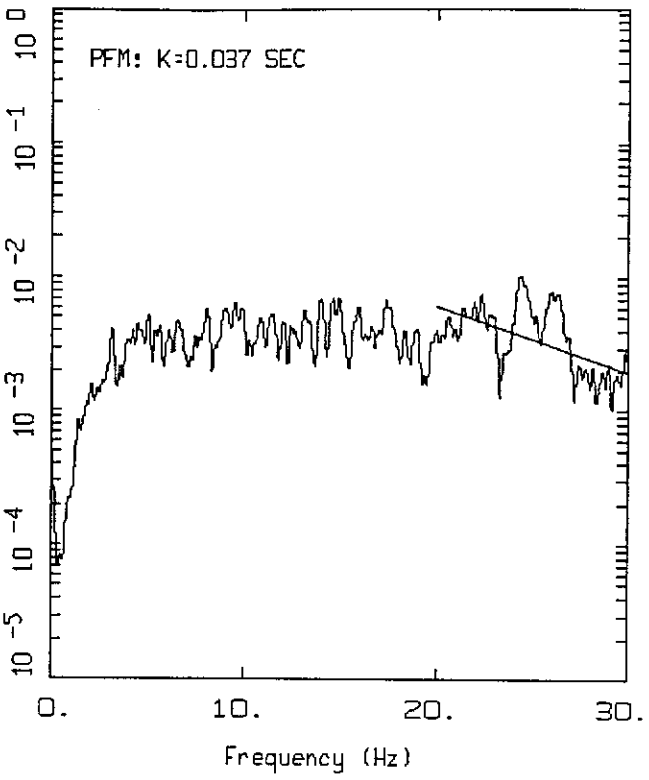


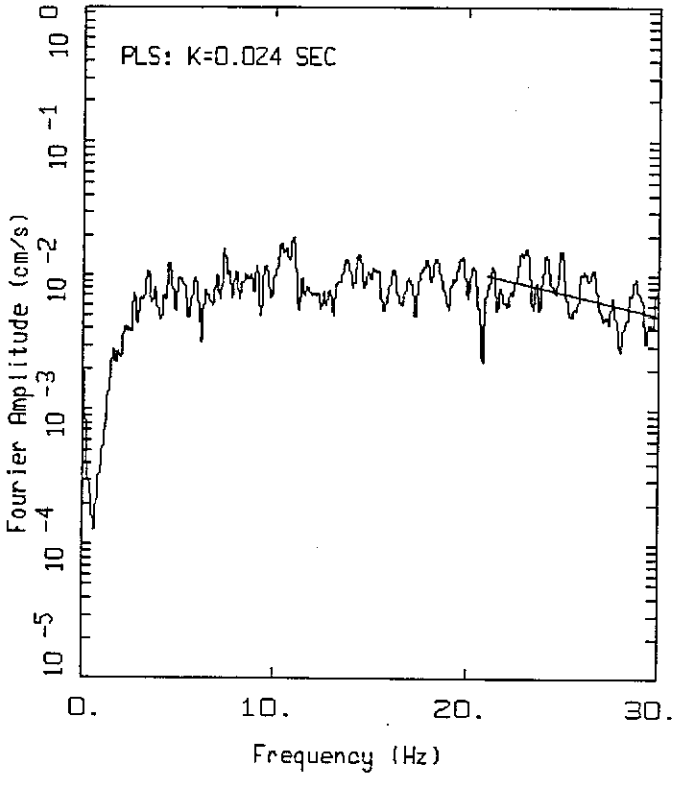


Note: 0.25 Hz smoothing

Project No. 91C0509	Los Alamos Seismic Hazards	LEAST-SQUARES FITS TO THE VECTOR-SUM FOURIER SPECTRA FOR 5 JULY 1990 EARTHQUAKE	Figure 8-15
Woodward-Clyde Federal Services			

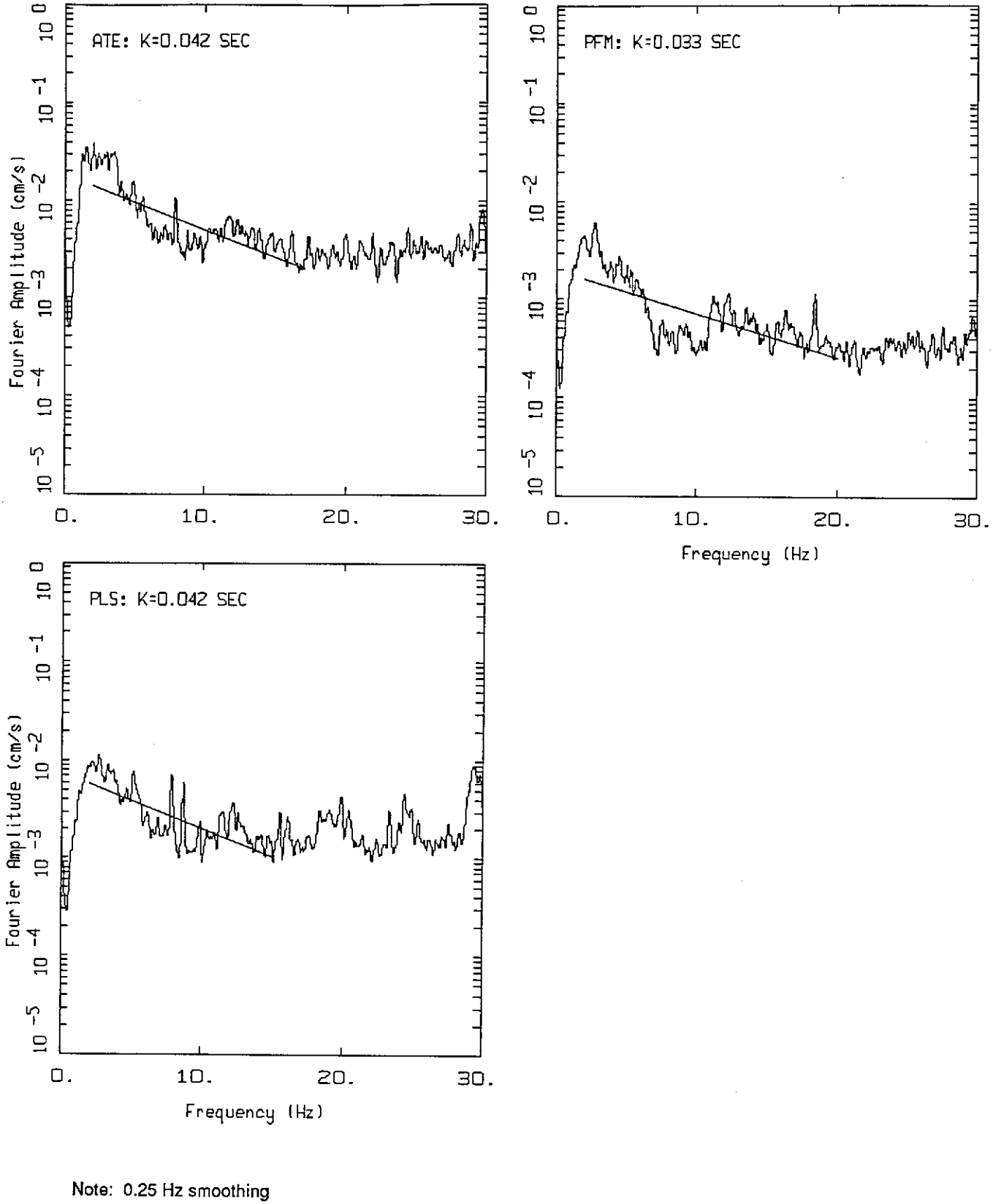






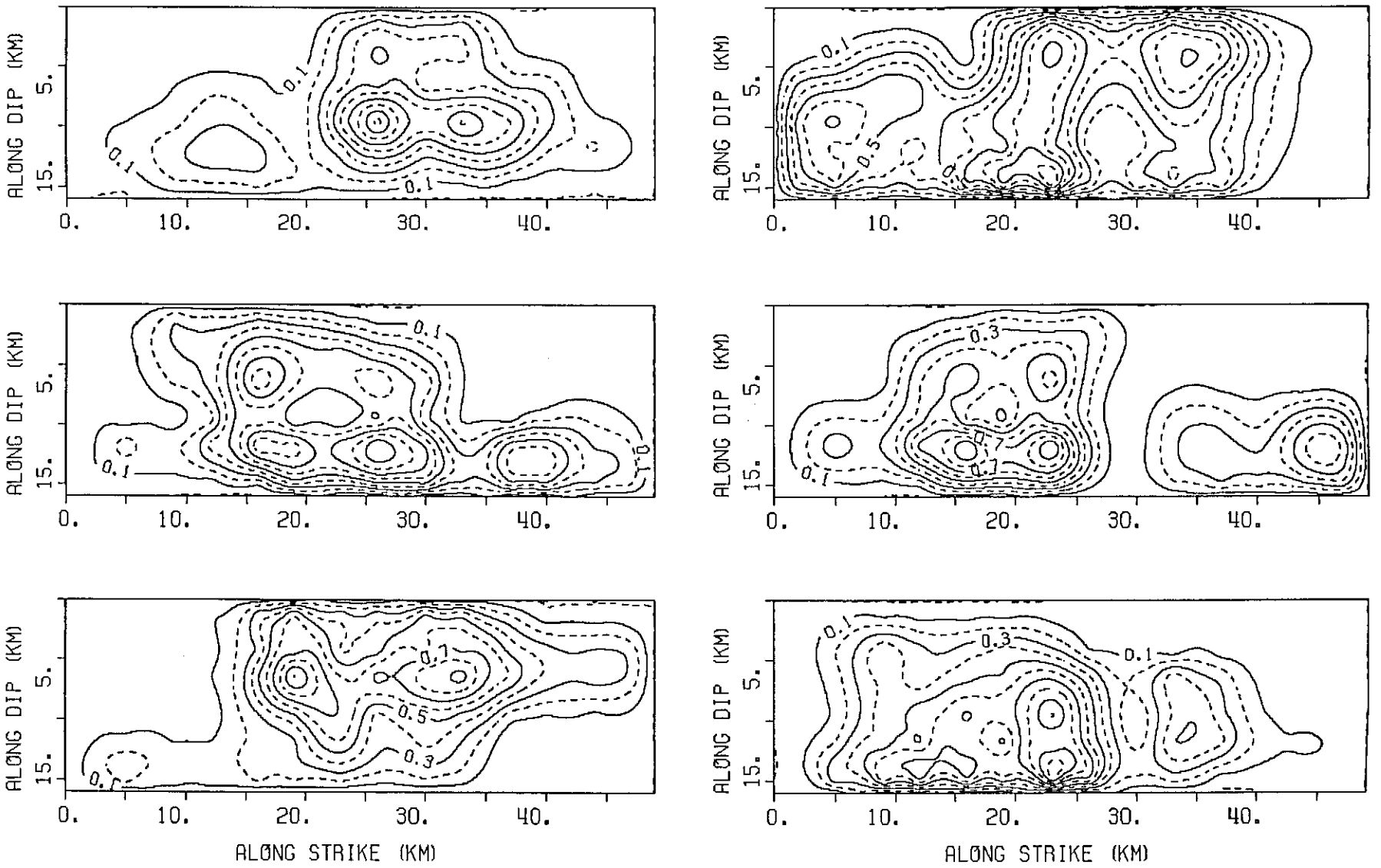
Note: 0.25 Hz smoothing

Project No. 91C0509	Los Alamos Seismic Hazards	LEAST-SQUARES FITS TO THE VECTOR-SUM FOURIER SPECTRA FOR 3 SEPTEMBER 1990 EARTHQUAKE	Figure 8-16
Woodward-Clyde Federal Services			



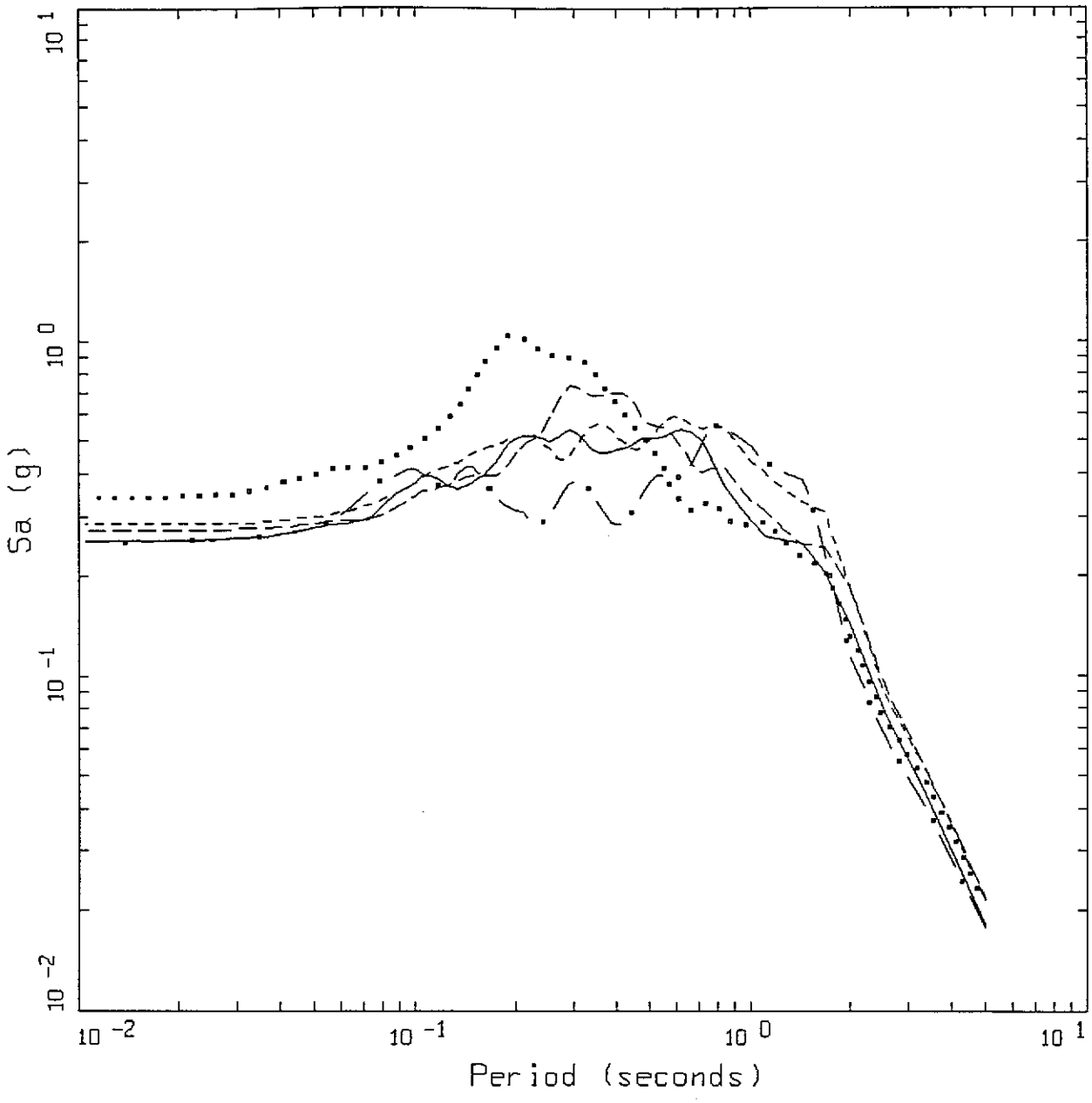
Note: 0.25 Hz smoothing

Project No. 91C0509	Los Alamos Seismic Hazards	LEAST-SQUARES FITS TO THE VECTOR-SUM FOURIER SPECTRA FOR 13 SEPTEMBER 1990 EARTHQUAKE	Figure 8-17
Woodward-Clyde Federal Services			



Note: Slip is normalized to maximum value.

Project No. 91C0509	Los Alamos Seismic Hazards	SAMPLE OF RANDOMIZED SLIP MODELS FOR THE PAJARITO FAULT M_W 7 EARTHQUAKE	Figure 8-18
Woodward-Clyde Federal Services			



LEGEND

TA-3, 50TH PERCENTILE, PROFILE VARIATION

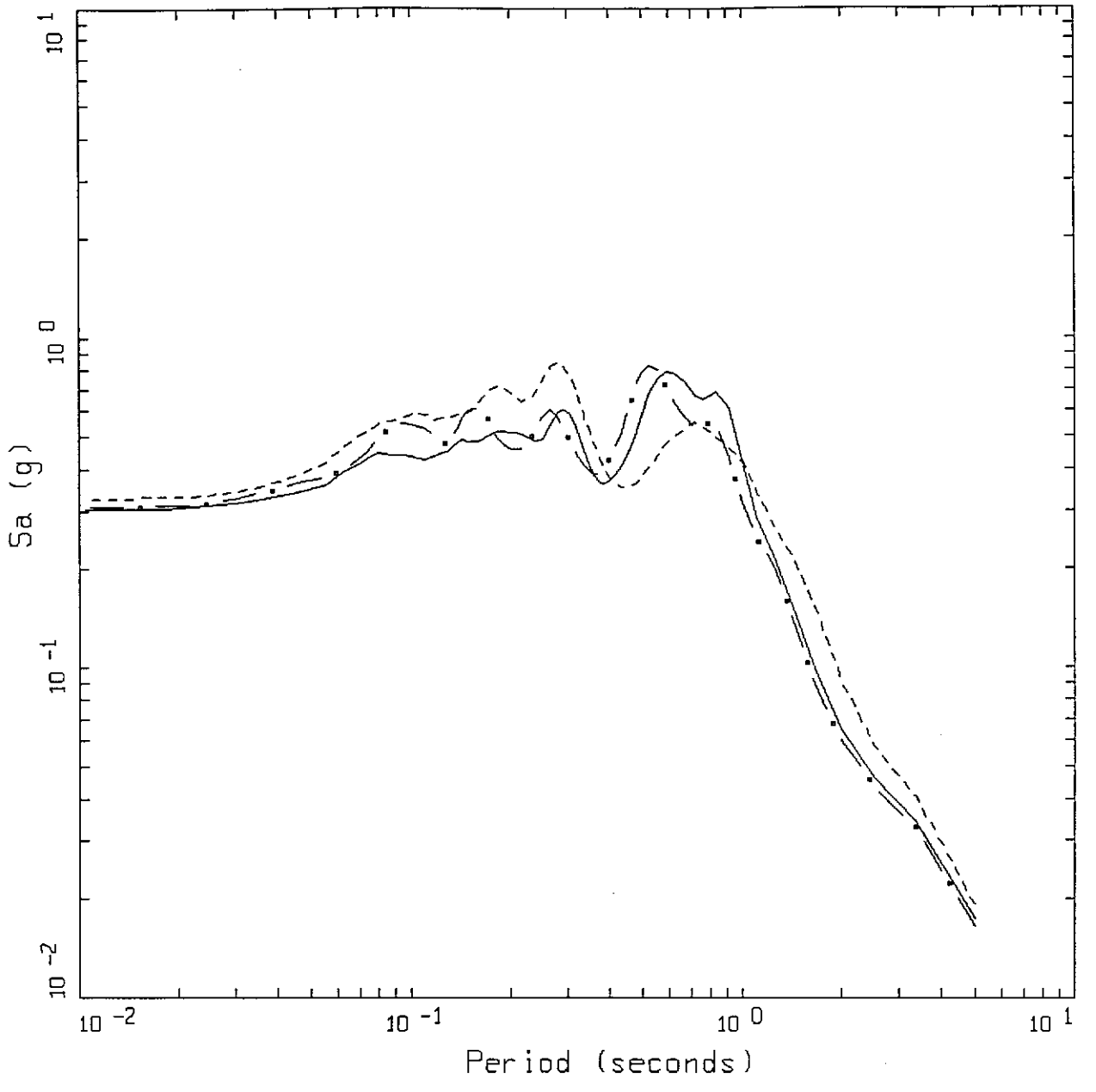
TA-16, 50TH PERCENTILE, PROFILE VARIATION

TA-21, 50TH PERCENTILE, PROFILE VARIATION

TA-46, 50TH PERCENTILE, PROFILE VARIATION

TA-55, 50TH PERCENTILE, PROFILE VARIATION

Project No. 91C0509	Los Alamos Seismic Hazards	AVERAGE RESPONSE SPECTRA FOR M_W 5.9 EARTHQUAKE AT 6 KM AT MESA TOP SITES	Figure 8-19
Woodward-Clyde Federal Services			



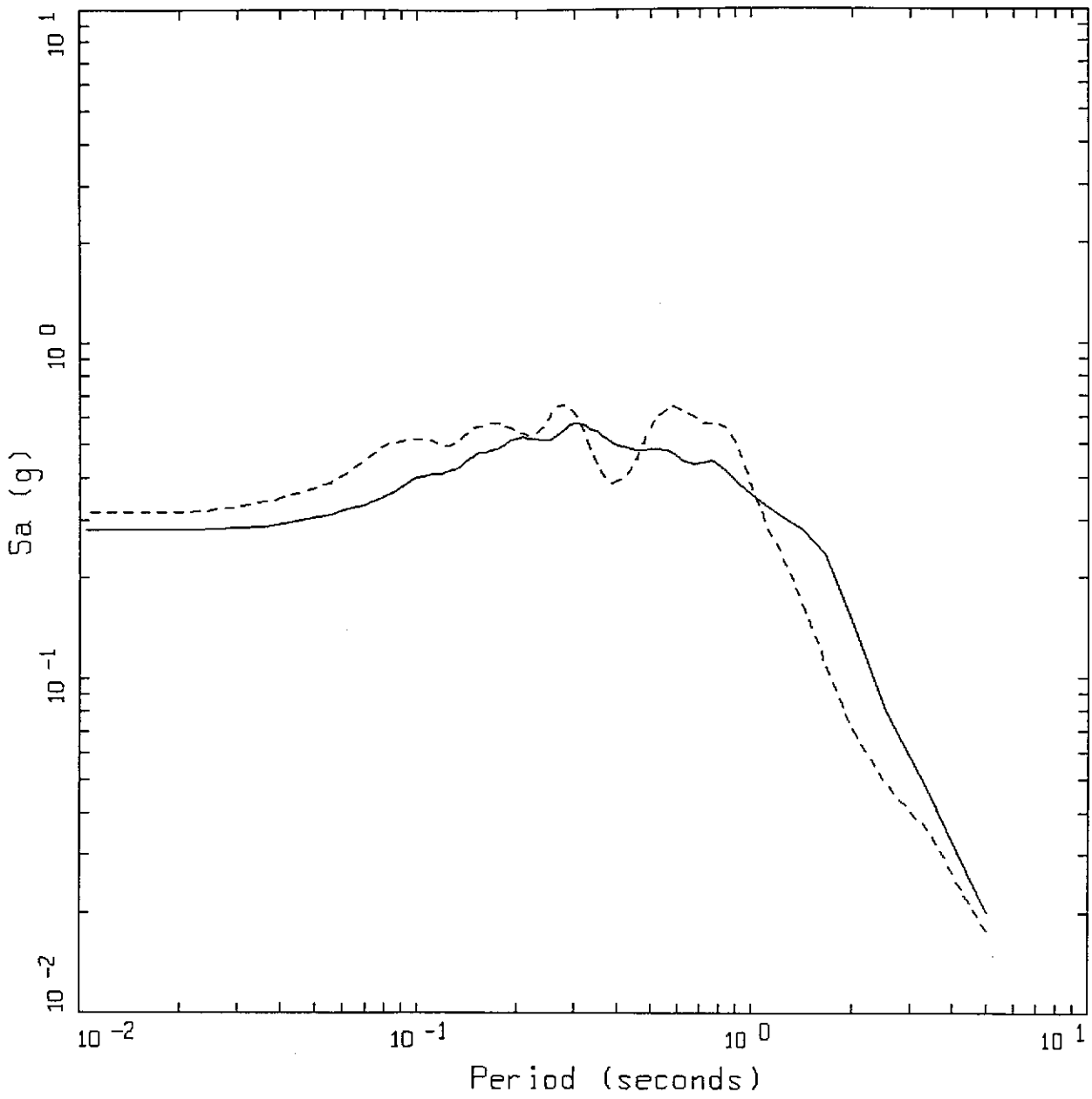
LEGEND

TA-2, 50TH PERCENTILE, PROFILE VARIATION

TA-18, 50TH PERCENTILE, PROFILE VARIATION

TA-41, 50TH PERCENTILE, PROFILE VARIATION

Project No. 91C0509	Los Alamos Seismic Hazards	AVERAGE RESPONSE SPECTRA FOR M_W 5.9 EARTHQUAKE AT 6 KM AT CANYON SITES	Figure 8-20
Woodward-Clyde Federal Services			

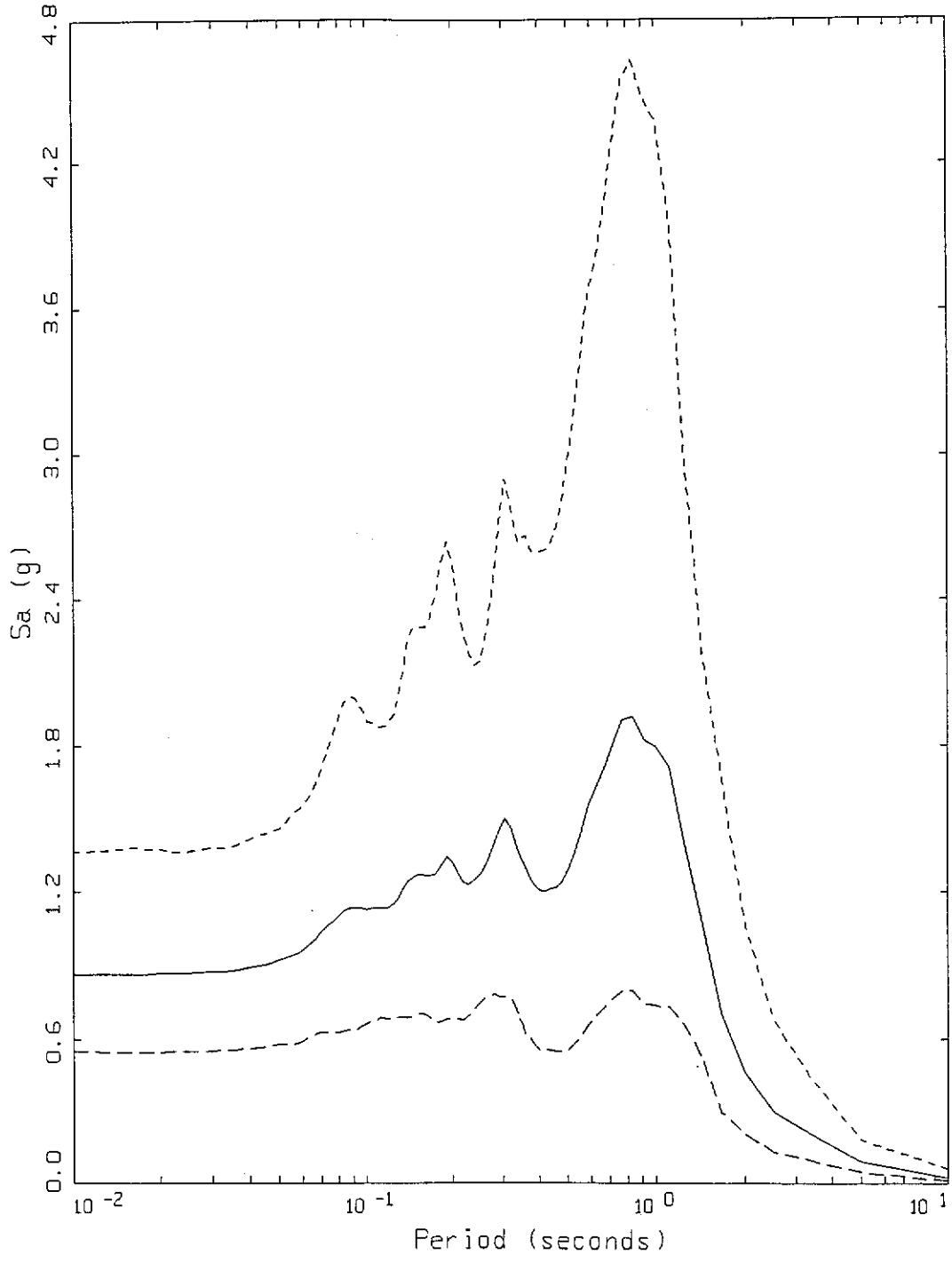


Legend:

——— Average of Mesa Sites

- - - - - Average of Canyon Sites

Project No. 91C0509	Los Alamos Seismic Hazards	AVERAGE RESPONSE SPECTRA FOR M_W 5.9 EARTHQUAKE AT 6 KM AT CANYON AND MESA TOP SITES	Figure 8-21
Woodward-Clyde Federal Services			



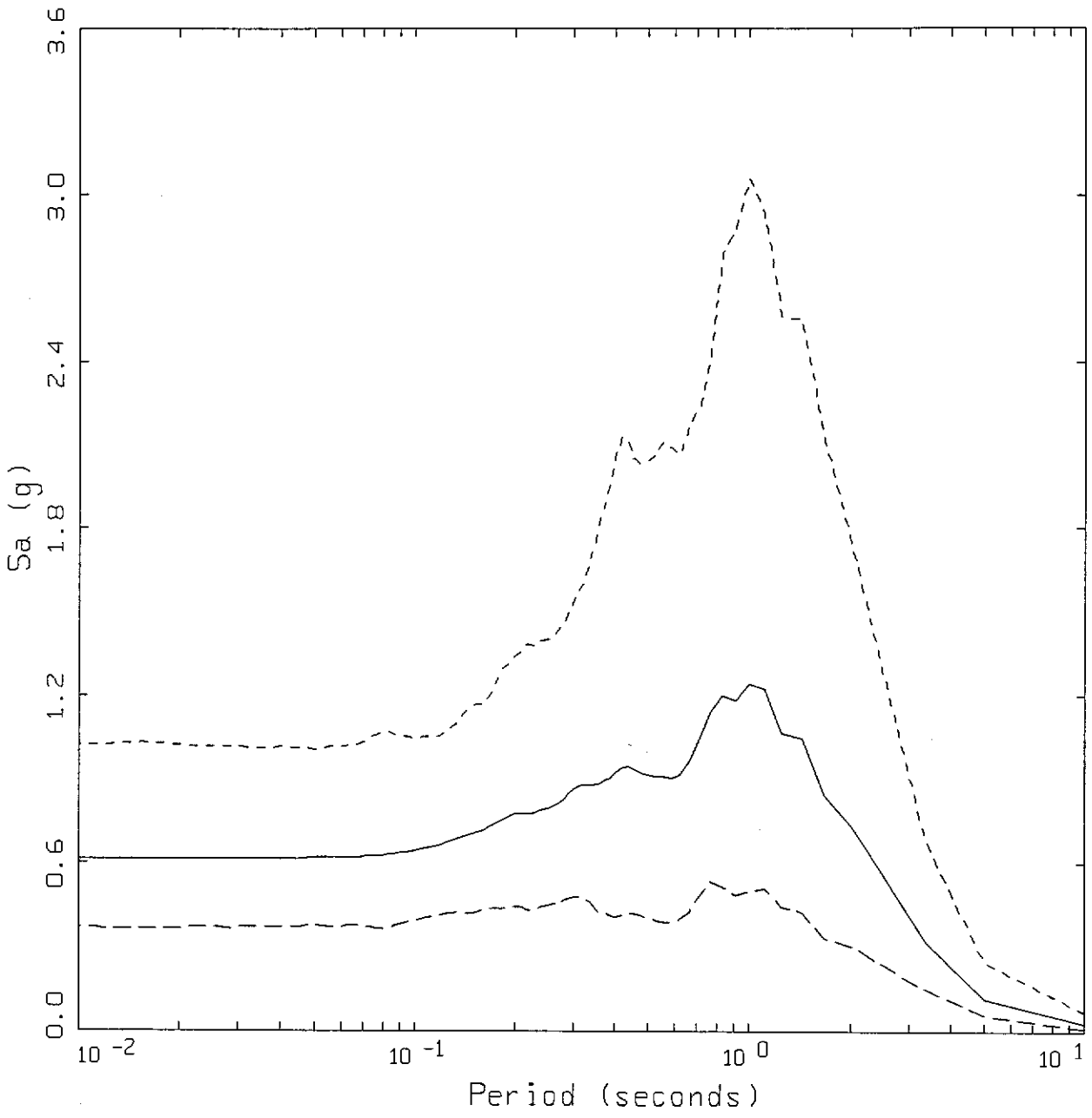
LEGEND

- - - - - 5 %, 84th PERCENTILE, PARAMETRIC + MODELING UNCERTAINTY, AMAX = 1.36 g

——— 5 %, 50th PERCENTILE, PARAMETRIC + MODELING UNCERTAINTY, AMAX = 0.87 g

— — — — 5 %, 16th PERCENTILE, PARAMETRIC + MODELING UNCERTAINTY, AMAX = 0.55 g

Project No. 91C0509	Los Alamos Seismic Hazards	STOCHASTIC ACCELERATION RESPONSE SPECTRA FOR PAJARITO FAULT M_w 7 EARTHQUAKE AT TA-2	Figure 8-22
Woodward-Clyde Federal Services			



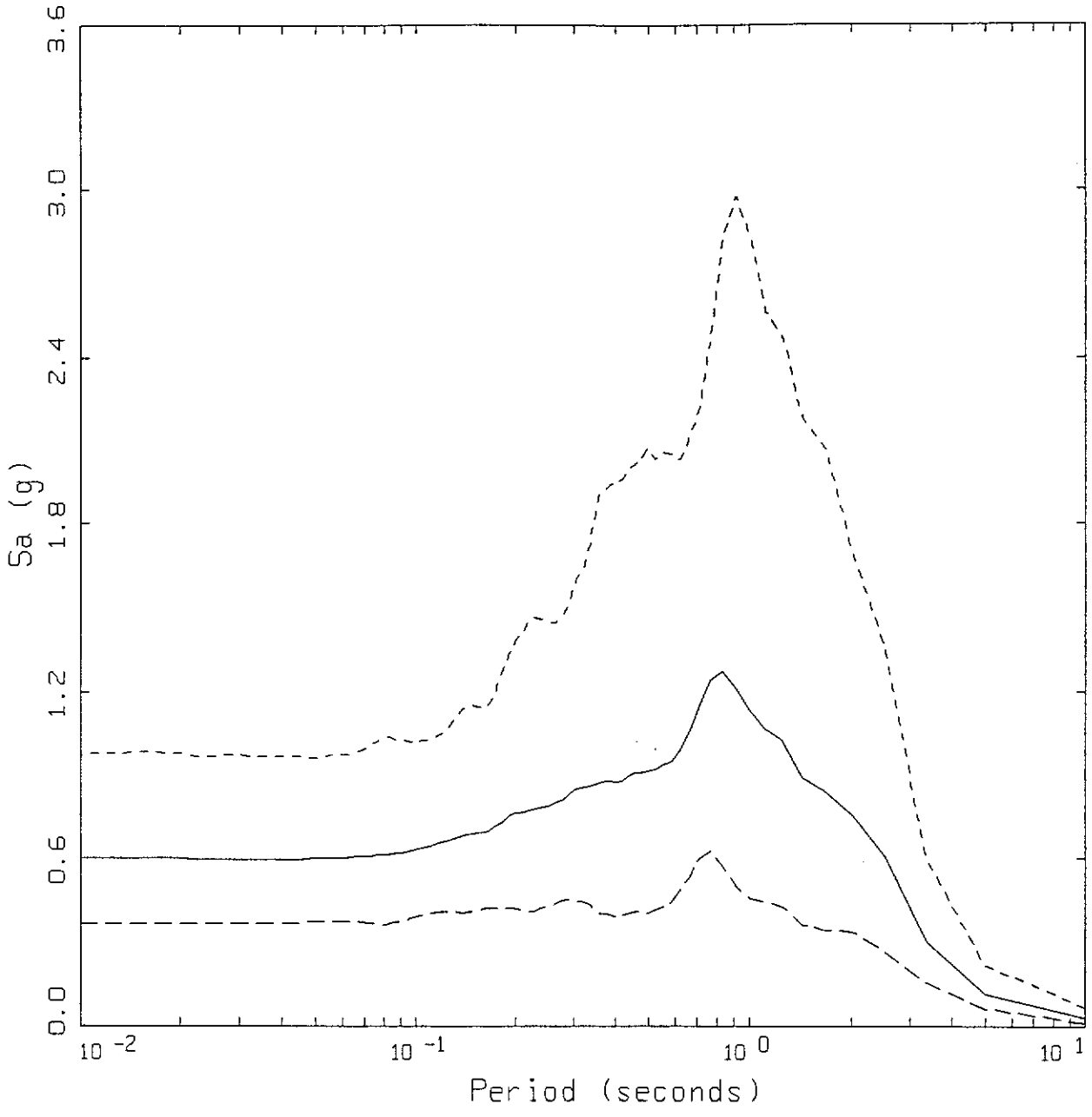
LEGEND

- - - - - 5 %, 84th PERCENTILE, PARAMETRIC + MODELING UNCERTAINTY, AMAX = 1.02 g

——— 5 %, 50th PERCENTILE, PARAMETRIC + MODELING UNCERTAINTY, AMAX = 0.62 g

— — — 5 %, 16th PERCENTILE, PARAMETRIC + MODELING UNCERTAINTY, AMAX = 0.37 g

Project No. 91C0509	Los Alamos Seismic Hazards	STOCHASTIC ACCELERATION RESPONSE SPECTRA FOR PAJARITO FAULT M_w 7 EARTHQUAKE AT TA-3	Figure 8-23
Woodward-Clyde Federal Services			



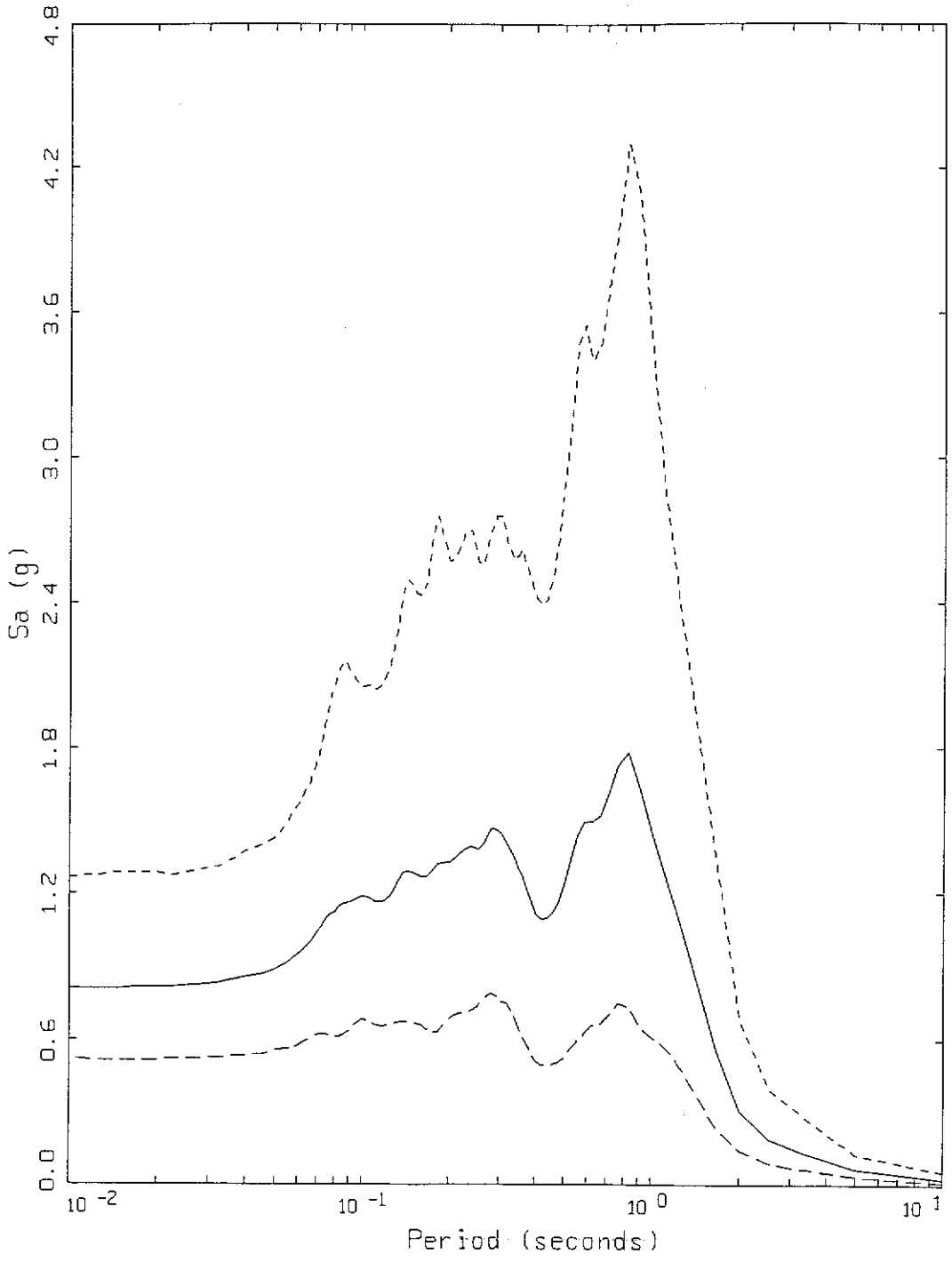
LEGEND

- - - - - 5 %, 84th PERCENTILE, PARAMETRIC + MODELING UNCERTAINTY, AMAX = 0.97 g

——— 5 %, 50th PERCENTILE USING ALL MESA PROFILES, AMAX = 0.60 g

– – – – 5 %, 16th PERCENTILE, PARAMETRIC + MODELING UNCERTAINTY, AMAX = 0.37 g

Project No. 91C0509	Los Alamos Seismic Hazards	STOCHASTIC ACCELERATION RESPONSE SPECTRA FOR PAJARITO FAULT M_w 7 EARTHQUAKE AT TA-16	Figure 8-24
Woodward-Clyde Federal Services			



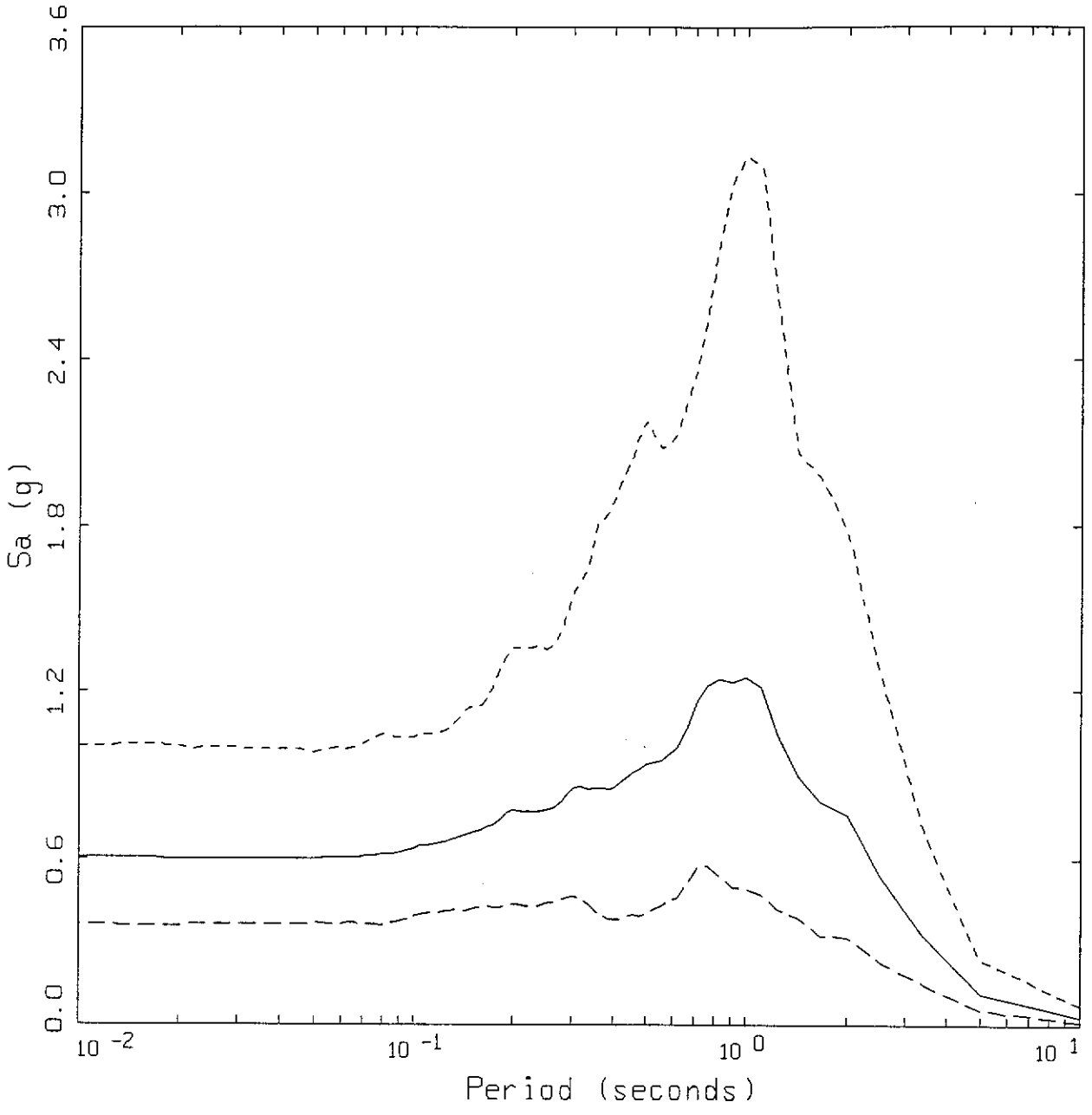
LEGEND

- - - - - 5 %, 84th PERCENTILE, PARAMETRIC + MODELING UNCERTAINTY, AMAX = 1.27 g

——— 5 %, 50th PERCENTILE, PARAMETRIC + MODELING UNCERTAINTY, AMAX = 0.81 g

— — — — 5 %, 16th PERCENTILE, PARAMETRIC + MODELING UNCERTAINTY, AMAX = 0.52 g

Project No. 91C0509	Los Alamos Seismic Hazards	STOCHASTIC ACCELERATION RESPONSE SPECTRA FOR PAJARITO FAULT M_w 7 EARTHQUAKE AT TA-18	Figure 8-25
Woodward-Clyde Federal Services			



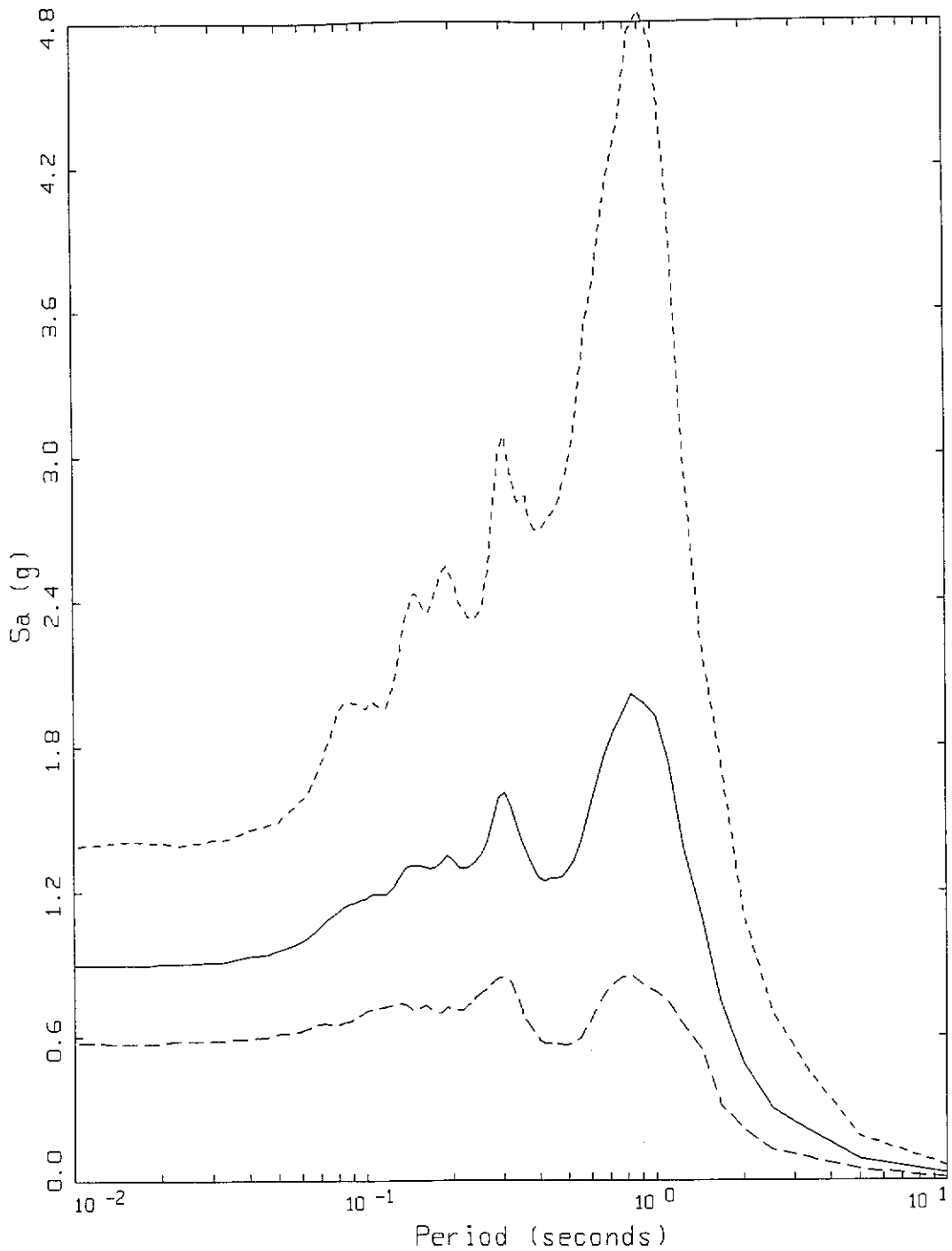
LEGEND

- - - - - 5 %, 84th PERCENTILE, PARAMETRIC + MODELING UNCERTAINTY, AMAX = 1.00 g

——— 5 %, 50th PERCENTILE, PARAMETRIC + MODELING UNCERTAINTY, AMAX = 0.61 g

— — — 5 %, 16th PERCENTILE, PARAMETRIC + MODELING UNCERTAINTY, AMAX = 0.37 g

Project No. 91C0509	Los Alamos Seismic Hazards	STOCHASTIC ACCELERATION RESPONSE SPECTRA FOR PAJARITO FAULT M_w 7 EARTHQUAKE AT TA-21	Figure 8-26
Woodward-Clyde Federal Services			



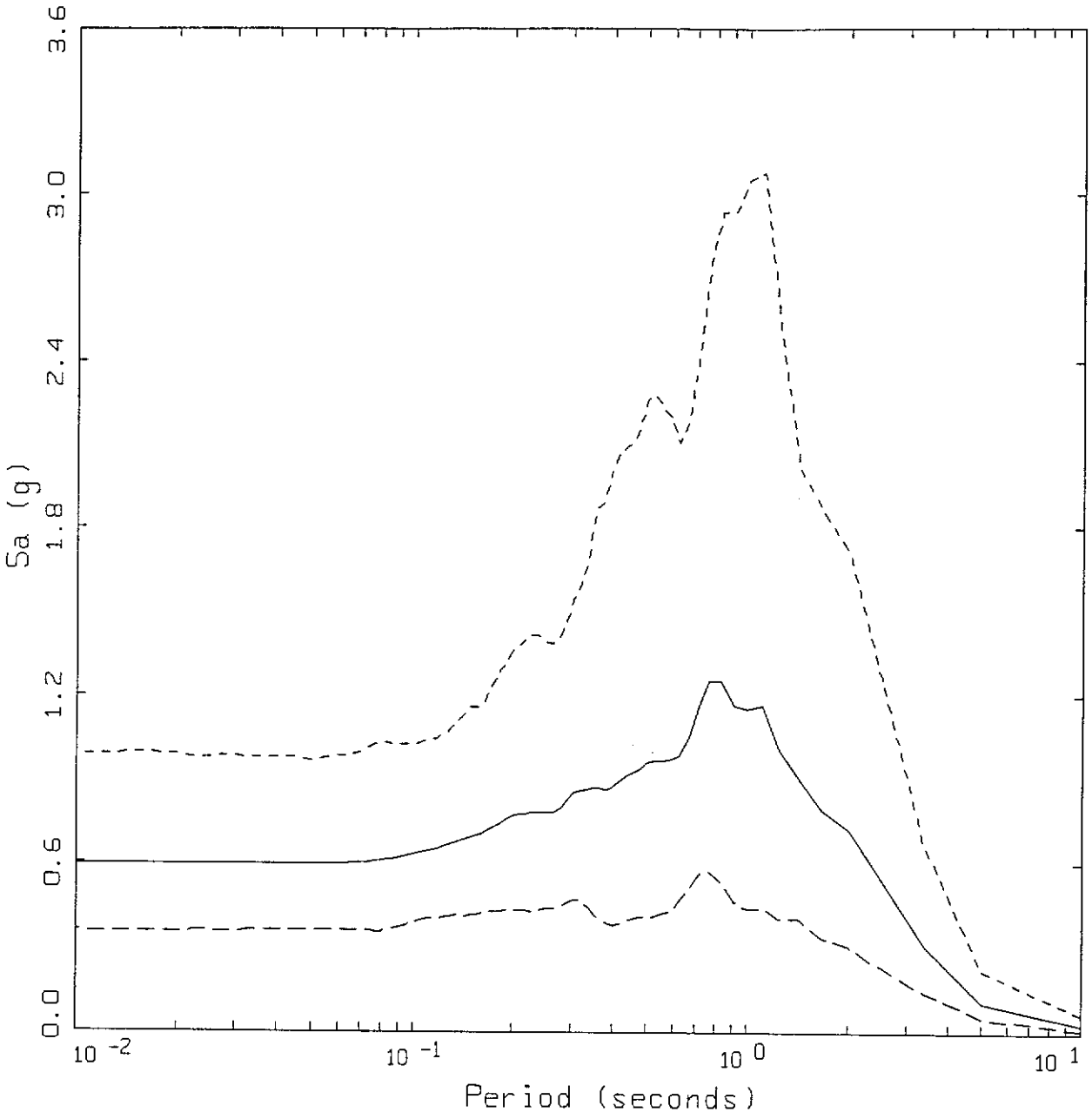
LEGEND

- - - - - 5 %, 84th PERCENTILE, PARAMETRIC + MODELING UNCERTAINTY, AMAX = 1.39 g

——— 5 %, 50th PERCENTILE, PARAMETRIC + MODELING UNCERTAINTY, AMAX = 0.90 g

— — — 5 %, 16th PERCENTILE, PARAMETRIC + MODELING UNCERTAINTY, AMAX = 0.58 g

Project No. 91C0509	Los Alamos Seismic Hazards	STOCHASTIC ACCELERATION RESPONSE SPECTRA FOR PAJARITO FAULT M_w 7 EARTHQUAKE AT TA-41	Figure 8-27
Woodward-Clyde Federal Services			



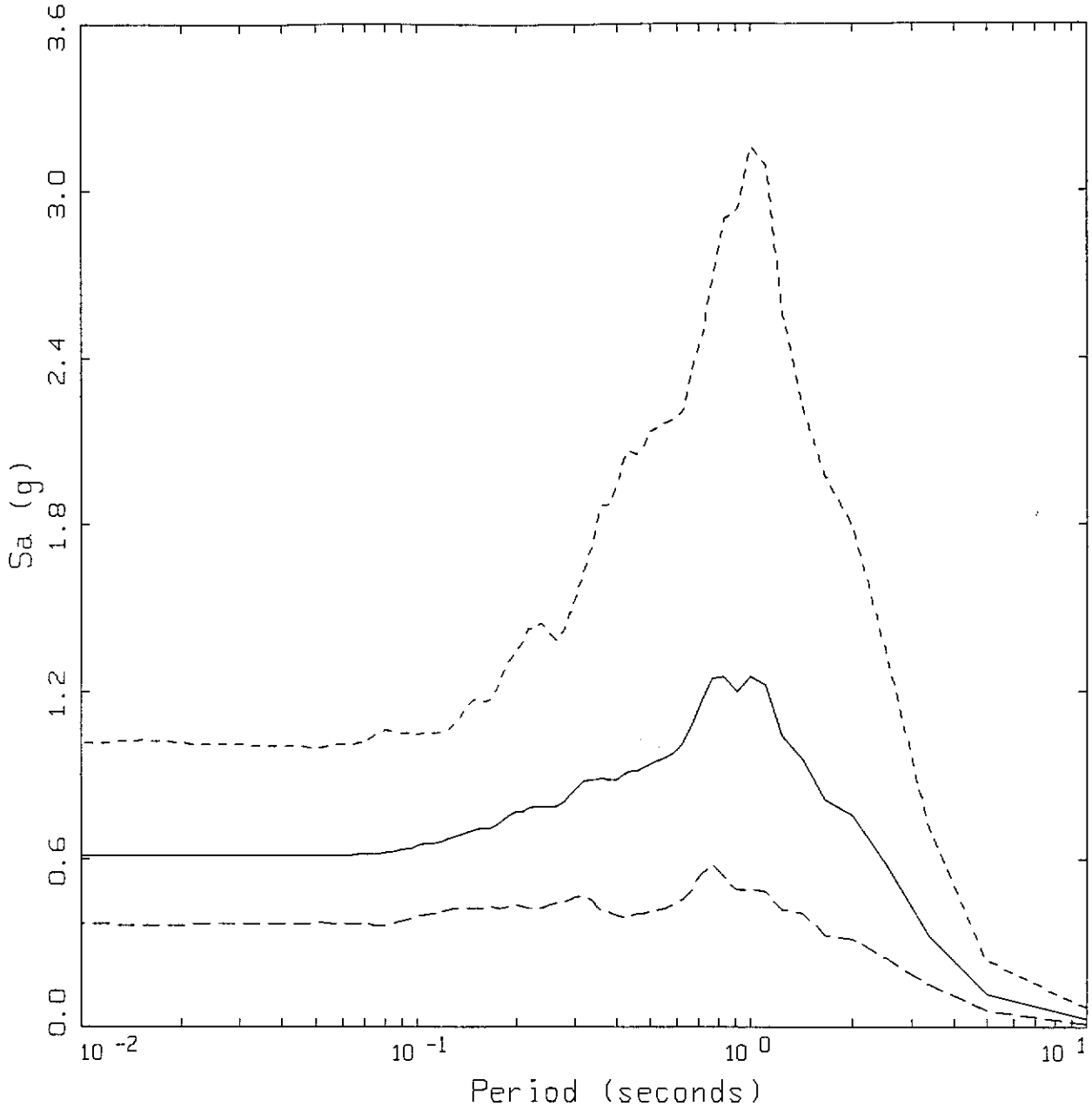
LEGEND

- - - - - 5 %, 84th PERCENTILE, PARAMETRIC + MODELING UNCERTAINTY, AMAX = 0.99 g

——— 5 %, 50th PERCENTILE, PARAMETRIC + MODELING UNCERTAINTY, AMAX = 0.60 g

– – – – 5 %, 16th PERCENTILE, PARAMETRIC + MODELING UNCERTAINTY, AMAX = 0.36 g

Project No. 91C0509	Los Alamos Seismic Hazards	STOCHASTIC ACCELERATION RESPONSE SPECTRA FOR PAJARITO FAULT M_w 7 EARTHQUAKE AT TA-46	Figure 8-28
Woodward-Clyde Federal Services			



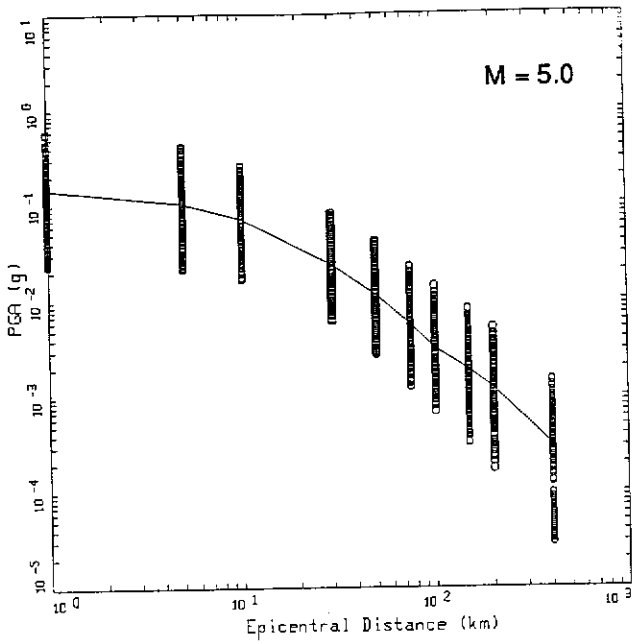
LEGEND

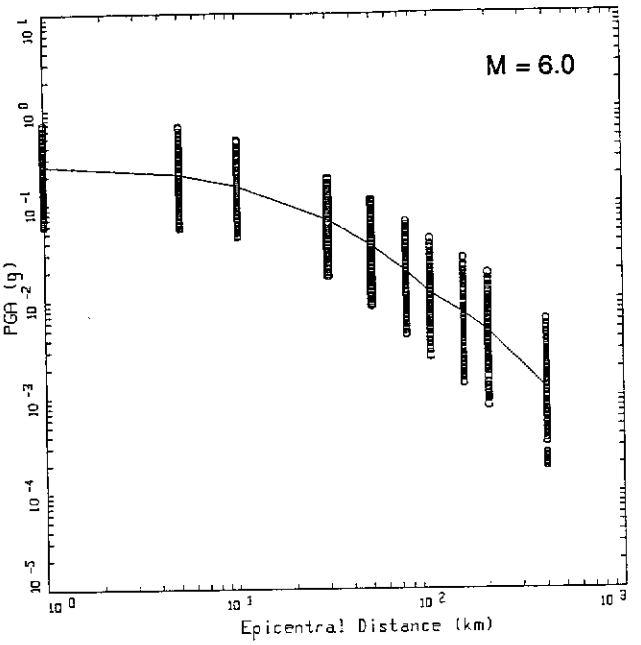
- - - - - 5 %, 84th PERCENTILE, PARAMETRIC + MODELING UNCERTAINTY, AMAX = 1.01 g

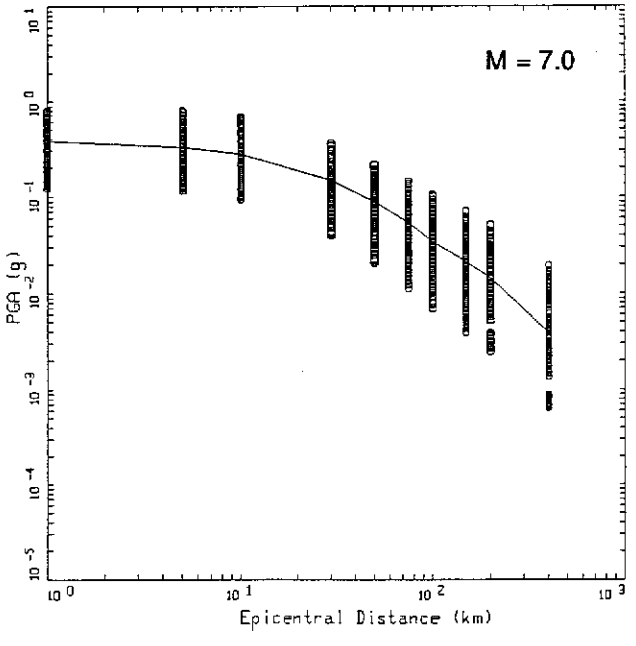
——— 5 %, 50th PERCENTILE, PARAMETRIC + MODELING UNCERTAINTY, AMAX = 0.62 g

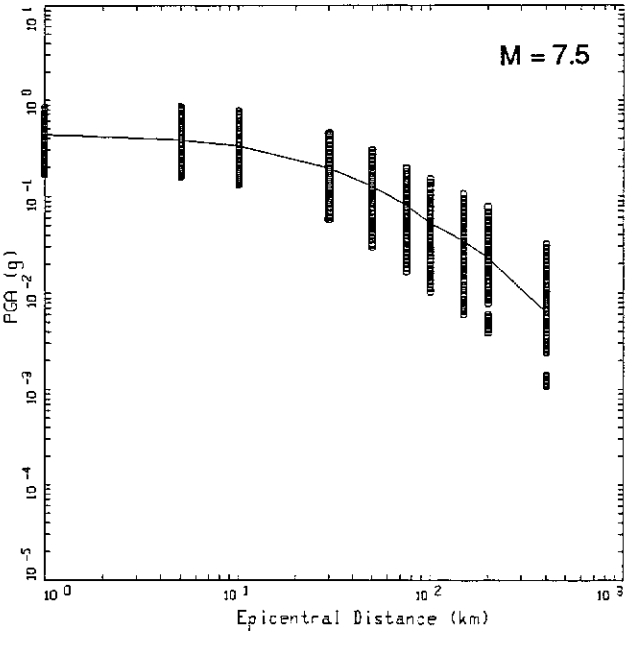
— — — 5 %, 16th PERCENTILE, PARAMETRIC + MODELING UNCERTAINTY, AMAX = 0.37 g

Project No. 91C0509	Los Alamos Seismic Hazards	STOCHASTIC ACCELERATION RESPONSE SPECTRA FOR PAJARITO FAULT M_w 7 EARTHQUAKE AT TA-55	Figure 8-29
Woodward-Clyde Federal Services			







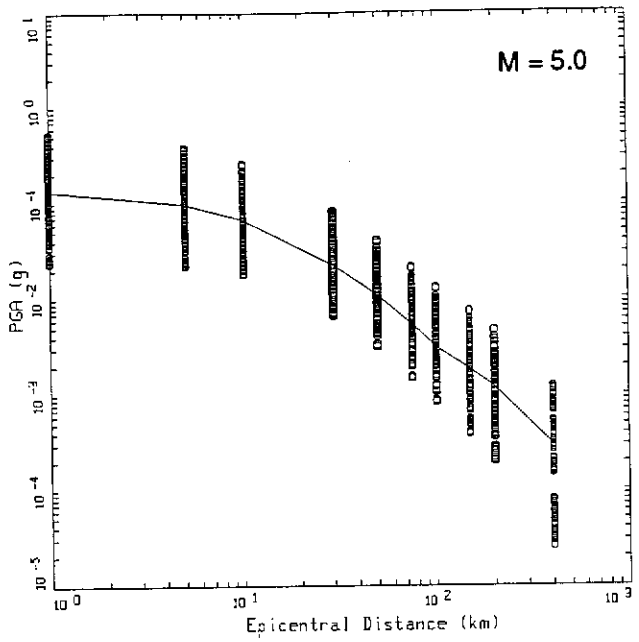


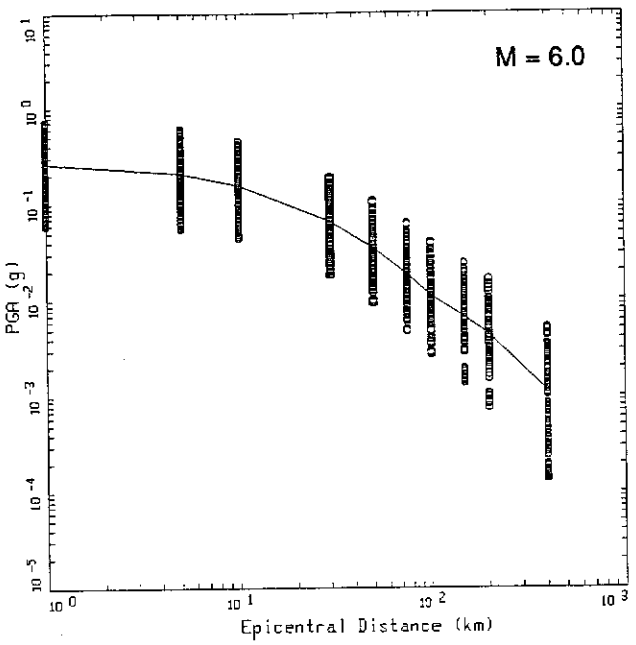
LEGEND

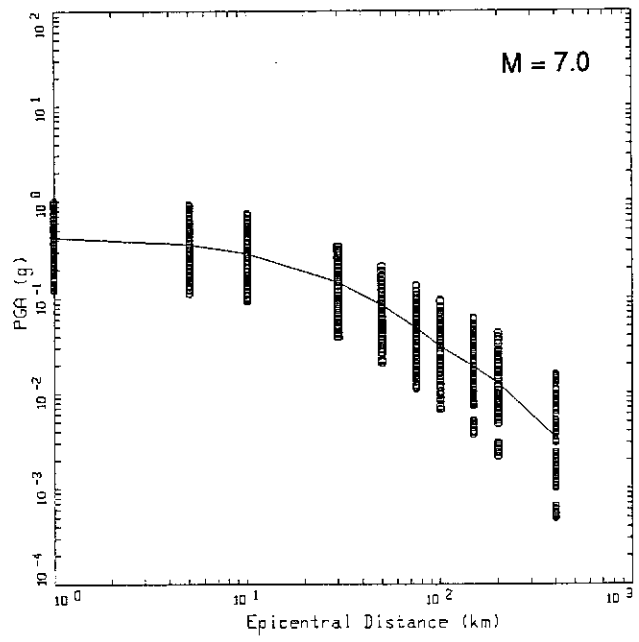
o Data

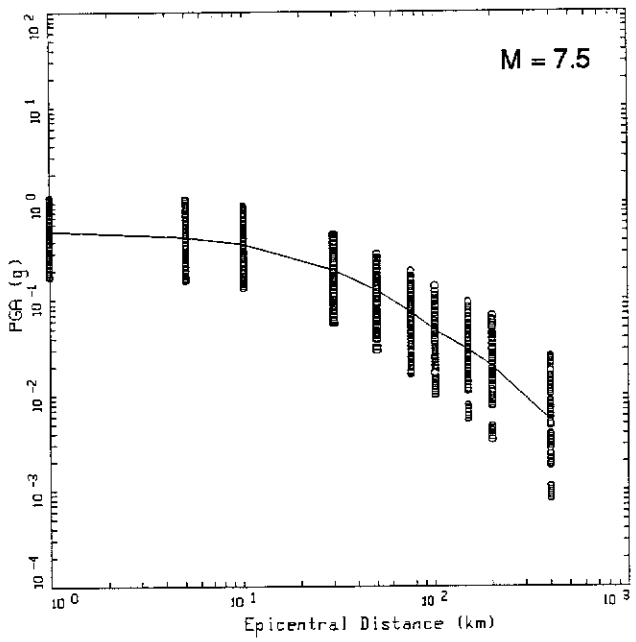
—— Regression of Data

Project No. 91C0509	Los Alamos Seismic Hazards	STOCHASTIC PEAK ACCELERATION ATTENUATION RELATIONSHIPS FOR MESA TOP SITES	Figure 8-30
Woodward-Clyde Federal Services			







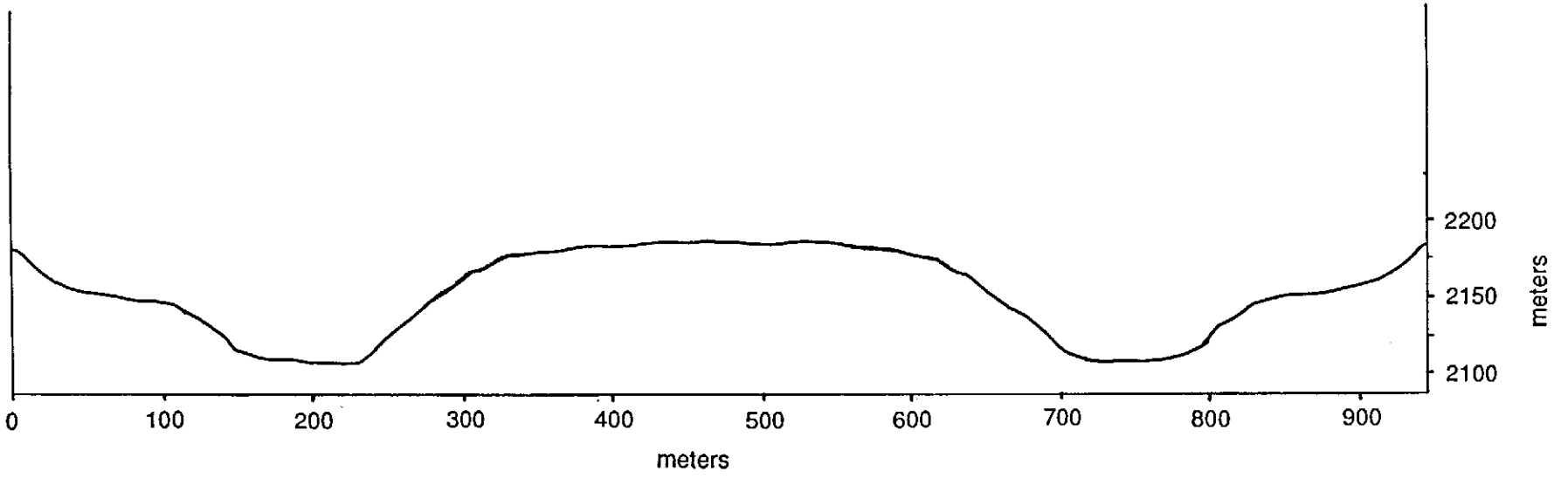


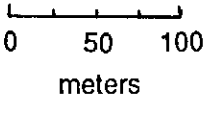
LEGEND

o Data

—— Regression of Data

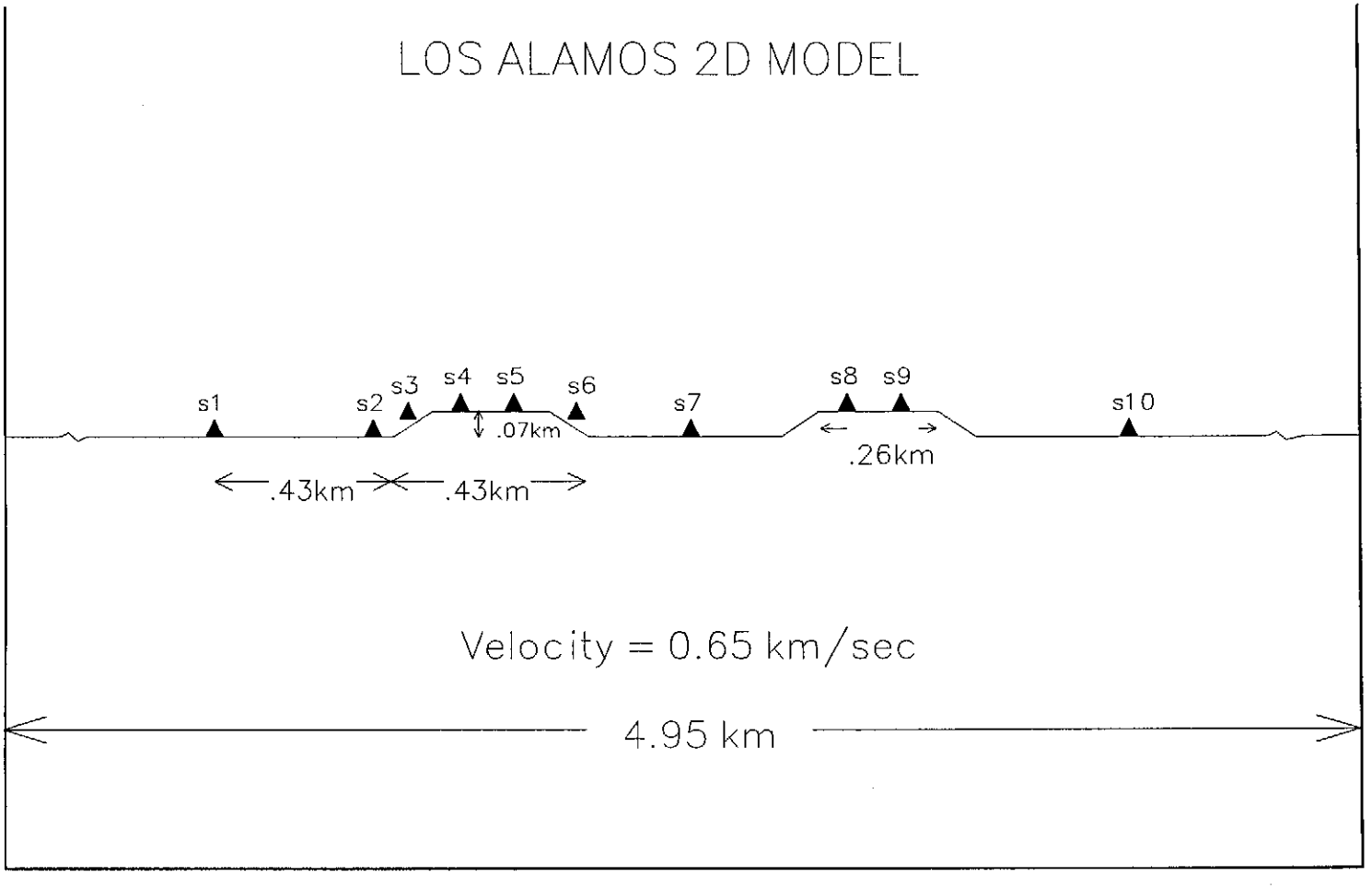
Project No. 91C0509	Los Alamos Seismic Hazards	STOCHASTIC PEAK ACCELERATION ATTENUATION RELATIONSHIPS FOR CANYON SITES	Figure 8-31
Woodward-Clyde Federal Services			



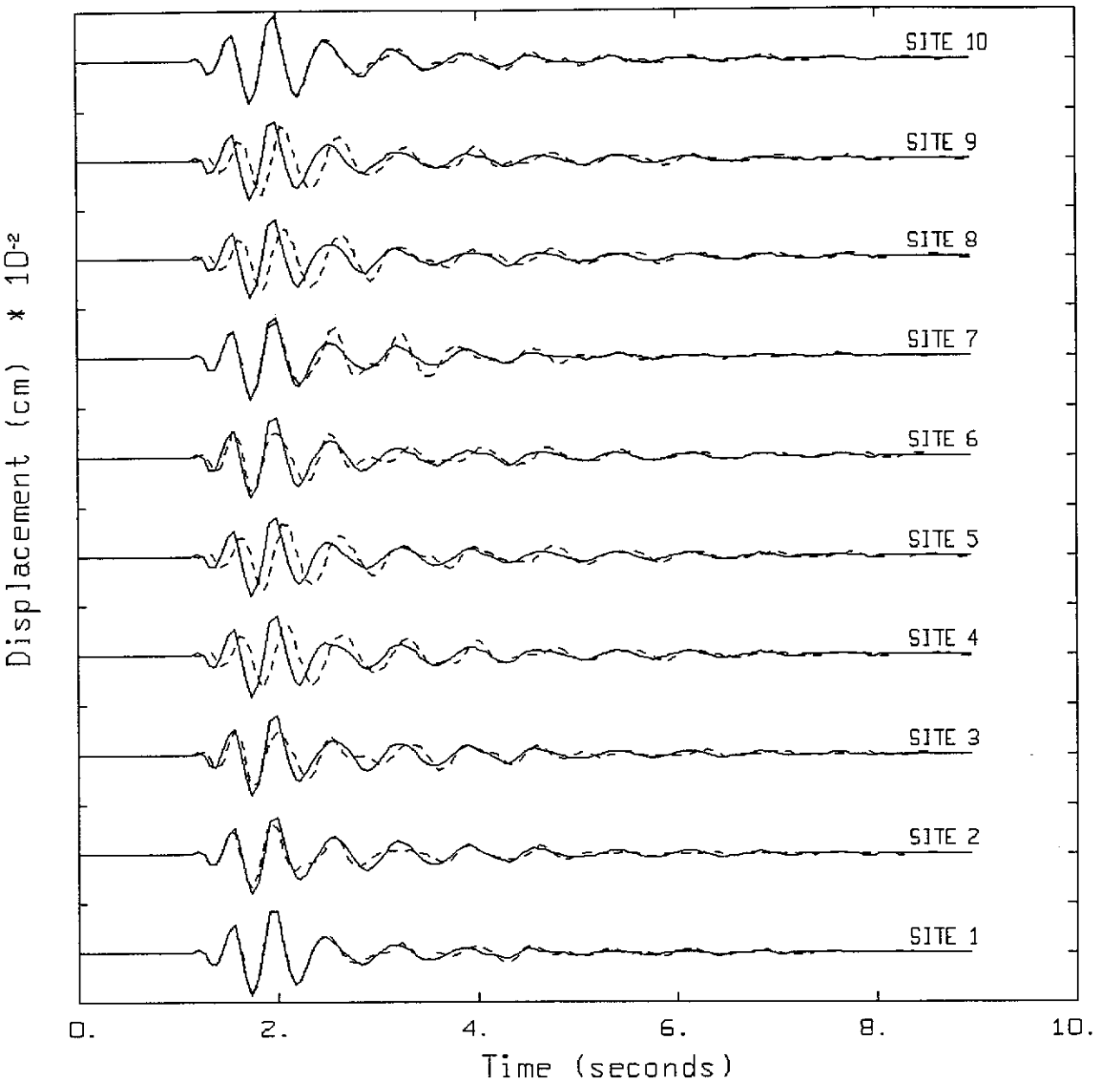


Note: View normal to long axis of a generic mesa.

Project No. 91C0509	Los Alamos Seismic Hazards	GENERALIZED MESA CROSS-SECTION USED IN TOPOGRAPHIC MODELING	Figure 8-32
Woodward-Clyde Federal Services			



Project No. 91C0509	Los Alamos Seismic Hazards	TWO-DIMENSIONAL MODEL USED IN THE FINITE DIFFERENCE SIMULATIONS	Figure 8-33
Woodward-Clyde Federal Services			



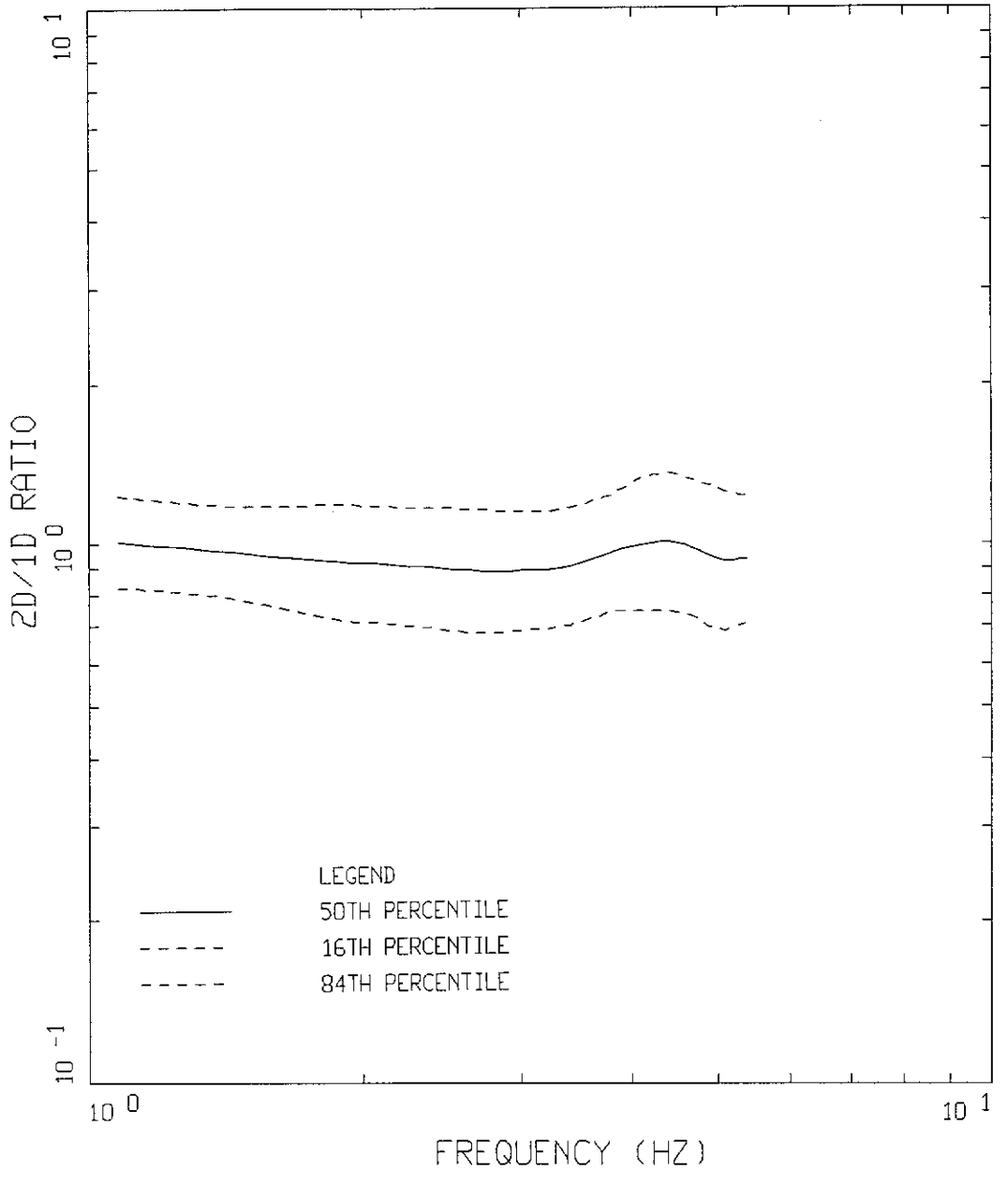
Legend

——— 1-D Structure

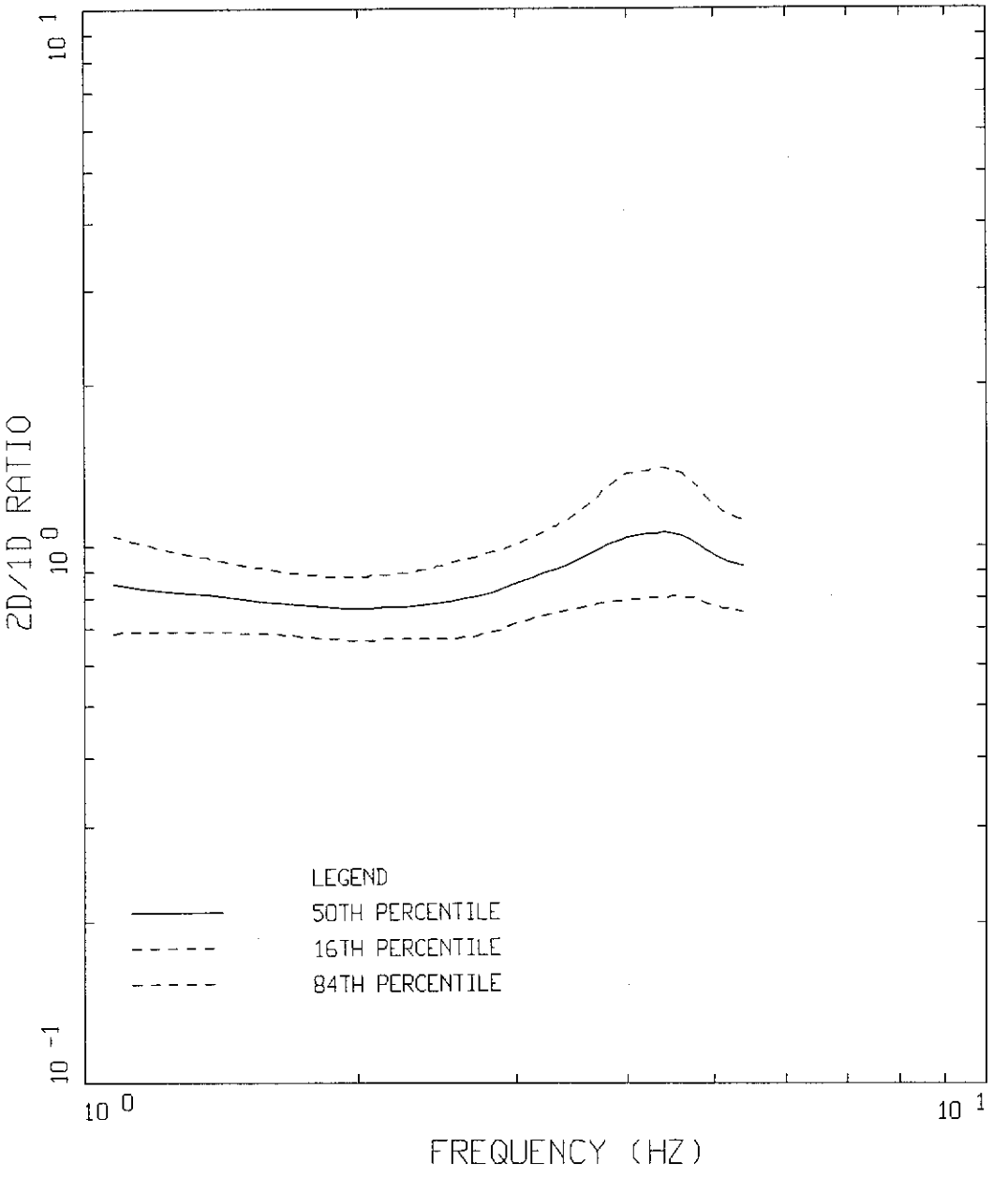
— — — 2-D Structure

Note: Sites 3, 4, 5, 6, 8, and 9 are mesa sites and reflect a slight delay in arrival.

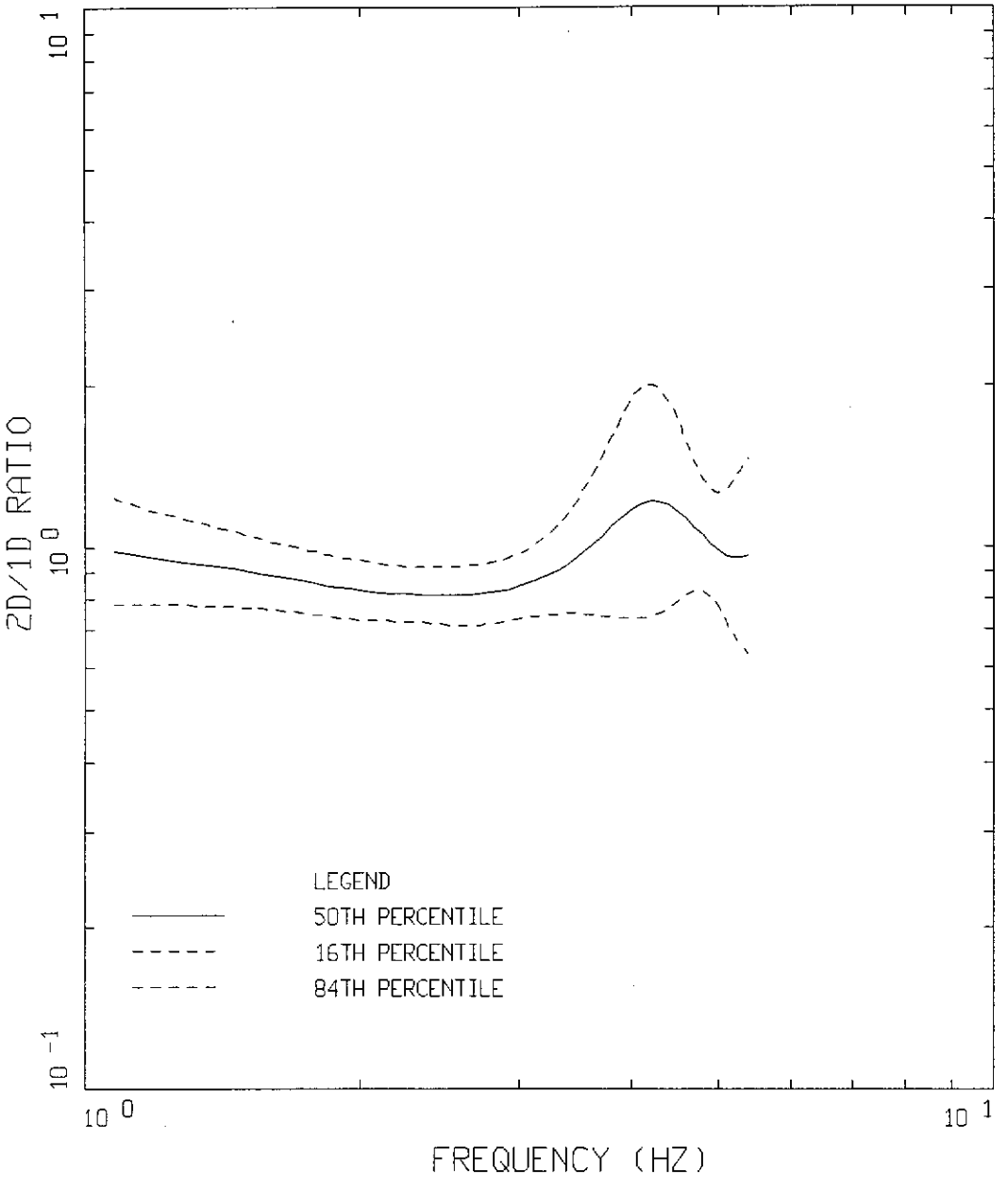
Project No. 91C0509	Los Alamos Seismic Hazards	SIMULATED DISPLACEMENT TIME HISTORIES AT SITES 1-10 FOR A VERTICALLY PROPAGATING PLANE SH WAVE	Figure 8-34
Woodward-Clyde Federal Services			



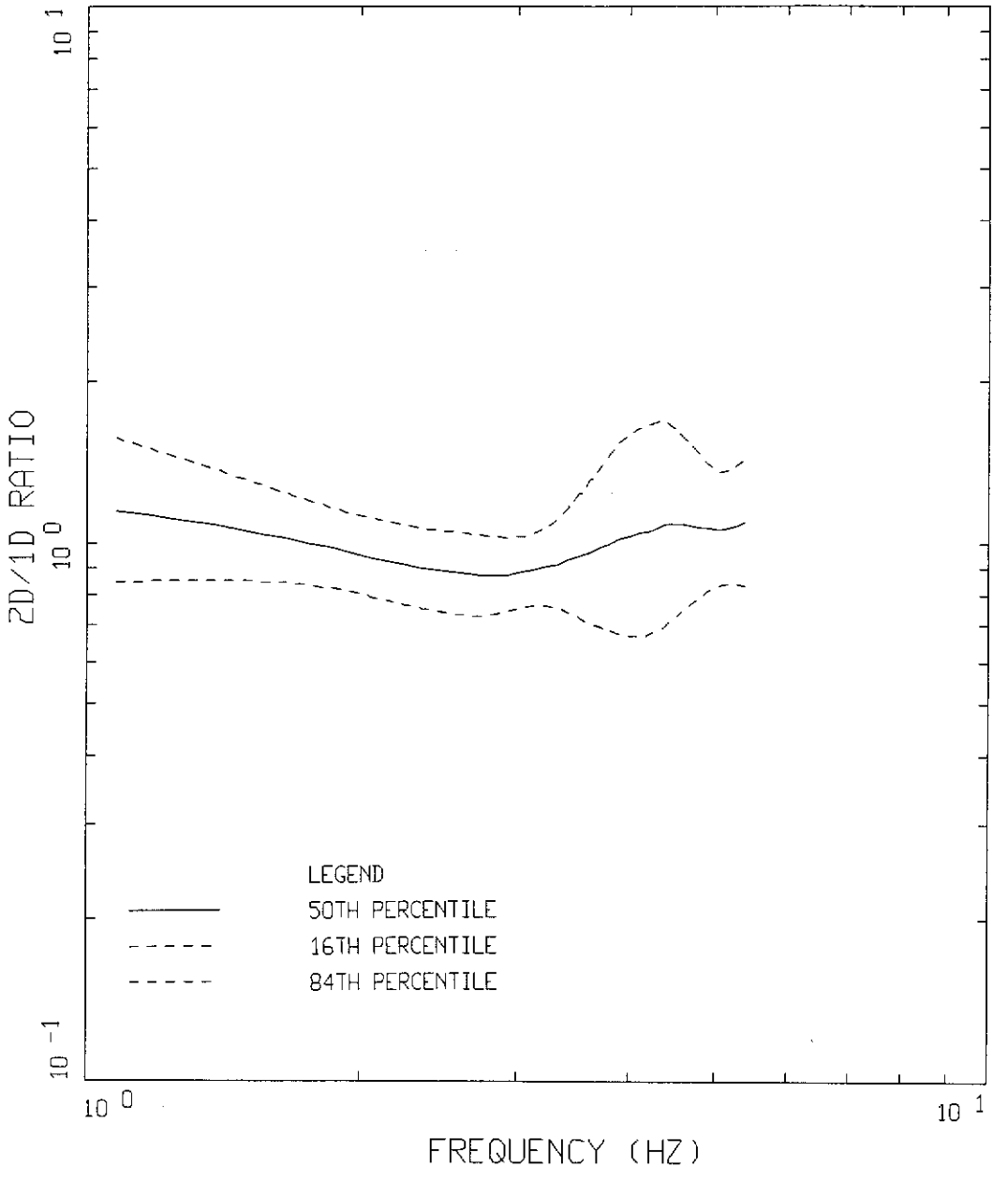
Project No. 91C0509	Los Alamos Seismic Hazards	SITE 1 FOURIER AMPLITUDE SPECTRAL RATIO (2D/1D)	Figure 8-35
Woodward-Clyde Federal Services			



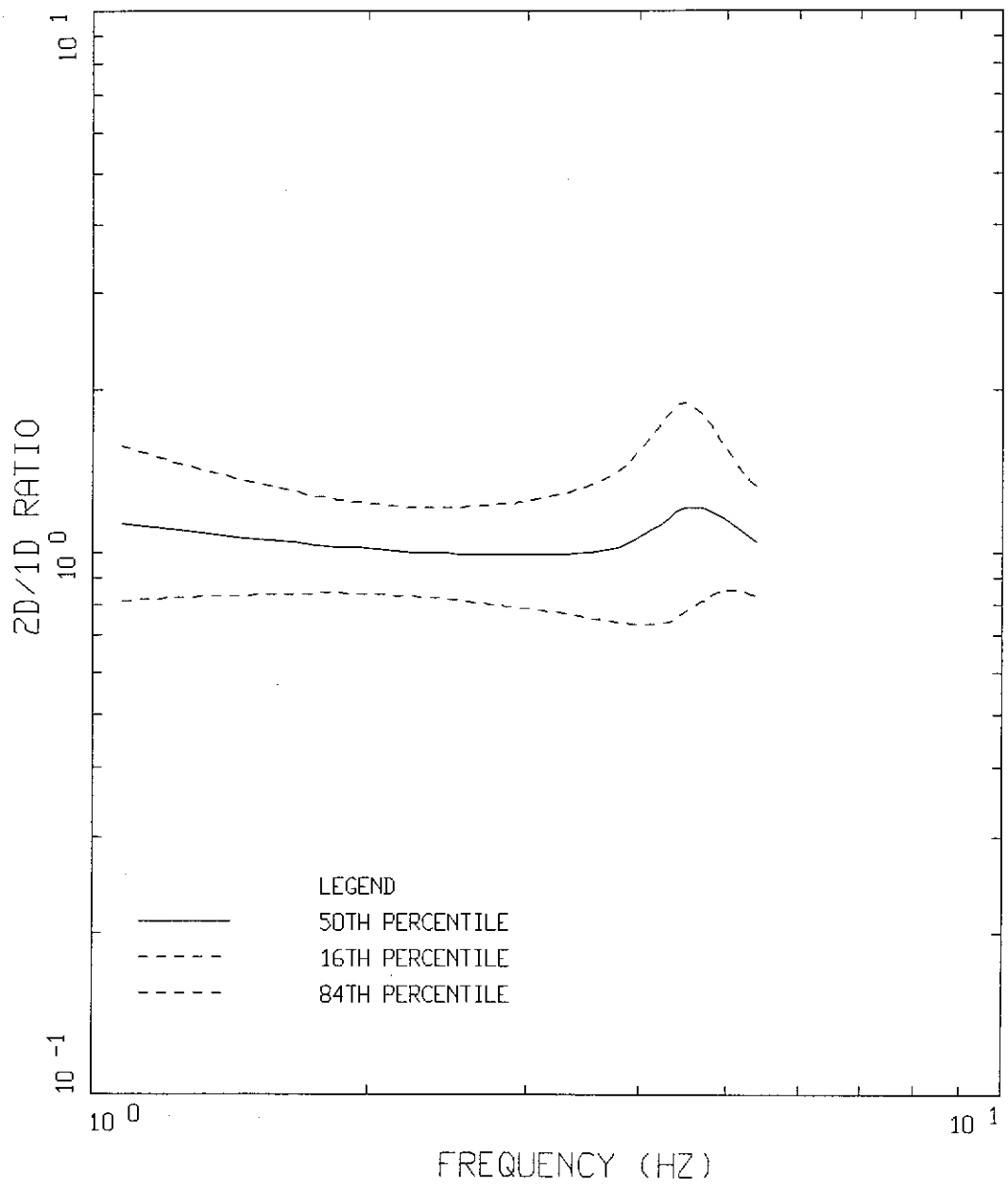
Project No. 91C0509	Los Alamos Seismic Hazards	SITE 2 FOURIER AMPLITUDE SPECTRAL RATIO (2D/1D)	Figure 8-36
Woodward-Clyde Federal Services			



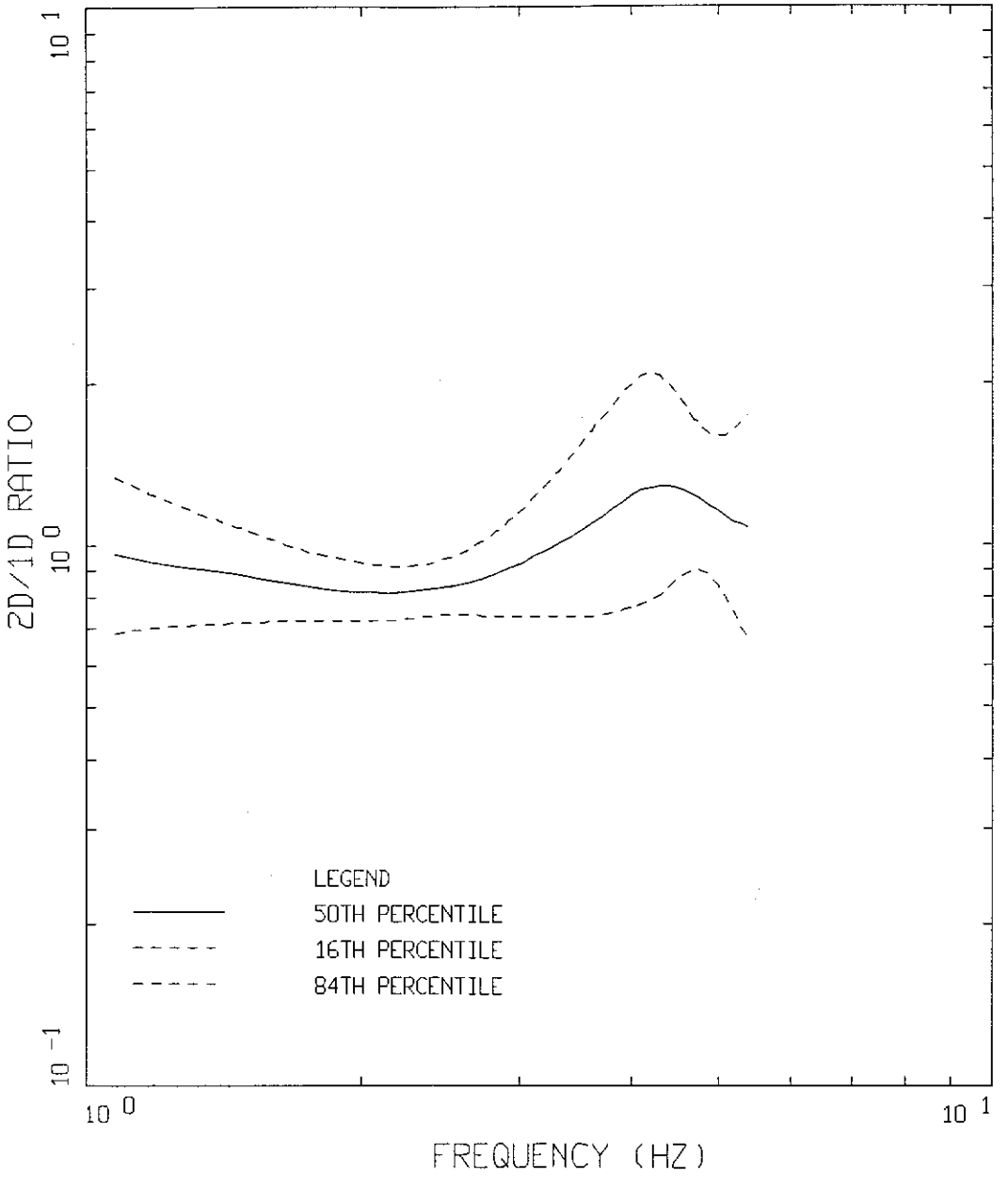
Project No. 91C0509	Los Alamos Seismic Hazards	SITE 3 FOURIER AMPLITUDE SPECTRAL RATIO (2D/1D)	Figure 8-37
Woodward-Clyde Federal Services			



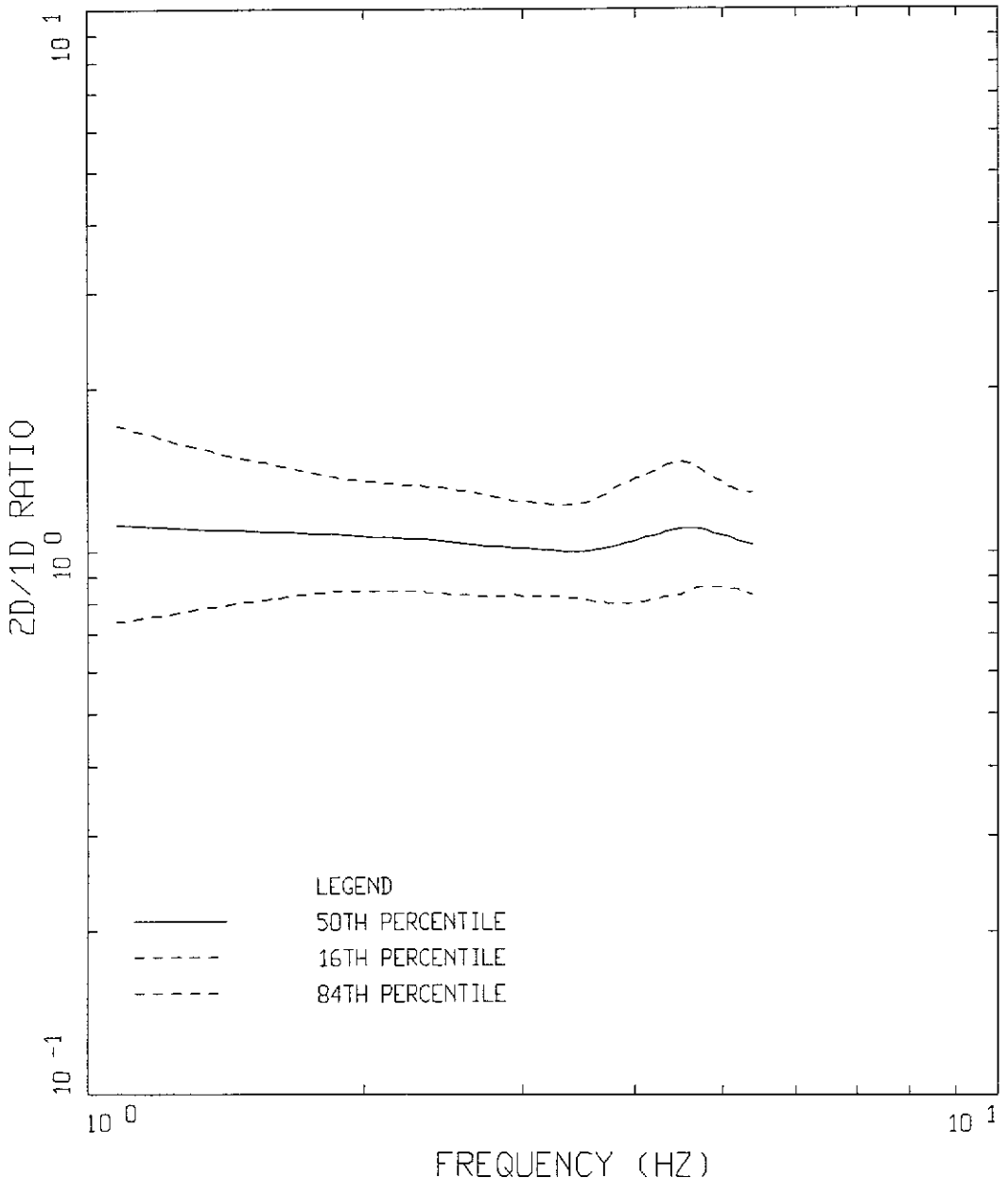
Project No. 91C0509	Los Alamos Seismic Hazards	SITE 4 FOURIER AMPLITUDE SPECTRAL RATIO (2D/1D)	Figure 8-38
Woodward-Clyde Federal Services			



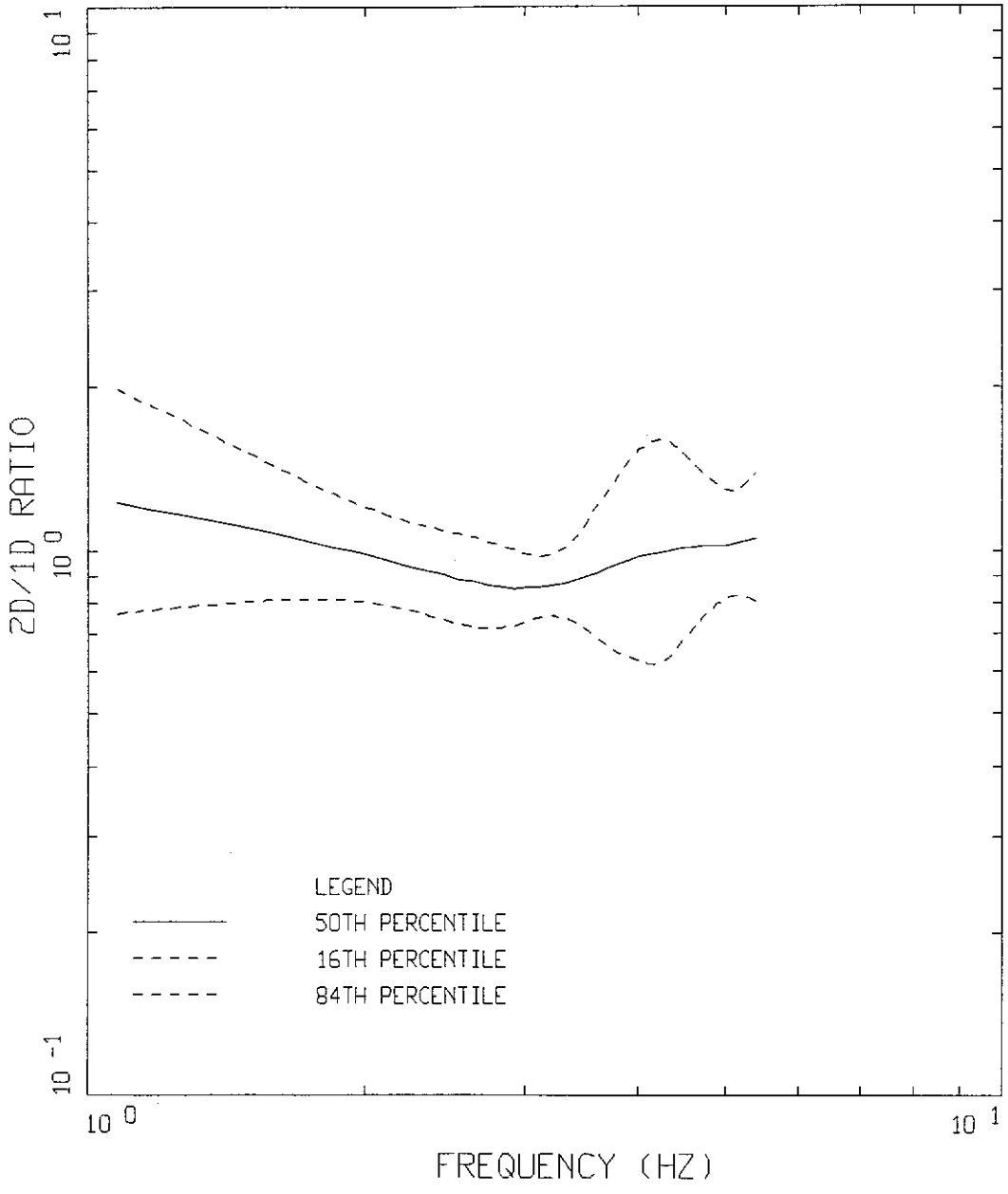
Project No. 91C0509	Los Alamos Seismic Hazards	SITE 5 FOURIER AMPLITUDE SPECTRAL RATIO (2D/1D)	Figure 8-39
Woodward-Clyde Federal Services			



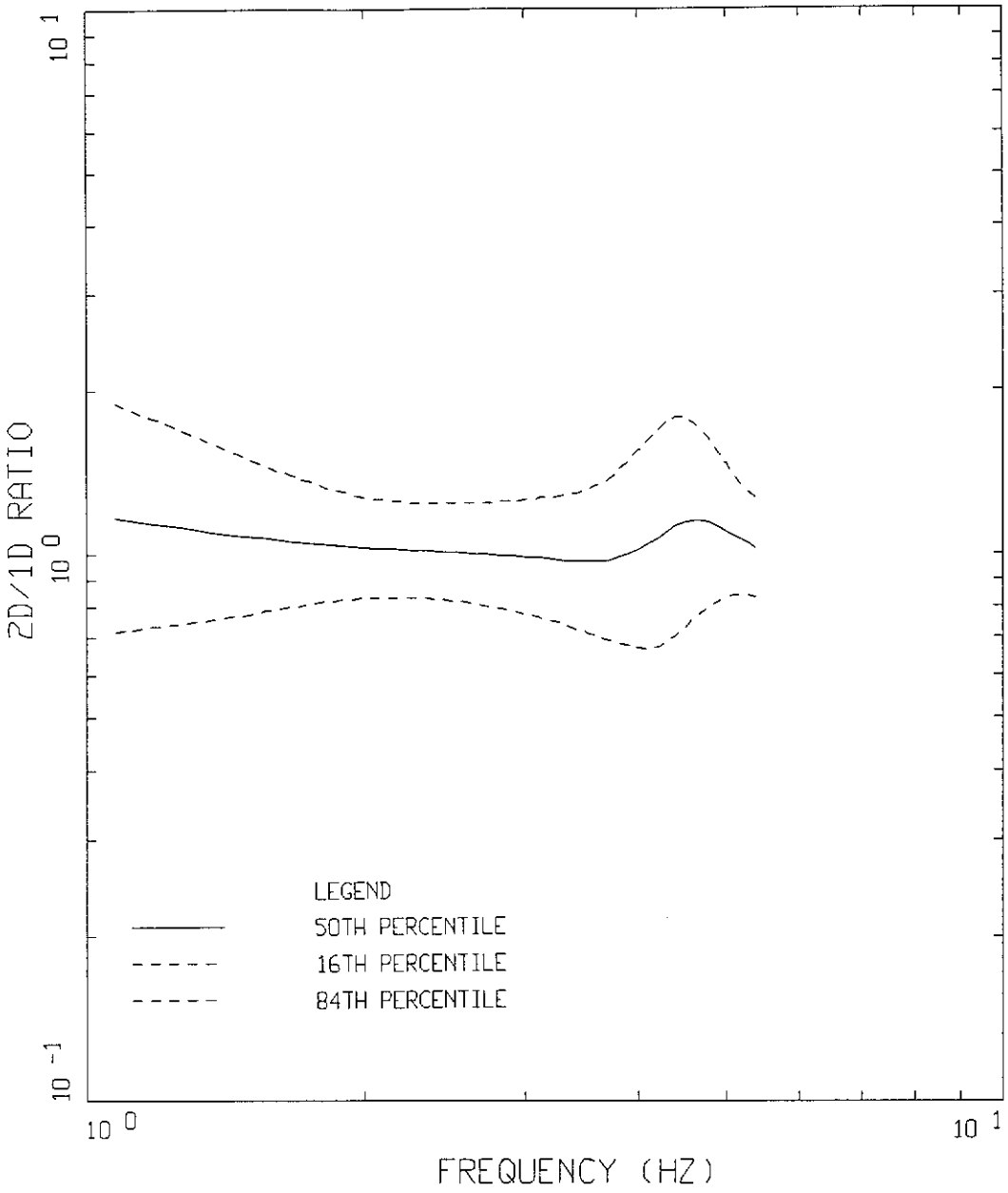
Project No. 91C0509	Los Alamos Seismic Hazards	SITE 6 FOURIER AMPLITUDE SPECTRAL RATIO (2D/1D)	Figure 8-40
Woodward-Clyde Federal Services			



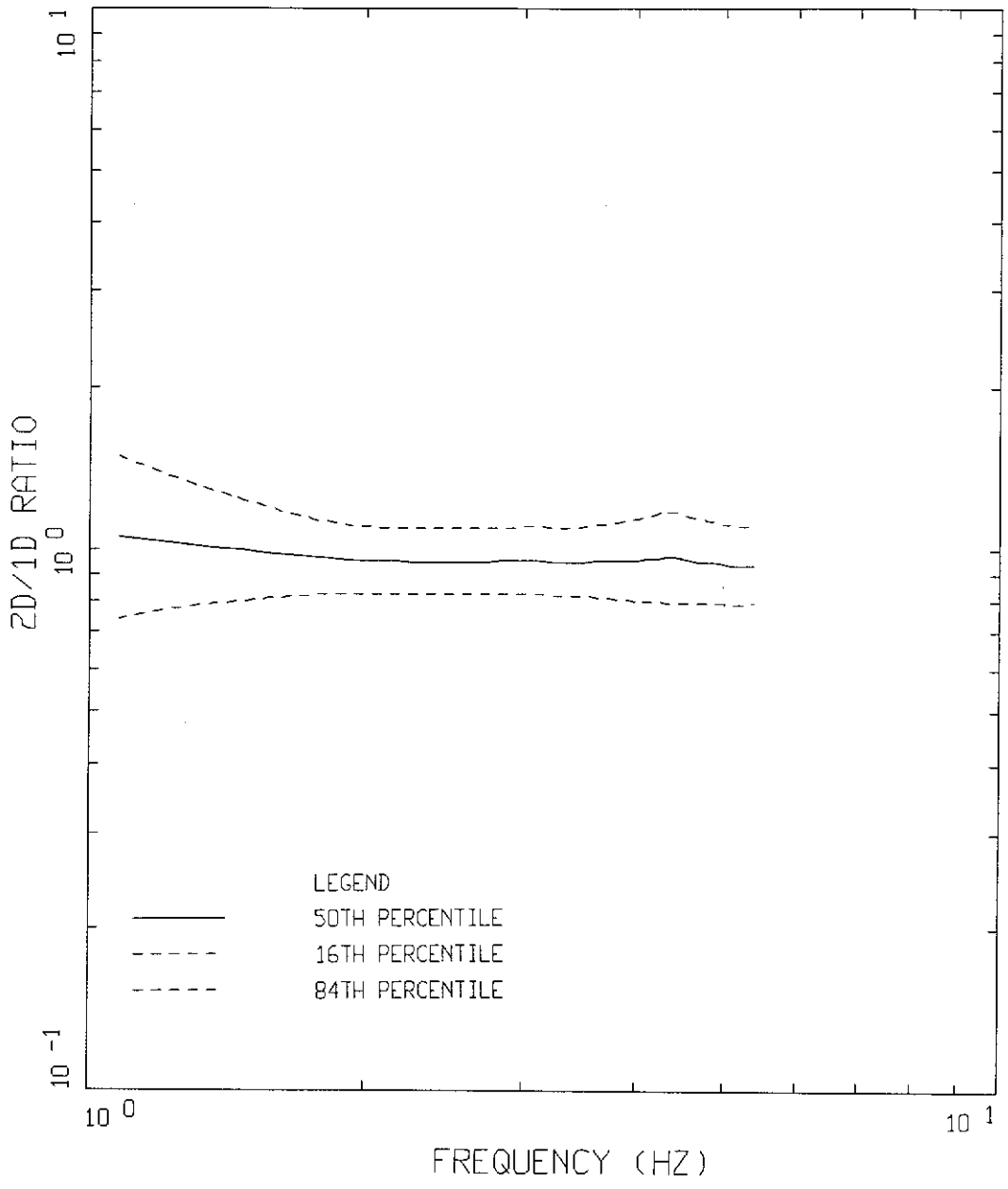
Project No. 91C0509	Los Alamos Seismic Hazards	SITE 7 FOURIER AMPLITUDE SPECTRAL RATIO (2D/1D)	Figure 8-41
Woodward-Clyde Federal Services			



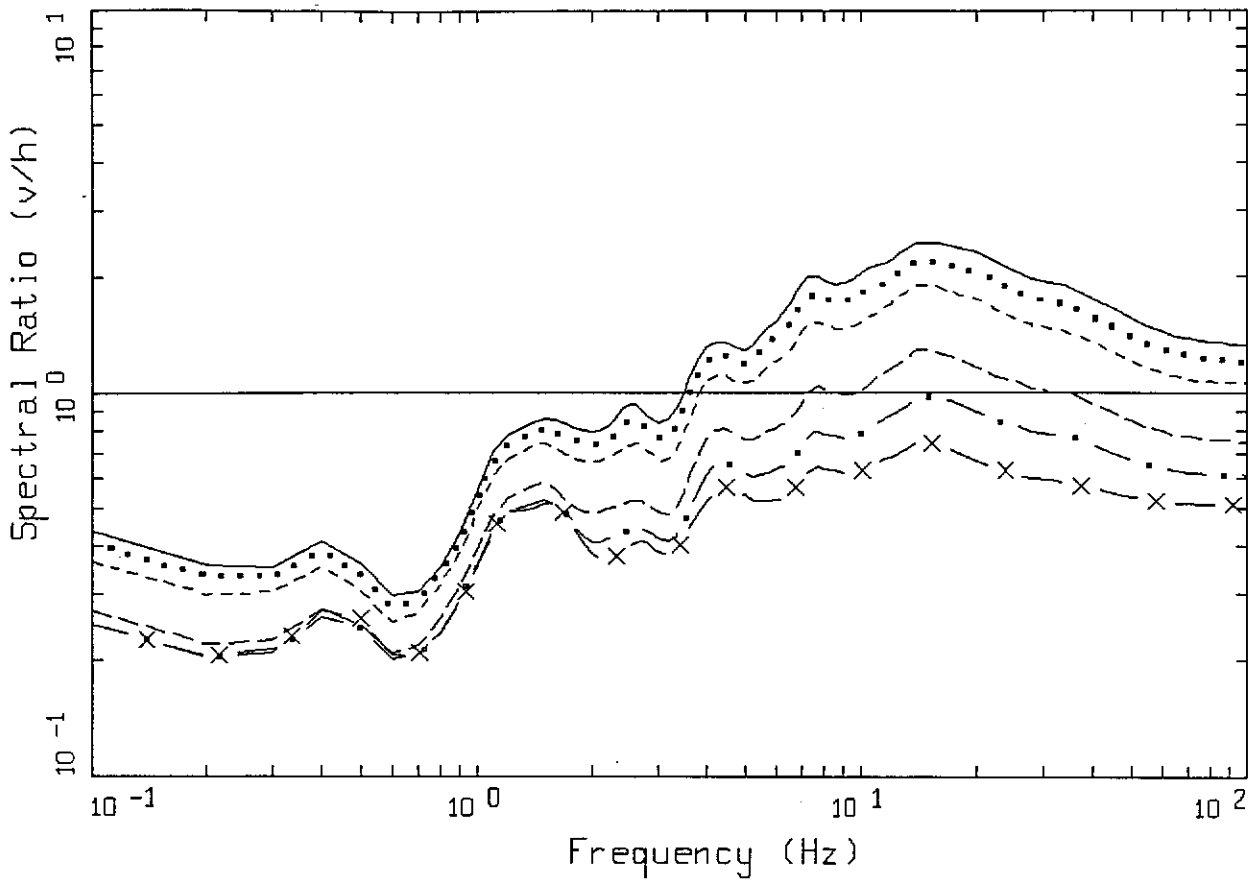
Project No. 91C0509	Los Alamos Seismic Hazards	SITE 8 FOURIER AMPLITUDE SPECTRAL RATIO (2D/1D)	Figure 8-42
Woodward-Clyde Federal Services			



Project No. 91C0509	Los Alamos Seismic Hazards	SITE 9 FOURIER AMPLITUDE SPECTRAL RATIO (2D/1D)	Figure 8-43
Woodward-Clyde Federal Services			



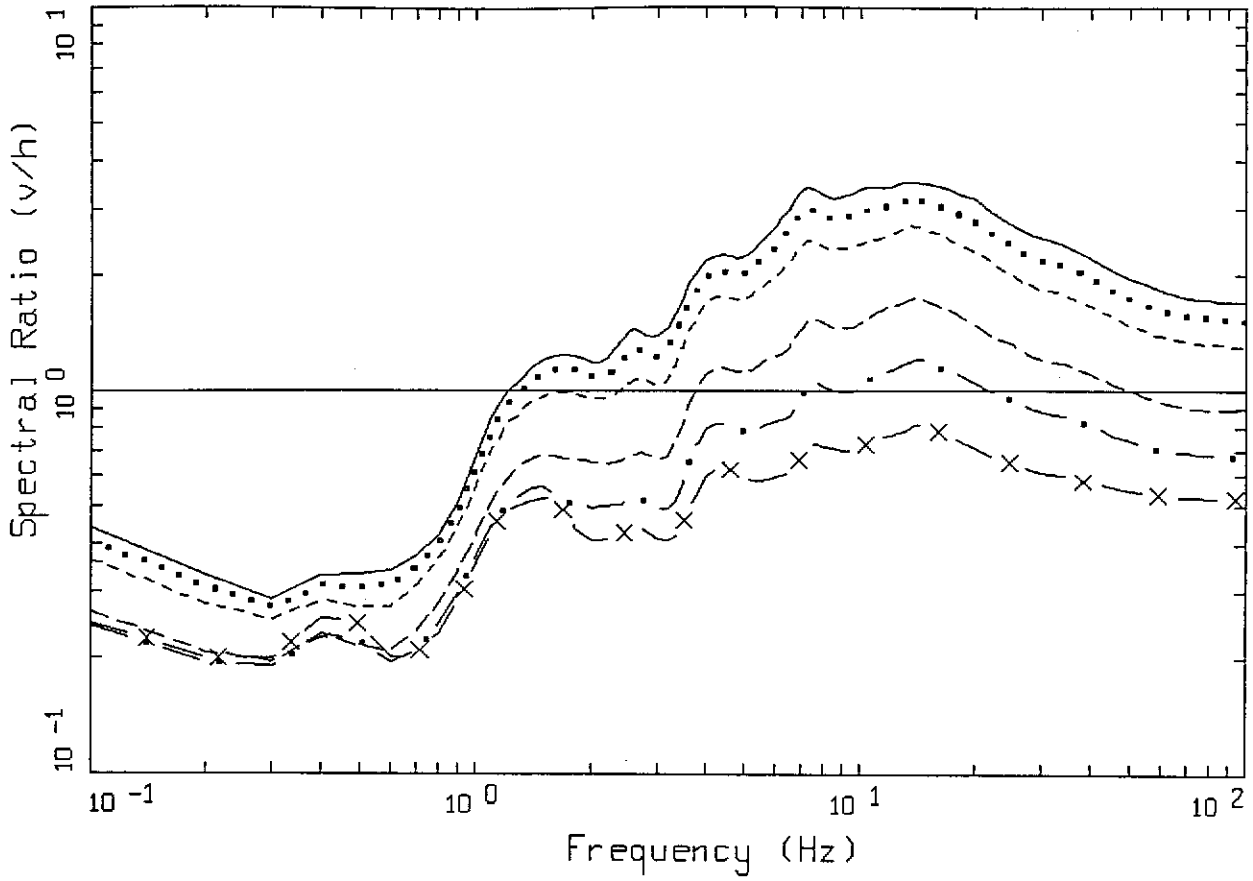
Project No. 91C0509	Los Alamos Seismic Hazards	SITE 10 FOURIER AMPLITUDE SPECTRAL RATIO (2D/1D)	Figure 8-44
Woodward-Clyde Federal Services			



LEGEND

- LOG-AVERAGE SA RATIO, D=1 KM
- LOG-AVERAGE SA RATIO, D=3 KM
- LOG-AVERAGE SA RATIO, D=5 KM
- LOG-AVERAGE SA RATIO, D=10 KM
- LOG-AVERAGE SA RATIO, D=20 KM
- LOG-AVERAGE SA RATIO, D=50 KM

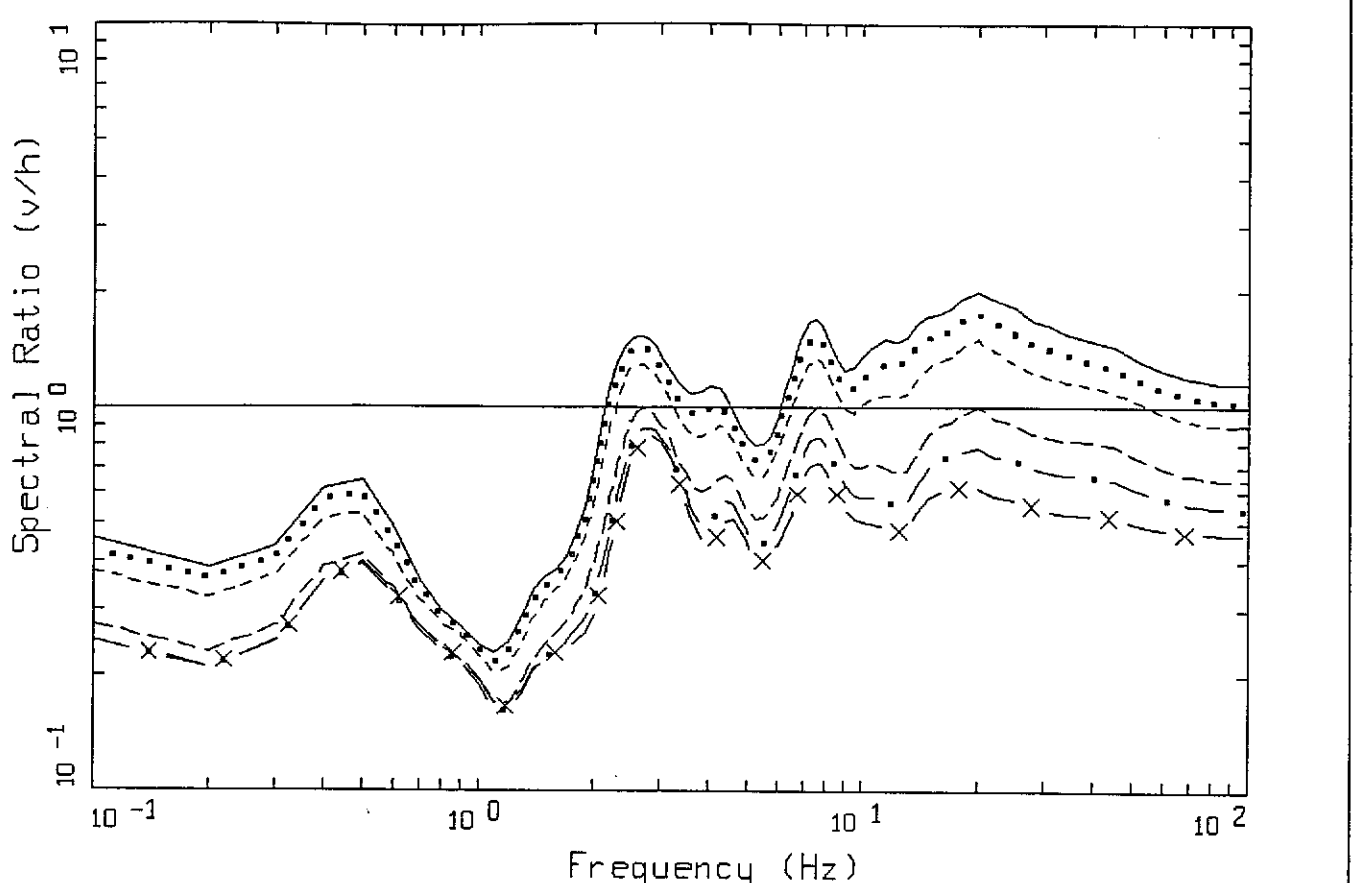
Project No. 91C0509	Los Alamos Seismic Hazards	LOG AVERAGE V/H RATIOS FOR M_W 6 AND MESA TOP SITES	Figure 8-45
Woodward-Clyde Federal Services			



LEGEND

- LOG-AVERAGE SA RATIO, D=1 KM
- LOG-AVERAGE SA RATIO, D=3 KM
- LOG-AVERAGE SA RATIO, D=5 KM
- LOG-AVERAGE SA RATIO, D=10 KM
- LOG-AVERAGE SA RATIO, D=20 KM
- LOG-AVERAGE SA RATIO, D=50 KM

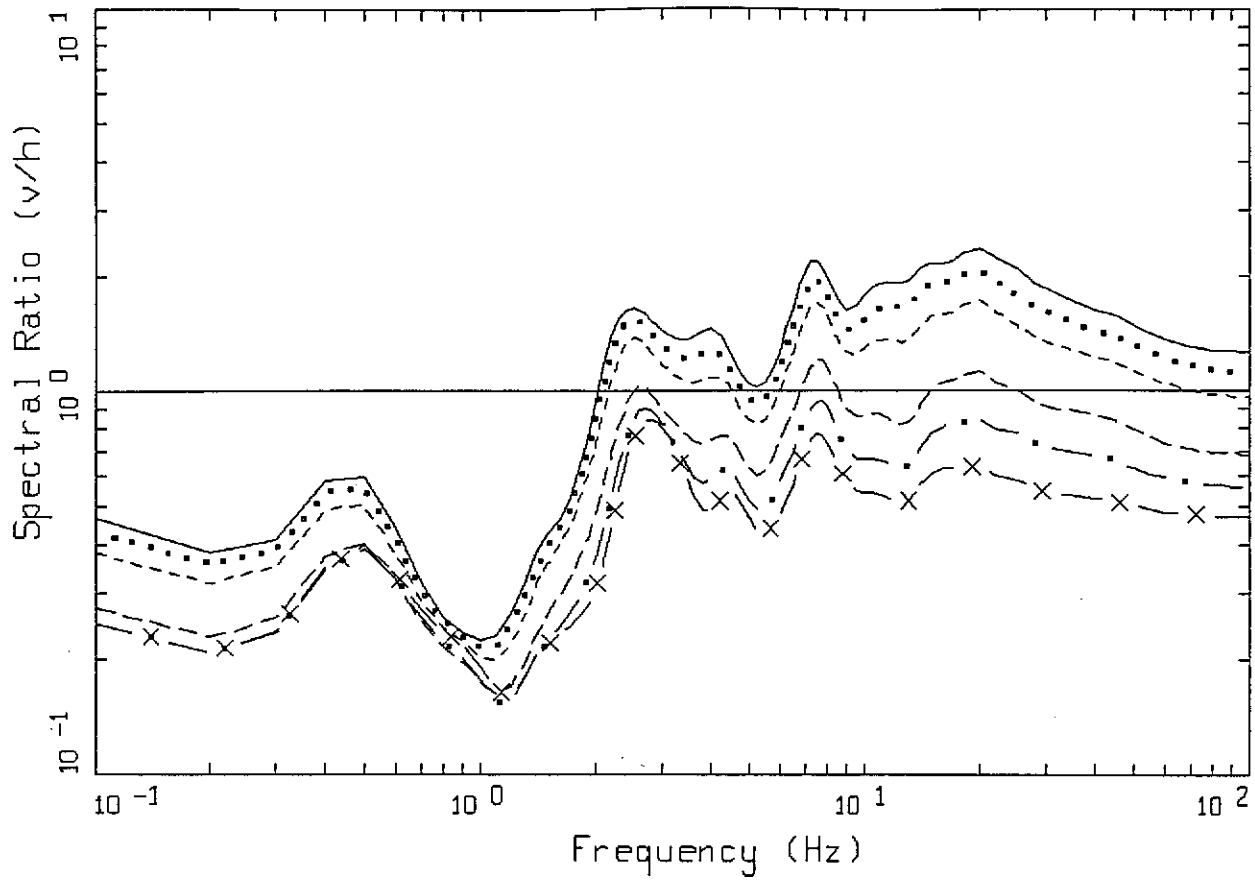
Project No. 91C0509	Los Alamos Seismic Hazards	LOG AVERAGE V/H RATIOS FOR M_W 7 AND MESA TOP SITES	Figure 8-46
Woodward-Clyde Federal Services			



LEGEND

- LOG-AVERAGE SA RATIO, D=1 KM
- LOG-AVERAGE SA RATIO, D=3 KM
- LOG-AVERAGE SA RATIO, D=5 KM
- LOG-AVERAGE SA RATIO, D=10 KM
- LOG-AVERAGE SA RATIO, D=20 KM
- LOG-AVERAGE SA RATIO, D=50 KM

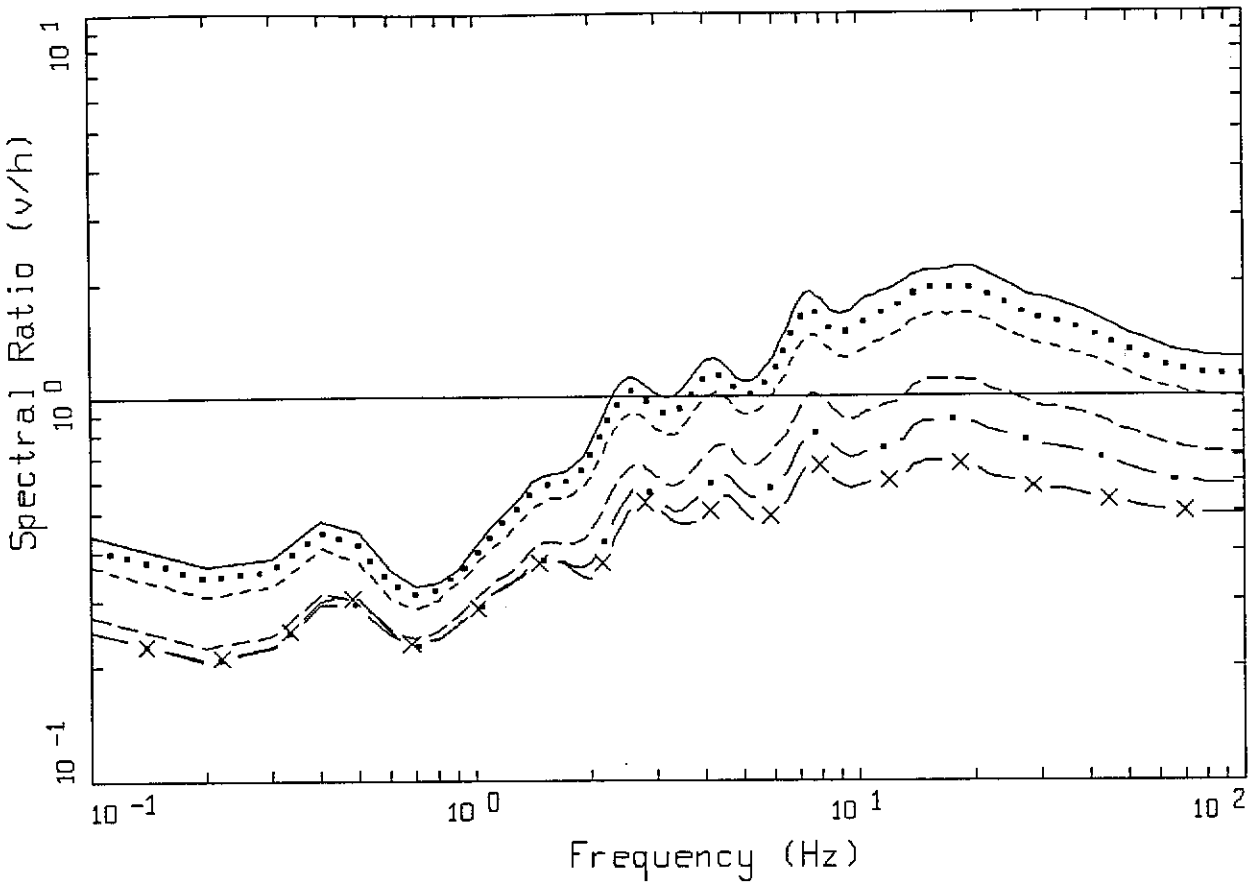
Project No. 91C0509	Los Alamos Seismic Hazards	LOG AVERAGE V/H RATIOS FOR M_W 6 AND CANYON SITES	Figure 8-47
Woodward-Clyde Federal Services			



LEGEND

- LOG-AVERAGE SA RATIO, D=1 KM
- LOG-AVERAGE SA RATIO, D=3 KM
- LOG-AVERAGE SA RATIO, D=5 KM
- LOG-AVERAGE SA RATIO, D=10 KM
- LOG-AVERAGE SA RATIO, D=20 KM
- LOG-AVERAGE SA RATIO, D=50 KM

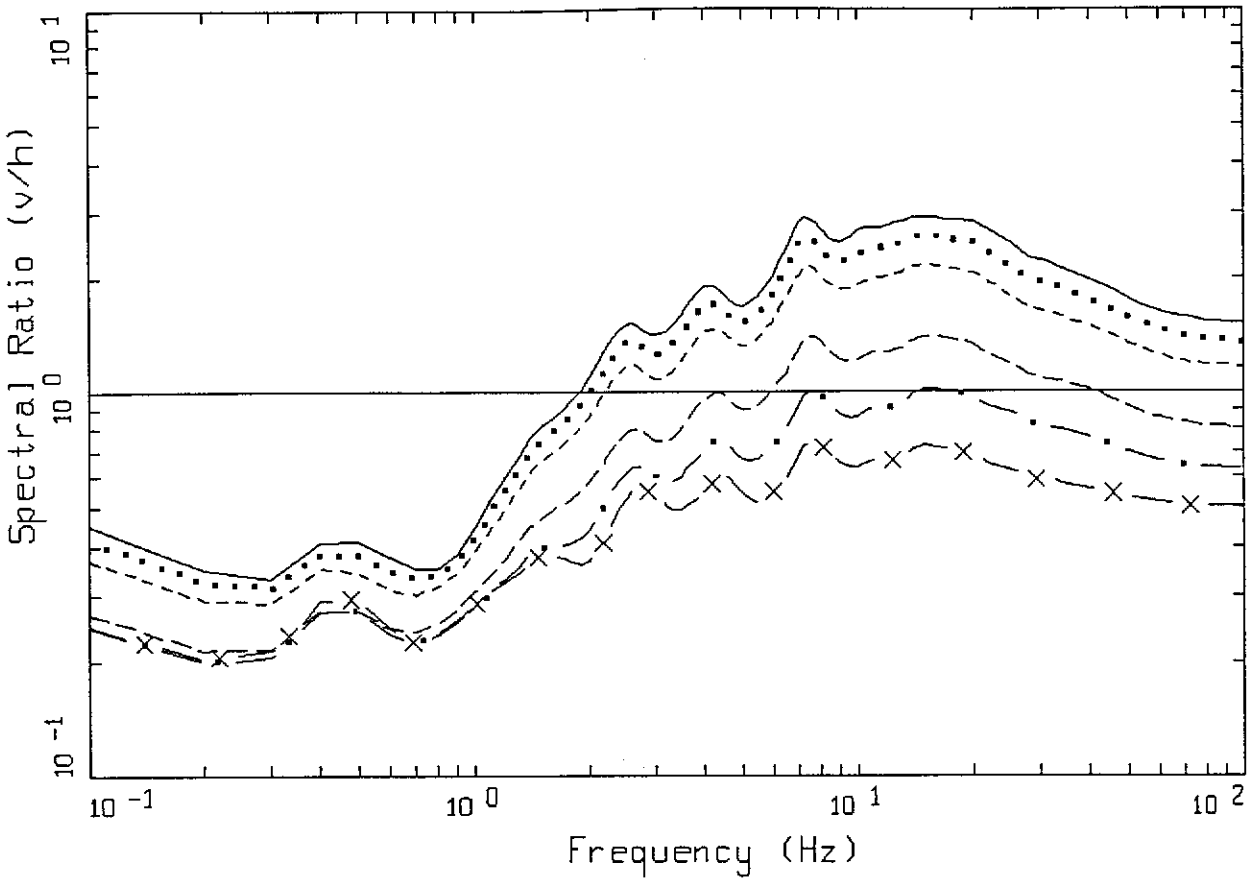
Project No. 91C0509	Los Alamos Seismic Hazards	LOG AVERAGE V/H RATIOS FOR M_W 7 AND CANYON SITES	Figure 8-48
Woodward-Clyde Federal Services			



LEGEND

- LOG-AVERAGE SA RATIO, D=1 KM
- LOG-AVERAGE SA RATIO, D=3 KM
- LOG-AVERAGE SA RATIO, D=5 KM
- LOG-AVERAGE SA RATIO, D=10 KM
- LOG-AVERAGE SA RATIO, D=20 KM
- LOG-AVERAGE SA RATIO, D=50 KM

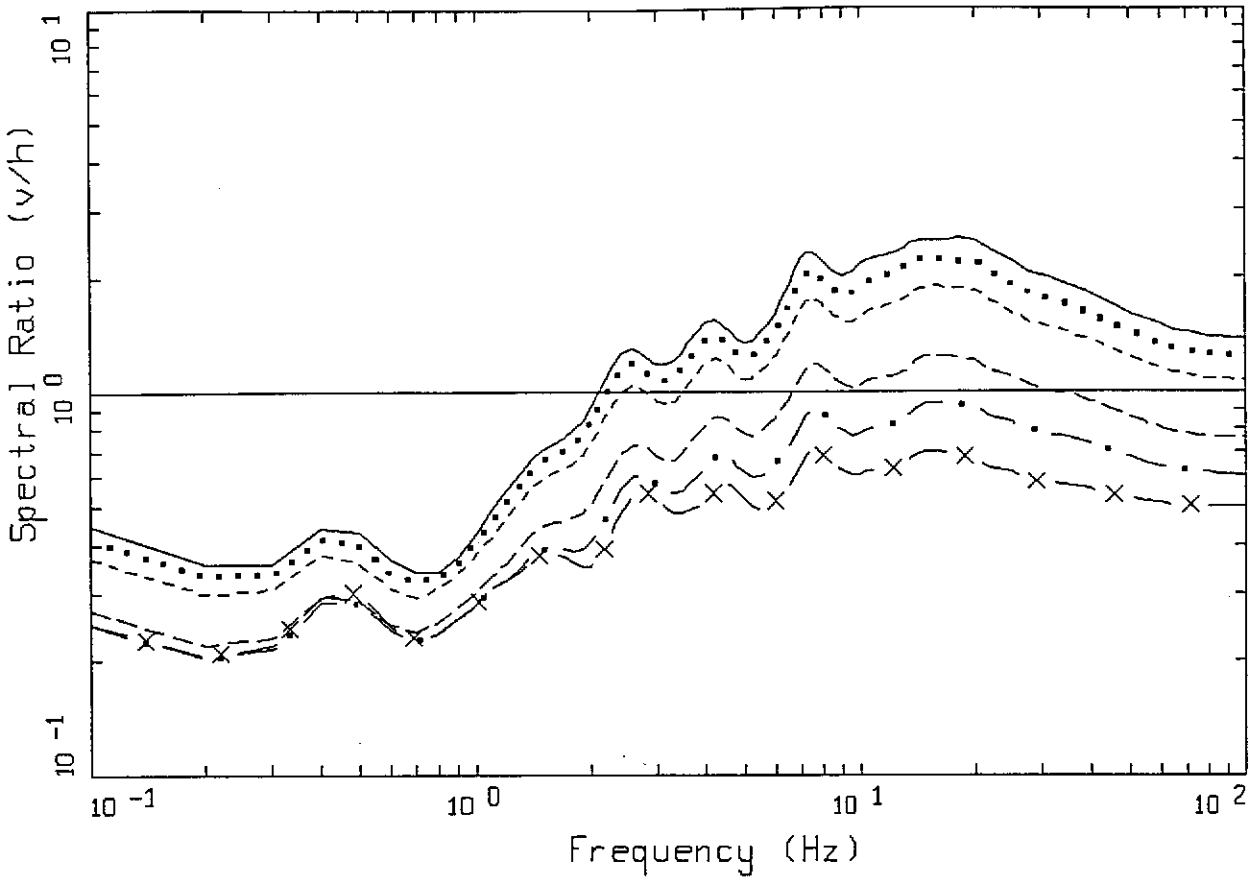
Project No. 91C0509	Los Alamos Seismic Hazards	LOG AVERAGE V/H RATIOS FOR M_W 6 AND ALL SITES	Figure 8-49
Woodward-Clyde Federal Services			



LEGEND

- LOG-AVERAGE SA RATIO, D=1 KM
- LOG-AVERAGE SA RATIO, D=3 KM
- LOG-AVERAGE SA RATIO, D=5 KM
- LOG-AVERAGE SA RATIO, D=10 KM
- LOG-AVERAGE SA RATIO, D=20 KM
- LOG-AVERAGE SA RATIO, D=50 KM

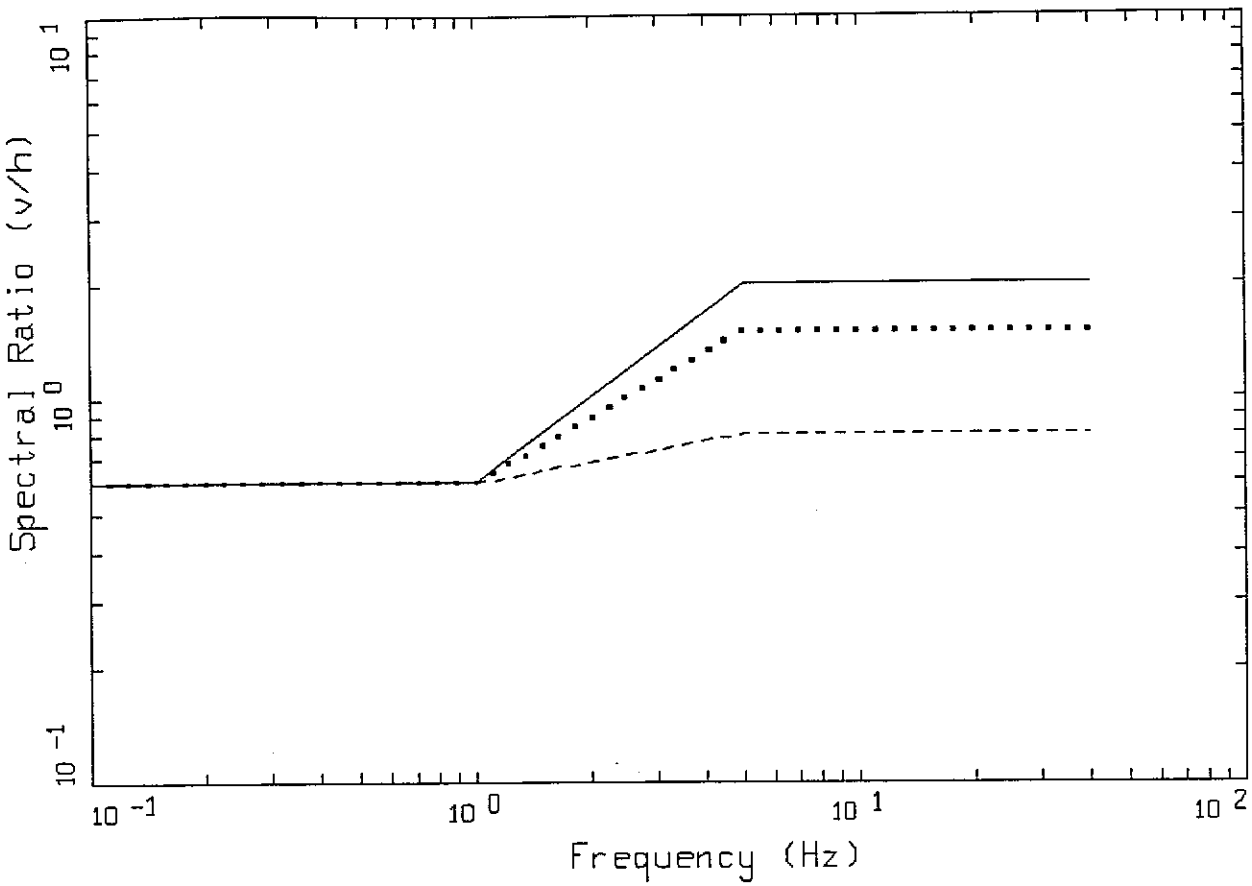
Project No. 91C0509	Los Alamos Seismic Hazards	LOG AVERAGE V/H RATIOS FOR M_W 7 AND ALL SITES	Figure 8-50
Woodward-Clyde Federal Services			



LEGEND

- LOG-AVERAGE SA RATIO, D=1 KM
- LOG-AVERAGE SA RATIO, D=3 KM
- LOG-AVERAGE SA RATIO, D=5 KM
- LOG-AVERAGE SA RATIO, D=10 KM
- LOG-AVERAGE SA RATIO, D=20 KM
- LOG-AVERAGE SA RATIO, D=50 KM

Project No. 91C0509	Los Alamos Seismic Hazards	LOG AVERAGE V/H RATIOS FOR M_W 6 and 7 AND ALL SITES	Figure 8-51
Woodward-Clyde Federal Services			



LEGEND

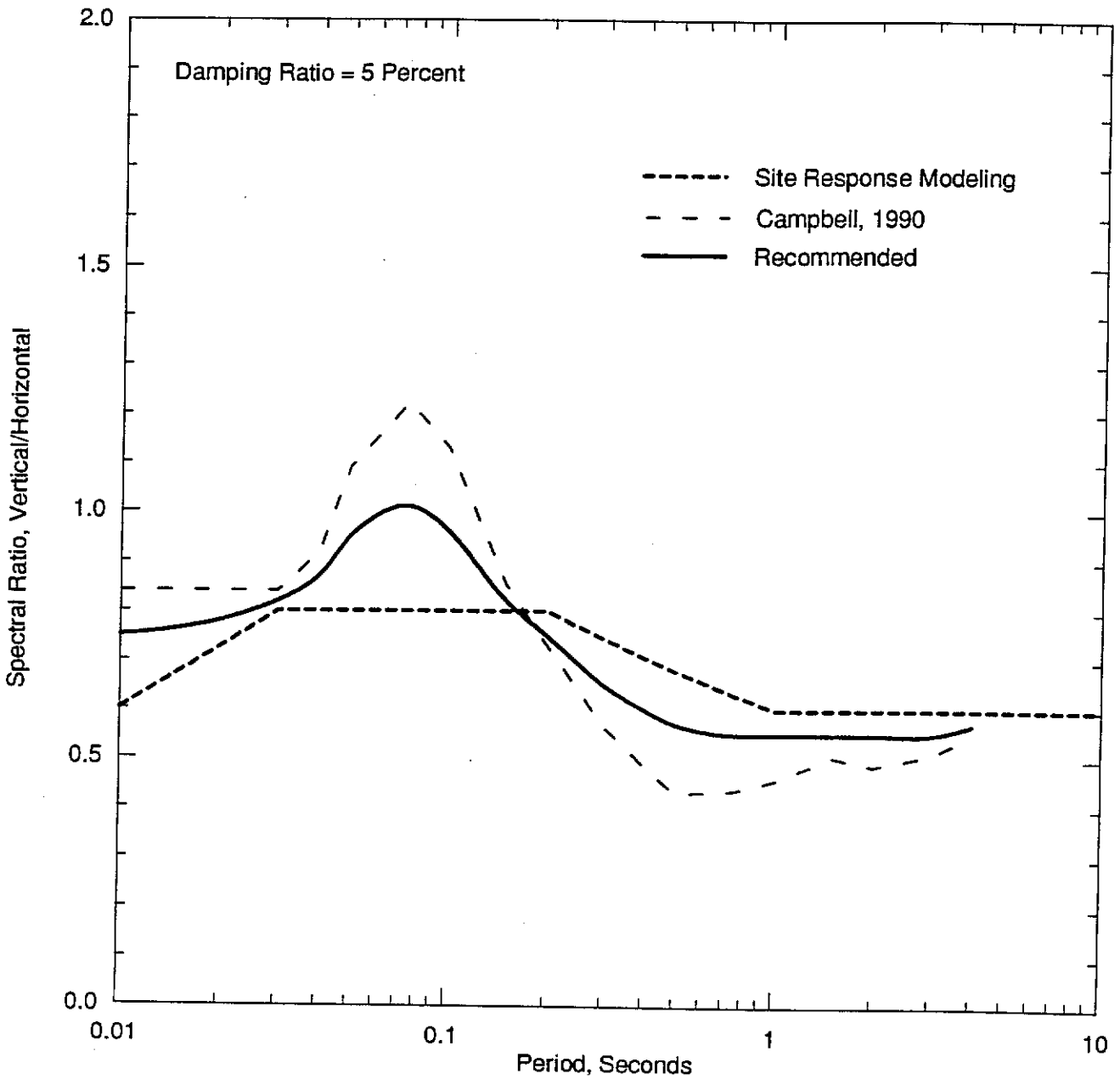
SA RATIO, D = 0 - 5 KM

SA RATIO, D = 5.1 - 10 KM

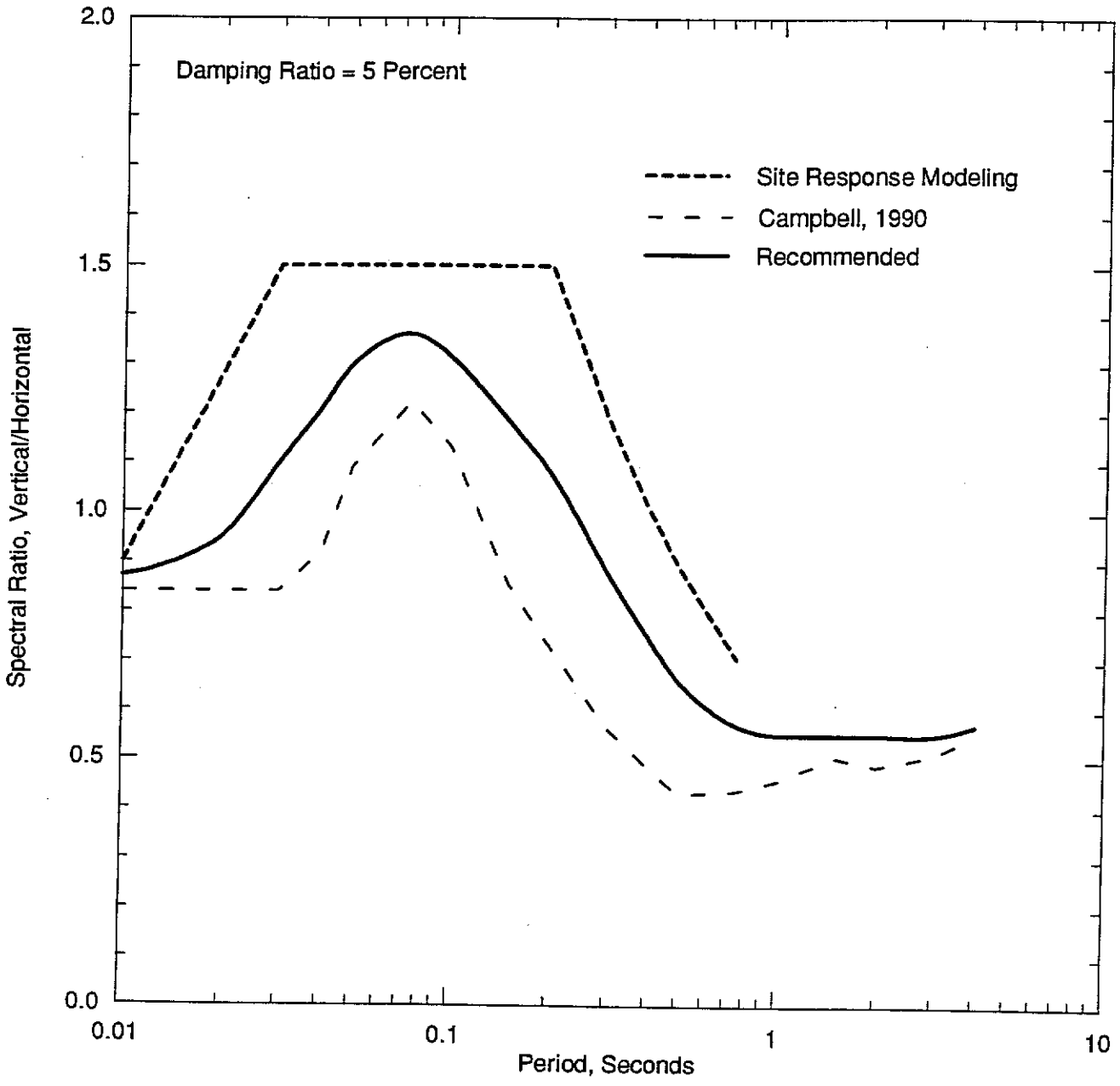
SA RATIO, D > 10 KM

Note: For PGA and D = 0 - 5 km SA Ratio = 1.2
D = 5.1 - 10 km SA Ratio = 0.9
D > 10 km SA Ratio = 0.6

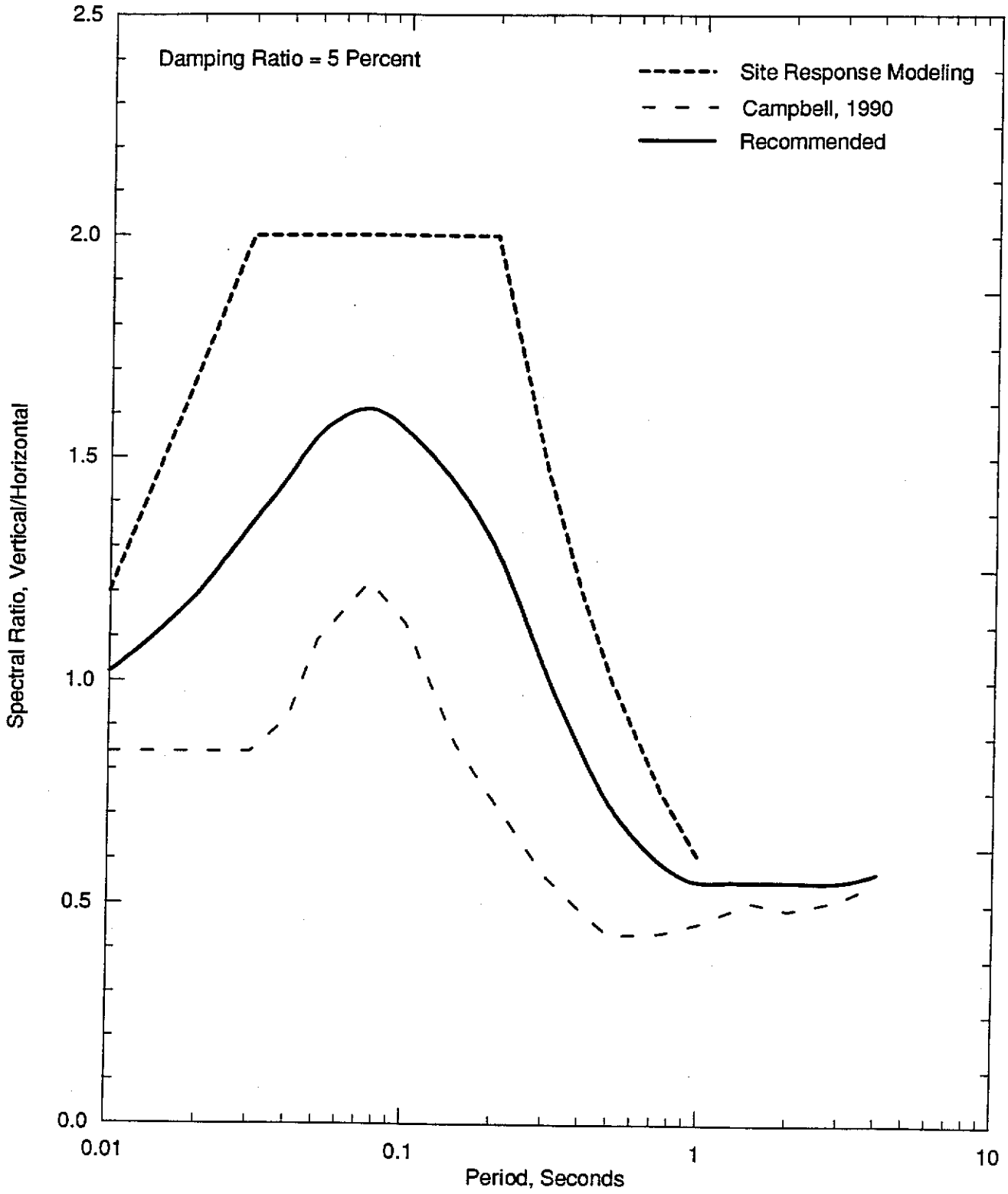
Project No. 91C0509	Los Alamos Seismic Hazards	RECOMMENDED 5 % DAMPED V/H RATIOS	Figure 8-52
Woodward-Clyde Federal Services			



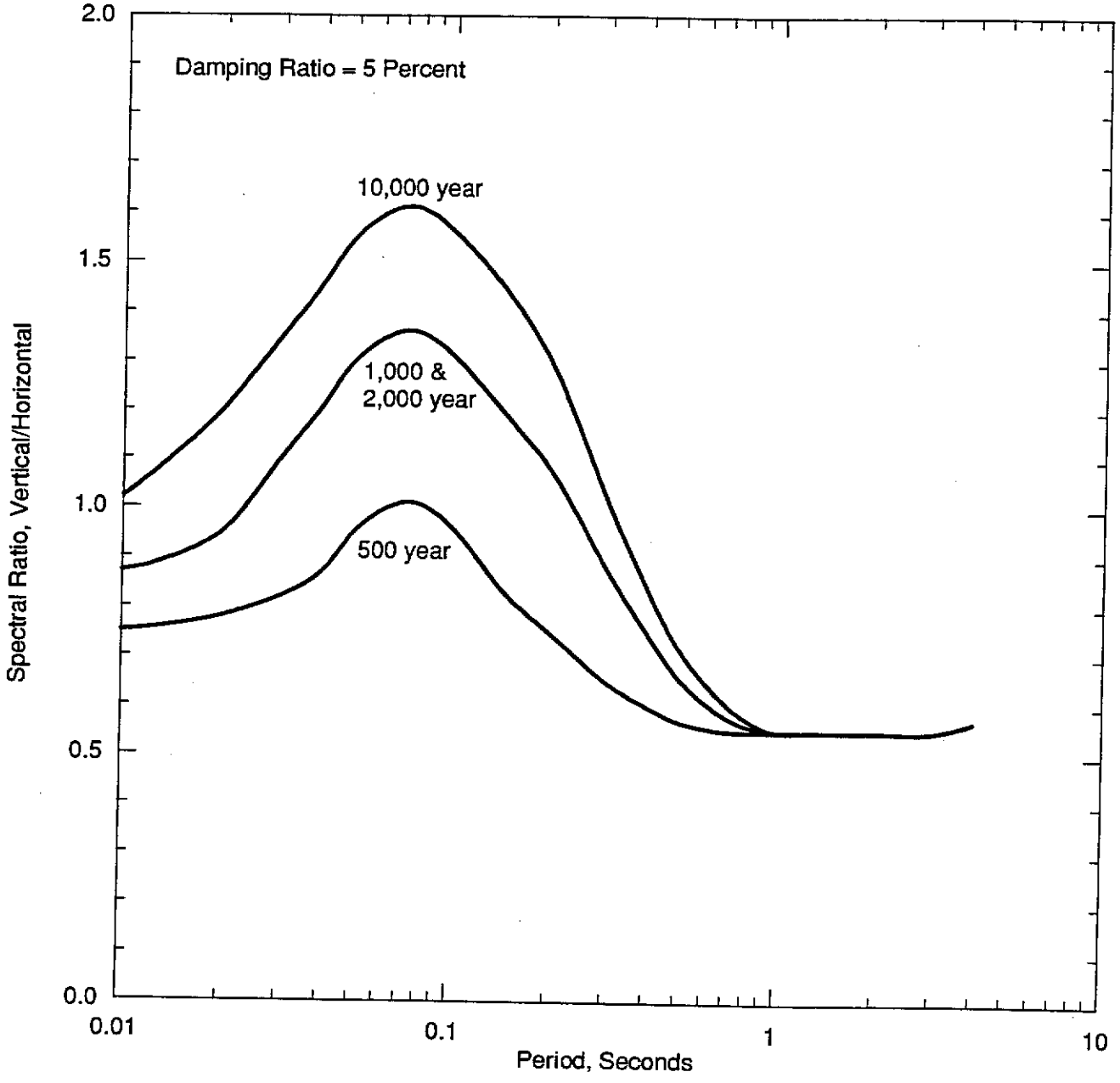
Project No. 91C0509	Los Alamos Seismic Hazards	RATIOS OF VERTICAL TO HORIZONTAL RESPONSE SPECTRA 500 YEAR RETURN PERIOD	Figure 8-53
Woodward-Clyde Federal Services			



Project No. 91C0509	Los Alamos Seismic Hazards	RATIOS OF VERTICAL TO HORIZONTAL RESPONSE SPECTRA 1,000 AND 2,000 YEAR RETURN PERIOD	Figure 8-54
Woodward-Clyde Federal Services			



Project No. 91C0509	Los Alamos Seismic Hazards	RATIOS OF VERTICAL TO HORIZONTAL RESPONSE SPECTRA 10,000 YEAR RETURN PERIOD	Figure 8-55
Woodward-Clyde Federal Services			



Project No. 91C0509	Los Alamos Seismic Hazards	RECOMMENDED RATIOS OF VERTICAL TO HORIZONTAL RESPONSE SPECTRA	Figure 8-56
Woodward-Clyde Federal Services			

9.0
PROBABILISTIC SEISMIC HAZARD ANALYSES

Seismic design criteria for DOE facilities are probabilistically based. To evaluate the levels of ground motions associated with the probability or likelihood of being exceeded in a specified time period, a probabilistic seismic hazard analyses was performed. Our analysis used geologic, seismologic and geophysical data to evaluate potential seismic sources, the likelihood of earthquakes of various magnitudes occurring on those sources, and the likelihood of the earthquakes producing ground motions greater than a specified level. The probabilistic seismic hazard analysis methodology used in this study provides for the explicit inclusion of the range of possible interpretations in components of the model including seismic source characterization and ground motion estimation. Uncertainties in models and parameters are incorporated into the hazard analysis through the use of logic trees. The following presents the methodology, input, and results of the probabilistic analysis of the eight LANL sites. The calculations were made using the computer programs XCEED (Woodward-Clyde Consultants, 1979) and EXPOSE. Both codes have been used extensively in the hazard analyses of DOE facilities, and specifically, they have been verified in a project for DOE Hanford.

9.1 SEISMIC HAZARD METHODOLOGY

A probabilistic seismic hazard analysis is an evaluation of the likelihood that specific ground motions will be exceeded during a specific time period. The analysis can also provide ground motions with specific probabilities of being exceeded. The seismic hazard model used in this study is based on the model presented by Kulkarni et al. (1979). This model is similar to other available seismic hazard analysis models (Cornell, 1968; McGuire, 1974, 1978; Der Kiureghian and Ang, 1977) but includes some additional features as described below.

The occurrence of earthquakes on a fault is assumed to be a Poisson process. The Poisson model is widely used and is a reasonable assumption in regions where data are sufficient to provide only an estimate of average recurrence rate (Cornell, 1968). When there is sufficient knowledge to permit a real-time estimate of the occurrence of earthquakes, the

probability of exceeding a given value can be modeled as an equivalent Poisson process in which a variable average recurrence rate is assumed. The occurrence of ground motions at the site in excess of a specified level is also a Poisson process, if:

(1) the occurrence of earthquakes is a Poisson process and

(2) the probability that any one event will result in ground motions at the site in excess of a specified level is independent of the occurrence of other events.

The probability that a ground motion parameter "Z" exceeds a specified value "z" in a time period "t" is given by:

$$p(Z > z) = 1\text{-}e^{-\nu(z)\bullet t} \qquad (9\text{-}1)$$

where $\nu(z)$ is the annual mean number (or rate) of events in which Z exceeds z. It should be noted that the assumption of a Poisson process for the number of events is not critical. This is because the mean number of events in time t, $\nu(z)\bullet t$ can be shown to be a close upper bound on the probability $p(Z > z)$ for small probabilities (less than 0.10) which generally are of interest for engineering applications. The annual mean number of events is obtained by summing the contributions from all sources, that is:

$$\nu(z) = \sum_{n} \nu_n(z) \qquad (9\text{-}2)$$

where $\nu_n(z)$ is the annual mean number (or rate) of events on source n for which Z exceeds z at the site. The parameter $\nu_n(z)$ is given by the expression:

$$\nu_n(z) = \sum_{i} \sum_{j} \beta_n(m_i) \bullet p(R=r_j \mid m_i) \bullet p(Z>z \mid m_i, r_j) \qquad (9\text{-}3)$$

where:

$\beta_n(m_i)$ = annual mean rate of recurrence of earthquakes of magnitude increment m_i on source n;

$p(R=r_j|m_i)$ = probability that given the occurrence of an earthquake of magnitude m_i on source n, r_j is the closest distance increment from the rupture surface to the site;

$p(Z>z|m_i,r_j)$ = probability that given an earthquake of magnitude m_i at a distance of r_j, the ground motion exceeds the specified level z.

The recurrence function, $ß_n(m_i)$, represents the average number of earthquakes of each magnitude expected on the seismic source. For the faults, both exponentially truncated (modified Gutenberg-Richter) and characteristic recurrence models are used as described subsequently in Section 9.2.2. The recurrence for the seismic source zones is modeled using the exponentially truncated model with the recurrence rates based on the historical seismicity, as described in Sections 5 and 7.2.

The distance function, $p(R=r_j|m_i)$, represents the probable distance at which earthquakes on a source will occur in the future. It is calculated from the geometry of the seismic source (distance from the site, dip, length, depth, and fault segmentation) and the geometry of the earthquake rupture (rupture length, rupture width, and depth of rupture).

The attenuation function, $p(Z>z|m_i,r_j)$, represents the probability of exceeding the ground motion given the magnitude and distance of the earthquake. This function is modeled using the attenuation relationships that are described in Sections 8.1.1 and 8.2.5. For the probabilistic analyses, the uncertainty is represented by the standard error in a lognormal distribution about the median value.

9.2 SEISMIC SOURCES

The seismic sources used in the hazard analyses include the 25 faults described in Section 7.1 and the four seismic source zones described in Section 7.2. The seismic sources are modeled in the hazard analysis in terms of geometry and earthquake recurrence. The geometric source parameters include fault location, segmentation model, dip, and depth of seismogenic zone. The recurrence parameters include recurrence model (exponential and characteristic), recurrence rate (slip rate or average return time for the maximum event on the faults or number of events over the minimum magnitude for the source zones), slope of

the recurrence curve (b-value), and maximum magnitude. Clearly, the geometry and recurrence are not totally independent. For example, if a fault is modeled with several small segments instead of longer segments, the maximum magnitude will be smaller, and a given slip rate requires many more small earthquakes to accommodate an accumulated seismic moment. Uncertainties in the source parameters are included in the hazard model using logic trees (Figure 9-1). In the logic tree approach, discrete values of the source input parameters have been included along with our estimate of the likelihood that the discrete value represents the actual value. Generally all input parameters have been represented by three values: a central value, which represents our best estimate of the parameter, and lower and higher values to represent the distribution around the best estimate. The characterization of an input parameter and its uncertainties using a simple three-point approximation and specific weights for the median and selected percentiles were generally used in this study based on the studies of Keefer and Bodily (1983). They recommend that this approximation is more accurate than other approximations in characterizing continuous probability distributions "typical of those elicited via judgmental assessments." Two sets of weights were used: 0.185, 0.63, and 0.185 to approximate the 5^{th}, 50^{th} and 95^{th} percentile values, respectively, and 0.3, 0.4, and 0.3 for 10^{th}, 50^{th}, and 90^{th} percentile values. The details of the selection of the parameter values and their probabilities are presented in the individual source characterizations in Section 7.

9.2.1 Source Geometry

The distance from an earthquake to the site is dependent on the source geometry, size and shape of the rupture on the fault plane, and the likelihood of the earthquake occurring at different points along the fault length. The distance to the fault is defined to be consistent with the specific attenuation relationship used to calculate the ground motions. The size and shape of the rupture on the fault plane is dependent on the magnitude of the earthquake, with larger events rupturing longer and wider portions of the fault plane. We modeled the rupture dimensions on rectangular planar surfaces following the magnitude-area, magnitude-rupture length, and magnitude-rupture width relationships of Wells and Coppersmith (1994). The magnitude-area relationship was used to calculate the recurrence as described in the following section, and the relationships for rupture length and rupture width with magnitude were used to calculate the appropriate source-to-site distances.

The seismicity that cannot be associated with any known structures has been modeled as area sources with randomly located seismicity within each source. We have assumed to a first-order that none of the historical seismicity is associated with any of the modeled faults, and have assigned all of the historical seismicity to the area sources. The boundaries of these area sources and their seismicity rates are described in Section 7.2. The area sources were modeled with a series of parallel planes representing locations of potential earthquake ruptures and these planes were treated as faults in the hazard calculations. Using this approach, the effects of rupture dimension are included in the distance distribution. The historical seismicity within each area source was proportioned to the planes within the area based on their lengths. The same relationships between magnitude and rupture area, rupture length, and rupture width (Wells and Coppersmith, 1994) were used for the planes within the area sources as were used for the faults. Because the tectonics of the region is dominated by the Rio Grande rift, the relationships for normal faults were used.

9.2.2 Recurrence

The recurrence relationships for the seismic sources are modeled using both the exponentially truncated Gutenberg-Richter relationship and the characteristic earthquake recurrence model. We have used the approach of Anderson (1979) to arrive at the recurrence for the exponentially truncated model. A relatively high likelihood has been included in the model that the faults rupture with a "characteristic" magnitude on specific segments. This model is described by Aki (1983), Schwartz and Coppersmith (1984), and the Working Group on California Earthquake Probabilities (1988, 1990). We have used the numerical model of Youngs and Coppersmith (1985) for the characteristic model. These exponential and characteristic models are weighted 0.3 and 0.7, respectively, to represent our judgment on their applicability to the sources. The higher weighting on the characteristic model reflects the lack of moderate to large historical seismicity along with geologic evidence that large events have occurred. The number of events exceeding a given magnitude, $N(m)$, for the truncated exponential relationship is

$$N(m)=\alpha(m^{o})\frac{10^{-b(m-m^{o})}-10^{-b(m^{u}-m^{o})}}{1-10^{-b(m^{u}-m^{o})}} \qquad (9\text{-}4)$$

where $\alpha(m^o)$ is the annual frequency of occurrence of earthquake greater than the minimum magnitude, m^o; b is the Gutenberg-Richter parameter defining the slope of the recurrence curve; and m^u is the maximum magnitude event that can occur on the source. A m^o 5 was used for the hazard calculations because smaller events are not considered likely to produce damaging ground motions to well-designed structures.

For the characteristic model, the number of events exceeding a given magnitude is the sum of the characteristic events and the non-characteristic events. The characteristic events are distributed uniformly over $\pm$ 0.3 magnitude units around the characteristic magnitude, and the remainder of the moment rate is distributed exponentially using the above equation with a maximum magnitude at the lower bound of the range around the characteristic magnitude (i.e. 0.3 magnitude below the characteristic magnitude). The slope of the exponential model and the exponential part of the characteristic model is based on the historical seismicity in the region.

The recurrence rates for the fault sources are defined by either the slip rate or the average return time for the maximum or characteristic event and the recurrence b-value. The slip rate is used to calculate the moment rate on the fault using the following equation defining the seismic moment.

$$M_o = \mu A D \qquad (9\text{-}5)$$

where M_o is the seismic moment, μ is the shear modulus of rupture, A is the area of the rupture plane, and D is the slip on the plane. Dividing both sides of the equation by time results in the moment rate as a function of slip rate:

$$\dot{M}_o = \mu A S \qquad (9\text{-}6)$$

where $\dot{M}_o$ is the moment rate and S is the slip rate. M_o has been related to the moment magnitude, M_w, by Hanks and Kanamori (1979):

$$M_w = 2/3 \log M_o - 10.7 \quad (9\text{-}7)$$

Using this relationship and the relative frequency of different magnitude events from the recurrence model, the slip rate can be used to estimate the absolute frequency of different magnitude events.

For the branches where the recurrence is specified by the average return time, the characteristic or maximum magnitude event defines the high magnitude (low likelihood) end of the recurrence curve. The maximum magnitude for this model is distributed in a range of $\pm$ 0.3 around the estimated maximum magnitude. The average return time is assigned to the lower bound of this range. When combined with the relative frequency of different magnitude events from either the exponential or characteristic recurrence model, the recurrence curve is established.

The recurrence rates and their weights for each of the potential seismic sources are described in Section 7. For the seismic source zones, the recurrence is modeled using the exponential model only with the rates defined by the historical seismicity as described in Sections 5 and 7.2. Uncertainty in the "a" and "b" values from the maximum likelihood evaluations is included in the hazard analyses using logic trees as shown in Figures 7-27 to 7-30.

The weighted combinations of all of the recurrence models, recurrence rates, and maximum magnitudes have been combined for each potentially significant seismic source to produce the recurrence curves presented in Figure 9-2. The mean number of events are shown exceeding various magnitudes for each source. Because the maximum (characteristic) magnitude is distributed over a $\pm$ 0.3 magnitude range, the highest magnitude for each source is 0.3 higher than the characteristic magnitude. The fault sources generally have return periods more than 1,000 years for earthquakes greater than M_w 5, over 5,000 years for events of $M_w > 6$, and more than 50,000 years for $M_w > 7$ (Figure 9-2). The recurrence curves for the seismic source zones show that the Rio Grande rift has the highest recurrence nearly up to its maximum of M_w 6¾. The rift has return periods of about 50, 400, and 4,000 years for earthquakes greater than M_w 5, 6, and 6½, respectively (Figure 9-2).

9.3 ATTENUATION RELATIONSHIPS

For the probabilistic analyses we used the same attenuation relationships as for the deterministic analyses. The empirical relationships appropriate for deep soil sites are Joyner and Boore (1988), a combined Campbell (1993) and Campbell and Bozorgnia (1994) (as recommended by Campbell, EQE, personnel communication, 1994), and Sadigh et al. (1987; described in Joyner and Boore, 1988); the latter using an updated standard error from Geomatrix (1993). These empirical relationships are described in Appendix L. In addition, we used one of the two attenuation relationships derived from the stochastic modeling (Section 8.2.5) for either mesa top or canyon sites. These attenuation relationships are illustrated in Figures 9-3 through 9-10 for peak horizontal acceleration and spectral accelerations from periods of 0.1 to 4 sec.

For the probabilistic analyses, the empirical relationships were each weighted 0.133, and the stochastic attenuation relationships were weighted 0.60 (Figure 9-1). This weighting favors the stochastic model, which reflects our judgment that the empirical relationships are comparatively less applicable in the LANL region, because they are based on data primarily from California, and because the stochastic model is more appropriate because of the inclusion of the regional seismic source, path and site parameters in the model.

9.4 SEISMIC HAZARD RESULTS

The seismic hazard was calculated at the eight Technical Areas for peak horizontal ground acceleration and response spectral acceleration for five percent damping at periods of 0.2 and 1.0 seconds (Figures 9-11 through 9-34). The results of the hazard analyses are presented in terms of the annual number of events exceeding the peak acceleration or spectral acceleration. The annual number of events is the reciprocal of the average return time.

9.4.1 Peak Acceleration

Figures 9-11 through 9-18 present the computed mean, median, 5^{th}, 16^{th}, 84^{th}, and 95^{th} percentile peak acceleration hazard curves for the eight sites. The mean peak horizontal accelerations for the four Performance Categories probabilities of being exceeded specified in DOE Standard 1020-94 are summarized in Table 9-1. The values are similar for all sites

because of their similar distances to the seismic sources, particularly the Pajarito fault. The canyon sites (TA-2, 18, and 41) have very slightly higher peak accelerations probably because they lack the high-frequency damping Bandelier Tuff beneath their locations as do the mesa top sites (TA-3, 16, 21, 46, and 55). The peak accelerations for a 500-year return period are lower than the UCRL-53582 values by 0.03 to 0.04 g (Section 1.2). The computed values for 1,000 years are generally identical to the UCRL-53582 peak accelerations.

The uncertainty band around the mean hazard curve is the result of the distribution of the results among all of the thousands of end branches of the logic trees. The difference between the mean and median curves reflects the skewed distribution of the slip rates (i.e., the mean slip rates are much higher than the median slip rates) and the attenuation relationships (i.e., the attenuation relationship based on the stochastic modeling is weighted 60 percent, which includes the median, and has a lower hazard than the empirical relationships [Figures 9-3 through 9-10]). The wide range between the 5th and 95th percentile hazard curves, especially for the longer return periods, shows the high degree of uncertainty in the source characterization and the differences in the attenuation relationships.

9.4.2 Response Spectral Acceleration

The seismic hazard was calculated for response spectral accelerations at periods of 0.2 and 1.0 sec using the same procedures as for peak acceleration. The only change in the calculations is the differences in the attenuation relationships and the levels of acceleration at which the calculations are being made. The mean, median, 5th, 16th, 84th, and 95th percentile hazard curves are presented in Figures 9-19 through 9-26 and 9-27 through 9-34, respectively. The results for response spectral acceleration show similar trends as the peak acceleration.

9.5 SENSITIVITY OF THE HAZARD RESULTS

To assess the sensitivity of the seismic hazard results to various input parameters, the contributions of several different parameters to total hazard have been examined. The results are most sensitive to the seismic sources and attenuation relationships that contribute significantly to the total hazard. Obviously, if parameters are changed sufficiently, then the

significant contributors could change and affect the total hazard. In this section, the sensitivity of the hazard results to selected significant contributors are described.

9.5.1 Seismic Source Contributions

The contributions of the various sources to the total peak acceleration hazard are presented in Figures 9-35 through 9-42. The seismic hazard is dominated by the closest sources with the highest likelihood of producing large earthquakes. The Pajarito fault, whose slip rate is about 0.1 mm/yr and which dips beneath the LANL is the most dominant contributor to the hazard at all eight sites at return periods beyond 1,000 years. The Rio Grande rift source zone, in which LANL is located, dominates hazard at return periods of less than 1,000 years and decreases in importance relative to the Pajarito fault system as return period increases (Figures 9-35 to 9-42). Faults such as the Embudo, Puye, Lobato Mesa, Sawyer Canyon, and Bajada-Rosario, contribute some hazard but only at return periods of 10,000 years or more. The remaining faults and source zones in the LANL region do not contribute significantly to the total hazard at the LANL because they are too distant and/or their recurrence rates are too low. Changes in the parameters for the other seismic sources within our range of probable values would result in insignificant changes in the total seismic hazard at the sites.

The contributions of the various sources to hazard for response spectral accelerations at 0.2 and 1.0 seconds are presented in Figures 9-43 through 9-50 and 9-51 through 9-58, respectively. The results for the response spectral acceleration show similar trends as the results for peak acceleration.

9.5.2 Sensitivity to Attenuation Relationship

In addition to the seismic sources, the contributions from the different attenuation relationships results in the widest variation in the total hazard. To assess the effects of the various empirical and site-specific stochastic attenuation relationships, Figures 9-59 through 9-66 present the weighted total hazard curves along with the hazard curve for each attenuation relationship if it were the only attenuation relationship used. For peak acceleration and 0.2 sec spectral acceleration (short periods), the stochastic attenuation relationships give lower ground motions at the sites due to most likely, the damping

characteristics of the LANL profiles, particularly for the mesa top sites, which are underlain by the Bandelier Tuff. Conversely, the stochastic peak acceleration attenuation curves for the canyon sites (TA-2, TA-18 and TA-41) are more similar to the empirical curves than the mesa top sites because of the missing tuff beneath the canyons (Figures 9-59 to 9-66).

At long periods, such as 1.0 sec, the Campbell (1994; consisting of Campbell and Bozorgnia [1994] and Campbell [1989]) curves are particularly low compared to the others. The stochastic attenuation relationship at 1.0 sec is consistent with the other empirical curves probably due to the long-period amplification of the LANL profiles.

9.5.3 Magnitude and Distance Contributions

As described in DOE Standard 1023-94, the mean seismic hazard can be deaggregated to determine the contributions of all earthquakes in a selected earthquake magnitude and distance range. These magnitude and distance contributions are presented as histograms of percent contribution to the total hazard from each 0.1 magnitude increment at selected ground motion levels (Figures 9-67 to 9-90). The contributions are presented for peak horizontal acceleration and spectral accelerations at 0.2 and 1.0 sec for the four Performance Category return periods. For peak acceleration, the background earthquake of the Rio Grande rift source zone, M_w 5 to 6½ at close-in distances of less than 10 km, appears to contribute most at short return periods of 500 and 1,000 years. As the return period increases, the contribution of the Pajarito fault system increases as shown by the shift to higher magnitudes (M_w 6¼ to 6¾) at distances of less than 10 km. In particular, the principal contribution at 10,000 years appears to be an earthquake of approximately M_w 6¼ to 6½ at less than 10 km distance. For longer-period spectral accelerations, the pattern is similar but with greater contributions from the larger magnitude near-field events in the range M_w 6 to 7. This is an expected result because the larger the magnitude, the larger the rupture dimensions and duration and hence, the greater amount of long-period ground motions which will be generated. For example, at 10,000 years, the largest contributor to 1.0 sec spectral acceleration is an event of about M_w 6½ at a distance of less than 10 km.

The dominant or controlling earthquake characterized by the mean magnitude $\bar{M}$ and mean distance $\bar{D}$ can also be determined through the deaggregation process (DOE-STD-1023-94). These values are shown in Table 9-2 as a function of return period and ground motion

parameter. The dominant earthquakes reflect the results shown in the magnitude and distance histograms (Figures 9-67 to 9-90).

9.5.4 Sensitivity to Site Location

The differences in the hazard at the different sites, which appear to be very small, are probably due to the minor differences in the distances to the various seismic sources and in the site geology as modeled in the stochastic attenuation relationships. These differences are only recognizable at very long return periods approaching 10,000 years.

9.6 EQUAL HAZARD SPECTRA

Equal hazard spectra were developed for each site by selecting the peak ground motion level from the mean hazard curves at the various spectral acceleration periods for return periods of 500, 1,000, 2,000 and 10,000 years (Figures 9-91 to 9-98). Smooth response spectral shapes are based on the peak spectral amplitudes at the periods of 0.01 (peak acceleration), 0.03, 0.1, 0.2, 0.3, 0.5, 1.0, 2.0 and 4.0 sec. The spectra show a gradual broadening in the shape as the return period increases resulting from the increased contributions from larger magnitude earthquakes. The equal hazard spectra for the canyon sites (TA-2, 18 and 41) for return periods of 500, 1,000 and 2,000 years exhibit a slight dip in their shapes at a period of 0.2 sec due to resonant peaks in the ground motions resulting from stochastic modeling using the site-specific geologic profiles.

Comparison of the spectra for each site for each return period (Figures 9-99 to 9-102) illustrate rather small differences. The spectra from the canyon sites are distinguishable from the mesa top sites by the 0.2 sec peak amplitudes. The canyon spectra are also slightly higher in amplitude at peak acceleration and high frequencies (less than 0.1 sec) than the mesa top sites due to the absence of the Bandelier Tuff and its high-frequency damping properties.

9.7 COMPARISON WITH OTHER PROBABILISTIC ESTIMATES

Algermissen et al. (1990) have produced maps of probabilistic accelerations, velocities, and response spectral values for the United States for return periods of 500 and 2,500 years.

Their seismic sources are typically area sources with the recurrence based in large part on historical seismicity. The maps are produced on a national scale, so do not include the level of source characterization detail that would generally be included in a site-specific probabilistic seismic hazard analysis. For the LANL area, the national maps show peak horizontal accelerations of less than 0.05 g and about 0.10 g for return periods of 500 and 2,500 years, respectively. These values are significantly lower than the site-specific values of about 0.14 g and 0.33 g determined in this study. The principal reason for these differences is most likely the absence of active faults as seismic sources in the Algermissen et al. (1990) maps and possibly, a lower recurrence for the area source zones. It is apparent that based on this study, the Pajarito fault system is a major source of seismic hazard in the LANL region. The lower uncertainty in models used to produce the national maps is also a possible reason for their lower values.

9.8 COMPARISON WITH DETERMINISTIC ESTIMATES

The deterministic empirical peak horizontal accelerations are similar to the values for Performance Category 4 (10,000-year return) (Table 8-4). The values estimated by the stochastic numerical modeling approach exceed the probabilistic peak accelerations for PC4. For the mesa top sites, the return period of the deterministic values is approximately 10,000 to 12,000 years (Figures 9-11 to 9-18). In contrast, the canyon sites with their high deterministic peak horizontal accelerations have return periods of greater than 40,000 years.

TABLE 9-1

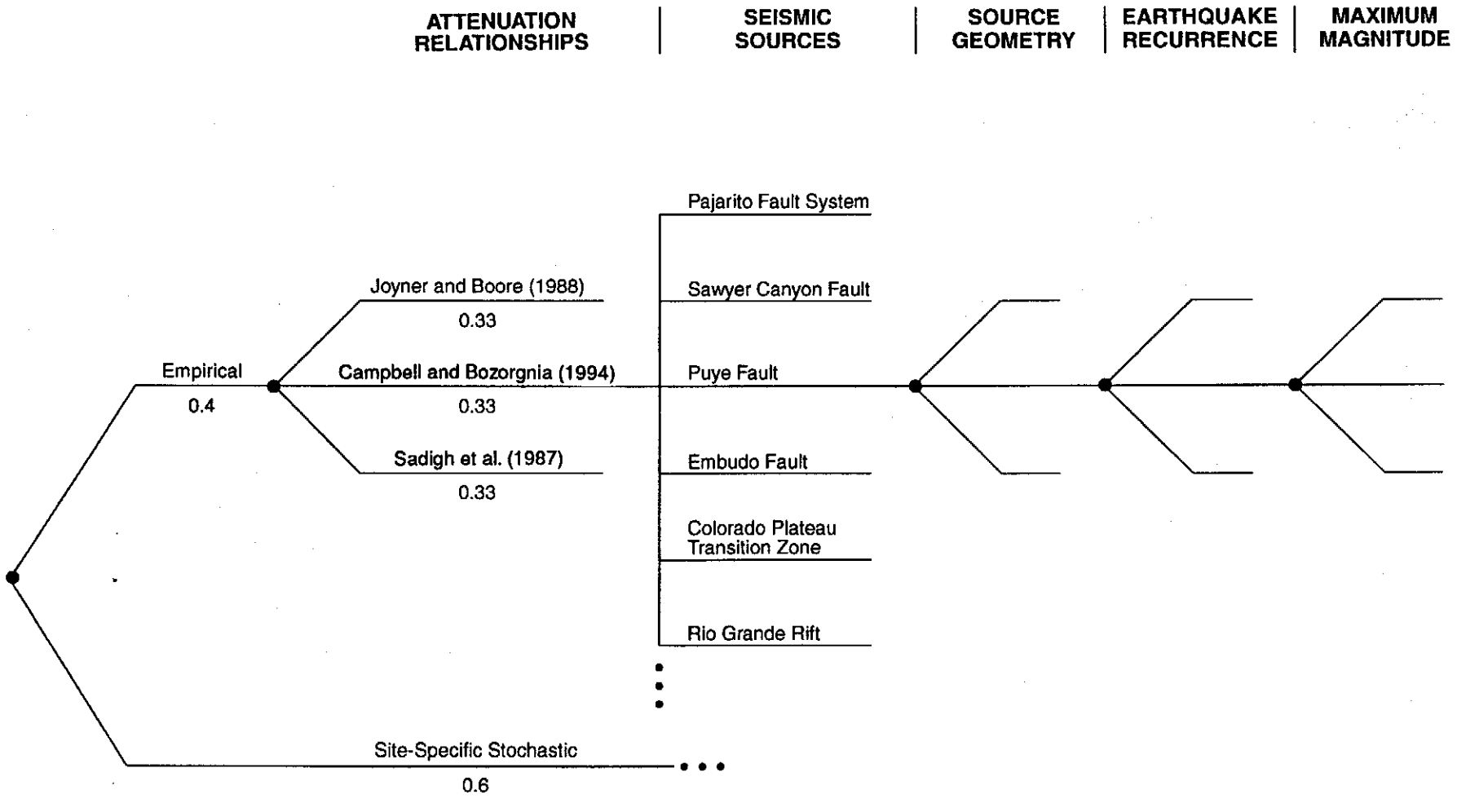
PROBABILISTIC PEAK HORIZONTAL ACCELERATIONS (in g's) for LANL

Site	Annual Exceedance Probability (Return Period)			
	PC1-$2x10^{-3}$ (500 yrs)	PC2-$1x10^{-3}$ (1,000 yrs)	PC3-$5x10^{-4}$ (2,000 yrs)	PC4-$1x10^{-4}$ (10,000 yrs)
TA-2	0.14	0.22	0.31	0.57
TA-3	0.14	0.21	0.30	0.56
TA-16	0.14	0.21	0.29	0.53
TA-18	0.14	0.22	0.31	0.57
TA-21	0.15	0.22	0.31	0.55
TA-41	0.14	0.22	0.31	0.57
TA-46	0.15	0.22	0.30	0.55
TA-55	0.15	0.22	0.30	0.56

TABLE 9-2

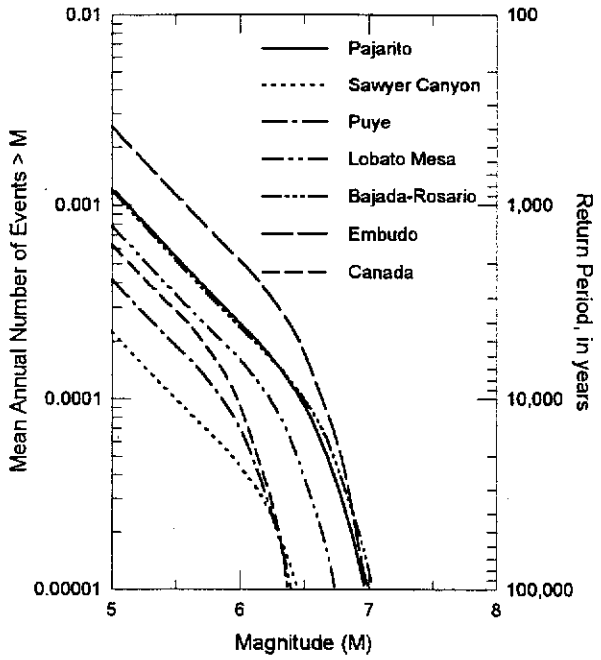
DOMINANT EARTHQUAKES

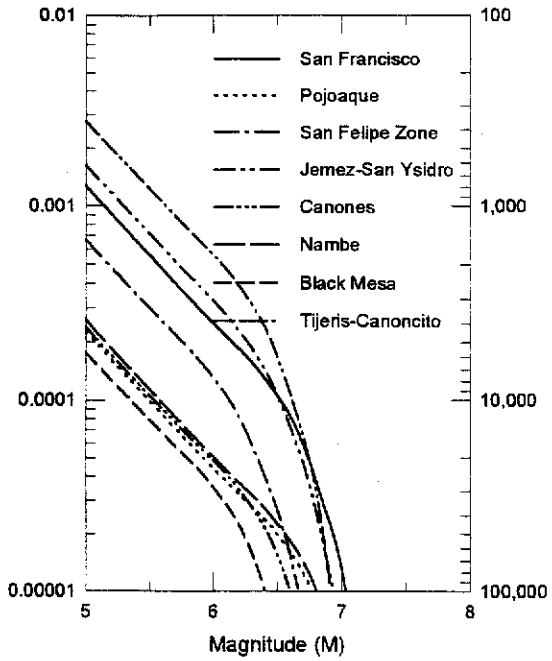
Return Period (yrs)	Peak Horizontal Acceleration		0.2 sec Spectral Acceleration		1.0 sec Spectral Acceleration	
	$\bar{M}$	$\bar{D}$ (km)	$\bar{M}$	$\bar{D}$ (km)	$\bar{M}$	$\bar{D}$ (km)
500	5.9	8.5	5.9	10.0	6.2	12.5
1,000	6.0	5.9	6.0	8.0	6.3	9.2
2,000	6.0	5.0	6.0	6.0	6.4	6.4
10,000	6.2	2.5	6.2	4.0	6.5	3.0

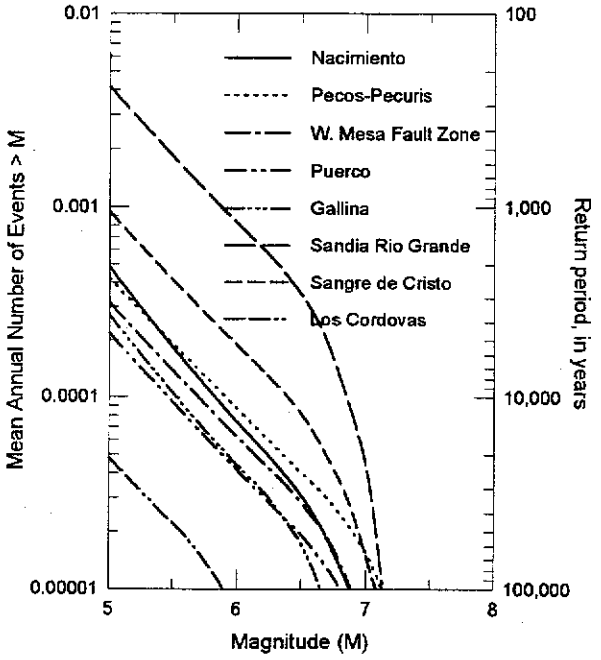


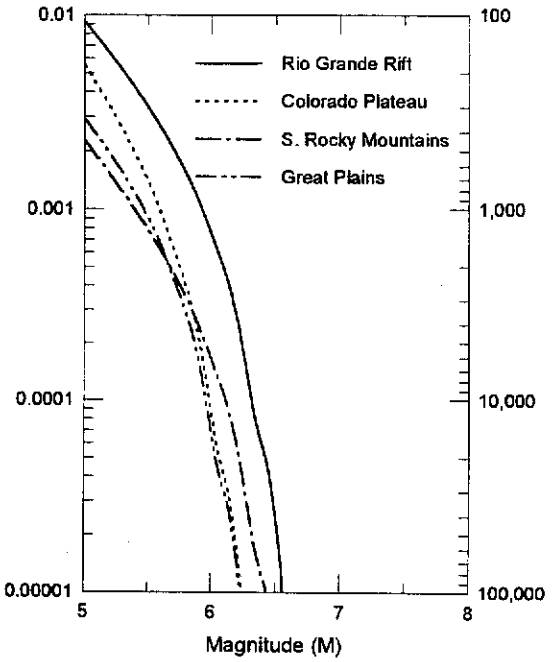
Project No. 91C0509	Los Alamos Seismic Hazards	SEISMIC HAZARD MODEL LOGIC TREE	Figure 9-1
Woodward-Clyde Federal Services			

SK9423-A9500/021095/gos



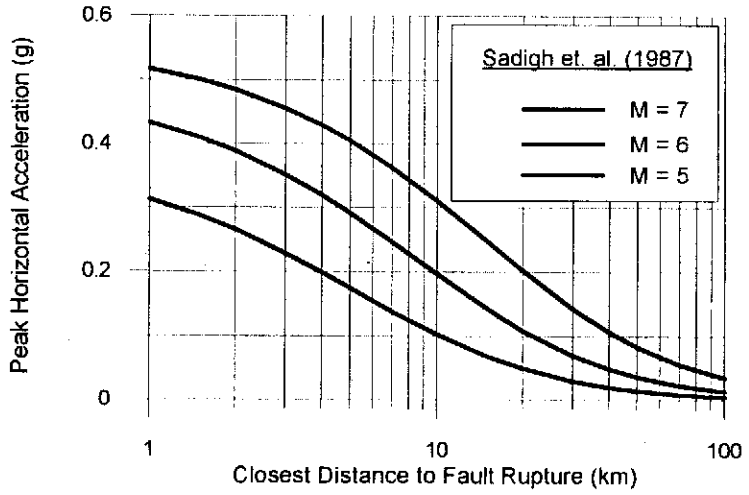


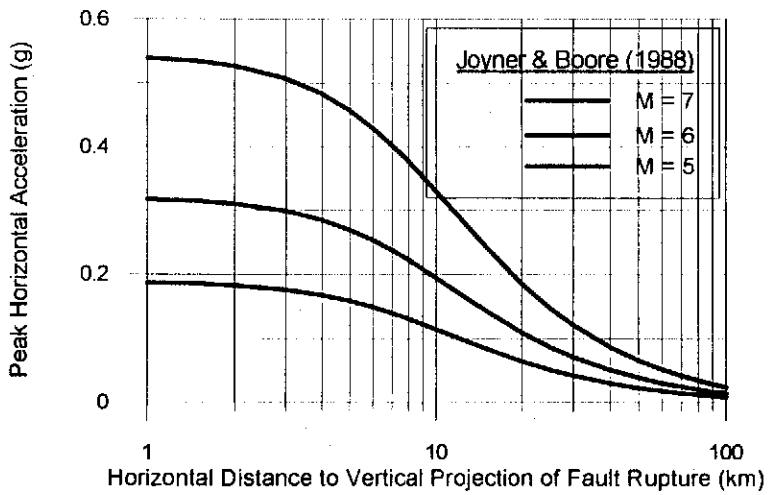


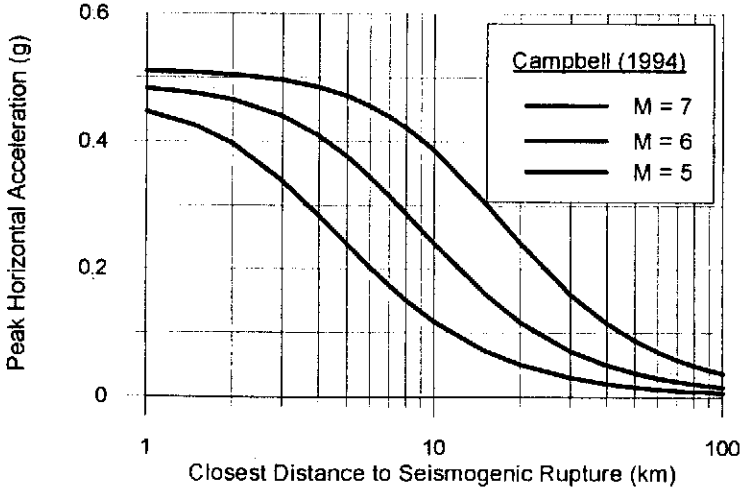


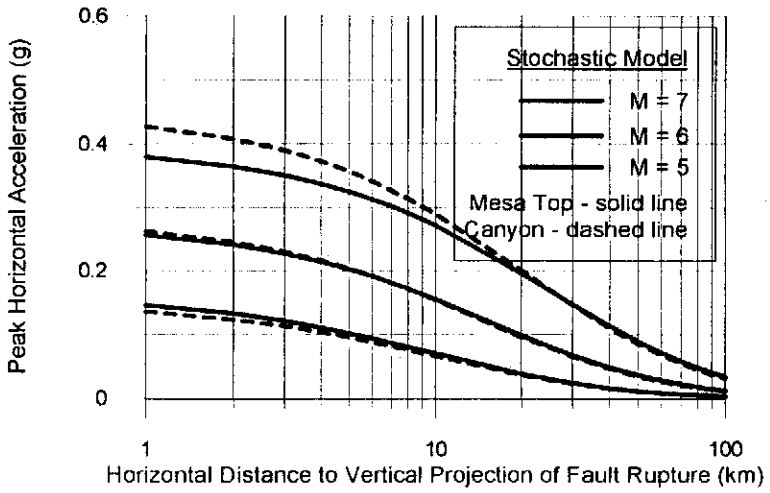
Project No. 91C0509	Los Alamos Seismic Hazards	SEISMIC SOURCE RECURRENCE	Figure 9-2
Woodward-Clyde Federal Services			

RECURN.GRF



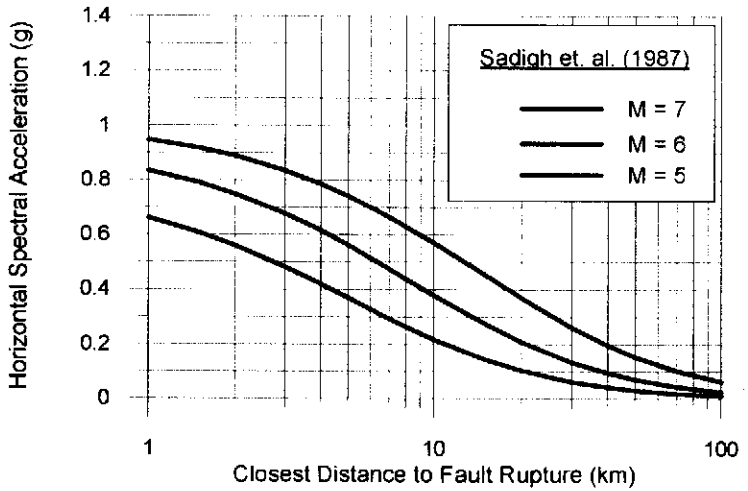


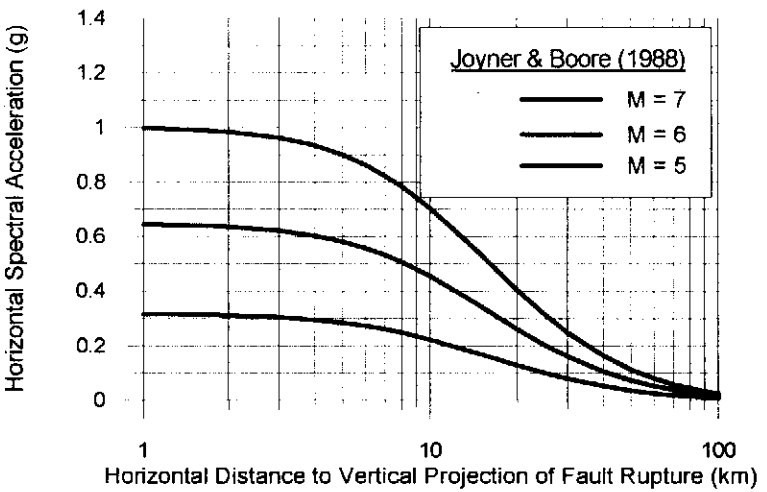


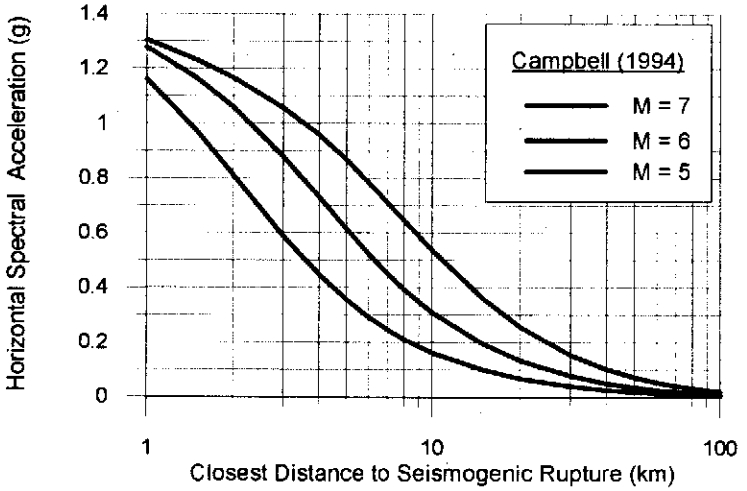


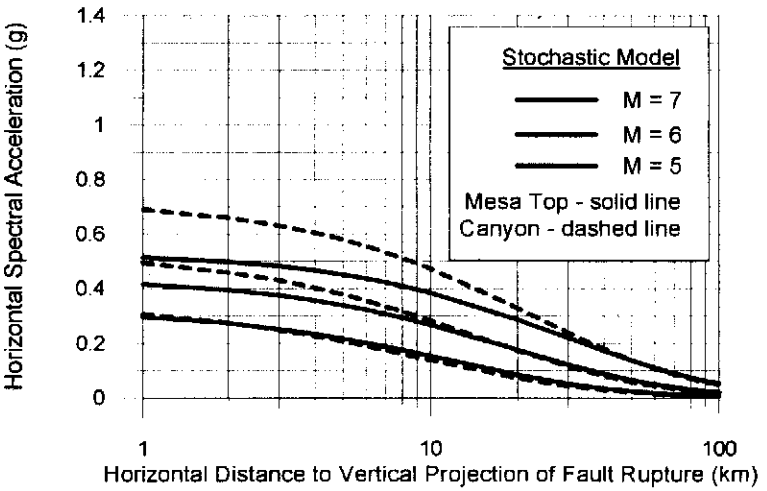
Project No. 91C0509	Los Alamos Seismic Hazards	ATTENUATION RELATIONSHIPS PEAK GROUND ACCELERATION	Figure 9-3
Woodward-Clyde Federal Services			

ATTEN.GRF



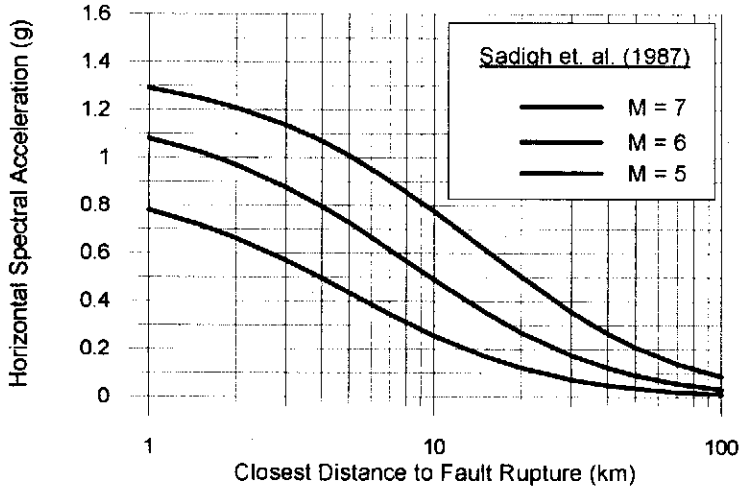


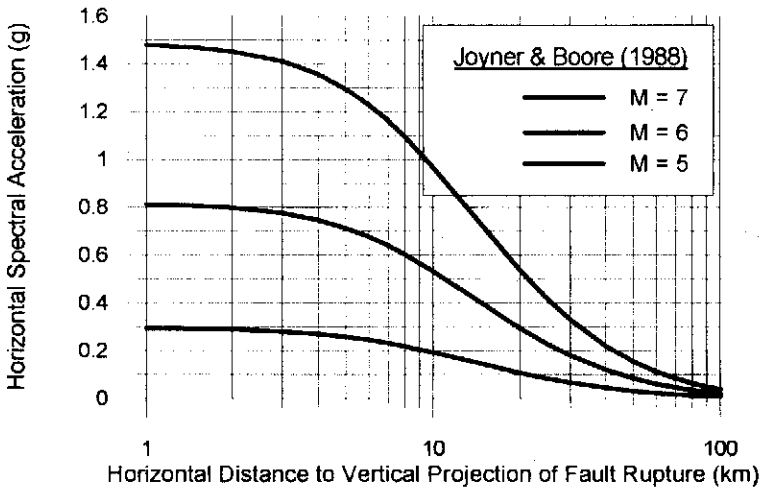


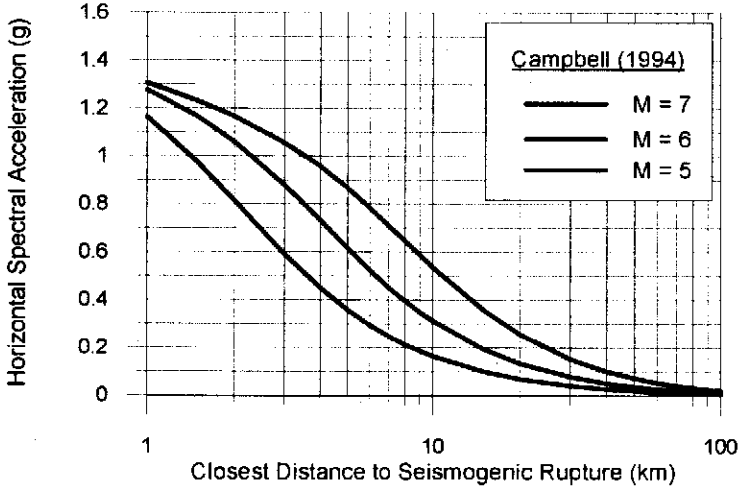


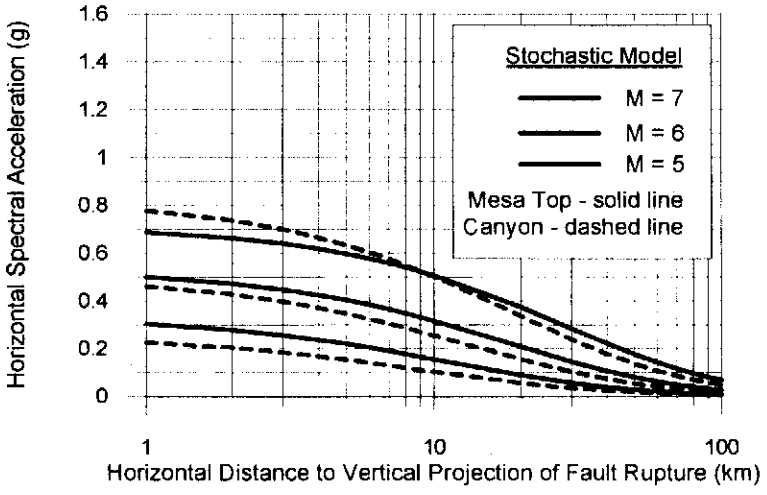
Project No. 91C0509	Los Alamos Seismic Hazards	ATTENUATION RELATIONSHIPS HORIZONTAL SPECTRAL ACCELERATION AT 0.1 SEC	Figure 9-4
Woodward-Clyde Federal Services			

ATTEN-1.GRF



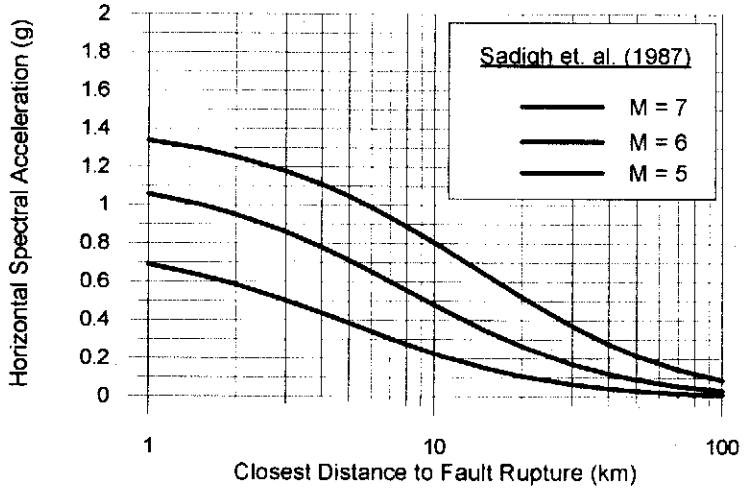


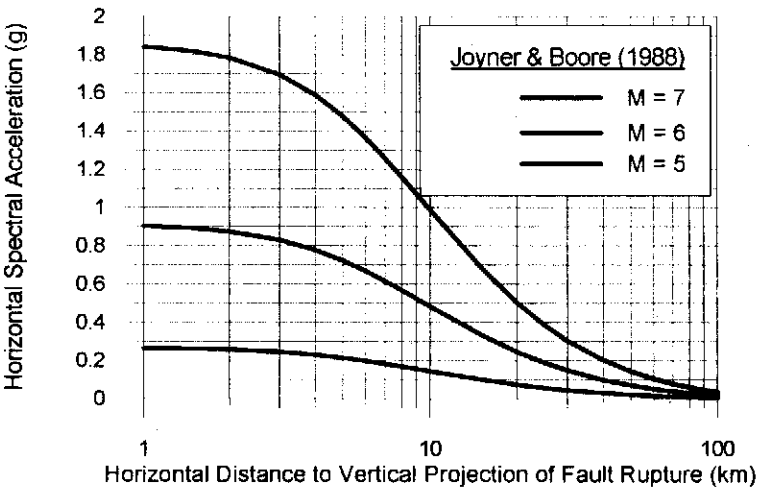


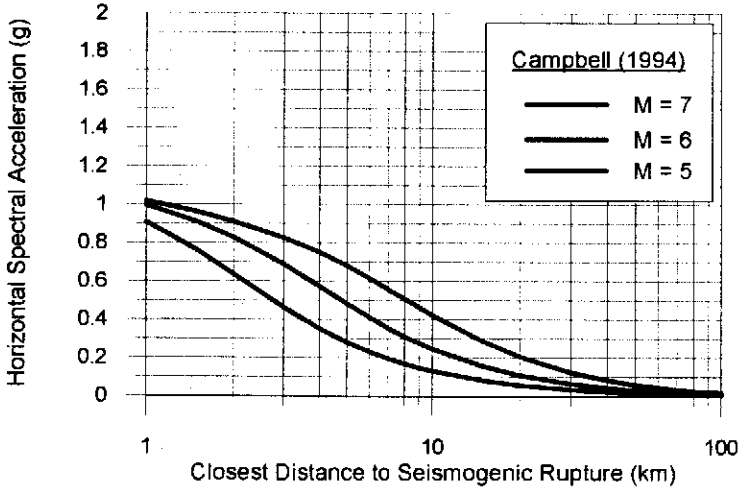


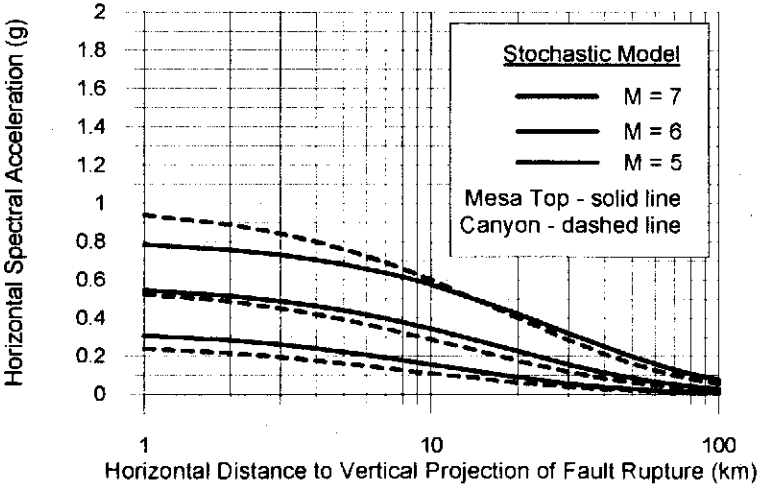
Project No. 91C0509	Los Alamos Seismic Hazards	ATTENUATION RELATIONSHIPS HORIZONTAL SPECTRAL ACCELERATION AT 0.2 SEC	Figure 9-5
Woodward-Clyde Federal Services			

ATTEN-2.GRF



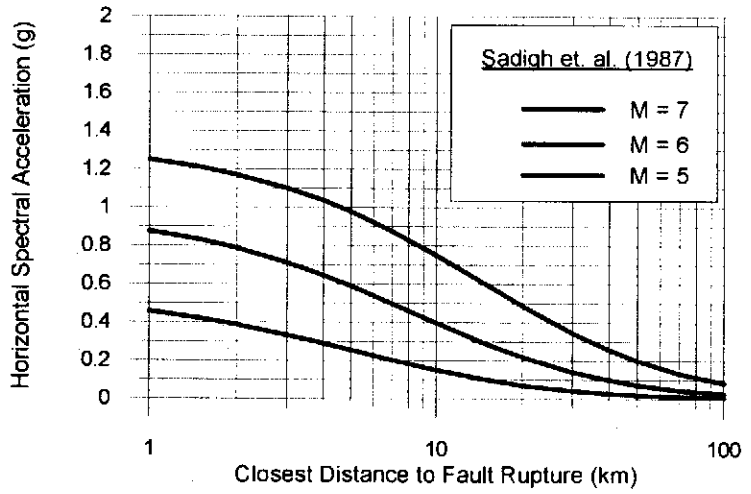


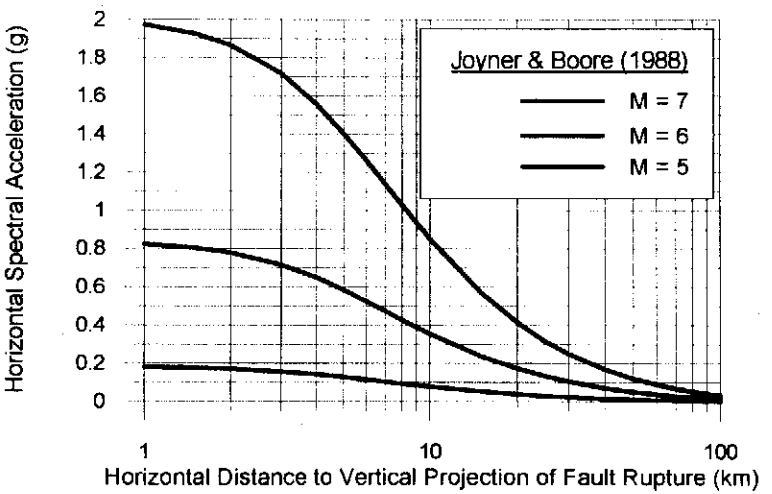


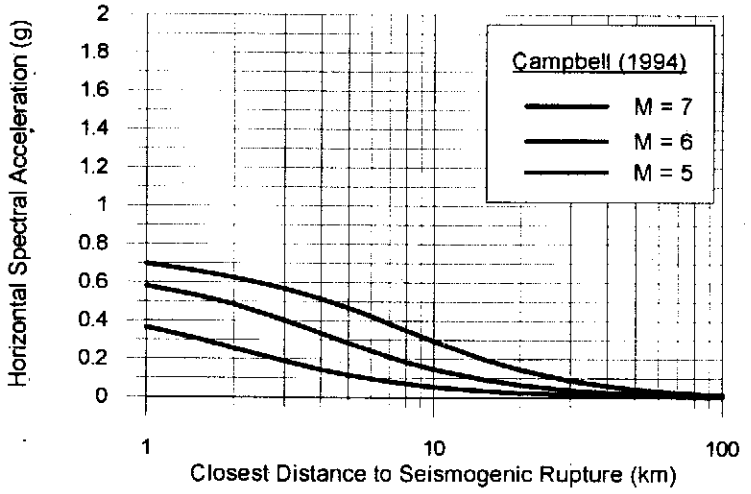


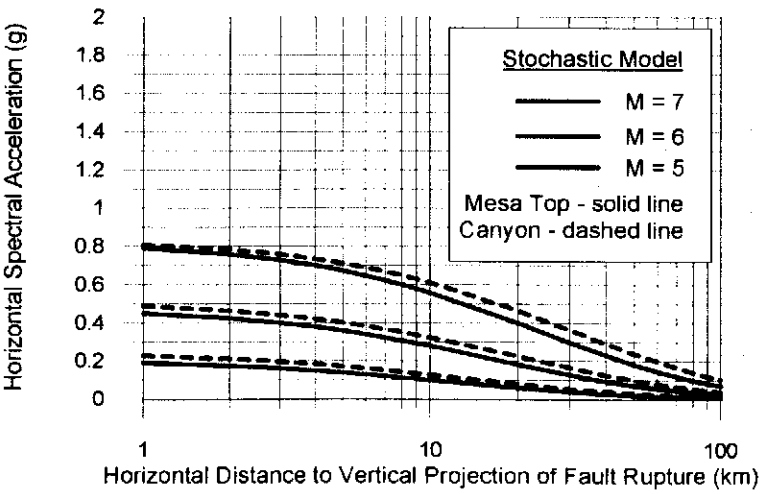
Project No. 91C0509	Los Alamos Seismic Hazards	ATTENUATION RELATIONSHIPS HORIZONTAL SPECTRAL ACCELERATION AT 0.3 SEC	Figure 9-6
Woodward-Clyde Federal Services			

ATTEN-3.GRF



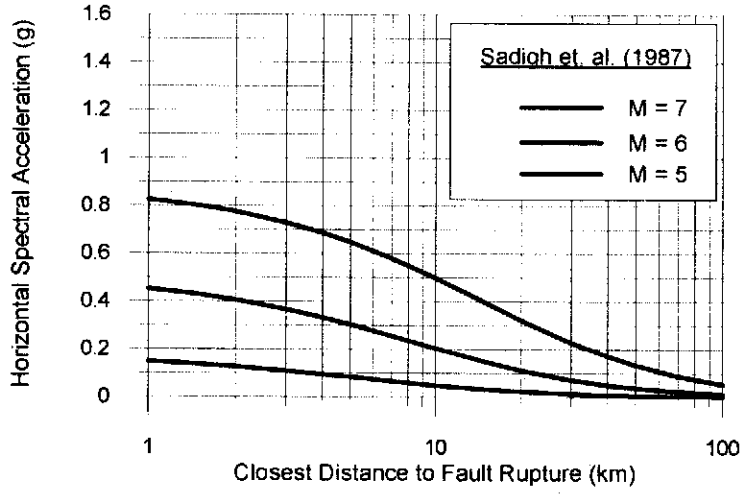


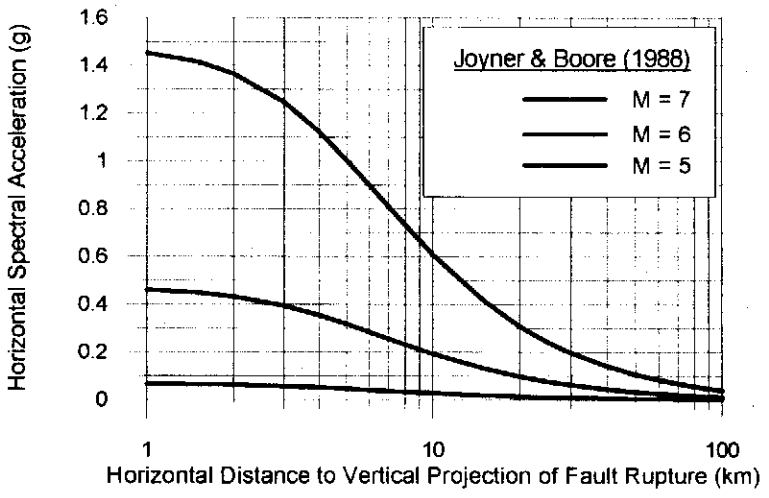


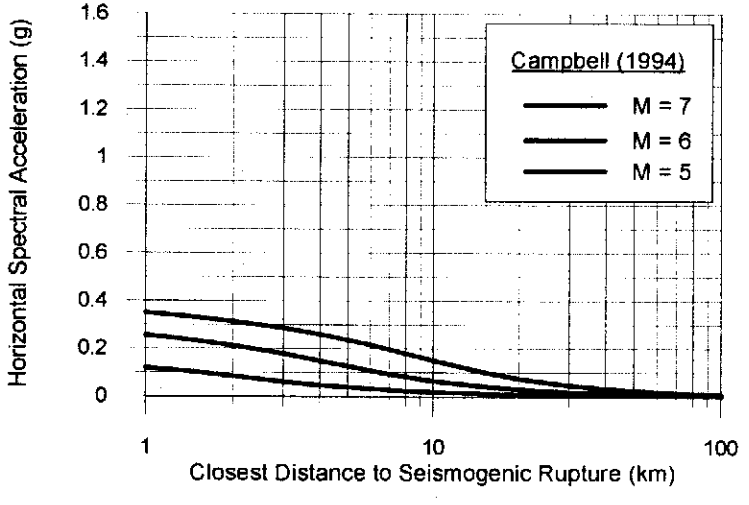


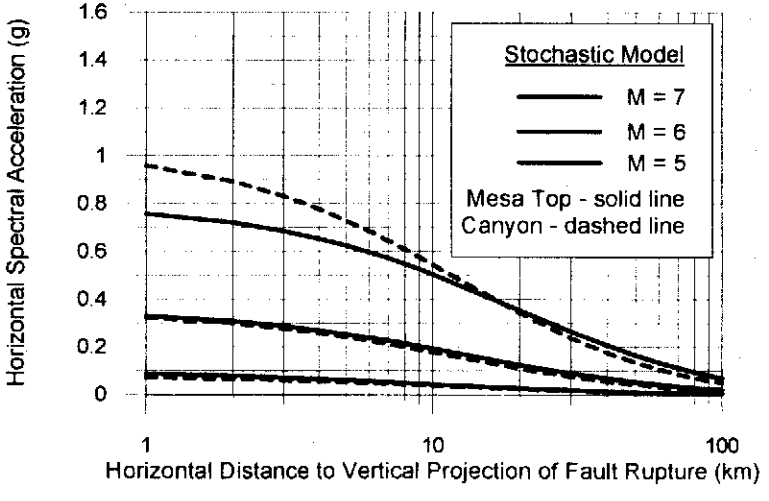
Project No. 91C0509	Los Alamos Seismic Hazards	ATTENUATION RELATIONSHIPS HORIZONTAL SPECTRAL ACCELERATION AT 0.5 SEC	Figure 9-7
Woodward-Clyde Federal Services			

ATTEN-4.GRF



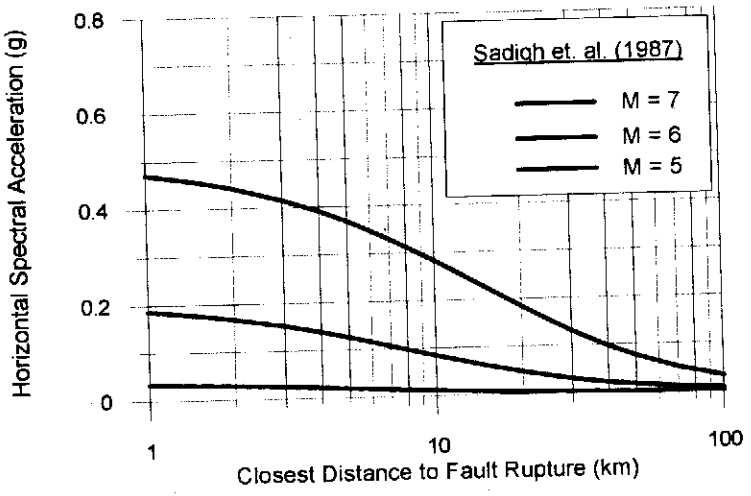


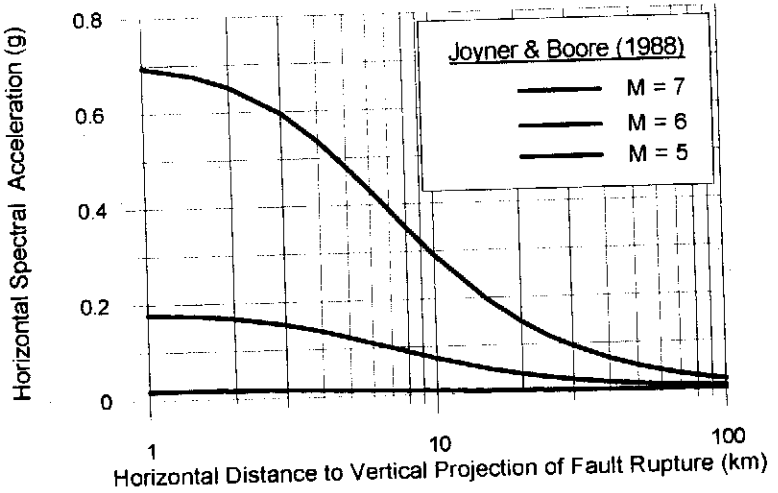


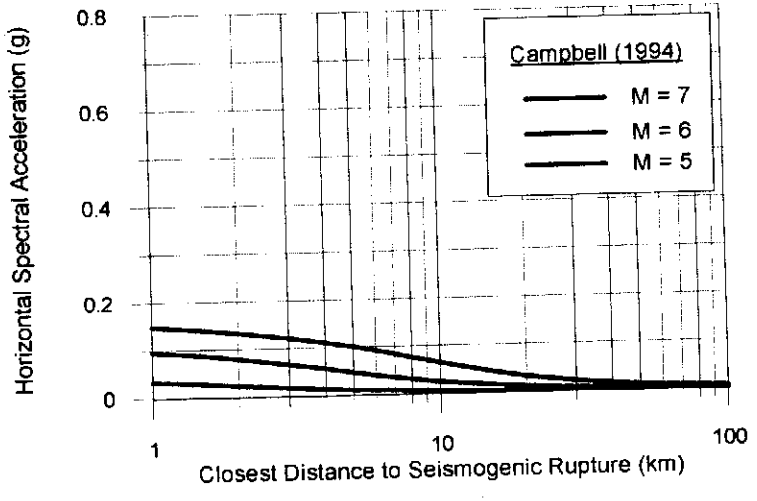


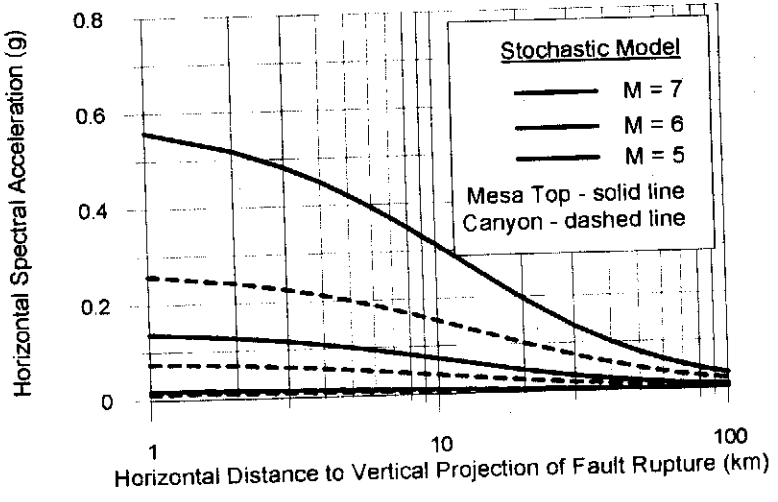
Project No. 91C0509	Los Alamos Seismic Hazards	ATTENUATION RELATIONSHIPS HORIZONTAL SPECTRAL ACCELERATION AT 1 SEC	Figure 9-8
Woodward-Clyde Federal Services			

ATTEN-5.GRF



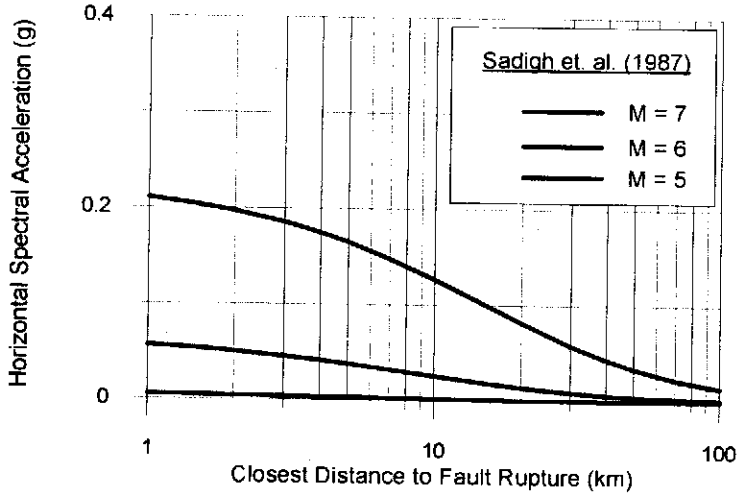


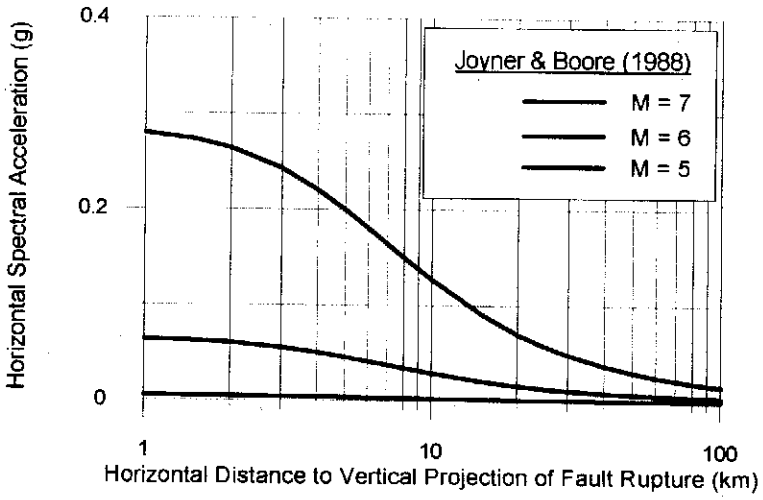


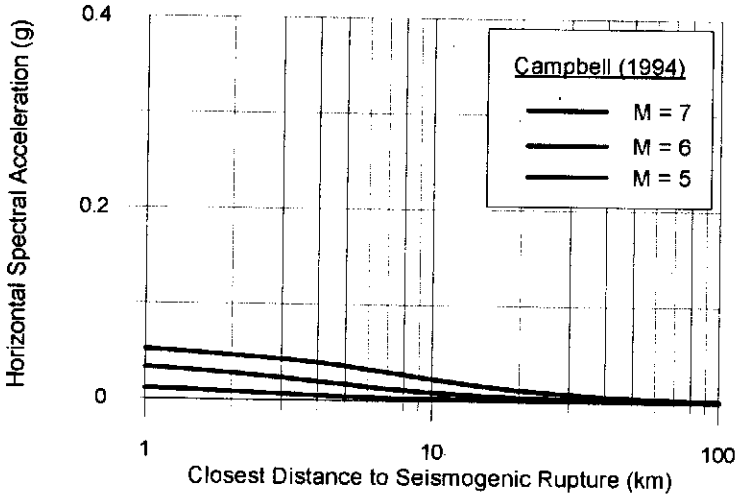


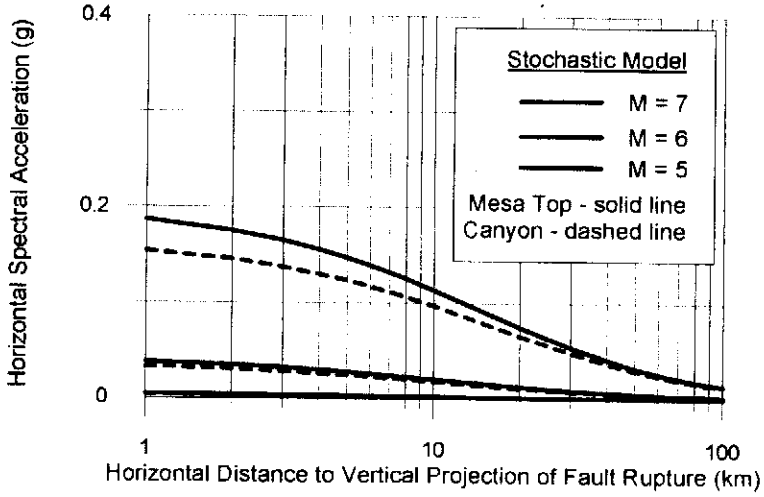
Project No. 91C0509	Los Alamos Seismic Hazards	ATTENUATION RELATIONSHIPS HORIZONTAL SPECTRAL ACCELERATION AT 2 SEC	Figure 9-9
Woodward-Clyde Federal Services			

ATTEN-6.GRF



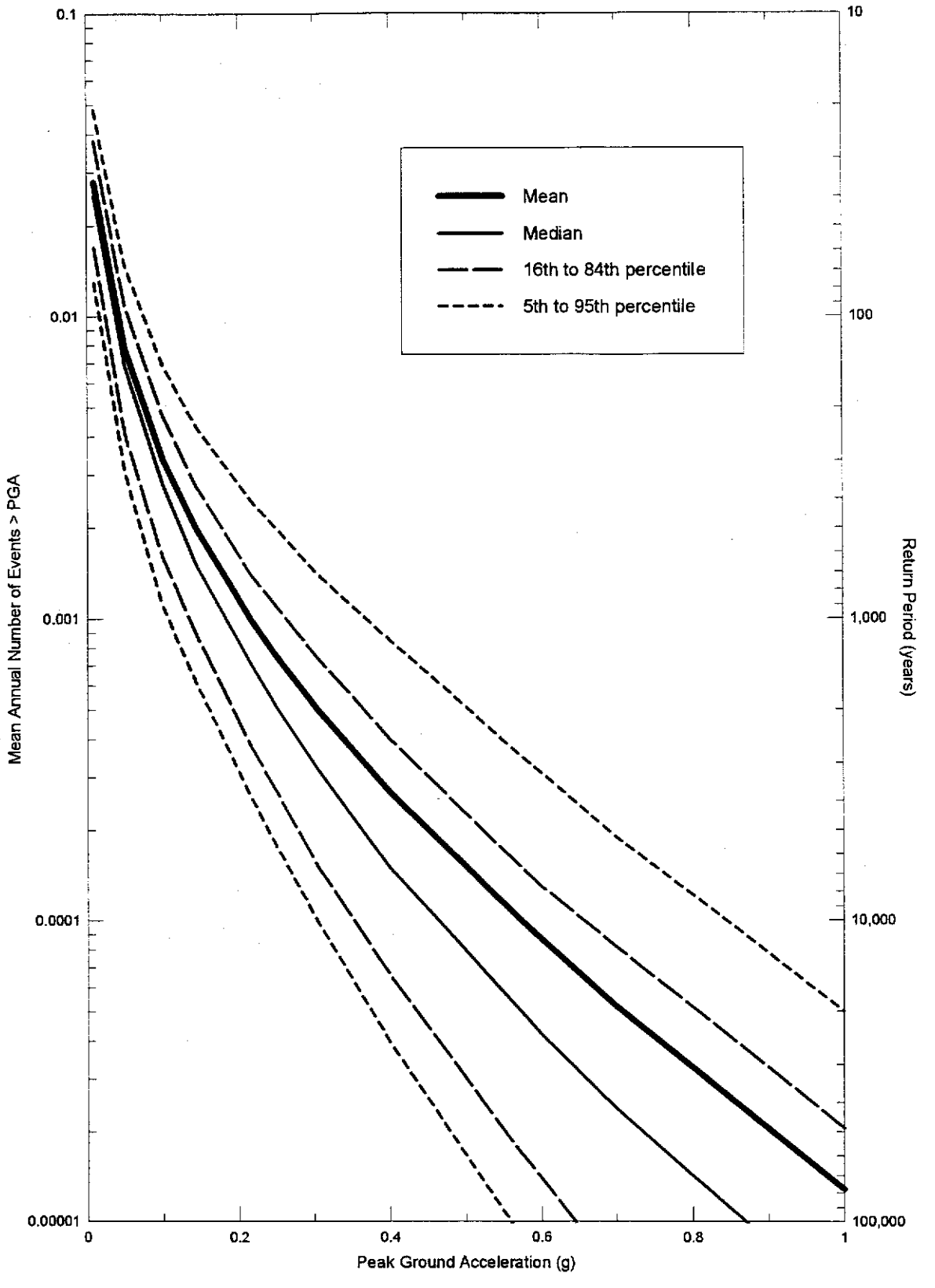






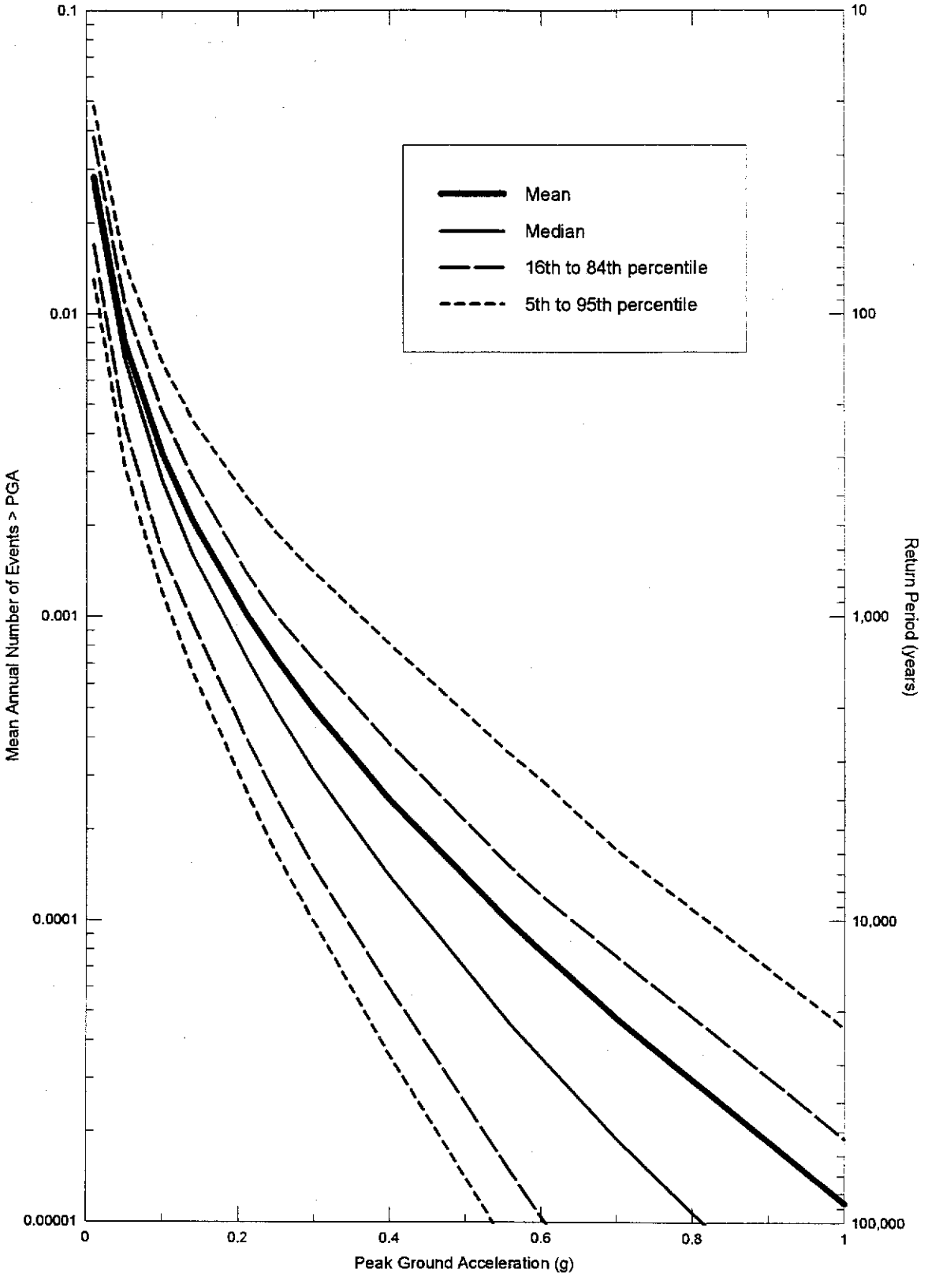
Project No. 91C0509	Los Alamos Seismic Hazards	ATTENUATION RELATIONSHIPS HORIZONTAL SPECTRAL ACCELERATION AT 4 SEC	Figure 9-10
Woodward-Clyde Federal Services			

ATTEN-7.GRF



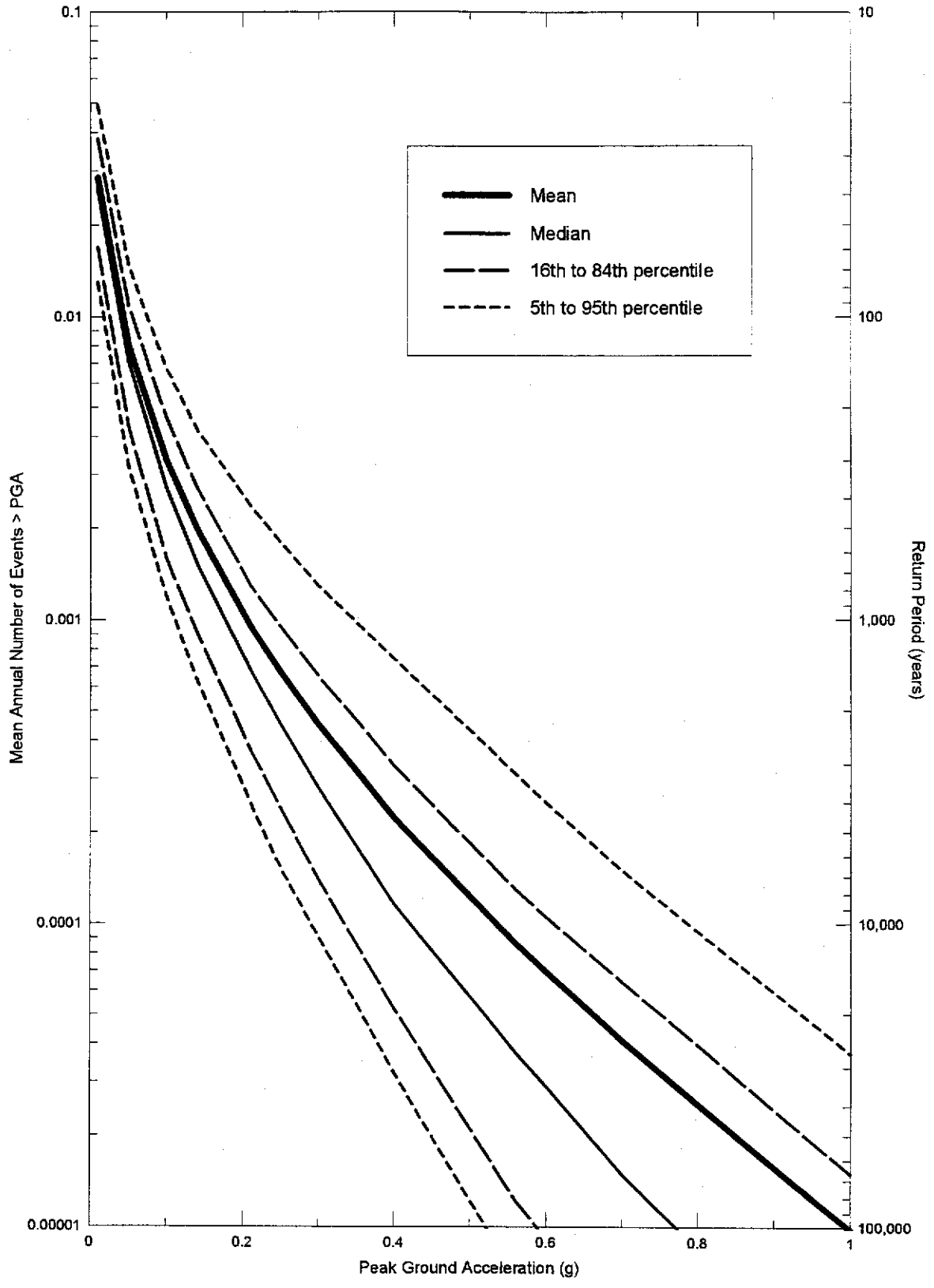
Project No. 91C0509	Los Alamos Seismic Hazards	MEAN AND 5th TO 95th PERCENTILE SEISMIC HAZARD CURVES FOR PEAK HORIZONTAL ACCELERATION AT TA-2	Figure 9-11
Woodward-Clyde Federal Services			

CON-REC.GRF



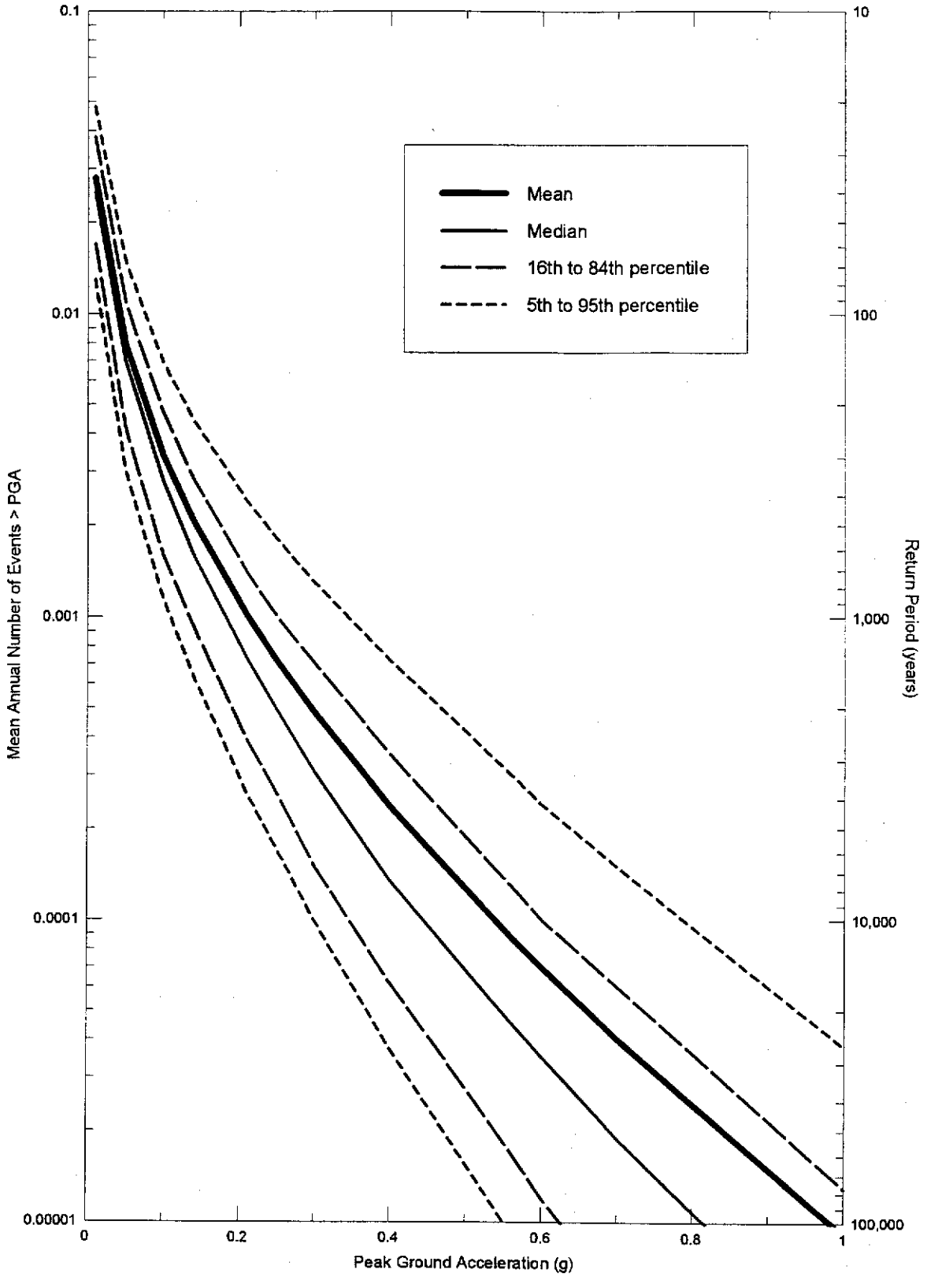
Project No. 91C0509	Los Alamos Seismic Hazards	MEAN AND 5th to 95th PERCENTILE SEISMIC HAZARD CURVES FOR PEAK HORIZONTAL ACCELERATION AT TA-3	Figure 9-12
Woodward-Clyde Federal Services			

CON-REC.GRF



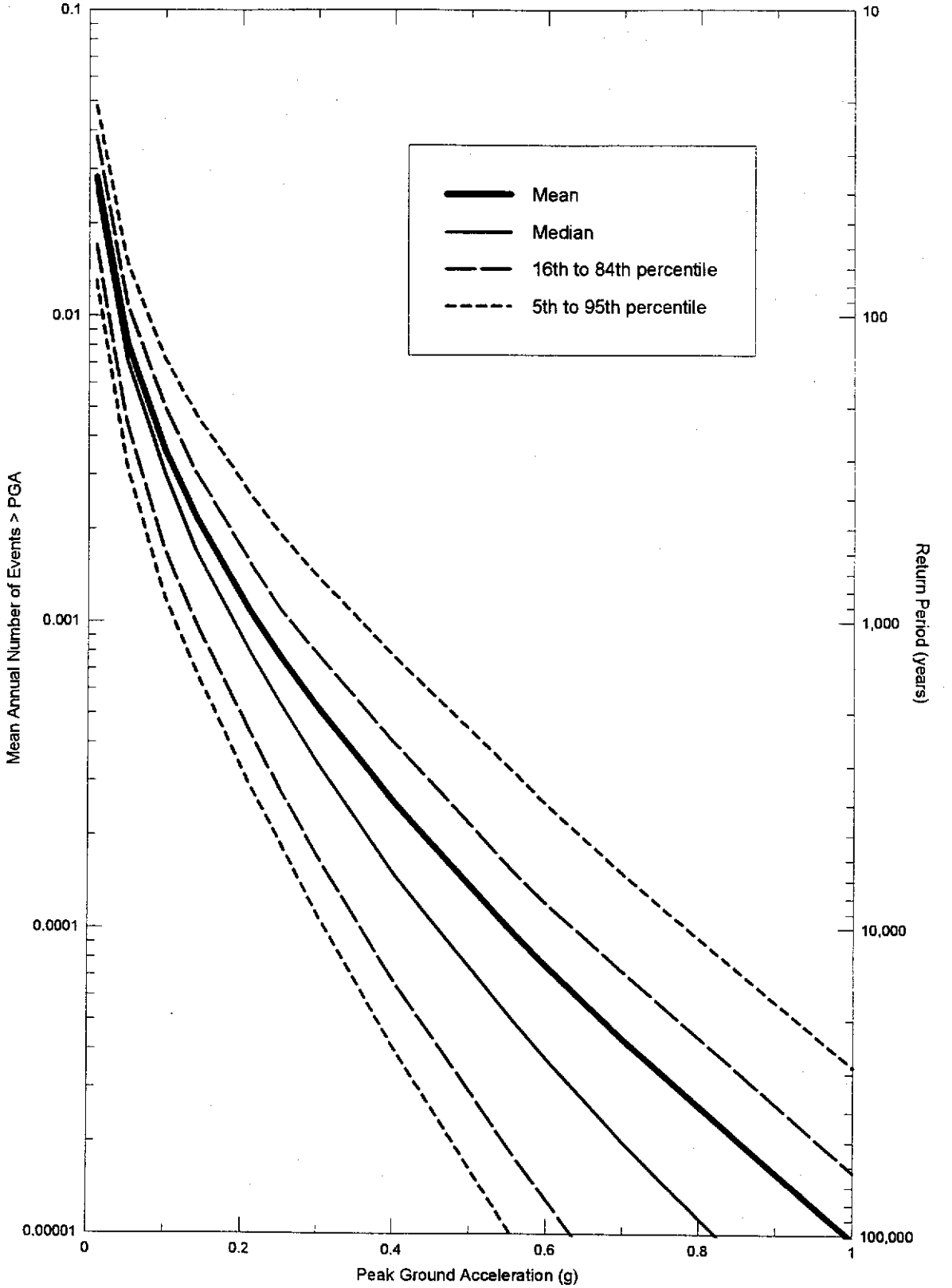
Project No. 91C0509	Los Alamos Seismic Hazards	MEAN AND 5th TO 95th PERCENTILE SEISMIC HAZARD CURVES FOR PEAK HORIZONTAL ACCELERATION AT TA-16	Figure 9-13
Woodward-Clyde Federal Services			

CON-REC.GRF



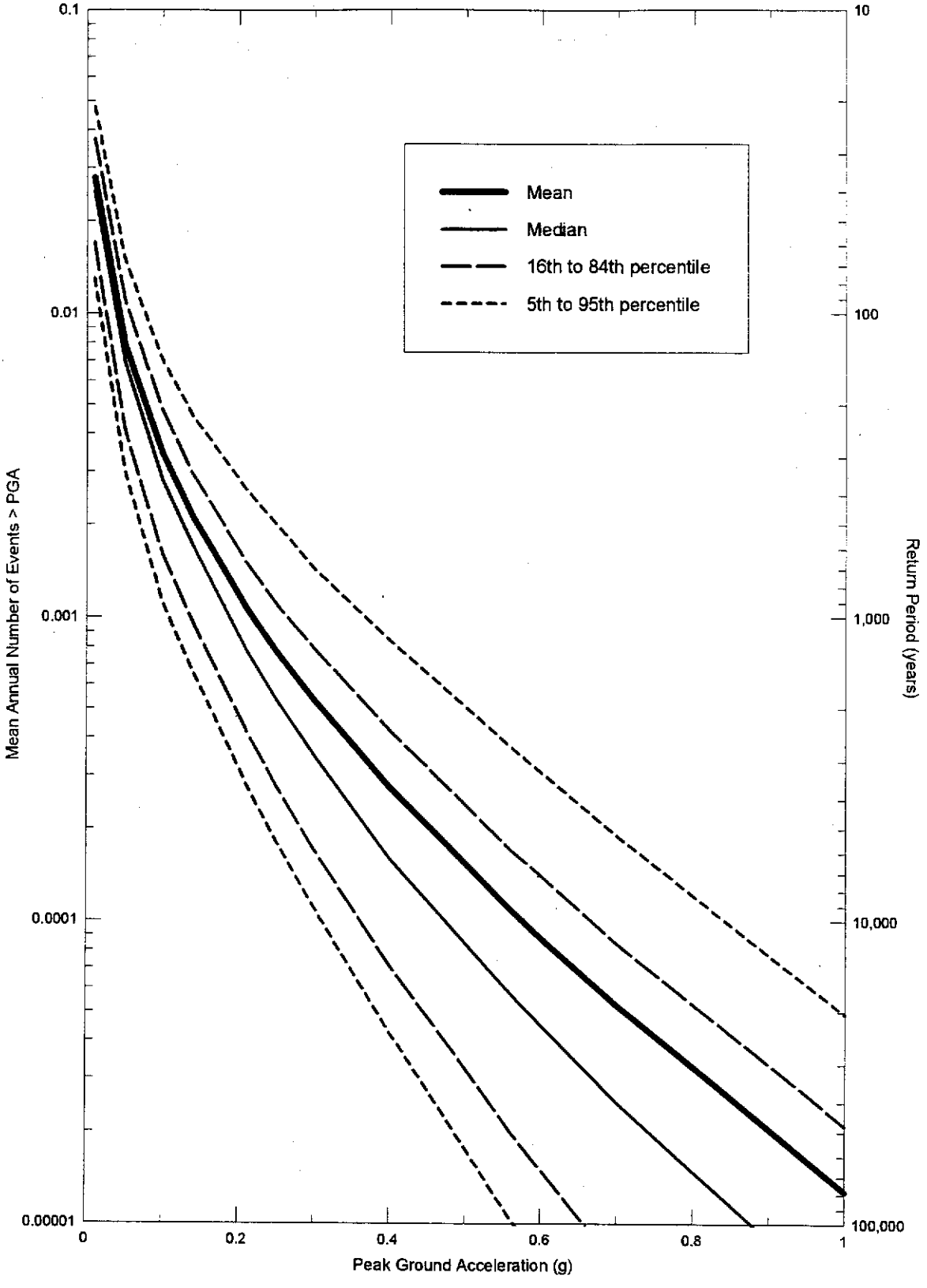
Project No. 91C0509	Los Alamos Seismic Hazards	MEAN AND 5th TO 95th PERCENTILE SEISMIC HAZARD CURVES FOR PEAK HORIZONTAL ACCELERATION AT TA-18	Figure 9-14
Woodward-Clyde Federal Services			

CON-REC.GRF



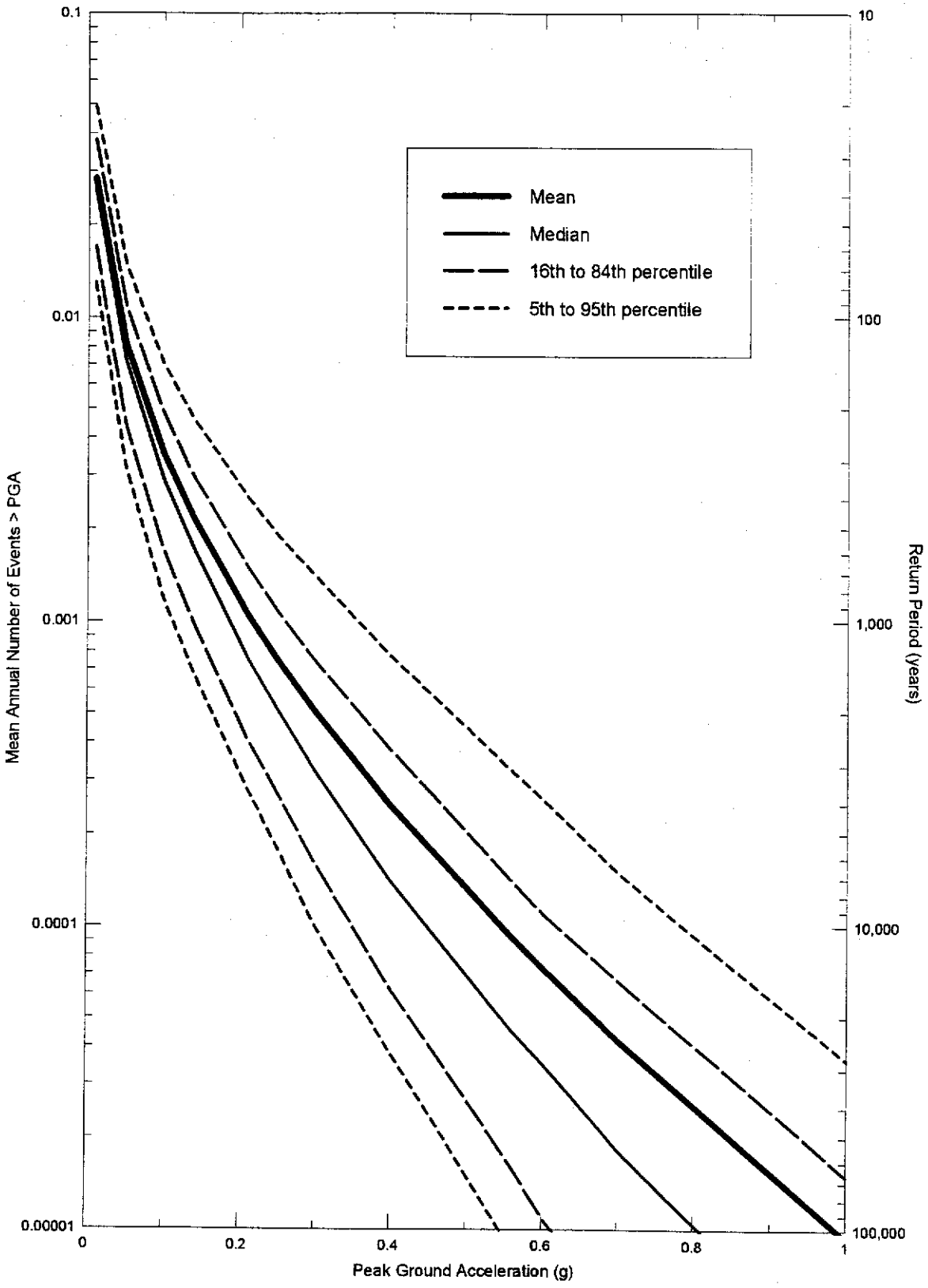
Project No. 91C0509	Los Alamos Seismic Hazards	MEAN AND 5th TO 95th PERCENTILE SEISMIC HAZARD CURVES FOR PEAK HORIZONTAL ACCELERATION AT TA-21	Figure 9-15
Woodward-Clyde Federal Services			

CON-REC.GRF



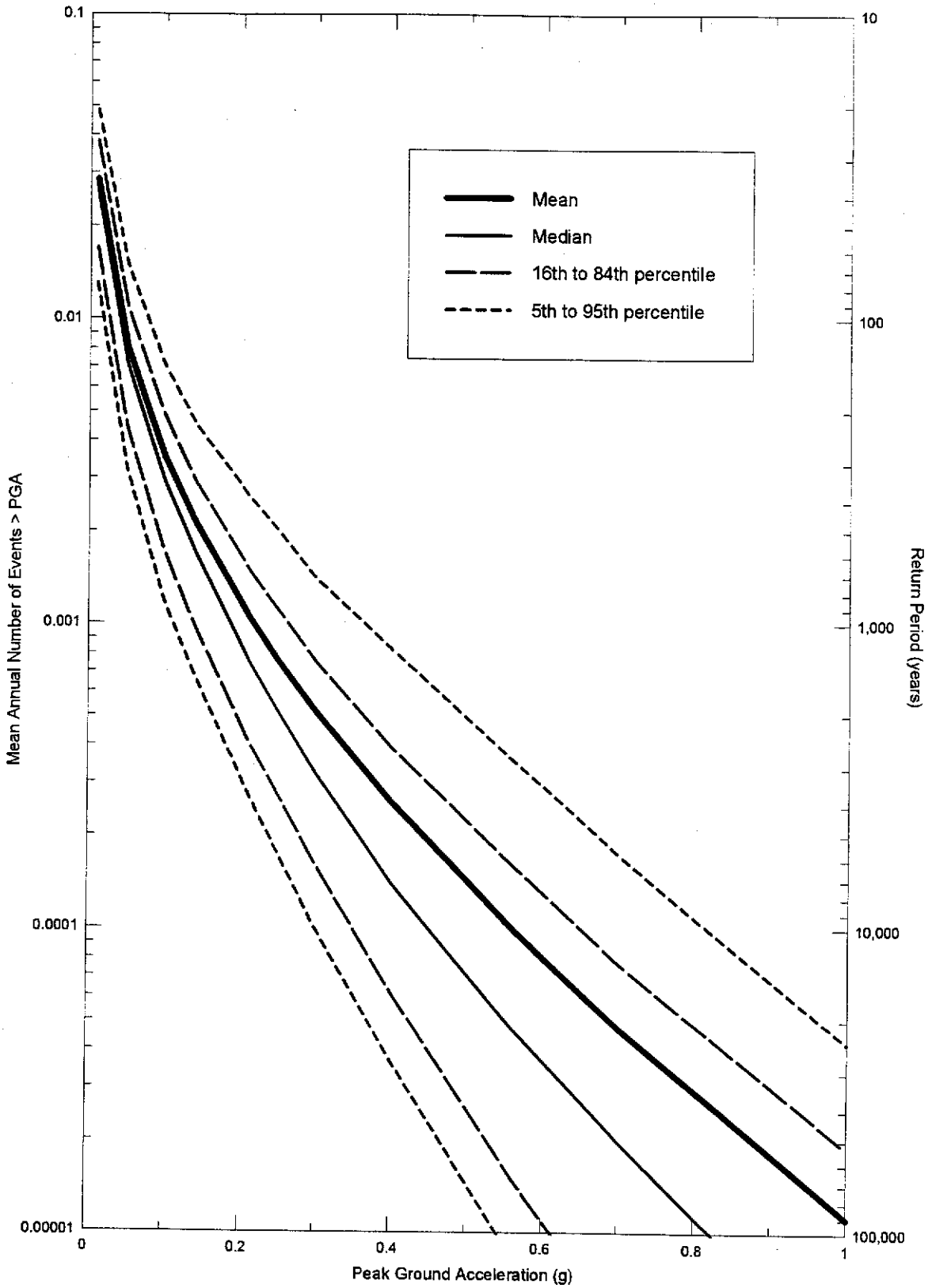
Project No. 91C0509	Los Alamos Seismic Hazards	MEAN AND 5th TO 95th PERCENTILE SEISMIC HAZARD CURVES FOR PEAK HORIZONTAL ACCELERATION AT TA-41	Figure 9-16
Woodward-Clyde Federal Services			

CON-REC.GRF



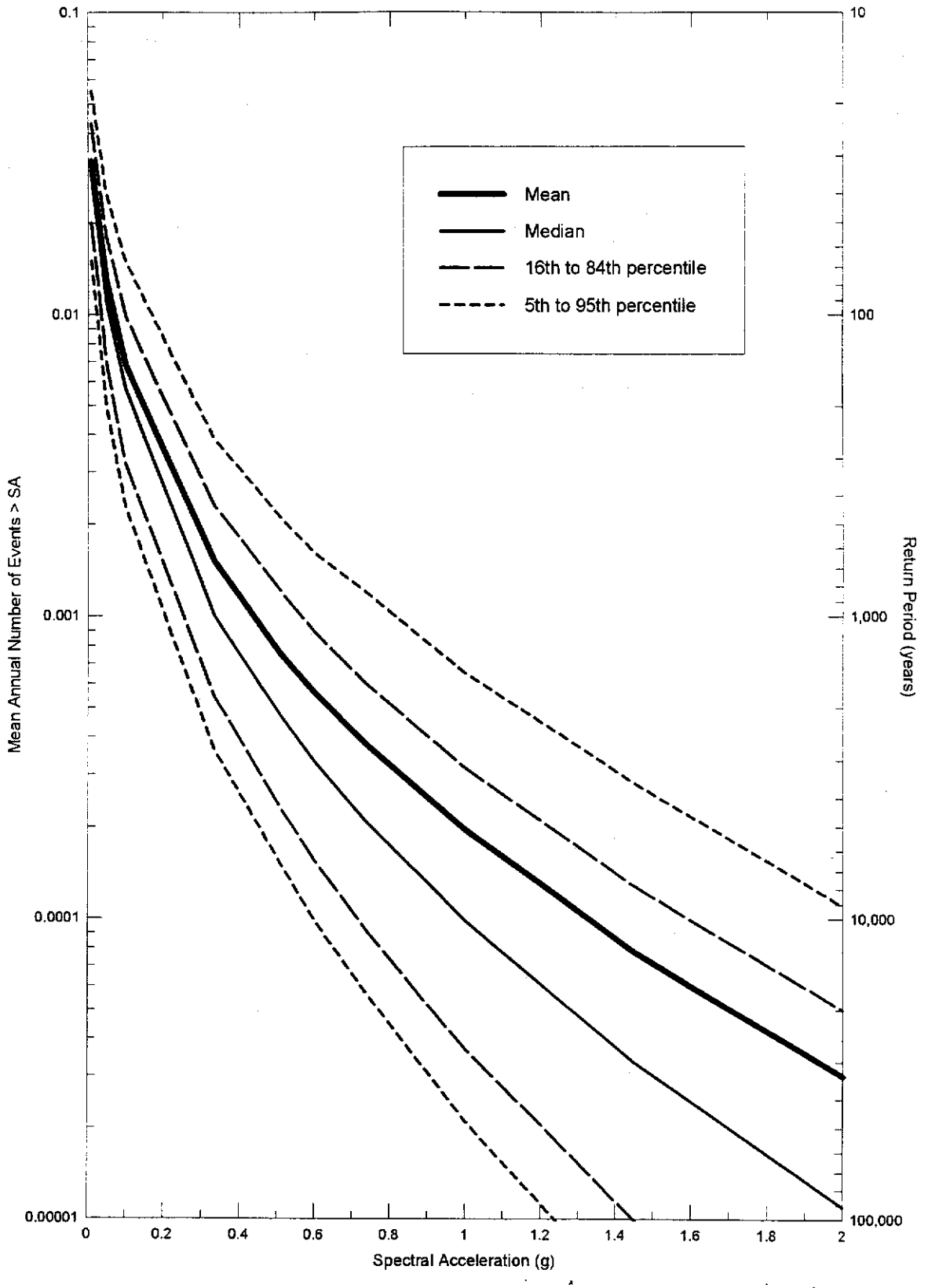
Project No. 91C0509	Los Alamos Seismic Hazards	MEAN AND 5th TO 95th PERCENTILE SEISMIC HAZARD CURVES FOR PEAK HORIZONTAL ACCELERATION AT TA-46	Figure 9-17
Woodward-Clyde Federal Services			

CON-REC.GRF



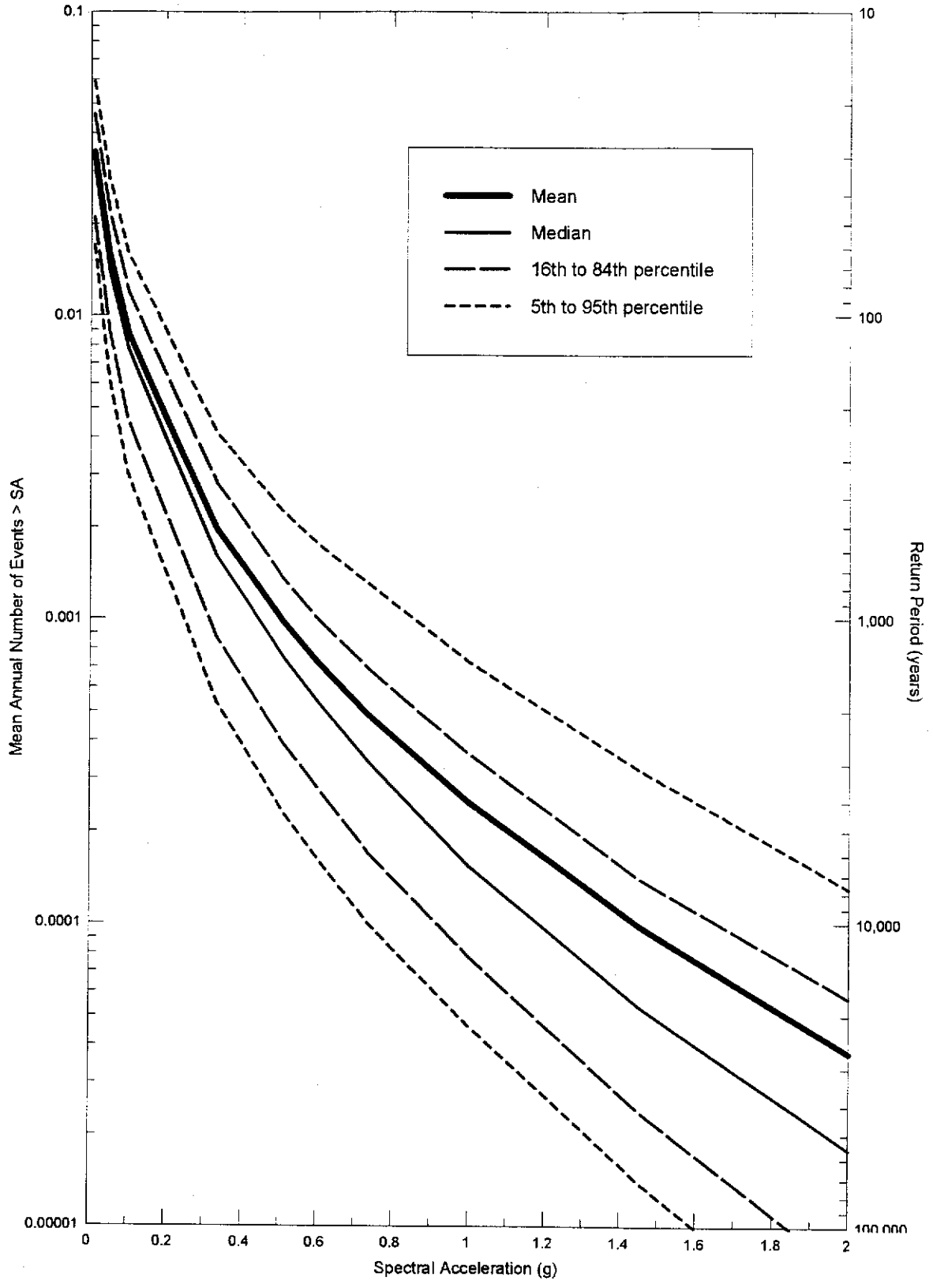
Project No. 91C0509	Los Alamos Seismic Hazards	MEAN AND 5th TO 95th PERCENTILE SEISMIC HAZARD CURVES FOR PEAK HORIZONTAL ACCELERATION AT TA-55	Figure 9-18
Woodward-Clyde Federal Services			

CON-REC.GRF



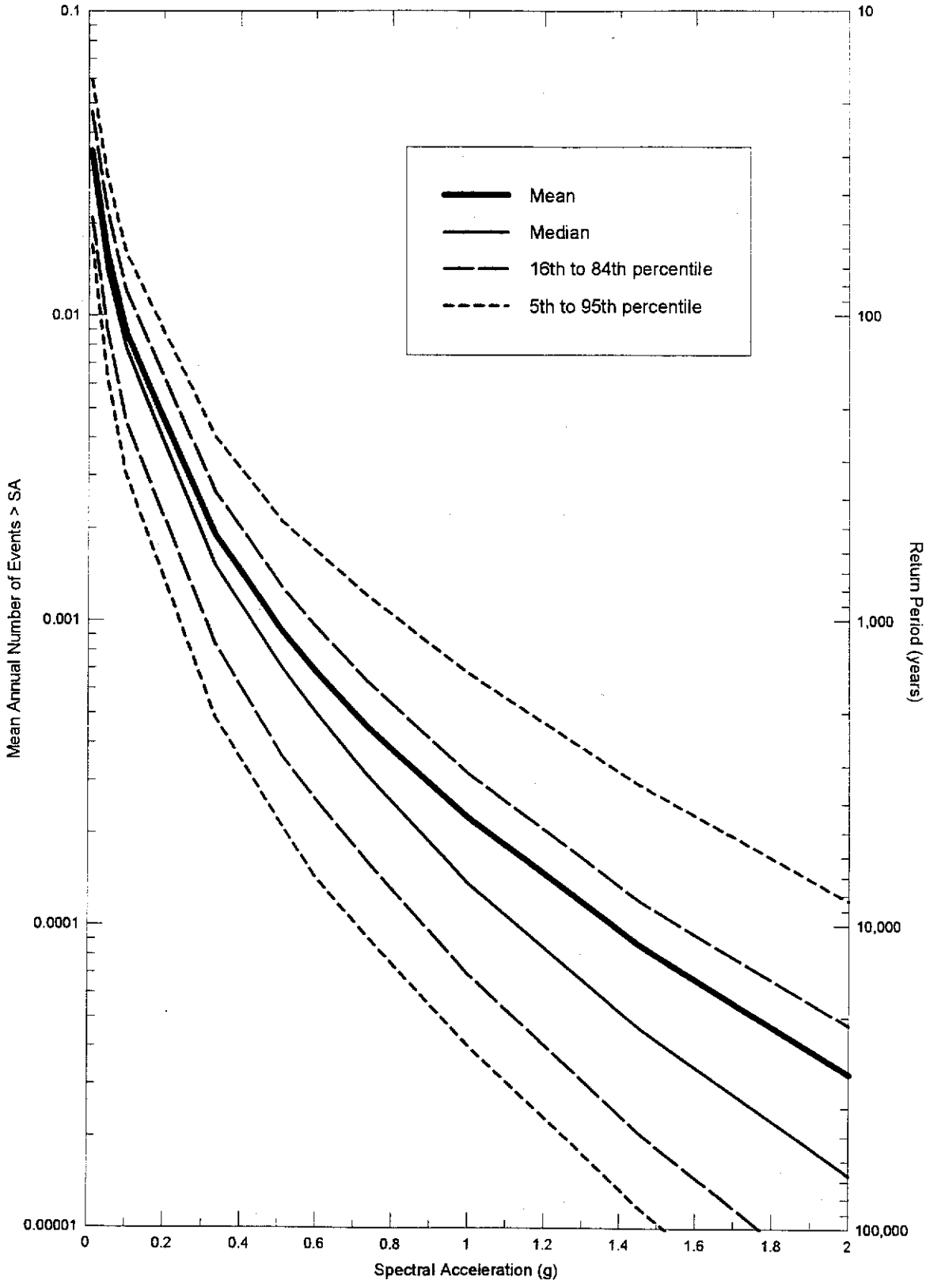
Project No. 91C0509	Los Alamos Seismic Hazards	MEAN AND 5th TO 95th PERCENTILE SEISMIC HAZARD CURVES FOR 0.2 SEC HORIZONTAL SPECTRAL ACCELERATION, TA-2	Figure 9-19
Woodward-Clyde Federal Services			

CON-REC.GRF



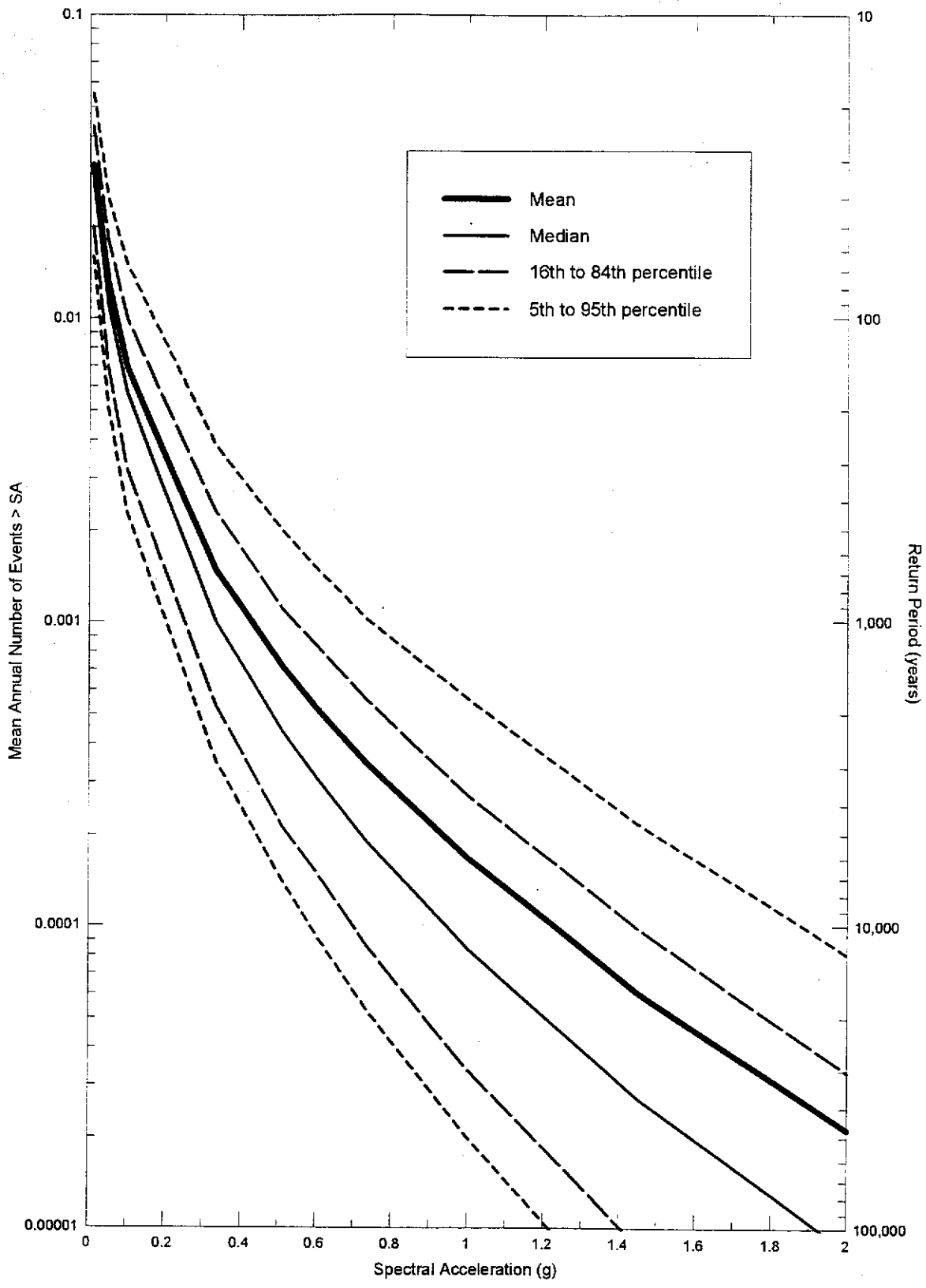
Project No. 91C0509	Los Alamos Seismic Hazards	MEAN AND 5th TO 95th PERCENTILE SEISMIC HAZARD CURVES FOR 0.2 SEC HORIZONTAL SPECTRAL ACCELERATION, TA-3	Figure 9-20
Woodward-Clyde Federal Services			

CON-REC.GRF



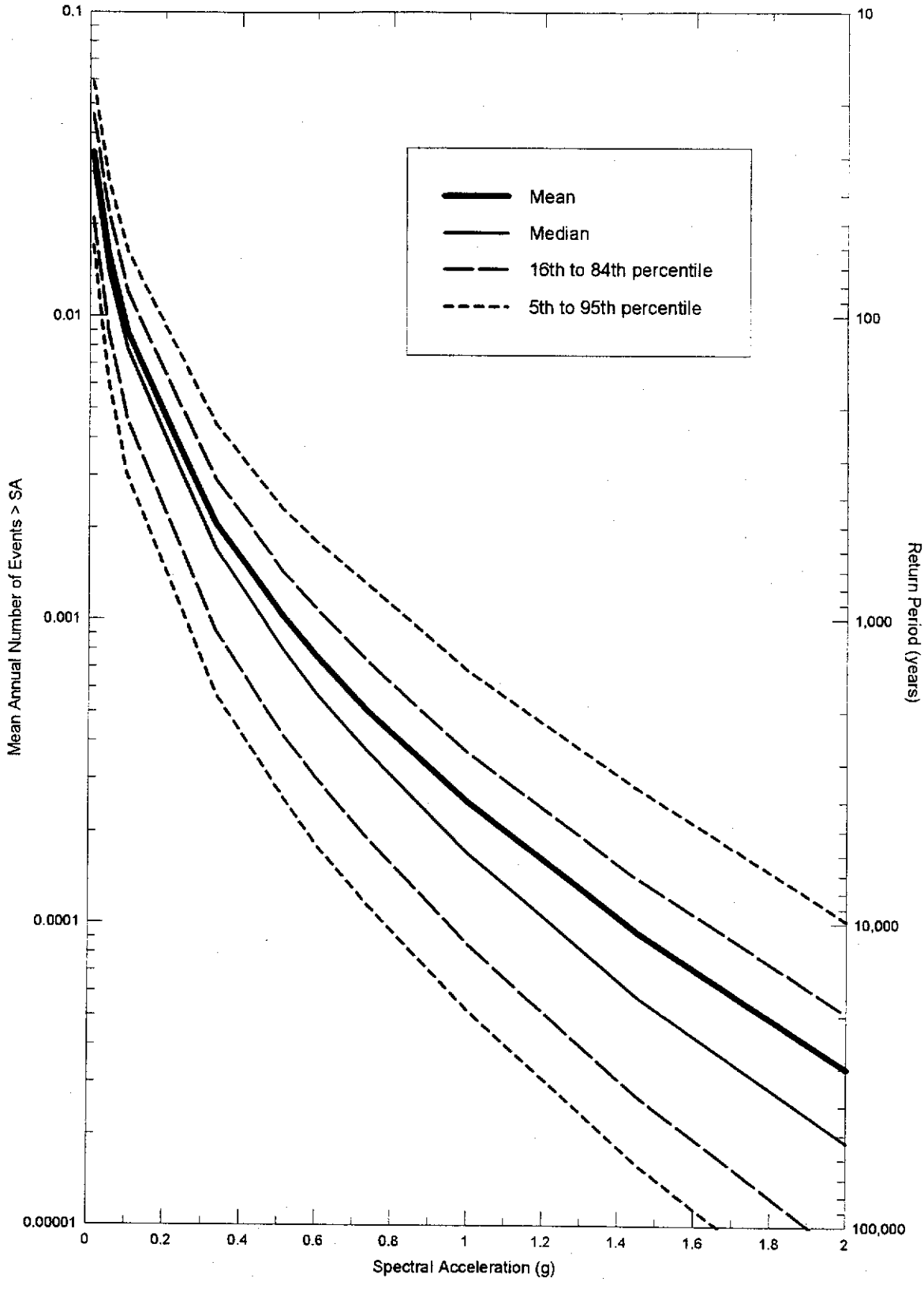
Project No. 91C0509	Los Alamos Seismic Hazards	MEAN AND 5th TO 95th PERCENTILE SEISMIC HAZARD CURVES FOR 0.2 SEC HORIZONTAL SPECTRAL ACCELERATION, TA-16	Figure 9-21
Woodward-Clyde Federal Services			

CON-REC.GRF



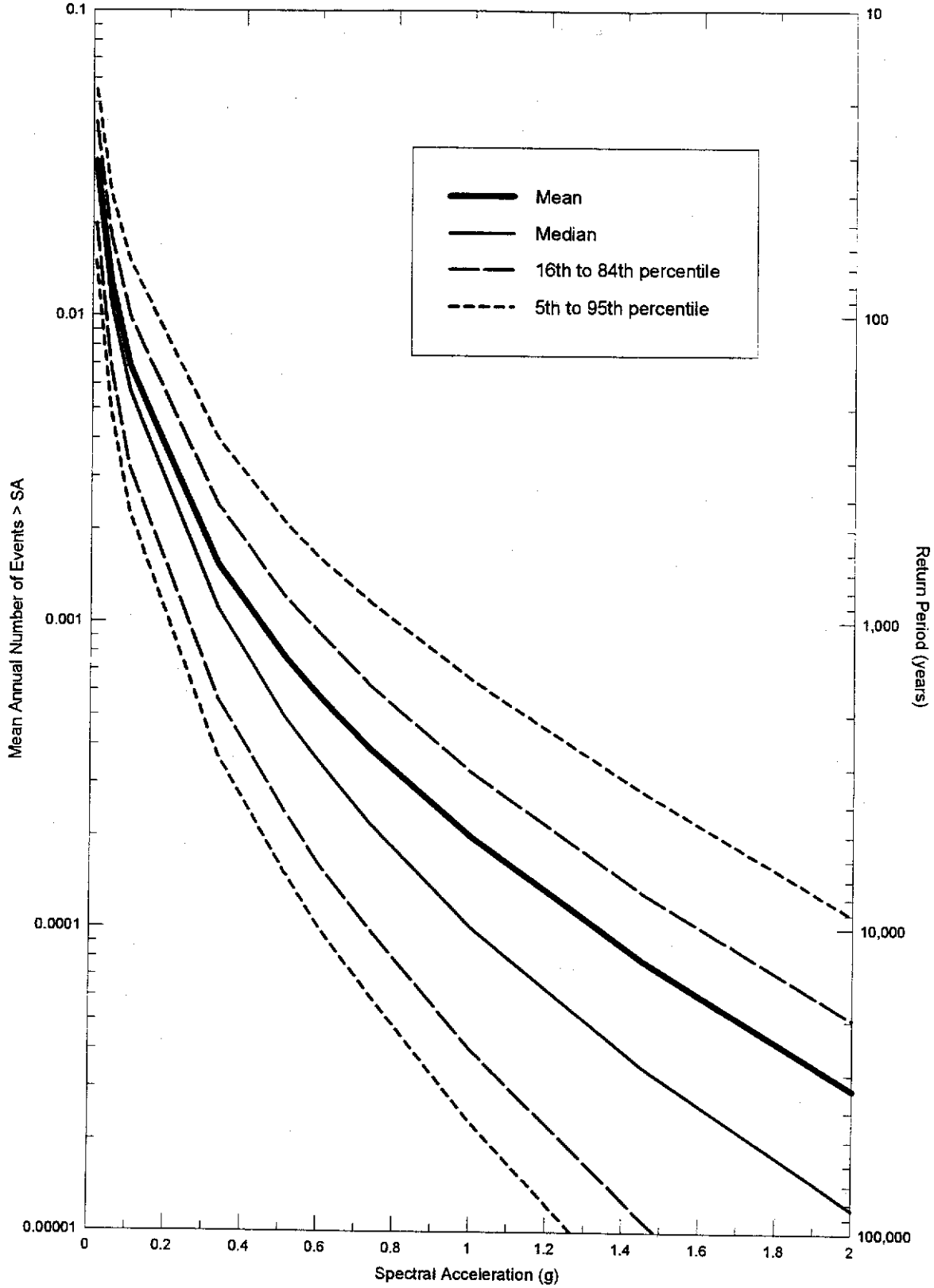
Project No. 91C0509	Los Alamos Seismic Hazards	MEAN AND 5th TO 95th PERCENTILE SEISMIC HAZARD CURVES FOR 0.2 SEC HORIZONTAL SPECTRAL ACCELERATION, TA-18	Figure 9-22
Woodward-Clyde Federal Services			

CON-REC.GRF



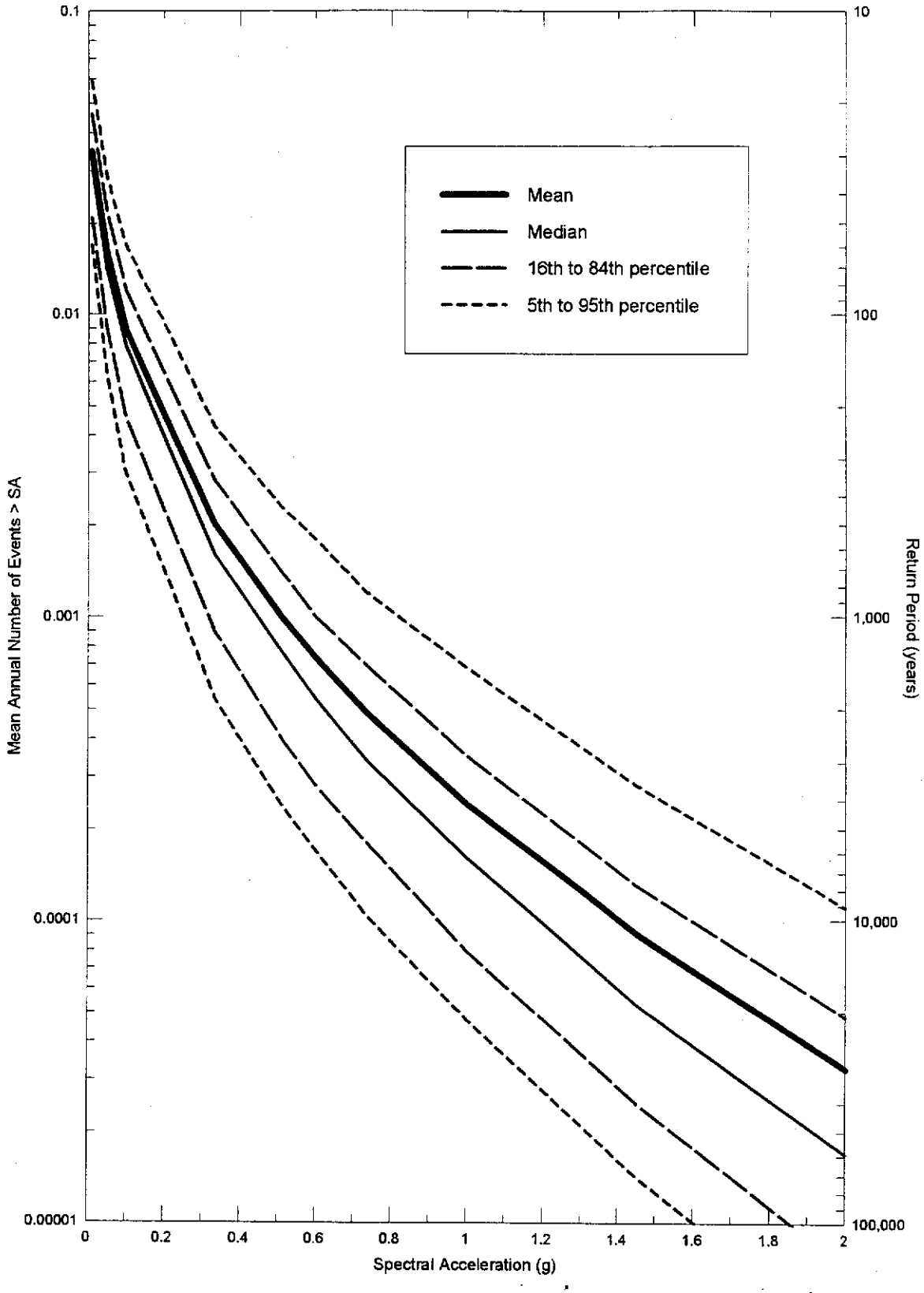
Project No. 91C0509	Los Alamos Seismic Hazards	MEAN AND 5th TO 95th PERCENTILE SEISMIC HAZARD CURVES FOR 0.2 SEC HORIZONTAL SPECTRAL ACCELERATION, TA-21	Figure 9-23
Woodward-Clyde Federal Services			

CON-REC.GRF



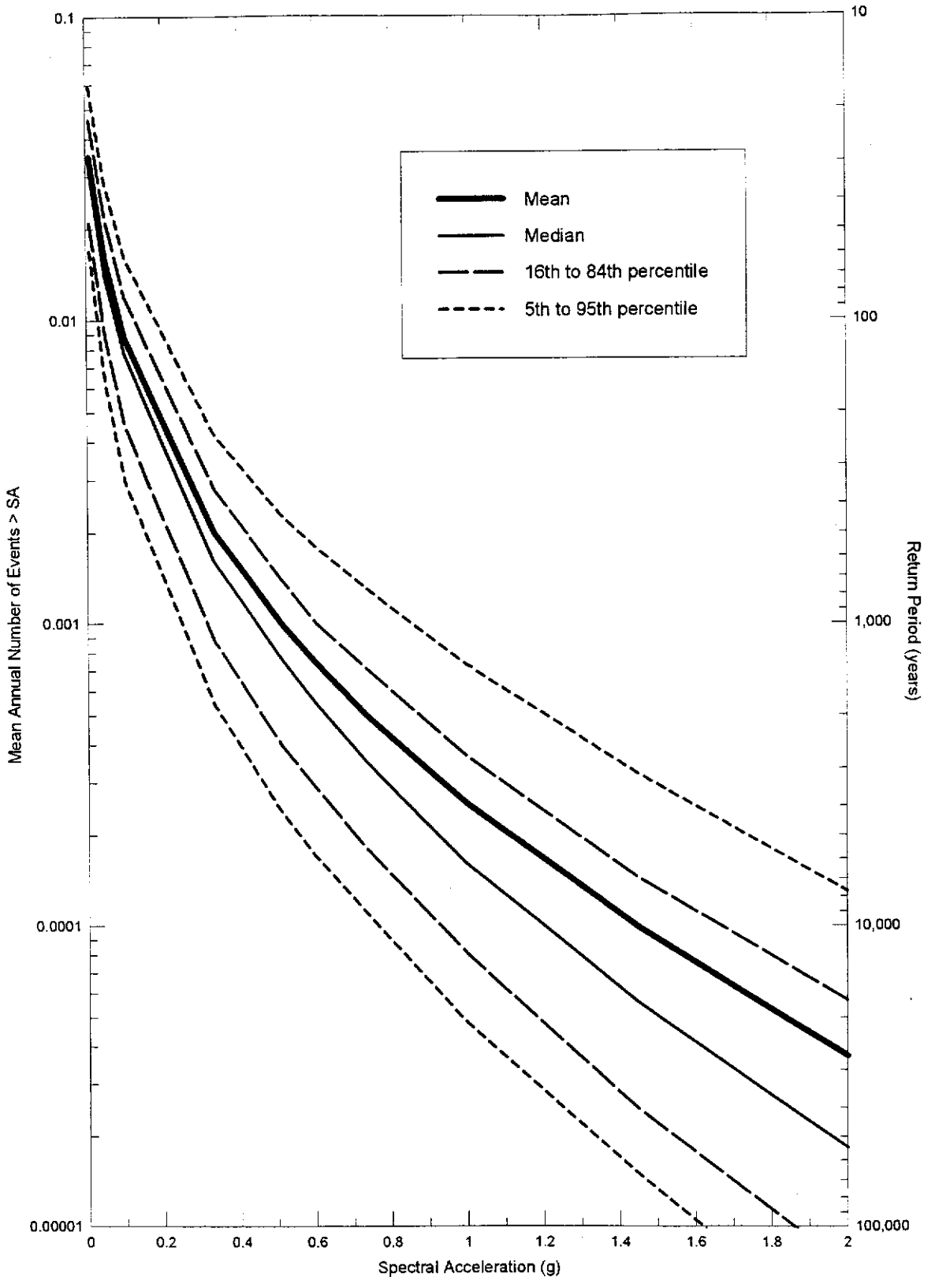
Project No. 91C0509	Los Alamos Seismic Hazards	MEAN AND 5th TO 95th PERCENTILE SEISMIC HAZARD CURVES FOR 0.2 SEC HORIZONTAL SPECTRAL ACCELERATION, TA-41	Figure 9-24
Woodward-Clyde Federal Services			

CON-REC.GRF



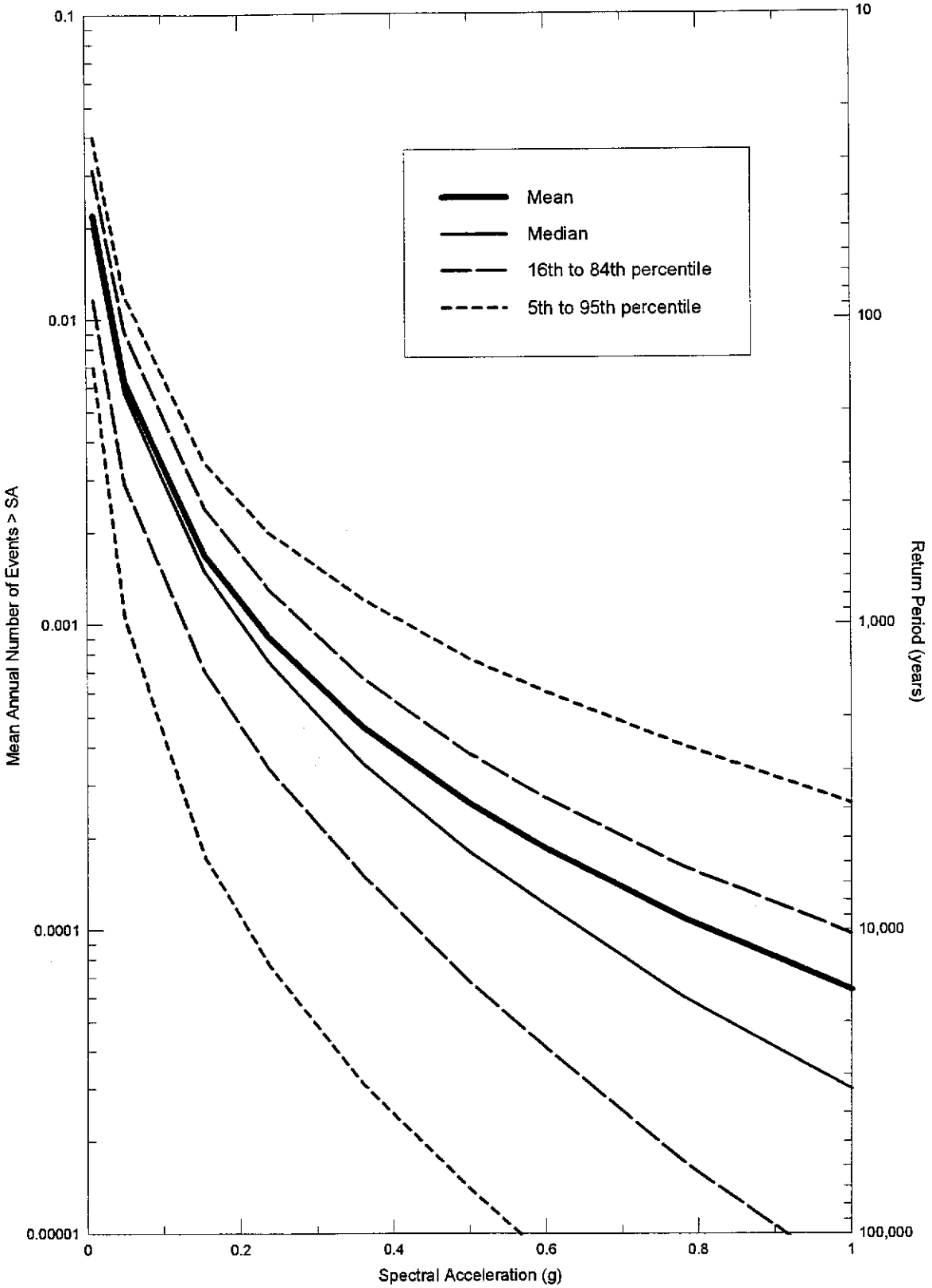
Project No. 91C0509	Los Alamos Seismic Hazards	MEAN AND 5th TO 95th PERCENTILE SEISMIC HAZARD CURVES FOR 0.2 SEC HORIZONTAL SPECTRAL ACCELERATION, TA-46	Figure 9-25
Woodward-Clyde Federal Services			

CON-REC.GRF



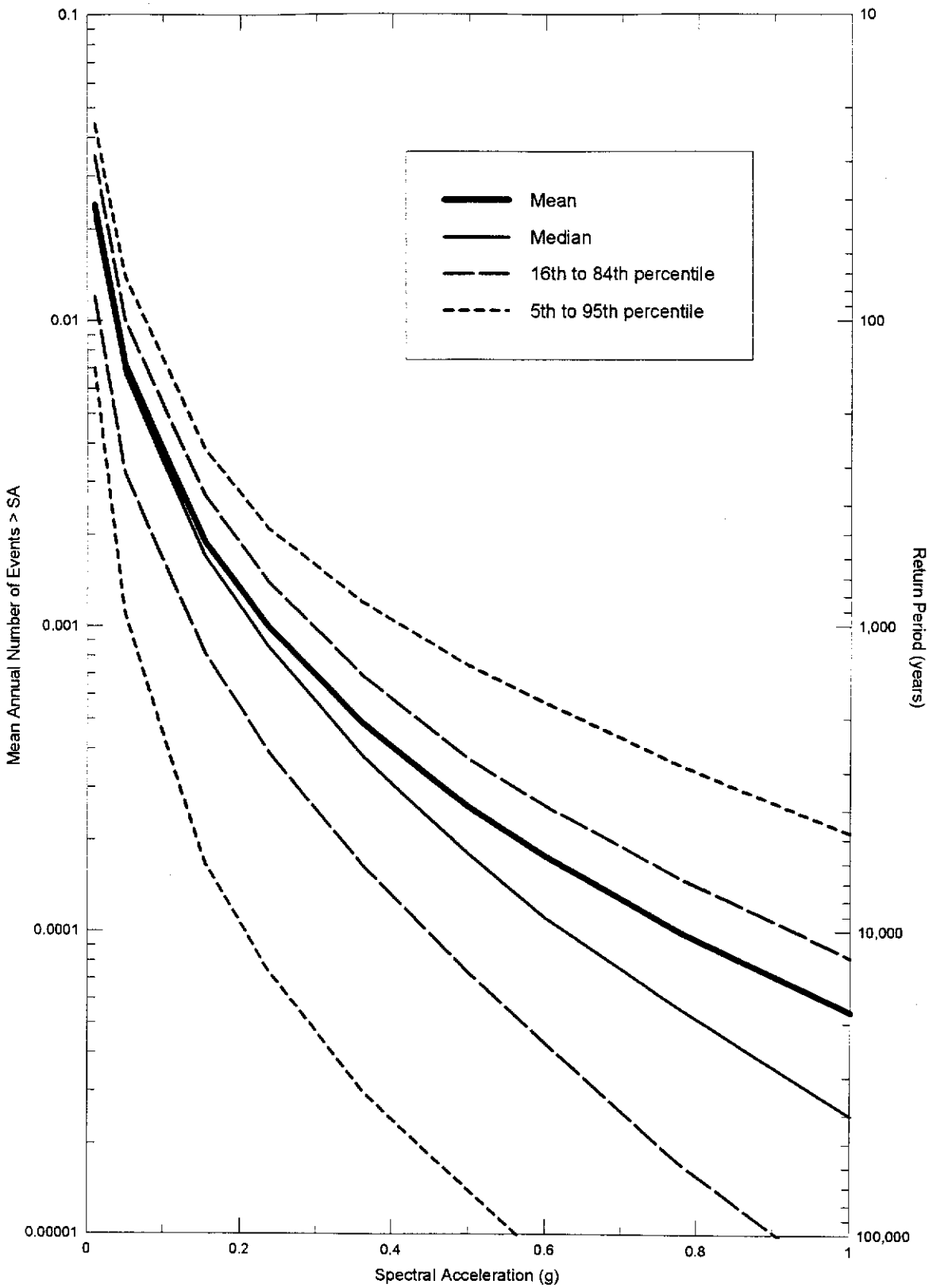
Project No. 91C0509	Los Alamos Seismic Hazards	MEAN AND 5th TO 95th PERCENTILE SEISMIC HAZARD CURVES FOR 0.2 SEC HORIZONTAL SPECTRAL ACCELERATION, TA-55	Figure 9-26
Woodward-Clyde Federal Services			

CON-REC.GRF



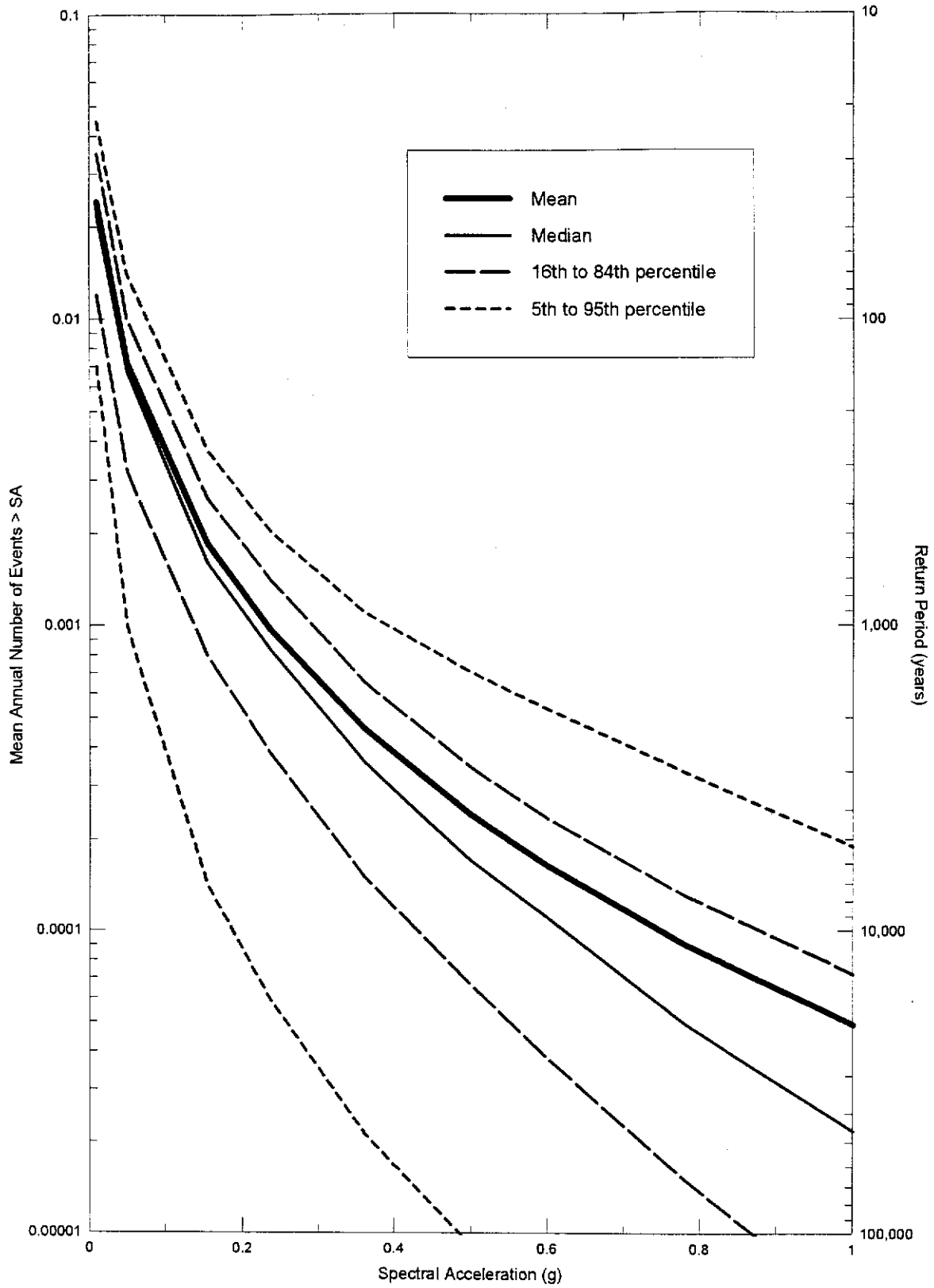
Project No. 91C0509	Los Alamos Seismic Hazards	MEAN AND 5th TO 95th PERCENTILE SEISMIC HAZARD CURVES FOR 1 SEC HORIZONTAL SPECTRAL ACCELERATION, TA-2	Figure 9-27
Woodward-Clyde Federal Services			

CON-REC.GRF



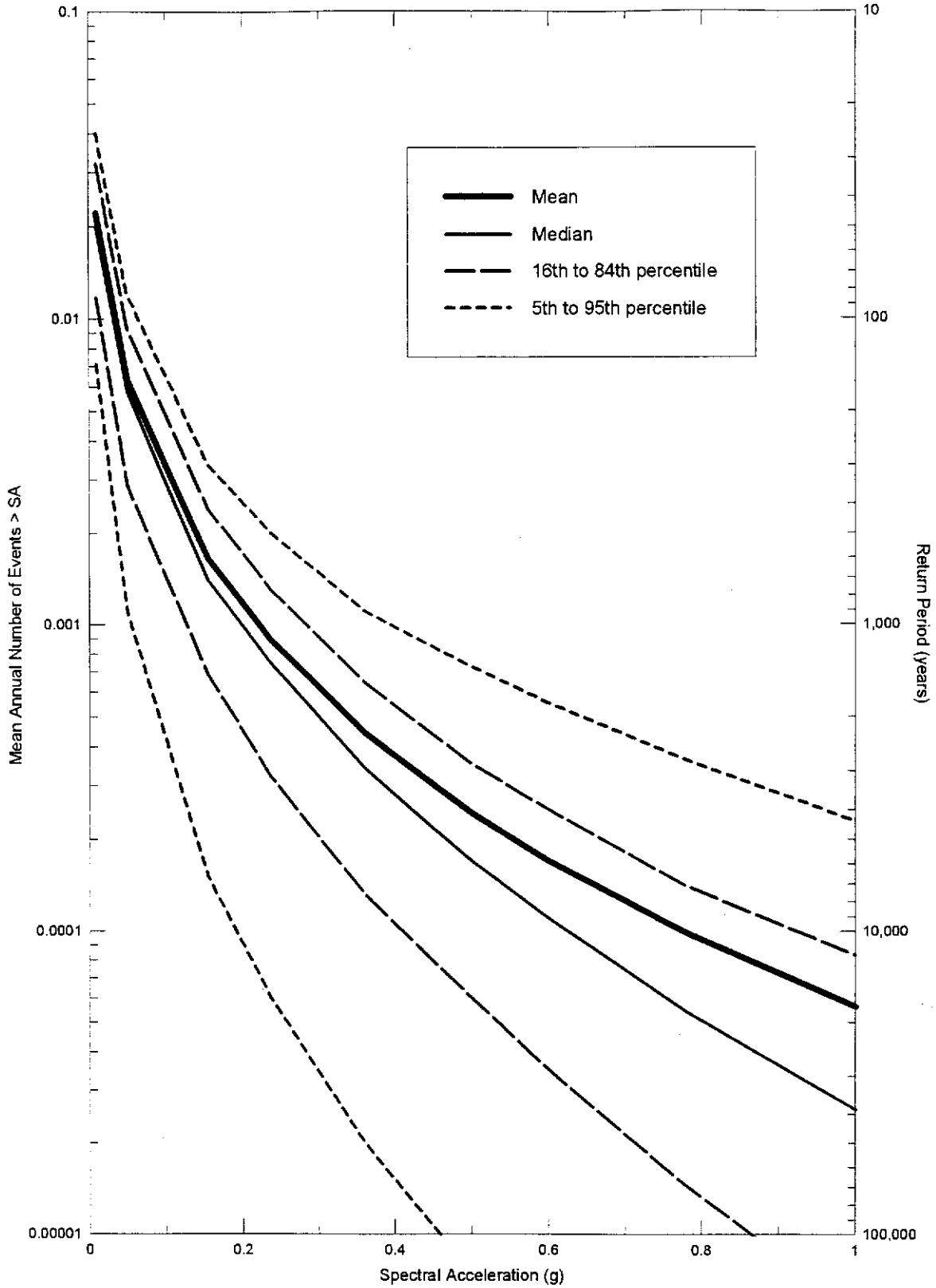
Project No. 91C0509	Los Alamos Seismic Hazards	MEAN AND 5th TO 95th PERCENTILE SEISMIC HAZARD CURVES FOR 1 SEC HORIZONTAL SPECTRAL ACCELERATION, TA-3	Figure 9-28
Woodward-Clyde Federal Services			

CON-REC.GRF



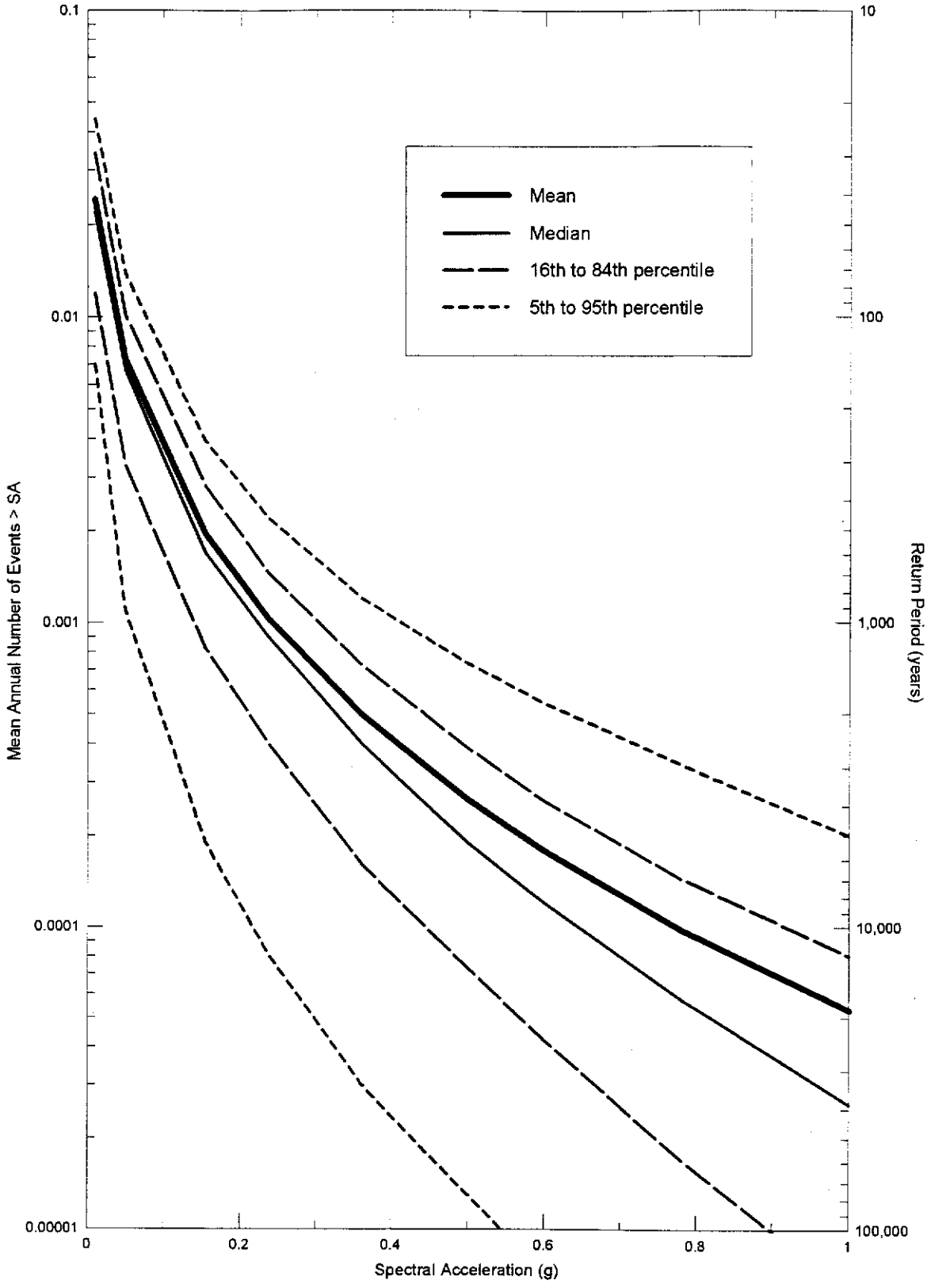
Project No. 91C0509	Los Alamos Seismic Hazards	MEAN AND 5th TO 95th PERCENTILE SEISMIC HAZARD CURVES FOR 1 SEC HORIZONTAL SPECTRAL ACCELERATION, TA-16	Figure 9-29
Woodward-Clyde Federal Services			

CON-REC.GRF



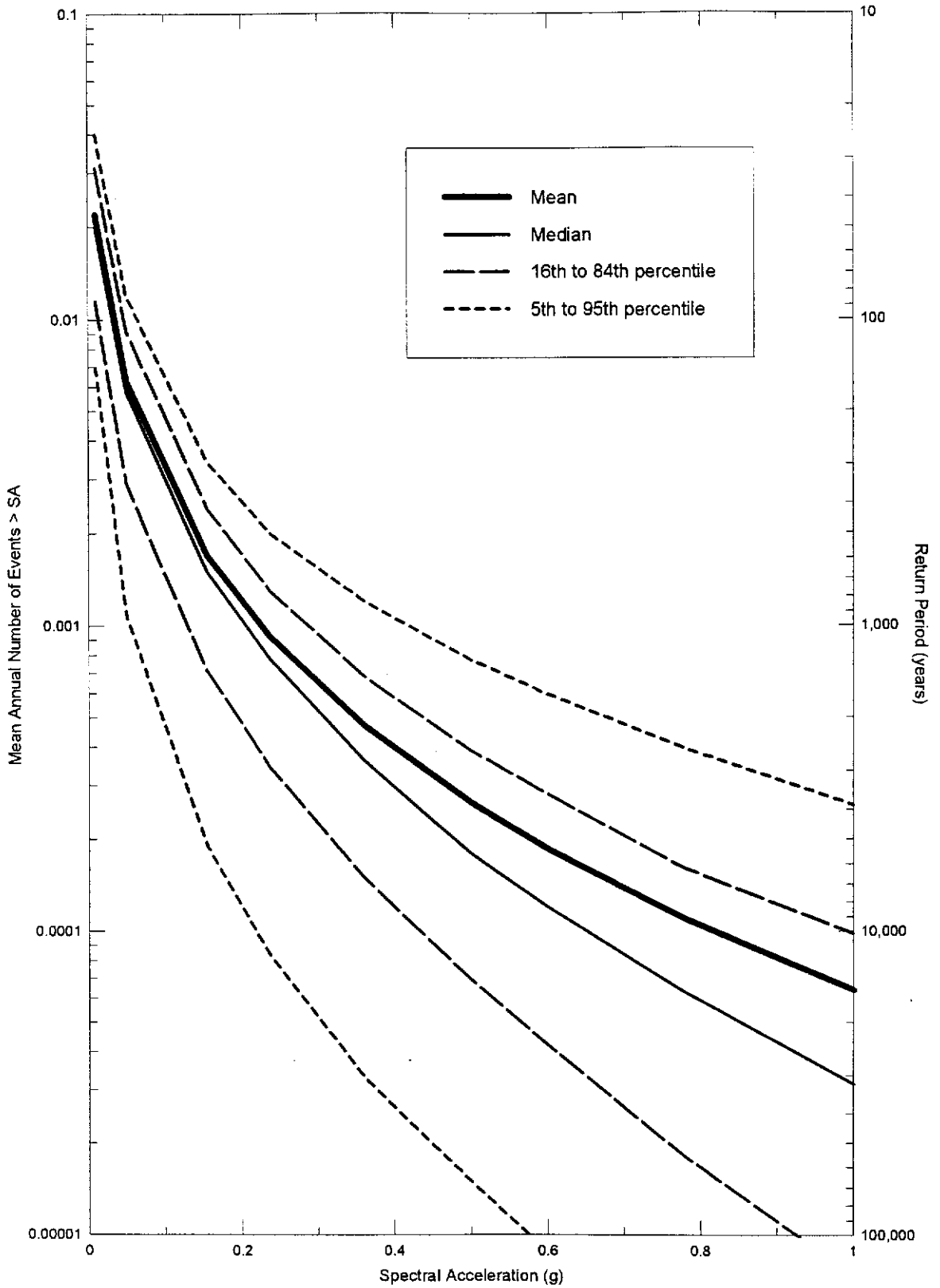
Project No. 91C0509	Los Alamos Seismic Hazards	MEAN AND 5th TO 95th PERCENTILE SEISMIC HAZARD CURVES FOR 1 SEC HORIZONTAL SPECTRAL ACCELERATION, TA-18	Figure 9-30
Woodward-Clyde Federal Services			

CON-REC.GRF



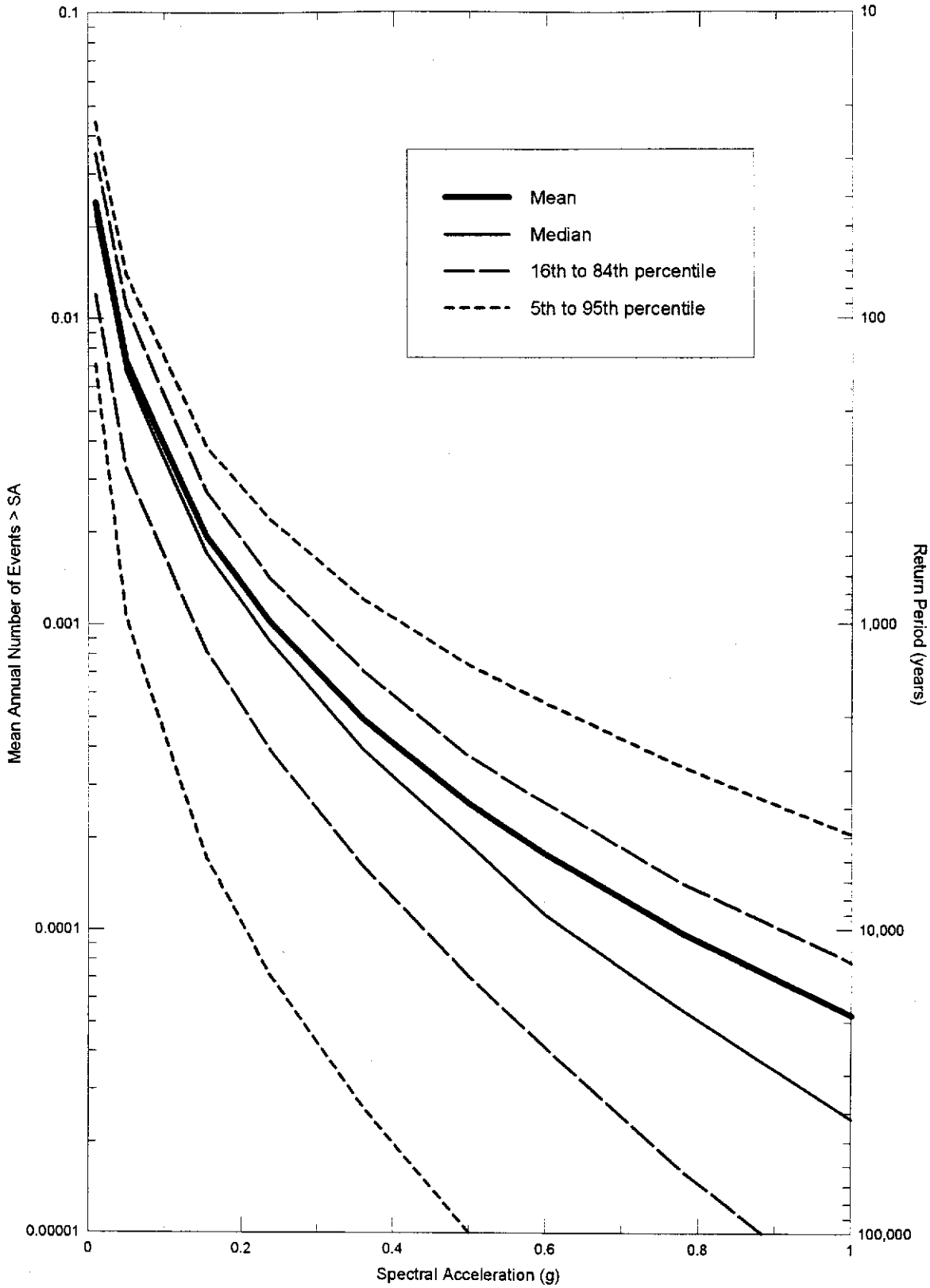
Project No. 91C0509	Los Alamos Seismic Hazards	MEAN AND 5th TO 95th PERCENTILE SEISMIC HAZARD CURVES FOR 1 SEC HORIZONTAL SPECTRAL ACCELERATION, TA-21	Figure 9-31
Woodward-Clyde Federal Services			

CON-REC.GRF



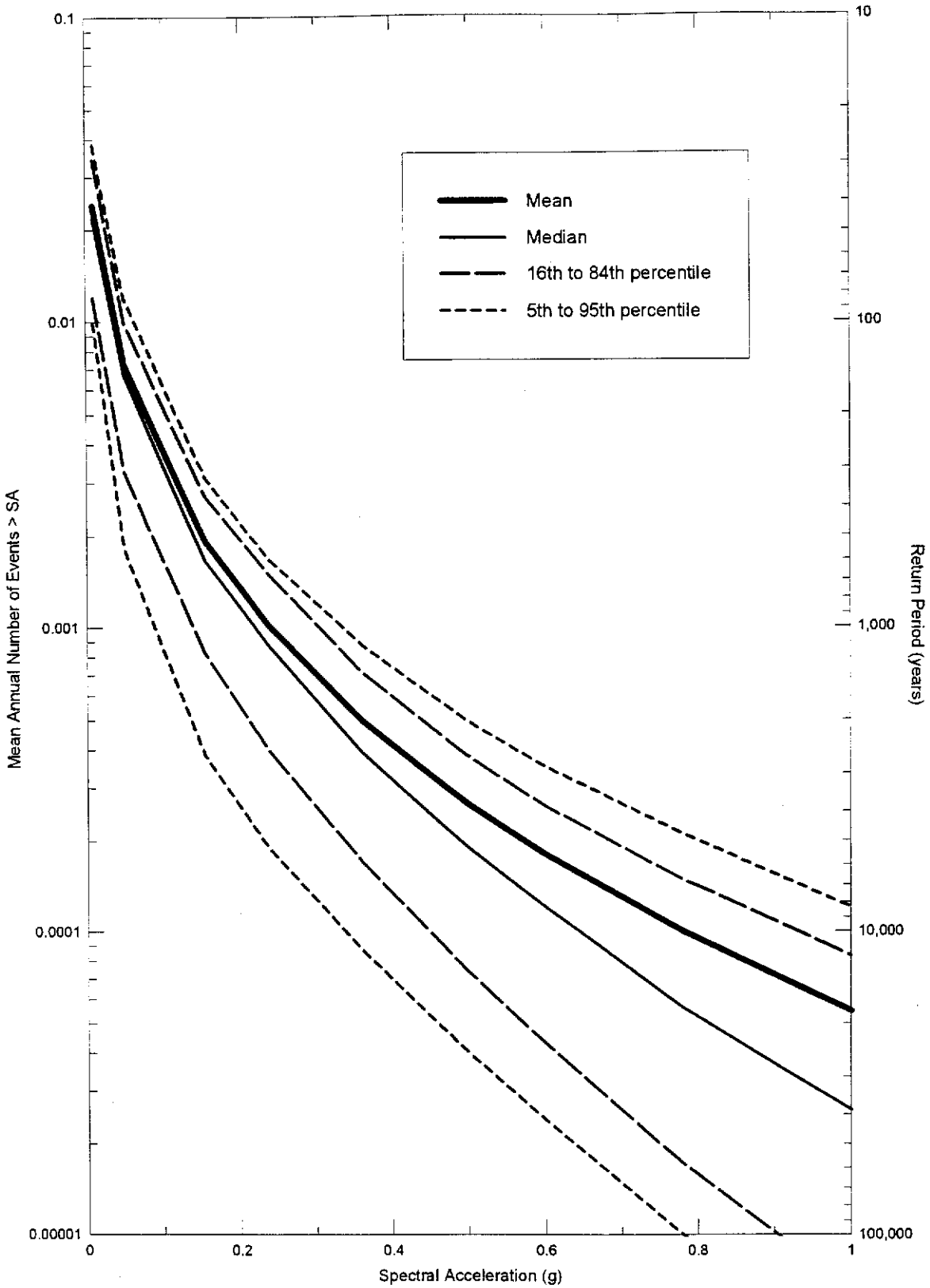
Project No. 91C0509	Los Alamos Seismic Hazards	MEAN AND 5th TO 95th PERCENTILE SEISMIC HAZARD CURVES FOR 1 SEC HORIZONTAL SPECTRAL ACCELERATION, TA-41	Figure 9-32
Woodward-Clyde Federal Services			

CON-REC.GRF



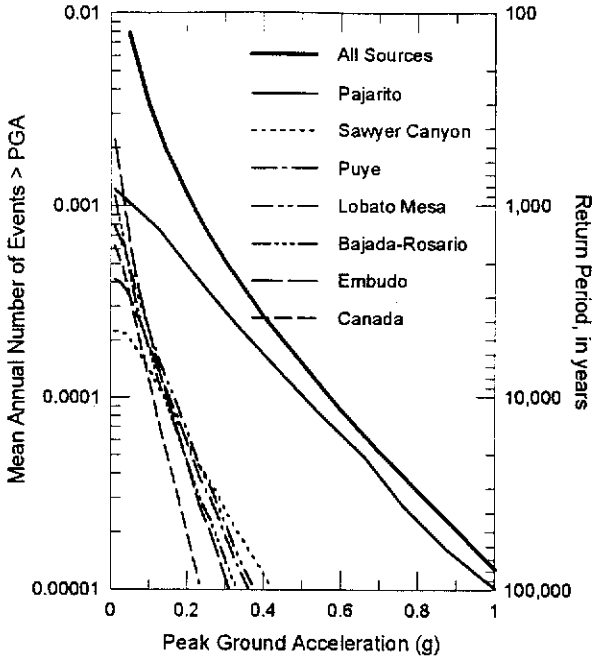
Project No. 91C0509	Los Alamos Seismic Hazards	MEAN AND 5th TO 95th PERCENTILE SEISMIC HAZARD CURVES FOR 1 SEC HORIZONTAL SPECTRAL ACCELERATION, TA-46	Figure 9-33
Woodward-Clyde Federal Services			

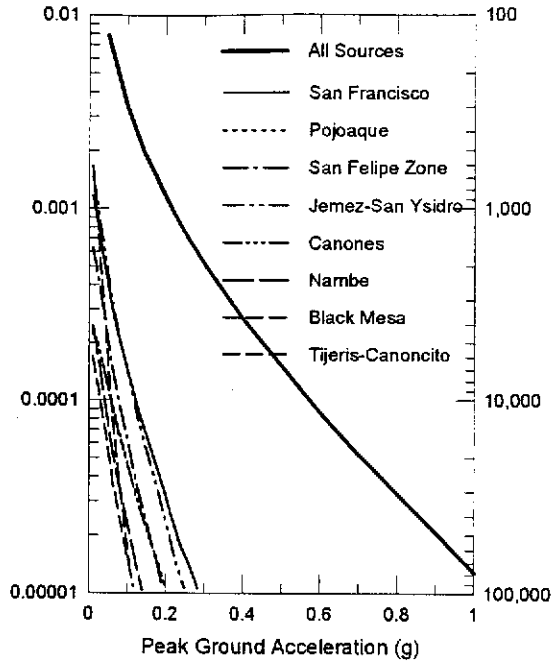
CON-REC.GRF

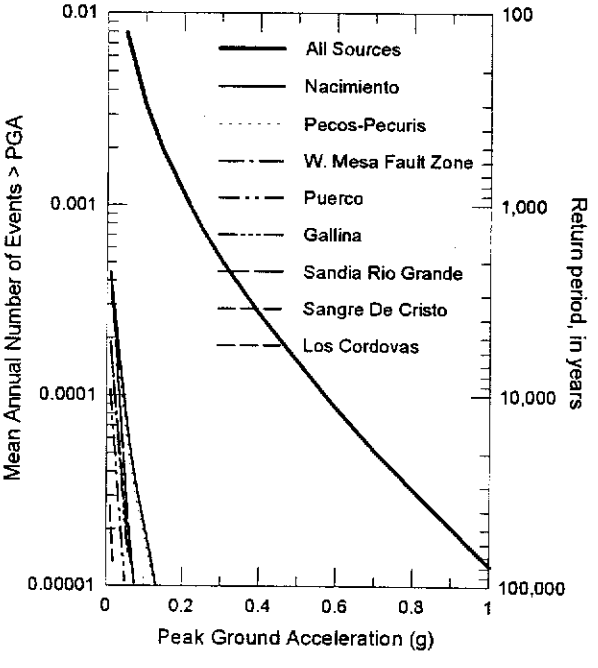


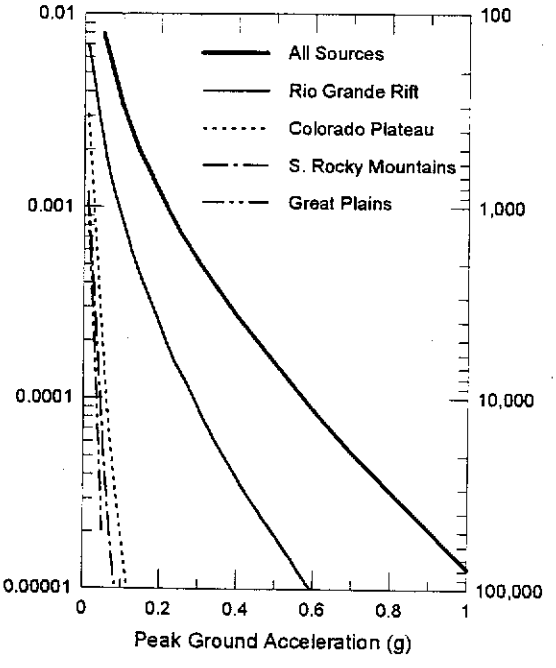
Project No. 91C0509	Los Alamos Seismic Hazards	MEAN AND 5th TO 95th PERCENTILE SEISMIC HAZARD CURVES FOR 1 SEC HORIZONTAL SPECTRAL ACCELERATION, TA-55	Figure 9-34
Woodward-Clyde Federal Services			

CON-REC.GRF



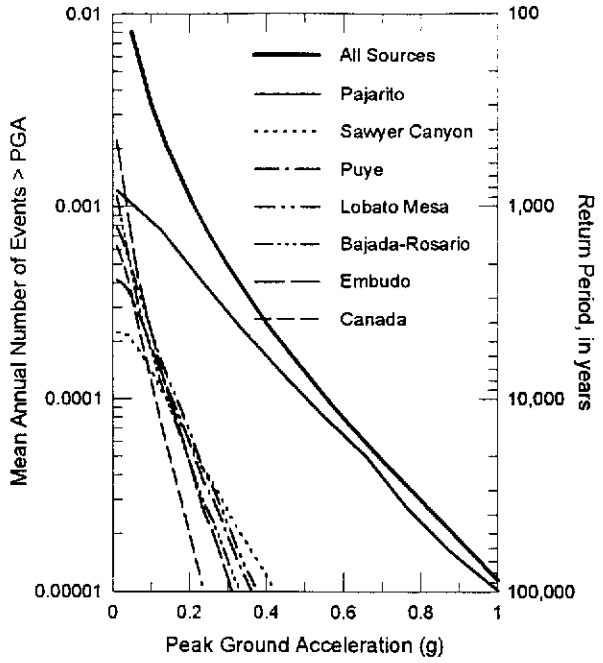


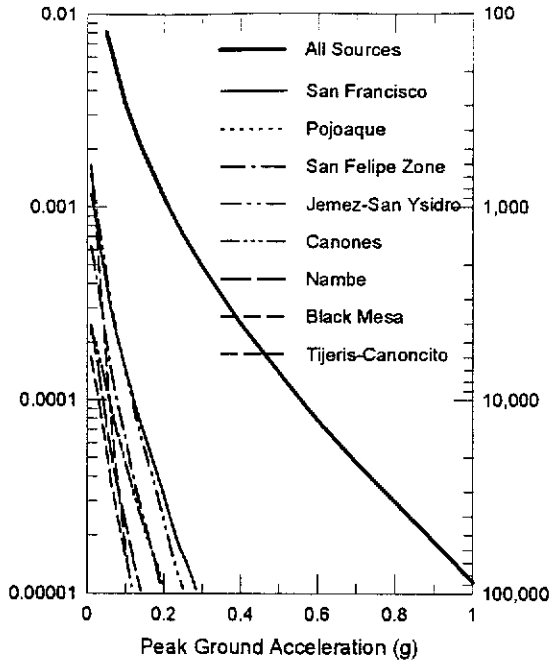


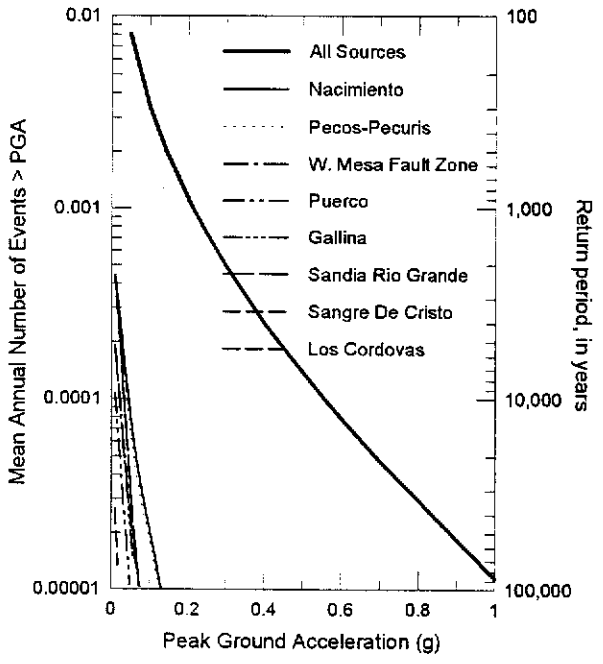


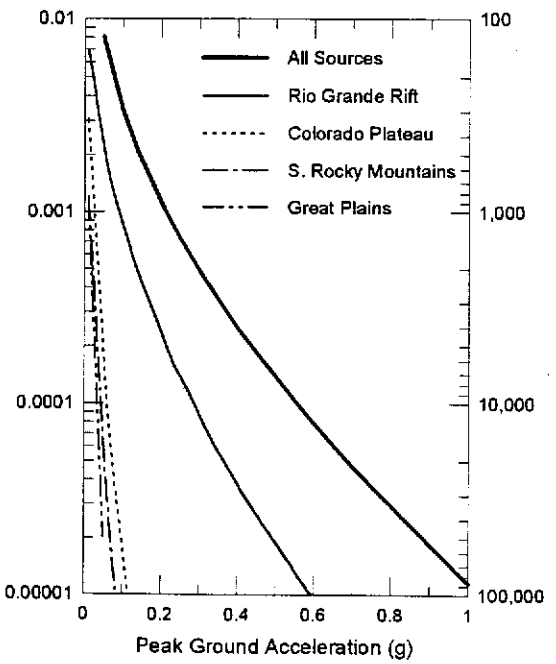
Project No. 91C0509	Los Alamos Seismic Hazards	CONTRIBUTION OF SEISMIC SOURCES TO THE MEAN SEISMIC HAZARD FOR PEAK HORIZONTAL ACCELERATION, TA-2	Figure 9-35
Woodward-Clyde Federal Services			

SRC-REC.GRF



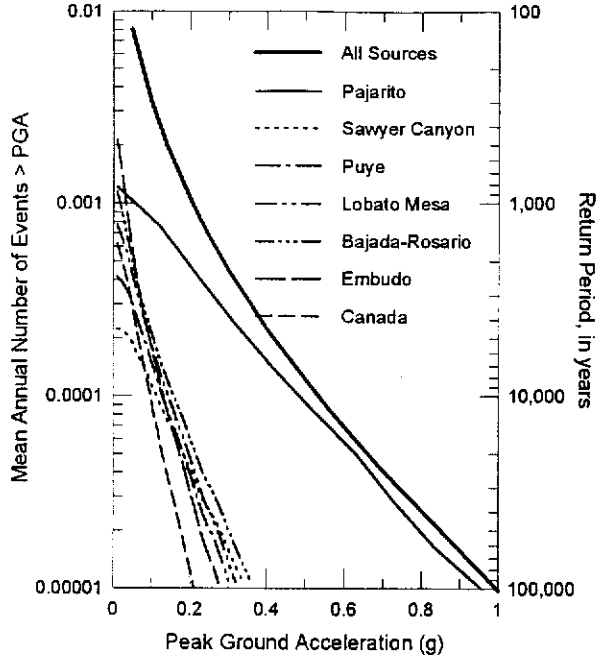


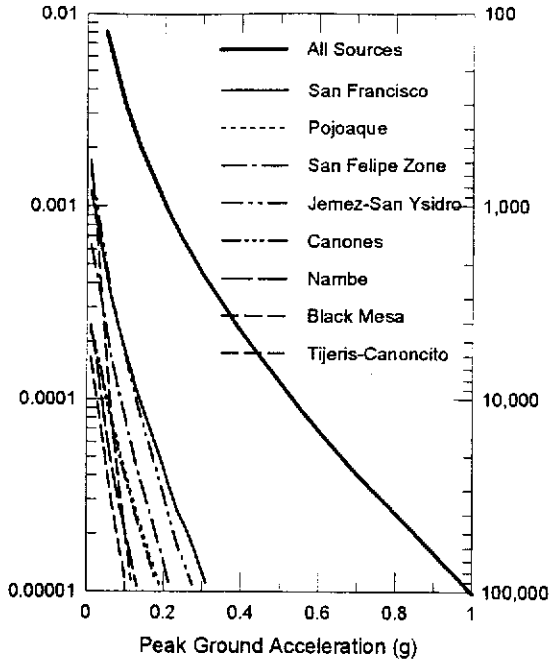


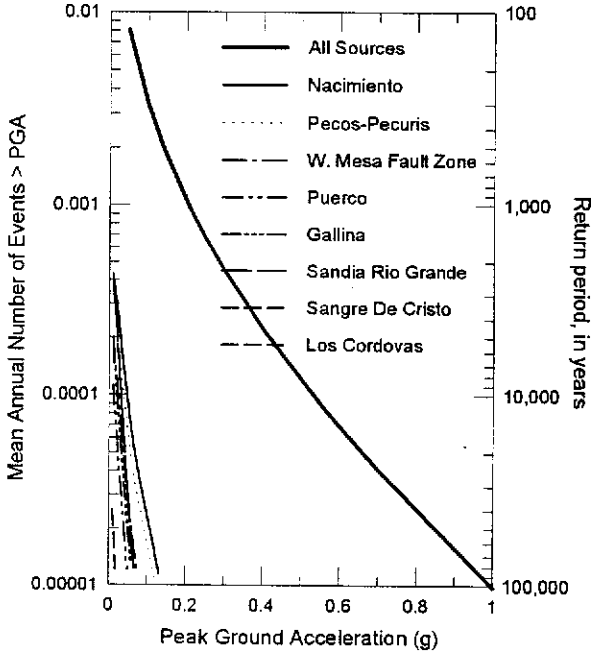


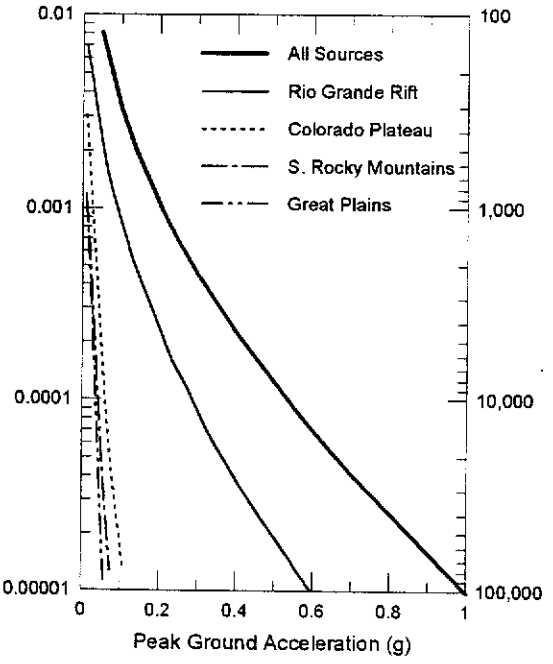
Project No. 91C0509	Los Alamos Seismic Hazards	CONTRIBUTION OF SEISMIC SOURCES TO THE MEAN SEISMIC HAZARD FOR PEAK HORIZONTAL ACCELERATION, TA-3	Figure 9-36
Woodward-Clyde Federal Services			

SRC-REC.GRF



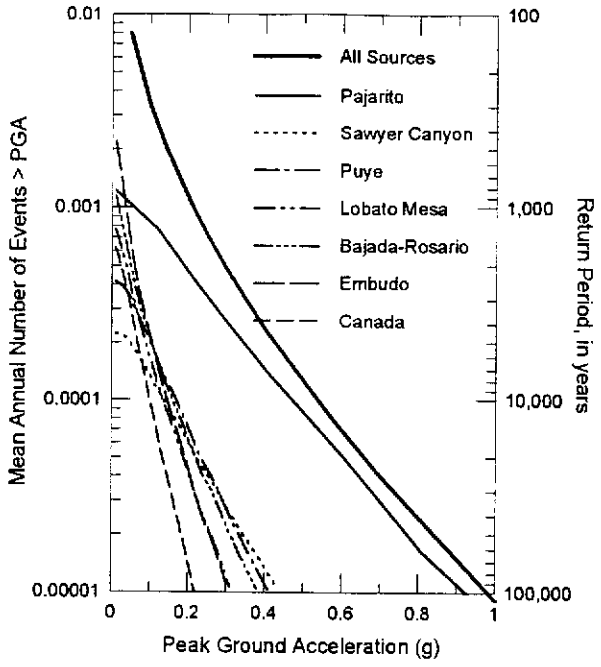


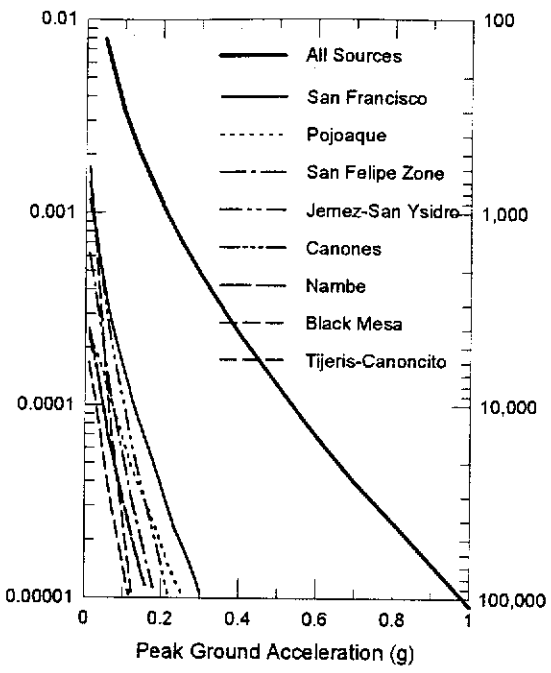


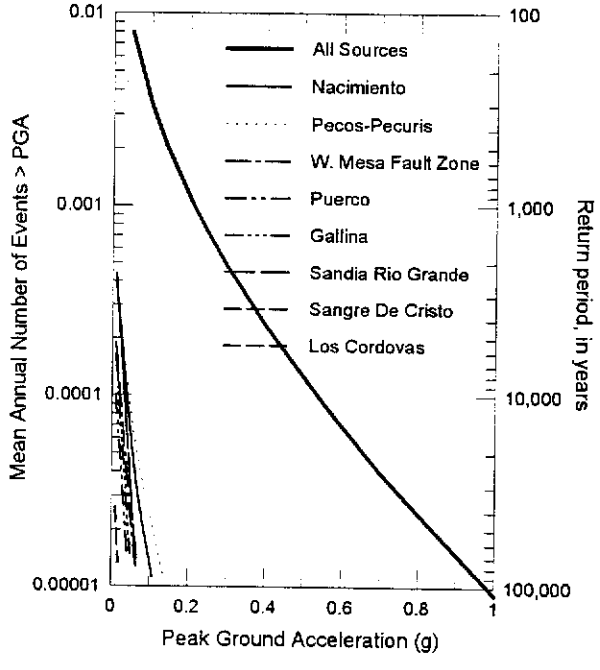


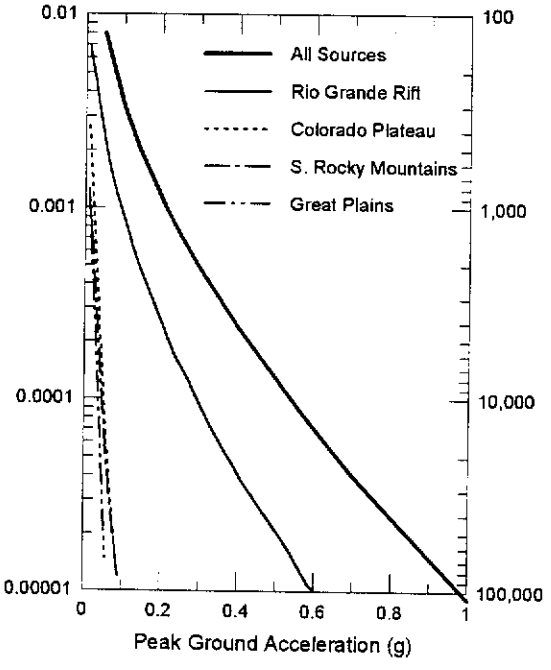
Project No. 91C0509	Los Alamos Seismic Hazards	CONTRIBUTION OF SEISMIC SOURCES TO THE MEAN SEISMIC HAZARD FOR PEAK HORIZONTAL ACCELERATION, TA-16	Figure 9-37
Woodward-Clyde Federal Services			

SRC-REC.GRF



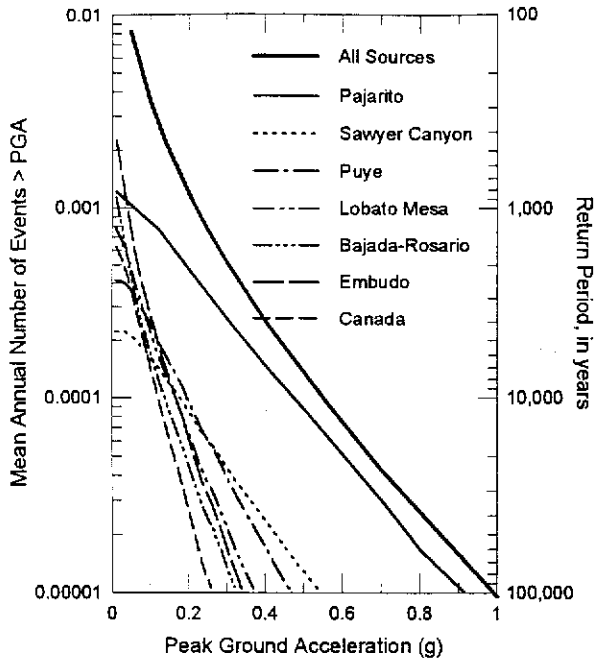


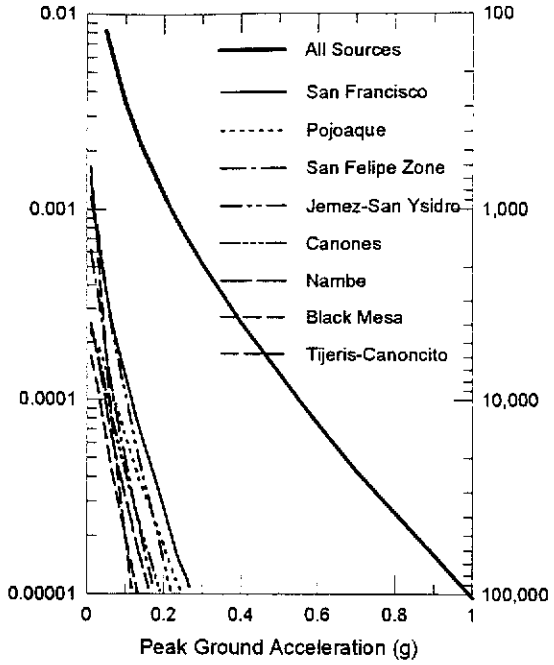


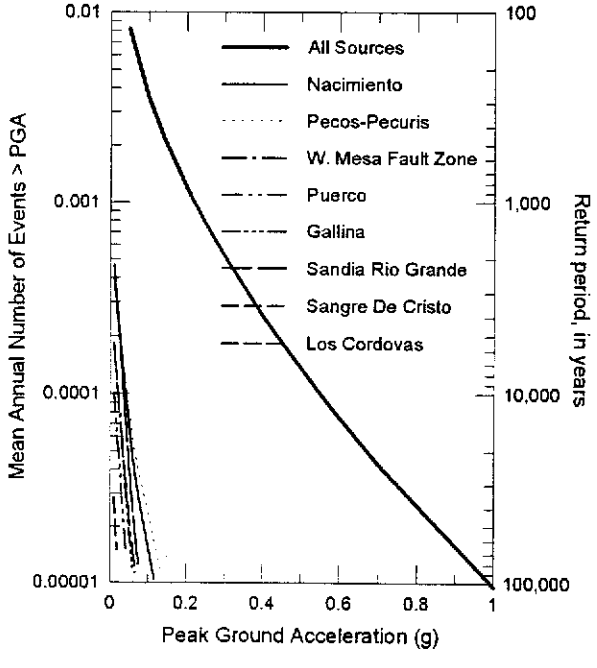


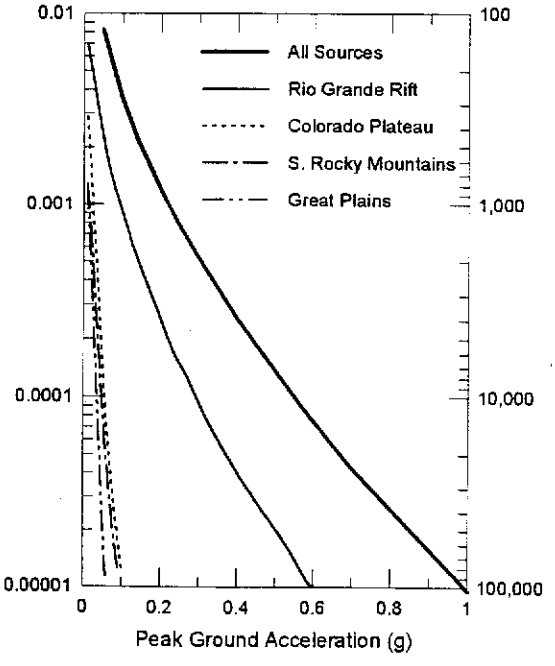
Project No. 91C0509	Los Alamos Seismic Hazards	CONTRIBUTION OF SEISMIC SOURCES TO THE MEAN SEISMIC HAZARD FOR PEAK HORIZONTAL ACCELERATION, TA-18	Figure 9-38
Woodward-Clyde Federal Services			

SRC-REC GRF



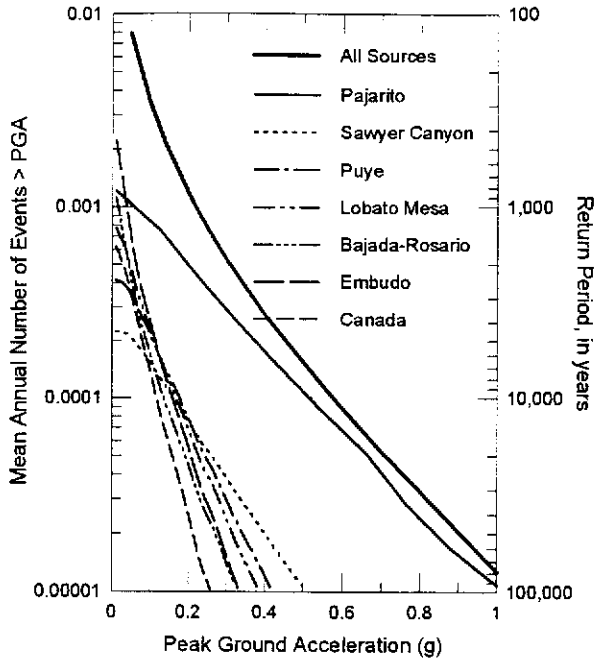


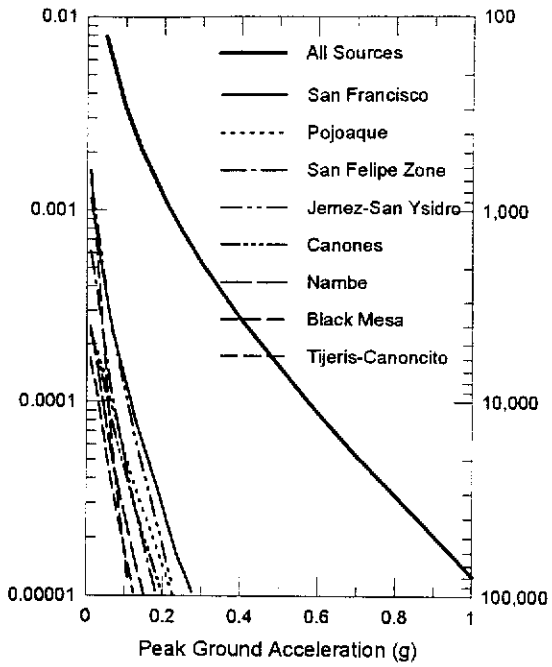


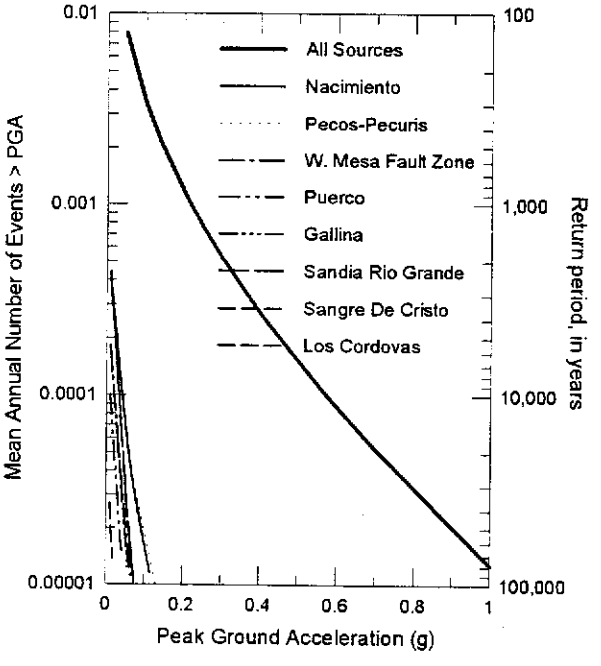


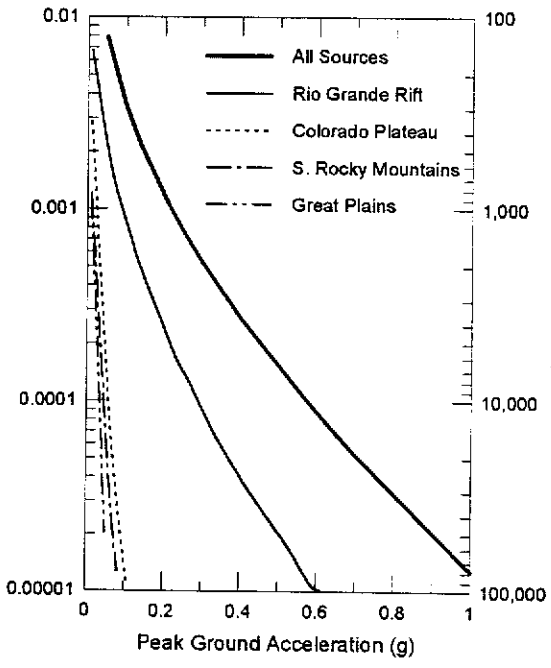
Project No. 91C0509	Los Alamos Seismic Hazards	CONTRIBUTION OF SEISMIC SOURCES TO THE MEAN SEISMIC HAZARD FOR PEAK HORIZONTAL ACCELERATION, TA-21	Figure 9-39
Woodward-Clyde Federal Services			

SRC-REC.GRF



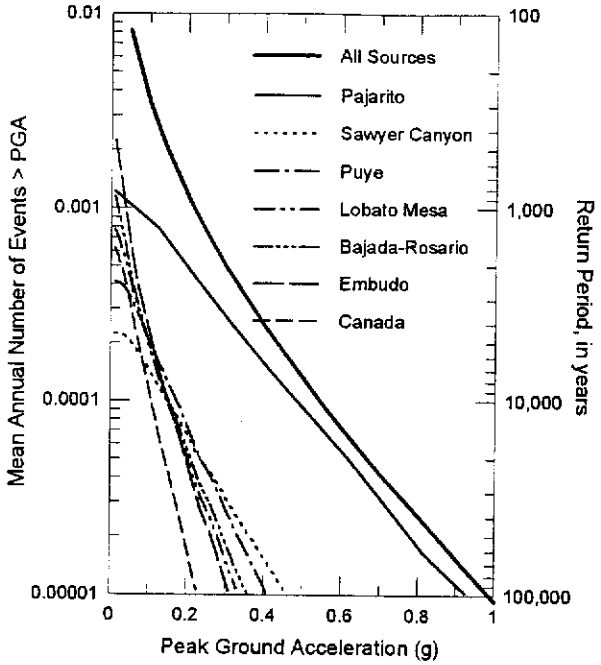


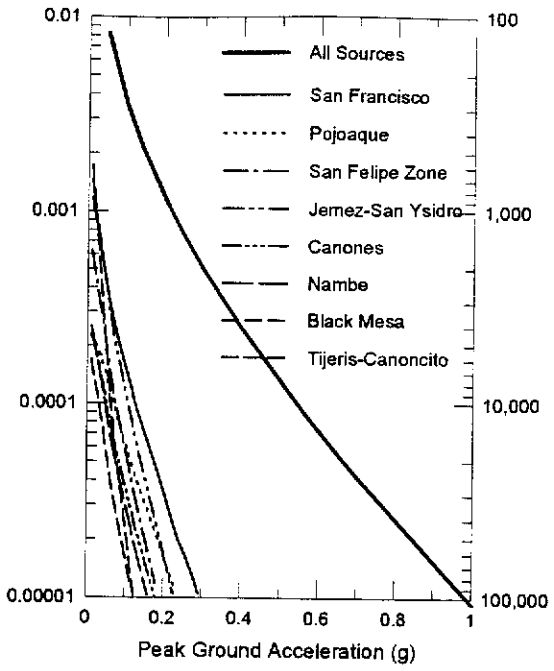


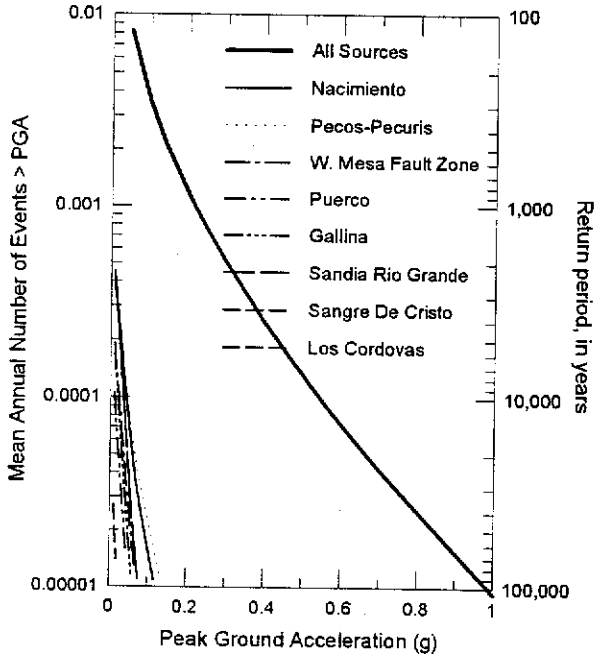


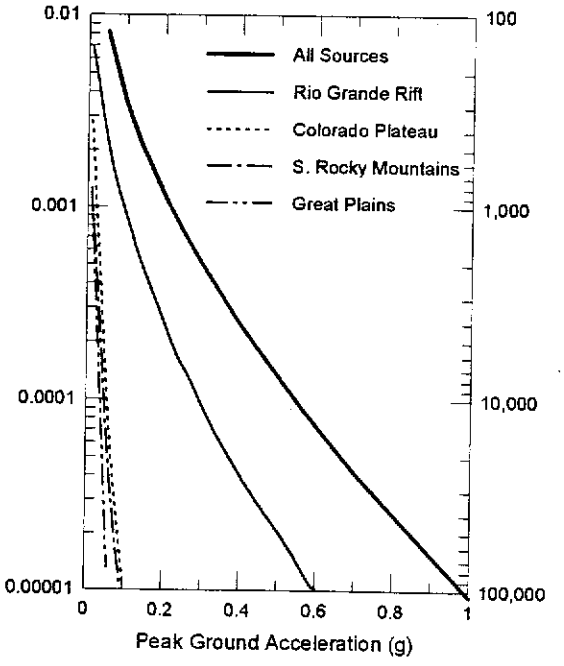
Project No. 91C0509	Los Alamos Seismic Hazards	CONTRIBUTION OF SEISMIC SOURCES TO THE MEAN SEISMIC HAZARD FOR PEAK HORIZONTAL ACCELERATION, TA-41	Figure 9-40
Woodward-Clyde Federal Services			

SRC-REC.GRF



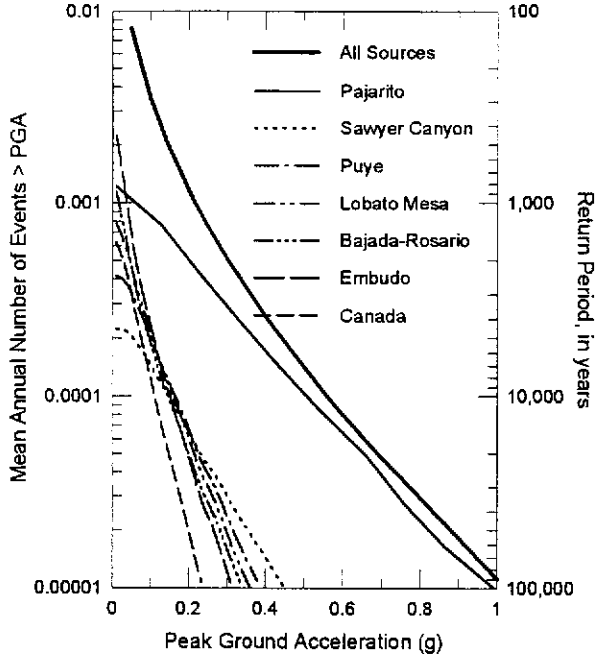


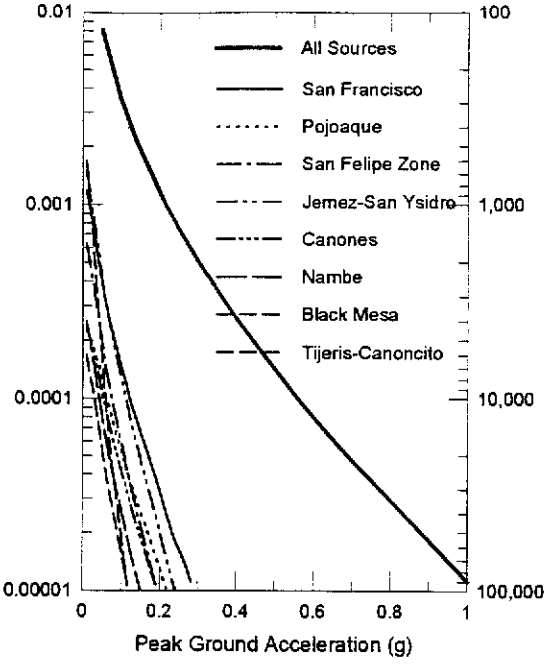


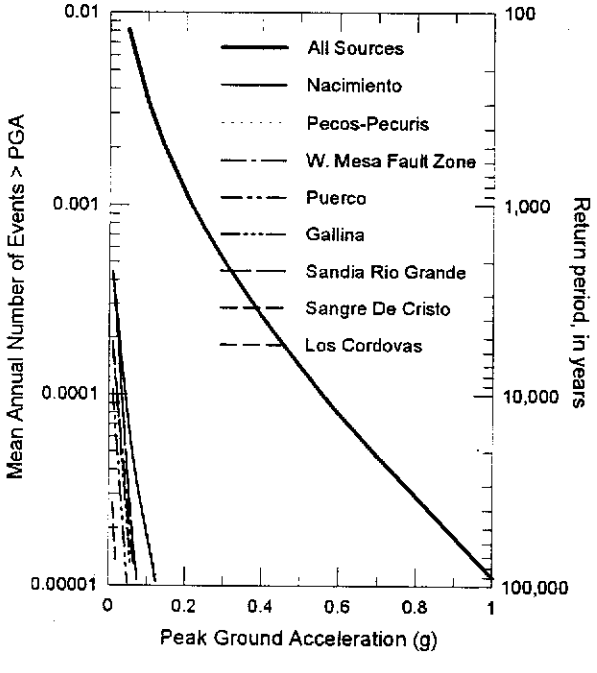


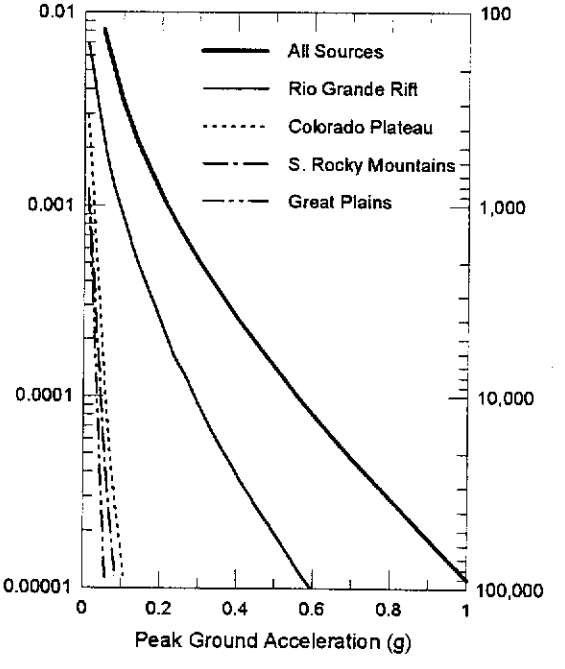
Project No. 91C0509	Los Alamos Seismic Hazards	CONTRIBUTION OF SEISMIC SOURCES TO THE MEAN SEISMIC HAZARD FOR PEAK HORIZONTAL ACCELERATION, TA-46	Figure 9-41
Woodward-Clyde Federal Services			

SRC-REC.GRF



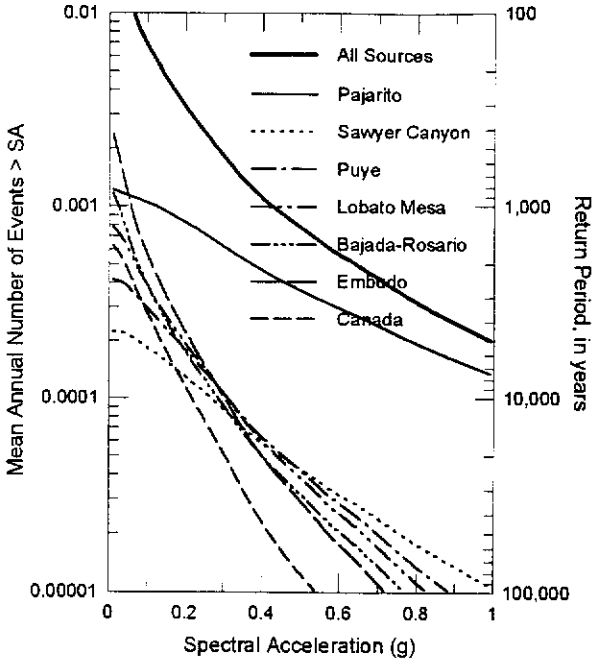


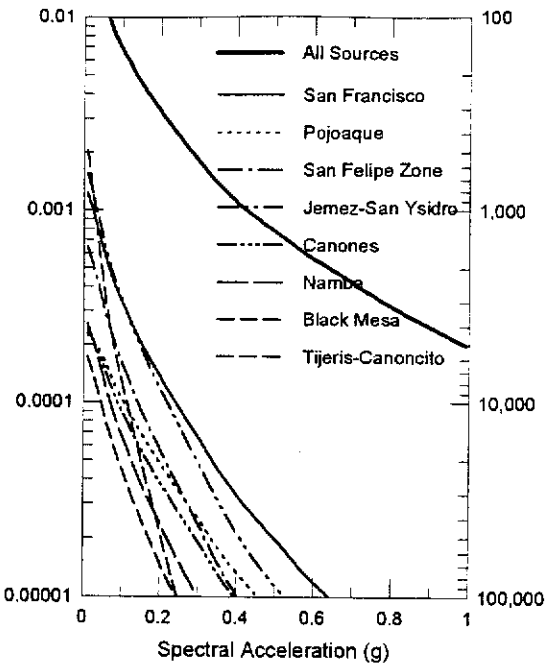


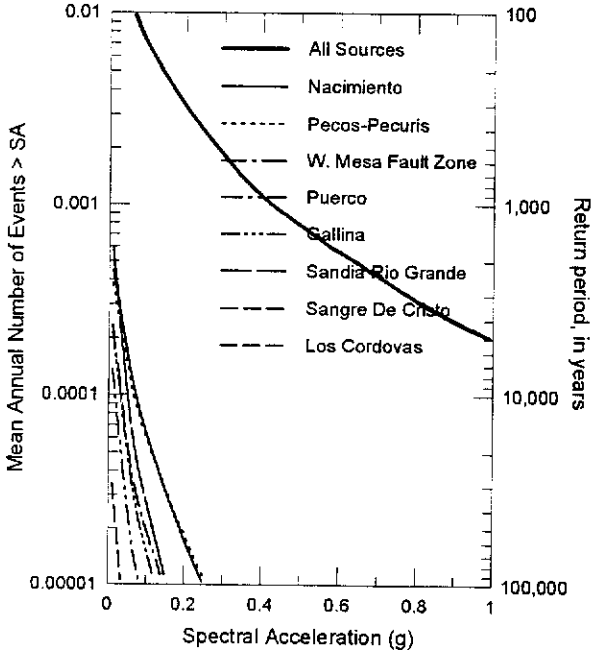


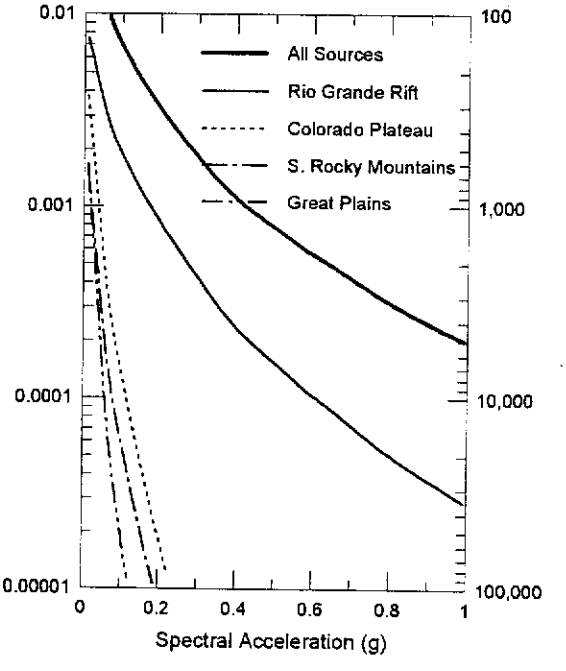
Project No. 91C0509	Los Alamos Seismic Hazards	CONTRIBUTION OF SEISMIC SOURCES TO THE MEAN SEISMIC HAZARD FOR PEAK HORIZONTAL ACCELERATION, TA-55	Figure 9-42
Woodward-Clyde Federal Services			

SRC-REC.GRF



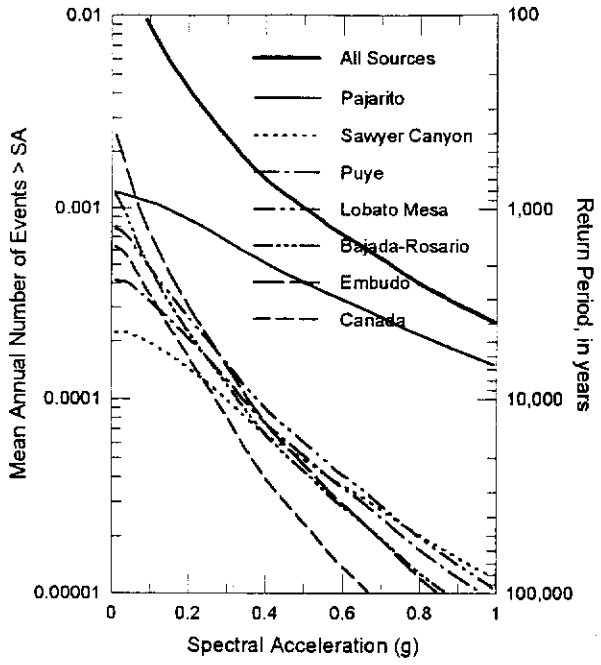


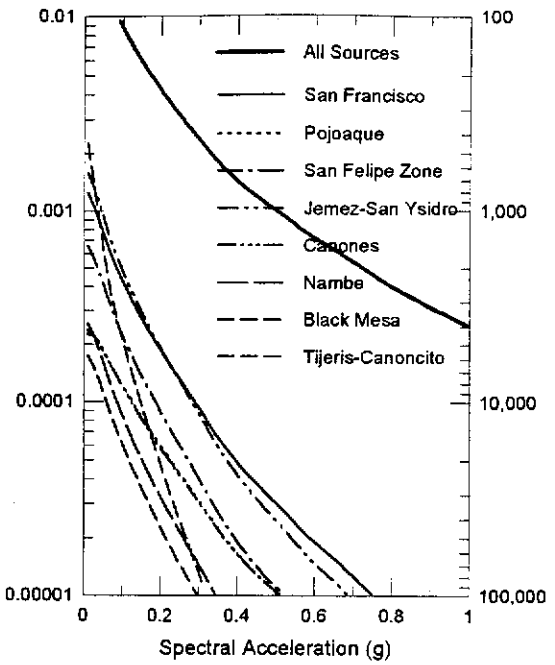


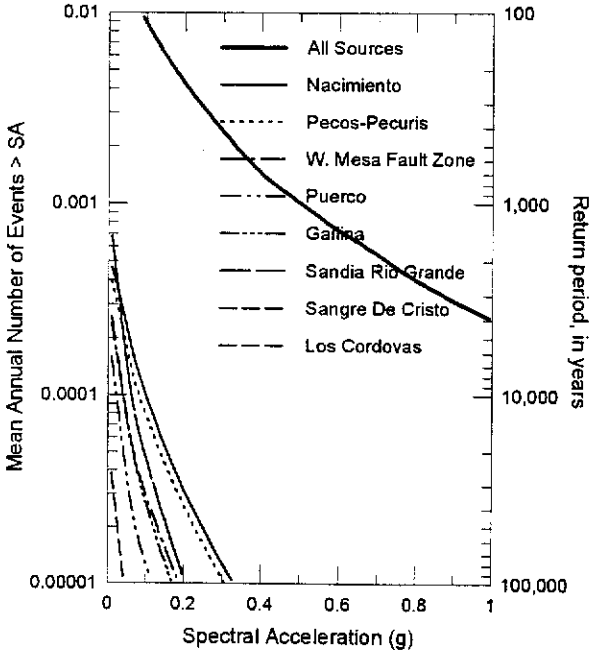


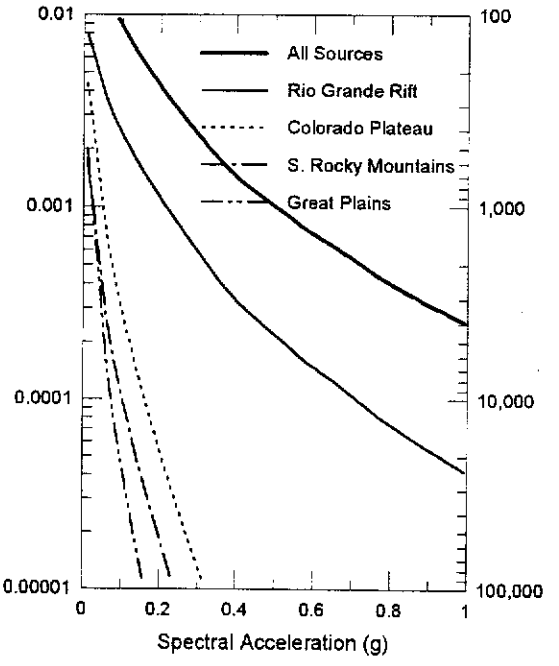
Project No. 91C0509	Los Alamos Seismic Hazards	CONTRIBUTION OF SEISMIC SOURCES TO THE MEAN SEISMIC HAZARD FOR 0.2 SEC HORIZONTAL SPECTRAL ACCELERATION, TA-2	Figure 9-43
Woodward-Clyde Federal Services			

SRC-REC.GRF



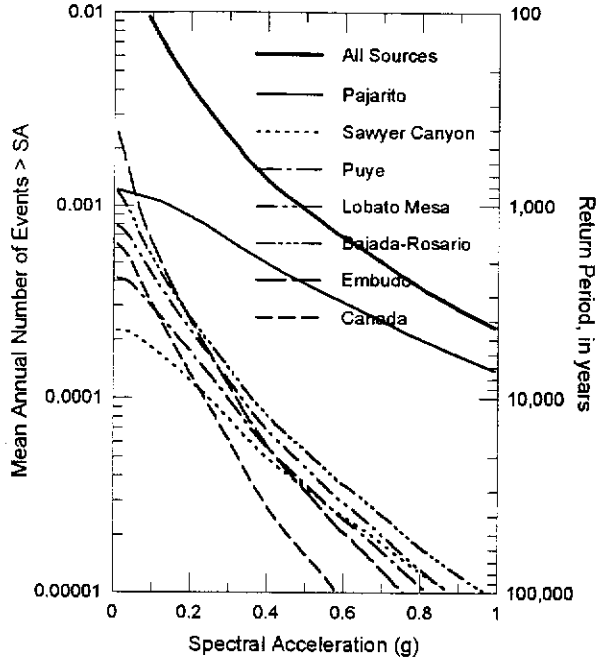


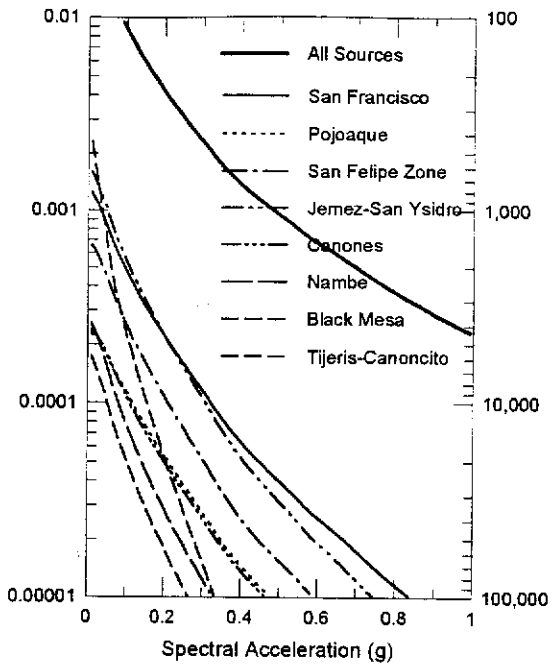


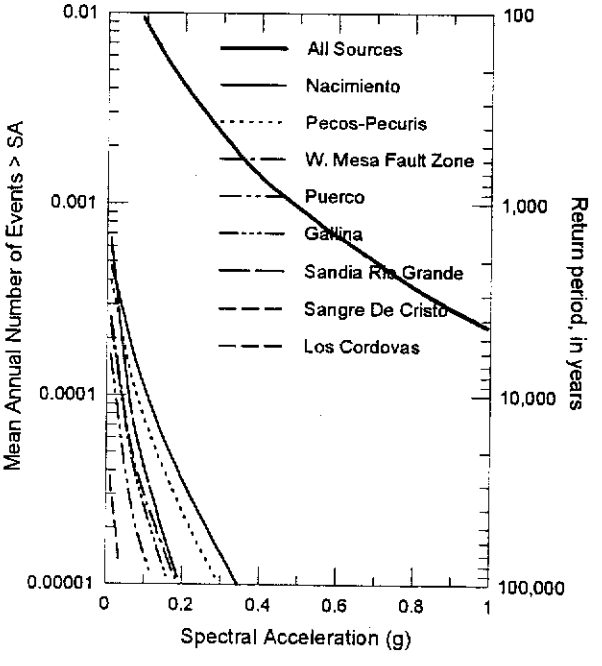


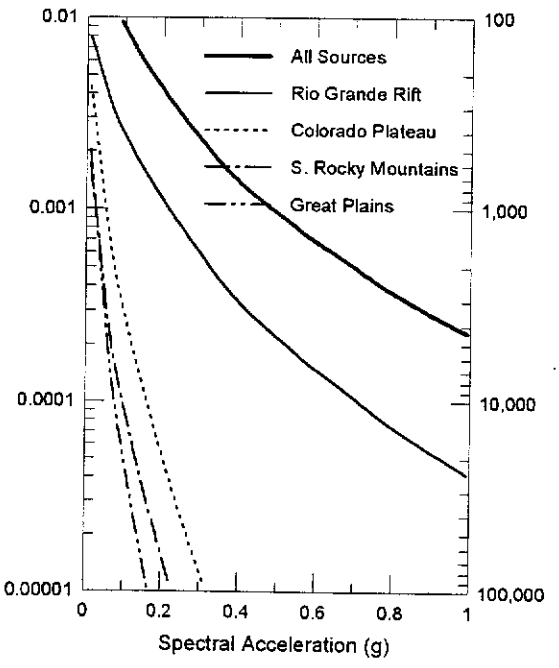
Project No. 91C0509	Los Alamos Seismic Hazards	CONTRIBUTION OF SEISMIC SOURCES TO THE MEAN SEISMIC HAZARD FOR 0.2 SEC HORIZONTAL SPECTRAL ACCELERATION, TA-3	Figure 9-44
Woodward-Clyde Federal Services			

SRC-REC.GRF



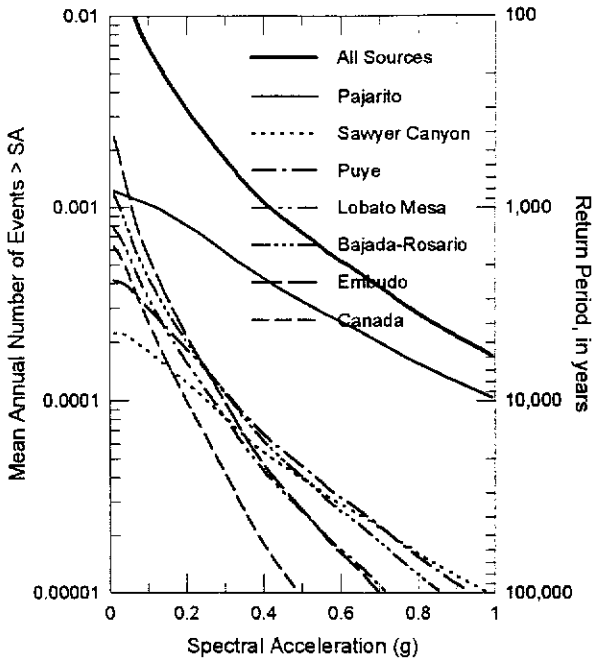


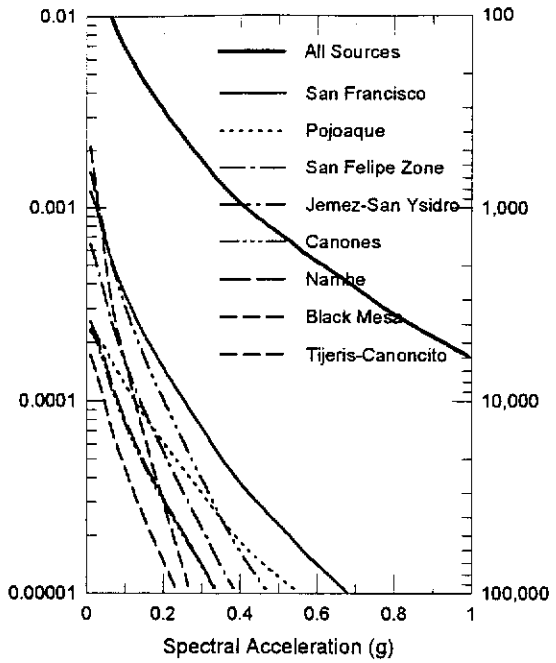


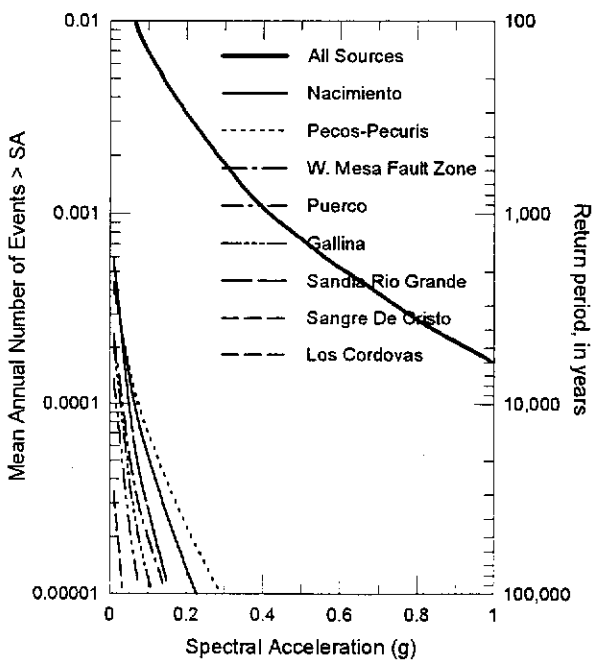


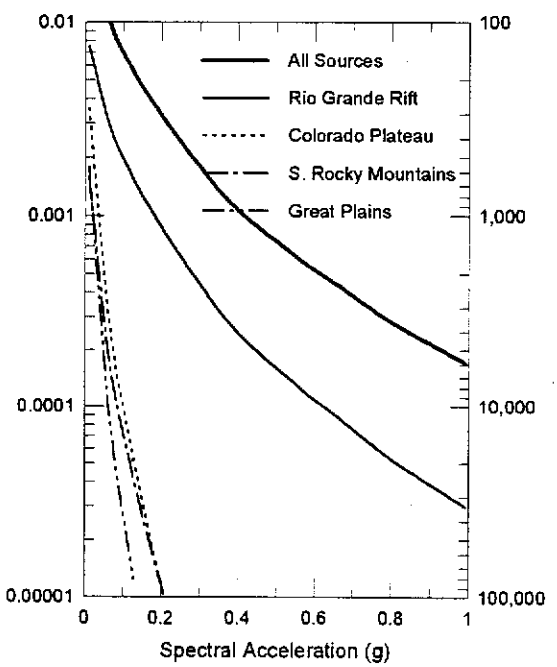
Project No. 91C0509	Los Alamos Seismic Hazards	CONTRIBUTION OF SEISMIC SOURCES TO THE MEAN SEISMIC HAZARD FOR 0.2 SEC HORIZONTAL SPECTRAL ACCELERATION, TA-16	Figure 9-45
Woodward-Clyde Federal Services			

SRC-REC.GRF



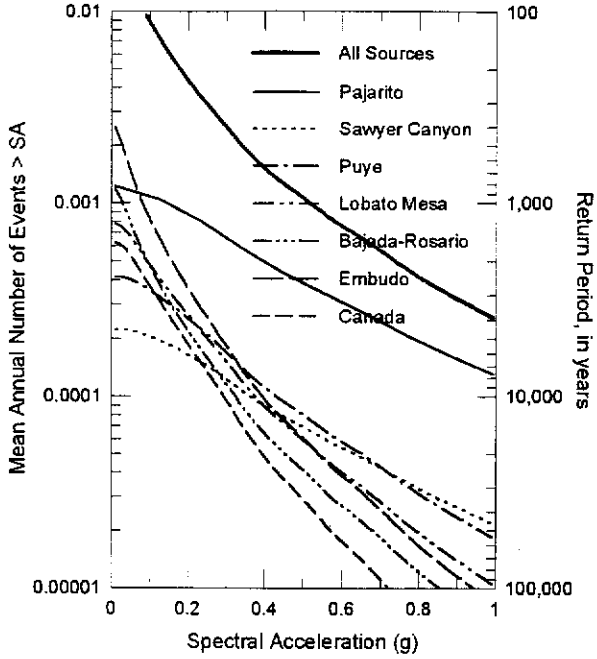


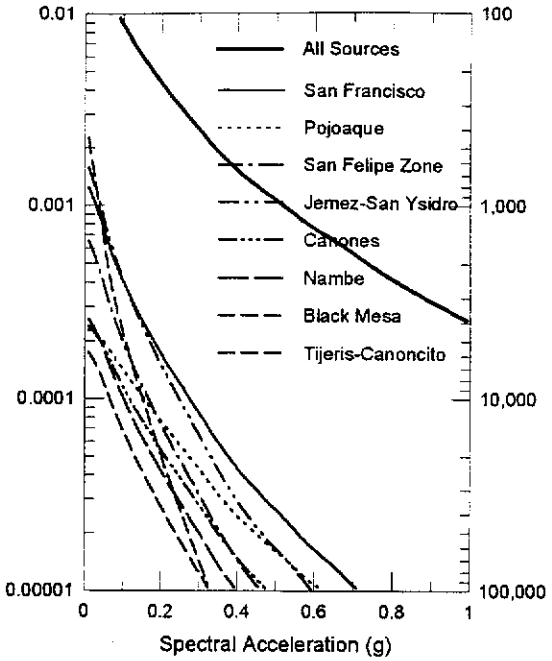


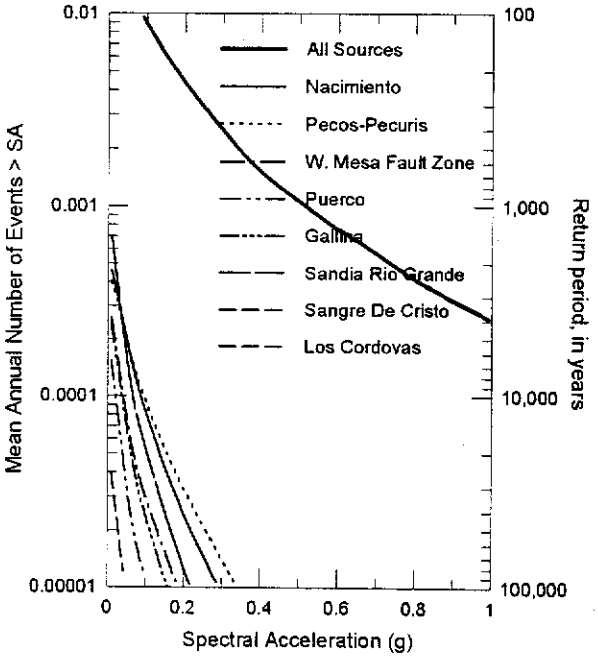


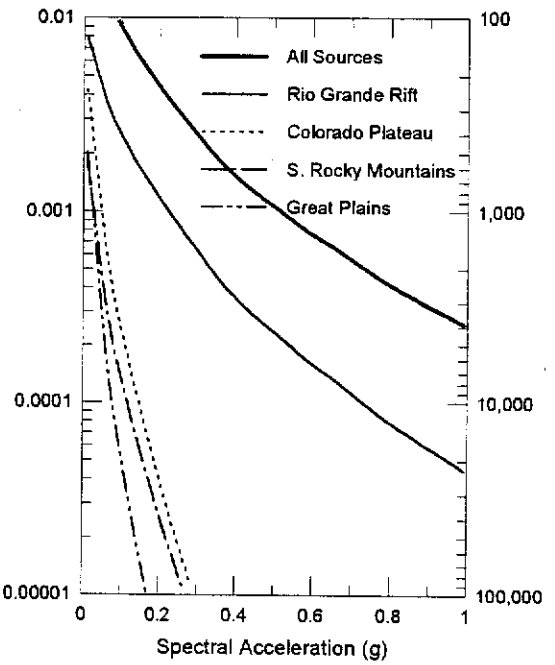
Project No. 91C0509	Los Alamos Seismic Hazards	CONTRIBUTION OF SEISMIC SOURCES TO THE MEAN SEISMIC HAZARD FOR 0.2 SEC HORIZONTAL SPECTRAL ACCELERATION, TA-18	Figure 9-46
Woodward-Clyde Federal Services			

SRC-REC.GRF



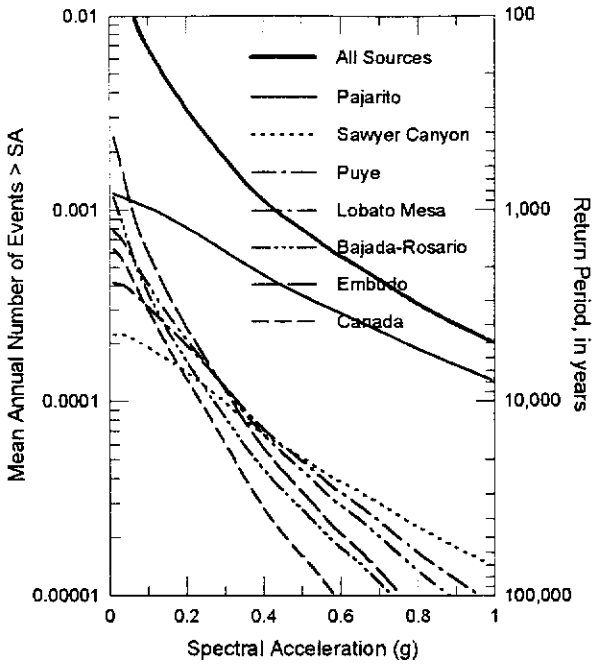


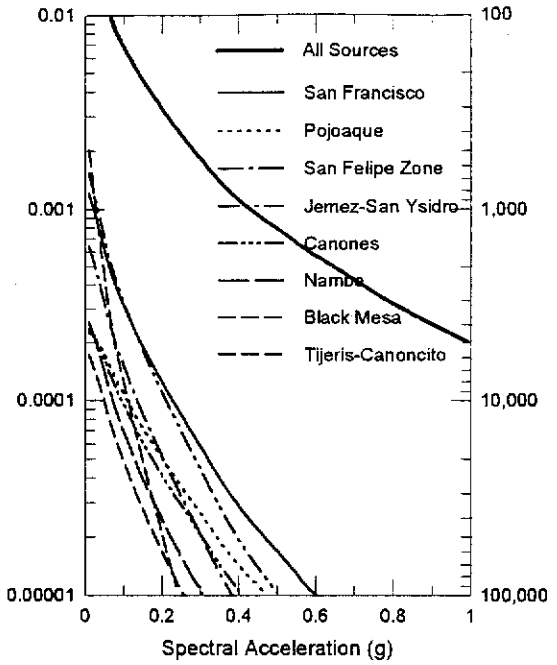


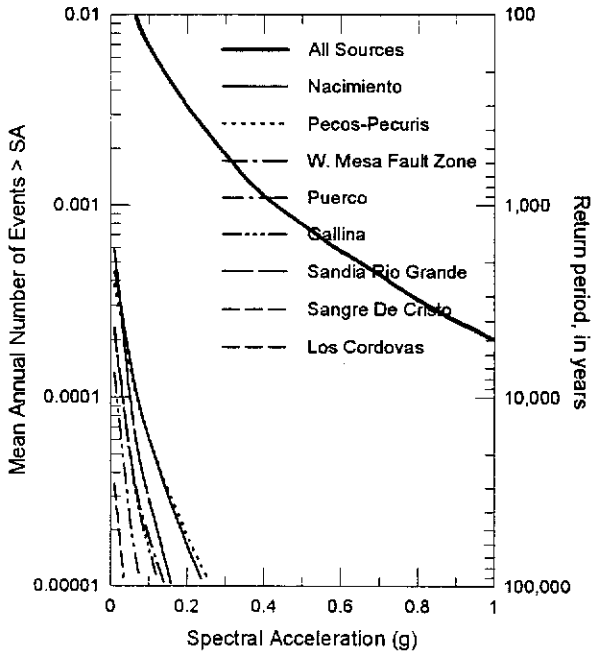


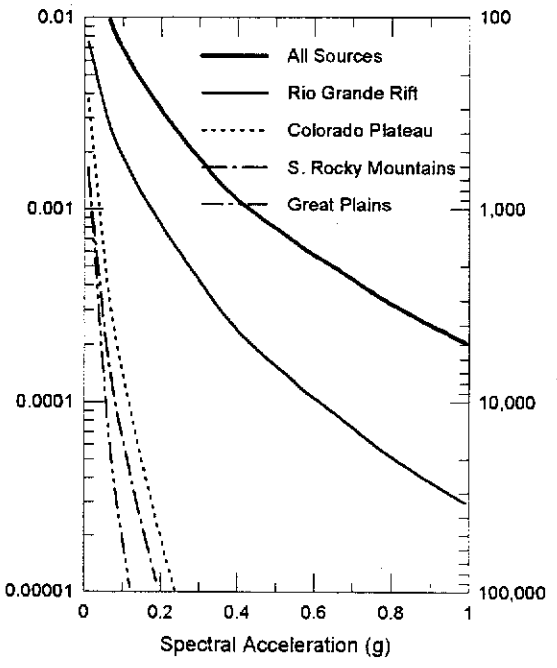
Project No. 91C0509	Los Alamos Seismic Hazards	CONTRIBUTION OF SEISMIC SOURCES TO THE MEAN SEISMIC HAZARD FOR 0.2 SEC HORIZONTAL SPECTRAL ACCELERATION, TA-21	Figure 9-47
Woodward-Clyde Federal Services			

SRC-REC.GRF



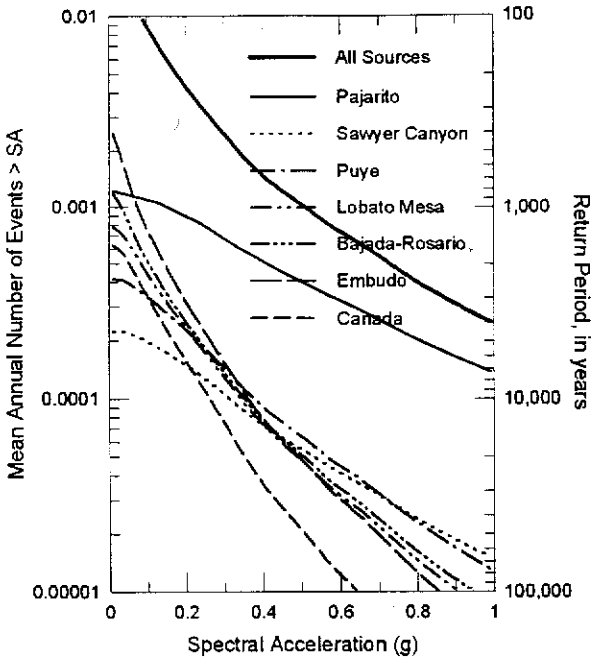


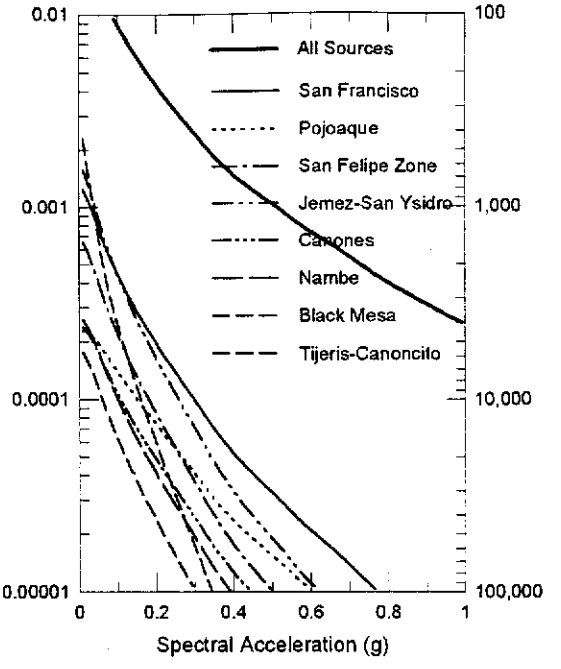


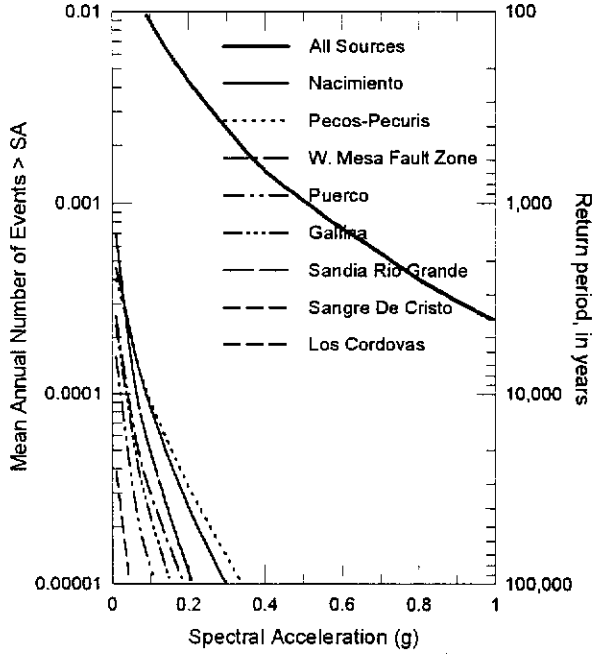


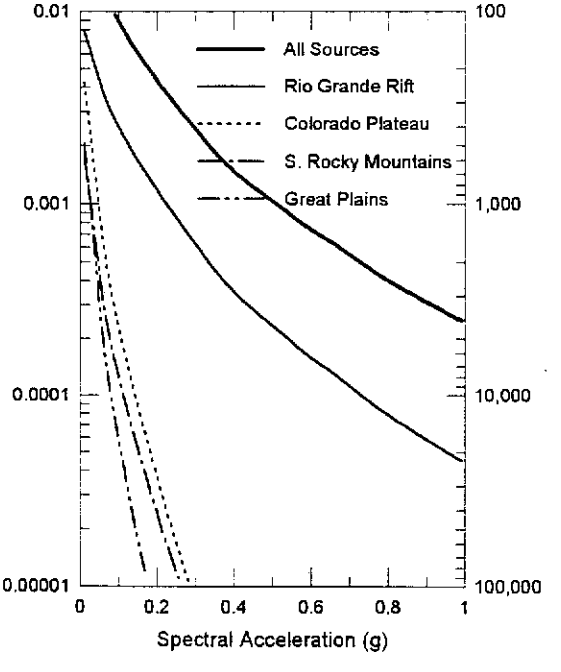
Project No. 91C0509	Los Alamos Seismic Hazards	CONTRIBUTION OF SEISMIC SOURCES TO THE MEAN SEISMIC HAZARD FOR 0.2 SEC HORIZONTAL SPECTRAL ACCELERATION, TA-41	Figure 9-48
Woodward-Clyde Federal Services			

SRC-REC.GRF



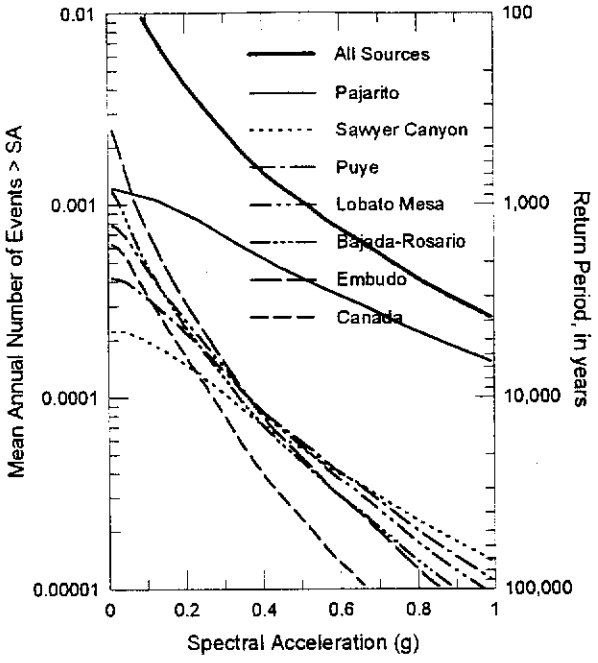


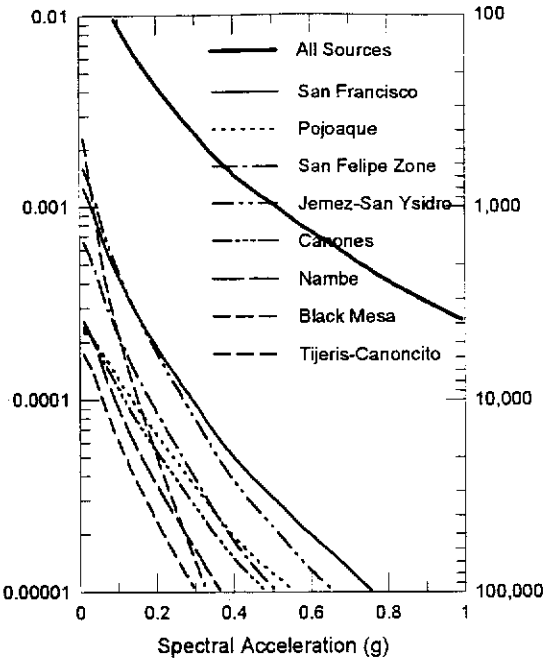


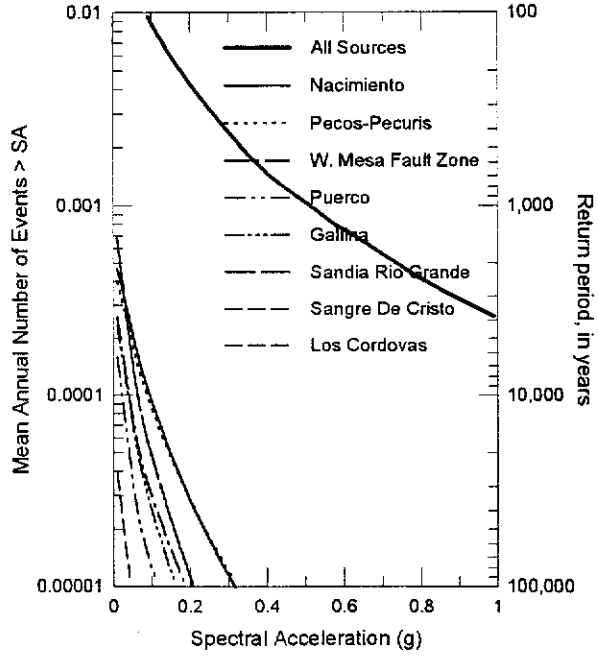


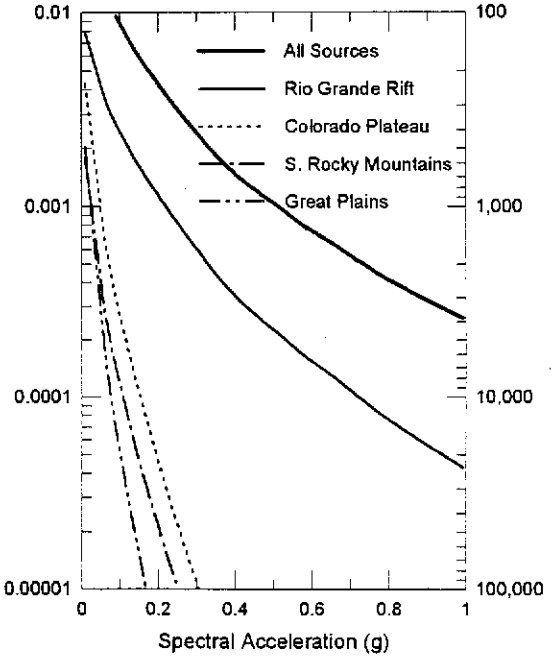
Project No. 91C0509	Los Alamos Seismic Hazards	CONTRIBUTION OF SEISMIC SOURCES TO THE MEAN SEISMIC HAZARD FOR 0.2 SEC HORIZONTAL SPECTRAL ACCELERATION, TA-46	Figure 9-49
Woodward-Clyde Federal Services			

SRC-REC.GRF



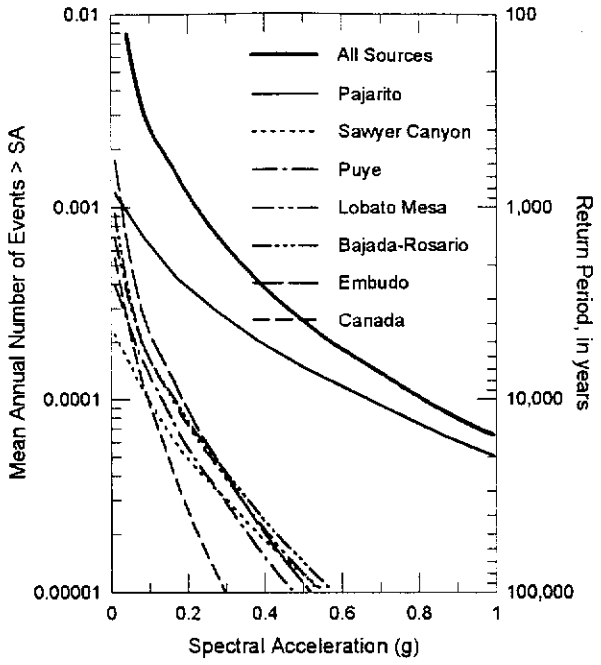


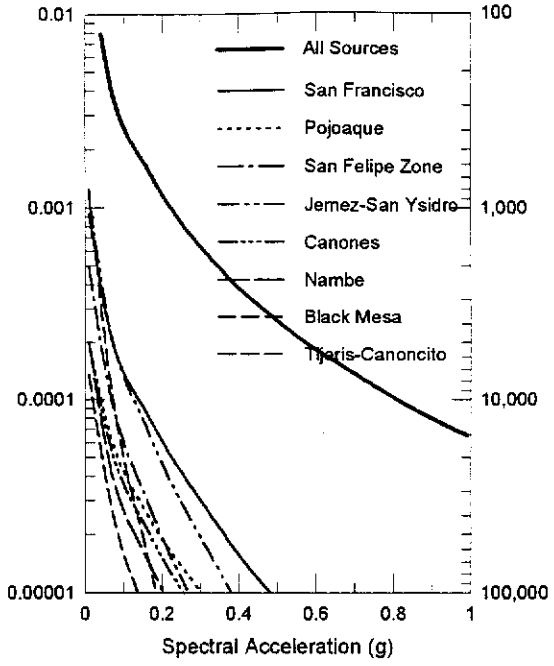


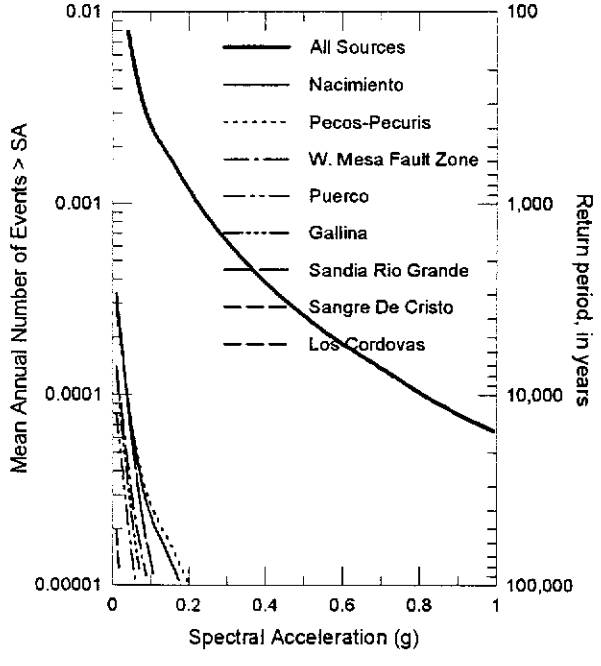


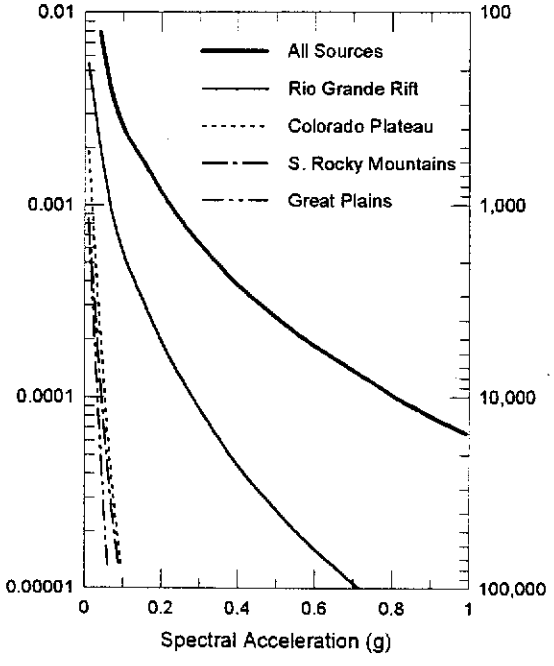
Project No. 91C0509	Los Alamos Seismic Hazards	CONTRIBUTION OF SEISMIC SOURCES TO THE MEAN SEISMIC HAZARD FOR 0.2 SEC HORIZONTAL SPECTRAL ACCELERATION, TA-55	Figure 9-50
Woodward-Clyde Federal Services			

SRC-REC.GRF



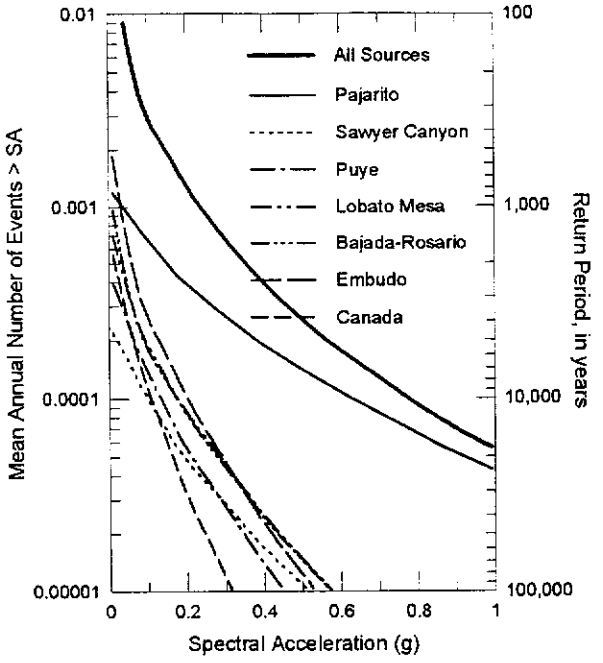


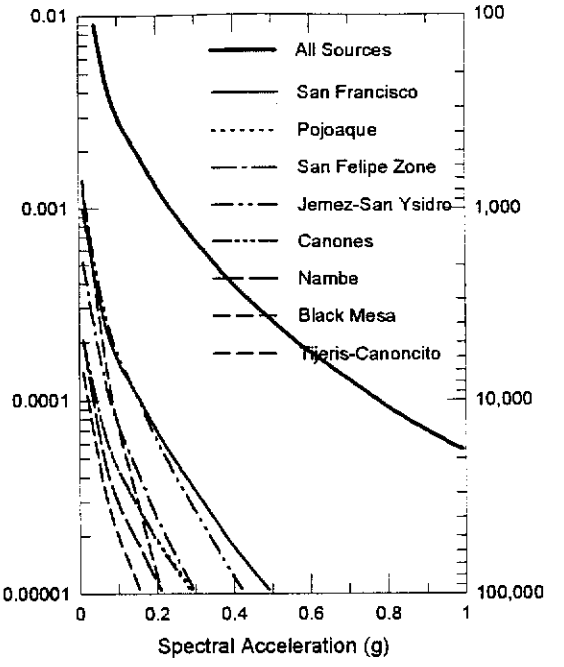


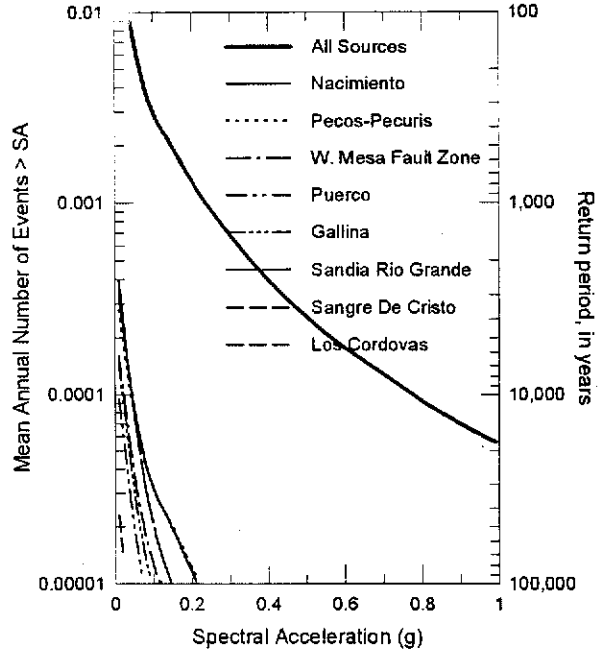


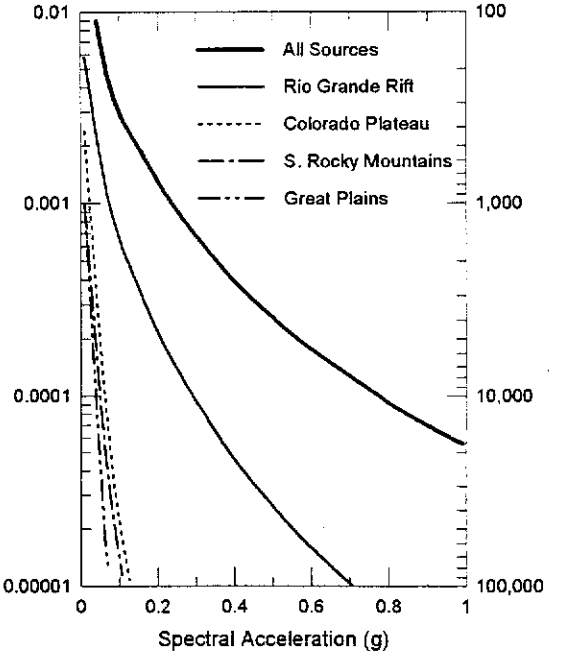
Project No. 91C0509	Los Alamos Seismic Hazards	CONTRIBUTION OF SEISMIC SOURCES TO THE MEAN SEISMIC HAZARD FOR 1 SEC HORIZONTAL SPECTRAL ACCELERATION, TA-2	Figure 9-51
Woodward-Clyde Federal Services			

SRC-REC GRF



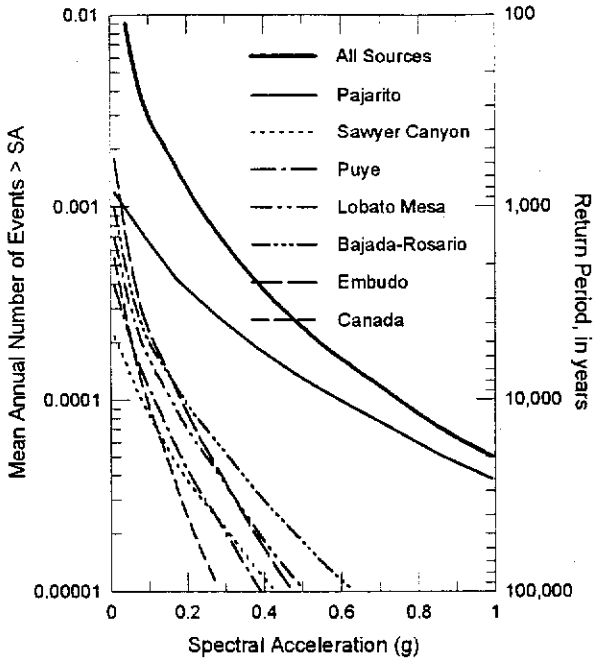


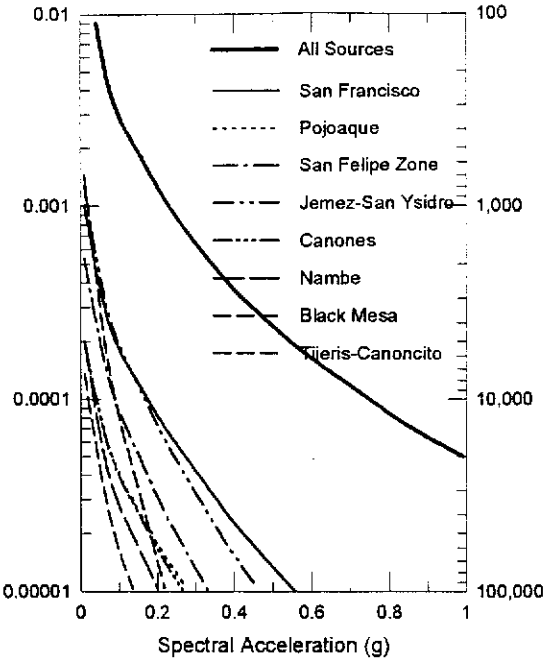


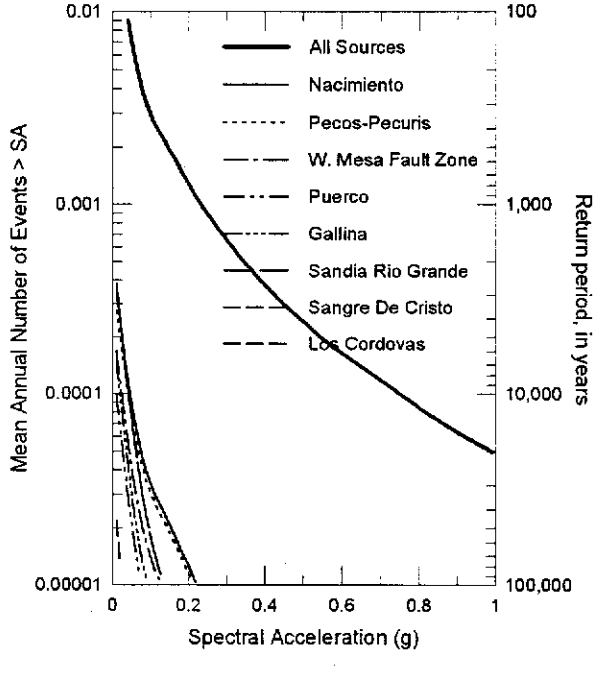


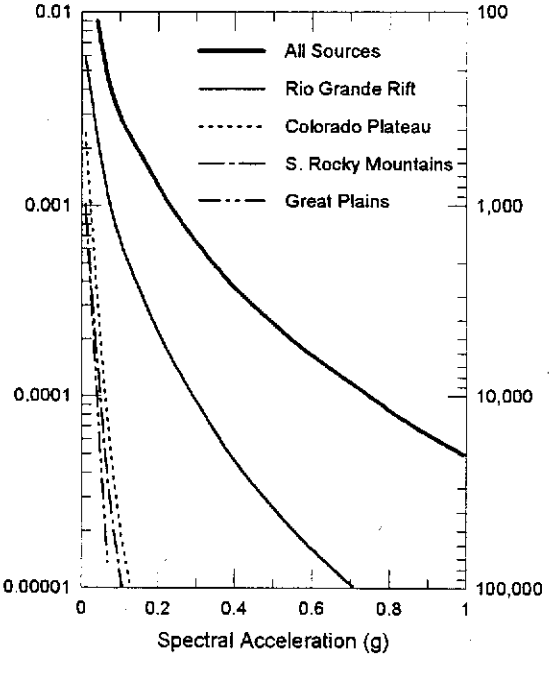
Project No. 91C0509	Los Alamos Seismic Hazards	CONTRIBUTION OF SEISMIC SOURCES TO THE MEAN SEISMIC HAZARD FOR 1 SEC HORIZONTAL SPECTRAL ACCELERATION, TA-3	Figure 9-52
Woodward-Clyde Federal Services			

SRC-REC.GRF



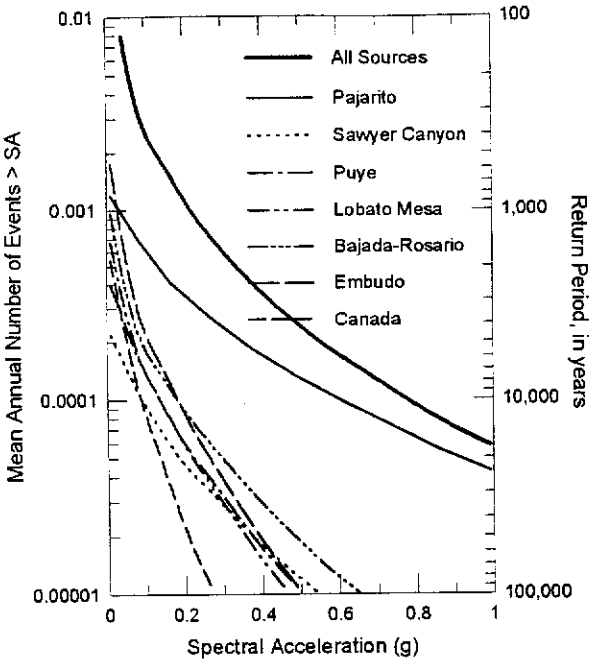


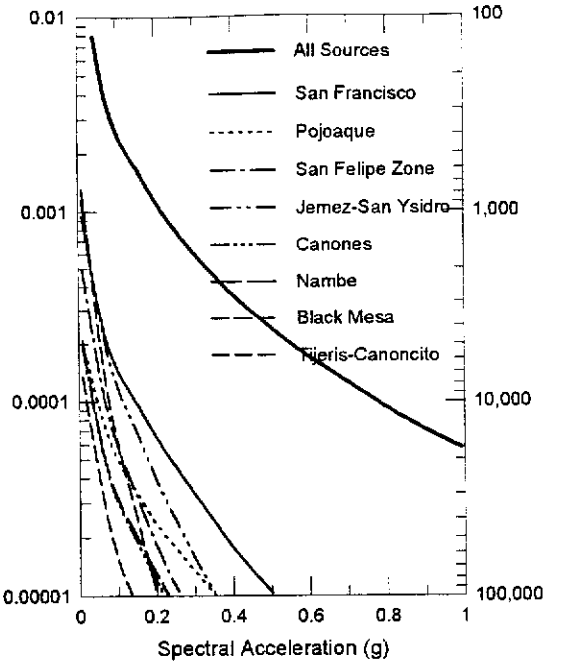


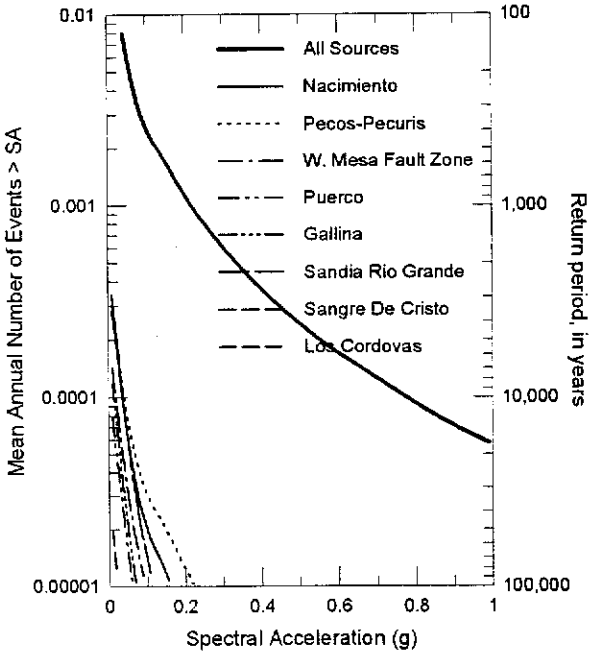


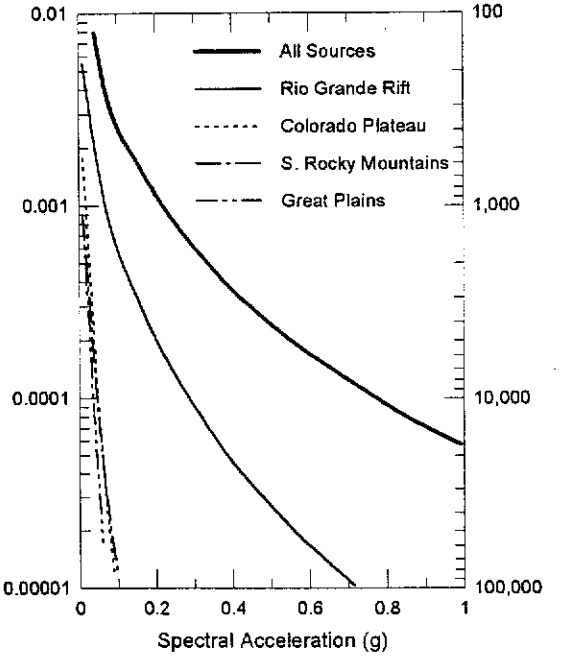
Project No. 91C0509	Los Alamos Seismic Hazards	CONTRIBUTION OF SEISMIC SOURCES TO THE MEAN SEISMIC HAZARD FOR 1 SEC HORIZONTAL SPECTRAL ACCELERATION, TA-16	Figure 9-53
Woodward-Clyde Federal Services			

SRC-REC.GRF



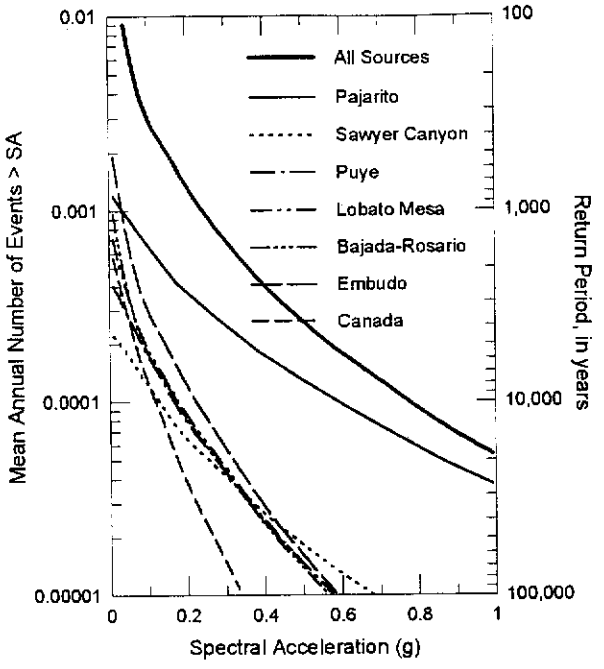


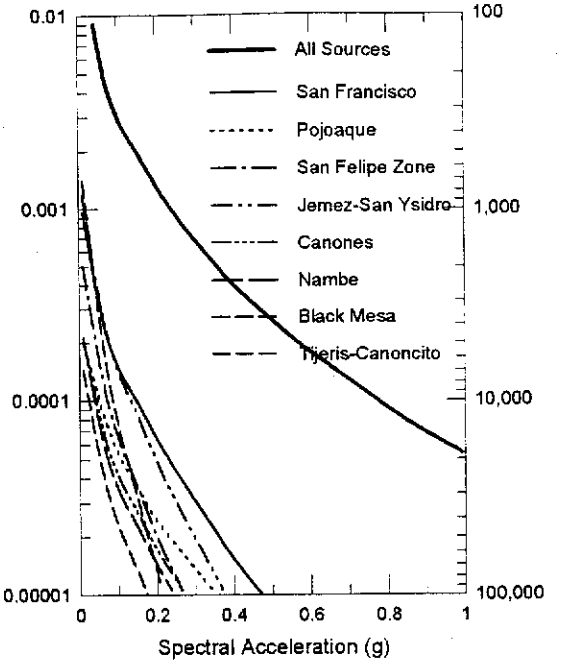


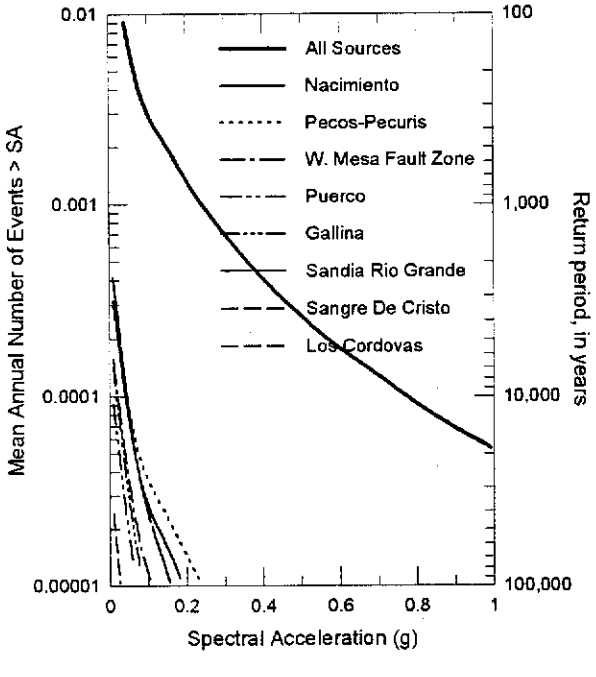


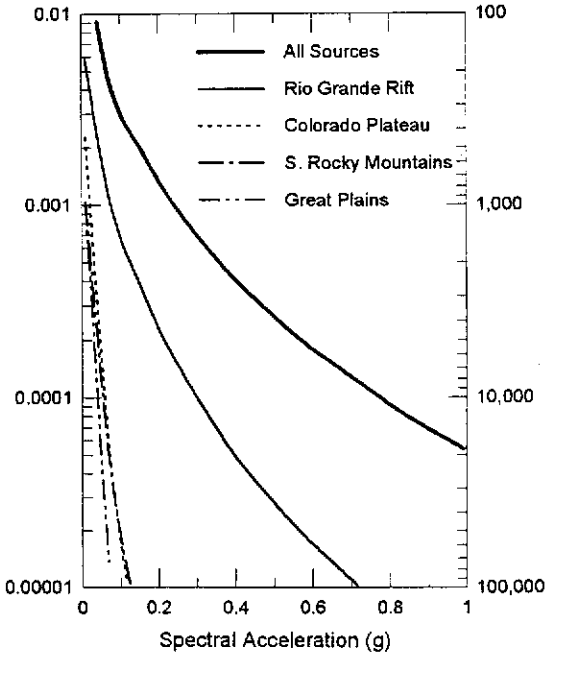
Project No. 91C0509	Los Alamos Seismic Hazards	CONTRIBUTION OF SEISMIC SOURCES TO THE MEAN SEISMIC HAZARD FOR 1 SEC HORIZONTAL SPECTRAL ACCELERATION, TA-18	Figure 9-54
Woodward-Clyde Federal Services			

SRC-REC.GRF



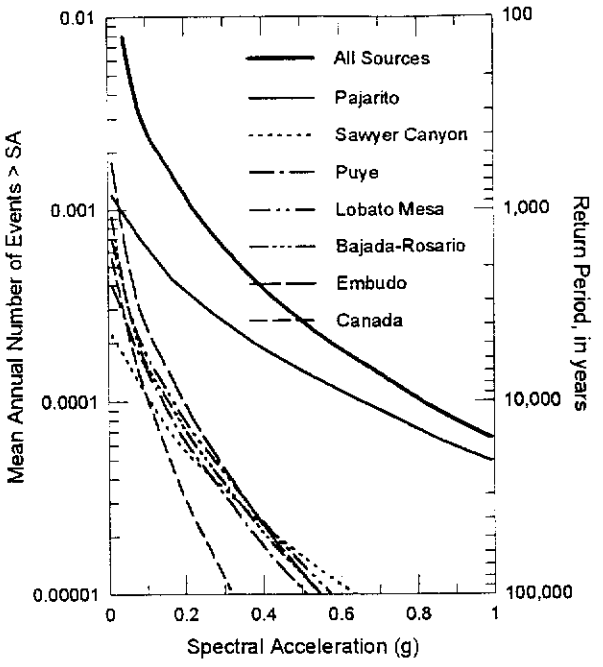


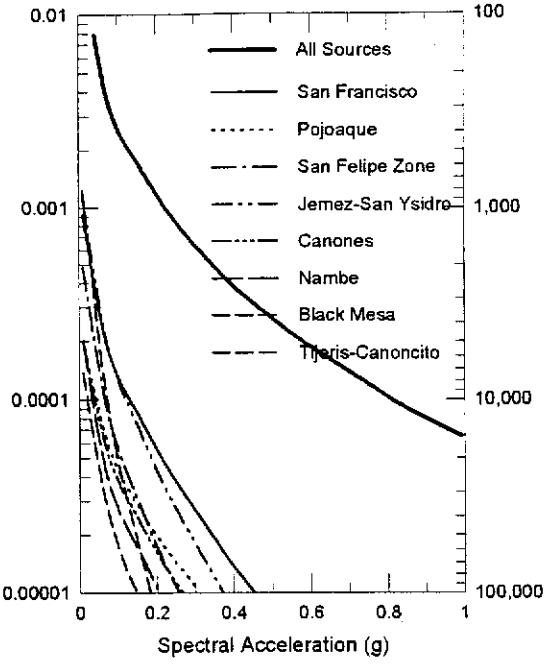


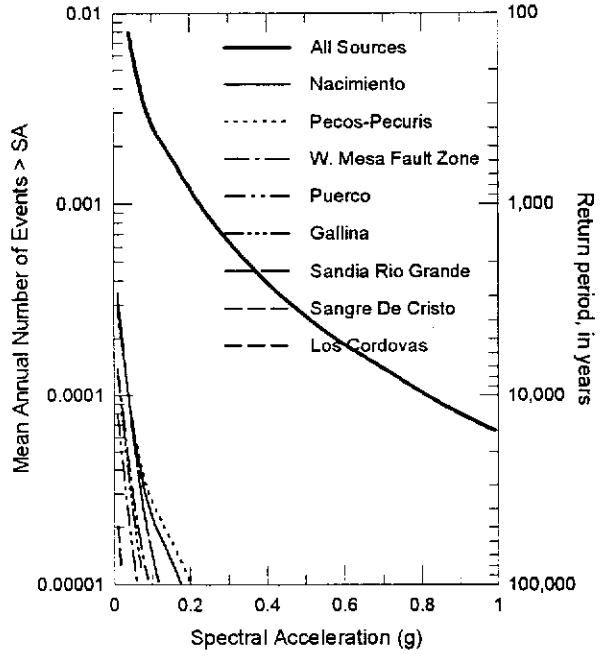


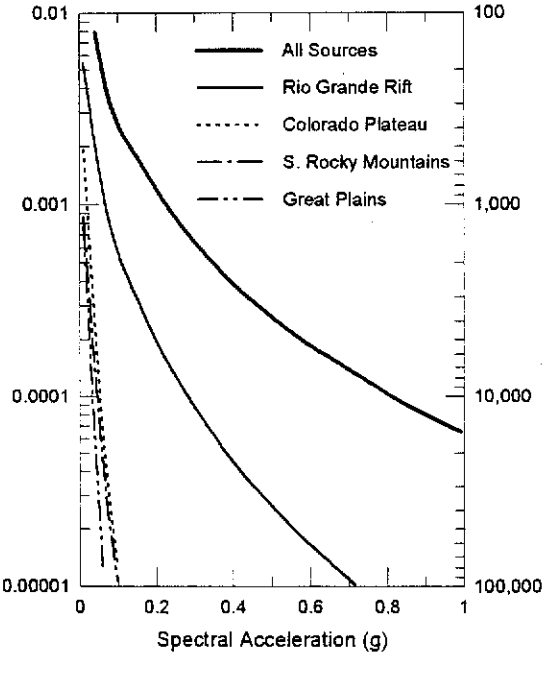
Project No. 91C0509	Los Alamos Seismic Hazards	CONTRIBUTION OF SEISMIC SOURCES TO THE MEAN SEISMIC HAZARD FOR 1 SEC HORIZONTAL SPECTRAL ACCELERATION, TA-21	Figure 9-55
Woodward-Clyde Federal Services			

SRC-REC.GRF



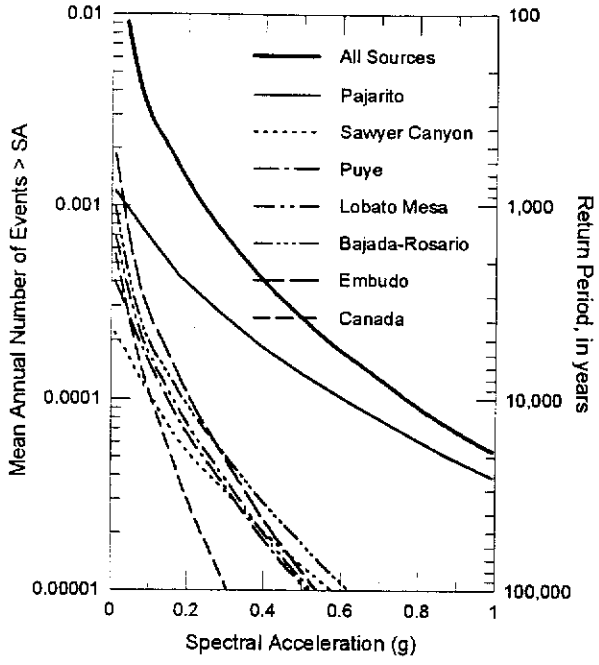


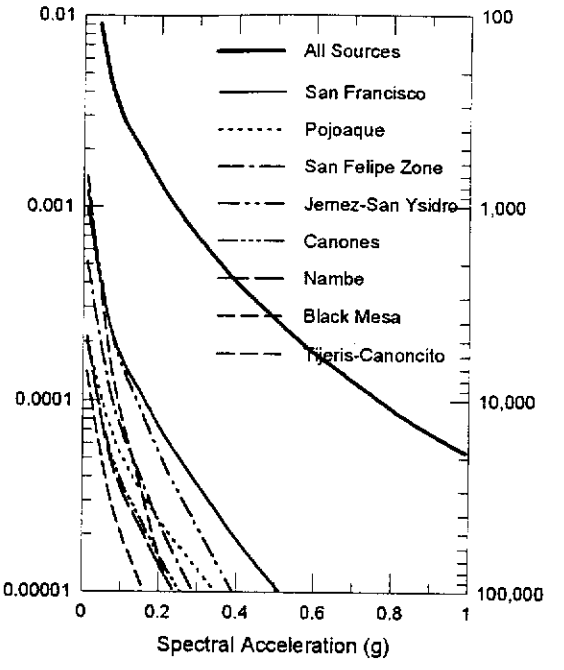


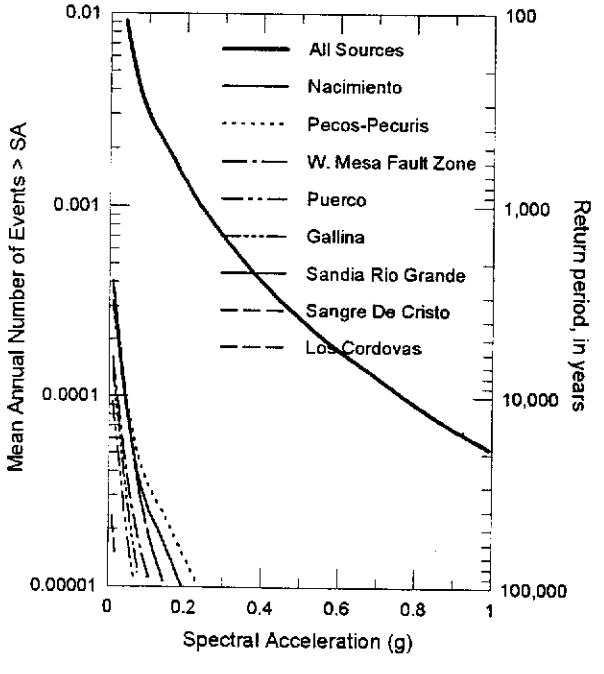


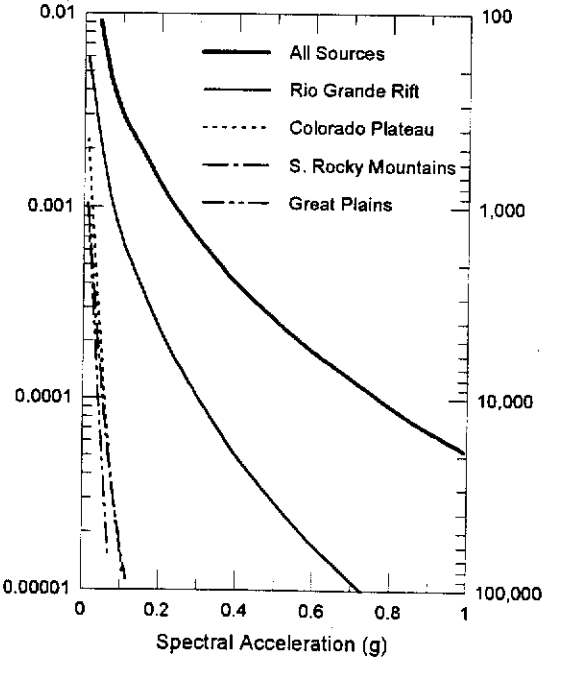
Project No. 91C0509	Los Alamos Seismic Hazards	CONTRIBUTION OF SEISMIC SOURCES TO THE MEAN SEISMIC HAZARD FOR 1 SEC HORIZONTAL SPECTRAL ACCELERATION, TA-41	Figure 9-56
Woodward-Clyde Federal Services			

SRC-REC.GRF



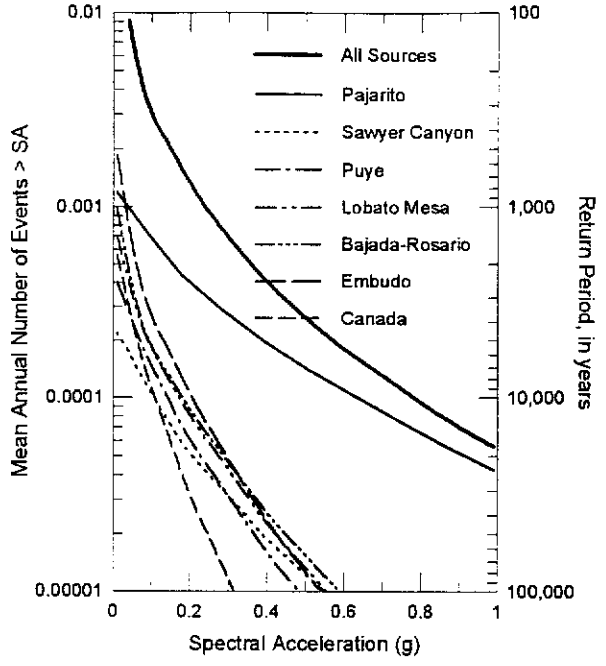


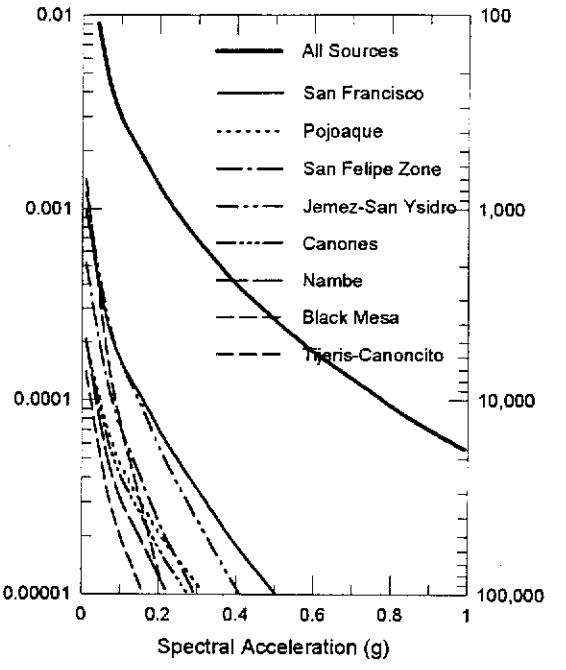


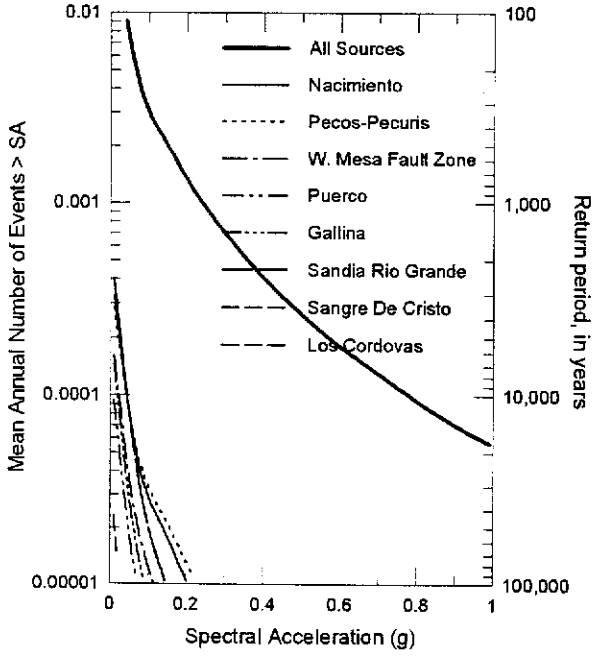


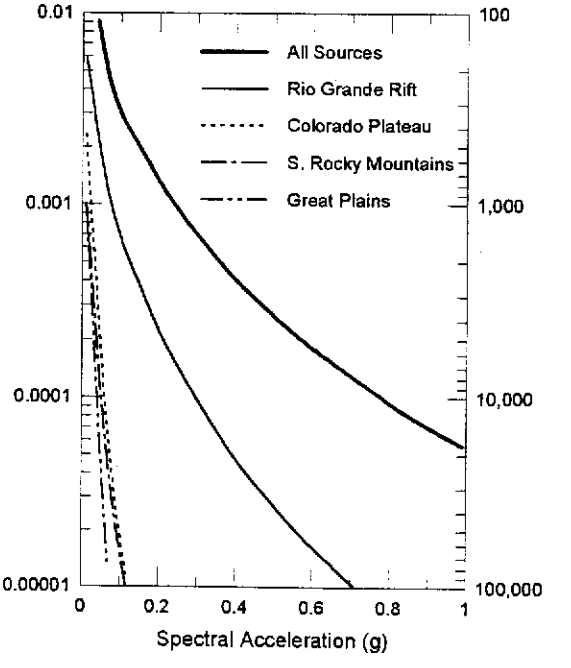
Project No. 91C0509	Los Alamos Seismic Hazards	CONTRIBUTION OF SEISMIC SOURCES TO THE MEAN SEISMIC HAZARD FOR 1 SEC HORIZONTAL SPECTRAL ACCELERATION, TA-46	Figure 9-57
Woodward-Clyde Federal Services			

SRC-REC.GRF



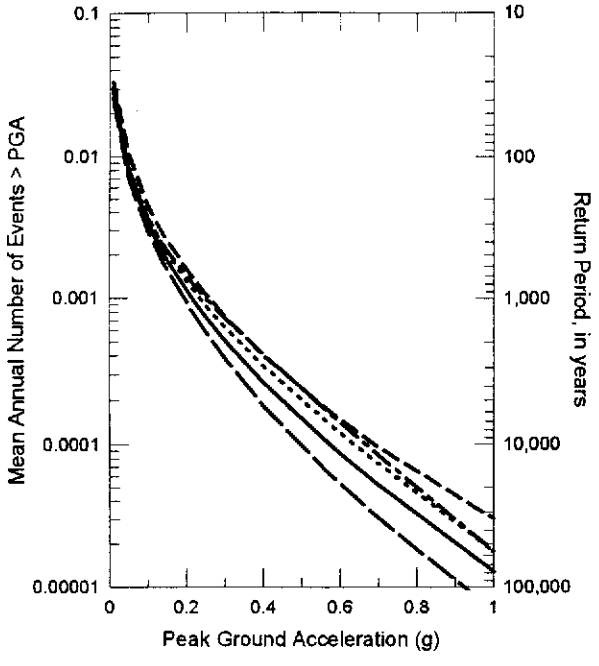


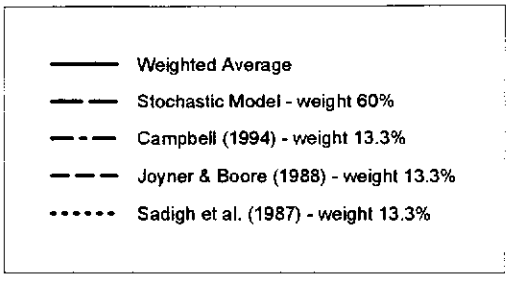


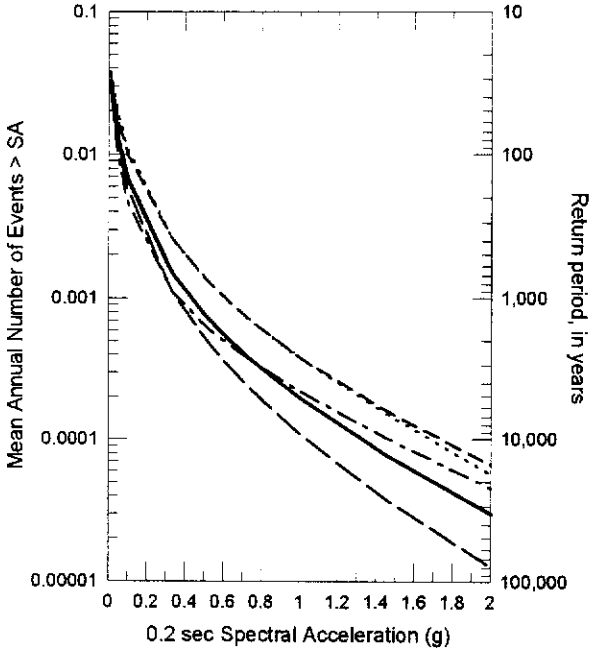


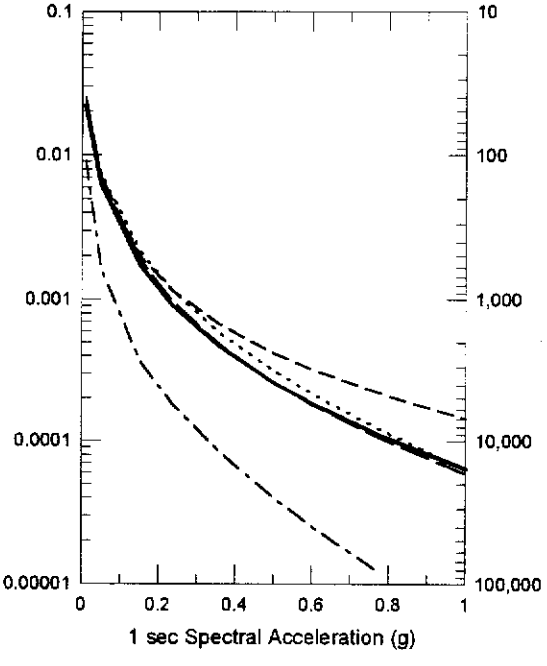
Project No. 91C0509	Los Alamos Seismic Hazards	CONTRIBUTION OF SEISMIC SOURCES TO THE MEAN SEISMIC HAZARD FOR 1 SEC HORIZONTAL SPECTRAL ACCELERATION, TA-55	Figure 9-58
Woodward-Clyde Federal Services			

SRC-REC GRF



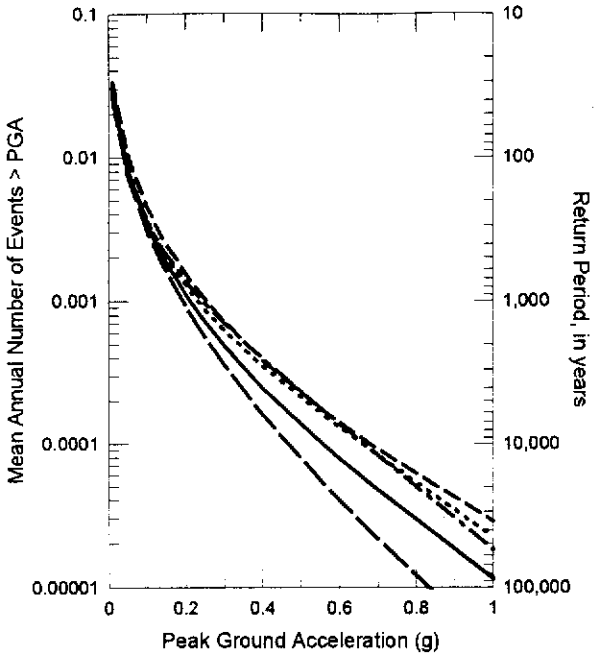


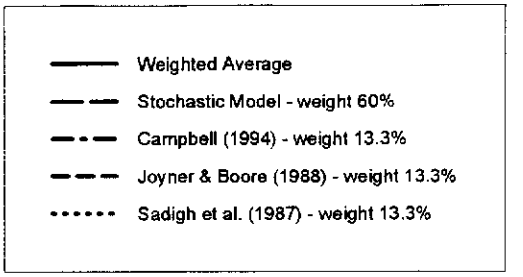


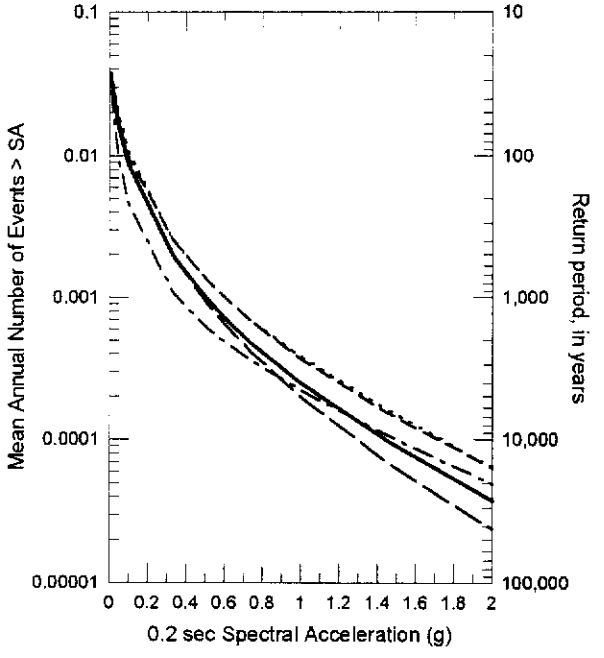


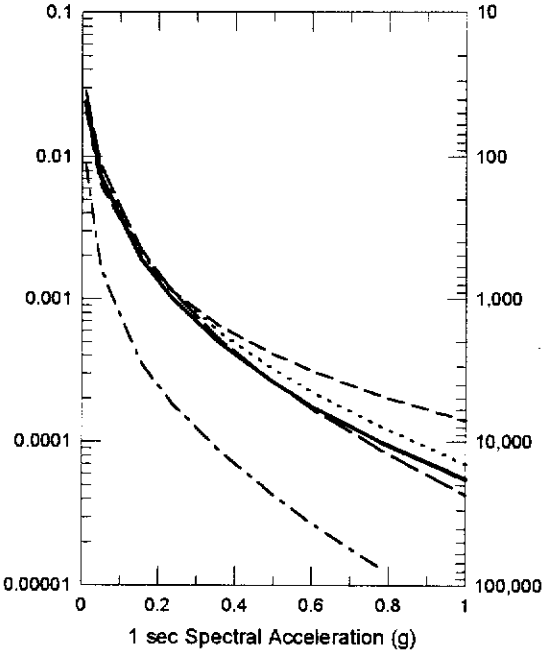
Project No. 938L410A	Los Alamos Seismic Hazards	EFFECT OF ATTENUATION RELATIONSHIPS ON MEAN SEISMIC HAZARD FOR PEAK ACCELERATION AND SPECTRAL ACCELERATIONS OF 0.2 AND 1 SEC, TA-2	Figure 9-59
Woodward-Clyde Federal Services			

2ATTENN.GRF



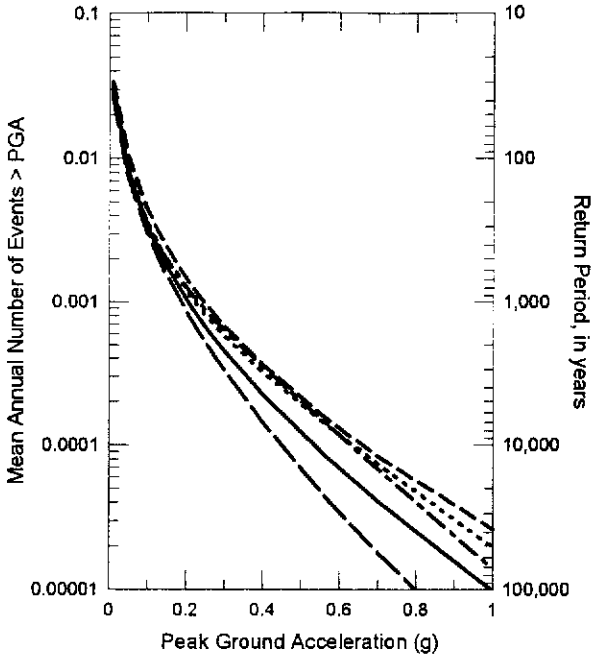


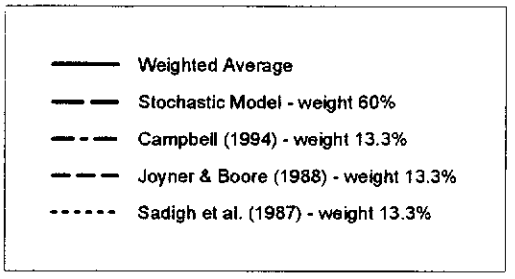


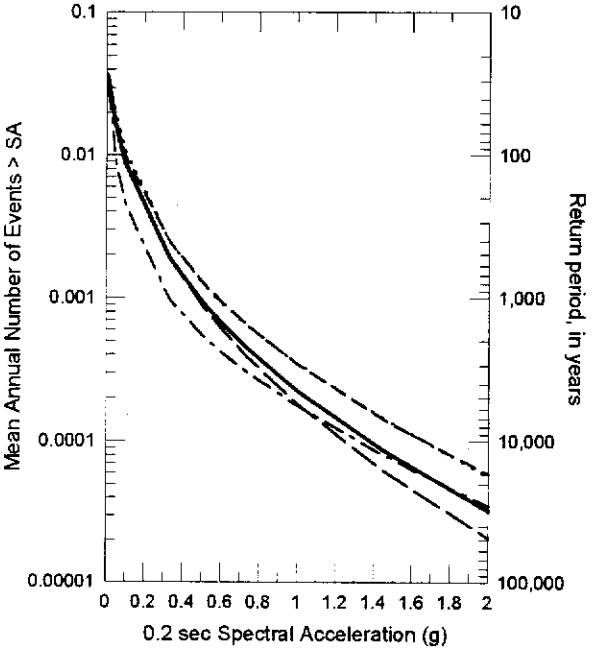


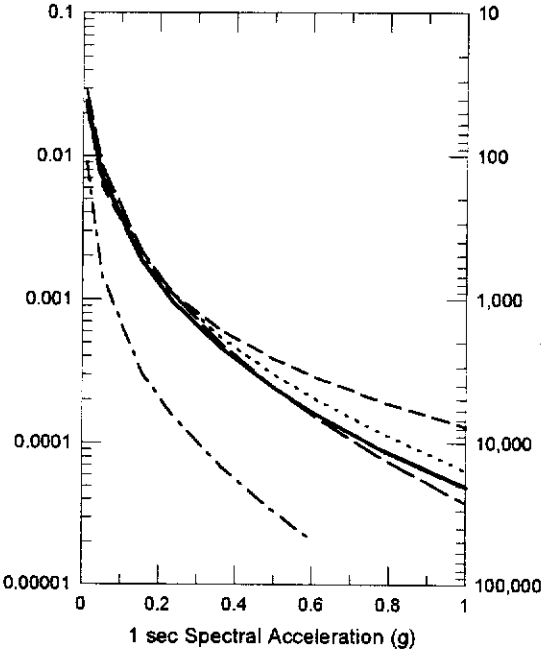
Project No. 938L410A	Los Alamos Seismic Hazards	EFFECT OF ATTENUATION RELATIONSHIPS ON MEAN SEISMIC HAZARD FOR PEAK ACCELERATION AND SPECTRAL ACCELERATIONS OF 0.2 AND 1 SEC, TA-3	Figure 9-60
Woodward-Clyde Federal Services			

3ATTENN.GRF



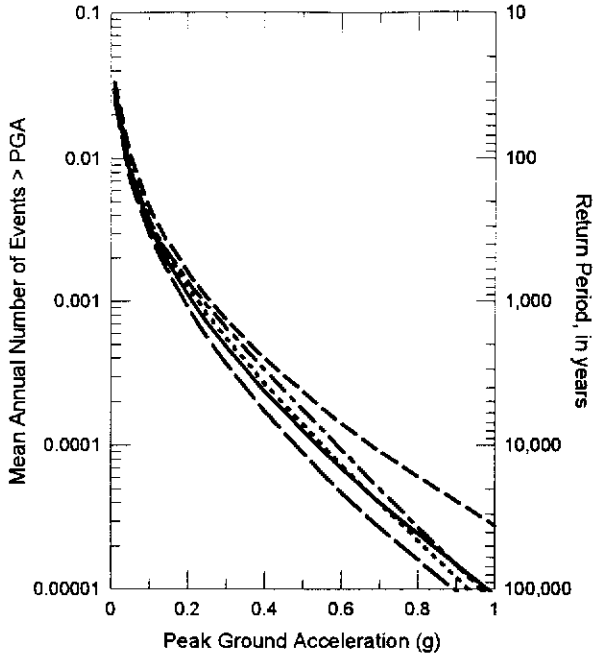


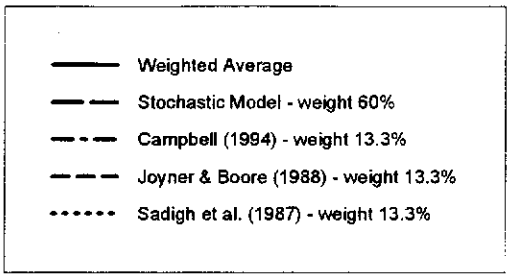


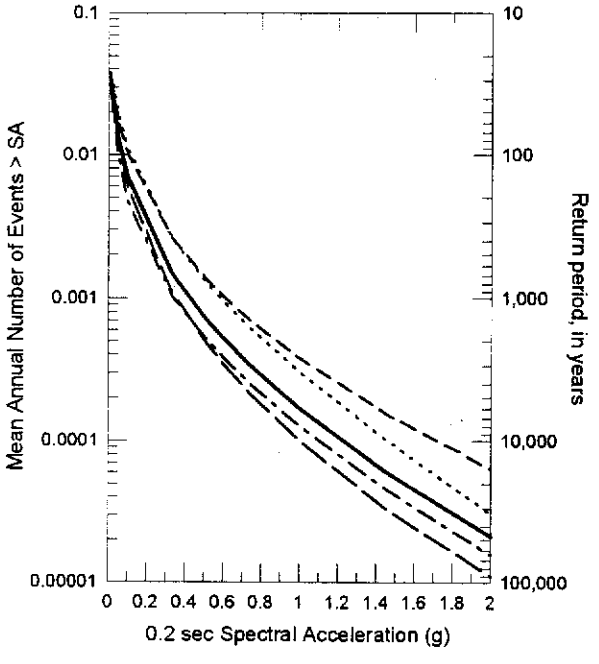


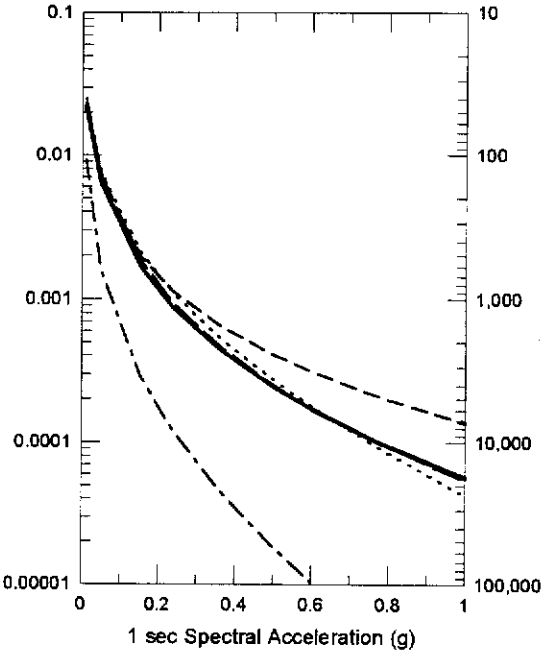
Project No. 938L410A	Los Alamos National Laboratories Los Alamos Seismic Hazards Los Alamos, New Mexico	EFFECT OF ATTENUATION RELATIONSHIPS ON MEAN SEISMIC HAZARD FOR PEAK ACCELERATION AND SPECTRAL ACCELERATIONS OF 0.2 AND 1 SEC, TA-16	Figure 9-61
Woodward-Clyde Federal Services			

16ATTENN.GRF



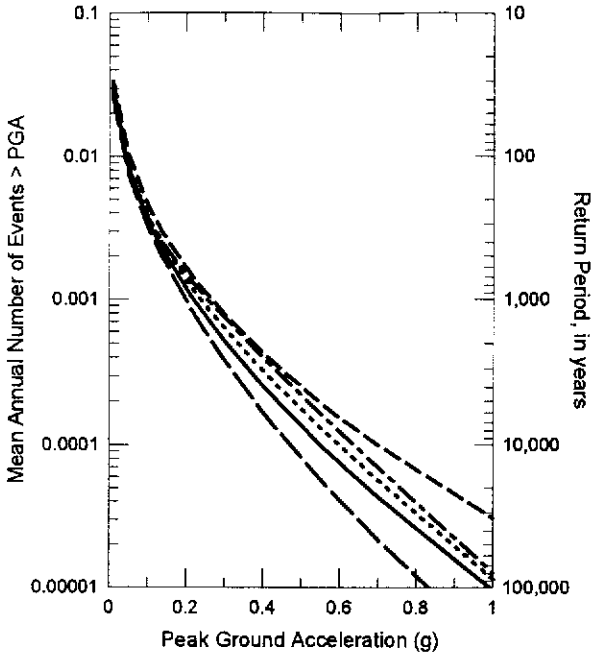


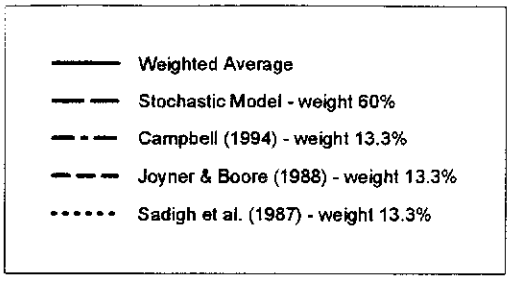


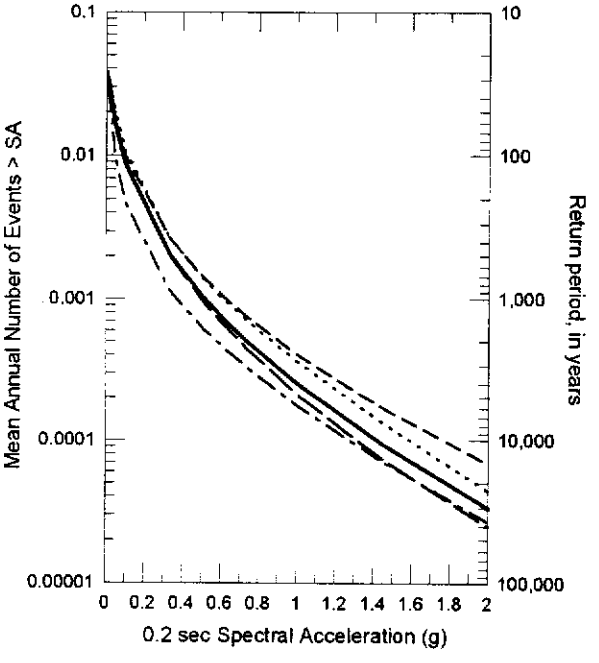


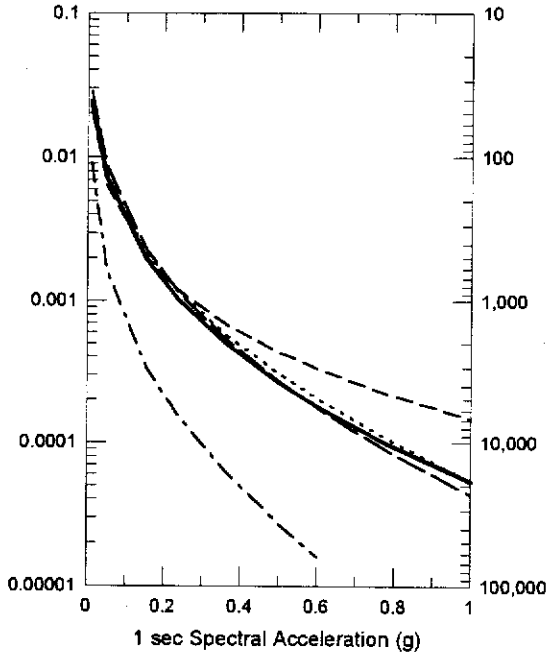
Project No. 938L410A	Los Alamos Seismic Hazards	EFFECT OF ATTENUATION RELATIONSHIPS ON MEAN SEISMIC HAZARD FOR PEAK ACCELERATION AND SPECTRAL ACCELERATIONS OF 0.2 AND 1 SEC, TA-18	Figure 9-62
Woodward-Clyde Federal Services			

18ATTENN.GRF



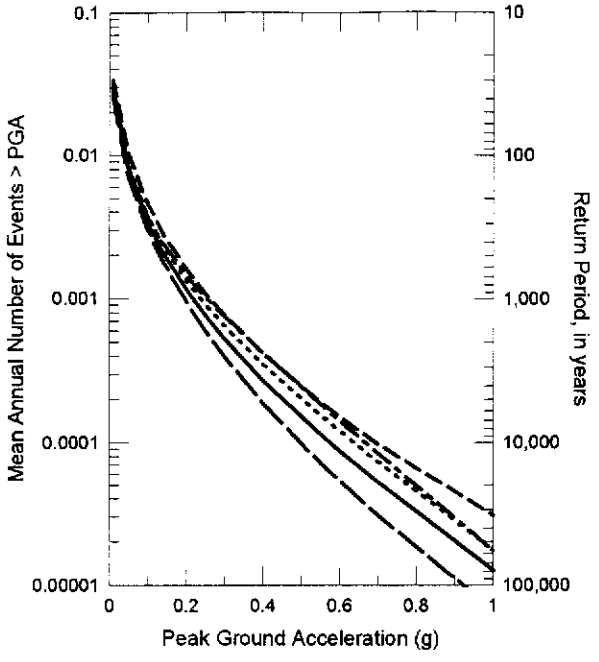


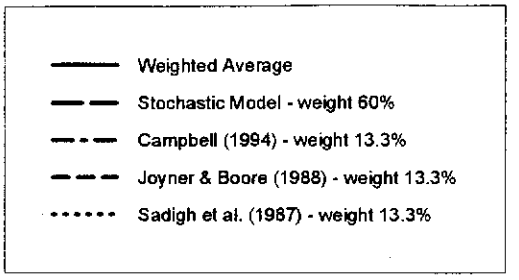


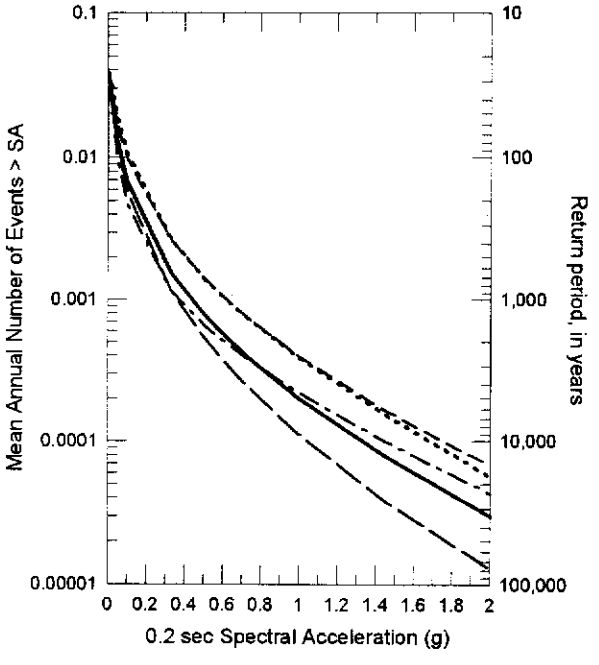


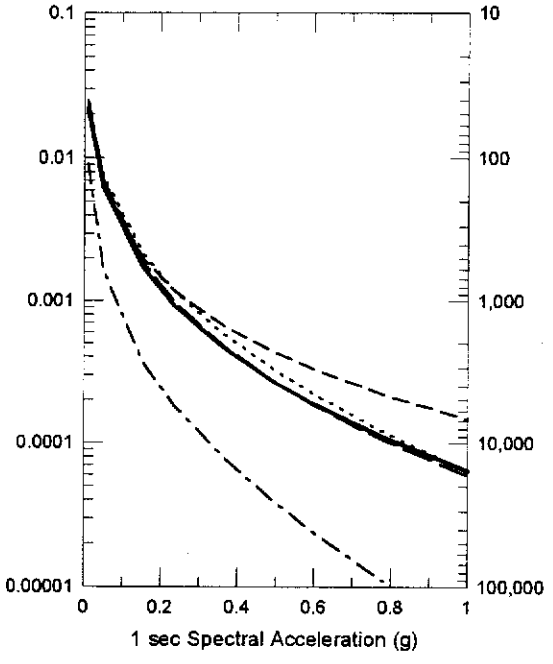
Project No. 938L410A	Los Alamos Seismic Hazards	EFFECT OF ATTENUATION RELATIONSHIPS ON MEAN SEISMIC HAZARD FOR PEAK ACCELERATION AND SPECTRAL ACCELERATIONS OF 0.2 AND 1 SEC, TA-21	Figure 9-63
Woodward-Clyde Federal Services			

21ATTENN.GRF



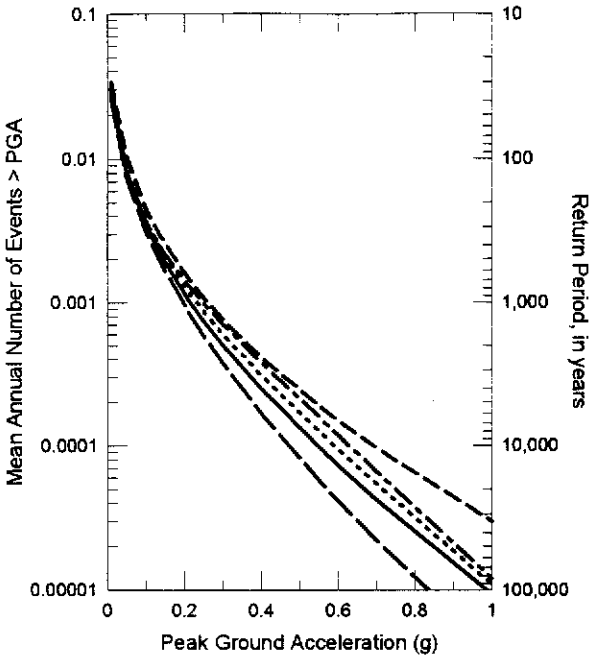


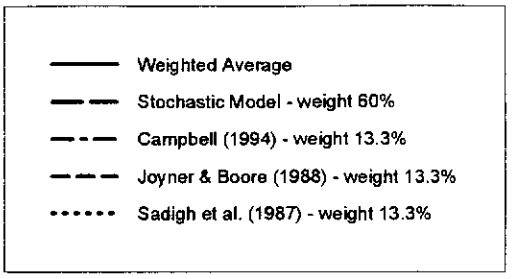


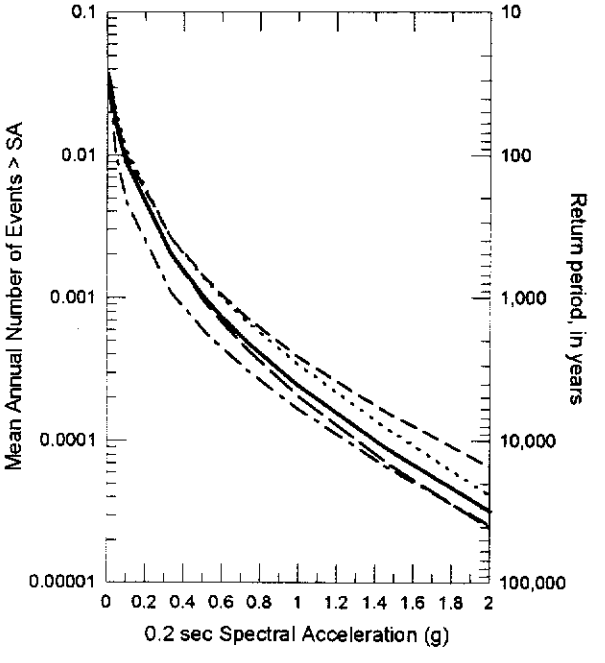


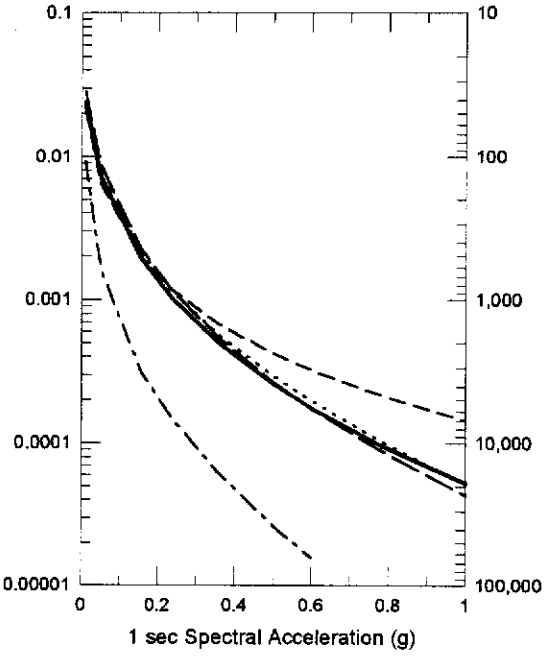
Project No. 938L410A	Los Alamos National Laboratories Los Alamos Seismic Hazards Los Alamos, New Mexico	EFFECT OF ATTENUATION RELATIONSHIPS ON MEAN SEISMIC HAZARD FOR PEAK ACCELERATION AND SPECTRAL ACCELERATIONS OF 0.2 AND 1 SEC, TA-41	Figure 9-64
Woodward-Clyde Federal Services			

41ATTENN.GRF



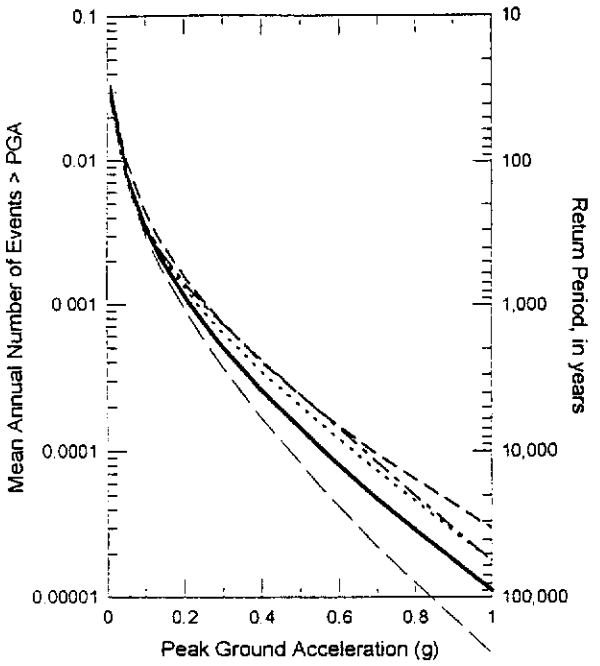


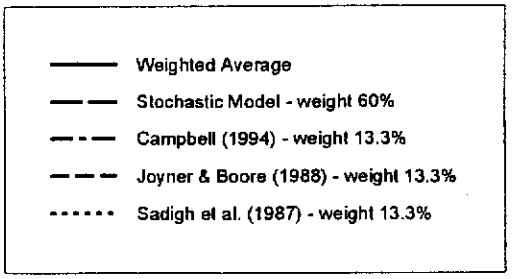


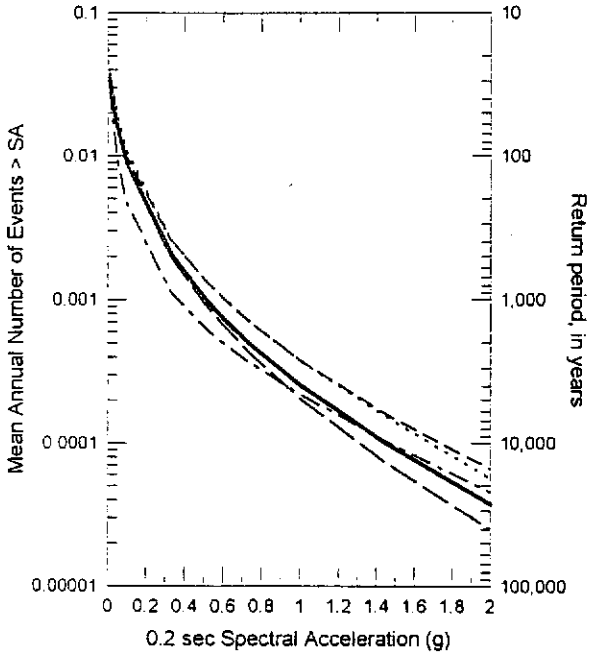


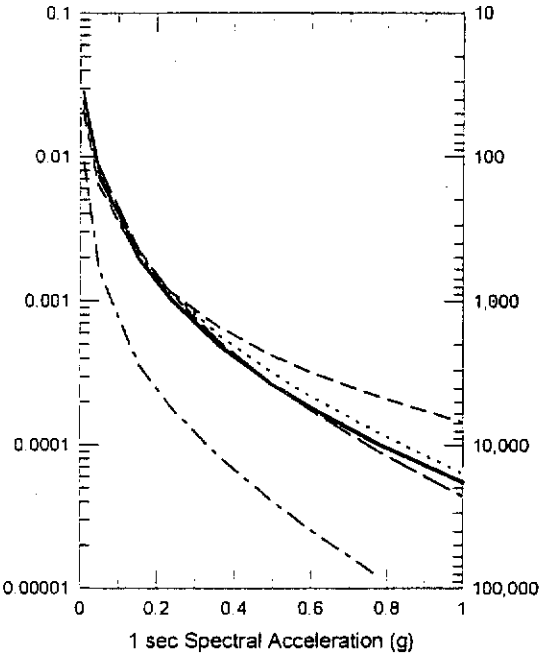
Project No. 938L410A	Los Alamos Seismic Hazards	EFFECT OF ATTENUATION RELATIONSHIPS ON MEAN SEISMIC HAZARD FOR PEAK ACCELERATION AND SPECTRAL ACCELERATIONS OF 0.2 AND 1 SEC, TA-46	Figure 9-65
Woodward-Clyde Federal Services			

46ATTENN.GRF

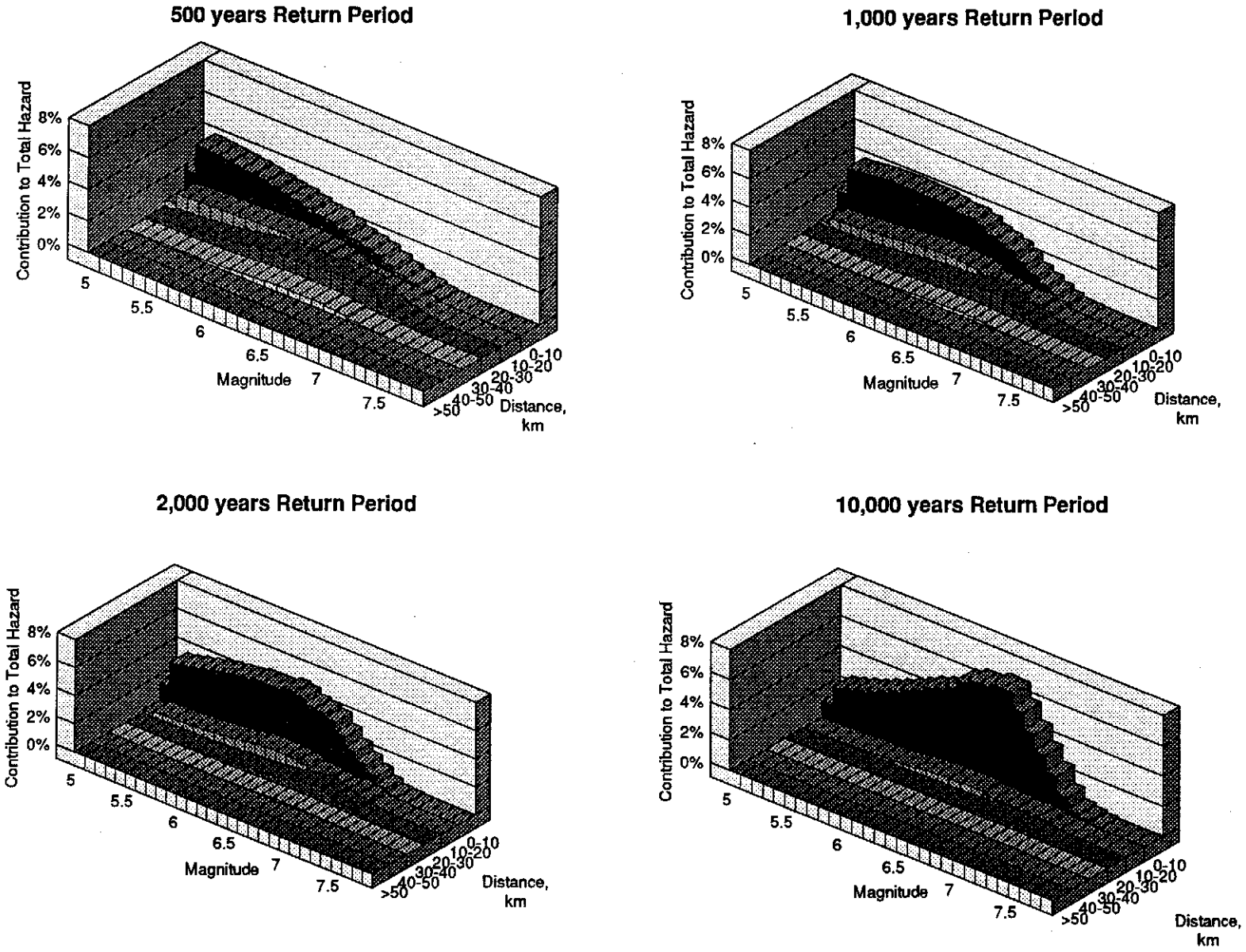




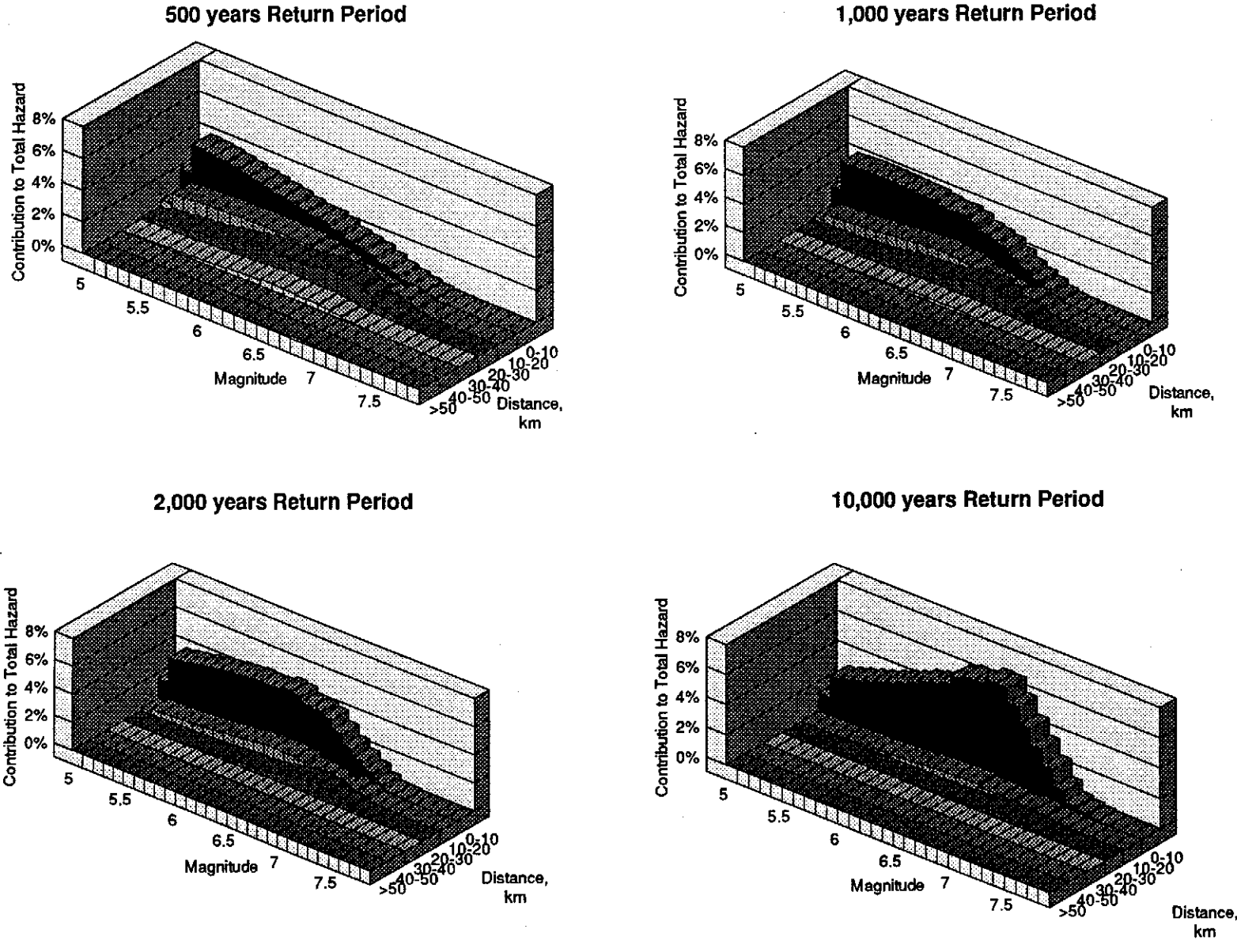




Project No. 91C0509	Los Alamos Seismic Hazards	EFFECT OF ATTENUATION RELATIONSHIPS ON MEAN SEISMIC HAZARD FOR PEAK ACCELERATION AND SPECTRAL ACCELERATIONS OF 0.2 AND 1 SEC, TA-55	Figure 9-66
Woodward-Clyde Federal Services			

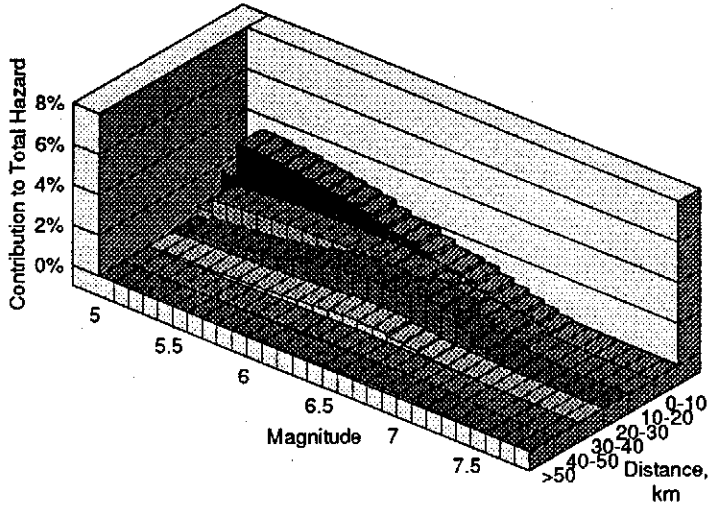


Project No. 91C0509	Los Alamos Seismic Hazards	MAGNITUDE AND DISTANCE CONTRIBUTIONS TO MEAN SEISMIC HAZARD FOR PEAK ACCELERATION, TA-2	Figure 9-67
WOODWARD-CLYDE FEDERAL SERVICES			

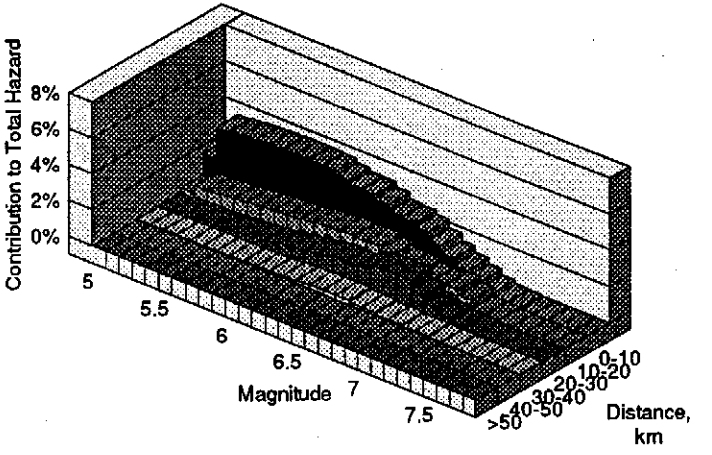


Project No. 91C0509	Los Alamos Seismic Hazards	MAGNITUDE AND DISTANCE CONTRIBUTIONS TO MEAN SEISMIC HAZARD FOR PEAK ACCELERATION, TA-3	Figure 9-68
WOODWARD-CLYDE FEDERAL SERVICES			

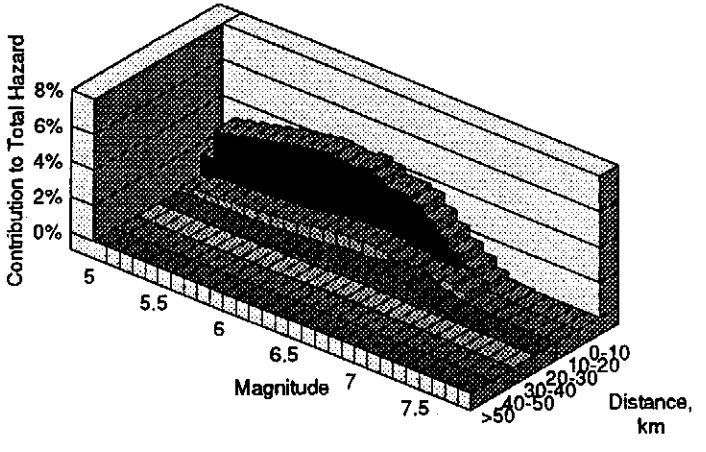
500 years Return Period



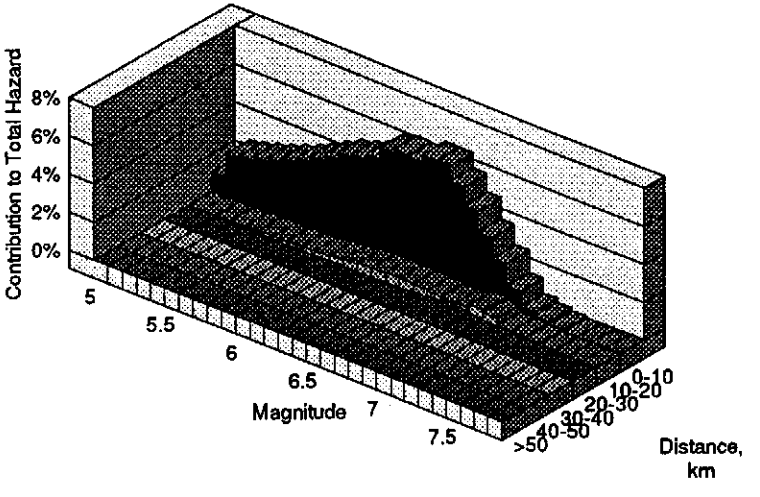
1,000 years Return Period



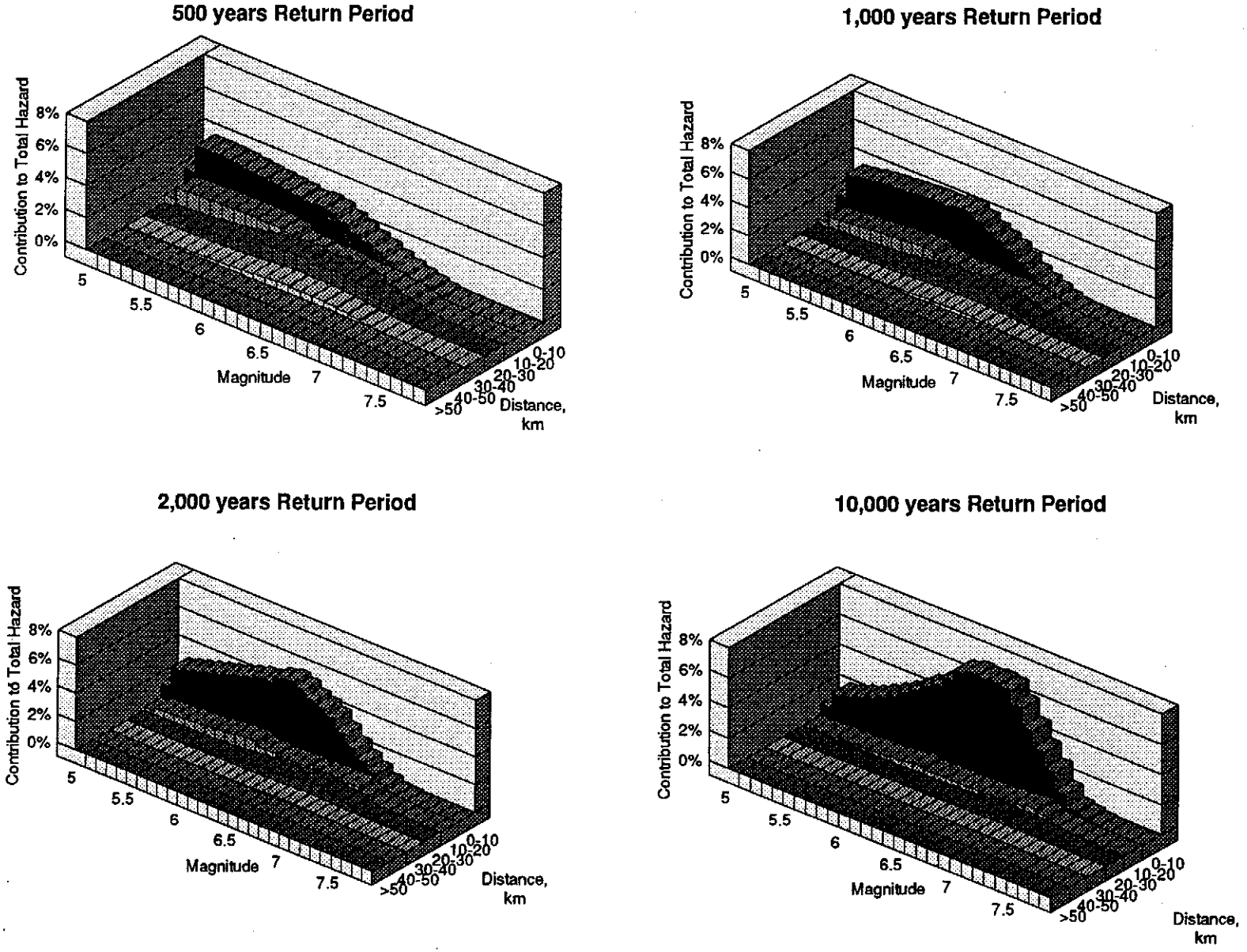
2,000 years Return Period



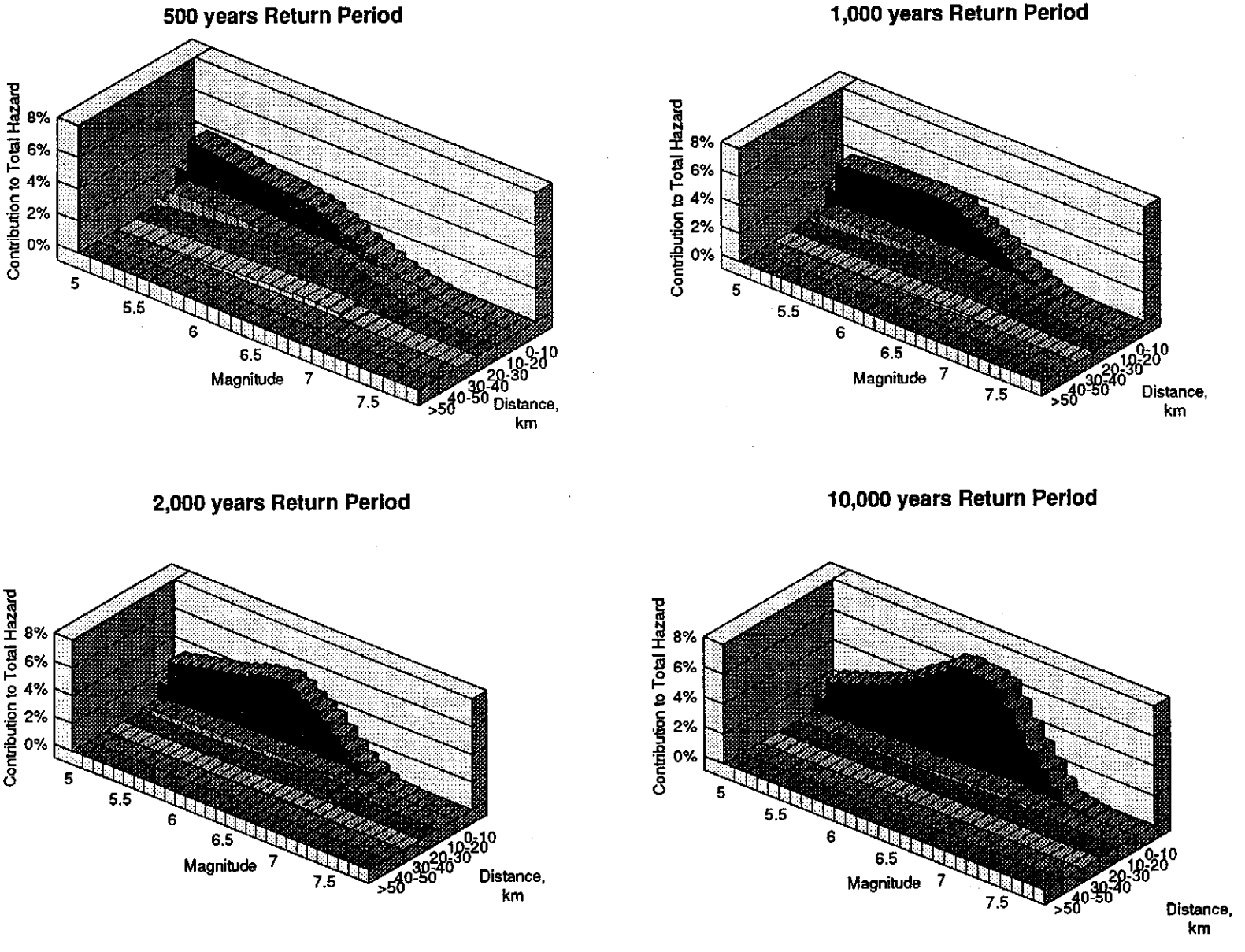
10,000 years Return Period



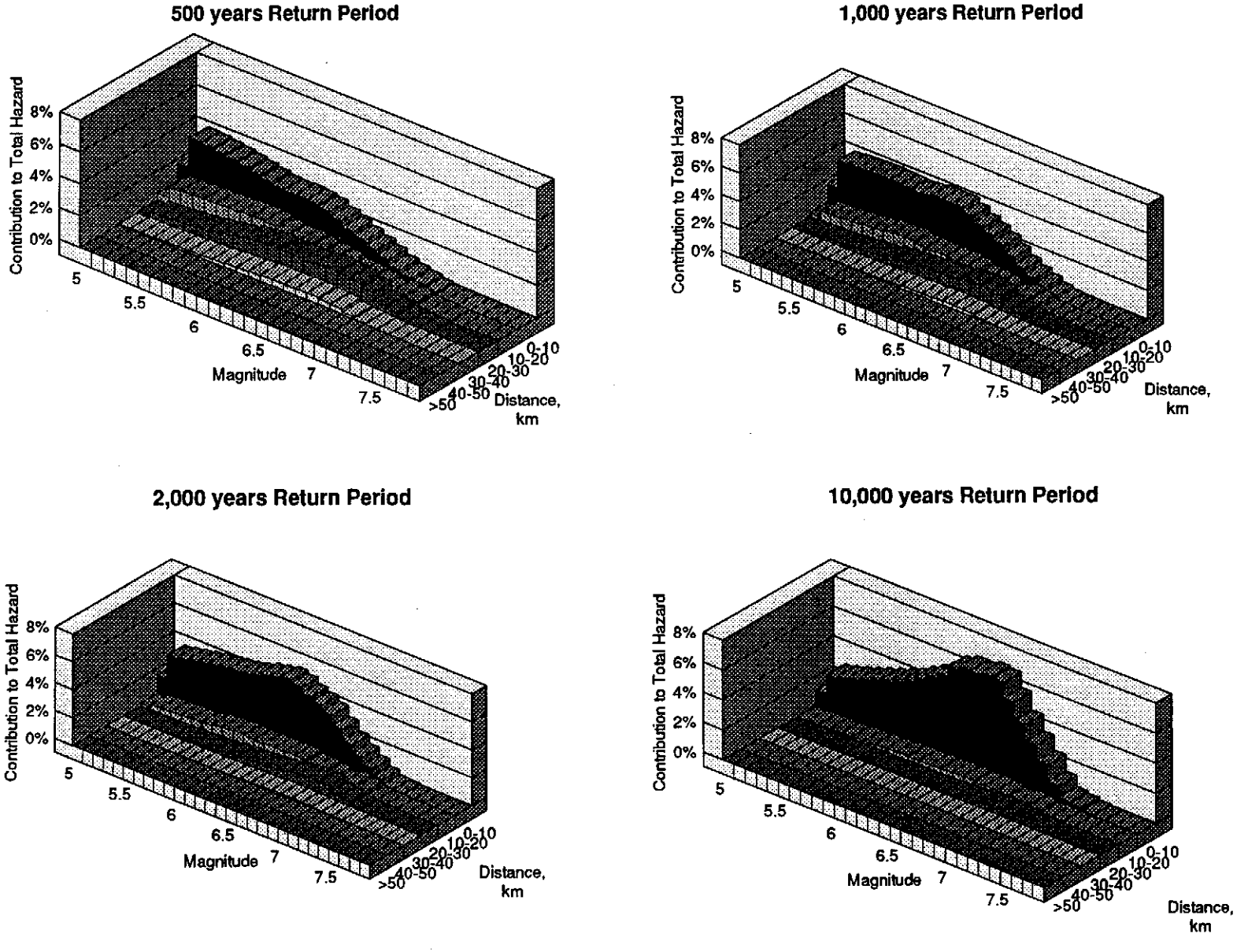
Project No. 91C0509	Los Alamos Seismic Hazards	MAGNITUDE AND DISTANCE CONTRIBUTIONS TO MEAN SEISMIC HAZARD FOR PEAK ACCELERATION, TA-16	Figure 9-69
WOODWARD-CLYDE FEDERAL SERVICES			



Project No. 91C0509	Los Alamos Seismic Hazards	MAGNITUDE AND DISTANCE CONTRIBUTIONS TO MEAN SEISMIC HAZARD FOR PEAK ACCELERATION, TA-18	Figure 9-70
WOODWARD-CLYDE FEDERAL SERVICES			

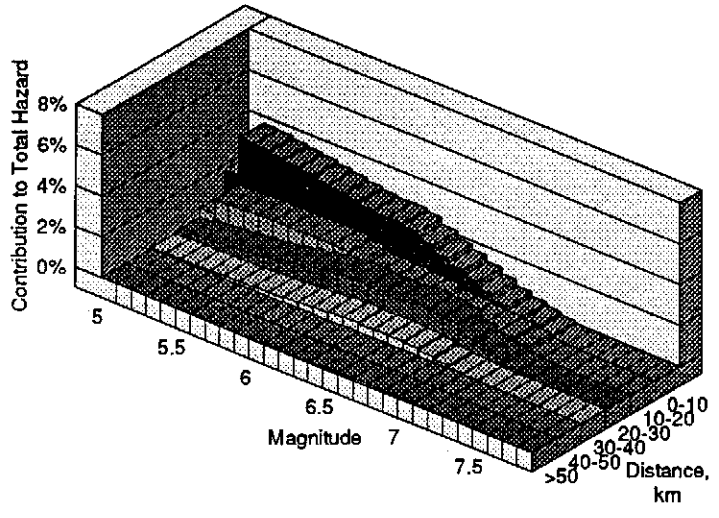


Project No. 91C0509	Los Alamos Seismic Hazards	MAGNITUDE AND DISTANCE CONTRIBUTIONS TO MEAN SEISMIC HAZARD FOR PEAK ACCELERATION, TA-21	Figure 9-71
WOODWARD-CLYDE FEDERAL SERVICES			

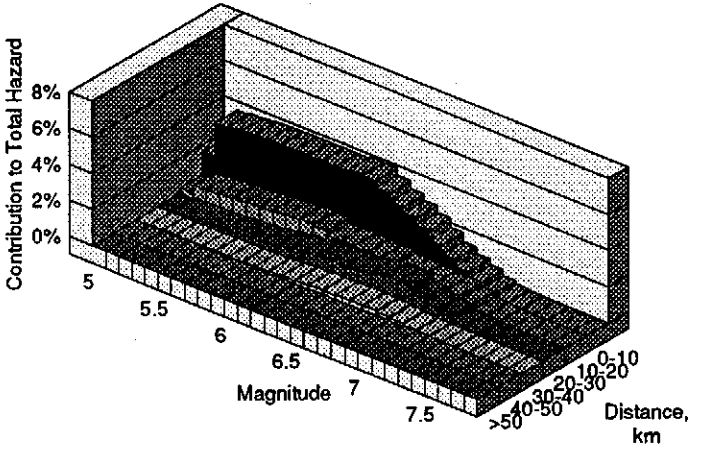


Project No. 91C0509	Los Alamos Seismic Hazards	MAGNITUDE AND DISTANCE CONTRIBUTIONS TO MEAN SEISMIC HAZARD FOR PEAK ACCELERATION, TA-41	Figure 9-72
WOODWARD-CLYDE FEDERAL SERVICES			

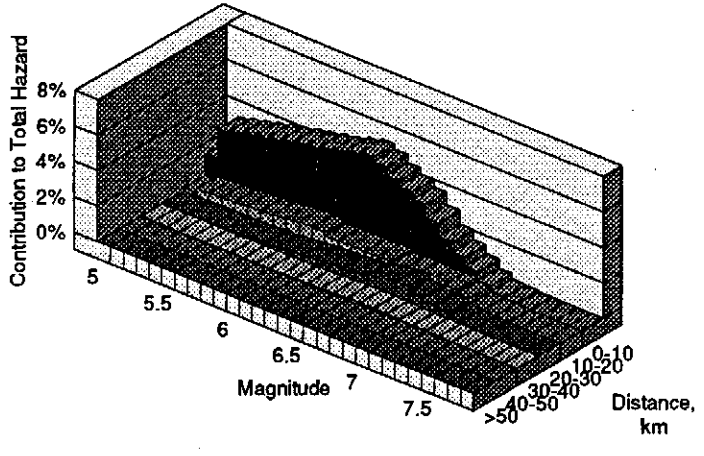
500 years Return Period



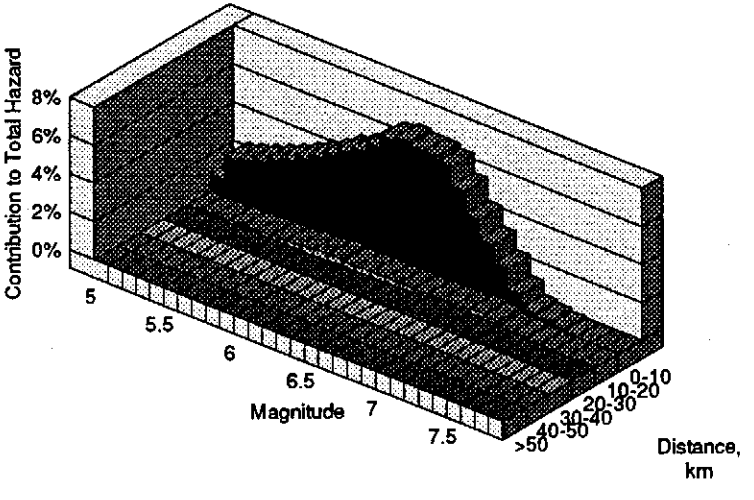
1,000 years Return Period



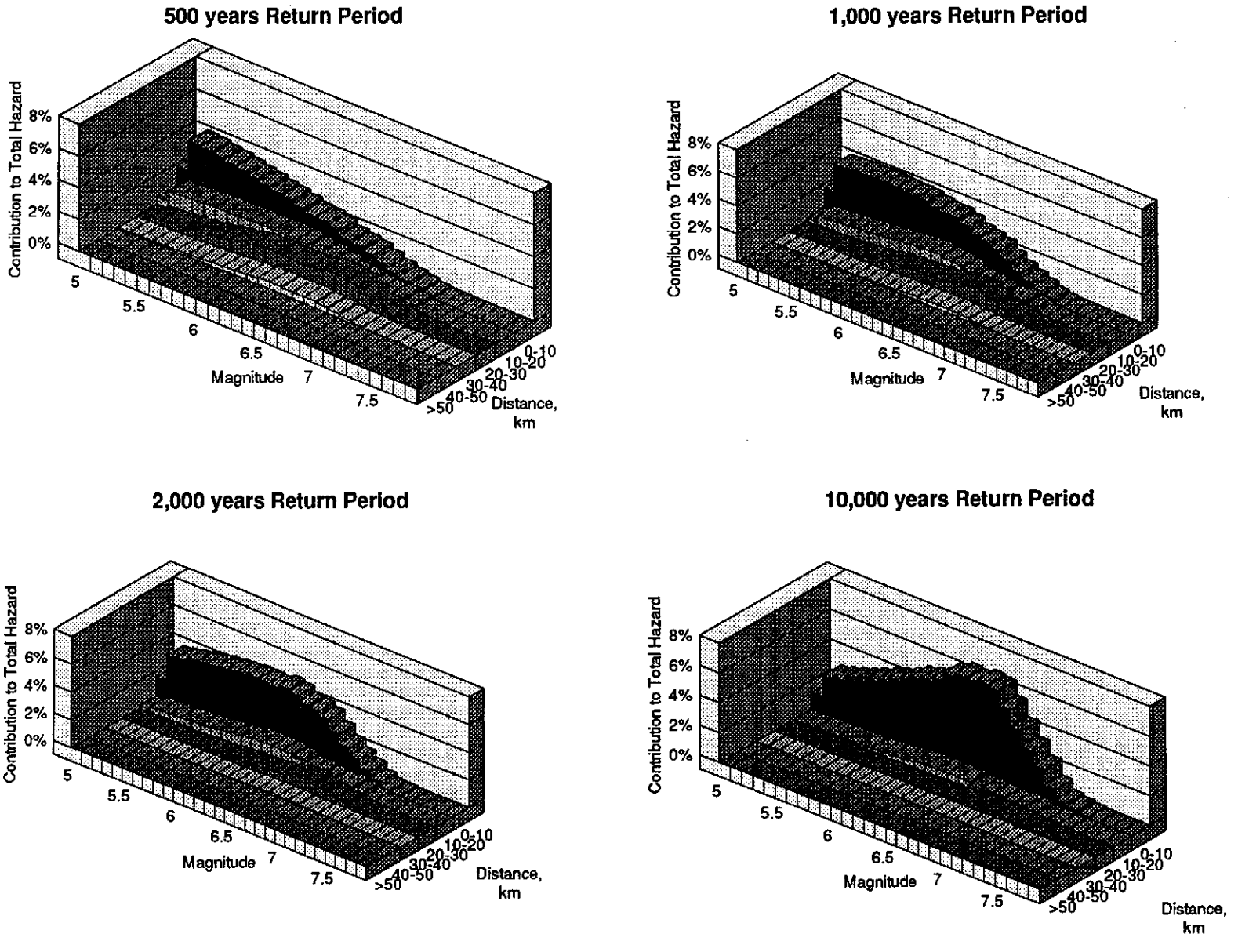
2,000 years Return Period



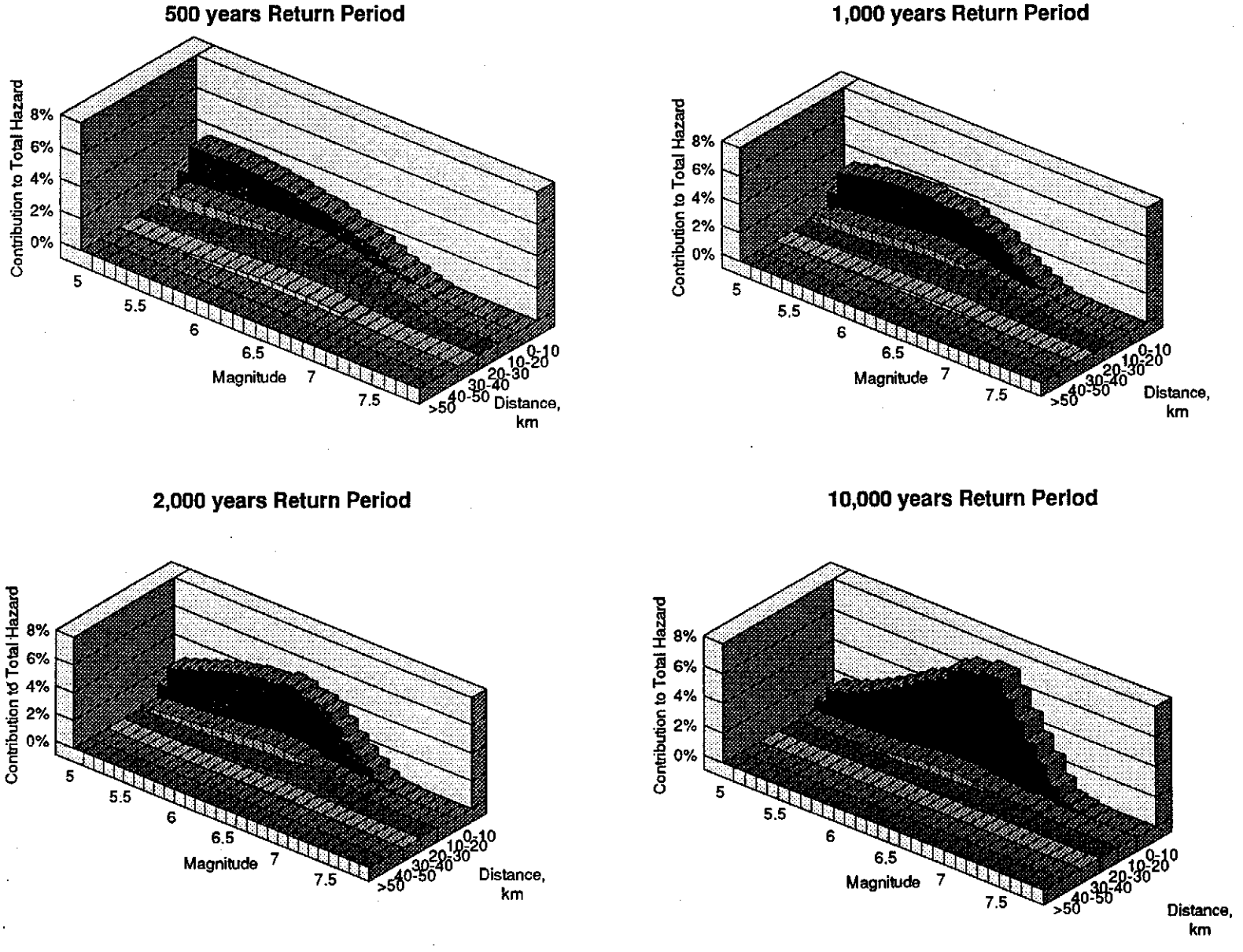
10,000 years Return Period



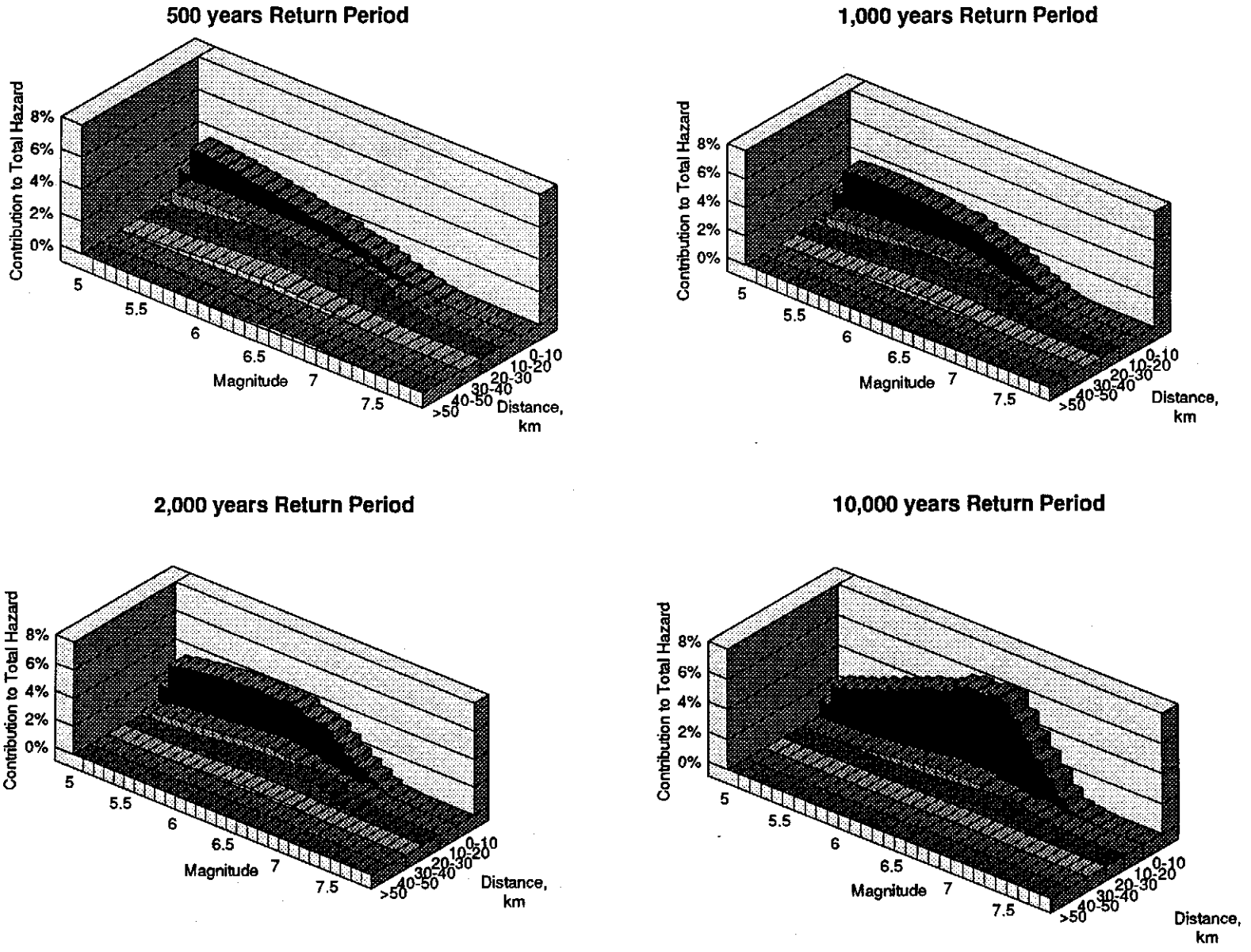
Project No. 91C0509	Los Alamos Seismic Hazards	MAGNITUDE AND DISTANCE CONTRIBUTIONS TO MEAN SEISMIC HAZARD FOR PEAK ACCELERATION, TA-46	Figure 9-73
WOODWARD-CLYDE FEDERAL SERVICES			



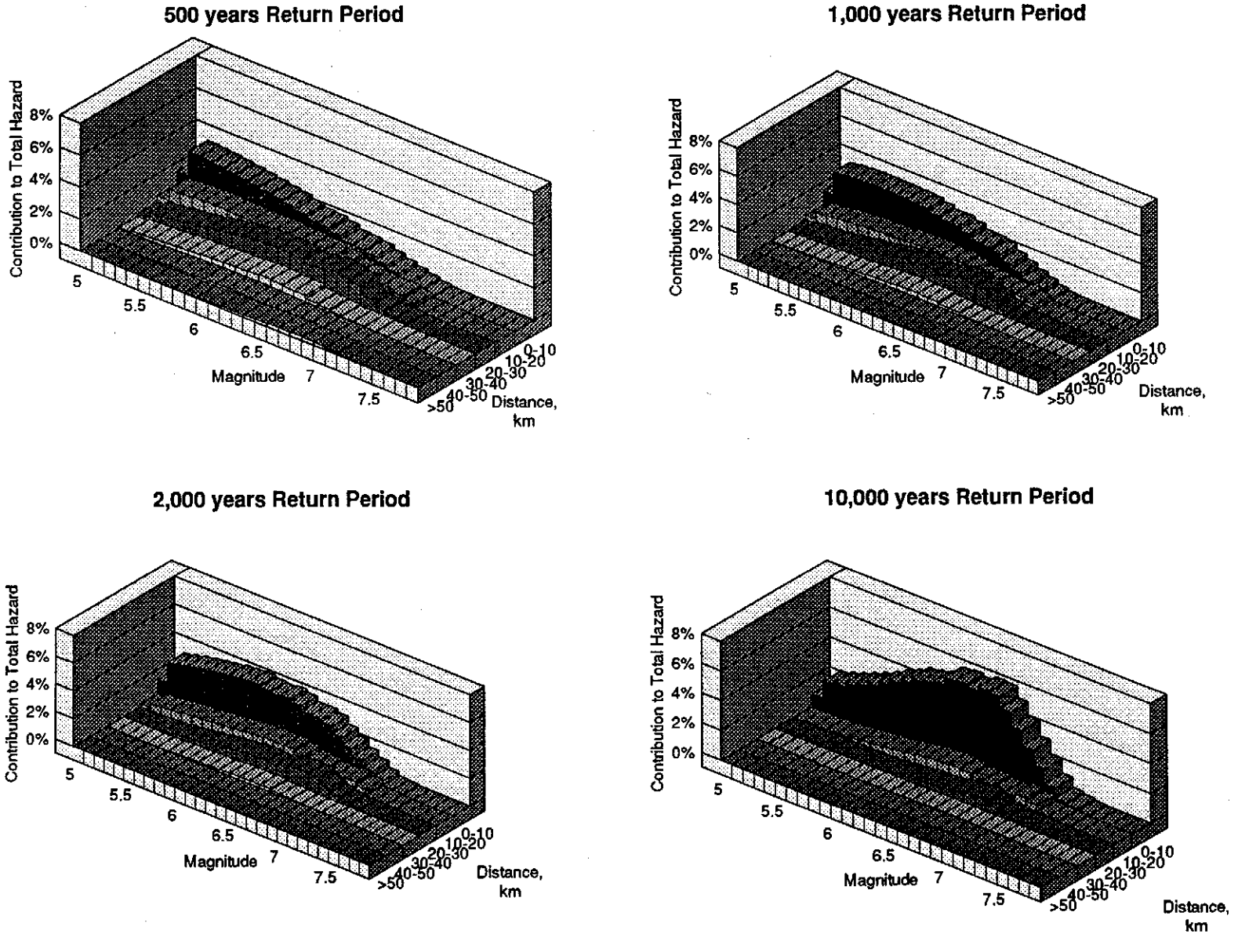
Project No. 91C0509	Los Alamos Seismic Hazards	MAGNITUDE AND DISTANCE CONTRIBUTIONS TO MEAN SEISMIC HAZARD FOR PEAK ACCELERATION, TA-55	Figure 9-74
WOODWARD-CLYDE FEDERAL SERVICES			



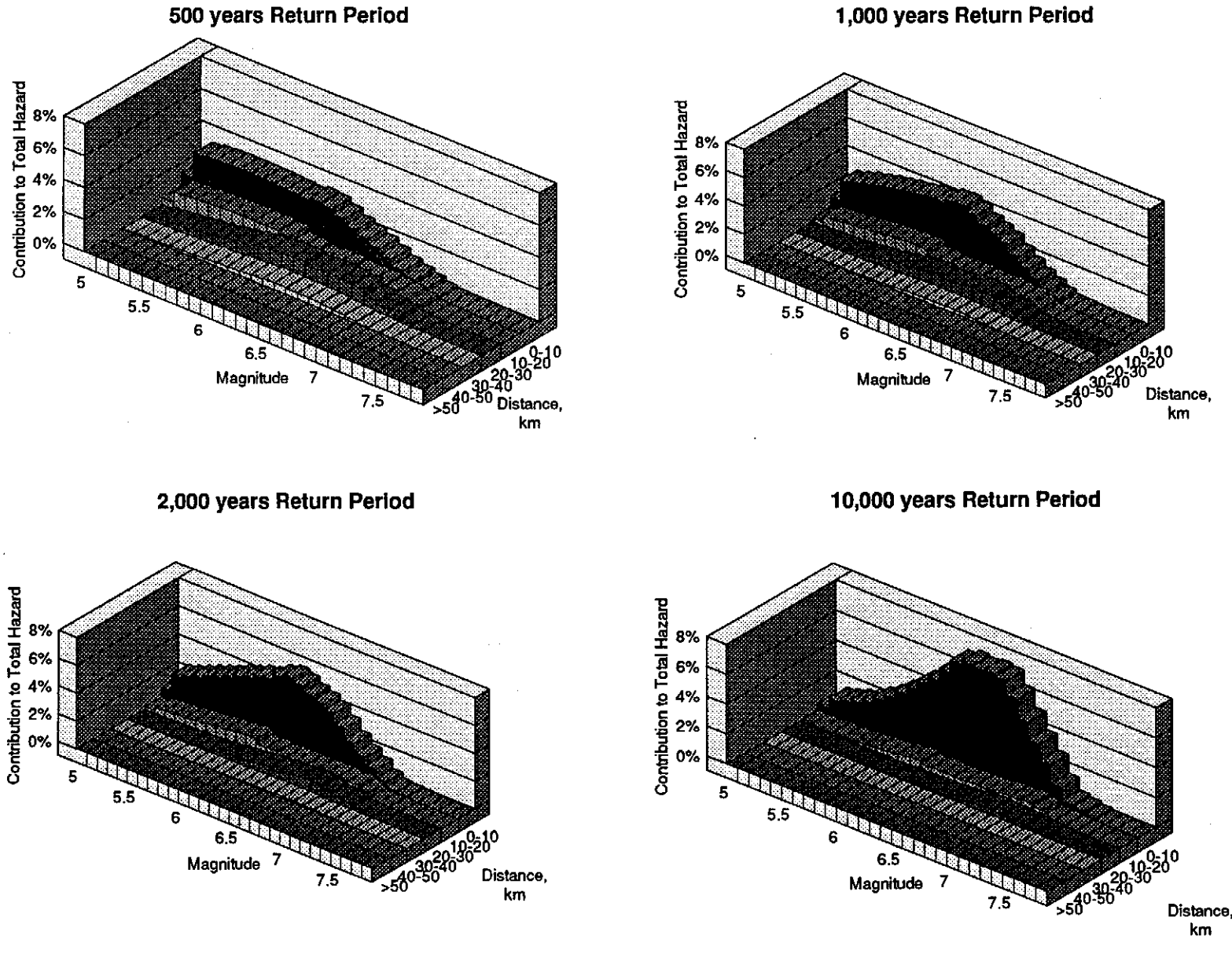
Project No. 91C0509	Los Alamos Seismic Hazards	MAGNITUDE AND DISTANCE CONTRIBUTIONS TO MEAN SEISMIC HAZARD FOR 0.2 SEC HORIZONTAL SPECTRAL ACCELERATION, TA-2	Figure 9-75
WOODWARD-CLYDE FEDERAL SERVICES			



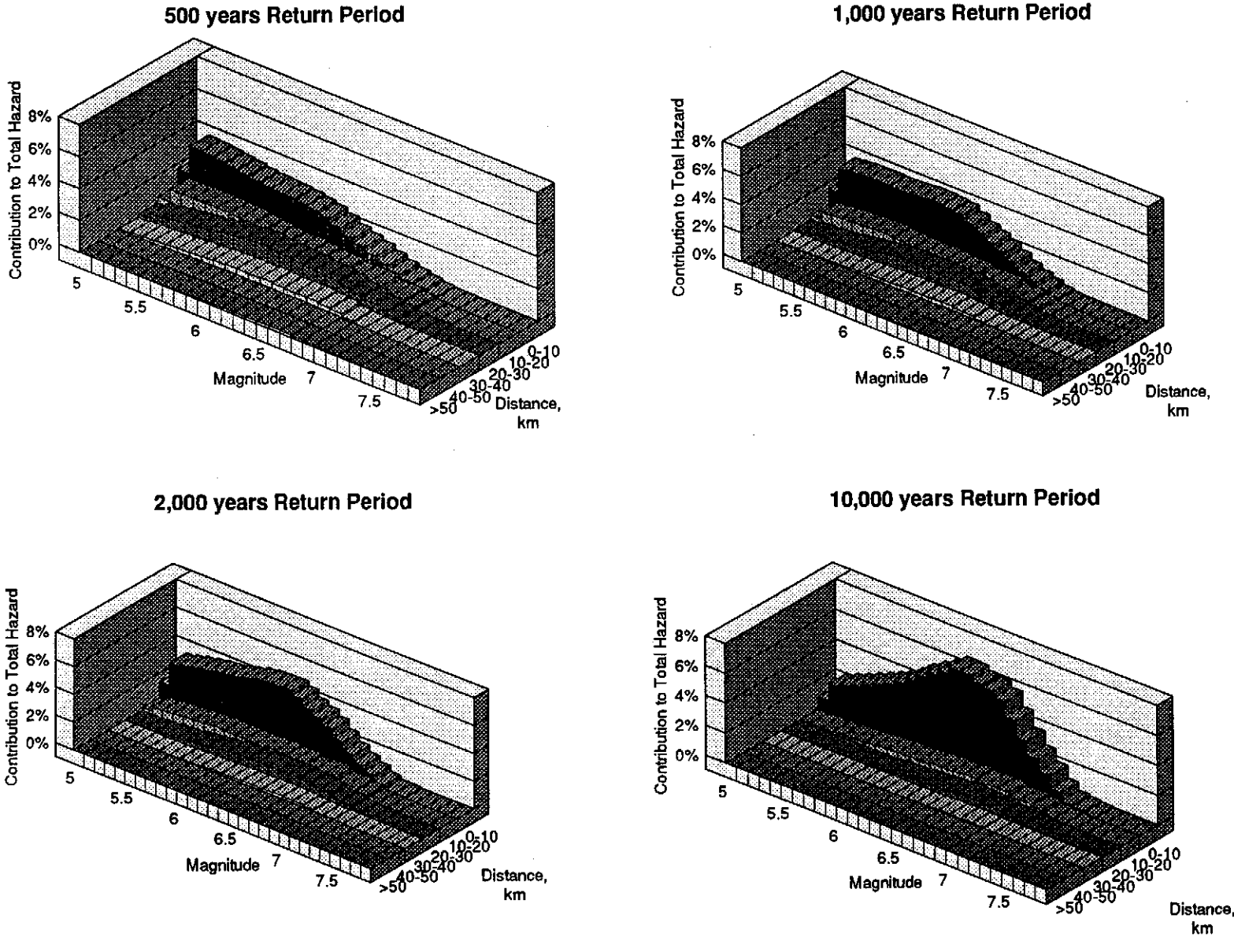
Project No. 91C0509	Los Alamos Seismic Hazards	MAGNITUDE AND DISTANCE CONTRIBUTIONS TO MEAN SEISMIC HAZARD FOR 0.2 SEC HORIZONTAL SPECTRAL ACCELERATION, TA-3	Figure 9-76
WOODWARD-CLYDE FEDERAL SERVICES			



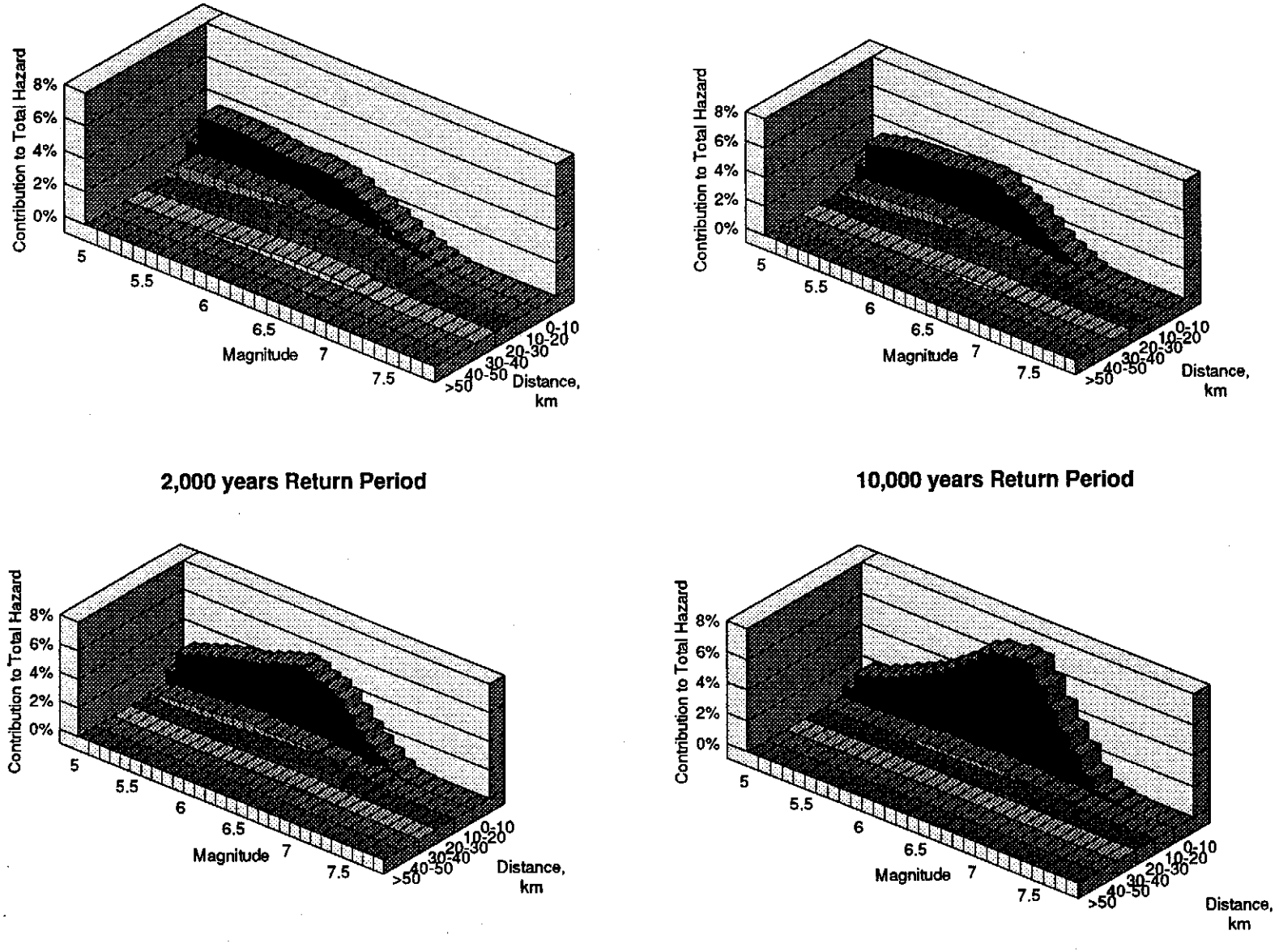
Project No. 91C0509	Los Alamos Seismic Hazards	MAGNITUDE AND DISTANCE CONTRIBUTIONS TO MEAN SEISMIC HAZARD FOR 0.2 SEC HORIZONTAL SPECTRAL ACCELERATION, TA-16	Figure 9-77
WOODWARD-CLYDE FEDERAL SERVICES			



Project No. 91C0509	Los Alamos Seismic Hazards	MAGNITUDE AND DISTANCE CONTRIBUTIONS TO MEAN SEISMIC HAZARD FOR 0.2 SEC HORIZONTAL SPECTRAL ACCELERATION, TA-18	Figure 9-78
WOODWARD-CLYDE FEDERAL SERVICES			

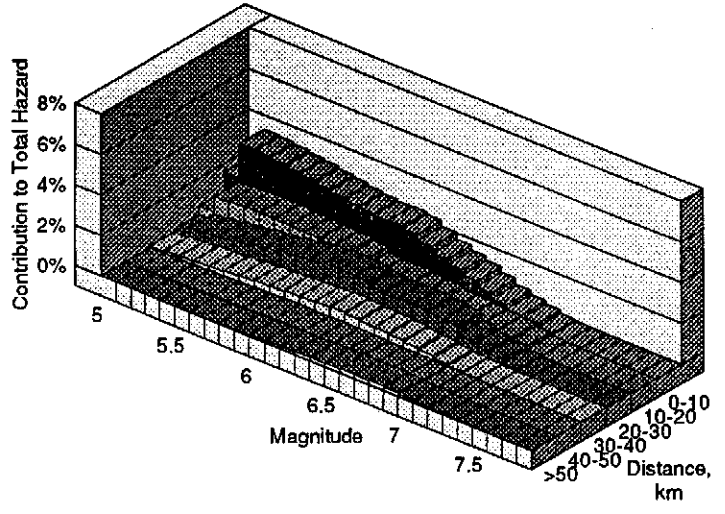


Project No. 91C0509	Los Alamos Seismic Hazards	MAGNITUDE AND DISTANCE CONTRIBUTIONS TO MEAN SEISMIC HAZARD FOR 0.2 SEC HORIZONTAL SPECTRAL ACCELERATION, TA-21
WOODWARD-CLYDE FEDERAL SERVICES		Figure 9-79

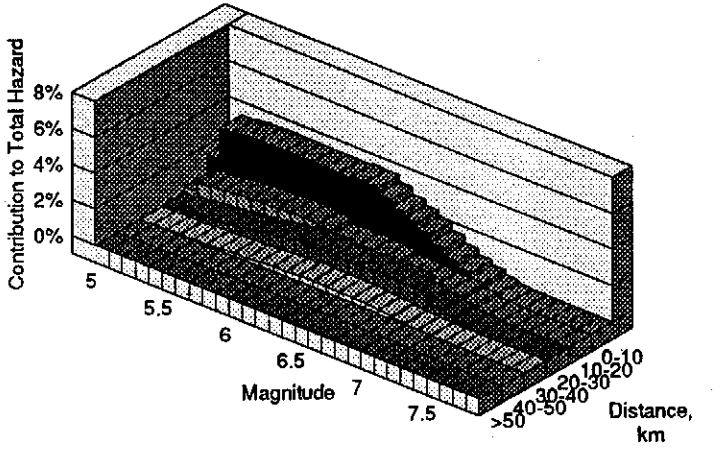


Project No. 91C0509	Los Alamos Seismic Hazards	MAGNITUDE AND DISTANCE CONTRIBUTIONS TO MEAN SEISMIC HAZARD FOR 0.2 SEC HORIZONTAL SPECTRAL ACCELERATION, TA-41	Figure 9-80
WOODWARD-CLYDE FEDERAL SERVICES			

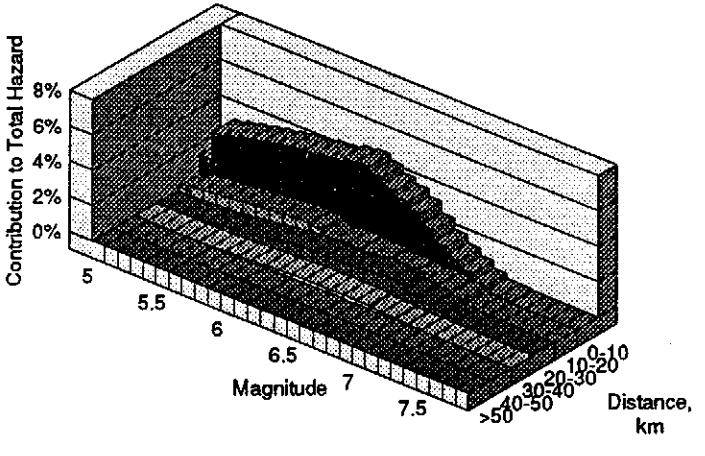
500 years Return Period



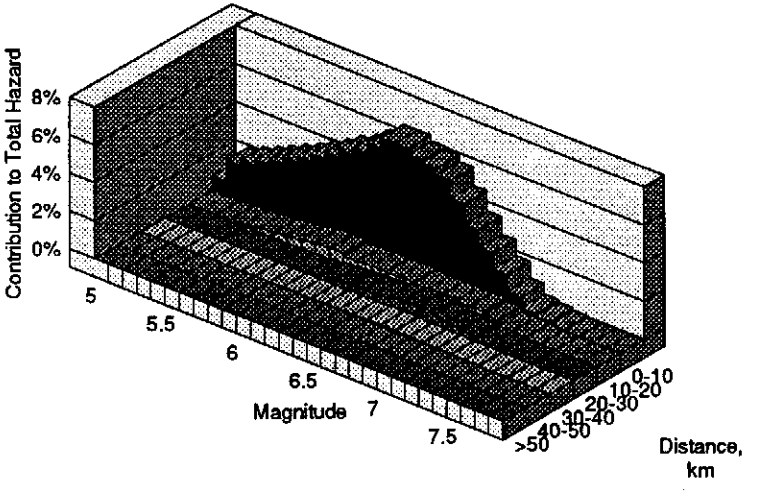
1,000 years Return Period



2,000 years Return Period

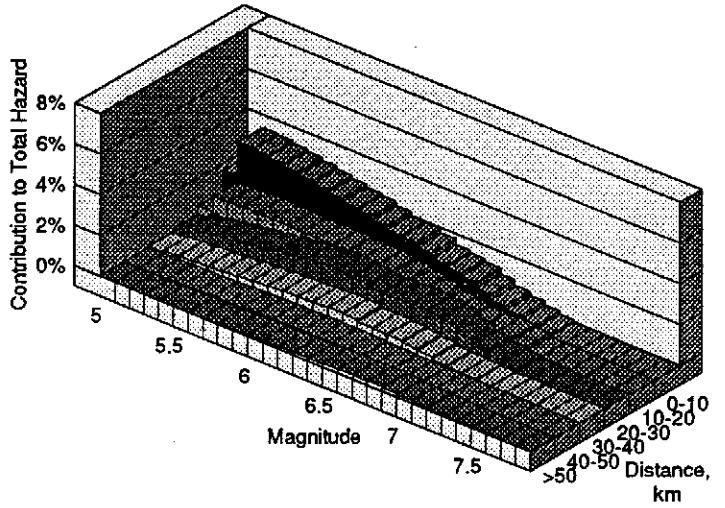


10,000 years Return Period

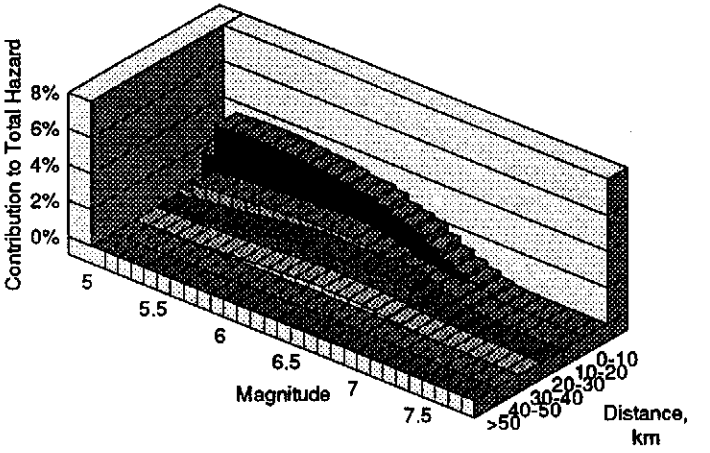


Project No. 91C0509	Los Alamos Seismic Hazards	MAGNITUDE AND DISTANCE CONTRIBUTIONS TO MEAN SEISMIC HAZARD FOR 0.2 SEC HORIZONTAL SPECTRAL ACCELERATION, TA-46	Figure 9-81
WOODWARD-CLYDE FEDERAL SERVICES			

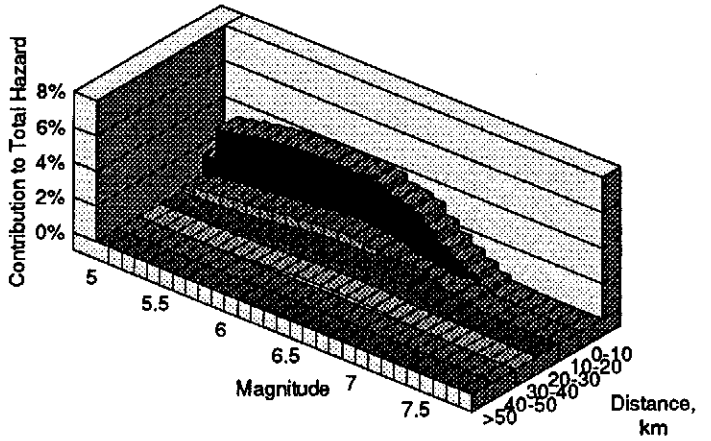
500 years Return Period



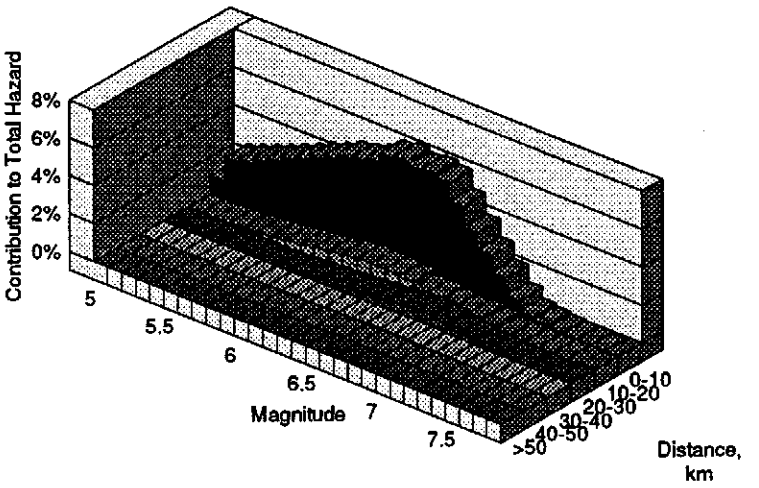
1,000 years Return Period



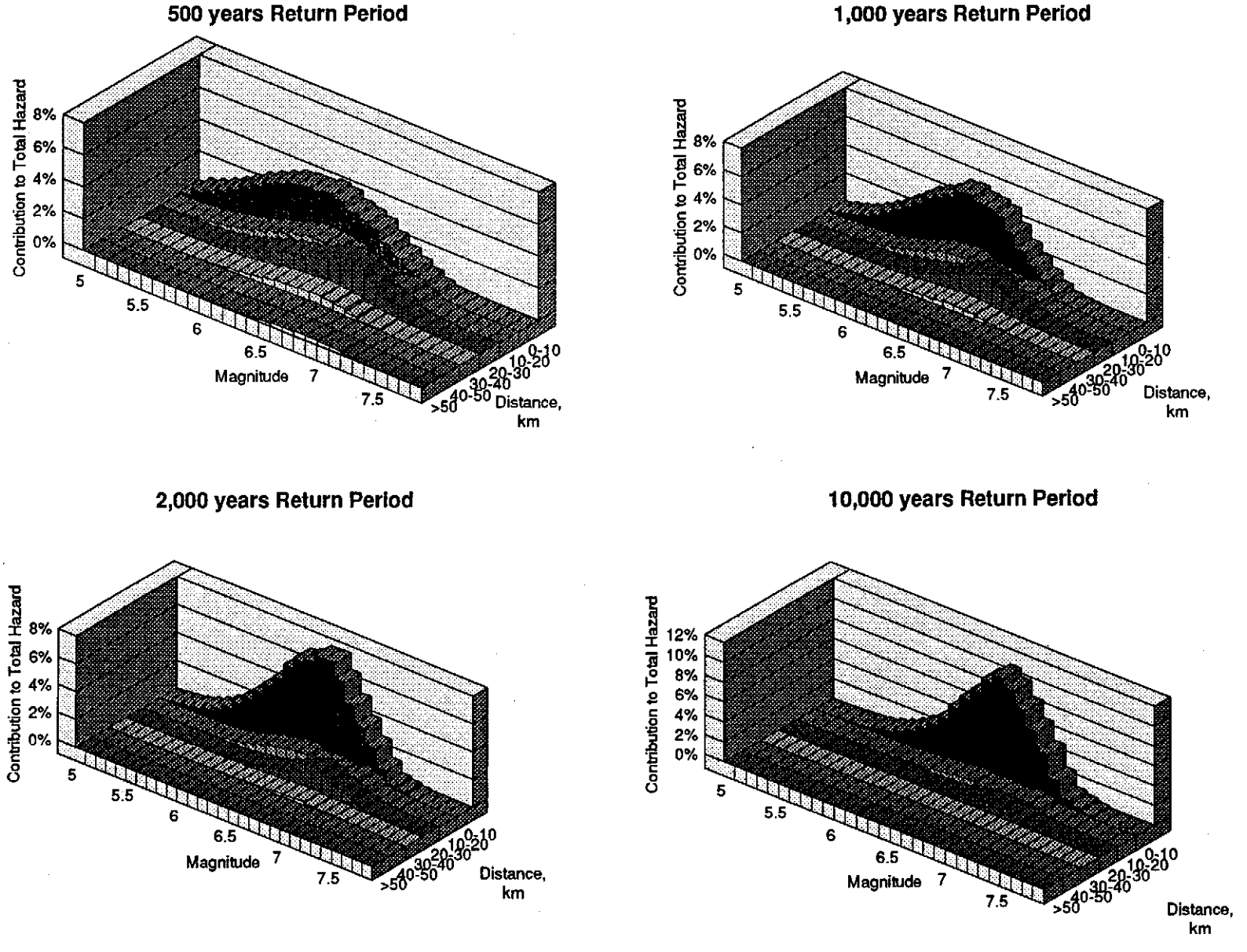
2,000 years Return Period



10,000 years Return Period

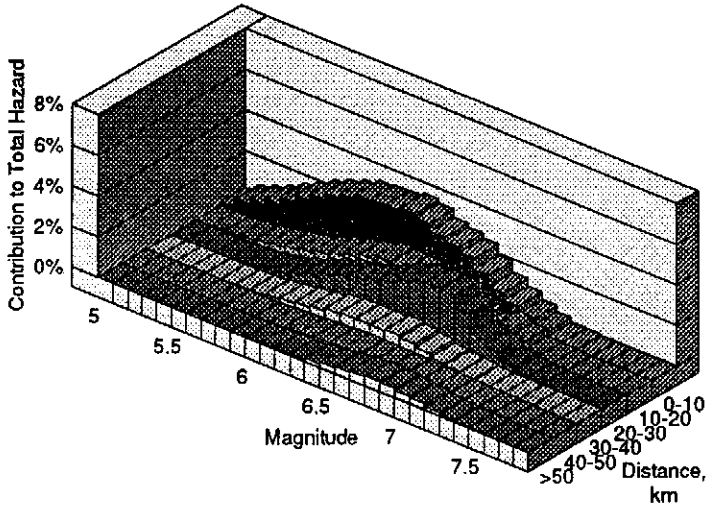


Project No. 91C0509	Los Alamos Seismic Hazards	MAGNITUDE AND DISTANCE CONTRIBUTIONS TO MEAN SEISMIC HAZARD FOR 0.2 SEC HORIZONTAL SPECTRAL ACCELERATION, TA-55	Figure 9-82
WOODWARD-CLYDE FEDERAL SERVICES			

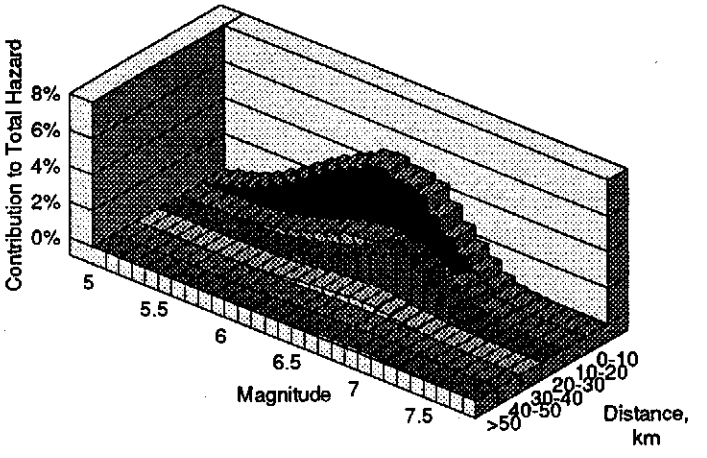


Project No. 91C0509	Los Alamos Seismic Hazards	MAGNITUDE AND DISTANCE CONTRIBUTIONS TO MEAN SEISMIC HAZARD FOR 1.0 SEC HORIZONTAL SPECTRAL ACCELERATION, TA-2	Figure 9-83
WOODWARD-CLYDE FEDERAL SERVICES			

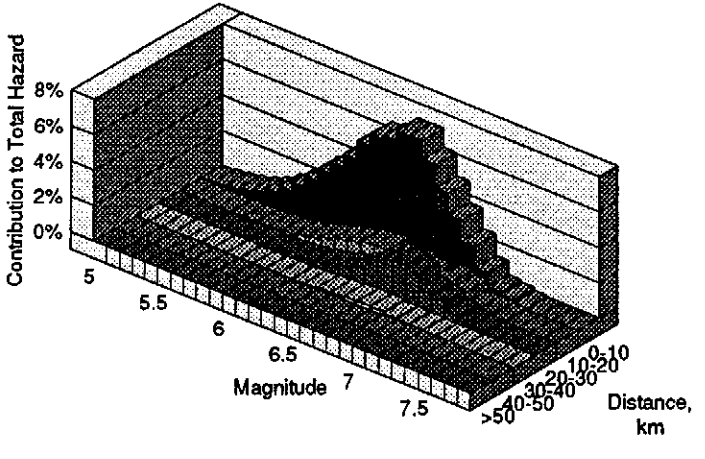
500 years Return Period



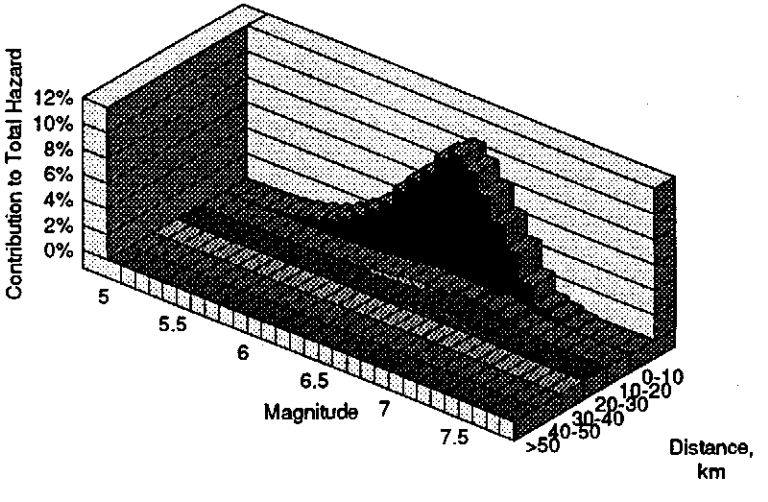
1,000 years Return Period



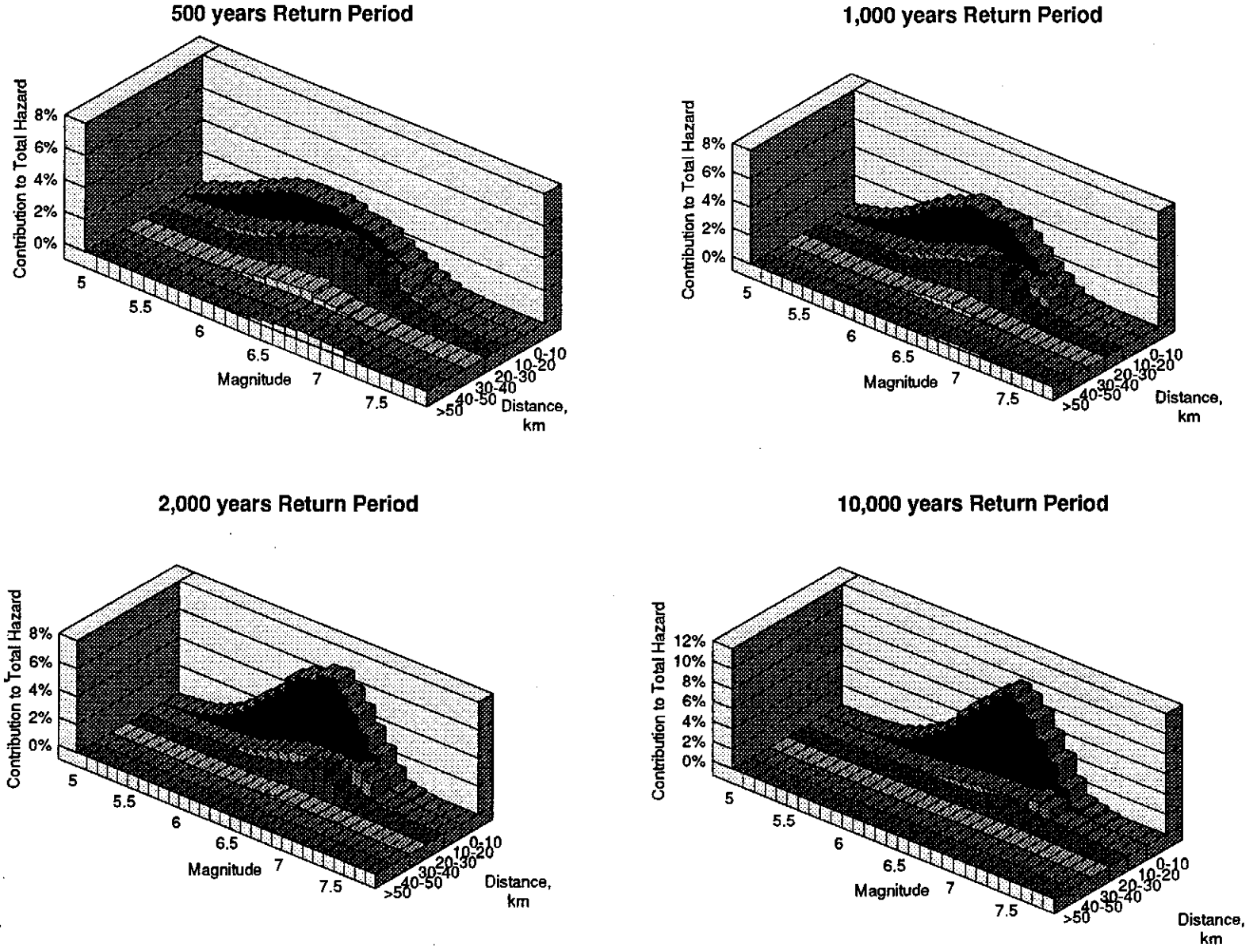
2,000 years Return Period



10,000 years Return Period

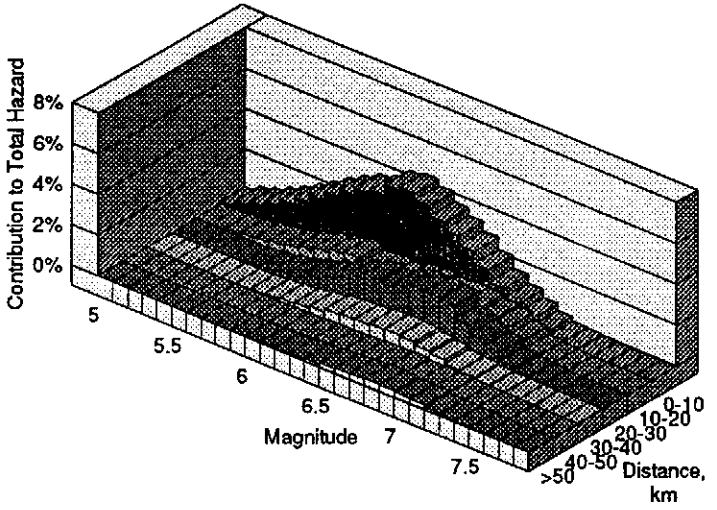


Project No. 91C0509	Los Alamos Seismic Hazards	MAGNITUDE AND DISTANCE CONTRIBUTIONS TO MEAN SEISMIC HAZARD FOR 1.0 SEC HORIZONTAL SPECTRAL ACCELERATION, TA-3	Figure 9-84
WOODWARD-CLYDE FEDERAL SERVICES			

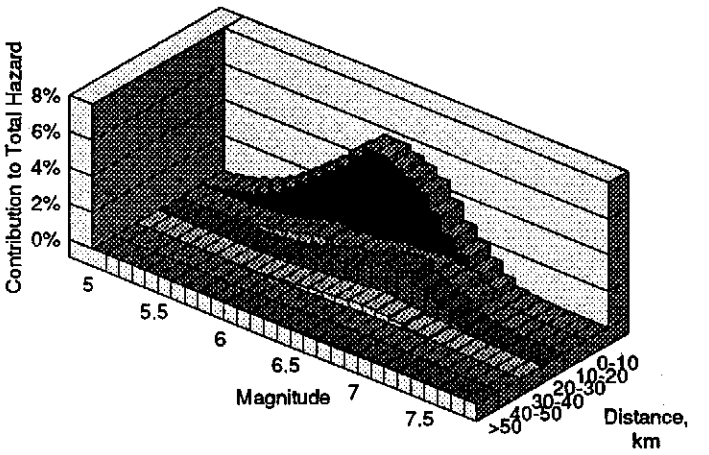


Project No. 91C0509	Los Alamos Seismic Hazards	MAGNITUDE AND DISTANCE CONTRIBUTIONS TO MEAN SEISMIC HAZARD FOR 1.0 SEC HORIZONTAL SPECTRAL ACCELERATION, TA-16	Figure 9-85
WOODWARD-CLYDE FEDERAL SERVICES			

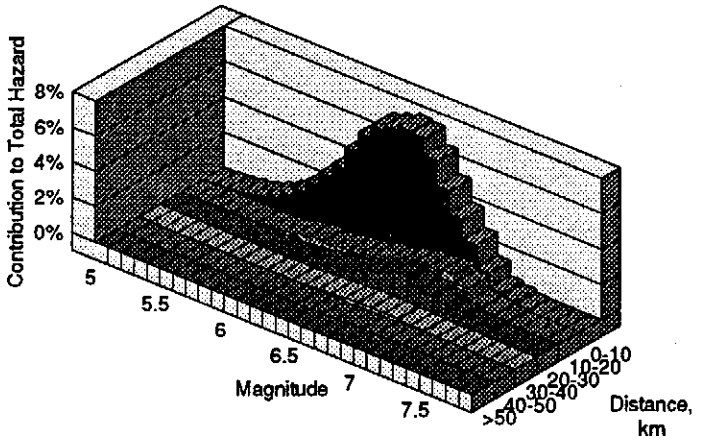
500 years Return Period



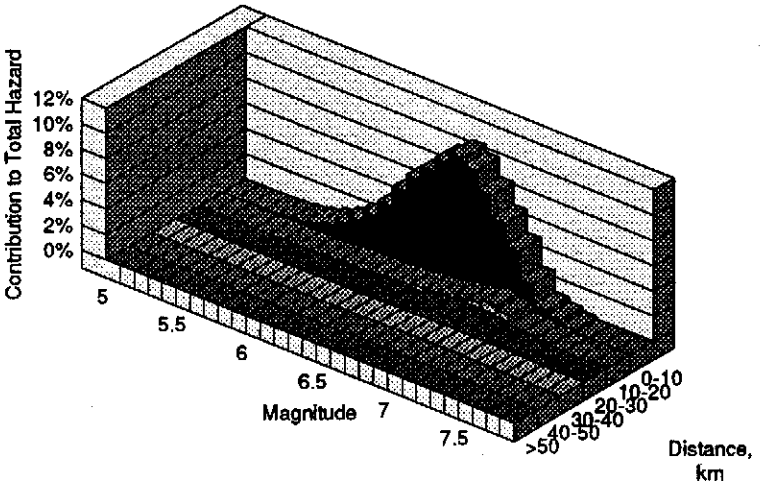
1,000 years Return Period



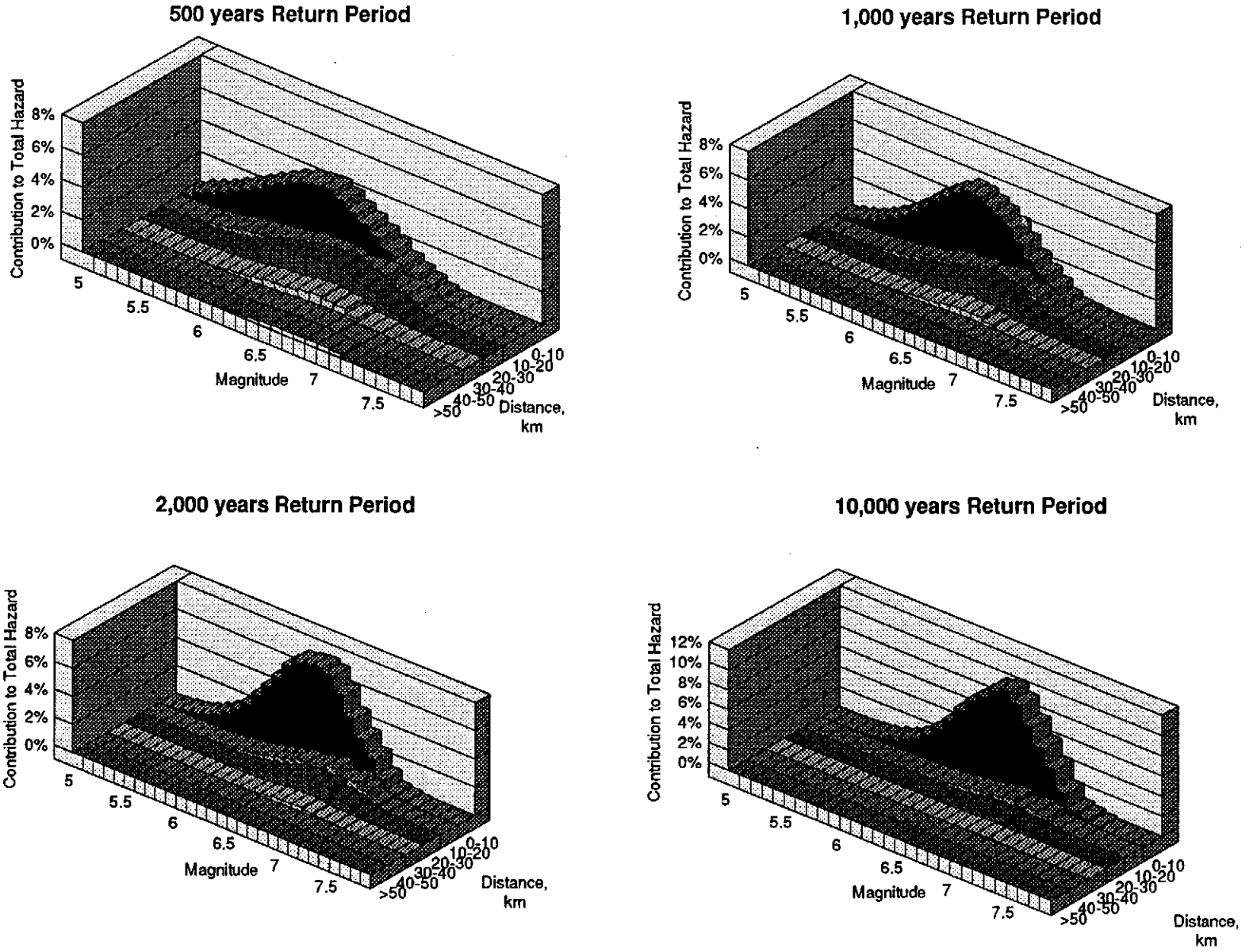
2,000 years Return Period



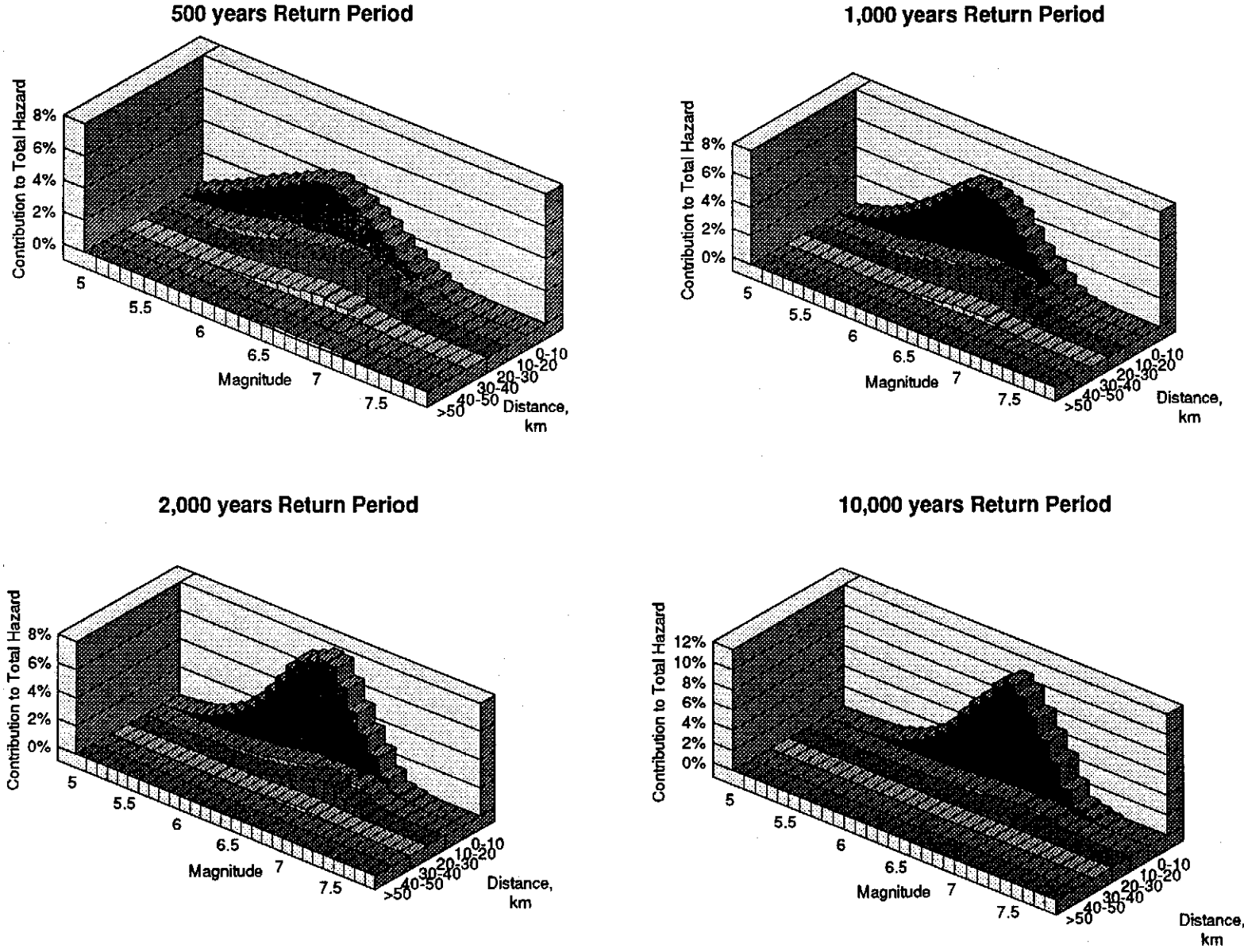
10,000 years Return Period



Project No. 91C0509	Los Alamos Seismic Hazards	MAGNITUDE AND DISTANCE CONTRIBUTIONS TO MEAN SEISMIC HAZARD FOR 1.0 SEC HORIZONTAL SPECTRAL ACCELERATION, TA-18	Figure 9-86
WOODWARD-CLYDE FEDERAL SERVICES			

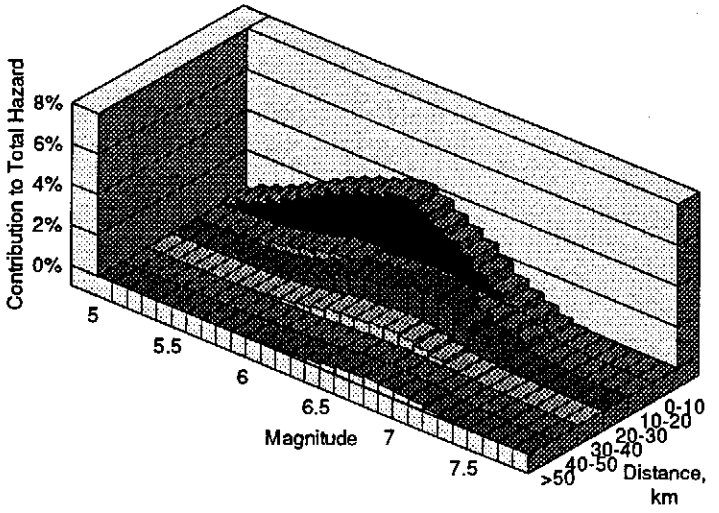


Project No. 91C0509	Los Alamos Seismic Hazards	MAGNITUDE AND DISTANCE CONTRIBUTIONS TO MEAN SEISMIC HAZARD FOR 1.0 SEC HORIZONTAL SPECTRAL ACCELERATION, TA-21	Figure 9-87
WOODWARD-CLYDE FEDERAL SERVICES			

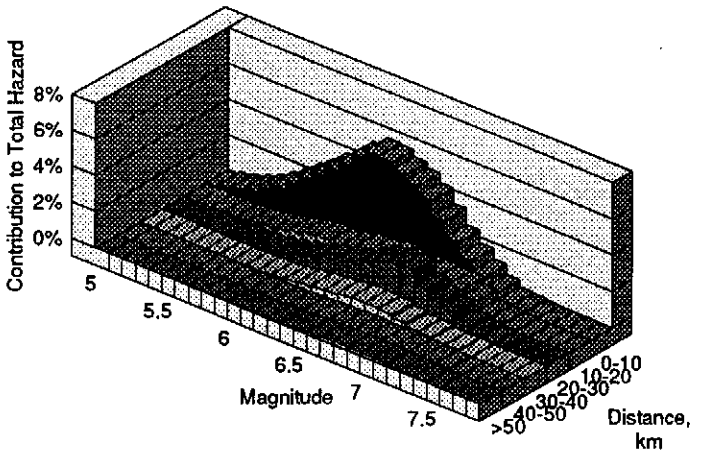


Project No. 91C0509	Los Alamos Seismic Hazards	MAGNITUDE AND DISTANCE CONTRIBUTIONS TO MEAN SEISMIC HAZARD FOR 1.0 SEC HORIZONTAL SPECTRAL ACCELERATION, TA-41	Figure 9-88
WOODWARD-CLYDE FEDERAL SERVICES			

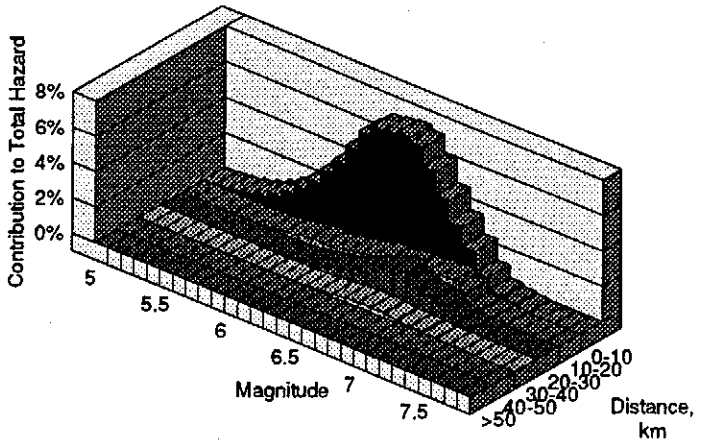
500 years Return Period



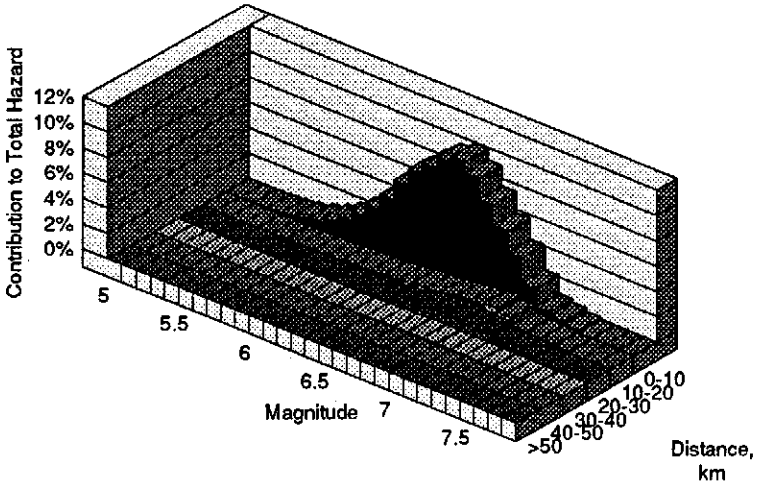
1,000 years Return Period



2,000 years Return Period

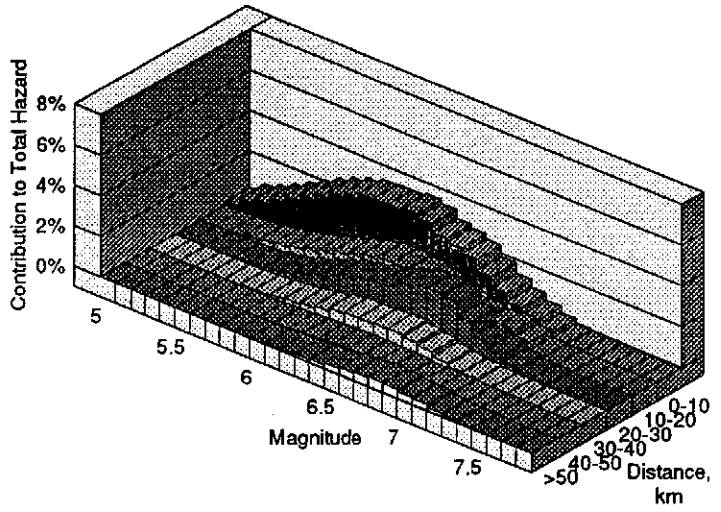


10,000 years Return Period

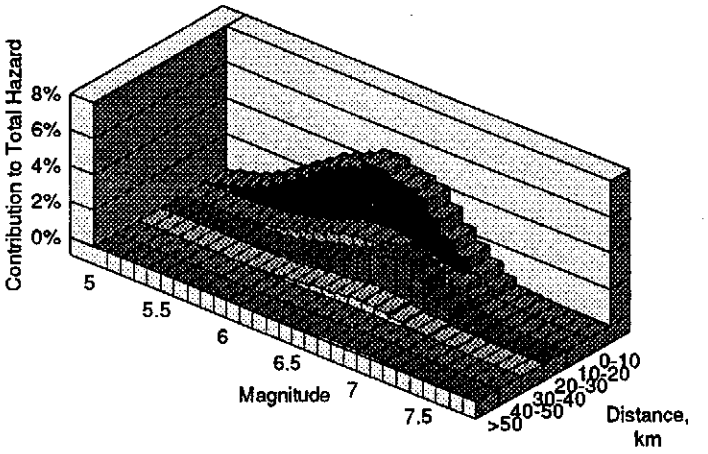


Project No. 91C0509	Los Alamos Seismic Hazards	MAGNITUDE AND DISTANCE CONTRIBUTIONS TO MEAN SEISMIC HAZARD FOR 1.0 SEC HORIZONTAL SPECTRAL ACCELERATION, TA-46	Figure 9-89
WOODWARD-CLYDE FEDERAL SERVICES			

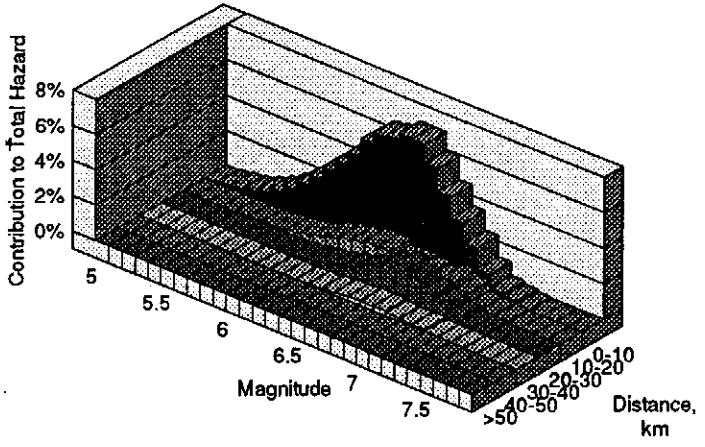
500 years Return Period



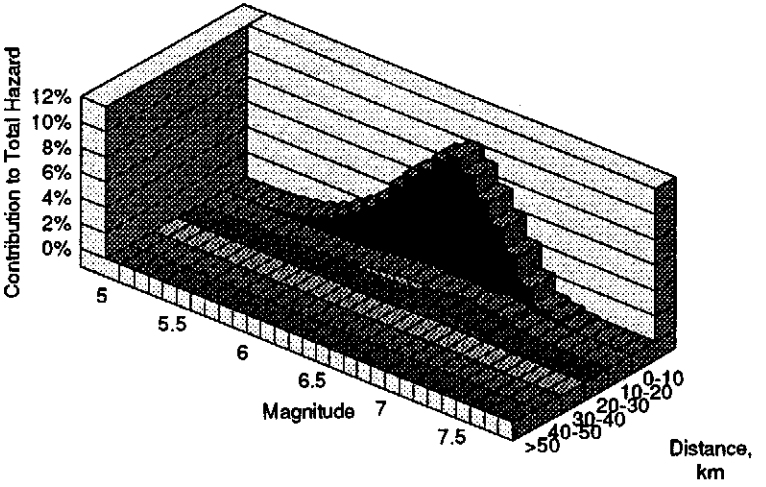
1,000 years Return Period



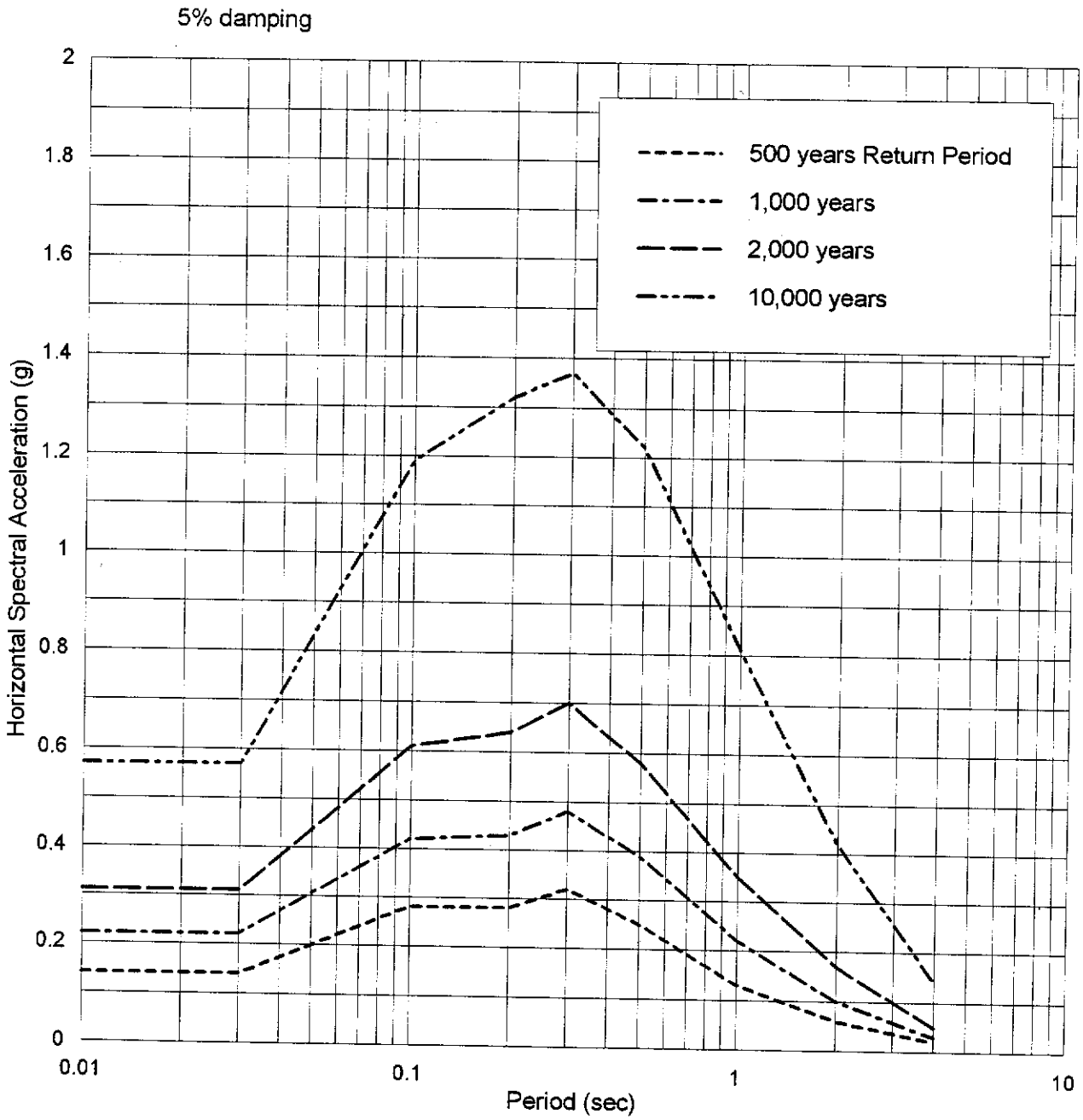
2,000 years Return Period



10,000 years Return Period

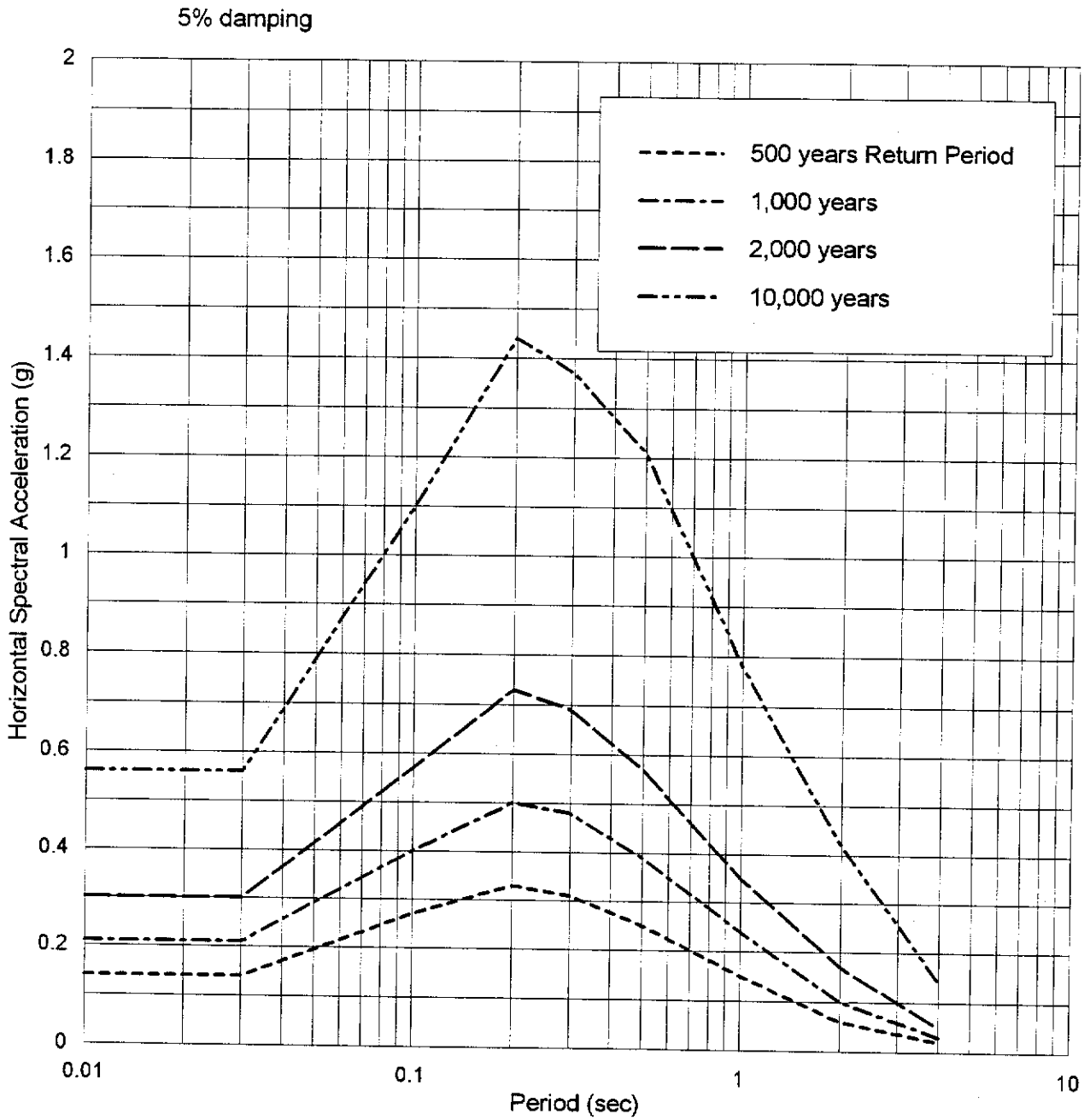


Project No. 91C0509	Los Alamos Seismic Hazards	MAGNITUDE AND DISTANCE CONTRIBUTIONS TO MEAN SEISMIC HAZARD FOR 1.0 SEC HORIZONTAL SPECTRAL ACCELERATION, TA-55	Figure 9-90
WOODWARD-CLYDE FEDERAL SERVICES			



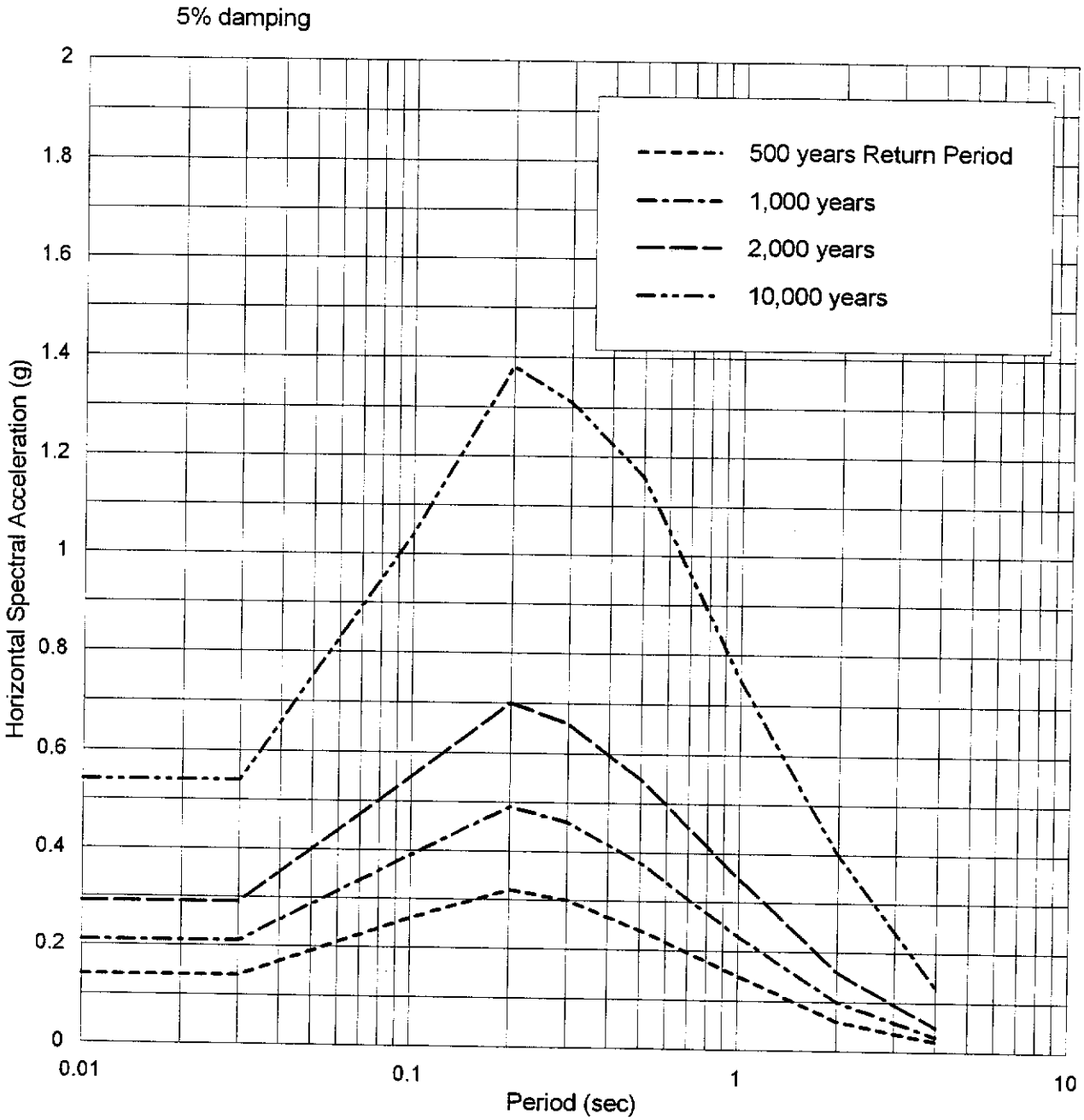
Project No. 91C0509	Los Alamos Seismic Hazards	MEAN EQUAL HAZARD SPECTRA AT TA-2	Figure 9-91
Woodward-Clyde Federal Services			

MEAN.GRF



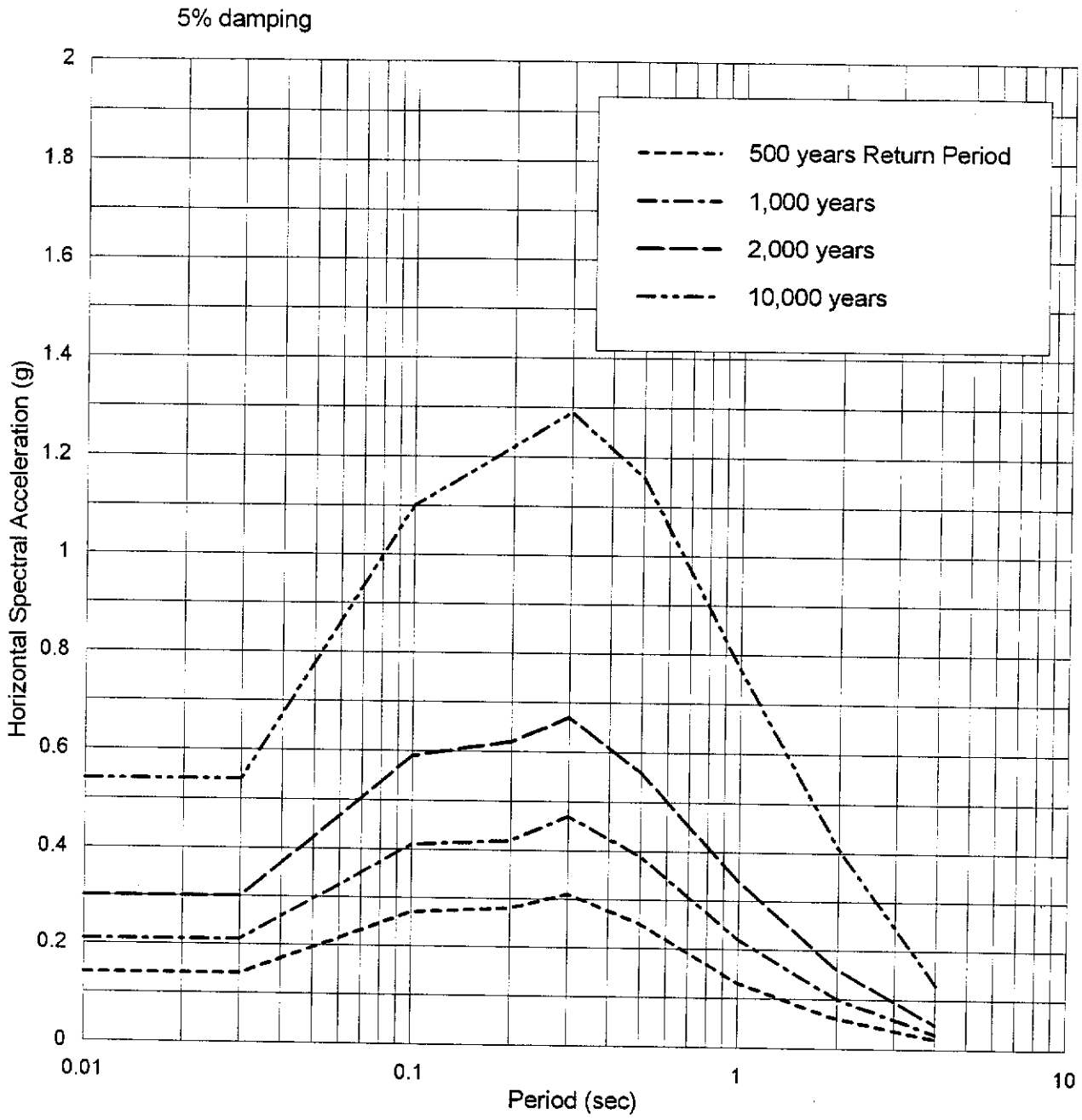
Project No. 91C0509	Los Alamos Seismic Hazards	MEAN EQUAL HAZARD SPECTRA AT TA-3	Figure 9-92
Woodward-Clyde Federal Services			

MEAN.GRF



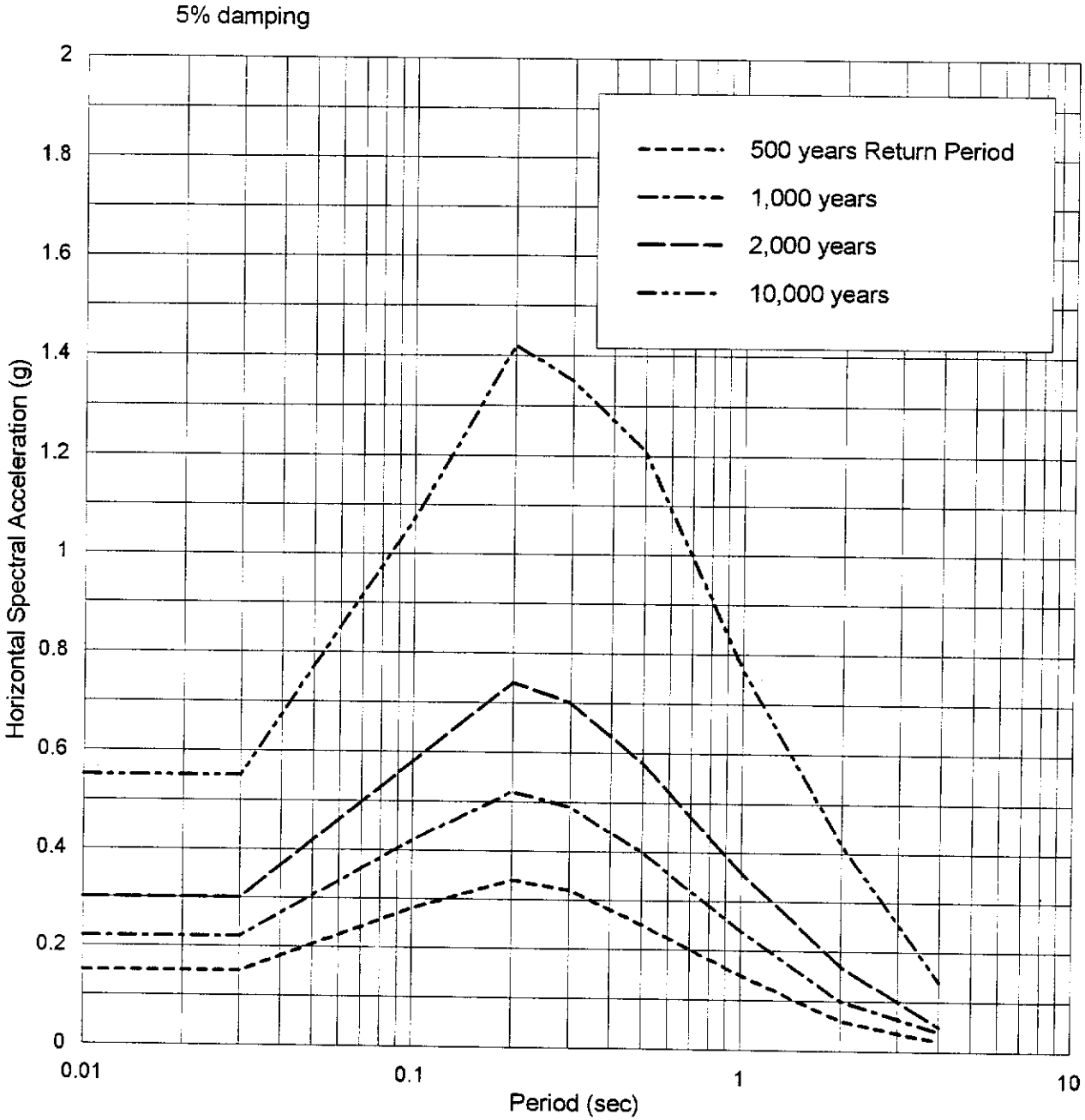
Project No. 91C0509	Los Alamos Seismic Hazards	MEAN EQUAL HAZARD SPECTRA AT TA-16	Figure 9-93
Woodward-Clyde Federal Services			

MEAN.GRF



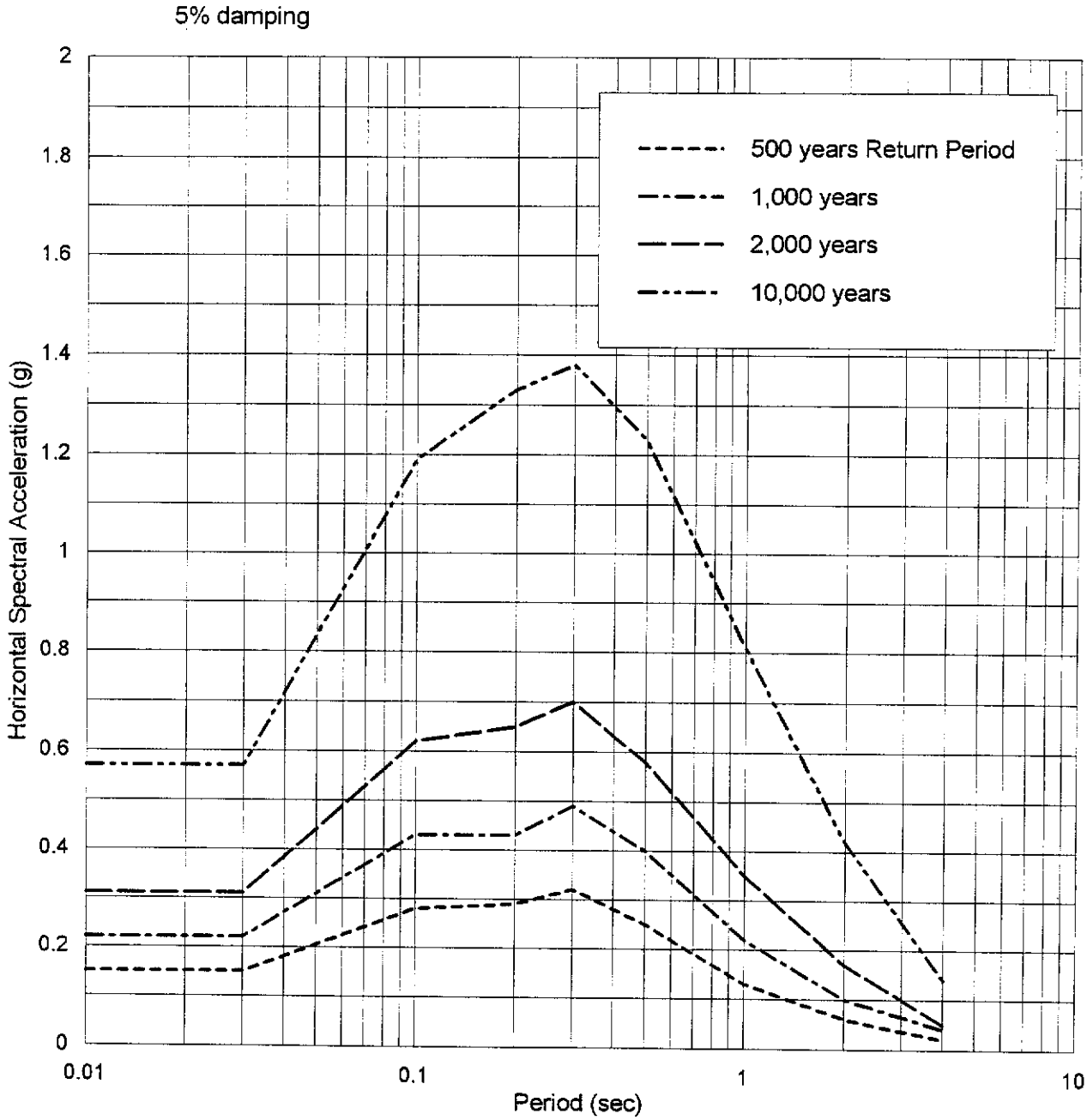
Project No. 91C0509	Los Alamos Seismic Hazards	MEAN EQUAL HAZARD SPECTRA AT TA-18	Figure 9-94
Woodward-Clyde Federal Services			

MEAN.GRF



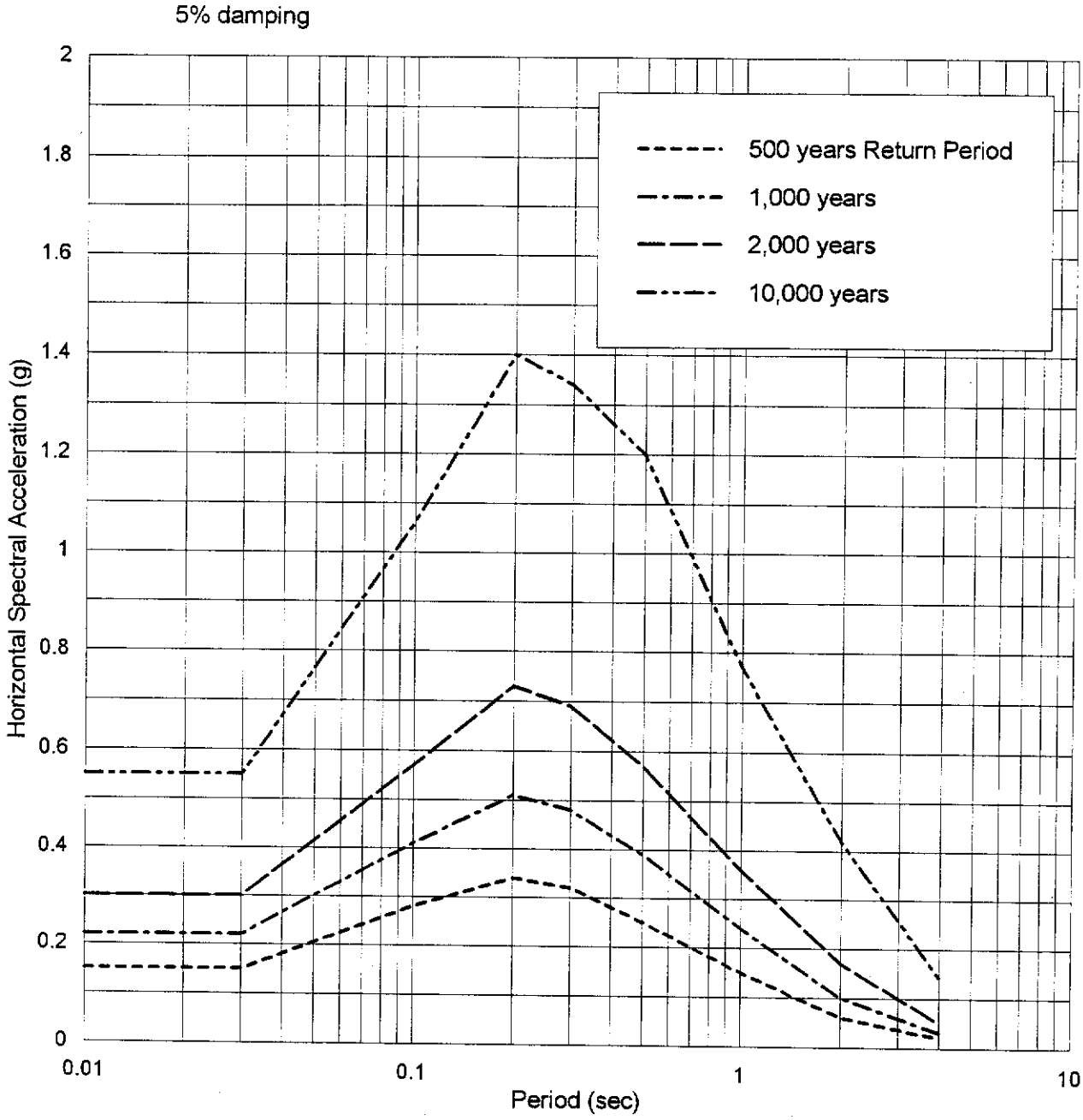
Project No. 91C0509	Los Alamos Seismic Hazards	MEAN EQUAL HAZARD SPECTRA AT TA-21	Figure 9-95
Woodward-Clyde Federal Services			

MEAN.GRF



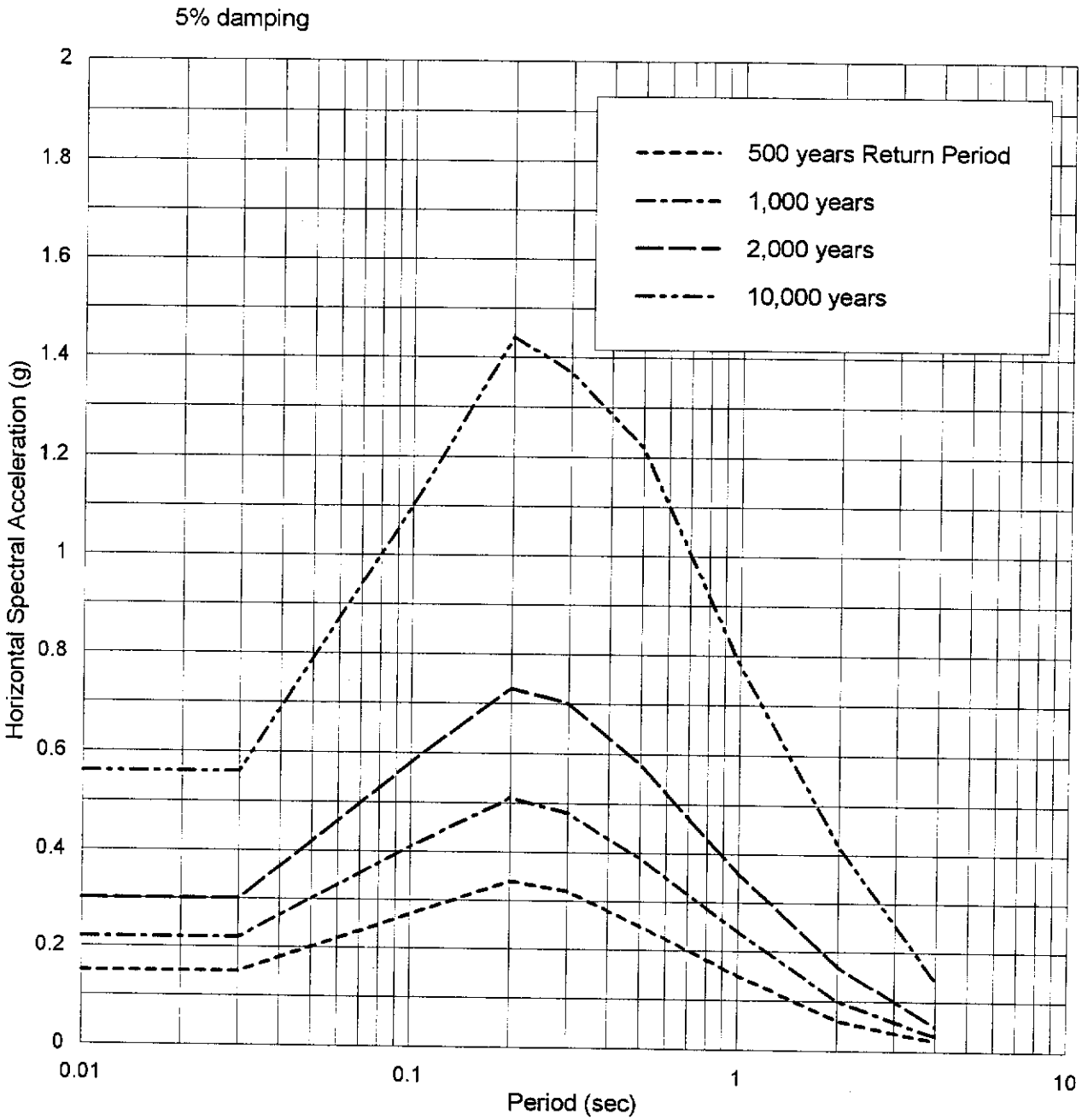
Project No. 91C0509	Los Alamos Seismic Hazards	MEAN EQUAL HAZARD SPECTRA AT TA-41	Figure 9-96
Woodward-Clyde Federal Services			

MEAN.GRF



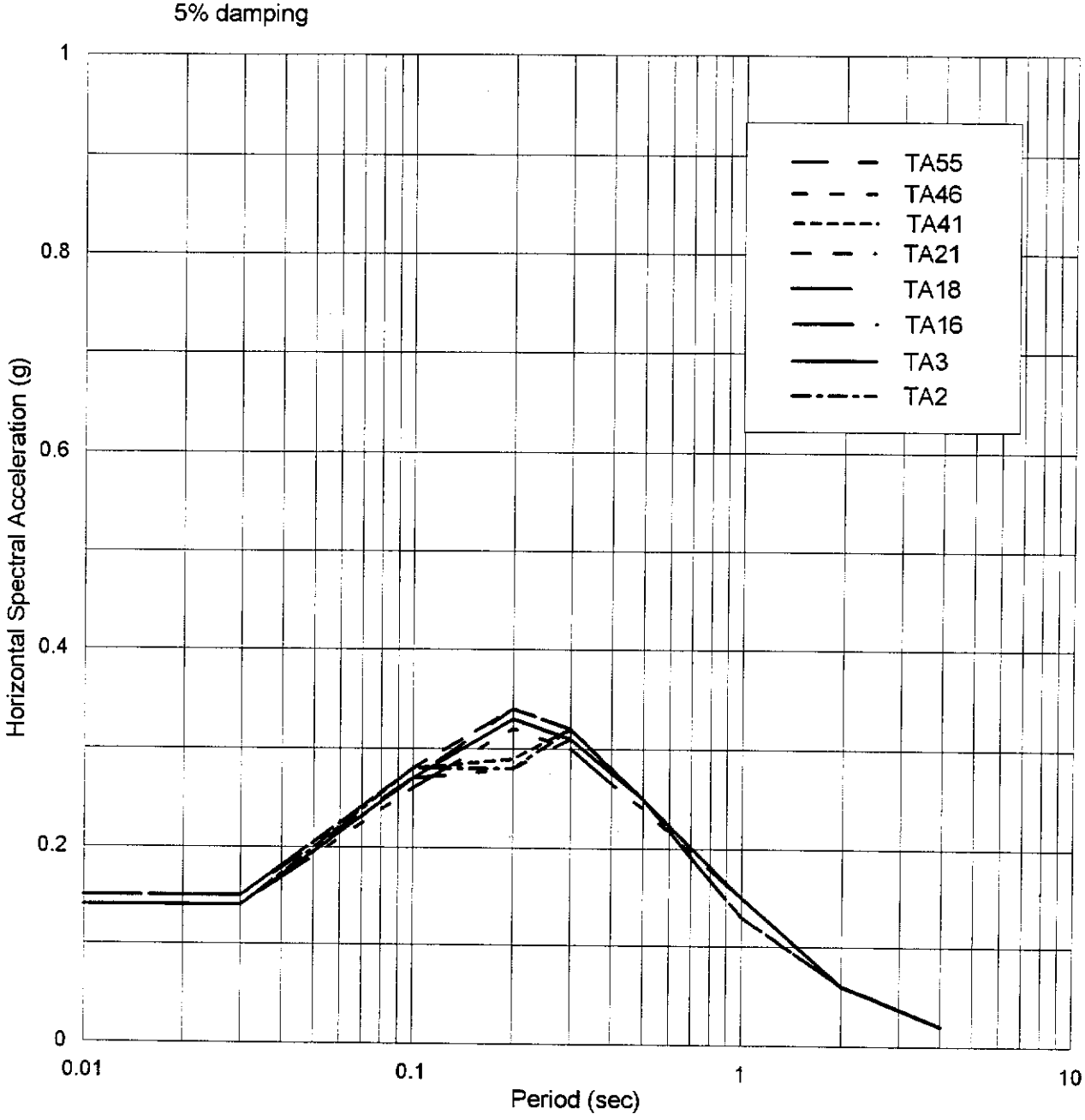
Project No. 91C0509	Los Alamos Seismic Hazards	MEAN EQUAL HAZARD SPECTRA AT TA-46	Figure 9-97
Woodward-Clyde Federal Services			

MEAN GRF



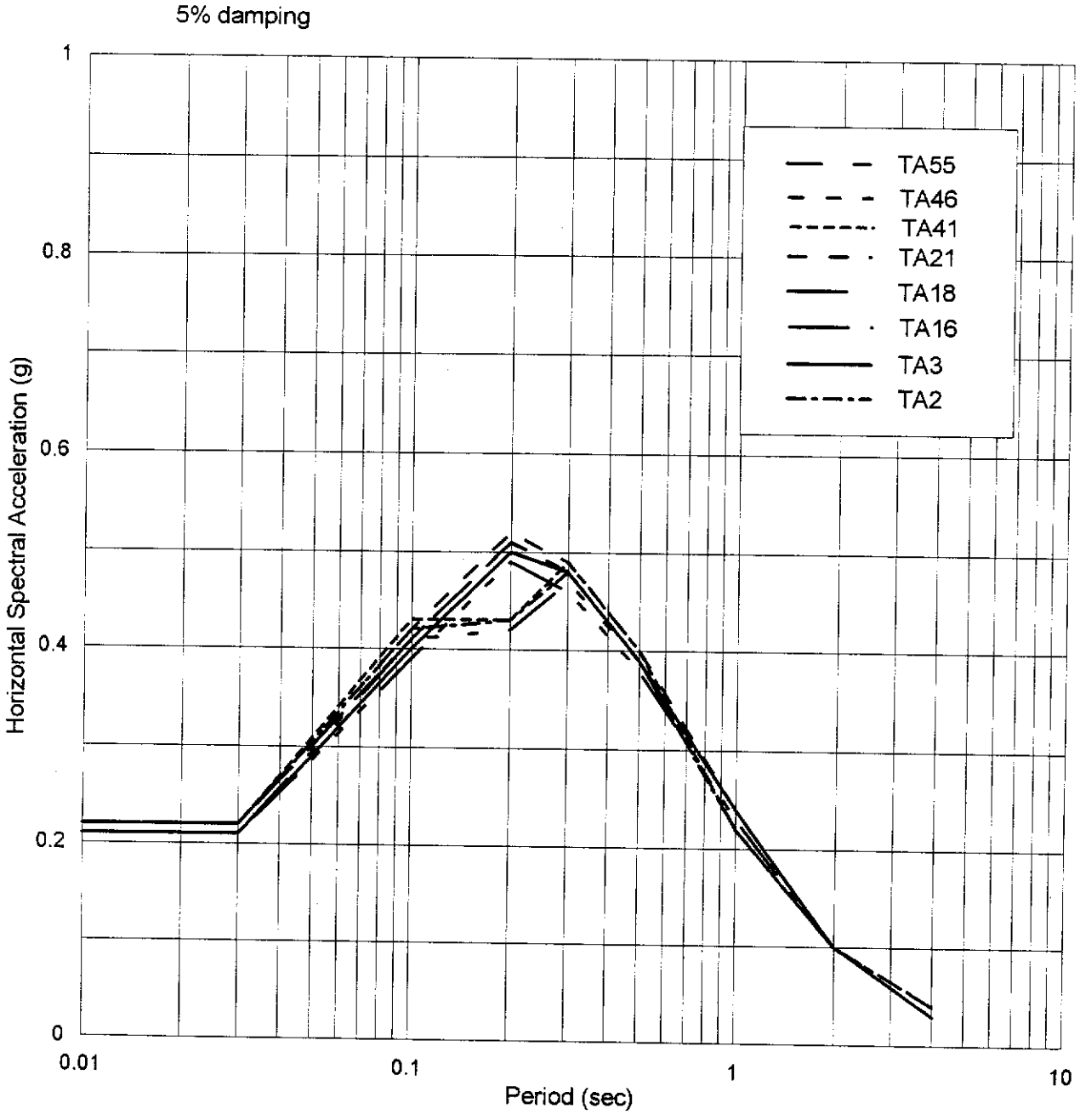
Project No. 91C0509	Los Alamos Seismic Hazards	MEAN EQUAL HAZARD SPECTRA AT TA-55	Figure 9-98
Woodward-Clyde Federal Services			

MEAN.GRF



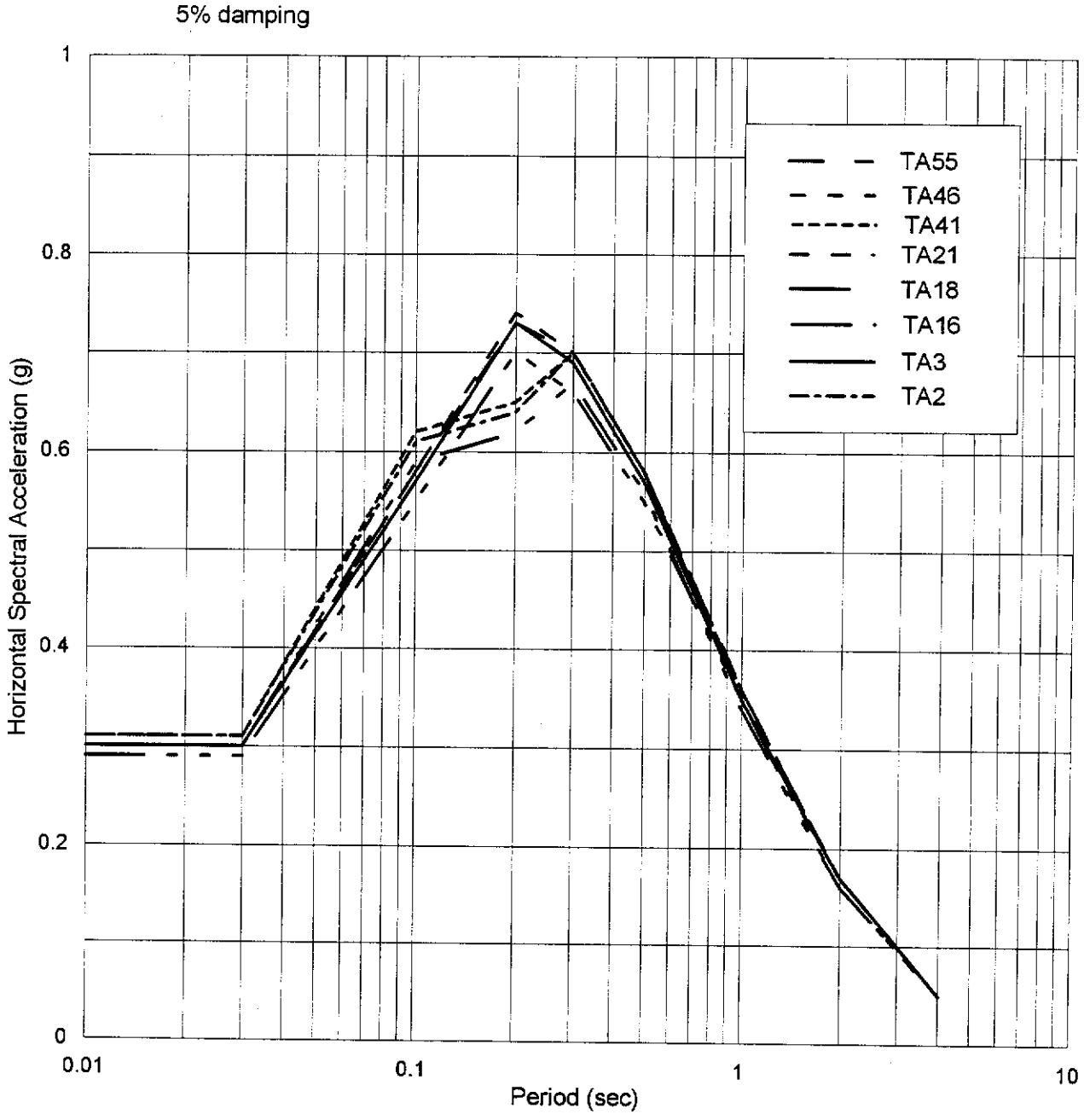
Project No. 91C0509	Los Alamos Seismic Hazards	COMPARISON OF THE MEAN EQUAL HAZARD SPECTRA FOR A 500-YEAR RETURN PERIOD	Figure 9-99
Woodward-Clyde Federal Services			

MEAN.GRF



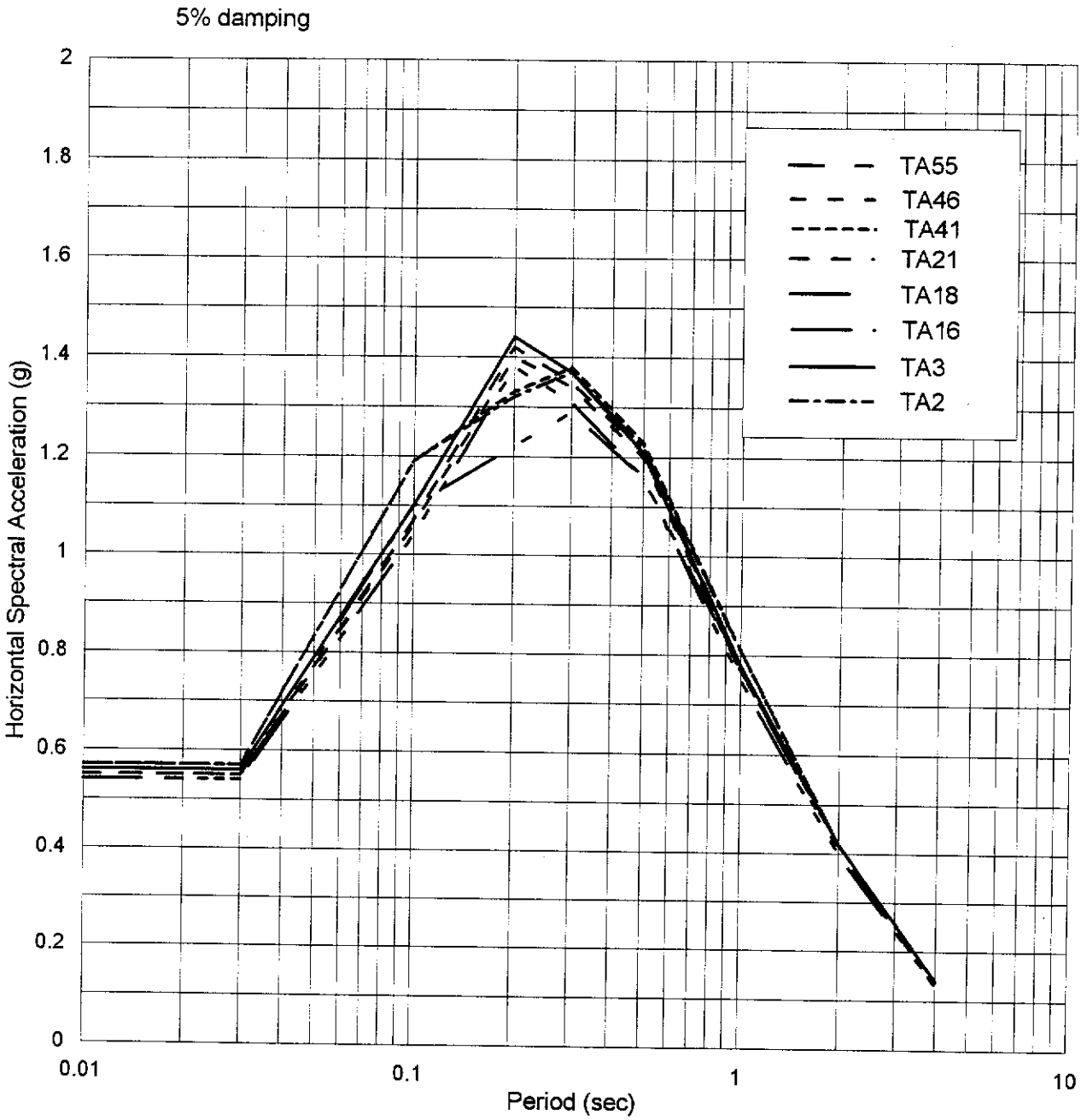
Project No. 91C0509	Los Alamos Seismic Hazards	COMPARISON OF THE MEAN EQUAL HAZARD SPECTRA FOR A 1000-YEAR RETURN PERIOD	Figure 9-100
Woodward-Clyde Federal Services			

MEAN.GRF



Project No. 91C0509	Los Alamos Seismic Hazards	COMPARISON OF THE MEAN EQUAL HAZARD SPECTRA FOR A 2000-YEAR RETURN PERIOD	Figure 9-101
Woodward-Clyde Federal Services			

MEAN.GRF



Project No. 91C0509	Los Alamos Seismic Hazards	COMPARISON OF THE MEAN EQUAL HAZARD SPECTRA FOR A 10,000-YEAR RETURN PERIOD	Figure 9-102
Woodward-Clyde Federal Services			

MEAN.GRF

10.0
DESIGN BASIS EARTHQUAKE PARAMETERS

Based upon the results of this study, the following Design Basis Earthquake (DBE) parameters are developed and recommended to LANL for their use in seismic safety evaluations and for future seismic design. It should be noted that these parameters do not directly incorporate possible mesa amplification (and valley deamplification) due to topographic effects (Section 8.4). However, these effects are present in strong motion recording sites and contribute to the variability in the empirical attenuation relations. The modeling uncertainty in the stochastic predictions may also encompass these effects. As a result, the equal hazard spectra reflect moderate topographic effects probably encompassing the 10 to 20% range estimated in the numerical study (Section 8.4). Further numerical as well as empirical studies are recommended to better constrain the degree and frequency range of the topographic effects.

10.1 DESIGN BASIS EARTHQUAKE RESPONSE SPECTRA

DOE Standard 1023-94 recommends that the equal hazard spectrum associated with the seismic hazard annual probability of exceedance should be supplemented by response spectral shapes of the dominant earthquakes at intermediate frequencies (5 to 10 Hz) and low frequencies (1 to 2.5 Hz) to arrive at the DBE response spectrum. Also "the DBE ground motion at a site shall be specified in terms of smooth and broad frequency content horizontal and vertical response spectra defined at a specific control point." In the case of LANL, because the site conditions most resemble those of a deep soil site, the control point is the free-field ground surface as specified by DOE Standard 1023-94.

In the development of the DBE spectra, we have followed the steps outlined in DOE Standard 1023-94. As previously noted, the equal hazard spectra for each site and Performance Category return period, are shown in Figures 9-99 through 9-102. At a meeting between LANL engineers and WCFS held on 13 January 1995, it was decided to develop a generalized response spectrum for the entire laboratory, for each Performance Category, because of the similarities between the site-specific spectra. By generally enveloping spectra for all sites, a single slightly conservative spectra can be used lab-wide.

To check the reasonableness of the composite equal hazard spectral shape, it was compared with shapes of the dominant earthquakes at 0.2 and 1.0 sec (Table 9-2). The shapes were computed by taking the average of three empirical response spectra using the same attenuation relationships used in both the deterministic and probabilistic ground motion estimates (Sections 8.1.1 and 9.3) (Figures 10-1 through 10-8). These average spectra were then normalized per DOE Standard 1023-94 by the spectral acceleration at either 0.2 or 1.0 sec as shown by the equal hazard spectra (Figures 10-9 through 10-16). These normalized spectra were then superimposed on the appropriate equal hazard spectra and all spectra were generally enveloped to arrive at the DBE horizontal spectra (Figures 10-17 through 10-20). Based on the recommended V/H ratios derived in this study (Figure 8-56), the DBE vertical response spectra have also been computed (Figure 10-21 through 10-24).

10.2 DESIGN BASIS EARTHQUAKE TIME HISTORIES

10.2.1 Recommended Stochastic Time Histories

Acceleration time histories or accelerograms can be produced by combining a Fourier amplitude spectrum (which is generated by matching the DBE target spectrum) with a phase spectrum from an observed strong ground motion recording using the technique described by Silva and Lee (1987). This approach has been used extensively for DOE and the other Federal agencies in developing appropriate time histories for seismic hazard analysis. To improve the fit to the target spectrum, additional spectral matching is performed using the response spectrum computed from the synthetic time history. Additionally, a baseline correction is included by high-pass filtering the record at 10 sec. The result is a synthetic time history which closely matches the target spectrum and which possesses realistic integrations to velocity as well as displacement.

The two most important criteria in selecting the phase from a recorded earthquake for the hypothetical event are that the seismic moment (or M_w) and the source-to-site distance should be comparable. These criteria produce synthetic records with appropriate durations and timing of the major phase arrivals so that the distribution of energy with time in the synthetic record appears reasonable. The time histories are intended to approximate expected durations, and as such, they are appropriate for nonlinear analyses of structures, embankments, and soil profiles. DBE time histories for acceleration, velocity and

displacement were generated by spectrally matching the DBE response spectra (Figures 10-25 through 10-32). The phase spectrum were taken from the following records: (1) the Gilroy Array #4 recordings of the 1979 M_L 5.9 Coyote Lake, California earthquake for the 500 year DBE; (2) the Gilroy #3 record for the 1982 M_L 6.2 Morgan Hill, California earthquake for the 1,000 year DBE; (3) the Holtville record of the 1979 M_L 6.6 Imperial Valley, California event for the 2,000 year DBE; and (4) the El Centro #2 records of the 1979 Imperial Valley earthquake for the 10,000 year DBE. The resulting DBE horizontal and vertical time histories are shown in Figures 10-33 through 10-36 and 10-37 through 10-40, respectively.

10.2.2 Recommended Empirical Time Histories

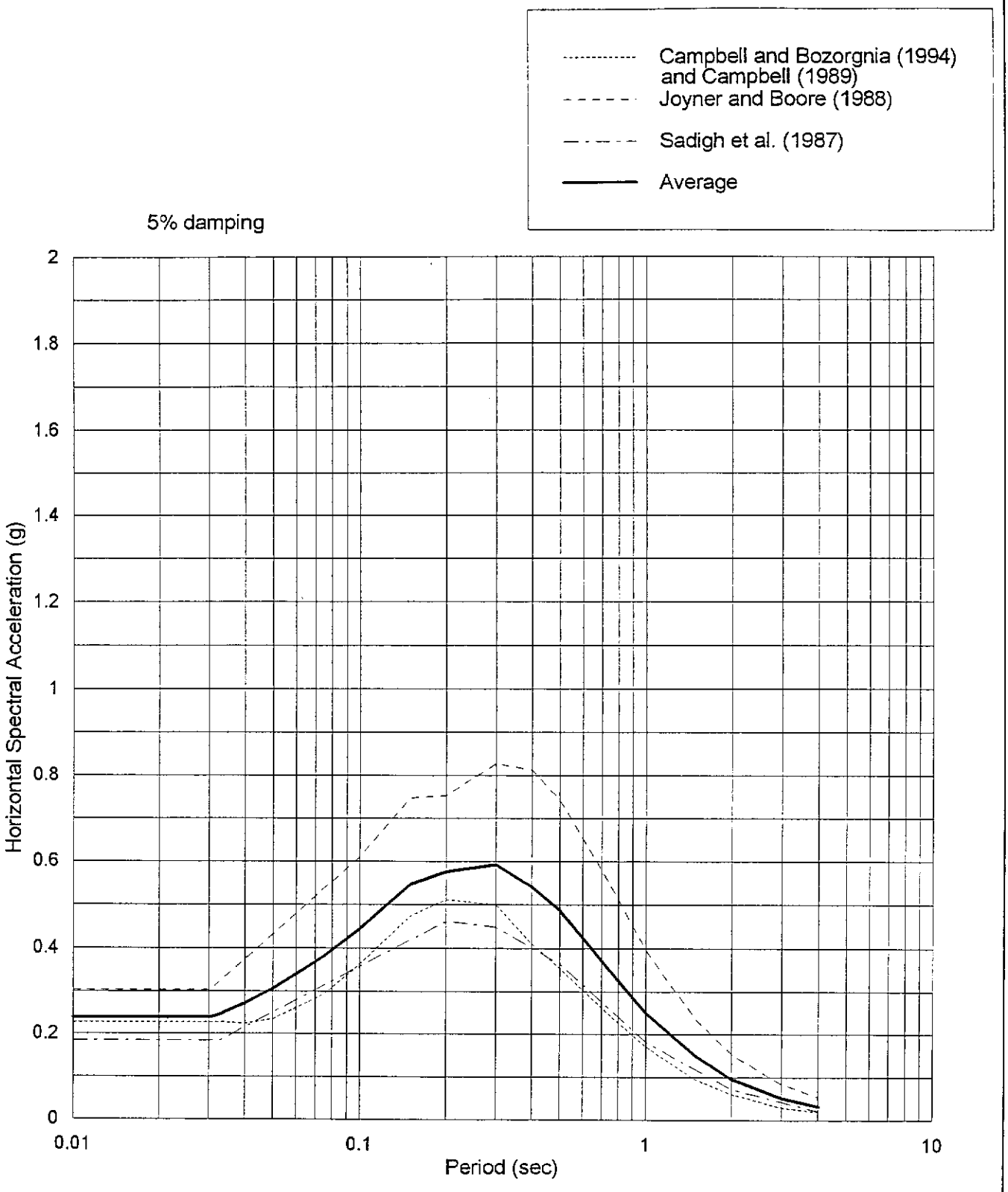
Based on our analysis, the DBE for the 10,000-year return period will most likely be a large earthquake on the Pajarito fault. Unfortunately, few strong motion records exist for normal faulting earthquakes in the western U.S. and for use in seismic stability analyses. An alternate approach is to use records from large magnitude California strike-slip earthquakes of similar size at similar distances. The 1979 Imperial Valley and 1989 Loma Prieta events could be used to simulate the 10,000 year DBE.

The DBEs at return periods of 500, 1,000, and 2,000 years are representative of the background earthquake. Earthquakes resulting from strike-slip faulting (preferably in extensional regimes) are appropriate for these DBEs because this style of faulting also characterizes the background seismicity in the northern Rio Grande rift (Section 5.2). The Coyote Lake, Mammoth Lakes, Friuli, and Morgan Hill earthquakes would be suitable for analyses for the 500, 1,000, and 2,000 year DBEs.

Given the available strong motion data, the following records (Table 10-1) are recommended for use together with the stochastic time histories in any dynamic analysis. These records should be scaled to the peak horizontal acceleration as specified by the appropriate Performance Category (Table 9-1). We also strongly recommend that a suite of records be used in any analysis since no single empirical earthquake can capture all aspects of the DBE ground motions.

TABLE 10-1 RECOMMENDED EMPIRICAL TIME HISTORIES

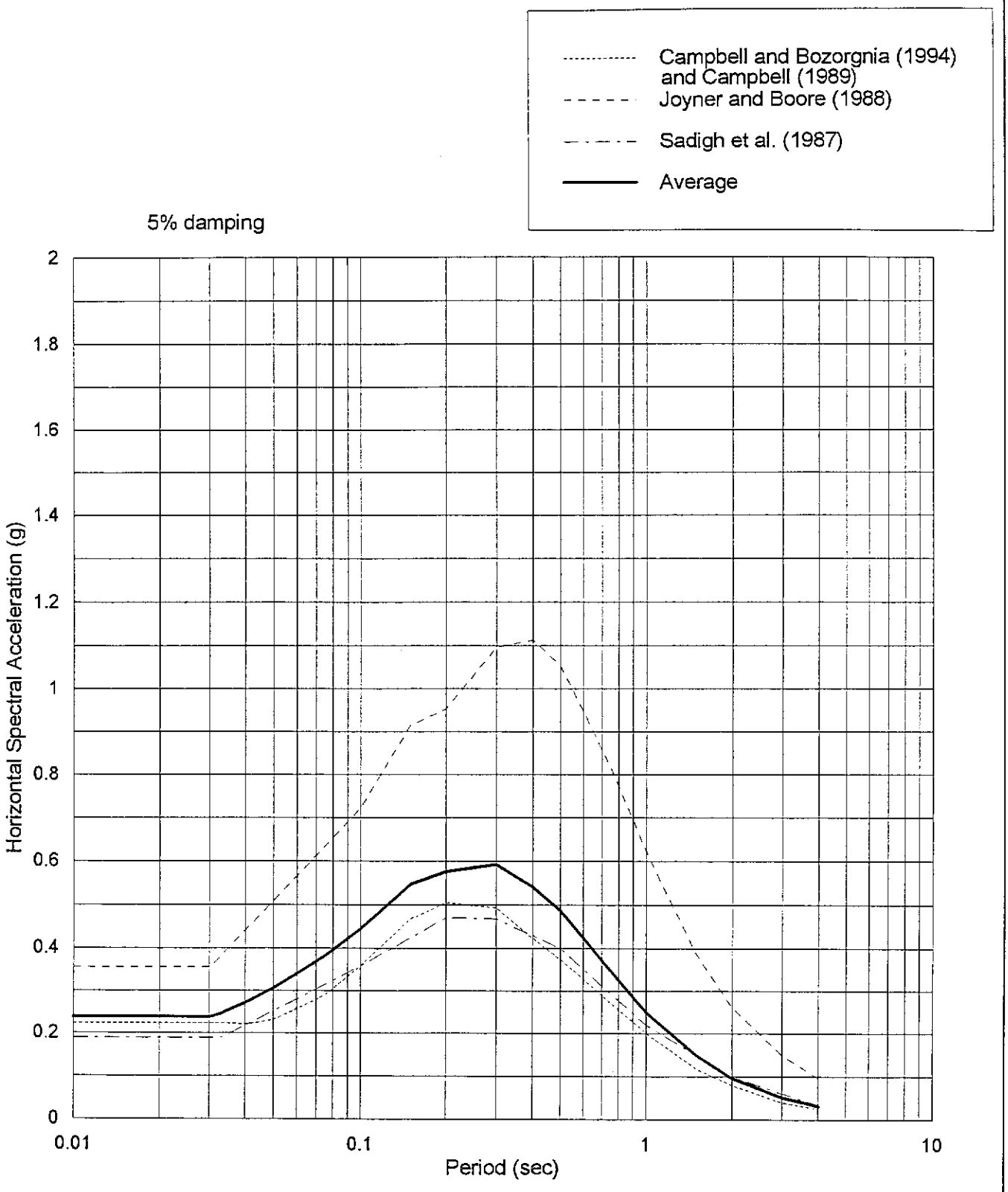
Event (Magnitude, Faulting Type)	Station (Site Conditions)	Rupture Distance (km)	Peak Horizontal Acceleration (g) (Component)
6 August 1979 Coyote Lake, CA (M_L 5.9, strike-slip)	Gilroy #3 (deep soil)	6.0 km	0.27 (N40°W) 0.26 (S50°W) 0.15 (VERT)
6 August 1979 Coyote Lake, CA (M_L 5.9, strike-slip)	Gilroy #4 (deep soil)	4.5 km	0.26 (N-S) 0.24 (E-W) 0.44 (VERT)
25 May 1980 Mammoth Lakes, CA 0949 GMT (M_L 6.0, oblique strike-slip)	Convict Creek (deep soil)	1.0 km	0.20 (N-S) 0.17 (E-W) 0.14 (VERT)
25 May 1980 Mammoth Lakes, CA 0933 GMT (M_L 6.1, oblique strike-slip)	Mammoth Lakes HS (deep soil)	3.2 km	0.33 (S74°W) 0.26 (N16°W) 0.26 (VERT)
15 November 1976, Friuli, Italy 0315 GMT (M_L 6.1, normal)	Buia (soil)	9 km (epicentral)	0.07 (N-S) 0.12 (E-W) 0.06 (VERT)
24 April 1984, Morgan Hill, CA (M_L 6.2, strike-slip)	Gilroy #4 (deep soil)	15 km	0.33 (N-S) 0.22 (E-W) 0.40 (VERT)
24 April 1984, Morgan Hill, CA (M_L 6.2, strike-slip)	Gilroy #3 (deep soil)	16 km	0.18 (N-S) 0.19 (E-W) 0.36 (VERT)
15 October 1979 Imperial Valley, CA 2316 GMT (M_L 6.6, strike-slip)	Calexico Fire Station (deep soil)	10.6 km	0.28 (S45°W) 0.22 (N45°W) 0.21 (VERT)
15 October 1979 Imperial Valley, CA 2316 GMT (M_L 6.6, strike-slip)	Holtville P.O. (deep soil)	7.5 km	0.22 (N45°W) 0.26 (S45°W) 0.31 (VERT)
15 October 1979 Imperial Valley, CA 2316 GMT (M_L 6.6, strike-slip)	El Centro Station #9 (deep soil)	6.2 km	0.40 (N-S) 0.27 (E-W) 0.38 (VERT)
15 October 1979 Imperial Valley, CA 2316 GMT (M_L 6.6, strike-slip)	El Centro Station #8 (deep soil)	3.8 km	0.50 (S50°W) 0.64 (S40°E) 0.55 (VERT)
18 October 1989 Loma Prieta, CA (M_w 7.0, oblique strike-slip)	Gilroy #3 (deep soil)	18 km	0.37 (E-W) 0.55 (N-S) 0.38 (VERT)



M 5.9, Distance = 10.0 km

Project No. 91C0509	Los Alamos Seismic Hazards	AVERAGE EMPIRICAL ACCELERATION RESPONSE SPECTRA FOR 500-YEAR DOMINANT EARTHQUAKE AT 0.2 SEC	Figure 10-1
Woodward-Clyde Federal Services			

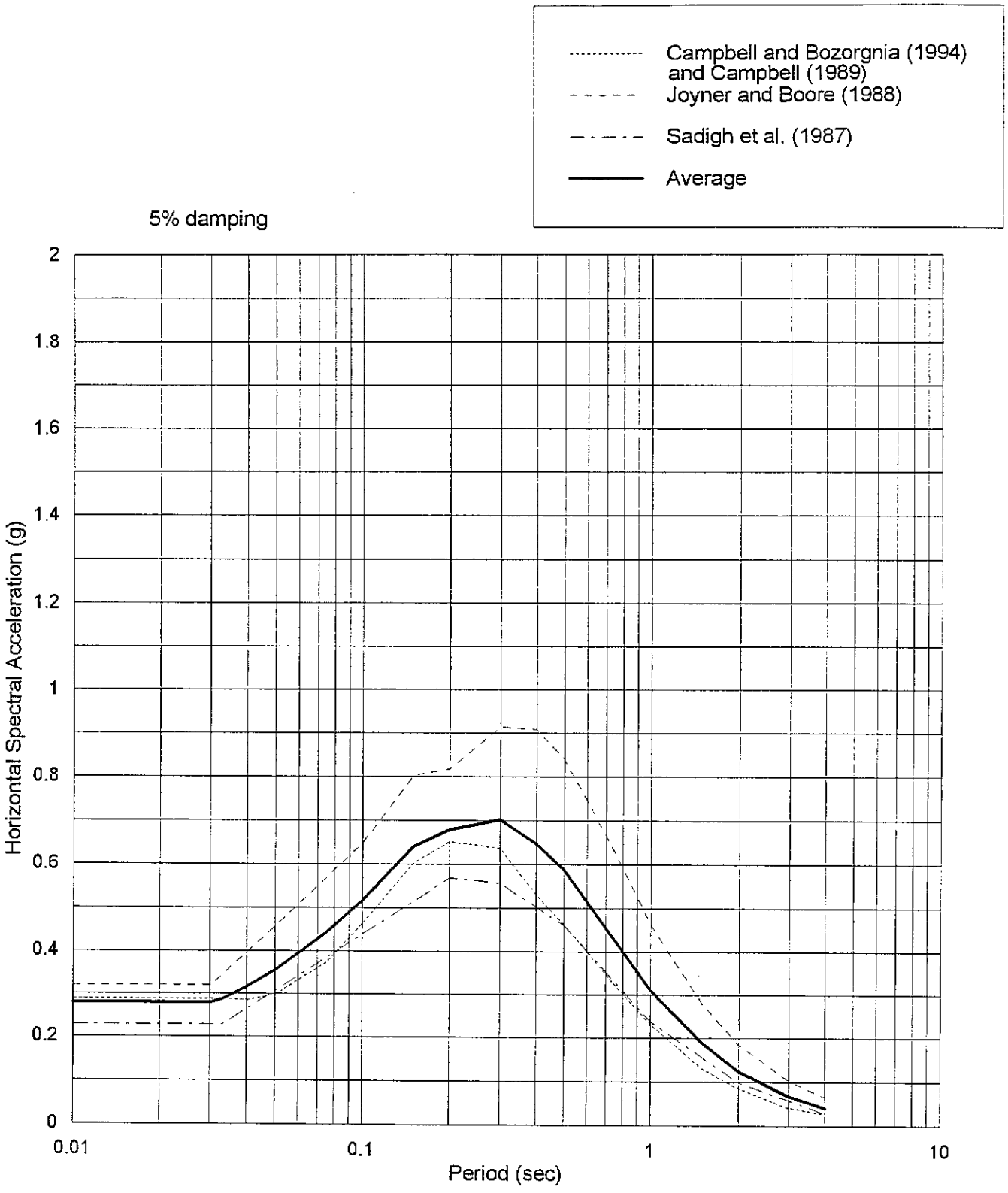
MEAN.GRF



M 6.2, Distance = 12.5 km

Project No. 91C0509	Los Alamos Seismic Hazards	AVERAGE EMPIRICAL ACCELERATION RESPONSE SPECTRA FOR 500-YEAR DOMINANT EARTHQUAKE AT 1.0 SEC	Figure 10-2
Woodward-Clyde Federal Services			

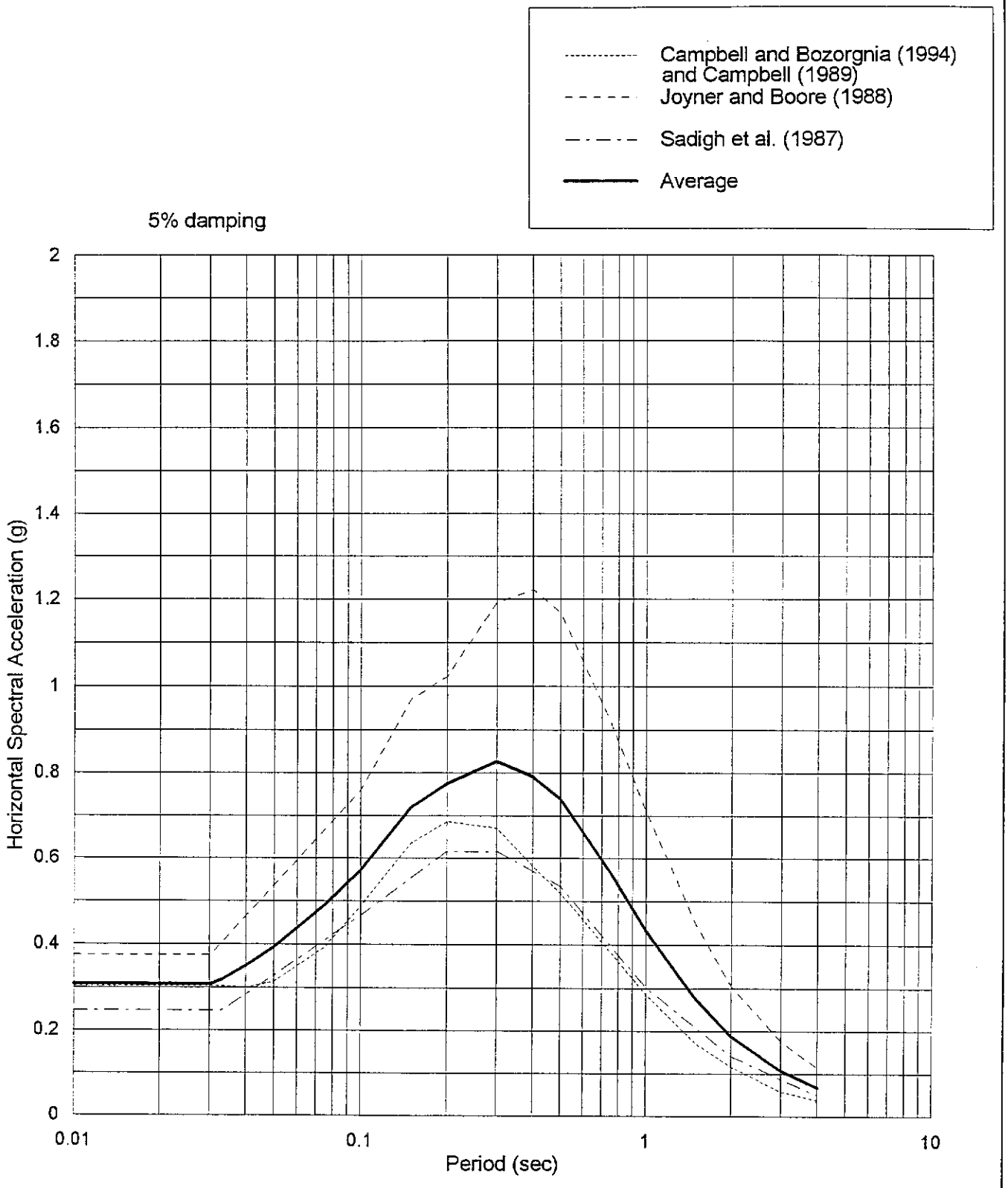
MEAN.GRF



M 6.0, Distance = 8.0 km

Project No. 91C0509	Los Alamos Seismic Hazards	AVERAGE EMPIRICAL ACCELERATION RESPONSE SPECTRA FOR 1000-YEAR DOMINANT EARTHQUAKE AT 0.2 SEC	Figure 10-3
Woodward-Clyde Federal Services			

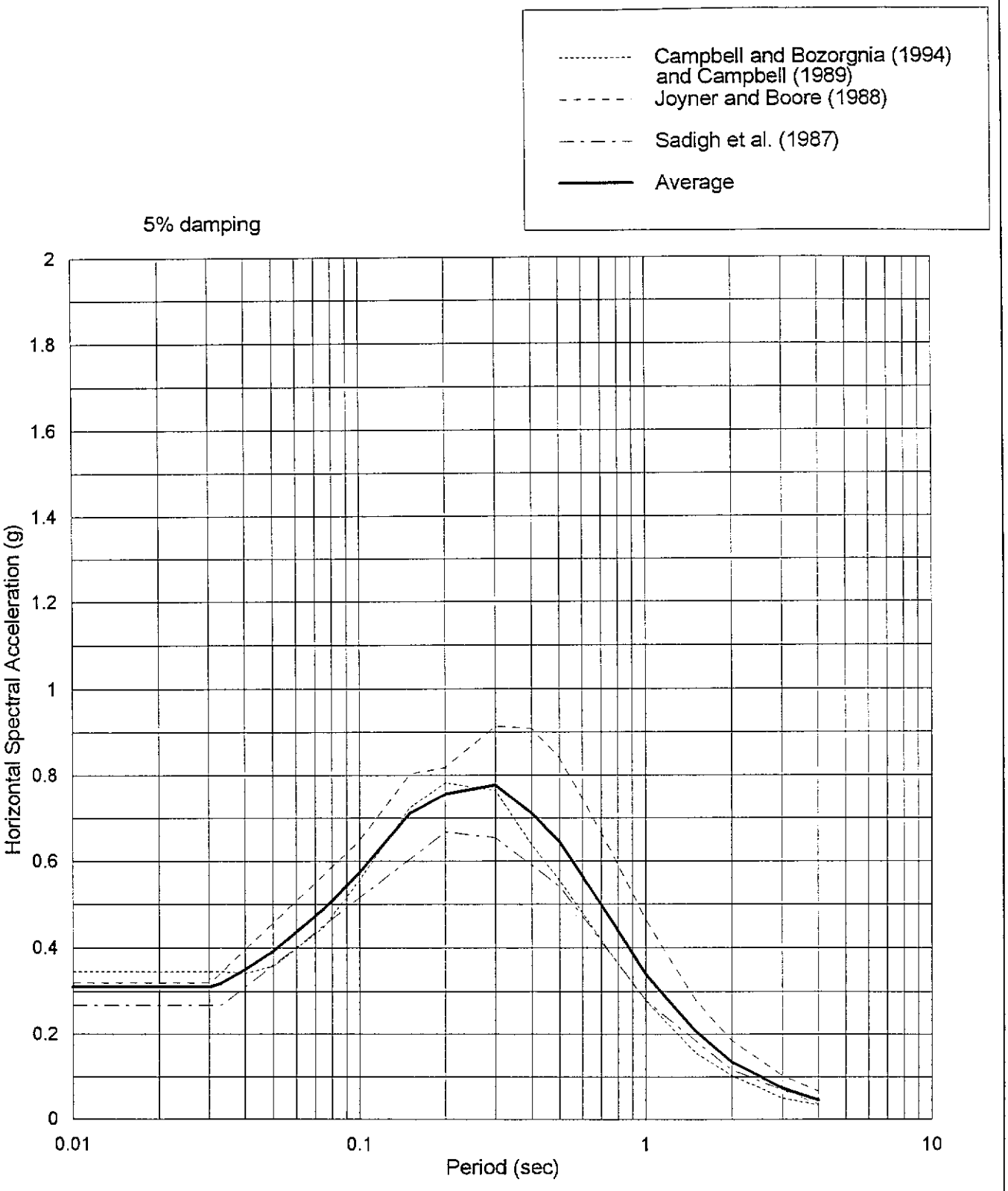
MEAN.GRF



M 6.3, Distance = 9.2 km

Project No. 91C0509	Los Alamos Seismic Hazards	AVERAGE EMPIRICAL ACCELERATION RESPONSE SPECTRA FOR 1000-YEAR DOMINANT EARTHQUAKE AT 1.0 SEC	Figure 10-4
Woodward-Clyde Federal Services			

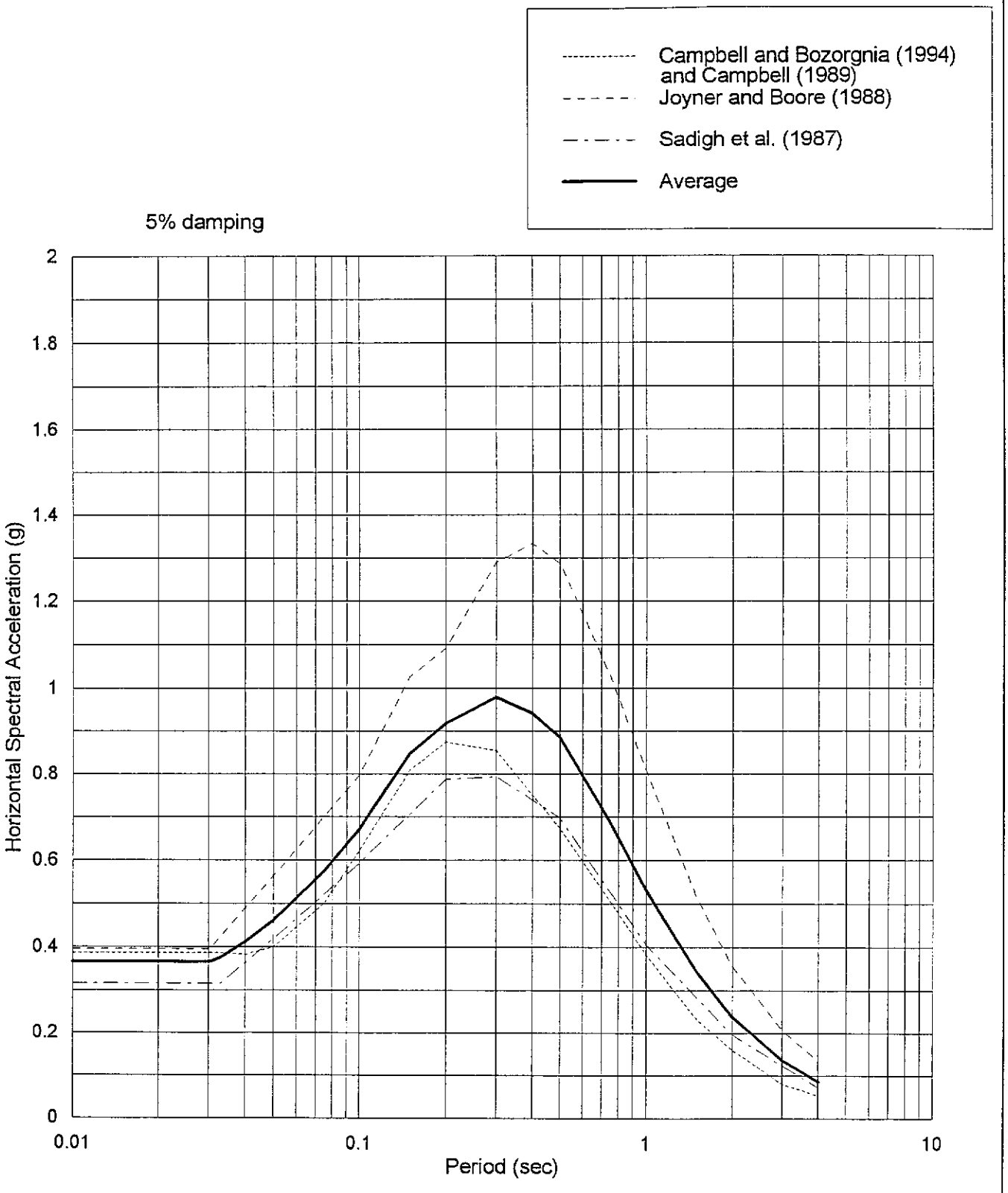
MEAN.GRF



M 6.0, Distance = 6.0 km

Project No. 91C0509	Los Alamos Seismic Hazards	AVERAGE EMPIRICAL ACCELERATION RESPONSE SPECTRA FOR 2000-YEAR DOMINANT EARTHQUAKE AT 0.2 SEC	Figure 10-5
Woodward-Clyde Federal Services			

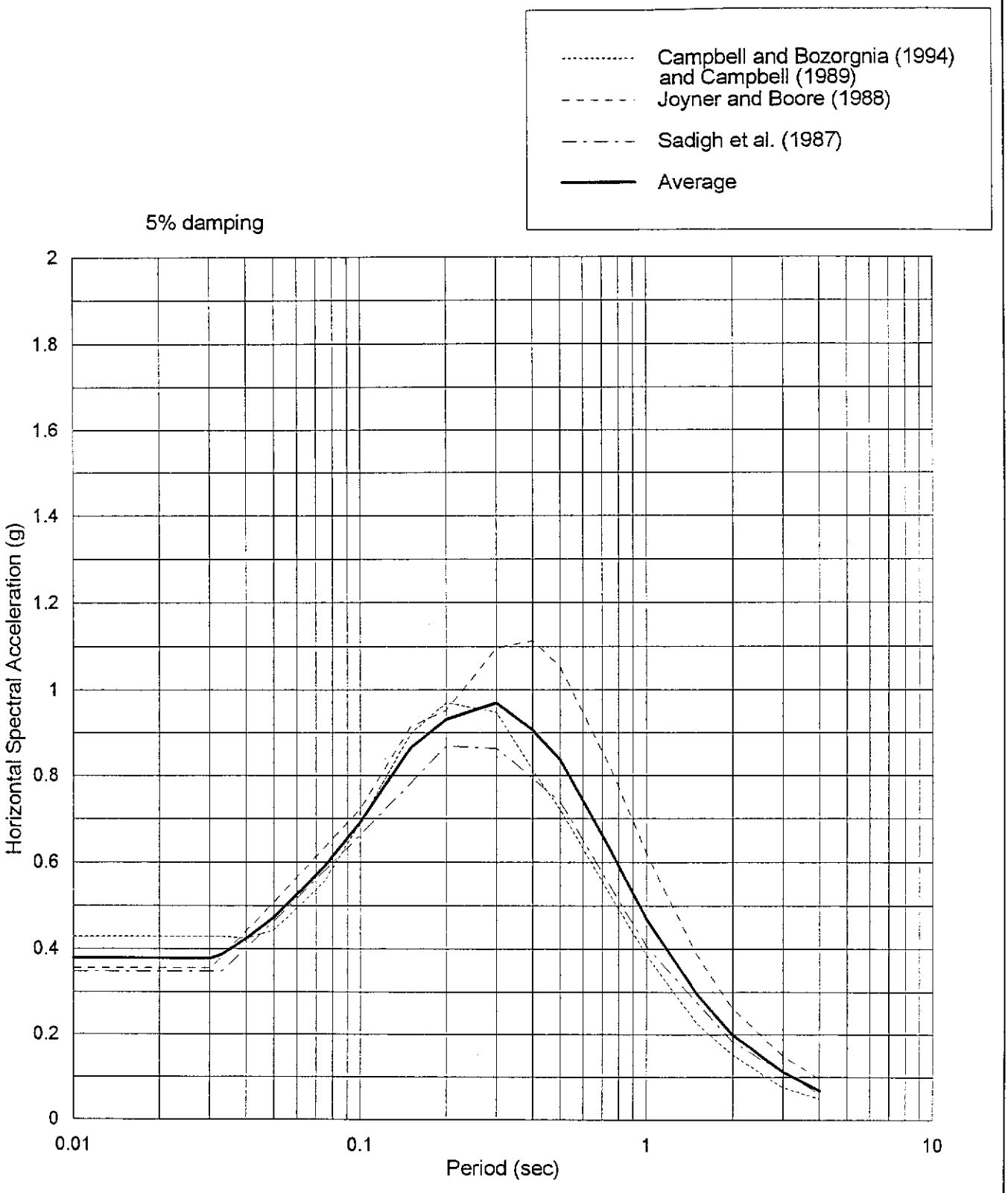
MEAN.GRF



M 6.4, Distance = 6.4 km

Project No. 91C0509	Los Alamos Seismic Hazards	AVERAGE EMPIRICAL ACCELERATION RESPONSE SPECTRA FOR 2000-YEAR DOMINANT EARTHQUAKE AT 1.0 SEC	Figure 10-6
Woodward-Clyde Federal Services			

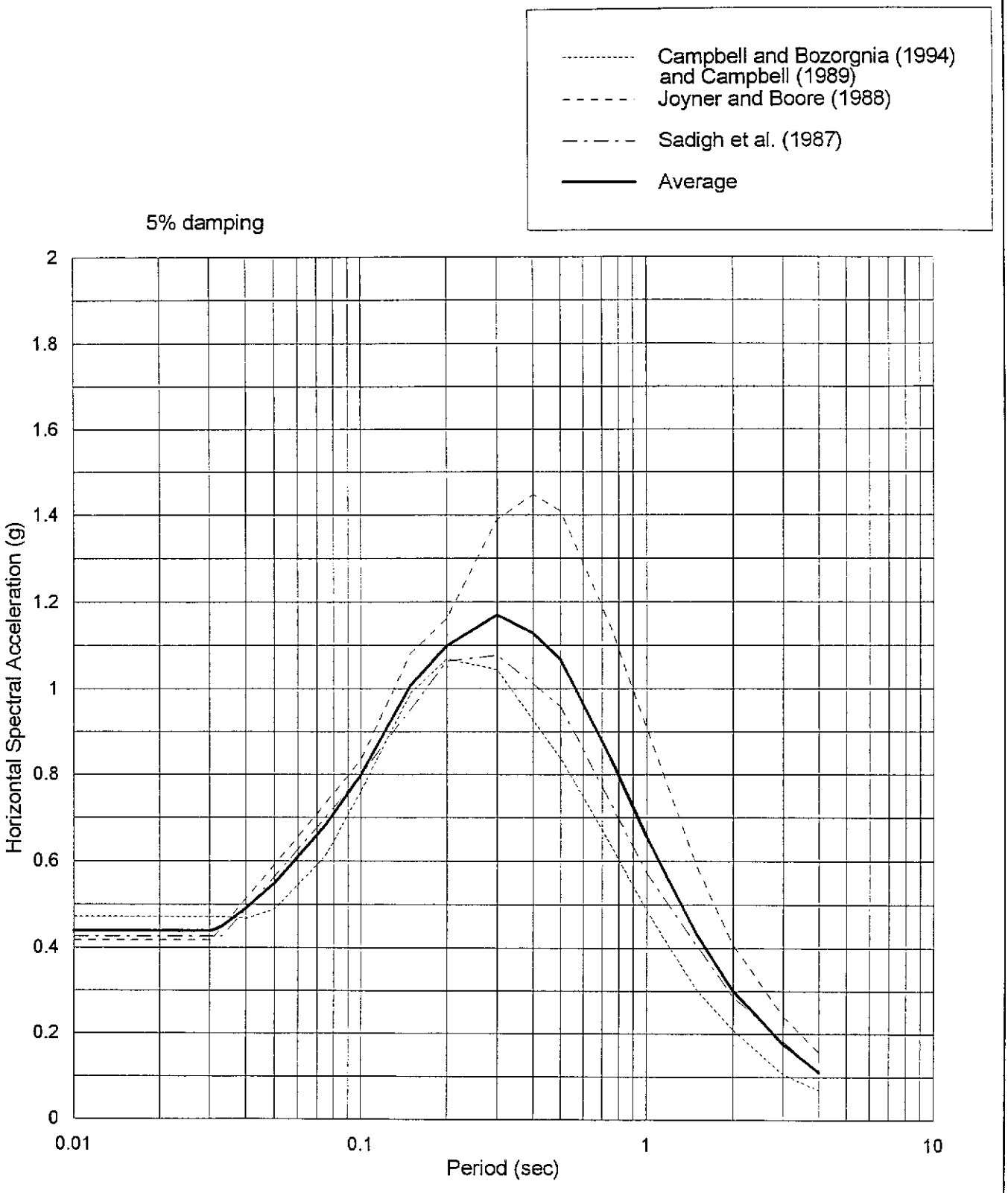
MEAN.GRF



M 6.2, Distance = 4.0 km

Project No. 91C0509	Los Alamos Seismic Hazards	AVERAGE EMPIRICAL ACCELERATION RESPONSE SPECTRA FOR 10,000-YEAR DOMINANT EARTHQUAKE AT 0.2 SEC	Figure 10-7
Woodward-Clyde Federal Services			

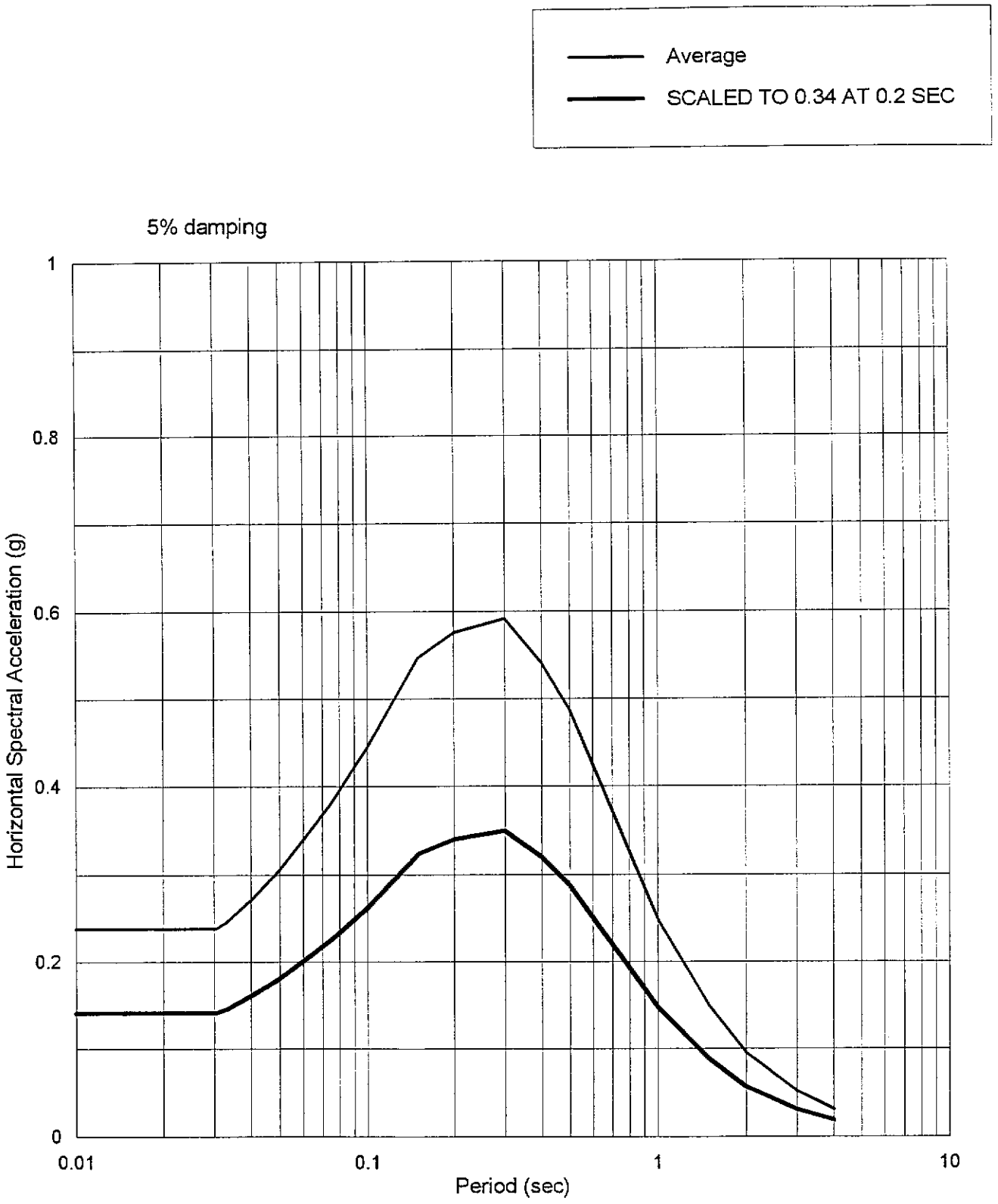
MEAN GRF



M 6.5, Distance = 3.0 km

Project No. 91C0509	Los Alamos Seismic Hazards	AVERAGE EMPIRICAL ACCELERATION RESPONSE SPECTRA FOR 10,000-YEAR DOMINANT EARTHQUAKE AT 1.0 SEC	Figure 10-8
Woodward-Clyde Federal Services			

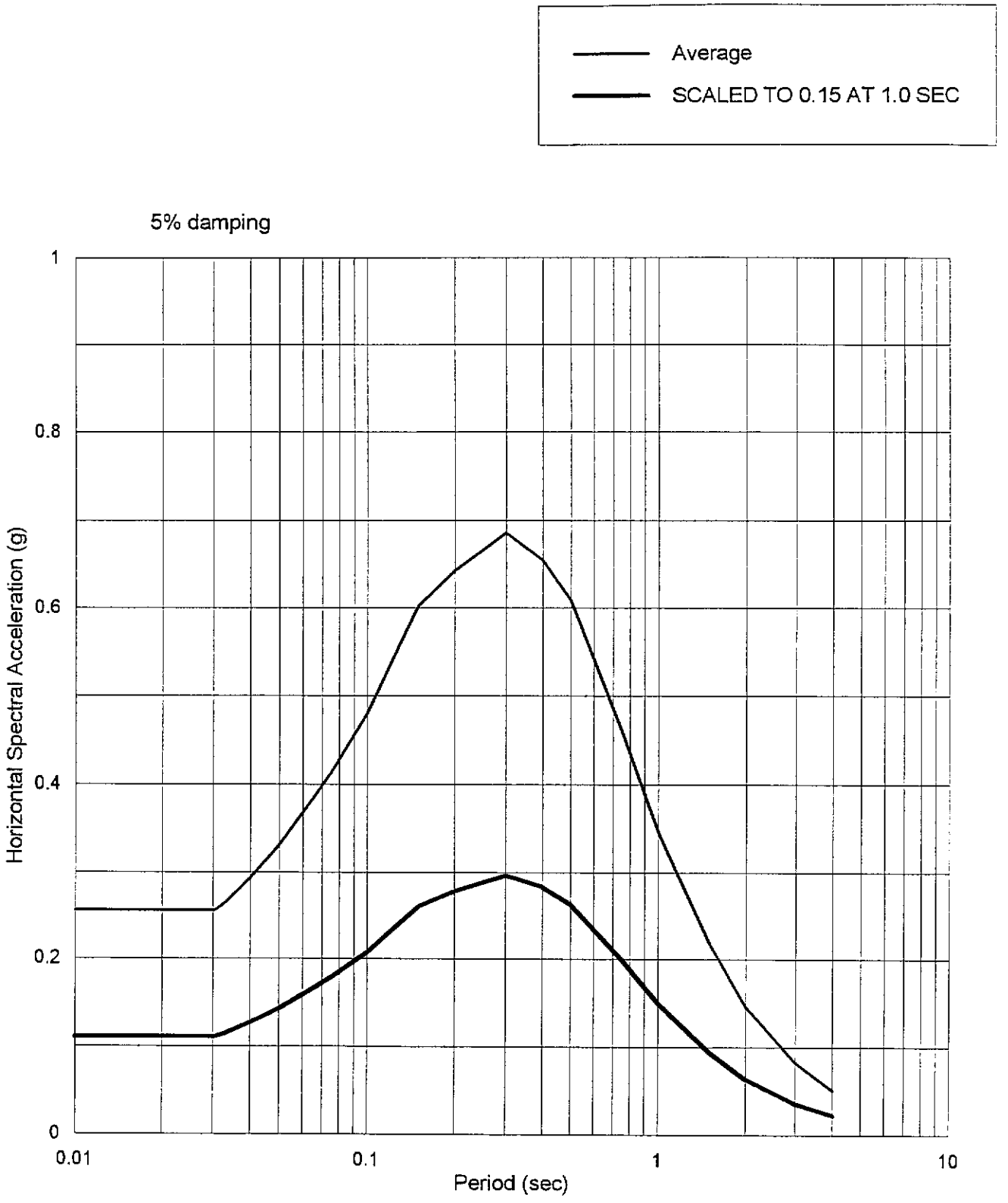
MEAN.GRF



M 5.9, Distance = 10.0 km

Project No. 91C0509	Los Alamos Seismic Hazards	NORMALIZED EMPIRICAL ACCELERATION RESPONSE SPECTRA FOR 500-YEAR DOMINANT EARTHQUAKE AT 0.2 SEC	Figure 10-9
Woodward-Clyde Federal Services			

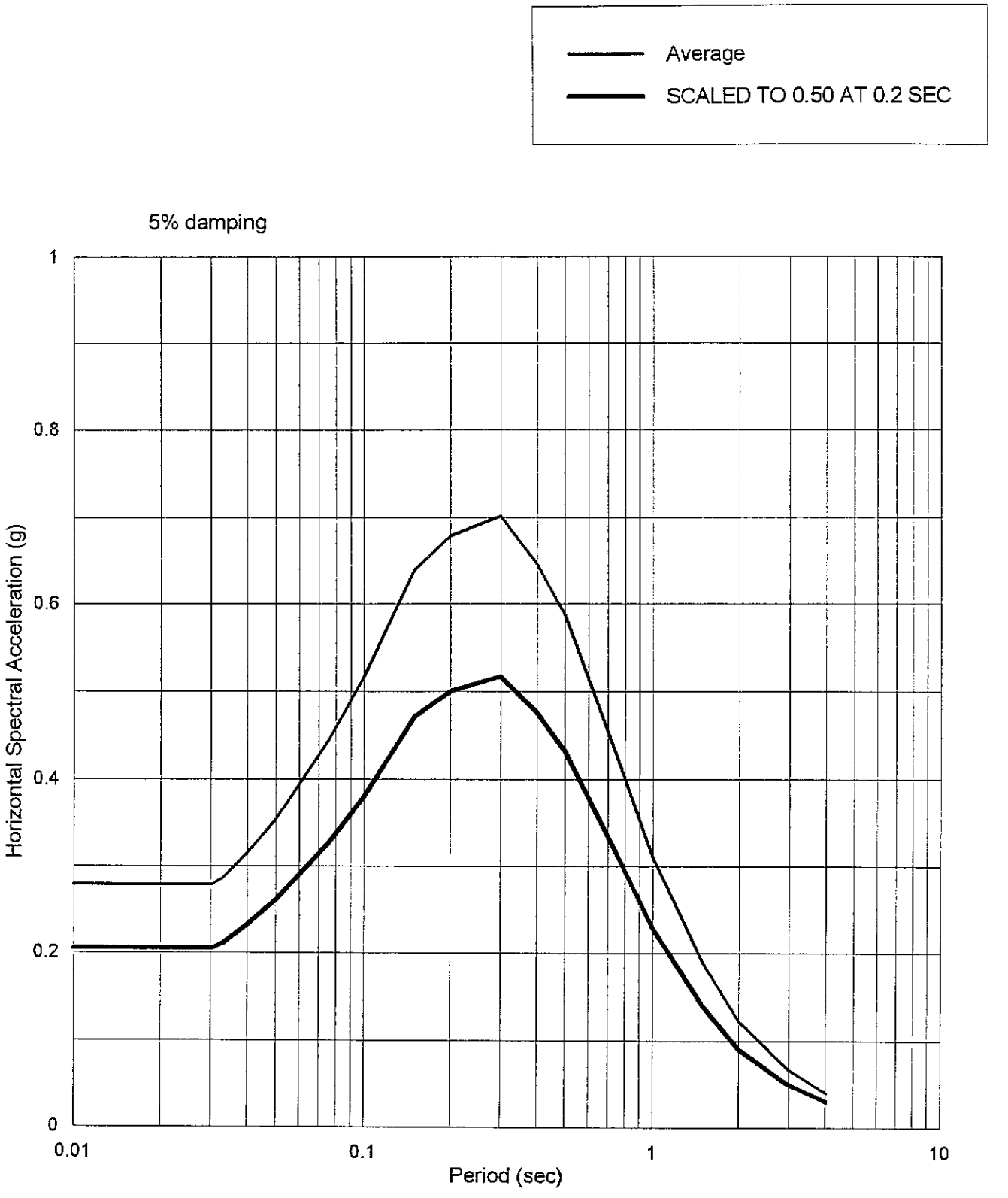
MEAN.GRF



M 6.2, Distance = 12.5 km

Project No. 91C0509	Los Alamos Seismic Hazards	NORMALIZED EMPIRICAL ACCELERATION RESPONSE SPECTRA FOR 500-YEAR DOMINANT EARTHQUAKE AT 1.0 SEC	Figure 10-10
Woodward-Clyde Federal Services			

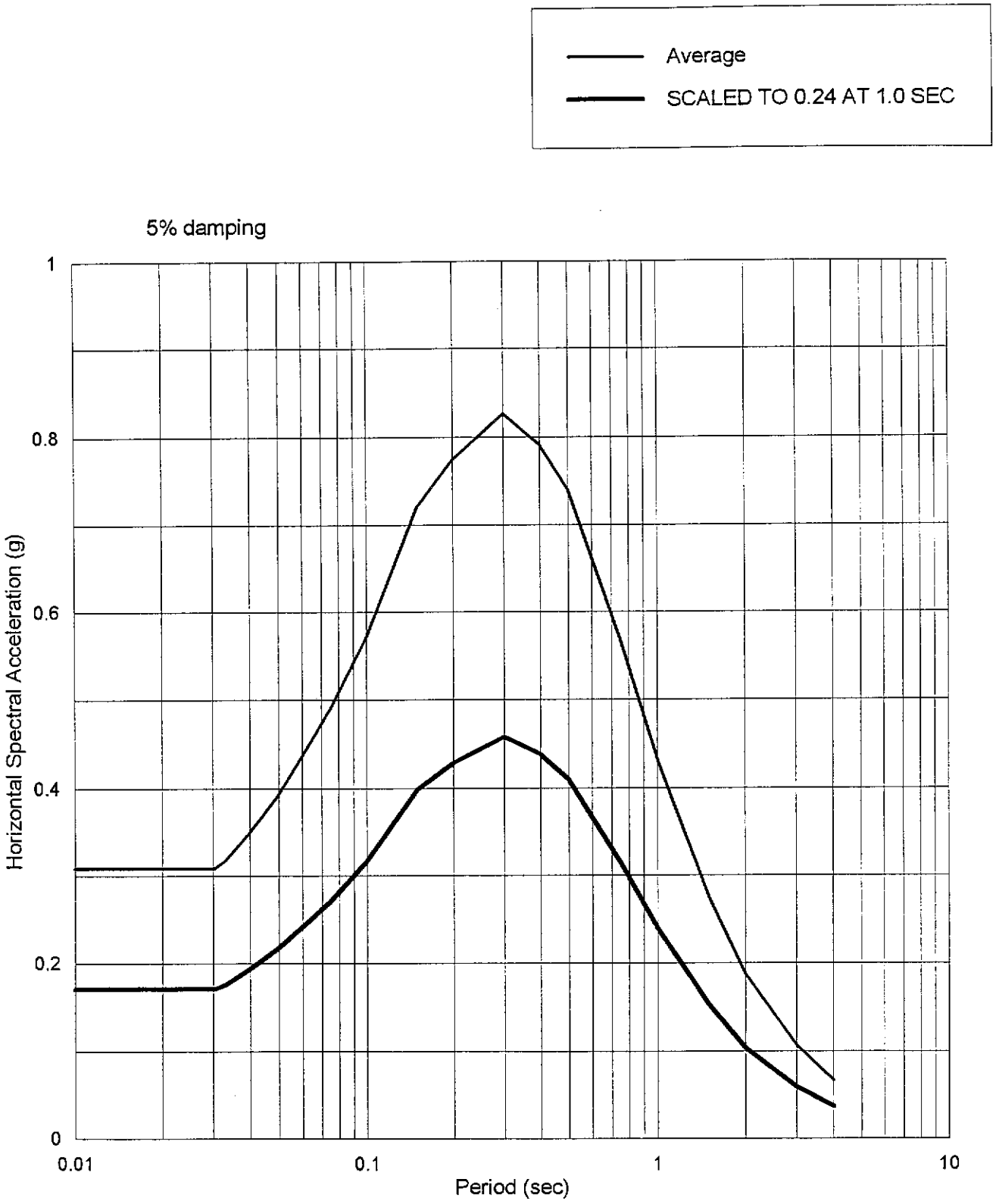
MEAN.GRF



M 6.0, Distance = 8.0 km

Project No. 91C0509	Los Alamos Seismic Hazards	NORMALIZED EMPIRICAL ACCELERATION RESPONSE SPECTRA FOR 1000-YEAR DOMINANT EARTHQUAKE AT 0.2 SEC	Figure 10-11
Woodward-Clyde Federal Services			

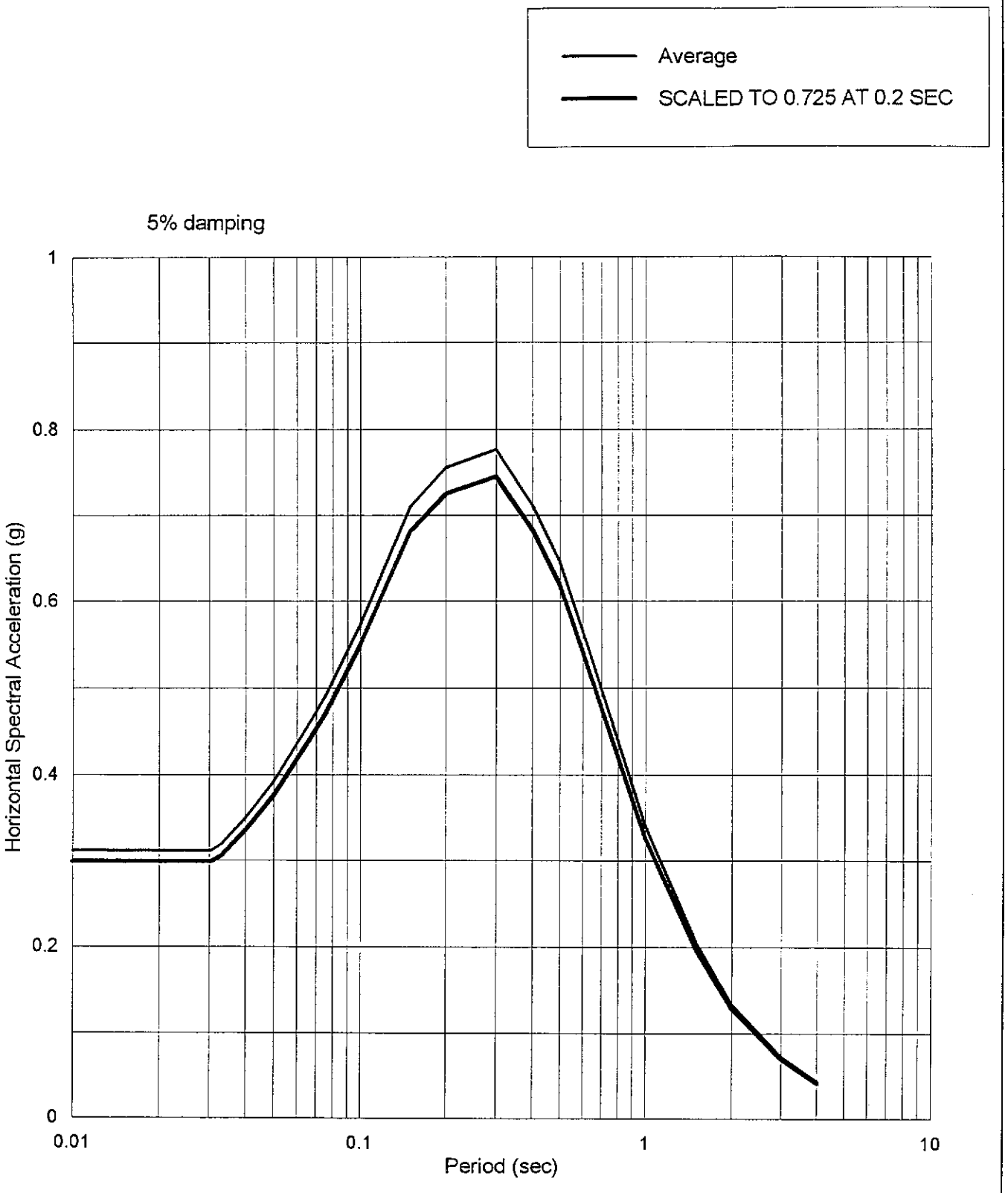
MEAN.GRF



M 6.3, Distance = 9.2 km

Project No. 91C0509	Los Alamos Seismic Hazards	NORMALIZED EMPIRICAL ACCELERATION RESPONSE SPECTRA FOR 1000-YEAR DOMINANT EARTHQUAKE AT 1.0 SEC	Figure 10-12
Woodward-Clyde Federal Services			

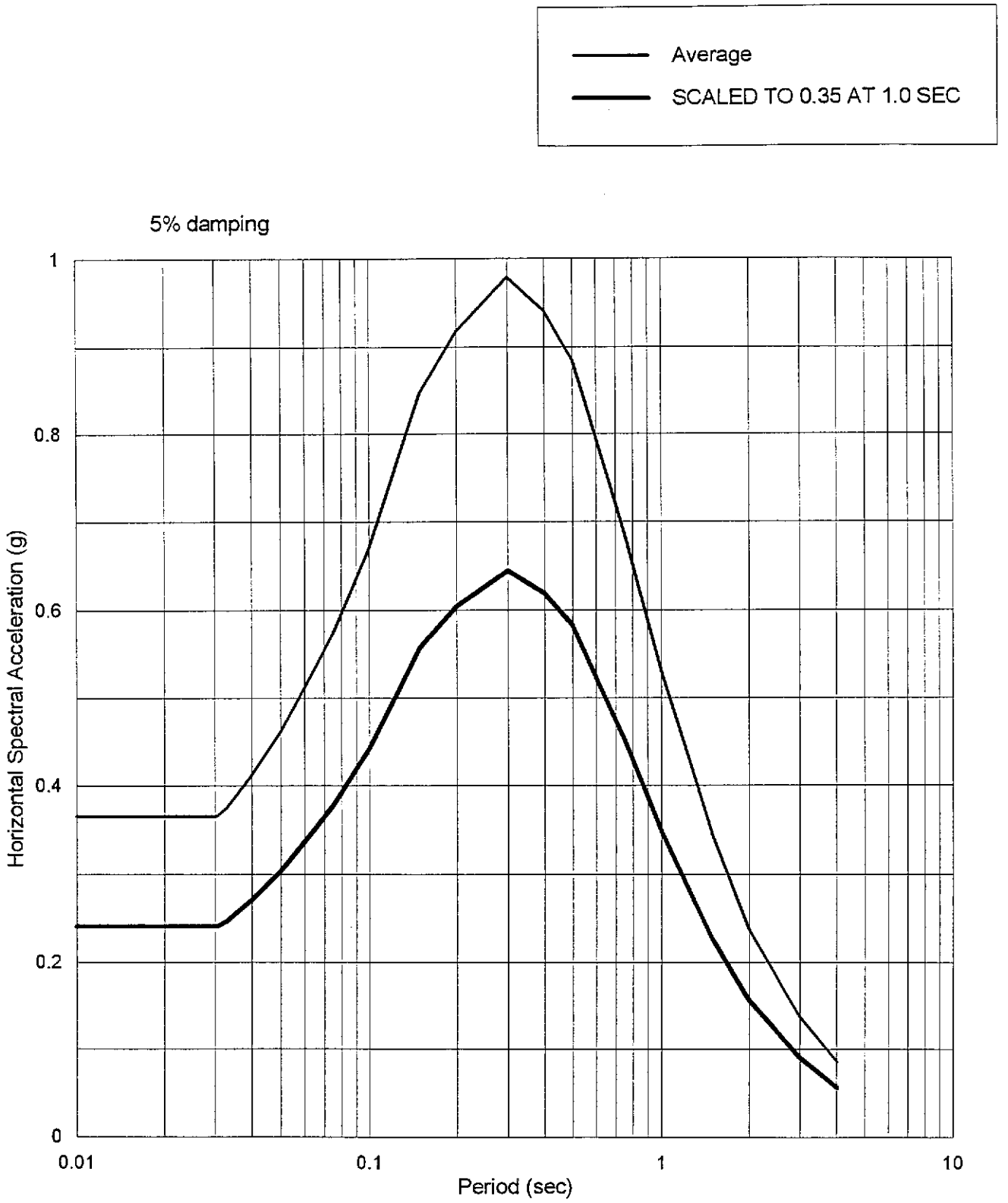
MEAN GRF



M 6.0, Distance = 6.0 km

Project No. 91C0509	Los Alamos Seismic Hazards	NORMALIZED EMPIRICAL ACCELERATION RESPONSE SPECTRA FOR 2000-YEAR DOMINANT EARTHQUAKE AT 0.2 SEC	Figure 10-13
Woodward-Clyde Federal Services			

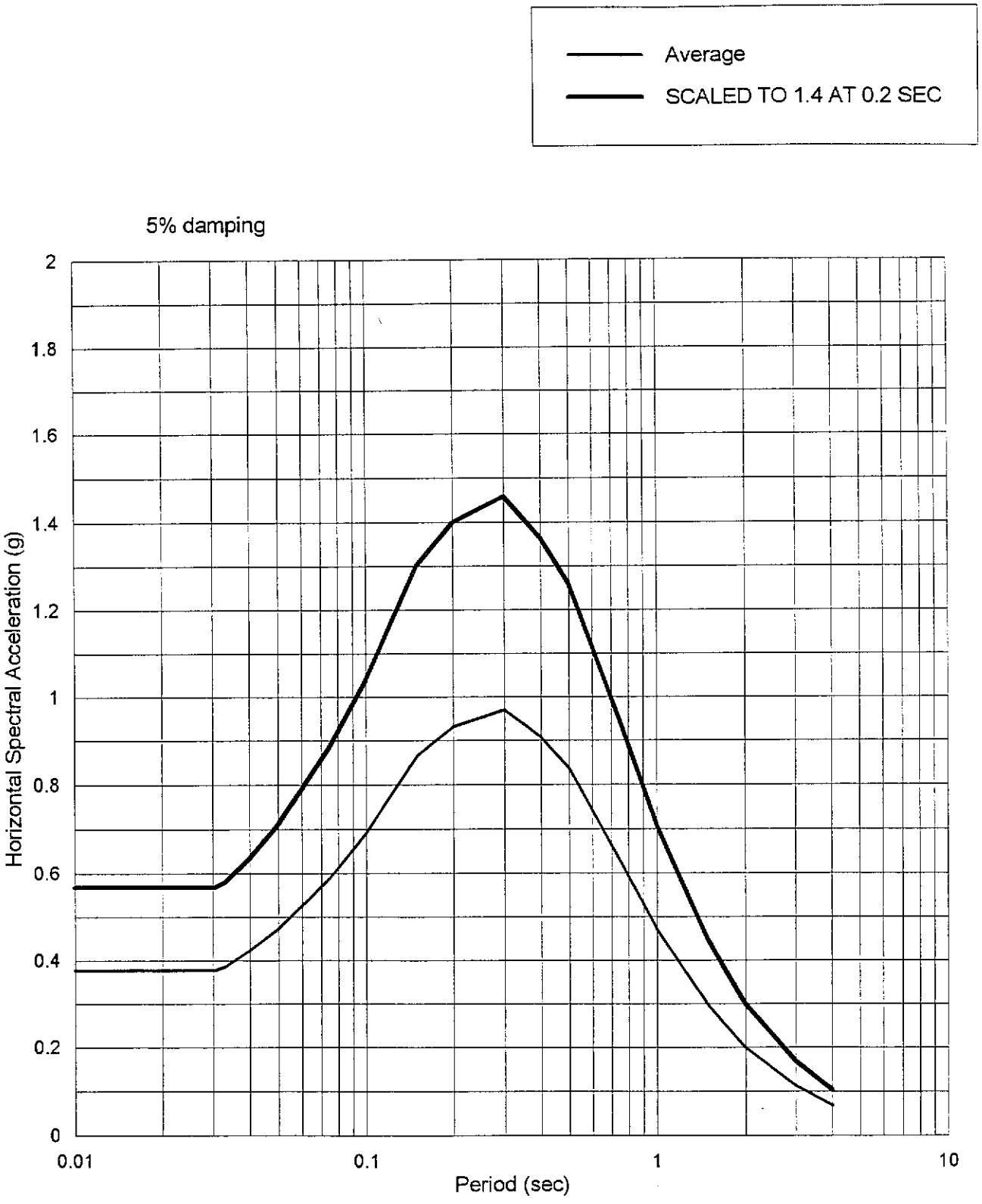
MEAN.GRF



M 6.4, Distance = 6.4 km

Project No. 91C0509	Los Alamos Seismic Hazards	NORMALIZED EMPIRICAL ACCELERATION RESPONSE SPECTRA FOR 2000-YEAR DOMINANT EARTHQUAKE AT 1.0 SEC	Figure 10-14
Woodward-Clyde Federal Services			

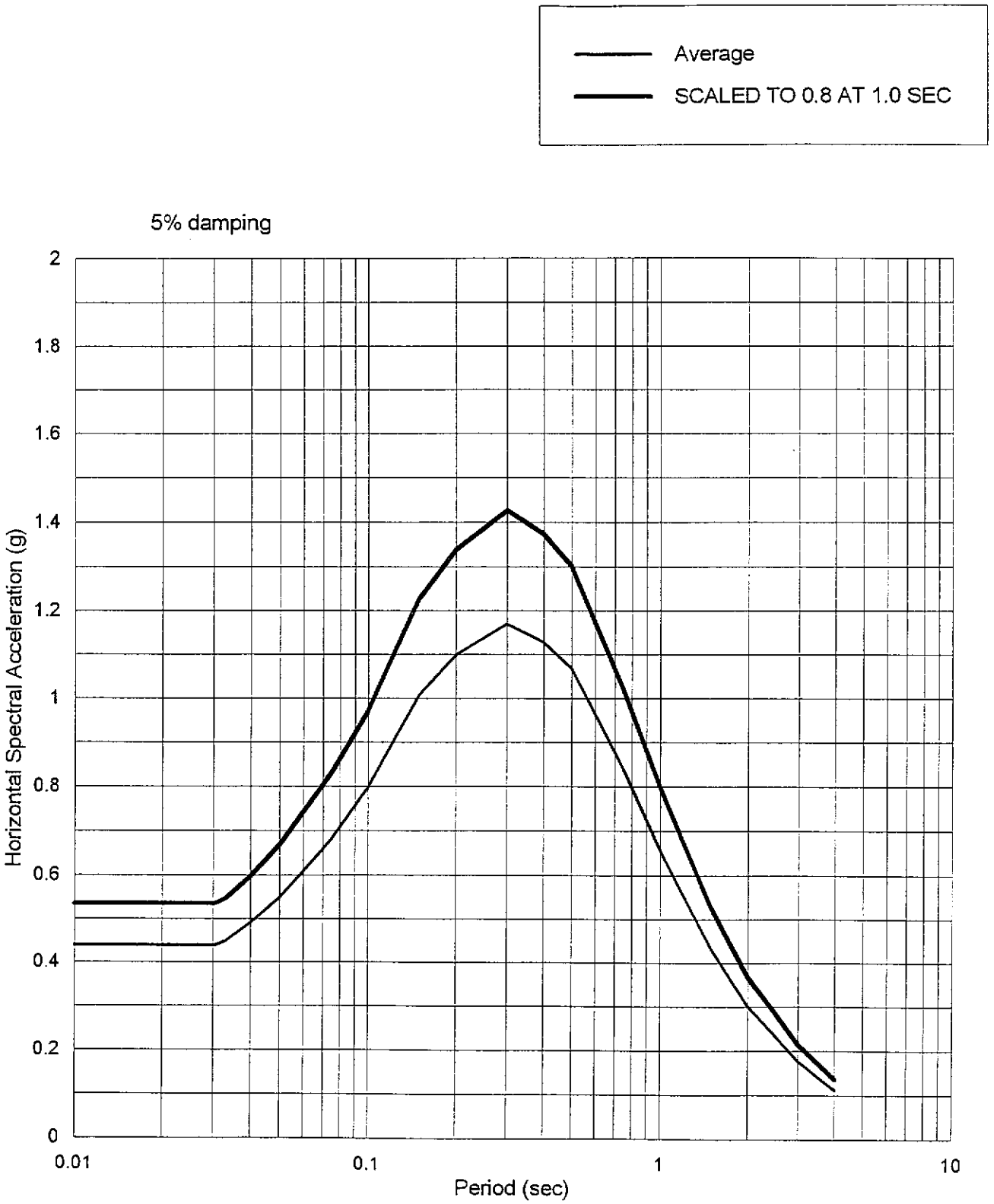
MEAN.GRF



M 6.2, Distance = 4.0 km

Project No. 91C0509	Los Alamos Seismic Hazards	NORMALIZED EMPIRICAL ACCELERATION RESPONSE SPECTRA FOR 10,000-YEAR DOMINANT EARTHQUAKE AT 0.2 SEC	Figure 10-15
Woodward-Clyde Federal Services			

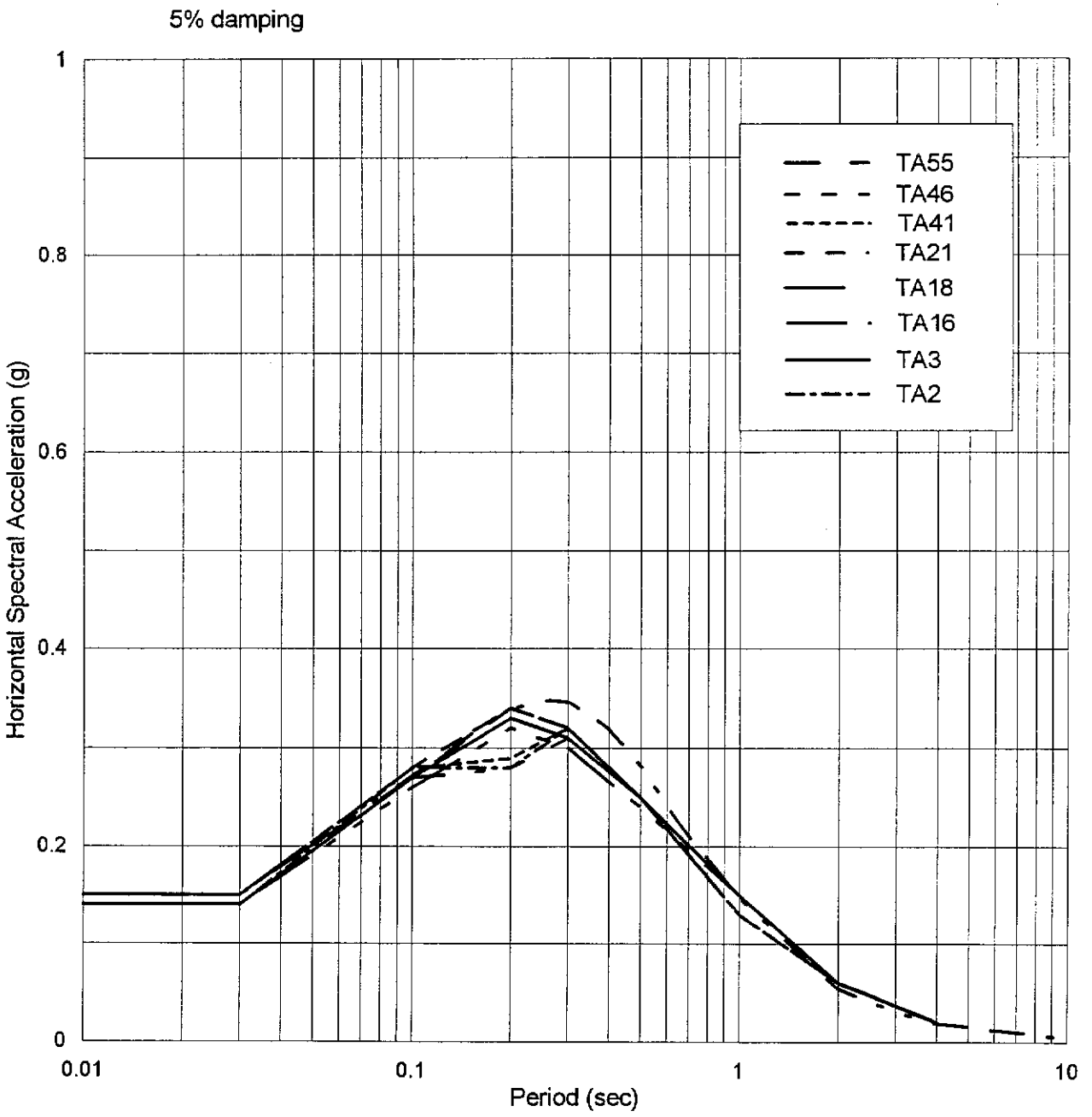
MEAN.GRF



M 6.5, Distance = 3.0 km

Project No. 91C0509	Los Alamos Seismic Hazards	NORMALIZED EMPIRICAL ACCELERATION RESPONSE SPECTRA FOR 10,000-YEAR DOMINANT EARTHQUAKE AT 1.0 SEC	Figure 10-16
Woodward-Clyde Federal Services			

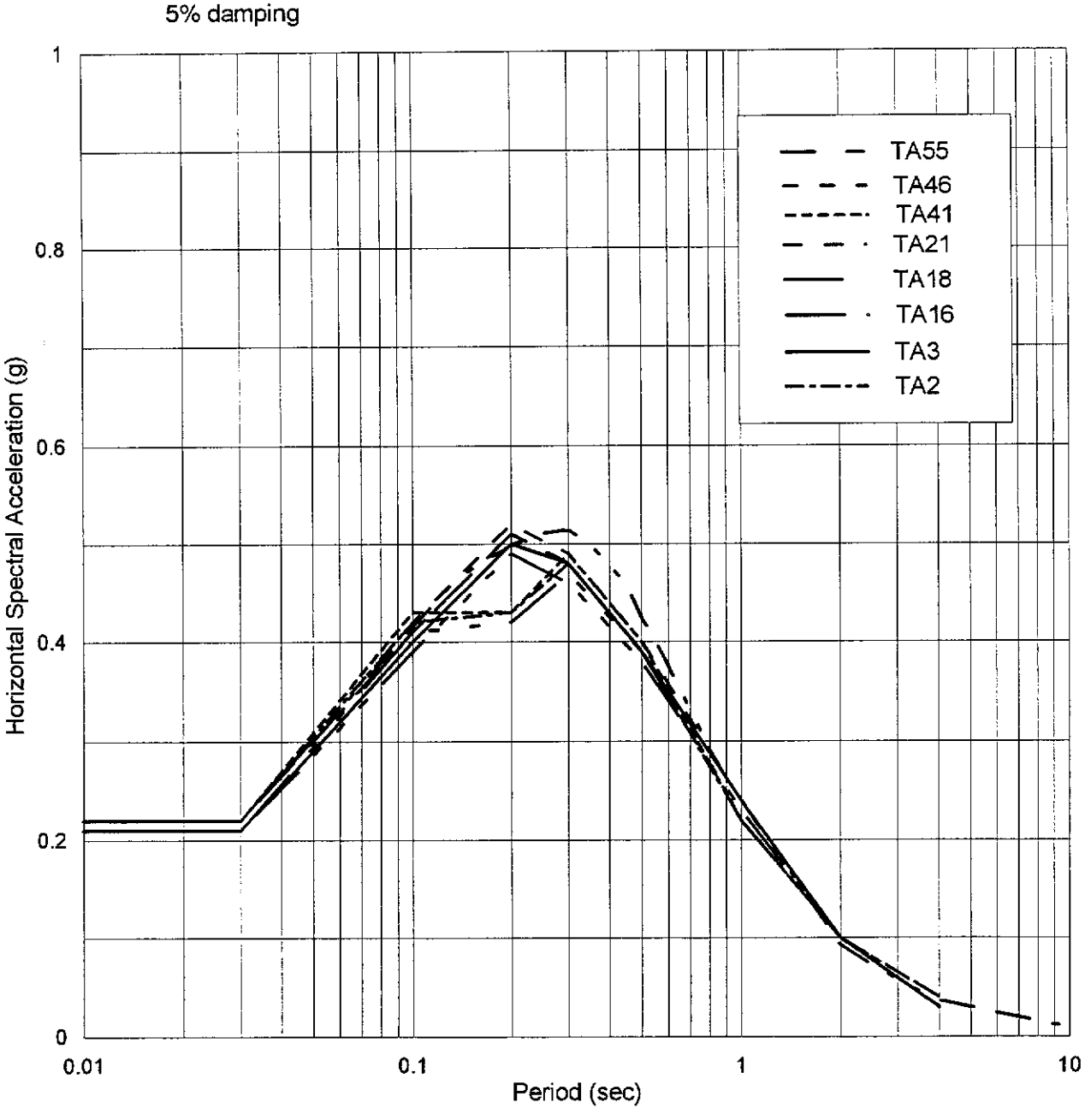
MEAN.GRF



DBE 500-year Horizontal Response Spectrum
Design PGA = 0.15 g

Project No. 91C0509	Los Alamos Seismic Hazards	RECOMMENDED DBE HORIZONTAL RESPONSE SPECTRUM FOR 500-YEAR RETURN PERIOD	Figure 10-17
Woodward-Clyde Federal Services			

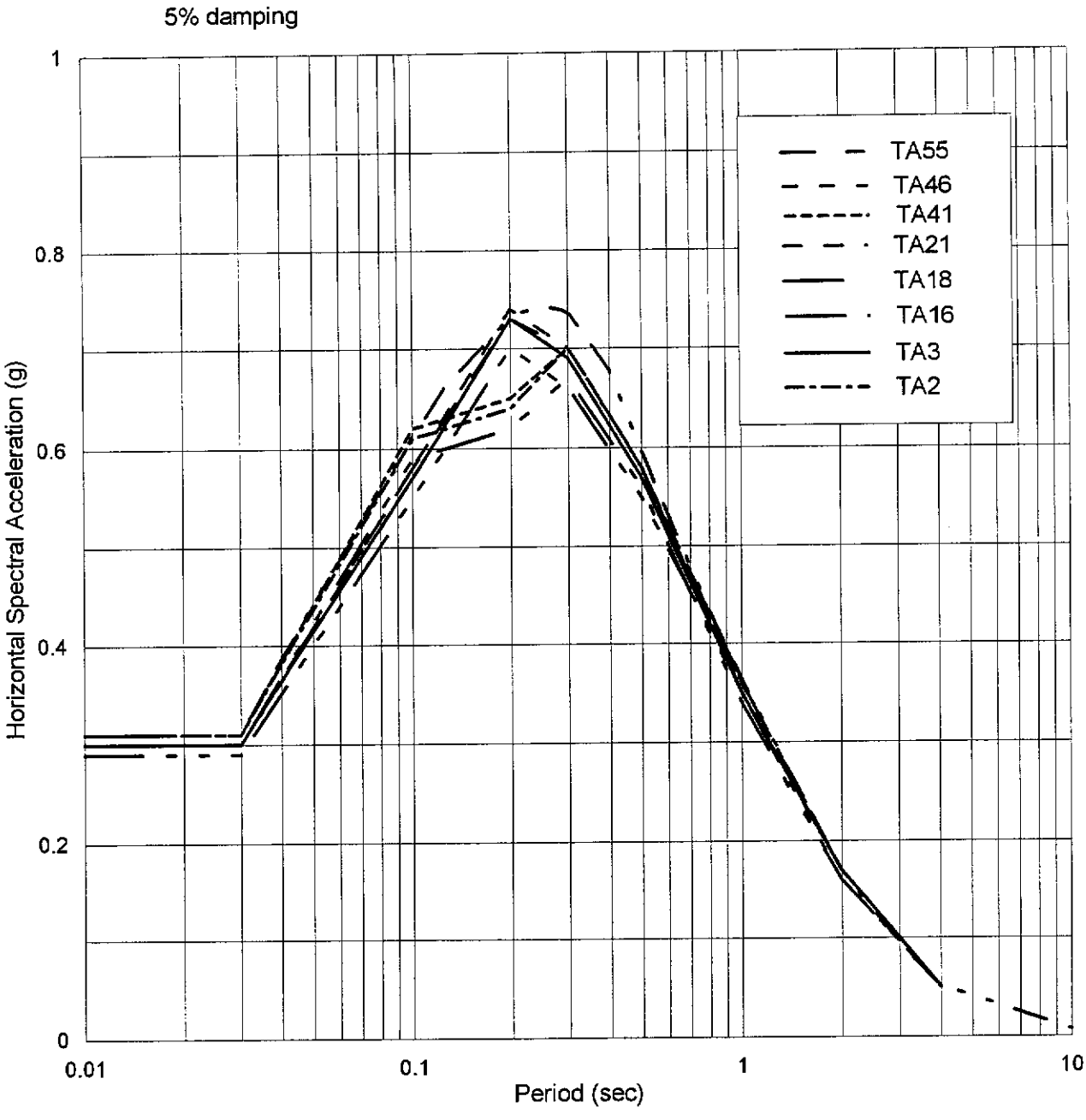
S-500.GRF



DBE 1000-year Horizontal Response Spectrum
Design PGA = 0.22 g

Project No. 91C0509	Los Alamos Seismic Hazards	RECOMMENDED DBE HORIZONTAL RESPONSE SPECTRUM FOR 1000-YEAR RETURN PERIOD	Figure 10-18
Woodward-Clyde Federal Services			

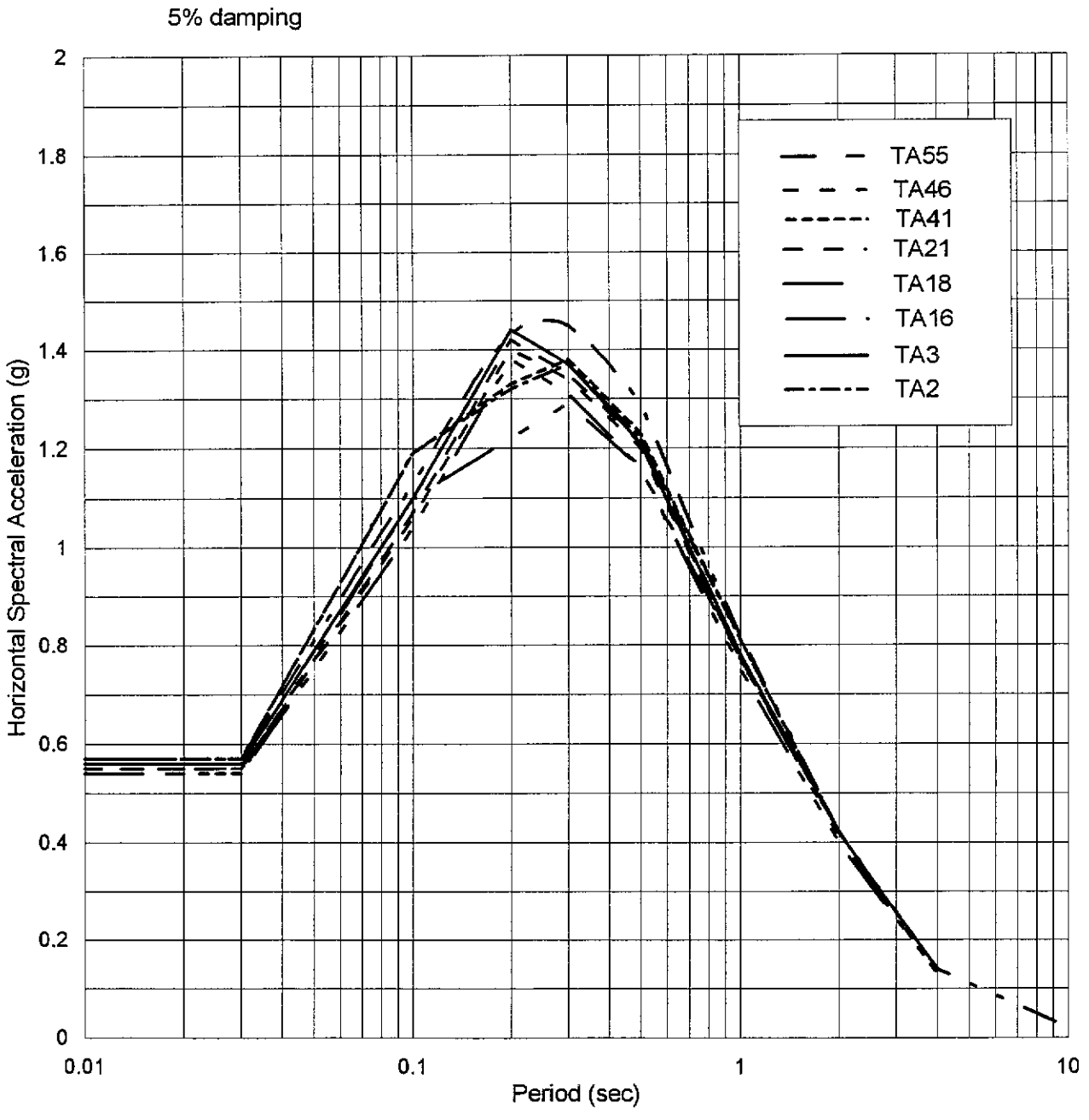
S-1000.GRF



DBE 2000-year Horizontal Response Spectrum
Design PGA = 0.31 g

Project No. 91C0509	Los Alamos Seismic Hazards	RECOMMENDED DBE HORIZONTAL RESPONSE SPECTRUM FOR 2000-YEAR RETURN PERIOD	Figure 10-19
Woodward-Clyde Federal Services			

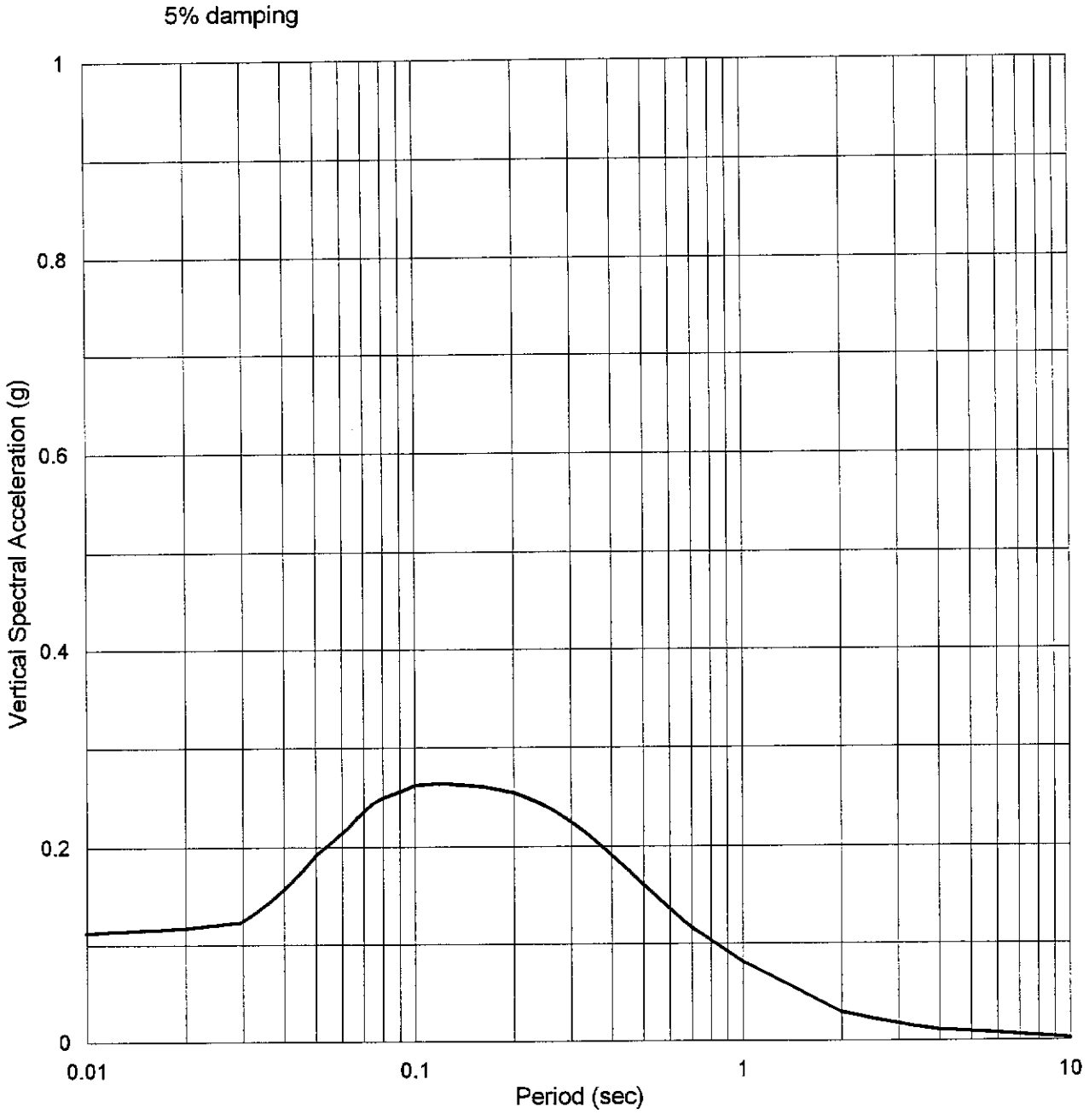
S-2000.GRF



DBE 10,000-year Horizontal Response Spectrum
Design PGA = 0.57 g

Project No. 91C0509	Los Alamos Seismic Hazards	COMPARISON OF THE MEAN EQUAL HAZARD SPECTRA FOR A 10,000-YEAR RETURN PERIOD	Figure 10-20
Woodward-Clyde Federal Services			

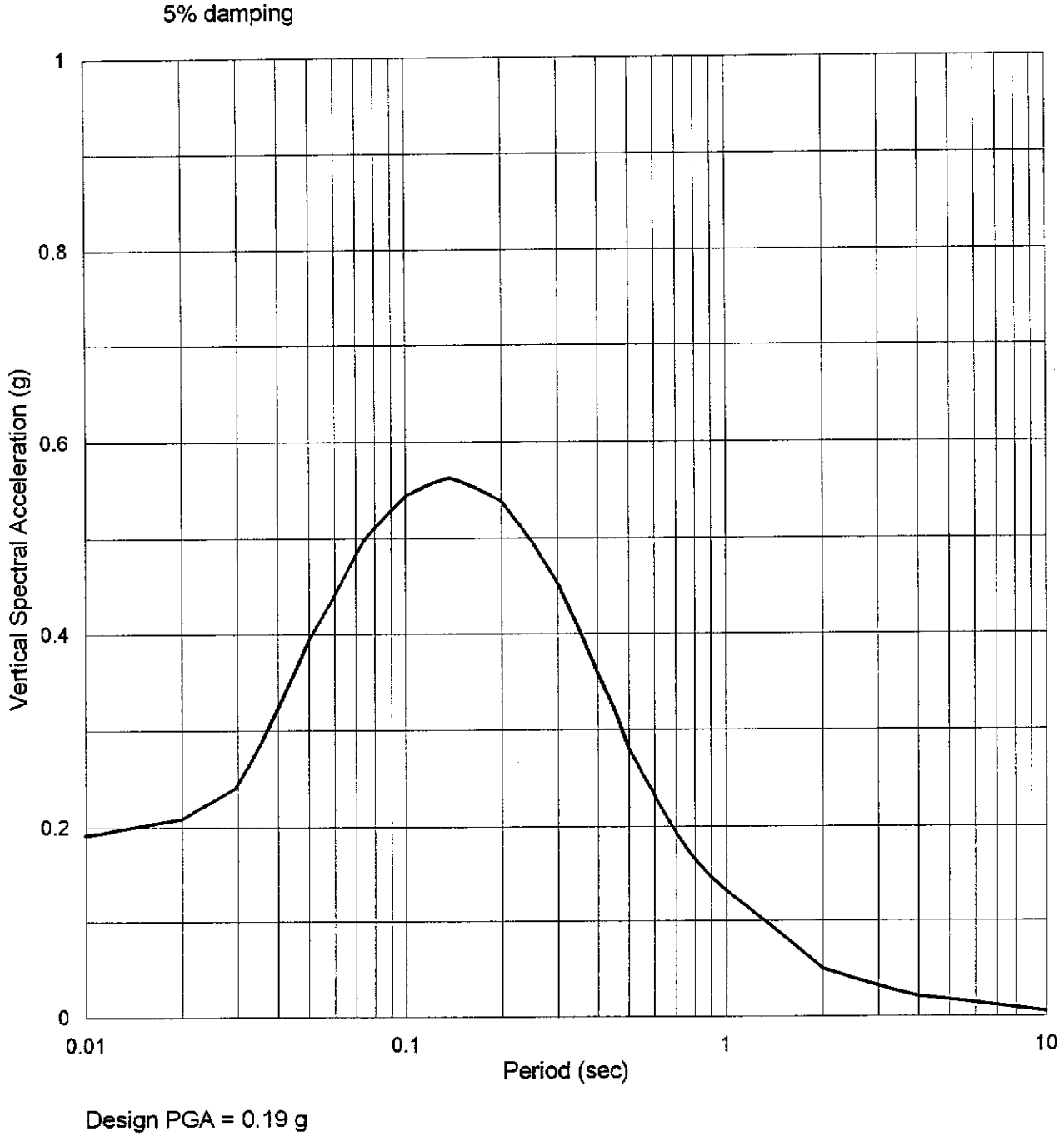
S-10000.GRF



Design PGA = 0.11 g

Project No. 91C0509	Los Alamos Seismic Hazards	RECOMMENDED DBE VERTICAL RESPONSE SPECTRUM FOR 500-YEAR RETURN PERIOD	Figure 10-21
Woodward-Clyde Federal Services			

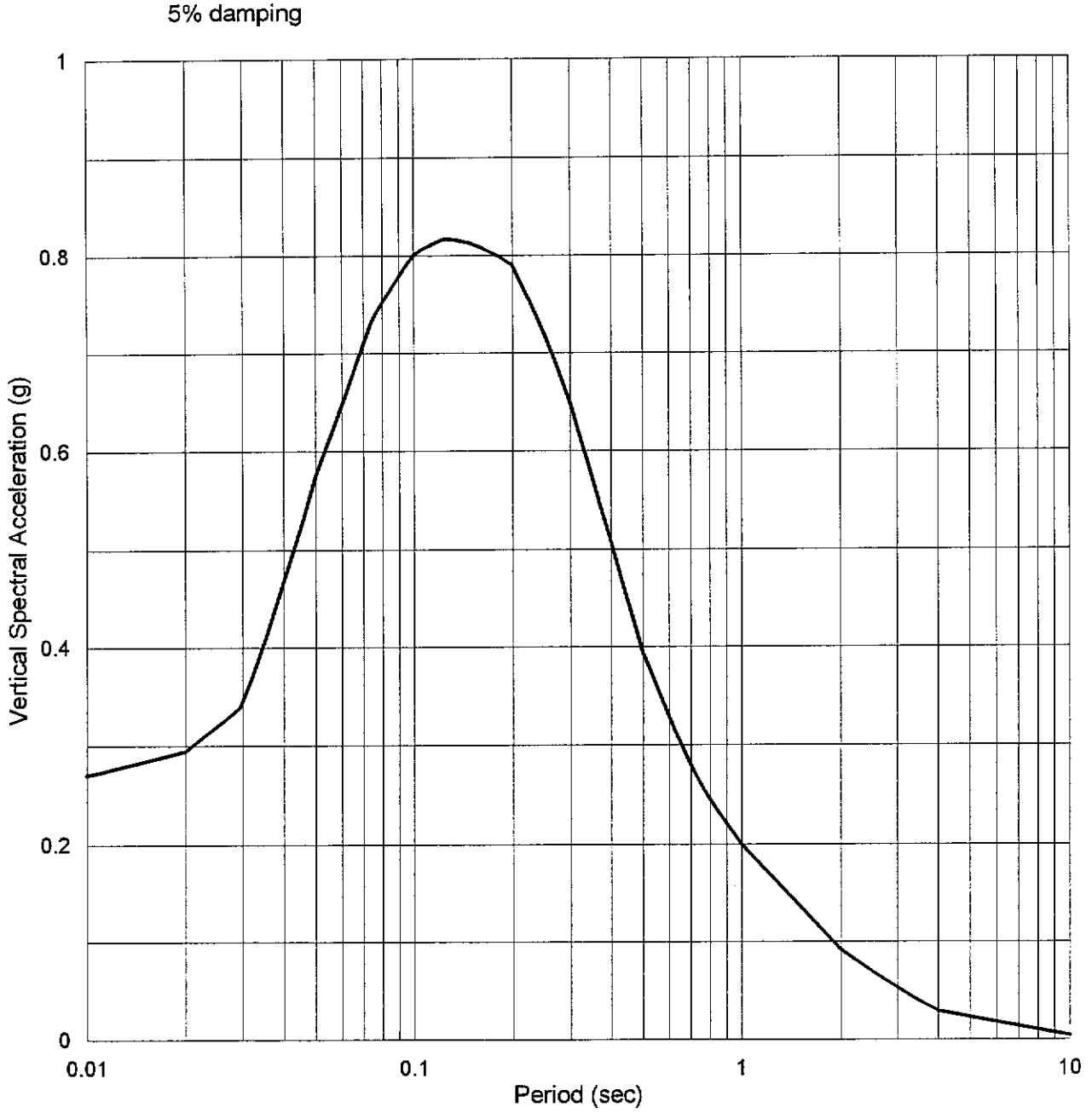
S-500.GRF



Design PGA = 0.19 g

Project No. 91C0509	Los Alamos Seismic Hazards	RECOMMENDED DBE VERTICAL RESPONSE SPECTRUM FOR 1000-YEAR RETURN PERIOD	Figure 10-22
Woodward-Clyde Federal Services			

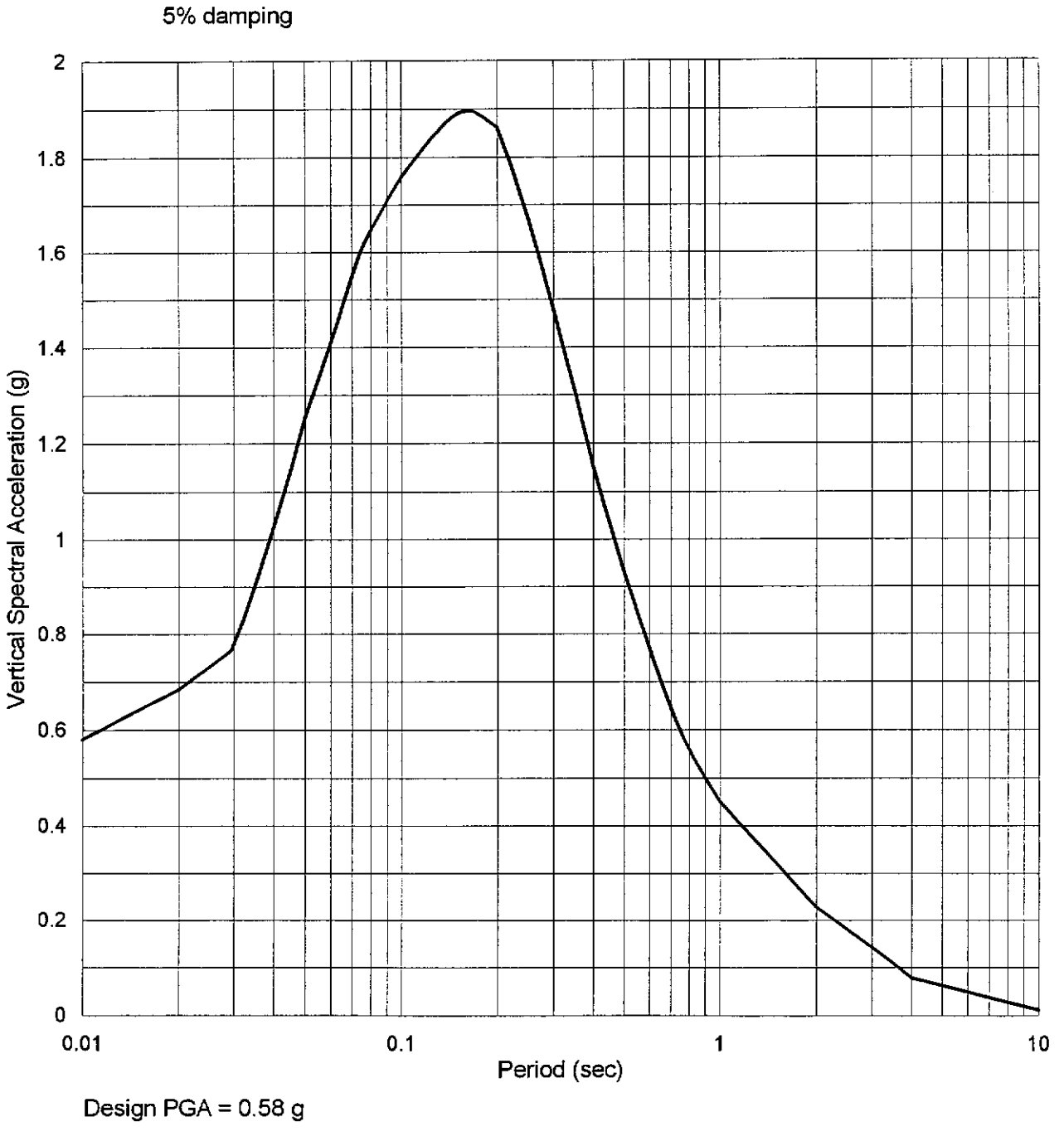
S-500.GRF



Design PGA = 0.27 g

Project No. 91C0509	Los Alamos Seismic Hazards	RECOMMENDED DBE VERTICAL RESPONSE SPECTRUM FOR 2000-YEAR RETURN PERIOD	Figure 10-23
Woodward-Clyde Federal Services			

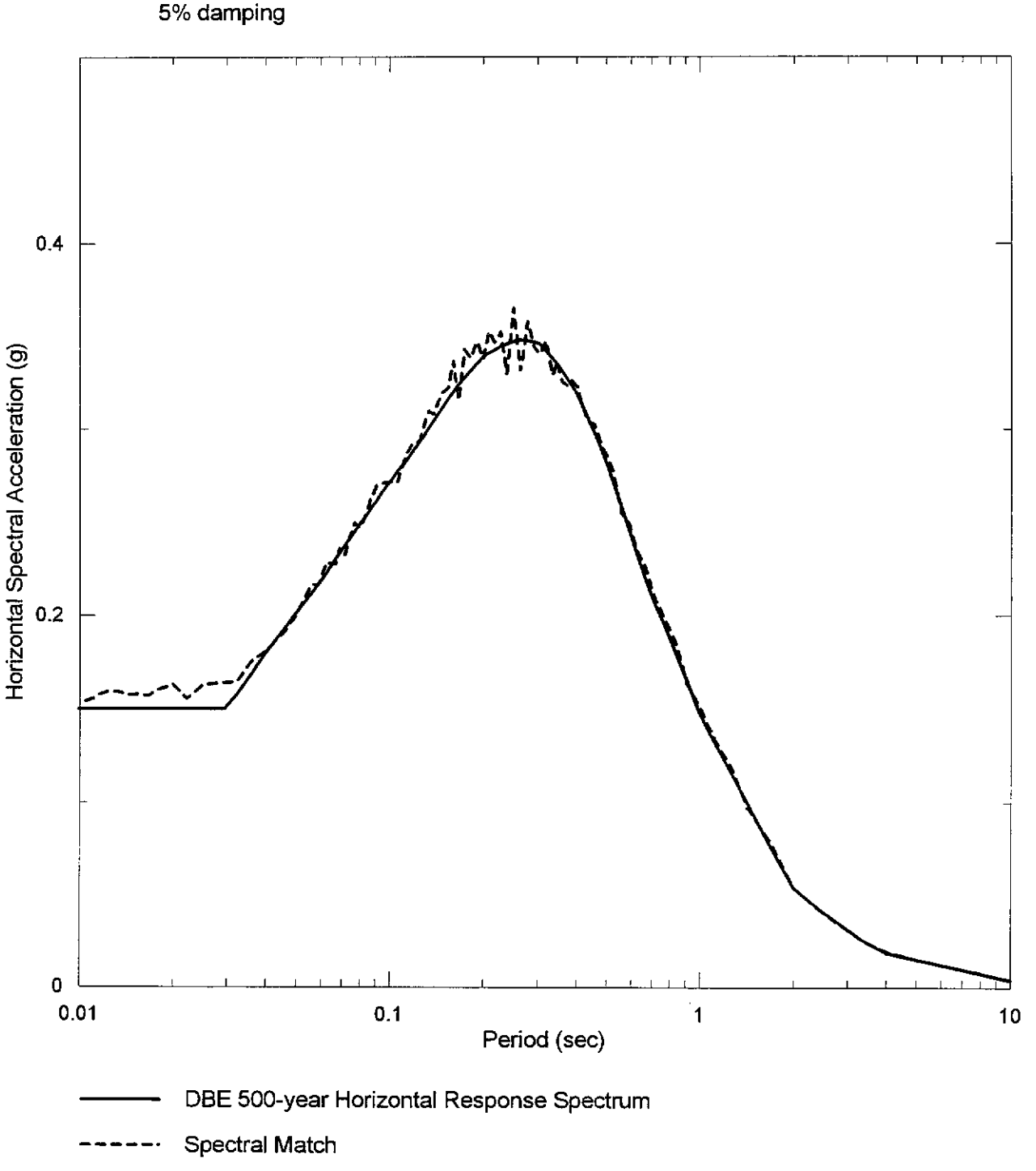
S-500.GRF



Design PGA = 0.58 g

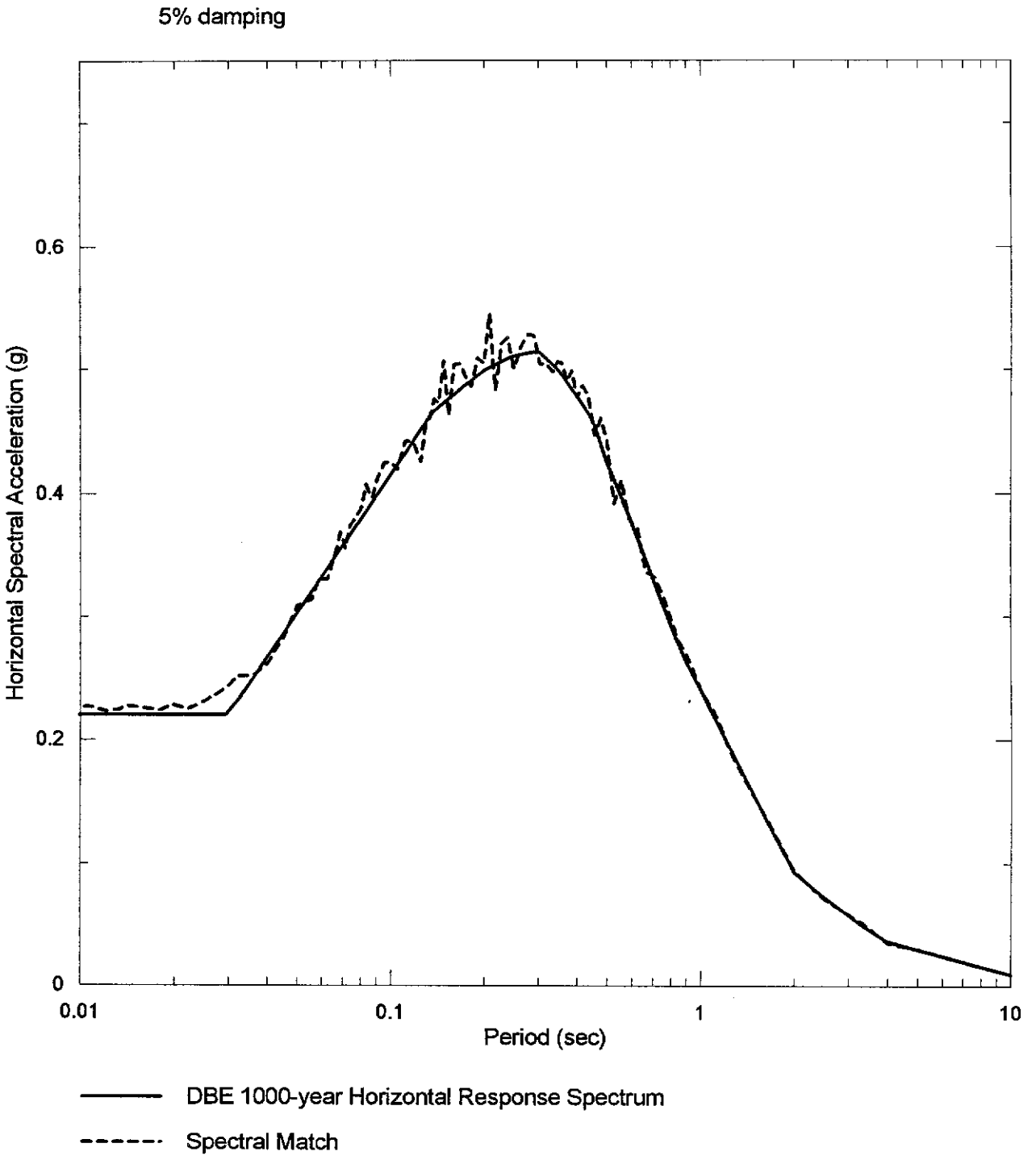
Project No. 91C0509	Los Alamos Seismic Hazards	RECOMMENDED DBE VERTICAL RESPONSE SPECTRUM FOR 10,000-YEAR RETURN PERIOD	Figure 10-24
Woodward-Clyde Federal Services			

S-500.GRF



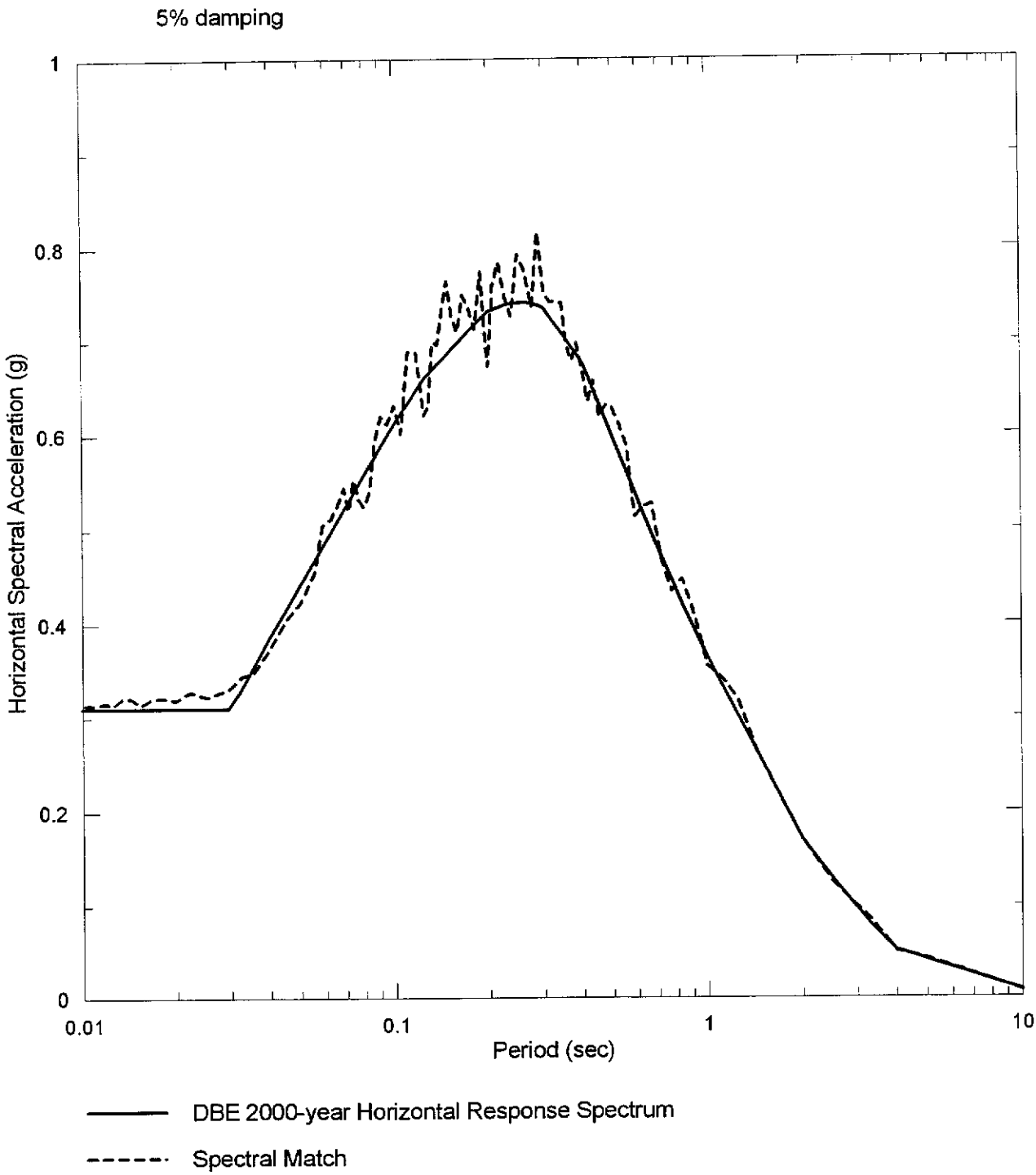
Project No. 91C0509	Los Alamos Seismic Hazards	SPECTRAL MATCH TO DBE HORIZONTAL RESPONSE SPECTRUM FOR 500-YEAR RETURN PERIOD	Figure 10-25
Woodward-Clyde Federal Services			

S-500.GRF



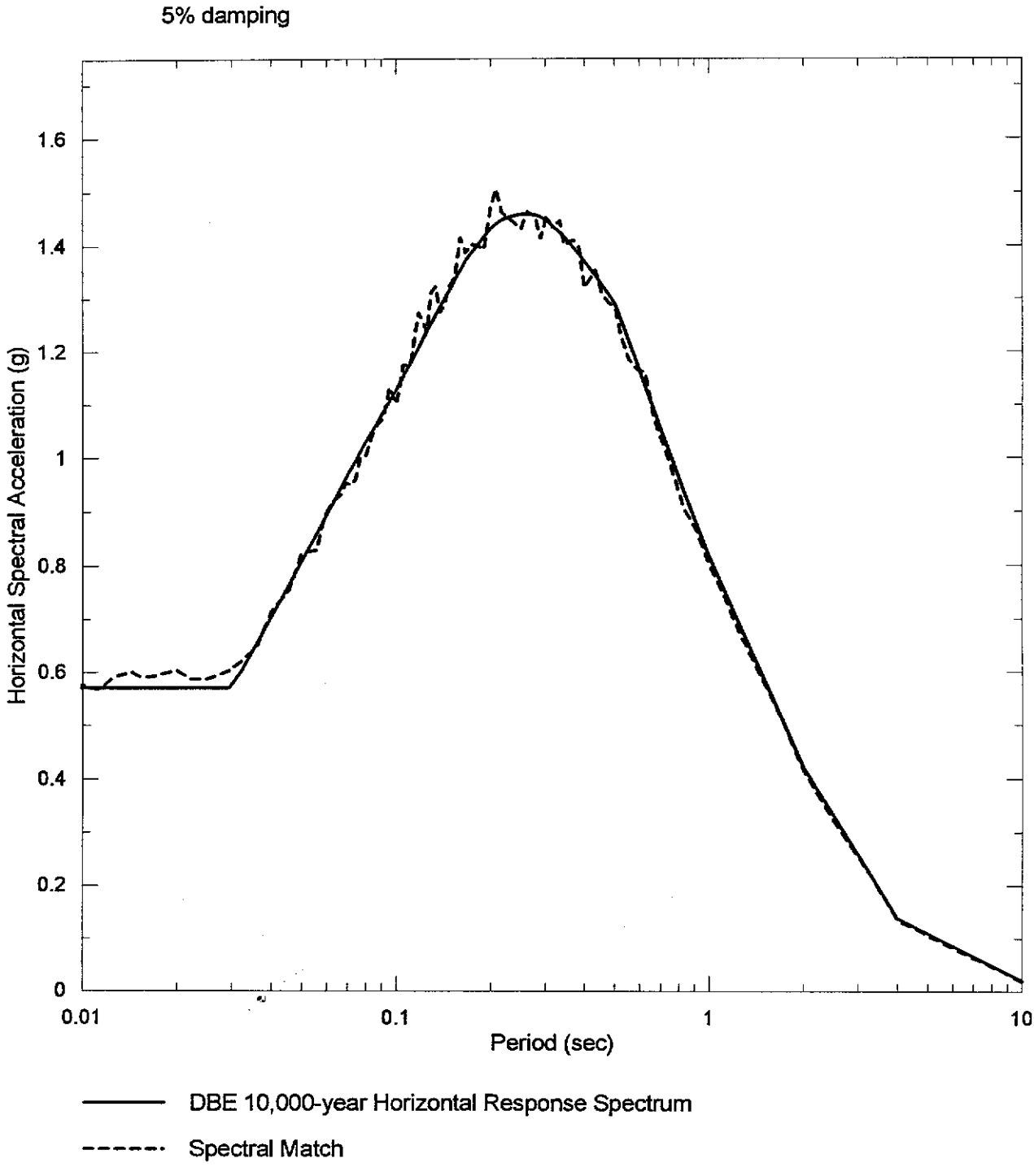
Project No. 91C0509	Los Alamos Seismic Hazards	SPECTRAL MATCH TO DBE HORIZONTAL RESPONSE SPECTRUM FOR 1000-YEAR RETURN PERIOD	Figure 10-26
Woodward-Clyde Federal Services			

S-500.GRF



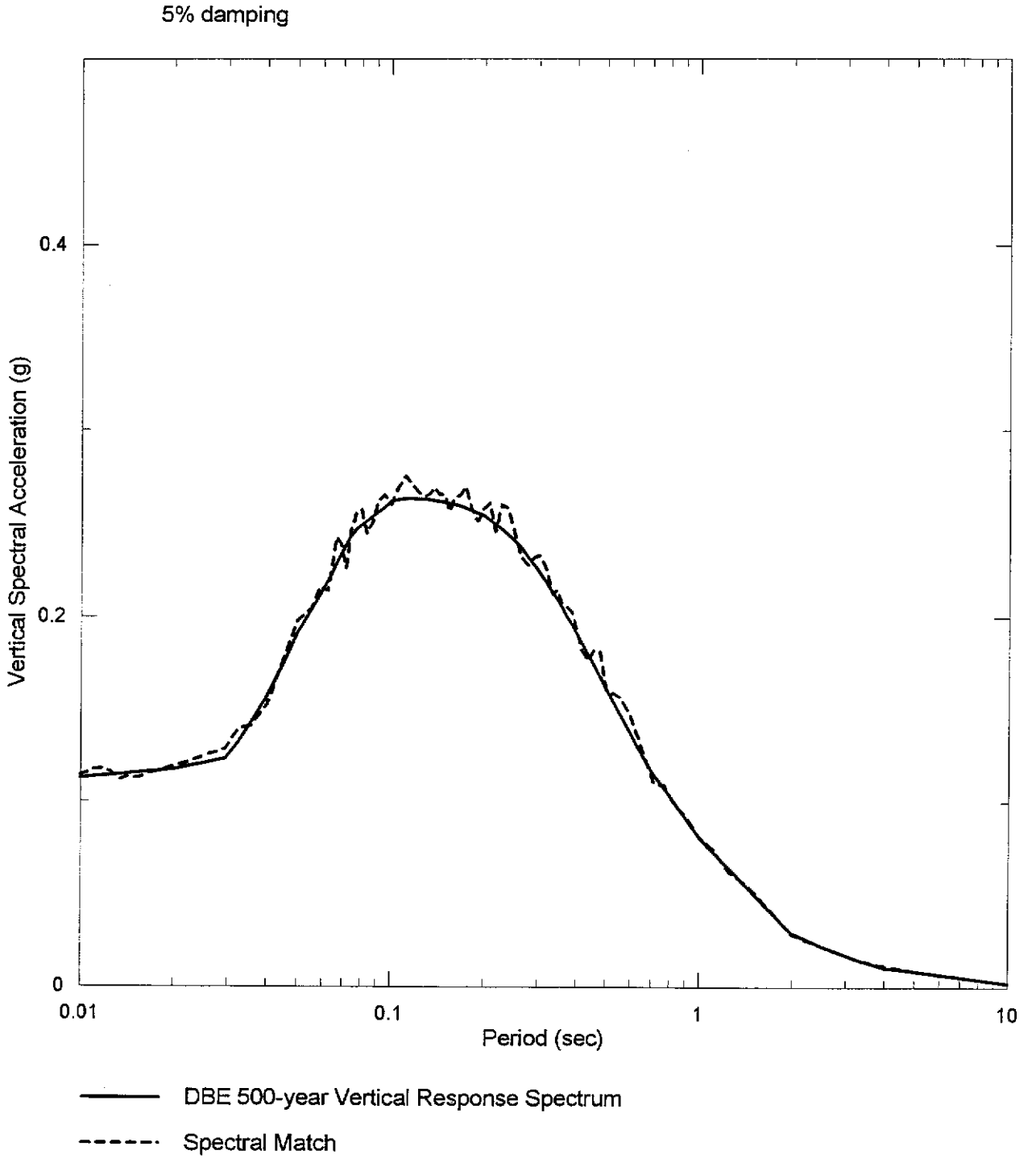
Project No. 91C0509	Los Alamos Seismic Hazards	SPECTRAL MATCH TO DBE HORIZONTAL RESPONSE SPECTRUM FOR 2000-YEAR RETURN PERIOD	Figure 10-27
Woodward-Clyde Federal Services			

S-500.GRF



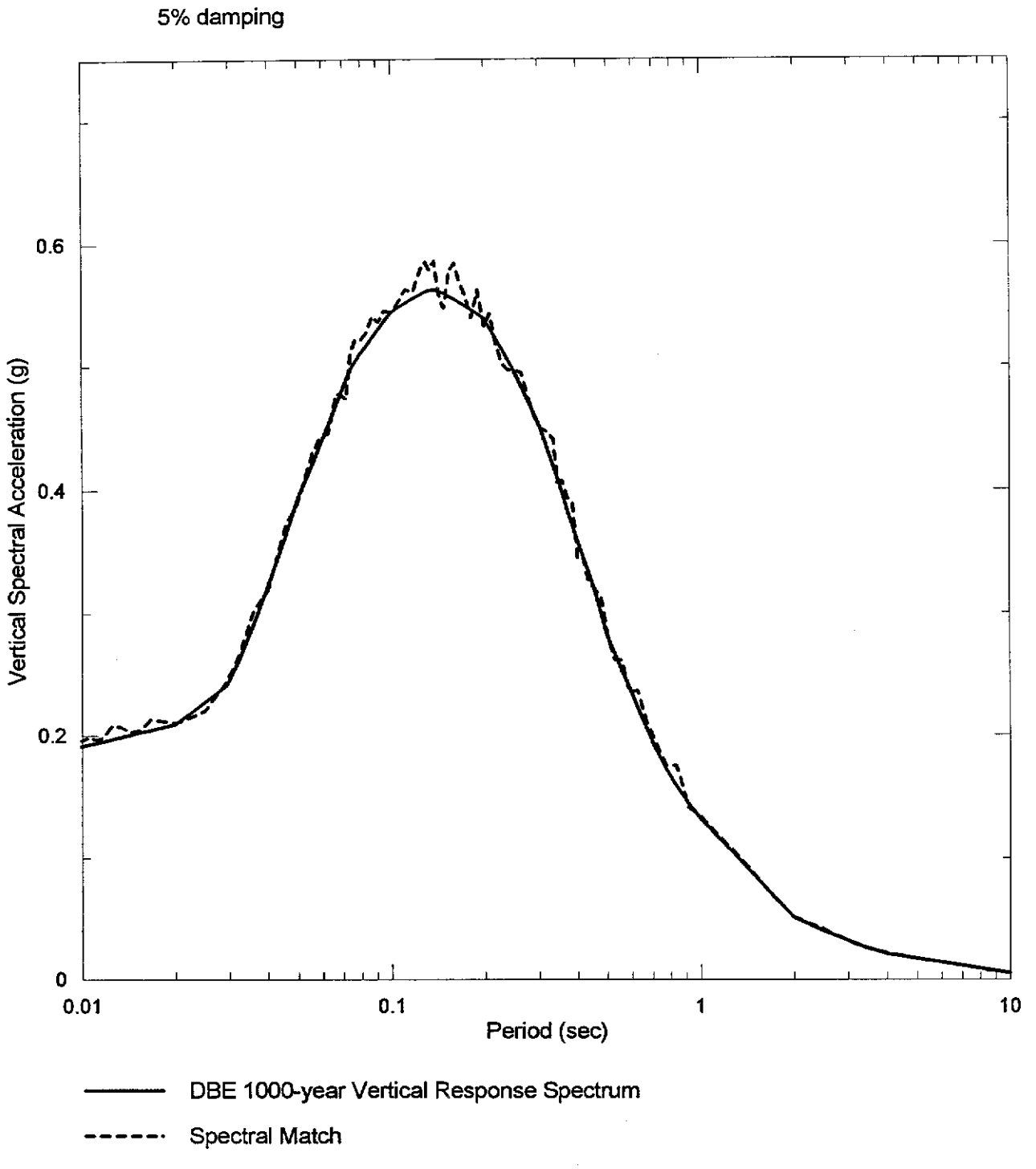
Project No. 91C0509	Los Alamos Seismic Hazards	SPECTRAL MATCH TO DBE HORIZONTAL RESPONSE SPECTRUM FOR 10,000-YEAR RETURN PERIOD	Figure 10-28
Woodward-Clyde Federal Services			

S-500.GRF



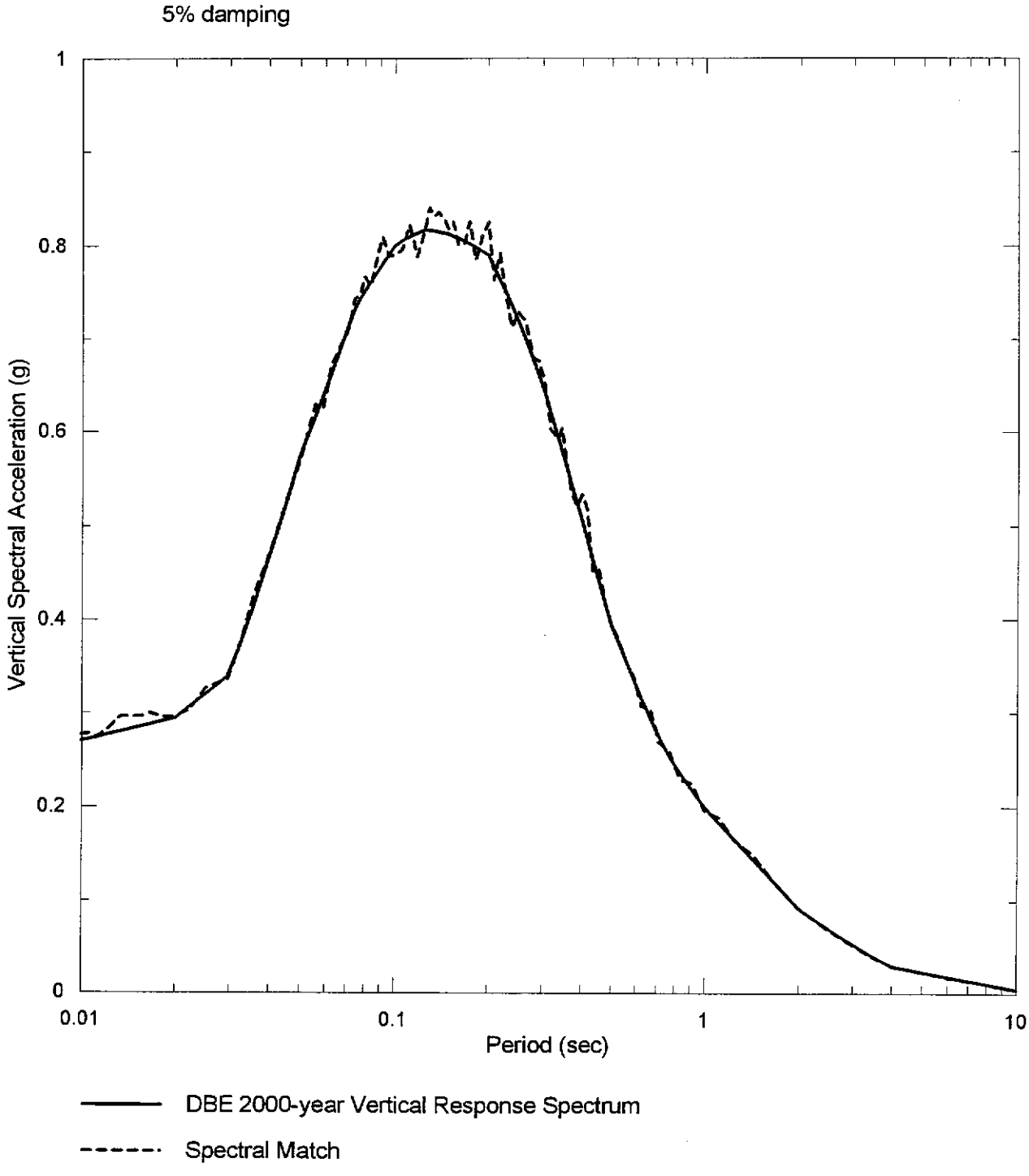
Project No. 91C0509	Los Alamos Seismic Hazards	SPECTRAL MATCH TO DBE VERTICAL RESPONSE SPECTRUM FOR 500-YEAR RETURN PERIOD	Figure 10-29
Woodward-Clyde Federal Services			

S-500.GRF



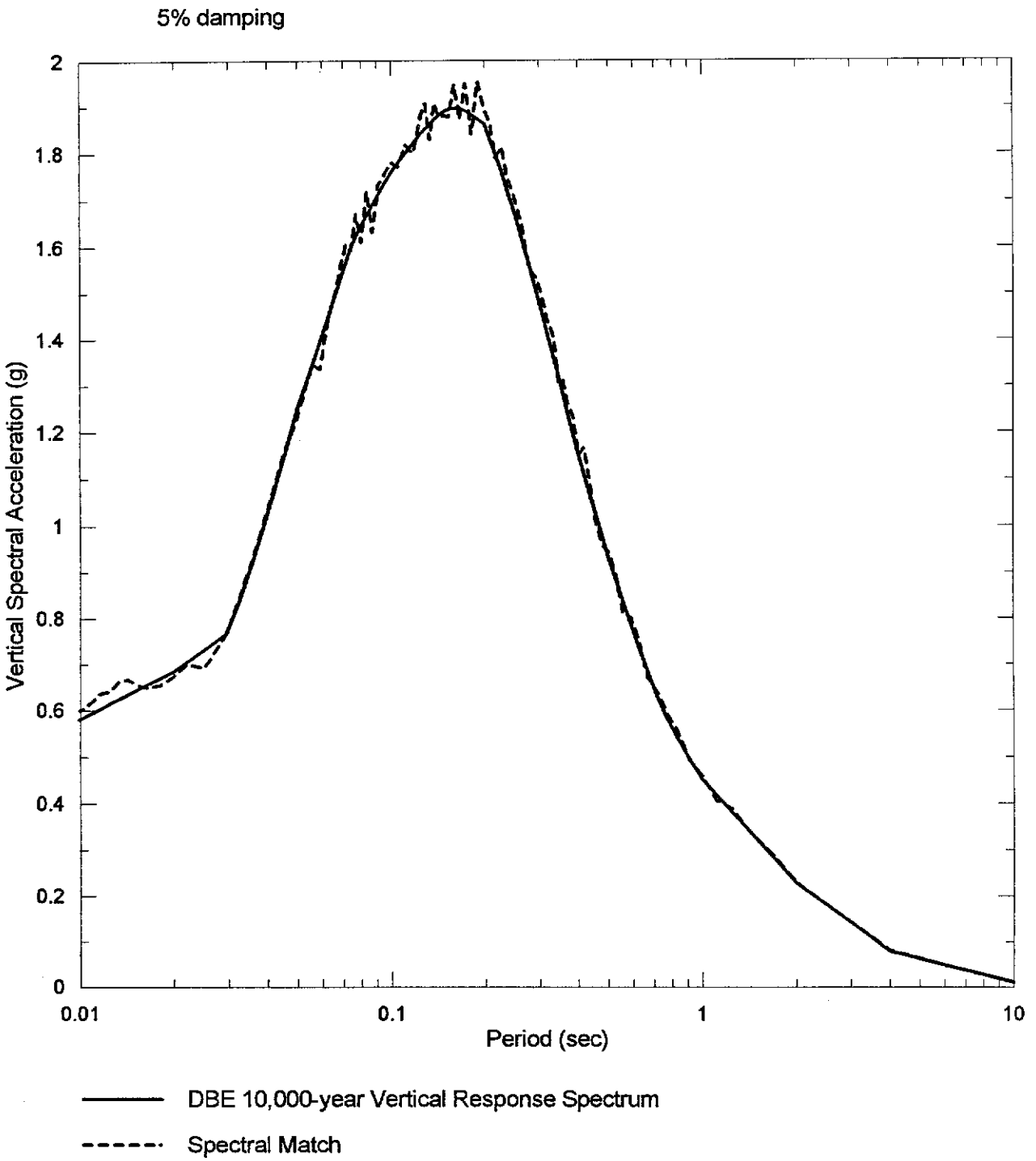
Project No. 91C0509	Los Alamos Seismic Hazards	SPECTRAL MATCH TO DBE VERTICAL RESPONSE SPECTRUM FOR 1000-YEAR RETURN PERIOD	Figure 10-30
Woodward-Clyde Federal Services			

S-500.GRF



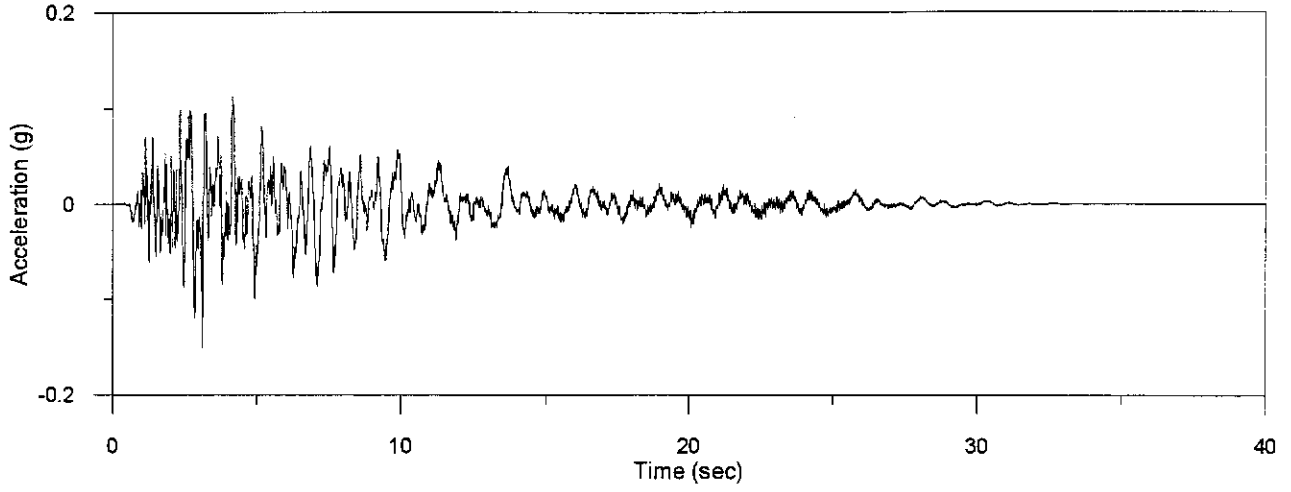
Project No. 91C0509	Los Alamos Seismic Hazards	SPECTRAL MATCH TO DBE VERTICAL RESPONSE SPECTRUM FOR 2000-YEAR RETURN PERIOD	Figure 10-31
Woodward-Clyde Federal Services			

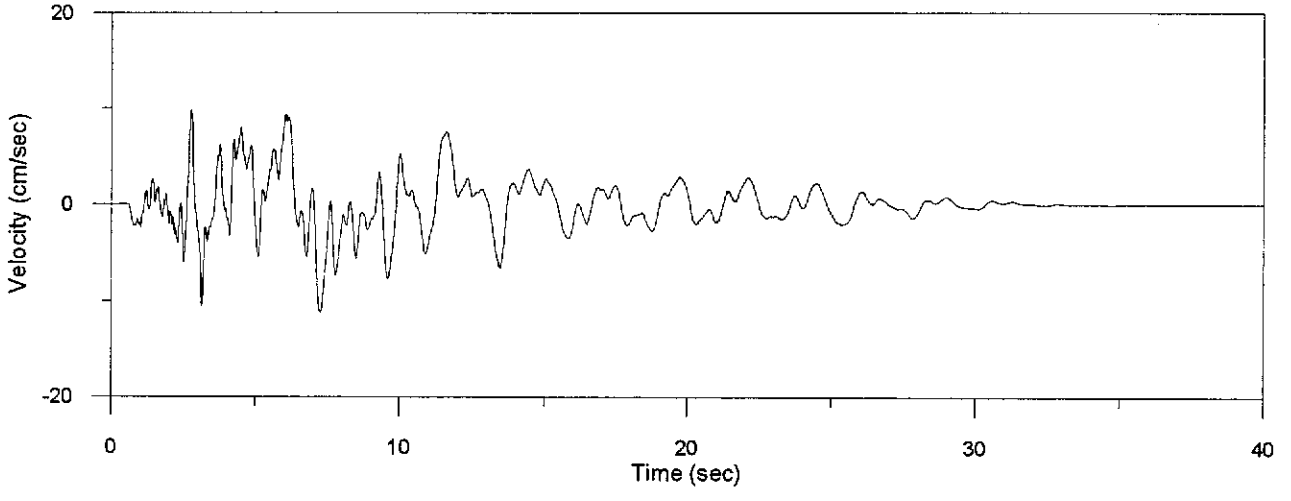
S-500.GRF

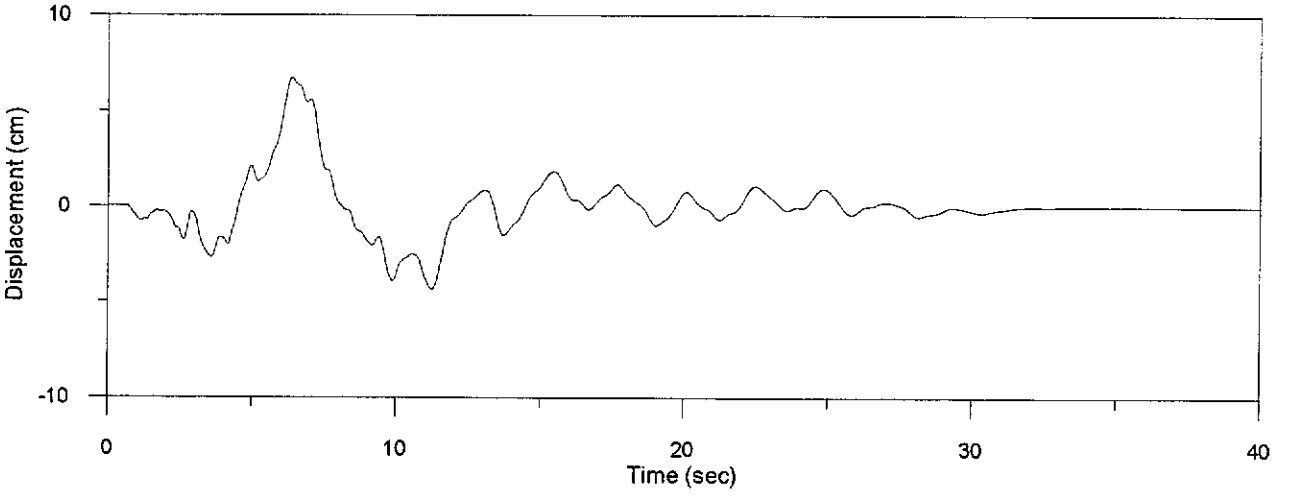


Project No. 91C0509	Los Alamos Seismic Hazards	SPECTRAL MATCH TO DBE VERTICAL RESPONSE SPECTRUM FOR 10,000-YEAR RETURN PERIOD	Figure 10-32
Woodward-Clyde Federal Services			

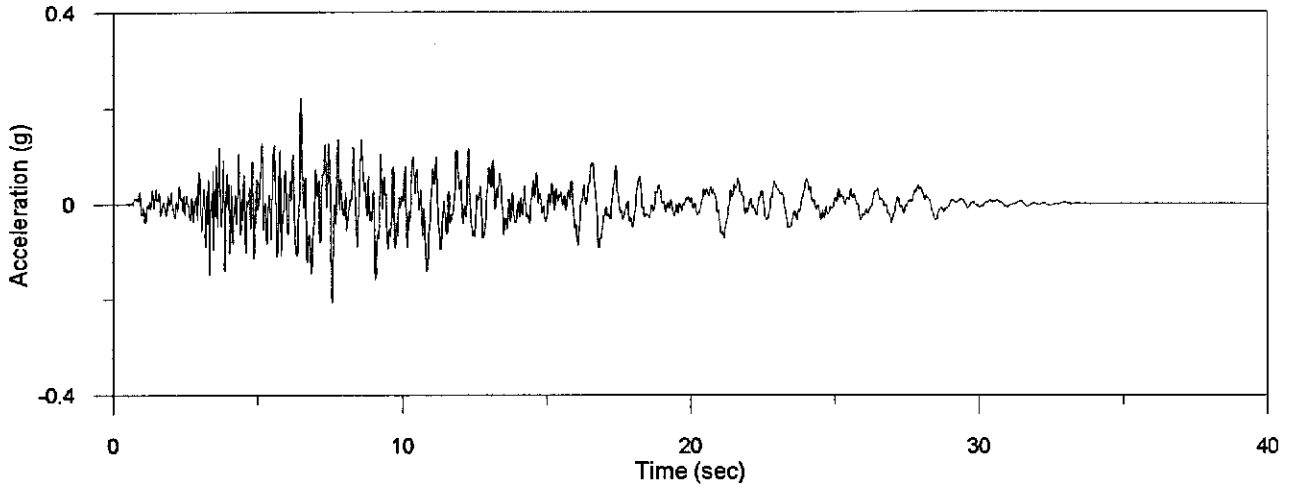
S-500.GRF

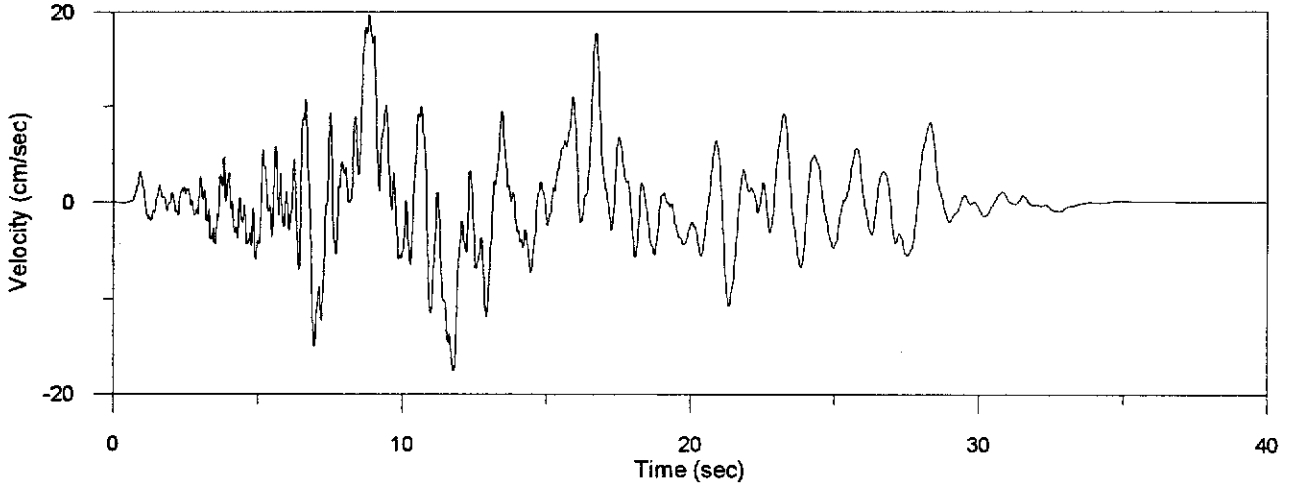


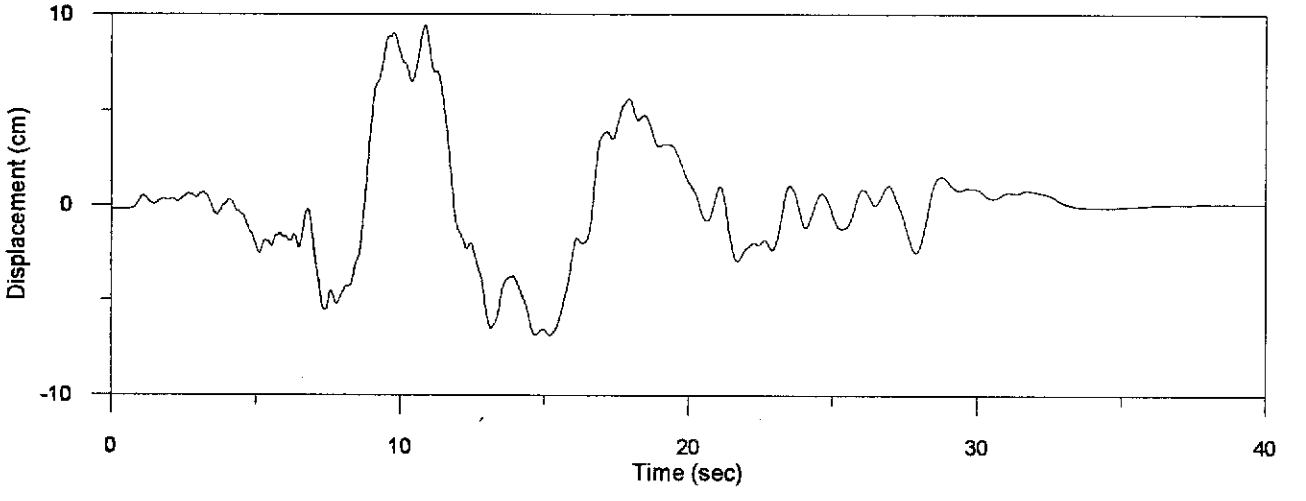




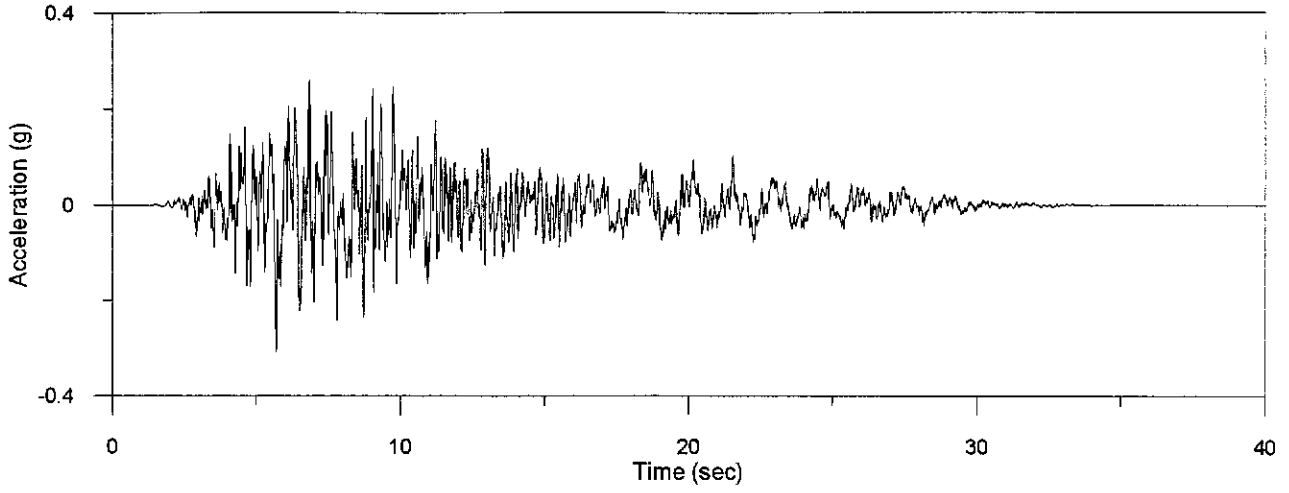
Project No. 91C0509	Los Alamos Seismic Hazards	RECOMMENDED DBE HORIZONTAL TIME HISTORIES FOR 500-YEAR RETURN PERIOD	Figure 10-33
Woodward-Clyde Federal Services			

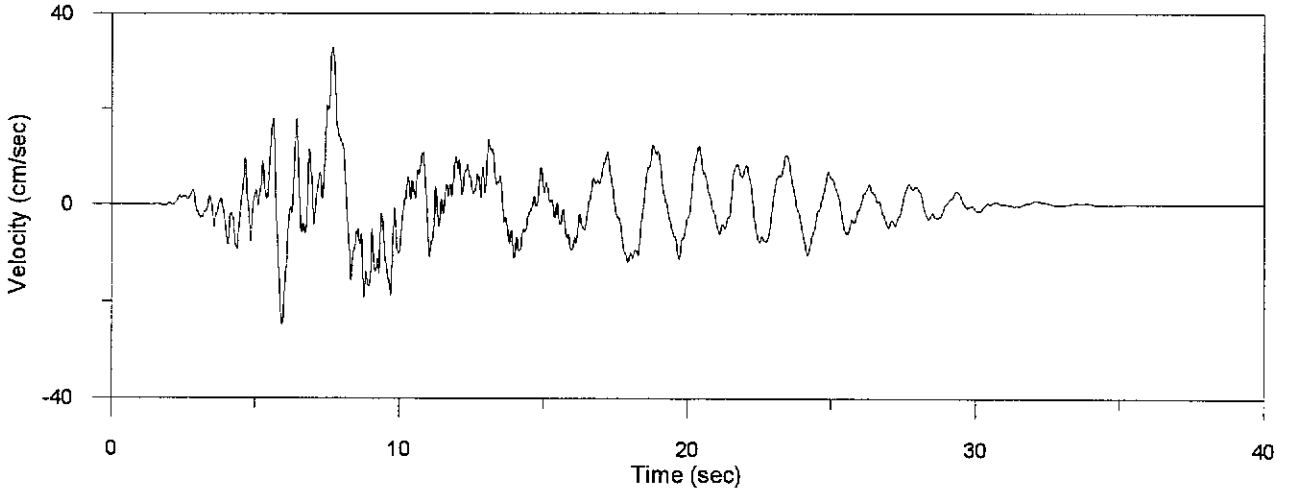


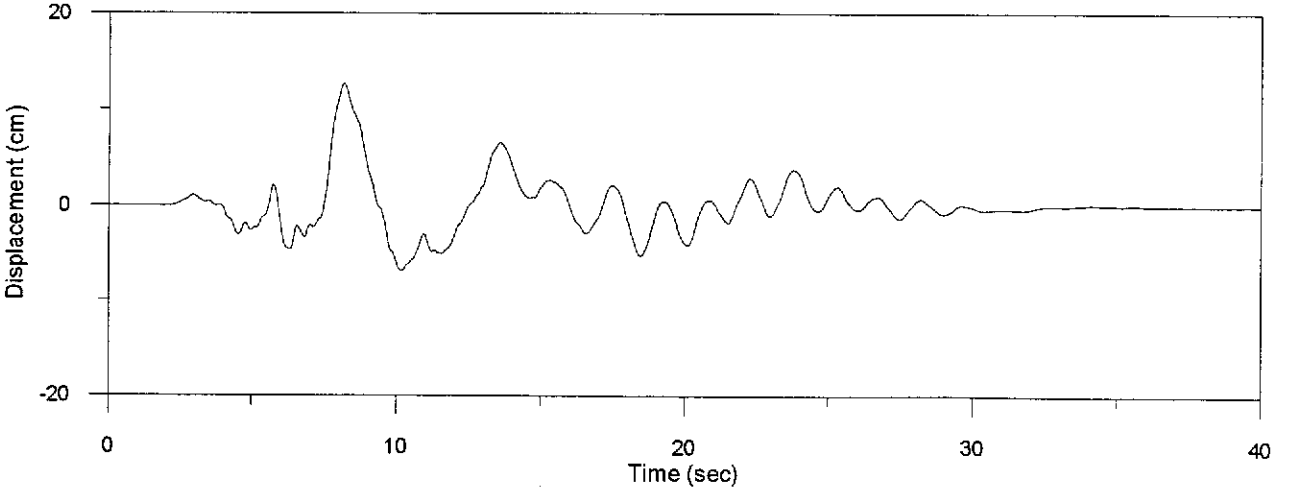




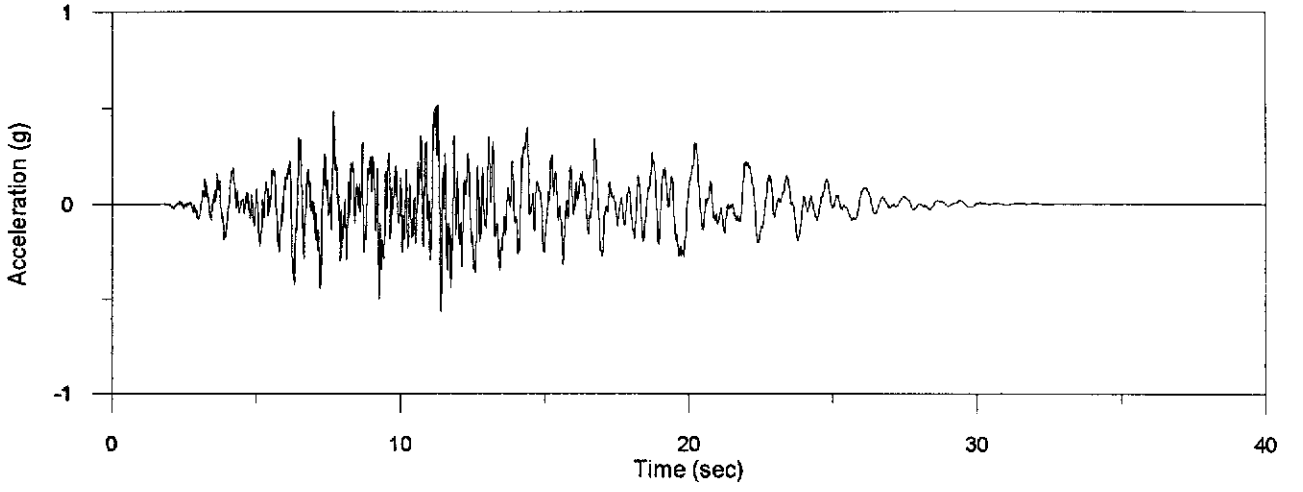
Project No. 91C0509	Los Alamos Seismic Hazards	RECOMMENDED DBE HORIZONTAL TIME HISTORIES FOR 1000-YEAR RETURN PERIOD	Figure 10-34
Woodward-Clyde Federal Services			

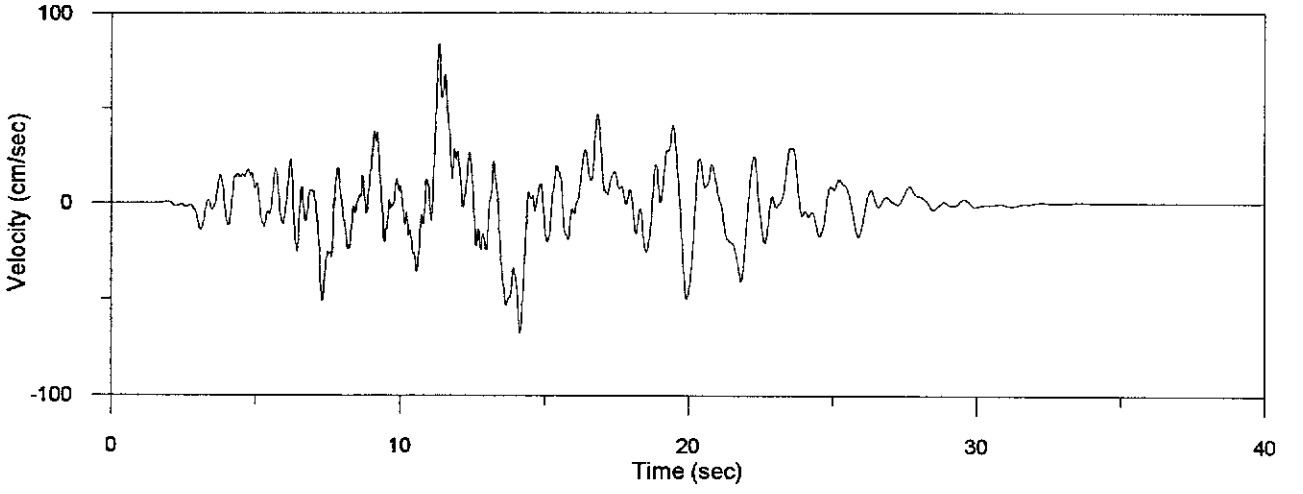


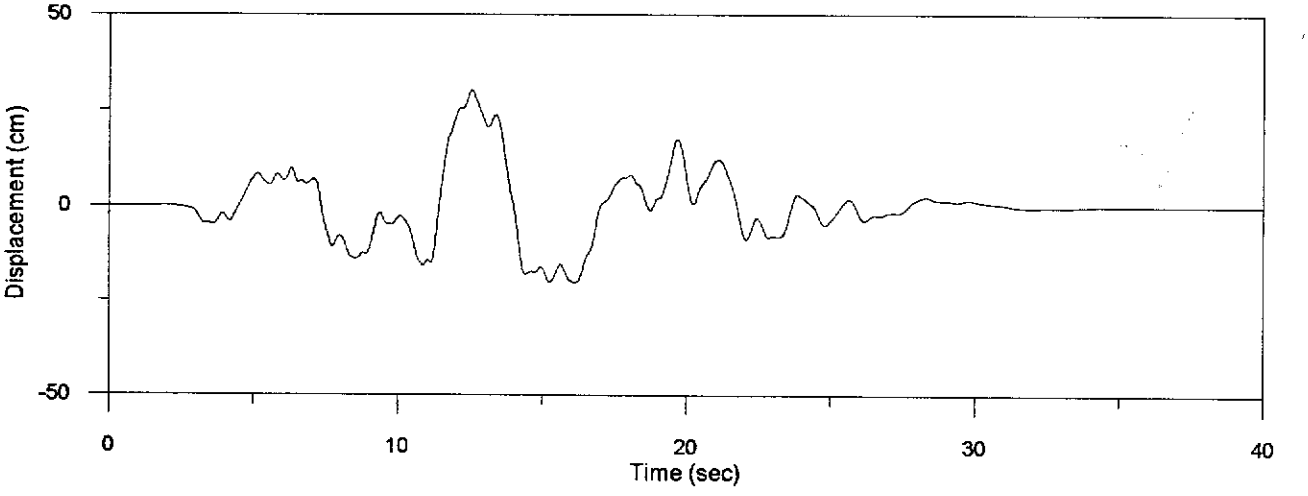




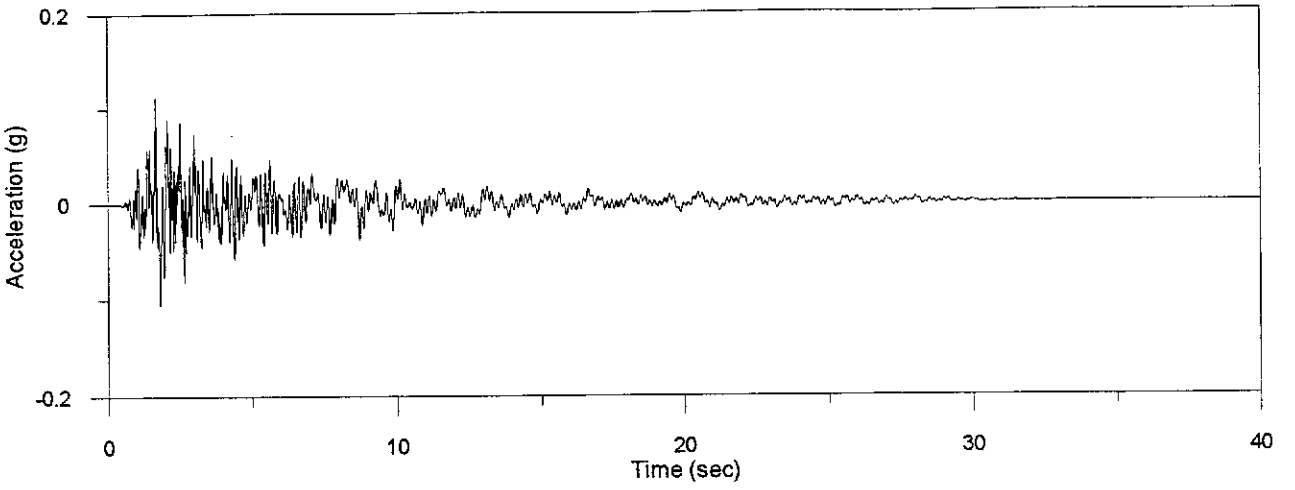
Project No. 91C0509	Los Alamos Seismic Hazards	RECOMMENDED DBE HORIZONTAL TIME HISTORIES FOR 2000-YEAR RETURN PERIOD	Figure 10-35
Woodward-Clyde Federal Services			

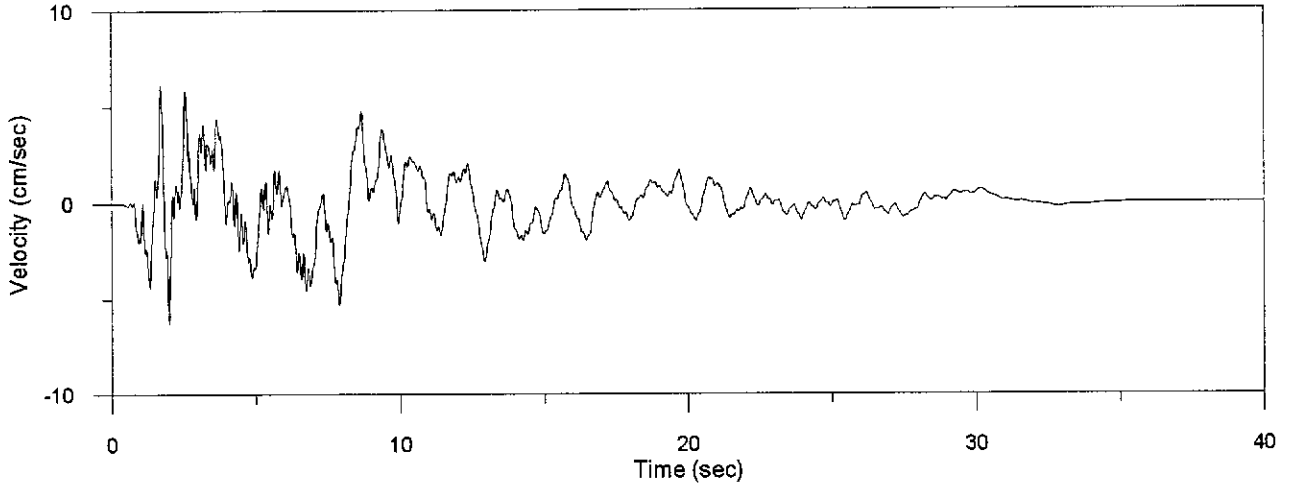


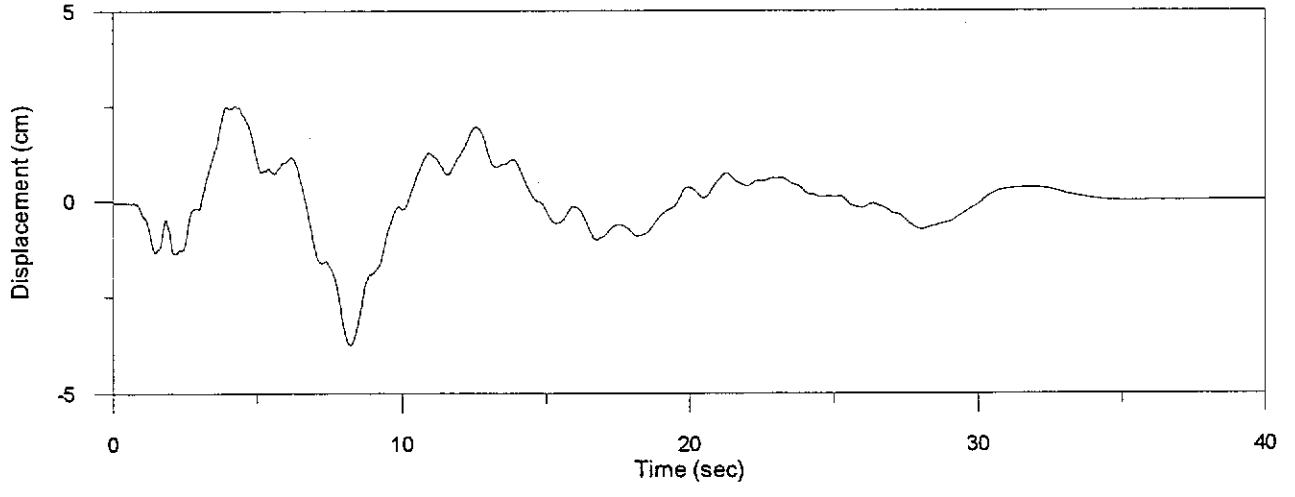




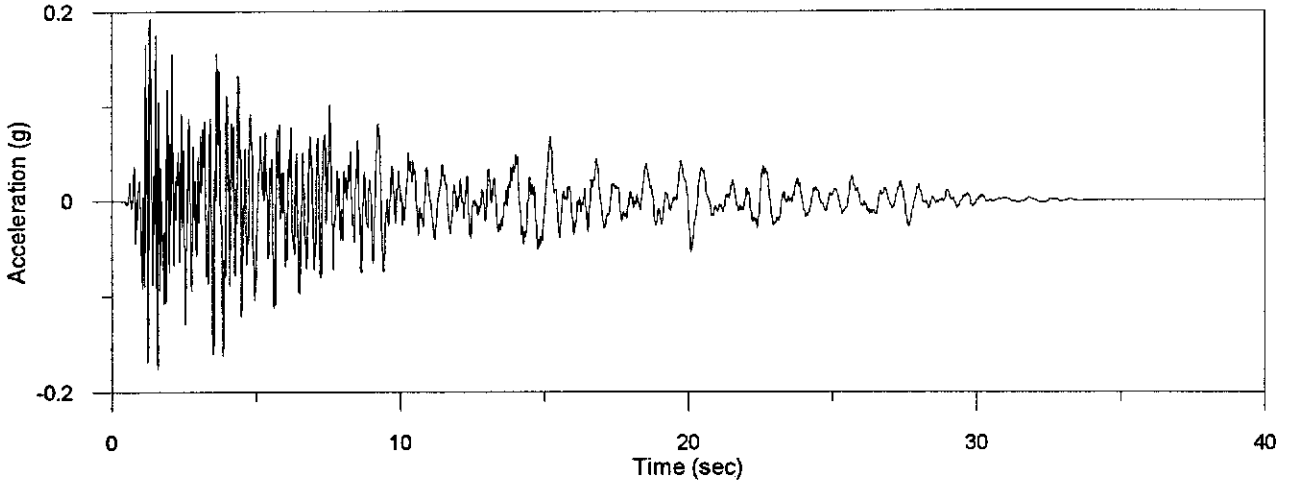
Project No. 91C0509	Los Alamos Seismic Hazards	RECOMMENDED DBE HORIZONTAL TIME HISTORIES FOR 10,000-YEAR RETURN PERIOD	Figure 10-36
Woodward-Clyde Federal Services			

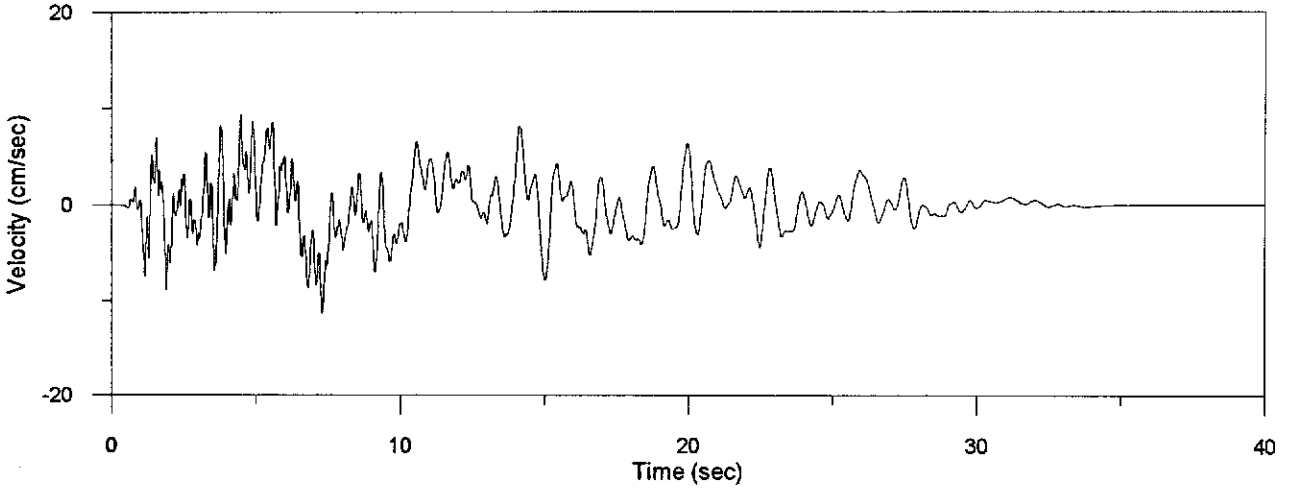


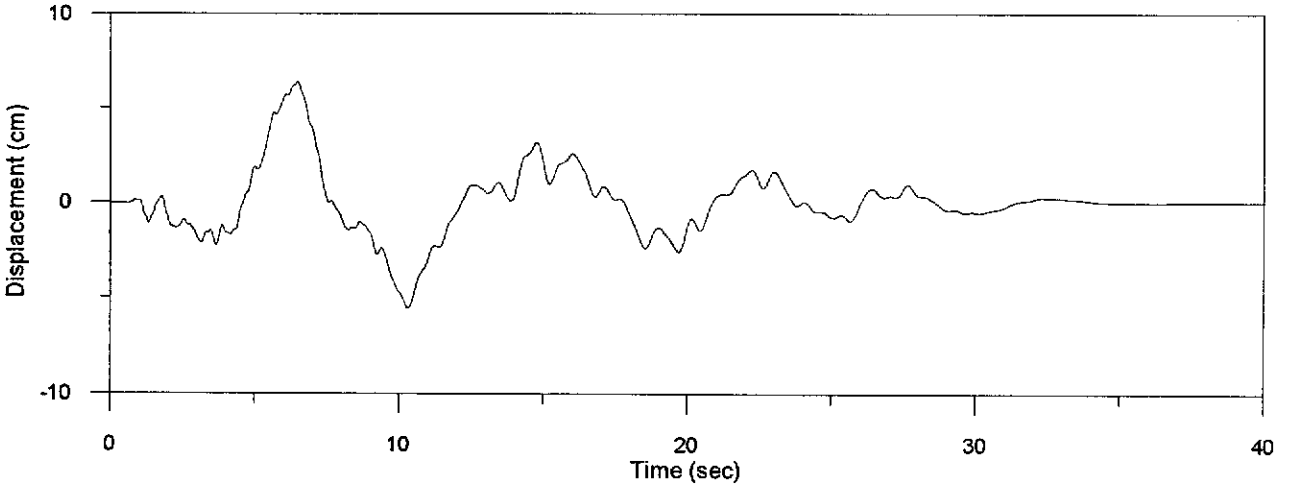




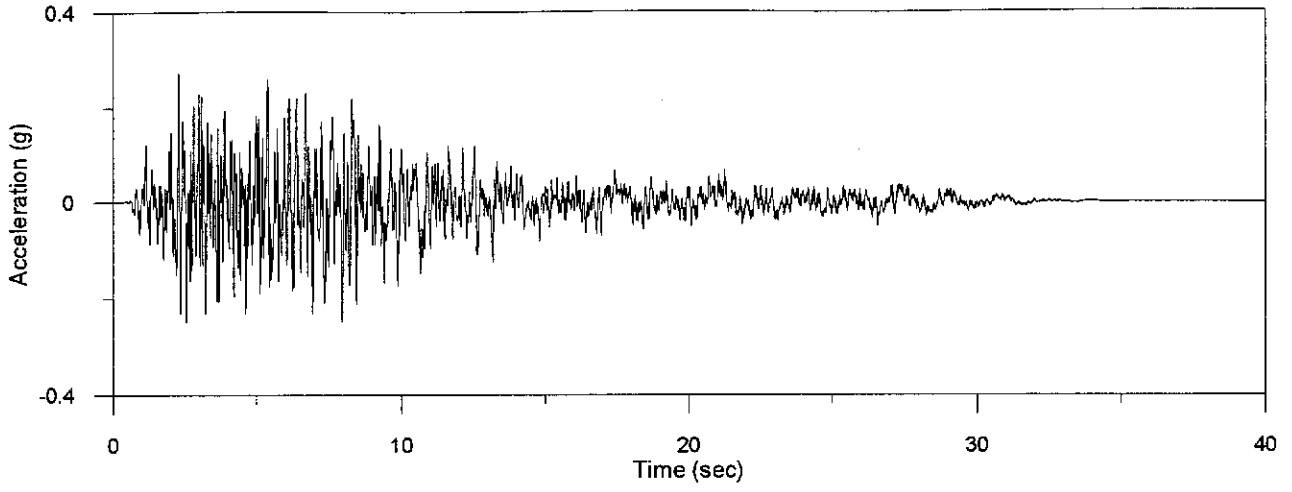
Project No. 91C0509	Los Alamos Seismic Hazards	RECOMMENDED DBE VERTICAL TIME HISTORIES FOR 500-YEAR RETURN PERIOD	Figure 10-37
Woodward-Clyde Federal Services			

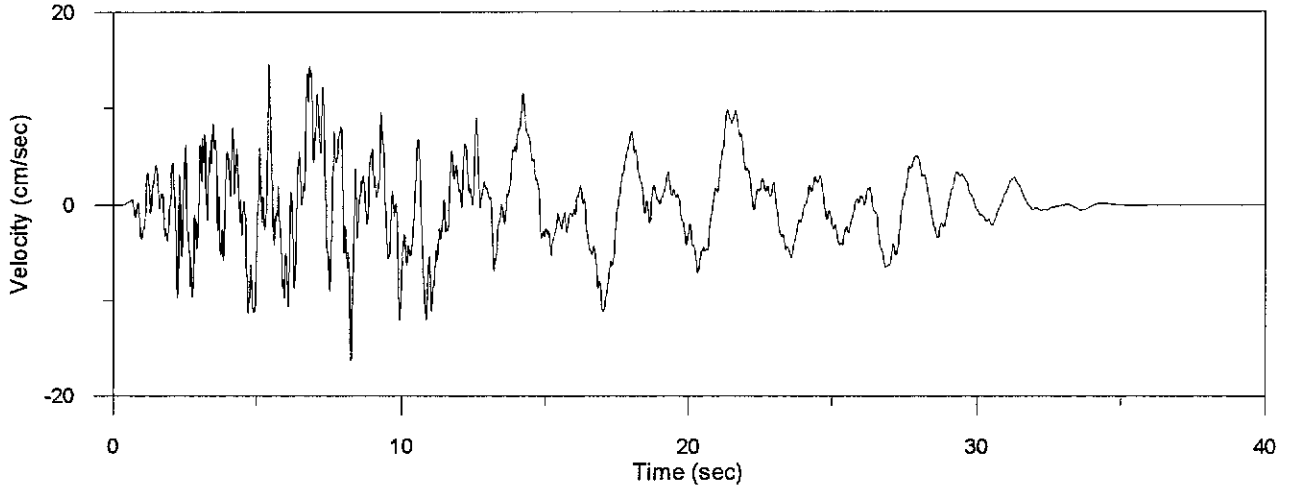


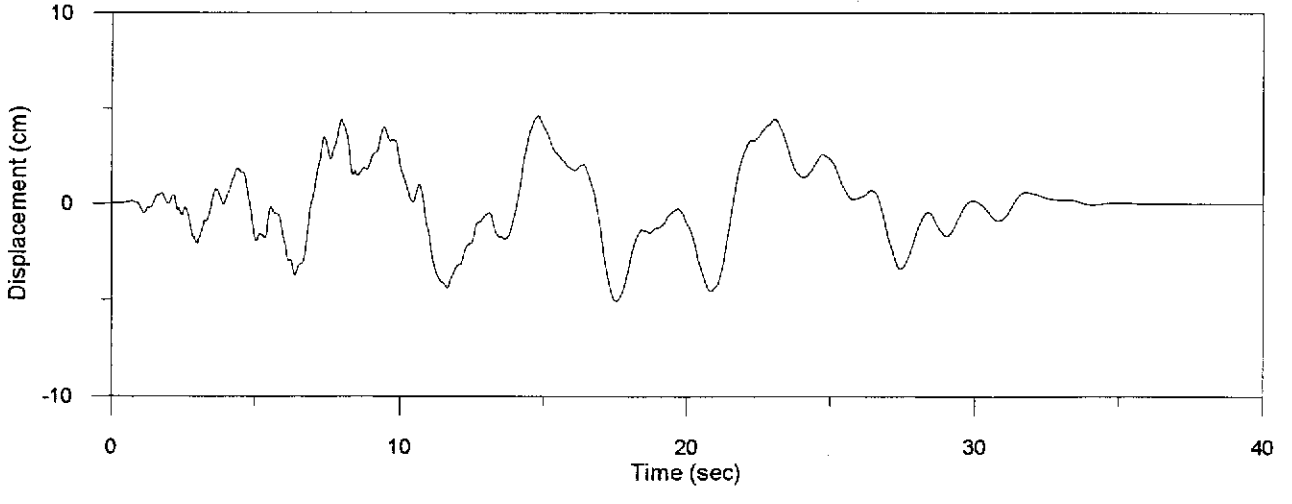




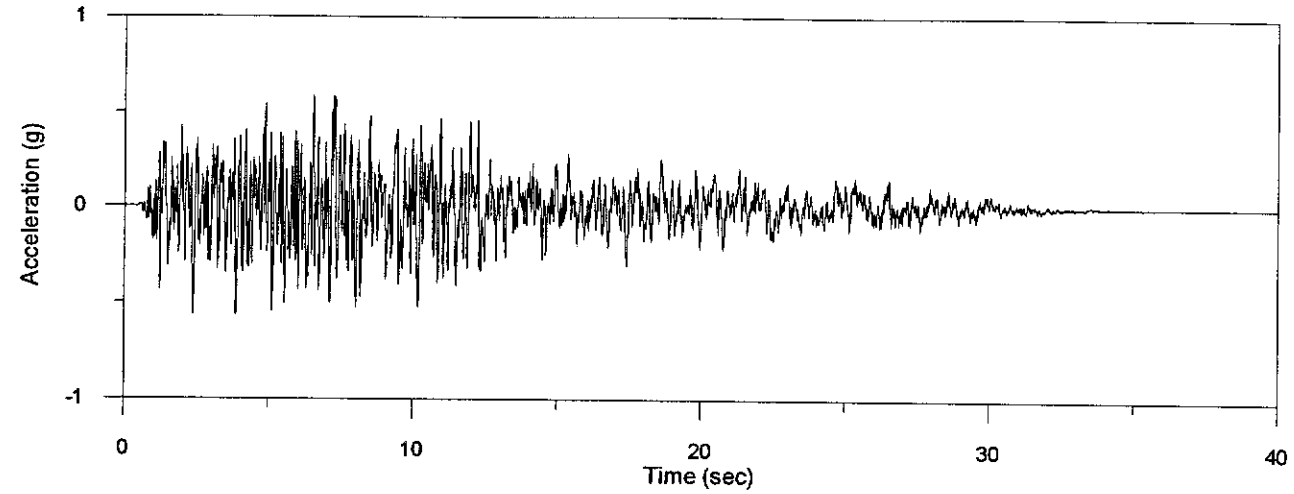
Project No. 91C0509	Los Alamos Seismic Hazards	RECOMMENDED DBE VERTICAL TIME HISTORIES FOR 1000-YEAR RETURN PERIOD	Figure 10-38
Woodward-Clyde Federal Services			

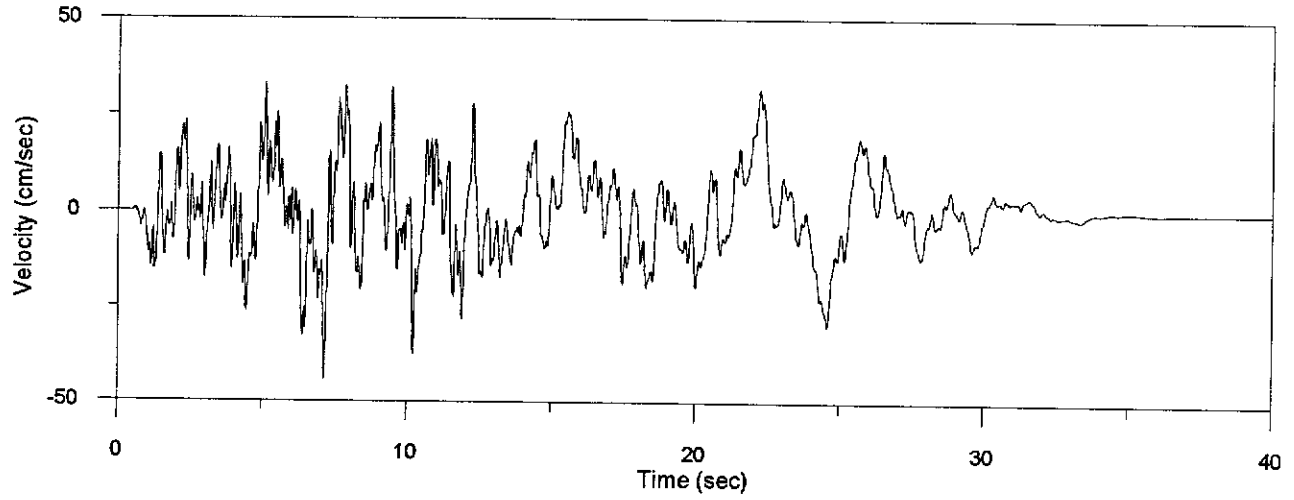


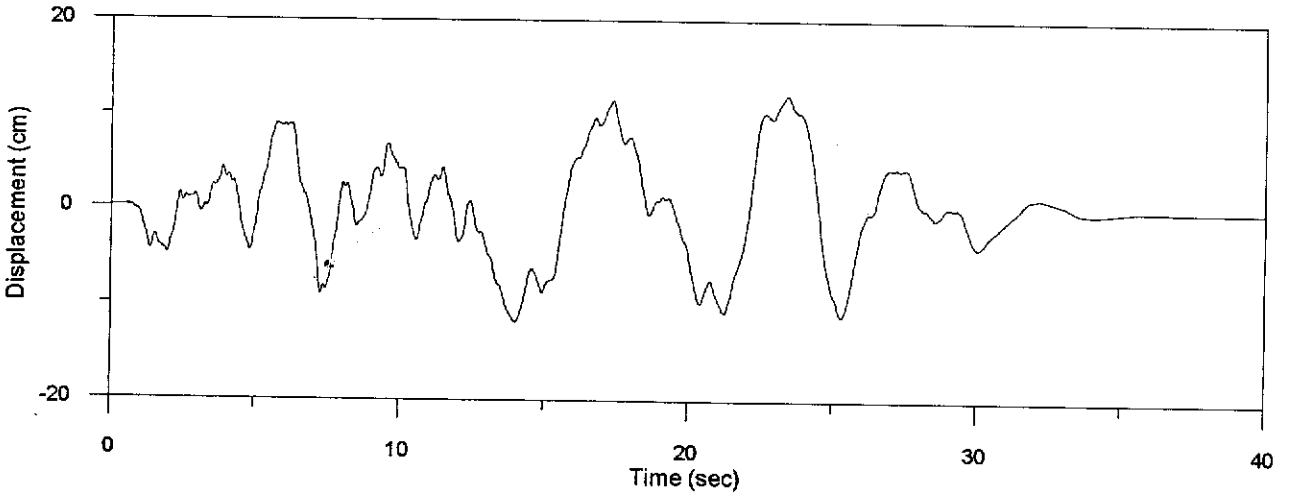




Project No. 91C0509	Los Alamos Seismic Hazards	RECOMMENDED DBE VERTICAL TIME HISTORIES FOR 2000-YEAR RETURN PERIOD	Figure 10-39
Woodward-Clyde Federal Services			







Project No. 91C0509	Los Alamos Seismic Hazards	RECOMMENDED DBE VERTICAL TIME HISTORIES FOR 10,000-YEAR RETURN PERIOD	Figure 10-40
Woodward-Clyde Federal Services			

11.0
RECOMMENDATIONS FOR FUTURE STUDIES

Based on the studies completed to date, the following are recommendations for future investigations. The results of such studies will aid in refining specific seismic source and site parameters, which have been incorporated into both the deterministic and probabilistic seismic hazard analysis, and reduce their associated uncertainties. Gardner et al. (1994) developed a draft plan for the LANL seismic program, which itemizes specific tasks and is a more comprehensive discussion of some of the recommendations that are highlighted here. The recommended studies are divided into three major categories: the Pajarito fault system, ground motion evaluations, and seismic monitoring.

11.1 PAJARITO FAULT SYSTEM

11.1.1 Faulting History

Paleoseismic investigations along the Pajarito fault system provide evidence of multiple late Quaternary displacements. However, considerable uncertainties remain concerning the recurrence intervals, the timing of the most recent surface ruptures along the faults, displacements per individual events, and late Quaternary slip rates. Specific issues of particular interest include: (1) did surface faulting younger than 45 to 55 ka occur on the Pajarito fault; (2) did the most-recent rupture on the Rendija Canyon fault occur between 8 to 9 ka or around 23 ka; (3) when did the penultimate event occur on the Guaje Mountain fault; and (4) is the Sawyer Canyon fault part of the Pajarito fault system? Uncertainties in the behavior of the fault system can be decreased via an integrated program of detailed mapping, topographic profiling, geophysical surveys, trench excavations, and applications of appropriate age-dating methods to better understand fault behavior.

The general lack of fault scarps on alluvium and the geomorphic expression of the Pajarito fault as primarily a Quaternary bedrock escarpment pose considerable logistical and interpretive challenges to deciphering the fault's late Pleistocene earthquake history. Additional trenching along the Pajarito fault, perhaps including exposure of stratigraphic and structural features across the entire Pajarito fault escarpment, has been recommended by

reviewers of our paleoseismic studies to obtain better paleoseismic data. However, such an effort would be logistically difficult, extremely costly, and speculative as to its effectiveness without more information to select an optimal site. Additional trenching investigations on the Pajarito, Rendija Canyon, Guaje Mountain, and Sawyer Canyon faults are definitely needed to develop a comprehensive paleoseismic record and better characterize these faults. However, it would seem prudent to first maximize surficial information by constructing a detailed strip map of the entire Pajarito fault system and the Sawyer Canyon fault. Due to the nature of the fault system, and based on our findings in this study, detailed mapping would be a necessary and cost-effective prerequisite to selecting optimal future sites for paleoseismic trench investigations. In particular, to fully understand the most-recent behavior of the Pajarito fault system, individual fault strands that potentially will show the youngest activity need to be identified within the Pajarito escarpment.

We recommend an integrated approach of investigating the Quaternary stratigraphic and structural framework that includes: 1) detailed mapping of stratigraphic units in the Bandelier Tuff to help identify fault traces lacking geomorphic expression; 2) detailed mapping of geomorphic features and Quaternary sediments along the faults; 3) supporting geochronological and pedogenic-soils studies; and 4) supplemental geomorphic profiling. Mapping units in the tuff is time-intensive, but has been done in some areas (e.g., Reneau, 1991; Carter and Winter, 1995) and has proved effective. Although mapping geomorphic features is hindered by the tree-cover and post-World War II development, recently developed FIMAD maps and a variety of remote-sensing imagery (possibly including 1951 aerial photographs, thematic, SPOT, and radar imagery) could greatly assist in developing a sufficiently detailed map. The application of thermoluminescence methods to dating Quaternary sediments at the LANL has provided constraints on the age of both volcanic and faulting events, and the extensive distribution of eolian deposits on the plateau indicates that this method would be useful in future studies. Geochemical studies and a better understanding of older pumice deposits would also provide useful constraints on faulting history (e.g., Section 4.2.2.2 and Kolbe et al., 1994). A better understanding of soil chronosequences in the area could provide some age control in areas where other methods cannot be applied. Finally, supplemental profiling of stream terraces (e.g., Section 4.2.3.1 and Reneau, 1992) and fault escarpments (Section 4.1.2) can provide displacement data, aid in identifying individual fault strands, and provide information on the geomorphic evolution of the Pajarito Plateau that is vital to understanding the behavior of the Pajarito fault system.

A detailed strip map of the Pajarito fault system could then be used to develop a surface faulting hazards map for the LANL (see below) and as a database for selecting sites for further geomorphic, geophysical, or trench investigations. Potential future paleoseismic sites identified in this and previous studies, such as the graben north of Cañon de Valle along the western escarpment of the Pajarito fault (Section 4.1.2.3) or the fault exposure and stream terraces in Bland Canyon (Gardner et al., 1994), could be better evaluated within the context of a strip map of the entire fault system.

11.1.2 Tectonic Model

In addition to a better understanding of faulting history, an evaluation of fault geometry and kinematics is needed to better characterize the Pajarito fault system for seismic hazard analysis. Recommended additional studies to accomplish this include: 1) compiling, processing, and interpreting existing geophysical data across the fault system and the Española Basin; 2) conducting a seismic refraction survey to characterize deeper subsurface structure of the faults; 3) compilation and structural analysis of fault-slip data; and 4) constructing balanced cross-sections across the fault system. Indeed, cross-sections across the entire Española Basin may provide insights into fault growth and rift development that would be useful for modeling other nearby faults as well, such as the Puye and Embudo faults. Ongoing mapping studies by K. Carter (LANL) of the Puye fault zone and other nearby faults will provide vital information for constructing cross-sections and gaining a better understanding of kinematics in the region.

11.1.3 Surface Rupture Potential

As discussed in Section 4.3, major strands of the Rendija Canyon and Guaje Mountain faults, as well as secondary splays of the Pajarito fault, pose a potential surface rupture threat to some laboratory facilities. This study and other recent studies demonstrate the need to develop a detailed surface faulting hazards map for the LANL because faulting is younger than previously thought for the Rendija Canyon and Guaje Mountain faults (Section 4.2.2 and Gardner et al., 1990) and Quaternary faulting is more widely distributed than previously thought on the Pajarito Plateau, including the LANL area (e.g., Reneau, 1991; Vaniman and Wohletz, 1990; Kolbe et al., 1994). This surface faulting hazards map needs to define active faults and associated areas of potential hazard at an adequate scale, and differentiate levels

of hazard where possible, as some fault strands have been active since the latest Pleistocene (past 35 ka), whereas others have not and show lower rates of activity. For those LANL facilities identified by the mapping as having potential surface rupture hazards, site-specific evaluations need to be conducted.

11.2 GROUND MOTION EVALUATIONS

11.2.1 Site Response of Other Technical Areas

Site-specific ground motion estimates have been computed for the eight most significant facility sites at the LANL. The results of these evaluations strongly emphasize the effects of site-specific subsurface geology on ground motions. In particular, the Bandelier Tuff beneath the laboratory provides a unique volcanic geology whose site response effects on ground motion appear to be unusual. Based on the results of this study, the tuff appears to damp out intermediate frequency ground motions in the bandwidth of engineering significance but amplify motions at periods of 1 second and greater. The presence of pumice and dacite layers beneath the LANL can also have significant effects on ground motions.

For future facility siting, a geotechnical borehole program should be undertaken with core holes drilled to a depth at least beneath the Bandelier Tuff. Such a program should attempt to characterize the variability of the subsurface geology across the Technical Areas. Downhole shear-wave velocity measurements are critical and should be performed in these holes. Dynamic laboratory testing of samples collected in the borehole program should be performed. The resulting data will be important to improve the basis for site-specific seismic design and will aid in a possible future microzonation of the laboratory.

11.3 SEISMIC MONITORING

11.3.1 LANL Seismographic Network

Seismic monitoring with the intent of addressing issues of both seismic and volcanic hazards and as a possible means of hazard mitigation has long been recognized as a valuable tool by the scientific and engineering communities. Historically, DOE has strongly supported the use of seismic monitoring for such purposes. For example, regional networks exist at the

Lawrence Livermore National Laboratory, the Hanford Reservation, and the Idaho National Engineering Laboratory. In addition, the current network at the Savannah River Laboratory is being greatly expanded. The present LANL network suffers from inadequate funding and technical support. It is recommended that the current network be reconfigured and stations added to adequately monitor seismicity in the vicinity of and around the LANL and to provide quality data for characterizing seismic sources, specifically the Pajarito fault system, Puye, La Bajada, and Embudo faults and any precursory seismicity associated with magmatic activity.

11.3.2 LANL Strong Motion Network

Currently there are only a few strong motion recorders operating at the LANL. A key element in assessing strong ground shaking, the effects of the subsurface geology on such motions, and the structural response of facilities to shaking are strong motion data. The 1983 M_w 6.8 Borah Peak, Idaho earthquake, was recorded by 13 accelerographs located near or at the major facilities at the INEL. These data have been invaluable in evaluating potential strong ground shaking at the INEL. The strong motion network was installed despite the fact that the INEL had not been previously subjected to any significant levels of shaking in the past. We believe that the capability to record potential future ground shaking at LANL is inadequate compared to other major DOE facilities. One or more strong motion recorders should be installed at each major facility with some instruments at free-field sites.

REFERENCES

Abrahamson, N.A. and Litehiser, J.J., 1989, Attenuation of vertical peak acceleration, Bulletin of the Seismological Society of America, v. 79, p. 549-580.

Abrahamson, N.A., Silva, W., and Schneider, J., 1994, Variability of strong ground motion due to the variability of the seismic slip distribution (abs.), Seismological Research Letters, v. 65, p. 35.

Abrahamson, N.A., Somerville, P.G., and Cornell, C.A., 1990, Uncertainty in numerical strong motion predictions, Proceedings, Fourth U.S. National Conference on Earthquake Engineering, v. 1, p. 407-416.

Achauer, U., Maguire, P.K.H., Mechie, J., Green, W.V., and the KRISP Working Group, 1992, Some remarks on the structure and geodynamics of the Kenya rift, in P.A. Ziegler (ed.), Geodynamics of rifting, Volume II, Case history studies on rifts: North and South America and Africa, Tectonophysics, v. 213, p. 257-268.

Aki, K., 1983, Seismological evidence in support of the existence of "Characteristic Earthquakes", Earthquake Notes, v. 54, p. 60-61.

Aki, K., 1988, Local site effect on ground motion, in J.L. Von Thun (ed.), Earthquake Engineering on Soil Dynamics 11: Recent Advances in Ground Motion Evaluation, American Society of Civil Engineering Geotechnical Special Publications, v. 20, p. 103-155.

Aldrich, M.J., Jr., 1986, Tectonics of the Jemez Lineament in the Jemez Mountains and Rio Grande rift, Journal of Geophysical Research, v. 91, p. 1753-1762.

Aldrich, M.J., Jr. and Dethier, D.P., 1990, Stratigraphic and tectonic evolution of the northern Española Basin, Rio Grande rift, New Mexico, Geological Society of America Bulletin, v. 102, p. 1695-1705.

Algermissen, S.T., Perkins, D.M., Thenhaus, P.C., Hanson, S.L., and Bender, B.L, 1990, Probabilistic earthquake acceleration and velocity maps for the United States and Puerto Rico, U.S. Geological Survey Miscellaneous Field Studies Map MF-2120, scale: 1:7,500,000.

Anderson, J.G., 1979, Estimating the seismicity from geological structure for seismic risk studies, Bulletin of the Seismological Society of America, v. 69, p. 135-158.

Anderson, J.G., 1986, Implication of attenuation for studies of the earthquake source, in S. Das, J. Boatwright, and C. Scholz (eds.), Earthquake Source Mechanics, American Geophysical Union Monograph 37, p. 311-318.

Anderson, J.G., 1991, A preliminary descriptive model for the distance dependence of the spectral decay parameter in southern California, Bulletin of the Seismological Society of America, v. 81, p. 2186-2193.

Anderson, J.G. and Hough, S.E., 1984, A model for the shape of the Fourier amplitude spectrum of acceleration at high frequencies, Bulletin of the Seismological Society of America, v. 74, p. 1969-1993.

Anderson, L.W., Piety, L.A., and LaForge, R.C., 1987, Seismotectonic Investigation for Theodore Roosevelt Dam, Arizona, U.S. Bureau of Reclamation, Seismotectonic Report 87-5, 46 p.

Ankeny, L.A., Braile, L.W., and Olsen, K.H., 1986, Upper crustal structure beneath the Jemez Mountains volcanic field, New Mexico, determined by three-dimensional simultaneous inversion of seismic refraction and earthquake data, Journal of Geophysical Research, v. 91, p. 6188-6198.

Arabasz, W.J. and Julander, D.R., 1986, Geometry of seismically active faults and crustal deformation with the Basin and Range-Colorado Plateau transition in Utah, Geological Society of America Special Paper 208, p. 43-74.

Arabasz, W.J., Pechmann, J.C., and Brown, E.D., 1992, Observational seismology and the evaluation of earthquake hazards and risk in the Wasatch Front area, Utah, in P.L. Gori and W.W. Hays (eds), Assessment of Regional Earthquake Hazards and Risk Along the Wasatch Front, Utah, U.S. Geological Survey Professional Paper 1500-A-J, p. D1-D36.

Arabasz, W.J. and Robinson, R., 1976, Microseismicity and geologic structure in the northern South Island, New Zealand, New Zealand Journal of Geology and Geophysics, v. 19, p. 561-601.

Armstrong, R.L., Leeman, W.P., and Malde, H.E., 1975, K-Ar dating, Quaternary and Neogene volcanic rocks of the Snake River Plain, Idaho, American Journal of Science, v. 275, p. 225-251.

Ashcroft, B., 1974, The July 1906 earthquake in Socorro, New Mexico Historical Review, v. 49, p. 325-330.

Atkinson, G.M., 1984, Attenuation of strong ground motion in Canada, Bulletin of the Seismological Society of America, v. 74, p. 2629-2953.

Aubele, J.C., 1978, Geology of the Cerros del Rio volcanic field, New Mexico, MS thesis, University of New Mexico, 136 p.

Bachman, G.O., 1975, Geologic map of the Madrid quadrangle, Santa Fe and Sandoval Counties, New Mexico, U.S. Geological Survey Quadrangle Map GQ-1268, scale 1:62,500.

Bachman, G.O. and Mehnert, H.H., 1978, New K-Ar dates and the late Pliocene to Holocene geomorphic history of the central Rio Grande region, New Mexico, Geological Society of America Bulletin, v. 89, p. 283-292.

Bagg, R.M., 1904, Earthquakes in Socorro, New Mexico, American Geologist, v. 34, p. 102-104.

Bailey, R.A. and Smith, R.L., 1978, Guide to Jemez Mountains and Española Basin, New Mexico Bureau of Mines and Mineral Resources Circular 163, p. 184-196.

Bailey, R.A., Smith, R.L., and Ross, C.S., 1969, Stratigraphy and nomenclature of volcanic rocks in the Jemez Mountains, New Mexico, U.S. Geological Survey Bulletin, 1274-P, 19 p.

Baldridge, W.S., Ferguson, J.F., Braile, L.W., Wang, B., Eckhardt, K., Evans, D., Schultz, C., Gilpin, B., Jiracek, G.R., and Biehler, S., 1994, The western margin of the Rio Grande rift in northern New Mexico: An aborted boundary?, Geological Society of American Bulletin, v. 105, p. 1538-1551.

Baldridge S., Gardner, J.N., and Reneau, S.L., 1990, Transfer faulting in the central Rio Grande rift: Oblique slip on the Pajarito fault system, EOS Transactions. American Geophysical Union, v. 71, 1584 p.

Baldridge, W.S. and Jiracek, G.R., 1992, SAGE program explores the Rio Grande rift, EOS Transactions, American Geological Union, v. 73, p. 145-148.

Baldridge, W.S., Olsen, K.H., and Callender, J.F., 1984, Rio Grande rift: Problems and perspectives, New Mexico Geological Society Guidebook, v. 35, p. 1-12.

Baltz, E.H., 1976, Seismotectonic analysis of the central Rio Grande rift, New Mexico, A progress report on geological investigations, Preliminary Report, 93 p.

Baltz, E.H., 1978, Resume of Rio Grande depression in north-central New Mexico, New Mexico Bureau of Mines & Mineral Resources, Circular 163, p. 210-228.

Biehler S., Ferguson, J., Baldridge, W.S., Jiracek, G.R., Aldern, L.W., Martinez, M., Fernandez, R., Romo, J., Gilpir, B., Braile, L.W., Hersey, D.R., Luyendyk, B.P., and Aiken, C.L., 1991, A geophysical model of the Española Basin, Rio Grande rift, New Mexico, Geophysics, v. 56, p. 340-353.

Blackwell, D.D., Steele, J.L., and Carter, L.S., 1991, Heat-flow patterns of the North American continent, A discussion of the Geothermal Map of North America, in D.B. Slemmons, E.R. Engdahl, M.D. Zoback, and D.D. Blackwell (eds.), Neotectonics of North America, Geological Society of America, Decade Map Volume 1, p. 457-466.

Boden, D.R., 1980, Stratigraphy of the Tshirege Member of the Bandelier Tuff and structural analysis of the Pajarito fault zone, Bandelier National Monument Area, Jemez Mountains, New Mexico, M.S. Thesis, Colorado School of Mines, 187 p.

Boore, D.M., 1983, Stochastic simulation of high-frequency ground motions based on seismological models of the radiated spectra, Bulletin of the Seismological Society of America, v. 73, p. 1865-1984.

Boore, D.M., 1986, Short-period P- and S-wave radiation from large earthquakes: Implications for spectral scaling relations, Bulletin of the Seismological Society of America, v. 76, p. 43-64.

Boore, D.M. and Atkinson, G.M., 1987, Prediction of ground motion and spectral response parameters at hard-rock sites in eastern North America, Bulletin of the Seismological Society of America, v. 77, p. 440-467.

Boore, D.M. and Boatwright, J., 1984, Average body-wave radiation coefficients, Bulletin of the Seismological Society of America, v. 74, p. 1615-1621.

Boore, D.M. and Joyner, W.B., 1984, A note on the use of random vibration theory to predict peak amplitudes of transient signals, Bulletin of the Seismological Society of America, v. 74, p. 2035-2039.

Bosworth, W., 1985, Geometry of propagating continental rifts, Nature, v. 316, p. 625-627.

Brister, B.S. and Gries, R.R., 1994, Tertiary stratigraphy and tectonic development of the Alamosa basin (northern San Luis Basin), Rio Grande rift, south-central Colorado, in G.R. Keller and S.M. Cather (eds.), Basins of the Rio Grande Rift: Structure, Stratigraphy, and Tectonic Setting, Geological Society of America Special Paper 291, p. 39-58.

Brown, L.D., Chapin, C.E., Sanford, A.R., Kaufman, S., and Oliver, J.E., 1980, Deep structure of the Rio Grande rift from seismic reflection profiling, Journal of Geophysical Research, v. 85, p. 4,773-4,800.

Brown, L.L. and Golombek, M.P., 1985, Tectonic rotations within the Rio Grande rift: Evidence from Palaeomagnetic studies, Journal of Geophysical Research, v. 90, p. 790-802.

Brown, L.L. and Golombek, M.P., 1986, Block rotations in the Rio Grande rift, New Mexico, Tectonics, v. 5, p. 423-438.

Brown, L.D., Krumhansl, P.A., Chapin, C.E., Sanford, A.R., Cook, F.A., Kaufman, S., Oliver, J.E., and Schilt, F.S., 1979, COCORP seismic reflection studies of the Rio Grande rift, in R.E. Riecher (ed.), Rio Grande Rift: Tectonics and Magmatism, American Geophysical Union, p. 169-184.

Broxton, D.E., Byers, F.M. and Warren, R.G., 1989, Petrography and phenocryst chemistry of volcanic units at Yucca Mountain, Nevada: A comparison of outcrop and drill hole samples, Los Alamos National Laboratory Report, LA-10503-MS, p. 66.

Broxton, D.E., Heiken, G., Chipera, S.J., and Byers, F.M., Jr., 1993, Stratigraphy, petrography and mineralogy of tuffs at technical area 21, Los Alamos National Laboratory, New Mexico, Los Alamos National Laboratory Report, LAUR 93-2028.

Bruhn, R.L., Gilber, P.R., and Parry, W.T., 1987, Rupture characteristics of normal faults: An examples from the Wasatch fault zone, Utah, in M.P. Coward, J.F. Dewey, and P.L. Hancock (eds.), Continental Extensional Tectonics, Geological Society of London Special Paper 28, p. 337-353.

Brune, J.N., 1970, Tectonic stress and the spectra of seismic shear waves from earthquakes, Journal of Geophysical Research, v. 75, p. 4997-5009.

Brune, J.N., 1971, Correction, Journal of Geophysical Research, v. 76, p. 5002.

Bryan, K., 1938, Geology and ground-water conditions of the Rio Grande depression in Colorado and New Mexico, in U.S. Natural Resources Planning Board, The Rio Grande Joint Investigations in the Upper Rio Grande Basin, Washington, v. 1, Pt. 2, p. 197-225.

Bryan, K. and McCann, F.T., 1937, The Ceja Del Rio Puerco-a border feature of the Basin and Range province in New Mexico: Pt. 1, Stratigraphy and structure, Journal of Geology, v. 45, p. 801-828.

Bryan K., and McCann, F.T., 1938, The Ceja del Rio Puerco-a border feature of the Basin and Range province in New Mexico: Pt. 2, Geomorphology, Journal of Geology, v. 46, p. 1-16.

Budding, A.J., 1978, Subsurface geology of the Pajarito Plateau: Interpretation of gravity data, New Mexico Bureau of Mines and Mineral Resources, Circular 163, p. 196-198.

Budding, A.J. and Purtymun, W.D., 1976, Seismicity of the Los Alamos area based on geologic data, Los Alamos Scientific Laboratory, Report LA-6278-MS, 7 p.

Cabot, E.C., 1938, Fault border of the Sangre de Cristo Mountains north of Santa Fe, New Mexico, Journal of Geology, v. 46, p. 88-105.

Campbell, K.W., 1989, Empirical prediction of near-source ground motion for the Diablo Canyon Power plant site, San Luis Obispo County, California, U.S. Geological Survey Open-File Report 89-484.

Campbell, K.W., 1990, Empirical prediction of near-source soil and soft-rock ground motion for the Diablo Canyon Power Plant site, San Luis Obispo County, California, Report prepared for Lawrence Livermore National Laboratory by Dames & Moore, 110 p.

Campbell, K.W., 1993, Empirical prediction of near-source ground motion from large earthquakes: International Workshop on Earthquake Hazard and Large Dams in the Himalaya, Indian National Trust for Art and Cultural Heritage (INTACH), New Delhi, India.

Campbell, K.W. and Bozorgnia, Y., 1994, Near-source attenuation of peak horizontal acceleration from worldwide accelerograms recorded from 1957 to 1993, Fifth U.S. International Conference on Earthquake Engineering, Chicago, Illinois.

Carroll, R.D. and Paul, J.E., 1970, The estimation of in situ acoustic properties of volcanic rocks from compressional velocity measurements--Central Nevada, U.S. Geological Survey No. 474-69, 25 p.

Carter, K.E. and Gardner, J.N., 1993, Quaternary fault kinematics in the northern Española Basin, Rio Grande rift, New Mexico: Implications for early rift development (abs.), EOS Transactions, American Geophysical Union, v. 74, p. 611.

Carter, K.E. and Winter, C.L., 1995, Fractal nature and scaling of normal faults in the Española Basin, Rio Grande rift, New Mexico: Implications for growth and strain, Journal of Structural Geology (in press).

Cash, D.J., 1971, The Dulce, New Mexico, earthquake of January 23, 1966: Location, focal mechanism, magnitude, and source parameters, Ph.D. Thesis, New Mexico Institute of Mining and Technology.

Cash, D.J., 1975, The focal mechanism of the Dulce, New Mexico, earthquake of January 23, 1966, EOS Transactions, American Geophysical Union, v. 56, p. 1022.

Cash, D.J., McFarland, N.J., and Headdy, J.J., 1978, Seismicity of northern New Mexico, 1973-1978, submitted to Rio Grande Rift Symposium, Los Alamos Scientific Laboratory, University of California, Los Alamos, New Mexico.

Cash, D.J. and Wolff, J.J., 1984, Seismicity of the Rio Grande rift in northern New Mexico, 1973-1983, New Mexico Society Guidebook, v. 35, p. 25-28.

Cather, S.M., 1992, Suggested revisions to the Tertiary tectonic history of north-central New Mexico, New Mexico Geological Society, 43rd Field Conference Guidebook, p. 109-122.

Cather, S.M., Chamberlin, R.M., Chapin, C.E., and McIntosh, W.C., 1994, Stratigraphic consequences of episodic extension in the Lemitar Mountains, Central Rio Grande Rift, in G.R. Keller and S.M. Cather (eds.), Basins of the Rio Grande Rift: Structure, Stratigraphy, and Tectonic Setting, Geological Society of America Special Paper 291, p. 157-170.

Chapin, C.E. and Cather, S.M., 1994, Tectonic setting of the axial basins of the northern and central Rio Grande rift, in G.R. Keller and S.M. Cather (eds.), Basins of the Rio Grande Rift: Structure, Stratigraphy, and Tectonic Setting, Geological Society of America Special Paper 291, p. 5-25.

Coffman, J.L. and von Hake, C.A., 1972, United States earthquakes 1970, National Oceanic and Atmospheric Administration, 81 p.

Coffman, J.L. and von Hake, C.A., 1973, Earthquake history of the United States, National Oceanic and Atmospheric Administration, Publication 41-1, 208 p.

Coffman, J.L., von Hake, C.A., and Stover, C.W., 1982, Earthquake history of the United States, National Oceanic and Atmospheric Administration and U.S. Geological Survey, Publication 41-1 with supplement.

Coffman, J.L., von Hake, C.A., Spence, W., Carver, D.L., Covington, P.A., Dunphy, G.J., Irby, W.L., Person, W.J., and Stover, C.W., 1975, United States earthquakes 1973, National Oceanic and Atmospheric Administration, 112 p.

Cooper, J.B., Purtymun, W.D., and John, E.C., 1965, Records of water-supply wells Guaje Canyon 6, Pajarito Mesa 1, and Pajarito Mesa 2, Los Alamos, New Mexico, Basic data report, U.S. Geological Survey, 62 p.

Cordell, L., 1976, Aeromagnetic and gravity studies of the Rio Grande graben in New Mexico between Belen and Pilar, in L.A. Woodward and S.A. Northrop (eds), Tectonics and Mineral Resources of Southwestern North America - A Volume Honoring Vincent C. Kelley, New Mexico Geological Society Special Publication 6, p. 62-70.

Cordell, L., 1978, Complete Bouguer anomaly map of the Taos Basin section of Rio Grande rift, U.S. Geological Survey Open-File Report 78-317.

Cordell, L., 1979, Gravimetric expression of graben faulting in Santa Fe County and the Española basin, New Mexico, New Mexico Geological Society Guidebook 30, p. 59-64.

Cornell, C.A., 1968, Engineering seismic risk analysis, Bulletin of the Seismological Society of America, v. 58, p. 1583-1606.

Costantino, C.J., 1967, Finite element approach to wave propagation problems, Journal of Engineering Mechanics Division, 93 p.

Costantino, C.J., 1969, Two dimensional wave propagation through nonlinear media, Journal of Computational Physics, 4 p.

Crone, A.J. and Haller, K.M., 1991, Segmentation and the coseismic behavior of Basin and Range normal faults: Examples from east-central Idaho and southwestern Montana, U.S.A., Journal of Structural Geology, v. 13, p. 151-164.

Crone, A.J., Machette, M.N., Bonilla, M.G., Lienkaemper, J.J., Pierce, K.L., Scott, W.E., and Bucknam, R.C., 1987, Surface faulting accompanying the Borah Peak earthquake and segmentation of the Lost River fault, central Idaho, Bulletin of the Seismological Society of America, v. 77, p. 739-770.

Crowe, B.M., Linn, G.W., Heiken, G., and Bevier, M.L., 1978, Stratigraphy of the Bandelier Tuff in the Pajarito Plateau, Los Alamos National Laboratory Report LA-7225-MS, 45 p.

Dames and Moore, 1972, Report of geologic, foundation, hydrologic, and seismic investigation: Plutonium Processing Facility, Los Alamos Scientific Laboratory, Los Alamos, NM, unpublished report prepared by Dames and Moore.

Davis, P.M., 1991, Continental rift structures and dynamics with reference to teleseismic studies of the Rio Grande and East African rifts, in A.F. Gangi (ed.), World Rift Systems, Tectonophysics, v. 197, p. 309-325.

Davis, P.M., Parker, E.C., Evans, J.R., Iyer, H.M., and Olsen, K.H., 1984, Teleseismic deep sounding of the velocity structure beneath the Rio Grande rift, in Rio Grande rift: Northern New Mexico, New Mexico Geological Society Guidebook, v. 35, p. 29-38.

dePolo, C.M., 1994, The maximum background earthquake for the Basin and Range Province, western North America, Bulletin of the Seismological Society of America, v. 84, p. 466-472.

dePolo, C.M., Clark, D.G., Slemmons, D.B., and Ramelli, A.R., 1991, Historical surface faulting in the Basin and Range Province, western North America: Implications for faulting segmentation, Journal of Structural Geology, v. 13, p. 123-136.

dePolo, C.M. and Slemmons, D.B., 1990, Estimation of earthquake size for earthquake hazards, Geological Society of America Reviews in Engineering Geology, v. 8, p. 1-28.

Der Kiureghian, A. and Ang, A.H., 1977, A fault-rupture model for seismic risk analysis, Bulletin of the Seismological Society of America, v. 67, p. 1173-1194.

Dethier, D.P. and Demsey, K.A., 1984, Erosional history and soil development on Quaternary surfaces, northwest Española Basin, New Mexico, in Rio Grande Rift: Northern New Mexico, New Mexico Geological Society Guidebook, 35th Field Conference, p. 227-233.

Dethier, D.P., Harrington, C.D., and Aldrich, M.J., 1988a, Late Cenozoic rates of erosion in the western Española Basin, New Mexico: Evidence from geologic dating of erosion surfaces, Geological Society of America Bulletin, v. 100, p. 928-937.

Dethier, D.P., Harrington, C.D., and Aldrich, M.J., 1988b, Cenozoic erosion rates, Española Basin, New Mexico, Geological Society of America Bulletin, v. 100, p. 928-937.

Dethier, D.P. and Manley, K., 1993, Geology of the White Rock quadrangle, Los Alamos County, New Mexico, New Mexico Bureau of Mines and Mineral Resources, Scale 1:24,000 (in press).

Dethier, D.P. and Manley, K., 1985, Geologic map of the Chili quadrangle, Rio Arriba County, New Mexico, U.S. Geological Survey Miscellaneous Field Studies Map MF-1814, Scale 1:24,000.

Dethier, D.P. and Martin, B.A., 1984, Geology and structure along the northeast Jemez Mountains, New Mexico, in Rio Grande Rift: Northern New Mexico, New Mexico Geological Society Guidebook, 35th Field Conference, p. 145-150.

Doser, D.I., 1985, The 1983 Borah Peak, Idaho and 1959 Hebgen Lake, Montana earthquakes--Models for normal fault earthquakes in the Intermountain seismic belt, in R.S. Stein and R.C. Bucknam (eds.), Proceedings of Workshop XXVIII on the Borah Peak, Idaho, Earthquake, U.S. Geological Survey Open-File Report 85-290, p. 368-384.

Doser, D.I. and Smith, R.B., 1989, An assessment of source parameters of earthquakes in the Cordillera of the western U.S., Bulletin of the Seismological Society of America, v. 79, p. 1383-1409.

Doser, D.I. and Yarwood, D.R., 1991, Strike-slip faulting in continental rifts: Examples from Sabukia, East Africa (1928), and other regions, in A.F. Gangi (ed.), World Rift Systems, Tectonophysics, v. 197, p. 213-224.

Dransfield, B.J. and Gardner, J.N., 1985, Subsurface Geology of the Pajarito Plateau, Española Basin, New Mexico, Los Alamos National Laboratory Report LA-10455-MS, 15 p.

Dungan, M.A., Muehlberger, W.R., Leininger, L., Peterson, C., McMillan, N.J., Gunn, G., Lindstrom, M., and Haskin, L., 1984, Volcanic and sedimentary stratigraphy of the Rio Grande gorge and the late Cenozoic geologic evolution of the southern San Luis Valley, New Mexico Geological Society Guidebook, 35th Field Conference, p. 157-170.

Eaton, G.P., 1987, Topography and origin of the southern Rocky Mountains and the Alvarado Ridge, in M.P. Coward, J.F. Dewey, and P.L. Hancock (eds.), Continental Extensional Tectonics, Geological Society of London Special Publication, No. 28, p. 355-369.

Egan, J.A., Makdisi, F.I., and Rosidi, D., 1994, Near-field vertical ground motions from the 17 January 1994 Northridge earthquake; were they unusual?, informal abstract and figures presented at Structural Engineers Association of Northern California Seismology Committee meeting.

El-Hussain, I.W. and Carpenter, P.J., 1990, Reservoir induced seismicity near Heron and El Vado reservoirs, northern New Mexico, Bulletin of the Association of Engineering Geologists, v. 27, p. 51-59.

Electric Power Research Institute, 1993, Guidelines for determining design basis ground motions, Volume 1, Method and guidelines for estimating earthquake ground motion in eastern north America, Final Report TR-102293.

Engdahl, E.R. and Rinehart, W.A., 1988, Seismicity map of North America: DNAG, The Geological Society of America, Scale 1:5,000,000.

Engdahl, E.R. and Rinehart, W.A., 1991, Seismicity map of North America Project, in D.B. Slemmons, E.R. Engdahl, M.D. Zoback, and D.D. Blackwell (eds.), Neotectonics of North America, Geological Society of America, Decade Map Volume 1.

Fisher, R.V. and Schmincke, H.U., 1984, Pyroclastics rocks, Springer-Verlag, New York, 472 p.

Forman, S.L., Nelson, A.R., and McCalpin, J.P., 1991, Thermoluminescence dating of fault-scarp-derived colluvium: Deciphering the timing of paleoearthquakes on the Weber segment of the Wasatch fault zone, north central Utah, Journal of Geophysical Research, v. 96, p. 595-605.

Galusha, T., 1966, The Zia Sand Formation, new early to medial Miocene beds in New Mexico, American Museum Novitates, No. 2271, 12 p.

Galusha, T. and Blick, J.C., 1971, Stratigraphy of the Santa Fe Group, New Mexico, American Museum of Natural History Bulletin, v. 144, art. 1.

Gardner, J.N., 1985, Tectonic and petrologic evolution of the Keres group: Implications for the development of the Jemez volcanic field, New Mexico, PhD Thesis, University of California, Davis, 293 p.

Gardner, J.N., 1986, Results of first geological and geophysical assessment and selection of first trench site, Los Alamos National Laboratory Memorandum, 4 p.

Gardner, J.N., Baldridge, W.S., Gribble, R., Manley, K., Tanaka, K., Geissman, J.W., Gonzalez, M., and Baron, G., 1990, Results from seismic hazards trench #1 (SHT-1) Los Alamos Seismic Hazards Investigations, Los Alamos National Laboratory Report No. EES1-SH90-19, 57 p.

Gardner, J.N., Goen, L.K., House, L.S., Keller, M.D., Volkman, D.E., 1994, Los Alamos National Laboratory draft seismic program plan, prepared for the U.S. Department of Energy, 100 p. plus appendices.

Gardner, J.N. and Goff, F., 1984, Potassium-argon dates from the Jemez volcanic field: implications for tectonic activity in the north-central Rio Grande rift, New Mexico Geological Society Guidebook 35, p. 75-81.

Gardner, J.N., Goff, F., Garcia, S., and Hagan, R.C., 1986, Stratigraphic relations and lithologic variations in the Jemez Volcanic field, New Mexico, Journal of Geophysical Research, v. 91, p. 1763-1778.

Gardner, J.N. and House, L., 1987, Seismic hazards investigations at Los Alamos National Laboratory, 1984-1985, Los Alamos National Laboratory Report LA-11072-MS, 76 p. +maps.

Gardner, J.N. and House, L., 1994, Surprisingly high intensities from two small earthquakes, northern Rio Grande rift, New Mexico (abs.), EOS Transactions, Americal Geophysical Union, v. 75, p. 240.

Gardner, J.K. and Knopuff, L., 1974, Is the sequence of earthquakes in Southern California, with aftershocks removed Poissonian, Bulletin of the Seismological Society of America, v. 65, p. 1363-1367.

Gardner, J.N., Kolbe, T., and Chang, S. 1993, Geology, drilling, and some hydrologic aspects of seismic hazards program core holes, Los Alamos National Laboratory, New Mexico, Los Alamos Miscellaneous Report, LA-12460-MS.

Geli, L., Bard, P.Y., and Jullien, B., 1988, The effect of topography on earthquake ground motion: A review and new results, Bulletin of the Seismological Society of America, v. 78(1), p. 42-63.

Geomatrix Consultants, 1993, Final Report, Seismic ground motion study for the San Joaquin-Antioch Bridge, Contra Costa County, unpublished report prepared for California Department of Transportation.

Gibbs, A.D., 1984, Structural evolution of extensional basin margins, Geological Society of London Journal, v. 141, p. 609-620.

Goff, F., Gardner, J.N., Baldridge, W.S., Hulen, J.B., Nielson, D.L., Vaniman, D., Heiken, G., Dungan, M.A., and Broxton, D., 1989, Excursion 17B: Volcanic and hydrothermal evolution of Valles caldera and Jemez volcanic field, New Mexico Bureau of Mines & Mineral Resources Memoir 46, p. 381-433.

Goff, F.E., Grigsby, C.O., Trujillo, P.E., Jr., Counce, D., and Kron, A., 1981, Geology, water chemistry and geothermal potential of the Jemez Springs area, Canon de San Diego, New Mexico, Journal of Volcanology and Geothermal Research, v. 10, p. 227-244.

Goff, F. and Kron, A., 1980, In-progress geologic map of Canon de San Diego, Jemez Springs, New Mexico, and lithologic log of Jemez Springs geothermal well, Los Alamos Scientific Laboratory, Report LA-8276-MAP, Scale 1:12,000.

Goff, F. and Shevenell, L., 1987, Travertine deposits of Soda Dam, New Mexico, and their implications for the age and evolution of the Valles caldera hydrothermal system, Geological Society of America Bulletin, v. 99, p. 292-302.

Golombek, M.P., 1981, Structural analysis of the Pajarito fault zone in the Española Basin of the Rio Grande rift, New Mexico, PhD Thesis, University of Massachusetts, Amherst, 129 p.

Golombek, M.P., 1983, Geology, structure, and tectonics of the Pajarito fault zone in the Española basin of the Rio Grande rift, New Mexico, Geological Society of America Bulletin, v. 94, p. 192-205.

Gonzalez, M.A. and Dethier, D.P., 1991, Geomorphic and neotectonic evolution along the margin of the Colorado Plateau and Rio Grande rift, northern New Mexico, New Mexico Bureau of Mines and Mineral Resources Bulletin 137, p. 29-45.

Grant, L.B. and Sieh, K., 1994, Paleoseismic evidence of clustered earthquakes on the San Andreas fault in the Carrizo Plain, California, Journal of Geophysical Research, v. 99, p. 6819-6841.

Gridley, J.M. and Keller, G.R., 1990, Reinterpretation of crustal structure in the central Rio Grande rift from integrated analysis of gravity, drilling and seismic data, EOS, Transactions of the American Geophysical Union, v. 71, p. 1584.

Griggs, R.L., 1964, Geology and groundwater resources of the Los Alamos area, New Mexico, U.S. Geological Survey Water Supply Paper 1753.

Gutenberg, G.B. and Richter, C.F., 1956, Magnitude and energy of earthquakes, Annales Geofisica, v. 9, p. 1-15.

Hammond, J.F., 1966, A surgeon's report on Socorro, N.M., 1852: Santa Fe, Stagecoach Press, 47 p.

Hanks, T.C., 1979, b-values and ω-τ seismic source models: Implications for tectonic stress variations along active crustal fault zones and the estimation of high-frequency strong ground motion, Journal of Geophysical Research, v. 84, p. 2235-2242.

Hanks, T.C., 1982, fmax, Bulletin of the Seismological Society of America, v. 72, p. 1867-1879.

Hanks, T.C. and Kanamori, H., 1979, A moment magnitude scale, Journal of Geophysical Research, v. 84, p. 2981-2987.

Hanks, T.C. and McGuire, R.K., 1981, The character of high-frequency strong ground motion, Bulletin of the Seismological Society of America, v. 71, p. 2071-2095.

Hardin, B.O., 1978, The nature of stress-strain behavior for soils, in Proceedings, Geotechnical Engineering Division Specialty Conference on Earthquake Engineering and Soil Dynamics, v. 1, p. 3-90.

Harrington, C.D. and Aldrich, M.J., 1984, Development and deformation of Quaternary surfaces on the northeastern flank of the Jemez Mountains, New Mexico Geological Society, Guidebook 35, p. 235-239.

Harrington, C.D. and Dethier, D.P., 1987, Geomorphic and stratigraphic evidence for Quaternary displacement along the northern Pajarito fault system near Hernandez, New Mexico, Geological Society of America Abstracts with Programs, v. 17, p. 281.

Hartzell, S., 1978, Earthquake aftershocks as Green's functions, Geophysical Research Letters, v. 5, p. 1-4.

Hauksson, E., Teng, T-L., and Henyey, T.L., 1987, Results from a 1500 deep, three-level downhole seismometer array: Site response, low Q values and f_{max}, Bulletin of the Seismological Society of America, v. 77, p. 1883-1904.

Hawley, J.W. (ed), 1978, Guidebook to Rio Grande rift in New Mexico and Colorado, New Mexico Bureau of Mines & Mineral Resources Circular 163, 241 p.

Hawley, J.W., Bachman, G.O., and Manley, K., 1976, Quaternary stratigraphy in the Basin and Range and Great Plains provinces, New Mexico and Texas, in W.C. Mahaney (ed.), Quaternary stratigraphy of North America, Dowden, Huchinson, and Ross, Inc., Stroudsburg, Pennsylvania, p. 235-274.

Hawley, J.W. and Galusha, T., 1978, Southern Rift Guide 2, Soccorro-Santa Fe, New Mexico: Bernalillo to south of San Ysidro, in J.W. Hawley (ed.), Guide to Rio Grande rift in New Mexico and Colorado, New Mexico Bureau of Mines & Mineral Resources Circular 163, p. 177-183.

Hawley, J.W. and Haase, C.S., 1992, Hydrologic framework of the northern Albuquerque basin, New Mexico Bureau of Mines and Mineral Resources, New Mexico Institute of Mining and Technology Open-File Report 387.

Heaton, T.H., 1990, Evidence for an implications of self-healing pulses of slip in earthquake rupture, Physical Earth and Planetary Interiors, v. 64, p. 1-20.

Heiken, G., Goff, F., Stix, J., Tamanyu, S., Shafiqullah, M., Garcia, S., and Hagan, R., 1986, Intracaldera volcanic activity, Toledo caldera and embayment, Jemez mountains, New Mexico, Journal of Geophysical Research, v. 91, p. 1799-1815.

Herrmann, R.B., Dewey, J.W., and Park, S.F., 1980, The Dulce, New Mexico, earthquake of 23 January 1966, Bulletin of the Seismological Society of America, v. 70, p. 2171-2183.

Hoek, E. and Bray, J., 1977, Rock slope engineering, London, Institution of Mining and Metallurgy, second edition.

Hoffman, J.P. and Northrop, S.A., 1977, The Dulce, New Mexico, earthquake of January 23, 1966, Earthquake Notes, v. 48, p. 3-20.

Hoge, H.P., 1970, Neogene stratigraphy of the Santa Ana area, Sandoval County, New Mexico, Ph.D. Thesis, University of New Mexico, 14 p.

Hough, S.E. and Anderson, J.G., 1988, High-frequency spectra observed at Anza, California: Implications for Q structure, Bulletin of the Seismological Society of America, v. 78, p. 692-707.

Hough, S.E., Anderson, J.G., Brune, J., Vernon, F., Berger, J., Fletcher, J., Haar, L., Hanks, T., and Baker, L., 1988, Attenuation near Anza, California, Bulletin of the Seismological Society of America, v. 78, p. 672-691.

House, L.S. and Cash, D.J., 1988, A review of historic and instrumental earthquake activity and studies of seismic hazards near Los Alamos, New Mexico, Los Alamos National Laboratory Report LA-11323-MS, 41 p.

House, L. and Phillips, W.S., 1989, Variability of relative seismic site response at Los Alamos, New Mexico, in Proceedings, Second DOE National Phenomena Hazards Mitigation Conference, CONF-8910192, p. 179-183.

Humphrey, J.R., Jr. and Anderson, J.G., 1992, Shear wave attenuation and site response in Guerrero, Mexico, Bulletin of the Seismological Society of America, v. 81, p. 1622-1645.

Hunt, C.B., 1936, Geology and fuel resources of the southern part of the San Juan Basin, New Mexico, Pt. 2, the Mount Taylor oil field, U.S. Geological Survey Bulletin 860-B, p. 31-80.

Ingersoll, R.V., Cavazza, W., Baldridge, W.S., Shafiqullah, M., 1990, Cenozoic sedimentation and paleotectonics of north-central New Mexico: Implications for initiation and evolution of the Rio Grande rift, Geological Society of America Bulletin, v. 102, p. 1280-1296.

Irikura, K., 1983, Semi-empirical estimation of strong ground motions during large earthquakes, Bulletin of the Disaster Prevention Research Institute, Kyoto University, v. 33, p. 63-104.

Izett, G.A. and Obradovich, J.D., 1994, $^{40}Ar/^{30}Ar$ age constraints for the Jaramillo Normal Subchron and the Matuyama-Brunhes geomagnetic boundary, Journal of Geophysical Research, v. 99, p. 2925-2934.

Jaksha, L.H., 1985, Seismicity of the San Juan Basin, New Mexico 1980-1981, U.S. Geological Survey Open-File Report 85-665, 16 p.

Jaksha, L.H. and Locke, J., 1978, Seismicity near Albuquerque, New Mexico, 1976-1977, U.S. Geological Survey Open-File Report 78-1054.

Jaksha, L.W., Locke, J., and Gebhart, H.J., 1981, Microearthquakes near the Albuquerque volcanoes, New Mexico, Geological Society of America Bulletin, v. 92, p. 31-36.

Jaksha, L.H., Locke, J., Thompson, J.B., and Garcia, A., 1978, Reconnaissance seismology near Albuquerque, New Mexico, U.S. Geological Survey Open-File Report 78-339.

John, E.C., Enyart, E., and Purtymun, W.D., 1967, Records of wells, test holes, springs and surface-water stations in the Los Alamos area, New Mexico, U.S. Geological Survey Open-File Report, Lab Job. 3274, ER ID No. 8796.

Johnson, L.R. and Silva, W.J., 1981, The effects of unconsolidated sediments upon the ground motion during local earthquakes, Bulletin of the Seismological Society of America, v. 71, p. 127-142.

Joyner, W.B. and Boore, D.M., 1981, Peak horizontal acceleration and velocity from strong-motion records including records from the 1979 Imperial Valley, California Earthquake, Bulletin of the Seismological Society of America, v. 71, p. 2011-2038.

Joyner, W.B. and Boore, D.M., 1982, Prediction of earthquake response spectra, U.S. Geological Survey Open-File Report 82-977, 16 p.

Joyner, W.B. and Boore, D. M., 1988, Measurement, characterization and prediction of strong ground motion, in J.L. Von Thun (ed.), Proceedings of the Conference on Earthquake Engineering and Soil Dynamics: Recent Advances in Ground Motion Evaluation, American Society of Civil Engineers, p. 43-103.

Joyner, W.B. and Fumal, T.E., 1985, Predictive mapping of earthquake ground motions, in J.I. Ziony (ed.), Evaluating Earthquake Hazards in the Los Angeles Region - An

Earth-Science Perspective, U.S. Geological Survey Professional Paper 1360, p. 203-220.
Keefer, D.I. and Bodily, S.E., 1983, Three-point approximations for continuous random variables, Management Science, v. 26, p. 595-609.
Keller, M.D. (ed.), 1968, Geologic studies and material properties investigations of Mesita de Los Alamos, Los Alamos Scientific Laboratory Report LA-3728.
Keller, G.R. and Cather, S.M., 1994, Introduction, in G.R. Keller and S.M. Cather (eds.), Basins of the Rio Grande Rift: Structure, Stratigraphy, and Tectonic Setting, Geological Society of America Special Paper 291, p. 1-3.
Keller, G.R., Braile, L.W., and Schlue, J.W., 1979, Region crustal structure of the Rio Grande rift from surface wave dispersion measurements, in R.E. Riecker (ed.), Rio Grande Rift: Tectonics and Magmatism, American Geophysical Union, p. 115-126.
Keller, G.R., Cordell, L., Davis, G.H., Peeples, W.J., and White, G., 1984, A Geophysical study of the San Luis Basin, New Mexico Geological Society Guidebook, 35th Field Conference, p. 51-57.
Keller, G.R., Khan, M.A., Morgan, P., Wendlandt, R.F., Baldridge, W.S., Olsen, K.H., Prodehl, C., and Braile, L.W., 1991, A comparative study of the Rio Grande and Kenya rifts, in A.F. Gangi (ed.), World Rift Systems, Tectonophysics, v. 197, p. 355-371.
Kelley, V.C., 1954, Regional tectonics of the Colorado Plateau and relationship to the origin and distribution of uranium, University of New Mexico Publications in Geology, No. 5, 120 p.
Kelley, V.C., 1952, Tectonics of the Rio Grande depression of central New Mexico, New Mexico Geological Society Guidebook 3rd Field Conference, p. 92-105.
Kelley, V.C., 1954, Tectonic map of a part of the upper Rio Grande area, New Mexico, U.S. Geological Survey Oil and Gas Investigation, Map OM-157.
Kelley, V.C., 1977, Geology of the Albuquerque Basin, New Mexico, New Mexico Bureau of Mines & Mineral Resources Memoir 33, 60 p.
Kelley, V.C., 1978, Geology of the Española Basin, New Mexico, New Mexico Bureau of Mines & Mineral Resources Geologic Map 48.
Kelley, V.C., 1979, Tectonics, middle Rio Grande rift, New Mexico, in R.E. Riecker (ed.), Rio Grande Rift: Magmatism and Tectonics, American Geophysical Union, p. 57-70.
Kelley, S.A. and Duncan, I.J., 1984, Tectonic history of the northern Rio Grande Rift derived from apatite fission-track geochronology, in Rio Grande Rift: Northern New Mexico, 1985, New Mexico Society Guidebook, 35th Field Conference, p. 67-73.
Kelley, V.C. and Northrop, S.A., 1975, Geology of Sandia Mountains and vicinity, New Mexico, New Mexico Bureau Mines & Mineral Resources Circular 156, 30 p.
Kelson, K.I., 1986a, Long-term tributary adjustments to base-level lowering northern Rio Grande rift, New Mexico, MS thesis, University of New Mexico, Albuquerque, 210 p.
Kelson, K.I., 1986b, Long-term tributary adjustments to base-level lowering, northern New Mexico (abs.), Geological Society of America, Abstracts with Programs, v. 18, 366 p.

Kelson, K.I. and Wells, S.G., 1987, Present-day fluvial hydrology and long-term tributary adjustments, northern New Mexico, in C.M. Menges (ed.), Quaternary Tectonics, Landform Evolution, Soil Chronologies and Glacial Deposits–Northern Rio Grande Rift of New Mexico, Friends of the Pleistocene Field-trip Guidebook, p. 95-109.

King, G.C.P., 1986, Speculations on the geometry of the initiation and termination processes of earthquake rupture and its relation to morphology and geological structure, Pure and Applied Geophysics, v. 124, p. 567-585.

Kluth, C.F. and Schaftenaar, C.H., 1994, Depth and geometry of the northern Rio Grande rift in the San Luis Basin, south-central Colorado, in G.R. Keller and S.M. Cather (eds.), Basins of the Rio Grande Rift: Structure, Stratigraphy, and Tectonic Setting, Geological Society of America Special Paper 291, p. 27-37.

Knuepfer, P.L.K., 1989, Implications of the characteristics of end-points of historical surface fault ruptures for the nature of fault segmentation, U.S. Geological Survey Open-File Report 89-315, p. 193-228.

Knuepfer, P.L.K., Bamberger, M.J., Turko, J.M., and Coppersmith, K.J., 1987, Characteristics of the boundaries of historic surface faults ruptures, Seismological Research Letters, v. 58, p. 31.

Kolbe, T., Sawyer, J., Gorton, A., Olig, S., Simpson, D., Fenton, C., Reneau, S., Carney, J., Bott, J., and Wong, I., 1994, Evaluation of the potential for surface faulting at the proposed mixed waste disposal facility, TA-67, unpublished report for the Los Alamos National Laboratory.

Kolbe, T., Sawyer, J., Springer, J., Olig, S., Reneau, S., Hemphill-Haley, M., and Wong, I., 1995, Evaluation of the potential for surface faulting at TA-63, unpublished report prepared for the Los Alamos National Laboratory.

Kulkarni, R.B., Sadigh, K., and Idriss, I.M., 1979, Probabilistic evaluation of seismic exposure, in Proceedings, Second U.S. National Conference on Earthquake Engineering, p. 90-99.

La Forge, R.C. and Anderson L.W., 1988, Seismotectonic study for Santa Cruz dam, Santa Cruz dam modification project, New Mexico, U.S. Bureau of Reclamation Seismotectonic Report 88-2, 31 p.

Lahr, J.C., 1984, HYPOELLIPSE/VAX, A computer program for determining local earthquake hypocentral parameters, magnitude and first motion patterns, U.S. Geological Survey Open-File Report 84-519, 66 p.

Lambert, W., 1966, Notes on the late Cenozoic geology of the Taos-Questa area, New Mexico, New Mexico Geological Society Guidebook, 17th Field Conference, p. 43-50.

Lambert, P.W., 1978, Rio Grande bridge (I-25) to Bernalillo, in J.W. Hawley (ed.), Guidebook to Rio Grande rift in New Mexico and Colorado, New Mexico Bureau of Mines & Mineral Resources Circular 163, p. 144-158.

Lambert, P.W., Hawley, J.W., and Wells, S.G., 1982, Supplemental Road-log segment III-S: Urban and environmental geology of the Albuquerque area, New Mexico Geological Society, Guidebook 33rd Field Conference, p. 97-124.

Langer, C.J., Martin, R.A., Wood, C.K., Snyder, G.L. and Bollinger, G.A., 1991, The Laramie Mountains, Wyoming earthquake of 18 October 1984: A report on its

aftershocks and seismotectonic setting, U.S. Geological Survey Open-File Report 91-258, 41 p.

Laughlin, A.W., Woldegabriel, G., and Dethier, D., 1993, Volcanic stratigraphy of the Pajarito Plateau, Preliminary Report FY93 prepared for the Los Alamos National Laboratory.

Leininger, R.L., 1982, Cenozoic evolution of the southernmost Taos plateau, New Mexico, MS thesis, The University of Texas at Austin, 110 p.

Lew, M., 1991, Characteristics of vertical ground motions recorded during the Loma Prieta earthquake, Proceedings, Second International Conference on Recent Advances in Geotechnical Earthquake Engineering and Soil Dynamics, v. 2, p. 1661-1666.

Li, S.X., Wang, Z.L., and Shen, C.K., 1992, SUMDES: A nonlinear procedure for response analysis of horizontally-layered sites subjected to multi-directional earthquake loading, Department of Civil Engineering, University of California, Davis.

Lindsey, D.A., Johnson, B.R., and Andriessen, P.A.M., 1983, Laramide and Neogene structure of the northern Sangre de Cristo Range, south-central Colorado, Rocky Mountain Association of Geologists, Symposium, p. 219-228.

Lisenbee, A.L., Woodward, L.A., and Connolly, J.R., 1979, Tijeras-Canoncito fault system-a major zone of recurrent movement in north-central New Mexico, New Mexico Geological Society, Guidebook 30, p. 89-100.

Logatchev, N.A. and Zorin, Y.A., 1992, Baikal rift zone: Structure and geodynamics, in P.A. Ziegler (ed.), Geodynamics of rifting, Volume II, Case history studies on rifts: North and South America and Africa, Tectonophysics, v. 213, p. 273-286.

Lozinsky, R.P., 1988, Stratigraphy, sedimentology and sand petrology of the Santa Fe Group and pre-Santa Fe Tertiary deposits in the Albuquerque Basin, central New Mexico, unpublished Ph.D. dissertation, New Mexico Institute of Mining and Technology, 298 p.

Lozinsky, R.P., 1994, Cenozoic stratigraphy, sandstone petrology, and depositional history of the Albuquerque Basin, central New Mexico, in G.R. Keller and S.M. Cather (eds.), Basins of the Rio Grande Rift: Structure, Stratigraphy, and Tectonic Setting, Geological Society of America Special Paper 291, p. 73-81.

Lozinsky, R.P., Hawley, J.W., and Love, D.W., 1991, Geologic overview and Pliocene-Quaternary history of the Albuquerque Basin, central New Mexico, Field Guide to Geologic excursions in New Mexico and adjacent areas of Texas and Colorado, New Mexico Bureau of Mines & Mineral Resources, Bulletin 137, p. 157-163.

Machette, M.N., 1978a, Dating Quaternary faults in the southwestern United States by using buried calcic paleosols, U.S. Geological Survey Journal of Research, v. 6, p. 369-382.

Machette, M.N., 1978b, Late Cenozoic geology of the San Acecia-Bernardo area, New Mexico Bureau of Mines & Mineral Resources Circular 163, p. 135-137.

Machette, M.N., 1982, Quaternary and Pliocene faults in the La Jencia and southern part of the Albuquerque-Belen basins, New Mexico: Evidence of fault history from fault-scarp morphology and Quaternary geology, New Mexico Geological Society Guidebook, 33rd Field Conference, p. 161-169.

Machette, M.N., 1985, Calcic soils of the southwestern United States, in D.L. Weide (ed.), Soils and Quaternary Geology of the Southwestern United States, U.S. Geological Survey Special Paper 203, p. 1-22.

Machette, M.N., 1986, History of Quaternary offset and paleoseismicity along the La Jencia fault, central Rio Grande rift, New Mexico, Bulletin of the Seismological Society of America, v. 76, p. 259-272.

Machette, M.N. and McGimsey, 1983, Quaternary and Pliocene faults in the Socorro and western part of the Fort Sumner 1° x 2° quadrangles, central New Mexico, U.S. Geological Survey Miscellaneous Field Studies Map MF-1465-A, scale 1:250,000.

Machette, M.N. and Personius, S.F., 1984, Quaternary and Pliocene faults in the eastern part of the Aztec quadrangle and the western part of the Raton quadrangle, Northern New Mexico, U.S. Geological Survey Map MF-1465-B, Scale 1:250,000.

Machette, M.N., Personius, S.F., and Nelson, A.R., 1992, Paleoseismology of the Wasatch fault zone: A summary of recent investigations, conclusions and interpretations, Chapter A, in Assessment of Regional Earthquake Hazards and Risk Along the Wasatch Front Area, Utah, U.S. Geological Survey Professional Paper 1500, p. A1-A71.

Manley, K., 1976a, The late Cenozoic history of the Española Basin, New Mexico, unpublished Ph.D. dissertation, University of Colorado, Boulder, 171 p.

Manley, K., 1976b, K-Ar age determinations of Pliocene basalts from the Española Basin, New Mexico, Isochron/West, No. 16, p. 29-30.

Manley, K., 1978, Pliocene deformation along the Rio Grande rift in the Española basin, New Mexico, Geological Society of America Abstracts with Programs, v. 10, p. 233.

Manley, K., 1979a, Stratigraphy and structure of the Española Basin, in R.E. Riecker (ed.), Rio Grande Rift: Tectonics and Magmatism, American Geophysical Union, p. 71-86.

Manley, K., 1979b, Tertiary and Quaternary stratigraphy of the northeast plateau, Española Basin, New Mexico, New Mexico Geological Society Guidebook 30, p. 231-236.

Manley, K., 1982, Geologic map of the Cañones quadrangle, Rio Arriba County, New Mexico, U.S. Geological Survey Miscellaneous Field Studies Map MF-1440, Scale 1:24,000.

Manley, K., 1987, Geologic map of the Aztec quadrangle, northwestern New Mexico and southern Colorado, U.S. Geological Survey Map I-1730, Scale 1:250,000.

Manley, K. and Mehnert, H.H., 1981, New K-Ar ages for Miocene and Pliocene volcanic rocks in the northwestern Española Basin and their relationships to the history of the Rio Grande Rift, Isochron/West, p. 5-8.

Manley, K., Scott, G.R., and Wobus, R.A., 1987, Geologic map of the Aztec 1° x 2° Quadrangle, northwestern New Mexico and southern Colorado, U.S. Geological Survey Miscellaneous Investigation Series Map I-1730.

Marvin, R.F. and Dobson, S.W., 1979, Radiometric ages: Compilation B, U.S. Geological Survey, Isochron West, v. 26, p. 25.

May, S.J. and Russell, L.R., 1994, Thickness of the syn-rift Santa Fe Group in the Albuquerque Basin and its relation to structural style, in G.R. Keller and S.M.

Cather (eds.), Basins of the Rio Grande Rift: Structure, Stratigraphy, and Tectonic Setting, Geological Society of America Special Paper 291, p. 113-123.

May, S.J., Kelley, S.A., and Russell, L.R., 1994, Footwall unloading and rift shoulder uplifts in the Albuquerque Basin: Their relation to syn-rift fanglomerates and apatite fission-track ages, in G.R. Keller and S.M. Cather (eds.), Basins of the Rio Grande Rift: Structure, Stratigraphy, and Tectonic Setting, Geological Society of America Special Paper 291, p. 125-134.

Maynard, S.R., Woodward, L.A., and Giles, D.L., 1991, Tectonics, intrusive rocks, and mineralization of the San Pedro-Ortiz porphyry belt, north-central New Mexico, Field guide to geologic excursions in New Mexico and adjacent areas of Texas and Colorado, New Mexico Bureau of Mines and Mineral Resources Bulletin 137, p. 57-70.

McCalpin, J., 1982, Quaternary geology and neotectonics of the west flank of the Northern Sangre de Cristo Mountains, south-central Colorado, Colorado School of Mines Quarterly, v. 77, 89 p.

McCalpin, J., 1987, Geologic criteria for recognition of individual paleoseismic events in extensional environments, U.S. Geological Survey Open-File Report 87-673, p. 102-114.

McCalpin, J.P., Zuchiewicz, W., and Jones, L.C.A., 1993, Sedimentology of fault-scarp-derived colluvium from the 1983 Borah Peak rupture, central Idaho, Journal of Sedimentary Petrology, v. 63, p. 120-130.

McGuire, R.K., 1974, Seismic structural response risk analysis incorporating peak response regressions on earthquake magnitude and distance, Massachusetts Institute of Technology Department of Civil Engineering/Research Report R74-51.

McGuire, R.K., 1978, FRISK: Computer program for seismic risk analysis using faults as earthquake sources, U.S. Geological Survey Open-File Report 78-1007.

Menges, C.M, 1988, The tectonic geomorphology of mountain front landforms in the northern Rio Grande rift, New Mexico, Albuquerque, Ph.D. Thesis, University of New Mexico, 140 p.

Menges, C.M., 1990a, Late Cenozoic rift tectonics and mountain-front landforms of the Sangre de Cristo Mountains near Taos, Northern New Mexico, New Mexico Geological Society Guidebook, 41st Field Conference, New Mexico, p. 113-122.

Menges, C.M., 1990b, Late Quaternary fault scarps, mountain-front landforms, and Pliocene-Quaternary segmentation on the range-bounding fault zone, Sangre de Cristo Mountains, New Mexico, in E.L. Krinitzsky and D.B. Slemmons (eds.), Neotectonics in Earthquake Evaluation: Boulder, Colorado, Geological Society of America Reviews in Engineering Geology, v. 8, p. 131-156.

Miller, J.P., Montgomery, A., and Sutherland, P.K., 1963, Geology of part of the southern Sangre de Cristo Mountains, New Mexico, New Mexico Bureau of Mines and Mineral Resources Memoir 11, 106 p.

Miyachi, M., Izett, G.A., Naeser, C.W., Naeser, N.D., and Andreissen, P.A.M., 1985, Zircon fission-track ages on some volcanic rocks and pyroclastic flow deposits of the Jemez Mountains, New Mexico, Bulletin Volcanological Society of Japan, v. 30, p. 90.

Moench, R.H., Grambling, J.A., Robertson, J.M., 1988, Geologic map of the Pecos wilderness, Santa Fe, San Miguel, Mora, Rio Arriba, and Taos Counties, New Mexico, U.S. Geological Survey Map MF-1921-B, Scale 1:48,000.

Molnar, P., 1979, Earthquake recurrence intervals and plate tectonics, Bulletin of the Seismological Society of America, v. 69, p. 115-133.

Morgan, P., Seager, W.R., and Golombek, M.P., 1986, Cenozoic thermal, mechanical and tectonic evolution of the Rio Grande rift, Journal of Geophysical Research, v. 91, p. 6263-6276.

Morley, C.K., Nelson, R.A., Patton, T.L., and Munn, S.G., 1990, Transfer zones in the East African rift system and their relevance to hydrocarbon exploration in rifts, American Association of Petroleum Geologists Bulletin, v. 74, p 1234-1253.

Muehlberger, W.R., 1979, The Embudo fault between Pilar and Arroyo Hondo, New Mexico: An active intracontinental transform fault, New Mexico Geological Society Guidebook, 30th Field Conference, p. 77-82.

Murdock, J.N. and Jaksha, L.J., 1981, The P-wave velocity of the uppermost mantle of the Rio Grande rift region of north central New Mexico, Journal of Geophysical Research v. 86, p. 7055-7063

Murphy, L.M., 1950, United States Earthquakes 1947, U.S. Coast and Geodetic Survey Serial No. 730, 62 p.

Murphy, L.M. and Cloud, W.K., 1954, United States earthquakes 1952, U.S. Coast and Geodetic Survey Serial No. 773, 112 p.

Nash, D.B., 1986, Morphologic dating and modeling degradation of fault scarps, in Active Tectonics - Studies in Geophysics, National Academy Press, p. 181-194.

Nelson, A.R., 1987, A facies model of colluvial sedimentation adjacent to a single-event normal-fault scarp, Basin and Range province, Western United States, in A.J. Crone, and E.M. Omdahl (eds.), Directions in Paleoseismology - Proceedings of Conference XXXIX, U.S. Geological Survey Open-File Report 87-673, p. 136-145.

Nelson, A.R., 1992, Lithofacies analysis of colluvial sediments - an aid in interpreting the recent history of Quaternary normal faults in the Basin and Range province, western U.S., Journal of Sedimentary Petrology, v. 63, p. 607-621.

Neumann, F., 1932, United States Earthquakes 1931, U.S. Coast and Geodetic Survey Serial No. 553, 26 p.

Neumann, F. and Bodle, R.R., 1932, United States Earthquakes 1930, U.S. Coast and Geodetic Survey Serial No. 539, 25 p.

Newmark, N.M. and Hall, W.J., 1978, Development of criteria for seismic review of selected nuclear power plants, Nuclear Regulatory Commission, Report NUREG/CR-0098, 49 p.

Newton, C.A., Cash, D.J., Olsen, K.H., and Homuth, E.F., 1976, LASL seismic programs in the vicinity of Los Alamos, New Mexico, Los Alamos Scientific Laboratory Informal Report LA-6406-MS.

Northrop, S.A., 1961, Earthquakes of central New Mexico, New Mexico Geological Society, Guidebook 12th Field Conference, p. 151-152.

Northrop, S.A., 1976, New Mexico's earthquakes history, 1849-1975, in L.E. Woodward, and S.A. Northrop (eds.), Tectonics and Mineral Resources of Southwestern North America, New Mexico Geological Society Special Publication No. 6, p. 77-87.

Nuttli, O.W., Bollinger, G.A., and Griffiths, D.W., 1979, On the relation between modified Mercalli intensity and body-wave magnitude, Bulletin of the Seismological Society of America, v. 69, p. 893-909.

Ohtani, K., 1993, Design spectra of U-D motion (phase I), Proceedings, International Workshop on Strong Motions, Menlo Park, California, Port and Harbor Research Institute, v. 2, p. 167-178.

Olig, S.S., Gorton, A.E., Bott, J.D., Wong, I.G., Knuepfer P.L.K., Forman, S.L., and Smith, R.P., 1994, Preliminary interpretations of temporal surface-faulting patterns on the southern Lost River fault zone, northeastern Basin and Range Province, U.S.A., in Proceedings on the Workshop for Paleoseismology, U.S. Geological Survey Open-File Report 94-568, p. 145-147.

Olsen, K.H., 1979, The seismicity of north-central New Mexico with particular reference to the Cerrillos earthquake of May 28, 1918, New Mexico Geology Society Guidebook v. 30, p. 65-75.

Olsen, K.H., Keller, G.R., and Stewart, J.N., 1979, Crustal structure along the Rio Grande rift from seismic refraction profiles, in R.E. Riecker (ed.), Rio Grande Rift: Tectonics and magmatism, American Geophysical Union, p. 127-143.

Olsen, K.H., Baldridge, W.S., and Callender, J.F., 1987, Rio Grande rift: An overview, Tectonophysics, v. 143, p. 119-139.

Ortiz, T.S., Williams, R.L., Nimick, F.B., Whittet, B.C., and South, D.L., 1985, A three dimensional model of reference thermal/mechanical and hydrological stratigraphy of Yucca Mountain, southern Nevada, SAND84-1076.

Ostenaa, D., 1984, Relationships affecting estimates of surface fault displacements based on scarp-derived colluvial deposits, Geological Society of America, Abstracts With Programs, v. 16, p. 327.

Ou, G.B. and Herrmann, R.B., 1990, A statistical model for ground motion produced by earthquakes at local and regional distances, Bulletin of the Seismological Society of America, v. 80, p. 1397-1417.

Papageorgiou, A.S. and Aki, K., 1983, A specific barrier model for the quantitative description of inhomogeneous faulting and the prediction of strong motion, Part I, description of the model, Bulletin of the Seismological Society of America, v. 73, p. 693-672.

Personius, S.F. and Machette, M.N., 1984, Quaternary faulting in the Taos Plateau region, northern New Mexico, in W.S. Baldridge, P.W. Dickerson, R.E. Riecker and J. Zidek (eds.), Tertiary and Quaternary stratigraphy of the northeast plateau, Española Basin, New Mexico, New Mexico Geological Society, Guidebook 30, p. 83-90.

Phillips, J.S., 1991a, Analysis of component surface/downhole ground motions at Yucca Mountain for underground nuclear explosions in Pahute Mesa, SAND87-2381, 199 p.

Phillips, J.S., 1991b, Prediction of pseudo relative velocity response spectra at Yucca Mountain for underground nuclear explosions conducted in the Pahute Mesa testing area at the Nevada Test Site. SAND88-3032, 208 p.

Prescott, W.H., Savage, J.C., and Kinoshita, W.T., 1979, Strain accumulation rates in the western United States between 1970 and 1978, Journal of Geophysical Research, v. 84, p. 5,423-5,435.

Press, F., 1966, Seismic velocities, in S. Clark (ed.), Handbook of Physical Constants, The Geological Society of America Memoir 97, p. 195-218.

Purtymun, W.D., 1993, Records of observation wells, test holes, test wells, supply wells, springs, and surface water stations at Los Alamos; with reference to the geology and hydrology, draft manuscript.

Ramelli, A.R. and dePolo, C.M., 1993, Examples of Holocene and latest Pleistocene faulting in northern and eastern Nevada, Geological Society of America Abstracts with Programs, v. 25, p. 136.

Reasenberg, P.A. and Oppenheimer, D.H., 1985, FPFIT, FPPLOT and FPPAGE: FORTRAN computer programs for calculating and displaying earthquake fault plane solutions, U.S. Geological Survey Open-File Report 85-739, 109 p.

Redpath Geophysics, 1992, Subsurface velocity and damping measurements at Los Alamos National Laboratory, report prepared for Woodward-Clyde Consultants.

Reid, H.F., 1911, Remarkable earthquakes in central New Mexico in 1906 and 1907, Bulletin of the Seismological Society of America, v. 1, p. 10-16.

Reilinger, R.E., Brown, L.D., Oliver, J.E., and York, J.E. 1979, Recent vertical crustal movements from leveling observations in the vicinity of the Rio Grande rift, in R.E. Riecker (ed), Rio Grande Rift: Tectonics and Magmatism, American Geophysical Union, p. 223-236.

Reilinger, R.E. and Oliver, J.E., 1976, Modern uplift associated with a proposed magma body in the vicinity of Socorro, New Mexico, Geology, v. 4, p. 583-586.

Reilinger, R., Oliver, J., Brown, L., Sanford, A., and Balazs, E., 1980, New measurements of crustal doming over the Socorro magma body, New Mexico, Geology, v. 8, p. 291-295.

Reiter, M., Clarkson G., and Shearer, C., 1979, Geothermal characteristics of the Rio Grande rift within the southern Rocky Mountain complex, in R.E. Riecker (ed.), Rio Grande Rift-Tectonics and Magmatism, American Geophysical Union, p. 253-267.

Reiter, M., Baroll, M.W., and Minier, J., 1991, An overview of heat flow in southwestern United States and northern Chihuahua, Mexico, in D.B. Slemmons, E.R. Engdahl, M.D. Zoback, and D.D. Blackwell (eds.), Neotectonics of North America, Geological Society of America, Decade Map Volume 1, p. 457-466.

Reneau, S.L., 1991, Report on geologic studies in Bandelier National Monument, Los Alamos National Laboratory unpublished report, 5 pg. plus figures.

Reneau, S.L., 1992, Report on geologic studies in Bandelier National Monument in 1992, Los Alamos National Laboratory unpublished report, p. 1-2.

Reneau, S.L., Gardner, J.N., Kelson, K.I., and Hemphill-Haley, M.A., 1993, Holocene stream aggradation and degradation, Pajarito Plateau, Northern New Mexico, Geological Society of America Abstracts with Programs, v. 25, p. 138.

Reneau, S.L., Kolbe, T.R., Simpson, D.T., Carney, J.S., Gardner, J.N., and Vaniman, D.T., 1994, Surficial materials and structure at Pajarito mesa, Los Alamos National

Laboratory, New Mexico, Chapter of Planned LA-MS report on MWDF Geologic Studies, unpublished draft report, 26 p.

Rinehart, E.J., Sanford, A.R., and Ward, R.M., 1979, Geographic extent and shape of an extensive magma body at midcrustal depths in the Rio Grande rift near Socorro, New Mexico, in R.E. Riecker (ed.), Rio Grande Rift-Tectonics and Magmatism, America Geophysical Union, p. 237-251.

Roberts, P.M., Aki, K., and Fehler, M.C., 1991, A low-velocity zone in the basement beneath the Valles caldera, New Mexico, Journal of Geophysical Research, v. 96, p. 21,583-21,596.

Rogers, K.L. et al., 1985, Middle Pleistocene (late Irvingtonian-Nebraskan) climatic changes in south-central Colorado, National Geographic Review, v. 1, p. 535-563.

Roller, J.C., 1965, Crustal structure in the eastern Colorado Plateau province from seismic-refraction measurements, Bulletin of the Seismological Society of America, v. 55, p. 107-119.

Rosendahl, B.R., 1987, Architecture of continental rifts with special reference to East Africa, Annual Review of Earth and Planetary Sciences, v. 15, p. 445-503.

Rowley, J., Hawkins, W., and Gardner, J., 1987, Drilling report first CSDP/thermal regimes core hole project at Valles Caldera, New Mexico (VC-1), Los Alamos National Laboratory Report LA-10934-OBES.

Russell, L.R. and Snelson, S., 1990, Structural style and tectonic evolution of the Albuquerque basin segment of the Rio Grande rift, in B. Pinet and C. Bois (eds.), The Potential of Deep Seismic Profiling for Hydrocarbon Exploration, p. 175-207.

Russell, L.R. and Snelson, S., 1994, Structure and tectonics of the Albuquerque Basin segment of the Rio Grande rift: Insights from reflection seismic data, in G.R. Keller and S.M. Cather (eds.), Basins of the Rio Grande Rift: Structure, Stratigraphy, and Tectonic Setting, Geological Society of America Special Paper 291, p. 83-112.

Sadigh, K.J., Chang, N.A., Abrahamson, N.A., Chiou, S.J., and Power, M., 1991, Specification of long period ground motions, Proceedings ATC-17-1, Seismic Isolation Systems., v. 1 (in press).

Salyards, S.L. and Ni, J.F., 1990, Kinematics of the Española Basin, Rio Grande rift, New Mexico from net, non-vertical Paleomagnetic rotations, EOS Transactions, American Geophysical Union, v. 71, p. 1584.

Salyards, S.L., Ni, J.F., and Aldrich, M.J., 1991, Kinematics of the Española Basin, Rio Grande rift, New Mexico, and implications for continental rift architecture, Geological Society of America Abstracts with Program, v. 23, p. 89.

Salyards, S.L., Ni, J.F., and Aldrich, M.J., Jr., 1994, Variation in paleomagnetic rotations and kinematics of the north-central Rio Grande rift, New Mexico, in G.R. Keller and S.M. Cather (eds.), Basins of the Rio Grande Rift: Structure, Stratigraphy, and Tectonic Setting, Geological Society of America Special Paper 291, p. 59-71.

Sanford, A.R., 1976, Seismicity of the Los Alamos region based on seismological data, Los Alamos Informal Report LA-6416-MS, 9 p.

Sanford, A.R., 1978, Earthquake activity in New Mexico (1849 through 1977), New Mexico Institute of Mining and Technology, Geophysics Open-File Report 26.

Sanford, A.R., Budding, A.J., Hoffman, J.P., Alptehin, O.S., Rush, C.A., and Toppozada, T.R., 1972, Seismicity of the Rio Grande rift in New Mexico, New Mexico State Bureau of Mines and Mineral Resources Circular 120.

Sanford, A.R., Jaksha, L.H., and Cash, D.J., 1991, Seismicity of the Rio Grande rift in New Mexico, in D.B. Slemmons, E.R. Engdahl, M.D. Zoback, and D.D. Blackwell (eds.), Neotectonics of North America, Geological Society of America Decade Map, v. 1, p. 229-244.

Sanford, A., Jaksha, L.W., and Wieder, D., 1983, Seismicity of the Socorro area of the Rio Grande rift, New Mexico Geological Society Guidebook, v. 34, p. 127-131.

Sanford, A.R., Olsen, K.H., and Jaksha, L.H., 1979, Seismicity of the Rio Grande rift, in R.E. Riecker (ed.), Rio Grande Rift: Tectonics and Magmatism, American Geophysical Union, p. 145-168.

Sanford, A.R., Olsen, K.H., and Jaksha, L.H., 1981, Earthquakes in New Mexico, 1849-1977, New Mexico Bureau of Mines and Mineral Resources, Circular 171, 20 p.

Sanford, A.R., Toppozada, T.R., Ward, R.M., and Wallace, T.C., 1976, The seismicity of New Mexico--1962 through 1972, New Mexico Institute of Mining and Technology, Geophysics Open-File Report 7b, 16 p.

Schnabel, P.B., Lysmer, J., and Seed, H.B., 1972, SHAKE - a computer program for earthquake analysis of horizontally layered sites, Earthquake Engineering Research Center, University of California, Report No. EERC 72-12.

Schwartz, D.P., 1988, Geologic characterization of seismic sources: Moving into the 1990s, Proceedings of the Conference on Earthquake Engineering and Soil Dynamics: Recent Advances in Ground Motion Evaluation, American Society of Civil Engineering, 42 p.

Schwartz, D.P. and Coppersmith, K.J., 1984, Fault behavior and characteristic earthquakes--examples from the Wasatch and San Andreas fault zones, Journal of Geophysical Research, v. 89, p. 5681-5698.

Schwartz, D.P. and Coppersmith, K.J., 1986, Seismic hazards: New trends in analysis using geologic data, in R.E. Wallace (ed.), Active Tectonics, Academic Press, p. 215-230.

Seager, W.R. and Morgan, P., 1978, Rio Grande rift in southern New Mexico, west Texas, and northern Chichuahua, in R.E. Riecker (ed.), Rio Grande Rift: Tectonics and Magmatism, American Geophysical Union, p. 87-106.

Seager, W.R., Shafiquallah, M., Hawley, J.W., and Marvin, R.F., 1984, New K-Ar dates from basalts and the evolution of the southern Rio Grande rift, Geological Society of America Bulletin, v. 95, p. 87-99.

Seed, H.B. and Idriss, I.M., 1970, Analyses of ground motions at Union Bay, Seattle, during earthquakes and distant nuclear blasts, Bulletin of the Seismological Society of America, v. 60, p. 125-136.

Self, S., Kircher, D.E., and Wolff, J.A., 1988, The El Cajete Series, Valles caldera, New Mexico, Journal of Geophysical Research, v. 93, p. 6113-6127.

Sherman, S.I., 1992, Faults and tectonic stresses of the Baikal rift zone, in P.A. Ziegler (ed.), Geodynamics of Rifting, v. I, Case History Studies on Rifts: Europe and Asia, Tectonophysics, v. 208, p. 297-307.

Sibson, R.H., 1985, Stopping of earthquake ruptures at dilational fault jogs, Nature, v. 316, p. 248-251.

Silva, W., 1976, Body waves in a layered anelastic solid, Bulletin of the Seismological Society of America, v. 66, p. 1539-1554.

Silva, W.J. and Darragh, R.B., 1990, Engineering characterization of strong ground motion recorded at rock sites, unpublished report submitted to Electric Power Research Institute Research Project RP 2556-48.

Silva, W.J. and Darragh, R.B., 1994, Engineering characterization of strong ground motion recorded at rock sites, unpublished draft report submitted to Electric Power Research Institute, Research Project RP-2556-48.

Silva, W.J. and Lee, K., 1987, WES RASCAL code for synthesizing earthquake ground motions: State-of-the-art for assessing earthquake hazards in the United States, Report 24, U.S. Army Engineer Waterways Experiment Station, Miscellaneous Paper S-73-1, 120 p.

Silva, W., Darragh, R., Stark, C., Wong, I., Stepp, J.C., Schneider, J.F., and Chiou, S., 1990, A methodology to estimate design response spectra in the near-source region of large earthquakes using the Band-Limited-White-Noise ground motion model, Proceedings, Fourth U.S. National Conference on Earthquake Engineering, v. 1, p. 487-494.

Silva, W.J. and Stark, C.L., 1992, Source, path, and site ground motion model for the 1989 M 6.9 Loma Prieta earthquake, unpublished draft final report submitted to the California Division of Mines and Geology.

Silva, W.J., Turcotte, T., and Moriwaki, Y., 1987, Soil response to earthquake ground motion, Electric Power Research Institute Report NP-5747.

Silva, W.J., Wong, I.G., and Darragh, R.B., 1991, Engineering characterization of earthquake strong ground motions with applications to the Pacific Northwest, in A.M. Rogers, T.J. Walsh, W.J. Kockelman, and G.R. Priest (eds.), Assessing Earthquake Hazards and Reducing Risk in the Pacific Northwest, U.S. Geological Survey Open-File Report 91-441H, 24 p.

Singh, S. and Herrmann, R.B., 1983, Regionalization of crustal coda Q in the continental United States, Journal of Geophysical Research, v. 88, p. 527-538.

Slack, P.B., 1975, Tectonic development of the northeast part of the Rio Puerco fault zone, Sandoval County, New Mexico, MS Thesis, University of New Mexico, Albuquerque, 74 p.

Slack, P.B. and Campbell, J.A., 1976, Structural geology of the Rio Puerco fault zone and its relationship to central New Mexico tectonics, New Mexico Geological Society Special Publication 6, p. 46-52.

Smith, R.L. and Bailey, R.A., 1968, Resurgent cauldrons, Geological Society of America Memoir 116, p. 613-662.

Smith, R.L., Bailey, R.A., and Ross, C.S., 1970, Geologic map of the Jemez Mountains, New Mexico, U.S. Geological Survey Miscellaneous Investigation Map I-571.

Soil Survey Staff, 1975, Soil taxonomy - A basic system of soil classification for making and interpreting soil surveys, U.S. Department of Agriculture, Soil Conservation Service, 754 p.

Soister, P.E., 1952, Geology of Santa Ana Mesa and adjoining areas, New Mexico, M.S. Thesis, University of New Mexico, 126 p.

Spell, T.L. and Harrison, T.M., 1993, $^{40}Ar/^{39}Ar$ Geochronology of post-Valles caldera rhyolites, Jemez volcanic field, New Mexico, Journal of Geophysical Research, v. 98, p. 8031-8051.

Spell, T., Harrison, M.T., and Wolff, J.A., 1990, $^{40}Ar/^{39}Ar$ dating of the Bandelier Tuff and San Diego Canyon ignimbrites, Jemez Mountains, New Mexico: Temporal constraints on magmatic evolution, Journal of Volcanology and Geothermal Research, v. 43, p. 175-193.

Spence, W. and Gross, R.S., 1990, A tomographic glimpse of the upper mantle source of magmas of the Jemez Lineament, New Mexico, Journal of Geophysical Research, v. 95, p. 10,829-10,849.

Spiegel, Z.B. and Baldwin, B., 1963, Geology and water resources of the Santa Fe area, New Mexico, U.S. Geological Survey Water-Supply Paper 1525, 258 p.

Stark, C.L., Silva, W.J., Wong, I.G., and Jackson, S.M., 1992, Assessment of stress drops of normal faulting earthquakes in the Basin and Range province, Seismological Research Letters, v. 63, p. 39.

Stearns, C.E., 1953, Tertiary geology of the Galisteo-Tonque area, New Mexico, Geological Society of America Bulletin, v. 64, p. 459-508.

Steven, T.A., 1975, Middle Tertiary volcanic field in the southern Rocky Mountains, in Cenozoic history of the southern Rocky Mountains, Geological Society of America Memoir 144, p. 75-94.

Stokoe, K.H., Hwang, S.K., and Laird, J.P., 1993, Dynamic properties of undisturbed soil samples from Los Alamos, New Mexico, unpublished report prepared for Woodward-Clyde Federal Services.

Stover, C.W., Reagor, B.G., and Algermissen, S.T., 1988, Seismicity map of the state of New Mexico, U.S. Geological Survey Miscellaneous Field Studies Map MF-2035, Scale 1:100,000.

Stuiver, M. and Reimer, P.J., 1993, Extended ^{14}C data base and revised CALIB 3.0 ^{14}C age calibration, Radiocarbon, v. 35, p. 215-230.

Susong, D.D., Janecke, S.U., and Bruhn, R.L., 1990, Structure of a fault segment boundary in the Lost River fault zone, Idaho, and possible effect on the 1983 Borah Peak earthquake rupture, Bulletin of the Seismological Society of America, v. 80, p. 57-68.

Swan, F.H., III, Schwartz, D.P., and Cluff, L.S., 1980, Recurrence of moderate to large magnitude earthquakes produced by surface faulting on the Wasatch fault zone, Utah, Bulletin of the Seismological Society of America, v. 70, p. 1431-1462.

Taggart, J. and Baldwin, F., 1982, Earthquake sequence of 1938-1939 in Mogolon Mountains, New Mexico, New Mexico Geology v. 4 , p. 49-52.

Tandon, K., 1992, Deep structure beneath the San Luis Basin in Colorado from reprocessing of an industry reflection survey, Ph.D. Thesis, Cornell University, 285 p.

Toppozada, T.R., 1975, Earthquake magnitude as a function of intensity data in California and western Nevada, Bulletin of the Seismological Society of America, v. 65, p. 1,223-1,238.

Toppozada, T.R. and Sanford, A.R., 1976, Crustal structure in central New Mexico interpreted from the Gasbuggy explosion, Bulletin of the Seismological Society of America, v. 66, p. 877-886.

Toro, G.R. and McGuire, R.K., 1987, An investigation into earthquake ground motion characteristics in eastern North America, Bulletin of the Seismological Society of America, v. 77, p. 468-489.

Toro, G.R., McGuire, R.K., and Silva, W.J., 1988, Engineering model of earthquake ground motion for eastern North America, EPRI Final Report NP-6074.

Toyoda, S., Goff, F., Ikeda, S., and Ikeya, M., 1995, ESR dating of quartz phenocrysts in the El Cajete and Battleship Rock Members of Valles Rhyolite, Valles Caldera, New Mexico, Journal of Volcanology and Geothermal Research (in press).

Trifunac, M.D., 1990, How to model amplification of strong earthquake motions by local soil and geologic site conditions, Earthquake Engineering and Structural Dynamics, v. 19, p. 833-846.

Turko, J.M. and Knuepfer, P.L.K., 1991, Late Quaternary fault segmentation from analysis of scarp morphology, Geology, v. 19, p. 718-721.

Tweto, O., 1979, The Rio Grande rift system in Colorado, in R.E. Riecker (ed.), The Rio Grande Rift: Tectonics and Magmatism, American Geophysical Union, p. 33-56.

Uhrhammer, R.A., 1986, Characteristics of northern and central California seismicity, Earthquake Notes, v. 57, p. 21.

U.S. Geological Survey, 1974, Abstracts of earthquake reports for the United States, January-March 1971, prepared by National Oceanic and Atmospheric Administration MSA-149, Open-File Report, 142 p.

von Hake, C.A. and Cloud, W.K., 1968, United States earthquakes 1966, U.S. Coast and Geodetic Survey, 110 p.

Vaniman, D. and Chipera, 1990, Results of geologic mapping/fracture studies: TA-55 area, Los Alamos National Laboratory Memorandum No. EES1-SH90-17.

Vaniman, D. and Wohletz, K., 1994, Mesa-penetrating fractures, fracture mineralogy, and projected fault traces at Pajarito Mesa, unpublished report, Los Alamos National Laboratory, Los Alamos, New Mexico.

Vernon, J.H. and Riecker, R.E., 1989, Significant Cenozoic faulting, east margin of the Española Basin, Rio Grande rift, New Mexico, Geology, v. 17 p. 230-233.

Vidale, J.E. and Helmberger, D.V., 1988, Elastic finite-difference modeling of the 1971 San Fernando, California earthquake, Bulletin of the Seismological Society of America, v. 78(1), p. 122-141.

Vortman, L.J. and Long, J.W., 1982a, Effects of repository depth on ground motion - The Pahute Mesa Data, SAND82-0174, 294 p.

Vortman, L.J. and Long, J.W., 1982b, Effects of repository depth on ground motion - The Yucca Flat Data, SAND82-1647, 668 p.

Wachs, D., Harrington, C.D., Gardner, J.N., Maassen, L.W., 1988, Evidence of young fault movements on the Pajarito fault system in the area of Los Alamos, New Mexico, Los Alamos National Laboratory Report LA-11156-MS, 23 p.

Wallace, R.E., 1977, Profiles and ages of young fault scarps, north-central Nevada, Geological Society of America Bulletin, v. 88, p. 1267-1281.

Wallace, R.E., 1978, Geometry and rates of change of fault-generated range fronts, north-central Nevada, U.S. Geological Survey Journal of Research, v. 6, p. 637-650.

Waresback, D.B. and Turbeville, B.N., 1990, Evolution of a Plio-Pleistocene volcanogenic-alluvial fan: The Puye Formation, Jemez Mountains, New Mexico, Geological Society of America Bulletin, v. 102, p. 298-314.

Weichert, D.H., 1980, Estimation of the earthquake recurrence parameters for unequal observation periods for different magnitudes, Bulletin of the Seismological Society of America, v. 70, p. 1337-1346.

Weir, J.E. and Purtymun, W.D., 1962, Geology and hydrology of Technical Area 49, Frijoles Mesa, Los Alamos County, New Mexico, U.S. Geological Survey, 225 p.

Wells, D.L. and Coppersmith, K.J., 1994, New empirical relationships among magnitude, rupture length, rupture width, rupture area, and surface displacement, Bulletin of the Seismological Society of America, v. 84, p. 974-1002.

Wells, S.G., Kelson, K.I., and Menges, C.M., 1987, Quaternary evolution of fluvial systems in the northern Rio Grande rift, New Mexico and Colorado: Implications for entrenchment and integration of drainage systems, in C.M. Menges (ed.), Quaternary Tectonics, Landform Evolution, Soil Chronologies and Glacial Deposits - Northern Rio Grand Rift of New Mexico, Field trip Guidebook, Friends of the Pleistocene - Rocky Mountain Cell.

Westaway, R. and Smith, R.B., 1989, Strong ground motion in normal-faulting earthquakes, Geophysical Journal, v. 96, p. 529-559.

Wheeler, R.L., 1987, Boundaries between segments of normal faults: Criteria for recognition and interpretation, U.S. Geological Survey Open-File Report 87-673, p. 385-398.

Wheeler, R.L. and Krystinik, K.B., 1988, Segmentation of the Wasatch fault zone, Utah - summaries, analyses, and interpretations of geological and geophysical data, U.S. Geological Survey Bulletin 1827, 47 p.

Wheeler, R.L. and Krystinik, K.B., 1992, Persistent and non-persistent segmentation of the Wasatch fault zone, Utah, statistical analysis for evaluation of seismic hazard, in P.L. Gori and W.W. Hays (eds.), Assessment of Regional Earthquake Hazards and Risk Along the Wasatch Front, Utah, U.S. Geological Survey Professional Paper 1500-B, p. B1-B47.

Windley, B.F. and Allen, M.B., 1993, Mongolian Plateau: Evidence for a late Cenozoic mantle plume under central Asia, Geology, v. 21, p. 295-298.

Wobus, R.A., 1984, An overview of the Precambrian geology of the Tusas range, north-central New Mexico, New Mexico Geological Society, 35th Annual Field Conference, p. 193-198.

Wolff, J.J., Cash, D.J., Olsen, K.H., and Stewart, J.N., 1984, Earthquake catalog for northern New Mexico, Los Alamos National Laboratory Report, LA-10598-PR, 16 p.

Wong, I.G., Cash, D.J., and Jaksha, L.H., 1984, The Crownpoint, New Mexico, earthquakes of 1976 and 1977, Bulletin of the Seismological Society of America, v. 74, p. 2,435-2,449.

Wong, I.G. and Chapman, D.S., 1990, Deep intraplate earthquakes in the western U.S. and their relationship to lithospheric temperatures, Bulletin of the Seismological Society of America, v. 80, p. 589-599.

Wong, I., Coppersmith, K., Silva, W., Youngs, R., Sawyer, T., Hemphill-Haley, M., Stark, C., Knuepfer, P., Castro, R., Makdisi, F., Wells, D., Chiou, S., Bruhn, R., and Daning, W., 1992, Earthquake ground motion evaluations for the proposed New Production Reactor at the Idaho National Engineering Laboratory Volume I: Deterministic Evaluation, EG&G Idaho Inc. Report EGG-GEO-10304.

Wong, I., Hemphill-Haley, M., Kelson, K., Kolbe, T., Green, R., Kanakari, H., Bott, J., Silva, W., Haraden, C., Gardner, J., House, L., and Reneau, S., 1993, Seismic hazards evaluation of the Los Alamos National Laboratory, unpublished draft report prepared for the Los Alamos National Laboratory, three volumes.

Wong, I.G. and Humphrey, J.R., 1989, Contemporary seismicity, faulting and the state of stress in the Colorado Plateau, Geological Society of America Bulletin, v. 101, p. 1127-1146.

Wong, I.G. and Silva, W.J., 1993, Site-specific strong ground motion estimates for the Salt Lake Valley, Utah, Utah Geological Survey Special Publication (in press).

Wong, I.G., Silva, W.J., Wright, D.H., and Olig, S.S., 1991, Preliminary site-specific strong ground motion estimates for the Salt Lake Valley, Utah, Proceedings, Fourth International Conference on Seismic Zonation, Earthquake Engineering Research Institute, v. 2, p. 203-210.

Woodward, L.A., 1977, Rate of crustal extension across the Rio Grande rift near Albuquerque, New Mexico, Geology, v. 5, p. 269-272.

Woodward, L.A., 1987, Geology and mineral resources of Sierra Nacimiento and vicinity, New Mexico, New Mexico Bureau of Mines and Mineral Resources, Memoir 42.

Woodward, L.A and DuChene, H.R., 1975, Geometry of the Sierrita fault and its bearing on the tectonic development of the Rio Grande rift, New Mexico, Geology, v. 3, p. 114-116.

Woodward, L.A., DuChene, H.R., and Martinez, R., 1977, Geology of Gilman quadrangle, New Mexico, New Mexico Bureau of Mines and Mineral Resources Geologic Map 45, Scale 1:24,000.

Woodward, L.A., Kaufman, W.H., and Anderson, J.B., 1972, Nacimiento fault and related structures, northern New Mexico, Geological Society of America Bulletin, v. 83, p. 2383-2396.

Woodward, L.A. and Ruetschilling, R.L., 1976, Geology of San Ysidro quadrangle, New Mexico, New Mexico Bureau of Mines and Mineral Resources Geologic Map 37, Scale 1:24,000.

Woodward-Clyde Consultants, 1979, Development of seismic exposure model, Report to Woodward-Clyde Consultants Professional Development Committee by R. Kulkarni, K. Sadigh and I.M. Idriss.

Woodward-Clyde Consultants, 1991, Data review and evaluation and recommendations for Task 2 Seismic Hazard Studies, unpublished report prepared for Los Alamos National Laboratory.

Working Group on California Earthquake Probabilities (Agnew, D.C., Allen, C.R., Cluff, L.S., Dieterich, J.H., Ellsworth, W.L., Keeney, R.L., Lindh, A.G., Nishenko, S.P., Schwartz, D.P., Sieh, K.E., Thatcher, W., and Wesson, R.L.), 1988, Probabilities of large earthquakes occurring in California on the San Andreas fault, U.S. Geological Survey Open-File Report 88-398, 62 p.

Working Group on California Earthquake Probabilities (Dieterich, J.H., Allen, C.R., Cluff, L.S., Cornell, C.A., Ellsworth, W.L., Johnson, L.R., Lindh, A.G., Nishenko, S.P., Scholz, C.H., Schwartz, D.P., Thatcher, W., and Williams, P.L.), 1990, Probabilities of large earthquakes in the San Francisco Bay region, California, U.S. Geological Survey Circular 1053, 51 p.

Wright, H.E., 1946, Tertiary and Quaternary geology of the lower Rio Puerco area, New Mexico, Geological Society of America Bulletin, v. 57, p. 383-456.

Youd, T.L., 1980, Ground failure displacement and earthquake damage to buildings, American Society of Civil Engineers Conference on Civil Engineering and Nuclear Power, v. 2, p. 7-6-2 - 7-6-26.

Youngs, R.R. and Coppersmith, K.J., 1985, Implications of fault slip rates and earthquake recurrence models to probabilistic seismic hazard estimates, Bulletin of the Seismological Society of America, v. 75, p. 939-964.

Youngs, R.R., Swan, F.H., Power, M.S., Schwartz, D.P., and Green, R.K., 1987, Probabilistic analysis of earthquake ground shaking hazard along the Wasatch Front, Utah, in P.L. Gori and W.W. Hays (eds.), Assessment of Regional Earthquake Hazards and Risk Along the Wasatch Front, Utah, U.S. Geological Survey, Open-File Report 87-585, v. 2, p. M1-M110.

Zhang, P., Slemmons, D.B., and Mao, F., 1991, Geometric pattern, rupture termination and fault segmentation of the Dixie Valley-Pleasant Valley active normal fault system, Nevada, U.S.A., Journal of Structural Geology, v. 13. 165-176.

Zoback, M.L. and Zoback, M.D., 1989, Tectonic stress field of the continental United States, in L.C. Pakiser and W.D. Mooney (eds.), Geophysical Framework of the Continental United States, Geological Society of America Memoir 172, p. 523-540.